

Transactions of the ASME®

Editor
L. S. LANGSTON (2006)
Associate Editors
Advanced Energy Systems
G. REISTAD (2005)
Fuels and Combustion Technologies
S. GOLLAHALLI (2004)
Internal Combustion Engines
D. ASSANIS (2002)
Nuclear
R. DUFFY (2004)
International Gas Turbine Institute
IGTI Review Chair
D. R. BALLAL (2000)
R. NATOLE (2001)
E. BENVENUTI (2002)
Combustion and Fuels
P. MALTE (2003)
Structures and Dynamics
N. ARAKERE (2004)
M. MIGNOLET (2002)

BOARD ON COMMUNICATIONS
Chair and Vice-President
OZDEN OCHOA

OFFICERS OF THE ASME
President, **S. H. SKEMP**
Executive Director, **V. R. CARTER**
Treasurer, **R. E. NICKELL**

PUBLISHING STAFF
Managing Director, Engineering
THOMAS G. LOUGHLIN
Director, Technical Publishing
PHILIP DI VIETRO
Managing Editor, Technical Publishing
CYNTHIA B. CLARK
Production Coordinator
JUDITH SIERANT
Production Assistant
MARISOL ANDINO

Transactions of the ASME, Journal of Engineering for Gas Turbines and Power (ISSN 0742-4795) is published quarterly (Jan., April, July, Oct.) by The American Society of Mechanical Engineers, Three Park Avenue, New York, NY 10016. Periodicals postage paid at New York, NY and additional mailing offices. POSTMASTER: Send address changes to Transactions of the ASME, Journal of Engineering for Gas Turbines and Power, c/o THE AMERICAN SOCIETY OF MECHANICAL ENGINEERS, 22 Law Drive, Box 2300, Fairfield, NJ 07007-2300. **CHANGES OF ADDRESS** must be received at Society headquarters seven weeks before they are to be effective. Please send old label and new address. **STATEMENT from By-Laws.** The Society shall not be responsible for statements or opinions advanced in papers or ... printed in its publications (B7.1, par. 3). **COPYRIGHT © 2002** by the American Society of Mechanical Engineers. For authorization to photocopy material for internal or personal use under circumstances not falling within the fair use provisions of the Copyright Act, contact the Copyright Clearance Center (CCC), 222 Rosewood Drive, Danvers, MA 01923, Tel: 978-750-8400, www.copyright.com. **INDEXED** by Applied Mechanics Reviews and Engineering Information, Inc. Canadian Goods & Services Tax Registration #126148048

Journal of Engineering for Gas Turbines and Power

Published Quarterly by The American Society of Mechanical Engineers

VOLUME 124 • NUMBER 4 • OCTOBER 2002

TECHNICAL PAPERS

Fuels and Combustion Technology

- 749 Mass Spectrometric Detection of Ionic and Neutral Species During Highly Preheated Air Combustion by Alkali Element Ion Attachment
T. Ishiguro, A. Matsunami, K. Matsumoto, K. Kitagawa, N. Arai, and A. K. Gupta

Gas Turbines: Coal, Biomass, and Alternative Fuels

- 757 Performance Analysis of Evaporative Biomass Air Turbine Cycle With Gasification for Topping Combustion (01-GT-367)
J. Wolf, F. Barone, and J. Yan

Gas Turbines: Combustion and Fuels

- 762 Fuel Droplet Evaporation in a Supercritical Environment (99-GT-301)
G. S. Zhu and S. K. Aggarwal

- 771 Performance of a Dry Low-NO_x Gas Turbine Combustor Designed With a New Fuel Supply Concept (01-GT-050)
T. Wakabayashi, S. Ito, S. Koga, M. Ippommatsu, K. Moriya, K. Shimodaira, Y. Kurosawa, and K. Suzuki

- 776 NO_x Formation in High-Pressure Jet-Stirred Reactors With Significance to Lean-Premixed Combustion Turbines (01-GT-067)
T. Rutar and P. C. Malte

- 784 Investigation of Two Advanced Cooling Mixing Concepts for a Rich Quench Lean Combustor (01-GT-085)
O. Diers, J. Koopman, M. Fischer, and C. Hassa

Gas Turbines: Controls, Diagnostics and Instrumentation

- 792 Gas Turbine Mach Number Control With Simplified Fuel System (00-GT-044)
G. J. Dadd and K. K. Chan

- 801 Uncertainty Reduction in Gas Turbine Performance Diagnostics by Accounting for Humidity Effects (01-GT-010)
K. Mathioudakis and T. Tsalavoutas

- 809 Data Rectification and Detection of Trend Shifts in Jet Engine Path Measurements Using Median Filters and Fuzzy Logic (01-GT-014)
R. Ganguli

- 817 Global Nonlinear Modeling of Gas Turbine Dynamics Using NARMAX Structures (01-GT-019)
N. Chiras, C. Evans, and D. Rees

- 827 A Multiple Harmonic Open-Loop Controller for Hydro/Aerodynamic Force Measurements in Rotating Machinery Using Magnetic Bearings (01-GT-023)
D. O. Baun, E. H. Maslen, C. R. Knospe, and R. D. Flack

(Contents continued on inside back cover)

This journal is printed on acid-free paper, which exceeds the ANSI Z39.48-1992 specification for permanence of paper and library materials. ©™
♻️ 85% recycled content, including 10% post-consumer fibers.

Gas Turbines: Cycle Innovations

- 835 The Ubiquitous Personal Turbine—A Power Vision for the 21st Century (01-GT-100)
C. F. McDonald and C. Rodgers

Gas Turbines: Cycle Innovations, and Combustion and Fuels

- 845 Tubular Solid Oxide Fuel Cell/Gas Turbine Hybrid Cycle Power Systems: Status (00-GT-550)
S. E. Veyo, L. A. Shockling, J. T. Dederer, J. E. Gillett, and W. Y. Lundberg
- 850 A Hybrid System Based on a Personal Turbine (5 kW) and a Solid Oxide Fuel Cell Stack: A Flexible and High Efficiency Energy Concept for the Distributed Power Market (01-GT-092)
L. Magistri, P. Costamagna, A. F. Massardo, C. Rodgers, and C. F. McDonald
- 858 Efficiency Upgrading of an Ambient Pressure Molten Carbonate Fuel Cell Plant Through the Introduction of an Indirect Heated Gas Turbine (01-GT-381)
P. Lunghi and S. Ubertini

Gas Turbines: Electric Power

- 867 Development of a Maintenance Program for Major Gas Turbine Hot Gas Path Parts (00-GT-187)
H. Moritsuka, T. Fujii, and T. Takahashi

Gas Turbines: Heat Transfer, and Turbomachinery

- 874 Droplet Entrainment From a Shear-Driven Liquid Wall Film in Inclined Ducts: Experimental Study and Correlation Comparison (01-GT-115)
J. Ebner, M. Gerendás, O. Schäfer, and S. Wittig

Gas Turbines: Industrial and Cogeneration

- 881 A Unique Approach for Thermoeconomic Optimization of an Intercooled, Reheat, and Recuperated Gas Turbine for Cogeneration Applications (01-GT-206)
R. Bhargava and A. Peretto
- 892 Thermoeconomic Analysis of an Intercooled, Reheat, and Recuperated Gas Turbine for Cogeneration Applications—Part II: Part-Load Operation (01-GT-207)
R. Bhargava, G. Negri di Montenegro, and A. Peretto
- 904 Conformable Eddy-Current Sensors and Arrays for Fleetwide Gas Turbine Component Quality Assessment (01-GT-212)
N. Goldfine, D. Schlicker, Y. Sheiretov, A. Washabaugh, V. Zilberstein, and T. Lovett

Gas Turbines: Industrial and Cogeneration, and Controls, Diagnostics and Instrumentation

- 910 Real-Time On-Line Performance Diagnostics of Heavy-Duty Industrial Gas Turbines (00-GT-312)
S. C. Gülen, P. R. Griffin, and S. Paolucci

Gas Turbines: Manufacturing, Materials, and Metallurgy

- 922 Delamination Cracking in Thermal Barrier Coating System
Y. C. Zhou and T. Hashida
- 931 Designing Hot Working Processes of Nickel-Based Superalloys Using Finite Element Simulation (01-GT-429)
R. Kopp, M. Tschirnich, M. Wolske, and J. Klöwer

Gas Turbines: Oil and Gas Applications

- 936 Series of Parallel Arrangement in a Two-Unit Compressor Station (01-GT-230)
S. Ohanian and R. Kurz

Gas Turbines: Structures and Dynamics

- 942 A Comparison of Two Finite Element Reduction Techniques for Mistuned Bladed Disks (00-GT-362)
F. Moyroud, T. Fransson, and G. Jacquet-Richardet
- 953 Effects of Wheel-Shaft-Fluid Coupling and Local Wheel Deformations on the Global Behavior of Shaft Lines (01-GT-233)
D. Lornage, E. Chatelet, and G. Jacquet-Richardet
- 958 Measurements Versus Predictions for the Dynamic Impedance of Annular Gas Seals—Part I: Test Facility and Apparatus (01-GT-237)
M. P. Dawson, D. W. Childs, C. G. Holt, and S. G. Phillips
- 963 Measurements Versus Predictions for the Dynamic Impedance of Annular Gas Seals—Part II: Smooth and Honeycomb Geometries (01-GT-238)
M. P. Dawson and D. W. Childs
- 971 Using Guided Balls to Auto-Balance Rotors (01-GT-243)
H. L. Wettergren

- 976 Estimation of Distributed Unbalance of Rotors (01-GT-245)
T. Yang and C. Lin
- 984 Transient Rotordynamic Modeling of Rolling Element Bearing Systems (01-GT-255)
A. Liew, N. Feng, and E. J. Hahn
- 992 Optimum Design of Squeeze Film Dampers Supporting Multiple-Mode Rotors (01-GT-256)
A. El-Shafei and R. Y. K. Yakoub
- 1003 A Framework for Flutter Clearance of Aeroengine Blades (01-GT-270)
A. Khalak
- 1011 Eigensolutions of Grouped Turbo Blades Solved by the Generalized Differential Quadrature Method (01-GT-273)
J. H. Kuang and M. H. Hsu
- 1018 Friction Damping of Interlocked Vane Segments: Experimental Results (01-GT-432)
T. Berruti, S. Filippi, M. M. Gola, and S. Salvano
- Gas Turbines: Structures and Dynamics, and Controls, Diagnostics, and Instrumentation*
- 1025 Three Practical Examples of Magnetic Bearing Control Design Using a Modern Tool (00-GT-407)
M. Spirig, J. Schmied, P. Jenckel, and U. Kanne
- Gas Turbines: Vehicular and Small Turbomachines*
- 1032 Application of Foil Bearings to Turbomachinery Including Vertical Operation (99-GT-391)
J. F. Walton II and H. Hesmat
- Internal Combustion Engines*
- 1042 Applying the Representative Interactive Flamelet Model to Evaluate the Potential Effect of Wall Heat Transfer on Soot Emissions in a Small-Bore Direct-Injection Diesel Engine
C. Hergart and N. Peters
- 1053 Author Index

ANNOUNCEMENTS AND SPECIAL NOTES

- 1060 Information for Authors
- 1061 Preparing and Submitting a Manuscript for Journal Production and Publication
- 1062 Preparation of Graphics for ASME Journal Production and Publication

T. Ishiguro

Department of Applied Chemistry,
Graduate School of Engineering

A. Matsunami

Research Center for Advanced Energy
Conversion

K. Matsumoto

Department of Applied Chemistry,
Graduate School of Engineering

K. Kitagawa

Research Center for Advanced Energy
Conversion

N. Arai

Research Center for Advanced Energy
Conversion

Nagoya University,
Furo-cho, Chikusa-ku,
Nagoya 464-8603, Japan

A. K. Gupta

Department of Mechanical Engineering,
University of Maryland,
College Park, MD 20742
e-mail: akgupta@end.umd.edu

Mass Spectrometric Detection of Ionic and Neutral Species During Highly Preheated Air Combustion by Alkali Element Ion Attachment

The use of high temperature and low oxygen concentration air as the oxidizer for regenerative combustion has become of increasing interest because this technology results in higher thermal efficiency, low energy consumption, and reduced emission of pollutants, such as NO_x and CO_2 , and compact size of the equipment. In this study information is provided on the effect of preheating the low oxygen concentration air on the formation and detection of chemical ions and neutral species formed in flames. These ions and species were detected directly using mass spectrometry. Such information also assists in determining the combustion mechanism. The intact ionic species have been detected only at downstream position of the flames. By applying an alkali element (Li^+) ion attachment technique, neutral species, such as Li^+ -attached ions have been also detected successfully. Three specific flame cases have been examined. They include using normal air (flame I), preheated air (flame II), and preheated air with low (diluted) oxygen concentration in air (flame III). The results show significant change in the spectra of the intact ionic species and the Li^+ -adduct neutral species amongst the three flames. The results also show that preheating the combustion air increases the number of chemical species formed in the flames. However, these chemical species decrease with low oxygen concentration (diluted) combustion air. [DOI: 10.1115/1.1473158]

Introduction

Combustion with high temperature air at low oxygen concentration has become of increasing interest for achieving very high thermal efficiency and very low emission of pollutants including NO_x and CO_2 [1–7]. The results obtained from several pilot plant and full-scale studies have shown energy savings of up to about 60% without any adverse effect on the product quality and other desirable parameters [8,9]. The thermal field uniformity in the combustion zone using high-temperature air combustion technology is far superior to any other combustion methodology [7–10]. This then results better quality of the resulting product due to far uniform thermal field in the combustion region. Flames with highly preheated air with normal and low oxygen concentration (herein called diluted air for low oxygen concentration) have been studied using a spectral-video camera [4]. This diagnostics allowed us to examine several important effects of highly preheated and diluted combustion air on flames and flame signatures.

In this study, a new mass spectrometric detection method has been developed that also allowed additional information during combustion with highly preheated and diluted combustion air. A wide variety of chemical species are produced in a flame during combustion. Information on these intermediate species is very useful to determine the combustion mechanism in addition to determining the effect of preheating and diluting the combustion air. In this study, our focus has been on direct detection of ionic and neutral species produced in hydrocarbon flames using a quadrupole mass spectrometer (Q-MS, Shimadzu QP-1100EX) fitted with a sampling interface. The diluted combustion air is preheated to a temperature of $T_{\text{air}}=1000^\circ\text{C}$, having 10% O_2 concentration in air, using a specially designed combustion air preheat facility [6].

Neutral species have been successfully detected by applying an alkali element (Li^+) ion attachment technique [11].

Experimental Apparatus

A schematic diagram of the experimental apparatus used for this study is shown in Fig. 1. A test flame was formed with $\text{C}_3\text{H}_8/\text{air}$ (N_2+O_2) mixture using a laboratory scale triple concentric burner having inner diameter of the outermost burner tube =4.0 mm. A mixture of (N_2+O_2) and fuel passed through the inner and outer openings of the concentric burner, respectively. This produced “inverse” diffusion flame. A mixture of N_2+O_2 was used instead of the normal combustion air. By changing the ratio between O_2 and N_2 , the concentration of oxygen in the air could be easily controlled (O_2 could be varied from 21 to 10%). The flow rates of the fuel and air (mixture of N_2+O_2) were regulated at 0.22 and 5.5 l/min, respectively. The equivalence ratio, ϕ , of the flame was changed from 1.0 to 2.0 by changing the oxygen concentration in the N_2+O_2 mixture. The mixture of N_2+O_2 gas was electrically heated up to 1000°C before introducing to the burner head. Without any heating, the N_2+O_2 mixture remains at the room temperature. A dual-cone interface was fitted on the mass spectrometer Q-MS (M/Z 10~1000 u) operating under high vacuum condition so as to introduce the ion species from the flame (burning under atmospheric pressure conditions) directly into the Q-MS. The sampling cone and the skimmer cone of this interface had 0.2-mm diameter opening. The mass spectrometer was scanned in 1s from m/z 10 to 1000. Mass spectra were obtained by averaging 30 scans over 30 s time duration.

The length of the flames was as follows: 100 mm with the normal air (flame I) and highly preheated air (flame II), and 140 mm with the highly preheated and diluted air (flame III). The flame length was considerably higher with diluted high-temperature combustion air with low oxygen concentration. This increase in flame length is due to the increase in flow velocity associated with the volumetric expansion of N_2+O_2 gas from the

Contributed by the Fuels and Combustion Division of THE AMERICAN SOCIETY OF MECHANICAL ENGINEERS for publication in ASME JOURNAL OF ENGINEERING FOR GAS TURBINES AND POWER. Manuscript received by the FC Division Oct. 3, 2000; final revision received by the ASME Headquarters Jan. 28, 2002. Associate Editor: S. R. Gollahalli.

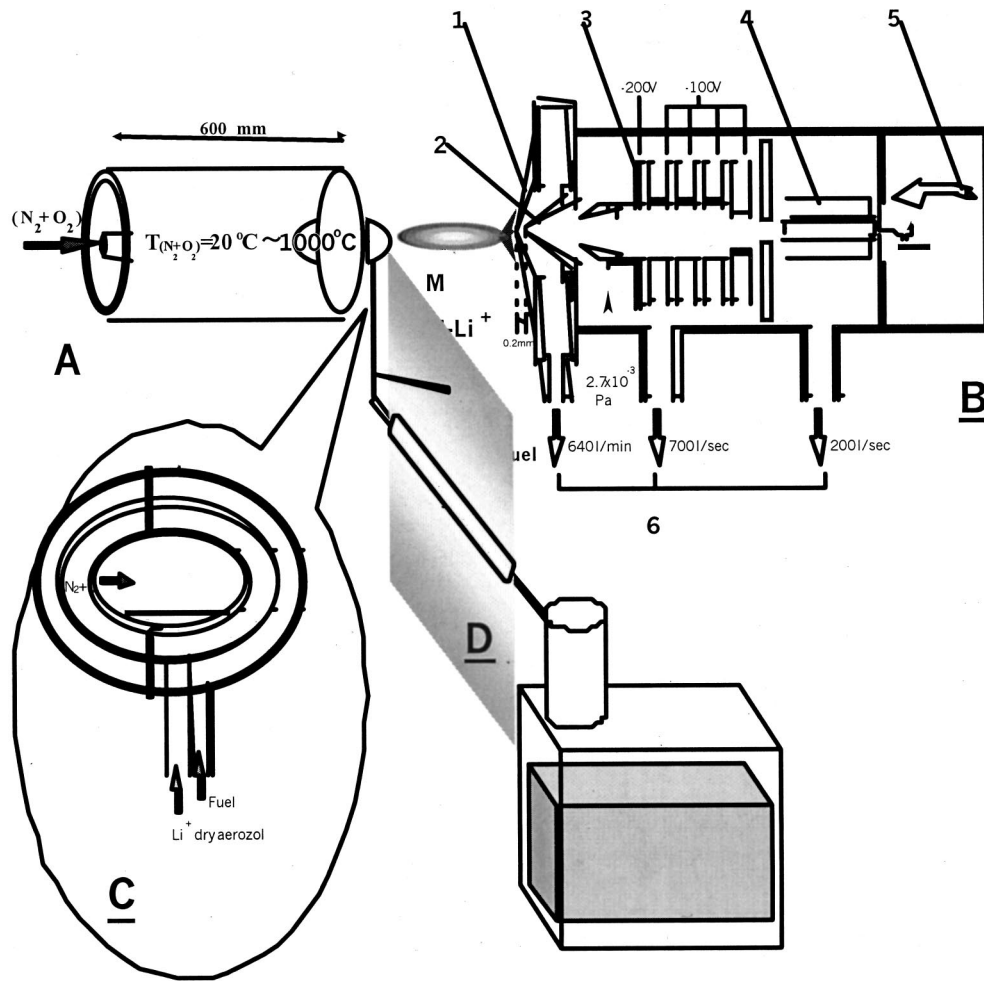


Fig. 1 Experimental setup for the detection of ionic species and neutral species in flames. **A**: Electric heater; **B**: mass spectrometer (Shimadzu QP1100EX); 1 sampling cone interface (orifice diameter 0.2 mm); 2 skimmer cone interface (orifice diameter 0.2 mm); 3 ion lens (15 mm i.d., 54 mm o.d., and 14 mm in thickness); 4 quadrupole mass analyzer; 5 channeltron detector; 6 vacuum pump (pressure in MS: 2.7×10^{-3} Pa); **C**: quartz burner head (4.0 mm i.d.); **D**: lithium dry aerosol generator.

air preheats. Low O_2 concentration diluted air decreased the burning rate. The spatial features of the flame were investigated by taking measurements at several spatial positions from within the flame as shown in Fig. 2. The top of the interface was inserted to a position of 10 mm from the burner head along the central axis of the flame (upstream position P_A), 50 and 70 mm from the burner

head (middle stream position P_B), and 20, 15, and 10 mm from the top of the flame (downstream positions P_C , P_D , and P_E , respectively).

A lithium ion attachment technique has been utilized to detect the neutral species. Dry aerosol containing lithium was generated from a solution of lithium hydroxide (1.2 M) using an ultrasonic

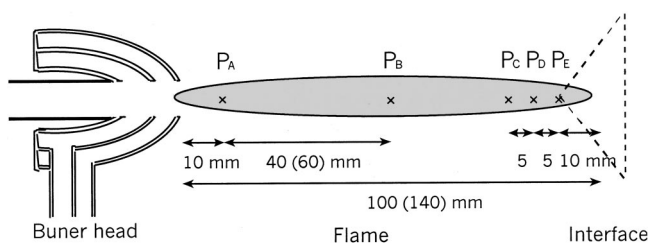


Fig. 2 The measurement locations used for investigating the spatial profiles in the flames. The value in the parentheses represents the relatively long flame obtained with highly preheated and diluted air under conditions of $T_{N_2+O_2} = 1000^\circ\text{C}$, O_2 conc. in air=10%, and $\phi=2.0$.

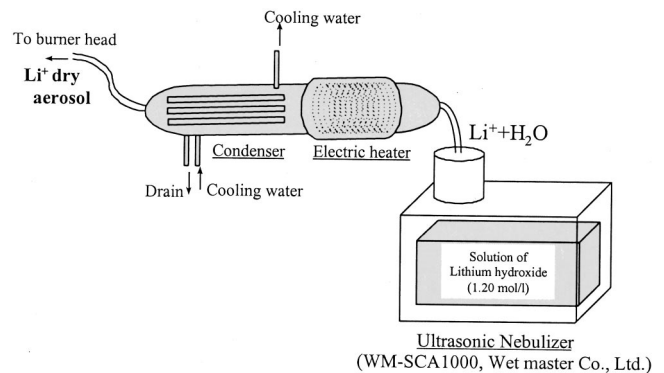
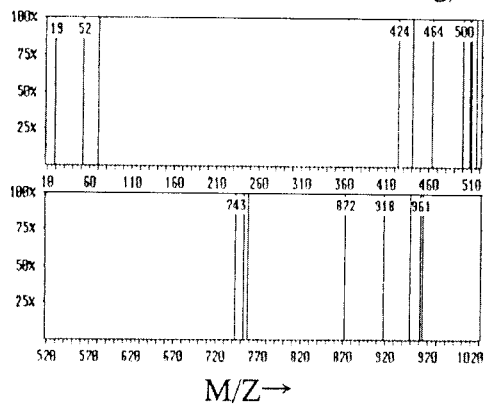


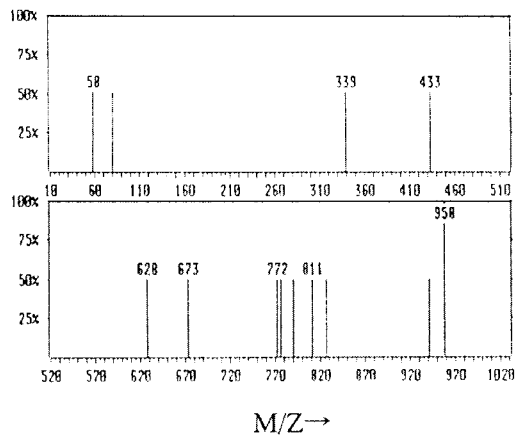
Fig. 3 Lithium dry aerosol generator

[P_A] B.I.(Base Intensity)=10
TIM_{ave} (averaged Total Ion Monitoring)=712



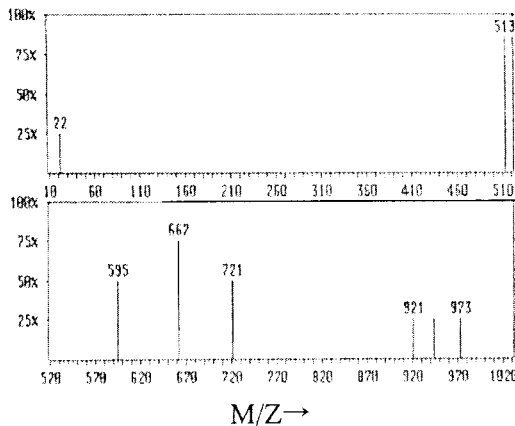
(a) M/Z →

[P_B] B.I.=20 TIM_{ave}=911



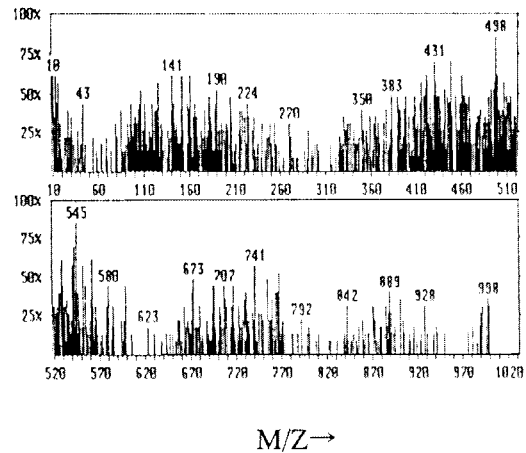
(b) M/Z →

[P_C] B.I.=40 TIM_{ave}=19862



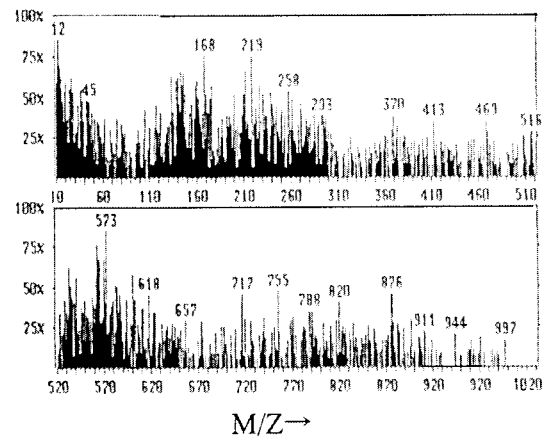
(c) M/Z →

[P_D] B.I.=230 TIM_{ave}=39062



(d) M/Z →

[P_E] B.I.=550 TIM_{ave}=106380



(e) M/Z →

Fig. 4 The mass spectra detected at five different locations in the flame (from the upstream position P_A to the downstream P_E shown in Fig. 2). Conditions: $T_{N_2+O_2}=20^\circ\text{C}$, O_2 conc. in air=21%, and $\phi=1.0$ (flame I).

nebulizer and electrical heating system as shown in Fig. 3. This aerosol was introduced into the flow of fuel and $N_2 + O_2$ gas mixture (from the opening between the inner and outer annuli of the burner head) at a flow rate of 2.52×10^{-3} mol/sec. Thus, the lithium ion was attached to the neutral species present in the flame. Consequently, the neutral species became detectable as Li^+ ion adducts by the mass spectrometer. The effect of air preheat and diluted air on combustion characteristics have been investi-

gated by comparing the features of mass spectra obtained for the three specific flames having normal air (flame I), highly preheated air (flame II), and highly preheated and diluted air (flame III).

Results and Discussion

Detection of Intact Ions. Figure 4(a)–(e) shows the mass spectra of the intact ionic species for flame 1 with normal air at room temperature, i.e., $T_{N_2+O_2} = 20^\circ\text{C}$, $[O_2] = 21\%$ at stoichio-

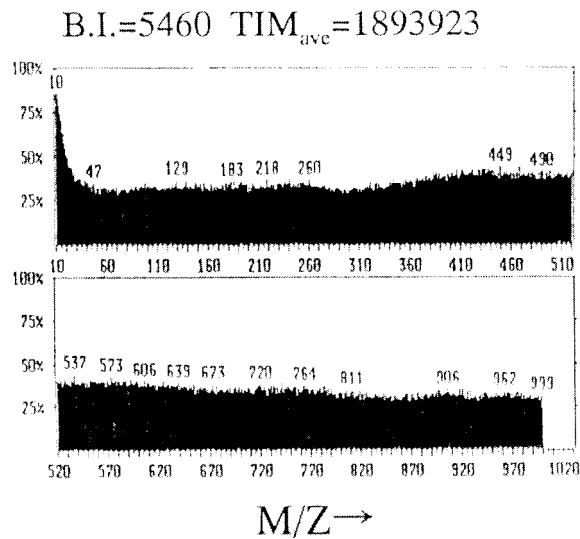


Fig. 5 The mass spectra detected at the downstream position P_E (10 mm from the flame tip). Conditions of $T_{N_2+O_2} = 1000^\circ\text{C}$, O_2 conc. in air=21%, and $\phi=1.0$ (flame II).

metric condition ($\phi=1.0$). The data, averaged over 30 seconds (30 scans), is shown at various points (from the upstream position P_A to the downstream position P_E) in the flame. The results show that the ionic species are hardly detected at the upstream position P_A (at a position of 10 mm downstream from the burner head) and the middle position P_B (at a position of 50 mm downstream from the burner head) in the flame. Even at position P_C (which is quite farther downstream of the flame) no ionic species could be detected, see Fig. 4 (a), (b), and (c). However, at position P_D the ion currents could be clearly detected (see Fig. 4(d)). Most intense peaks were observed at the top of the flame (e.g., at position P_E , see Fig. 4(e)). The results show that many species having various mass numbers are formed at the downstream positions of the flame.

Figure 5 shows the mass spectrum of the ionic species detected at downstream position P_E (10 mm from the flame tip) for flame II using highly preheated combustion air with $T_{N_2+O_2} = 1000^\circ\text{C}$, $[O_2]=21\%$, and $\phi=1.0$. The results show that similar to flame I,

B.I.=320 $TIM_{avc}=53873$

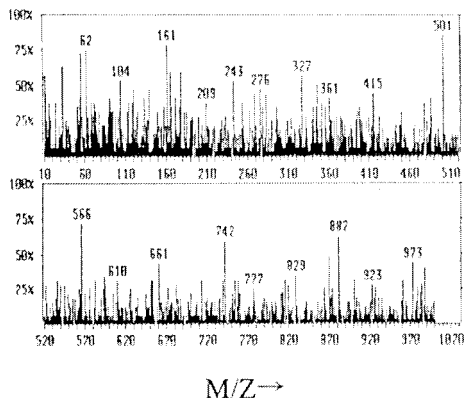
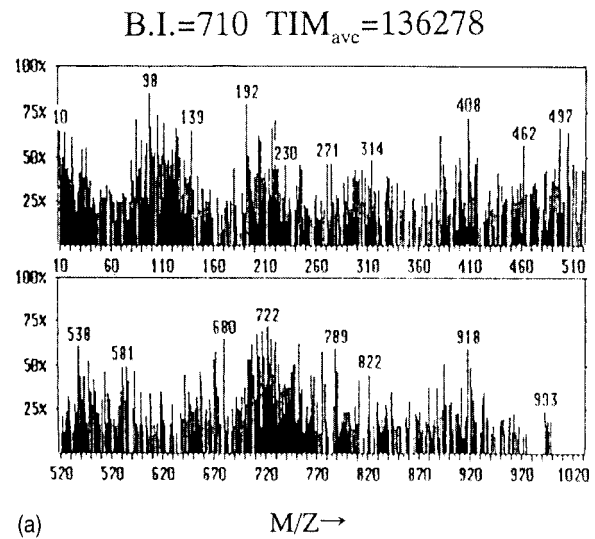
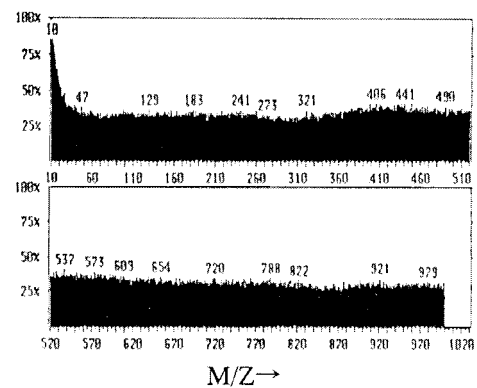


Fig. 6 The mass spectra at the downstream position P_E (10 mm from the flame tip). Conditions $T_{N_2+O_2}=1000^\circ\text{C}$, O_2 conc. in air=10%, and $\phi=2$ (flame III).



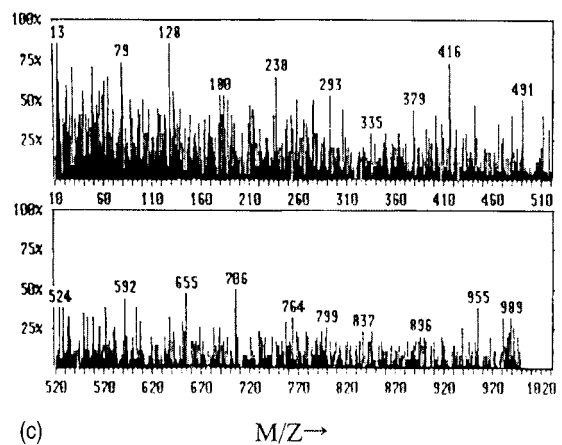
(a)

b B.I.=6010 $TIM_{avc}=1997318$



(b)

b B.I.=320 $TIM_{avc}=66523$

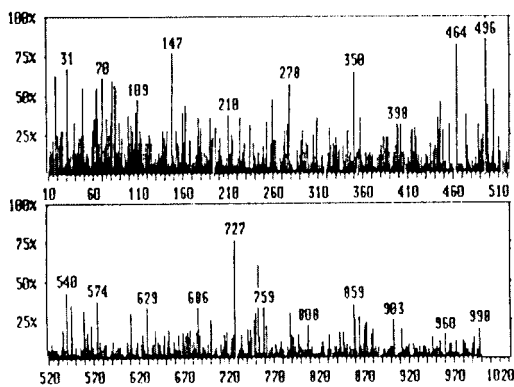


(c)

Fig. 7 The mass spectra detected with lithium ion attachment technique at position P_E (10 mm from the flame tip). The flame conditions used were (a) $T_{N_2+O_2}=20^\circ\text{C}$, O_2 conc. in air=21%, and $\phi=1.0$ (flame I); (b) $T_{N_2+O_2}=1000^\circ\text{C}$, O_2 conc. in air=21%, and $\phi=1.0$ (flame II); (c) $T_{N_2+O_2}=1000^\circ\text{C}$, O_2 conc. in air=10%, and $\phi=2.0$ (flame III).

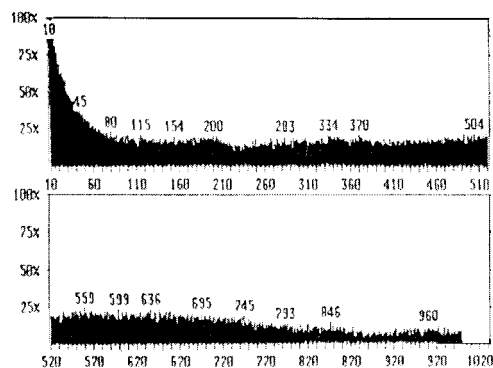
the peaks are negligibly small (near to the lower detection limits of the mass spectrometer) at the upstream position P_A and middle position P_B of the flame at all combustion conditions. These results suggest that ionization of the chemical species must take place only at the downstream positions of flame II. In other words,

a B.I.=510 $TIM_{ave}=66891$



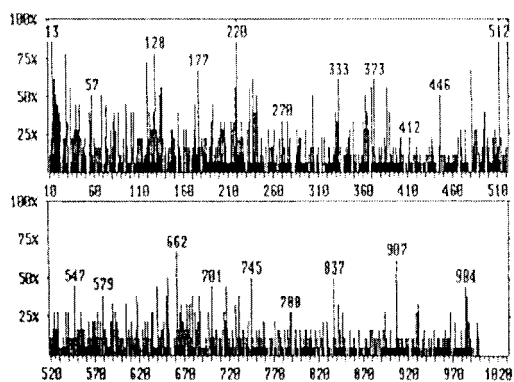
(a) $M/Z \rightarrow$

a B.I.=3650 $TIM_{ave}=591618$



(b) $M/Z \rightarrow$

a B.I.=180 $TIM_{ave}=35319$

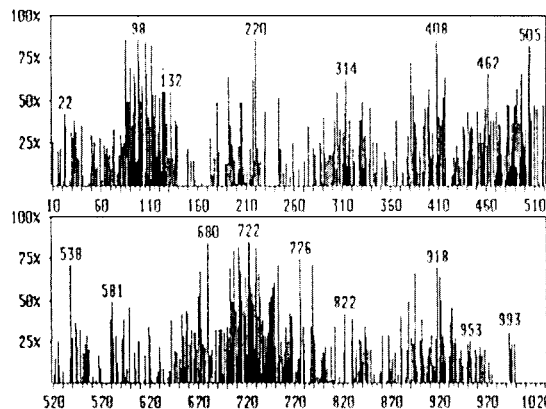


(c) $M/Z \rightarrow$

Fig. 8 The mass spectra obtained at position P_B with lithium ion attachment technique. The flame conditions used were (a) $T_{N_2+O_2}=20^\circ\text{C}$, O_2 conc. in air=21%, and $\phi=1.0$ (flame I); (b) $T_{N_2+O_2}=1000^\circ\text{C}$, O_2 conc. in air=21%, and $\phi=1.0$ (flame II); (c) $T_{N_2+O_2}=1000^\circ\text{C}$, O_2 conc. in air=10%, and $\phi=2.0$ (flame III).

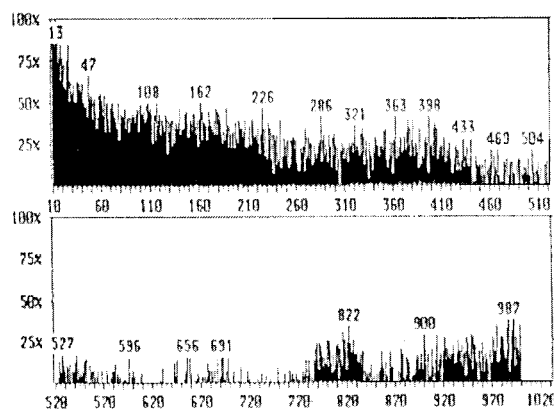
it takes some time for neutral species to accumulate enough thermal energy to be ionized. Figure 5 also indicates that peak ion intensity for flame II increases significantly as compared to that observed for flame I (compare results shown in Fig. 5 with the results shown in Fig. 4(e) for position P_E). The spectrum shown

B.I.=550 $TIM_{ave}=29898$



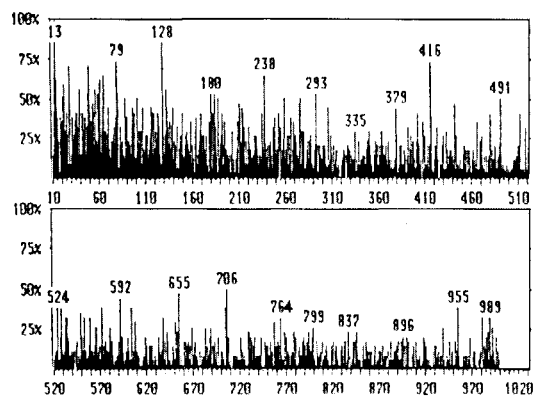
(a) $M/Z \rightarrow$

B.I.=590 $TIM_{ave}=103395$



(b) $M/Z \rightarrow$

B.I.=320 $TIM_{ave}=66523$



(c) $M/Z \rightarrow$

Fig. 9 The calculated mass spectra of neutral species at position P_E with lithium ion attachment technique. The flame conditions were (a) $T_{N_2+O_2}=20^\circ\text{C}$, O_2 conc. in air=21%, and $\phi=1.0$ (flame I); (b) $T_{N_2+O_2}=1000^\circ\text{C}$, O_2 conc. in air=21%, and $\phi=1.0$ (flame II); (c) $T_{N_2+O_2}=1000^\circ\text{C}$, O_2 conc. in air=10%, and $\phi=2.0$ (flame III).

Table 1 Average value of total ion monitoring (TIM) for three experimental condition at position P_B and P_E .

Position	Flame I		Flame II		Flame III	
		Li*	(Ionic Species, TIC)	Li*		Li*
P_B	N.D.	66,891	N.D.	591,618	N.D.	35,319
P_E	106,380	136,278	1,893,923	1,997,318	55,873	66,523
			(Neutral Species)			
P_B	66,891		591,618		35,319	
P_E	29,898		103,395		12,650	

*TIC total ion current

*N.D. not detected

*Lithium ion attachment

in Fig. 5 is mostly flat, which suggests that ionic species having M/Z from low to high values are produced concurrently in this flame. The temporal fluctuation of the total ion monitoring signals was drastically decreased for the highly preheated air flame case. This suggests that the ionic species produced in this flame are more stable. Therefore one can conclude that preheated air has a stabilizing effect on flames. This stabilizing effect is also supported by our previous paper, which utilized optical measurements [1].

Figure 6 shows the mass spectrum of ionic species detected at the downstream position P_E (10 mm from the flame tip) of flame III using highly preheated and diluted air combustion conditions ($T_{N_2+O_2}=1000^\circ\text{C}$, O_2 concentration in air=10%, and $\phi = 2.0$). Both the peak intensity of the mass spectrum and number of total ionic species are found to decrease as compared to those presented in Fig. 5 for flame II. These results, therefore, show that the formation of the ionic species is suppressed under condition of high temperature and low oxygen concentration combustion air.

Detection of Intact Ions and Neutral Species as Li^+ Adduct Ions. Figures 7(a), (b), and (c) show the mass spectra obtained with the lithium ion attachment technique at the position P_E for flames I, II, and III, respectively. By comparing the total ion monitoring (TIM) in Fig. 4(e) (TIMave.=106,380) with Fig. 7(a) (TIMave.=136,278) for flame I, one can observe an increase in peak intensity by attaching lithium ion. Similar conclusions can be made for flame II when Fig. 5 (TIMave.= 1,893,923) is compared with Fig. 7(b) (TIMave.=1,997,318), and also for flame III when Fig. 6 (TIMave.=53,873) is compared with Fig. 7(c) (TIMave.=66,523).

Measurement of Neutral Species. Figures 8(a), (b), and (c) show the mass spectra detected at the middle position P_B (50, 50, 70 mm from the burner head) of the flames I, II, and III, respectively, using lithium adducted ion technique. Although the intact ions are hardly detected at the middle position P_B (as mentioned above) neutral species were clearly detected as Li^+ adduct ions. Considering that these peaks are due to the Li^+ adducts of neutral species, the mass numbers of the species are smaller than the ions. The results show that various chemical species exist as neutral species at middle position of the flame, which have been detected by the lithium ion attachment technique. Similar to the intact ionic species, they are affected by the combustion conditions, such as temperature and oxygen concentration of the gas (N_2+O_2) mixture.

It is to be noted that no ionic species could, however, be detected at position P_A of the flames for the three experimental flame conditions examined. A reason for this could be that the lithium elements have not yet ionized at the position P_A . The ionizing energy of lithium element is 518 kJ/mol. The bond energy of C-H and C-C bonds is 410 and 350 kJ/mol, respectively. We also assume that no reaction, and hence the radicals, occurs before position A.

Figures 7(a), (b), and (c) show the mass spectra obtained with the lithium ion attachment technique at the downstream position

P_E (10 mm from the flame top) for flame I, II, and III, respectively. Since the intact ionic species also exist at this position P_E (as shown in Figs. 4, 5, and 6), these spectra are regarded as the sum of the intact and Li^+ -adduct ions. The differences in intensity between the spectra shown in Figs. 7(a), (b), and (c) and those of the intact ionic species alone (shown in Figs. 4, 5, and 6) are shown in Figs. 9(a), (b), and (c), respectively. One can view this as the net peak generated from the neutral species present at the downstream position P_E . It was experimentally confirmed that beyond a Li^+ concentration of Ca.1.2 M, the ion current becomes independent of the Li^+ concentration and is proportional to the number density of the radicals. The peak intensity in these spectra is smaller than that of intact ionic peaks. Thus, the chemical species exist as ions at downstream positions of the flame. The averaged TIM (total ion monitoring) under the three experimental flame conditions is summarized in Table 1. The relative standard deviation of these results is less than 10%.

The features observed for flames I and III are very similar. The only apparent difference is the abundance of ionic and neutral species in the flames. At every measured experimental position, the intensity for flame I is about 2 times larger than that for flame III. In contrast, the most abundant peaks of ionic and neutral species are observed for flame II. At position P_B , the intensity of neutral species is about ten times larger for flame II (TIC=ca. 590,000) than for flame I (TIC=ca. 67,000). However at position P_E , it is about three times larger for flame II (TIC=ca. 104,000) than for flame I (TIC=ca. 30,000). The intensity of ionic species is about 18 times larger for flame II than for flame I at position P_E . The intensity ratio of neutral species to ionic species at position P_E is 0.28 and 0.05 for flame I and flame II, respectively. These results indicate that at position P_E most of the species are ionized in flame II. However, neutral species exist in flame I. Excitation and ionization of a large amount of species in flame II have been confirmed experimentally.

At position P_B (e.g., flame I, in Table 1), no ionic species were detected and Li^+ attached species were found to have about 67,000 counts. However, at position P_E (within the flame), ions without Li^+ had an intensity count of about 106,000 counts and Li^+ attached species plus ions had a count of about 136,000. Thus, Li^+ can only attach to the neutral species but not to ionic species in the flames. This is also reflected in the results obtained with Li^+ , which showed ion intensities of about 67,000 and 30,000 counts at locations P_B and P_E , respectively. This also suggests that at location P_B neutral species are abundant while at position P_E , ionic species are predominant and the neutral species decrease in number. The rate of Li^+ attaching to the neutral species seems to be very fast which aids in the detection of species by this method.

Relationship Between Mass Spectrometry and Emission Spectroscopy Results. Figure 10 shows the emission spectra of C_2 band (from 450 to 530 nm) for the three flames examined. The experimental conditions examined here are the same as that given in our previous paper [4]. The spectra show good similarity except

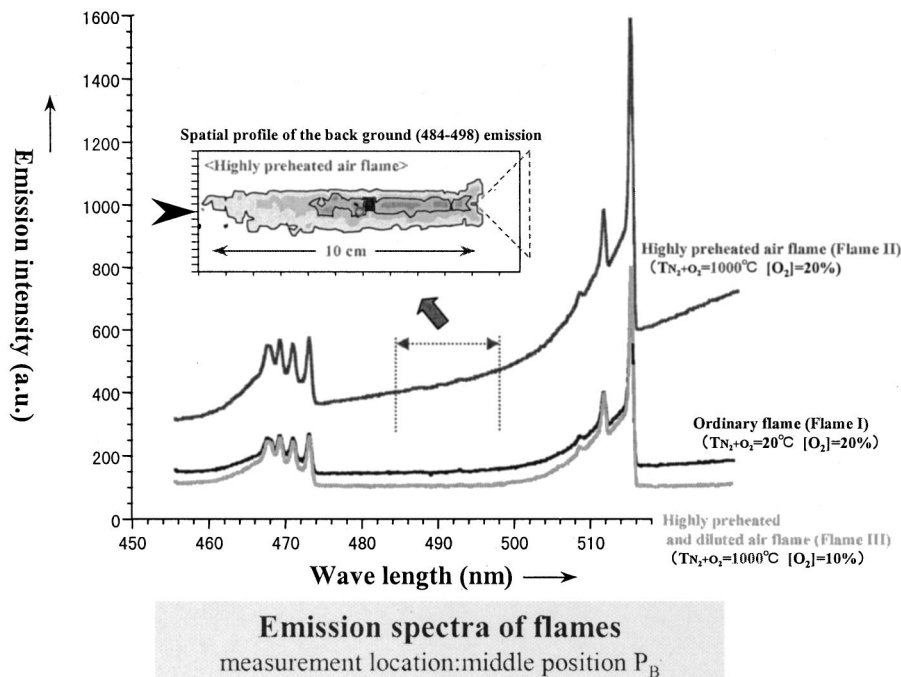


Fig. 10 The spectra of the C2 swan band from the flames; (a) flame I, (b) flame II, (c) flame III

for the intensity. The three emission spectra show the continuum background emission, which results from the carbon cluster, or soot. The intensity of flame I is slightly stronger than that of flame III. In contrast flame II gives strong background emission and very well-defined spectra. These results indicate the formation of carbon cluster, or soot nearly uniformly in Flame I and larger amounts in flame II. The good agreement obtained between mass spectrometry and emission spectroscopy results for the flame properties implies that both techniques provide important features and flame phenomena in combustion systems (compare Table 1 and Fig. 10).

Figures 11(a), (b), and (c) show the TIM chromatograms for 50 seconds for the three flames at position P_B using Lithium attachment technique. The CV values are 24.2, 11.9, and 20.6% for flames I, II, and III, respectively. The values provide an indication on the rate of fluctuation of ion formation in flames. Flame II had the least value of flame fluctuation (11.9%). The large and close values were observed for flames I and III. These results provide good agreement with the results obtained using spectroscopy [4].

Conclusions

In this study, the intact ionic species and neutral species that exist in flames have been detected using mass spectrometry. For detecting neutral species, the Li^+ adduct technique was developed and applied. The experimental results have indicated the following:

1 The neutral species exist predominantly at the mid position of the flames examined and decrease at downstream position of the flames. In contrast, the ionic species gradually increase and exist predominantly at the downstream positions of the flames examined.

2 Preheating the air results in significant increase in the number of ionic species and neutral species produced in the flame.

3 Diluting the air results in decrease in the number of ionic and neutral species produced in the flame.

4 Good agreement has been found between the results obtained using mass spectrometry and emission spectroscopy.

Acknowledgments

We would like to thank Dr. T. Tanaka of Nagoya University for helpful discussions, and Mr. S. Takahashi and Mr. K. Tachibana for making the mass spectrometer interface.

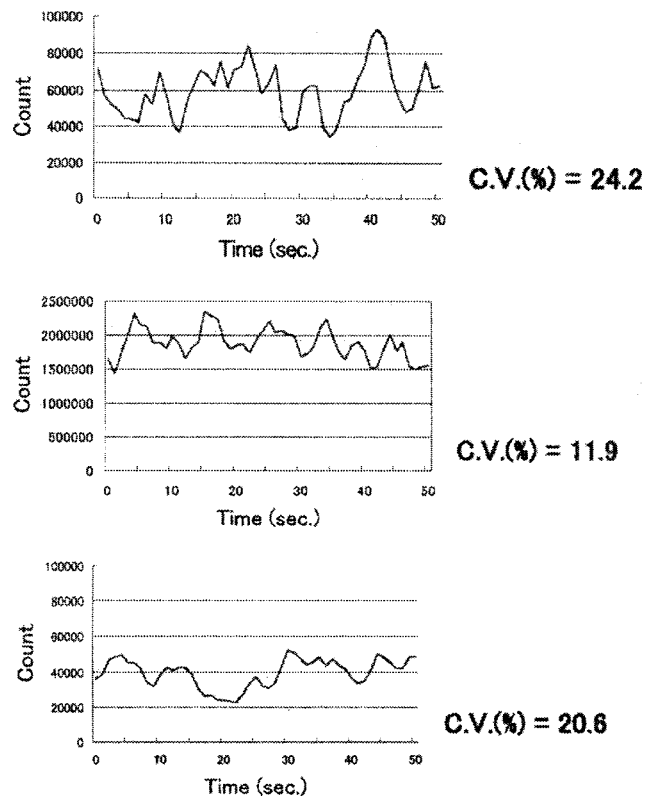


Fig. 11 Fluctuation of TIM at positions P_B in the flame; (a) flame I, (b) flame II, (c) flame III

References

- [1] Gupta, A. K., and Li, Z., 1997, "Effect of Property on the Structure of Highly Preheated Air Flames," *Proc. of the ASME 1997 International Joint Power Generation Conference (IJPGC)*, Denver, CO, ASME EC-Vol. 5, ASME, New York, pp. 247–258.
- [2] Choi, G.-M., and Katsuki, M., 2000 "New Approach to Low Emission of Nitric Oxides from Furnaces Using Highly Preheated Air Combustion," *J. Inst. Energy*, **73**, pp. 18–24.
- [3] Katsuki, M., and Ebisui, K., 1997 "Possibility of Low Nitric Oxides Emissions From Regenerative Combustion Systems using Highly Preheated Air," *Proc. Asian Pacific Combustion Conference (ASPACC-97)*, Osaka University, Osaka, Japan, May 12–15, 1997, pp. 294–297.
- [4] Ishiguro, T., Tsuge, S., Furuhata, T., Kitagawa, K., Arai, N., Hasegawa, T., Tanaka, R., and Gupta, A. K., 1998, "Homogenization and Stabilization During Combustion of Hydrocarbons with Preheated Air," *Proc. 27th Symposium (Intl.) on Combustion*, The Combustion Institute, Pittsburgh, PA, pp. 3205–3213.
- [5] Gupta, A. K., Bolz, S., and Hasegawa, T., 1999, "Effect of Air Preheat and Oxygen Concentration on Flame Structure and Emission," *ASME J. Energy Resour. Technol.*, **121**, pp. 209–216.
- [6] Konishi, N., Kitagawa, K., Arai, N., and Gupta, A. K., 2000 "Two-Dimensional Spectroscopic Analysis of Spontaneous Emission From a Flame Using Highly Preheated Air Combustion," *J. Propul. Power*, to appear in Jan.-Feb. issue.
- [7] Hasegawa, T., Mochida, S., and Gupta, A. K., 2001, "Development of Advanced Industrial Furnace using Highly Preheated Air Combustion," *J. Propul. Power*, to appear in Jan-Feb issue.
- [8] Weber, R., Verlaan, A. L., Orsino, S., and Lallemand, N., 1999, "On Emerging Furnace Design Methodology that Provides Substantial Energy Savings and Drastic Reductions in CO₂, CO, and NO_x Emissions," *J. Inst. Energy, UK*, **72**, pp. 77–83.
- [9] Katsuki, M., and Hasegawa, T., 1998, "The Science and Technology of Combustion in Highly Preheated Air," *Proc. 27th Symposium (Intl.) on Combustion*, The Combustion Institute, Pittsburgh, PA, **27**, pp. 3135–3146.
- [10] Tsuji, H., Gupta, A. K., Katsuki, M., Hasegawa, T., Kishimoto, K., and Morita, M., 2002, *High Temperature Air Combustion: From Energy Conservation to Pollution Reduction*, CRC Press, Boca Raton, FL.
- [11] Fujii, T., 1992, "A Novel Method for Detection of Radical Species in the Gas Phase: Usage of Li⁺ ion Attachment to Chemical Species," *Chem. Phys. Lett.*, **191**, Nos. 1 and 2, pp. 162–168.

Performance Analysis of Evaporative Biomass Air Turbine Cycle With Gasification for Topping Combustion

J. Wolf

F. Barone

J. Yan

Department of Chemical Engineering and
Technology/Energy Processes,
Royal Institute of Technology,
SE-100 44 Stockholm, Sweden

This paper investigates the performance of a new power cycle, a so called evaporative biomass air turbine (EvGT-BAT) cycle with gasification for topping combustion. The process integrates an externally fired gas turbine (EFGT), an evaporative gas turbine (EvGT), and biomass gasification. Through such integration, the system may provide the potential for adapting features from different advanced solid-fuel-based power generation technologies, e.g., externally fired gas turbine, integrated gasification combined cycle (IGCC), and fluidized bed combustion, thus improving the system performance and reducing the technical difficulties. In the paper, the features of the EvGT-BAT cycle have been addressed. The thermal efficiencies for different integrations of the gasification for topping combustion and the heat recovery have been analyzed. By drying the biomass feedstock, the thermal efficiency of the EvGT-BAT cycle can be increased by more than three percentage points. The impact of the outlet air temperature of the high-temperature heat exchanger has also been studied in the present system. Finally, the size of the gasifier for topping combustion has been compared with the one in IGCC, which illustrates that the gasifier of the studied system can be much smaller compared to IGCC. The results of the study will be useful for the future engineering development of advanced solid fuel power generation technologies. [DOI: 10.1115/1.1492834]

Introduction

Gas turbine systems that enable the use of solid fuels such as biomass and coal are of importance for future technologies for electricity production. The issues of the nuclear power phaseout in some European countries increase the interests for using other energy resources including biomass for electricity generation. For example, in Germany, 161 TWh/year of nuclear power will be replaced by other energy resources by 2021 according to a recent agreement between the German Government and the nuclear power industry (European Union [1] and IZE [2]). In Sweden, nuclear power today provides about 50% of the total electricity (Energikommissionen [3]) and the phaseout of nuclear power has already started. At the same time, the reduction of CO₂ emissions has recently been given great attention by the OECD countries due to their commitment to Kyoto agreement. Since biomass is a renewable energy resource and does not contribute to CO₂ emissions, using biomass in the place of fossil fuels for power generation has the potential for reducing CO₂ emissions. Therefore, developing an energy efficient, economically affordable, and technically reliable power generation system by using biomass becomes more important.

Sweden has large resources of biomass and the energy supply from biomass and peat reached 15% of the total energy supply in 1998 (Energimyndigheten [4]). However, the existing biomass power plants have low electrical efficiencies (Wahlund et al. [5]). Therefore, it is of importance to find a new approach for improving the biomass power generation systems.

The characteristics of fuels are of major importance when choosing an option in gas turbine systems. The use of solid fuels in gas turbines requires the resolution of technology issues which

are of little, or no consequence for conventional natural gas and refined oil fuels. Some options for producing power and heat using solid fuels are under development. These are direct solid-fuel fired gas turbine, integrated gasification combined cycle (IGCC), pressurized fluidized-bed combustion (PFBC), and externally fired gas turbines (EFGT). Each of these advanced technologies is at a different stage of development, but all face some barriers, as for example, limited operating experience and unproven long-term reliability, an unwillingness by the risk-averse utilities to accept products with limited operating experiences, lack of ability to deal with fluctuating loads and alternative modes of operation, and high capital costs. Today, the market of cheap natural gas brings another challenge for using solid fuels such as coal and biomass for power generation. Therefore, the R&D strategy should focus on the integration of features of different technologies, e.g., PFBC, IGCC, and EFGT (Yan and Eidensten [6]).

In this paper, a new power cycle so called evaporative biomass air turbine (EvGT-BAT) cycle with gasification for topping combustion has been studied. The system integrates the externally fired gas turbine (EFGT), the evaporative gas turbine (EvGT) and biomass gasification to improve the performance and use existing technologies as much as possible.

System Description

Previous work on biomass fired evaporative gas turbine can be found in Yan et al. [7–9]. The gasification process for topping combustion has been studied by Wolf and Yan [10]. This paper is a continued work of these previous studies with the focus on the integration of the various processes studied earlier. Figure 1 gives a flowsheet of an existing model presented in Yan et al. [8]. The model contains the gas turbine system, the solid fuel (biomass) combustion (SFC), and the heat recovery (HR) subsystem. The fuel for the topping combustor in the previous work was natural gas. For the present paper, natural gas has been replaced with syngas produced by a steam-based gasification process. Figure 2 shows the integrated system that has been studied in this paper,

Contributed by the International Gas Turbine Institute (IGTI) of THE AMERICAN SOCIETY OF MECHANICAL ENGINEERS for publication in the ASME JOURNAL OF ENGINEERING FOR GAS TURBINES AND POWER. Paper presented at the International Gas Turbine and Aeroengine Congress and Exhibition, New Orleans, LA, June 4–7, 2001; Paper 01-GT-367. Manuscript received by IGTI, Dec. 2000, final revision, Mar. 2001. Associate Editor: R. Natole.

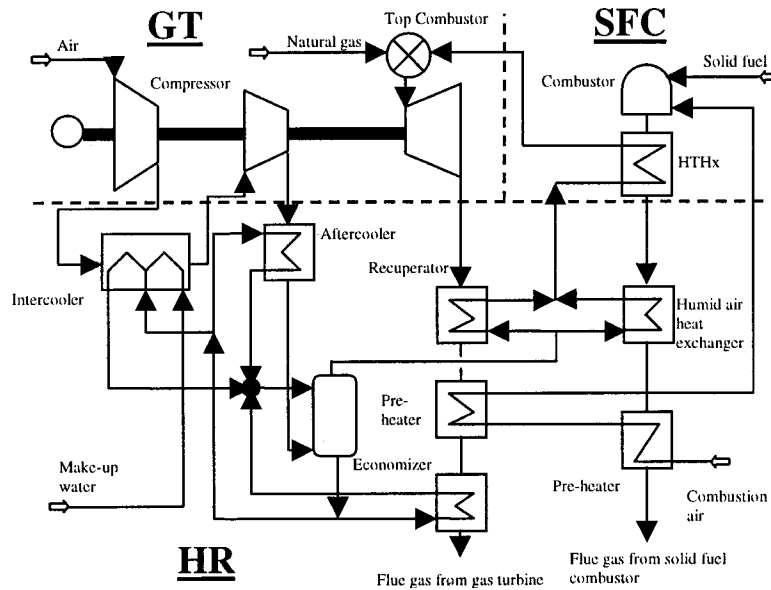


Fig. 1 The system without the gasification unit: GT= gas turbine, SFC = solid fuel combustion (biomass), HR=heat recovery (Yan et al. [8])

the so-called EvGT-BAT. The furnace provides the main part of the thermal energy for producing electricity. The high-temperature heat exchanger (HTHx) heats the air to about 900°C. Before entering the turbine, the air temperature is further increased by mixing with the flue gas from the topping combustion to the required turbine inlet temperature of 1100°C. In order to further increase the thermal efficiency of the process, the technology of evaporative gas turbines (EvGT) is used. The thermal energy of the exhaust gas from the turbine and the furnace is used for preheating and humidifying the compressed air before it enters the HTHx. To produce the fuel gas, steam-based pyrolysis of biomass conducted in an entrained flow tubular reactor is used. This process is discussed by Wolf and Yan [10]. A screw feeder transports the feedstock to a carrier gas injector. The carrier gas is a high-temperature product gas, which is accelerated and slightly pressurized by a compressor. The carrier gas conveys the biomass very rapidly through an entrained flow tubular reactor. The mix-

ture of product gas and biomass that enters the reactor is heated up to about 800°C in less than 1 sec. Under these conditions flash pyrolysis occurs. After pyrolysis, the gaseous products are separated from the pyrolysis char by a cyclone and the char is transported into the SFC. The stream of gaseous products is divided into a recycle stream, which flows back into the carrier gas injector, and the product gas stream. The product gas stream passes a gas cleaning system and if necessary, a water knock out unit. Since the gasifier suggested in this work operates close to atmospheric pressure, the product gas has to be compressed before it can be fed into the topping combustor. Syngas leaves the gasifier at about 800°C and is cooled down to 40°C and then compressed from 1 to 12 bar. After compression, the syngas of 12 bar and about 130°C is supplied to the topping combustor. Heat from the syngas cooler can be recovered in three ways, preheating the syngas stream after the compression, preheating the combustion air

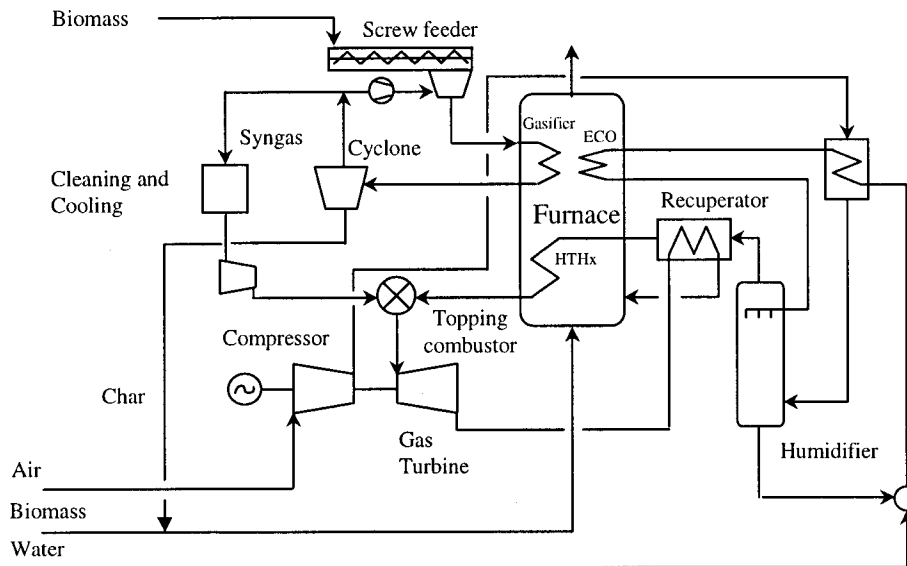


Fig. 2 Flow sheet of the EvGT-BAT process integrated with gasification

for the HITAF, or increasing the amount of water evaporated in the humidifier. In this paper three combinations of these options have been studied.

Features of the System

The studied system is an approach to use commercially available equipment as much as possible and new developing technologies only when necessary. For example, combustion occurs in a conventional atmospheric furnace. By using topping combustion to increase the turbine inlet temperature, the temperature of the high-temperature heat exchanger (HTHx) can be selected in a reasonable temperature range based on the development of the material and manufacturing technique. The gasification of biomass to produce the additional fuel for the topping combustion can be a simple pyrolysis process, which does not require a high conversion rate from biomass to gaseous fuel because the unconverted char can be further used in the SFC. The entrained flow tubular reactor, where the pyrolysis occurs, is housed in the SFC. In this way an extra building and combustor for the gasification is not necessary. Cooling down the syngas enables not only the use of a conventional cool gas cleaning, but also leading to a higher heating value of the fuel gas (Wolf and Yan [10]). Besides a high heating value, steam-based gasification supplies a syngas that contains a very low amount of nitrogen (about 1 Vol%).

Assumptions for the Process Model

The gasifier is modeled by a heat exchanger for heating the solid and moist biomass, a yield reactor for simulating the devolatilization reaction and a second heat exchanger for heating the syngas up to the final pyrolysis temperature of about 800°C. The gas composition listed in Table 1 is assumed to be achieved at a heating rate of about 1000°C/sec and an operating temperature of 800°C. The heating value of this gas has been calculated as 16 MJ/Nm³.

The heat requirement for the devolatilization reactions has been calculated by a heat balance based on the lower heating values of the biomass input and the output of syngas and char. Calculations showed that most of the energy needed for the pyrolysis is used to heat the biomass, the syngas, and the char to the required pyrolysis temperature. The required amount of energy for the devolatilization reactions is relatively small (Table 2). In this paper, the values from Table 2 are used in the model of the gasifier.

Further main assumptions used in the simulations are listed in Table 3. More detailed assumptions related to externally fired evaporative gas turbine can be found from the references (Yan et al. [9] Barone [11]). The pressure drop in the gasifier has not been considered in this study.

Table 1 Pyrolysis gas compositions for flash pyrolysis of woody biomass with a moisture content of about 14wt% (Wolf and Yan [10])

Component	N ₂	CO	H ₂	CO ₂	CH ₄	C ₂ H ₄	H ₂ O
Vol %	1	47	16	7	14	5	9

Table 2 Results of the heat balance for the devolatilization reactions (Yan et al. [7], Wolf [14], and Williams and Beslere [15])

Stream	LHV (MJ/kg)	wt %	Total Energy (MJ/kg _{Biomass})
Biomass	8.25	100	8.25
Syngas	7.9	93	9.59
Char	32	7	
Required devolatilization energy			1.34

Table 3 Input data

Subsystem	Description	Assumption
Gasifier	operating temperature	800°C
	fuel gas compressor isentropic efficiency	0.9
	pressure ratio	2.5
Turbine	air compressor isentropic efficiency	0.88
	turbine isentropic efficiency	0.9
	inlet temperature	1100°C
Solid Fuel	pressure ratio	12
	biomass LHV	8.25 MJ/kg
	moisture content	50%
Heat Generation	outlet temp. topping combustor	1120°C
Heat Recovery Subsystem	HTHx outlet air temperature	900°C
	syngas temperature	800°C
	preheated combustion air	365°C
Heat Recovery Subsystem	make up water	9°C
	max. outlet air temp. of the recuperator	500°C
	minimum stack gas temperature	100°C

Results and Discussion

The EvGT-BAT system with biomass gasification for fuel gas production for topping combustor has been compared with the EvGT-BAT system with natural gas as the additional fuel (reference system). The gasification is integrated into the whole power process. Thus, excess heat from the gasification process is recovered as much as possible to reduce any efficiency drops due to the introduction of gasification. The use of a dryer has been considered for both biomass streams, one entering the gasifier and one entering the SFC. The impact of the HTHx temperature on the systems performance is discussed, and finally the flow rate of biomass feedstock passing the gasifier is compared to the flow rate required in IGCC.

Efficiency of EvGT-BAT Systems When Introducing Biomass Gasification. The reference system for the present study is the EvGT-BAT system with natural gas as the additional fuel. Under the assumptions listed in Table 3, the thermal efficiency of this process is 42%. When gasification is used, due to the extra energy demand and the losses during the syngas cooling before the compression, the total thermal efficiency decreases by almost four percentage points if heat from the gasification is not recovered. The main loss appears in the product gas cooler. In this paper three options have been studied to increase the thermal efficiency:

- using the excess heat for raising the water-to-air ratio of the compressed air (HR 1),
- preheating the combustion air entering the HITAF and the syngas before entering the topping combustor (HR 2), and
- increasing the water-to-air ratio and preheating the combustion air (HR 3).

The possible increase in efficiency if the three modified heat recovery systems (HR 1–HR 3) are used is shown in Fig. 3. The first modification of the heat recovery system (HR 1) achieves an

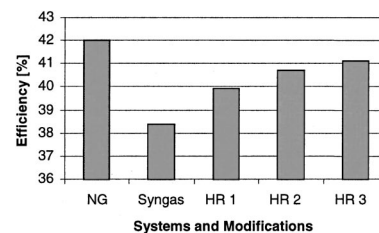


Fig. 3 Comparison of efficiencies between the reference system with natural gas as additional fuel (NG) and the EvGT-BAT system with an integrated gasification (Syngas) and its modification to improve the heat recovery (HRx)

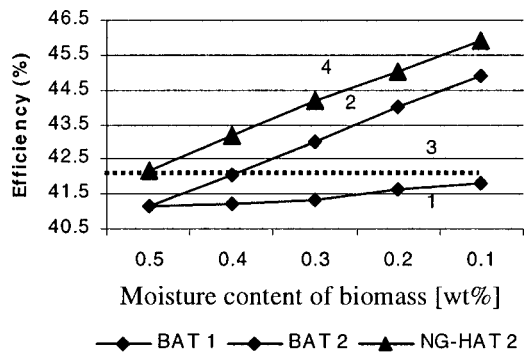


Fig. 4 Efficiency improvements when drying the biomass feedstock. 1=only the biomass for the gasification process is dried; 2=all biomass is dried; 3=reference system with natural gas and no drying; 4=reference system with natural gas when all biomass is dried.

efficiency increase of 1.5 percentage points compared to the syngas case, where heat from the gasifier is not recovered. The water-to-air ratio raises to 23.6%, thus the larger mass flow through the turbine results in a higher work output from the turbine. The second modification (HR 2) achieves an efficiency increase of 2.3 percentage points without changing the water-to-air ratio. This case leads to a decrease in the fuel consumption of the furnace (7.9% less biomass) and in the gasification process (1.5% less biomass). However, the low temperature heat ($<130^{\circ}\text{C}$) cannot be used because after compression, the syngas has a temperature of about 120°C . A combination of both modifications, preheating the combustion air, and raising the water-to-air ratio from 19.5 to 21% (HR 3) leads to an overall thermal efficiency of 41.13%. This efficiency is less than one percentage point lower than the reference system with natural gas. This shows the gasification process, if well integrated into the whole process, does not inevitably cause a large drop in efficiency.

Increase of Efficiency When a Drier is Used. A further increase in the thermal efficiency can be achieved by drying the biomass feedstock. It has been assumed that the biomass leaves the drier at a temperature of 70°C . Figure 4 shows that drying only the biomass that enters the gasification does not lead to a significant increase in efficiency. This is because the flow rate of biomass feedstock to the gasifier is smaller. A different result is achieved by drying both biomass streams entering the gasifier and the furnace. This leads to a significant increase in the overall efficiency. It is also important to consider that the lower amount of flue gas from the furnace means less energy is available for the HR. Thus, the water-to-air ratio and the net power decrease.

Regardless of whether natural gas or syngas is used for the topping combustion, the thermal efficiency increases with 8% if the biomass is dried from 50% to 10% moisture content.

Impacts of the HTHx Operation Temperature. The development of HTHx is of importance for externally fired gas turbine systems. Thus, the impact of the HTHx temperature on system performance has been studied. The temperature of HTHx will affect the feedstock flow rate (biomass) into the topping combustion via the gasifier and into the solid fuel furnace. Figure 5 shows the flow rate of the feedstock and the efficiency versus the HTHx temperature. The simulations show that at higher temperatures, the major part of biomass feedstock is consumed in the solid fuel combustion. The higher the HTHx operation temperature is, the less fuel gas is required to increase the temperature to the TIT. Thus the gasifier can be designed smaller. On the other hand, the less fuel gas that enters the topping combustor, the less its exhaust mass flow, thus the air stream has to be increased in order to produce the same amount of power in the turbine. Therewith, in the case of a higher HTHx temperature, the heat requirement for

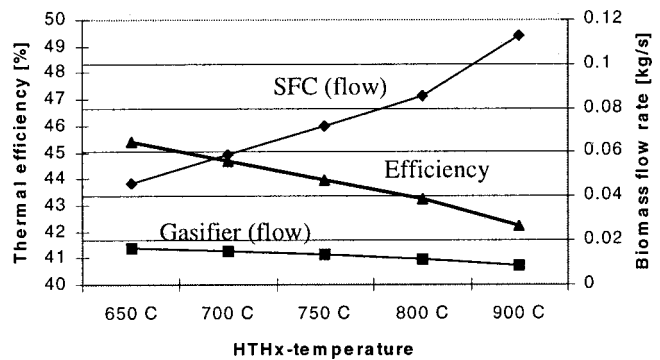


Fig. 5 Biomass flow rate into the furnace (SFC) and the gasifier and the resulting efficiency versus HTHx operation temperature (TIT constant at 1100°C)

the SFC increases because the temperature that must be reached is higher while at the same time the mass flow rate of the compressed air is larger. The efficiency of the process confirms that for the above-mentioned reason, very high HTHx temperatures are not meaningful in the EvGT-BAT system. This effect is a special feature of the present system in which the gasifier is housed in the solid fuel combustion chamber like a heat exchanger. An increased syngas production leads simultaneously to an increased amount of char, which is used as additional fuel in the solid fuel combustion. However, it is not possible to decrease the input in the furnace by much, because the increasing biomass stream passing the gasifier has to be heated and gasified. It will increasingly become complicated to design the solid fuel furnace if the size of the entrained flow tubular gasifier increases and at the same time the feedstock for the furnace and its dimension decreases. Furthermore, the investment cost for the gasifier, the gas compressor, the gas cooler, and the syngas cleaning system will rise. However, by further analyzing the EvGT-BAT system, an optimum HTHx temperature considering the overall efficiency and the investment cost might be found.

Comparison of the Size of the Gasifier in EvGT-BAT and IGCC. The high investment cost for gasification in IGCC is one of the obstacles for adopting this technology in commercial applications. An advantage of the EvGT-BAT system in comparison to IGCC is the lower flow rate of fuel gas that is needed to heat the compressed air to the turbine inlet temperature. This will greatly reduce the size of gasifiers in EvGT-BAT compared to the IGCC by reaching about the same thermal efficiency between 41–46% (Foster-Pegg [12]). In IGCC, the compressed air has a temperature of about 190°C when it leaves the compressor and enters the turbine combustor. This temperature is much lower than the one of the compressed air that enters the topping combustor in the present system. As the gasifier is housed in the solid fuel combustion, the present system gives a further advantageous feature. All required energy for heating the biomass feedstock and sustaining the devolatilization during the gasification comes from the solid fuel furnace. In an IGCC, this energy must also be produced in the gasifier by either burning syngas or using partial oxidation, which increases the biomass throughput in the gasifier. In the EvGT-BAT system, a steam-based gasification is suggested. Steam-based gasification supplies a fuel gas with a heating value up to $16\text{ MJ}/\text{Nm}^3$ when the water vapor concentration of the product gas is about 7 Vol% (Wolf and Yan [10]). If steam-based gasification is used in both technologies and for the EvGT-BAT system a HTHx temperature of 750°C is assumed, the biomass stream passing the gasifier in EvGT-BAT is one-sixth the one in IGCC. This means the reactor volume of the gasifier in IGCC will be six times the one in EvGT-BAT. When increasing the HTHx temperature to 900°C , the biomass flow rate in IGCC will be about 12 times the one in the EvGT-BAT system (Fig. 6).

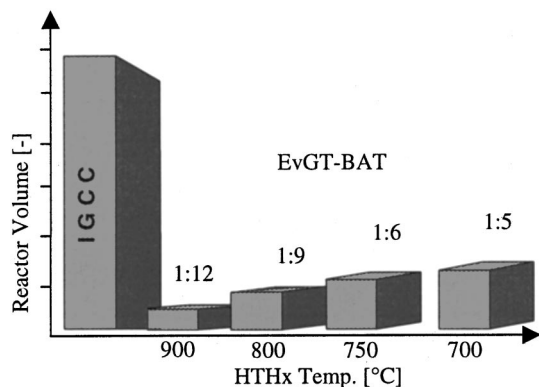


Fig. 6 Comparison between the theoretic dimension of a gasifier in EvGT-BAT at different HTHx temperature with a comparable gasifier in IGCC

The advantages of a smaller size and no requirement for high gasification conversion for the gasification in EvGT-BAT (because the unconverted char can be further used in the furnace) give a great potential to reduce the investment cost.

Discussion on Technical Issues. Since the main objective of this paper is to investigate the performance of the system, some of the technical issues have not been studied. For example biomass fuels contain a significant amount of fuel-bound nitrogen, which may convert into NO_x in the combustion process. Topping combustion is still a relatively new and novel concept and needs further development. Some work regarding topping combustion in PFBC applications has been carried out by Domeracki et al. [13]. Combustion of humid air with lower or medium-heating-value fuels is an interesting area for further investigation.

Conclusions

A new process, called EvGT-BAT, which integrates the features of IGCC, EFGT, and EvGT is introduced. The efficiency and main flow rates have been studied while changing the moisture content of the biomass feedstock and the temperature of the high-temperature heat exchanger. The results of the study are:

- the process converts solid fuel as biomass into electrical power with a thermal efficiency of more than 41% if the raw biomass has a moisture content of 50% and the temperature in the high-temperature heat exchanger is 900°C. If a drier is used this efficiency can be increased to about 44.5%.
- it is possible to integrate the gasification process into the whole cycle so that the efficiency drop is just 1% in comparison to a system with natural gas as the additional gaseous fuel for topping combustion.
- a comparison between the required fuel gas generation for IGCC and the presented EvGT-BAT system shows that the EvGT-BAT system has a great potential to reduce investment costs for the gasification section of the cycle.
- contrary to EFGT, the optimum temperature of the high-temperature heat exchanger is not as high as the turbine inlet temperature. A lower temperature results in higher requirements for the gasification process, but also a higher efficiency, while a higher temperature leads to a smaller gasifier, but efficiency decreases.

Acknowledgments

Financial supports from the Swedish National Energy Administration (Energimyndigheten) and Angpannefö-ningen's Foundation for Research and Development (Angpanneföreningens Forskningsstiftelse) are gratefully acknowledged.

Nomenclature

- EFGT = externally fired gas turbine
 EvGT = evaporative gas turbine
 EvGT-BAT = evaporative biomass air turbine
 HITAF = high-temperature air heater furnace
 HR = heat recovery
 HTHx = high-temperature heat exchanger
 IGCC = integrated gasification combined cycles
 PFBC = pressurized fluidized bed combustion
 R&D = research and development
 SFC = solid fuel combustion
 TIT = turbine inlet temperature

References

- [1] European Union, 1998, "1998 Annual Energy Review, Part II."
- [2] IZE, 2000, "Verständigung auf Atomkompromiss—Regierung und Unternehmen vereinbaren eine Laufzeit von 32 Jahren," Informationszentrale der Elektrizitätswirtschaft e.V., 2000-07-07, <http://oneworldweb.de/castor/presse/stromthemen/2000/nr7.html>.
- [3] Energikommisionen, 1995, "Omställning av energi-systemet—Slutbetänkande av Energikommisionen," SOU 1995:139, Stockholm, Sweden.
- [4] Energimyndigheten, 1999, "Energy in Sweden 1999," Swedish National Energy Administration, Eskilstuna, Sweden.
- [5] Wahlund, B., Yan, J., and Westermark, M., 2000, "Comparative Assessment of Biofuel-Based Combined Heat and Power Generation Plants in Sweden," 1st World Conference on Biomass for Energy and Industry, Sevilla, Spain, June 5–9.
- [6] Yan, J., and Eidensten, L., 2000, "Status and Perspective of Externally Fired Gas Turbines," *J. Propul. Power*, **16**(4), pp. 572–575.
- [7] Yan, J., Eidensten, L., and Svedberg, G., 1994, "Performance Evaluation of Biomass Externally Fired Evaporative Gas Turbine System," *IGTI-Vol. 9, ASME Cogen-Turbo*, ASME, New York, pp. 663–671.
- [8] Yan, J., Eidensten, L., and Svedberg, G., 1995, "An Investigation of the Heat Recovery System in Externally Fired Evaporative Gas Turbines," *International Gas Turbine and Aeroengine Congress and Exposition*, Houston, TX, June 5–8.
- [9] Yan, J., Eidensten, L., and Svedberg, G., 1996, "Externally Fired Evaporative Gas Turbine with a Condensing Heat Exchanger," *International Gas Turbine and Aeroengine Congress and Exposition*, Birmingham, UK, June 10–13.
- [10] Wolf, I., and Yan, J., 2000, "Simulation of Steam-Based Gasification Processes for Topping Combustion in the Biomass Air Turbine (BAT) Cycle," *International Gas Turbine & Aeroengine Congress & Exhibition*, Munich, Germany, May 8–11.
- [11] Barone, F., 2000, "Integration of Biomass Air Turbine and Evaporative Gas Turbine with Gasification for Topping Combustion," MS thesis, Department of Chemical Engineering and Technology, Energy Processes, Royal Institute of Technology, Stockholm, Sweden.
- [12] Foster-Pegg, R. W., 1990, "A Small Air Turbine Power Plant Fired With Coal in an Atmospheric Fluid Bed," *ASME J. Eng. Gas Turbines Power*, **112**, pp. 21–27.
- [13] Domeracki, W. F., Dowdy, T. E., and Bachovchin, D. M., 1994, "Topping Combustor Development for Second-Generation Pressurized Fluidized Bed Combined Cycles," *International Gas Turbine and Aeroengine Congress and Exhibition*, The Hague, Netherlands, June 13–16.
- [14] Wolf, J., 1999, "Simulation of a Steam-Based Gasification Process for Top Firing in Externally Fired Gas Turbine Systems," Master of Science thesis (Diplomarbeit), Department of Chemical Engineering and Technology, Energy Processes, Royal Institute of Technology, Stockholm, Sweden.
- [15] Williams, P. T., and Besler, S., 1996, "The Influence of Temperature and Heating Rate on the Slow Pyrolysis of Biomass," *Renewable Energy*, **7**, pp. 233–250.

Fuel Droplet Evaporation in a Supercritical Environment

G. S. Zhu¹

S. K. Aggarwal²

Department of Mechanical Engineering,
University of Illinois at Chicago,
Mail Code 251,
Chicago, IL 60607-7022

This paper reports a numerical investigation of the transcritical droplet vaporization phenomena. The simulation is based on the time-dependent conservation equations for liquid and gas phases, pressure-dependent variable thermophysical properties, and a detailed treatment of liquid-vapor phase equilibrium at the droplet surface. The numerical solution of the two-phase equations employs an arbitrary Eulerian-Lagrangian, explicit-implicit method with a dynamically adaptive mesh. Three different equations of state (EOS), namely the Redlich-Kwong (RK), the Peng-Robinson (PR), and Soave-Redlich-Kwong (SRK) EOS, are employed to represent phase equilibrium at the droplet surface. In addition, two different methods are used to determine the liquid density. Results indicate that the predictions of RK-EOS are significantly different from those obtained by using the RK-EOS and SRK-EOS. For the phase-equilibrium of n-heptane-nitrogen system, the RK-EOS predicts higher liquid-phase solubility of nitrogen, higher fuel vapor concentration, lower critical-mixing-state temperature, and lower enthalpy of vaporization. As a consequence, it significantly overpredicts droplet vaporization rates, and underpredicts droplet lifetimes compared to those predicted by PR and SRK-EOS. In contrast, predictions using the PR-EOS and SRK-EOS show excellent agreement with each other and with experimental data over a wide range of conditions. A detailed investigation of the transcritical droplet vaporization phenomena indicates that at low to moderate ambient temperatures, the droplet lifetime first increases and then decreases as the ambient pressure is increased. At high ambient temperatures, however, the droplet lifetime decreases monotonically with pressure. This behavior is in accord with the reported experimental data. [DOI: 10.1115/1.1385198]

Introduction

Droplet gasification in high-pressure environments, where the thermodynamic conditions correspond to the supercritical state of the liquid fuel, is important in diesel engines, liquid rockets, and gas turbine combustors. In jet engines used in military applications, the liquid fuel is the primary coolant for on-board heat sources, and may attain a critical state before it is "atomized." The gas turbine combustors used in propulsion applications are being designed to operate at increasingly higher pressures, which may exceed the critical pressure of the fuel. The modeling of transcritical droplet vaporization also represents a scientifically challenging problem, since the conventional "low-pressure" droplet models are generally not valid at high-pressure conditions. For example, the gas-phase nonidealities and the liquid-phase solubility of gases are negligible at low pressures, but become essential considerations at high pressures. Consequently, a single-component fuel droplet would assume a multicomponent behavior, and liquid mass transport in the droplet interior would become an important process. Secondly, as the droplet surface approaches the transcritical state, the latent heat reduces to zero, and the gas and liquid densities become equal at the droplet surface. Then, transient effects in the gas phase would become as important as those in the liquid phase, since the characteristic times for transport processes in the two phases become comparable. In addition, the liquid and gas-phase thermophysical properties become pressure-dependent. Also, under convective conditions, the drop-

let distortion and breakup become important processes, as the surface tension is greatly diminished and approaches zero at the critical point.

Due to its significant practical and fundamental relevance, the supercritical droplet gasification phenomena has been a subject of many theoretical and experimental investigations. Manrique and Borman [1] presented a methodology to consider several high-pressure effects in a quasi-steady model that was based on the Redlich-Kwong (RK-EOS) equation of state ([2]). In a subsequent study ([3]), it was demonstrated that the effects due to thermodynamic nonidealities and property variations modified the vaporization behavior significantly. Lazar and Faeth [4] and Canada and Faeth [5] also employed RK-EOS to develop a high-pressure model to investigate steady-state droplet vaporization and combustion for hydrocarbon fuels. They found the droplet burning-rate predictions of the high-pressure model to be similar to those of a conventional low-pressure model. In addition, the results of both models were in fair agreement with their experimental data. Matlosz et al. [6] developed a high-pressure model in which the gas-phase unsteadiness and real gas effects were included, while the gas absorption in liquid droplet was neglected.

Curtis and Farrell [7,8] developed a high-pressure model, using the Peng-Robinson (PR-EOS) equation of state ([9]) that predicted the droplet vaporization rate, temperature, and the critical mixing state. It was shown that for droplet vaporization under conditions similar to those in diesel engines, the anomalies in transport properties near the critical mixing state were insignificant. Hsieh et al. [10] reported a comprehensive analysis of the high-pressure droplet vaporization phenomena in binary and ternary systems at a temperature of 2000 K. The Soave-Redlich-Kwong equation of state (SRK-EOS) ([11]) was employed in the analysis. In a subsequent study, Shuen et al. [12] extended their high-pressure model to examine the combustion behavior of an n-pentane droplet under subcritical and supercritical conditions. Their results indicated a continuous increase in the droplet gasification rate with pressure, with a more rapid increment occurring near the critical burning pressure of the fuel. Delpanque and Sirignano [13] also

¹Currently at the University of Wisconsin at Madison.

²To whom all correspondence should be addressed.

Contributed by the International Gas Turbine Institute (IGTI) of THE AMERICAN SOCIETY OF MECHANICAL ENGINEERS for publication in the ASME JOURNAL OF ENGINEERING FOR GAS TURBINES AND POWER. Paper presented at the International Gas Turbine and Aeroengine Congress and Exhibition, Indianapolis, IN, June 7–10, 1999; ASME Paper 99-GT-301. Manuscript received by IGTI, March 1999; final revision received by the ASME Headquarters, August 2000. Associate Editor: H. D. Nelson.

considered a transient, spherically symmetric model to investigate transient gasification of a liquid oxygen droplet in gaseous hydrogen at high pressures. It was noted that at supercritical pressures, the droplet surface temperature reaches the critical mixing value. Jia and Gogos [14,15] employed the PR-EOS to quantify the effect of liquid-phase gas solubility on the vaporization of an n-hexane droplet for a range of ambient pressures and temperatures. The variation of droplet lifetime with pressure was shown to exhibit a maximum at low ambient temperatures, but to decrease monotonically with pressure at high ambient temperatures. Stengel et al. [16] employed the SRK-EOS to examine the vaporization behavior of freely falling n-heptane droplets in a nitrogen environment. Results from a quasi-steady droplet model were compared with measurements for ambient pressure up to 40 atm. Aggarwal et al. [17] also reported a quasi-steady high-pressure model that used the PR-EOS and considered the thermophysical properties to be pressure-dependent. The transient liquid-phase processes were also included in the model. The computed vaporization histories were shown to compare well with the measurements of Stengel et al. [16].

An important result from several numerical and experimental investigations ([18–21]) is that a droplet does not immediately attain the critical mixing state as it is introduced into an ambient where the pressure and temperature exceed the thermodynamic critical point of the liquid fuel. Also, while most studies indicate that the droplet surface generally reaches the critical mixing state at some pressure that is much higher than the fuel critical pressure, they report a wide scatter in the minimum ambient pressure required for the attainment of the critical state. The literature review also indicates that several different EOS have been employed to represent the liquid-vapor phase equilibrium at the droplet surface. Clearly, an accurate representation of phase equilibrium is essential for a realistic simulation of droplet evaporation at high pressures. Previous studies have not examined in detail the accuracy of various EOS and their effects on the predicted transcritical/supercritical droplet vaporization behavior. The present study is motivated by these considerations.

In the present study, a comprehensive model is developed to investigate the transcritical droplet vaporization phenomena. The model is first used to examine the effects of different EOS on the prediction of phase equilibrium for an n-heptane-nitrogen system, as well as on the prediction of droplet gasification rate in a supercritical environment. A detailed numerical study is then conducted to characterize the transcritical vaporization phenomena, including the transition from subcritical to supercritical state, and the subsequent supercritical droplet gasification behavior.

Problem Formulation

The physical problem described here considers the transient gas and liquid-phase processes associated with an isolated fuel droplet. The droplet, which is initially at a subcritical state, is suddenly introduced into a stagnant gas environment with its thermodynamic state in the supercritical regime of the fuel species. In the following, we describe the transient two-phase governing equations in a spherical coordinate system, along with the interphase conditions at the droplet surface.

For the gas-phase region, $r > r_s(t)$, the governing equations include the conservation equations for species, momentum, energy, and the equation of state (EOS):

$$\frac{\partial \rho_k}{\partial t} + \frac{1}{r^2} \frac{\partial}{\partial r} (\rho_k u r^2) = \frac{1}{r^2} \frac{\partial}{\partial r} \left[\rho D_k r^2 \frac{\partial}{\partial r} \left(\frac{\rho_k}{\rho} \right) \right] \quad (1)$$

$$\begin{aligned} \frac{\partial \rho u}{\partial t} + \frac{1}{r^2} \frac{\partial}{\partial r} (\rho u^2 r^2) + \frac{\partial p}{\partial r} &= \frac{1}{r^2} \frac{\partial}{\partial r} \left[2\mu r^2 \frac{\partial u}{\partial r} + \lambda \frac{\partial}{\partial r} (u r^2) \right] \\ &- \frac{2}{r^2} \left[2\mu u + \frac{\lambda}{r} \frac{\partial}{\partial r} (u r^2) \right] \quad (2) \end{aligned}$$

$$\begin{aligned} \frac{\partial \rho I}{\partial t} + \frac{1}{r^2} \frac{\partial}{\partial r} (\rho I u r^2) + \frac{p}{r^2} \frac{\partial}{\partial r} (u r^2) \\ = \frac{1}{r^2} \left\{ \frac{\partial}{\partial r} r^2 \rho D_k \left[\sum_{k=1}^N h_k \frac{\partial}{\partial r} \left(\frac{\rho_k}{\rho} \right) \right] \right\} + \frac{1}{r^2} \frac{\partial}{\partial r} \left(k r^2 \frac{\partial T}{\partial r} \right) \\ + \frac{\partial u}{\partial r} \left[2\mu \frac{\partial u}{\partial r} + \frac{\lambda}{r^2} \frac{\partial}{\partial r} (u r^2) \right] + \frac{2u}{r^2} \left[2\mu u + \frac{\lambda}{r} \frac{\partial}{\partial r} (u r^2) \right] \quad (3) \end{aligned}$$

$$f_1(p, T, \rho_1, \rho_2, \dots, \rho_N) = 0. \quad (4)$$

In the above equations, D_k , ρ_k , and h_k are, respectively, the diffusion coefficient, density, and specific enthalpy of k th species. N is the total number of species. Further, k , μ , and λ are the thermal conductivity, viscosity, and second viscosity coefficient, respectively. Equation (4) represents a P-V-T relation for the fluid mixture. A cubic EOS is employed, which can be written in a general form as ([22])

$$p = \frac{RT}{V-b} - \frac{a}{V^2 + u b V + w b^2} \quad (5)$$

where a and b are functions of temperature and species mole fractions. u and w are constants. Their values are: $u=2$, $w=-1$ for PR-EOS; and $u=1$, $w=0$ for SRK-EOS and RK-EOS.

For the liquid-phase region, $r < r_s$, the governing equations for the liquid temperature and species mass fractions are

$$\frac{\partial}{\partial t} (\rho_l C_{\rho l} T_l) = \frac{1}{r^2} \frac{\partial}{\partial r} \left(k_l r^2 \frac{\partial T_l}{\partial r} \right) + \frac{1}{r^2} \frac{\partial}{\partial r} \left[r^2 \sum_{k=1}^N \rho_l D_{lk} h_k \frac{\partial}{\partial r} \left(\frac{\rho_{lk}}{\rho_l} \right) \right] \quad (6)$$

$$\frac{\partial \rho_{lk}}{\partial t} = \frac{1}{r^2} \frac{\partial}{\partial r} \left[\rho_{lk} D_{lk} r^2 \frac{\partial}{\partial r} \left(\frac{\rho_{lk}}{\rho_l} \right) \right]. \quad (7)$$

Boundary Conditions

The boundary conditions at the droplet center ($r=0$) are: $\partial T_l / \partial r = 0$ and $\partial \rho_k / \partial r = 0$, and those at $r \rightarrow \infty$ are: $T \rightarrow T_\infty$, $p \rightarrow p_\infty$, and $\rho_k \rightarrow \rho_{k\infty}$. At the droplet surface, $r=r_s$, the condition of mass and energy conservation, and thermodynamic equilibrium are

$$\dot{m} X_k - \rho_{lk} D_l \frac{\partial X_k}{\partial r} \Big|_{r=r_s^-} = \dot{m} Y_k - \rho_k D_k \frac{\partial Y_k}{\partial r} \Big|_{r=r_s^+} \quad (8)$$

$$\begin{aligned} -k_l \frac{\partial T_l}{\partial r} \Big|_{r=r_s^-} &= -k \frac{\partial T}{\partial r} \Big|_{r=r_s^+} + \sum_{k=1}^N \left(\dot{m} Y_k - \rho_k D_k \frac{\partial Y_k}{\partial r} \right) \Big|_{r=r_s^+} \Delta H_{v,k} \\ &+ \dot{m} \left[\frac{u^2}{2} - u \frac{dr_s}{dt} - \frac{1}{\rho} \left(2\mu \frac{\partial u}{\partial r} + \frac{\lambda}{r^2} + \frac{\partial}{\partial r} \frac{\partial}{\partial r} (u r^2) \right) \right] \quad (9) \end{aligned}$$

$$f_2(T_s, P_s, X_{1s}, X_{2s}, \dots, X_{Ns}, Y_{1s}, Y_{2s}, \dots, Y_{Ns}) = 0 \quad (10)$$

where X_{is} and Y_{is} represent, respectively, the liquid and gas-phase mole fractions of i th species at the droplet surface. The specific form of Eq. (10) can be derived from the condition of thermodynamic and mechanical equilibrium at the droplet surface. At low pressures, the equilibrium is normally expressed by the Raoult's law. At elevated pressures, however, it should be described from a more general thermodynamic consideration, as discussed in the next section.

In a supercritical environment, depending on the ambient and droplet properties, the droplet may experience a thermodynamic

state transition from subcritical to supercritical. Equations (8)–(10) are only applicable until the droplet surface reaches a critical mixing point. The subsequent droplet regression is then characterized by the motion of the critical surface which moves inward continuously.

Vapor-Liquid Equilibrium at the Drop Surface

The vapor-liquid equilibrium at the droplet surface is represented by the equality of temperature and pressure, and the fugacity of each species in the gas and liquid phases. The equality of fugacity of species k is expressed as

$$\phi_k^v Y_k = \phi_k^l X_k \quad (11)$$

where the superscripts v and l refer to the vapor and liquid phase, respectively. ϕ_k is a function of pressure, temperature, and composition. It is given by the following relation:

$$RT \ln(\phi_k) = \int_v^\infty \left[\left(\frac{\partial P}{\partial n_k} \right)_{T,v,n_j} - \frac{RT}{v} \right] dv - RT \ln z \quad (12)$$

where n_j is the mole number of j th species. By substituting the equation of state (5) into Eq. (12), the fugacity of the k th species in the liquid and gas phase mixture is given by ([22]):

$$\ln \phi_k = \frac{b_k}{b} (z-1) - \ln(z-B) + \frac{A}{B\sqrt{u^2-4w}} \left(\frac{b_k}{b} - \delta_k \right) \times \ln \frac{2Z+B(u+\sqrt{u^2-4w})}{2Z+B(u-\sqrt{u^2-4w})} \quad (13)$$

where

$$\frac{b_k}{b} = \frac{T_{ck}/P_{ck}}{\sum_j y_j T_{cj}/P_{cj}} \quad \text{and}$$

$$\delta_k = \frac{2\sqrt{a_k}}{a} \sum x_j \sqrt{a_j} (1 - k_{kj}).$$

The binary interaction coefficient k_{kj} in the above equation is taken from Knapp et al. [23]. It is 0.1441 for PR-EOS, and 0.1422 for SRK and RK-EOS. Equations (11)–(13) provide the basic relations for vapor-liquid equilibrium calculation. These equations along with Eqs. (8)–(9) provide a closed system to determine the temperature and species mole fractions at the droplet surface. It represents a system of highly nonlinear algebraic equations that need to be solved iteratively at each time-step.

For a multicomponent mixture, the latent heat of vaporization of each species is defined as the difference between the partial molar enthalpy of that species in the vapor and liquid phases. The following thermodynamic relation then gives the partial molar enthalpy of k th species:

$$\bar{H}_k - \bar{H}_k^0 = -RT^2 \frac{\partial}{\partial T} (\ln \phi_k) \quad (14)$$

where the superscript 0 denotes the quantity in an ideal state. Equation (14) is solved iteratively along with Eqs. (8)–(9) and (11)–(13).

Thermophysical Properties

The gas and liquid-phase thermo-transport properties are considered function of pressure, temperature, and composition. The method suggested by Chung et al. [24] is employed to calculate the thermal conductivity and viscosity of the gas mixture at high pressures. The binary mass diffusivity is calculated by using the Chapman-Enskog theory in conjunction with the collision inte-

grals given by Neufeld et al. ([25]). It is then corrected for pressure effects by using the Takahashi correlation ([26]). For a multicomponent mixture, the effective diffusivity is obtained by using the formula given by Bird et al. [27]. The gas density is calculated directly from the EOS employed. For the enthalpy of gas mixture, the enthalpy of pure components is obtained from JANAF tables. A generalized thermodynamic correlation based on three-parameter corresponding states ([28]) is then used to calculate the enthalpy correction for high-pressure effects. Then, the specific internal energy of gas mixture in Eq. (3) is given by

$$l = \sum_{k=1}^N \frac{\rho_k}{\rho} h_k(T) - \frac{P}{\rho} \quad (15)$$

which relates the energy Eq. (3) to the equation of state (4) through the gas temperature.

The heat capacity of pure liquid components is calculated by a fourth-order polynomial of temperature, and then extended to liquid mixture using the mixture rule of Filippov [29]. The liquid mass diffusivity and thermal conductivity are obtained by using the correlations of Nakanishi [30] and Chung [24] respectively. In the present study, two different methods are employed to determine the liquid density. In the first, the liquid density is obtained directly from the EOS employed, while in the second, it is calculated by using the formulas suggested by Hankinson and Thomson [31] along with the high-pressure correction given by Thomson et al. [32].

Numerical Method

An arbitrary Lagrangian-Eulerian numerical method with a dynamically adaptive mesh is used to solve the governing equations. The solution procedure is as follows: (i) calculate explicitly the contributions of the diffusion and source terms in the gas-phase equations; (ii) calculate implicitly the terms associated with the acoustic pressure in the gas-phase equations; (iii) compute new mesh distribution with the adaptive mesh method, and then the convection terms in the gas-phase equations; and (iv) based on the solutions of above steps, solve implicitly the gas-phase equations, along with the liquid-phase equations as well as the droplet surface and vapor-liquid equilibrium equations.

The adaptive mesh technique is very effective in improving the calculation efficiency. For the supercritical vaporization calculations here, the results show that the minimum number of grid points required to get a grid-independent solution is about 600 for a uniform grid. However, using the adaptive mesh technique, the number of grid points is reduced to 180. A variable time-step is employed. It is calculated automatically based on the stability restrictions of explicit convection and diffusion processes.

Results and Discussion

The present simulations consider an n-heptane droplet evaporating in a high-pressure nitrogen environment. The first set of results focuses on a comparison of the thermodynamic phase equilibrium obtained by using the PR, SRK, and RK-EOS. Figure 1 shows a comparison of the phase-equilibrium predictions of PR, SRK, and RK-EOS at four different pressures. An important observation is that PR and SRK-EOS predict essentially the same equilibrium composition, including the fuel vapor mole fraction and the liquid-phase solubility of nitrogen, over a wide pressure range. In contrast, the predictions of RK-EOS exhibit significant differences from those of PR and SRK-EOS. In both the subcritical and supercritical regimes, the RK-EOS predicts higher fuel vapor mole fraction, which implies that it would yield higher droplet gasification rate compared to that using the PR and SRK-EOS. In addition, the RK-EOS predicts higher liquid-phase solubility of nitrogen in the supercritical regime ($P_r > 1.0$). The critical mixing point obtained by using RK-EOS is also different from that using the other two EOS. The temperatures at the critical

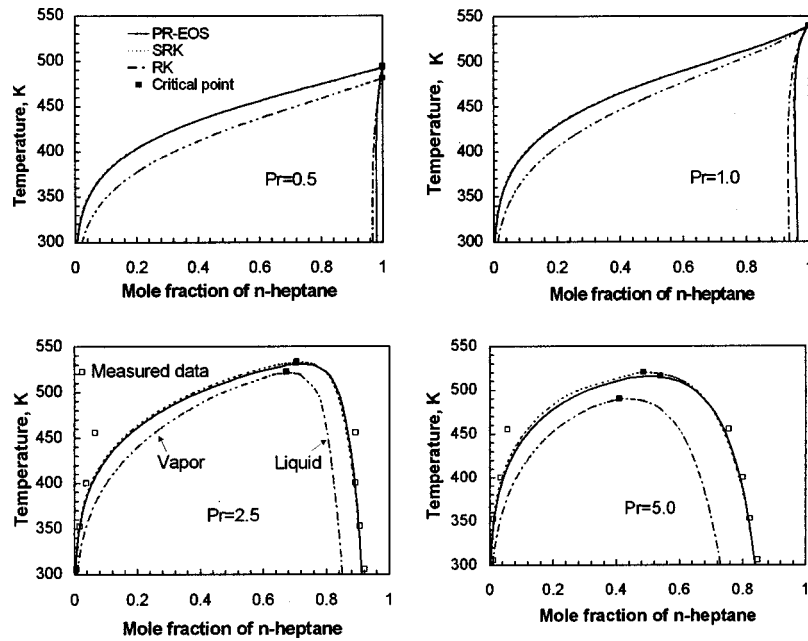


Fig. 1 Mole fraction of n-heptane predicted by PR, SRK, and RK-EOS for an n-heptane-nitrogen system in thermodynamic equilibrium at four different pressures. P_r is the reduced pressure normalized by the critical pressure of pure n-heptane. The experimental data from Chung et al. [23], for $P_r=2.5$ and 5.0, are also included in the plots.

mixing point predicted by RK-EOS are 1.9 and 8.4 percent lower than those predicted by the other two EOS at $P_r=2.5$ and 5.0, respectively. In addition, results for $P_r=2.5$ and 5.0 indicate that while the phase-equilibrium predictions of PR and SRK-EOS show good agreement with the experimental data [23] those of RK-EOS show significant differences.

Another important observation from Fig. 1 deals with the solubility of nitrogen into liquid at different ambient pressures and temperatures. At supercritical pressures, the amount of gas absorbed in liquid becomes significant, and increases as the ambient temperature and pressure are increased. This implies that in supercritical environments, the liquid mass transport becomes important and a pure fuel droplet exhibits multicomponent behavior. Also notable in Fig. 1 is that the critical mixing temperature (defined by the critical mixing point) decreases as the pressure is increased. This is indicated more clearly in Fig. 2(a), which shows the pressure-temperature diagram for an n-heptane-nitrogen system in equilibrium. Again, the difference between the prediction of RK-EOS and those of SRK and RK-EOS at supercritical pres-

ures is significant. Figure 2(b) shows the variation of latent heat of vaporization of n-heptane with temperature as predicted by PR, SRK, and RK-EOS. The heat of vaporization decreases as the temperature and/or pressure is increased, and drops to zero at the critical point. The predictions of PR and SRK-EOS are again in good agreement with each other, while those of RK-EOS exhibit noticeable differences, with RK-EOS underpredicting the heat of vaporization significantly. Clearly, this has important implications for predicting the droplet vaporization rate at supercritical conditions using different EOS.

We now focus on the transient vaporization behavior of an n-heptane droplet which at time $t=0$ is introduced into a high-pressure nitrogen environment. Figure 3 shows the droplet lifetime computed by using different EOS and plotted as a function of ambient pressure and temperatures. Here, the droplet lifetime is defined when the nondimensional droplet surface area reaches a value of 0.2, and it is normalized by using a characteristic time as d_o^2/β , where d_o is the initial diameter, and β is the vaporization

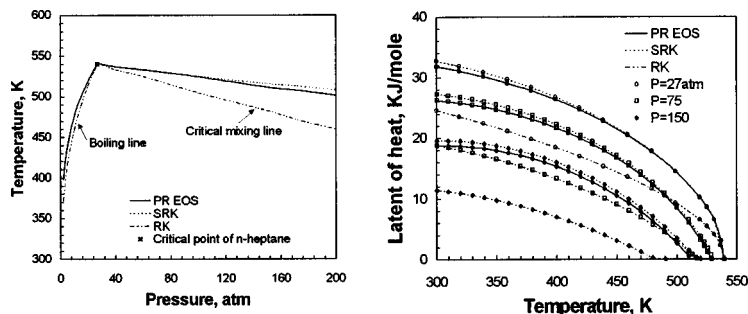


Fig. 2 (a) Phase equilibrium in terms of the pressure-temperature diagram and (b) latent heat of vaporization of n-heptane versus temperature for n-heptane-nitrogen system in thermodynamic equilibrium, as predicted by PR, SRK, and RK-EOS at three different pressures. See Fig. 1 for additional details.

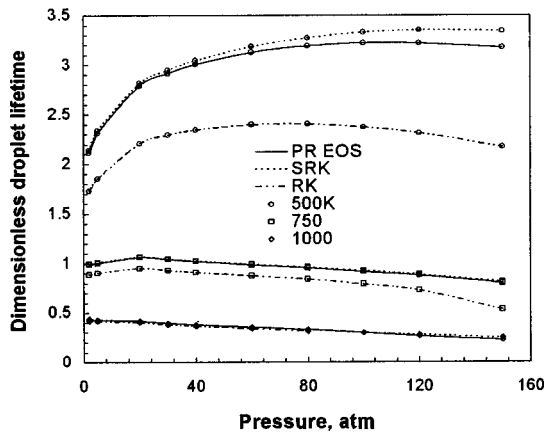


Fig. 3 Non-dimensional droplet lifetime, predicted by PR, SRK, and RK-EOS, plotted versus pressure at three different ambient temperatures

constant computed at $p=1$ atm and $T_a=750$ K. At high ambient temperatures, the droplet lifetime decreases monotonically as the ambient pressure is increased. However, at low to moderate ambient temperatures, the droplet lifetime first increases and then decreases as the ambient pressure is increased. This behavior is consistent with the reported experimental results ([18]), and can be explained as follows:

An increase in ambient pressure leads to the following effects: (i) the droplet heatup time increases and becomes a more significant part of droplet lifetime, since the fuel boiling temperature increases continuously with pressure until the droplet surface reaches a critical state, see Fig. 2(a); (ii) the mass transfer number B , which is generally expressed as $B=c_p \cdot (T_a - T_s)/L$, decreases as p is increased, since T_s increases with pressure; and (iii) the latent heat of vaporization (L) decreases and goes to zero as the droplet surface reaches a critical mixing point, see Fig. 2(b). At low to moderate ambient temperatures, the first two effects dominate, and, consequently, the droplet lifetime increases with pressure. At higher pressures, however, the third effect becomes dominant, since the heat of vaporization decreases drastically and goes to zero at the critical mixing point. Consequently, as indicated in Fig. 3 for ambient temperatures of 500 and 750 K, the droplet lifetime decreases with pressure at high pressures. Also, when the ambient temperature is sufficiently high, the first two effects become relatively less sensitive to pressure compared with the third effect, and the droplet lifetime decreases continuously as the ambient pressure is increased. These results also imply that the lifetime of a combusting droplet would decrease monotonically with increasing ambient pressure. This observation is well corroborated by experimental studies ([20]).

The sensitivity of the computed droplet lifetime to different EOS is also illustrated in Fig. 3. For all the cases examined, the lifetime predictions using PR-EOS and SRK-EOS are in good agreement with each other, except for small differences at low ambient temperatures ($T=500$ K) and at high pressures ($p > 60$ atm). In contrast, at moderate ambient temperatures ($T_a = 750$ K), RK-EOS significantly underpredicts the droplet lifetime compared with those obtained by using PR and SRK-EOS. This can be attributed to the fact that for given ambient temperature and pressure, RK-EOS predicts higher fuel vapor mole fraction at the droplet surface and lower heat of vaporization compared with those predicted by PR and SRK-EOS, see Figs. 1 and 2(b). At high ambient temperatures, however, the differences in the lifetime predictions using the three EOS are insignificant. This implies that the predicted gasification behavior of a combusting droplet may not be very sensitive to the particular EOS used.

Figure 4 shows the final temperature and fuel vapor mass fraction at the droplet surface plotted versus the ambient pressure.

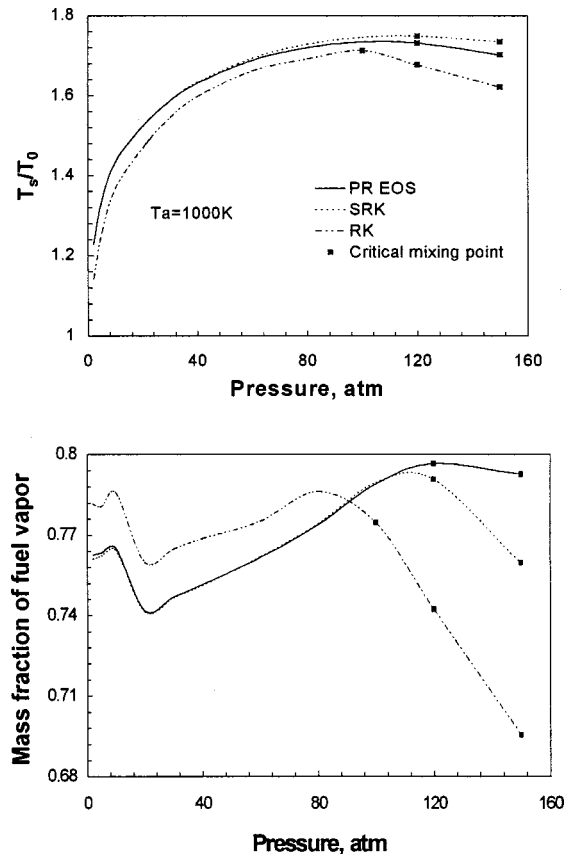


Fig. 4 Final temperature and fuel vapor mass fraction at the droplet surface plotted as functions of pressure. The ambient temperature (T_a) is 1000 K, and initial droplet temperature (T_0) 300 K. The final time corresponds to a time when $(d/d_0)^2 = 0.2$.

Again, the predictions of SRK and PR-EOS are in close agreement with each other over a wide pressure range, except for small deviations after the droplet surface reaches the critical mixing state. The predicted droplet surface temperature using RK-EOS is lower than that predicted by the other two EOS. More importantly, the predicted fuel vapor mass fraction using RK-EOS is higher compared to those obtained by using SRK and PR-EOS prior to the attainment of critical state and lower after the critical state. This is consistent with the phase-equilibrium results presented in Fig. 1, which indicates higher fuel vapor mass fraction for RK-EOS. The results for $P_r=5.0$ in Fig. 1 also indicate that with RK-EOS, the critical mixing point is attained at a lower temperature compared to that with the other two EOS. After the critical mixing point, the final temperature and fuel vapor mass fraction at the droplet surface decrease as the pressure is increased. This behavior is consistent with the phase-equilibrium results shown in Fig. 2(a), which indicates that the critical temperature decreases with critical pressure, as well as with those reported by Shuen et al. [12] and Jia and Gogos [14].

The literature indicates a wide scatter in the minimum ambient pressure required for attaining a critical mixing state at the droplet surface. Clearly, a reliable supercritical droplet gasification model should provide an accurate value of this pressure. As indicated in Fig. 4, at an ambient temperature of 1000 K, the minimum ambient pressure predicted by using PR and SRK-EOS is 120 atm ($P_r=4.44$), while that by using RK-EOS is 100 atm ($P_r=3.70$).

Figure 5 shows a comparison between our predictions and the measurements of Nomura et al. [21]. Results are presented in terms of the temporal variation of nondimensional surface area

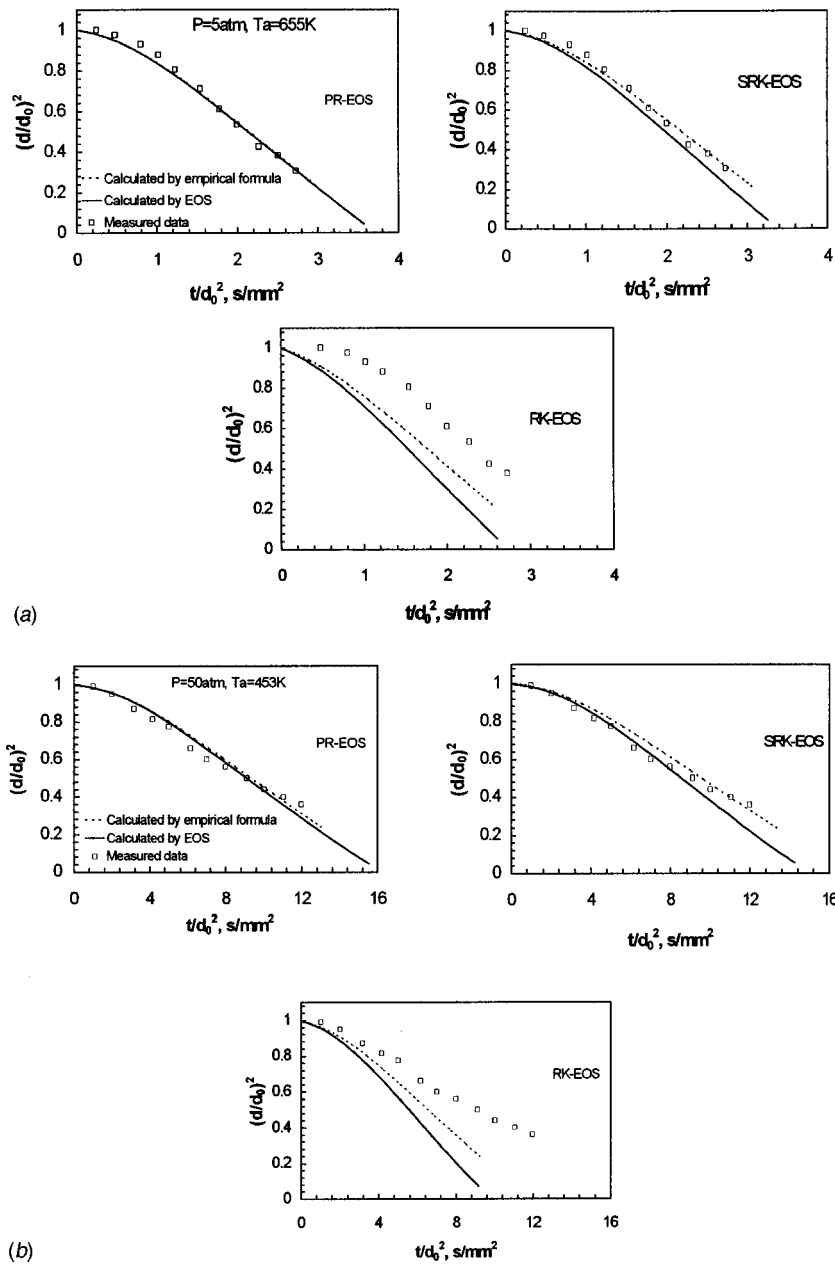


Fig. 5 (a) Comparison between the predictions using PR, SRK, and RK-EOS and the measured data of Nomura et al. [21] at $P=5$ atm and $T_a=655$ K. (b) comparison between the predictions using PR, SRK, and RK-EOS and the measured data of Nomura et al. [21] at $P=50$ atm and $T_a=453$ K.

obtained by using the three EOS for two different ambient conditions. In order to examine the effect of liquid density on predictions, the computed results are shown for two cases. An important observation is that using PR-EOS, the simulations reproduce experimental results quite well over a wide range of pressures. The numerical results obtained by using SRK-EOS are also in good agreement with experimental data, while those obtained by using RK-EOS exhibit significant differences, especially for the high-pressure case. Consistent with the earlier discussion, the RK-EOS significantly overpredicts the vaporization rate. For example, for $p=50$ atm and at a nondimensional time of 8, the numerical model based on RK-EOS predicts a nondimensional surface area of 0.2 compared to the experimental value of 0.6. The predictions

of RK-EOS show improvement when the liquid density is calculated by the empirical formula, but still deviate noticeably from the experimental data.

In order to examine the supercritical droplet vaporization phenomena, we plot some important gas and liquid-phase properties during the transcritical state. Figure 6 shows the temporal variation of droplet surface area, surface temperature and liquid temperature at the droplet center for an ambient pressure of 120 atm. The predictions are based on PR-EOS with liquid density calculated by using the empirical formula. As indicated, the droplet surface, which is initially at a subcritical state, reaches the critical mixing state during later part of droplet lifetime. Furthermore, as the ambient temperature is increased, the surface temperature rises

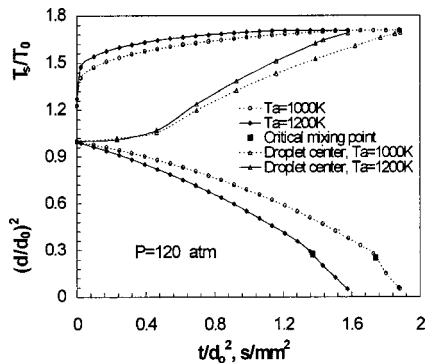


Fig. 6 Supercritical vaporization behavior in terms of the temporal variation of nondimensional droplet surface area, surface temperature and liquid temperature at the droplet center as predicted by PR-EOS

at a faster rate, and the droplet surface reaches the critical mixing state earlier in droplet lifetime.

When the droplet surface approaches the critical mixing state, the difference between the gas and liquid phases disappears. In the present model, it is assumed that once the surface reaches the critical mixing state, it is maintained at that state. Note, however, that the critical mixing state varies with ambient temperature and pressure. The velocity of the critical mixing surface moving inwards to the droplet center then determines the vaporization rate. This velocity depends on how fast the inner liquid layer adjacent to the droplet surface attains the critical mixing temperature, which in turn depends on the distributions of liquid-phase properties within the droplet. It is also important to note that our simulations did not indicate any anomalous behavior during the transcritical stage of droplet evaporation.

In order to examine the multicomponent behavior of a pure fuel droplet at high pressure, we plot in Fig. 7 the radial distribution of liquid temperature and dissolved nitrogen within the droplet during different stages of droplet lifetime. The ambient conditions are the same as those in Fig. 6. As expected, the liquid nitrogen mass fraction has its maximum value at the droplet surface, and increases continuously with time until the droplet surface reaches a critical mixing state. Note that the critical mixing state for this case is attained at a nondimensional time of 0.69. This plot demonstrates that a pure fuel droplet evaporating in a supercritical environment exhibits multicomponent behavior. It is also noteworthy that while the liquid nitrogen mass fraction drops rapidly to a negligible value within a thin layer near the surface, the liquid temperature shows a more gradual decrease. This is indicative of small liquid mass diffusivity (relative to thermal diffusivity) or high liquid Lewis number.

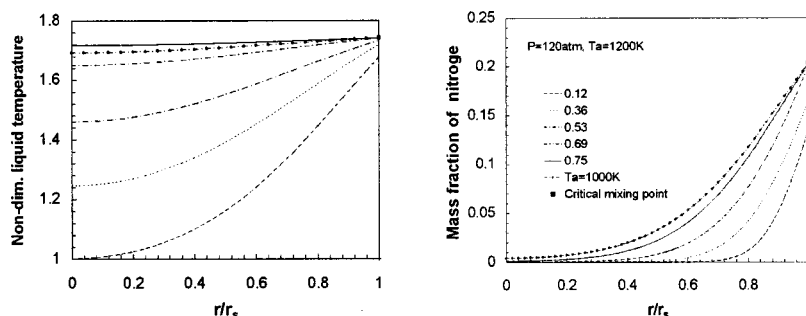


Fig. 7 Radial distribution of liquid temperature (a) and dissolved nitrogen (b) in the droplet interior at different stage of droplet lifetime, as predicted by PR-EOS. The number for each curve represents a fraction of droplet lifetime.

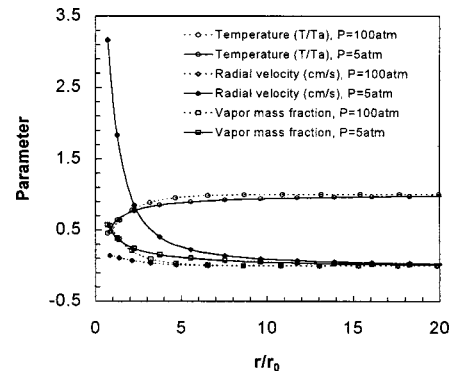


Fig. 8 Radial distribution of gas temperature, velocity, and fuel vapor mass fraction in the gas-phase region as predicted by PR-EOS for ambient pressures of 5 and 150 atm

Figure 8 shows the radial distribution of gas temperature, velocity, and fuel vapor mass fraction in the gas-phase region at two different ambient pressures. For these results, the PR-EOS has been employed. An important observation is that the radial distance over which the gas-phase properties vary significantly decreases as the ambient pressure is increased. For example, it decreases from ten to four times the droplet radius as the pressure is increased from 5 to 150 atm. This implies that the rates of heat and mass transport are enhanced, and, consequently, the vaporization rate is increased at higher pressures. It can be seen that the maximum gas velocity decreases dramatically when the pressure is increased from 5 to 150 atm, which also implies a change in the gas-phase unsteadiness.

The literature indicates a wide scatter in the minimum ambient pressure required for a droplet to attain a critical mixing state at its surface. Clearly, this value depends on several liquid and gas-phase properties including ambient temperature and composition, initial droplet diameter, and liquid fuel properties. Figure 9 shows the minimum ambient pressure as a function of ambient temperature. In order to obtain this minimum pressure value, simulations were performed for increasingly higher pressures, but at fixed ambient temperature, until a critical mixing state is observed at the droplet surface. The plot in Fig. 9 represents a boundary (in terms of the ambient temperature and pressure) between the subcritical and supercritical vaporization. Any point above the curve indicates that a critical mixing state will be reached sometime during the droplet lifetime, or the droplet will undergo transcritical evaporation during its lifetime. On the other hand, any point below the curve implies that the droplet is not likely to attain a supercritical state during its lifetime. Also, farther a point is from the curve (in the supercritical region), earlier in its lifetime does the droplet reach the critical mixing state.

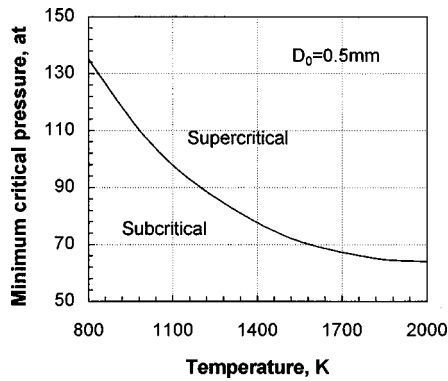


Fig. 9 Minimum pressure, required for an n-heptane fuel droplet to attain a critical mixing state, plotted as a function of ambient temperature

Conclusions

In this paper, the transcritical droplet vaporization phenomena has been investigated. The computational model considers the transient, spherically symmetric conservation equations for gas and liquid phases, pressure-dependent variable thermophysical properties, and a detailed treatment of the liquid-vapor phase equilibrium at the droplet surface. The model is shown to reproduce the subcritical, transcritical, and supercritical vaporization behavior of a liquid fuel droplet over a wide range of ambient conditions. In addition, the effects of using different EOS on predicting the equilibrium composition and transcritical droplet vaporization have been examined. Important observations are as follows:

1 For an n-heptane-nitrogen system, the phase-equilibrium predictions using RK-EOS show significant differences from those using PR and SRK-EOS. The RK-EOS yields higher fuel vapor concentration, higher solubility of nitrogen into liquid, lower critical-mixing-state temperature, and lower latent heat of vaporization compared to those obtained by using PR and SRK-EOS.

2 At low to moderate ambient temperatures, RK-EOS significantly overpredicts the droplet vaporization rate, and underpredicts the droplet lifetime compared to that using the other two EOS. Also, using RK-EOS, the critical mixing state at the droplet surface is reached earlier in droplet lifetime compared to that by using the other two EOS. These differences become less noticeable at higher ambient temperatures ($T_a \geq 1000$ K), implying that for a combusting droplet, differences in the predictions of three EOS may not be significant. The droplet lifetime predictions of PR-EOS are in excellent agreement with measurements ([21]) over a wide range of ambient pressures. In contrast, the predictions based on RK-EOS show significant differences with measurements, while those based on SRK-EOS are in reasonable agreement with measurements.

3 At low to moderate ambient temperatures, the predicted droplet lifetime first increases reaching a maximum value, and then decreases as the ambient pressure is increased. At high ambient temperatures ($T_a \geq 1000$ K), however, the droplet lifetime decreases monotonically with increasing pressure. These results are in agreement with the reported experimental and numerical results ([19–21]).

Acknowledgment

This work was partially funded by the GE Aircraft Engines.

Nomenclature

c_p = specific heat at constant pressure
 h = enthalpy
 H = partial molar enthalpy

I = internal energy
 k = thermal conductivity
 \dot{m} = droplet vaporization rate
 r = spatial variable
 p = pressure
 $r_s(t)$ = instantaneous droplet radius
 R = gas constant
 t = temporal variable
 T = temperature
 V = specific volume
 ρ = mixture density
 z = compressibility factor

Subscripts

k = gas species
 l = liquid-phase property

References

- [1] Manrique, J. A., and Borman, G. L., 1969, "Calculation of Steady State Droplet Vaporization at High Ambient Pressures," *Int. J. Heat Mass Transf.*, **12**, pp. 1081–1095.
- [2] Chueh, P. L., and Prausnitz, J. M., 1968, "Calculation of High Pressure Vapor-Liquid Equilibria," *Ind. Eng. Chem.*, **60**, pp. 34–52.
- [3] Savery, C. W., and Borman, G. L., 1970, "Experiments on Droplet Vaporization at Supercritical Pressures," AIAA Paper No. 70-6.
- [4] Lazar, R. S., and Faeth, G. M., 1971, "Bipropellant Droplet Combustion in the Vicinity of the Critical Point," *Proc. 13th Symp. on Combustion*, The Combustion Institute, Pittsburgh, PA, pp. 801–811.
- [5] Canada, G. S., and Faeth, G. M., 1973, "Fuel Droplet Burning Rates at High Pressures," *Proc. of 14th Symp. on Combustion*, The Combustion Institute, Pittsburgh, PA, pp. 1345–1354.
- [6] Matlosz, R. L., Leipziger, S., and Torda, T. P., 1972, "Investigation of Liquid Drop Evaporation in a High Temperature and High Pressure Environment," *Int. J. Heat Mass Transf.*, **15**, pp. 831–852.
- [7] Curtis, E. W., and Farrell, P. V., 1988, "Droplet Vaporization in a Supercritical Microgravity Environment," *Acta Astronaut.*, **17**, pp. 1189–1193.
- [8] Curtis, E. W., and Farrell, P. V. A., 1992, "Numerical Study of High-Pressure Droplet Vaporization," *Combust. Flame*, **90**, pp. 85–102.
- [9] Peng, D., and Robinson, D. B., 1976, "A New Two-Constant Equation of State," *Ind. Eng. Chem. Fundam.*, **15**, pp. 59–64.
- [10] Hsieh, K. C., Shuen, J. S., and Yang, V., 1991, "Droplet Vaporization in High Pressure Environments I: Near Critical Conditions," *Combust. Sci. Technol.*, **76**, pp. 111–132.
- [11] Graboski, M. S., and Daubert, T. E., 1987, "A Modified Soave Equation of State for Phase Equilibrium Calculations I: Hydrocarbon Systems," *Ind. Eng. Chem. Process Des. Dev.*, **17**, pp. 443–337.
- [12] Shuen, J. S., Tang, V., and Hsiao, C. C., 1992, "Combustion of Liquid-Fuel Droplets in Supercritical Conditions," *Combust. Flame*, **89**, pp. 299–319.
- [13] Delplanque, J. P., and Sirignano, W. A., 1993, "Numerical Study of the Transient Vaporization of an Oxygen Droplet at Sub- and Super-Critical Conditions," *Int. J. Heat Mass Transf.*, **36**, pp. 303–314.
- [14] Jia, H., and Gogos, G., 1993, "High Pressure Droplet Vaporization; Effects of Liquid-Phase Gas Solubility," *Int. J. Heat Mass Transf.*, **36**, pp. 4419–4431.
- [15] Jia, H., and Gogos, G., 1992, "Investigation of Liquid Droplet Evaporation in Subcritical and Supercritical Gaseous Environments," *J. Thermophys. Heat Transfer*, **6**, pp. 738–745.
- [16] Stengele, J., Bauer, H. J., and Wittig, S., 1996, "Numerical Study of Bicomponent Droplet Vaporization in a High Pressure Environment," Presented at the International Gas Turbine and Aeroengine Congress & Exhibition, Birmingham, UK, Paper No. 96-GT-442.
- [17] Aggarwal, S. K., Shu, Z., Mongia, H., and Hura, H. S., 1998, "Multicomponent and Single-Component Fuel Droplet Evaporation Under High Pressure Conditions," AIAA Paper No. 98-3833.
- [18] Faeth, G. M., 1977, "Current Status of Droplet and Liquid Combustion," *Prog. Energy Combust. Sci.*, **3**, pp. 191–224.
- [19] Givler, S. D., and Abraham, J., 1996, "Supercritical Droplet Vaporization and Combustion Studies," *Prog. Energy Combust. Sci.*, **22**, pp. 1–28.
- [20] Kadota, T., and Hiroyasu, H., 1982, "Combustion of a Fuel Droplet in Supercritical Gaseous Environments," *Proc. 18th Symp. on Combustion*, The Combustion Institute, Pittsburgh, PA, pp. 275–282.
- [21] Nomura, H., Ujiie, Y., Rath, H. J., Sato, J., and Kono, M., 1996, "Experimental Study of High-Pressure Droplet Evaporation Using Microgravity Conditions," *Proc. 26th Symp. on Combustion*, The Combustion Institute, Pittsburgh, PA, pp. 1267–1273.
- [22] Reid, R. C., Prausnitz, J. M., and Poling, B. E., 1987, *The Properties of Gases and Liquids*, McGraw-Hill, New York.
- [23] Knapp, H., Doring, R., Oellrich, L., Plocker, U., and Prausnitz, J. M., 1982, "Vapor-Liquid Equilibria for Mixture of Low Boiling Substances," *Chem. Eng. Data*, Series, Vol. VI, DEHEMA, Frankfurt.
- [24] Chung, T. H., Ajlan, M., Lee, L. L., and Starling, K. E., 1988, "Generalized Multiparameter Correlation for Nonpolar and Polar Fluid Transport Properties," *Ind. Eng. Chem.*, **27**, pp. 671–679.

- [25] Neufeld, P. D., Janzen, A. R., and Aziz, R. A., 1972, "Empirical Equations to Calculate 16 of the Transport Collision Integrals $\Omega^{(l,s)}$ for the Lennard-Jones Potential," *J. Chem. Phys.*, **57**, pp. 1100–1102.
- [26] Takahashi, S., 1974, "Preparation of a Generalized Chart for the Diffusion Coefficients of Gases at High Pressures," *J. Chem. Eng.*, **6**, pp. 417–420.
- [27] Bird, R. B., Stewart, W. E., and Lightfoot, E. N., 1960, *Transport Phenomena*, John Wiley and Sons, New York.
- [28] Byung, I. L., and Michael, G. K., 1975, "A Generalized Thermodynamic Correlation Based on Three-Parameter Corresponding States," *AIChE J.*, **21**, pp. 510–527.
- [29] Filippov, L. P., 1956, "Thermal Conduction of Solutions in Associated Liquids: Thermal Conduction of 50 Organic Liquids," *Chem. Abstr.*, **50**, Col. 8276.
- [30] Nakanishi, K., 1978, "Prediction of Diffusion Coefficients of Nonelectrolytes in Dilute Solution Based on Generalized Hammond-Stokes Plot," *Ind. Eng. Chem. Fundam.*, **17**, pp. 253–256.
- [31] Hankinson, R. W., and Thomson, G. H., 1979, "A New Correlation for Saturated Densities of Liquids and Their Mixtures," *AIChE J.*, **25**, pp. 653–663.
- [32] Thomson, G. H., Brobst, K. R., and Hankinson, R. W., 1982, "An Improved Correlation for Densities of Compressed Liquids and Liquid Mixtures," *AIChE J.*, **28**, pp. 671–676.

T. Wakabayashi

e-mail: twakaba@osakagas.co.jp

S. Ito

e-mail: ito@osakagas.co.jp

S. Koga

e-mail: s-koga@osakagas.co.jp

M. Ippommatsu

e-mail: m-ippommatsu@osakagas.co.jp

K. Moriya

e-mail: moriya@osakagas.co.jp

Osaka Gas Co., Ltd.,

6-19-9, Torishima,

Konohana-ku,

Osaka 554-0051, Japan

K. Shimodaira

e-mail: simo@nal.go.jp

Y. Kurosawa

e-mail: kuro@nal.go.jp

K. Suzuki

e-mail: suzukazu@nal.go.jp

National Aerospace Laboratory,

7-44-1 Jindaiji-higashi,

Chofu, Tokyo 182-8522, Japan

Performance of a Dry Low-NO_x Gas Turbine Combustor Designed With a New Fuel Supply Concept

This paper describes the performance of a dry low-NO_x gas turbine combustor designed with a new fuel supply concept. This concept uses automatic fuel distribution achieved by an interaction between the fuel jet and the airflow. At high loads, most of the fuel is supplied to the lean premixed combustion region for low-NO_x, while at low loads, it is supplied to the pilot combustion region for stable combustion. A numerical simulation was carried out to estimate the equivalence ratio in the fuel supply unit. Next, through the pressurized combustion experiments on the combustor with this fuel supply unit using natural gas as fuel, it was confirmed that NO_x emissions were reduced and stable combustion was achieved over a wide equivalence ratio range. [DOI: 10.1115/1.1473154]

Introduction

The reduction of NO_x emissions from stationary gas turbines is necessary to meet the increasingly stringent emissions standards imposed by regulatory agencies worldwide. Current practices involve the injection of water or steam and the use of selective catalytic reduction. These abatement methods have specific limitations and problems, including high installation and operating costs and the requirement of large installation space.

Lean premixed combustion is an effective way to reduce these emissions, and development programs of dry low-NO_x combustors using lean premixed combustion concepts are being actively conducted by several gas turbine manufacturers ([1]). However, the stable operating range becomes narrow when this method is applied without any supplementary control. Many techniques have been developed to solve this problem: parallel fuel staging ([2–5]), series fuel staging ([6]), and variable geometry systems, such as, inlet guide vane modulation ([7]), air bleed ([8]), and swirler inlet air control ([7,9]).

However, parallel or series fuel staging requires individual fuel supply devices for each group of burners, and variable geometry systems have problems in reliability and durability, since movable parts are needed in the high-pressure high-temperature gas stream. Furthermore, neither can respond smoothly to rapid load changes.

In order to solve these problems, a new fuel supply concept has been proposed. This concept uses automatic fuel distribution

achieved by an interaction between the fuel jet and the airflow. A schematic diagram of the new concept is shown in Fig. 1. A fuel supply unit is placed at the forward part of a combustor. This unit has an outer main region for lean premixed combustion and an inner pilot region for stable combustion. The air velocity in the main region is higher than in the pilot region. Fuel is supplied through only one line. A fuel passage hole (B) is located at the outer position of a fuel injection nozzle (A). There is a gap between these parts, and combustion air flows through this gap.

At high loads, the fuel jet has so much momentum that it penetrates the airflow through the gap. More fuel is supplied to the main region than to the pilot region and consequently the rate of lean premixed combustion increases. At low loads, the fuel jet has low momentum. More fuel is supplied to the pilot region than to the main region and consequently the combustion becomes stable.

As the fuel distribution ratio between the main and the pilot region changes automatically when the load of the gas turbine is changed, this combustion system offers good response for rapid load changes.

Design of Fuel Supply Unit by Numerical Simulation

Figure 2 shows a cross section of the prototype combustor and the test rig. This combustor is one of six can-annular-type combustors (4000 kW class). This combustor has a fuel supply unit, a liner (ID: 142.3 mm) and a transition piece.

The details of the fuel supply unit are shown in Fig. 3. The unit has an outer main region for lean premixed combustion and an inner pilot region for stable combustion. The air velocity in the main region is higher than in the pilot region.

A fuel passage hole (B: 2.6 mm dia.) is located at the outer position of the fuel injection nozzle (A: 1.6 mm dia.). There is a

Contributed by the International Gas Turbine Institute (IGTI) of THE AMERICAN SOCIETY OF MECHANICAL ENGINEERS for publication in the ASME JOURNAL OF ENGINEERING FOR GAS TURBINES AND POWER. Paper presented at the International Gas Turbine and Aeroengine Congress and Exhibition, New Orleans, LA, June 4–7, 2001; Paper 01-GT-050. Manuscript received by IGTI, December 2000, final revision, March 2001. Associate Editor: R. Natole.

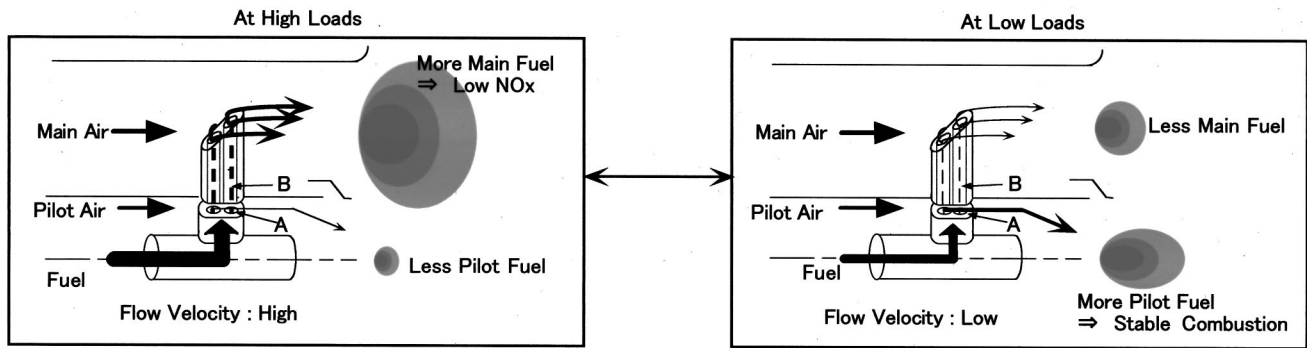


Fig. 1 New Fuel supply concept

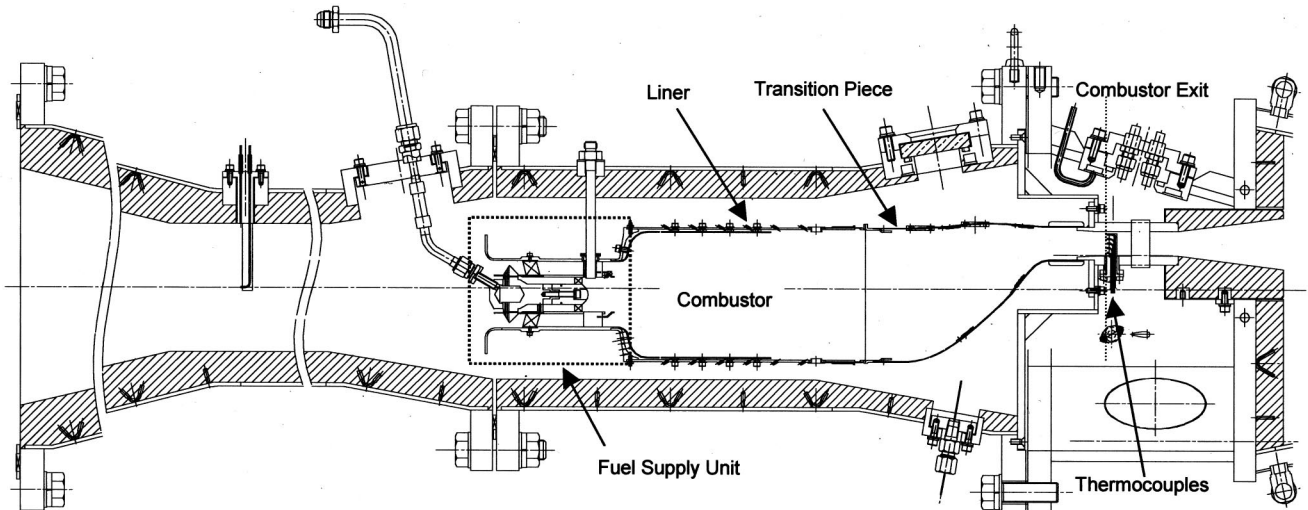


Fig. 2 Cross section of the prototype combustor and the test rig

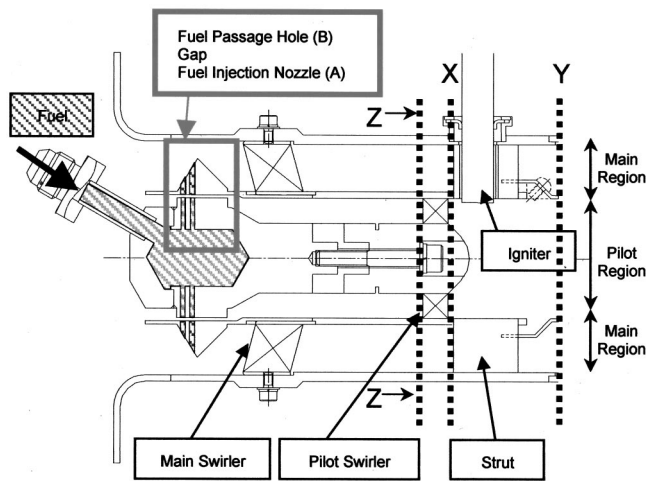


Fig. 3 Details of the fuel supply unit

gap (1.2 mm) between these parts, and the pilot air for combustion flows through this gap. Two sets of this device were positioned axially at each of eight locations arranged in a circle.

The temperature of the inlet air is 623 K and the combustor air velocity at the liner is 24 m/s.

First, in order to verify that more fuel is distributed to the main region at high loads and to the pilot region at low loads, the

equivalence ratio in the fuel supply unit shown in Fig. 3 was calculated by numerical simulation in a noncombusting state. The standard $k-\epsilon$ model was used to take account of turbulence. A multiblock grid system was adopted to make the mesh configuration sufficiently fine around the zone adjacent to the fuel jet, in order to precisely analyze the interaction between the free stream fluid and the fuel jets. All significant parts were three dimensionally modeled, including swirlers, which would be relative to the pressure resistance and fuel mixing, and important in prediction of the flow rates in the main and pilot region as well as the profile of the fuel concentrations.

The equivalence ratio patterns in the fuel supply unit and at the exit of the fuel supply unit (dotted line Y) were calculated at six different total equivalence ratios (ϕ_t), i.e., 0.05, 0.10, 0.15, 0.20, 0.25, and 0.30 (see Fig. 4). Figure 4 indicates that more fuel is distributed to the main region at high loads and to the pilot at low loads. Further at high load ($\phi_t=0.3$) the equivalence ratio pattern at the exit of the fuel supply unit is very uniform for the reduction of NO_x , and at low load ($\phi_t=0.2$) less fuel is distributed to the tip side in the main region for the improvement of combustion efficiency.

Figure 5 shows the dependence of the average equivalence ratio in the main region at the dotted line X (ϕ_m) on the total equivalence ratio (ϕ_t) by numerical simulation. In the equivalence range of 0.00 to 0.15, ϕ_m is estimated to be almost zero. Further, it is estimated that above 0.15, the higher ϕ_t becomes, the higher ϕ_m becomes linearly. These results support the new fuel supply concept shown in Fig. 1.

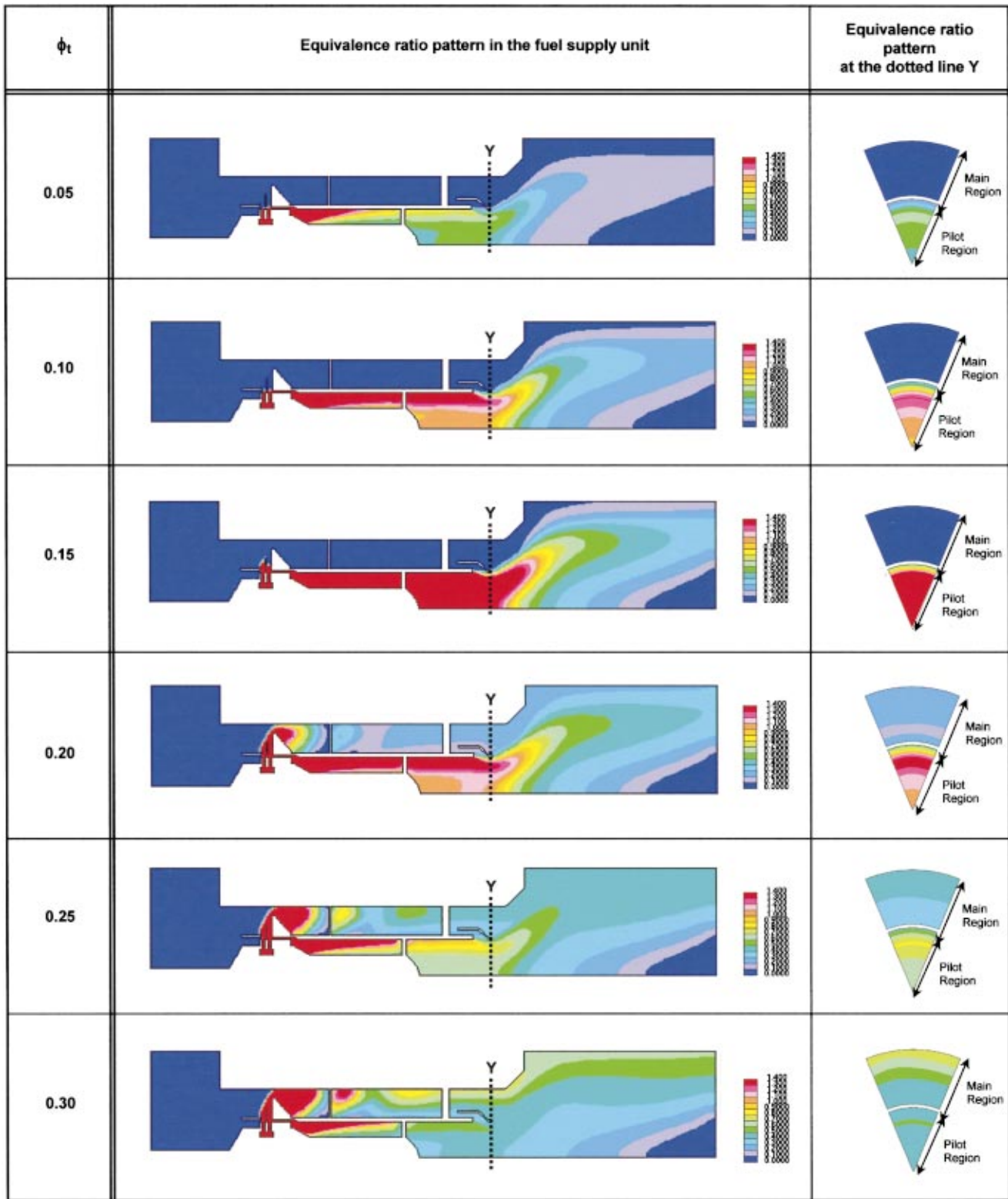


Fig. 4 Equivalence ratio pattern in the fuel supply unit by numerical simulation

Therefore, we decided to measure the pressurized combustion performance on the combustor with the fuel supply unit shown in Fig. 3.

Experimental Apparatus

The pressurized combustion test facility is shown in Fig. 6. The temperature of the inlet air was 623 K, and the combustor air

velocity at the liner was 24 m/s. Combustion tests were conducted at four different compressor discharge pressures (CDP), i.e., 0.15, 0.40, 0.60, and 0.80 MPa. Natural gas (methane: 88%, ethane: 6%, propane: 4% and butane: 2%) was used as fuel.

The NO_x , O_2 , CO , CO_2 , and THC concentrations were measured in the exhaust gas. A water-cooled sampling probe was mounted at a location about 1 m downstream from the combustor

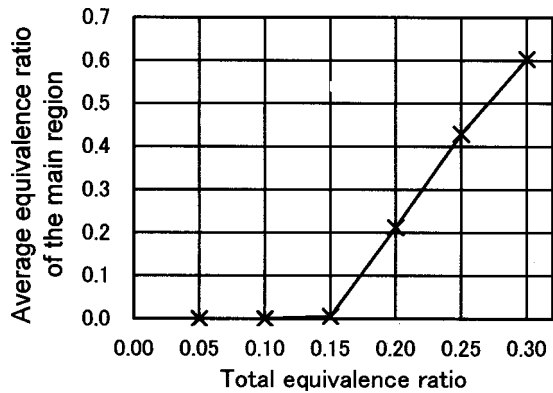


Fig. 5 Average equivalence ratio of the main region by numerical simulation

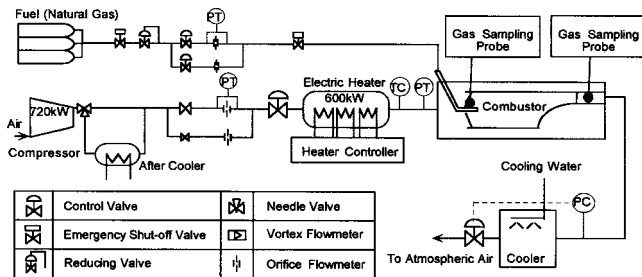


Fig. 6 Pressurized combustion test facility

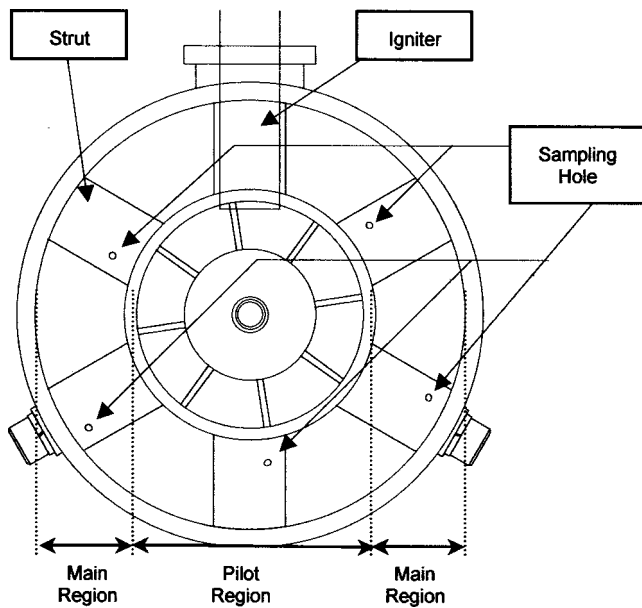


Fig. 7 Cross section (Z-Z) of fuel supply unit (see Fig. 3)

exit. This probe was designed to mix equal amounts of exhaust gas sampled from seven holes, each measuring 1.0 mm in diameter. The combustion efficiency and the total equivalence ratio (ϕ_t) were calculated from the measured exhaust gas compositions.

To evaluate experimentally whether the fuel distribution shown in Fig. 1 was actually achieved, THC and O_2 concentrations in the main mixture at the fuel supply unit were also measured. There were six structures, termed struts, in the main region (see Figs. 3 and 7). Sampling holes (1.3 mm dia.) were in five of the struts excluding the one that houses the igniter. The sampling holes were

dispersed in the tip side and hub side of the main region. Equal amounts of the sampling gas from five holes were mixed and sent to the gas analyzer. The main equivalence ratio (ϕ_m) was calculated from the measured gas compositions.

The average temperature of the exhaust gas at the combustor exit, called BOT, was measured by 50 thermocouples (R-type, inconel sheath, 1.6 mm dia., see Fig. 2).

Experimental Results and Discussion

First, it was confirmed that ignition was possible and stable combustion was achieved in all loads even with only one fuel line in this prototype combustor.

Figure 8 shows the relation between the average equivalence ratio in the main region (ϕ_m) and the total equivalence ratio (ϕ_t). The numerical prediction shows good agreement with the experimental results. The CDP difference does not affect this relation. In the equivalence ratio range of 0.00 to 0.15, ϕ_m is almost zero. Above 0.15, the higher ϕ_t becomes, the higher ϕ_m becomes linearly. The reason for this is as follows. The fuel jet in the equivalence ratio range of 0.00 to 0.15 does not have enough momentum to penetrate the gap. At the equivalence ratio of 0.15, the fuel jet is able to penetrate the gap and a part of the fuel starts being supplied to the main region. Above 0.15, the fuel jet has enough momentum to penetrate the gap, and the higher ϕ_t becomes, the more momentum the jet has.

Figure 9 shows the relation between NO_x emissions (at 0% O_2) and the total equivalence ratio (ϕ_t). The CDP difference affects this relation intensely. The higher the CDP becomes, the higher NO_x emissions become. Figure 10 shows the relation between

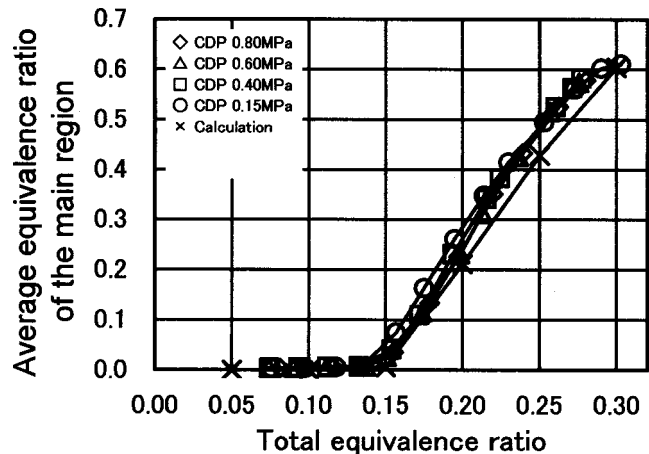


Fig. 8 Average equivalence ratio of the main region

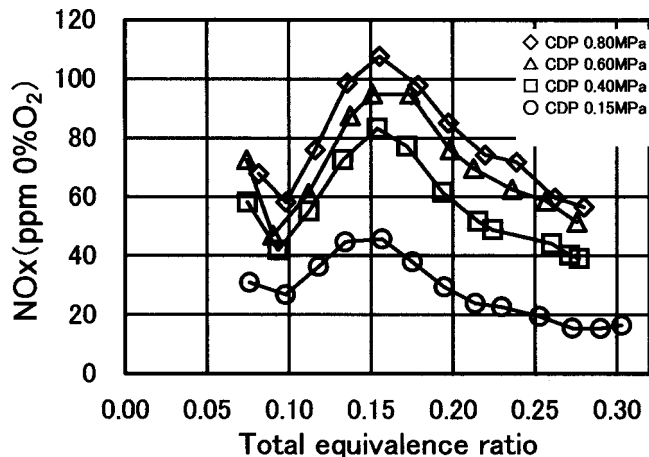


Fig. 9 NO_x emissions (at 0% O_2)

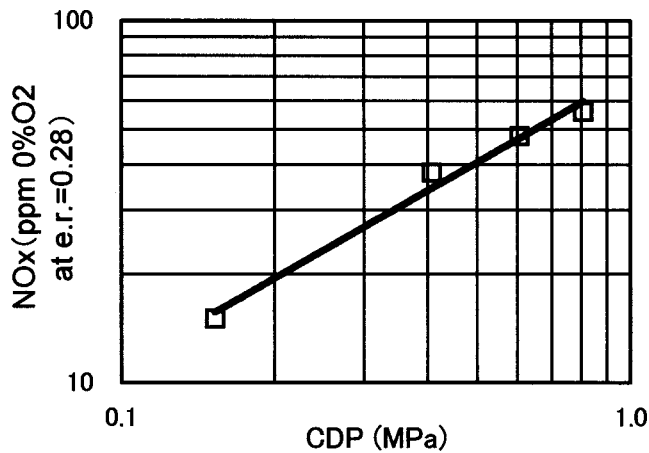


Fig. 10 Dependence of NO_x emissions on CDP

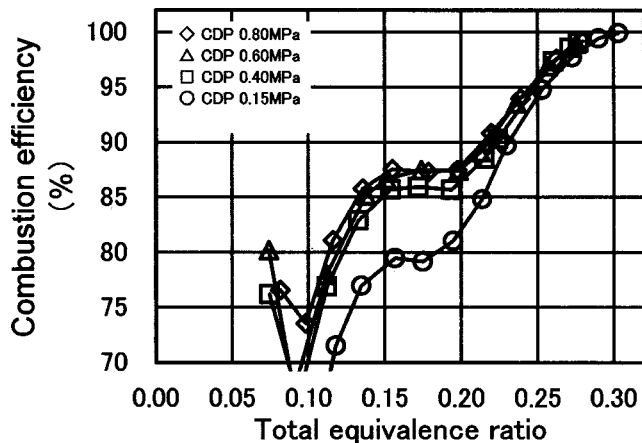


Fig. 11 Combustion efficiency

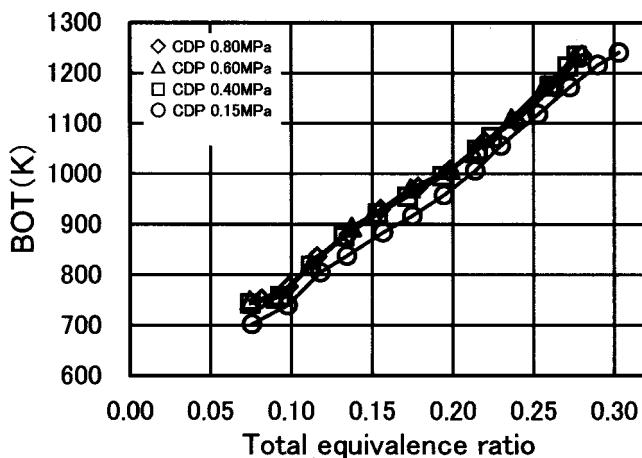


Fig. 12 Average temperature of exhaust gas at the exit of the combustor

NO_x emissions (at 0% O₂) and CDP at an equivalence ratio of about 0.28. NO_x emissions are proportional to the CDP to the power of about 0.81 in this prototype combustor.

NO_x emissions increase up to an equivalence ratio of 0.15 and decrease above 0.15. This behavior is the same under all CDP values. The reason for this performance is estimated as follows, using the results of the numerical simulation and the combustion experiment above (see Figs. 4 and 8). Under any CDP value, in

the equivalence ratio range of 0.00 to 0.15, ϕ_m is almost zero. But above 0.15, the higher ϕ_t becomes, the higher ϕ_m becomes linearly. Further, the uniform equivalence ratio pattern at the dotted line Y makes it possible to reduce NO_x emissions at high loads. It was confirmed that NO_x emissions (at 0% O₂) were below 60 ppm under the condition that CDP was 0.80 MPa and ϕ_t was about 0.28.

Figure 11 shows the relation between the combustion efficiency and the total equivalence ratio (ϕ_t). The CDP difference affects this relation moderately. At the same equivalence ratio, the higher the CDP becomes, the higher the combustion efficiency becomes. The tendency of the relation is the same under any CDP value. In the equivalence ratio range from 0.20 to 0.30, the lower the combustion efficiency becomes, the lower ϕ_t becomes. However, even if ϕ_t decreases in the equivalence ratio of 0.15 to 0.20, the combustion efficiency does not decrease. The reason for this is assumed to be that in this equivalence range, the fuel distribution ratio to the pilot increases intensely when ϕ_t decreases. Therefore stable combustion is achieved at low loads and the combustion efficiency does not decrease.

Figure 12 shows the relation between BOT and the total equivalence ratio (ϕ_t). The CDP difference affects this relation moderately. When CDP is 0.80 MPa and the equivalent ratio is 0.28, the BOT is about 1240 K.

Conclusion

In order to obtain low-NO_x characteristics over a wide operating range without any supplementary control, a new fuel supply concept was proposed in this paper. This concept uses automatic fuel distribution achieved by an interaction between the fuel jet and the airflow. At high loads, most of the fuel is supplied to the lean premixed combustion region to reduce NO_x emissions, while at low loads, it is supplied to the pilot combustion region to stabilize combustion.

First, the fuel distribution of a prototype combustor was calculated by numerical simulation, and it was confirmed that the results of the numerical simulation support the new fuel supply concept described above.

Next, through pressurized combustion experiments on the combustor with this fuel supply unit using natural gas as fuel, it was confirmed that NO_x emissions were reduced (under 60 ppm at 0% O₂ $\phi_t=0.28$) and stable combustion was achieved over a wide equivalence ratio range.

This simple structure makes it possible to reduce NO_x emissions without additional apparatus, helping to lower the cost of equipment and to improve the reliability and durability of combustors.

References

- [1] Solt, J. C., and Tuzson, J., 1993, "Status of Low NO_x Combustor Development," ASME Paper No. 93-GT-270.
- [2] Aigner, M., and Muller, G., 1993, "Second-Generation Low-Emission Combustors for ABB Gas Turbines: Field Measurements with GT11N-EV," ASME J. Eng. Gas Turbines Power, **115**, pp. 533–536.
- [3] Kitajima, J., Kimura, T., Sasaki, T., Okuto, A., Kajita, S., Ohga, S., and Ogata, M., "Development of a Second Generation Dry Low NO_x Combustor for 1.5MW Gas Turbine," ASME Paper No. 95-GT-255.
- [4] Ishii, J., 1999, "The Next Generation High-Efficiency Combined-Cycle Power Plants which used 1500C-class Steam Cooled Gas Turbine," Journal of the Gas Turbine Society of Japan, **27**(3), pp. 161–165.
- [5] Akita, E., and Nishida, M., 1999, "Development and Verificational Operation of 1500C Class Next Generation High Efficient G series Gas Turbine," Journal of the Gas Turbine Society of Japan, **27**(3), pp. 138–145.
- [6] Sato, H., Amano, T., Iiyama, Y., Mori, M., and Nakamura, T., 1999, "Development of a Three-Stage Low Emissions Combustor for Industrial Small-Size Gas Turbines," ASME Paper No. 99-GT-236.
- [7] Smith, K. O., 1992, "Engine Testing of a Prototype Low NO_x Gas Turbine Combustor," ASME Paper No. 92-GT-116.
- [8] Etheridge, C. J., 1994, "Mars SoLoNo_x-Lean Premix Combustion Technology in Production," ASME Paper No. 94-GT-255.
- [9] Smith, K. O., Holsapple, A. C., Mak, H. K., and Watkins, L., 1991, "Development of a Natural Gas Fired, Ultra-Low NO_x Can Combustor for 800 kW Gas Turbine Engines," ASME Paper No. 91-GT-303.

NO_x Formation in High-Pressure Jet-Stirred Reactors With Significance to Lean-Premixed Combustion Turbines

T. Rutar

Department of Mechanical Engineering,
Seattle University,
900 Broadway,
Seattle, WA 98122-4340

P. C. Malte

Department of Mechanical Engineering,
University of Washington,
Box 352600,
Seattle, WA 98195-2600

Measurements of NO_x and CO in methane-fired, lean-premixed, high-pressure jet-stirred reactors (HP-JSRs), independently obtained by two researchers, are well predicted assuming simple chemical reactor models and the GRI 3.0 chemical kinetic mechanism. The single-jet HP-JSR is well modeled for NO_x and CO assuming a single PSR for Damköhler number below 0.15. Under these conditions, the estimates of flame thickness indicate the flame zone, that is, the region of rapid oxidation and large concentrations of free radicals, fully fills the HP-JSR. For Damköhler number above 0.15, that is, for longer residence times, the NO_x and CO are well modeled assuming two perfectly stirred reactors (PSRs) in series, representing a small flame zone followed by a large post-flame zone. The multi-jet HP-JSR is well modeled assuming a large PSR (over 88% of the reactor volume) followed by a short PFR, which accounts for the exit region of the HP-JSR and the short section of exhaust prior to the sampling point. The Damköhler number is estimated between 0.01 and 0.03. Our modeling shows the NO_x formation pathway contributions. Although all pathways, including Zeldovich (under the influence of super-equilibrium O-atom), nitrous oxide, Fenimore prompt, and NNH, contribute to the total NO_x predicted, of special note are the following findings: (1) NO_x formed by the nitrous oxide pathway is significant throughout the conditions studied; and (2) NO_x formed by the Fenimore prompt pathway is significant when the fuel-air equivalence ratio is greater than about 0.7 (as might occur in a piloted lean-premixed combustor) or when the residence time of the flame zone is very short. The latter effect is a consequence of the short lifetime of the CH radical in flames. [DOI: 10.1115/1.1492829]

Introduction

Fundamental research on NO_x formation from methane-fired, lean-premixed combustion in high-pressure jet-stirred reactors (HP-JSRs) has developed through stages. First, the work of Nicol et al. [1] showed the significance of the nitrous oxide pathway to NO_x formation in high-pressure combustion reactors operating at temperatures up to about 1800 K. Then Steele [2] built and operated a HP-JSR for residence times of 2.0 and 4.0 ms, pressures up to 7.1 atm, and combustion temperatures up to about 1900 K. Steele et al. [3] reported a weak decrease in NO_x for the pressure increase from 1.0 to 7.1 atm, and an activation temperature of about 24,000 K for the NO_x increase with combustion temperature. In fact, the NO_x data obtained in Steele's HP-JSR resemble in magnitude and in trends for pressure and temperature, the data obtained in the porous-plate combustor of Leonard and Stegmaier [4] and the gas turbine type combustor of Joshi et al. [5].

The investigation of the effect of pressure (1 to 20 bar) on NO_x in a HP-JSR operated at a fuel-air equivalence ratio of 0.55, at short residence times (1.0 to 2.0 ms), and at combustion temperatures around 1800 K, is contained in [6,7]. The work shows NO_x decreases with pressure, and that the decrease is more pronounced at pressures up to 5 bar than for pressures above 5 bar. Furthermore, the effect of pressure is most pronounced for the 2.0 ms data, for which the NO_x varies between about 8.5 ppmv, wet, at 1.0 bar, to about 5 ppmv, wet, at 5 bar. However, for the same pressure range, and for 1.0 ms residence time, the NO_x decreases

only from about 5.4 ppmv, wet, to about 4.5 ppmv, wet. The multi-jet reactor of Bengtsson [6] was sampled for species and temperature in the exhaust section attached to the reactor, close to the reactor outlet. The volume of the exit tubes up to the sampling point is approximately equal to 16% of the reactor volume. The data in [6,7] was modeled as two PSRs followed by a PFR, with the PFR representing the exit tubes.

Studies of NO_x formation in a single-jet HP-JSR are contained in [8,9]. In Rutar et al. [9], the focus is on interpreting the NO_x measurements in terms of the flame structure. It is determined how well the turbulent flame zone, that is, the zone of rapid oxidation and large concentrations of free radicals, fills the HP-JSR.

The HP-JSR of Rutar [8] was operated for residence times between 0.5 and 4.0 ms, for unheated and preheated reactants, and for pressures of 3.0, 4.7, and 6.5 atm. The temperature of the reactor gas, as measured by a thermocouple (type R, coated) placed in the recirculation zone of the reactor, was held constant at 1800 K by making adjustments to the fuel-air ratio. Calculation of the corrected temperature is conducted by two methods (Rutar et al. [10]). The primary method is based on the heat balance for the thermocouple, and the confirming method is based on the wall heat loss of the HP-JSR. These methods indicate a corrected temperature of 1825 ± 10 K for runs at short residence times (<2 ms). For the largest residence times (of up to 4 ms), the corrected temperature increases to about 1880 K for pressures of 4.7 and 6.5 atm, and to about 1940 K for 3 atm. Probe measurements of species were obtained in the recirculation zone, which represents the bulk of the reactor and exhibits nearly uniform composition and temperature under most running conditions.

The measurements show a small decrease in NO_x with increasing pressure (pronounced only above 1.5 ms), and lower NO_x when the inlet is preheated (pronounced only below 1.5 ms). With

Contributed by the International Gas Turbine Institute (IGTI) of THE AMERICAN SOCIETY OF MECHANICAL ENGINEERS for publication in the ASME JOURNAL OF ENGINEERING FOR GAS TURBINES AND POWER. Paper presented at the International Gas Turbine and Aeroengine Congress and Exhibition, New Orleans, LA, June 4–7, 2001; Paper 01-GT-067. Manuscript received by IGTI, December 2000, final revision, March 2001. Associate Editor: R. Natole.

respect to residence time, the behavior of the NO_x is complex. Under several running conditions, minimum NO_x is obtained when the residence time is about 2.0 ms.

In references [8,9], size estimates are made of the turbulent flame zone. When the residence time is short, and thus, the velocities in the reactor are high, estimates of the turbulent flame thickness indicate the turbulent flame zone fully fills the HP-JSR. Under this condition, the NO_x and CO are well modeled assuming the full reactor to be a single perfectly stirred reactor (PSR). Typically, a critical residence time of $\tau \approx 1.5$ ms satisfies this condition, though as pressure decreases and inlet temperature increases, the critical residence time decreases. For long residence times, and thus, for relatively low velocities in the reactor, the turbulent flame zone is reduced in size. The flame zone now is situated around the centered jet of the reactor, and is surrounded by the recirculation zone of the reactor acting as a post-flame zone. Over the eightfold increase in the residence time of the reactor, estimates indicate about a tenfold decrease in the volume of the turbulent flame zone. Thus, for the largest residence times, the flame zone is a relatively small part of the reactor volume. Outside of the single PSR regime, that is, typically for $\tau > 1.5$ ms, the HP-JSR is modeled as two PSRs in series (PSR-PSR). Generally good agreement of the modeled NO_x and CO to the experimental values is obtained by using a small initial PSR, representing the flame zone, followed by a large concluding PSR, representing the recirculating post-flame zone. The residence time split between the two PSRs is set by optimizing the agreement between the measured and modeled NO_x and CO. The volumes of the two PSRs obtained by this procedure are similar to the volumes of the flame zone and post-flame zone independently determined by the turbulent flame thickness estimates.

The present paper goes beyond the papers of Bengtsson et al. [7] and Rutar et al. [9]. It models the data of Bengtsson [6] and Rutar [8] for the pathways responsible for the NO_x formation. It shows the NO_x and CO data of the HP-JSRs are well modeled with the simple PSR, PSR-PSR, and PSR-PFR chemical reactor configurations and the GRI 3.0 chemical kinetic mechanism (Smith et al. [11]).

The authors believe the measurements of Bengtsson et al. [7] and Rutar et al. [9] represent important databases for the fundamental study of methane-air combustion at conditions of lean-premixed combustion turbines. The particular value is in testing of chemical kinetic mechanisms, in development of global mechanisms (underway), in determining contributions of each of the NO_x formation pathways, and, consequently, in finding optimal operating conditions for lean-premixed combustors. The short residence times of less than 2 ms are used to drive the reactors to the well-stirred condition, which permits full chemical kinetic mechanisms to be applied to the datasets via PSR modeling. The longer residence times of 2 to 4 ms are useful, since they simulate the flame zone residence times of lean-premixed gas turbine combustors.

Modeling and Discussion of Experimental Data

The Damköhler number, $Da = \text{turbulent mixing time}/\text{chemical time}$, and the turbulence Reynolds number, $Re = u'd_o/\nu$, are estimated for the flames of the work of Bengtsson [6] and Rutar [8]. The estimates of Da and Re are made based on the paper by Abraham et al. [12]. The mixing time is calculated as d_o/u' , where d_o is the jet nozzle diameter, which is assumed to be the turbulent integral scale, and u' is the turbulent intensity, which is assumed to be 10% of the inlet jet velocity (u_o). The kinematic viscosity (ν) is determined for the inlet temperature and reactor pressure.

Figure 1, redrawn from Abraham et al. [12], is used to identify regimes of turbulent combustion. The limiting experimental conditions are shown for the two data sets. Operation of the HP-JSR of Rutar [8] is shown for the minimum and maximum residence times and for the minimum and maximum pressures, both for

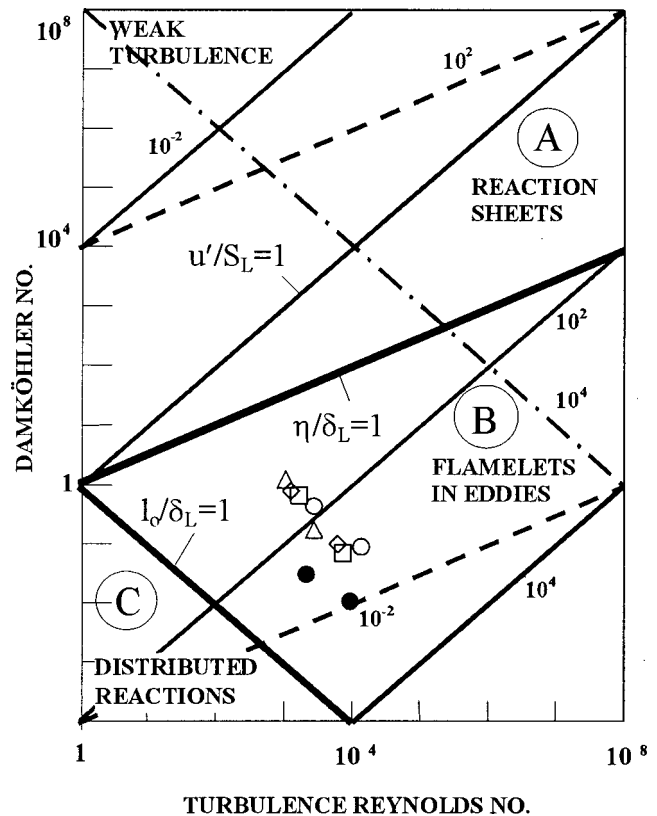


Fig. 1 Parameters characterizing turbulent premixed combustion (Abraham et al. [12]). Operation of the HP-JSR of Rutar [8] at the minimum and maximum residence times are identified for the conditions: 6.5 atm (open circles), 3.0 atm (diamonds), 6.5 atm at 573 K inlet temperature (squares), and 3.0 atm at 573 K inlet temperature (triangles). Operation of the HP-JSR of Bengtsson [6] is for pressures between 5 and 20 bar (black circles).

unheated and preheated inlets. Operation of the HP-JSR of Bengtsson [6] is shown for the pressure range between 5 and 20 bar. As shown in Fig. 1, both reactors operated at very low Damköhler numbers and very high turbulent intensities, hence in the flamelets-in-eddies regime (Turns [13]). Kobayashi et al. [14] have visualized flamelets in eddies by instantaneous Schlieren photography and laser tomography. They explain that the flames wrinkle significantly, and, consequently, parcels of unburned gas are engulfed into the flame. In their experimental work, the Damköhler number was above 1.0 and the turbulent Reynolds number was below 3000. Because of the low Da and high Re , the flames in the present work are assumed to contain a significant number of parcels of unburned gas. These parcels, embedded into the thick flame, are strained by the flow while the reaction front moves into their periphery. It should be mentioned that the division between regimes of turbulent combustion is rather arbitrary, and that flames in the present work could be considered to be in the distributed reaction regime. This is based on Bray [15] and Chomiak [16], who call the regime of $Da < 1$ the distributed reaction regime. Regardless of the name for the regime, and keeping the physical picture in mind, the present flames can certainly be labeled as highly stirred with comparably slow chemistry.

For the cases for which the HP-JSR of Rutar [8] is operated in the regime of the single-PSR modeling ($\tau \leq 1.5$ ms), the Damköhler number is 0.06 to 0.15. For the HP-JSR of Bengtsson [6], our estimate indicates the Damköhler number is between 0.01 and 0.03. Under these conditions, the turbulent flame zone fills the reactors. Utilizing a PSR to model the flame is reasonable for thick turbulent flames with low Damköhler numbers. Mixing of

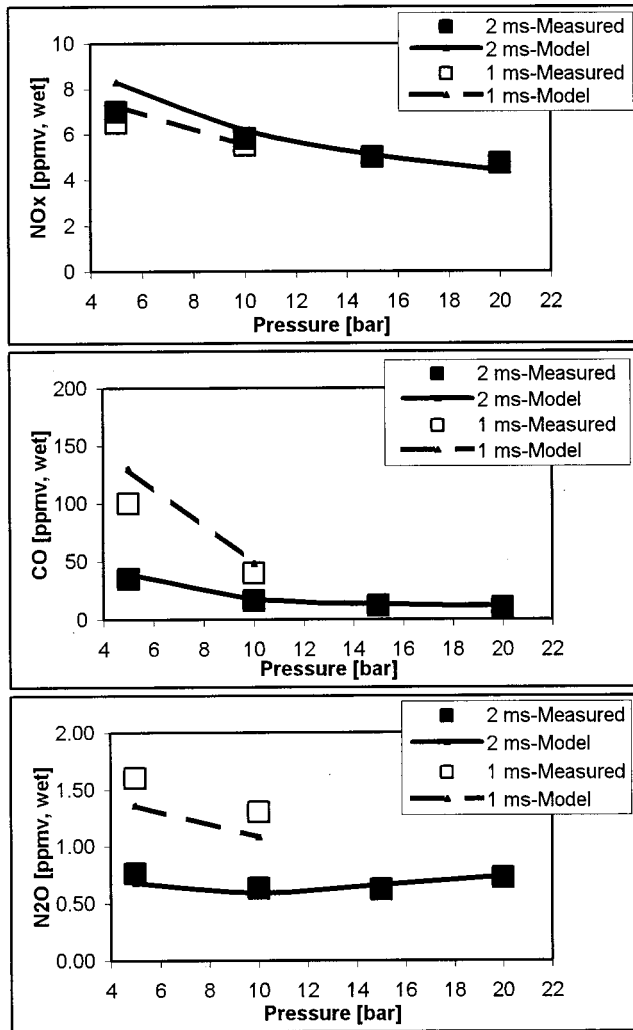


Fig. 2 NO_x, CO, and N₂O data of Bengtsson [6] compared to the results obtained using chemical reactor model PSR-PFR, where $V_{PSR}/V_{reactor}=88\%$. Fuel-air equivalence ratio is 0.55. Reactor temperature is 1828 K.

reactants and products in the turbulent flame is improved compared to molecular diffusion, which is the only mechanism for mixing within thin laminar or wrinkled laminar flames. Flames are thicker than the smallest turbulent eddies, that is, the Kolmogorov scale eddies roll within the flames, thus enhancing the mixing. The high mixing intensity at low Da establishes that the flame zone is reasonably well represented by the perfectly stirred reactor model. Such results provide support for modeling the HP-JSR as a single PSR.

Figure 2 shows the comparison between the modeled and measured NO_x, CO, and N₂O of Bengtsson [6]. The premixed and preheated methane and air enter the 19 cm³ HP-JSR through twenty nozzles, each with a diameter of $d_o=0.6$ mm. The jets penetrate at 12-deg radial angle designed to create a highly swirling flow in the reactor. The chemical reactor configuration in the model is determined by matching both NO_x and CO—a process described in [8,9]. The model consists of a PSR (with a volume of 88% of the HP-JSR volume) followed by a PFR (with a volume of the remaining 12% of the HP-JSR plus an additional 16% for the exit tubes). The existence of a PFR is an indicator that the HP-JSR may not be completely filled by the flame zone and that regions closest to the exit may not be as well stirred as the bulk of the reactor.

The PSR-PFR reactor configuration is different from the 30%

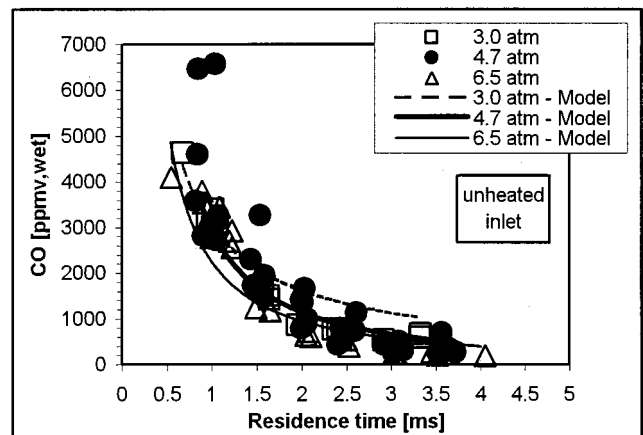
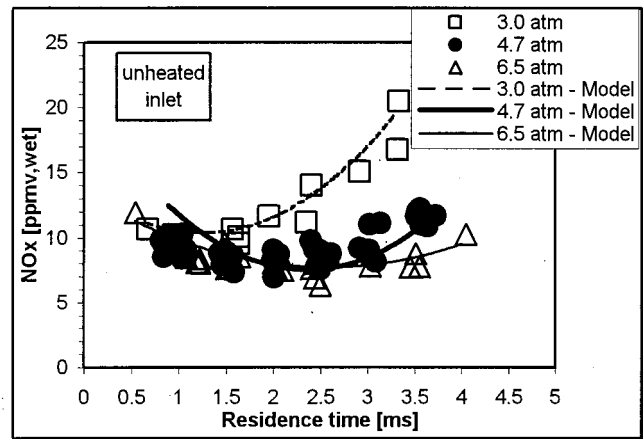


Fig. 3 NO_x and CO data of Rutar [8] compared to the results obtained using chemical reactor models PSR (at short residence times) and PSR-PSR (at long residence times). Inlet air and methane are not preheated.

first-PSR / 60% second-PSR / 10% PFR configuration used in Bengtsson [6] and Bengtsson et al. [7]. The 30%/60%/10% configuration was chosen to match the measured blowout conditions with a chemical kinetic mechanism available prior to the release of GRI 3.0. (It should be noted the GRI 3.0 mechanism is still unable to predict the reactor blowout conditions.)

Figures 3 and 4 show the comparison between the model and the NO_x and CO measurements of Rutar [8]. The premixed methane and air enter the 1.5-cm³ HP-JSR through a nozzle with a diameter of $d_o=1.4$ mm, which is positioned on the axis of symmetry for the reactor. The jet penetrates the recirculating flow in the reactor, hits the top of the reactor, and back-mixes to create that recirculation. The short residence time data were modeled as a single PSR, whereas the long residence time data were modeled as two PSRs in series. The transition occurs always for $Da=0.15$, irrespective of the reactor pressure or inlet temperature. At $Da=0.15$, the height to which the inlet reactants reach, estimated as $h=5d_o u'/S_T$ in [8,9], where S_T is the turbulent burning velocity, is equal to the height of the reactor. Any increase in the flow rate results in reactant back-mixing, and, coupled with the increasing flame thickness, leads to filling of the reactor with flame. The relation between Da and the turbulent flame thickness and flame volume is given in [8,9]. As mentioned earlier, the first PSR (PSR1) represents the flame zone. The recirculating post-flame zone is also modeled with a PSR (PSR2). For the recirculating post-flame zone, the characteristic turbulent mixing time is longer than in the flame zone, because the characteristic length scale is

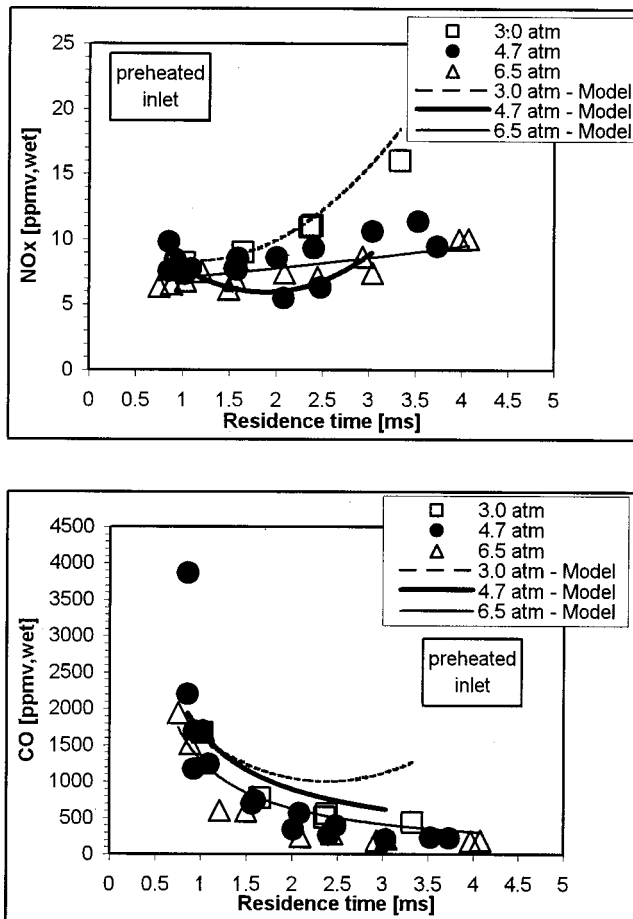


Fig. 4 NO_x and CO data of Rutar [8] compared to the results obtained using chemical reactor models PSR (at short residence times) and PSR-PSR (at long residence times). Inlet air and methane are preheated to 573 K.

the overall reactor dimension and not the inlet jet diameter. The chemical time is also longer than in the flame zone, since the rate of chemistry slows in the post-flame zone. Therefore, the Damköhler number remains relatively low and the recirculating post-flame zone is reasonably well represented by the perfectly stirred reactor model. Since conversion in PSR2 is highly dependent on the gas temperature, PSR2 is run at the corrected measured temperature. Adiabatic conditions are assumed for PSR1 because the chemical energy release rate in the flame zone is sufficiently high that any heat transfer is negligible. The volume (or residence time) of PSR1 is an adjustable parameter—as indicated above, this is determined by optimizing the agreement between the modeled and measured NO_x and CO values.

The main trends in the experimental data of Rutar [8] are summarized in the following paragraphs.

Residence Time. As stated above and also noted in Figs. 3 and 4, the variation of NO_x with residence time is complex. There are several reasons for this. Over the eightfold increase in the residence time of the experiment, more time is available for NO_x to form. However, more time is also available for the super-equilibrium concentrations of the O-atom and CH-radical to decay, thereby decreasing the rate of NO_x formation. Further, as the residence time increases, the fraction of the reactor filled with the highly reactive flame zone decreases. Additionally, because of the manner in which the experiment was conducted, the combustion temperature, as expressed by the corrected measured temperature of the recirculation zone, increases from a nearly constant value of 1825 K for $\tau < 2$ ms to 1880 K for the longest residence times

(1940 K in the case of the 3 atm experiments). For runs at constant pressure and inlet temperature, the fuel-air ratio was adjusted upward at both the short and long residence time limits. Minimum fuel-air ratio was set at the intermediate residence times. Enrichment at the short residence times overcame the trapping of chemical energy by the unburned CO, and enrichment at the long residence times overcame reactor heat transfer losses.

The NO_x data in Fig. 3, for the unheated inlet, show minimum NO_x at a residence time of about 2 ms. With decreasing residence time the NO_x increases, an effect most likely associated with an increase in the free radical concentrations at the short residence times. The CH-radical appears to be important to this regard. Modeling indicates [CH] grows significantly as the residence time decreases. (This is shown later in the paper.) Thus, an increase in prompt NO_x could be responsible for a significant part of the increase in NO_x with decreasing residence time for the NO_x data of Fig. 3. Interestingly, the NO_x data of Fig. 4 show little increase in NO_x with decreasing residence time. However, these runs are made with a preheated inlet, and thus, are leaner than the data of Fig. 3 and consequently contain a lesser fraction of prompt NO_x in the total NO_x.

For residence times greater than about 2 ms, the NO_x data in Fig. 3 show an increase in NO_x with increasing residence time. This increase is also noted in the NO_x data of Fig. 4. The increase is mainly associated with the increase in the temperature of the experiment with increasing residence time. A weaker contributing factor is the greater residence time available for NO_x to form. This is noted in Rutar [8] through adjustment of all of the NO_x data to 1820 K constant temperature (which is the approximate temperature of the short residence time runs), using the NO_x activation temperature of Steele et al. [3]. The adjustment leads to a reduction of NO_x for the intermediate and long residence times compared to the results in Figs. 3 and 4. Nevertheless, a mild increase in NO_x with residence time remains in the adjusted data for $\tau > 2.5$ ms.

Pressure. NO_x shows a mild decrease with increasing pressure for the intermediate and long residence times. This can be noted in Figs. 3 and 4 by comparing the 4.7 and 6.5 atm data. For given residence time, the combustion temperature is essentially identical for the two pressures—thus, the decrease in the NO_x is indeed caused by the increasing pressure.

Inlet Temperature. The effect of inlet temperature (and thus, equivalence ratio for given combustion temperature) is weak at the long residence times (above 2 ms). However, as noted above in the discussion of the effect of residence time on NO_x, comparison of Figs. 3 and 4 indicates a decrease in NO_x with increasing inlet temperature for the short residence times runs (of less than 2 ms).

Carbon Monoxide. CO markedly decreases with residence time, falling from values as large as 6700 ppmv at short residence times to as low as 100 ppmv at the long residence times. This behavior is consistent with the significant change in the combustion structure within the reactor over the eightfold change in residence time.

Exit Emissions. Although the present sampling measurements were conducted within the recirculation zone of the reactor, they represent exit emissions, since the recirculation zone is nearly uniform (especially in NO_x) and the gases exit the reactor from the recirculation zone.

Also plotted in Figs. 3 and 4 are the curves obtained from the modeling. The modeling is conducted with either the PSR or PSR-PSR configuration, depending on the residence time, and is based on the experimental fuel-air ratio and the corrected measured temperature (except for the assumption of adiabaticity for PSR1 in the PSR-PSR model). The modeling shows good agreement to the measurements, except for a few situations. One such situation is the peak CO concentrations, seen in both Figs. 3 and 4 for the 4.7

atm runs at the short residence times. These CO concentrations are underpredicted by the PSR model. Another situation is noted in Fig. 4 for the 3.0 atm runs at intermediate and long residence times, where the CO is overpredicted by the model. Although not done in the present modeling, the addition of a small PFR zone to the PSR-PSR model reduces the CO to the experimental levels. A final situation is noted in the NO_x predictions for 4.7 atm, which show more curvature with respect to residence time than seen in the measurements.

Discussion on NO_x Formation Pathways

The simple reactor configurations, particularly the single-PSR and PSR-PFR configurations, are useful for assessing the importance of the several chemical pathways that can form NO_x. The four NO_x formation pathways under lean premixed combustion of methane in air are the Zeldovich, nitrous oxide, Fenimore prompt, and NNH pathways. The exact algorithm for assessing the contribution of each pathway is described below.

Each NO_x formation pathway exchanges species that form NO_x with two or more other pathways. For example, N-atom, which oxidizes into NO primarily through the second and third Zeldovich reactions, i.e., $N + O_2 \rightarrow NO + O$ and $N + OH \rightarrow NO + H$, is formed via the first Zeldovich reaction ($N_2 + O \rightarrow N + NO$), the prompt reaction ($N_2 + CH \rightarrow HCN + N$), as well as through a series of reactions involving short-lived species such as NH and CN. However, the maximum contribution of each pathway is easily estimated. The present work uses estimates based on the discussion by Nicol et al. [17]. This is summarized in the following paragraphs.

The Zeldovich contribution to the total NO_x can be easily determined by considering the first (or initiating) Zeldovich reaction, $N_2 + O \rightarrow N + NO$. Two NO molecules are formed from this reaction, one directly and the other from the oxidation of the N-atom. Thus, the rate of Zeldovich NO formation is $(dNO/dt)_{ZELD} = 2k_{N_2+O} [O] [N_2]$, where k_{N_2+O} is the rate constant of the first Zeldovich reaction and [O] and [N₂] are the concentrations predicted by the integration of the GRI 3.0 mechanism in either the PSR, PSR-PSR, or PSR-PFR configuration.

Some of the collisions between N₂ and O result in the third-body-stabilized reaction to N₂O nitrous oxide. The overall reaction is $N_2 + O + M \rightarrow N_2O + M$. Some of the nitrous oxide formed by this reaction is attacked by O-atom, and thus, converted to two NO molecules by the reaction, $N_2O + O \rightarrow 2NO$. Other N₂O molecules are attacked by H-atom, leading to a molecule of NO and a molecule of NH. The reaction is $N_2O + H \rightarrow NO + NH$. Under lean-premixed combustion, the NH oxidizes to NO. Thus, two NO molecules are formed by the reaction $N_2O + H \rightarrow NO + NH$. The total rate of NO formation from N₂O may thus be expressed as $(dNO/dt)_{N_2O} = 2k_{N_2O+O} [O] [N_2O] + 2k_{N_2O+H} [H] [N_2O]$, where k_{N_2O+O} and k_{N_2O+H} are the respective rate constants, and [O], [H], and [N₂O] are predicted by the integration of the GRI 3.0 mechanism.

Within flame zones, N₂ is also attacked by CH. The reaction given in GRI 3.0 for this "prompt" NO is $N_2 + CH \rightarrow HCN + N$. Under lean-premixed combustion the HCN and N-atom are oxidized to NO. Thus, the reaction yields two NO molecules, and the rate of NO formation is $(dNO/dt)_{PROMPT} = 2k_{N_2+CH} [CH] [N_2]$. The term k_{N_2+CH} is the rate constant for the prompt NO reaction and the concentrations [CH] and [N₂] are predicted by the integration of the GRI 3.0 mechanism.

The final NO_x pathway in GRI 3.0 arises from the NNH radical. This radical forms by the reaction of N₂ with H-atom. Once formed, the NNH can be oxidized by the reaction $NNH + O \rightarrow NO + NH$. Since under lean-premixed combustion, NH is oxidized to NO, the NNH reaction yields two NO molecules. The resultant rate of formation is $(dNO/dt)_{NNH} = 2k_{NNH+O} [O] [NNH]$, where k_{NNH+O} is the rate constant and [NNH] and [O] are predicted by the integration of the GRI 3.0 mechanism.

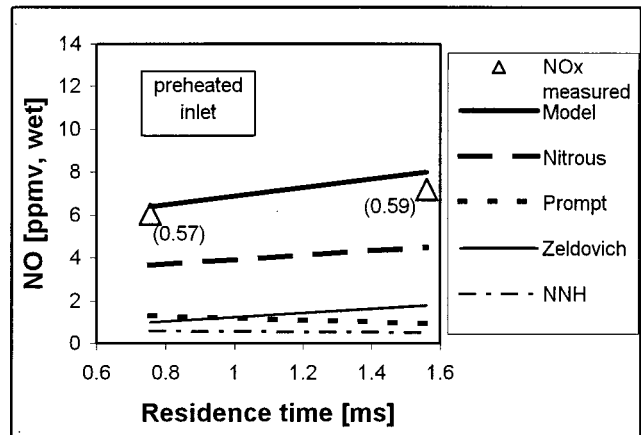
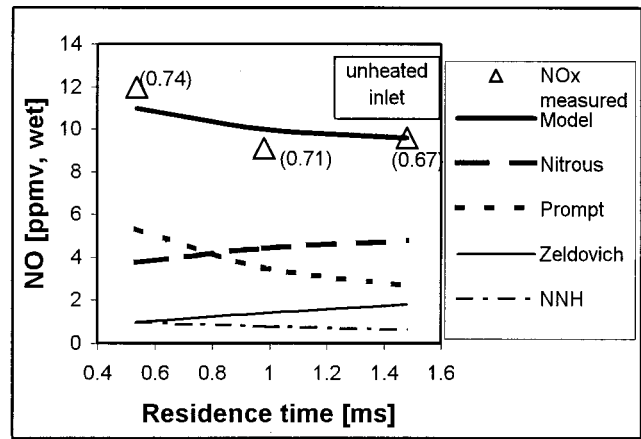


Fig. 5 Amount of NO formed by each of the four pathways in a single-PSR at 6.5 atm with and without preheat. Also shown is the NO from the PSR output (model) and the measured NO_x (data of Rutar [8]).

Summation of the NO separately calculated by the four rate equations just derived equals the NO predicted by the full GRI 3.0 mechanism within $\pm 5\%$. Because of the small concentrations of NO in lean-premixed combustion, reverse reaction of the NO-forming reactions is not a significant factor in accounting for the difference. However, reduction of NO by hydrocarbon attack, leading to cyano species such as HCN and HCNO, can occur in lean-premixed combustion. These molecules quickly form and then are reconverted to NO. This can lead to a slight distortion in the sum of the NO predicted by the separated pathways, yielding slightly less NO at short residence times, and slightly greater NO at long residence times.

Nitrogen dioxide (NO₂) is not a factor in the modeling, since only negligible amounts of NO are oxidized to NO₂ by the application of the GRI 3.0 mechanism. The experimental sampling is conducted for the sum of NO and NO₂, that is, for NO_x, since some NO can be oxidized to NO₂ in the sample probe and line. Thus, in this work, NO predicted can be directly compared to NO_x measured.

The NO computed using the separated rate equations for each pathway and multiplied by the residence time in the PSR is plotted in Figs. 5–7. The figures also contain the experimental data and the full mechanism predictions. Figure 5 compares the contribution of each pathway for the Rutar [8] data for unheated and preheated inlets at 6.5 atm for short residence times, i.e., for cases modeled with a single PSR. Fuel-air equivalence ratios for each data point are shown in parentheses. When the inlet is not pre-

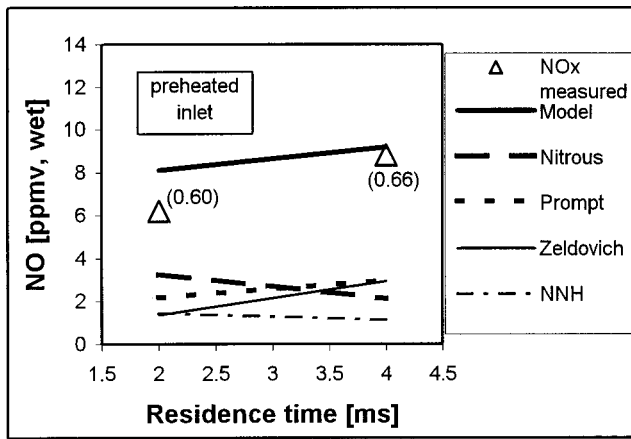


Fig. 6 Amount of NO formed by each of the four pathways in two-PSR model at 6.5 atm with preheat. Also shown are the NO from the PSR2 output (model) and the measured NO_x (data of Rutar [8]).

heated (upper graph), both the nitrous oxide and the prompt pathways dominate the NO formation. Prompt contributes as much as 5.3 ppmv, wet, at 0.5 ms reactor residence time (i.e., 48% of the total NO), but then decreases to approximately 2.7 ppmv, wet, at 1.5 ms. The trend is opposite for the contribution of the nitrous oxide pathway to NO. At 0.5 ms, it contributes 3.8 ppmv, wet, but

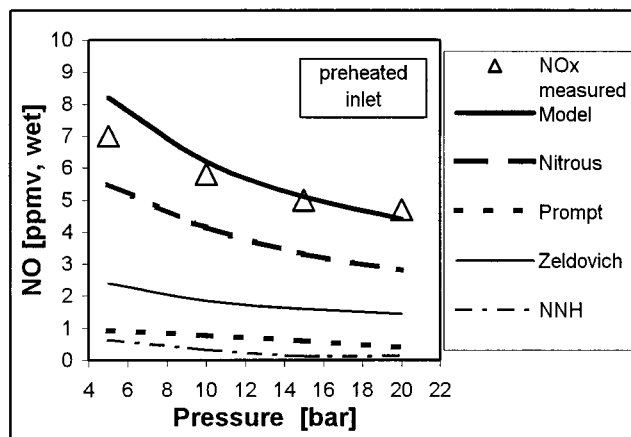
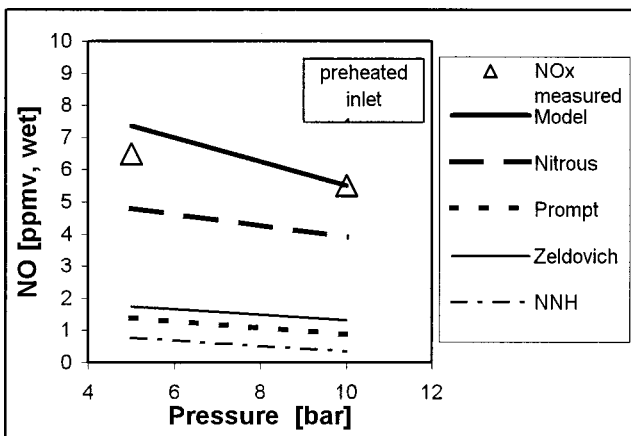


Fig. 7 Amount of NO formed by each of the four pathways in a PSR-PFR at 1 and 2 ms with preheat. Also shown is the NO from the PFR output (model) and the measured NO_x (data of Bengtsson [6]).

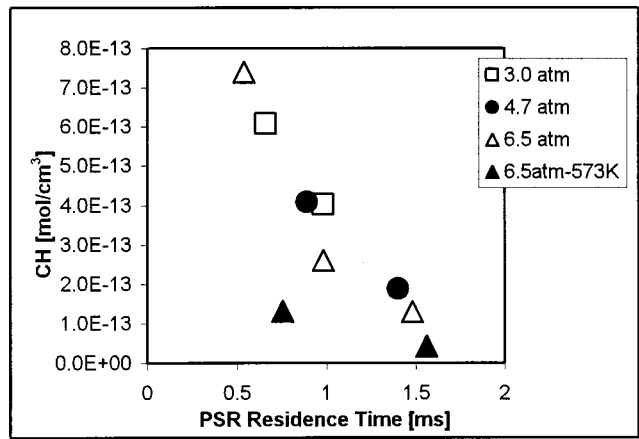


Fig. 8 Concentration of CH radical versus reactor residence time for single-PSR cases

at 1.5 ms, it contributes 4.8 ppmv, wet. The decrease in the prompt NO is explained by the decrease in the CH-radical concentration, [CH], with residence time. The CH-radical has a short lifetime in flame zones, so the only way to capture its existence in a PSR is if the PSR residence time is short. Figure 8 depicts [CH] versus PSR residence time for the single-PSR cases. It shows the [CH] decreases an order of magnitude over 0.5 to 1.5 ms. Also noted is the decrease in [CH] as the inlet temperature is increased, and thus, the reactor is operated leaner.

The NO formed by the nitrous oxide and Zeldovich pathways increases with residence time. The nitrous oxide NO and Zeldovich NO increase with residence time because the time available to form NO increases and overcomes decreases in [O] and [H]. Temperature is nearly constant (at about 1825 K) at these short residence times. The decrease of O-atom with residence time is plotted in Fig. 9 for the single-PSR cases. It is apparent the decrease in O-atom with residence time is weaker than the decrease in [CH], shown in Fig. 8. The O-atom also decreases with pressure, but the inlet temperature does not influence it.

For the preheated inlet cases at short residence times, shown in the bottom graph of Fig. 5, the nitrous oxide pathway is the predominant NO pathway, yielding 56–58% of the total NO. The prompt NO contribution is similar to the contributions of the Zeldovich and the NNH pathways. The decrease in NO obtained by preheating the inlet air is consistent with a diminished influence of the prompt pathway. The concentration of the CH-radical is sig-

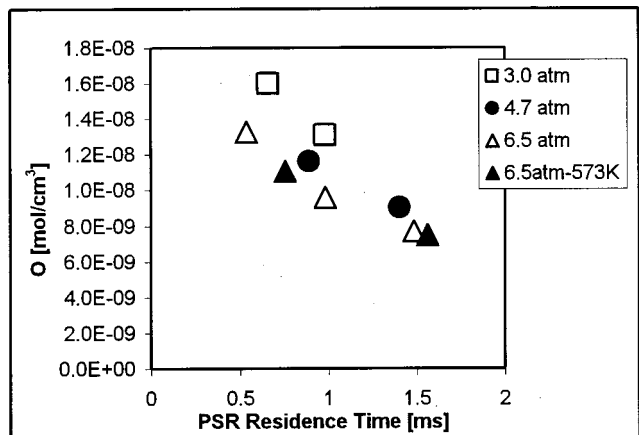


Fig. 9 Concentration of O-atom versus reactor residence time for single-PSR cases

Table 1 Numerical results for two-PSR model (for 6.5 atm)

	6.5 atm Unheated				6.5 atm Preheated			
	2 ms		4 ms		2 ms		4 ms	
Overall residence time (ms)	2 ms		4 ms		2 ms		4 ms	
Fuel-air equivalence ratio	0.7		0.73		0.6		0.66	
Measured NO (ppmv,wet)	7.5		10.3		6.2		8.8	
PSR number	PSR1	PSR2	PSR1	PSR2	PSR1	PSR2	PSR1	PSR2
PSR residence time (ms)	0.126	1.897	0.0695	3.833	0.231	1.847	0.045	3.892
Temperature (K)	1757	1836	1748	1880	1820	1840	1764	1884
Zeldovich NO (ppmv,wet)	0.20	0.74	0.11	2.36	0.74	0.63	0.11	2.85
Nitrous NO (ppmv,wet)	1.19	0.71	0.65	1.30	2.82	0.44	0.55	1.57
Prompt NO (ppmv,wet)	3.07	0.06	3.93	0.05	2.19	0.01	2.91	0.05
NNH NO (ppmv,wet)	1.24	0	1.00	0.07	1.45	0.01	1.06	0.08
Zone NO (ppmv,wet)	5.69	1.51	5.69	3.79	7.2	1.09	4.63	4.56
Modeled NO (ppmv,wet)	7.2		9.5		8.3		9.2	

nificantly lower, because of the lower fuel-air equivalence ratio (shown in parentheses). The [O] is nearly insensitive to preheat, while [H] and [NNH] decrease slightly.

For the longer residence times, the influence of each pathway differs for the first PSR (PSR1), i.e., the flame zone, and the second PSR (PSR2), i.e., the post-flame zone. Figure 6 shows the experimental data of Rutar [8], the total GRI 3.0 prediction, and the contribution (summing each zone) of each of the four pathways, along with the fuel-air equivalence ratio (shown in parentheses) for 6.5 atm with preheated inlet. Table 1 contains the information used in the analysis of the PSR-PSR modeling. In the table, the experimental conditions, i.e., the residence time, corrected measured temperature, and fuel-air equivalence ratio, are presented first. The measured NO_x [ppmv, wet] is also included for comparison with the modeling results. The next section of Table 1 contains the values of the NO in [ppmv, wet] that are formed via the Zeldovich, nitrous oxide, prompt, and NNH pathways, as well as the sum of the NO formed by the four pathways in each zone (termed Zone NO), and the sum of NO for the two zones (termed modeled NO).

Results from the chemical kinetic modeling for the reactor operating in the PSR-PSR regime (i.e., for $2 \leq \tau \leq 4$ ms) are summarized as follows:

- The amount and the fraction of NO formed in PSR2 increase as the overall reactor residence time increases. This is caused by two effects: the increasing residence time and the increasing temperature of PSR2.
- The amount of Zeldovich NO formed in PSR2 increases as the overall reactor residence time increases, and becomes an important part of the total NO formed in the reactor.
- The formation of the nitrous oxide NO shifts from PSR1 to PSR2 as the overall reactor residence time increases.
- The volume and residence time of PSR1 decreases as the overall reactor residence time increases. This is linked to decreasing inlet jet velocity and reactor pressure drop, which lead to decreasing mixing intensity and flame zone thickness. The reduction in the residence time of PSR1 leads to greater [CH] and thus more prompt NO formation in PSR1. This leads to a significant impact of prompt NO to the total NO predicted for the reactor.
- The increase in NO with decreasing pressure is caused by the increase in free-radical concentrations in both zones. In PSR1, between 6.5 and 3.0 atm, [O] increases by threefold, [CH] by seven to eightfold, [H] by four to fivefold, and [NNH] by twofold. The NO formation rates in PSR1 increase between the two pressure levels from 2.2-fold at 2.0 ms to 3-fold at 4.0 ms. The contribution of each pathway changes, however. For example, at 2.0 ms, between 6.5 and 3.0 atm, the prompt NO contribution increases from 54 to 65%, the NNH contribution to NO increases from 22 to 28%, the nitrous oxide contribution to NO decreases from 21 to 6%, and Zeldovich contribution to NO decreases from 3 to 1%. In PSR2, the O-atom concentration increases with decreasing pressure. This causes Zeldovich and nitrous oxide path-

ways to increase, which in turn, increase NO formation rates in the PSR2 as the pressure drops from 6.5 atm to 3.0 atm. The increase is 1.8-fold at 2.0 ms to 2.8-fold at 4.0 ms. The prompt and NNH pathways have little contribution to the overall NO production in PSR2.

The contribution of each NO pathway for the reactor of Bengtsson [6] is shown in Fig. 7, for both the 1 ms and 2 ms data. For both residence times, the nitrous oxide pathway is predominant, followed by the Zeldovich pathway. The small influence of the prompt pathway is caused by the lean fuel-air equivalence ratio (0.55). It is beneficial to compare the single-PSR results for the HP-JSR of Rutar [8] for 6.5 atm, preheated inlet, and 1.5 ms (Fig. 5, lower section), to the results for the HP-JSR of Bengtsson [6] for the same pressure. In both cases the nitrous oxide pathway is predominant. The Zeldovich pathway follows it, then the prompt pathway and lastly the NNH pathway.

Conclusions

The paper uses the experimental data obtained in the HP-JSRs of [6,8], and the modeling approach of [8,9] for a study of methane-air combustion at conditions of lean-premixed combustion turbines. Both reactors operate at low Damköhler numbers, i.e., between 0.01 and 1, which make them suitable for the study of chemical kinetic effects. The results are of significance to predicting and understanding NO_x formation in lean-premixed combustion turbines. Points in this regard are the following:

- 1 The results indicate the GRI 3.0 mechanism is appropriate for modeling combustion pollutant formation/emission at the pressure, temperature, and equivalence ratio conditions of lean-premixed combustion turbines. (The conditions of high-pressure ratio aeroderivative engines have not been explored—however, if the trend of weak dependency of the NO_x on pressure extends to 30–40 atm, the results of [6,7] should apply.)
- 2 The results substantiate databases for developing reduced and global mechanisms for lean-premixed combustion.
- 3 The results provide additional understanding on the importance of the several pathways to NO_x formation in lean-premixed combustion. The nitrous oxide pathway is important at all conditions, whereas the Zeldovich mechanism is important only at long-residence times and high temperatures. Additionally, the Fenimore prompt NO_x must be carefully considered for lean-premixed combustion.

References

- [1] Nicol, D. G., Steele, R. C., Marinov, N. M., and Malte, P. C., 1995, "The Importance of the Nitrous Oxide Pathway to NO_x in Lean-Premixed Combustion," *ASME J. Eng. Gas Turbines Power*, **117**, pp. 100–111.
- [2] Steele, R. C., 1995, "NO_x and N₂O Formation in Lean-Premixed Jet-Stirred Reactors Operated From 1 to 7 atm," Ph.D. Thesis, University of Washington, Seattle, WA.
- [3] Steele, R. C., Tonouchi, J. H., Nicol, D. G., Horning, D. C., Malte, P. C., and Pratt, D. T., 1998, "Characterization of NO_x, N₂O, and CO for Lean-

- Premixed Combustion in a High-Pressure Jet-Stirred Reactor," ASME J. Eng. Gas Turbines Power, **120**, pp. 303–310.
- [4] Leonard, G. and Stegmaier, J., 1993, "Development of an Aero-derivative Gas Turbine Dry Low Emissions Combustion System," ASME Paper 93-GT-288.
- [5] Joshi, N. D., Epstein, M. J., Durlak, S., Marakovits, S., and Sabla, P. E., 1994, "Development of a Fuel Air Premixer for Aero-Derivative Dry Low Emissions Combustors," ASME Paper 94-GT-253.
- [6] Bengtsson, K. U. M., 1998, "Experimental and Numerical Study of the NO_x Formation in High-Pressure Lean Premixed Combustion of Methane," Ph.D. Thesis, Swiss Federal Institute of Technology, Zürich, Switzerland.
- [7] Bengtsson, K. U. M., Benz, P., Schaeren, R., and Frouzakis, C. E., 1998, "NyOx Formation in Lean Premixed Combustion of Methane in a High-Pressure Jet-Stirred Reactor," Proc. Combust. Inst., **27**, pp. 1393–1401.
- [8] Rutar, T. (as Shuman, T. Rutar) 2000, "NO_x and CO Formation for Lean-Premixed Methane-Air Combustion in a Jet-Stirred Reactor Operated at Elevated Pressure," Ph.D. Thesis, University of Washington, Seattle, WA.
- [9] Rutar, T., Malte, P. C., and Kramlich, J. C., 2000, "Investigation of NO_x and CO Formation in Lean Premixed, Methane-Air, High-Intensity, Confined Flames at Elevated Pressures," Proc. Combust. Inst., **28**, pp. 2435–2441.
- [10] Rutar, T., Horning, D. C., Lee, J. C. Y., and Malte, P. C., 1998, "NO_x Dependence on Residence Time and Inlet Temperature for Lean-Premixed Combustion in Jet-Stirred Reactors," ASME Paper No. 98-GT-433.
- [11] Smith, G. P., Golden, D. M., Frenklach, M., Moriarty, N. W., Eiteneer, B., Goldenberg, M., Bowman, C. T., Hanson, R., Song, S., Gardiner, W. C. Jr., Lissianski, V., and Qin, Z., 1999, http://www.me.berkeley.edu/gri_mech/.
- [12] Abraham, J., Williams, F. A., and Bracco, F. V., 1985, "A Discussion of Turbulent Flame Structure in Premixed Charges," SAE Paper 850345, *Engine Combustion Analysis: New Approaches*, P-156, Society of Automotive Engineers, Warrendale, PA, pp. 27–43.
- [13] Turns, S. T., 2000, *An Introduction to Combustion*, McGraw-Hill, New York.
- [14] Kobayashi, H., Nakashima, T., Tamura, T., Maruta, K., and Niioka, T., 1997, "Turbulence Measurements and Observations of Turbulent Premixed Flames at Elevated Pressures up to 3.0 MPa," Combust. Flame, **108**, pp. 104–117.
- [15] Bray, K. N. C., 1980, "Turbulent Flows With Premixed Reactants," *Turbulent Reacting Flows*, P. A. Libby and F. A. Williams, eds., Springer-Verlag, New York, pp. 115–183.
- [16] Chomiak, J., 1990, *Combustion: A Study in Theory, Fact and Application*, Gordon and Breach, New York.
- [17] Nicol, D. G., Malte, P. C., and Steele, R. C., 1994, "Simplified Models for NO_x Production Rates in Lean-Premixed Combustion," ASME Paper 94-GT-432.

Investigation of Two Advanced Cooling Mixing Concepts for a Rich Quench Lean Combustor

O. Diers

J. Koopman

M. Fischer

C. Hassa

e-mail: Christoph.Hassa@DLR.DE

German Aerospace Center,
Institute of Propulsion Technology,
51170 Köln, Germany

To support the development of a rich quench lean pilot zone for a staged aeroengine combustor, two rectangular rich quench lean (RQL) combustor sectors have been investigated under atmospheric conditions. Two advanced cooling mixing concepts, effusion and impingement cooling, with one and two rows of secondary air inlet holes in the mixing zone, have been measured using intrusive and nonintrusive measurement techniques. The results elucidate the interrelations between the cooling concepts and the respective mixing and emissions performances. The measurements were accompanied by numerical calculations supporting the interpretations of the measured data. Drawbacks were observed for the near stoichiometric conditions of the effusion cooling concept near the wall, however, the quench zone design with two rows of staggered holes performs well. On the contrary, the impingement cooling system shows good results for the homogeneity of the primary zone, but since less quench air is available with impingement cooling, optimum mixing is more difficult to achieve. [DOI: 10.1115/1.1473823]

Introduction

The growing concerns about the production of nitrogen oxides by aviation have been answered by the aeroengine manufacturers with the development of low-emission combustor concepts. This contribution is a part of such an effort with the low-emission combustor technology (LOWNOX) program supported by the European commission. In the ongoing third phase of the program, the aeroengine manufacturers SNECMA, MTU, and FIAT cooperate to build a staged combustor having a lean premixing, pre-vaporizing (LPP) combustor as main stage and a rich quench lean (RQL) combustor as pilot stage, developed by MTU (cf. Verdier [1]). This application presents a new and particularly stringent set of conditions to the RQL design. Since some features of the two investigated designs have been studied before, the specific consequences of their use in this application are discussed while reviewing those studies.

Background

Earlier investigation considered RQL combustors for fuel flexibility of aircraft with high fuel bound nitrogen fuels (Briehl et al. [2]). The primary zone of the tubular combustor was water cooled. For lean-lean operation, that has to be demonstrated for aeroengine part-load conditions, air swirler resonance occurred in the undamped liner. Novick et al. [3] investigated combustion of heavy distillate fuels for industrial gas turbines. Fuel preparation required a long primary zone, which was convectively cooled with fins augmenting the outer liner surface area. The pressure drop of the combustor was 6%. Differences of these studies to the current application are the long primary zone making convective cooling necessary because of the large stoichiometric area that would result from film cooling and lower preheat temperatures and inlet pressures, making it feasible, although with higher pressure loss. Hasegawa et al. [4] studied burning low BTU gas for an integrated coal gasification combined cycle. The fuel required similar primary zone residence time. Due to the high preheat and exit temperature, the primary zone was cooled by a combination of

impingement and film cooling, the effect of the film cooling being limited by the low adiabatic flame temperature of the fuel. For kerosene combustion with preheat temperatures up to 850 K and a homogeneous primary one, Griebel et al. [5] found only negligible increase of CO for residence times above 4 ms already at atmospheric pressure, hence shorter primary zones can be used in aeroengines. The primary zone was convectively cooled, however, with a velocity in the secondary channel, which was higher than used for civil applications, requiring small channel heights. Due to the advanced cycle of the intended application and the given position of the pilot combustor in the casing of the staged combustor with small velocities at the backside of the liner, convective cooling could be ruled out as satisfactory means to cool the rich primary zone. Zarzalis et al. [6] demonstrated satisfactory performance for a short effusion cooled RQL combustor up to 19 bar. Hence effusion and impingement cooling were chosen as technically feasible cooling methods for the primary zone length shortened to 50 mm to yield the smallest possible pilot combustor.

Since the choice of the cooling method influences the amount of air and the pressure drop available for quenching, different mixing concepts have to be chosen for both configurations. Lisinsky et al. [7] and Doerr and Hennecke [8] investigated isothermal mixing from one row of holes into a rectangular duct. They found more intense mixing of staggered holes compared to inline holes, provided the nondimensional distance between holes S/D was at least two. However, the amount of quenching air corresponding to convectively cooled RQL combustors leads to less than optimal mixing for annular liners with one row of holes compared to tubular liner because of the lower combustor height H/D . Hence Miguez [9] investigated mixing from two or more rows of holes. He concluded that mixing has to be optimized for fastest near-field homogenization in the stoichiometric zone, the final homogeneity being of secondary importance. For two closely spaced rows staggered axially and circumferentially, quick large-scale mixing especially in the circumferential direction was observed, which was driven by the interaction of the counterrotating vortices produced by each pair of staggered jets. Noncircular holes for single-sided injection were investigated by Holdeman et al. [10] Differences in mixing from circular and noncircular holes were limited to distances upstream of x/H less than one. Bluff slots were more two dimensional in the row plane and had less penetration than equivalent circular holes.

This contribution now focuses on the question of how to keep

Contributed by the International Gas Turbine Institute (IGTI) of THE AMERICAN SOCIETY OF MECHANICAL ENGINEERS for publication in the ASME JOURNAL OF ENGINEERING FOR GAS TURBINES AND POWER. Paper presented at the International Gas Turbine and Aeroengine Congress and Exhibition, New Orleans, LA, June 4–7, 2001; Paper 01-GT-085. Manuscript received by IGTI, Dec. 2000, final revision, Mar. 2001. Associate Editor: R. Natole.

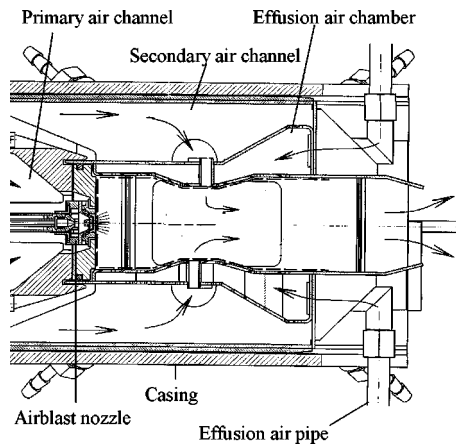


Fig. 1 Side view of combustor first configuration

as much of the NO_x -reduction potential of the RQL method demonstrated earlier while using cooling technologies for high temperature and pressure combustors. MTU and DLR together with other partners split work to characterize two combustors, utilizing the two different cooling and mixing concepts. While MTU designed and investigated two rectangular four-nozzle sector combustors under pressure conditions up to 800 K and 20 bars, DLR took up the part of building atmospheric, rectangular five-sector combustors of the same design with optical access and measure species, temperature, and velocity.

Experimental Setup

The DLR combustors are shown in Figs. 1 and 2. Both combustors have the same geometrical dimensions in length, height, and width. The combustor air is preheated to 650 K by an electrical heater. Before passing the heater, the total air mass flow is measured by passing a critical nozzle.

For the first configuration the air is separated in primary, secondary, and effusion air by critical nozzles behind the preheater. So the three air flows are separated from each other, the air split is listed in Table I. The primary air gets into the combustor from the primary air channel by passing five air blast nozzles. One of them is depicted in the center plane of Fig. 1. In the combustor three zones can be seen. The primary (rich) zone is the part of the combustor from the dome up to the axial position with the minimum height. The part of the combustor with the minimum height is the mixing zone, where the secondary air is brought in. The divergent part downstream is the secondary zone. The secondary air flows through two channels situated on the upper and the lower part inside the casing. To get into the combustor the secondary or

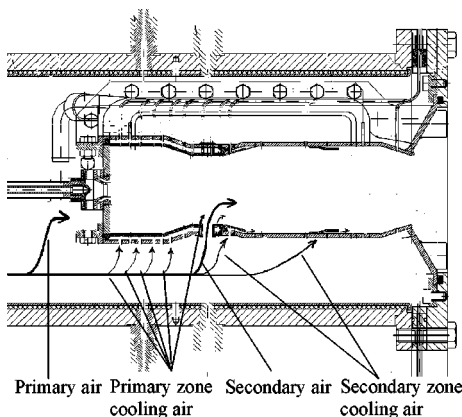


Fig. 2 Side view of second configuration

Table 1 Air split of first and second configuration

Airsplit (%)	1st Configuration	2nd Configuration
Primary air	22	20
Secondary air	52	28
Effusion air (PZ)	11	-
Effusion air (SZ)	15	-
Primary zone cooling air (impingement cooling)	-	39
Secondary zone cooling air	-	13

mixing air flows through two rows of pipes traversing the effusion air chamber, ending in two rows of secondary air inlet holes on each side of the liner. These secondary air inlet holes are arranged staggered in the direction of the mean flow (x -direction) as well as in the circumferential (z -) direction, as shown in Fig. 3. Between the combustion chamber and the secondary air channel the effusion air chamber can be seen (Fig. 1). The effusion air enters into this chamber from the back side through the effusion air pipes. This cooling air gets into the combustor by passing the diagonal effusion air holes which are situated over the whole liner wall in the primary, the mixing, and the secondary zone. The backside of the combustor is open so the exhaust gas can escape through a chimney. To allow nonintrusive measurement techniques, two rectangular windows are mounted in the sidewalls of the combustor. These sidewalls are convectively cooled. The windows are cooled by a cooling film. For laser Doppler anemometry (LDA) measurements, only the primary and secondary air is seeded to prevent clogging of the effusion air holes.

In the second configuration (Fig. 2) the primary and secondary air is split according to the ratio of the effective areas in the combustor liner, also shown in Table 1. The primary air gets into the combustor by passing the five air blast nozzles. The secondary air is divided into three parts on each side of the liner: in primary zone cooling air, mixing or secondary air and secondary zone cooling air. In this configuration the primary zone cooling concept has changed into an impingement cooling. Between the liner wall and the secondary air channel a chamber can be seen along the length of the primary and the mixing zone in Fig. 2. The outer wall of this chamber is perforated so that cooling air for the liner wall of the primary zone can enter through several holes into the casing, cooling there the backside of the liner. This primary zone cooling air is brought into the mixing zone through one row of concentric holes on each side of the liner, arranged staggered in circumferential (z -) direction. The pipes of the secondary air are situated in the center of these holes. So the primary zone cooling air enters into the mixing zone of the combustor through annular gaps and encapsulates the secondary air. The secondary zone is cooled by two cooling films on each side of the liner. As a further means to protect the primary zone, the liner and the dome are coated with thermal barrier coatings. The design of the combustor sidewalls and the outlet is identical to the first configuration.

Most of the measurements were performed in the central sector of the five sectors, where sidewall effects are believed to be minimal. The position of the measurement planes is shown in Figs. 3 and 4. For both configurations, three measurement planes perpen-

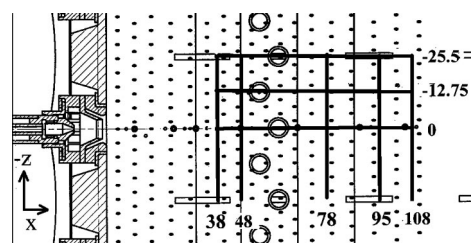


Fig. 3 Measurement planes and upper side of first configuration, axial plane positions in mm behind the nozzle exit

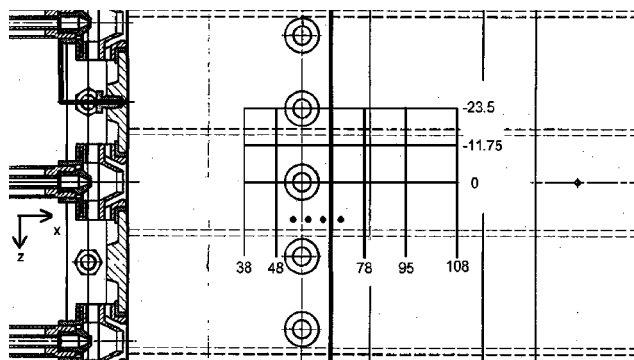


Fig. 4 Measurement planes and lower side of liner second configuration, axial plane positions in mm behind the nozzle exit

dicular to the tangential direction cutting every secondary air inlet hole in one half of the center sector and up to five measurement planes perpendicular to the axial direction have been investigated (two in the primary and three in the secondary zone, depending on the measurement method). All investigations have been performed with a preheating temperature of 650 K, except the gas analysis and temperature measurement of the first configuration. Here the temperature had to be decreased to 550 K due to structural problems. In order to preserve the mixing behavior for all experiments, the pressure drop dp/p of the combustor was held constant at 3%.

Numerical Method

Code and Methods. The numerical simulations of the fluid mechanical and chemical processes of the first geometry have been performed with the unstructured three-dimensional Navier–Stokes code “TRUST,” developed in DLR by Schütz et al. [11] for gas turbine applications, and is based on the KIVA II code of Amsden et al. [12].

In the TRUST code, the time-dependent conservation equations for the turbulent flow of a chemically reacting mixture of ideal gases are solved on a three-dimensional grid of body-fitted cells. The TRUST code uses an ALE-solver (arbitrary Lagrange Eulerian method). The half empirical $k-\epsilon$ model is used. Processes in gas turbine combustion chambers are usually very fast and highly turbulent. Therefore the chemical timescale was assumed to be small compared to the turbulent time scale, such that the equilibrium assumption for the mixture would be valid. This assumption will be discussed in the Results section. In turbulent reacting flows the local values of temperature, composition, and density generally fluctuate. These fluctuations can dominate their averaged counterparts. The transport of the species mass fraction is therefore characterized by the transport of the mixture fraction f and its fluctuating counterpart $g=f^*f'$. The assumption of a Gaussian behavior of the mixture fluctuations around their average closes the heat release model ($f-g$ model).

In earlier publications (Griebel et al. [5]), the importance of the interaction between secondary jet flow and rich primary zone flow for the performance of RQL combustors was pointed out. Therefore we included the primary zone in the calculation domain. Because no measurements of the nozzle outlet were available, the calculation domain of the first geometry was extended to include the flow in the fuel nozzle.

Measurement Techniques

The local gas concentration was measured using a suction probe and several analyzers for CO_2 , CO , O_2 , H_2 , UHC, and NO (NO_x). For the analysis of NO_x the analyzer has been modified to be able to measure not only NO , but also nitrogen containing species like NH_3 or HCN . These species are mostly built under

rich conditions in the flame front and oxidize to NO under leaner combustion conditions. In a converter of the analyzer which is heated up to 650°C these species were oxidized with a sufficient dilution of oxygen into NO_2 . Hence the measured NO_x is the sum of all molecular bound nitrogen and will be called TFN (total fixed nitrogen). The sum of the preliminary products of NO like NH_3 and HCN but also NO_2 is called RTFN (rest total fixed nitrogen). The accuracy of the gas composition measurements was about 4%.

The temperatures inside the combustor were measured with an Al_2O_3 layered PtRh–Pt thermocouple. For the second configuration the temperatures are corrected for radiation effects, in the first configuration a correction has not been made, due to the redundancy reached by the CARS measurements. Comparison of both methods showed that for the low temperatures measured, thermocouple measurements did not need a radiation correction.

Laser Doppler Anemometry. Velocities were measured with LDA in forward scattering using TSI (model 9107 and 9155) optics and Dantec electronics (model BSA). The airflow was seeded with titanium dioxide particles ($<1 \mu\text{m}$) which are added to the combustor inlet before division in primary and secondary flow. The accuracy of the mean velocities was about 5% (Hassa et al. [13]).

Coherent AntiStokes Raman Scattering. Temperatures of the first configuration were also measured with a BOX CARS arrangement using single shot N_2 thermometry. The accuracy of the mean temperatures was about 3% (Fischer et al. [14]).

Results

First Configuration With Effusion Cooling

Experimental Observations. The radial staging of the staged combustor enforced a very short primary zone for its pilot stage. Hence effusion cooling seemed to be possible even for RQL combustion, where a homogeneously rich primary zone is the ultimate goal. Investigations of Stursberg et al. [15] showed a strong influence of liner cooling air on the effective equivalence ratio of the combustion in the primary zone. For a homogeneous primary zone Griebel [5] found a minimum of the TFN concentrations at an equivalence ratio of $\Phi=2.22$ at the end of the primary zone, but also a strong soot formation for equivalence ratios higher than $\Phi=2$. Considering this result, higher equivalence ratios are not of practical interest. Based on these results all investigations of the effusion air-cooled combustor have been made at an equivalence ratio of $\Phi=1.96$ at the end of the primary zone, including effusion air.

The axial development of combustion efficiency and nitrogen species resulting in the measurement planes at constant x positions is depicted in Fig. 5.

At the end of the primary zone, combustion efficiency as well as RTFN is rather low. Ideally only CO should remain as carbon species at the end of the primary zone, which would give a combustion efficiency above 50% and RTFN should have reached its maximum. Substantial RTFN formation is found in the mixing zone, which is not fully reacted to NO up until the position at $x=108 \text{ mm}$ where the pilot combustor would end in the staged combustor. Here the combustion efficiency is also lower than desired, although it would improve at higher pressure. At $x=78 \text{ mm}$, the reaction progress is like the one that the ideal RQL combustor should have at the end of the primary zone, since production of RTFN is limited to rich zones. To explain this behavior, we now examine in more detail the development of the combustor flow.

In the primary zone the recirculation of the air blast nozzle extends up to the end of the reduction of the liner height at 48 mm behind the nozzle exit (Fig. 6). At $x=38 \text{ mm}$ the recirculation areas of neighboring nozzles combine over the whole width of the nozzle sector, however, with no measured backflow of secondary air into the primary zone.

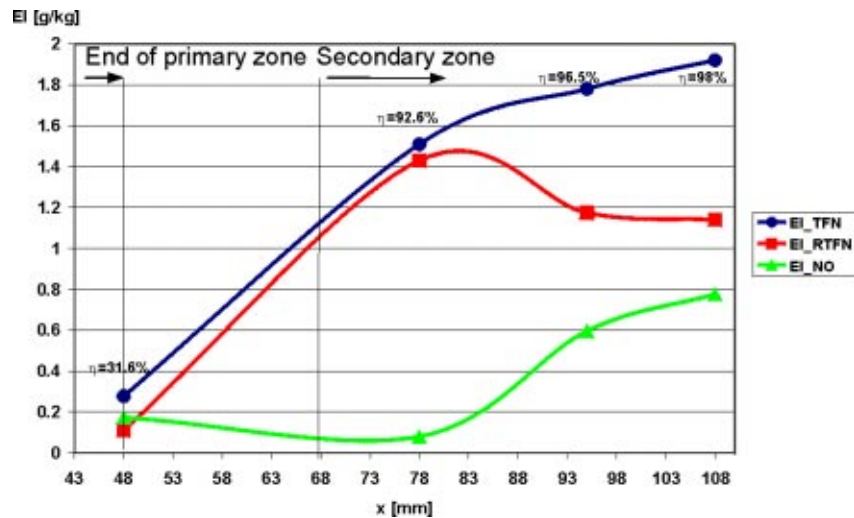


Fig. 5 TFN, RFTN, NO, and combustion efficiency average of measurement of planes at $x=48, 78, 95,$ and 108 mm

Due to the wide extension of the recirculation, the maximum possible residence time for the given primary zone length is attained. It was estimated to $\tau=5$ ms. This residence time is calculated by the division of primary zone length over axial velocity, which can be calculated by the mass flow and the estimated mean primary zone temperature of 1300 K. The CARS temperature measurements taken in the same plane at the primary zone exit show that no reaction between the primary air and the effusion air in the primary zone takes place.

Near the liner walls on the lower and the upper side of the combustor, the temperature is very low. These low temperatures result from the interaction between fuel placement and effusion air cooling. By using an airblast nozzle with a wide cone angle and a wall attached gas flow, a huge part of fuel is placed in the effusion air zone. The remainder of that fuel was found in the UHC measurements at the end of the primary zone. The result of this fuel placement is a quench effect near the liner walls in the primary zone. Only in the recirculation area the reaction has started to yield higher heat release rates, thus higher temperatures have been measured. However, at higher preheat temperature the evaporation would be faster and higher pressure would accelerate the reaction, such that less unreacted fuel would reach the effusion cooling zone. It seems, that due to the improved protection of the liner against hot reaction products by the effusion cooling compared to the film cooling configuration of Stursberg et al. [15], most of the

cooling air remains inert and just bypasses the primary zone reaction, thus resulting in a too high fuel loading of the reaction zone, delaying the reaction progress, such that our wrong assumption about the interaction between cooling and nozzle air has led us to choose a nonoptimum operating point.

In this atmospheric case, high heat release has been measured in the mixing and secondary zone, as can be seen in Fig. 7. Due to the slow reaction in the primary zone, fuel rich bubbles reach the mixing and secondary zone and produce RTFN there (cp. Fig. 5). There is also rather considerable buildup of thermal NO in the secondary zone. Due to the reaction delay, the quench zone mixing cannot prevent the production of thermal NO, but without the mixing as good as it is, the TFN concentration would be worse. This can be seen in a measured EI_{NO_x} ($=EI_{TFN}$) of 1.924 g/kg at the measurement plane at $x=108$ mm. Due to the atmospheric pressure and the elevated equivalence ratio, the measurements at the primary zone exit exhibit an incompleteness of the chemical reaction.

Nevertheless the mixing induced by the two rows of axially and circumferentially staggered secondary air holes is very good (cp. Fig. 6). The first injected secondary air stream penetrates nearly 3/4 of the height of the mixing zone. For the generation of the counter rotating vortices described by Miguez [9], that enhance turbulence and mixing, at least the first pair of jets needs to penetrate well into the opposed half of the combustor height. The second jet is rapidly turned around in the main flow direction, the collision between first and second jet resulting in a very high vertical turbulence level measured at the $x=78$ mm plane. From the jet injection to that plane, the mean temperature distribution is already reduced to a spread of 250 K. In the next measurement plane, situated in the middle of the secondary zone, this high turbulence is not measurable anymore and the vertical velocities are small.

After the decision for the number of rows and the staggered configuration, hole diameter and axial distance are the only free parameters of the mixing. Since the jet to mainstream momentum ratio is given by the liner pressure loss and the combustor height, and the mass flow by the equivalence ratios chosen for the combustor zones, the hole spacing follows from the hole diameter. Here a big hole diameter was chosen for the first row for good penetration. Following that, a rather wide hole spacing S/D had to be used. To limit the axial extension of stoichiometric zones emerging between the holes, the axial row distance was chosen much smaller than $x/S=0.5$ proposed by Miguez [9]. However,

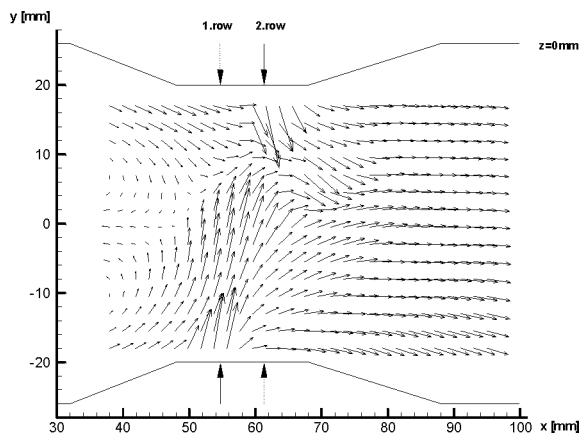


Fig. 6 Interpolated vector plot of measured velocities in nozzle center area

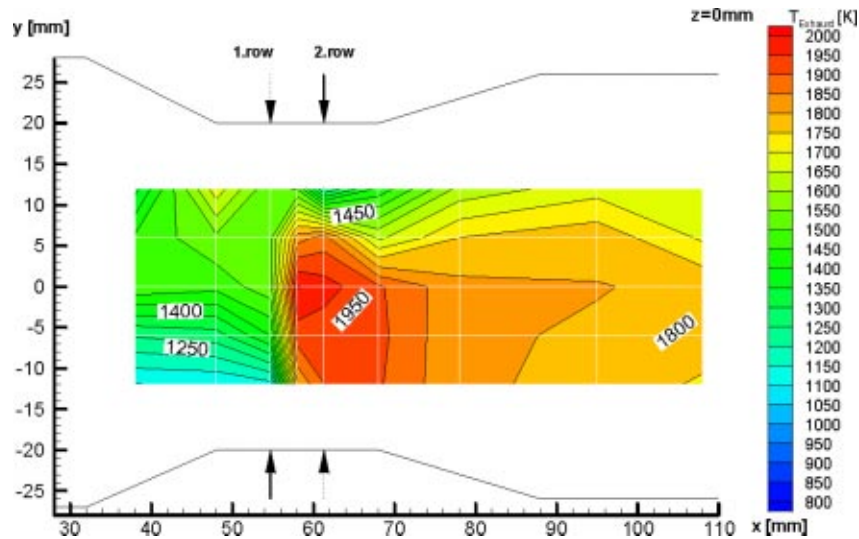


Fig. 7 Thermocouple temperatures in nozzle center plane

the good vertical and circumferential homogeneity at the beginning of the secondary zone shows that the right priorities have been set in the choice of geometrical parameters.

Numerical Results. At the considered operating conditions and atmospheric pressures the reaction process appears to be severely delayed. However, at higher pressures the chemical reaction process will be accelerated. To study the influence of pressure, the numerical results describe the heat release to be infinitely fast. In this model reaction delay is only produced by turbulent mixture fluctuations but not by kinetical effects.

Contrary to the observations made at atmospheric pressure, the highest temperatures of the primary zone in Fig. 8 are located near the effusion air holes. Whereas at atmospheric pressure effusion air quenches reaction even more, it can be expected that raising the operating pressure will accelerate chemical reaction processes and the quenching effect diminishes. The numerical results show the situation where no quenching is present anymore and heat will be released next to the wall. In this way the effusion cooling turns out to stimulate heat release in an undesired part of the combustion chamber.

Second Configuration With Impingement Cooling

Experimental Observations. The main difference to the first configuration is the cooling concept, that has changed to impingement cooling in the primary zone, so that no extra air is brought into the rich zone. Due to the decreased efficiency of the impingement cooling compared to the effusion cooling, the amount of cooling air has to be increased to the expense of the mixing air.

Having learned that the optimum staging of small pilot RQL combustors cannot be deduced from experience gained with larger single-stage RQL combustors, a minimum of the TFN concentration has been searched at the combustor outlet. As can be seen in Fig. 9, the curve of EI_{NO_x} ($\equiv EI_{TFN}$) is very flat over a wide operating range with a minimum of 1.92 g/kg for a primary zone air fuel ratio (AFR) of 8.4 which is equal to an equivalence ratio of $\Phi=1.72$.

Because nearly no difference between arithmetical and mass averaging was detected, only the arithmetically averaged values will be used from now on. In the optimum operating point at primary zone $AFR=8.4$, the combustion efficiency is very respectable for atmospheric pressure. The remainder of the investi-

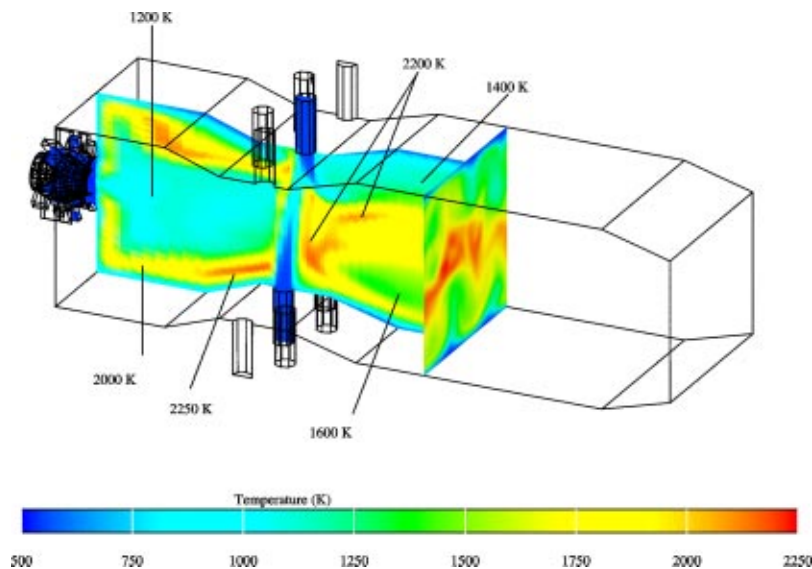


Fig. 8 Calculated temperature distribution of first configuration

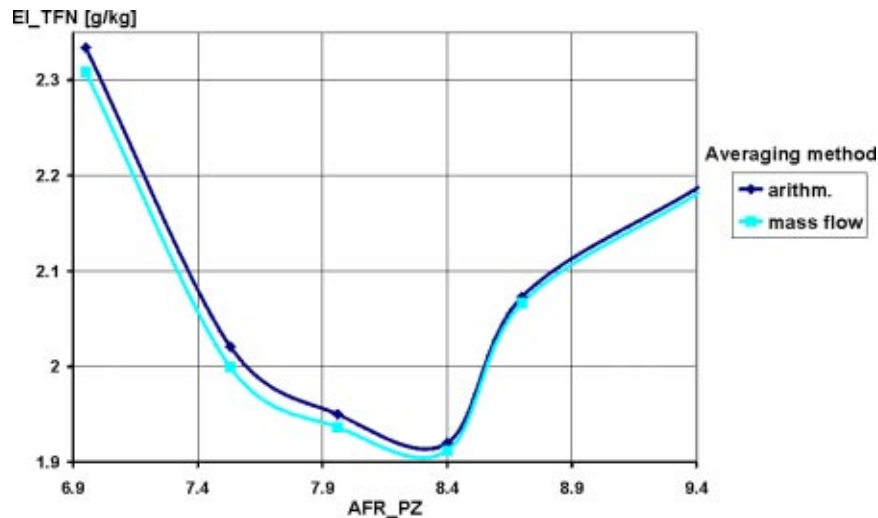


Fig. 9 Mass and arithmetically averaged EI_TFN for several primary zone air fuel ratios (AFR)

gation of the combustor was therefore performed at this AFR. Again the axial development of nitrogen species is shown in Fig. 10.

In comparison to the first configuration, where the combustion efficiency at the end of the primary zone was 32%, the combustion efficiency in the leaner primary zone is now much better with 58%, a reaction delay can't be seen any longer. Nevertheless, there is still RTFN formation in the mixing zone. At the combustor exit it's part in the total fixed nitrogen is still bigger than that of NO. The less than optimal quality of mixing becomes also apparent with the increasing TFN concentration in the secondary zone (see Fig. 10). As for the first configuration, results from the detailed investigation of the combustor flow are now presented to explain these results.

Surprisingly, the recirculation zones of this combustor are isolated from each other and much smaller although the same nozzles are used. Apparently the increased heat release in the primary zone causes a larger decrease in the effective swirl due to the lower density as the relative increase of the swirl in the primary zone connected with the absence of unswirled effusion air.

Although the conversion of the fuel in the primary zone is faster than in the first configuration, chemical equilibrium is not reached at it's end. The thermocouple measurement at the axial position gives a spatially averaged temperature of about 1600 K which would be much higher if a CO concentration near equilibrium would have been reached, consequently rather high UHC concentration in the percent range were measured. In this atmospheric test case, caused by a small primary zone, the residence time was too short ($\tau \approx 6.4$ ms) to allow completeness of the chemical reaction process. Under realistic pressure conditions this problem wouldn't exist due to faster reaction rates.

The measurements of the mixing zone of Fig. 11 shows a clear separation of axial mean velocities of the primary and the mixing zone. Nevertheless, a turbulent exchange, as it is often the case in the wall jet primary zone interaction, is possible between the primary and the mixing zone. If there is enough turbulent exchange producing a transport of mixing air into the primary zone it is not secondary but cooling air: in Fig. 11, two histograms of the axial velocity are shown.

The upper histogram represents the axial velocity distribution

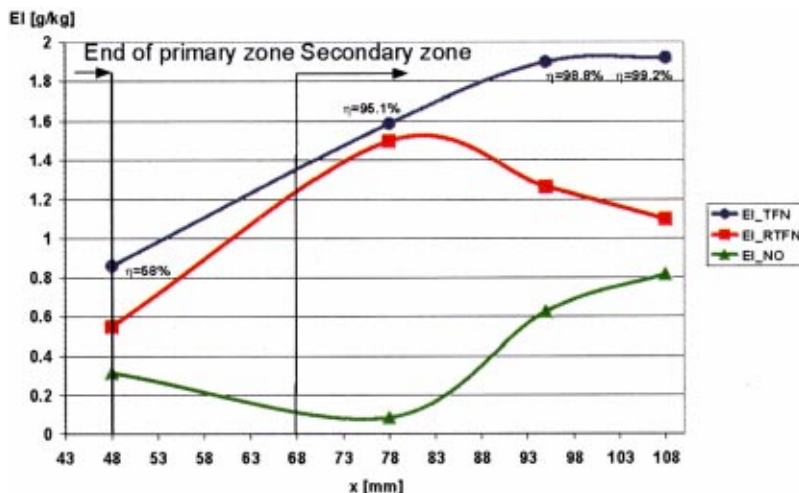


Fig. 10 Axial development of nitrogen emission indices (upper: EI_TFN, middle: EI_RT FN, lower: EI_NO), calculated with molecular weight of NO_2 for a primary zone AFR of 8.4

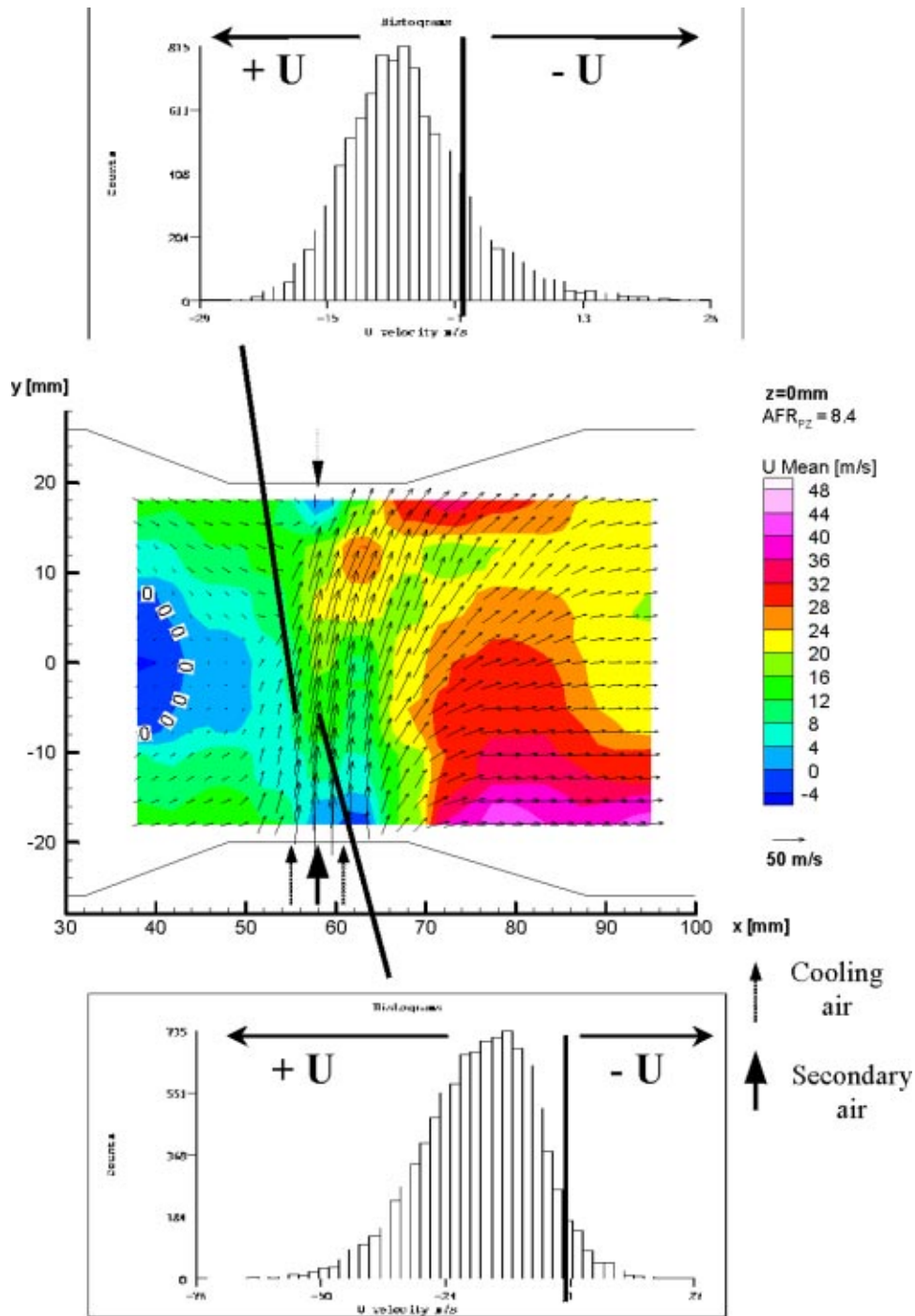


Fig. 11 Interpolated velocity vectors, axial velocity as gray scale, histograms with axial velocities in nozzle area (upper: position over primary zone cooling air orifice, lower: position over secondary air inlet hole)

off axis of the jet, the radius corresponds to a position over the concentric orifice, the lower one presents the axial velocity on the axis of a mixing jet. Here it can be clearly seen that directly over the secondary air inlet hole only very few samples with negative velocities have been detected. In the primary zone cooling air stream, a higher part flows back in axial direction, but not much. By inspection of the interpolated vector field of Fig. 11, an overpenetration of the secondary air jets becomes apparent. The experiments have shown that the encapsulating primary zone cooling air prevents good mixing of primary and secondary air. Only the primary zone cooling air and the primary air are well mixed.

The secondary air overpenetrates, because it is shielded from the attack of the primary zone fluid by the surrounding cooling air.

In the secondary zone the situation is reflected in the measured local equivalence ratios that are lower than the secondary zone average in the central area of the combustor ($12 \text{ mm} < y < -12 \text{ mm}$). Lean secondary air is concentrated near the liner walls and due to the incomplete mixing of primary and secondary air, the gas mixture around the center axis is much richer. The resulting measured equivalence ratio $\Phi=0.62$, can also be calculated by the air mass flow ratios of primary and cooling air, omitting the secondary air mass flow. All measurement planes with constant

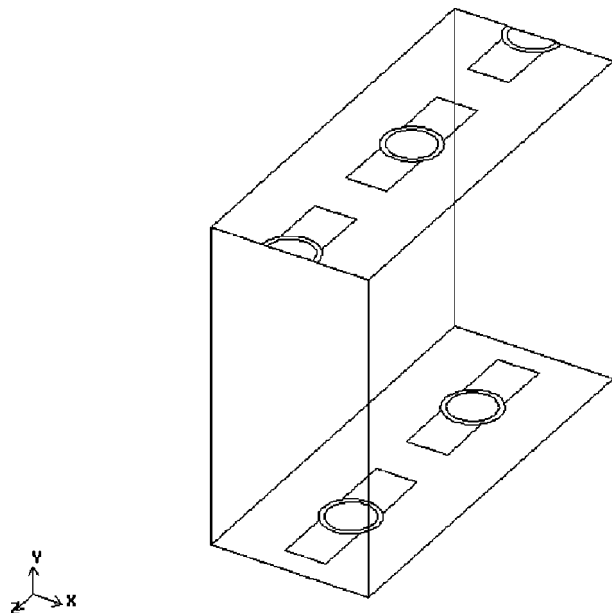


Fig. 12 Flame tube boundary and mixing hold configuration for modified mixing hold design

z -positions cut one secondary air inlet hole, so no fuel rich area has been detected. However, the existence of rich pockets can be presumed in the flow between the holes that will prevail longer for a single than for a double row configuration.

Due to those bubbles and nonequilibrium in the primary zone, a high heat release is produced up to the middle of the secondary zone so that additional thermal NO is formed in these areas. More downstream a homogenization takes place and the production of TFN is stopped. In difference to the first configuration this homogenization does not take place until downstream to the second measurement plane of the secondary zone. By improvement of the mixing process, this extra production of thermal NO can be avoided.

Taking into account results of the second configuration, a design modification was proposed with cooling air holes elongated in the circumferential direction (see Fig. 12) preserving the effective hole area. Because the area of the shear layers is increased, the overpenetration is avoided and at the same time, the distance between the jets is reduced, thus reducing the volume of the rich bubbles of primary air. Calculations show a more homogeneous temperature distribution at the outlet, where the hot core is effectively mixed out. Meanwhile the configuration has been successfully tested by MTU and results will be reported in the future.

Summary

A rectangular sector combustor with two different cooling mixing concepts was investigated. The combustor configuration with an effusion air cooling concept shows incomplete combustion in the primary zone for the chosen operating point being too far on the rich side. The reaction is delayed into the mixing and secondary zone, exhibiting high RTFN and thermal NO_x building rates there. Nevertheless the quench zone mixing concept with two staggered rows of secondary air inlet holes works well and an acceptable NO_x emission index at the defined combustor end is obtained.

The second configuration with impingement cooling showed a faster chemical reaction in the primary zone, but the desired reaction progress of the primary zone was not fully reached. Fuel rich bubbles pass between the jets producing relatively high RTFN. The mixing concept with one row of secondary air jets encapsulated by primary zone cooling air shows not so good mixing in the quench zone. The problem was alleviated by a modified mixing

concept. The resulting production of thermal NO could be reduced by alternative quench zone designs. The numerical results and the pressure tests of the final configuration will be reported by MTU after the completion of the project.

Acknowledgments

The present work was supported by European Commission as part of the Brite-Euram Research Program "Low Emission Technology Program Phase III/Low NO_x III Part 1" under contract number BRPR-CT95-0122, which is gratefully acknowledged.

The authors are indebted to F. Turrini, FIAT Avio, for the use of his numerical results.

This work only could have been performed with the help of technical and scientific persons of the Institute of Propulsion Technology. For the support and their effort we want to thank Mr. S. Cordes, Mr. M. Pütz, Mr. A. Winandy, Mr. A. Langfeld, Mr. T. Behrendt, Mr. N. Heltsch, and Mrs. A. Dreizner.

Nomenclature

AFR	=	air fuel ratio
EI	=	emission index
CARS	=	coherent antiStokes Raman scattering
LDA	=	laser Doppler anemometry
LPP	=	lean premixed prevaporized
RMS	=	root mean square
RQL	=	rich quench lean
RTFN	=	rest total fixed nitrogen
TFN	=	total fixed nitrogen
η	=	combustion efficiency
Φ	=	equivalence ratio

References

- [1] Verdier, L., 1997, "The European Low NO_x Emission Combustor Technology Initiative," Aeroday Conference.
- [2] Briehl, D., Schultz, D. F., and Ehlers, R., 1983, "A Variable Geometry Combustor to Study Primary and Secondary Zone Stoichiometry," ASME Paper 83-GT-00-9.
- [3] Novick, A. S., Troth, D. L., and Yacobucci, H. G., 1982, "Design and Preliminary Results of a Fuel Flexible Industrial Gas Turbine Combustor," ASME J. Eng. Gas Turbines Power, **104**, pp. 368–376.
- [4] Hasegawa, T., Sato, M., and Ninomiya, T., 1997, "Effect of Pressure on Emission Characteristics in LPG-Fueled 1500°C-Class Gas Turbine," ASME Paper 97-GT-277.
- [5] Griebel, P., Fischer, M., Hassa, C., Magens, E., Nannen, C., Winandy, A., Chrysostomou, A., Meier, U., and Stricker, W., 1997, "Experimental Investigation of an Atmospheric Rich Quench Lean Combustor Sector for Aeroengines," ASME Paper 97-GT-146.
- [6] Zarzalis, N., Hohmann, S., Hettel, M., Merkle, K., Klose, G., Meier, R., Koch, R., Wittig, S., Carl, M., Behrendt, T., Hassa, C., Meier, U., Lückerrath, R., and Stricker, W., 2000, "Rich-Lean Combustor Development," submitted to Aerospace Science & Technology.
- [7] Liscinsky, D. S., True, B., and Holdeman, J. D., 1993, "Experimental Investigation of Crossflow Jet Mixing in a Rectangular Duct," AIAA Paper 93-2037.
- [8] Doerr, Th. and Hennecke, D. K., 1993, "The Mixing Process in the Quenching Zone of the Rich-Lean-Combustion Concept," AGARD-CP-536.
- [9] Migueis, C. E., 1996, "Untersuchung zur Optimierung einer fett-mager gestuften Ringbrennkammer," DLR FB 96-33.
- [10] Holdeman, J., Srinivasan, R., Coleman, E., Meyers, E., and White, C., 1987, "Effects of Multiple Rows and Noncircular Orifices on Dilution Jet Mixing," J. Propul. Power **3**, pp. 219–226.
- [11] Schütz, H., Eickhoff, H., Theisen, P., and Koopman, J., 1997, "Analysis of the Mixing Zone of an Air Staged Combustor," ISABE Paper 97-7225.
- [12] Amsden, A. A., O'Rourke, P. J., and Butler, T. D., 1989, "KIVA II: A Computer Program for Chemically Reacting Flows With Sprays," Los Alamos Laboratory Report LA-11560-MS.
- [13] Hassa, C., Behrendt, T., and Griebel, P., 1996, "LDA-Messungen in Einem Atmosphärischen Fett-Mager-Brennkammersektor für Flugtriebwerke, Lasermessmethoden in der Strömungstechnik," **5**, Fachtagung der GALA, Shaker Verlag, Aachen, pp. 35.1–7.
- [14] Fischer, M., Griebel, P., Magens, E., and Winandy, A., 1996, "CARS Temperature Measurements in a Rich Quench Lean Combustion Chamber for Aeroengines," DLR IB-325-11-96.
- [15] Stursburg, K., Behrendt, T., Heinze, J., and Hassa, C., 1999, "Druckeinfluß auf die magere Stabilitätsgrenze, KEROMIX Abschlußbericht," DLR-IB-325-09-99.

Gas Turbine Mach Number Control With Simplified Fuel System

G. J. Dadd

Defence Research and Evaluation Agency,
Pyestock, Farnborough,
Hampshire GU14 0LS, UK
e-mail: gjdadd@dera.gov.uk

K. K. Chan

Frazer-Nash Consultancy Ltd,
Stonebridge House, Dorking Business Park,
Dorking, Surrey RH4 1HJ, UK
e-mail: info@fnc.co.uk

The compressor exit Mach number control theory presented here will enable improved control of transient compressor working point trajectories of a turbine engine. This will allow the steady working line to be raised towards the surge boundary with the advantage of increased thrust and reduced specific fuel consumption. This new control method can replace the rigid acceleration and deceleration limiters of the fuel control loop, and achieve superior surge avoidance performance. This paper documents the theoretical and practical study of Mach number controllers designed for implementation with a simplified fuel pump system and the subsequent testing of the controllers on an aeroengine in the sea level test bed in DERA Pyestock. The new controller incorporated two Mach number dynamic limiting control loops (one each for acceleration and deceleration) besides the NH controller. Several designs were tested successfully and demonstrated not only Mach number control from idle to full power, but also surge avoidance. Engine start control was also tested in the latest engine test. [DOI: 10.1115/1.1359785]

Introduction

A standard practice in modern advanced military engines is to implement high pressure compressor surge avoidance and flame out by precise closed-loop control of spool accelerations and decelerations (NHdot) through fuel flow. The benefits are considerable. For instance, thrust response times are repeatable, and transient trajectories on the compressor map are consistent in spite of fuel type and temperature variations. What is more, the accuracy to which the compressor trajectories can be controlled allows the working line to be raised towards the surge boundary with the advantage of increased thrust and reduced specific fuel consumption. On the debit side, the closed-loop NHdot control is *obstructive* in that the occurrence of surge invokes an *increase* in fuel flow in order to maintain NHdot. This problem is conventionally countered by open-loop fuel flow limits, which may be sensitive to high pressure compressor (HPC) delivery pressure (Pt3), to ensure that excessive over-fuelling cannot occur. Accurate metering of fuel flow therefore remains a prime requirement for the fuel system and the much sought after mechanical simplifications, with reliability and cost improvements, have not so far been achieved.

The positions of the constant NHdot lines are not unique. Levels of power extraction from the HP spool and the general heat soak condition of the engine tend to move these lines bodily relative to the axes of the compressor map. In times of heavy power extraction, the steady working line will move towards the compressor surge line. This movement effectively reduces the maximum acceleration rate before initiating surge. If the surge margin and the fuel limit are set using the worst power off-take scenario over the whole flight envelope, the engine performance will be seriously restricted. This issue is particularly relevant to the "More Electric Engine" concept¹ (Toyne and Hodges [1], Cronin [2], and Chan [3]) when significant power off-take from the engine is anticipated. A back-up limiter implemented in terms of compressor exit Mach number (General Electric Company [4]) will intercede an NHdot acceleration control loop in this situation,

removing the need for the less accurate fixed schedule fuel limiting. Much improved transient performance can be obtained for all levels of power off-take operation. The reduced reliance on fuel scheduling will enable hardware simplification of the fuel system.

Engine control law research at DERA Pyestock in the past has centered on active closed-loop control of fan and compressor working lines and trajectories. Currently, fan and compressor working lines are set by open-loop scheduling of propulsion nozzle area and inlet guide vane position. A closed-loop working line Mach number controller has been considered in this paper. Previous work covering sensor requirements, inlet distortion effect and surge recovery performance has been published (Dadd and Porter [5]). Successive Mach number controllers have been developed, optimized, and tested on a typical military aero-engine equipped with a simplified fuel system. To assess the capability of the Mach number control, there was no requirement for stringent fuel metering accuracy. While not representative of a flight worthy fuel system, many of the simplifications tested could be incorporated in flight standard hardware leading to reliability improvements and cost savings.

The engine trials discussed in this paper include the investigation of Mach number characteristics in the whole power range including engine subidle. Besides normal acceleration and deceleration loops, engine startup has also been demonstrated.

Test Set-up

The control concept has been investigated in a sea-level test bed in DERA Pyestock and successfully demonstrated its capability. The test vehicle is a conventional two-spool military engine equipped with a simplified fuel system with no fuel flow feedback.

The simplified fuel system concerned was a variable capacity fuel pump with significantly simpler system design compared with its predecessors. Furthermore, it differed from the conventional scheme in that the required fuel flow was adjusted by metering the spill flow.

Instrumentation

For the purposes of the engine test work reported here, Mach number measurements were inferred from dynamic head and local pressure. The conventional absolute and differential diaphragm pressure transducers used were engine mounted. Although turn-down effects on the measured Mach number are small, even across the flight envelope, there are significant turndown effects

¹Contributed by the International Gas Turbine Institute (IGTI) of THE AMERICAN SOCIETY OF MECHANICAL ENGINEERS for publication in the JOURNAL OF ENGINEERING FOR GAS TURBINES AND POWER. Paper presented at the International Gas Turbine and Aeroengine Congress and Exhibition, Munich, Germany, May 8–11, 2000; Paper 00-GT-044. Manuscript received by IGTI Feb. 2000; final revision received by ASME Headquarters Jan. 2001. Associate Editor: M. Magnolet.

¹This is an engine system concept in which the power off takes from the engine are electrical in nature so the need for on-engine hydraulic power generation and bleed air off takes is removed.

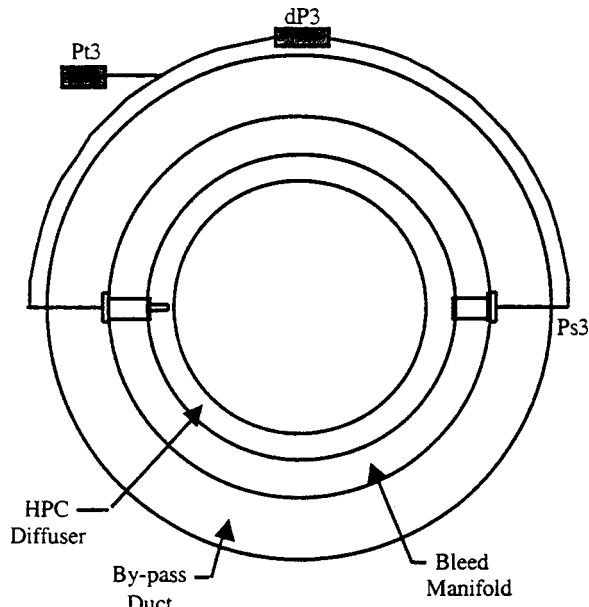


Fig. 1 HPMN probe arrangement

on the individual pressure measurements used to derive Mach number. These effects reduce the precision with which Mach number can be measured for high altitude and low speed flight. Dadd and Porter [5] has documented the scale of Mach number uncertainty at different flight conditions. Measurement of HPMN forms the basis of the control laws defined in the next section.

Figure 1 shows the instrumentation layout for these tests. The total and static pressure probes required for these measurements are positioned on opposite sides of the compressor casing. This is a constraint imposed by the engine architecture, which could lead to dynamic errors due to rotational compressor flow effects. The Mach number response to rotating stall cells could be particularly affected. The instrumentation could be much improved if considered at the engine design stage.

Functional Requirements

The control law requirements considered are based on control of fuel flow in the dry engine regime. Final nozzle area and HPC inlet guide vanes are to be controlled to open-loop schedules as is the current convention. Control of fuel is therefore to be used for the following features:

- 1 Steady state thrust level control (i.e., range governing)
- 2 Acceleration control
- 3 HPC surge avoidance
- 4 Turbine temperature limiting
- 5 Recovery from HPC surge
- 6 Avoidance of flame-out during deceleration.

Control of thrust relies on stable, closed-loop fuel control of an engine thrust-related parameter such as HPC shaft speed (NH), fan speed (NL), or engine pressure ratio (PR). Closed-loop fuel control of turbine temperature (and/or other physical limits) is used to override the main thrust control as the need arises. The major problem faced in the design of these closed-loop functions is to ensure that stability and response are retained over the operational envelope of the aircraft despite the corresponding variations in engine and fuel system characteristics.

First line avoidance of HPC surge in these existing systems relies heavily upon accurate closed-loop fuel control of HPC acceleration (NHdot). This control limits acceleration over-fuelling at all flight conditions, and gives useful accurate time control of thrust transients, but suffers in having undesirable behavior in

response to surge. Surge results in an immediate reduction in NHdot and a consequent increase in fuel flow to restore NHdot through the action of the closed-loop. Second line protection is provided by means of a scheduled open-loop limit on fuel flow excursion. This is the feature that imposes stringent requirements on fuel flow control accuracy and which, in turn, leads to the need for complex fuel system designs.

The Mach number control law described in the next section provides an alternative approach to engine control, which is independent of absolute fuel metering accuracy and provides robust stability and response even with large variations in fuel system dynamics.

Control Law Configuration

The engine control laws implemented were devised during a feasibility study (Dadd, Shutler, and Greig [6]). The control structure, or configuration, is repeated here in order to clarify the reasoning behind the type of test imposed on the engine and the assessment of the test results.

Figure 2 gives a general view of the control configuration adopted. The fuel control concept employed is to use a carefully chosen engine parameter in an inner closed loop to set the fuel valve area. In effect this closed loop is the alternative to the combination of pressure drop regulator and valve position control loop of the conventional fuel control system. The outer engine control loops, such as thrust and acceleration and turbine blade temperature limiter loops are then designed to work via the inner control loop. Given the availability of a suitable engine parameter for the inner control loop, the advantages expected from this structure are

- 1 The anticipated uncertainty of the fuel system dynamic characteristics are included in an inner closed loop so that the effect of these uncertainties on the response and stability of the outer engine control loops can be minimized by good design.
- 2 If the selected engine parameter is one that shows high sensitivity to HPC surge margin, or working line displacement, then limits applied to the inner control loop demand can provide the necessary back-up control to the outer NHdot acceleration and deceleration control loops.

Ideally, the selected inner loop parameter must exhibit *constructive* behavior in the presence of surge. That is, its action must be to reduce fuel flow in the event of surge. With this provision a third advantage might be claimed,

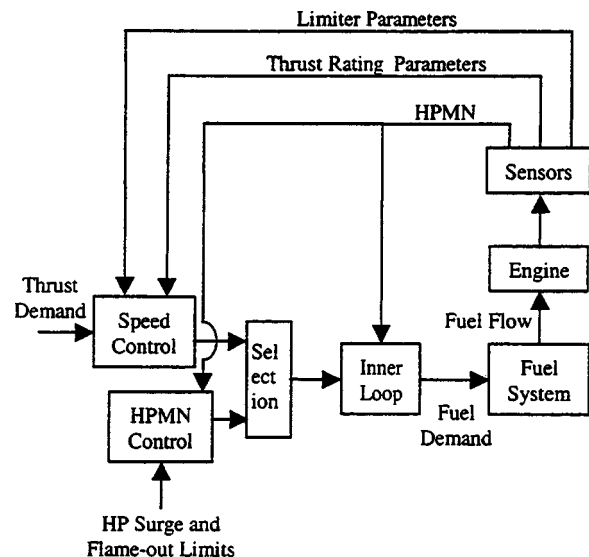


Fig. 2 Mach number control law configuration

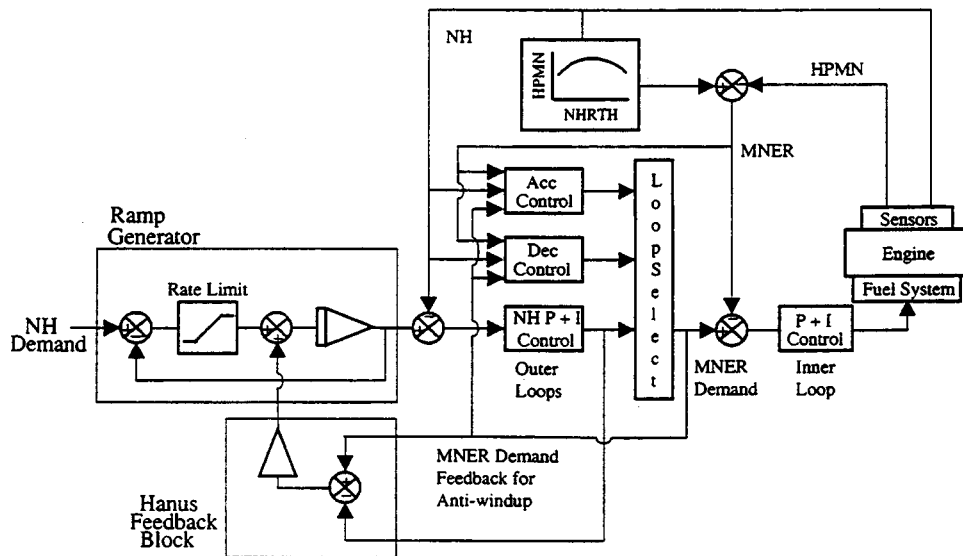


Fig. 3 Engine control law using MNER selection

3 Under all steady-state and transient engine conditions the primary loop will act, initially, in such a way as to reduce fuel flow in the event of surge.

The control structure chosen for the engine tests is shown in greater detail in Fig. 3. The inner/outer loop configuration follows the suggestions made above in all respects. Note that the parameter selected to provide the inner closed-loop control is the HPC exit Mach number (HPMN) as recommended by Dadd et al. [5,6]. HPMN is a direct compressor working point measure, i.e.

$$HPPR = f(W\sqrt{T/P}),$$

maps into

$$HPMN = g(NH/\sqrt{T}),$$

which is invariant provided compressor geometry does not change. Moreover, it can be shown that HPMN shows approximately two to three times the sensitivity to displacement from the working line than does HPC pressure ratio, while having an extremely low turn-down ratio over the engine operating range. Since it also shows rapid dynamic response to fuel flow changes, HPMN is considered an acceptable candidate parameter for the inner loop control in accordance with the statements (a) and (b) above. More significantly, HPMN exhibits *constructive* behavior in the presence of surge and therefore meets requirement (c). This surge behavior and a demonstration of successful surge recovery have been described by Dadd and Porter [5].

Engine thrust level in these tests is determined by outer loop control of HP compressor speed (NH) from pilot's lever command. The choice of NH has no particular significance to either the relevance of the demonstration or to future fuel system work. HP compressor acceleration (NHdot) control is applied as a rate limit on the outer loop command. Additional outer loops (acceleration and deceleration) for HPMN limiting, which restrict HPMN deviation during fast engine transients, override the NHdot acceleration control if the predicted boundaries for surge or flame-out are encountered. The surge and flame-out limits are applied to these outer Mach number loops for acceleration and deceleration. Not shown in the diagram are other limiting control loops, such as turbine blade temperature control, which are applied as other outer loops, replacing the thrust control loop at high temperature conditions. Selection of the outer control loop from those competing is achieved through the action of lowest and highest wins signal gates.

Controller Design. The control structure selected on the basis of the arguments presented in the last section means that the inner (Mach number) loop is common to all of the dry engine control loops, which include the outer NH governor loop, the NHdot acceleration and deceleration loops. Mach number limiting loops, and other temperature and pressure limiter loops.

This control mode has been shown to be fundamental to the success of the fuel system simplification concept (refer to control law configuration section). In the event that engine HPMN should approach a limit set to define surge, for whatever reason, then control is switched from the speed control loop and one of the MNER limiting loops must accept full authority for the control of fuel flow. Operation in the Mach number acceleration control mode maintains surge margin by restricting HPMN excursions, or MNER, to a defined limit, ALMT. Two design schemes were developed for comparison. Their differences are explained here.

Acceleration Control Via Mach Number Error Selection. In this control scheme, the outer loops output Mach number error (MNER) demands selection. Figure 3 shows the overall block diagram of this scheme. A Hanus (Hanus, Kinnaert, and Henrotte [7]) feedback block and a demand ramp generator were included. The Hanus block prevented the integrator in the demand ramp generator from winding up when the main speed loop lost control to either of the Mach number limiting loops.

The Mach number dynamic limiting control blocks (namely "Acc Control" and "Dec Control" in the figures) are primarily proportional plus integral (*P+I*) controllers which compare the MNER feedback with scheduled limits and deliver the demands for selection. With the right set of gains, one of these demands will become dominant when the scheduled limit is reached. A Hanus feedback block is also incorporated to maintain an appropriate integrator output when the loop is not selected.

Acceleration Control Via NHdot Selection. Figure 4 shows an overall block diagram of this second method of Mach number control. It is very similar to the first scheme: the main differences are change of the parameter used for loop selection and removal of the inner loop feedback path. The selection of the loop in control of the engine is now the parameter NHdot demand instead of Mach number error demand. This method eliminates the necessity for an integrator in the main speed control loop with its inherent need for resetting during a transient.

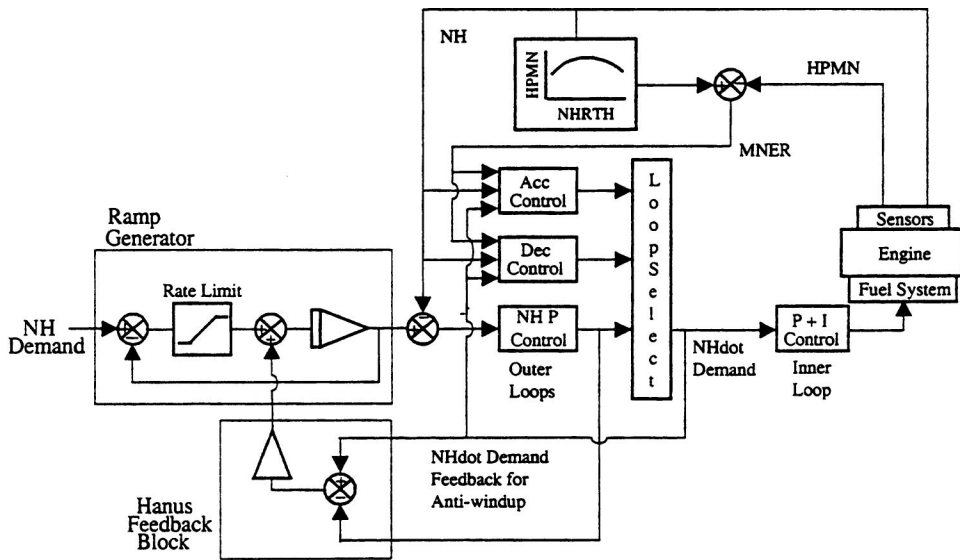


Fig. 4 Engine control law using NHdot selection

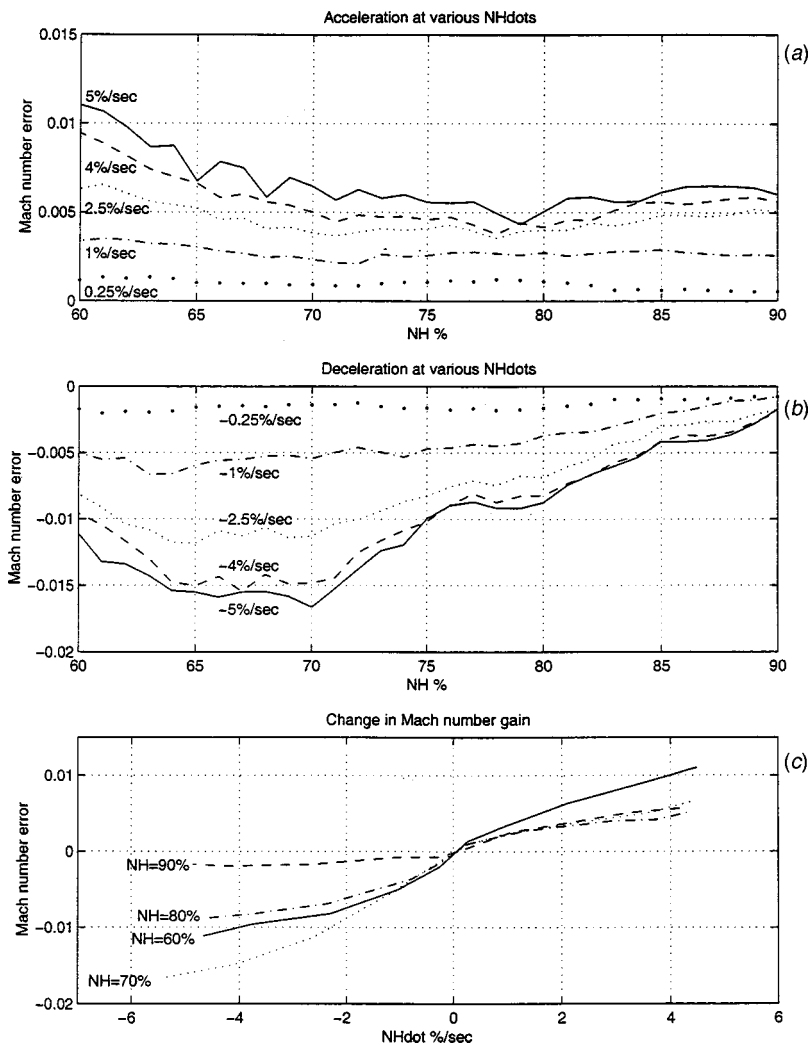


Fig. 5 Mach number signal characteristics

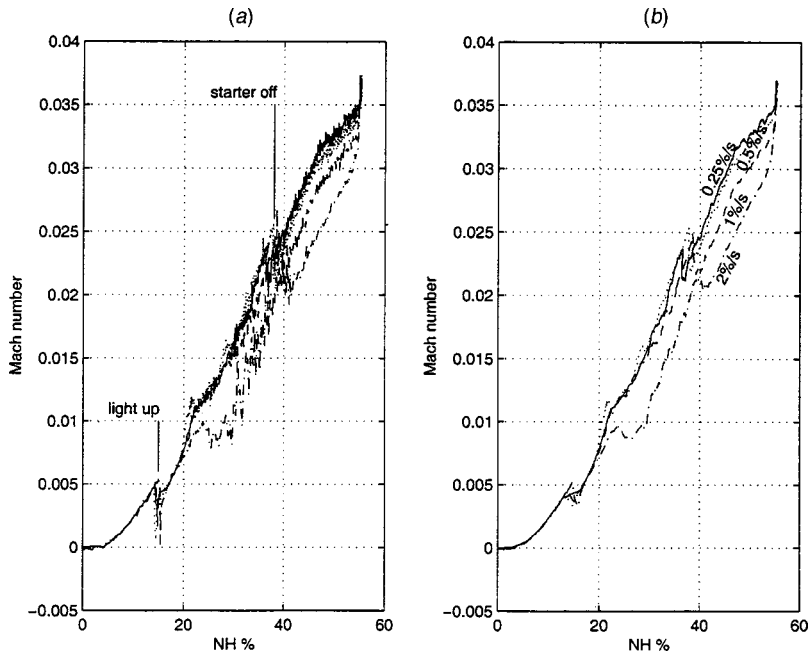


Fig. 6 Mach number signal from various NHdot starts

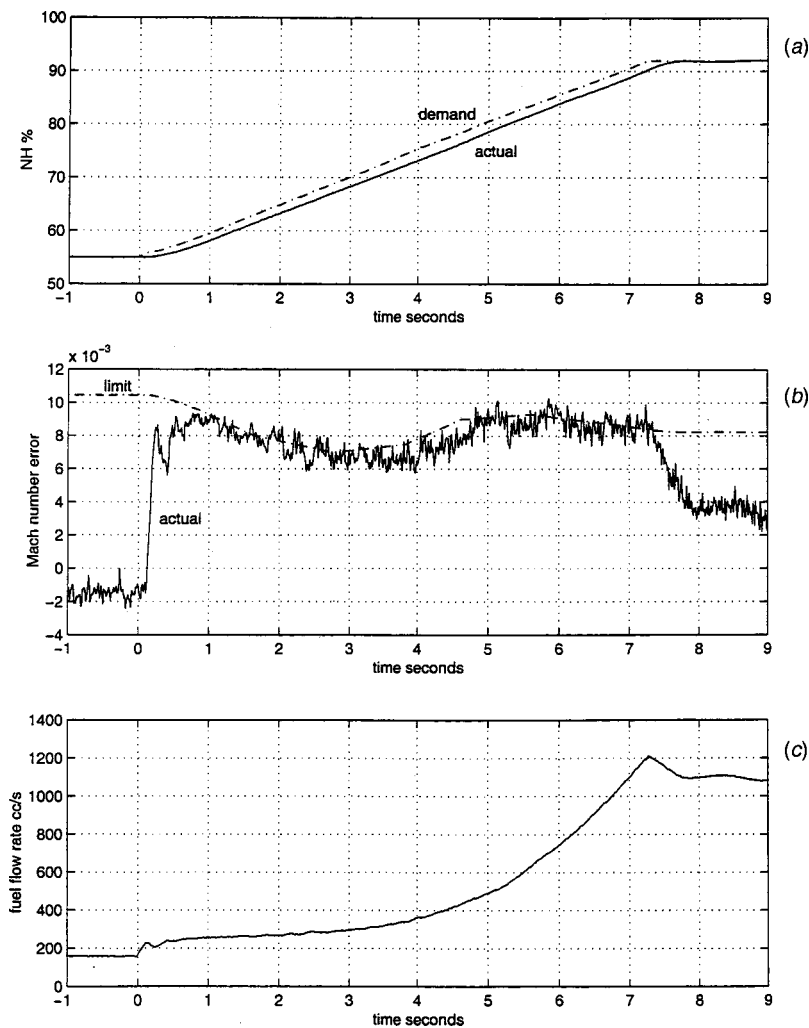


Fig. 7 HPMN acceleration control using MNER selection

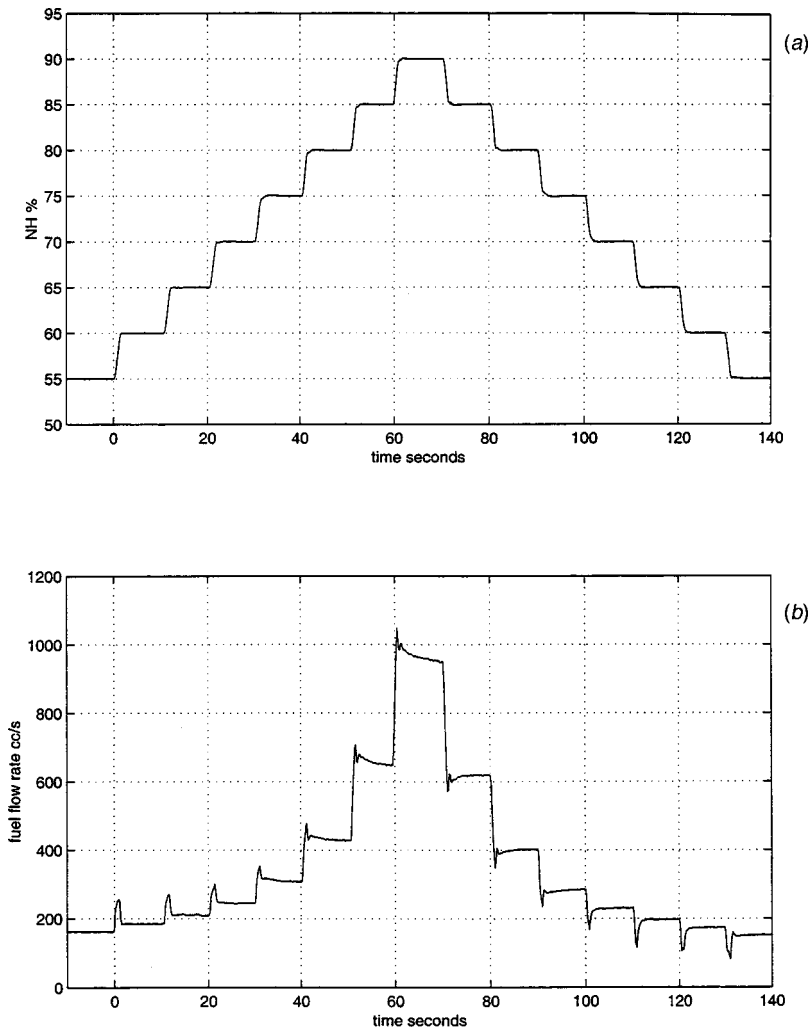


Fig. 8 NH governor performance under HPMN control

The Mach number dynamic limiting control blocks for this scheme have identical structure to those used in the first scheme.

Start Control. Due to time and financial constraints, only one of the two control schemes was tested in the engine starting regime. The controller with the NHdot selection (Fig. 4) was chosen.

Since the Mach number controller will only be effective when combustion is confirmed and when the influence of the air starter has subsided, the following criteria have to be satisfied before control can commence.

1 The igniters must have ignited the fuel; this was detected by observing a pre-determined increase in T6.

2 The engine acceleration rate must have been reduced to that set by the controller. The air starter produces an initial acceleration much higher than achievable by burning the start fuel alone. This extra check before the closed-loop control took over attempts to prevent the start fuel flow being reduced by an appreciable amount during the start.

As the differentiation of NH to derive NHdot produces a very noisy signal, a first-order low pass filter was used to smooth this parameter. During the period before closed-loop engine control is activated, the start fuel schedule is used. Simultaneously, the integrators of the control loops are initialized.

In these tests, a volume flow meter was used to set light-off fuel level. This represents the only remaining requirement for open-

loop scheduling of fuel, assuming that the concepts presented in this paper are an acceptable alternative when the engine is operating. Future work will address how the light-off requirements can best be met without recourse to reintroduction of significant hardware complexity.

Engine Test Result and Analysis

The main objectives of the trial were to verify the Mach number control schemes, and to test the feasibility of Mach number control during the starting of a gas turbine engine. Prior to the trial of the controllers, the schedules for HPMN and MNER limit have to be constructed using data from engine identification.

Engine Identification. Above idle conditions, the engine characteristics were obtained by analyzing data from a series of engine manoeuvres. Figures 5(a) and 5(b) show the recorded data from a series of accelerations and decelerations at various rates of change in NH. Figure 5(c) shows the Mach number deviation plotted against NHdot for selected values of NH.

All lines show an apparent increase in gain near the steady-state condition, which may be associated with the heat soaking effect. These results also highlight the different gains during deceleration, compared with the almost constant gain during acceleration. It is not known if these results are typical or due to the total and static probes measuring Mach number being located on opposite sides of the engine as a result of physical constraints.

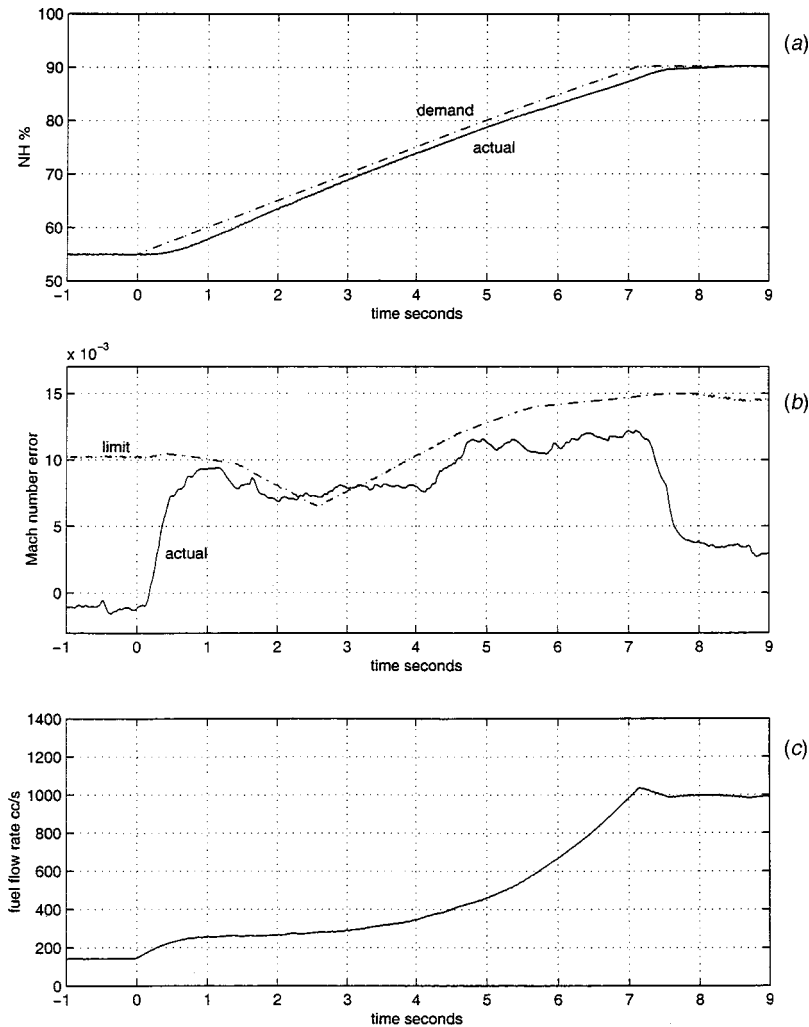


Fig. 9 HPMN acceleration control using NHdot selection

During the tests described in this paper, the single control gain used was the mean value of the gains required for all acceleration deceleration rates. This did not take into account the sense of the Mach number error signal. On reflection it may have been prudent to account for the nonlinearity shown in Fig. 5(c) when choosing control gains. Oscillations during decelerations through 70 percent NH were observed, which were subsequently resolved by reducing the loop gains.

It is difficult to identify the characteristics of the engine in the range below idle, and in particular the range below the self-sustaining speed. The main method chosen for this regime was to start the engine under NHdot control with the rate set to 2, 1, 0.5, and 0.25 percent/s. It was arranged that the control would not come into action until the achieved NHdot was less than the value in demand. The results from these starts are shown in Fig. 6(a).

It is difficult to extract meaningful results from this figure because of the noise on the traces, although it can be seen that the Mach number signal gives a good indication of engine light up. The data of Fig. 6(a) are replotted in Figure 6(b) following filtering to reveal more clearly the underlying trends.

The first point to note is that the Mach number signal has possibly shown up some form of stall (indicated by the significantly lowered Mach number) occurring at about 25 percent NH during the 2 percent/s start. Secondly it can be seen that below 30 percent NH there is no noticeable difference in the Mach number signals from the 1, 0.5, and 0.25 percent/s starts. Between 30 percent and 38 percent (where the starter disengaged) there is a small deviation

in the Mach number. Without assistance from the starter motor (i.e., above 40 percent NH) there is a considerable change in the Mach number signal with NHdot thus allowing it to be used confidently for Mach number control after this event.

From this set of data, a steady-state Mach number relationship was estimated. To avoid a possible engine stall, a Mach number limiting schedule was also chosen to give approximately a 1 percent/s acceleration rate. Trials of engine start control are discussed in the section on "Starting Under Mach Number Control."

Acceleration Control Via Mach Number Error Selection (Idle and Above).

One of the main aims of the Mach number control law was to achieve accurate Mach number excursion control. The control scheme (Fig. 3) was tested by setting the Mach number error limit, ALMT, to a level predicted to correspond to an acceleration NHdot of 5 percent/s and increasing the requested NHdot to 5.5 percent/s. Figure 7 shows that the acceleration of 5 percent/s was achieved (Fig. 7(a)) and the Mach number error (MNER) is controlled to the required limit (ALMT) with good accuracy (Fig. 7(b)). The overall control stability was also demonstrated (see Fig. 8) during a series of 5 percent step changes ("stair case" test) in demand speed. By normal control standards these are good control responses.

Acceleration Control Via NHdot Selection (Idle and Above).

The test described in the previous section was repeated with the control architecture shown in Fig. 4. This simpler control scheme

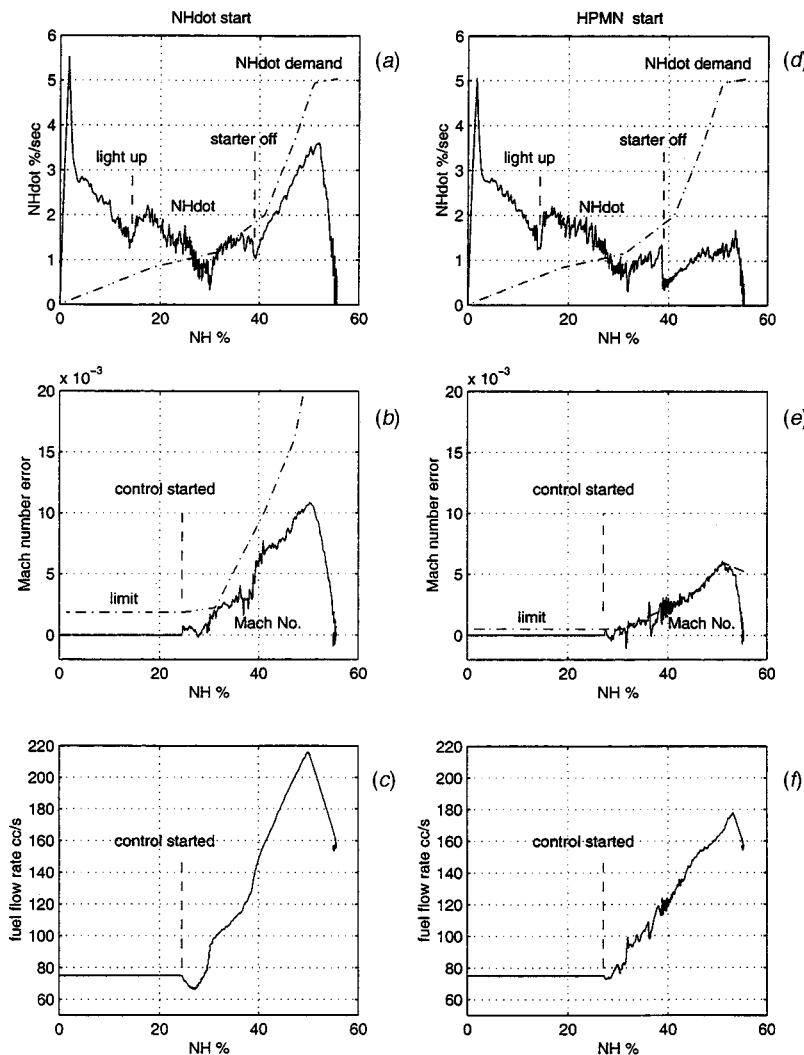


Fig. 10 Mach number control start with NHdot selection

did not perform as well as the first scheme, as is shown in Fig. 9. Here the acceleration control loop (“Acc Control” block in Fig. 4) tended to keep control even though the Mach number error was significantly below its limiting value (between 5 and 7/s in Fig. 9(b)). In addition, the gains for acceptably stable control were not high enough for good responsive handling. It is apparent at the beginning that the Mach number changed slower (Fig. 9(b)) and the fuel flow rate (Fig. 9(c)) did not increase as fast as the responses (Fig. 7(b) and 7(c)) obtained previously. The overall control stability was also checked to be comparable with previous results.

Starting Under Mach Number Control. Figure 10 shows two engine starts under the NHdot controller and the Mach number controller separately. In both cases the results are plotted against NH to allow direct comparisons to be made without the complexity of a differing times to reach idle.

Figures 10(a), 10(b) and 10(c) show the start under conventional NHdot control. During these tests the closed-loop control of fuel demand starts when the engine is alight and the achieved NHdot is less than the demanded value (Fig. 10(a)). For future application, a highest wins selection between the fixed starting fuel flow and the output of the controller can be applied, once light-up has been identified. It can be seen that in this particular start, the controller started prematurely as indicated by the fuel flow (Fig. 10(c)) dropping below its starting value for a brief

period of time. This was most likely due to a noise spike on the computed NHdot signal. The demanded NHdot (Fig. 10(a)) was achieved up to the point when the starter automatically disengaged (at around 38 percent NH). After this point the demanded NHdot rises rapidly, which the achieved value never quite meets. For this start the Mach number control limit (Fig. 10(b)) was raised to prevent unwanted selection which would have corrupted the desired results.

Figures 10(d), 10(e), and 10(f) show a Mach number controlled start with the Mach number limit scheduled against NH (Fig. 10(e)) to maintain nominally a 1 percent/s NHdot as described in the engine identification section. In this start the change over to closed-loop control operated as expected and the fuel flow (Fig. 10(f)) increased from its initial light-off value (unlike the experience with the NHdot control). The Mach number error (Fig. 10(e)) tracks the limit value very successfully, and the achieved NHdot (Fig. 10(d)) was near to the intended value (1 percent) except when the starter disengaged. While there was no noticeable change in Mach number error, or fuel flow, there was a large step change in NHdot. The limiting value of Mach number error is scheduled against NH and was set to be a smooth line with no discontinuities. If the Mach number limiting schedule was set to respect compressor operating boundaries, faster, safe, and reliable starts might be achieved.

While these tests demonstrated that starting could be achieved

using Mach number control, it was not considered sufficiently robust for normal use below the self-sustaining condition due to the insensitivity of the feedback signal.

Conclusion

It is sufficient here to note that, being based on closed-loop control of appropriate engine parameters, the Mach number limiters (working line controls) can be designed to be independent of fuel metering accuracy or variable geometry position control accuracy. This implies that the working line controls will be effective despite engine degradation which affect the open-loop engine calibrations.

The work at DERA Pyestock has confirmed engine parameter, HPMN, which is sensitive to working line displacement and has dynamic characteristics suitable for surge avoidance and control. This parameter is said to be *constructive* in their response to surge in that it responds in a sense that causes the closed-loop working line control to reduce fuel flow.

In the Mach number controller design, two Mach number dynamic limiting blocks (for acceleration and deceleration) have been incorporated into the outer loop, which aim to provide accurate control of Mach number during fast engine transients. With this basic design, two control schemes of different architectures have been developed for comparison.

By using dynamic instead of static limiting of Mach number error, the first control scheme (Fig. 3, Acceleration control via MNER selection in the Acceleration control via Mach number error selection section) achieved accurate control of Mach number. The control of the Mach number becomes independent of the inner loop gain, which will allow flexible Mach number control design. Therefore, the control of the working line of the high pressure compressor can be improved. The second scheme tested (Fig. 4, in the Acceleration control via NHdot selection section) did not perform as well as the first in terms of Mach number accuracy. However, both control schemes achieved good control stability.

Engine starting with Mach number control was demonstrated, but only considered really practical at speeds greater than self-sustaining level (i.e., without starter assist). Below this level, the gain between Mach number error and NHdot becomes too small for reliable control application. It is most probable that NHdot control will be adequate below this condition but some strategy for achieving light-off fuel flow will be needed. In order to secure the fuel system simplifications being pursued in this paper, this strategy will have to operate without a requirement for accurate scheduling. This remains the target of current research at DERA Pyestock.

Acknowledgments

The technical research documented in this paper was conducted by DERA Pyestock in the last three years under different programs funded by DTI CARAD and MOD. The researchers included M. J. Porter, A. G. Shutler, and the authors. This is a joint paper between DERA and Frazer-Nash Consultancy Ltd.

Nomenclature

ALMT	=	Mach number error limit during engine acceleration
dP3	=	Dynamic pressure at high pressure compressor exit, Pt3-Ps3 (KPa)
HPC	=	High pressure compressor
HPMN	=	HPC exit Mach number represented as dP3/Pt3
MNER	=	Mach number error
NH	=	High pressure compressor spool speed (percent)
NHdot	=	Rate of change of NH (percent/sec)
NL	=	Low pressure compressor spool speed (percent)
P	=	Proportional
P+I	=	Proportional plus integral
PI	=	Engine intake pressure (KPa)
PR	=	Engine pressure ratio
Ps3	=	High pressure compressor exit static pressure (KPa)
Pt3	=	High pressure compressor exit total pressure (KPa)
T	=	Flow temperature (°K)
W	=	Mass flow rate (kg/s)

References

- [1] Toyne, G. B., and Hodges, G. S., 1983, "All-Electric Accessory Drive Systems: Implications on Engine Design and Performance," AGARD Conference Proceedings No. 352.
- [2] Cronin, M. J., 1983, "All Electric vs Conventional Aircraft: The Production/Operational Aspects," J. Aircr., **20**, No. 6.
- [3] Chan, K. K., 1998, "More Electric Engine Controls Technology Report," DERA Technical Report.
- [4] General Electric Company, 1967, "Improvements in Control Systems for Axial Flow Compressors, Particularly Adapted for Use in Gas Turbine Engines," British Patent 1184369.
- [5] Dadd, G. J., and Porter, M. J., 1992, "Surge Recovery and Compressor Working Line Control using Compressor Exit Mach Number Measurement," Proceedings, Aerotech '92 Conference, Session 33.
- [6] Dadd, G. J., Shutler, A. G., and Greig, A. W. M., 1993, "Pump and Tap Control Laws using an HP Compressor-based Inner Loop," DRA Technical Memorandum Aero/Prop 30.
- [7] Hanus, Kinnaert, and Henrotte, 1987, "Conditioning Technique, a General Anti-windup and Bumpless Transfer Method," Automatica, **23**, No. 6.

Uncertainty Reduction in Gas Turbine Performance Diagnostics by Accounting for Humidity Effects

K. Mathioudakis
Associate Professor

T. Tsalavoutas
Research Assistant

Laboratory of Thermal Turbomachines,
National Technical University of Athens,
Iroon Polytechniou 9,
Athens 15773, Greece

The paper presents an analysis of the effect of ambient humidity on the performance of industrial gas turbines and examines the impact of humidity on methods used for engine condition assessment and fault diagnostics. First, the way of incorporating the effect of humidity into a computer model of gas turbine performance is described. The model is then used to derive parameters indicative of the "health" of a gas turbine and thus diagnose the presence of deterioration or faults. The impact of humidity magnitude on the values of these health parameters is studied and the uncertainty introduced, if humidity is not taken into account, is assessed. It is shown that the magnitude of the effect of humidity depends on ambient conditions and is more severe for higher ambient temperatures. Data from an industrial gas turbine are presented to demonstrate these effects and to show that if humidity is appropriately taken into account, the uncertainty in the estimation of health parameters is reduced. [DOI: 10.1115/1.1470485]

Introduction

Use of monitoring systems for assessing the condition of a gas turbine and its components is widespread today. Such systems provide substantial information, which helps, on one hand, minimizing outages and on the other hand optimizing engine usage. It is thus desirable that the information provided is as accurate and as reliable as possible.

Current day trends favor the implementation of monitoring and diagnostic procedures with a high degree of automation, minimizing the need for specialized personnel. Moreover, it is recognized that on-line implementation gives a substantial benefit to engine operators. Cases of on-line systems operating in industrial gas turbines have been reported by Andersen [1], Gulen et al. [2], and Razak and Carlyle [3], who have commented on advantages over off-line processing. In the case of on-line systems with high degree of automation, it is important that the techniques employed provide information with a high confidence level and do not produce false alarms.

In order to achieve high accuracy, all possible factors influencing performance should be accounted for. One factor which is often considered to not influence performance significantly is ambient humidity. Many gas turbines operate in environments in which absolute humidity is very small, does not vary significantly and has therefore small influence on performance (as, for example, reported by Cloyd and Harris [4]). This is the reason why ambient humidity effects have not received much attention in industrial gas turbines. On the contrary, the stringent requirements posed on aviation gas turbines have led to numerous investigations on ambient humidity effects. An extensive reference to such effects has been given in AGARD-AR-332 [5], while effects of humidity on jet engines have been studied by Bird and Grabe [6] and Gu and Palmer [7]. A presentation of such effects for jet engines and aero derivative gas turbine gas turbines has been given by Walsh and Fletcher [8].

The purpose of the present paper is to investigate the impact of the presence of air humidity on monitoring procedures for industrial gas turbines. Humidity effects are first discussed and the way

of introducing them in engine models is presented. Influence of humidity level on the values of monitored parameters and their interrelations is then examined. The predictions are substantiated through measurement data from an operating gas turbine.

Study of these effects, their incorporation into monitoring procedures and relevant measurement data have not been previously presented in the open literature to the knowledge of the authors.

Modeling Humidity Effects on Gas Turbine Performance

Humidity influences the performance of a gas turbine because it changes the thermodynamic properties of the working medium, which is a mixture of dry air and water vapor. This means that the interrelations between various thermodynamic quantities characterizing engine performance will be modified accordingly. In the following, the way of incorporating humidity effects in gas turbine calculations will be outlined. The particular approach followed by the authors in the present work will be highlighted.

The effect of different levels of humidity on the values of measured quantities can be evaluated with the aid of an engine model. By using a component-based computer engine model, values of measured quantities can be computed and compared for different humidity levels. The case of a twin shaft gas turbine is analyzed here. This particular configuration is chosen for the reason that test data are available from such an engine, and will be used later in the paper to demonstrate the principles discussed. The layout of such a turbine, indicating the subdivision into main modules for modeling purposes is shown in Fig. 1. The discussion is general enough, however, and gives the basis for implementation to any type of gas turbine.

The model is formulated as a solver of a set of nonlinear equations, relating various thermodynamic quantities at the inlet and outlet of engine components, ensuring compatibility between their operation. Modifications introduced in order to account for humidity are mainly in two levels:

- All calculations of thermodynamic processes use properties (C_p , R , γ) of a working medium which is considered to be a mixture of air and water vapor. Mixture properties are calculated on the basis of its constitution according to well-known principles of thermodynamics. The water content is taken into account through the magnitude of absolute humidity, also called water-air ratio, defined as the ratio of water vapor to dry air mass:

Contributed by the International Gas Turbine Institute (IGTI) of THE AMERICAN SOCIETY OF MECHANICAL ENGINEERS for publication in the ASME JOURNAL OF ENGINEERING FOR GAS TURBINES AND POWER. Paper presented at the International Gas Turbine and Aeroengine Congress and Exhibition, New Orleans, LA, June 4–7, 2001; Paper 01-GT-010. Manuscript received by IGTI, December 2000, final revision, March 2001. Associate Editor: R. Natole.

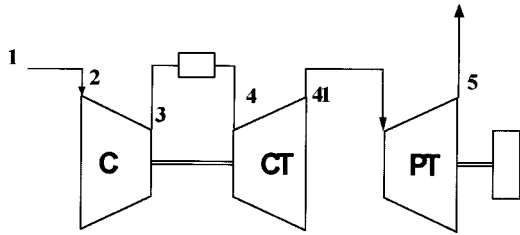


Fig. 1 Layout of twin shaft gas turbine, used for constituting a component based performance model

$$\text{WAR} = \frac{m_w}{m_{d,a}} \quad (1)$$

This quantity may be derived in different possible ways, as for example from relative humidity measurement or from dry and wet bulb temperature measurements. Relations for estimating the difference if C_p , R , γ , between wet and dry air are derived in Appendix A.

• Calculation of component performance parameters is based on performance maps for each component with dry air as working medium, by applying appropriate transformations to include humidity. The relations used to transform quantities for dry air operation to quantities for wet operation are based on methods reported in AGARD [5] and are as follows:

Compressor

$$\left(\frac{N}{\sqrt{T}} \right)_w \bigg/ \left(\frac{N}{\sqrt{T}} \right)_d = \sqrt{R_w \cdot \gamma_w / R_d \cdot \gamma_d} \quad (2.1)$$

$$\left(\frac{W\sqrt{T}}{P} \right)_w \bigg/ \left(\frac{W\sqrt{T}}{P} \right)_d = \sqrt{R_d \cdot \gamma_w / R_w \cdot \gamma_d} \quad (2.2)$$

$$\left(\frac{\Delta h}{T} \right)_w \bigg/ \left(\frac{\Delta h}{T} \right)_d = R_w \cdot \gamma_w / R_d \cdot \gamma_d \quad (2.3)$$

Turbines

$$\left(\frac{N}{\sqrt{T}} \right)_w \bigg/ \left(\frac{N}{\sqrt{T}} \right)_d = \sqrt{R_w \cdot \gamma_w \cdot (1 + \gamma_d) / R_d \cdot \gamma_d \cdot (1 + \gamma_w)} \quad (3.1)$$

$$\left(\frac{W\sqrt{T}}{P} \right)_w \bigg/ \left(\frac{W\sqrt{T}}{P} \right)_d = \sqrt{\frac{R_d \cdot \gamma_w}{R_w \cdot \gamma_d} \cdot \left(\frac{2}{1 + \gamma_w} \right)^{(\gamma_w + 1)/(2 \cdot (\gamma_w - 1))} \cdot \left(\frac{1 + \gamma_d}{2} \right)^{(\gamma_d + 1)/(2 \cdot (\gamma_d - 1))}} \quad (3.2)$$

$$\left(\frac{\Delta h}{T} \right)_w \bigg/ \left(\frac{\Delta h}{T} \right)_d = R_w \cdot \gamma_w \cdot (1 + \gamma_d) / R_d \cdot \gamma_d \cdot (1 + \gamma_w) \quad (3.3)$$

Subscript d in all the above relations denotes properties of working medium at the corresponding component, when the air at gas turbine inlet is dry. Subscript w denotes the same quantities in operation with wet air at gas turbine inlet.

When data from operation at different ambient conditions (pressure, temperature, and humidity) are to be compared, they should be referred to the corresponding quantities at some reference condition. Such comparisons need usually to be done when analyzing measurement data from different time instants. The above relations can serve as a basis for deriving referred (corrected) quantities for this purpose. We will choose dry air at standard day as a reference.

A direct consequence of Eqs. (2.1) and (2.2) is that referred (corrected) rotational speed and mass flow rate will be

$$N_{\text{cor}} = N \bigg/ \sqrt{\frac{\gamma \cdot R}{1.4 \times 287} \cdot \theta} \quad (5.1)$$

$$W_{\text{cor}} = \frac{W}{\delta} \sqrt{\frac{R}{287} \times \frac{1.4}{\gamma} \cdot \theta} \quad (5.2)$$

Concerning temperature, given that $\Delta h = C_p \Delta T$, Eq. (2.3) can be used to show that temperature ratio depends only on γ . For applications involving ambient humidity, it is shown in Appendix A that changes in γ are very small and in any case about one order of magnitude smaller than changes in R . We can therefore consider that temperature ratio does not change, which gives the following formula for corrected temperature:

$$T_{\text{cor}} = T / \theta \quad (5.3)$$

Similar arguments can be used for pressure. Using a generalized relation (given, for example, by Walsh and Fletcher [8]) the corrected pressure can be given by the following relation:

$$P_{\text{cor}} = \left(1 + \frac{\gamma - 1}{0.4} \left(\left(\frac{P}{\delta} \right)^{\gamma - 1/\gamma} - 1 \right) \right)^{3.5} \quad (5.4)$$

Finally, corrected power can be derived using relations for referred mass flow and temperature:

$$P_{\text{cor}} = P \bigg/ \frac{\gamma}{1.4} \cdot \delta \sqrt{\frac{\gamma}{1.4} \cdot \frac{R}{287} \cdot \theta} \quad (5.5)$$

It is understood from the discussion above that the change in performances is directly dependent on the change of the properties of the working medium. Changes of air properties are proportional to water-air ratio. It is the value of this parameter therefore which will determine how much deviation from dry air performances is expected. This parameter is the one which will be used for presenting the effect of humidity in the following. Relative humidity, although a customary humidity measure, because of its relevance to human comfort and process industries, is not appropriate in this case. For the same relative humidity, different inlet temperatures will provide different water-air ratios.

Effect of Humidity on Quantities Used for Monitoring

The presence of humidity in the compressor inlet air results in a change of the engine cycle for certain operating conditions. This means that quantities measured for monitoring will have different values from those for dry inlet air operation. Monitoring techniques based either on direct observation of measured quantities or on parameters derived from them will thus be influenced.

Effect on Measured Quantities. The percentage change of various quantities that can be measured, for different humidity levels is shown in Fig. 2. The abscissa in this figure is the absolute humidity (= water/air ratio), preferred for the reasons explained previously. The range of values of absolute humidity is the one considered to be of practical interest for gas turbine operation ([8]). For reasons of comparison the corresponding relative humidity for different temperatures, dry bulb of 15, 25, 35°C, is indicated above the upper abscissa axis.

The changes presented in this figure have been estimated with the aid of the engine performance model for given inlet pressure and temperature and for operation holding different operating parameters constant, namely power output, gas generator speed N_{GG} , turbine inlet temperature (TIT), and exhaust gas temperature (EGT). Some remarks to the use of such quantities for monitoring are

- The change in various quantities, for humidity changes expected to occur in the field, may be rather large and quite larger than expected measurement uncertainty for the corresponding quantity. For example, for constant turbine inlet temperature, a load variation of about 1% is expected for a change in absolute humidity from 0.015 to 0.025 (Fig. 2b).

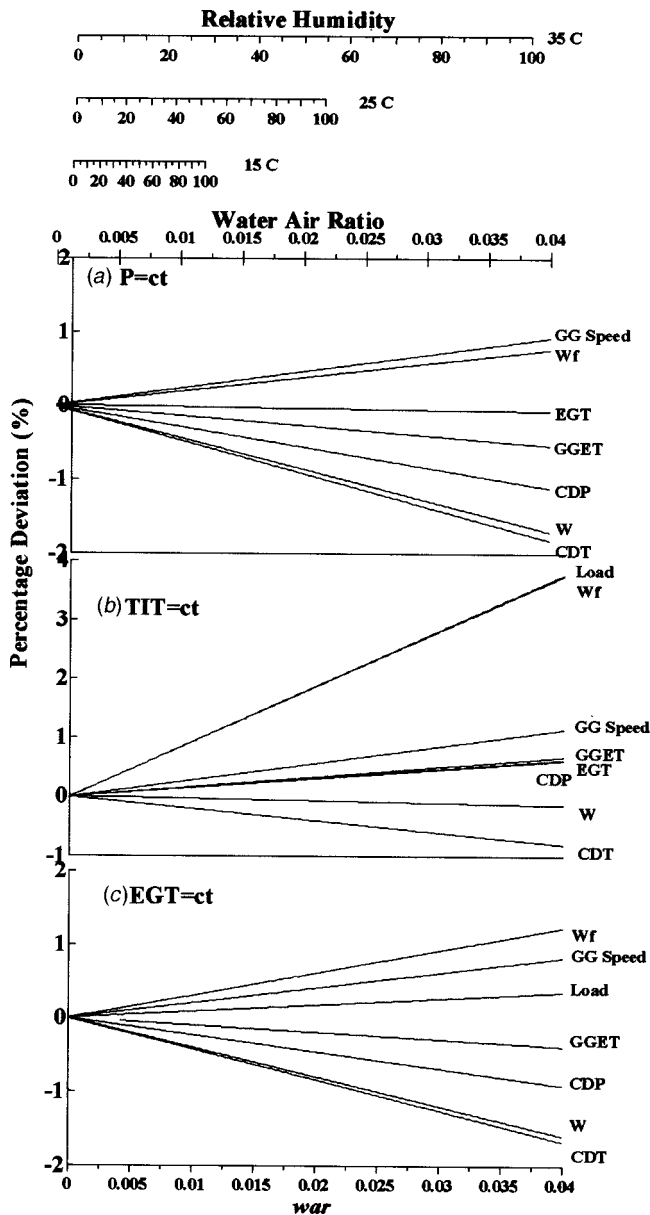


Fig. 2 Percentage change of performance related quantities, in function of water/air ratio. Changes evaluates at constant (a) power output, (b) TIT, (c) EGT.

- The way the different quantities change depends much on how the differences are taken, namely on which quantity is held constant. For example, compressor delivery pressure decreases with increasing humidity, when power output is held constant, while it increases, when comparison is done at given TIT.

The results shown correspond to a high power setting. It was found that the trends remain the same, with minor changes in magnitude, at part power settings.

The results shown here are in agreement with the trends of the results presented by Bird and Gabe [6]. It must be noted, however, that the parameter changes they presented, mainly for aircraft engines, have shown a considerable variability for different types of engines.

The interrelations of Fig. 2 are derived by keeping the actual parameter constant, for certain inlet pressure and temperature. In practice, data are usually available from operation at different ambient conditions. It is thus useful to refer all quantities to the same conditions and derive signatures from the values of referred pa-

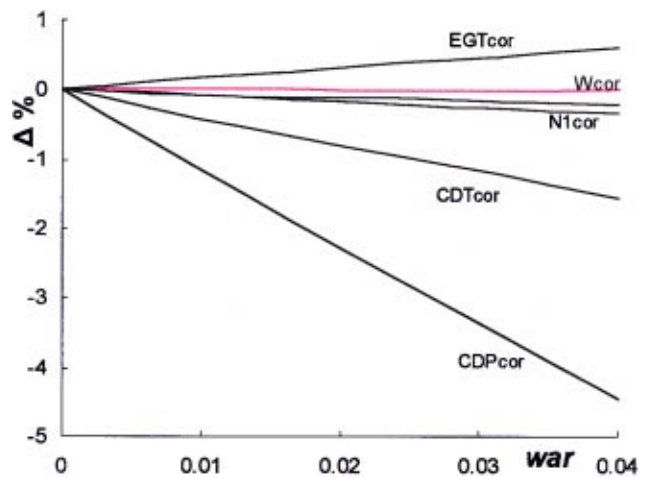


Fig. 3 Percentage change of referred quantities for constant referred load

rameters. The dependence of corrected parameters on WAR can be derived also with the help of a model. An example of such a dependence for constant corrected load, obtained by using an engine model, is shown in Fig. 3. It can be seen that the variation of referred quantities for constant referred load does not show the same trend as the actual values of Fig. 2(a). For example, CDP_{cor} comes as the most sensitive quantity, while for constant load com-

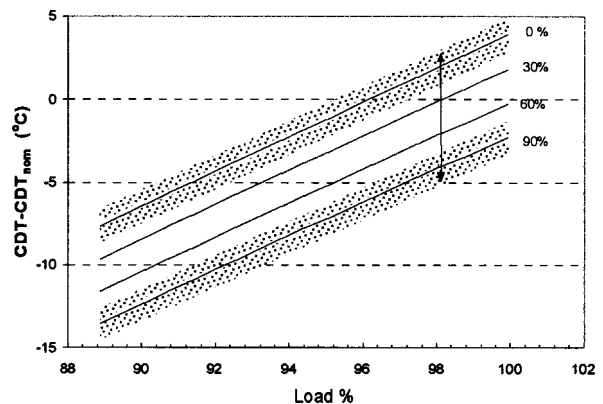


Fig. 4 Interrelation of compressor delivery temperature and power output for different relative humidity levels, and related uncertainty bands

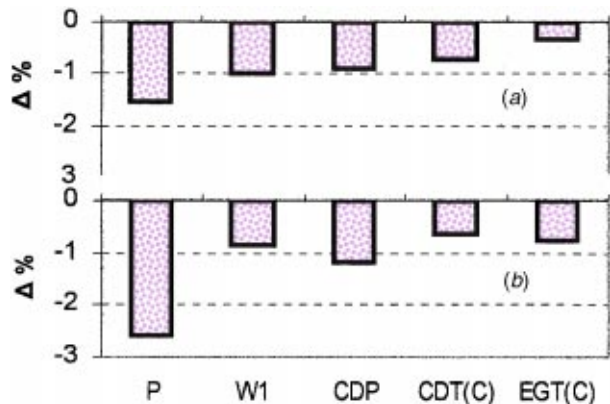


Fig. 5 Measurement deviations: (a) WAR=0.009 (b) IGV fault. Signatures for N1 constant.

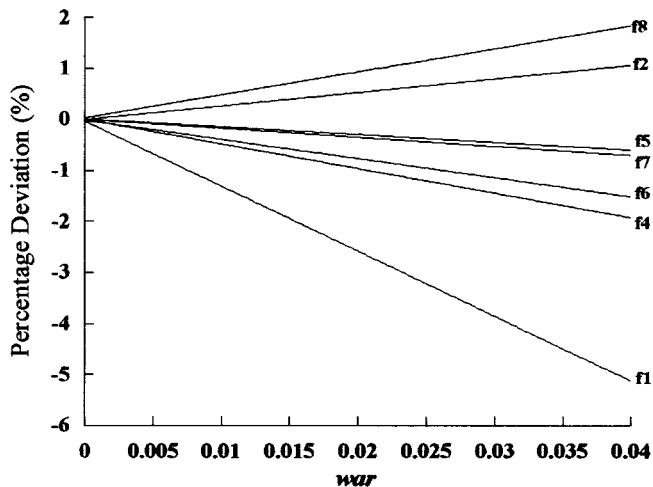


Fig. 6 Deviation of modification factors if humid air data are processed by adaptive model with dry air

pressor delivery temperature (CDT) was the most sensitive, Fig. 2(a). Trends for EGT_{cor} and $N1_{cor}$ are in a direction opposite to the ones of EGT and $N1$ for constant load.

It can be now shown that the band of uncertainty within which the values of measured quantities are considered acceptable will be larger, if humidity effect is not taken into account. Let's take for example compressor delivery temperature. The relation of CDT to engine load for dry inlet conditions is shown in Fig. 4.

An uncertainty band is related to this interrelation, because of measurement uncertainties in both power output and pressure measurement. It is indicated by the shaded area around the corresponding line. The meaning of this uncertainty band is that, for values within it, it cannot be sure whether a deviation was actually caused by change in condition of a component or if it is merely a measurement error. If now the possibility of having different inlet humidity levels has to be encountered for, then the width of this band increases, as shown in Fig. 4. The reason for this increase is that for a given load, the compressor delivery temperature will be different for different humidity levels, as shown in the figure. Adding to that the uncertainties mentioned above, gives the larger uncertainty band, for "healthy" engine operation. The range of values which will have to be considered as "healthy" is quite large.

A direct consequence of this fact is that if humidity is not accounted for, the ability for diagnosing malfunction is reduced, when based on performance quantity interrelations. It is obvious that large uncertainties will "bury" measurements deviations until their cause is more severe than it would have if humidity was taken care of. A different kind of consequence may be as follows: if variation of measured quantities is monitored, changes caused by humidity may be large enough to be misinterpreted as the occurrence of a fault, and thus have a false alarm.

Effect on Measurement Deviation Patterns. The simplest form of engine monitoring consists in observing the values of various measured quantities and see if they exhibit changes from their expected values, at certain operating conditions (see for example, [9,10]). The pattern of changes in these measured values can be used as a "signature" for identifying the engine fault that caused them.

As we have seen, measurements for operation with wet air differ from those with dry air, as demonstrated in Fig. 2. This means that change in humidity will actually produce a pattern of deviations, such as the one of Fig. 5(a). The existence of such a pattern may have two types of negative effects in a diagnostic procedure: (a) it may overlap with a fault pattern and alter its signature, so that it cannot be recognized, (b) it may mistakenly be taken as a

fault (false alarm). In Fig. 5(b), the signature of a possible variable geometry IGV fault (see [10]) is shown. It can be observed that the two signatures of the figure are similar.

If a monitoring procedure based on the recognition of difference patterns is employed, the occurrence of patterns like the ones mentioned above may thus present a difficulty in producing a diagnosis (such methods have been, for example, proposed in [9,11]). It will be shown later how such shortcoming can be overcome.

Component Health Indices. Effects on methods based on component "health indices" will now be discussed. A technique of this kind is the method of adaptive modeling. Its general principles have been introduced by Stamatis et al. [12,13] and are summarized in Appendix B, for completeness of the present paper. Implementation on different gas turbine configurations has been presented by Tsalavoutas et al. [14,15] and Mathioudakis et al. [10].

The condition of the gas turbine is assessed from the values of "health indices," characterizing individual engine components. Health indices employed for monitoring the twin shaft gas turbine are defined in Appendix B.

When an engine is operating in a humid air environment and the air humidity is not properly taken into account into an adaptive model used for monitoring, then health indices will deviate from their reference values, even though the components have not undergone any condition change. This means that erroneous information may be derived concerning engine health. This is demonstrated from the results shown in Fig. 6. The deviation of modification factors caused by not taking into account air humidity is shown, and has been derived as follows: For certain operating conditions with humid air, performance simulation provides values for all measured quantities on an engine. With these values, an adaptive model is employed to derive "health indices," but using dry air. Matching of the measurements with dry air produces values of indices deviating from their baseline, by the amounts shown in Fig. 6, depending on the level of humidity. The values have been derived by using measurements sufficient in number and suitable for definition of all health indices.

Although the components have not undergone any change, they appear to have a modified performance. The presence of humidity changes the different mass and energy balances in the engine and is thus interpreted by the engine adaptive model as a change of component characteristics. The mere presence of humidity may thus be interpreted as a change in the condition of components, which could wrongly be attributed to deterioration or faults.

It is noticed that the quantity which is mostly influenced is compressor flow capacity. This is a very useful quantity for monitoring compressor condition. The conclusion drawn from this figure is that, unless humidity is taken into account, it is possible that incorrect decisions may be taken about deteriorated or faulty compressor.

We will now present some experimental evidence to support the previous observations.

Measurement Data From an Industrial Gas Turbine

Data have been collected from a twin shaft industrial gas turbine, operating as a part of a cogeneration system in an oil refinery. This gas turbine is the SULZER TYPE 10 and is equipped with an on-line monitoring system, which among other methods uses also the technique of adaptive modeling and trends the health indices derived. The layout of the gas turbine is presented in Fig. 7, where also measured quantities are indicated. The mass flow measurement indicated in the figure comes from a differential pressure measured at the gas turbine inlet.

Operation during the hot months of the year is mostly affected by humidity, the reason being that hot air can withhold larger amounts of water vapor. Ambient conditions for every day over a period of one week are shown in Fig. 8. This figure is used to show the periodic daily patterns. Typical daily variations of tem-

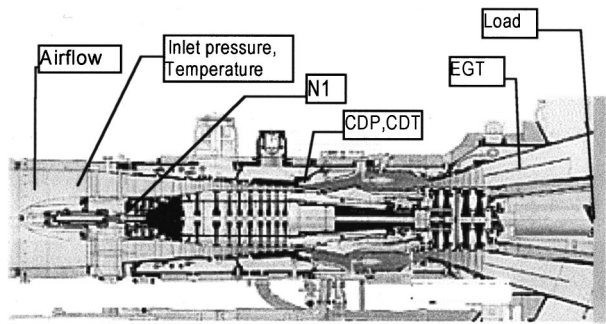


Fig. 7 Layout of the SULZER TYPE 10 gas turbine and quantities measured for monitoring

perature and humidity are observed. Early morning hours are characterized by low temperatures and high relative humidity, but not essentially high absolute humidity. Highest temperatures are during afternoon. Although relative humidity drops, absolute one is quite high, through to early evening.

The time evolution of engine load, temperature, and absolute humidity over this period is shown in Fig. 9. It is interesting that over this period the difference of minimum and maximum temperature is about 18°C while absolute humidity reaches a maximum value nearly double its minimum one. This particular time interval of one week has been chosen, in order to show the short-term effect on monitoring.

If, for example, operation between winter and summer time is considered, then differences may be much larger. Absolute humid-

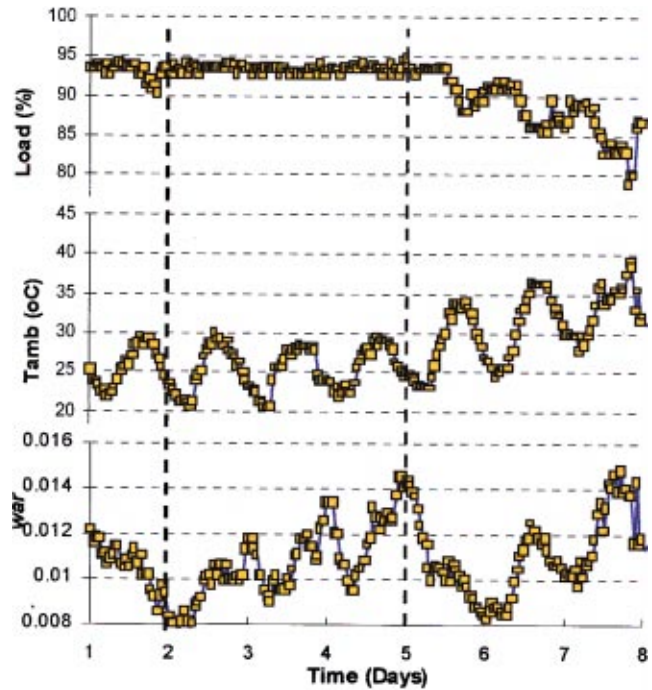


Fig. 9 Ambient conditions over a period of a week

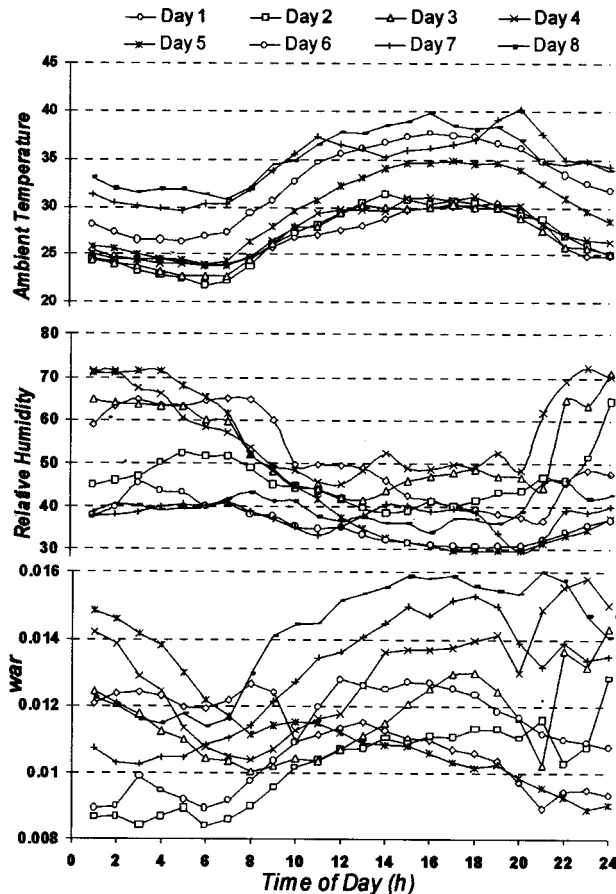


Fig. 8 Daily variations of ambient conditions over a period of a week

ity during a “humid” summer day is much larger than a “dry” winter day. Such differences do not present much interest from the monitoring point of view, apart from the fact that they may be related to observation of long-term deterioration.

Humidity Effect on Measured Quantities. In order to show the effect of humidity on the quantities measured for monitoring, data from two operating conditions are compared: the instants **A** of lowest and **B** of highest absolute humidity (Fig. 9). For a number of operating points in the vicinity of these operating conditions, corrected measurements in function of corrected load are shown in Fig. 10. It is observed that the various quantities on this figure exhibit systematic deviations, which are in very good agreement with the trends predicted in Fig. 3.

In order to demonstrate how accurate the predictions of the present model are, in Fig. 11 measured and predicted quantities are shown. The bars for measured quantities indicated the difference as a percentage of the value of the low humidity operating point, calculated from the measurement data. Local least-square lines were fitted to the two groups of data, in order to obtain an accurate estimation of the differences. Bars for calculated values represent the same quantities, as they are reproduced by running the engine model at the operating conditions, for which data were collected. A very good agreement between measured and predicted values can be observed.

Health Parameters. An adaptive model has been formulated for this engine. For a given operating point, defined through ambient conditions and load, five measured values are input to the model: N_1 , CDP, CDT, EGT, and W_2 . Five health indices are determined by the model and used for assessing engine health: f_1 , f_2 , f_5 , f_6 , and f_7 . When the problem is formulated this way, the sensitivity of the individual indices to humidity is shown in Fig. 12. It is observed that the indices mostly influence are f_1 and f_7 .

Measurement data can now be used to show the effect of humidity on monitored health parameters. We will concentrate on f_1 and f_7 , for which the influence of humidity was observed to be noticeable.

The time evolution of compressor flow capacity health index is shown in Fig. 13. The upper part shows the value calculated by

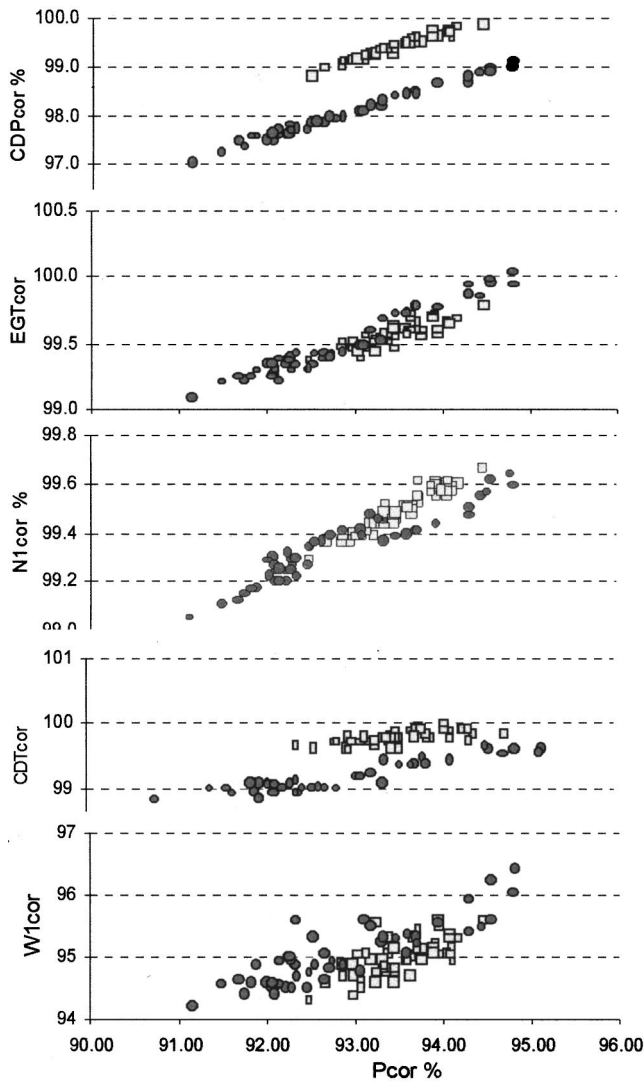


Fig. 10 Referred measured quantities for low and high humidity level. Points around Instants A ■ and B ●, Fig. 9.

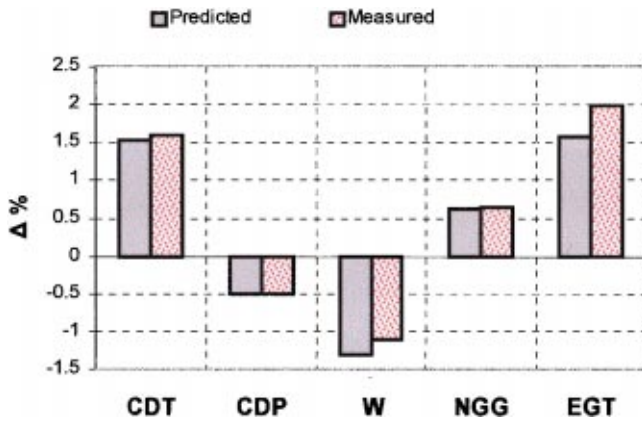


Fig. 11 Comparison of predicted and measured differences for operating conditions of low and high ambient humidity (Instants A and B of Fig. 9)

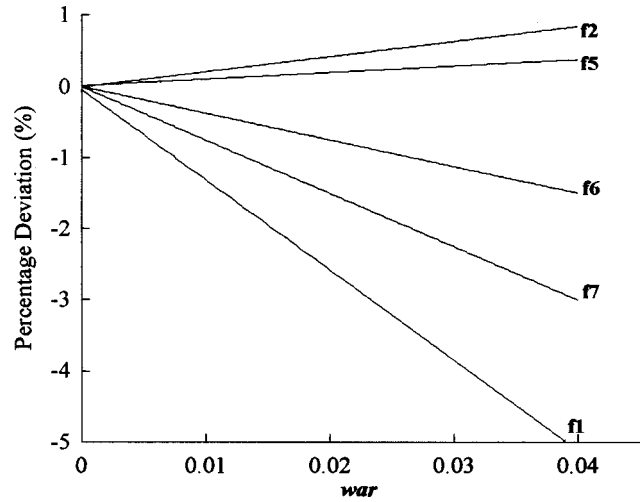


Fig. 12 Health indices deviation for different levels of humidity, when f_1 , f_2 , f_5 , f_6 , and f_7 are estimated from N_1 , CDP, CDT, EGT, and W_2

not taking into account the actual humidity level but considering that there is a constant relative humidity of 60% (this is value for the ISO standard day). The lower part shows the values calculated using the measured humidity.

It is observed that when the humidity is not correctly taken into account, large daily variations of flow capacity are observed (amplitude of about 2%). Such variations are only apparent and disappear when the correct humidity is used by the monitoring model, as shown in the lower part of the figure. Flow capacity shows a trend of decrease over time. This is a result of compressor fouling, which builds up during engine operation. The particular engine considered here is regularly washed in intervals of about one month. The time evolution of compressor flow capacity be-

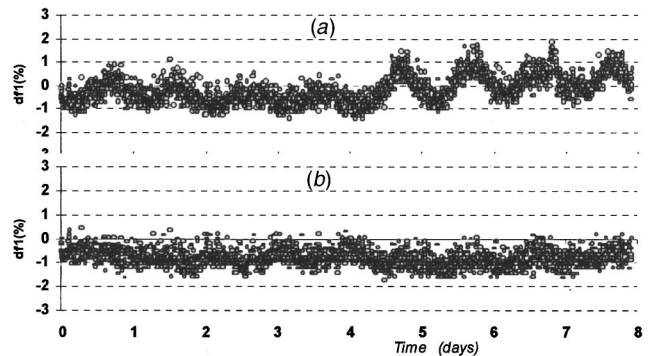


Fig. 13 Compressor flow capacity evaluated (a) with a standard humidity of 60%, (b) using actual measured humidity

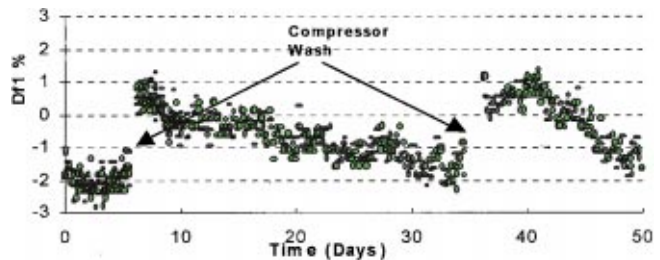


Fig. 14 Compressor flow capacity, resulting from fouling, and the effect of compressor washes

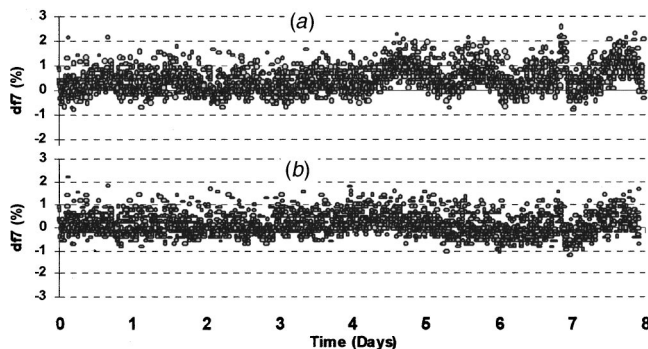


Fig. 15 Power turbine swallowing capacity evaluated (a) with a standard humidity of 60%, (b) using actual measured humidity

tween successive washes can be seen in Fig. 14. This figure is presented here to show that the amounts of pumping capacity deterioration, considered to be severe enough for washing to be needed, are comparable to the fluctuations which are caused by insufficient humidity modeling.

The effects of humidity are less pronounced for the turbine section. Figure 15 compares power turbine swallowing capacity evolution over the period considered. It is shown that incorporating humidity correctly reduces the scatter of points, but again the effect is not as dramatic as on compressor flow capacity.

Discussion

From the results shown above it is obvious that inclusion of humidity in monitoring calculations is necessary if an accurate picture of engine condition is desired. If humidity is not taken into account, the uncertainty bands for acceptable conditions may be too wide. A consequence of these observations is that humidity measurements should be an essential measurement if accurate monitoring is desired.

The influence of humidity becomes more important when large variations in ambient absolute humidity are expected. This would be the case more for hot and humid climates. Use of referred variables gives the possibility of comparing data from operation in different humidity levels. The reference condition can be chosen to be representative of an average day, but it does not practically influence the magnitude of observed changes, if it is consistently used. For the results presented here, dry air at standard day was used as reference; however, if the standard humidity of 60% is used, the same results are obtained. Attention must be paid when an average humidity is used for calculations, in the lack of a humidity measurement. In that case, it would be preferable to use the standard absolute humidity for all calculations instead of keeping the relative humidity constant or assuming dry air.

A situation in which humidity changes dramatically and very fast is when inlet humidification is used to increase gas turbine power output (see, for example, [16]). It is obvious that when such a turbine is monitored, for the monitoring system to keep providing correct assessments (and avoid false alarms) during inlet air humidification, it is essential to be supported by a model incorporating humidity and include the relevant measurement.

Conclusions

The effect of humidity on quantities related to gas turbine performance monitoring has been analyzed. A twin shaft industrial gas turbine was used as a test case for this analysis.

The method of incorporating humidity effects in a component based engine performance model was briefly described, as well as the method to refer measured performance variables to one ambient condition. The model was used to demonstrate how measured quantities deviate from their values in operation with dry air. It

was shown that if humidity is not taken into account, uncertainty bands in measured quantities may be too broad reducing thus the discriminative ability for diagnostics. On the other hand, deviations caused by humidity changes may be of magnitude similar to the magnitude of deviation caused by faults, a fact that may lead to either false alarms or obscure the effects of faults.

The effect of humidity is also significant on methods using component "health" parameters for monitoring. It was shown that such parameters will exhibit apparent deviations if humidity is not correctly accounted for. Incorporating a measurement of humidity in calculations eliminates apparent trends, while it reduces the scattering of "health" parameter values.

Nomenclature

CDP	=	compressor delivery pressure (bar)
CDT	=	compressor delivery temperature (K)
C_p	=	specific heat for constant pressure
EGT	=	exhaust gas temperature (K)
f	=	modification factor (Eqs. (B3) to (B10))
GG	=	gas generator
GGET	=	gas generator exhaust temperature
h	=	specific enthalpy
N1	=	compressor rotational speed.
P	=	gas turbine shaft output power
p	=	pressure
R	=	gas constant
T	=	total temperature (Kelvin)
TIT	=	turbine inlet temperature
WAR	=	water to air ratio, Eq. (1)
W_f	=	fuel flow rate (kg/sec)
W_i	=	gas flow rate at station i along the engine
Y	=	quantity measured for monitoring
γ	=	isentropic exponent, $\gamma = C_p / C_v$
Δ	=	operator denoting difference
δ	=	reduced (nondimensional) pressure: $\delta = p / 1.013$ (p in bar)
η_{is}	=	isentropic efficiency of turbine or compressor
θ	=	reduced (nondimensional) temperature: $\theta = T / 288$ (temperature in K)

Subscripts

1, . . . , 5	=	station numbering along the gas path (Fig. 3)
a	=	property of air
C	=	compressor
cor	=	referred (corrected) performance parameter (Eqs. (5))
CT	=	compressor turbine
d	=	quantity for operation in dry air
f	=	fuel
PT	=	power turbine
s	=	property of steam (water vapor)
w	=	quantity for operation in wet air

Appendix A

Variation of Wet Air Properties With Water-Air Ratio
The difference of C_p , R , γ for wet air from the corresponding values for dry air can be estimated by using small perturbation analysis, given that water-air ratio (WAR) is a small number. Starting with specific heat, we have

$$C_{p,wa} = (C_{p,da} + \text{WAR}C_{p,s}) / (1 + \text{WAR}). \quad (A1)$$

Change of C_p derived from this relation is

$$\frac{\delta C_p}{C_p} = \frac{C_{p,wa} - C_{p,da}}{C_{p,da}} = \frac{\text{WAR}}{1 + \text{WAR}} \left(\frac{C_{p,s}}{C_{p,da}} - 1 \right). \quad (A2)$$

For ambient conditions typical values are $C_{p,s} = 1810$ J/Kg, $C_{p,da} = 1005$ J/Kg. This relation thus gives

$$\frac{\delta C_p}{C_p} = 0.8 \cdot \frac{\text{WAR}}{1 + \text{WAR}} \approx 0.8 \text{WAR}. \quad (A3) \quad f_4 = \eta_b / \eta_{b,\text{ref}} \quad (B5)$$

Similarly, for the change of gas constant we get

$$\delta R / R \approx 0.6 \text{WAR}. \quad (A4)$$

For the isentropic exponent, starting from the relation

$$\frac{\gamma - 1}{\gamma} = \frac{R}{C_p}$$

we get

$$\frac{\delta \gamma}{\gamma} = (\gamma - 1) \left(\frac{\delta R}{R} - \frac{\delta C_p}{C_p} \right). \quad (A5)$$

From Eqs. (A3), (A4), for a typical $\gamma = 1.4$, we get

$$\delta \gamma / \gamma \approx -0.08 \text{WAR}. \quad (A6)$$

It should be noted that the change in γ is about one order of magnitude smaller than the changes in R , C_p .

This analysis also applies when a change of properties between two humidity levels is considered. In that case WAR should stand for the difference in absolute humidity between the two conditions.

Appendix B

The Principle of Adaptive Modeling. Adaptive modelling employs the values of measured quantities to determine parameters characteristic to the performance of each gas turbine component, which can in turn be used to assess its health. If a particular component parameter has a value X_{ref} on the reference map and a value X_{act} on the actual “on engine” map, then a modification factor f is defined as follows:

$$f = X_{\text{act}} / X_{\text{ref}}. \quad (B1)$$

Given that the occurrence of faults or component deterioration leads to a change of the component performance characteristics, f can be used as a health indicator. Usually, two such factors are defined to describe the health of one engine component.

The values of modification factors for a certain test data set are derived through the solution of a multidimensional optimization problem, which ensures that predicted and measured variable values match.

The health indices used for the twin shaft gas turbine of Fig. 1 are

Compressor:

$$f_1 = (W_2 \sqrt{T_2} / P_2) / (W_2 \sqrt{T_2} / P_2)_{\text{ref}} \quad (B2)$$

$$f_2 = \eta_C / \eta_{C,\text{ref}} \quad (B3)$$

Combustor:

$$f_3 = \Delta p_b / (\Delta p_b)_{\text{ref}} \quad (B4)$$

Gas Generator Turbine:

$$f_5 = (W_4 \sqrt{T_4} / P_4) / (W_4 \sqrt{T_4} / P_4)_{\text{ref}} \quad (B6)$$

$$f_6 = \eta_{CT} / \eta_{CT,\text{ref}} \quad (B7)$$

Power Turbine:

$$f_7 = (W_{4.1} \sqrt{T_{4.1}} / P_{4.1}) / (W_{4.1} \sqrt{T_{4.1}} / P_{4.1})_{\text{ref}} \quad (B8)$$

$$f_8 = \eta_{PT} / \eta_{PT,\text{ref}} \quad (B9)$$

References

- [1] Andersen, H., 2000, “Early Detection of Combustor Pulsations and Optimized Operation Through On-Line Monitoring Systems,” ASME Paper No. 2000-GT-0180.
- [2] Gülen, S. C., Griffin, P. R., and Paolucci, S., 2000, “Real-Time On-Line Performance Diagnostics of Heavy-Duty Industrial Gas Turbines,” ASME Paper No. 2000-GT-0312.
- [3] Razak, A. M. Y., and Carlyle, J. S., 2000, “An Advanced Model Based Health Monitoring System To Reduce Gas Turbine Ownership Cost,” ASME Paper No. 2000-GT-627.
- [4] Cloyd, S. T., and Harris, A. J., 1995, “Gas Turbine Performance—New Application and Test Correction Curves,” ASME Paper No. 95-GT-167.
- [5] AGARD-AR-332, 1995, *Recommended Practices for the Assessment of the Effects of Atmospheric Water Injection on the Performance and Operability of Gas Turbines Engines*, Sept.
- [6] Bird, J., and Grabe, W., 1991, “Humidity Effects on Gas Turbine Performance,” ASME Paper No. 91-GT-329.
- [7] Gu, Y. G., and Palmer, J. R., 1985, “A Mathematical Model for Computing the Effects of Air Humidity, Fuel Composition and Gas Dissociation on Gas Turbine Performance and Its Application,” ASME Paper No. 86-GT-114.
- [8] Walsh, P. P., and Fletcher, P., 1998, *Gas Turbine Performance*, Blackwell Oxford, UK.
- [9] Dundas, R., Sullivan, D., and Abegg, F., 1992, “Performance Monitoring of Gas Turbines for Failure Prevention,” ASME Paper No. 92-GT-267.
- [10] Mathioudakis, K., Stamatis, A., Tsalavoutas, A., and Aretakis, N., 2001, “Performance Analysis of Industrial Gas Turbines for Engine Condition Monitoring,” *ImechE J. Power Energy*, **215**(A2), p. 1.
- [11] Lee, Y. H., and Singh R., 1996, “Health Monitoring of Turbine engine Gas Path Components and Measurements Instruments,” ASME Paper No. 96-GT-242.
- [12] Stamatis, A., Mathioudakis, K., and Papailiou, K. D., 1990, “Adaptive Simulation of Gas Turbine Performance,” *ASME J. Eng. Gas Turbines Power*, **112**, pp. 168–175.
- [13] Stamatis, A., Mathioudakis, K., Smith, M., and Papailiou, K. D., 1990, “Gas Turbine Component Fault Identification by Means of Adaptive Performance Modelling,” ASME Paper No. 90-GT-376.
- [14] Tsalavoutas, A., Aretakis, N., Stamatis, A., and Mathioudakis, K., 2000, “Combining Advanced Data Analysis Methods for the Constitution of an Integrated Gas Turbine Condition Monitoring and Diagnostic System,” ASME Paper No. 2000-GT-0034.
- [15] Tsalavoutas, A., Pothos, S., Mathioudakis, K., and Stamatis, A., 1999, “Monitoring the Performance of a Twin-Shaft Ship Propulsion Turbine by Means of Adaptive Modeling,” *RTO Symposium on Gas Turbine Operation and Technology for Land, Sea and Air Propulsion and Power Systems*, Ottawa, Oct. 18–21.
- [16] Meher-Homji, C. B., and Mee, T. R., III, 2000, “Inlet Fogging of Gas Turbine Engines: Part A—Theory, Psychrometrics and Fog Generation,” ASME Paper No. 2000-GT-307.

Data Rectification and Detection of Trend Shifts in Jet Engine Path Measurements Using Median Filters and Fuzzy Logic

R. Ganguli

Assistant Professor,
Department of Aerospace Engineering,
Indian Institute of Science,
Bangalore 560 012, India

Filtering methods are explored for removing noise from data while preserving sharp edges that many indicate a trend shift in gas turbine measurements. Linear filters are found to have problems with removing noise while preserving features in the signal. The nonlinear hybrid median filter is found to accurately reproduce the root signal from noisy data. Simulated faulty data and fault-free gas path measurement data are passed through median filters and health residuals for the data set are created. The health residual is a scalar norm of the gas path measurement deltas and is used to partition the faulty engine from the healthy engine using fuzzy sets. The fuzzy detection system is developed and tested with noisy data and with filtered data. It is found from tests with simulated fault-free and faulty data that fuzzy trend shift detection based on filtered data is very accurate with no false alarms and negligible missed alarms.

[DOI: 10.1115/1.1470482]

Introduction

Gas turbines are susceptible to faults because of a harsh aerothermodynamic environment and rapidly rotating blades. Measurement deviations between a baseline “good” engine and a “faulty” engine are often used to detect that a fault has occurred. There are two broad classifications of measurement trend changes: A slow change over time indicates deterioration in the modules and a rapid trend shift indicates a new fault. Many engine problems leading to in-flight shut downs manifest themselves as a sudden change in engine gas path measurements. Recent work has shown that following a sudden measurement trend change, identification and pattern recognition algorithms can be used to isolate module as well as system faults. The trend shift in measurements is assumed to be a precursor to an engine fault. Kalman filter approach has been demonstrated for fault isolation in gas turbine engines (Urban [1], Volponi [2], Luppold [3], Stamastis [4], Kerr [5], Gallops [6], Volponi [7], and Doel [8]). More recently, neural network approaches have also been studied ([9]) and similarities between neural network and Kalman filter approaches for the single-fault detection pointed out in [10]. Some attempts have also been made to detect trend shifts in gas path measurements using a neural network-based approach ([11]).

Fault detection is based on some health measure of the system. The health measure has a bounded value for a healthy system. However, when the system becomes unhealthy, the fault measure exceeds some threshold and maintenance action may be needed. For an ideal system, the health residual or delta between the unhealthy and healthy system should be zero if the system has no faults ([12]).

In reality, errors due to sensor noise, disturbances, instrument degradation, and human errors usually contaminate measured data. Since the fault detection task depends on quality of the information extracted from measured data, the collected data needs to be cleaned or “rectified” for efficient fault detection ([13]).

Further, fault isolation methods based on Kalman filtering and neural networks work better with low noise data.

Most popular data rectification methods rely on information about the nature of the errors or smoothness of the underlying signal and include various univariate filtering methods. Linear, univariate, low-pass filtering methods such as mean filtering and exponential smoothing are commonly used in industry ([14]), as they are simple and can be easily used online. However, linear filters are not very effective in filtering signals containing features with different localization in time and frequency (Gallagher [15] and Heinonen [16]). There are many natural signals with smooth behavior most of the time, but occasionally there are fast changes. If the point where the trend shifts are not important for the signal analysis, the traditional linear filters designed for stationary signal periods are often the optimal solution. In applications such as fault detection, however, the trend shift points are the most critical and should be preserved intact. In these applications, nonlinear filters have found widespread use, as many nonlinear filters are able to preserve edges and simultaneously attenuate noise levels ([17]).

Some work has been done in chemical engineering process flow models for data rectification (Albuquerque [18], Johnston [19], Karjala [20], and Kramer [21]). Chemical processes generate lot of data that can be used for fault detection if trends can be obtained from the noisy data. Therefore, they are similar to gas turbines that also generate considerable measurement data which could be used for fault detection. Linear and nonlinear filters were used for these studies. Linear filters include finite impulse response (FIR), and infinite impulse response (IIR) filters and nonlinear filters include finite median hybrid (FMH) ([17]), recurrent neural networks ([20]) and auto-associative neural networks ([21]).

Among the various nonlinear filtering methods, median filters have emerged as a powerful nonlinear filter for removal of noise from signals with sharp trend shifts, and continue to be an active research area in signal processing ([22,23]). Median filters are easy to design and can be implemented in hardware. Even after noisy data is filtered, the effect of uncertainty should be modeled in the thresholding process. After white noise is removed from data, model related uncertainties are still present. Fuzzy logic offers a way to handle this uncertainty ([12]). Fuzzy logic can be simply interpreted as a way of computing with words ([24]).

Contributed by the International Gas Turbine Institute (IGTI) of THE AMERICAN SOCIETY OF MECHANICAL ENGINEERS for publication in the ASME JOURNAL OF ENGINEERING FOR GAS TURBINES AND POWER. Paper presented at the International Gas Turbine and Aeroengine Congress and Exhibition, New Orleans, LA, June 4–7, 2001; Paper 01-GT-014. Manuscript received by IGTI, December 2000, final revision, March 2001. Associate Editor: R. Natole.

In this paper, linear and nonlinear FMH filters are compared for reducing the noise inherent in gas turbine measurements. Simulation studies are used to show the performance of the filters with realistic data and a trend shift detection method using health residuals and fuzzy thresholds is proposed.

Background on Filters

Technologies related to linear and nonlinear filtering are used in this paper and a brief introduction is provided below. Linear filters are widely used in the industry as moving averages.

Linear Filtering. Linear filtering methods rectify the signal by taking a weighted sum of previous measurements in a window of finite or infinite length. These techniques are computationally efficient and easy to implement and can be readily used for on-line identification. Linear filters belong to the class of low-pass filters and can be represented as

$$\hat{x}_t = \sum_{i=0}^{I-1} b_i x_{t-i}$$

where I is the filter length and $\{b_i\}$ is the sequence of weighting coefficients which define the characteristics of the filter. These weighting coefficients satisfy the following conditions:

$$\sum_i b_i = 1.$$

The weighting sequence $\{b_i\}$ is the impulse response of the linear filters. Linear filters with finite window size are called finite impulse response (FIR) filters. Linear filters with infinite window size are called infinite impulse response (IIR) filters. When all coefficients $\{b_i\}$ are equal, the FIR filter reduces to the mean filter. For a filter of length I , any mean filtered data point can be represented in terms of the last I measured data points as

$$\hat{x}_t = \frac{1}{I} (x_t + x_{t-1} + \dots + x_{t-I+1}).$$

The mean filter is a convolution of the measured signal with a vector of I constant coefficients, each equaling $(1/I)$.

Infinite impulse response (IIR) filters are linear filters with infinite filter length. IIR filters rectify a data point by using a weighted sum of all previous measurements. Exponentially weighted moving average is a popular IIR filter which smoothes a measured data point by exponentially averaging it with all previous measurements. The exponentially weighed moving average filter is a recursive low-pass filter that eliminates high-frequency components from the measured signal. Computationally, it is implemented as

$$\hat{x}_t = a x_t + (1-a) \hat{x}_{t-1}.$$

The parameter a is an adjustable smoothing parameter between 0 and 1. A value of $a=1$ corresponds to no smoothing and a value of $a=0$ corresponds to keeping only the first measured point. Expanding the above equation, we can write

$$\hat{x}_t = \sum_{i=0}^{\infty} a(1-a)^i x_{t-i}.$$

The weights of the exponentially weighted moving average filter drop exponentially depending on the smoothing parameter and more weight is given to more recent measurements. Strum and Kirk [13] give more details about different types of linear filters.

Drawbacks of Linear Filters. The basis functions representing raw measured data have a temporal localization equal to the sampling interval. Linear filters represent the measurements with basis functions with a broader temporal localization and a narrower frequency localization. These filters are single scale in nature since all basis functions have the same fixed time-frequency

localization. Consequently linear filters face a tradeoff between accurate representation of temporally localized changes and efficient removal of temporally global noise. Therefore, simultaneous noise removal and accurate feature representation on nonstationary measured signals cannot be effectively achieved by linear filtering methods. Since trend detection of gas turbine measurements require isolation of local trend shifts from globally noisy data, linear filters are of limited use for that problem.

Nonlinear Filters. Nonlinear filtering techniques are multi-scale in nature and have been developed to overcome the inability of linear filters to capture features at different scales. The FMH filter is used in this study.

Finite Median Hybrid (FMH) Filters. A FIR median hybrid filter (FMH) is a median filter that uses preprocessed inputs from M linear FIR filters ([16,17]). The FMH filter output is the median of M values, which in turn are outputs of M FIR filters. An FMH filter of length $2I+1$ and three FIR substructures can be written as

$$y_1 = \frac{1}{I} (x_{t-1} + x_{t-2} + \dots + x_{t-I})$$

$$y_2 = x_t$$

$$y_3 = \frac{1}{I} (x_{t+1} + x_{t+2} + \dots + x_{t+I})$$

$$y = \text{median}(y_1, y_2, y_3)$$

where $2I+1$ data points filtered by the FMH filter. The values y_1 , y_2 , and y_3 are called the backward predictor, central value, and forward predictor, respectively. FMH filtering is a batch filtering technique and is most effective in capturing sharp changes in piece wise constant signals. The lengths of the FIR filters are selected to preserve the signal features while eliminating high frequency noise. Long FIR filters may cause sharp edges to be oversmoothed. Short FIR filters may not remove enough noise. Since the central part of the FMH filter is the original noisy data, FMH filters tend to return some noise. Better noise removal is possible by repeated applications of the FMH filter, which will result in a root signal that does not change with further filtering. It has been suggested that the windows of the FIR substructures underlying the FMH filter be slowly increased in length and the FMH filter performed repeatedly. This method has been shown to be efficient if the signal is heavily embedded with noise, and it is important to preserve the exact shapes of the sharp edges ([16,17]).

FMH is superior to linear filters because of the ability to preserve temporally linearized features while eliminating errors. However, because FMH filters use a forward predictor, they have a time delay of I . The time delay is a price that has to be paid for feature recognition since it is very difficult to predict sharp trend shifts from backward data only. In this study, we assume that data is rapidly measurement received from the engine by the trend detection system, at the rate of at least I points per flight. A typical value of I is 10.

Problem Formulation

Gas path measurement deltas are obtained by subtracting the baseline measurements for a good engine from the actual measurement. The baseline measurements often come from an engine model, and various correction factors are used to reduce the measured data to standard sea level conditions ([25]). Gas path measurement deltas contain high levels of uncertainty due to sensor errors and modeling assumptions.

For a trend shift to be detectable, it must show up beyond the scatter band caused by noise for the measurements. For simplicity,

consider the case of the basic four measurement deltas, ΔEGT , $\Delta N1$, $\Delta N2$, and ΔWF . Thus, we can write the measurement deltas as follows:

$$z = z^0 + \theta \quad (1)$$

where θ is noise and z^0 is the baseline measurement delta. The baseline measurement delta can be representative of either a good engine, or a faulty engine. A trend shift in the baseline measurement delta will result in a trend shift in the measurement delta. The problem is therefore to find the trend shift in the presence of noise in the data.

Healthy Engine. For a healthy engine, the pure measurement deltas are zero and the measurements contain only noise. As an example, simulated data for the ΔEGT measurement for a healthy engine is shown in Fig. 1 over 150 discrete time points. Both the pure signal and the realistic noisy signal are shown. Equation (1) then takes the following form for measurements of a healthy engine:

$$z = \theta. \quad (2)$$

Noise is added to the simulated measurement deltas using the typical standard deviations for ΔEGT , $\Delta N1$, $\Delta N2$, and ΔWF as 4.23C, 0.25%, 0.17%, and 0.50%, respectively ([9]).

Faulty Engine. The engine is assumed to have a module fault. The modules considered are the FAN, LPC, HPC, HPT, and LPT. The module faults are modeled using influence coefficients and couplings for a jet engine obtained from Volponi [10]. The couplings used for the five implanted faults are as follows:

1. FAN coupled FAN (-2% η , -2.5 FC)
2. LPC coupled LPC (-2% η , -2.2% FC)
3. HPC coupled HPC (-2% η , -1.6 FC)
4. HPT coupled HPT (-2% η , 1.5% FP4)
5. LPT coupled LPT (-2% η , +3.3% FP45)

Each implanted fault corresponds to a 2% decrease in module efficiency. The influence coefficients used are shown in Table 1. These influence coefficients represent a linearized model of the

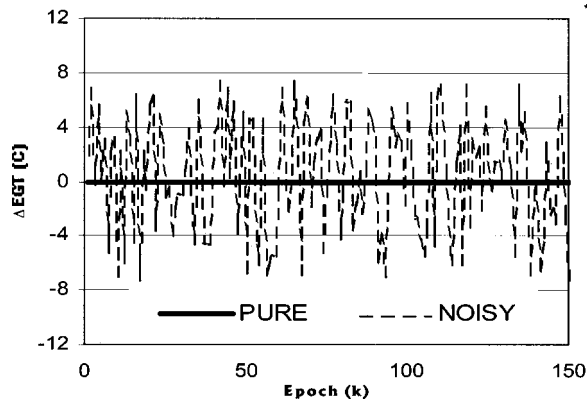


Fig. 1 Pure and noisy ΔEGT signals for a healthy (no fault) gas turbine

Table 1 Sample module fault influence coefficients

	ΔEGT (°C)	ΔWF (%)	$\Delta N2$ (%)	$\Delta N1$ (%)
FAN	3.86	0.70	0.30	-0.68
LPC	-4.54	-0.66	-0.29	-0.14
HPC	-6.80	-0.80	0.06	-0.05
HPT	-10.88	-1.29	0.57	-0.08
LPT	-1.19	0.96	-0.63	0.98

engine. The measurements corresponding to the implanted fault are calculated after adding noise. Equation (1) then assumes the form:

$$z = Hx + \theta \quad (3)$$

where H contains the influence coefficients in matrix form and x contains the module efficiencies in vector form. Simulated data for each fault is generated at 150 discrete time points for each fault. For the first 50 points, the engine has no fault and the measurement deltas come only from noise (Eq. (2)). After the first 50 points, there is a fault that remains for the next 50 points. Measurement deltas for the faulty engine are obtained from Eq. (3). After the first 100 points, the measurement deltas again reflect a healthy engine and are derived using Eq. (2).

Health Residual and Threshold. For the purpose of quantifying the health of the gas turbine engine, we define the following residual as the root-mean square value of the measurement deltas

$$u = \sqrt{\Delta EGT^2 + \Delta WF^2 + \Delta N2^2 + \Delta N1^2}. \quad (4)$$

For an ideal healthy engine, the residual u should be zero. In reality, there is always noise in measurements and modeling uncertainties that cause the residual to have some value for a healthy engine. However, the residual for a healthy engine will be lower than for a faulty engine. Next, a threshold for fault detection is defined:

$$u \leq \text{threshold (normal)}$$

$$u > \text{threshold (faulty)}$$

Hard limits as well as fuzzy limits can be used to define such thresholds. A standard way to define such thresholds is to run a fault free simulation and then set the threshold to be slightly larger than the maximum residual norm for a healthy system ([12]).

Numerical Results

Healthy and faulty simulated data are used to test linear and nonlinear filters and select the best filters for the gas turbine measurement trend shift problem. The simulated filtered data is then used to get health residuals and define thresholds. Finally, the system is tested with simulated data for trend detection.

Healthy Engine. Simulated measurements for ΔEGT for a healthy engine are shown in Fig. 1. The pure signal represents a noise-free environment and is called the root signal. The noisy signal is obtained by adding Gaussian noise to the pure signal. The Gaussian noise is high frequency in nature, and can often confuse a trend detection system because of sharp spikes.

Figure 2 shows the effect of passing the noisy data shown in Fig. 1 once through three different FIR filters with window

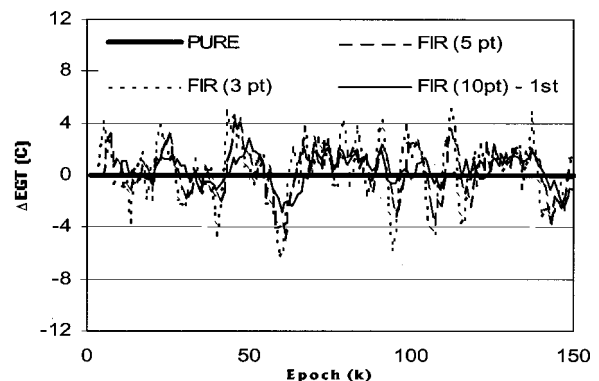


Fig. 2 Effect of a single pass through linear finite impulse response (FIR) filters with varying window lengths on noisy ΔEGT for a healthy gas turbine

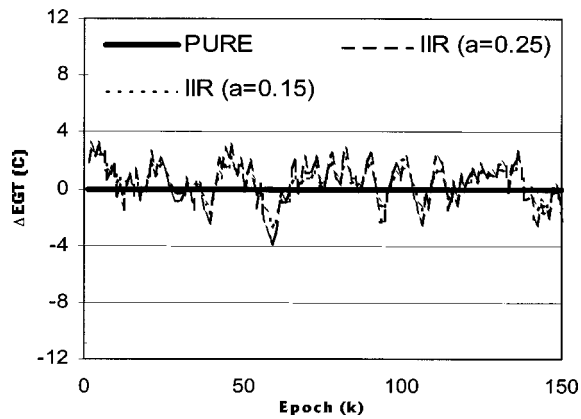


Fig. 3 Effect of a single pass through linear infinite impulse response (IIR) filters with varying smoothing factors on noisy ΔEGT for a healthy gas turbine

lengths of $I=3$, $I=5$, and $I=10$. Larger window lengths more smoothing out of the high-frequency noise. Figure 3 shows the effect of passing the noisy data shown in Fig. 1 through two different IIR filters with $a=0.15$ and $a=0.25$.

Both the FIR and IIR filters cause some reduction in noise that can be observed by comparing Figs. 1, 2, and 3. Figures 4 and 5 show the effect of recursive filtering with linear filters. Figure 4 shows noisy data shown in Fig. 1 as it passes through an FIR filter with window length $I=10$.

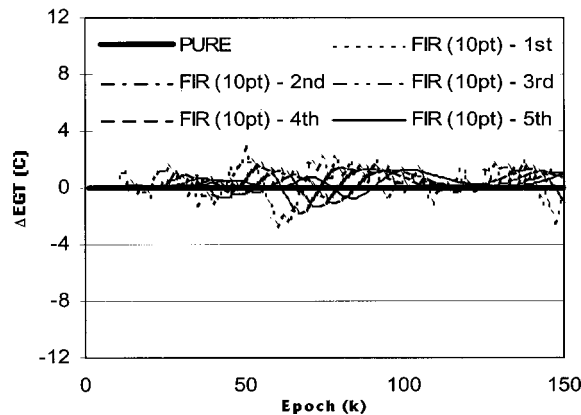


Fig. 4 Effect of recursive FIR filtering on ΔEGT noisy data for healthy gas turbine engine

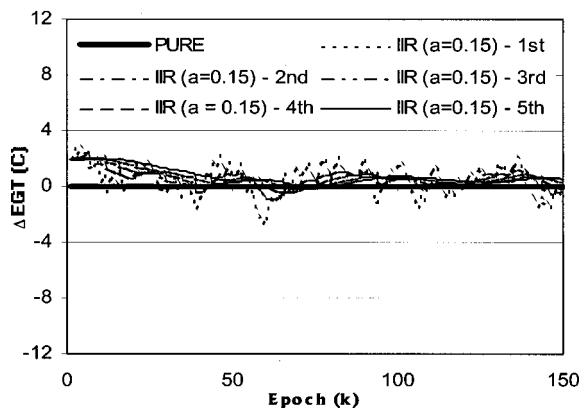


Fig. 5 Effect of recursive IIR filtering on ΔEGT noisy data for healthy gas turbine engine

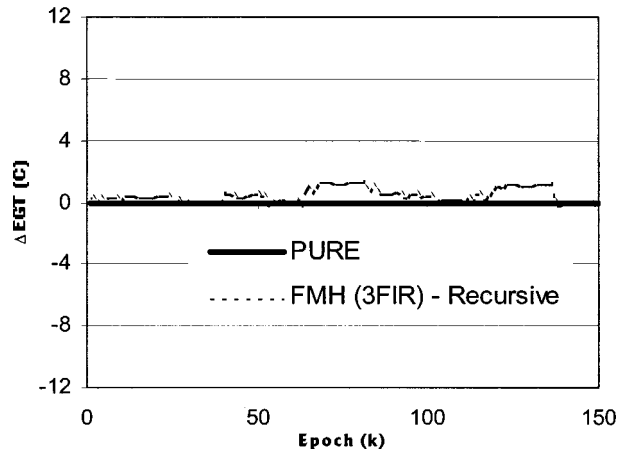


Fig. 6 Effect of recursive finite median hybrid (FMH) filtering on ΔEGT noisy data for healthy gas turbine engine

Figure 5 shows the same noisy data as it passes through an IIR filter with $a=0.15$ five times. In both these cases, each pass removes high-frequency noise and squashes the noisy signal to bring it closer to the noise-free root signal. Several passes of the filters are required to significantly remove high-frequency noise from the signal of the healthy engine.

Figure 6 shows the effect of the nonlinear FMH filter. Here, the FMH includes three FIR filters in the substructure. The window lengths of the FIR filters underlying the FMH filters are set to I

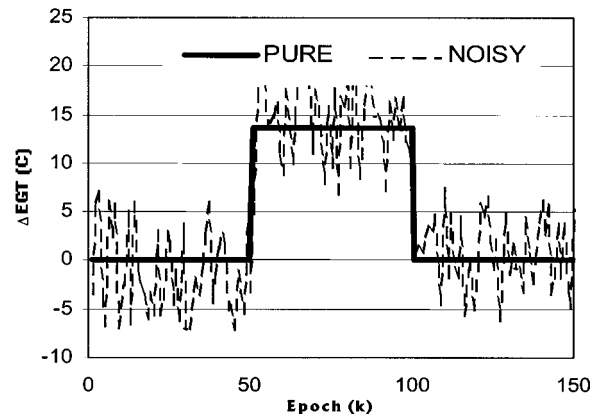


Fig. 7 Pure and noisy ΔEGT signal for HPC fault (onset at $k=51$, ends at $k=100$)

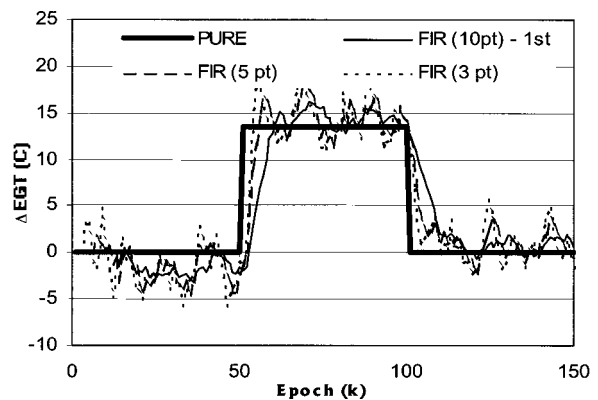


Fig. 8 Effect on noisy data of one pass through FIR filters for a faulty engine

$=2, I=3, I=5, I=7,$ and $I=10$ for five passes through the FMH. Following the five passes, the FMH gives a good approximation to the noise-free root signal as shown in Fig. 6. The important thing to note here is that repeated passes through the filters are needed to significantly reduce noise.

Faulty Engine. Figure 7 shows pure and noisy signal for ΔEGT corresponding to a faulty engine. This signal assumes an HPC fault occurs at discrete time $k=51$ and ends at discrete time $k=101$. There is no fault in the region $k=1$ to $k=50$ and from $k=101$ to $k=150$. The simulated data shown here is used as a test case for trend shift detection.

Figures 8 and 9 show the results of passing the noisy data shown in Fig. 7 through FIR filters and IIR filters. While these linear filters remove noise from the data, they also result in smoothing out of the sharp trend shifts.

Figures 10 and 11 show the effect of recursive passes of the noisy data shown in Fig. 7 through FIR and IIR filters, respectively. The FIR filter used here has a window length $I=10$ and the IIR filter has a smoothing factor $a=0.15$. It is clear that recursive runs remove noise. However, the removal of noise comes at the cost of smoothing out of the sharp edges of the signal, which inhibits trend detection.

In sharp contrast, the result of passing noisy data through the FMH filter is shown in Fig. 12. It is clear that the FMH filter removes noise while preserving the features of the signal along with the sharp edges. The FMH filter therefore minimizes any delay in trend detection while making the data much cleaner.

In industry applications in the gas turbine field, a single pass of FIR or IIR filters is sometimes used to smooth data. In common

parlance, FIR filters are called moving averages and IIR filters are called exponential smoothing. From the above results, we can see that such practices are fraught with danger. To really remove Gaussian noise from a signal, we need recursive passes through the linear filters. However, recursive passes through linear filters causes smoothing out of sharp edges that may be caused by faults, and may be one of the main reasons for data analysis. The FMH filter allows an easily applicable way to solve this paradox of recursion than afflicts linear filters.

Health Residuals. The health residuals given by Eq. (4) are calculated for each discrete time, fault and number of sets of simulation. For this study, we use $M=150$ discrete time points per set of data, $N=10$ sets of data and $P=5$ faults. The five faults are the five module faults and are simulated over the entire epoch ($k=1$ to 150) and not just between $k=50$ and $k=100$ as shown in the figures related to signal processing results. We can then define the entire data used in these numerical experiments in terms of three indexes ($k=1, M; j=1, P; i=1, N$). The health residual for each point is obtained and the mean and the standard deviations for the noisy and FMH filtered data for a faulty engine are calculated. All results that follow use FMH filtering when filtered data is mentioned.

The above process assumes module faults with an efficiency reduction of 2%. The above process is repeated with module faults with an efficiency reduction of 1%. This allows a middle ground between the healthy and faulty engine and can be called a deteriorated engine.

The no-fault data uses $M=150$ and $N=10$ but does not include the fault index j . Also, the no fault region spans the entire $k=1$ to $k=150$ time points. Again, health residuals at each point are ob-

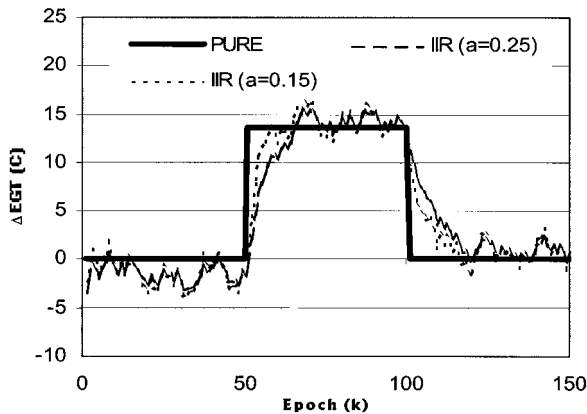


Fig. 9 Effect on noisy data of one pass through IIR filters for a faulty engine

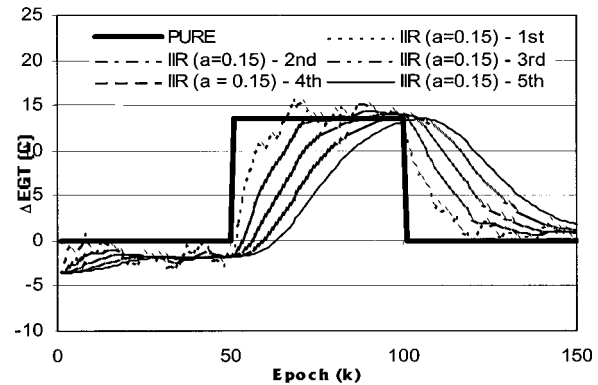


Fig. 11 Effect on noisy data of recursive passes through IIR filters for a faulty engine

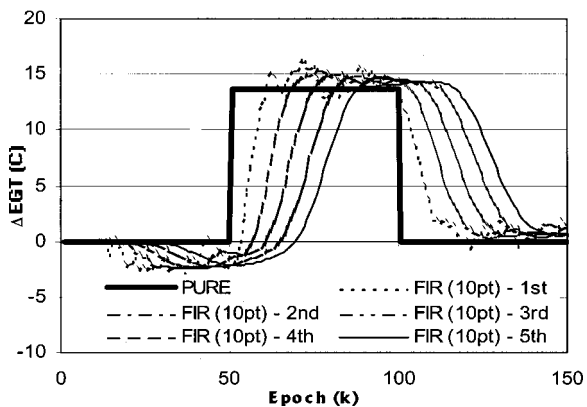


Fig. 10 Effect on noisy data of recursive passes through FIR filters for a faulty engine

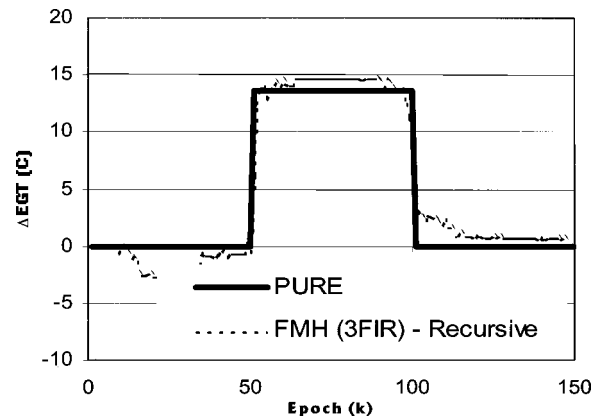


Fig. 12 Effect on noisy data of recursive passes through FMH filter for a faulty engine

tained and the mean and standard deviation for the noisy and FMH filtered data for a healthy engine is calculated.

At this point, we have the characteristics of health residuals for a healthy, deteriorated and faulty gas turbine. Using the mean and standard deviations for these residuals, we define Gaussian membership functions for fuzzy sets named low, medium, and high. These sets are shown in Figs. 13 and 14 for cases with noisy and filtered data and are mathematically represented by the following equation:

$$\mu(x) = e^{-0.5(x-m/\sigma)^2}$$

where m is the mean and σ is the standard deviation.

Thresholds. The Gaussian functions in Figs. 13 and 14 show the separability of the healthy, deteriorated and faulty residuals. For a given engine, the health residual can be used to predict the engine fault condition using the Gaussian fuzzy sets.

For the purposes of trend shift detection, we use a fuzzy logic system to get a binary output saying “faulty” or “healthy.” For example, such problems occur in optical image thresholding where image pixels must be labeled as 1 or 0 corresponding to background and foreground respectively, assuming the background is brighter than the foreground, as in text documents ([26]).

Given $R1$, $R2$, and $R3$ are three patterns, the overlapping areas between the Gaussian fuzzy sets shown in Figs. 13 and 14 represent a measure of the probability of error in pattern separation ([27]). No intersection shows a completely separable problem. The error can be reduced by increasing the difference between means of the two classes (increasing fault size) or by decreasing the variance of each class (reduce noise while preserving features). Increasing fault size is not a viable option as we don't want

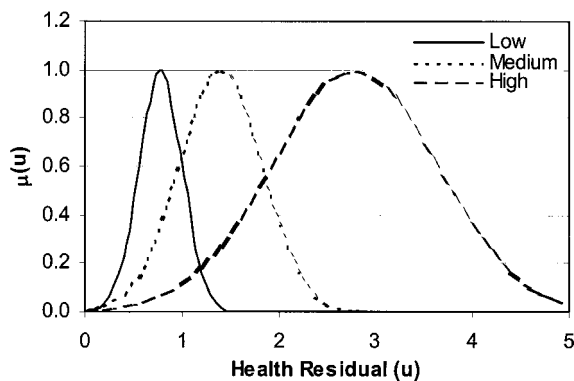


Fig. 13 Fuzzy sets representing linguistic measures of health residual for noisy data

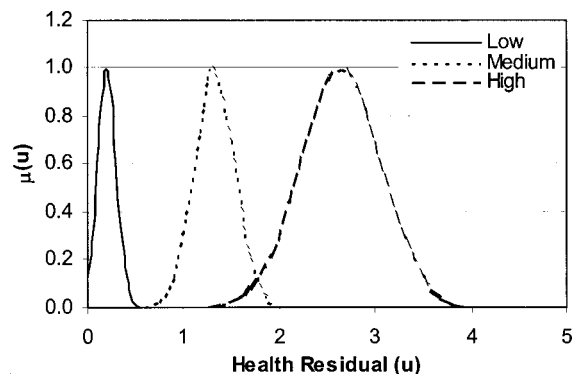


Fig. 14 Fuzzy sets representing linguistic measures of health residual for FMH filtered data

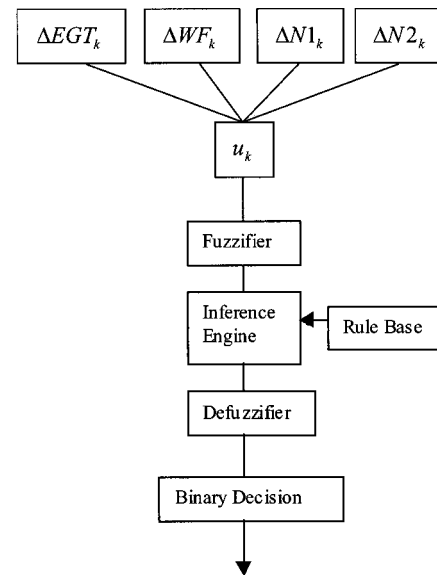


Fig. 15 Schematic representation of fuzzy system for trend shift detection

to detect faults after they have reached catastrophic proportions. Figure 14 clearly shows that classification error is considerably reduced by using FMH filtering.

Statistical decision theory tells us that the optimal threshold between two patterns represented by Gaussian functions lies at the point of intersection of the Gaussian functions that are located between the two mean values. This solution point minimizes the statistical error ([28]). We obtain this point by using the following fuzzy decision rules using the health residuals after they have been fuzzified and expressed as linguistic variables ([27]). This represents a single-output single-input fuzzy system. The fuzzy logic system is shown in Fig. 15 and consists of a fuzzifier, inference engine, rule base, defuzzifier, and binary decision logic. The fuzzifier maps crisp input numbers into fuzzy sets. It is needed to activate rules that are expressed in terms of linguistic variables. An inference engine maps fuzzy sets to fuzzy sets and determines the way in which the fuzzy sets are combined. A defuzzifier is used to calculate crisp values from fuzzy values or the best class. Details about fuzzy set theory are available from textbooks ([29]).

The fuzzy rules used here are

- IF u is low THEN engine is healthy,
- IF u is medium THEN engine is deteriorated, and
- IF u is high THEN engine is faulty.

These fuzzy decision rules are applied at each discrete point of the test data. Maximum matching defuzzification is used to obtain the engine fault condition ([27]). While centroid defuzzification is widely used for control problems where a crisp output is required ([29]), maximum matching is popular for pattern recognition problem where only the correct class is needed ([27]). Once the engine fault condition is obtained, binary trend shift decisions are made using the following crisp decision rules:

- IF engine is healthy THEN trend shift=0 and
- IF engine is faulty THEN trend shift=1.

Testing. Simulated faulty and no fault noisy data is created for testing the detector. Faults are simulated with efficiency reduction of 2%. Test data is created at 150 points including 50 samples of faulty data and 100 samples of no fault data. Each sample contains a time series of 150 discrete points, in a manner similar to Fig. 7. The samples follow the pattern shown in Fig. 7, with a

Table 2 Missed and false alarms

Module Faults	Noisy Data/Fuzzy System		FMH Filtered Data/Fuzzy System	
	Missed Alarm (%)	False Alarm (%)	Missed Alarm (%)	False Alarm (%)
FAN	1	8	0	0
LPC	4	9	1	0
HPC	2	7	0	0
HPT	1	3	0	0
LPT	2	3	1	0

fault starting at $k=51$ and ending at $k=100$. Ten such samples of data are used for each fault to obtain the statistics shown in Table 2.

Correct fault detection occurs when the detector gives the correct binary decision about the trend shift at a given discrete time point. When a faulty engine is misdiagnosed as healthy, a missed alarm is indicated. When a healthy engine is misdiagnosed as faulty, a false alarm is indicated. Table 2 shows the false alarm and missed alarm statistics for each of the five module faults for noisy and filtered data. For the noisy data, thresholds corresponding to noisy data are used to define the “high,” “medium,” and “low” fuzzy sets. For the filtered data, thresholds corresponding to filtered data are used to define the “high,” “medium,” and “low” fuzzy sets. The filtered data uses an FMH filter operating on 21 ($2I+1, I=10$) points of data at a time using the recursive scheme discussed earlier with $I=2, I=3, I=5, I=7$, and $I=10$. The detection results are expressed in binary form with a healthy engine being 0 and faulty engine being 1.

The noisy data and corresponding fuzzy system shows several missed and false alarms. The filtered data and corresponding fuzzy system shows no false alarms for the faults and a few missed alarms. False alarms are eliminated from the filtered data because of the lack of intersection of the “low” and “high” fuzzy sets for the filtered case (Fig. 14). However, some missed alarms occur when some faults in the “medium” zone are misdiagnosed because of the intersection between “medium” and “high” fuzzy sets in Fig. 14. For the noisy data, there is considerable intersection between the “high” and “low” fuzzy sets leading to several false alarms, which are a great handicap for a diagnostic system. False alarms are more unwanted than missed alarms as they lower the faith of a user in the diagnostics system. It is clear that using the FMH filter reduces the noise in the data and improves the separability of the faulty engine and the healthy engine.

Concluding Remarks

Filtering methods are explored for removing noise from data while preserving sharp edges that many indicate a trend shift in gas turbine measurements. Linear FIR and IIR filters are found to be have problems with removing noise while preserving features in the signal. Linear filters need to be used recursively to remove noise. However, recursive use of linear filters smoothed out sharp edges in data that might indicate a fault. The nonlinear FMH filter is found to accurately reproduce the root signal from noisy data. FMH filters can be used in recursive mode to remove noise without smoothing out features in the signals. However, FMH filters are batch filters and have a time lag while linear filters are instantaneous. This shortcoming of FMH filters can be removed by faster sampling of measurement data.

Simulated faulty data and fault-free gas path measurement data are passed through FMH filters and health residuals for the data set are created. The health residual is a scalar norm of the gas path measurement deltas and is used to partition the faulty engine from the healthy engine using fuzzy sets. The fuzzy detection system is developed and tested with noisy data and with filtered data. It is found from tests with simulated fault free and faulty data that trend shift detection based on filtered data is very accurate with no false alarms and negligible missed alarms. In sharp contrast, the

fuzzy detector based on noisy data gives several false alarms and missed alarms, which is unacceptable for a fault detection algorithm as it would dramatically increase maintenance costs instead of saving costs.

Nomenclature

EGT	= exhaust gas temperature
FC	= flow capacity
FIR	= finite impulse response
FMH	= FIR median hybrid
FP4	= high-pressure turbine area
FP45	= low-pressure turbine area
IIR	= infinite impulse response
N1	= low-pressure rotor speed
N2	= high-pressure rotor speed
WF	= fuel flow
x	= element of fuzzy set
\mathbf{x}	= module faults
\mathbf{z}	= measurement deltas
Δ	= change from baseline “good” engine
η	= efficiency
$\mu_A(x)$	= degree of membership of x in fuzzy set A
σ	= uncertainty as standard deviation

References

- [1] Urban, L. A., 1972, “Gas Path Analysis Applied to Turbine Engine Conditioning Monitoring,” AIAA/SAE Paper 72-1082.
- [2] Volponi, A., 1983, “Gas Path Analysis: An Approach to Engine Diagnostics,” *Time-Dependent Failure Mechanisms and Assessment Methodologies*, Cambridge University Press, Cambridge, UK.
- [3] Luppold, R. H., et al., 1989, “Estimating In-Flight Engine Performance Variations Using Kalman Filter Concepts,” AIAA Paper 89-2584.
- [4] Stamatis, A., et al., 1991, “Jet Engine Fault Detection With Discrete Operating Points Gas Path Analysis,” *J. Propul.*, **7**(6), pp. 1043–1048.
- [5] Kerr, L. J., et al., 1991, “Real-Time Estimation of Gas Turbine Engine Damage Using a Control Based Kalman Filter Algorithm,” ASME Paper 91-GT-216.
- [6] Gallops, G. W., et al., 1992, “In-Flight Performance Diagnostic Capability of an Adaptive Engine Model,” AIAA Paper 92-3746.
- [7] Volponi, A. J., and Urban, L. A., 1992, “Mathematical Methods of Relative Engine Performance Diagnostics,” SAE Trans., **101**, Journal of Aerospace Technical Paper 92-2048, pp. 1–26.
- [8] Doel, D. L., 1993, “An Assessment of Weighted-Least-Squares Based Gas Path Analysis,” ASME Paper 93-GT-119.
- [9] Lu, P. J., Hsu, T. C., Zhang, M. C., and Zhang, J., 2001, “An Evaluation of Engine Fault Diagnostics Using Artificial Neural Networks,” ASME J. Gas Eng. Power, **123**, pp. 240–246.
- [10] Volponi, A. J., Depold, H., Ganguli, R., and Daguang, C., 2000, “The Use of Kalman Filter and Neural Network Methodologies in Gas Turbine Performance Diagnostics: A Comparative Study,” ASME Paper 00-GT-547.
- [11] DePold, H., and Gass, F. D., 1999, “The Application of Expert Systems and Neural Networks to Gas Turbine Prognostics and Diagnostics,” ASME J. Eng. Gas Turbines Power, **121**, pp. 607–612.
- [12] Chen, J., Lopez-Toribio, C. J., and Patton, R. J., 1999, “Nonlinear Dynamic Systems Fault Detection and Isolation Using Fuzzy Observers,” *J. Syst. Control Eng., Part 1*, **213**(6), pp. 467–476.
- [13] Strum, R. D., and Kirk, D. E., 1989, *First Principles of Discrete Systems and Digital Signal Processing*, Addison-Wesley, Reading, MA.
- [14] Tham, M. T., and Parr, A., 1994, “Succeed at On-Line Validation and Reconstruction of Data,” *Chem. Eng. Prog.*, **90**(4), pp. 46–58.
- [15] Gallagher, Jr., N. C., and Wise, G., 1981, “Theoretical Analysis of the Properties of Median Filters,” *IEEE Trans. Acoust., Speech, Signal Process.*, **29**, pp. 1136–1141.
- [16] Heinson, P., and Neuvo, Y., 1987, “FIR-Median Hybrid Filters,” *IEEE Trans. Acoust., Speech, Signal Process.*, **35**, pp. 832–838.
- [17] Heinson, P., and Neuvo, Y., 1988, “FIR-Median Hybrid Filters With Predictive FIR Substructures,” *IEEE Trans. Acoust., Speech, Signal Process.*, **36**, pp. 892–899.
- [18] Albuquerque, J., and Biegler, J., 1995, “Data Reconciliation and Gross Error Detection for Dynamic Systems,” *AIChE J.*, **42**(10), pp. 2841–2856.
- [19] Johnston, P. M., and Kramer, M. A., 1995, “Maximum Likelihood Data Rectification: Steady State Systems,” *AIChE J.*, **41**, pp. 2415–2421.
- [20] Karjala, T. W., and Himmelblau, D. M., 1994, “Dynamic Data Rectification by Recurrent Neural Networks vs. Traditional Methods,” *AIChE J.*, **40**, pp. 1865–1875.
- [21] Kramer, M. A., 1991, “Non linear Principal Components Analysis Using Auto Associative Neural Networks,” *AIChE J.*, **37**, pp. 233–243.
- [22] Arce, G. R., et al., 1998, “Affine Order Statistic Filters: Mediatization of FIR Filters,” *IEEE Trans. Signal Process.*, **46**(8), pp. 2101–2112.

- [23] Arce, G. R., Grabowski, N. A., and Gallagher, N. C., 2000, "Weighted Median Filter With Sigma-Delta Modulation Encoding," *IEEE Trans. Signal Process.*, **48**(2), pp. 489–498.
- [24] Zadeh, L., 1996, "Fuzzy Logic=Computing With Words," *IEEE Trans. Fuzzy Syst.*, **4**(2), pp. 103–111.
- [25] Volponi, A. J., 1999, "Gas Turbine Parameter Corrections," *ASME J. Eng. Gas Turbines Power*, **121**, pp. 613–621.
- [26] Gonzales, R. C., and Woods, R. E., 1992, *Digital Image Processing*, Addison-Wesley, Reading, MA.
- [27] Chi, Z., Yan, H., and Pham, T., 1998, *Fuzzy Algorithms: With Applications to Image Processing and Pattern Recognition*, World Scientific, Singapore.
- [28] Therrien, C. W., 1989, *Decision Estimation and Classification: An Introduction to Pattern Recognition and Related Topics*, John Wiley and Sons, New York.
- [29] Kosko, B., 1997, *Fuzzy Engineering*, Prentice-Hall, Englewood Cliffs, NJ.

Global Nonlinear Modeling of Gas Turbine Dynamics Using NARMAX Structures

N. Chiras

C. Evans

D. Rees

School of Electronics,
University of Glamorgan,
Pontypridd CF27 1DL
Wales, UK

This paper examines the estimation of a global nonlinear gas turbine model using NARMAX techniques. Linear models estimated on small-signal data are first examined and the need for a global nonlinear model is established. A nonparametric analysis of the engine nonlinearity is then performed in the time and frequency domains. The information obtained from the linear modeling and nonlinear analysis is used to restrict the search space for nonlinear modeling. The nonlinear model is then validated using large-signal data and its superior performance illustrated by comparison with a linear model. This paper illustrates how periodic test signals, frequency domain analysis and identification techniques, and time-domain NARMAX modeling can be effectively combined to enhance the modeling of an aircraft gas turbine. [DOI: 10.1115/1.1470483]

Introduction

Gas turbines were originally designed for aircraft propulsion but are now extensively used in aero, marine, and industrial applications. With such widespread and increasing applications, the modeling of such engines is an issue of some importance.

Modeling of gas turbines is required both in the development and operational stages of an engine's life. Design of control systems can be facilitated and, once the model has been verified against real engine data, a physical interpretation of the model parameters can often be made. This allows initial assumptions about the engine characteristics to be checked.

This paper deals with the relationship between the fuel flow and shaft speed dynamics of an aircraft gas turbine. The shaft speeds are the primary outputs of a gas turbine, from which the internal pressures and the thrust can be calculated. Modern gas turbines usually have two shafts, one connecting a high-pressure (HP) compressor to a HP turbine, the other connecting the low-pressure (LP) compressor to a LP turbine. The Rolls Royce Spey Mk202 turbofan modeled in this paper is an example of such an engine. Although no longer in service, the Spey possess the same characteristics, for control purposes, as a modern engine such the EJ200 fitted to the Eurofighter ([1]).

Recent work by Evans et al. [2–5] concentrated on testing the engine using small-amplitude multisine signals and then using frequency-domain techniques to identify linear models of high accuracy. The errors due to noise and nonlinearities were assessed and found to be small for these small-signal models. The same techniques were used to estimate models at a range of different operating points. Data were gathered under sea level static conditions at the Defense Evaluation & Research Agency (DERA) at Pyestock. Multisine and inverse repeat maximum length binary sequences (IRMLBS) were used at amplitudes of up to $\pm 10\%$ of the steady-state fuel flow ($\pm 10\% W_f$).

However, all physical systems are nonlinear, to a greater or lesser extent, so the need is apparent for a more complete gas turbine description using nonlinear models. Rodriguez [6,7] used a multiobjective genetic programming approach on the same data and allocated weights to various objectives to assess their significance in the identification of Nonlinear Autoregressive Moving

Average with eXogenous inputs (NARMAX) models of the engine. Higher-amplitude signals, such as triangular waves and three-level periodic signals with input amplitudes of up to $\pm 40\% W_f$, were used to validate the estimated models. These caused the HP shaft speed to vary between 65% and 85% of its maximum value ($\%N_H$).

In this paper, a review of the linear models previously estimated is presented and their properties are discussed. The variation of the linear models with operating point clearly shows the need for a global nonlinear model. The presence of this nonlinearity is then detected using nonparametric analysis of the engine data. Knowledge gained from this analysis is used *a priori* to restrict the search space of nonlinear models under consideration. The estimation of NARX models (NARMAX models with the noise terms excluded) of the HP shaft dynamics is then discussed. Finally, the performance of the linear and nonlinear models is compared.

Linear Modeling

Small-signal linear models were estimated using frequency-domain techniques, which have a number of clear advantages when applied to this problem. First, the measured fuel-flow is both noise corrupted and band limited, which matches the basic assumptions of the frequency-domain approach ([8]). In addition, the engine has an unknown combustion delay, which can be included as an estimated parameter in the frequency-domain estimator. Finally, *s*-domain models can be directly estimated in the frequency-domain and compared to the linearized thermodynamic models of the engine ([5]). A physical interpretation can thus be made of the model poles and zeros and the estimated time delay.

The basic input-output relationship in the frequency domain is given by

$$H(j\omega) = \frac{Y(j\omega)}{U(j\omega)}, \quad (1)$$

$H(j\omega)$ being the frequency response function and $Y(j\omega)$ and $U(j\omega)$ the Fourier transforms of the output and input signals. The use of periodic signals allows the direct estimation of the frequency response function as the ratio of the mean values of the output and input Fourier coefficients, at the discrete test frequencies ω_k

Contributed by the International Gas Turbine Institute (IGTI) of THE AMERICAN SOCIETY OF MECHANICAL ENGINEERS for publication in the ASME JOURNAL OF ENGINEERING FOR GAS TURBINES AND POWER. Paper presented at the International Gas Turbine and Aeroengine Congress and Exhibition, New Orleans, LA, June 4–7, 2001; Paper 01-GT-019. Manuscript received by IGTI, December 2000, final revision, March 2001. Associate Editor: R. Natole.

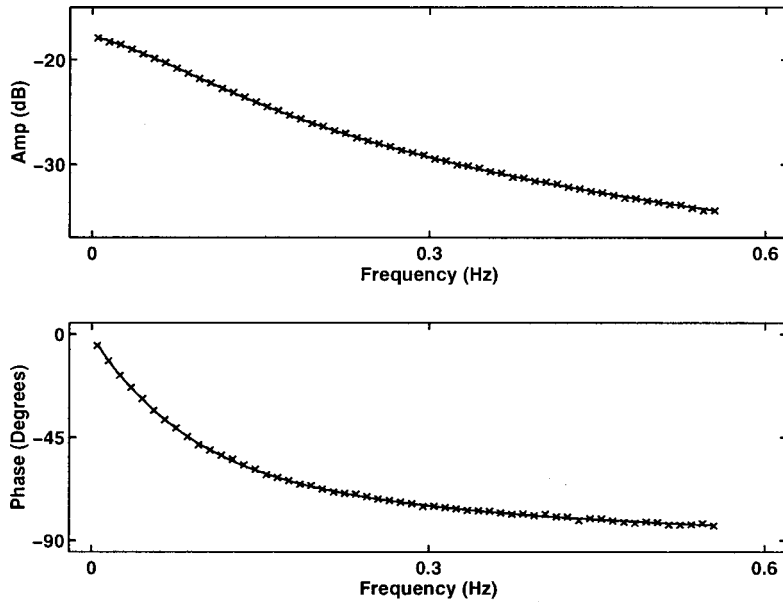


Fig. 1 Frequency response of high-pressure shaft model at 75% N_H (solid), with estimated frequency response function (crosses)

$$\hat{H}(j\omega_k) = \frac{\frac{1}{M} \sum_{m=1}^M Y_m(j\omega_k)}{\frac{1}{M} \sum_{m=1}^M U_m(j\omega_k)} = \frac{\bar{Y}(j\omega_k)}{\bar{U}(j\omega_k)} \quad (2)$$

where M is the number of periods measured. This is termed the EV estimator and it has been shown that it is a maximum likelihood estimator if the input and output noises have a complex normal distribution, even if they are mutually correlated ([9]). Multisine signals were used to excite the engine and by averaging over multiple periods signal-to-noise ratios (SNRs) of greater than 40 dB were obtained for the input and output.

Parametric identification involves estimating continuous s -domain models with a pure time delay T_d ([10,11]).

$$H(s) = \frac{b_0 + b_1 s + \dots + b_{nb} s^{nb}}{a_0 + a_1 s + \dots + a_{na} s^{na}} e^{-j\omega T_d} \quad (3)$$

These models can be validated by comparison of their frequency responses with the frequency response functions of the engine. Tests were conducted at several operating points along the turbine running range, from 55% N_H to 90% N_H , at input amplitudes of $\pm 10\%$ W_f .

Parametric models were estimated at each operating point, us-

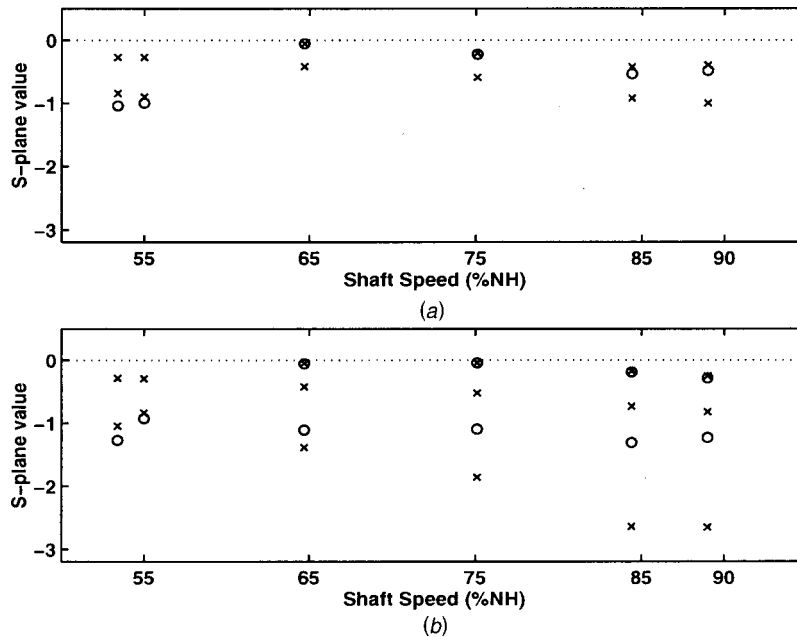


Fig. 2 Poles and zeros of the linear frequency-domain models (a) high-pressure shaft and (b) low-pressure shaft. Showing: poles (x) and zeros (o).

Table 1 Model DC gains at different operating points

Operating Point	HP Shaft DC Gain	LP Shaft DC gain
53	0.262	0.195
65	0.177	0.141
75	0.127	0.098
85	0.088	0.067

ing a model selection and validation procedure which has been described in detail in [2–5]. The frequency fit of one such model, with a transfer function

$$G(s) = \frac{0.06733(s + 0.1514)}{(s + 0.1388)(s + 0.5742)} e^{-0.012s}, \quad (4)$$

is shown in Fig. 1. This pattern was repeated across the range of operating points, with all of the models obtained having poles and zeros lying on the real axis of the left-hand s -plane. The variation of the poles and zeros with operating point is shown in Fig. 2 and several features can be deduced from the plot. It is clear that the HP and LP shafts have different order dynamics. Canceling pole-zero pairs suggest that the HP shaft is predominantly first order, across most of the operating range, and that the LP shaft is second order. It is also clear from Fig. 2 that the position of the poles and zeros change with the operating point. The DC gains of these models also decrease as the operating point is increased, as shown in Table 1. This shows clearly that the gas turbine is nonlinear ([12]).

It can be concluded that for linear models representing the small-signal dynamics of the gas turbine the frequency-domain identification of s -domain models is a good approach. This provides an accurate representation of the system, incorporating the pure time delay in the model, and a physical interpretation can be made of the model poles and zeros. This work has been recently extended to the multivariable case ([13]), where frequency techniques were used to estimate linear state-space models.

Detecting the Nonlinearity

It is possible to detect the presence of the engine nonlinearity by analyzing the small-signal data at a single operating point. If a signal contains only harmonics that are odd multiples of the fundamental (such as an IRMLBS or an odd-harmonic multisine) then all the frequency contributions at the output resulting from any even-order nonlinearities will fall at even harmonics ([14]). Thus the even nonlinearities can be detected just by inspection of the frequency content of the system input and output signals.

Similarly if an odd-odd multisine is used (a signal where every other odd harmonic is also excluded) both even-order and odd-order nonlinearities can be detected, since the odd-order nonlinear contributions will fall at the omitted odd harmonics. A useful tool with which to assess the periodicity of the generated harmonics, and distinguish them from noise harmonics, is the squared coherence function

$$\gamma_{nl}(\omega) = \frac{\left| \frac{1}{M} \sum_{m=1}^M Y_m(j\omega) \right|^2}{\frac{1}{M} \sum_{m=1}^M Y_m(j\omega) Y_m^*(j\omega)} = \frac{|\bar{Y}(j\omega)|^2}{G_{YY}(\omega)} \quad (5)$$

where $Y_m(j\omega)$ is the output spectrum at the excited and non-excited frequencies, $Y_m^*(j\omega)$ its complex conjugate, and $G_{YY}(\omega)$ the autospectrum of the output. The coherence represents the ratio of the periodic power to the total power at the output frequencies and if there is no periodic power at a given output frequency then the coherence will assume a value of $1/M$.

The periodic power due to nonlinearities can be detected since the coherence function at those frequencies will rise well above the $1/M$ bound.

The nonlinear coherence of an odd-odd multisine at an input amplitude of $\pm 10\%$ W_f is plotted in Fig. 3, along with the $1/M$ bound, in order to assess the nonlinear contributions. It is seen that the coherence of the even harmonics in the input spectrum is close to the $1/M$ bound whereas the coherence of the even har-

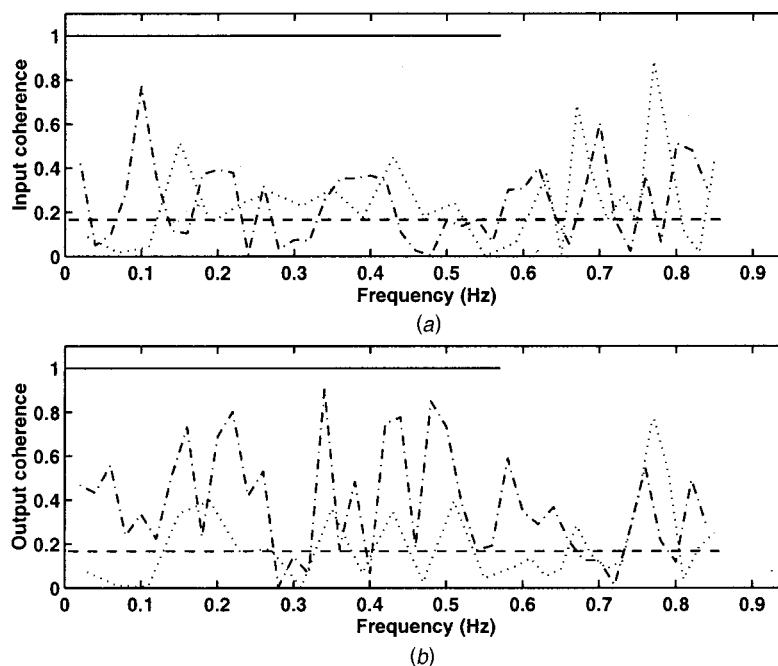


Fig. 3 Nonlinear coherence of an odd-odd multisine at (a) input and (b) output. Input harmonics (solid), even harmonics (dashdot) and omitted odd harmonics (dotted). With $1/M$ bound (dashed).

monics at the output is more significant. It can be also seen that the coherence of the omitted odd harmonics is consistently lower on both the input and output.

This suggests the presence of a weak even-order nonlinearity in the engine, for small input amplitudes. More information about this nonlinear effect can be gathered by looking at the input-output properties of the triangular test shown in Fig. 4. Most of the power is concentrated at low frequencies for this signal, thus making it unsuitable for exciting the engine dynamics. However, this property allows the use of these data as a pseudo-static test, which can provide a very good approximation of the static behavior of the engine. The static polynomial

$$u(t) = 445 - 13y(t) + 0.14y^2(t) \quad (6)$$

was then fitted to these data and it can be seen from the fit in Fig. 5, that a second-order polynomial is sufficient to model the static behavior of the engine. It must be stressed here that this even-order nonlinearity did not influence the estimated linear models, due to the use of odd harmonic test signals.

Nonlinear Modeling

Having detected the nonlinearity, the need to develop a nonlinear model for the gas turbine is apparent. Leontaritis and Billings [15] introduced the NARMAX approach as a means of describing the input-output relationship of a nonlinear system. The model represents the extension of the well-known ARMAX model to the nonlinear case, and is defined as

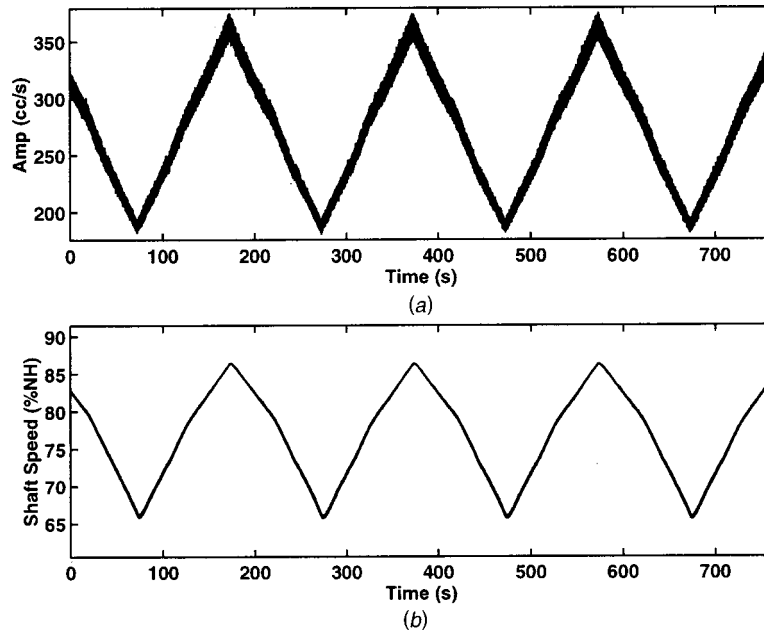


Fig. 4 Triangular test (a) measured fuel flow (b) high-pressure shaft response

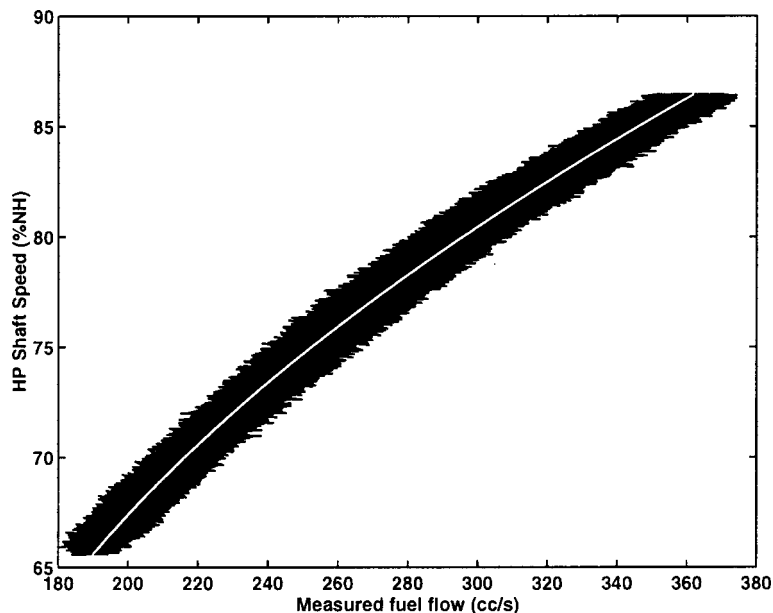


Fig. 5 Input-output relationship for the gas turbine when using a high-amplitude triangular wave (black), nonlinear fit (white)

$$y(k) = F(y(k-1), \dots, y(k-n_y), u(k-1), \dots, u(k-n_u), e(k-1), \dots, e(k-n_e)) + e(k) \quad (7)$$

where F is a nonlinear function; $y(k)$, $u(k)$, and $e(k)$ represent the output, input, and noise signals, respectively; and n_y , n_u , and n_e are their associate maximum lags. Billings and Tsang [16] used an orthogonal estimator for the identification of a NARMAX model. This estimator is a very simple and efficient algorithm that allows each coefficient in the model to be estimated, while at the same time providing an indication of the contribution that the term makes to the system output using the error reduction ratio (ERR) defined as

$$ERR_i = \frac{g_i^2 \sum_{k=1}^N w_i^2(k)}{\sum_{k=1}^N y^2(k)} \quad (8)$$

where g_i are the coefficients and $w_i(k)$ are the terms of an auxiliary model constructed in such a way that the terms $w_i(k)$ are orthogonal to the data records. A forward-regression algorithm is employed to select at each step the term with the highest error reduction ratio, in other words the term which contributes most to the reduction of the residual variance. The procedure is usually stopped using an information criterion such as the Akaike information criterion (AIC), defined as

$$AIC = N \log_e(\sigma_\varepsilon^2(\theta_p)) + kp \quad (9)$$

where $\sigma_\varepsilon^2(\theta_p)$ is the variance of the residuals associated with a p -term model and k is a penalizing factor.

In this paper a priori knowledge of the engine dynamics will be used (obtained from the previous section) to identify NARX models with the nonlinear terms restricted to the second order. The selection of an appropriate signal for use in nonlinear identification is an issue of some importance. Schoukens et al. [17] showed that multisine signals with a user-defined amplitude distribution can be designed. The authors suggest that a nonlinear system

should be tested with a signal whose amplitude distribution matches as closely as possible that of a typical input to the system.

This poses a challenge for gas turbine modeling, since a typical input is difficult to define due to the diversity of inputs to the engine. To this end, a concatenated set of small-signal IRMLBS tests was used for the identification of the nonlinear model. A single period of one of these signals, at an operating point of 75% N_H and input amplitude of $\pm 10\%$ W_f , is shown in Fig. 6. The spectra of these signals are shown in Fig. 7. It can be seen that the signal-to-noise ratios are very good for this input amplitude, up to 0.6 Hz. The concatenated data used for nonlinear model estimation are shown in Fig. 8.

From linear modeling it was established that a second-order input-output lag would be sufficient to capture the engine dynamics. In addition it was shown that the nonlinearity in the engine could be approximated by a second-order term. Setting the maximum input and output lags n_u and n_y to 2, the forward-regression orthogonal estimation algorithm was applied for a maximum order of nonlinearity of 2. The selected terms with their associated error reduction ratios and the coefficients of the selected model 1 are shown in Table 2. The model terms are listed in the order of their qualification.

Mendes [18] showed that standardization can aid structure selection and avoid the problem of wrongly qualifying spurious terms before significant terms are selected. Standardization involves removing the means from the data and normalizing the variance of the data records to unity. A new model shown in Table 3 was then estimated using the forward-regression orthogonal algorithm but in this case the data were standardized before entering the estimator.

The model quality can be assessed using higher-order correlation functions ([19]), but no definite conclusion can be drawn unless cross validation is employed. This is a nonparametric approach, which consists of simulating the candidate model with different engine inputs and a comparison of the results with the

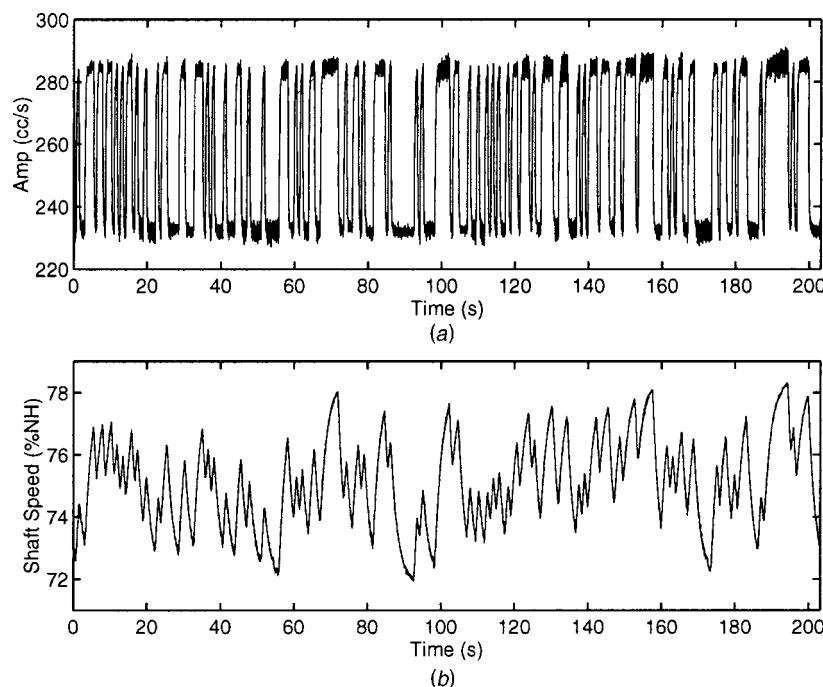


Fig. 6 One period of an IRMLBS test (a) measured fuel flow (b) high-pressure shaft response

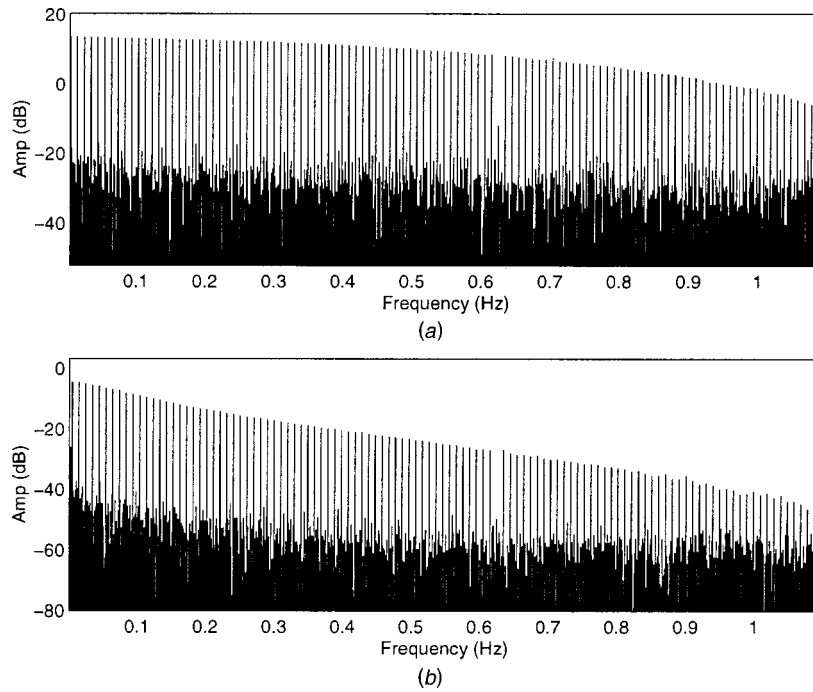


Fig. 7 Spectra of the IRLBS test (a) measured fuel flow (b) high-pressure shaft response

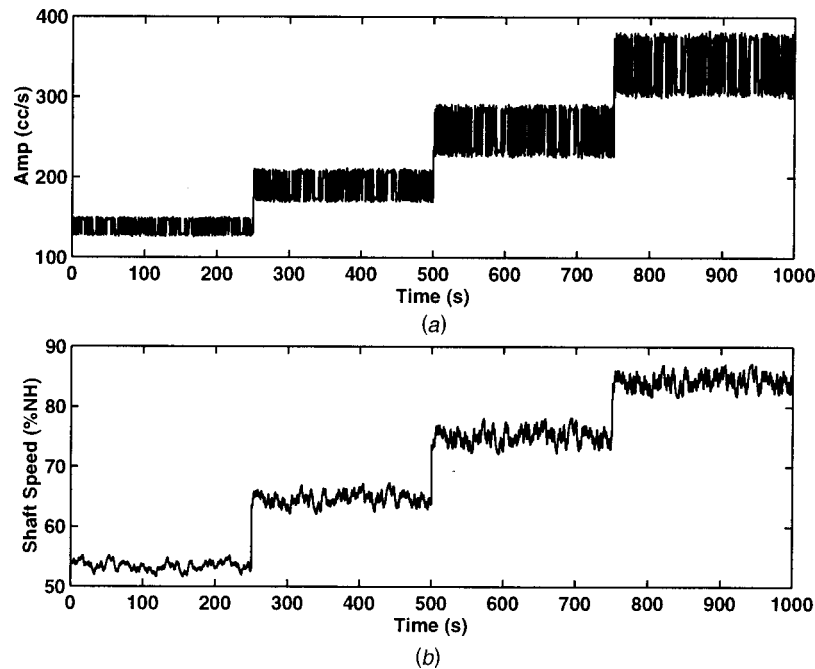


Fig. 8 Concatenated data set used for estimation (a) measured fuel flow (b) high-pressure shaft response

Table 2 Quadratic NARX model 1

Model Terms	ERR _i	θ _i
y(k-1)	9.9 e-1	6.998e-1
y(k-2)	1.8 e-7	2.867e-1
u(k-1)	1.6 e-7	9.725e-3
u(k-1)*y(k-2)	8.8 e-7	-1.158e-4
u(k)*y(k-1)	8.5 e-8	4.277e-5
Constant	3.1 e-9	-8.595e-2

Table 3 Quadratic NARX model 2

Model Terms	ERR _i	θ _i
y(k-1)	9.9 e-1	1.0998
u(k-1)	1.9 e-5	4.208 e-3
y(k-2)	1.3 e-5	-5.863 e-2
y(k-1)*y(k-2)	3.2 e-6	-9.563 e-2
Constant	8.8 e-6	-1.3577
y ² (k-2)	4.4 e-6	5.166 e-2
y ² (k-1)	1.0 e-5	4.343 e-2
u(k-2)	1.4 e-7	7.546 e-4

measured engine outputs. A range of tests is available for this purpose which consists of low-amplitude IRMLBS and multisine tests and high-amplitude tests such as triangular waves and three-level sequences.

The difference between the performance of the two nonlinear models will be illustrated using high-amplitude data. Figure 9 shows a test in which the engine input was a triangular wave of period 100s and amplitude of $\pm 35\% W_f$. The measured engine

output is plotted, along with the responses of models 1 and 2. It can be seen that the two model outputs follow the measured output very well, without any significant difference between their behavior.

The next test, shown in Fig. 10, consists of a three-level sequence of period 100s with an input amplitude of $\pm 22\% W_f$. This is effectively a series of positive and negative step inputs. Again in this test the models show a good response, with model 2 per-

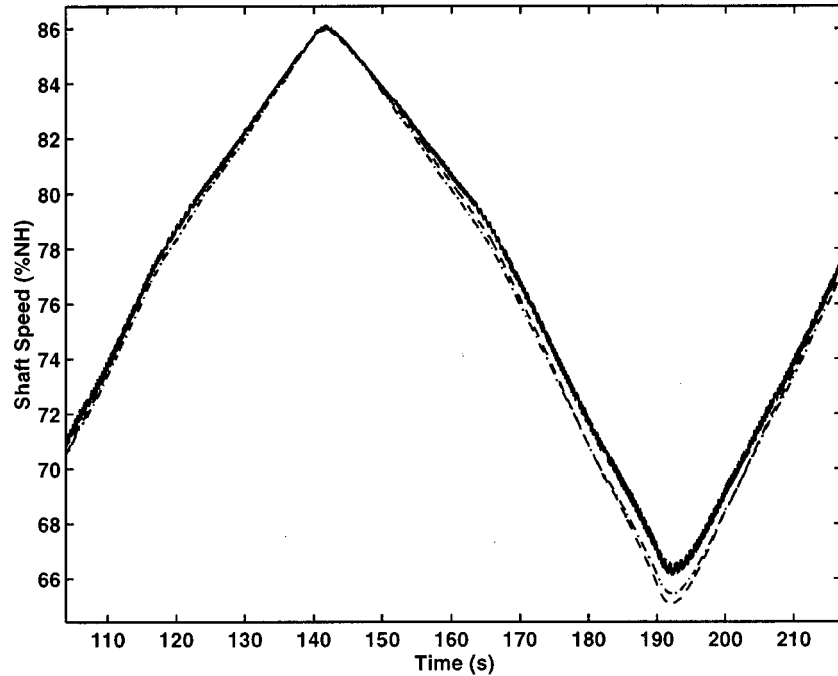


Fig. 9 Output of triangular wave high-pressure shaft test. Measured output (solid), model 1 output (dashed), model 2 output (dash-dot).

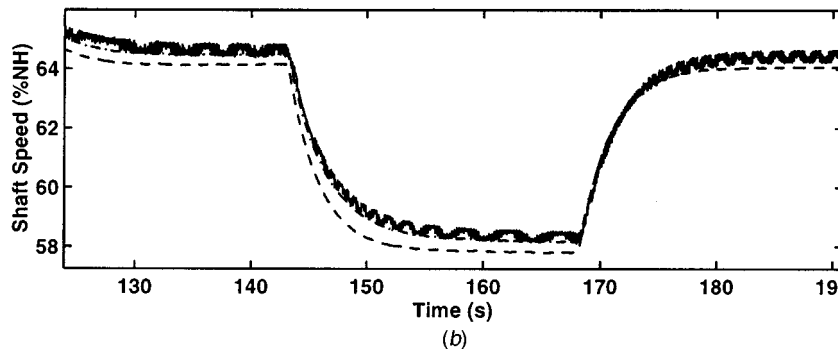
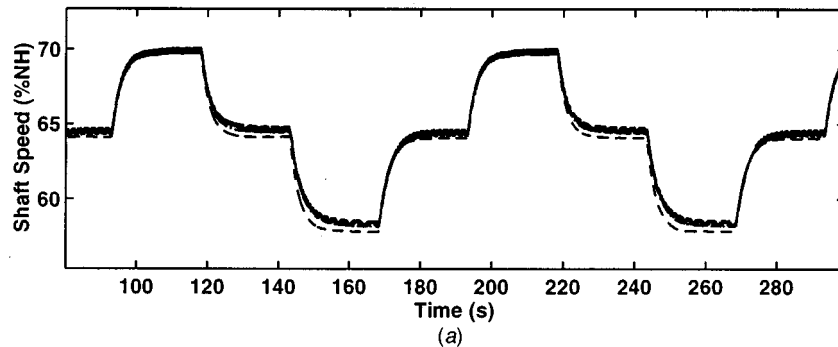


Fig. 10 Output of three-level high-pressure shaft test. (a) Complete signal (b) portion of the signal. Measured output (solid), model 1 output (dashed), model 2 output (dash-dot).

forming somewhat better than model 1. Model 2 was selected for this reason. It is similar in structure to a model previously estimated by Chiras et al. [20], using an approach based simply on monitoring the model cost function.

After establishing the quality of the model using cross validation, the model parameters were examined in order to identify any possible similarities with the previously identified linear models. It was noticed that the linear part of nonlinear model 2 is unstable, having a discrete pole outside the unit circle at $z=1.043$. This should not be taken to mean in any way that the model is unstable in its operating region. On the contrary, if model 2 is linearized at different operating points, the resulting locally linear models are stable. It is thus necessary for the control engineer to take care when using a nonlinear model of this kind since it is only valid in the region for which it was identified.

Linear Versus Nonlinear

In this section a comparison is made between the performance of the linear models obtained using frequency-domain techniques and nonlinear model 2 obtained in the previous section. Figure 11 shows a time-domain comparison between the linear and nonlinear model outputs and the measured gas turbine output for a small signal IRMLBS test. It can be seen that both the linear and nonlinear models are capable of modeling the low-amplitude dynamics of the engine. Close inspection shows that the linear model performs slightly better. This can be attributed to the inclusion of the time delay into the model.

Similar results are obtained when the performance of the nonlinear model is compared with the different s -domain models at different operating points, suggesting that the nonlinear model is capable of modeling the small-signal engine dynamics throughout the operating range. This allows the single nonlinear model to be used in place of the family of linear models previously estimated.

Figure 12 shows a comparison of the performance of a linear model (estimated at 75% N_H) and the nonlinear model, on high-amplitude data. It can be seen from this triangular test that the linear model does not follow the engine data at high shaft speeds, whereas the nonlinear model has some problems at the lower shaft

speeds. The difference is even more apparent in the next test, shown in Fig. 13, where a three-level sequence was used as the input. Here, the linear model is completely unable to capture the high-amplitude dynamics.

It can be concluded that the nonlinear model is capable of modeling both high and low-amplitude engine dynamics. The linear models obtained perform very well with small-signal data at different operating points but cannot model the engine response to all large-signal tests. The results can also be extended to the LP shaft case, where a nonlinear model of similar structure (but different parameter values) was estimated.

Conclusions

The linear and nonlinear modeling of a gas turbine was discussed in this paper. Linear models were estimated in the frequency domain using small-signal data. The models perform really well with these data and allow a physical interpretation of the linear modes (and the pure time delay) of the engine to be made. The fact that these models vary with operating point suggests the need for a global nonlinear model. The order of the linear dynamics can be used as *a priori* information in the nonlinear modeling.

A simple method to identify a nonlinear NARX model of a gas turbine was proposed. This consisted of a nonparametric analysis of the engine data, in both time and frequency domains, to establish the existence and approximate order of the nonlinearity.

This allowed the search space of the potential NARX models to be considerably narrowed and facilitated the straightforward selection of an appropriate model structure. A model was estimated which performs well with both small-amplitude and high-amplitude tests. The performance of the model was illustrated on a range of signals and shown to follow the output behavior of the engine extremely well. However, the physical interpretability of the model is lost. This is due to inherent problems with discrete-time estimation using band-limited input signals and also to the great variability of the model parameters when different nonlinear terms are included. Nevertheless, such a model could provide the basis for a global nonlinear controller of the engine.

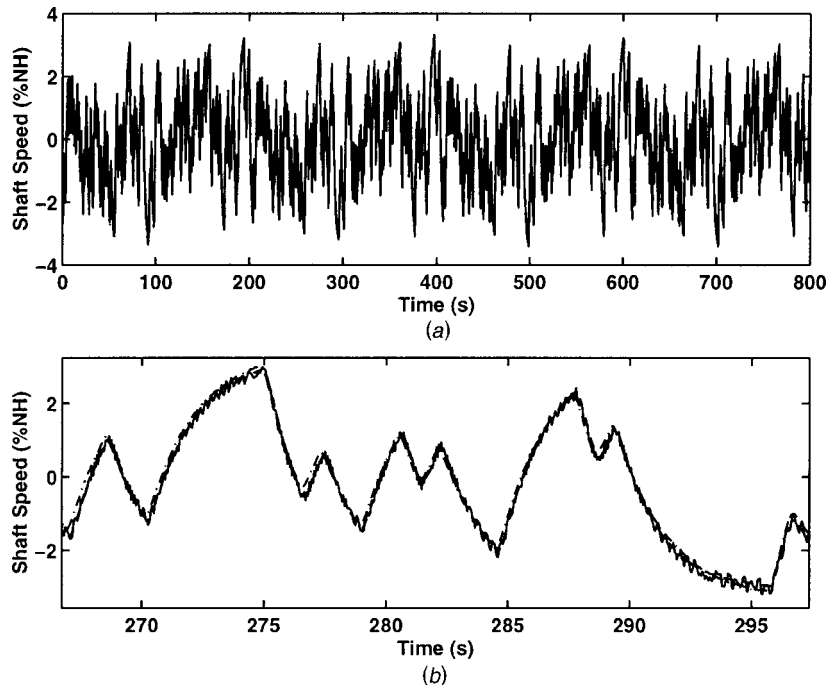


Fig. 11 Output of IRMLBS high-pressure shaft test. (a) Complete signal (b) portion of the signal. Measured output (solid), linear s -domain model (dashed), nonlinear model output (dash-dot).

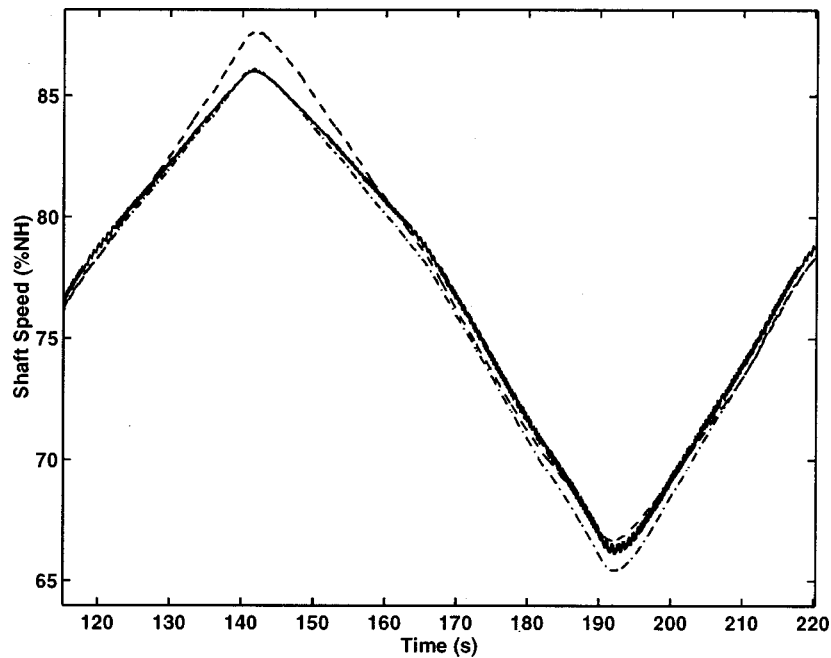


Fig. 12 Output of triangular wave high-pressure shaft test. Measured output (solid), linear s -domain model (dashed), nonlinear model output (dash-dot).

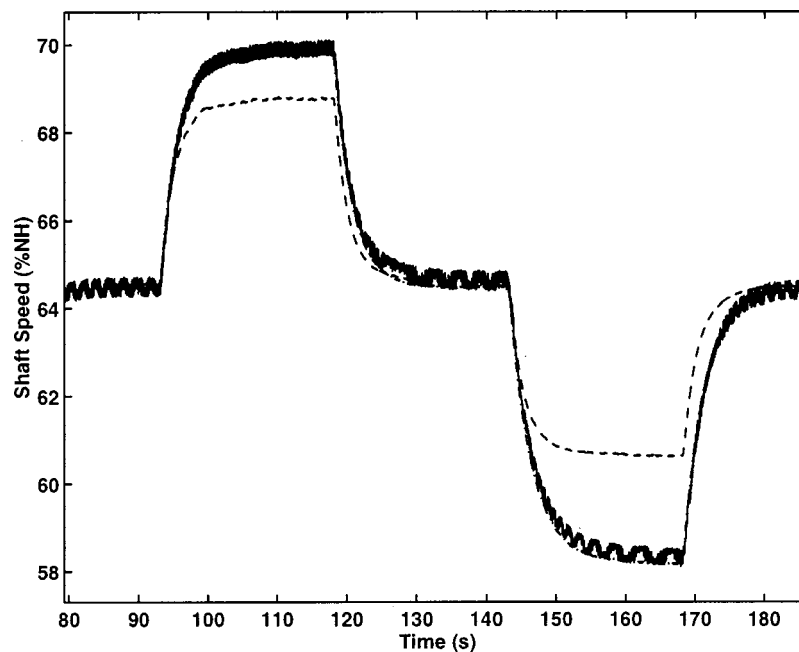


Fig. 13 Output of three-level high pressure shaft test. Measured output (solid), linear s -domain model (dashed), nonlinear model output (dash-dot).

This paper illustrates how periodic test signals, frequency domain analysis, and identification techniques, and time-domain NARMAX modeling can be effectively combined to enhance the modelling of an aircraft gas turbine.

Acknowledgment

This work was conducted on data gathered at the Defense Evaluation & Research Agency at Pyestock with the support of Rolls Royce plc. The authors would like to thank all the staff involved.

References

- [1] Dadd, G. J., Sutton, A. E., and Greig, A. W. M., 1996, "Multivariable Control of Military Engines," *AGARD Conference Proceedings No. 572—Advanced Aero-Engine Concepts and Controls*, Paper 28, pp. 1–12.
- [2] Evans, C., Rees, D., and Jones, L., 1995, "Identifying Linear Models of Systems Suffering Nonlinear Distortions, With a Gas Turbine Application," *IEE Proc.-D: Control Theory Appl.*, **142**(3), pp. 229–240.
- [3] Evans, C., Rees, D., and Hill, D., 1998, "Frequency-Domain Identification of Gas Turbine Dynamics," *IEEE Trans. Cont. Syst. Technol.*, **6**(5), pp. 651–662.
- [4] Evans, C., Borrell, A., and Rees, D., 1999, "Testing and Modelling Gas Turbines Using Multisine Signals and Frequency-Domain Techniques," *ASME J. Eng. Gas Turbines Power*, **121**, pp. 451–457.
- [5] Evans, C., Rees, D., and Borrell, A., 2000, "Identification of Aircraft Gas

- Turbine Dynamics Using Frequency-Domain Techniques," *Cont. Eng. Pract.*, **8**(4), pp. 457–467.
- [6] Rodriguez, K., and Fleming, P. J., 1998, "Multiobjective Genetic Programming for Gas Turbine Engine Model Identification," *UKACC International Conference on Control*, **2**(455), pp. 1385–1390.
- [7] Rodriguez, K., 1999, "Multiobjective Evolutionary Algorithms in Non-linear System Identification," Ph.D. thesis, Department of Automatic Control and Systems Engineering, University of Sheffield, Sheffield, UK.
- [8] Schoukens, J., Pintelon, R., and Van Hamme, H., 1994, "Identification of Linear Dynamic Systems Using Piecewise Constant Excitations: Use, Misuse and Alternatives," *Automatica*, **30**(7), pp. 1153–1169.
- [9] Guillaume, P., 1992, "Identification of Multi-Input Multi-Output Systems Using Frequency-Domain Methods," Ph.D. thesis, Department ELEC, Vrije Universiteit Brussel, Brussels, Belgium.
- [10] Pintelon, R., Guillaume, P., Rolain, Y., and Verbeyst, F., 1992, "Identification of Linear Systems Captured in Feedback Loop," *IEEE Trans. Instrum. Meas.*, **41**(6), pp. 747–754.
- [11] Kollár, I., 1997, *Frequency Domain System Identification Toolbox for Use With Matlab*, Mathworks, Natick, MA.
- [12] Haber, R., 1985, "Non-linearity Tests for Dynamic Processes," *Proc. 7th IFAC Symp. Identification and System Parameter Estimation*, York, pp. 409–414.
- [13] Evans, C., Chiras N., Guillaume P., and Rees D., 2001, "Multivariable Modelling of Gas Turbine Dynamics," ASME Paper No. 2001-GT-0018.
- [14] Evans, C., and Rees, D., 1999, "Assessing the Errors in Practical Gas Turbine Modelling," ASME Paper No. 99-GT-138.
- [15] Leontaritis, I. J., and Billings, S. A., 1985, "Input-Output Parametric Models for Nonlinear Systems," *Int. J. Control*, **41**(2), pp. 311–341.
- [16] Billings, S. A., and Tsang, K. M., 1989, "Spectral Analysis of Non-linear Systems, Part 1. Parametric Non-linear Spectral Analysis," *J. Mechanical Systems and Signal Processing*, **3**(4), pp. 319–339.
- [17] Schoukens, J., and Dobrowiecki, T., 1998, "Design of Broadband Excitation Signals With a User Imposed Power Spectrum and Amplitude Distribution," *IEEE Instrumentation and Measurement Technology Conference*, pp. 1002–1005.
- [18] Mendes, E. M. A. M., and Billings, S. A., 1996, "An Important Issue of System Identification Using Algorithms for Structure Selection," *Proceedings of the Twelfth International Conference on CAD/CAM Robotics and Factories of the Future*, Middlesex University Press, Middlesex, UK, pp. 544–549.
- [19] Billings, S. A., and Zhu, Q. M., 1994, "Nonlinear Model Validation Using Correlation Tests," *Int. J. Control*, **60**(6), pp. 1107–1120.
- [20] Chiras, N., Evans, C., and Rees, D., 2000, "Nonlinear Gas Turbine Computer Modelling Using NARMAX Structures," *Proceedings IEEE Instrumentation and Measurement Technology Conference*, **3**, Baltimore, pp. 1278–1284.

A Multiple Harmonic Open-Loop Controller for Hydro/Aerodynamic Force Measurements in Rotating Machinery Using Magnetic Bearings

D. O. Baun

Project Engineer,
e-mail: dob@concepts-nrec.com

E. H. Maslen

Associate Professor,
e-mail: ehm7s@virginia.edu

C. R. Knospe

Associate Professor,
e-mail: crk4y@virginia.edu

R. D. Flack

Professor,
e-mail: rdf@virginia.edu

Department of Mechanical and Aerospace
Engineering,
University of Virginia,
Charlottesville, VA 22903

Inherent in the construction of many experimental apparatus designed to measure the hydro/aerodynamic forces of rotating machinery are features that contribute undesirable parasitic forces to the measured or test forces. Typically, these parasitic forces are due to seals, drive couplings, and hydraulic and/or inertial unbalance. To obtain accurate and sensitive measurement of the hydro/aerodynamic forces in these situations, it is necessary to subtract the parasitic forces from the test forces. In general, both the test forces and the parasitic forces will be dependent on the system operating conditions including the specific motion of the rotor. Therefore, to properly remove the parasitic forces the vibration orbits and operating conditions must be the same in tests for determining the hydro/aerodynamic forces and tests for determining the parasitic forces. This, in turn, necessitates a means by which the test rotor's motion can be accurately controlled to an arbitrarily defined trajectory. Here in, an interrupt-driven multiple harmonic open-loop controller was developed and implemented on a laboratory centrifugal pump rotor supported in magnetic bearings (active load cells) for this purpose. This allowed the simultaneous control of subharmonic, synchronous, and superharmonic rotor vibration frequencies with each frequency independently forced to some user defined orbital path. The open-loop controller was implemented on a standard PC using commercially available analog input and output cards. All analog input and output functions, transformation of the position signals from the time domain to the frequency domain, and transformation of the open-loop control signals from the frequency domain to the time domain were performed in an interrupt service routine. Rotor vibration was attenuated to the noise floor, vibration amplitude $\approx 0.2 \mu\text{m}$, or forced to a user specified orbital trajectory. Between the whirl frequencies of $\frac{1}{4}$ and 2 times running speed, the orbit semi-major and semi-minor axis magnitudes were controlled to within 0.5% of the requested axis magnitudes. The ellipse angles and amplitude phase angles of the imposed orbits were within 0.3 deg and 1.0 deg, respectively, of their requested counterparts. [DOI: 10.1115/1.1473159]

Introduction

A common experimental technique for measuring dynamic fluid-structure interaction forces is to impose a controlled or known excitation to a test structure and measure the resulting reaction forces due to the structure's interaction with the surrounding fluid. In the case of a rotating structure (compressor, turbine or pump impeller, seal or bearing) this experimental technique usually implies superimposing a controlled excitation onto the rotating assembly. Many researchers have used variations of this basic procedure to measure hydrodynamic interaction forces. Jery et al. [1] used circular whirl orbits at various whirl ratios (Ω/ω) to excite a centrifugal pump impeller operating in a spiral volute. A linear skew symmetric impeller force model was assumed. Quadratic curve fits of the measured radial and tangential interaction forces as functions of whirl ratio provided the six impeller force coefficients for the model. Bolleter et al. [2] used swept sine excitation on a boiler feed pump impeller operating in a vaned diffuser. Impedance functions were related to the mea-

sured radial and tangential forces. A linear skew-symmetric impeller coefficient model was assumed where the six model coefficients were obtained from quadratic curve fits of the impedance functions. These two procedures require the a priori assumptions that the force coefficients are frequency independent and that the coefficient matrices are skew symmetric. While these methods, with their associated assumptions, may be applicable in some circumstances they are limited and do not provide a general technique for determining hydrodynamic interaction forces. Murphy et al. [3] reviewed a number of test methods for extracting hydrodynamic forces. He concluded that the single-frequency dual ellipse approach was the best way to fit a linear model to a nonlinear system. However, the method suffers from the drawback of being time intensive. Flack et al. [4] describe a hydrodynamic test facility that uses single frequency elliptical orbits to extract bearing coefficients. The dual ellipse method facilitated a detailed uncertainty analysis and was shown to provide low uncertainties in the measured bearing coefficients. Kostrzewsky and Flack [5] give a detailed assessment of the various factors contributing to the total uncertainty for experimentally derived bearing coefficients using the single-frequency dual ellipse excitation method. The authors showed that the largest contribution to the derived bearing coefficient uncertainties came from the velocity terms which were obtained from the first time derivative of the position

Contributed by the International Gas Turbine Institute (IGTI) of THE AMERICAN SOCIETY OF MECHANICAL ENGINEERS for publication in the ASME JOURNAL OF ENGINEERING FOR GAS TURBINES AND POWER. Paper presented at the International Gas Turbine and Aeroengine Congress and Exhibition, New Orleans, LA, June 4–7, 2001; Paper 01-GT-023. Manuscript received by IGTI, December 2000, final revision, March 2001. Associate Editor: R. Natole.

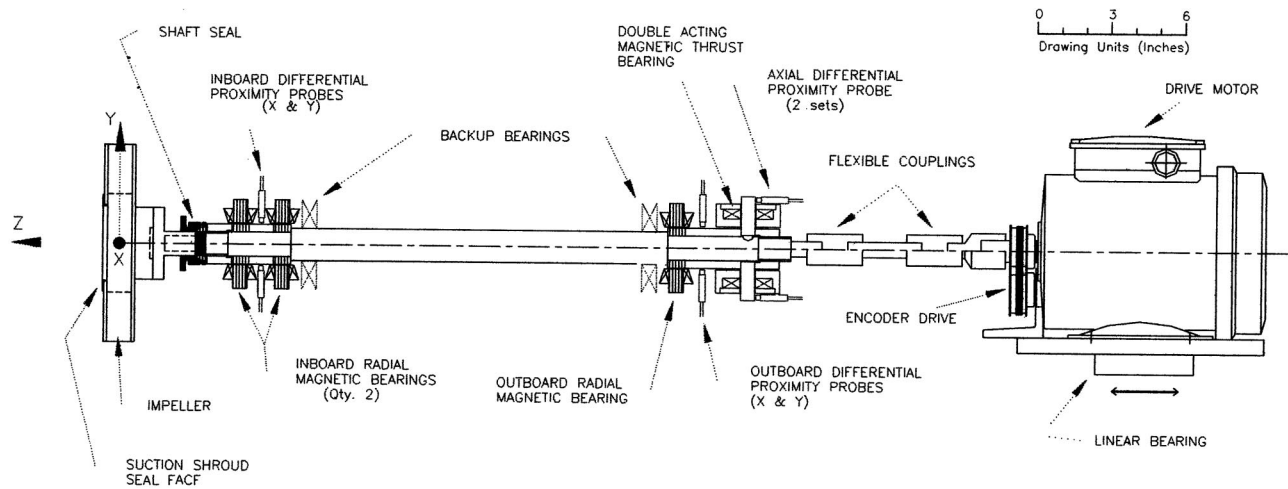


Fig. 1 Plexiglas pump rotor

signals. The uncertainties in the velocities contributed from two to ten times as much uncertainty to the derived bearing coefficients as the next most significant factor.

When applying the single-frequency dual ellipse method, or any other excitation method, to a hydro/aerodynamic force testing apparatus the fluid dynamic forces, $F(t)$, must be resolved from parasitic forces. In the case of the pump apparatus shown in Fig. 1, these parasitic forces arise due to the shaft seal, suction shroud face seal, shaft couplings, and hydraulic and mass unbalance. One method of extracting the impeller forces from the parasitic forces would be to obtain a set of reference forces with a blank disk installed in place of the test impeller. If the blank disk mimics the test impeller in every aspect except for the fluid passages and vanes, the reference forces thus obtained will include all the unwanted parasitic forces, but exclude the desired impeller force. If the reference forces are subtracted from test forces the desired impeller hydrodynamic interaction forces remain. Applying the single-frequency dual ellipse method detailed by Flack et al. [4] requires multiple single frequency orbits at various whirl rates. In general, parasitic forces will vary with each whirl orbit. Therefore, a means by which the rotor whirl orbits can be forced to an arbitrarily defined path and exactly duplicated between the impeller hydrodynamic force test cases (impeller installed) and the reference force cases (blank disk installed) is required.

The present work details the implementation and quantifies the performance of a multiple harmonic open-loop controller on a laboratory centrifugal pump rotor supported in magnetic bearings. The pump apparatus is intended for studying hydrodynamic impeller interaction forces, which are measured directly by the magnetic bearings. The utility of the open-loop controller is demonstrated by forcing precise user defined and repeatable motion on the pump rotor. The multiple harmonic open-loop controller produced sinusoidal current signals at subharmonic, synchronous and superharmonic frequencies of the rotor's angular velocity. When the open-loop control signals were added to the suspension feedback currents of the magnetic bearings they produced rotating forces at the bearing locations at the selected frequencies. The rotor's lateral vibration at each frequency was automatically forced to an arbitrary condition by altering the phase and amplitude of the sinusoidal open-loop control signals.

Apparatus

The multiple harmonic open-loop controller was applied to the plexiglas pump rotor, Fig. 1, which is detailed by Baun and Flack [6]. The pump has a nominal speed of 620 rpm. The magnetic bearing system has five control degrees-of-freedom, four lateral and one axial; open-loop control was applied to the four lateral

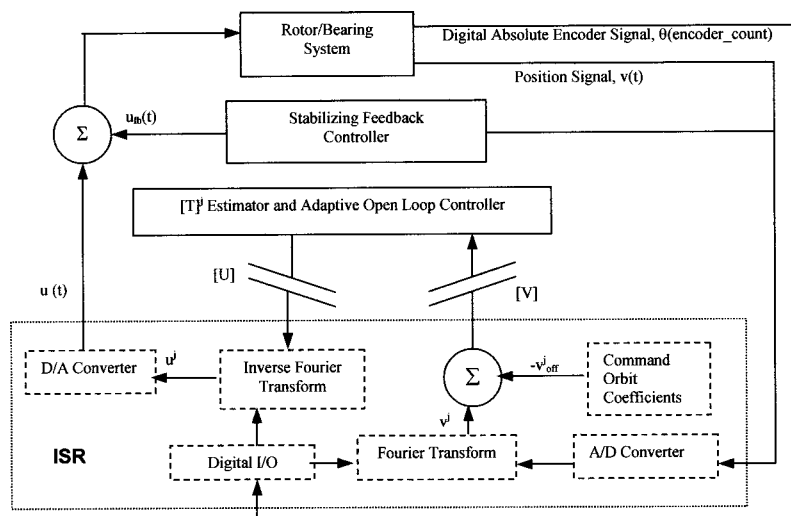


Fig. 2 System block diagram

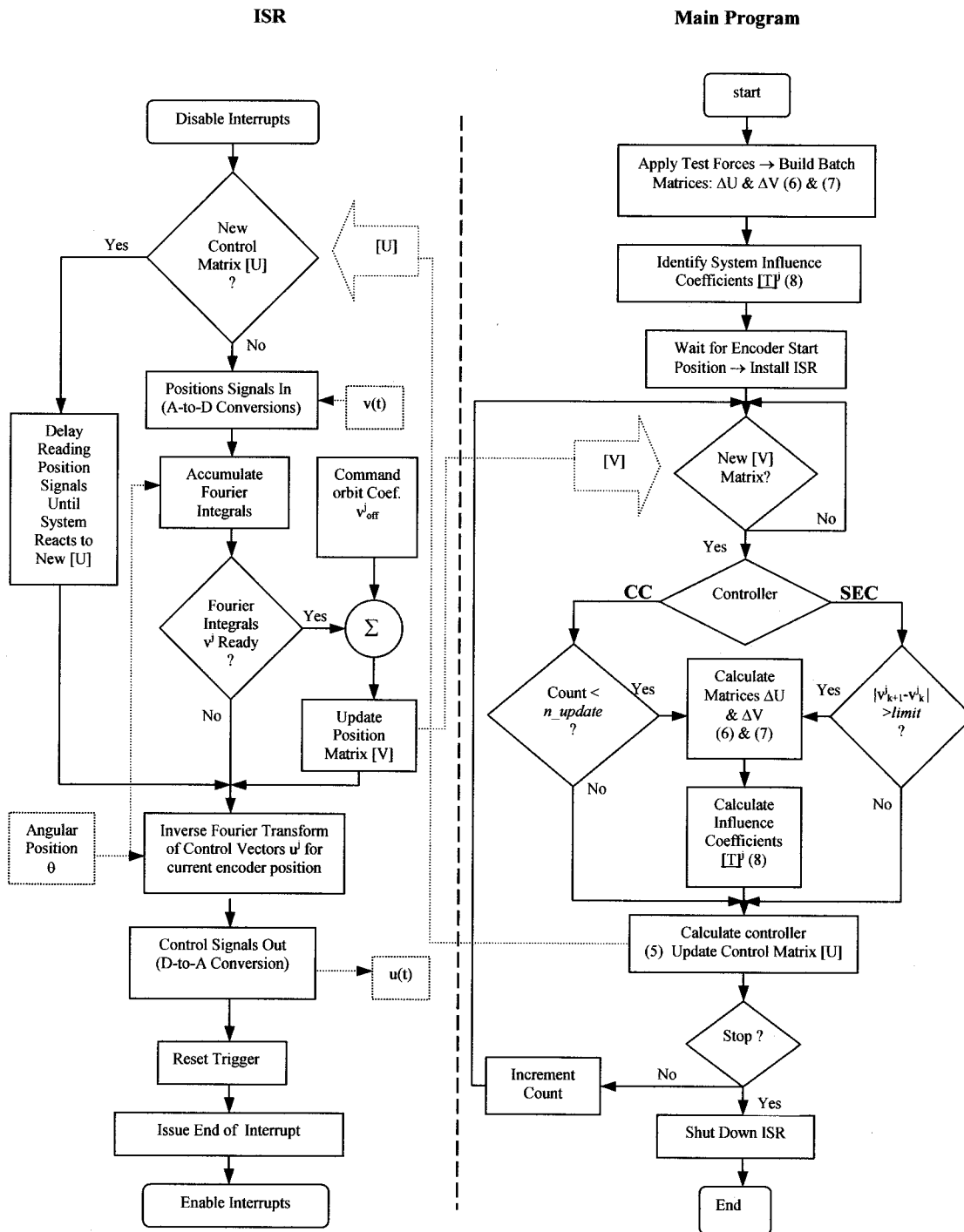


Fig. 3 Open-loop controller and interrupt service routine block

control axes. The open-loop controller was implemented on a standard 166 MHz Pentium PC using a commercially available 100 kHz analog-to-digital (A/D) converter card and a digital-to-analog (D/A) converter card for vibration signal input and open-loop control signal output, respectively. Figure 2 gives a block diagram of the rotor/bearing system, stabilizing feedback controller, open-loop controller, and interrupt service routine. An eight-bit absolute encoder driven directly by the pump shaft generated a 256 times running speed phase-locked digital signal.

Open-Loop Controller

Theoretical Background. In open-loop control a precalculated schedule of control signals, $u(t)$, are applied to a system to

tailor its forced response. In this case, the open-loop signals are superimposed on the stabilizing feedback control signals, $u_{fb}(t)$ (Fig. 2). If the elements in the system influence coefficient matrix, $[T]^j$, are updated or adapted based on the system's response, v_{k-1}^i , to the previous schedule of open-loop signals, the controller is said to be adaptive. The adaptive open-loop control process is particularly well suited to turbomachine rotors which are subjected to synchronous and/or integer multiple supersynchronous disturbance forces which may change as the machine wears or as the operating point or speed of the machine changes. This utility has been well documented in the literature (Burrows and Sakhkaya [7] and Higuchi et al. [8]).

Open-loop control requires a priori knowledge of the system

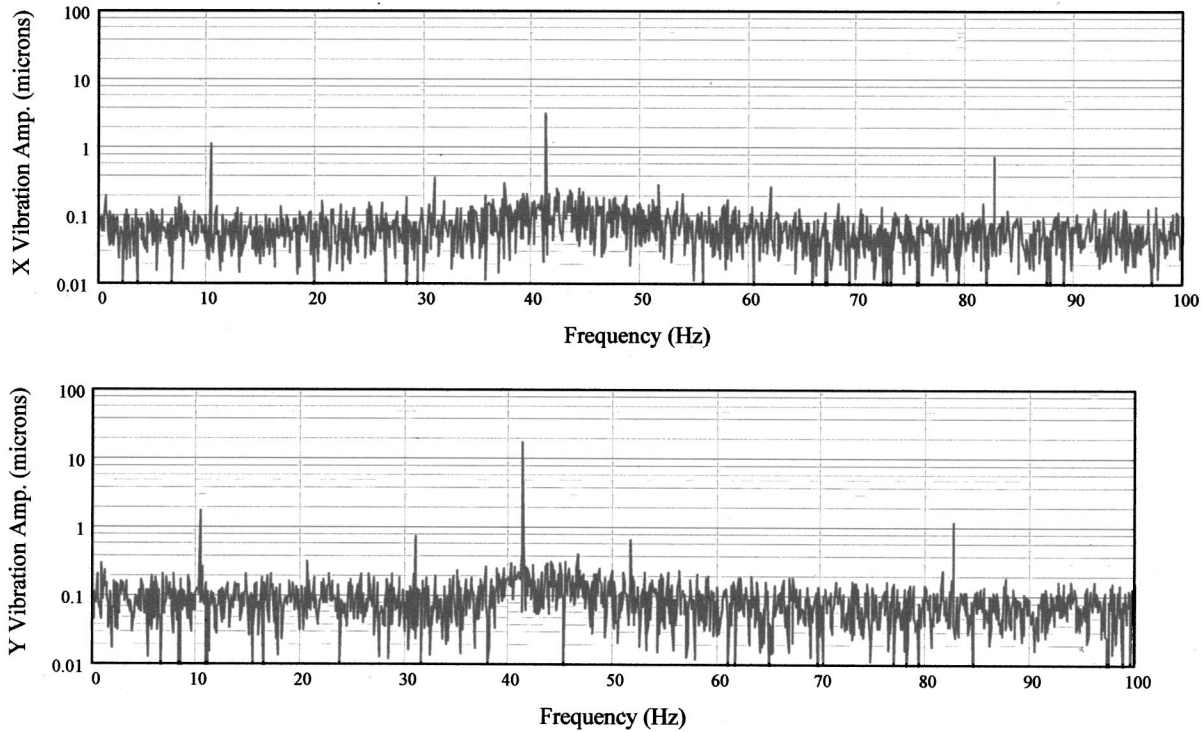


Fig. 4 Frequency spectra (no open-loop control applied)

since the control signals are precalculated. To determine the appropriate amplitude and phase of the open-loop control signals, it is necessary to estimate a system influence coefficient matrix, $[T]^j$, which relates the system response at the j th frequency, v^j , due to the open-loop control signals, u^j , at the same frequency. The method used to estimate the system influence coefficient matrix is similar to the well-established least-squares balancing technique where influence coefficients are determined by applying known unbalance forces at balancing planes along a shaft and measuring the rotors' response at position sensor locations. In the case of a rotor supported in magnetic bearings, the bearings themselves are used to apply rotating magnetic forces and the position sensors, required to close the feedback loop in a magnetic bearing system, provide the system response. The open-loop control method is well documented by Knospe et al. [9] from which a brief summary follows with an extension to the case with multiple harmonics.

A forced response model of a rotor system is given by

$$v' = [T]^j u^j + v_0^j. \quad (1)$$

Equation (1) describes the rotor vibration at the j th frequency, v^j , as the uncontrolled vibration, v_0^j , superimposed with the vibration due to the applied control forces, u^j , times the system influence matrix, $[T]^j$. To apply open-loop control using this model, an estimate of both, the system influence coefficient matrix, $[T]^j$, and the uncontrolled vibration, v_0^j , must be made. However, if the open-loop control forces are applied incrementally, then the vibration at the k th iteration will be given by

$$v_k^j = [T]^j u_k^j + v_0^j. \quad (2)$$

Assuming a time invariant system and subtracting the k th iteration from the $(k+1)$ th iteration gives

$$v_{k+1}^j - v_k^j = [T]^j [u_{k+1}^j - u_k^j] \quad (3a)$$

or

$$\Delta v^j = [T]^j \Delta u^j. \quad (3b)$$

Equation (3) only requires an estimate of the influence coefficient matrices, $[T]^j$, at each open-loop control frequency, and is the preferred system model for developing a control law. A performance function

$$J^j = v^{jT} [W] v^j \quad (4)$$

defines a performance surface which weights the norm of the vibration vector at each open-loop control frequency. The system model (3a) is substituted into the performance function (4) with $v_k^j = v_{k+1}^j$. To minimize the performance function, the first derivative of J^j with respect to Δu_{k+1}^j is set to zero which yields

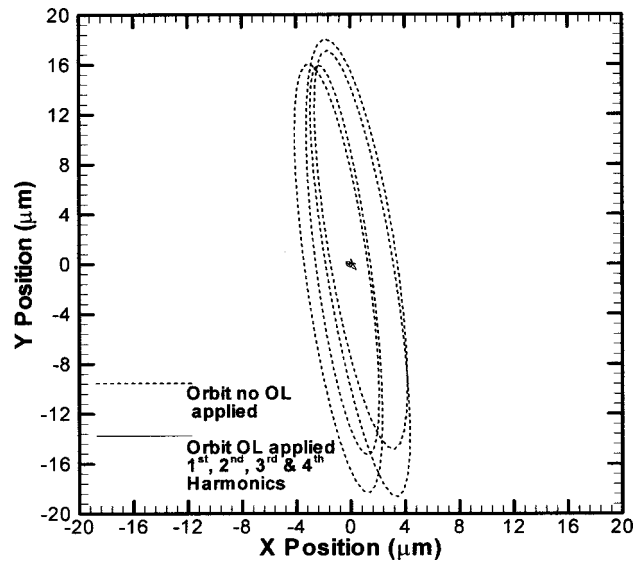


Fig. 5 Orbit comparison (no open-loop control and open-loop control applied)

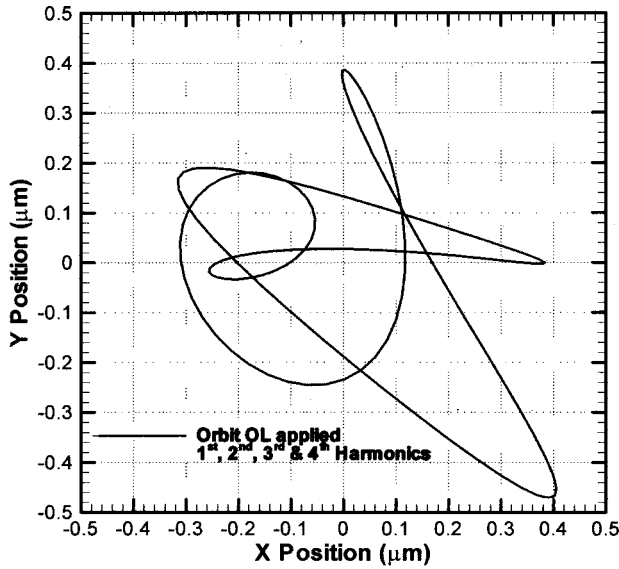


Fig. 6 Orbit (open-orbit control applied at 1×, 2×, 3×, and 4×)

$$u_{k+1}^j = u_k^j - (T^{jT} W T^j)^{-1} T^{jT} W v_k^j. \quad (5)$$

An estimate, $[T]^j$, for T^j is easily obtained by injecting a set of p test forces at each open-loop control frequency where $p \geq 2m + 1$, and measuring the resulting vibration at the same frequency. The difference in successive test forces and the difference in the resulting vibrations are then formed in two batch matrices,

$$\Delta V^j = [v_1^j - v_2^j \quad v_2^j - v_3^j \quad \cdots \quad v_{p-1}^j - v_p^j] \quad (6)$$

and

$$\Delta U^j = [u_1^j - u_2^j \quad u_2^j - u_3^j \quad \cdots \quad u_{p-1}^j - u_p^j]. \quad (7)$$

Substituting (6) and (7) into (3b) and solving for $[T]^j$ gives the estimator

$$[T]^j = \Delta V^j \Delta U^{jT} [\Delta U^j (\Delta U^j)^T]^{-1}. \quad (8)$$

Now, if we relax the constraint of a time invariant system and instead allow the system to be slowly time varying, the quantities, Δv^j and Δu^j in (3) can be used directly for the implementation of adaptive control. If the magnitude of Δv^j after any loop cycle is greater than some threshold level (limit), the estimator $[T]^j$ can be reevaluated by substituting new values of Δv^j and Δu^j into the appropriate columns of (6) and (7), respectively, and resolving for $[T]$ using (8).

Software Implementation. Equations (5), (6), (7), and (8) were coded into a C program. Figure 3 shows a block diagram of the basic structure of the open-loop control code. The right-hand side of Fig. 3 shows the layout for the main code while the left-hand side shows the same for the interrupt service routine. The implementation of the control algorithm shown on the right-hand side of Fig. 3 shows both the simultaneous estimation and control (SEC) and convergent control (CC) algorithms (Knospe et al. [9]). The SEC algorithm allows the system influence coefficient matrix $[T]$ to be updated based on the magnitude of the difference in the rotor vibration vectors between successive loop iterations. The SEC algorithm is sensitive to the value of the threshold criterion (limit) used to determine whether or not to update the $[T]$ matrix. If the criterion (limit) is too low, the individual differences that constitute the batch matrices (6) and (7), become small and similar in magnitude. This, in turn, produces an ill-conditioned estimate of the system influence matrix (8) and the performance will be erratic (perhaps unstable). This sensitivity is compounded when multiple open-loop control frequencies are employed, as each open-loop frequency will, in general, have a different threshold criterion (limit). An alternative algorithm, convergent control

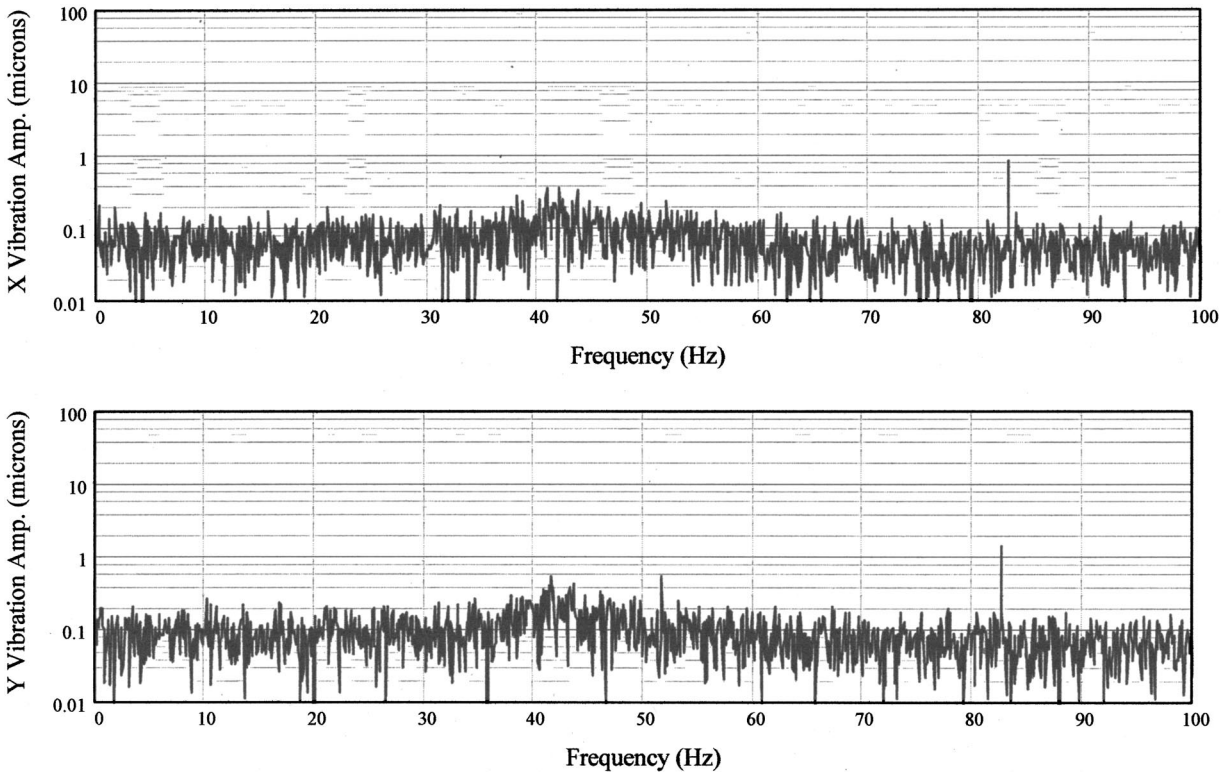


Fig. 7 Frequency spectra (open-loop applied at 1×, 2×, 3×, and 4×)

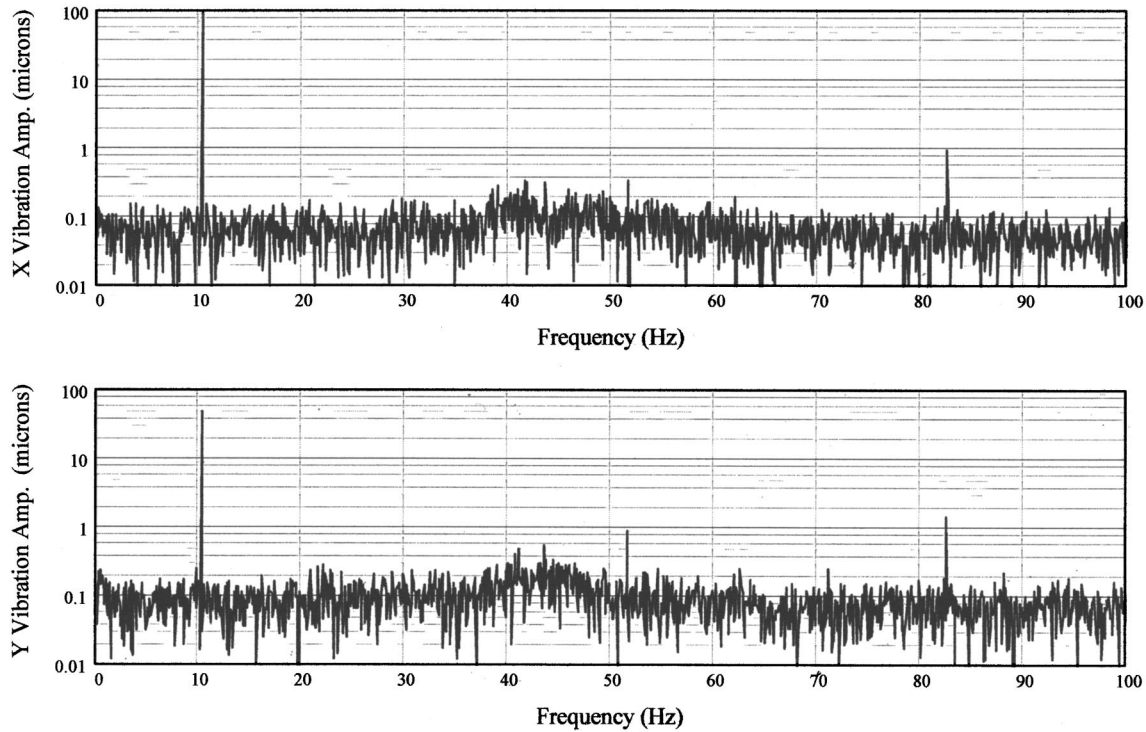


Fig. 8 Frequency spectra (open-loop control applied 1X, 2X, 3X, and 4X; orbit at 1X)

(CC) (Knospe et al. [9]), updates the system influence coefficient matrix, $[T]$, a preset number of times (n_{updates}). Both the SEC and CC open-loop control algorithms were used on the plexiglas pump apparatus with comparable performance. The SEC algorithm requires considerable setup effort to get the threshold criterion (limit) set for each open-loop control frequency. For this reason the CC algorithm was the preferred for implementing multiple harmonic open-loop control on the plexiglas pump test apparatus. Typically the system influence coefficient matrix, $[T]$, was updated on the first two or three-loop iterations only.

The least significant bit from the absolute encoder signal acted as a trigger for the A/D converter. For each trigger pulse the analog-to-digital card generated an interrupt service request which invoked the interrupt service routine, left-hand side of Fig. 3. An interrupt service routine (ISR) is essentially the same as a standard function or subroutine, except that it can be initiated by a hardware event. When an interrupt service routine is initiated, other programs that are running (open-loop controller in this case, the right-hand side of Fig. 3) are suspended until the ISR is finished executing. The encoder signal also provided an absolute angular position index, $\theta(\text{encoder_count})$, from which discrete Fourier transforms and discrete inverse Fourier transforms of the rotor lateral position signals, v^j , and open-loop control signals, u^j , respectively, were calculated. Since the absolute encoder provided a fixed number of trigger signals at equal angular increments on each shaft rotation, the use of an interrupt service routine to handle all input/output functions was the logical and most computationally efficient technique for interfacing with the rotor/bearing system. All timing was intrinsic to the encoder signal. Therefore, absolute angular position error, associated with the conventional method of tracking a rotor's angular velocity and angular position by means of a clock signal and a key phasor reference was eliminated. The encoder signal provided a simple and robust method for fixing the integration angular increment for the Fourier and inverse Fourier transforms, determining the shaft's absolute angular position and synchronizing all input/output events.

Command orbit coefficients, v_{off}^j , were added to the rotor po-

sition coefficients, v^j . By specifying nonzero Fourier command orbit coefficients for a particular frequency, the rotor motion at that frequency, was forced to an orbit defined by the command orbit coefficients. In addition to whirl orbit control the command orbit coefficients provide a simple means of apply runout compensation. If the runout can be characterized by a set of Fourier coefficients at any combination of the open-loop control frequencies, then these coefficients can be superimposed on the command orbit coefficients such that the runout-induced shaft motion is canceled.

A hand-shaking protocol consisting of a series of flags was used to coordinate the various decision paths and provide synchroniza-

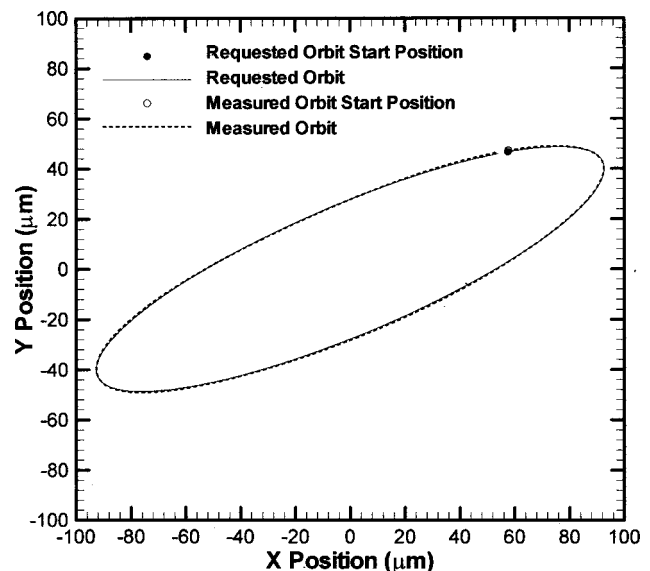


Fig. 9 Comparison between requested and measured orbits (1X)

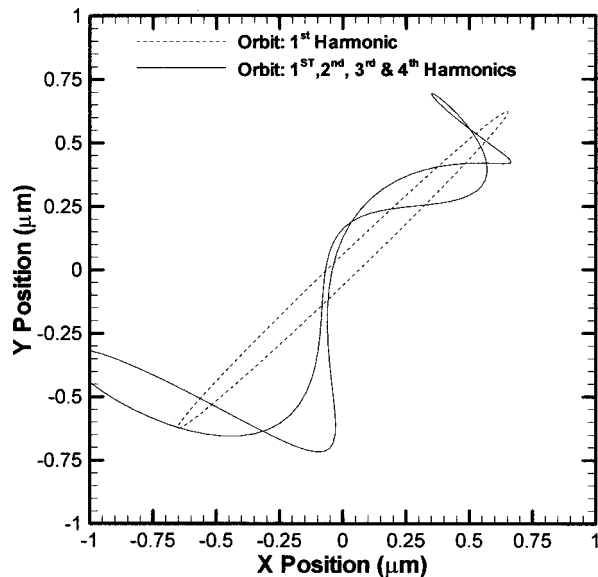


Fig. 10 Difference between measured and requested orbits (1X)

tion between the main code and the interrupt service routine. In addition, a local copy of the open-loop control coefficient matrix, $[U]$, was defined in both the main code and the interrupt service routine. This was necessary since the interrupt service routine needed access to the coefficients at all times (each trigger event) while the main section of the code may take several trigger periods to complete control calculations and updates on the matrix. A convolution period of 12 revolutions for the Fourier integrals and a delay period of three revolutions after a new control coefficient matrix, $[U]$, was introduced proved to be a good compromise between noise reduction benefits with longer convolution periods and controller performance benefits with more frequent controller updates.

To streamline the code execution, several techniques were employed. Function calls were avoided whenever possible. Matrix operations were coded as macros and sine and cosine values (used to evaluate Fourier transforms and inverse transforms at each trigger event) were precalculated and stored in lookup tables and accessed directly based on the encoder position. Pointers were used throughout and in particular for swapping matrices in the controller calculations (5), and for passing coefficient matrices back and forth between the main part of the control code and the interrupt service routine.

Testing and Utility

To demonstrate the utility of the open-loop controller a few representative vibration case studies are presented here. The open-loop controller was used to manipulate the lateral ($x-y$ plane) motion of the rotor in Fig. 1. Runout compensation was applied for all test cases. The total shaft runout at each position sensor

location was mapped by supporting the shaft in a set of roller blocks and performing a slow roll test. The slow roll test was performed insitu with the axial thrust bearing on to prevent axial movement of the rotor. Total indicated mechanical runout (TIR) at the roller block locations was below the resolution of the digital dial gauge, less than 0.0001 inches. The position sensors, Fig. 1, were used to map the target runout as the shaft was slowly turned on the roller blocks. Fourier coefficients of the runout position signals were superimposed with the command orbit Fourier coefficients, v_{off}^j .

Figure 4 show the frequency spectra for the vibration at one control plane of the plexiglas pump without open-loop control applied. The predominant vibration occurs at four times running speed, 41.33 Hz, and is due to the vane passing frequency (4 vane impeller interacting with a single tongue volute) with smaller vibration levels at $1\times$, $2\times$, $3\times$, $4\times$, $5\times$, $6\times$, and $8\times$ running speed. The resulting rotor vibrations for one complete shaft revolution, the dashed line in Fig. 5, clearly shows the dominant $4x$ vibration. Applying the open-loop control reduces the orbit size to the dot at the origin of Fig. 5. Figure 6 shows the resulting rotor orbit with the open-loop controller applied at the first four harmonics of the pumps rotational speed. The rotor orbit is shown with only the $1x$, $2x$, $3x$, and $4x$ components included and the scale magnified by a factor of 40 (as compared to Fig. 5) emphasizing the effectiveness of the open-loop controller. The solid line in Fig. 5 is the orbit from Fig. 6 plotted to the same scale as the orbit without open-loop control applied. Relative to the orbit without open-loop control applied, the orbit with open-loop control applied appears as a dot at the origin of Fig. 5. Figure 7 is the direct counterpart to Fig. 4 with the open-loop controller applied to the first four harmonics of the pumps rotational frequency, $1\times$, $2\times$, $3\times$, and $4\times$. Figure 7 clearly shows that these four frequencies in the X and Y vibration spectra have been attenuated to the sensor noise floor.

The open-loop controller was designed to accept a user requested command orbit at any of the open-loop control frequencies. The command orbit is entered as a vector whose components represent the semi-major axis (a), semi-minor axis (b), ellipse angle (Ψ), and amplitude phase angle (γ) of an ellipse. Figures 8 and 9 show the resulting rotor vibration spectra and orbit, respectively, for a synchronous command orbit vector $\{0.004'', 0.001'', 25 \text{ deg}, 45 \text{ deg}\}$ or $\{101.6 \mu\text{m}, 25.4 \mu\text{m}, 25 \text{ deg}, 45 \text{ deg}\}$ while the $2\times$, $3\times$, and $4\times$ vibration components were attenuated to zero (noise floor). Within the range of open-loop control frequencies, only a synchronous vibration component is observed in the frequency spectra of the X and Y position signals (Fig. 8). The resulting rotor orbit shown as a dashed line in Fig. 9 is a superposition of the $1x$, $2x$, $3x$, and $4x$ vibration components. The elliptical rotor orbit is oriented with the semi-major axis inclined at 25 deg relative to the positive x -axis. The unfilled circle represents the orbit starting point, or phase, and is controlled by the amplitude phase angle, γ , argument. The orbit whirl direction is counterclockwise starting from the open circle. A qualitative comparison between the actual rotor orbit, the dashed line in Fig. 9, and the requested orbit, solid line in Fig. 9, shows that the open-loop controller was successful in controlling the rotor to the

Table 1 Quantitative comparison between requested and measured orbits

Whirl Freq. {multiple of synch.}	Orbit Parameter								Difference (Requested–Measured)			
	Requested				Measured							
	a (μm)	b (μm)	ψ (deg)	γ (deg)	a (μm)	b (μm)	ψ (deg)	γ (deg)	a (μm)	b (μm)	ψ (deg)	γ (deg)
1/4	101.60	25.40	-35.0	45.0	101.83	25.50	-35.3	45.0	-0.23	0.10	0.3	0.0
1/2	101.60	25.40	55.0	45.0	102.06	25.50	55.1	44.6	-0.46	0.10	-0.1	0.4
1	101.60	25.40	25.0	45.0	101.55	25.68	25.1	44.5	0.05	0.28	-0.1	0.5
2	101.60	25.40	-65.0	45.0	101.83	25.22	-65.4	44.0	-0.23	-0.18	0.2	1.0

requested orbit. Figure 10 is plot of the difference between the requested orbit and the measured orbit and is provided to facilitate a more detailed qualitative comparison between the two orbits. The solid line in Fig. 10 shows the difference between the actual orbit, a superposition of the first four harmonics, and the requested synchronous orbit. The dashed line shows the difference between the first harmonic of the actual orbit and the requested orbit. The difference between these two curves represents rotor motion resulting from 2x, 3x, and 4x vibration (noise).

Table 1 provides a quantitative comparison between measured rotor orbits and requested orbits at four different whirl frequencies. For the whirl frequencies of, $\frac{1}{2}$ and $\frac{1}{4}$ running speed, the open-loop controller was set to control five harmonics simultaneously, $\frac{1}{2}\times$, $1\times$, $2\times$, $3\times$, and $4\times$ and $\frac{1}{4}\times$, $1\times$, $2\times$, $3\times$, and $4\times$, respectively. The differences between the various requested and measured orbit parameters, as shown in Table 1, appear to be random and unrelated to the orbit orientation or whirl frequency with the exception of the amplitude phase angle (γ). The amplitude phase angle is systematically increasing from 0 deg to 1 deg between the whirl frequencies of $\frac{1}{4}$ and two times running speed. This systematic trend appears to be the result of force slewing limitations of the magnetic actuators. As the whirl frequency increases, the inertial reaction forces due to the rotors mass also increase. The largest difference between the magnitudes of the requested and measured ellipse axis, as shown in Table 1, is -0.46 microns or expressed as a percent of the requested semi-major axis amplitude, -0.5% , while the largest difference in the ellipse angle is 0.3 deg.

The examples discussed above and shown in Fig. 4 through 10, while not exhaustive, demonstrate the effectiveness of the open-loop controller to simultaneously control multiple harmonics to a user prescribed condition. In the selected test cases open-loop control was simultaneously applied to four or five harmonics. While in principle any number of harmonics can be simultaneously controlled, in practice, the number will be limited by the controller processor speed and the sampling frequency of the input/output hardware. Poor signal-to-noise ratio, aliasing, and coupling between harmonics can degrade the controller performance, particularly for higher harmonics.

Summary

To facilitate the measurement of hydrodynamic forces on a laboratory centrifugal pump rotor supported in magnetic bearings, a PC-based interrupt-driven adaptive open-loop controller was developed and implemented for the purpose of orbit control. The open-loop controller provides a critical function in the measurement procedure and determination of the hydrodynamic impeller forces coefficients as precisely controlled arbitrarily defined user prescribed orbits are required between independent tests. The open-loop controller provided a flexible platform from which sub-harmonic, synchronous, and superharmonic rotor vibration frequencies were simultaneously controlled with each open-loop control frequency independently forced to some user prescribed orbit. The open-loop controller was implemented using common off-the-shelf IO hardware and a standard PC. The open-loop controller and all IO functions were coded in a C program. An interrupt service routine and an absolute angular encoder were used to synchronize all IO functions. The utility and effectiveness of the open-loop controller to force arbitrary user-defined whirl orbits on a test rotor was quantified by example. The controller performance was dictated by the system noise floor and the force slewing limitations of the magnetic actuators.

Acknowledgments

This research was sponsored by the Rotating Machinery and Controls (ROMAC) Industrial Research Program at the University of Virginia. Acknowledgment is given to Dr. José Vázquez, ROMAC Research Scientist.

Nomenclature

$F(t)$	= hydro/aerodynamic force vector
i	= $\sqrt{-1}$ complex number
J	= performance function
m	= number of independent control axis
n	= number of position signal locations on shaft
$[T]^j$	= $2n \times 2m$ matrix of system influence coefficients
u^j	= $2m \times 1$ vector of j th frequency open-loop Fourier coefficients
$[U]$	= matrix of u^j vectors (frequency domain)
$u(t)$	= time domain control signal
$[W]$	= diagonal weighting matrix
v^j	= $2n \times 1$ vector of j th frequency position Fourier coefficients
v_{off}^j	= $2n \times 1$ vector of the j th frequency command orbit Fourier coefficients
$[V]$	= matrix of v^j vectors (frequency domain)
$v(t)$	= time domain motion
θ	= angular position of shaft on rotation (rad)
τ	= period of shaft revolution (sec)
ω	= rotor spin frequency
Ω	= rotor whirl frequency
Ω/ω	= whirl ratio
limit	= SEC threshold value
n_updates	= CC threshold value

Subscript

k	= adaptation or iteration index
fb	= feedback signals

Superscript

j	= frequency index
-----	-------------------

References

- [1] Jery, B., Acosta, A. J., Brennen, C. E., and Caughey T. K., 1984, "Hydrodynamic Impeller Stiffness, Damping, and Inertia in the RotorDynamics of Centrifugal Flow Pumps," Proc. of the workshop on Rotordynamic Instability Problems in High Performance Turbomachinery, May, Texas A&M University, NASA Publication No. 2338.
- [2] Bolleter, U., Wyss, A., Welte, I., and Sturchler, R., 1987, "Measurement of Rotordynamic Interaction Matrices of Boiler Feed Pump Impellers," ASME J. Vib. Stress, Reliab. Des. **109**, pp. 144–151.
- [3] Murphy, B. T., Scharrer, J. K., and Sutton, R. F., 1990, "The Rocketdyne Multifunction Tester. Part I: Test Method," Proc. of the Workshop on Rotordynamic Instability Problems in High Performance Turbomachinery, NASA Conference Publication CP-3122, pp. 347–359.
- [4] Flack, R. D., Kostrzewsky, G. J., and Taylor, D. V., 1993, "A Hydrodynamic Journal Bearing Test Rig with Dynamic Measurement Capabilities," STLE Tribol. Trans., **36**(4), pp. 497–512.
- [5] Kostrzewsky, G. J., and Flack, R. D., 1990, "Accuracy Evaluation of Experimentally Derived Dynamic Coefficients of Fluid Film Bearings, Part I: Development of Method," STLE Tribol. Trans., **33**(1), pp. 105–114.
- [6] Baun, D. O., and Flack, R. D., 1999, "A Plexiglas Research Pump with Calibrated Magnetic Bearings/Load Cells for Radial and Axial Hydraulic Force Measurements," ASME J. Fluids Eng., **121**, pp. 126–132.
- [7] Burrows, C. R., and Sahinkaya, M. N., 1983, "Vibration Control of Multi-Mode Rotor-Bearing Systems," Proc. R. Soc. London, Ser. A, **A386**, pp. 77–94.
- [8] Higuchi, T., Otsuka, M., Mizuno, T., and Ide, T., 1990, "Application of Periodic Learning Control With Inverse Transfer Function Compensation in Totally Active Magnetic Bearings," Proc. 2nd Int. Symp. Of Magnetic Bearings, July 12–14, Tokyo, Japan, Technomic, Lancaster, PA.
- [9] Knospe, C. R., Hope, R. W., Fedigan, S. J., and Williams, R. D., 1995, "Experiments in the Control of Unbalance Response Using Magnetic Bearings," Mechatronics, **5**(4), pp. 385–400.

The Ubiquitous Personal Turbine—A Power Vision for the 21st Century

C. F. McDonald

McDonald Thermal Engineering,
1730 Castellana Road,
La Jolla, CA 92037
e-mail: kmcadona1@san.rr.com

C. Rodgers

ITC,
3010 N. Arroyo Drive,
San Diego, CA 92103
e-mail: crodgers@4dcomm.com

Having a personal computer (PC) and related electronic equipment in the majority of U.S. homes today is accepted without question. In the same vein, having a personal turbine (PT) in the home could also be taken for granted in coming decades to assure a constant and reliable source of electrical power, which is paramount in the e-business era. As addressed in this paper, gas turbine technology has advanced to the point where a natural gas-fired PT, rated at about 5 kW could reliably provide the total energy needs of an average home. The Industrial Revolution of the 18th century, in which a centralized factory replaced cottage industries, was made possible by introduction of the steam engine. In the 21st century IT Revolution, the situation will have essentially gone the full circle, with a high percentage of service industry work being done in the home. For individuals using the internet for conducting business a reliable source of electrical power is mandatory. Alas, this can no longer be assured by the U.S. power grid which is quickly reaching its capacity, and increasing outages will become more commonplace. One solution to this could be the use of PTs in homes in both cities and remote areas. Also it would be ideally suited to applications in the developing countries, where it could provide the total energy needs of villages and small communities. In this introductory paper it is projected that when mass produced in very large quantities like automobile turbochargers, the PT unit cost would be competitive. [DOI: 10.1115/1.1473826]

1 Introduction

Currently microturbine efforts are being strongly focused on units in the 30–100 kW range, and these are expected to be produced in significant quantities within the next two years or so, to meet the energy needs of many distributed power users. The successful introduction of these first-generation microturbines could pave the way for smaller PTs in the future, with a postulated much larger market potential.

The aforementioned analogy between the 18th century steam engine and the 21st century PT is felt to be valid in the same evolutionary sense, in light of the drastically changing work environment brought about by the IT era.

A compact, natural gas-fired silent running PT with very low emissions would operate unattended, and be essentially maintenance-free. In this introductory paper on the potential of the PT, no attempt has been made to optimize the small turbogenerator. Design simplicity is of the essence, and this point is stressed for this futuristic power generation option. The use of existing materials and proven technology is paramount for the initial introduction of such a new prime mover. The PT package is compact, and could be installed in about the same space as a domestic dish washer.

Generator sets have the potential of becoming a standard item in new homes in coming decades. For installation today, the user is limited to the utilization of reciprocating engines burning either gasoline or diesel fuel. The use of fuel cells sounds attractive, but they are several years away from being economically viable. In light of this, where does the PT fit in?

The technology to deploy a compact 5 kW PT exists today, and commercialization could be achieved within four years, it really being just a matter of resolve. Compared with contemporary gen-

erator sets, the PT offers many advantages including, a smaller and lighter weight package, multifuel capability, very low emissions, silent running, vibration-free, minimum maintenance, and moderate to high fuel utilization efficiency dependent upon waste heat recovery. With such obvious advantages, why are they not in service today? The answer is, of course, their perceived high cost, and poor economic payback.

Design simplicity was adhered to in establishing the PT concept outlined in this paper, but whether the configuration stands the test of time remains to be seen. It is the authors' view that analytical and design engineers do not have the background to establish a minimum-cost small turbogenerator. They can generate an elegant preconceptual design, which would then have to be essentially re-engineered by manufacturing and production specialists to yield a practical engine with minimum cost for mass production. With some crystal ball gazing at this stage, a market potential for many millions of units can be projected, with the most obvious manufacturing technology base being the automobile industry. As outlined in the paper, this could include the transfer of know-how from the high-volume manufacture of automobile turbochargers, heat exchangers, and electrical and electronic components.

While viewed as an introductory paper on the merits of PT utilization, it includes what technical studies are necessary to establish an optimized very small turbogenerator that meets economic, performance, and reliability goals. A vision expressed in the early 1930s of having a car in every garage, and a chicken in every pot, could without much stretch of the imagination be extended in the 21st century IT era to include a PT in every basement!

2 Microturbine Deployment

Following deregulation of the utility industry, a need became apparent for modern, and much smaller and more efficient turbogenerators for the distributed generation (DG) market. About a dozen companies in the USA, Europe, and Japan have microturbine programs in progress. Units in the 30–100 kW power range are expected to be produced in significant quantities within the next two years or so. Applications include restaurants, supermar-

Contributed by the International Gas Turbine Institute (IGTI) of THE AMERICAN SOCIETY OF MECHANICAL ENGINEERS for publication in the ASME JOURNAL OF ENGINEERING FOR GAS TURBINES AND POWER. Paper presented at the International Gas Turbine and Aeroengine Congress and Exhibition, New Orleans, LA, June 4–7, 2001; Paper 01-GT-100. Manuscript received by IGTI, December 2000, final revision, March 2001. Associate Editor: R. Natole.



Fig. 1 Capstone 30-kW microturbine (courtesy Capstone Turbine Corp.)

kets, schools, hospitals, office buildings and apartment houses. In addition, there may be microturbine variants produced to meet specific defense needs.

The first generation of recuperated microturbines are based on the use of existing materials and proven technology, and typically have an efficiency close to 30%. An excellent example of an operating microturbine embodying state-of-the-art technology is the Capstone 30 kW compact turbogenerator ([1]) shown on Fig. 1. Over a thousand of these units are in service for a variety of power generation applications, and it has been demonstrated for vehicular use ([2]).

The many variants of microturbines being developed have major features that reflect particular vendors technology bases. One common aspect is the use of radial flow turbomachinery. Variables in the selection of the components include the following: (1) single or two-shaft arrangement, (2) an integrated annular or separately installed recuperator, (3) lubricant-free or oil bearings, (4) annular or single can combustor, and (5) air or liquid-cooled generator.

Within the microturbine industry common goals include low emissions, high reliability, low cost, good performance, long-life, minimum maintenance, and being amenable to high-volume production. As will be outlined in following sections, the successful introduction of these first-generation microturbines could pave the way for smaller PT's in the future.

3 Very Small Gas Turbines

3.1 Background. Very small gas turbines for a variety of applications have been demonstrated, but never manufactured in large numbers for commercial power generation. The smallest and perhaps the most fascinating are turbojet engines for model aircraft ([3]), their size being similar to a cylindrical flashlight. In the propulsion field, engines include jet fuel starters and expendable turbojets ([4]), and related technologies for various applications ([5]). Also a variety of small generator sets have been deployed for defense applications over the years ([6]).

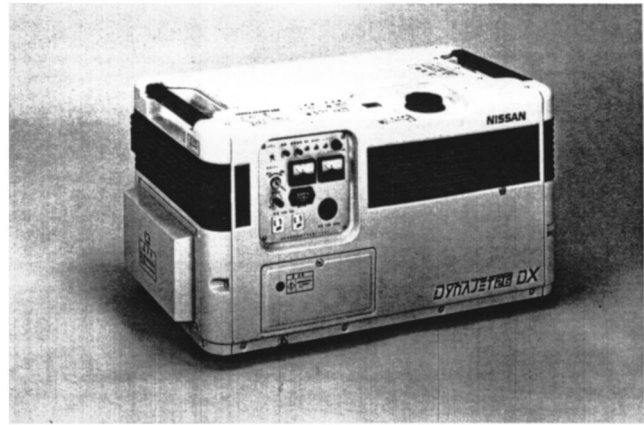


Fig. 2 Micro gas turbine (2.6 kW) (courtesy Nissan Motor Co. Ltd.)

Over the last five decades small aircraft auxiliary power units (APU's) have been produced in large quantities. Many of these machines are complex, having multiple spools and power plus bleed air capability ([7]). A major design requirement for these machines is light weight, and a compact package, hence the reliance on the nonrecuperative approach. These machines have very high reliability, and utilize sophisticated controls to facilitate integration with the main propulsion engines and the aircraft environmental system, with the result that by commercial standards their cost is high.

A very small turbogenerator that was introduced for commercial use was the Nissan micro gas turbine rated at 2.6 kW ([8]). The package envelope for this microturbine (shown on Fig. 2) is similar in size to a picnic ice chest. While never produced in large quantities, it nevertheless represents a valuable point of reference, particularly in terms of efficient packaging. Studies have also been carried out in Japan on a 3-kW mini-cogeneration system, based on the exhaust-heated cycle, and using turbocharger technology ([9]).

3.2 Why the Personal Turbine (PT) Now? Several of the following considerations, when combined, would seem to indicate that it is now opportune to launch a PT development program. With increasing economic growth in the U.S., the expansive use of electronic equipment will outpace the supply of electrical power. This is particularly acute in California where a new major power plant hasn't been built since 1984. A solution to this problem is DG, where the energy source is located near the user. With an ever-increasing amount of service-related work being done in the home, assurance of a constant and reliable source of electrical power in this location is mandatory.

The dominant factor in the development of all new heat engines today is low emissions. Until low-cost fuel cells become commercially available in perhaps a decade or so, the "greenest" small prime mover available is the microturbine. These very small gas turbines can operate on a variety of fuels with single-digit emissions. The acceptance of microturbines of different types for commercial service in the power range of 30–100 kW will give future users added confidence regarding the installation and operation of a PT in their home.

The PT does not require any technology breakthroughs, and could be introduced using existing materials and gas turbine know-how, accordingly an extensive and prolonged development program is not foreseen. The major challenge is to optimize a 5-kW PT for low cost by taking advantage of automated high-volume manufacturing expertise from the automobile industry. The potential worldwide market for perhaps millions of units should be attractive in terms of finding financial backing to make the PT a reality.

3.3 Potential PT Applications. As touched on previously, the main application of a natural gas-fired 5-kW PT would be to provide the total energy needs of an average home. This would include electrical power, space heating, air conditioning, and hot water. The unit installation would be such that the computer control system would assure that the user has the lowest cost of electricity. At times when the cost of electricity from an external source was lower, the PT would automatically cut out. At other times, the PT would operate to meet the needs of the user, and excess power could possibly be fed back into the grid, and thus become a revenue generator for the owner.

The PT is by no means limited to home users in the industrialized nations. In developing countries, a PT could provide the total energy needs of a village, small community, or in a newly constructed business or factory. Operating perhaps on methane derived from animal residues, the PT could provide the following: electrical power, low-grade steam, hot water, refrigeration, hot air bleed for crop drying, desalination, and provide power for irrigation water pumps. The operation and performance of such a facility could perhaps be remotely monitored from a satellite-based diagnostic system.

Characteristics of the PT such as silent and vibration-free operation, no visible exhaust smoke, together with a low IR signature, would seem to make it ideal for a variety of defense applications. The small size and light-weight PT package, capable of being handled by one person, could be used for field communications. Perhaps even smaller PT's, rated at 1 kW or less could be backpack mounted for mobile power generation, or for battery charging. These compact units would operate on the same liquid fuel used in current army vehicles, helicopters and aircraft, thus eliminating any battlefield fuel logistic problems.

In addition to the above applications, there are several others that could utilize a compact and light weight PT, and these include recreational vehicles, boats, refrigerated trucks and rail cars, and power for emergency shelters set up quickly in disaster areas.

Studies have been conducted in the past on very small gas turbines ([10]), but it was a recent publication exploring the merits of microturbines in the power range of 5 to 25 kW ([11]) that has attracted potential user attention. The following sections address design considerations for a 5-kW PT concept.

4 Personal Turbine Technology

4.1 Thermodynamic Cycle/Performance. Large gas turbines have the advantage of both economy of performance and scale. The reverse is true for very small gas turbines. Small engines, like the PT, with a radial flow compressor and turbine have significantly lower aerodynamic efficiencies. This is a result of smaller blade heights, Reynolds number effects, tip clearance effects, manufacturing tolerances, surface finish, and engine-to-engine variation all of which adversely affect efficiency. Also geometries associated with radial turbines make blade cooling very difficult, and thus advances in turbine inlet temperature are solely dependent on materials technology.

For many, initiating studies of very small gas turbines has involved the direct utilization of automobile turbochargers. While this would seem to have merit at first sight, the performance achievable from these simplistic rotating assemblies is not very attractive for power generation ([12]). However, as will be discussed in a following section, the know-how from the manufacture of turbochargers in very large quantities is viewed as a major technology base for the PT.

For very small simple cycle gas turbines demonstrated to date, their efficiencies have been modest. While a recuperator may be a user's option for larger industrial gas turbines, it is mandatory to achieve acceptable efficiency for small units, and the majority of microturbines being developed utilize a recuperated cycle ([13,14]). For the even smaller PT, the inclusion of a recuperator is vital to achieve a thermal efficiency of over 20%.

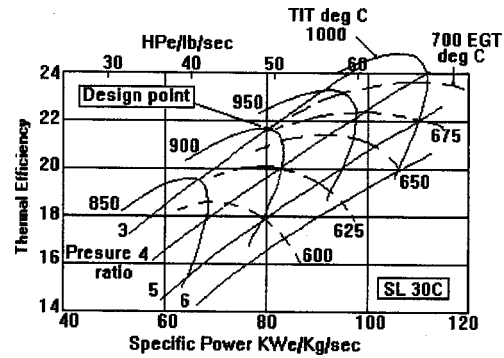


Fig. 3 Performance array for 5-kW personal turbine

Based on state-of-the-art component efficiencies, analyses were undertaken to study the effect of the various parameters on PT performance. A representative performance array is shown on Fig. 3. The turbine inlet temperature is essentially determined by the turbine rotor alloy stress rupture and low-cycle fatigue strength, duty cycle, and rotor cooling systems. Another important factor is the recuperator hot gas inlet temperature, which is limited by oxidation and creep considerations, together with life requirements for the selected matrix material. The pressure ratio is dictated by compressor type and material. The rotational speed is determined by rotor dynamic and bearing considerations, together with rotor stress limitations commensurate with the machine life requirement.

The selected design point parameters are based on conservative values of the various aerodynamic, thermal, and stress loading criteria. As can be seen from Fig. 3 the estimated design point thermal efficiency is 21.5%, and the specific power 80 kW/ kg/ sec. As mentioned previously, the recuperator plays an important role in contributing to thermal efficiency, and this is illustrated on a carpet plot (Fig. 4). The selected value of effectiveness is 0.85. It is of interest to note that at this value the internal heat transfer in the recuperator is actually greater than the heat input value of the fuel. A gain in thermal efficiency of about 1.9 percentage points would be achieved if this was increased to 0.90 as shown on Fig. 4, but the recuperator matrix size and cost would increase by about 60%. The need for a comprehensive trade study involving the influence of such parameter changes is discussed in a later section. It is of interest to note that without a recuperator the PT simple-cycle efficiency would be only about 10%. The major parameters selected are given on Table 1.

A comment often given about single-shaft simple-cycle gas turbines is that their part-load efficiency is poor. In the case of the low-pressure ratio single-shaft PT, with variable speed operation and power conditioning, it is the inclusion of the recuperator that ameliorates the above criticism. At part-power the recuperator effectiveness increases significantly with decreasing air flow, until a very low value is reached (below 10%), where thermal perfor-

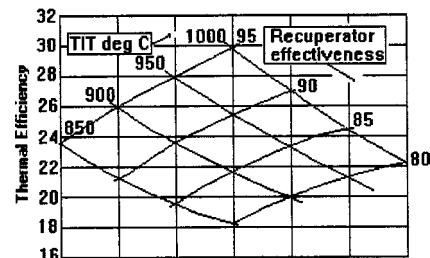


Fig. 4 Impact of recuperator effectiveness on thermal efficiency

Table 1 Salient features of personal turbine (PT)

Component	Feature
Thermodynamic cycle	Recuperated Brayton cycle
Fuel type	Natural gas or liquid fuels
Fuel flow	3 m ³ /hr (NG), 2.5 ltr/hr (Liquid)
Nominal rating, kW	5 (at 50/60 Hz)
Thermal Efficiency, %	21.5
Potential fuel utilization efficiency, %	70
Turbomachine type	Variable-speed single-shaft rotor
Rotational speed, rpm	Approx. 150,000
Compressor	Single-stage radial flow
Compressor pressure ratio	3.0
Turbine	Single-stage radial inflow
Turbine inlet temperature, °C	900
Combustor	Low-emission premix or catalytic type
Recuperator	Compact primary-surface type
Recuperator effectiveness	0.85
Bearing type	Air or magnetic bearings
Generator	Air-cooled samarium cobalt Permanent magnet type
Approx. PT package envelope	0.06 m×0.60 m×0.60 m
Approx. PT package weight, kg	35
Frequency control	Power electronics converter
Control system	Digital system
Natural gas supply	Electric motor driven compressor
Machine start	Generator run as motor from battery supply
Machine operational life, hrs	40,000
Technology status	State of the art
Commercialization	2004

mance is degraded by longitudinal conduction in the heat exchanger, particularly for matrices of very high surface compactness ([15]).

The typical part-load characteristics of a representative recuperated microturbine are shown on Fig. 5, for both constant-speed and variable turbine inlet temperature (TIT), or variable-speed and constant recuperator inlet temperature (RIT). It can be seen that when operating in the variable-speed mode a reasonable thermal efficiency is maintained down to about 20% of the rated PT power. The advantage of variable speed operation must, however, be traded against transient load capability.

4.2 PT Concept Definition . . . Simplicity is of the Essence!

The analyses and preconceptual design efforts expended on the 5-kW PT have essentially been driven by two major considerations, namely low emissions and low cost. These were manifest in establishing the ITC 5000 personal turbine concept layout shown on Fig. 6, which is viewed as being the simplest approach consistent with meeting major objectives, which include high reliability, and being amenable to high-volume production. From the engine cross section, the major features include the following; (1) single-stage radial compressor, (2) single-stage radial inflow turbine, (3) high-speed rotor supported on hydrodynamic air bearings, (4) direct-drive air-cooled generator, (5) annular combustor, (6) a compact prime surface recuperator, and (7) can be readily scaled up or down depending on the actual power rating selected.

To minimize the size of the overall PT installation the concept shown on Fig. 6 embodies a wrap-around recuperator that is inte-

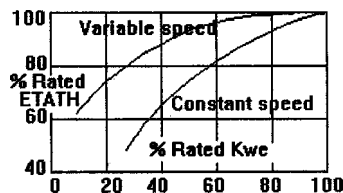


Fig. 5 Part-load characteristics

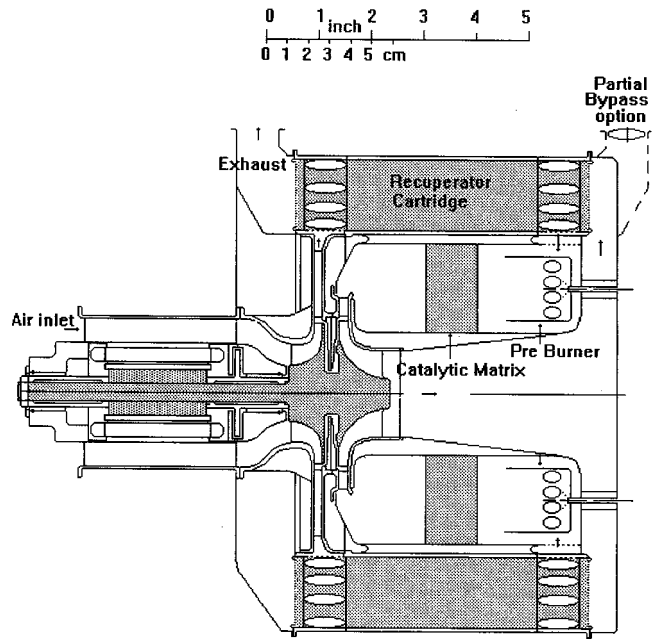


Fig. 6 5-kW personal turbine (PT) design concept

grated with the turbomachinery. The advantages of this arrangement include the following: (1) good aerodynamic gas flow paths resulting in low pressure losses, (2) very compact modular package, (3) lower acoustic signature, (4) built-in rotor burst shield, (5) the close coupling eliminates the need for external ducts and thermal expansion devices, and (6) minimizes the amount of external insulation needed. A mockup of the ITC 5000 turbogenerator rated at 5 kW is shown on Fig. 7.

It is recognized that flexibility exists in terms of overall PT configuration, and a brief discussion on alternative approaches is discussed in a later section. At this stage, however, it is germane to mention that it is the authors' view that the conservative concept shown on Fig. 6 will yield the lowest cost for a mass-produced PT. Since details of the major components have been discussed previously ([11]), they are only briefly addressed below.

4.2.1 Compressor and Turbine. The basic rotor consists of back-to-back compressor and turbine impellers and drive shaft. With a rotational speed of 150,000 rpm the compressor impeller diameter is 2.7" (68.5 mm), and would likely be cast from an



Fig. 7 ITC 5000 PT mockup



Fig. 8 Automobile turbocharger rotor (courtesy Honeywell)

aluminum alloy such as C355. The cast turbine impeller would be made from a high-temperature alloy such as INCO 713.

The rotor assembly would be completed by electron beam welding of the impellers and steel shaft. The size of the rotor assembly would be similar to that in an automobile turbocharger as shown on Fig. 8 ([16]). The manufacture of the PT rotor in very large quantities would draw heavily on well established production methods from the turbocharger industry.

The overall turbogenerator size (see Figs. 6 and 7) was basically defined by the recuperator effectiveness, rather than the choice of engine rotational speed. A conservative speed of 150,000 rpm was selected based upon the cycle optimization ([11]).

4.2.2 Bearings. From the standpoints of simplicity, high reliability, and zero maintenance, the high-speed rotor would be supported on lubricant-free bearings. Hydrodynamic air bearings operate free of contact with the shaft following lift off, and rotor dynamics are satisfactory. A well-established technology base exists for air bearings in aircraft rotating machinery, and would be used in a first-generation PT. As magnetic bearing technology matures, they may be a future candidate if they offer a lower cost approach.

4.2.3 Combustor. The issue of whether to use a single can or an annular combustor has a major impact on the engine configuration. For microturbines with very low fuel flows an advantage of the former is that it facilitates a single fuel injector. With an annular recuperator it has been found difficult to integrate a single can combustor with the turbomachinery because of the complex ducting, and the likelihood of flow maldistribution in the system, and this point will be discussed later. For the proposed PT concept an annular combustor was selected, and the choice of whether it should be of the premix or catalytic type could be made at a later date after detailed analysis. An initial PT would be natural gas-fired, but it could be engineered for a variety of liquid fuels. The major thrust of development for this component would be to identify the optimum fuel injector arrangement and combustor geometry for minimum emissions, and operational durability.

4.2.4 Recuperator. In a microturbine, the recuperator is not only one of the largest cost components, but it is also the least well developed. Existing recuperator types, while they have demonstrated good performance and structural integrity, are labor intensive to fabricate and have high costs. This is partially attributed to the fact that so far they have been produced in only small quantities, and were never designed for high-volume production in the first place.



Fig. 9 Small primary-surface annular recuperator (courtesy Turbulence Tubes)

In support of existing microturbines, and applicable to the PT, several new recuperator concepts are under development. To achieve low cost, most of these have prime surface geometries, have a minimum number of parts, and are amenable to continuous automated high-volume production methods. While the construction of the air-to-gas recuperator differs considerably from an air-to-water heat exchanger, manufacturing technology and know-how for the recuperator can be gained from the automobile radiator business where tens of millions of units are made each year, the completed heat exchanger being made for less than twice the material cost.

The compact annular prime surface stainless steel recuperator for the 5 kW PT shown on Fig. 6 has a matrix cartridge density of about 100 cubic centimeters per thermal kilowatt and weight of about 6 kilograms, its size being slightly larger than a two pound coffee can. New annular recuperator concepts include spirally wrapped variants ([17,18]), and those embodying stamped and folded surface geometries ([19]). An innovative annular prime surface counterflow recuperator, with a stamped and folded geometry formed from a single spool of thin foil, developed for a very small gas turbine is shown on Fig. 9 ([20]).

4.2.5 Generator. Improvements in permanent magnet materials have resulted in lighter and more efficient generators. The generator produces AC power at a frequency that varies directly in proportion to engine speed. Consistent with the goal of engine simplicity (particularly avoiding the use of liquid coolants and lubricants) an air cooled generator was selected, with ambient air being drawn through a finned passage surrounding the generator

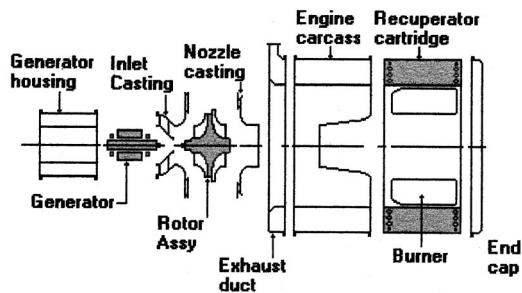


Fig. 10 Major turbogenerator components

casing. The air temperature rise in the generator does result in a small penalty in compressor power, but this approach was selected because of its simplicity. In the single-shaft PT, the generator is run as a motor to start the engine from the battery. The power conditioning system to provide commercial ac frequency is regarded as being state of the art, however, in mass production new fabrication and packaging approaches would be necessary to establish a minimum cost unit.

5 PT Construction/Cost

5.1 Modular Construction. The bare turbogenerator assembly shown on Fig. 6 is compact with an outer diameter of 24 cm (9.5") and length of 30 cm (12"). In establishing the design concept, efforts were expended to minimize the number of components to facilitate automated assembly and thus minimize cost. A simplistic exploded view of the turbogenerator is given on Fig. 10. Several components not shown on this figure include the control system, gas compressor, insulation, instrumentation, and other small accessories. When assembled within a paneled enclosure, the size of the package would be about 0.60 m × 0.60 m × 0.60 m, with an estimated weight on the order of 35 kg. This does not include the waste heat recovery unit, which would be a separate customized module.

5.2 Cost Target. Because of the competitive and proprietary nature of the business it is understandable that there is a paucity of microturbine cost data in the open literature. Thermo-economic design considerations for a small turbogenerator aimed at the identification of cost targets have been reported previously ([21]). Microturbine costs reported in the open literature range from \$1000/kW for fully equipped units currently being produced in limited quantities ([22]), to a projected \$400/kW for a 30 kW microturbine with an annual production of 100,000 units ([23]).

If one could say that the market potential for the PT is in the millions of units, a different cost estimating approach is necessary. A technology base where well established learning curves exist is the automobile industry, where many complex components are mass produced for about two times the material cost ([24]). Extrapolating from current gas turbine manufacturing technology it has been hypothesized ([12]) that \$/kW cost could increase significantly below 25 kW. Until a well-detailed PT design has been established, with strong input from manufacturing and production engineers, a definitive cost estimate can't be made, and indeed is beyond the scope of this introductory paper. Such a detailed cost estimate would involve the evaluation of each individual component in order to determine the lowest method of manufacture, such as castings, forgings, pressings, extrusions, rolled and welded structures, etc.

An effort was expended to establish a tentative cost target for the proposed 5 kW PT. Using available data, one approach was to identify which of the PT components were analogous to ones being mass produced in the automobile industry. These include the following: (1) the turbo rotor is quite similar to that in an automobile turbocharger, (2) the recuperator would be fabricated

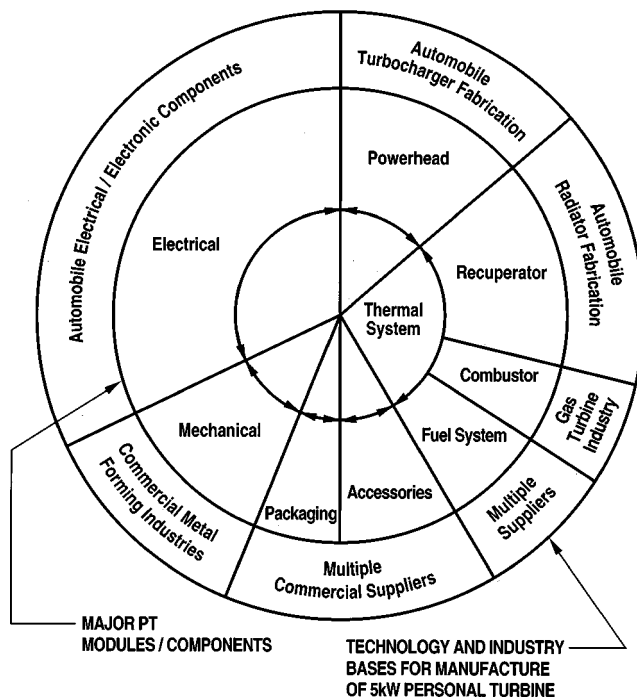


Fig. 11 Cost breakdown for 5-kW PT

in an automated facility like car radiators, (3) the generator could perhaps be viewed as having some similarity with mass produced automobile generators/alternators, and electric motors, (4) micro-processors, controls, and instrumentation perhaps similar to those in automotive diesel engines and generator sets, and (6) the small gas compressor driven by a 300 watt electric motor has features similar to many units produced in quantity for process industries. In addition to the above approach, the cost of some of the simpler static components were estimated by assuming a representative markup of the basic material cost. An approximate distribution of the costs of the major component groupings is shown in pie chart form on Fig. 11.

Bearing in mind that the proposed 5-kW PT is in only a very embryonic stage of design definition, and the tentative nature of the aforementioned cost estimating approach, a target cost of \$1000 (i.e., \$200/kW) was established and details are given on Table 2. It is recognized that a much more detailed economic evaluation is necessary to establish a firm cost, but at least a strawman has been put forward which will likely be the subject of many comments, and perhaps criticism by specialists. The authors would welcome the initiation of such a dialogue with others.

6 PT Rating and Deployment

Prior to initiating an extensive engineering study an applications and market assessment must be undertaken. A major decision to be made is the actual machine rating. Is the 5-kW PT discussed in this paper exactly the right size to meet the energy needs of an average home, and for a variety of applications in the developing nations? The proposed conservative concept (Fig. 6) has flexibility in that it is amenable to both scaling and speed changes depending on the final power rating selection. Recognizing that a major uncertainty in this introductory study is cost, an important part of the proposed pre-engineering investigation will be to establish a cost goal for the PT to be commercially viable.

6.1 Performance Optimization. As discussed in Section 4, using state-of-the-art technology, a set of basic thermodynamic parameters was selected that yielded a thermal efficiency of 21.5%. In establishing the PT preconceptual design no attempt

Table 2 Cost target for mass-produced personal turbine

Module/Assembly	Component	Material/Fabrication	Cost \$
Powerhead	Turbo rotor	Cast alum. comp. impeller cast super alloy turbine impeller steel shaft	140
	hydrodynamic air bearings Comp. inlet and diffuser	st. st. foils cast aluminum cast super alloy	
	Turbine nozzle assy. Seals and fasteners	miscellaneous	
Thermal system	Recuperator cartridge	st. st. prime surface geometry	275
	premix combustor fuel system	super alloy sheet metal miscellaneous	
Electrical	Generator power conditioning system Controls, instrumentation	miscellaneous miscellaneous miscellaneous	325
Mechanical	backbone structure ducts and closures	st. st. misc. fabrication stamped alum. and st. st.	120
Accessories	air filter air inlet silencer connections fittings battery	miscellaneous/ commercially available	90
Packaging	frame and enclosure insulation fan/cooling system	miscellaneous	50
Total Target Cost			\$1000

was made at this stage to optimize the performance. What needs to be undertaken are trade-off studies and sensitivity analyses for the complete system. For example what would be the effect on emissions and life cycle cost of increasing the turbine inlet temperature by 10 deg, or increasing the recuperator effectiveness by one percentage point? The results from these investigations would form the basis for preparing a detailed PT specification.

6.2 Evaluation of Alternative PT Concepts. In the micro-turbine field (i.e., 30–100 kW) different turbogenerator configurations and packaging arrangements are being pursued by the various vendors. While the authors view the configuration shown on Fig. 6 as being the most attractive in terms of gas flow path simplicity, compact size, and potential for low cost, it is recognized that in the 5-kW size different approaches will be evaluated by others. Two of the major layout considerations relate to the choice of combustor type (i.e., annular or single can), and the degree of recuperator integration. An alternate design concept is shown on Fig. 12, this embodying a single can combustor and a rear mounted recuperator. Such an installation has external ducts with the attendant need for thermal expansion devices such as bellows. There may be applications where this approach has advantages and these include the following: (1) hybrid variant involving the coupling of the PT with a solid oxide fuel cell (SOFC), (2) exhaust heated cycle, or (3) concepts with a specialized external combustor for burning biomass and low grade dirty fuels.

6.3 Manufacturing Considerations. The key to selection of the lowest cost PT will be innovativeness on the part of manufacturing engineers. Specialists with expertise in the mass production of automobile components and turbochargers will play the key role in establishing the optimum PT configuration in terms of low cost. It will then be the task of analysts and designers to engineer and refine it for high performance and low emissions. With a preliminary design established, an in-depth failure modes and effects analysis would be undertaken. The findings from this would be factored into the final design.

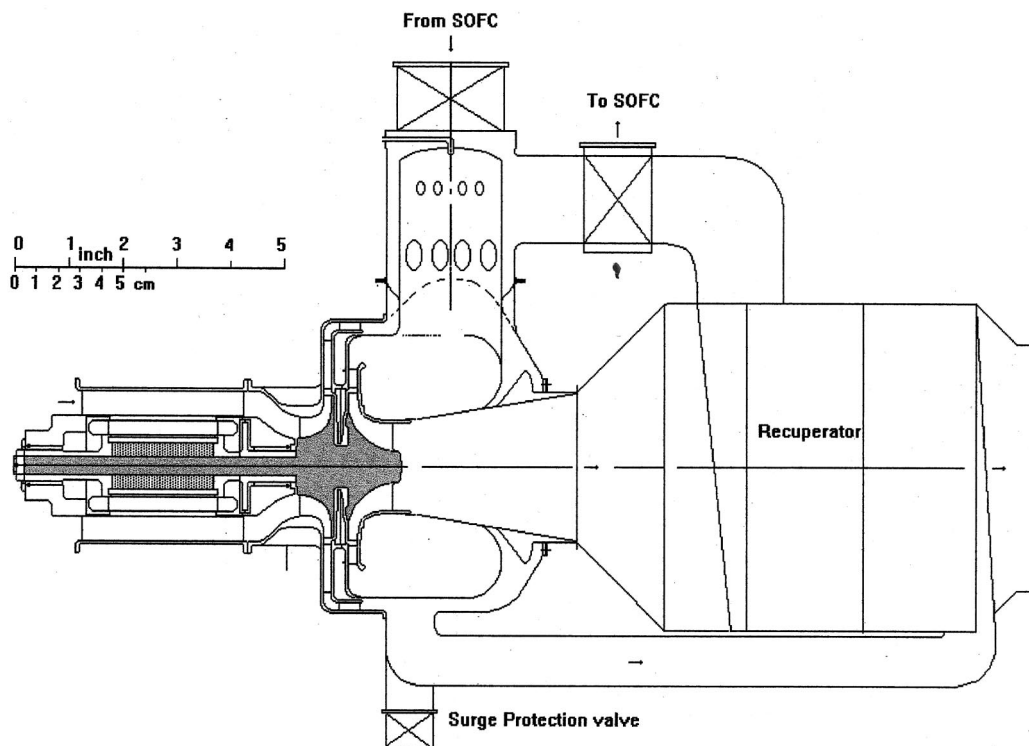


Fig. 12 -Alternate 5-kW personal turbine design concept with rear-mounted recuperator and can combustor

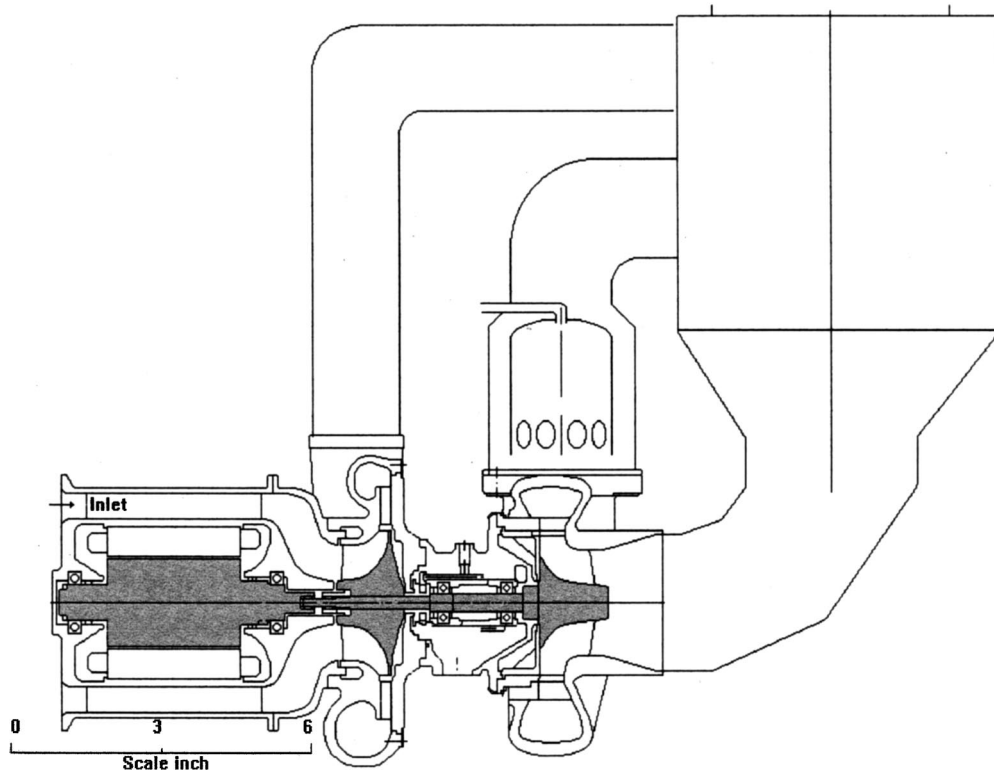


Fig. 13 Turbocharger-based 5-kW PT design concept

There are those who feel that the genesis of the PT is a modern automobile turbocharger, and we would be remiss not to address this point. A tentative layout of a 5 kW PT concept embodying a representative turbocharger is shown on Fig. 13. Modifications to the turbocharger to give the required flow characteristics and improved efficiency would include the following: (1) incorporation of a vaned diffuser in the compressor, (2) modifying the turbine inlet volute to include a nozzle assembly, (3) increasing the diameter of the turbine impeller to facilitate power to the generator, and (4) replacement of the oil bearings with a lubricant-free system. It is likely that other researchers will explore this PT variant.

6.4 Waste Heat Utilization. Microturbines have been demonstrated in a combined power and heat mode of operation ([25]) and this can be extended to the PT.

With a modest level of turbine inlet temperature, and a high degree of recuperation, the exhaust temperature from the turbogenerator is only 250°C, which is considerably lower than in larger gas turbines. Nevertheless this reject thermal energy has economic worth, and can be taken advantage of by using a waste heat recovery module. Even with a clean fuel like natural gas, the final reject temperature from the heat exchanger should be kept above the dew point of sulfuric acid to obviate corrosion in the exhaust system. With a heat exchanger module about 10 kW of thermal energy can be recovered from the exhaust, this giving a fuel utilization efficiency of about 70% for the cogeneration version of the 5-kW PT.

Details of the waste heat recovery module are not addressed in this paper, since it would be customized for a particular application. For installation in a home it would be engineered to give hot water, space heating, and air conditioning. For applications in the developing countries, the module could provide hot water, low grade steam, refrigeration, hot air supply for crop drying, and be used for desalination. The heat exchanger industry has been responsive to the needs of small users, and an example of a compact heat recovery exchanger developed for small engines is shown on Fig. 14 ([26]).

6.5 Hybrid PT. The next major technology advancement in the power generation field could well be the coupling of gas turbines with high-temperature fuel cells to give power plants with essentially zero emissions and very high levels of efficiency. This includes the coupling of microturbines with SOFCs, and a study for a 50 kW unit has shown very attractive results ([27]). The 900°C effluent temperature from a SOFC is perfectly matched to the turbine inlet temperature of the 5-kW PT. The PT concept shown on Fig. 12 is well suited for the hybrid variant, since as shown the external ducts facilitate ease of coupling between the turbogenerator and the SOFC stack. An initial investigation of a

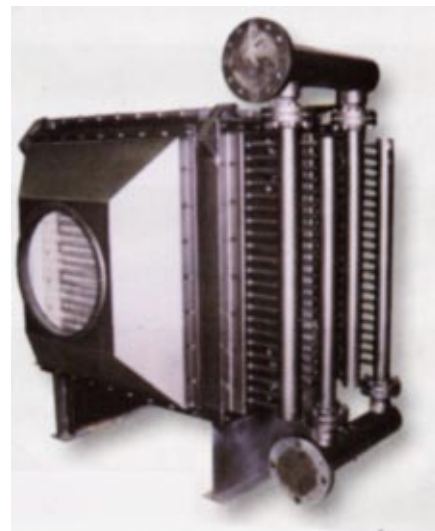


Fig. 14 Compact waste heat recovery exchanger (courtesy Cain Industries)

hybrid concept using the 5-kW PT has indicated that the total power output would increase to about 36 kW, with an overall efficiency on the order of 56% ([28]). This encouraging result will surely foster further work to yield maximum performance and minimum cost.

7 Summary

Those who had vision many years ago, that someday the majority of homes in the U.S. would have a PC, were of course absolutely right. The basis for a similar vision regarding widespread utilization of a PT is the rapidly expanding use of electronic equipment for the internet, e-business, and all commercial aspects in the IT era, and in coming decades the growing amount of service industry work that will be done in the home. In light of the current shortage of electrical power in some parts of the country, providing a constant and reliable source of power for home-based industries will be mandatory.

While installing a PT in many homes could be a big market, it may well be dwarfed by the power demand in the developing countries. In vast regions of the world, the inability to rapidly and cost effectively build a network of transmission lines, means that DG is the only option. The PT is ideally suited to provide the total energy needs of small communities and villages, and this will spawn new industries and contribute to improved living standards.

In addition there may be defense applications for a compact and light-weight PT. It is also of interest to note that if a 5-kW PT was coupled with a SOFC, the unit power output would be increased to 36 kW with an overall efficiency of 56%, and near zero emissions. The worldwide market for PT's could be in the millions in coming decades.

The perceived need for a viable PT is really more than just a vision, so how can it become a reality? All of the technology for the deployment of a PT exists today, and what must be done is an engineering effort to establish a concept that will yield low cost when mass produced. The major design drivers, as emphasized several times in this paper, are low emissions and low cost, together with design simplicity to ensure high reliability, and near zero maintenance.

Clearly, the automobile industry, where tens of millions of units are made each year, is the most germane technology base for a low-cost PT. The transfer of manufacturing know-how from the mass production of turbochargers, heat exchangers, electrical components and controls is viewed as being essential.

A paradigm shift in terms of cost estimating for a PT is necessary since if it becomes a reality it will be the most widely produced gas turbine ever. At the root of the matter will be what worth must be added to the basic material cost to mass produce each component. It is of interest to note that in the automobile industry many components are produced for about twice the material cost

Small emergency and standby generator sets (rated at 5 kW) can be purchased from home improvement stores for as low as \$500, but in the future their cost could increase substantially if they are to comply with ever-demanding emission requirements. It needs to be mentioned that a direct comparison can't really be made between these generator sets (that are operated intermittently as standby/backup power units for only a few hours each year) and the PT which has features and component stress levels commensurate with a life of several tens of thousand hours.

Automobile reciprocating engines are produced for about \$45/kW ([29]), but such a low value is not realizable with a PT because of the inclusion of high temperature materials, although in the proposed concept this has been minimized. A cost target of \$1000 for the mass produced ITC 5000 personal turbine has been proposed. Hopefully this will initiate a dialogue between specialists to see if this is can be realized. Important follow-on work will include an assessment of the O and M costs, and together with current and future fuel costs, a definitive projection of power generation cost made.

The use of natural gas as the fuel for the PT has been emphasized essentially because it is available in many homes and yields low emission levels. However, the PT can be readily adapted for service in the developing countries, to operate on a wide range of indigenous fuels.

In making projections for the 21st century the idea of a PT has fascinated others ([30]), and an engineering introduction to this topic has been given in this paper. Microturbines are currently attracting a lot of publicity in the press, and their successful penetration of the DG market could pave the way for the potentially much larger PT market. An attractive PT concept has been proposed, but whether it will stand the test of time after an assessment by manufacturing specialists who have expertise in the mass production of small engineering assemblies, remains to be seen. It is hoped that this introductory paper will foster and stimulate interest in others who are also fascinated by the unlimited potential of very small gas turbines.

Acknowledgments

The authors express their thanks to Keith Rochford (Honeywell Transportation and Power Systems) for his guidance on automotive turbochargers, and to Skip Carlson (Turbulence Tubes) for information on small recuperator technology. Thanks are also expressed to Tony Davies (Bowman Power Systems, U.K.) and Dave Dewis (Elliott Energy Systems) for their perspectives on small gas turbines. This paper has been enhanced by the inclusion of hardware photographs, and the authors are appreciative to all concerned with credits being duly noted.

References

- [1] Craig, P., 1997, "The Capstone Turbogenerator as an Alternative Power Source," SAE Paper 970292.
- [2] Clark, A., and McShane, D., 1999, "Hybrid Electric Vehicles Utilizing Capstone Microturbine Technology," SAE Paper 1999-01-2930.
- [3] Gerendas, M., and Pfister, R., 2000, "Development of a Very Small Aero Engine," ASME Paper 2000-GT-0536.
- [4] Rodgers, C., 1986, "A Jet Fuel Starter and Expendable Turbojet," ASME Paper 86-GT-001.
- [5] Rodgers, C., 1997, "Advances in Small Turbopropulsion Engine Technology," AIAA Paper 97-3289.
- [6] Thompson, T., et al., 1994, "Conversion of T-100 MPSU Technology," ASME Paper 94-GT-490.
- [7] Woodhouse, G. D., 1994, "Auxiliary Power Unit Evolution," *Aerosp. Eng.*, May, pp.19–23.
- [8] Nakajima, T., et al., 1995, "The Development of the Micro Gas Turbine Generator," paper presented at Yokohama International Gas Turbine Conference.
- [9] Sakakida, M., et al., 1999, "A Study of a Small Gas Turbine Engine for Mini-Cogeneration System," *Proceedings of the International Gas Turbine Congress*, Kobe, Japan, Nov. 14–17, Gas Turbine Society of Japan, Tokyo, pp. 1060–1074.
- [10] Rodgers, C., 1993, "Small (10–200 kW) Turbogenerator Design Considerations," ASME IGTI-Vol. 8, pp. 535–542.
- [11] Rodgers, C., 2000, "25.5 kW Microturbine Design Aspects," ASME Paper 2000-GT-0626.
- [12] Rodgers, C., 1997, "Turbochargers to Small Gas Turbines?" ASME Paper 97-GT-200.
- [13] McDonald, C. F., 1996, "Heat Recovery Exchanger Technology for Very Small Gas Turbines," *Intl. J Turbo Jet Eng.*, **13**(4), pp. 239–261.
- [14] McDonald, C. F., 1999, "Emergence of Recuperated Gas Turbines for Power Generation," ASME Paper 99-GT-067.
- [15] McDonald, C. F., 1975, "Recuperator Development Trends for Future High Temperature Gas Turbines," ASME Paper 75-GT-050.
- [16] Rochford, K., 2000, personal communication Aug. 18.
- [17] Oswald, J. I., et al., 1999, "A New Durable Gas Turbine Recuperator," ASME Paper 99-GT-369.
- [18] McDonald, C. F., 2000, "Low Cost Recuperator Concept for Microturbine Applications," ASME Paper 2000-GT-0167.
- [19] McDonald, C. F., 2000, "Low Cost Compact Primary Surface Recuperator for Microturbines," *J. Appl. Therm. Eng.*, **29**, pp. 471–497.
- [20] Carlson, S., 2000, personal communication June 6.
- [21] Rodgers, C., 1997, "Thermo—Economics of Small 50 kW Turbogenerator," ASME Paper 97-GT-260.
- [22] Gelsi, S., 2000, "Capstone Turbine Eyes PC-Like Role," *CBS Market Watch Publication*, Aug. 13.
- [23] Dunn, S., 2000, "Micropower: The Next Electrical Era," *Worldwatch Paper*, **151**, July, p. 22.
- [24] Myers, P. F., 1997, "Economics and Design Approaches for Small Commercial Turbogenerators," ASME Paper 97-GT-364.

- [25] Carno, J., et al., 1998, "Micro Gas Turbine for Combined Heat and Power in Distributed Generation," ASME Paper 98-GT-309.
- [26] Brezonick, M., 2000, "Cain Raising Its Sights in Cogeneration Markets," Diesel Gas Turb Worldwide, Jan., pp. 10–12.
- [27] Massardo, A. F., et al., 2000, "Microturbine/Fuel Cell Coupling for High Efficiency Power Generation," ASME Paper 2000-GT-0175.
- [28] Magistri, L., et al., 2001, "A Hybrid System Based on a Personal Turbine (5 kW) and a SOFC Stack: A Flexible and High Efficiency Energy Concept for the Distributed Power Market," ASME Paper No. 2001-GT-0092.
- [29] Rodgers, C., and McDonald, C. F., 1997, "Automotive Turbogenerator Design Considerations and Technology Evolution," SAE Paper 972673.
- [30] Armstrong, L., 1999, "Ideas for the 21st Century . . . I am Your Local Power Plant," Bus. Week, Aug. 30, p 84.

Tubular Solid Oxide Fuel Cell/Gas Turbine Hybrid Cycle Power Systems: Status

S. E. Veyo

L. A. Shockling

J. T. Dederer

J. E. Gillett

W. L. Lundberg

SOFC Power Generation,
Siemens Westinghouse Power Corporation,
1310 Beulah Road,
Pittsburgh, PA 15235-5098

The solid oxide fuel cell (SOFC) is a simple electrochemical device that operates at 1000°C, and is capable of converting the chemical energy in natural gas fuel to AC electric power at approximately 45% efficiency (net AC/LHV) when operating in a system at atmospheric pressure. Since the SOFC exhaust gas has a temperature of approximately 850°C, the SOFC generator can be synergistically integrated with a gas turbine (GT) engine generator by supplanting the turbine combustor and pressurizing the SOFC, thereby enabling the generation of electricity at efficiencies approaching 60% or more. Conceptual design studies have been performed for SOFC/GT power systems employing a number of the small recuperated gas turbine engines that are now entering the marketplace. The first hardware embodiment of a pressurized SOFC/GT power system has been built for Southern California Edison and is scheduled for factory acceptance tests beginning in Fall 1999 at the Siemens Westinghouse facilities in Pittsburgh, PA. The hybrid power cycle, the physical attributes of the hybrid systems, and their performance are presented and discussed. [DOI: 10.1115/1.1473148]

Introduction

The pressurized SOFC/GT hybrid cycle power system is depicted schematically simplified in Fig. 1.

The SOFC generator is pressurized, operating on recuperatively heated process air supplied by the compressor. The power system based upon this cycle achieves increased power output and higher efficiencies due to the utilization by the gas turbine generator of thermal energy in the pressurized solid oxide fuel cell (SOFC) exhaust stream. Power system performance is also enhanced by SOFC generator operation at elevated pressure. For a given cell operating current, cell voltage, cell power output, and efficiency increase logarithmically with pressure. The gas turbine combustor and the air heater are fired during system startup operations, and they could be fired during peak power or turndown periods. For maximum system efficiency during steady-state operation at system rating, neither combustor is fired.

Interest in the fuel cell/gas turbine hybrid cycle has increased in recent years. Discussion in Appleby and Foulkes [1] indicates that the integration of fuel cells and gas turbines and steam turbines was considered earlier. However, it was done then mostly in the context of the large power plant, primarily because the gas turbine experience base was there. With the advent of small gas turbines (ratings less than 250 kWe), and with the maturing of the modular fuel cell, there is now the promise that the high-performance hybrid cycle can be applied in small-capacity power systems, just at the time when interest in distributed generation is developing rapidly. Papers by Rokni [2], Harvey and Richter [3,4], and Massardo and Lubelli [5] provide recent examples of hybrid cycle performance analyses. The parametric study of Stephenson and Ritchey [6] focused specifically on the recuperated SOFC/GT cycle. It concluded that high cycle efficiencies will be achieved by directly expanding SOFC exhaust gas at the gas turbine without firing supplemental fuel at the gas turbine (GT) combustor, highlighting the synergy of SOFC and gas turbine integration. Veyo and Lundberg [7] predicted the performance of hybrid combined heat and

power (CHP) and advanced SOFC/GT hybrid cycle concepts. In the present paper, the projected performance of small-capacity SOFC/GT hybrid power systems based on specific small gas turbines is reported. In addition, performance estimates for the first constructed SOFC/GT hybrid power system are provided.

Siemens Westinghouse Program Status

Recently, our focus has been on the operation of a 100 kWe atmospheric-pressure SOFC-CHP demonstration power system in the Netherlands, and on the design and fabrication of a 220 kWe PSOFC/GT hybrid cycle power system. The 100 kWe system, sponsored by EDB/ELSAM, a consortium of Dutch and Danish energy generating and distribution companies, is installed on a utility site near Arnhem, and has logged over 6000 operating hours. It generates approximately 110 kWe net AC power at 46% efficiency (net AC/LHV) for the utility grid, and hot water for the local district heating system. The demonstrated energy efficiency is nearly 75%. The SOFC generator for this system uses a stack of 1152 tubular cells, each cell having a diameter of 22 mm and an active length of 1500 mm. The cell stack can be viewed as composed of two 576-cell substacks, each having its own ejector,

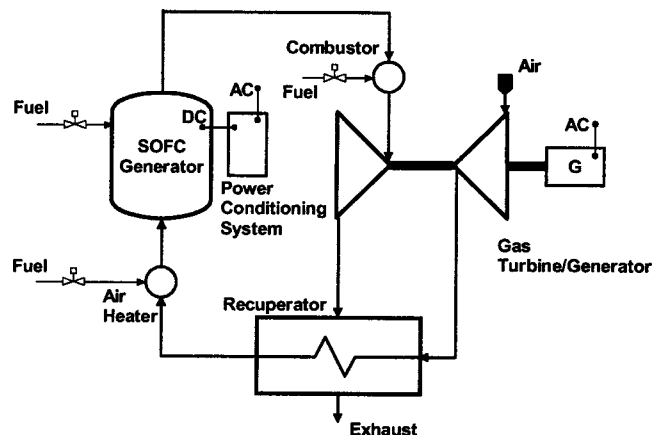
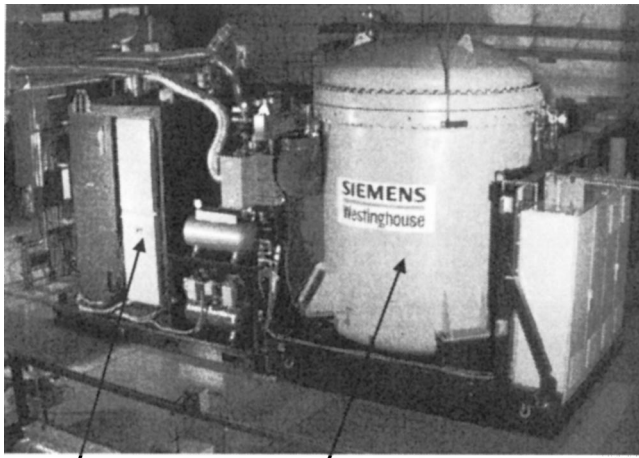


Fig. 1 PSOFC/GT hybrid power system cycle—simplified schematic

Contributed by the International Gas Turbine Institute (IGTI) of THE AMERICAN SOCIETY OF MECHANICAL ENGINEERS for publication in the ASME JOURNAL OF ENGINEERING FOR GAS TURBINES AND POWER. Paper presented at the International Gas Turbine and Aeroengine Congress and Exhibition, Munich, Germany, May 8–11, 2000; Paper 00-GT-550. Manuscript received by IGTI, November 1999; final revision received by ASME Headquarters, February 2000. Associate Editor: D. R. Ballal.



Gas Turbine
SOFC Generator

Fig. 4 220 kW PSOFC/GT power system

SOFC exhaust at the gas turbine combustor inlet, and it sends recuperatively heated process air to the SOFC generator inlet. The hot gas is expanded partially across the gasifier turbine, which rotates at approximately 70,000 rpm, and drives the compressor. The expansion of the hot gas is completed across the power turbine, where the derived shaft power turns the generator. A typical

Table 1 220 kW PSOFC/GT power system performance estimates

Cell current	267 amps
Cell voltage	0.610 V
Compressor pressure ratio	2.9:1
Air intake rate	0.58 kg/s
Turbine inlet temperature	780C
SOFC DC power	187 kW
SOFC gross AC power	176 kW
Gas turbine AC power	47 kW
System net AC power	217 kW
Efficiency (net AC/LHV)	57%

power turbine shaft speed is 44,000 rpm. Initially, the electric power produced by both the gas turbine and the SOFC generator will be dissipated.

As indicated in Fig. 3, the SOFC generator is valved to permit the flow of air around the cell stack. The gas turbine can therefore be started before the SOFC generator, by firing the gas turbine combustor, and air can be directed around and through the SOFC generator in desired proportions. With the gas turbine started, exhaust heat recovered at the recuperator is available to aid the SOFC heat-up process. The air heater is fired during this process, but the flow of fuel to the heater and to the GT combustor are turned back to zero as steady-state operation at the peak-efficiency rating point is achieved.

Power system performance estimates are presented in Table 1. For these estimates the efficiency is calculated assuming all power is exported to the AC grid, and reasonable power condi-

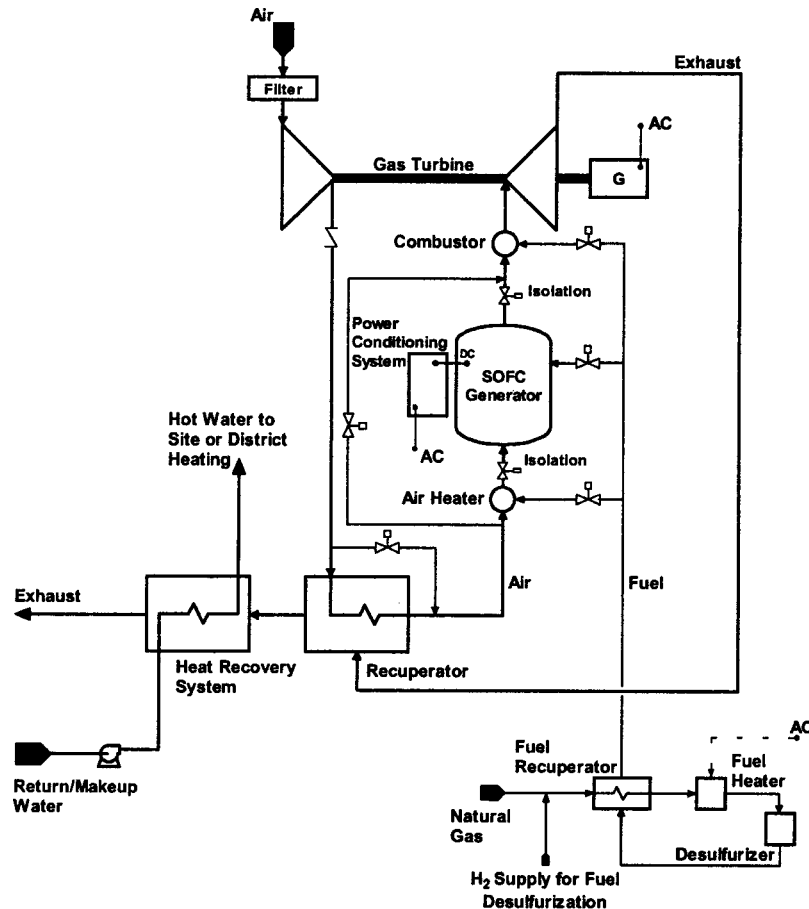


Fig. 5 320 kW PSOFC/GT power system cycle

Table 3 MWe-class PSOFC/GT power system performance estimates (precommercial)

Cell current	239 amps
Cell voltage	0.643 V
Compressor pressure ratio	3.3:1
Air intake rate	2.0 kg/s
Turbine inlet temperature	1144 K
Combustor and air heater fuel flow rate	0
SOFC dc power	879 kWe
SOFC gross AC power	818 kWe
Gas turbine AC power	218 kWe
System net AC power	1014 kWe
Efficiency (net AC/LHV)	59%
Exhaust flue temperature	515 K

The SOFC generator for this system uses ten 576-cell substacks in a horizontal pressure vessel. The power system is configured as two factory-assembled skids; the SOFC and gas turbine equipment is installed on one skid, and balance-of-plant hardware is installed on the second skid. Each skid will be transported to the installation site in a single truck shipment. At the site, trailer wheel assemblies are removed, and the transporter skids are lowered into place on prepared pads. Other installation activity at the site will involve, in addition to the site preparation work, the interconnection of the skids, and the completion of the system/site interfaces. Performance estimates for the MWe-class power system are presented in Table 3. For these particular estimates the gas turbine was modeled using information on a developmental 300 kWe Solar Turbines engine.

Conclusions

1 Atmospheric pressure tubular SOFC-CHP power systems can achieve electrical generating efficiencies greater than 45%, and energy efficiencies near 75%, as demonstrated by the operation of the EDB/ELSAM 100 kW SOFC power system.

2 Pressurized tubular SOFC/GT hybrid cycle power systems will exhibit more than ten points in electrical efficiency advantage over atmospheric pressure systems.

3 A MWe class PSOFC/GT power system conceptual design projects a precommercial electrical generation efficiency of 59% for a system that is factory assembled and tested prior to shipment on two over-the-road transporters/skids.

4 A 300 kWe class PSOFC/GT power system conceptual design projects a precommercial electrical generation efficiency of 57% for a system that is factory assembled and tested prior to shipment on one over-the-road transporter skid.

5 The world's first proof-of-concept test of a PSOFC/GT power system is scheduled for initiation in CY99.

Acknowledgment

The development of the Siemens Westinghouse tubular solid oxide fuel cell is supported by the United States Department of Energy, Federal Energy Technology Center, Morgantown, WV, under a cooperative agreement, contract DE-FC26-97FT34139. Pressurized SOFC testing is supported by the United States Department of Energy, Federal Energy Technology Center, Morgantown, WV; Siemens Westinghouse Power Corporation; Ontario Hydro Technologies and their Canadian funding partners (the Canadian Electrical Association, Natural Resources Canada, Gas Technology Canada, Consumers Gas, British Gas, Union Gas, and the Ontario Ministry of Environment and Energy). In addition, analysis and interpretation of data is sponsored by the preceeding plus the Institute for Advanced Energy of Japan.

References

- [1] Appleby, A. J., and Foulkes, F. R., 1989, *Fuel Cell Handbook*, van Nostrand Reinhold, New York.
- [2] Rokni, M., 1993, "Introduction of a Fuel Cell Into a Combined Cycle: A Competitive Choice for Future Cogeneration," *Proceedings of the ASME Cogeneration Turbo Power '93 Conference*, ASME, New York, pp. 255-261.
- [3] Harvey, S. P., and Richter, H. J., 1993, "Improved Gas Turbine Power Plant Efficiency by use of Recycled Exhaust Gases and Fuel Cell Technology," *ASME Heat Transfer Division*, **266**, pp. 199-207.
- [4] Harvey, S. P., and Richter, H. J., 1994, "Gas Turbine Cycles With Solid Oxide Fuel Cells: Parts I and II," *ASME J. Energy Resour. Technol.*, **118**, pp. 305-318.
- [5] Massardo, A. F., and Lubelli, F., 1998, "Internal Reforming Solid Oxide Fuel Cell-Gas Turbine Combined Cycles (IRSOFC-GT), Part A: Cell Model and Cycle Thermodynamic Analysis," *ASME Paper 98-GT-577*.
- [6] Stephenson, D., and Ritchey, I., 1997, "Parametric Study of Fuel Cell and Gas Turbine Combined Cycle Performance," *ASME Paper 97-GT-340*.
- [7] Veyo, S. E., and Lundberg, W. L., 1999, "Solid Oxide Fuel Cell Power System Cycles," *ASME Paper 99-GT-356*.
- [8] Leeper, J. D., 1999, "The Hybrid Cycle: Integration of a Fuel Cell With a Gas Turbine," *ASME Paper 99-GT-340*.

L. Magistri

TPG-DIMSET,
Università di Genova,
Via Montallegro 1,
Genova 16145, Italy

P. Costamagna

TPG-DICheP,
Università di Genova,
Via Montallegro 1,
Genova 16145, Italy

A. F. Massardo

TPG-DIMSET,
Università di Genova,
Via Montallegro 1,
Genova 16134, Italy
Mem. ASME

C. Rodgers

ITC,
3010 N. Arroyo Drive,
San Diego, CA 92103

C. F. McDonald

McDonald Thermal Engineering,
1730 Castellana Road,
La Jolla, CA 92037

A Hybrid System Based on a Personal Turbine (5 kW) and a Solid Oxide Fuel Cell Stack: A Flexible and High Efficiency Energy Concept for the Distributed Power Market

In this paper a high efficiency and flexible hybrid system representing a new total energy concept for the distributed power market is presented. The hybrid system is composed of a very small size (5 kW) micro gas turbine (named personal turbine—PT) presented in a companion paper by the authors coupled to a small size solid oxide fuel cell (SOFC) stack. The power of the whole system is 36 kW depending on the design parameters assumed for the stack. The design and off-design performance of the hybrid system have been obtained through the use of an appropriate modular code named “HS-SOFC” developed at the University of Genoa and described in detail in this paper. The results of the simulation are presented and discussed with particular regards to: choice of the hybrid system (HS) design point data, HS design point performance, off-design performance of PT and SOFC stack, and off-design performance of the whole HS. Some preliminary economic results are also included based on different fuel and capital cost scenarios and using the cost of electricity as the parameter for comparison between PT and HS.

[DOI: 10.1115/1.1473825]

Introduction

The increasing use of electronic equipment in the IT has put a strain on the existing electrical supply system, which if not resolved quickly, will mean increasing blackouts. Large centralized power plants, together with the necessary transmission lines, are not foreseen in the future because of extended and unacceptable times in permitting and construction. The growing trend of distributed generation will ensure that the power source is located near to the user. This will involve the installation of gas turbines from multi-megawatt industrial units down to the current range of microturbines. The internet has resulted in an increasing amount of work done in the home where a constant and reliable source of electrical power is mandatory. This trend could result in small turbogenerators such as the PT being used in the home, and this would represent the ultimate application in terms of distributed generation.

Microturbines in the 30–100 kW power range are expected to be produced in significant quantities within the next two years or so to meet the energy needs of many distributed power users. The successful introduction of these first generation microturbines could pave the way for smaller personal turbines (PT) in the future, with a postulated much larger market potential. This topic was discussed in a recent publication (Rodgers [1]).

Gas turbine technology has advanced to the point where a natural gas fired personal turbine, rated at say 5 kW, could provide the energy needs of an individual home, this including electrical power, heating, and cooling. The turbine-alternator, about the size

of a domestic dish washer, would operate unattended with no vibration or noise, have single-digit emissions, and would be essentially maintenance free.

Such a small turbo-generator, using natural gas fuel, is ideally suited for coupling with a solid oxide fuel cell (SOFC) stack, as already discussed by the authors (Massardo et al. [2]) for a larger microturbines (50 kW), could meet the power needs of business users, and also provide the total energy needs for villages and communities in the developing countries.

This natural extension of existing microturbines is addressed in this paper, and involves the coupling of a very small (PT) state-of-the-art recuperated gas turbine with a high-temperature SOFC stack. Such a hybrid plant, with an electrical output of about 36 kW, an overall efficiency of over 56%, a fuel utilization factor of over 80%, no NO_x emission, and very low carbon dioxide (CO₂) emissions—due to the very high fuel conversion efficiency—could meet the total clean energy needs of many users in both the individual nations and developing countries.

For the proposed hybrid concept, based on the state of the art technology, the following topics are discussed: concept definition, stack and system modeling, PT, SOFC, and HS performance at design and off design conditions, system and energy costs, and possible future developments.

Personal Turbine Technology

Large gas turbines have the advantage of both economy of performance and scale (Wilson and Korakianitis [3]). The reverse is true for very small gas turbines. Small engines, like the personal turbine (PT) discussed here, with a radial compressor and turbine have significantly lower aerodynamic efficiencies. This is a result of smaller blade heights, Reynolds number effects, tip clearance effects, manufacturing tolerances, and surface finish, all of which adversely affect efficiency. In addition, the geometries associated

Contributed by the International Gas Turbine Institute (IGTI) of THE AMERICAN SOCIETY OF MECHANICAL ENGINEERS for publication in the JOURNAL OF ENGINEERING FOR GAS TURBINES AND POWER. Paper presented at the International Gas Turbine and Aeroengine Congress and Exhibition, New Orleans, LA, June 4–7, 2001; Paper 01-GT-092. Manuscript received by ITGI, Dec. 2000, final revision, Mar. 2001. Associate Editor: R. Natole.

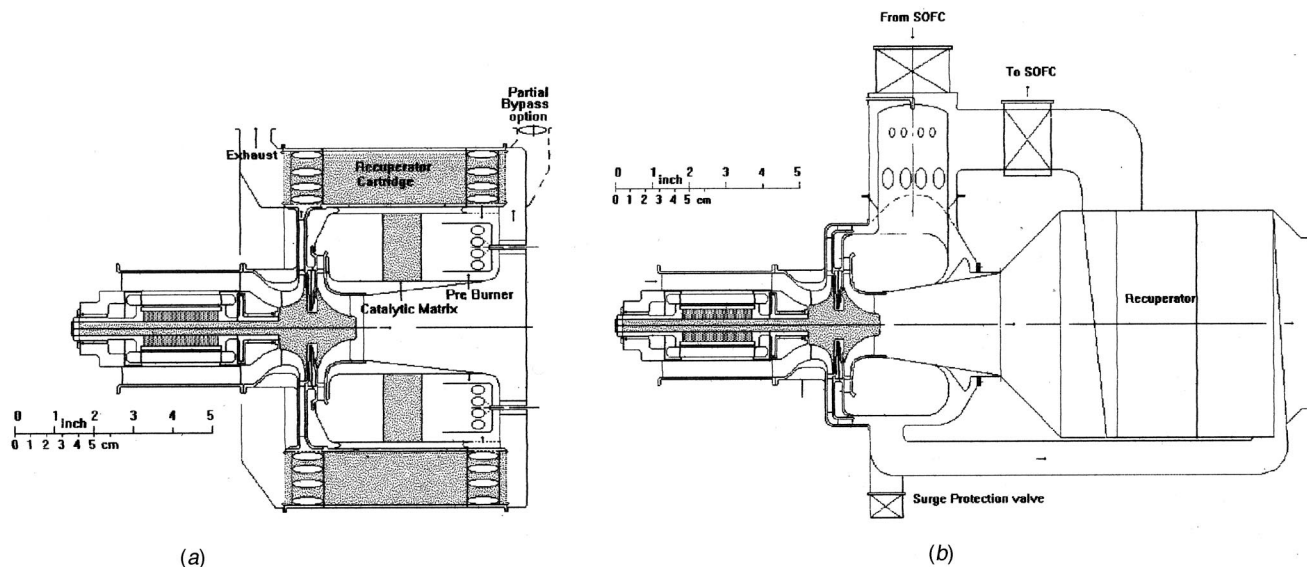


Fig. 1 Personal turbine: (a) microturbine configuration, (b) hybrid system configuration

with a radial turbine make blade cooling very difficult, and thus advances in turbine inlet temperature are solely dependent on material technology.

For very small simple cycle gas turbines demonstrated to date, their efficiencies have been modest. While a recuperator may be a user option for larger industrial gas turbines, it is mandatory to achieve acceptable efficiency for small size units, and the majority of microturbines being developed utilize a recuperated cycle. For the even smaller PT, the inclusion of a recuperator is vital to achieve a thermal efficiency of over 20%. Moreover, some technological constraints are present in this microturbine development:

- turbine inlet temperature: determined by the rotor alloy stress rupture and low cycle fatigue strength, duty cycle;
- recuperator hot side gas inlet temperature: limited by the oxidation and creep considerations, together with life requirements for the selected matrix material;
- pressure ratio: dictated by compressor type and material;
- rotational speed: determined by rotor dynamic and bearing considerations, together with rotor stress limitations commensurate with the machine life requirement.

A complete description of the PT technology is reported by the authors (Mc Donald and Rodgers [4]). Figure 1(a) [1] shows the ITC5000 personal turbine concept layout which is varied as being the simplest approach consistent with meeting major objectives, which include high reliability, and being amenable to high volume predictions. Figure 1(b) shows the modification necessary to use the personal turbine as part of a hybrid system (PT plus SOFC reactor).

Solid Oxide Fuel Cells (SOFC) Technology

Solid oxide fuel cells (SOFC) are electrochemical reactors currently under development for applications in the field of energy conversion (Hirschenhofer et al. [5] and Wolk [6]). The type of electrolyte which is usually employed (YSZ, yttria stabilized zirconia) requires a high operating temperature (about 1000°C) which imposes severe technological constraints on the materials or alternative multilayer deposition techniques which are expected to permit operation at temperatures of 700–800°C. Other intensive research efforts are being made in the field of electrode im-

provement, with particular attention to new electroactive materials and to optimization of the structure and morphology of composite electrodes.

Even if SOFCs have not yet reached a level where they can compete with conventional energy conversion techniques, a number of demonstration programs are currently in progress, including some hybrid plants based on SOFCs coupled with small gas turbines (Veyo et al. [7], George [8], and Bruch [9]).

Configuration and Model of the Personal Turbine–Solid Oxide Fuel Cell (PT-SOFC) Hybrid System (HS)

Solid oxide fuel cells (SOFCs) integrated with gas turbines of small size (less than 1 MW) are attracting wide interest as these systems are able to solve simultaneously some key problems of small gas turbines (low-efficiency and NO_x emissions due to the combustor) and of SOFCs (high cost, predicted around \$/kW 1000–1500) (Massardo and Magistri [10]). In the HS configuration the pressurized SOFC module substitutes the combustor of the regenerated PT, and the clean effluent at a temperature of about 900°C, which matches well the requirements on the inlet temperature of the very small microturbines, enters the expander to generate both electrical and mechanical power for the compressor. The value of the compressor discharge pressure of about 0.4 MPa facilitates increased power output and higher efficiency from a given SOFC frame size.

Figure 2 shows a flow schematic of the hybrid PT/SOFC power plant. The complete microturbine package is regarded as a stand-alone unit that can be operated independent of the fuel cell. However, plumbing and control modifications must be incorporated for the overall plant to operate in a hybrid mode. The flow schematic shown on Fig. 2 represents the system in a simple form, and it is recognized that more detailed analysis may necessitate changes that will make it more complex. A startup air heater is shown at the cell inlet. In its simplest form this could be an electric unit. Additions to the system for hybrid operation include a natural gas desulfurizer, and a purge gas unit. New sections of ducting, together with various valves requires alterations to the microturbine external plumbing (see Fig. 1(b)), and replacement of the natural gas compressor. The plant control system must also be updated.

Personal Turbine (PT) Model. The simplified layout of the recuperated micro gas turbine named PT (5 kW) is shown in Fig. 3. The PT consists of the following components: centrifugal com-

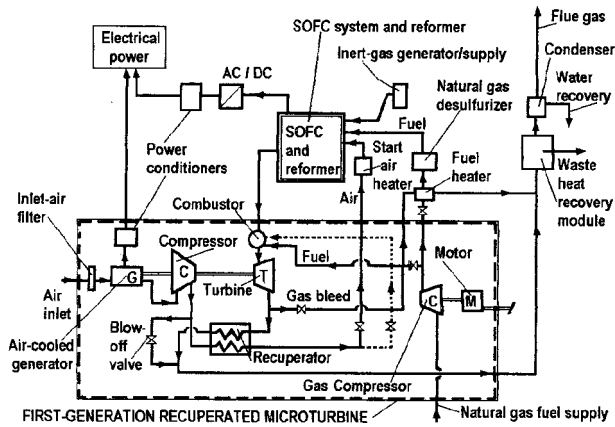


Fig. 2 Flow schematic of hybrid microturbine/fuel-cell power plant (Massardo et al. [2])

pressor, inflow expander, combustion chamber, recuperator, electrical generator, and natural gas compressor. The simulation program, named "MGT" is composed of several modules representing actual PT components and interconnected one to each other (Magistri [11]). The simulation of the compressor module is based on its maps (efficiency and pressure ratio versus non-dimensional flow rate) and the condition that the compressor surge margin is checked at each calculation. The input data of the compressor module are air inlet pressure and temperature, rotational speed, and a first attempt for pressure ratio. The actual pressure ratio value of the PT is determined using a matching technique between the compressor and the downstream components. In the combustion chamber the complete combustion reaction hypothesis is utilized, using as input the outlet compressor data and the fuel mass flow rate. The combustion chamber pressure losses (correlated to the combustion process and to the friction) are evaluated. The simulation of the expander is based on the turbine nondimensional maps, and utilizes as inputs the data at the combustion

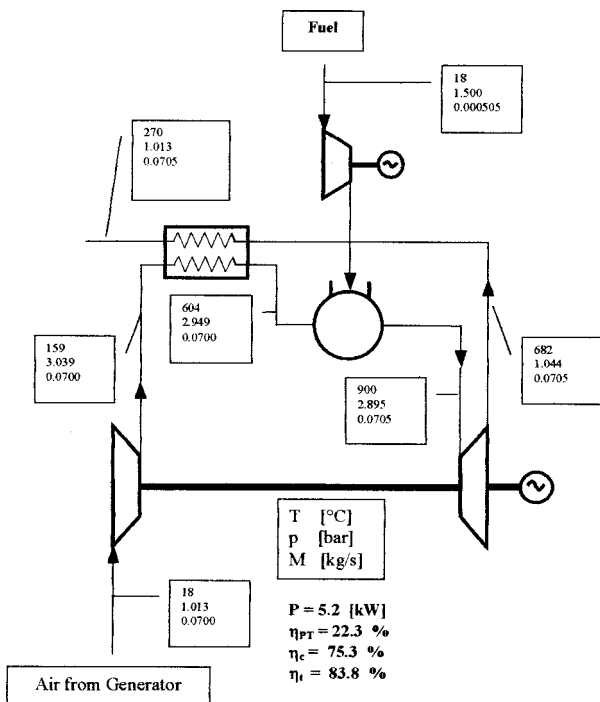
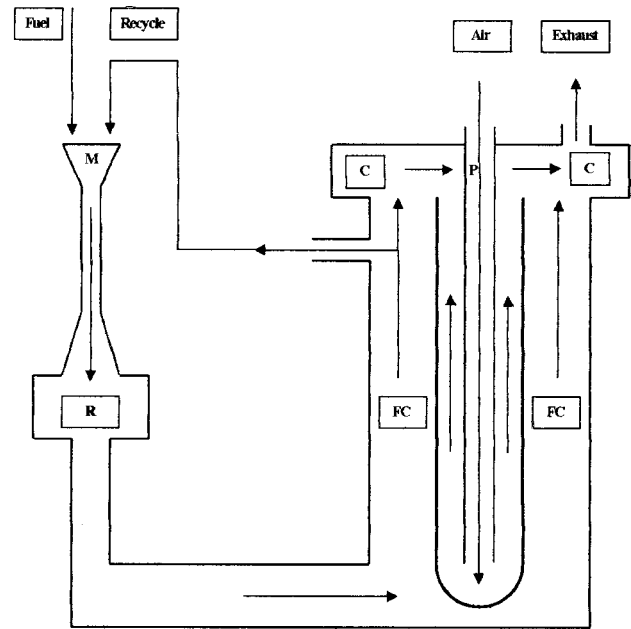


Fig. 3 Personal turbine simplified layout



M : Mixing
R : Sensible Heat Reforming
FC : Fuel Cell
C : Combustion
P : Air Pre-Heater

Fig. 4 Simplified tubular solid oxide fuel cell (M: mixing, R: sensible heat reforming, FC: fuel cell, C: combustion, P: air preheater)

chamber outlet and the regenerator downstream pressure losses. The mass flow rate and compressor-turbine work compatibility are checked to verify the correct matching of PT components; if the matching is not verified another suitable pressure ratio value is considered until convergence is reached. The recuperator module allows the evaluation of temperature distribution at design and off design operating conditions to be obtained both at the cold and hot side. At part load, keeping the heat transfer surface fixed, an appropriate correlation (Magistri [11]) is used to evaluate the heat transfer coefficient based on the value of the Reynolds number. The pressure losses at partial load are evaluated as a function of the density and mass flow rate. Finally, simplified models have been included in the code for the natural gas compressor (necessary to increase the fuel pressure up to the combustion chamber pressure) and the electrical generator. The overall model has been positively tested with medium and large-size gas turbine data available in the open literature (Pilidis [12] and Campanari [13]).

Figure 3 shows the design point data of the PT as already discussed (McDonald and Rodgers [4]). It is noteworthy observing that the PT efficiency is about 22% for 5.2 kW electrical power, with compressor efficiency of 75.3%, the expander efficiency of 83.8%, and the recuperator effectiveness of 85%. The fuel compressor power is 0.3 kW due to the very low efficiency of this auxiliary device already discussed by the authors (Massardo et al. [2]).

SOFC Group Model. The layout of the SOFC group, which includes both the reformer and the SOFC stack, is shown in Fig. 4 (Costamagna et al. [14]). The reformer is a typical catalytic reactor, where the reforming and shift reactions take place. The sensible heat of the reactants provides the energy necessary for the reforming reaction to occur. The reactants are methane and water, which are supplied to the reformer through the fuel and through the recycle of the water-rich anodic-exhaust of the SOFC. In this study, the recycle flow rate is chosen in order to meet the condi-

tion that the steam-to-carbon ratio is about 2.4. This steam-to-carbon ratio value ensures that the problem of carbon deposition is avoided in the SOFC group at all the operating conditions (off-design). The other components of the SOFC group are the mixer and the SOFC stack. The mixer is an ejector, where the fuel and the recycle flow rate mix prior to entering the reformer. The SOFC group is represented in the cited Fig. 4 as a bundle of tubular cells; however, no specific details of the tubular geometry have been taken into consideration in the present simulation. In the outlet part of the SOFC stack, after the recycle flow rate is discharged from the anodic side, the SOFC exhausts mix and burn, so that their temperature raises to the level required by the downstream PT group.

In this study the SOFC simulation is carried out with the code "SOFC-STACK" a submodule of the overall plant model (HS-hybrid system code), which requires many iterations before reaching convergence; in light of this, reliability and high calculation speed have been considered the most important requirements for the SOFC code. However, due to the high number of operating variables (temperature, current density, reactant utilization, pressure, etc.), a complete experimental database of SOFC performance under the different operating conditions is difficult to obtain, and no complete (geometry and performance) data are available in the open literature yet. Moreover, SOFC reactors are still under development and most of the data are "proprietary data." A "state-of-the-art" fuel cell performance cannot be easily defined, and thus it would be very useful to have a flexible simulation tool, which could be adapted in an easy way to different cells geometry and operating conditions. This is only possible with a model based on the overall mass and energy balances coupled with appropriate expressions for the reaction kinetics, thermodynamic constants, and material properties. Thus, such a model has been developed in order to evaluate the behavior of the SOFC group, including mixer, reformer, and SOFC stack (Costamagna et al. [14]). The balance equations have been solved between the inlet and outlet of each component of the group, allowing the evaluation of the average values of the physical-chemical variables (i.e., temperatures, concentrations, etc.) in each component, and the electrochemical performance of the group itself. In this way, some details of the distribution of the physical-chemical variables within the electrochemical SOFC reactor are not evaluated, as was done in previous studies at the University of Genoa (Costamagna et al. [15], Costamagna and Honegger [16], and Costamagna et al. [17]). This small loss of accuracy is fully acceptable in the framework of the overall plant evaluation, and, on the other hand, it allows a significant reduction of the computational time. Moreover, it is worthy to note that increasing the cell model complexity the data necessary for the calculation increases too, and they are very difficult to be obtained by companies or laboratories working in the SOFC field.

In the SOFC stack, the calculation of the electrical current-voltage relationship is done through the evaluation of the thermodynamic voltage, which is the voltage of the stack under open circuit conditions. When electrical current is drawn from the stack, voltage losses due to irreversibility arise, which can be classified as: (i) ohmic losses; (ii) activation losses, due to sluggish electrode kinetics; (iii) concentration losses, occurring when the diffusion of the reactants through the electrodes is slower than the electrochemical reaction. However, at the high operating temperature of SOFCs, diffusion is a very effective process, and thus the latter effect is usually negligible, unless under conditions of very high fuel or oxidant utilization, which are not taken under consideration here. Thus, concentration losses have been neglected in this work.

The current-voltage behavior of the stack is evaluated by subtracting the overall voltage losses from the thermodynamic potential for each value of the electrical current.

More details on the model are reported in Costamagna et al. [14], where all the parameters and constants used in the analysis

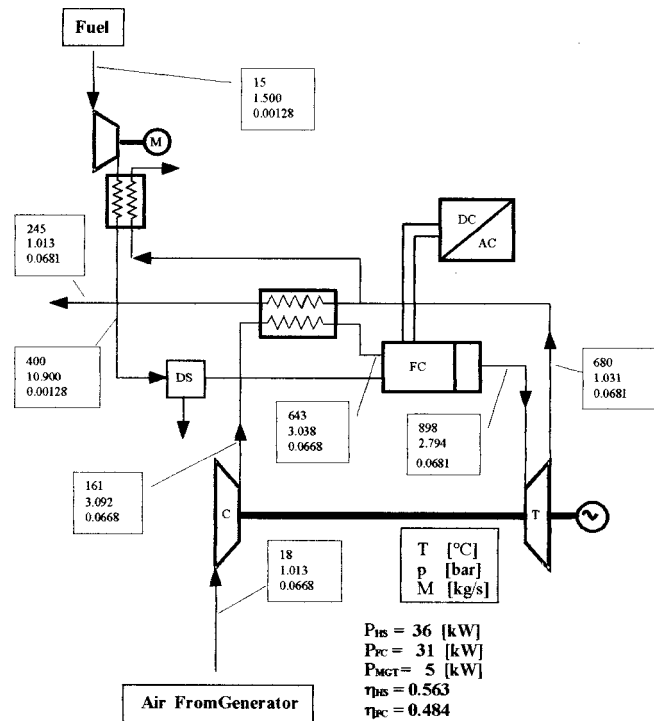


Fig. 5 Simplified layout of the hybrid plant (personal turbine and solid oxide fuel cell), and design point data

are fully presented and discussed. The design point and off-design performance of a SOFC group alone, both for fixed or variable SOFC temperatures are presented and discussed in depth in the cited reference.

Hybrid System Model

Figure 5 shows a very simplified layout of the hybrid system, which has been obtained by substituting the SOFC group to the combustor of the PT plant previously reported in Fig. 3. However, in the actual plant the combustion chamber is always present (see Fig. 2) to allow the start up of the system, and transients management (Massardo et al. [2]). The HS plant design point is the operating condition where the turbine flow rate, rotational speed, pressure, and turbine inlet temperature are compatible with the limitations of this technology and the size of the turbine under consideration. When the PT is already defined (as in this case), the SOFC group is designed to be fed with the same air flow rate, operated at the PT pressure, and have an exhaust temperature equal to the turbine inlet pressure (TIT) of the PT.

The plant design and the size of all the components have been chosen both on the basis of data from the open literature on combined SOFC/MGT plants and taking into account the PT size of 5 kW. The design point data for the SOFC stack have been evaluated on the basis of the SOFC alone system performance (SOFC-STACK code), and taking into account that the size of the cell together with its efficiency are the most important decision parameters. The overall active area of the cell has been fixed at 15 m², which leads to a SOFC power of about 31 kW at the design point, using a fuel utilization factor of 0.85, and a current density of 3850 A/m².

The simulation model of the hybrid system has been obtained using a combination of the previously PT and SOFC models, generating the code named "HS" as described by Costamagna et al. [14].

Even if the best operating condition for the combined plant is slightly different from the design point chosen on the basis of the previous procedure, the main goal of this work is the study of the

behavior of the HS under off-design conditions, which would only be marginally affected by the choice of the design point.

Hybrid System Performance

The HS has been investigated both at design and off-design conditions. At off-design operation it has been investigated using both a PT fixed or variable speed control system.

Design Point Analysis. The already cited Figs. 3 and 5 show the data for the PT and for the HS at the design point condition. At full load the cell efficiency is about 48% (the cell temperature is 965°C, the air utilization factor is 0.3114), which is heavily affected by the low efficiency of the electronic system (due to its size, just over 30 kW). The corresponding HS design point efficiency is 56.3% with a turbine inlet temperature of about 900°C (this value matches the value required by the PT expander). The power of the fuel compressor has been considered to be part of the PT power, so that the PT power now is more reduced than the PT alone system (the fuel compressor power is obviously different for PT and HS solutions taking into account the large increase of the fuel mass flow rate passing from PT to HS conditions: $\dot{m}_{fPT} = 0.0005$ kg/s, $\dot{m}_{fHS} = 0.00128$ kg/s).

It is worthy to note that the HS efficiency at design point is very high mainly taking into account its size (36 kW), and it is in the same range as large size combined plants (>100 MW). Moreover, if the design data of the cell are modified it is possible to obtain an increase of the HS efficiency, but with a simultaneous increase of the SOFC active area and size (i.e., SOFC cost).

Another interesting data is the ratio between PT and SOFC power at design point. In this case the ratio is about 16%. This value is lower than previously investigated systems rated at higher power (200–500 kW) as discussed by the authors (Massardo et al. [2], Costamagna et al. [14,17]) due to the high impact of the fuel compressor power on small size HS, and to the reduction of the gas turbine performance correlated to the size of the turbomachinery, while the cell performances are less influenced by the size of the system.

Off-Design Analysis. As already stated the off-design results are presented in two parts: one using a fixed PT speed control system, and the second using a variable speed control system (variable frequency control).

(a) *Fixed PT Speed Control.* When a variable speed control system is not available, the only possible way to vary the power supplied by the plant (part load operation) in a system including a PT is to vary the overall fuel flow rate to be fed to the plant. Some simulations have been made, where the fuel flow rate has been changed by keeping the SOFC fuel utilization factor constant at 0.85 (and thus different fuel flow rates correspond to proportionally different electrical currents supplied by the SOFC stack). On the other hand, the air flow rate is an independent parameters, which is evaluated on the basis of matching of PT expander, the PT compressor, and the SOFC stack, thus the oxygen utilization is not constant throughout the simulations.

Figure 6 shows the efficiency of the hybrid system at part load conditions in the range from about 55% to full load. The SOFC group efficiency is also shown in the figure. We would like to point out that a direct comparison between the SOFC and HS efficiencies is not possible, since they are evaluated with slightly different procedures. In fact, the efficiency of the plant is calculated as the ratio between the net power produced and the LHV of the fuel, while the efficiency of the stack is the ratio between the power supplied by the stack alone and the LHV of the fuel supplied to the plant. Thus, the power consumption of the air and fuel compressors and the mechanical losses are not taken into account in the efficiency of the fuel cell group, while they are considered in evaluating the efficiency of the whole plant. To give an idea of the relative importance of all the contributions, at design point the fuel cell and the PT expander supply 31 and 17.3 kW, respec-

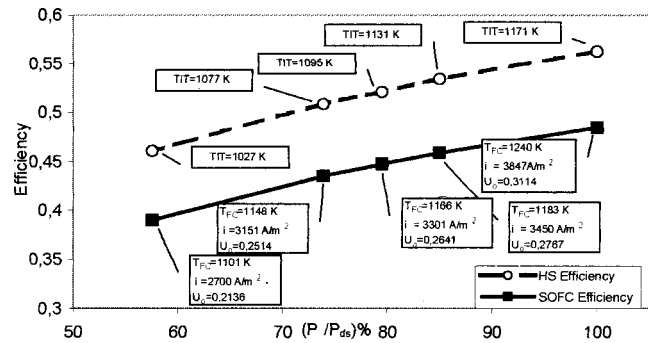


Fig. 6 Design and part-load performance of a hybrid system based on a solid oxide fuel cell reactor and a personal turbine (personal turbine-fixed speed control system)

tively, the air compressor consumes 9.7 kW, and the methane compressor, mechanical, electrical losses account for 2.6 kW. Thus, as the compressors serve the SOFC group as well as the PT expander, it would be realistic to subtract part of their power consumption from the power supplied by the SOFC group in evaluating the SOFC efficiency. In other words, the increase of efficiency due to the presence of the microturbine is not simply the difference between the overall plant and the SOFC group efficiencies (which would erroneously be calculated from Fig. 6 as about 9–10%). This aspect has been addressed also by Massardo and Lubelli [19].

The part load behavior of the SOFC group and the HS are very interesting, in fact with a reduction of 45% of the generated electrical power (from 100% to 55%) the cell efficiency reduction is about seven points, while the HS is about ten points. However, the HS efficiency is always higher than 45% (a very high value taking into account the size of the system—35 kW). Moreover, it is interesting to observe the reduction of the turbine inlet temperature value from the full to the part load conditions (from 898°C to 754°C), while the cell temperature reduces from 967°C to 828°C. This last value has been considered as the minimum temperature which allows good operation of the pre-reformer and of the stack. More details of this aspect are discussed by Costamagna et al. [14].

(b) *Variable PT Speed Control.* The typical operation mode of large-size gas turbine plants does not usually involve the possibility of changing the rotational speed of the turbine. The reason for this is that typical plants do not include an inverter, and thus the rotational speed of the turbine is chosen on the basis of the alternate frequency required by the end user/electrical network. On the contrary, an HS requires an inverter which converts the electrical current produced by both the fuel cell and the alternator, the latter one being rectified previously, to direct current. Thus, this configuration allows the operation of the turbine at variable rotational speed (variable frequency).

When the PT variable speed control is considered for the 36 kW hybrid system, the part-load operating zone can be increased without the need of air cell bypass (Fig. 7). Using this variable-speed solution the HS efficiency is always very high for a wide range of power values as shown in the cited figure. It is possible in fact to consider that the PT speed control could be used to maintain the maximum efficiency of the whole plant working where the HS efficiency values is higher than 54–55%, and where the cell works at conditions close to the design point data. If the power must be reduced more than 50% of the full load, the speed control system could be extended to very low speed. At the available minimum speed considered here the performance of the HS are similar to those shown at the full load speed (Fig. 6).

It is worthy to observe that taking into account the size of the system (36 kW) the efficiency is very high not only at the design

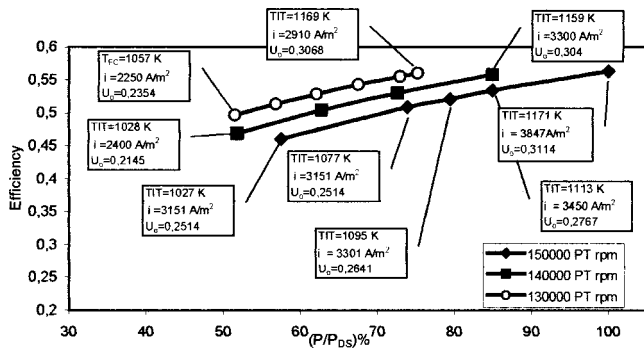


Fig. 7 Hybrid plant inefficiencies versus nondimensional power (personal turbine variable speed control system)

point but also at part-load conditions, where the system is expected to work in a distributed power market (the system could be often used at part load taking into account the load variation of the cost of the electricity from the grid, etc., with the time).

In order to investigate the performance of the different parts of the plant at part-load conditions in further detail, attention has been restricted to the SOFC group itself. The results are reported in Fig. 8 and show that at each fixed value of the turbine rotational speed the behavior of the SOFC group is very similar to that previously reported in Fig. 7 for the overall plant. The interesting feature reported in this figure is that the fuel cell efficiency increases by decreasing the turbine rotational speed, while the opposite is true for the overall plant. It is possible to give an explanation for this effect by considering the broken curve of Fig. 8, along which the efficiency increases by reducing the power. It can be noticed that along each broken line both the temperature and the oxygen utilization of the fuel cell remain fairly constant; this is due to the fact, when the SOFC module is integrated into the plant, there is an interesting effect of the recuperator module when the variable speed is utilized. In fact, in this case the load changes involve a reduction of the air flow rate correlated to the speed reduction, while for fixed speed control the load reduction is only due to the fuel mass flow rate variation (corresponding to a small air flow rate reduction (Costamagna et al. [14])). Therefore, under variable speed control conditions, at part load the recuperator effectiveness increases significantly with decreasing air flow, until a very low value is reached (below 10%), where thermal performance is degraded by longitudinal conduction in the heat exchanger, particularly for matrices of very high compactness (McDonald [20]). This behavior of the recuperator effectiveness allows the air temperature at the inlet of the stack (recuperator outlet) to increase at part load, and therefore the SOFC temperature remains fairly constant along the broken lines of Fig. 8. Since

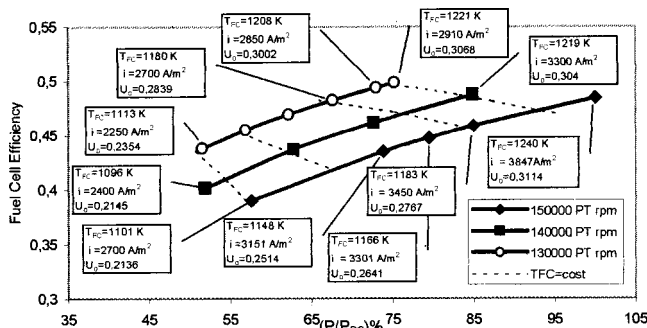


Fig. 8 Fuel cell efficiency versus nondimensional power in the hybrid system configuration (personal turbine speed control system)

both temperature and oxygen utilization factor remain constant along those curves, this explains the reason why they show an increase of fuel cell efficiency by decreasing the power.

The fact that in spite of the increased performance of the SOFC group under part load conditions, the overall plant shows a decreased performance under the same conditions is due to the fact that the efficiency of the fuel cell group alone does not take the power required by the compressor and the off design of the electrical part of the plant into account, as already mentioned. These effects, and also the effects related to the off-design of the PT group, the alternator, and the mechanical parts, explain the difference between SOFC and HS off-design performance.

Waste Heat Utilization

In the hybrid system the temperature of the gas leaving the recuperator is about 245°C (see Fig. 3). A waste heat module can be included to utilize this thermal energy after the power cycle. Depending on the end user, this could include the generation of low-grade steam, hot-water supply, chiller, hot-air supply for drying, and desalination.

Since the natural gas has been desulfurized before entering the fuel cell, there is no concern about sulfuric acid formation and corrosion in the exhaust system (as for combustion turbine), and the final discharge temperature can be reduced to a low value. If the discharge temperature to the atmosphere is 50°C, the available thermal energy in the exhaust would be about 15 kW. The overall fuel utilization efficiency of the hybrid plant is about 80%.

Downstream of the heat recovery module a flue gas condenser would be utilized. This would facilitate water recovery from the exhaust gas prior to discharge to the environment (Korakianitis et al. [21]). In some applications, this recovered water could have economic worth, particularly in arid regions.

Preliminary Evaluation of Energy Costs

There is a paucity of definitive cost data in the open literature for both microturbines and fuel cells. The range expected of the former is \$200–500/kW, and \$500–2000/kW for the latter. In light of this, establishing realistic capital and power generating costs for the hybrid plant is very difficult. Further, really meaningful costs for commercial units must come from industry, and even these are premature today since development programs are still in progress for both microturbines and SOFCs.

However, a preliminary economic investigation is carried out in this work just to compare the economic performance of PT and HS based on different capital and fuel cost scenarios. As a parameter for the comparison the cost of electricity is considered, taking into account the difficulty to evaluate the cost of the heat, and the fact that both the systems produce useful heat for cogeneration applications.

For microturbines, several capital cost data have been published in the open literature, however, they are very difficult to be used with confidence for an economic investigation of PT; for SOFC stacks this aspect is more difficult taking into account the paucity of data. The authors (Massardo and Magistri [10]) presented a thermo-economic analysis of large-size SOFC-GT combined cycles but the thermo-economic analysis cannot be used in this work since cost or costing equations necessary for thermo-economic analysis (Massardo et al. [18] and Agazzani and Massardo [22]) do not exist for PT at the moment.

To carry out the economic comparison between the PT and HS two different scenarios have been considered for fuel and capital costs. PT capital cost is assumed to be in the range 200–500 \$/kW, while the SOFC cost in the range 500–1000 \$/kW. The low-level scenario is optimistic, particularly for SOFC, but it can be considered as the lower bound of future SOFC and hybrid system costs. Taking into account the size of the PT and SOFC stack of the HS investigated here the capital cost of the HS is for the two scenarios about \$17,000 and \$33,000, respectively. While the PT cost is \$1250 and \$2500, respectively. Two fuel costs have

been considered (this aspect is very difficult to be fixed taking into account the different costs in U.S., Japan, and Europe and also the distributed power applications) 12 c\$/Nm³ and 25 c\$/Nm³, respectively. The life of the plant has been considered ten years, while the discount rate has been fixed at 0.08. Moreover, to take into account that during the year the PT and HS plants do not work always at full load, we use a simplified solution considering a full load operation for 70% of the time (6180 hours over 8760), as discussed by Dodero [23] for molten carbonate fuel cell–microgas turbine hybrid systems.

With the previous assumptions the annualized capital costs have been evaluated, and the following results for the electricity costs have been obtained.

- Scenario 1—High capital and fuel costs (PT 500 \$/kW; SOFC 1000 \$/kW; fuel 25 c\$/Nm³). The cost of the electricity is about 13 c\$/kWh for PT, a high value compared to the actual cost of the electricity from the grid (even if in Europe the cost of electricity for civil applications—houses—is sometimes higher). For HS the electricity cost is 6.15 c\$/kWh. The electricity cost ratio between HS and PT is 0.47.

- Scenario 2—High capital and low fuel costs (PT 500 \$/kW; SOFC 1000 \$/kW; fuel 12 c\$/Nm³). In this case the cost of the electricity is about 12.57 c\$/kWh for PT system, and 5.30 c\$/kWh for the HS solution. The electricity cost ratio is 0.42.

- Scenario 3—Low capital and high fuel costs (PT 200 \$/kW; SOFC 500 \$/kW; fuel 25 c\$/Nm³). The influence of the capital cost is more evident in this case where the PT electricity cost is about 7.35 c\$/kWh, while the HS cost is about 3.91 c\$/kWh. The electricity cost ratio is 0.53.

- Scenario 4—Low capital and fuel costs (PT 200 \$/kW; SOFC 500 \$/kW; fuel 12 c\$/Nm³). In this case the simultaneous effect of low fuel and capital cost effect is evident: PT electricity cost is 6.90 c\$/kWh, while HS cost is 3.07 c\$/kWh. The electricity cost ratio is 0.44.

The reduction of the electricity cost when only the capital costs reduce (scenario 2 versus scenario 4) is 55% for PT and 58% for HS, respectively. The influence of fuel cost is less evident if scenarios 3 and 4 are considered. In this case the reduction ratio is 94% for PT and 78.5% for HS. This confirms the importance of capital cost reduction and the influence of the microturbine to stack power ratio as discussed by Massardo and Magistri [10].

The low electricity cost of the HS solution is evident in all the cases investigated here; however, it is important to remember that the size of the two plants are different (5 and 36 kW). A more correct comparison should be carried out between the HS and a MGT rated at about 35 kW. In fact in this case the conversion efficiency of the MGT is higher than PT (about 28–29% against 21–22%) and the annual fuel cost is greatly reduced. It is worthwhile to note that the PT energy costs are very interesting when the size of the power plant is carefully taken into account.

Conclusions

In this paper a small size hybrid system (HS)—an interesting high efficiency and no pollution solution for the distributed energy market—based on the coupling of a recuperated very small size micro gas turbine, named personal turbine (PT), with a high-temperature solid oxide fuel cell (SOFC) stack have been presented and discussed.

The PT, the SOFC reactor, and the HS design and off-design models have been presented and discussed in depth.

The coupling of the PT (5 kW) with a SOFC reactor (31 kW) has shown a potential for an efficiency of over 56% at design point.

The HS off-design performance, analyzed here for two different PT rotational speed control systems: (i) fixed and (ii) variable, are very interesting. When a fixed PT rotational speed control system is utilized the performance are always high, taking into account the plant size, and only limited by the minimum TIT and SOFC

temperature values (based on the constraints assumed here). With a variable PT rotational speed control it is possible to obtain very high efficiency also at very low part load conditions. The efficiency is always higher than 50%, also at less than 50% of the design point power.

Some interesting considerations on the SOFC off-design performance have been presented and discussed observing and analyzing the increase of efficiency of the stack at part load conditions where the cell performance in the HS configuration is mainly dominated by the fuel and air flow rate, i.e., the air utilization coefficient (since the fuel utilization coefficient is considered constant). It is important to note that at part load the air mass flow rate is dependent on the matching between the compressor and the expander, obviously taking into account the behavior of the regenerator effectiveness and stack and regenerator pressure losses at part load conditions.

The results of a preliminary economic analysis, based on four different capital-fuel cost scenarios, have shown the better performance of the HS versus PT due mainly to the very high efficiency of HS compared to PT value (56% versus 22%). The influence of the capital cost has also been pointed out, while for very low SOFC capital cost the cost of electricity is particularly reduced taking also into account the size of the plant (36 kW). This aspect needs more work and more information from the companies involved in the HS development.

Moreover, it is very interesting to remember that due to its very high efficiency the HS shows very low CO₂ emissions (no NO_x emissions) and using an appropriate taxation for this pollutant, Carbon Tax or Carbon Exergy Tax as suggested by the authors [24], the superiority of HS versus traditional power systems in the small size range (less than 1 MW) will be more evident.

Acknowledgments

This work has been sponsored by University of Genoa, by the Ministry of University and Research of Italy, Grant “Cofinanziamento 1999.”

Nomenclature

HS = hybrid system
 P = electrical power
 P_{DS} = electrical power at design point condition
 PT = personal turbine

References

- [1] Rodgers, C., 2000, “25–5 kW Microturbine Design Aspects,” ASME Paper 00-GT-626.
- [2] Massardo, A. F., McDonald, C., and Korakianitis, T., 2000, “Microturbine/Fuel Cell Coupling for High Efficiency Electrical—Power Generation,” ASME J. Eng. Gas Turbine Power, **124**, pp. 110–116.
- [3] Wilson, D. G., and Korakianitis, T., 1997, *The Design of High Efficiency Turbomachinery and Gas Turbines*, Prentice-Hall, Englewood Cliffs, NJ.
- [4] McDonald, C., and Rodgers, C., 2001, “The Ubiquitous Personal Turbine (PT): A Power Vision for the 21st Century,” ASME Paper 01-GT-100.
- [5] Hirschenhofer, J. H., Stauffer, D. B., Engleman, R. R., and Klett, M. G., 1998, *Fuel Cell Handbook*, DOE report DOE/FETC-99/1076, U.S. Dept. of Energy, Morgantown, WV.
- [6] Wolk, R. H., 1999, *IEEE Spectrum*, pp. 36–45.
- [7] Veyo, S. E., and Forbes, C. A., 1998 *Proc. 3rd European SOFC Forum*, European Fuel Cell Forum Ed., Nantes, June, p. 79.
- [8] George, R. A. 1999, “Status of Tubular SOFC Field Unit Demonstrations,” *J. Power Sources*, **86**, pp. 134–139.
- [9] Bruch, C., 2000, “Future SOFC/GT demonstration project in Essen,” IEA Topical Meeting, Ystad (S), Sept. 2000.
- [10] Massardo, A. F., and Magistri, L., 2001 “Internal Reforming Solid Oxide Fuel Cell-Gas Turbine Combined Cycles. Part B,” ASME Paper 2001-GT-0380.
- [11] Magistri, L., 1999, “Microturbine a gas e Celle a Combustibile ad Ossidi Solidi per la generazione elettrica distribuita,” degree thesis, University of Genoa.
- [12] Pilidis, P., 1983, “Digital Simulation of Gas Turbine Performance,” Ph. D. thesis, University of Glasgow.
- [13] Campanari, S., 1998, “Impianti di potenza basati su Celle a Combustibile ad Ossidi Solidi integrate con Cicli di Turbina a Gas,” Ph. D. thesis, Politecnico of Milan.

- [14] Costamagna, P., Magistri, L., and Massardo, A. F., 2001, "Design and Part-Load Performance of a Hybrid System Based on a Solid Oxide Fuel Cell Reactor and a Micro-Gas Turbine," *J. Power Sources*, **96**, pp. 352–368.
- [15] Costamagna, P., Arato, E., Antonucci, P. L., and Antonucci, V., 1996, "Partial Oxidation of CH₄ in Solid Oxide Fuel Cells: Simulation Model of the Electrochemical Reactor and Experimental Validation," *Chem. Eng. Sci.*, **51**(11), pp. 3013–3018.
- [16] Costamagna, P., and Honnegger, K. 1998, "Modeling of Solid Oxide Heat Exchanger Integrated Stacks and Simulation at High Fuel Utilization," *J. Electrochem. Soc.*, **145**(11), pp. 3995–4007.
- [17] Costamagna, P., Massardo, A. F., and Bedont, P., 2000, "Techno-Economical Analysis of SOFC Reactor—Gas Turbine Combined Plants," 4th European SOFC Forum, Luzern (CH), July.
- [18] Massardo, A. F., Costamagna, P., and Magistri, L. 2000, "Techno Economical Analysis of SOFC Reactor Gas Turbine Combined Plants," IEA Topical Meeting, Ystad, Sept.
- [19] Massardo, A. F., and Lubelli, F. 2000, "Internal Reforming Solid Oxide Fuel Cell-Gas Turbine Combined Cycles: Part A," *ASME J. Eng. Gas Turbines Power*, **122**, pp. 1–27.
- [20] McDonald, C., 1975, "Recuperator Development Trends for Future High Temperature Gas Turbine," ASME Paper 75-GT-050.
- [21] Korakianitis, T., Grantstrom, J., Wassingbo, P., and Massardo, A. F., 1997, "Parametric Performance of Combined Cogeneration Power Plants With Various Power and Efficiency Enhancements," ASME Paper 97-GT-286.
- [22] Agazzani, A., and Massardo, A. F. 1997, "A Tool for Thermoeconomic Analysis and Optimization of Gas, Steam, and Combined Plants," *ASME J. Eng. Gas Turbines Power*, **119**, pp. 885–892.
- [23] Doderò, C., 2000, "Sistema Ibrido Cella a Combustibile a Carbonati Fusi (MCFC) e Microturbina a Gas (MGT) per la generazione elettrica di piccola potenza," degree thesis, University of Genoa.
- [24] Massardo, A. F., Santarelli, M., and Borchellini, R., 2000, "Carbon Exergy Tax (CET): Impact on Conventional Energy Systems Design and Its Contribution to Advanced Systems Utilisation," ECOS 2000, Twentee, The Netherlands, July.

Efficiency Upgrading of an Ambient Pressure Molten Carbonate Fuel Cell Plant Through the Introduction of an Indirect Heated Gas Turbine

P. Lunghi

e-mail: lunghi@unipg.it

S. Ubertini

Dipartimento di Ingegneria Industriale,
Università di Perugia
Via G. Duranti 1A/4,
06125 Perugia, Italy

The efficient and environmentally friendly production of electricity is undoubtedly one of the 21st century priorities. Since renewable sources will be able to guarantee only a share of the future demand, the present research activity must focus on innovative energy devices and improved conversion systems and cycles. Great expectations are reserved to fuel cell systems. The direct conversion from chemical to electrical energy eliminates environmental problems connected with combustion and bypasses the stringent efficiency limit due to Carnot's principle. Still in infancy, high-temperature fuel cells present the further advantage of feasible cycle integration with steam or gas turbines. In this paper, a molten carbonate fuel cell plant is simulated in a cycle for power generation. The introduction of an external combustion gas turbine is evaluated with the aim of efficiency and net power output increase. The results show that the proposed cycle can be conveniently used as a source of power generation. As compared to internal combustion gas turbine hybrid cycles found in the literature the plant is characterized by fuel cell greater simplicity, due to the absence of pressurization, and gas turbine increased complexity, due to the presence of the heat exchange system. [DOI: 10.1115/1.1492839]

Introduction

Fuel cell technology is considered an important element in meeting future distributed electricity generation market needs. Robust progress has been made in the last decade and phosphoric acid fuel cells have entered the marketplace with several units with more than 40,000 hours of operation. Polymer electric fuel cells (PEM), solid oxide fuel cells (SOFC), and molten carbonate fuel cells (MCFC) are now being tested at a commercial size in pilot power plants in Europe and the USA ([1,2]). MCFC full-scale power plants tests are needed to achieve 100% successful commercial-scale demonstration, which is foreseen in less than ten years ([3,4]). Open access and competition are expected to increase the opportunities for fuel cell technology within the coming decade, as the deregulation evolves in the USA and European markets.

High-temperature fuel cells, such as SOFC and MCFC, are especially attractive since, making high-temperature heat available at the exhaust, can be efficiently used in cogeneration applications or for hybrid cycle purposes. Hybrid systems have been extensively analyzed in the past five years by the DOE and similar institutions in Europe, in combination with industry. This combination is potentially superior to other power generation technologies, revealing remarkably high efficiency with an inherent low level of pollutant emissions. Moreover, it is largely believed that combining traditional cycles with fuel cells can accelerate the market introduction of the latter. In large fuel cell systems, a steam bottoming cycle can be conveniently combined. Lobachov et al. [5] predicted a 70% overall thermal efficiency for a hybrid fuel cell/steam cycle power plant for an existing intermediate scale MCFC (2.5 MW). The integration of a gas turbine is a natu-

ral evolution in a pressurized high-temperature fuel cell system, using the gas turbine compressor as the air mover and evolving the cell exhaust in the gas turbine. The first fuel cell/gas turbine hybrid system demonstration is a 250kW unit that utilizes a Siemens Westinghouse SOFC and a NERC gas turbine ([6]). A team led by MC power is studying the technical and economic feasibility of a 20 MW natural gas fueled MCFC bottomed by a gas turbine [6]. Rolls Royce has joined fuel cell manufacturers to develop pressurized fuel cell plants to be combined with gas turbines ([2]). The primary objective is to demonstrate successful operation at higher efficiencies than the traditional power plants. Randall et al. [7] describe some generic SOFC and MCFC systems combined with gas turbines. A preliminary analysis of a representative state-of-the-art 50kW microturbine coupled with a SOFC with an overall efficiency close to 60% is presented by Massardo et al. [8].

In a previous paper [9] the possible introduction of external heated closed gas turbine bottoming cycles has been investigated and the peculiarities of plants using different working fluids have been analyzed. Only Fuel Cell Energy Inc. seems to be currently working on a high efficiency MCFC/gas turbine hybrid system retaining the ambient pressure of the fuel cell ([10]). They estimate, for long-term fuel cell technology advances, an overall efficiency of the hybrid system of 74%.

In this paper an air gas turbine open cycle has been coupled with an ambient pressure 15 MW MCFC system, where the GT required thermal energy is extracted by heat exchange from the fuel cell exhaust. Performances of the plant have been evaluated in function of different parameters in order to identify optimal solutions. A second set of simulations has been focused on the introduction of steam in the GT working fluid. The steam is produced using the heat content of the gas turbine exhaust and mixed to the air stream at the exit of the GT cycle compressor. The performances of the system revealed to be improved both in terms of efficiency and reduction of plant size.

Contributed by the International Gas Turbine Institute (IGTI) of THE AMERICAN SOCIETY OF MECHANICAL ENGINEERS for publication in the ASME JOURNAL OF ENGINEERING FOR GAS TURBINES AND POWER. Paper presented at the International Gas Turbine and Aeroengine Congress and Exhibition, New Orleans, La., June 4–7, 2001; Paper 01-GT-381. Manuscript received by IGTI, December 2000; final revision, March 2001. Associate Editor: R. Natole.

Molten Carbonate Fuel Cell (MCFC) Plant Analysis

The configuration of the MCFC system is illustrated in Fig. 1. The process involves treating the natural gas to remove impurities, after which it is mixed with steam and sent to the fuel cell stack. An internal reforming solution for fuel/steam mixture has been chosen, eliminating the need for an external fuel processor. The endothermic oxidative reaction within the cell produces the heat necessary to the fuel reforming, while a supported catalyst (Ni supported on LiAlO_2) provides sufficient catalytic activity to sustain the steam reforming reaction at 923 K. The concept of internal reforming has been successfully demonstrated for 10,000 hours lifetime in MCFC system ([11]). The mixture fuel/steam enters the stack at 623 K. All the reactions in the cell take place at 923 K representing the state-of-the-art best compromise for reaction kinetics, voltage cell loss, and high-temperature corrosion problems.

The anode exhaust at 973 K is sent to a catalytic combustor ([12]) where the unoxidized part is burnt with the oxygen present in the air blown inside by an electric fan. The combustor inlet air quantity has been chosen in order to present an oxygen excess of 20% above the quantity necessary for the combustion plus the quantity required by the cathode. The combusted gas exits the burner at about 943 K and it is used as the oxidant for the cathode side of the cell.

The demonstration plant shown in Fig. 1 is the result of an optimization of the exploitation of the thermal streams presented by the authors in a previous paper ([13]), where detailed description of the simulation model developed by the authors with the Aspen Plus thermodynamic flow sheet code is also presented.

The heat content of the stream 1 is used to preheat the fuel before entering the anode with a minimum pinch temperature of 76 K. Steam is generated and superheated by means of the exhaust stream 2 with a minimum pinch temperature of 23 K. At full load operation the fuel enters the cell at 681 K and the steam at 824 K, thus maintaining the conditions for the fuel cell process requirements. The remaining exhaust gases (stream 3 in Fig. 1) preheat the air flow at the combustor inlet. The heat exchange occurs with a minimum pinch temperature of 76 K and the air enters the combustor at 753 K. As a result the temperature of the burner effluent is increased to 1146 K.

Before entering the cathode the hot effluent provides heat that can be used for cogeneration purpose or for a bottoming cycle.

The system has been designed considering 2.9% heat losses in the cell, 2% heat losses in the fuel and air preheaters, and 3% heat losses in the steam generator and superheater.

It should be noticed that changing the ambient conditions, the inlet flow rate and the heat losses the process operating conditions

could change. In order to maintain the inlet and outlet conditions to the fuel cell, the plant features three sensor probes that measure the temperatures of the steam and fuel streams at the cell inlet and the temperature of the air flow entering the catalytic combustor. The temperatures measured are communicated to a feedback system that controls the four-way valve (Fig. 1). The temperature gap for the fuel and the steam is fixed for the fuel cell internal reformer process requirements, while the air preheating can be changed, since the only consequence is the combustor outlet temperature.

The Nernst equation ([14]) predicts, for a MCFC operating at this temperature, a theoretical voltage of 1030 mV. Actual cells operate at voltages ranging between 750 and 900 mV. Among the various parameters that influence cell voltage are the stream pressures, the stream compositions, i.e., the partial pressures of the single reactants, and the voltage losses due to activation polarization, ohmic polarization and concentration polarization. Since cell performance degrades in time, (Ito et al. [4] proposed a line with negative slope in efficiency vs. log of time diagram) a working condition must be chosen for the evaluations. In this work, the beginning of life has been considered.

A global fuel utilization ($U_f = \text{H}_{2,\text{consumed}} / \text{H}_{2,\text{in}} + \text{CO}_{\text{in}}$) of 0.8 has been assumed.

The fuel utilization factor has a major impact on the theoretical voltage, which is related to the streams partial pressures according to the following equation:

$$E = E^0 + \frac{RT}{2F} \ln \frac{P_{\text{H}_2} \cdot P_{\text{O}_2}^{1/2}}{P_{\text{H}_2\text{O}}} + \ln \frac{P_{\text{CO}_2, \text{cathode}}}{P_{\text{CO}_2, \text{anode}}} \quad (1)$$

Assuming the same pressure for the anode and the cathode,

$$E = E^0 + \frac{RT}{2F} \ln \frac{X_{\text{H}_2} \cdot X_{\text{O}_2}^{1/2} \cdot X_{\text{CO}_2, \text{cathode}} \cdot P^{1/2}}{X_{\text{H}_2\text{O}, \text{anode}} \cdot X_{\text{CO}_2, \text{anode}}} \quad (2)$$

A high utilization factor brings to low molar fraction of the hydrogen and high molar fraction of water and carbon dioxide at anode outlet and to low molar fraction of the oxygen and carbon dioxide at cathode outlet ([14]). A high utilization factor thus brings to a voltage decrease; to understand this, it is necessary to consider the high conductivity of the cell electrodes that implies the equipotentiality of its surfaces; the potential becomes that of the most unfavored spot (i.e., the stream outlet).

To compensate for this, a quite low current density of 152 mA/cm² has been chosen resulting in a voltage of 820 mV. As compared to the system analyzed by Braun et al. [12], characterized by an average cell voltage of 760 mV, a current density of

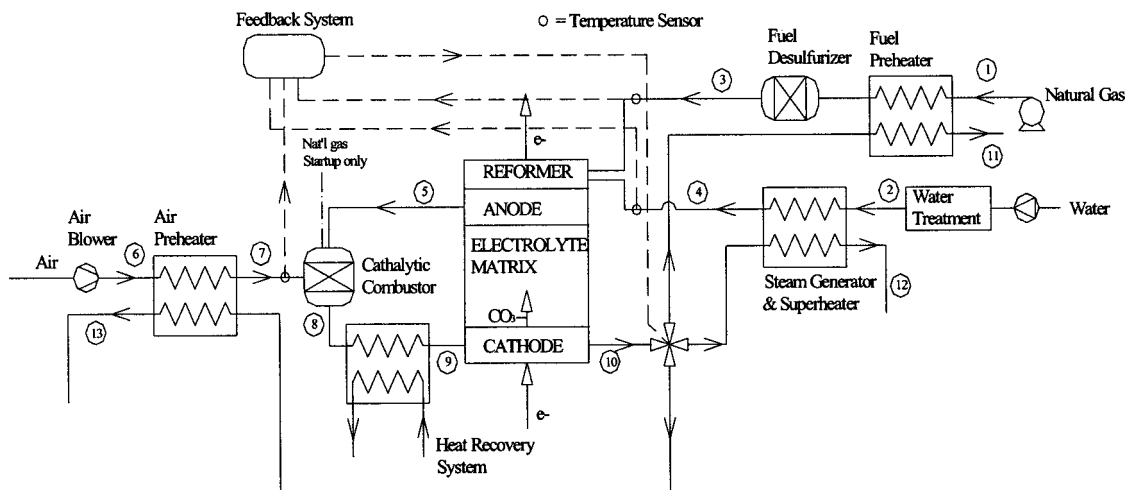


Fig. 1 Molten carbonate fuel cell (MCFC)

Table 1 Molten carbonate fuel cell (MCFC) plant operational parameters

Stack nominal power	16 MW
Stack temperature	650°C
Auxiliary absorption	700 kW
Stack heat losses	2.9% LHV
Combustor heat losses	1.8%
Heat exchangers losses	2%
DC-AC converter efficiency	98%
O ₂ excess in cathode	20%
Fuel utilization factor	0.80
Current density (mA/cm ²)	152
Cell voltage (mV)	820
Net power output (MWe)	14.8
Heat available (MWt)	5.55
First-law efficiency (% LHV)	0.82
Electrical efficiency (% LHV)	0.59
Second-law efficiency (% LHV)	0.75

215 mA/cm² and a fuel utilization factor of 78.5 percent, higher efficiency has been achieved at the expense of a lower power density. This results in decreased energy production costs and higher investment costs.

It must be observed that the ratio of the voltage rise to the current density rise is in very good agreement with the experimental law ([14]):

$$\frac{\Delta V}{\Delta A} = -1.21 \text{ mV/mA.} \quad (3)$$

Equilibrium reactions and thermal exchanges are simulated through the Grayson model, comprising the Redlich-Kwong equation of state for vapor state ([15]) and the Lee-Kesler equation of state for liquid and vapor enthalpy. Steam parameters have been calculated through NBS/NBC steam tables ([16]). All the calculations were performed with Aspen+ software ([17]). The main assumption and data used for the calculation of the system performance were selected with the objective of industrial realism.

The gross power output of the fuel cell plant is 15.8 MW and the power input of the fuel is 25 MW.

The heat required by the internal reforming process is entirely provided by the heat produced by the cell itself with a consequent heat loss of the cell of about 2.9%. Considering that the auxiliary power requirement is about 750 kW and 2% of the electric power is lost in the DC to AC conversion the net power output of the plant is 14.8 MW at beginning of life (Table 1).

The resulting electric efficiency, calculated as the ratio of the net electric power output to the product of the fuel mass flow rate and the fuel lower heating value (LHV), is 59%. This high efficiency, compared with traditional power plants, is due to the high electric efficiency of the cell itself. 5.55 MWt are available between 1146 K and 903 K in the heat recovery system, where the gas turbine bottoming cycle has been introduced. The first law efficiency is 81 percent, considering the recovery of 98 percent of the available heat between the catalytic combustor and the cathode inlet. This is not impressive if compared with conventional cogeneration system. The novelty aspect consists of the high electric production and the high temperature of the recoverable heat, allowing the use of a high efficiency bottoming cycle. The exergy gain obtained with this system is clearly detectable by the second law efficiency. If we consider the energy content of the output heat we obtain 75% exergetic efficiency. Even if the second-law efficiency is only a reference value for the possible electric production, since it does not take into account possible exergy dissipations in the bottoming cycle, it shows the potential of this kind of heat regeneration. Using the high-temperature stack gas for combustion air preheating, contributes to reducing exergy destruction in the catalytic burner and in the boiler and fuel-preheating units. The whole unused heat has been transferred at 1146 K in the burner effluent spreading the way to its exploitation. The system performance parameters are summarized in Table 1.

Molten Carbonate Fuel Cell/Gas Turbine (MCFC/GT) Plant Analysis

The very high electrical efficiency of the MCFC plant can be further improved through the introduction of a bottoming cycle. The high exergetic value of the MCFC waste heat opens the way to a sensible work production which theoretical maximum value,

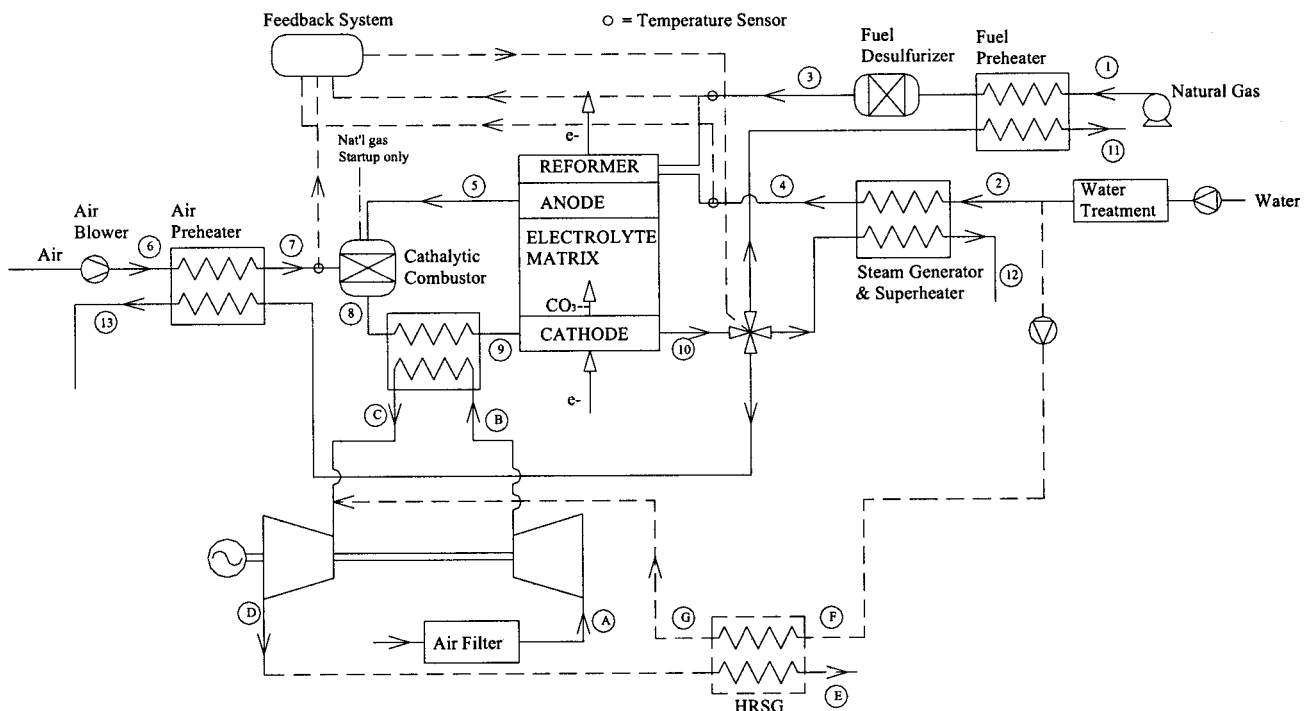


Fig. 2 Demonstration power plant diagram

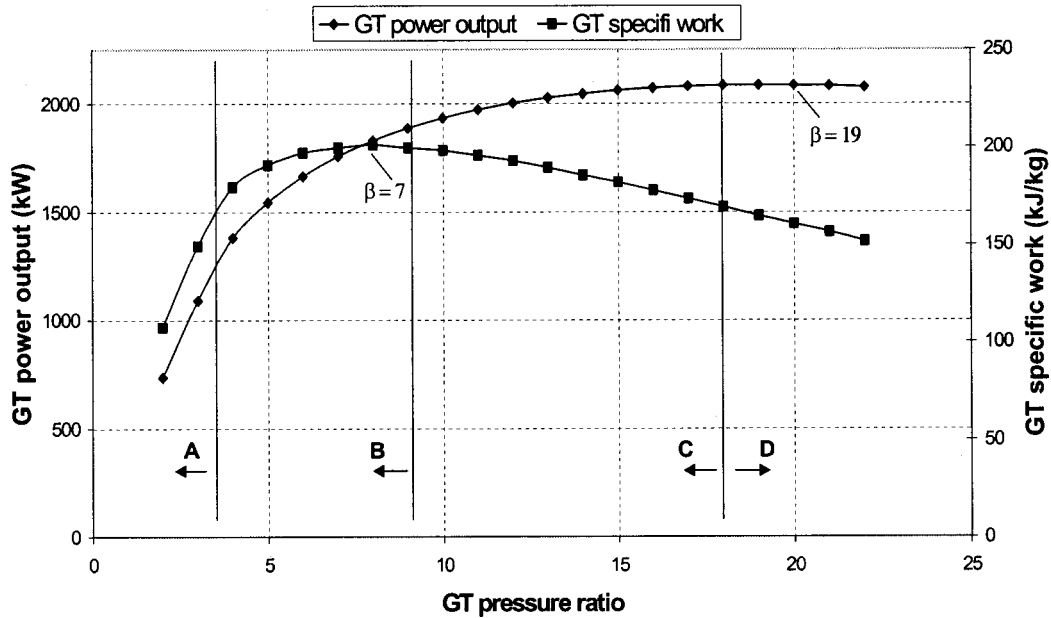


Fig. 3 Gas turbine (GT) power output and specific work

as a fraction of the “chemical power” introduced with the fuel, is expressed by the difference between the plant second law efficiency and the electrical efficiency. Given the relatively small dimension of the fuel cell plant, it does not seem advisable to introduce a steam turbine bottoming cycle. The chosen solution has been an indirect heated gas turbine.

The bottoming section features a compressor, a turbine and a heat exchanger: the fuel cell waste heat recuperator. The authors decided to focus on an indirect heated gas turbine, where the required thermal energy is extracted by heat exchange from the fuel cell exhaust. Most of the hybrid fuel cell/gas turbine systems proposed involve the pressurization of the fuel cell up to the pressure ratio desired for the turbine. Even if pressurization offers a power increase at a given level of stack efficiency, its pressurized reformer requires higher steam to carbon ratio to suppress carbon formation, thus causing a significant complication. Moreover, the high cost of vessels and piping to contain pressure at the high fuel cell operating temperatures, has a significant impact on the cost of energy.

The internal reforming, inhibited at higher operating pressures, can be carried out in the ambient pressure fuel cell at low steam-to-carbon ratio. This provides the anode with a more concentrated fuel stream, thus improving the performance of the anode itself. Another aspect in favor of atmospheric pressure fuel cells is that the life of the stack is longer, since some degradation phenomena increase with pressure rise and the cost is lower due to standardization.

The selected plant layout is presented in Fig. 2 (dotted components should not be considered). The heat available from the MCFC stream at the exit of the catalytic combustor is recovered for the heating of air at the exit of the GT cycle compressor. The indirect transfer of heat allows the turbine pressure ratio to be independent from the fuel cell operational parameters. As a consequence, it was possible to conduct the analysis for a range of GT pressure ratio from 2 to 22. The heat recovery occurs on the basis of a fixed approach point temperature, following the assumption of a consequent dimensioning of the heat exchanger surfaces. The approach point temperature difference, representing a compromise

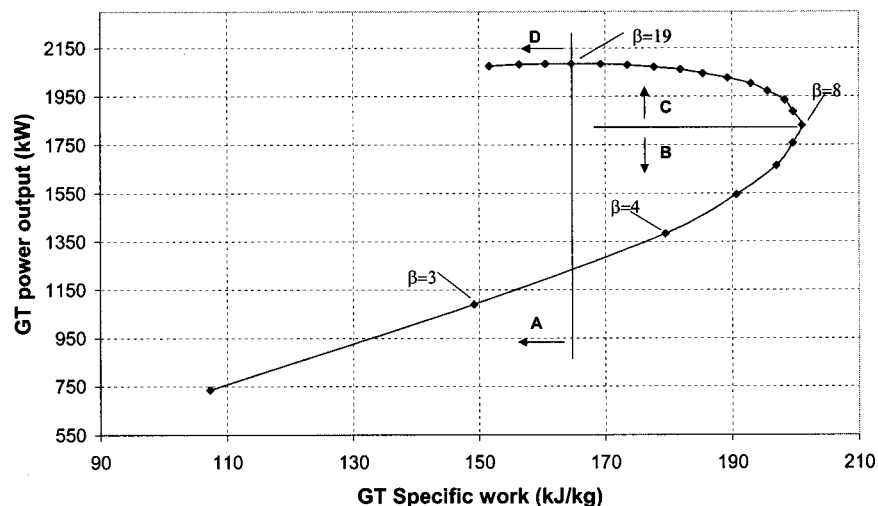


Fig. 4 Gas turbine (GT) power output versus specific work

Table 2 Optimized molten carbonate fuel cell/gas turbine (MCFC-GT) plant parameters

Optimized Plant Parameters	
GT air mass flow rate (kg/s)	10.7
GT pressure ratio β	13
GT power output (MWe)	2.025
Total net power output (MWe)	16.8
GT/MCFC power ratio (%)	13.7
Electrical efficiency (% LHV)	67.2

between low exergetic losses and affordable exchanger surfaces, has been fixed at 60 K. Any change in the MCFC inlet streams temperatures must be avoided to maintain the conditions for the fuel cell process requirements and this is ensured by a feedback regulating system (Fig. 2).

The isentropic efficiency of the gas turbine has been fixed at 0.92 and an isentropic efficiency of 0.9 was considered for the gas compressor. The mechanical into electrical energy conversion results in a 1.5% loss.

Since the different gas turbine configurations do not affect the fuel cell system, the various bottoming cycles have the peculiarity of a constant received heat power (under the hypothesis of a constant heat exchanger efficiency). Under this condition there is a direct proportionality between the net power output of the bottoming cycle and its first law efficiency. In Fig. 3, the trends of the GT power output and the GT specific work have been reported. The power output shows its maximum for a pressure ratio of 19, while the specific work trend is decreasing starting from a pressure ratio value of 8. This means that even if the increase in the pressure ratio has a beneficial effect on the system performances until a value of 19 is reached, this is obtained with a plant overdimensioning; in particular the decrease in the specific work shows that,

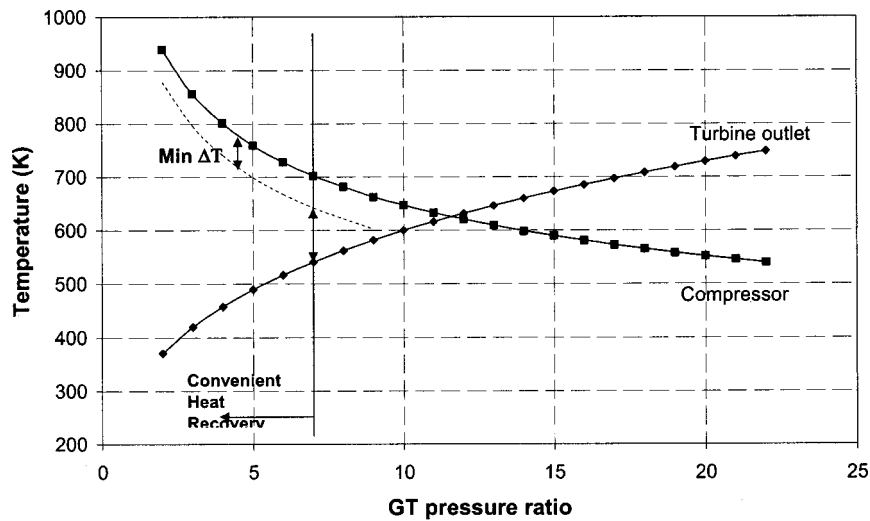


Fig. 5 Internal regeneration as a function of β

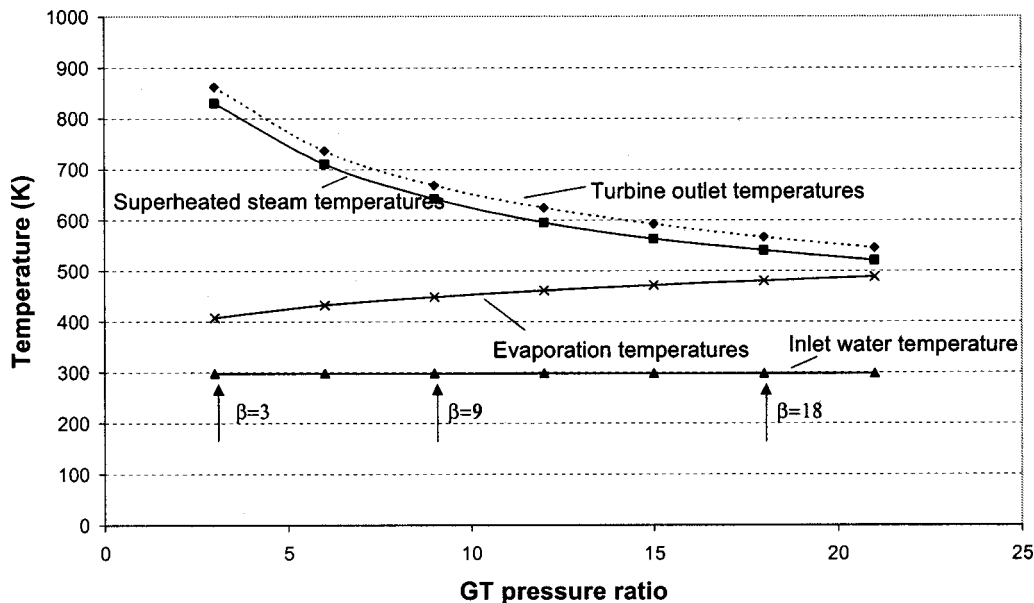


Fig. 6 Steam generation as a function of β

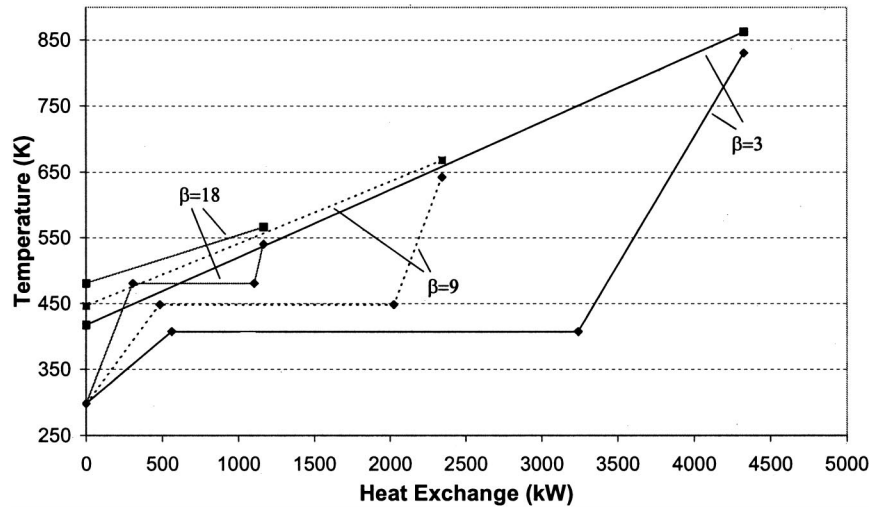


Fig. 7 Steam generation

in that pressure ratio range, an increase in power output can only be obtained with a more than proportional increase in flow rates.

Figure 4 shows that the trend of GT power output as a function of GT specific work can help in analyzing and determining the best solution. The graph has been divided in four zones. Zones A, B, and D comprise solutions that do not represent neither technical nor economical optimum values. The plant configurations that insist in Zone A, in fact, show both power outputs and specific works that are inferior to those in Zone C. The solutions that are comprised in Zone B presents specific works in the range of those in Zone C with inferior power outputs. Zone D is finally characterized by power outputs in the range of those in Zone C but presenting smaller specific works. The optimal solution must, therefore, be chosen in Zone C. The best choice is dependent on the relative weight of plant investment and fuel costs. The points in the proximity of Zone D are favored by high fuel costs and low specific investment costs since they guarantee higher power production at the expenses of bigger plants. Vice versa the points in the proximity of Zone B present lower energy yields but smaller plants. Any attempt of obtaining an exact solution in a moment in which fuel cell systems costs are very high and very rapidly decreasing would be at least presumptuous. All that can be observed is that moving towards Zone D from Zone C there is, in the last

segment, little power output increase and large specific work decrease. This suggests an optimal value of about 13 for the GT plant pressure ratio. As shown in Table 2, the optimized fuel cell/gas turbine hybrid system produces 16.8 MWe with an electrical efficiency of 67%.

With the aim of further improving the electrical efficiency, several heat recovery options have been analyzed. Simple heat regeneration from the gas turbine exhaust gases is not feasible as shown in Fig. 5.

As can be easily seen, even with an ideal heat recovery system, this kind of heat recovery is not possible for pressure range over 12. If we consider that a certain temperature difference is needed between the hot and the cold streams to have reasonable exchange surface areas, this value falls below 10. Moreover, since it is worth performing a heat recovery system only if a sensible temperature increase is feasible, it can be said that, in the present situation, no heat recovery is convenient for β over 7. A much more promising way of heat regeneration consists of using the exhaust gas heat content for steam generation in a sort of indirect heated STIG (steam injected gas turbine, copyright by General Electric, [18]).

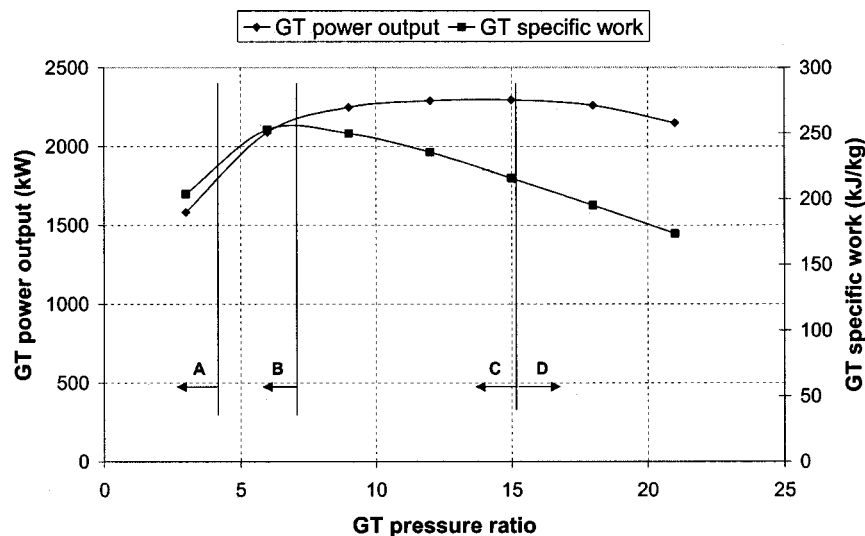


Fig. 8 Steam injected gas turbine (STIG) power output and specific work

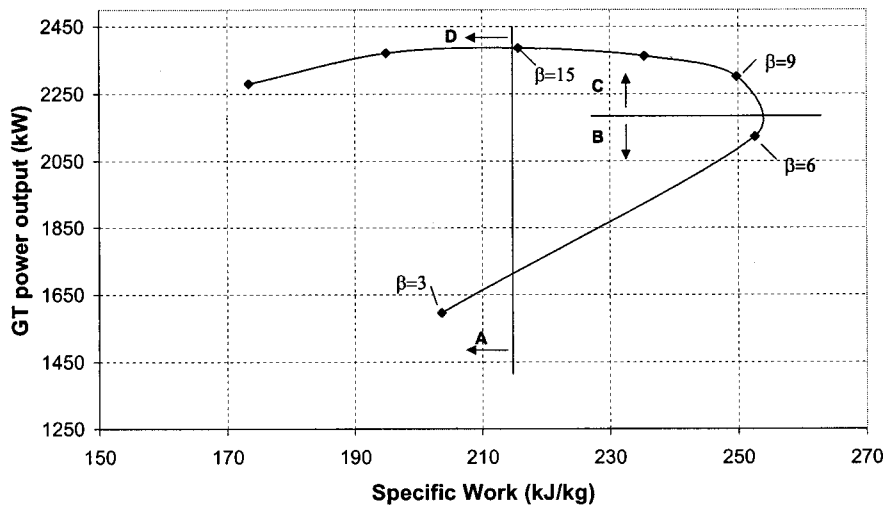


Fig. 9 Steam injected gas turbine (STIG) power output versus specific work

Steam Injected Gas Turbine (STIG) Cycle Analysis

The stream in the gas turbine is a mixture of compressed air and steam, produced in a heat recovery steam generator as shown in Fig. 2. The steam is produced at a pressure 1.3 times higher than the maximum pressure of the cycle, in order to allow the steam injection before the gas turbine. The steam injected must be demineralized to eliminate components that could damage the turbine blades: GE specifies a solid content inferior to 200 ppb ([18]). The heat needed for steam generation is recovered from gas turbine exhaust gases and the reduction of their temperature produces an efficiency rise, even if it must be outlined that a great part of the heat recovered is lost as latent heat, since at the turbine exhaust water is still vaporized.

Like for the simple GT cycle, the heat recovery from the fuel cell occurs on the basis of a fixed approach point temperature, following the assumption of a consequent dimensioning of the heat exchanger surfaces: With this assumption the heat available for gas heating is not a function of the GT cycle pressure ratio. System design has been performed for various pressure ratios using air mass flow rate and steam mass flow rates as operational parameters. The two constraints that allow their unique determination are the following:

$$(\dot{m}_w + \dot{m}_{air}) \int_{T_D}^{T_E} c_{p,mix} dT = \dot{m}_w (h_G - h_F) \quad (4)$$

$$(\dot{m}_w + \dot{m}_{air}) \int_{T_B}^{T_C} c_{p,mix} dT = \dot{Q}_{FC} \quad (5)$$

It must be noticed that the reported equations apparently introduce three further unknowns, i.e., T_B , T_E , and T_G . The system has, in fact, three implicit constraints due to pinch point analysis of the steam generator and to approach point temperature differences fixed in the two heat exchange processes.

This situation is much more convenient than the internal heat recovery for air preheating illustrated at the end of the previous paragraph. With this new solution, in fact, the heat recovery can be performed at all examined pressure ratios as shown in Fig. 6.

The maximum temperature of the water after heat recovery is some degrees below that of the exhaust gases to allow for reasonable heat exchanger surface areas. As can be easily seen, this temperature is always over the relative water phase transition (evaporation) temperature, while the water starting temperature

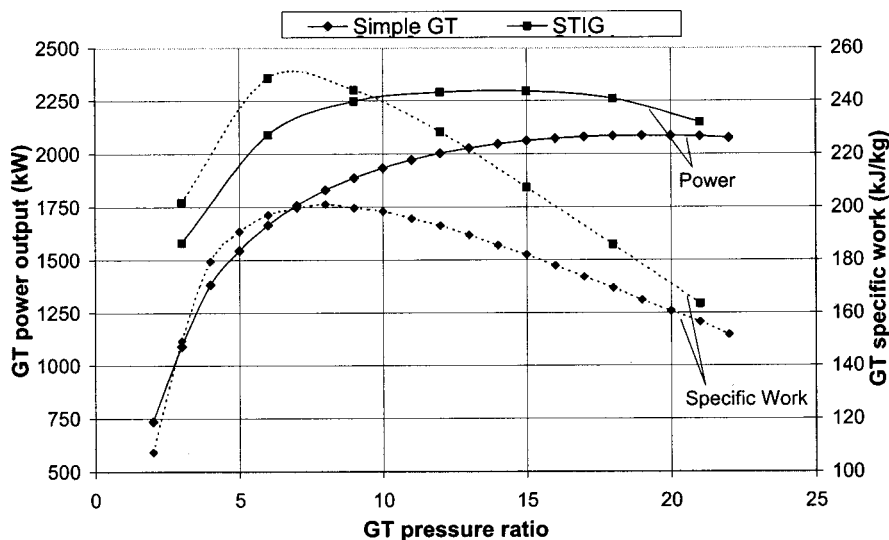


Fig. 10 Power output and specific work comparisons

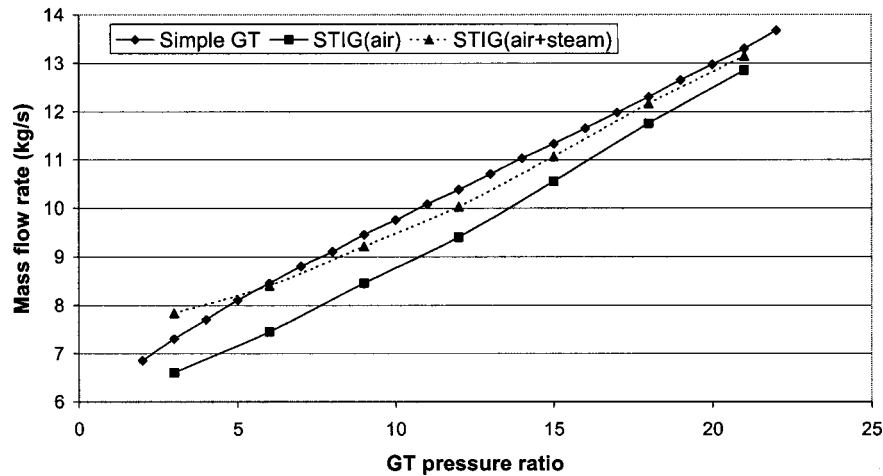


Fig. 11 Mass flow rates

is fixed at 298 K being not cycle related. The consequent heat exchange diagrams for three given GT pressure ratios are shown in Fig. 7.

As for all gas turbine regenerated cycles, the steam injection convenience tends to decrease at higher pressures. Figure 8 easily shows that the maximum work with this cycle is obtainable for a pressure ratio of about 15, while the maximum specific work is in correspondence of $\beta=7$. Similar considerations of those used for the simple cycle can bring to the conclusion that a pressure ratio of about 10 represents the best compromise between efficient electricity generation and affordable plant investment costs (Fig. 9).

Figure 10 shows the comparison of the specific and the total work of the steam injected cycle with the simple one. In all the pressure ratios, inside the range chosen for the simulations, both the specific work and the net power output are higher in the STIG cycle. The increase in specific work is drastic: compared to the simple GT cycle a 25% rise is obtained at $\beta=6$ and a 19% rise at $\beta=12$.

Since the heat content of the exhaust gases is recuperated, the STIG cycle behave similarly to a regenerated cycle with maximum performances obtained at lower pressure ratios. Moreover, as illustrated in Fig. 11, the air mass flow rate is decreased (12% at $\beta=6$) and even the total mass flow rate (air plus steam) is decreased in almost the whole range. This results in less loaded and smaller turbomachinery with evident advantages in terms of efficiency, costs and dimensions of the plant. Another advantage of the steam injection is its flexibility: the steam produced in the HRSG can be used for cogeneration or electricity production according to heat request. The disadvantages concern the necessity of a HRSG, even if not very expensive, and mainly on the necessity of demineralizing the water. In a hybrid cycle with the fuel cell, however, water treatment is necessary for the cell and the steam cycle involves only an increase in the treatment system dimensions.

Table 3 summarizes the parameters of an optimal hybrid plant with steam injection. The electrical efficiency is around 69% with a 1.5 points of increase compared to the simple GT cycle hybrid plant. As outlined before, the best performances are obtained at lower pressures and with lower mass flow rates. This means smaller turbomachinery with fewer stages.

The performance increment is limited by the low turbine inlet temperature. A necessary future step is the investigation of a post-combustion in the GT cycle.

A comparison with the results obtained by other researchers with pressurized cells and internal combustion gas turbines ([6,8,14]) shows that the global system performances are comparable. This is a result of higher pressurized cells performances and

Table 3 Optimized steam injected gas turbine (STIG) plant parameters

Air flow rate (kg/s)	6.25
GT air mass flow rate (kg/s)	8.75
Steam injected flow rate (kg/s)	0.715
GT pressure ratio	10
GT power output (MWe)	2.35
Total net power output (MWe)	17.2
GT/MCFC power ratio (%)	15.8
Electrical efficiency (% LHV)	68.6

lower internal combustion gas turbines performances; the first is due to the potential improvement predicted by Nernst equation and the second is due to the unfeasibility of turbine optimization caused by the low allowable pressure for fuel cells.

A development of such type of hybrid system is not problem free. High-temperature heat exchangers and the associated materials need to be developed and new gas turbine designs are required in order to meet cost criteria necessary to guarantee success in the market place. The study of high-efficiency cycles is necessary anyway, since it represents a first step in identifying performance goals and problems that must be resolved before fuel cell/gas turbine hybrid systems are commercialized for the electrical power generation market.

Conclusions

This paper presents the results of a simulation of a hybrid MCFC/gas turbine system. The upper cycle is a molten carbonate fuel cell system with a global utilization factor of 0.8, a current density of 152 mA/cm² and a cell voltage of 760 mV. The cell alone produces around 15 MW_{el} at beginning of life with 5.55 MW_t available at 1146 K.

The addition of a gas turbine bottoming cycle has also been investigated. An indirect heated gas turbine solution has been chosen, retaining the ambient pressure in the fuel cell. Since the indirect transfer of heat allows the maximum pressure to be set independently from the fuel cell parameters, plant simulations have been performed at various GT pressure ratios. The optimal solution chosen by the authors leads to a 14% net power output increase and to an overall electrical efficiency of 67%.

The plant has been improved introducing a heat recovery steam generator at the GT exhaust. Superheated steam is then injected in the air stream at the GT compressor outlet in a sort of STIG cycle. Specific work and electrical efficiencies result higher in all the simulation range, with lower mass flow rates evolving in the turbomachinery. Moreover, compared to the simple GT cycle, the

optimal performances are obtained at lower pressure ratios. Therefore the STIG solution requires less loaded and smaller turbomachinery with advantages in terms of costs, efficiency, and plant dimensions.

Nomenclature

C_p = constant pressure specific heat
 F = Faraday constant
 h = specific enthalpy
LHV = low heating value
 m = mass flow rate
HRSG = heat recovery steam generator
MCFC = molten carbonate fuel cell
MSW = municipal solid waste
SOFC = solid oxide fuel cell
PEM = polymer electric fuel cell
STIG = steam injected gas turbine
 U_f = fuel utilization factor
 V_m = molar volume
 X = molar fraction
 β = GT pressure ratio
 ΔV = voltage difference
 ΔA = current difference

References

- [1] Kordesch, K., and Simader, G., 1996, *Fuel Cells and Their Applications*, Weinheim.
- [2] Ali, S. A., and Moritz, R., 2000, "A Prototype for the First Commercial Pressurized Fuel Cell System," ASME Paper No. 2000-GT-551.
- [3] Hussey, L., 1999, "Room-Temperature Molten Salts: A Bright Future for Applications in Clean Technology," *Electrochem.*, **67**(16), p. 527.
- [4] Ito, K., Gamou, S., and Yokoyama, R., 1997, "Optimal Unit Sizing of Fuel Cell Cogeneration Systems in Consideration of Performance Degradation," *Proceedings of Flowers '97*, Florence World Energy Research Symposium, Florence, Italy.
- [5] Lobachyov, K. V. and Richter, H. J., 1997, "Performance and Economics of Advanced Integrated Biomass Gasification Carbonate Fuel Cell Power Systems," *Proceedings of Flowers '97*, Florence World Energy Research Symposium, Florence, Italy.
- [6] Layne, A., et al., 2000, "Hybrid Heat Engines: The Power Generation Systems of the Future," ASME Paper No. 2000-GT-0549.
- [7] Randall, G., et al., "Development of Dynamic Modeling Tools for Solide Oxide and Molten Carbonate Hybrid Fuel Gas Turbine Systems," ASME Paper No. 2000-GT-554.
- [8] Massardo, A., and Bosio, B., 2000, "Assessment of a Molten Carbonate Fuel Cell Models and Integration With Gas and Steam Cycles," ASME Paper No. 2000-GT-174.
- [9] Lunghi, P., Ubertini, S., and Desideri, U., 2000, "Highly Efficiently Electricity Generation Through a Hybrid Molten Carbonate Fuel Cell-Close Loop Gas Turbine Plant," *Energy Convers. & Manage.*, **42**(14), pp. 1657–1672.
- [10] Leo, A., et al., 2000, "Ultra High Efficiency Hybrid Direct Fuel Cell/Turbine Power Plant," ASME Paper No. 2000-GT-0552.
- [11] Farouque, M., 1993, "MCFC Power Plant System Verification," *Proceedings of FE Fuel Cells and Coal-Fired Heat Engines Conference*, Library Binding, US DOE/METC, Aug. 3–5.
- [12] Braun, R. J., Gaggioli, R. A., and Dunbar, W. R., 1999, "Improvements of a Molten Carbonate Fuel Cell Power Plant via Exergy Analysis," *Energy Resource Technol.*, **121**, pp. 277–285.
- [13] Desideri, U., Lunghi, P., and Ubertini, S., 2000, "Thermodynamic Analysis of a Molten Carbonate Fuel Cell System Using Waste Derived Fuel Gas," ASME IMECE, Orlando, Florida, Nov. 5–10.
- [14] Hirchenhofer, J. H., et al., 1998, *Fuel Cell Handbook*, 4th Ed., Persons Corp., Reading, PA.
- [15] Redlich, O., and Kwong, J. N. S., 1979, "On the Thermodynamics of Solutions V. An Equation-of-State. Fugacities of Gaseous Solutions," *Chem. Rev.*, **44**, pp. 223–244.
- [16] Haar, L., and Gallagher, J. S., and Kell, J. H., 1984, *NBS/NRC Steam Tables*, Hemisphere, Washington DC.
- [17] ASPEN PLUS Simulation Code, Release 10.1, 1999, Aspen Technology Inc., Cambridge, MA.
- [18] Lozza, G., 1996, *Turbine a Gas e Cicli Combinati*, Progetto Leonardo, Bologna.

Development of a Maintenance Program for Major Gas Turbine Hot Gas Path Parts

H. Moritsuka

e-mail: moritsuk@criepi.denken.or.jp

T. Fujii

T. Takahashi

Central Research Institute of Electric Power Industry (CRIEPI),
2-6-1 Nagasaka,
Yokosuka City, Kanagawa Prefecture,
240-0196 Japan

The thermal efficiency of gas turbine combined cycle power generation plants increase significantly in accordance with turbine inlet temperature. Gas turbine combined cycle power plants operating at high turbine inlet temperature are popular as a main thermal power station among our electric power companies in Japan. Thus, gas turbine hot gas parts are working under extreme conditions which will strongly affect their lifetime as well as maintenance costs for repaired and replaced parts. To reduce the latter is of major importance to enhance cost effectiveness of the plant. This report describes a gas turbine maintenance management program of main hot gas parts (combustor chambers, transition pieces, turbine first stage nozzles and first stage buckets) for management persons of gas turbine combined cycle power stations in order to obtain an optimal gas turbine maintenance schedule considering rotation, repair and replacement, or exchange of those parts. [DOI: 10.1115/1.1399055]

1 Introduction

Over the last few years, the gas turbine combined cycle power generation system has rapidly been accepted as the main type of thermal power generation system for many power plants in Japan. This is because increases in turbine inlet temperature have allowed thermal efficiency to increase.

Against this backdrop, one issue must be considered carefully: The gas turbine hot gas path parts, used under severe environmental conditions, usually have a relatively short lifespan (manufacturer's recommended lifespan) of four to eight years, depending on overall conditions. Cracks and other flaws occurring under operating conditions must be repaired or replaced during periodic inspections. The increased maintenance costs kill the benefit of the thermal efficiency. Reducing the gas turbine maintenance costs has recently become a tremendous challenge facing electric power companies.

The authors studied several main hot gas path parts of the gas turbine (combustor chambers, transition pieces, turbine first-stage nozzles, and turbine first-stage buckets), to help these companies design optimal maintenance plans for their gas turbine power plants. The authors developed a computer program for preparing maintenance plans for optimal parts rotation, and for repair and replacement work in gas turbines. The plans and maintenance cost estimates for gas turbines have been prepared manually. This program would allow the plants to draw up their own maintenance plans using a personal computer, and to reduce the total amount of maintenance planning and maintenance costs.

2 Maintenance of Gas Turbine Hot Gas Path Parts in Japan

The gas turbine consists of an air compressor, a combustor, and a turbine (see Fig. 1). The gas turbine inlet temperature has continuously been set at higher levels, in order to enhance overall thermal efficiency. Gas turbine hot gas path parts include the combustor chamber, transition piece, bucket, and nozzle.

Contributed by the International Gas Turbine Institute (IGTI) of THE AMERICAN SOCIETY OF MECHANICAL ENGINEERS for publication in the ASME JOURNAL OF ENGINEERING FOR GAS TURBINES AND POWER. Paper presented at the International Gas Turbine and Aeroengine Congress and Exhibition, Munich, Germany, May 8–11, 2000; Paper 00-GT-187. Manuscript received by IGTI November 1999; final revision received by ASME Headquarters February 2000. Associate Editor: D. Wisler.

A high-quality super alloy is used as the material for these parts. The parts are subjected to various processes to make bucket/nozzle cooling holes on the surface and to form a structure for the cooling air feed. This increases costs considerably. In addition, these parts are used under hard conditions—high flow rates, hot gases, and frequent temperature changes that occur during start-up and shut-down. Therefore, these parts often suffer degradation damage, such as cracking, creeping, and corrosion. Unlike the case of the steam turbine, such degradation damage is tolerated in these hot gas path parts. The parts are repaired periodically until

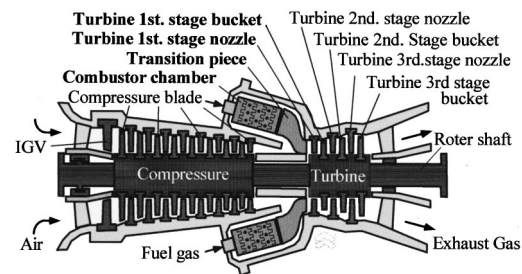


Fig. 1 Gas turbine main hot gas path parts (bold letters)

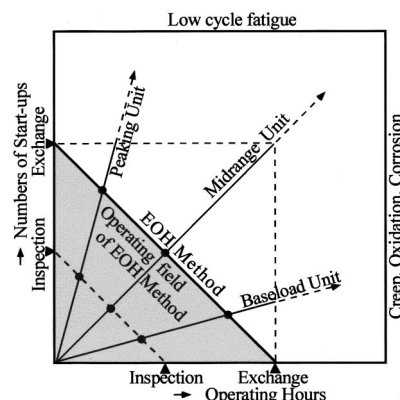


Fig. 2 Gas turbine hot gas path parts maintenance method

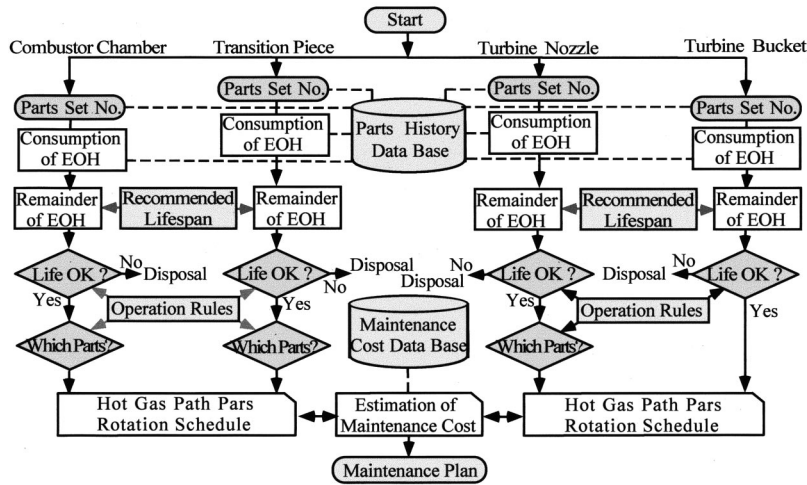


Fig. 3 Flow chart of the program

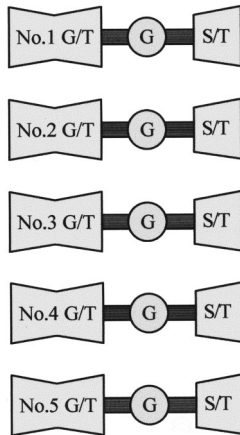


Fig. 4 Typical combined cycle power plant

the end of their manufacturer's recommended lifespan for each kind of the hot gas path parts, then decommissioned as expendables.

In Japan, the most commonly used maintenance method for hot gas path parts is the EOH (equivalent operating hours) management method. To the actual operation hours are added other relevant hours, the value for which is determined by converting the number of start-ups into EOH. When determining EOH values, the values for other lifespan-reducing factors are also taken into account—these factors include the number of trips, the number of load dumps, and the number of peak operating hours. Figure 2 shows a schematic diagram for the EOH management method.

EOH is defined with the following standard equation:

$$\text{EOH} = \text{actual operating hours} + k_1 \times (\text{number of start-ups} + \text{number of trips} \times k_2) + \text{peak operating hours} \times k_3$$

where k_1 is the conversion factor for the number of start-ups (=operating hours/number of trips);

k_2 is the conversion factor for the number of trips (=number of start-ups/number of trips);

k_3 is the conversion factor for peak operating hours (=operating hours/peak operating hours).

These conversion factors are determined specifically, in accordance with the actual operation performance of particular plants.

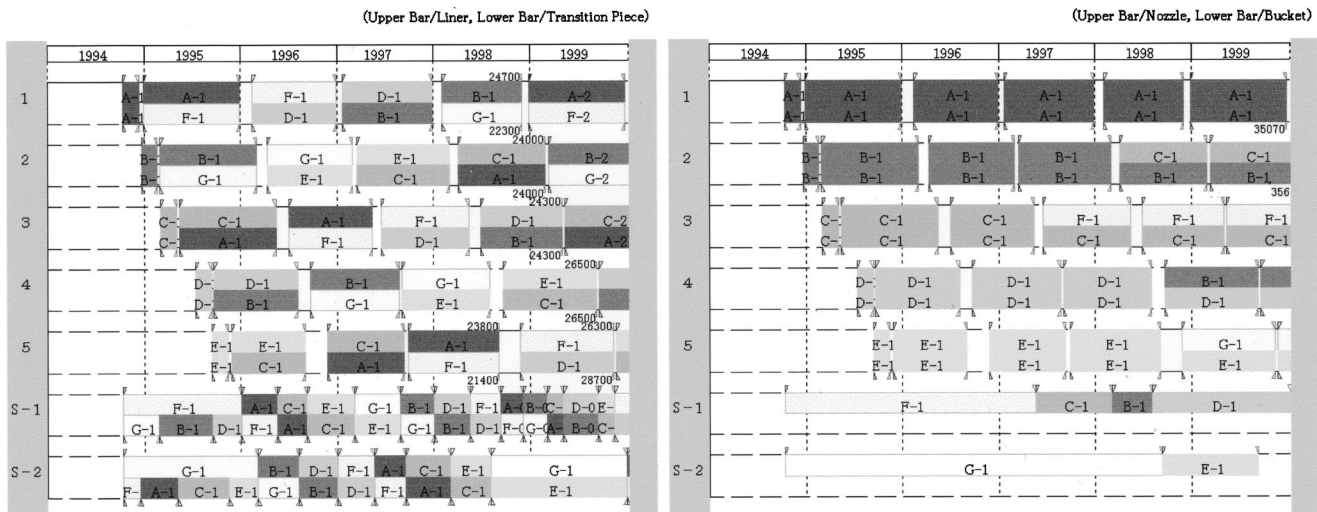


Fig. 5 Gas turbine hot gas path parts rotation history diagram

Table 1 Price, recommended lifespan, and inspection cost

Parts name	Price/numbers	Lifespan
Combustor chamber	1.0 Unit/10 pieces	32,000 EOH
Transition piece	2.0 Unit/10 pieces	32,000 EOH
Turbine first stage nozzle	4.0 Unit/18 segments	64,000 EOH
Turbine first stage bucket	4.0 Unit/92 pieces	64,000 EOH
Periodic inspection	1.25 Unit	
Combustor inspection	0.025 Unit	

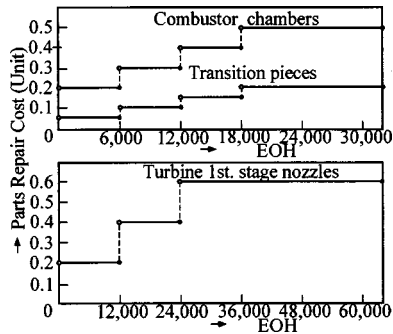


Fig. 6 Repair costs of hot gas path parts

An independent management method can also be used. Under this method, the value for operating hours is determined separately from the number of start-ups. The lifespan of a specific part is regarded as having expired whenever either of these two values reaches its upper limit.

The Electric Utilities Industry Law in Japan obliges Japanese electric power companies to carry out gas turbine inspections at least once every two years (these are called “periodic inspections”). Combustors subject to heavy deterioration or damage are to be inspected once or twice between these periodic inspections (during the so-called “combustor inspections”). During the periodic inspection, all casings of the air compressor and the turbine are opened in order to check, and repair if necessary, all hot gas path parts. During the combustor inspection, only the combustor chambers and transition pieces are removed for checking, then repaired if necessary. A repair takes several days or several weeks, depending on the degree of degradation or damage. This generally obliges the operator to stock several sets of spare parts for each of the gas turbines currently installed. During the inspection, the

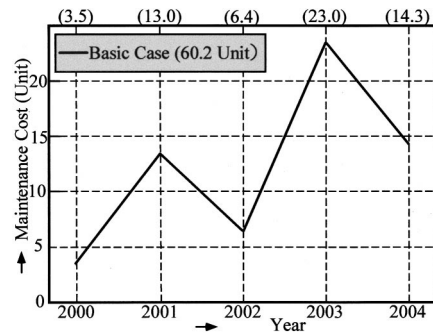


Fig. 8 Maintenance cost for the five-year period (standard case)

parts currently being used are replaced with some set of the spare parts. The replaced parts are then repaired and stored. If the lifespan (EOH) of any removed part does not extend beyond the time for the next planned inspection, the part is decommissioned, with a replacement spare part purchased.

During the inspection, if the combustor chambers, the transition pieces or the turbine first nozzles are found to have cracks exceeding allowable levels, they are repaired by welding and kept in use. However, the turbine buckets are prohibited from being repaired by welding for further usage. Instead, they are put back into use, until the end of their lifespan, only after their cracked zones have been subjected to a blending process. If the operator has a spare rotor, the entire rotor assembly can be replaced during the periodic inspections.

For such maintenance of hot gas path parts, power plant operators (repair personnel) draw up maintenance plans and prepare cost estimates.

3 Capabilities of the Gas Turbine Maintenance Program

Figure 3 shows a flow chart for the gas turbine maintenance program. The program has four basic capabilities:

1. computing required to prepare, in the parts history database, plans for the maintenance of hot gas path parts, especially plans for parts usage rotation, parts repair, and parts replacement;

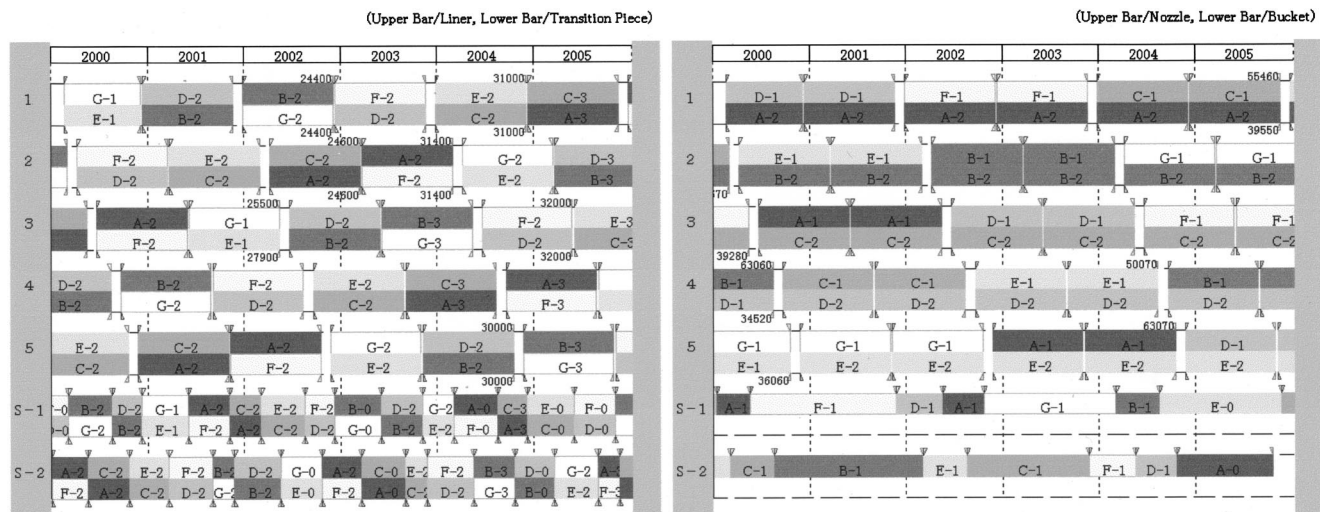


Fig. 7 Gas turbine hot gas path parts rotation plan diagram (basic case)

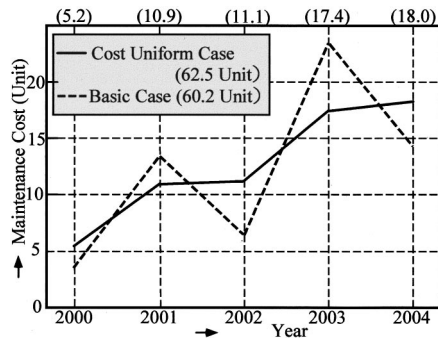


Fig. 12 Maintenance costs for the five-year period (cost uniform case)

Figure 6 shows repair costs for the main hot gas path parts. We assumed that repair costs would increase in a step-up pattern, according to the number of usages. The step-up pattern actually results from repair cost data of operation gas turbine power plants. These costs are represented as relative values, percentages of the price of a gas turbine.

A complete set of hot gas path parts for a single gas turbine is replaced at any one time, with the following principles applied:

- 1 The parts are used on a “first in, first out” basis—in other words, the parts set that has been stored for the longest period is to be used first.
- 2 Any combustor chamber and transition piece that have less than 8,000 EOH remaining, and any turbine first buckets and first nozzles that have less than 16,000 EOH remaining, should be considered useless and should be disposed of, and a new set of parts should be procured.

To prepare a maintenance plan, the set number and the EOH for the hot gas path parts currently used are retrieved from the parts history database. Then the values representing the capability of preparing hot gas path parts maintenance plans, and the values for mapping capability, are used to calculate the maintenance costs that would be incurred in the coming several years under the maintenance plan. The results are represented as line graphs.

Repeated use of these capability values for preparing maintenance plans allow us to conduct various case studies concerning the adjustment of the lifespan of specific hot gas path parts, EOH

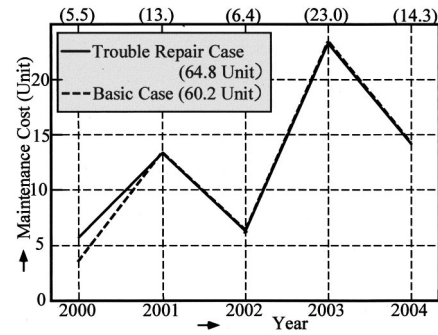


Fig. 14 Maintenance costs for the five-year period (trouble repair case)

factors and the timing of combustor inspections. In addition, unscheduled inspections can be carried out in the event any problem occurs suddenly.

4 Drawing Up Maintenance Plans for a Gas Turbine Program

We prepared sample maintenance plans for the main hot gas path parts of a gas turbine.

First, a basic maintenance plan was prepared according to the standard parts application rules. Figure 7 shows a parts rotation plan diagram. Figure 8 shows the maintenance costs for the five-year period, 2000 to 2004. Calculations revealed that costs incurred under the basic maintenance plan would be 60.2 Unit for the five-year period (as explained above, this cost is a relative value, the percentage of the price of a gas turbine).

Next, calculations were performed to determine costs in the case where the basic maintenance plan is modified. This maintenance plan modification assumes the case where the manufacturer’s recommended lifespan exceeds by 25 percent that of the standard case. Figure 9 shows a diagram for the parts rotation plan diagram, while Fig. 10 shows a diagram for maintenance costs for the five years. The extension of the parts’ lifespan helps reduce maintenance costs for the year 2003, and to reduce the total cost amount for the five years to 44.1 Unit (27 percent lower than costs for the basic case).

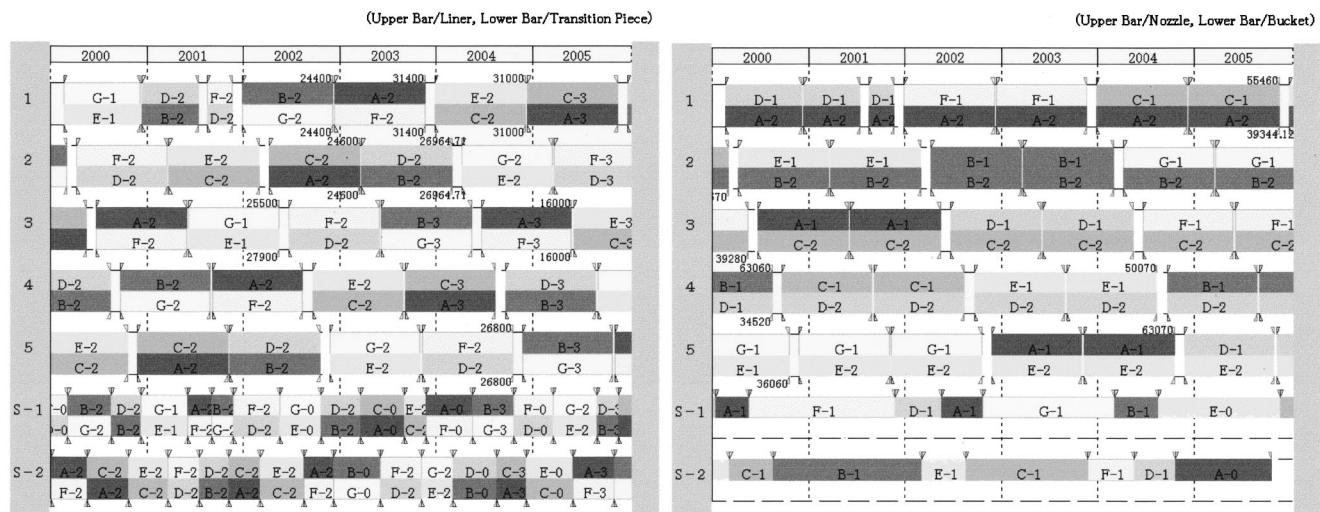


Fig. 13 Gas turbine hot gas path parts rotation plan diagram (trouble repair case)

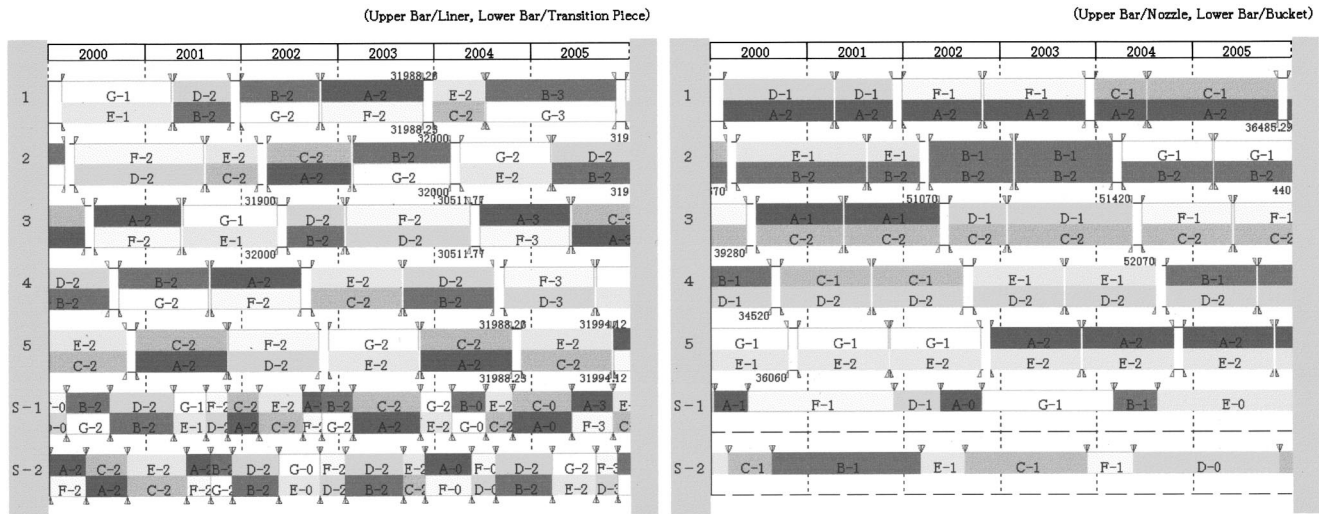


Fig. 15 Gas turbine hot gas path parts rotation plan diagram (combustor inspection optimizing case)

Another calculation was made for the case where the timing of periodic inspections is changed in order to make the cost of differently timed maintenance procedures relatively uniform. In the basic case, the periodic inspections for turbines No. 2 to No. 5 are concentrated in the years 2001 and 2003. In 2003, replacement of the combustor chamber and transition piece adds to the amount of maintenance costs.

To make the total cost for each of the five years more uniform, we assumed a case where the periodic inspections for gas turbine No. 2 are brought forward to the preceding year.

Figure 11 shows a parts rotation plan diagram, while Fig. 12 shows total maintenance costs. The parts rotation plan differs little from that of the basic case, although total maintenance costs are made considerably more uniform. Moving up periodic inspections increased the total number of periodic inspections for gas turbine No. 2. Thus, the total maintenance costs for the five years increase to 62.5.

The next example is a revision of the initial maintenance plan, in the case where a failure occurs in the combustor for gas turbine No. 1, thus making it necessary to remove failed parts and install spare parts in the combustor chamber and transition piece. Such a situation would require an additional repair period.

Figure 13 shows a parts rotation plan diagram, while Fig. 14 shows total maintenance costs for the five years. This parts rotation plan differs greatly from that of the standard case for the period after repair shut-down. Total maintenance costs are 64.8 (including the additional 2.0 points for repairing the combustor).

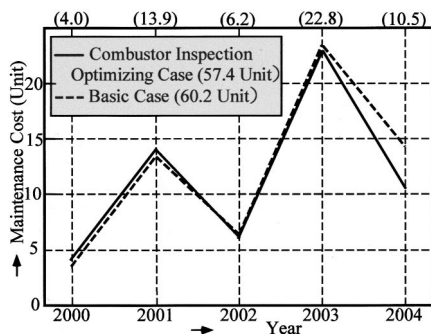


Fig. 16 Maintenance costs for the five-year period (combustor inspection optimizing case)

The last calculation was conducted for a case where the scheduling of the combustor inspections is optimized, in order to cut down on the cost of maintaining the hot gas path parts of the gas turbine. The ultimate aim of this optimization is use the combustor chamber and transition piece more efficiently, up to the end of their manufacturer's recommended lifespan, by adjusting the scheduling of combustor inspections to accord with the remaining lifespans of the combustor chambers and transition pieces.

In the basic case, the sets of combustor chambers and transition pieces A to G of the second generation have 600, 7600, 7400, 2000, 1000, and 0 remainder EOH, respectively (G is in use). These sets are disposed of in accordance with standard parts application rules, since all of the EOHs are lower than the specified level (8,000 EOH). In this optimized case, all parts A to G are used almost until the end of their recommended lifespan of 32,000 EOH.

Figure 15 shows a parts rotation plan diagram, while Fig. 16 shows total maintenance costs for the five-year period. These costs have been reduced to 57.4 (five percent lower than costs for the basic case).

These maintenance plans were prepared using calculations based on basic parts application rules, and could not be used as such for actual generation plants. Nevertheless, the maintenance plans could probably be approximated to plans that can be implemented, if they take into account various restrictive conditions (generated energy and fuel consumption), and if the application rules of particular plants are enhanced.

5 Conclusion

The authors developed a gas turbine maintenance program that is specifically designed to reduce maintenance costs for gas turbines. Our research proved that this program is useful for drawing up optimal maintenance plans for hot gas path parts and reducing required maintenance costs for gas turbines. The authors believe that the program will be useful as a supplementary tool for the repair personnel of a power generation plant, helping them draw up better maintenance plans for the plant's generating equipment. (Also, please see Refs. [1-4]).

Acknowledgment

The authors would like to express their gratitude to the staff of the Thermal Generation Department, the Thermal Power Center

and Yokkaichi Thermal Power Plant operated by Chubu Electric Power Co., Ltd. Their valuable information and advice for this study are much appreciated.

References

- [1] 1991, "Development and Evaluation of Life and Assessment and Reconditioning Methods for Gas Turbine Blading," EPRI GS-4302.
- [2] Soneda, N., and Takao, T., 1993, "Development of Integrated Evaluation Support System for Nuclear Plant Life Extension," CRIEPI Report T92061.
- [3] Moritsuka, H., Fujii, T., and Takahashi, T., 1999, "Development of the Gas Turbine Maintenance Optimization Supporting Program—First Report Maintenance Management Basic Program of Main Hot Gas Parts," CRIEPI Report W98020.
- [4] Hayakawa, Y., Isobe, N., Sakurai, S., and Kumata, K., 1999, "Life Management System for Hot-Gas-Path Components of Gas Turbine," ASME Paper 99-GT-428.

Droplet Entrainment From a Shear-Driven Liquid Wall Film in Inclined Ducts: Experimental Study and Correlation Comparison

J. Ebner

e-mail: Joachim.Ebner@its.uni-karlsruhe.de

M. Gerendás

O. Schäfer

S. Wittig

Lehrstuhl und Institut für Thermische
Strömungsmaschinen,
Universität Karlsruhe (T.H.),
Kaiserstrasse 12,
76128 Karlsruhe, Germany

The primary objective of the present study is to clarify the droplet disintegration mechanism and the film properties of liquid oil films driven by shear stress, which is induced by a co-current gas flow. This work focuses on the flow behavior within the starting length of the complex two-phase flow and the effect of inclination on the entrainment rate. Many investigations have been performed in the past to determine the droplet entrainment in the gas core for fully developed flow conditions with respect to their relevance in pipes of power plants and various chemical engineering systems. In more recent work the effect of inclination has been studied in detail. Nevertheless, a lack of knowledge can be realized for droplet entrainment within the starting length of this complex flow type. Thus, fundamental experiments have been carried out to provide a data base for droplet entrainment of liquid disintegrated from an oil film within its starting length at several inclination angles of the flow. The experimental results have been compared with correlations from literature. Additionally, the wall film thickness has been measured to allow a fully coupled modeling of entrainment and liquid film properties depending on global flow parameters. Based on film Reynolds number, Weber number, a dimensionless film flow length, and a modified Froude number, taking into account the angle of inclination, correlations have been developed, where those from literature are not applicable.

[DOI: 10.1115/1.1476926]

Introduction

A proper characterization of the air/oil flow in bearing compartments and many other cavities of the so-called secondary air system of modern aeroengines requires reliable models for droplet entrainment from shear-driven oil films. In particular the development of CFD-based design tools (computational fluid dynamics) to simulate this complex type of flow requires detailed information as shown by Glahn et al. [1]. The pressure drop of the two-phase flow as well as the heat transfer from the wall to the gas core is strongly affected by the distribution of oil as wall film and as droplets within the gas core ([2,3]). Thus, the thickness of the liquid film becomes a vitally important parameter for a proper description of the overall flow field.

A profound modeling of the droplet generation mechanism at the gas-liquid interface, caused by the co-current air stream is very demanding. For that reason, this type of flow is still under research. Extensive investigations have been performed in the past for fully developed two-phase flow with respect to their significance, e.g., for air/water flow in pipe systems of nuclear power plants or evaporators ([4–8]). In more recent work the effect of inclination has been studied in detail ([9–11]). The present work focuses on developing film flow, because the typical pipe lengths within the secondary air system of aeroengines and many other applications are by far too short to expect fully developed flow conditions. Thus, the film flow length has to be taken into account.

Measurements of the entrainment fraction and the oil film

thickness have been conducted for various air velocities, oil flow rates, test section slopes, and film flow lengths. Thus, the major parameters to describe the heat transfer and the propagation of the liquid wall film are available for the air/oil flow under investigation.

Experimental Setup and Operating Conditions

The measurements presented in this paper have been performed using an unheated rectangular duct (30 mm × 50 mm) with only the bottom wall wetted and a length of up to $l = 30H = 900$ mm. The air pressure is $p = 3$ bar absolute and the oil has a kinematic viscosity of $\nu_f = 5.2$ mm²/s (DOW: DC 200 Fluid 5 cs). Thereby, the film flows only on a width of $b = 40$ mm to minimize effects due to a three-dimensional air flow in the duct. It flows in a height adjustable groove such that it can be lowered a little bit more than its film thickness with respect to the bottom wall of the duct. By this method, the film remains in the restricted area and furthermore no point of discontinuity of the gas phase occurs at the start of the film.

A schematic diagram of the test section is given in Fig. 1. The air is supplied by a compressor at a constant pressure. A settling chamber with a nozzle is placed upstream of the rectangular duct to generate a constant velocity profile at the entrance. The oil film is formed by a device consisting of a small slit, through which the liquid flows into the test section at a shallow angle with respect to the main stream direction. Therewith, a point of discontinuity is avoided at the start of the film. For the same reason, the film flows on a plate, which can be adjusted in its height. Thus, the cross section of the gas flow remains constant changing the film loading. Three different film flow lengths can be installed ($l = 10 - 30H$). The film draining is realized via a variable slit to adjust it according to the present flow conditions. This procedure ensures

Contributed by the International Gas Turbine Institute (IGTI) of THE AMERICAN SOCIETY OF MECHANICAL ENGINEERS for publication in the ASME JOURNAL OF ENGINEERING FOR GAS TURBINES AND POWER. Paper presented at the International Gas Turbine and Aeroengine Congress and Exhibition, New Orleans, LA, June 4–7, 2001; Paper 01-GT-115. Manuscript received by IGTI, December 2000, final revision, March 2001. Associate Editor: R. Natole.

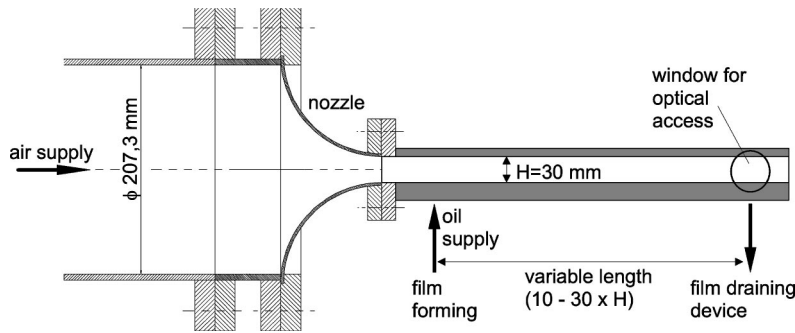


Fig. 1 Schematic of rectangular test section

the complete removal of the wall film with minimal air content for all test conditions. The performance of the device can be observed through a window.

Extensive measurements have been performed over a wide range of air and oil flow rates. Table 1 gives a detailed overview of the operating conditions and the fluid properties.

Table 1 Operating conditions of entrainment fraction and film thickness measurements

Hydraulic diameter D_h	37.5 mm
Width of film b	40 mm
Film length l	300 – 900 mm
Angle of inclination α	$-20^\circ - +40^\circ$
Mean gas velocity u_g	15 – 35 m/s
Film loading \dot{V}_f/b	2.5 – 15 cm^2/s
Temperature T	293 K
Kinematic viscosity ν_f	5.2 mm^2/s
Surface tension σ_f	0.02 N/m

Measurement Techniques

In the following a brief description of the measurement systems used to analyze the complex two-phase flow will be given. First of all, the mass flow rate measurement of the droplets in the gas core and the liquid wall film to determine the entrainment fraction with a high level of accuracy is described. The liquid flows in a closed circuit. It is supplied to the test rig by a pump out of a reservoir and is continuously drained by an adjustable slot. The functionality of the device can be observed optically. Thus, the slot can be adjusted according to the working conditions such that an additional drainage of droplets from the gas core can be avoided. Between the outlet of the filter system downstream and the inlet of the oil tank the liquid can be redirected by computer-controlled valves onto a high-accuracy scale (resolution: $\Delta m = 0.1 \text{ g}$) for a well defined period of time. By this procedure the oil flow rate of both, the droplets and the wall film can be determined with an accuracy of $\Delta \dot{m} \leq 0.05 \text{ g/s}$.

The measurement of film thickness is very demanding. In the past, several capacitive and inductive techniques have been applied (e.g., Hewitt [12]). A major restriction in the use of these sensors are their large dimensions. In order to obtain a better spatial resolution optical approaches have been suggested. An advanced system based on the absorption of infrared light is described by Samenfink et al. [13]. This technique is suitable for water and alcohols due to the strong absorption within the fluid. Unfortunately, nearly no absorption occurs for the oil under inves-

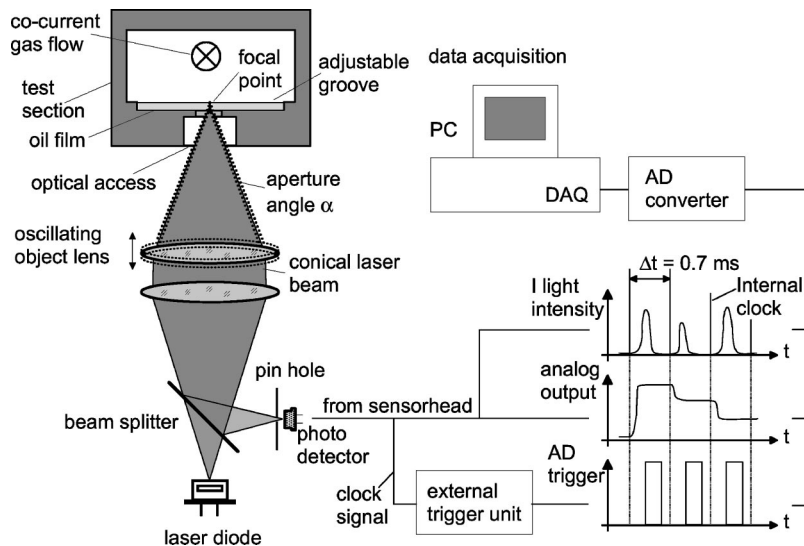


Fig. 2 Optical setup and the modified data acquisition of the nonintrusive laser-based film thickness measurement technique

tigation. Due to the closed circuit of the liquid including several filter systems the use of dye to increase absorption is not appropriate, because its concentration would not remain constant. Thus, a laser-based system, a so-called laser focus displacement meter, according to Takamasa et al. [14] is applied. The optical and electronic setup of the system is illustrated in Fig. 2.

The measurement principle is based on focusing the light cone of a laser diode (wavelength $\lambda = 670$ nm) onto the phase interface. One of the focusing lenses oscillates due to electric attenuation, shifting the spatial position of the focal point of the laser beam. At the gas-liquid interface the beam is reflected to a great extent back into the emitting optics. The reflected light is redirected through a pinhole onto a photo detector by a half-transparent mirror. For one cycle of oscillation the photo detector receives the maximum amount of light in the time instant, when the focal point is directly located on the phase interface as illustrated in Fig. 2. The relation of the spatial position of the objective lens and the peak in light intensity allows one to determine the distance of the film surface from the sensor. Since the spacing of the sensor and the glass window (on which the film flows) is known and remains constant, the film thickness can be determined. The sample frequency of the LFD sensor (Keyence: model LT-8110) is $f = 1.5$ kHz and the range of the sensor is $0 \leq h \leq 2.1$ mm in air. A spatial resolution of $\Delta h = 0.2 \mu\text{m}$ is specified by the manufacturer. This resolution can be obtained using the sensor with standard options, i.e., averaging two or even more samples, thereby taking into account a decrease in the data rate. In order to reach the maximal temporal resolution to perform detailed measurements of the film structure, the analog output of the LFD system has to be used. For this purpose, an external trigger unit was built to generate a suitable pulse for the analogue-to-digital conversion board of the data acquisition computer. Due to this method the spatial resolution decreases to a value of $\Delta h = 2 \mu\text{m}$, which is very accurate for the measurement of liquid films in the range of $0.1 \text{ mm} \leq h_f < 2 \text{ mm}$.

The refraction of the light at the glass/liquid interface as well as the reflection of the light at the wavy surface of the film has to be taken into account. According to Eq. (1) the measurement range of the sensor increases by a factor of $c(n, n_f) = 1.404$ due to the refraction index of $n_f = 1.390$ of the oil under investigation. On the other hand the half-angle of the aperture is reduced from a value of $\alpha/2 = 11.5$ deg in air to $\alpha_f/2 = 8.25$ deg in the liquid film.

$$h_f = h \cdot \frac{\tan(\alpha/2)}{\tan(\alpha_f/2)} = h \cdot c(n, n_f) \quad \text{with} \quad \alpha_f/2 = \arcsin\left[\frac{n}{n_f} \cdot \sin(\alpha/2)\right]. \quad (1)$$

Thus, the film structure can be detected as long as the surface angle of the film remains lower than $\alpha_f/2 \leq 8.0$ deg. Previous investigations on film flows at the Institute of Thermal Turbomachinery (Samenfink et al. [13,15]) revealed that the surface angles of shear-driven liquid films are mostly smaller. Therefore, the LFD technique can be applied in order to perform spatial resolved measurements of the film structure ([16,17]). In the case that the maximal angle is exceeded and no measurement can be performed the sensor gives a specific signal. This allows to discriminate those cases from valid measurements. Since such strong reflections are rare the wave structure can be reconstructed easily by interpolating the missing data points.

Theoretical Background

In this section dimensionless groups and fundamental equations are provided to characterize the overall flow field. They are all based on the forces acting in two-phase flows. In the following, a brief description of the forces dominating the interaction of liquid film and co-flowing air stream is given. Inertia F_I , friction F_F , and surface tension F_S can be identified as vitally important parameters to characterize the droplet generation from shear-driven liquid films (Kataoka et al. [18]). Due to the variation of the inclination of the flow and the large span of air velocities conducted,

Table 2 Dimensionless groups used to characterize the two-phase flow field

Reynolds number Re_f	$Re_f = \frac{\dot{V}_f}{b v_f} = \frac{u_f^* H}{\nu_f}$
Weber number We	$We = \frac{\rho_g u_g^2 D_h}{\sigma}$
Ohnesorge number On	$On = \frac{\mu_f}{\sqrt{\rho_f \sigma D_h}}$
Froude number Fr_f	$Fr_f = \frac{u_f^{*2}}{H g \sin(\alpha)}$
dimensionless length λ	$\lambda = \frac{l}{D_h}$

the film flow is not always dominated by shear stress at the phase interface. Thus, gravity F_G has to be taken into consideration (Spedding et al. [8]).

Based on this system, four dimensionless groups can be deduced for the purpose to describe the film disintegration mechanism: the film Reynolds number Re_f , the Weber number We , the Ohnesorge number On , and a modified Froude number Fr_f . The Froude number accounts for the inclination angle of the test section, i.e., the gravitational force acting in film flow direction. The superficial velocity u_f^* of the film is used in its definition, since no information of the film velocity is available yet. The behavior of the flow in the developing region is taken into consideration by a dimensionless film length λ depending on the hydraulic diameter of the duct $D_h = 4 \cdot A/P$. An overview of the definitions of all groups to characterize the flow is given in Table 2.

Especially the studies of Ishii and co-workers are used quite often for the prediction of the entrainment fraction. Those authors summarized a large amount of droplet entrainment measurements performed in the past. Based on these experimental data sets correlations have been developed, to predict the droplet entrainment fraction EF depending on the operating conditions. Those correlations mainly focus on fully developed flow. Nevertheless, an approach to describe the starting of the entrainment has been suggested. Thus, the experimental results of the present study are compared to the prediction according to Ishii and Mishima [19].

The prediction of the entrainment fraction EF according to Eq. (2) is done assuming that all liquid above the stability limit of the film is disintegrated. Two different entrainment mechanisms are introduced. The so-called wave undercut and shear off roll waves depending on the flow conditions. This contemplation leads to an equilibrium entrainment fraction EF_∞ (cp. Eq. (3)) of droplets in the gas core and liquid at the wall for a fully developed flow. It should be mentioned that the definition of both, the film Reynolds number Re_f^* as well as the Weber number We^* , differ from the definitions used in this paper as shown in Eqs. (4)–(5). Thus, these modified parameters are superscripted by an asterisk.

The following correlations have been introduced by Ishii and Mishima [19]:

$$EF = \frac{\dot{V}_{dr}}{\dot{V}_f + \dot{V}_{dr}} = \frac{\dot{V}_{dr}}{\dot{V}_{tot}} \quad (2)$$

$$EF_\infty = \tanh(7.25 \cdot 10^{-7} We^* 1.25 Re_f^{*0.25}) \quad (3)$$

$$Re_f^* = \frac{\rho_f u_f^* D_h}{\mu_f} \quad (4)$$

$$We^* = \frac{\rho_g u_g^2 D_h}{\sigma} \left(\frac{\Delta \rho}{\rho_g} \right)^{1/3} \quad \text{with} \quad u_f^* = \frac{\dot{V}_f}{A} = \frac{\dot{V}_f}{bH} \quad \text{and} \quad \Delta \rho = \rho_f - \rho_g. \quad (5)$$

In order to describe the entrainment in the developing region an exponential function has been suggested. A dimensionless length ζ

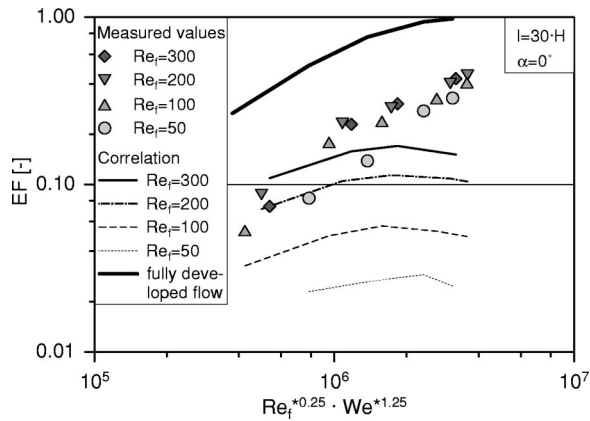


Fig. 3 Comparison of measured entrainment fraction with correlation according to Ishii and Mishima [19] (film length $l = 30H$)

depending on film Reynolds number Re_f^* and a gas phase velocity u_g^* corrected for the droplet content are used. An overview of the entrance correlation are given in Eq. (5).

$$EF(\zeta) = (1 - e^{-10^{-5}\zeta^2})EF_{\infty}$$

$$\text{with } \zeta = \frac{1}{D_h} \sqrt{\frac{Re_f^*}{u_g^*}} \text{ and } u_g^* = \frac{u_g}{\sqrt[4]{\frac{\sigma g \Delta \rho}{\rho_g^2} \left(\frac{\rho_g}{\Delta \rho}\right)^{2/3}}} \quad (6)$$

The value of the constant in the relation has been derived based on experimental data sets of Cousins et al. [20]. A comparison of the measured entrainment fraction of the present study and the half-empirical approach is presented in the following.

Experimental Results

Entrainment Fraction. A comparison of measured and calculated entrainment fraction is plotted in Fig. 3 in terms of the dimensionless numbers described above. The diagram shows measurements of entrainment fraction for horizontal flow. It displays some shortcomings in the accuracy of the prediction for the present application, especially taking into account the double-logarithmic scaling. The calculated values according to the entrance correlation (cp. Eq. (6)) do not match the measured data. On the other hand the comparison to fully developed flow conditions appears reasonable. Thus, it can be assumed that the deviations occur due to an incorrect characterization of the entrance effect.

In order to find out the origin of the discrepancies the entrance effect is analyzed in detail. Therefore, the experimental results are compared to data according to the exponential entrance function (cp. Eq. (6)). A comparison of measured entrainment fractions and data obtained by the correlation according to Ishii is given in Fig. 4. It can be seen clearly, that the run of the predicted curve does not match the measured data.

Figure 5 presents a plot of the exponential function defined by Eq. (6). The effect of the Reynolds number in the dimensionless length ζ is not described properly for the air/oil flow under investigation as evident in the diagram. The shape of the curve also differs from the trend given by the measured entrainment fractions. Thus, an adjustment of the model constants is not appropriate in order to improve the predicting quality significantly.

Therefore, a new correlation to characterize the entrainment of the developing air/oil flow has to be deduced. In order to obtain a model with a high accuracy, a correlation based on the dimensionless groups defined in Table 2 is presented in the following. A

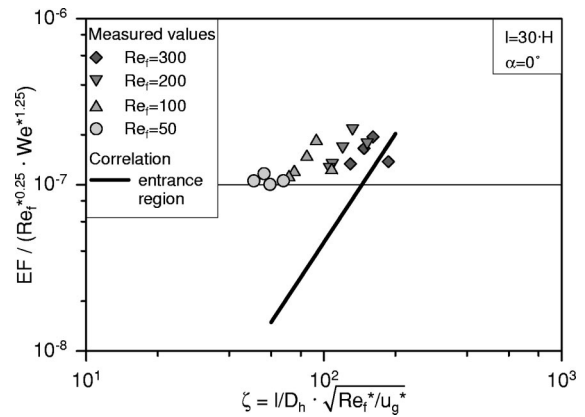


Fig. 4 Comparison of measured entrainment fraction with correlation in entrance region (Ishii and Mishima [19])

separation of the parameters controlling the droplet disintegration mechanism has been performed to derive singular relationships for each. Thus, Figs. 6–8 give an overview of measured data sets separating the parameters film loading (Reynolds number), shear stress (Weber number), film length, and inclination. The angle α in Fig. 8 is defined positive for upwards directed flow according to a force balance, which can be derived for a fluid element in the film.

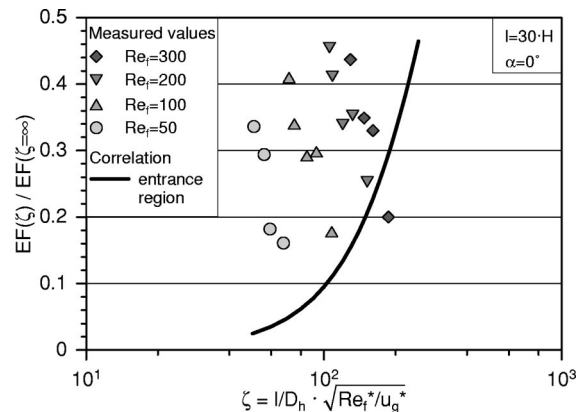


Fig. 5 Entrainment function in entrance region Ishii and Mishima [19]

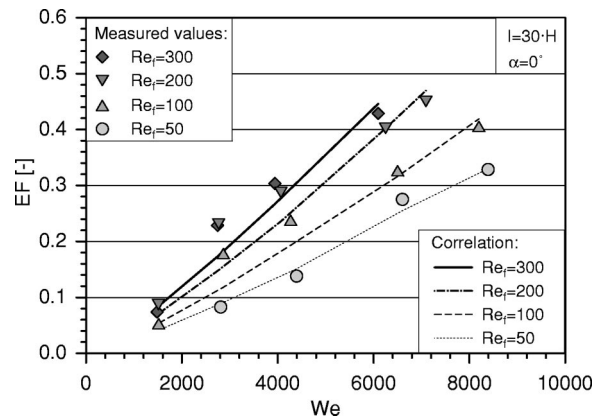


Fig. 6 Effect of Reynolds and Weber number on entrainment fraction (film length $l = 30H$; inclination $\alpha = 0$ deg)

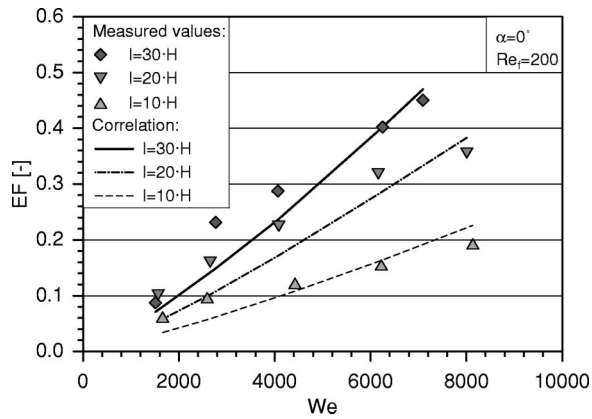


Fig. 7 Effect of film flow length on entrainment fraction

The correlation derived for the entrainment fraction by the least-squares method reads as follows:

$$EF = 1.042 \cdot 10^{-7} We^{1.2} Re_f^{0.4} \lambda^{0.8} \cdot \left(1 + 2.061 \cdot 10^{-4} \frac{Re_f^2}{We Fr_f} \right)^{2.25} \quad (7)$$

It has to be pointed out that the correlation has been derived from all data sets performed within this study (see Table 1). The calculated values of the entrainment fraction according to Eq. (7) are also plotted in the diagrams. In order to give a measure for the overall prediction accuracy a mean relative error of $\Delta EF/EF \approx 20\%$ of the measured data and the entrainment fraction correlation can be determined. Since no variation of the Ohnesorge number has been applied it should be mentioned that the applicability of the formula is restricted to two-phase flows under comparable operating conditions.

The overall accuracy in predicting the entrainment fraction with the newly developed correlation is also confirmed by the results presented in Figs. 9 and 10. The tests have been performed over a wide range of flow conditions which are typical for the secondary air system of modern aero engines. Even though minor deviations occur in some cases the correlation leads to a significant increase of accuracy in predicting the entrainment of the air/oil flow under investigation.

Film Thickness. Film thickness measurements have been conducted for all operating conditions (see Table 1). As mentioned above, time-resolved film thickness measurements can be performed with the LFD technique. Since modeling of liquid films is usually done by an analysis based on mean values only time-averaged film thickness are presented here. In order to deduce a correlation depending on the dimensionless groups according to

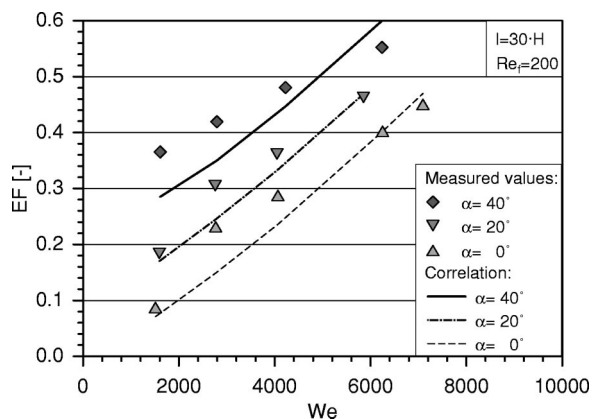


Fig. 8 Effect of inclination angle on entrainment fraction

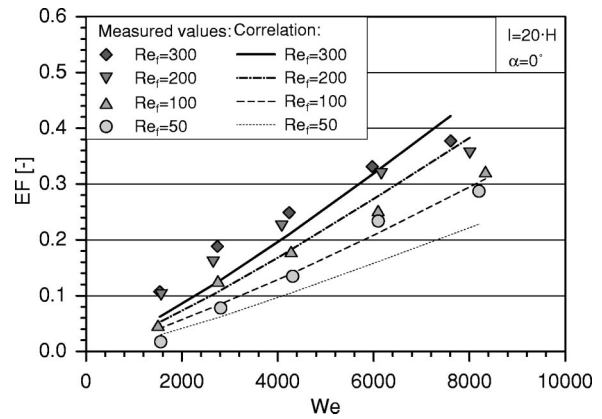


Fig. 9 Comparison of measured entrainment fraction and correlation (film length $l=20H$; inclination $\alpha=0$ deg)

Table 2, the experimental results are presented depending on film loading, air flow rate, and film flow length. Figure 11 shows that the film thickness decreases with higher air velocities (Weber number) due to the rising shear stress at the gas/liquid interface. The increase of shear accelerates the film and additionally increases the droplet generation (cp. Fig. 6). On the other hand no significant effect of the film length can be observed at first sight. This behavior can be explained with respect to the various interlocking effects. On the one hand the film loading decreases due to film disintegration. On the other hand the loss of momentum of the gas boundary layer leads to a decrease of the shear force. By this, the negligible influence of the length scale becomes evident.

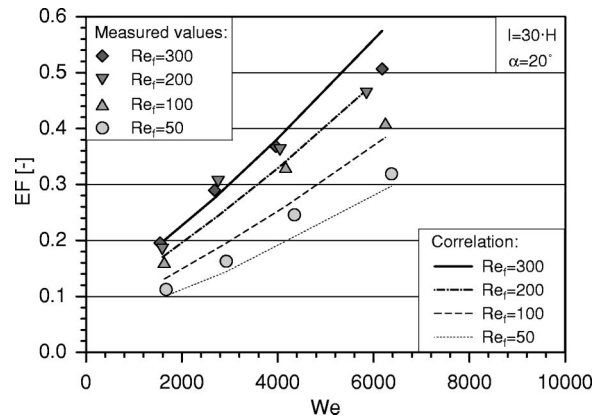


Fig. 10 Comparison of measured entrainment fraction and correlation (film length $l=30H$; inclination $\alpha=20$ deg)

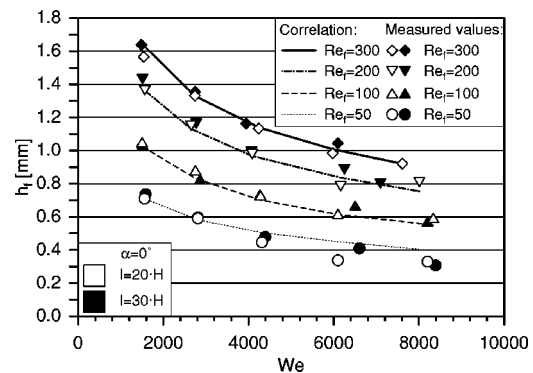


Fig. 11 Comparison of measured film thickness and correlation for different film flow lengths

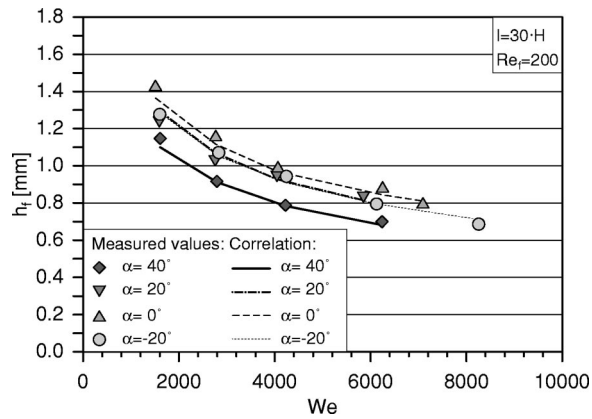


Fig. 12 Comparison of measured film thickness and correlation for different inclination angles

The impact of the inclination on the film thickness is displayed in Fig. 12. The effect is rather small as long as the slope of the duct is in the range of $-20 \text{ deg} < \alpha \leq 20 \text{ deg}$. Nevertheless, the inclination is taken into account in the correlation presented in the following. The film thickness decreases for a positive as well as for a negative inclination angle. An explanation can be derived by analyzing the gravity effect on the film propagation and the droplet generation. In upwards directed flow the force of gravity decelerates the film. On the one hand, the film thickness rises up due to the conservation of mass. On the other hand, a thicker film exhibits a higher roughness, thereby leading to a higher interfacial shear stress. This results in an increase of film disintegration according to Fig. 8. Since both effects are of same magnitude, the dependence of the film thickness on the inclination angle becomes clear. A similar contemplation can be conducted for downwards directed flow, respectively.

With respect to the findings presented above, the following correlation of the mean film thickness can be obtained:

$$h_f = 1.714 \text{We}^{-0.36} \text{Re}_f^{0.457} \cdot \left(1 - 1.096 \cdot 10^{-14} \frac{\text{Re}_f^4}{\text{Fr}_f^2} \right)^{0.375} \quad (\text{mm}). \quad (8)$$

The fraction term in the formula, taking into account the inclination angle, confirms the considerations discussed above. The effect of the inclination is controlled both by the stability of the film via the Reynolds number and by the gravity force via the Froude number. The predicted film thickness according to Eq. (8) are also presented in Figs. 11 and 12. The calculated curves match the measured values very well. A relative error lower than $\Delta h_f / h_f \leq 10\%$ of measured and predicted film thickness can be stated for all operating conditions.

Summary and Conclusions

This paper supplies detailed information on the complex two-phase flow. Extensive experimental work has been performed under operating conditions typical for the secondary air system of modern aero engines. Based on this experimental data and addressing the underlying physical relationships in terms of nondimensional parameters, correlations for the entrained liquid and the film thickness for air/oil flows have been developed with special emphasis to the starting length of the flow.

The study reveals that entrainment correlations from literature are not suitable for the present air/oil flow due to a lack in prediction accuracy. In order to develop detailed models for CFD-based design tools a relationship based on dimensionless groups is provided. The accuracy of the correlation is excellent for all test conditions performed. Due to its nondimensional form it can be scaled easily to similar applications. Nevertheless, the entrainment

correlation has to be verified for other liquids if the properties differ significantly from the oil used in the present study.

A global description of the air/oil flow requires not only detailed information of the droplet phase. The heat transfer as well as the pressure drop is also affected by the properties of the liquid wall film. Thus, based on experimental data a correlation for the mean film thickness is presented.

Acknowledgment

This work was supported by grant from the United Technology Research Center (UTRC), East Hartford (U.S.) which is gratefully acknowledged. Special thanks are due to A. Glahn for the valuable discussions on the subject and the excellent collaboration during the investigation.

Nomenclature

- $A = bH$ = cross-section area (m)
- b = width of film (m)
- c = conversion factor
- D = diameter (m)
- f = sample frequency (1/s)
- EF = entrainment fraction
- F = force (N)
- Fr = Froude number
- h = thickness, distance (m)
- H = height of duct (m)
- l = length (m)
- LFD = laser focus displacement meter
- \dot{m} = mass flow rate (kg/s)
- n = refraction index
- On = Ohnesorge number
- P = perimeter of duct (m)
- p = pressure (Pa)
- Re = Reynolds number
- u = velocity (m/s)
- $u_f^* = \dot{V}_f / A$ = superficial velocity (m/s)
- T = temperature (K)
- \dot{V} = volume flow rate (m³/s)
- We = Weber number

Greek Symbols

- α = aperture angle, angle of inclination (deg)
- λ = wavelength (m)
- λ, ζ = dimensionless film length
- ν = kinematic viscosity (mm²/s)
- σ = surface tension (N/m)

Indices

- dr = droplet
- f = film
- F = friction
- g = gas
- G = gravity
- h = hydraulic
- l = inertia
- S = surface tension
- tot = total
- ∞ = fully developed
- * = modified parameter

References

- [1] Glahn, A., Busam, S., Blair, M. F., Allard, K. L., and Wittig, S., 2000, "Droplet Generation by Disintegration of Oil Films at the Rim of a Rotating Disk," 45th ASME Paper 2000-GT-279.
- [2] Glahn, A., Busam, S., and Wittig, S., 1997, "Local and Mean Heat Transfer Coefficients along the Internal Housing Walls of Aero Engine Bearing Chambers," ASME Paper 97-GT-261.
- [3] Busam, S., Glahn, A., and Wittig, S., 1999, "Internal Bearing Chamber Wall Heat Transfer as a Function of Operating Conditions and Chamber Geometry," ASME J. Eng. Gas Turbines Power, **122**, pp. 314–320.

- [4] Hewitt, G. F., and Taylor, N. S., 1970, *Annular Two-Phase Flow*, Pergamon Press, Oxford, UK.
- [5] van Rossum, J. J., 1959, "Experimental Investigation of Horizontal Film Flow," *Chem. Eng. Sci.*, **11**, pp. 35–52.
- [6] Ishii, M., and Grolmes, M. A., 1975, "Inception Criteria for Droplet Entrainment in Two-Phase Concurrent Film Flow," *AIChE J.*, **21**(2), pp. 308–318.
- [7] Woodmansee, D. E., and Hanratty, T. J., 1969, "Mechanism for the Removal of Droplets from a Liquid Surface by a Parallel Air Flow," *Chem. Eng. Sci.*, **24**, pp. 299–307.
- [8] Spedding, P. L., Watterson, J. K., Raghuanthan, S. R., and Ferguson, M. E. G., 1998, "Two-Phase Co-Current Flow in Inclined Pipe," *Int. J. Heat Mass Transf.*, **41**, pp. 4205–4228.
- [9] Lee, C. K., and Mjani, A. M., 1995, "Enhancement of Droplet Entrainment From Liquid Film Flowing Over Horizontal Ribbed Surfaces," *Proceedings 1st Int. Symp. on Two-Phase Modelling and Experimentation*, G.-P. Celata and R. K. Shah, eds, Edizione ETS, Pisa, **1**, pp. 143–148.
- [10] Azzopardi, B. J., 1997, "Drops in Annular Two-Phase Flow," *Int. J. Multiphase Flow*, **23**, pp. 1–53.
- [11] Azzopardi, B. J., Zaidi, S. H., and Jepson, D. M., 1997, "Entrained Fraction in Inclined Annular Gas/Liquid Flow," *Proceedings of the ASME Fluid Eng Division*, ASME, New York, **244**, pp. 69–76.
- [12] Hewitt, G. F., 1978, *Measurement of Two Phase Flow Parameters*, Academic Press, London.
- [13] Samenfink, W., Elsäßer, A., Wittig, S., and Dullenkopf, K., 1996, "Internal Transport Mechanisms of Shear-Driven Liquid Films," *Proceedings of the Eighth International Symposium on Applications of Laser Techniques to Fluid Mechanics*, Lisbon, Portugal, July 8–11.
- [14] Takamasa, T., Tamura, S., and Kobayashi, K., 1998, "Interfacial Waves on a Film Flowing Down Plate Wall in an Entry Region Measured With Laser Focus Displacement Meters," 3rd International Conference on Multiphase Flow, Lyon, France, June 8–12.
- [15] Samenfink, W., 1997, "Fundamental Study of the Interaction of Droplets and Shear-Driven Liquid Films," Ph.D. thesis, Institute of Thermal Turbomachinery, University Karlsruhe, Germany.
- [16] Fujii, T., Asano, H., Takenaka, N., and Yamada, H., 1998, "The Liquid Film Structure in a Two-Phase Gas-Liquid Annular Flow," 3rd International Conference on Multiphase Flow, Lyon, France, June 8–12.
- [17] Busam, S., Ebner, J., and Wittig, S., 2001, "An Experimental Study of Liquid Film Thickness in Annular Air/Oil Flow in a Vertical Pipe Using a Laser Focus Displacement Meter," 46th ASME Paper 2001-GT-116.
- [18] Kataoka, I., Ishii, M., and Mishima, K., 1983, "Generation and Size Distribution of Droplet in Annular Two-Phase Flow," *Trans. ASME*, **105**, pp. 230–238.
- [19] Ishii, M., and Mishima, K., 1989, "Droplet Entrainment Correlation in Annular Two-Phase Flow," *Int. J. Heat Mass Transf.*, **32**(10), pp. 1835–1845.
- [20] Cousins, L. B., Denton, W. H., and Hewitt, G. F., 1965, "Liquid Mass Transfer in Annular Two-Phase Flow," *Symposium on Two-Phase Flow*, Exeter, U.K., **1** (Paper C4).

A Unique Approach for Thermoeconomic Optimization of an Intercooled, Reheat, and Recuperated Gas Turbine for Cogeneration Applications

R. Bhargava

Universal Ensco, Inc.,
1811 Bering Drive
Houston, TX 77057

A. Peretto

DIEM—University of Bologna,
Viale Risorgimento 2,
Bologna 40136, Italy

In the present paper, a comprehensive methodology for the thermoeconomic performance optimization of an intercooled reheat (ICRH) gas turbine with recuperation for cogenerative applications has been presented covering a wide range of power-to-heat ratio values achievable. To show relative changes in the thermoeconomic performance for the recuperated ICRH gas turbine cycle, results for ICRH, recuperated Brayton and simple Brayton cycles are also included in the paper. For the three load cases investigated, the recuperated ICRH gas turbine cycle provides the highest values of electric efficiency and Energy Saving Index for the cogenerative systems requiring low thermal loads (high power-to-heat ratio) compared to the other cycles. Also, this study showed, in general, that the recuperated ICRH cycle permits wider power-to-heat ratio range compared to the other cycles and for different load cases examined, a beneficial thermodynamic characteristic for the cogeneration applications. Furthermore, this study clearly shows that implementation of the recuperated ICRH cycle in a cogeneration system will permit to design a gas turbine which has the high specific work capacity and high electric efficiency at low value of the overall cycle pressure ratio compared to the other cycles studied. Economic performance of the investigated gas turbine cycles have been found dependent on the power-to-heat ratio value and the selected cost structure (fuel cost, electric sale price, steam sale price, etc.), the results for a selected cost structure in the study are discussed in this paper. [DOI: 10.1115/1.1476928]

Introduction

With the deregulation in power generation industry worldwide, the power generation market is becoming increasingly dynamic and competitive. In recent years, the observed performance enhancements in the gas turbine technologies can be attributed to the phenomenal advancements in the fields of aerodynamics, materials and coatings, blade cooling, and fabrication technologies. These technologies have allowed to achieve the turbine inlet temperature (TiT) value of 1500°C (2732°F) and simple cycle efficiency 40% and more ([1,2]). The use of the hybrid gas turbine technology, where both metal and ceramics are used for parts subjected to high temperature, with 8 MW capacity gas turbine under development for cogeneration applications is another approach to achieve high cycle efficiency ([3]).

An alternative approach to improve the gas turbine cycle efficiency which has been investigated and/or implemented is to modify the Brayton cycle by adopting intercooled compression or reheat expansion or recuperation or the combinations of one or more modifications. These modified gas turbine cycles, sometimes also referred as “complex cycles,” have been analyzed in the past ([4–10]). However, limited amount of studies have been made on the thermoeconomic performance evaluation of an intercooled, reheat, and recuperated gas turbine in cogeneration applications.

In a recent study by Bhargava et al. [11] a comprehensive ther-

moeconomic analysis of the recuperated intercooled reheat (ICRH) gas turbine cycle in cogeneration applications revealed some interesting results, which are summarized below:

1 It was shown that for the power-to-heat ratio value selected for each load case, the maximum values of cycle efficiency and Energy Saving Index could be realized with the use of recuperated ICRH gas turbine cycle in a cogeneration system compared to the other cycles (namely, ICRH, recuperated Brayton and Brayton cycles).

2 For a given load and the selected value of power-to-heat ratio, the recuperated ICRH gas turbine-based cogeneration system obtained the maximum specific work capacity compared to the other cycles investigated except for the small load case, implying a smaller size (overall dimensions) gas turbine system. For the small load case ($P_{el}=5$ MW) examined, the nonrecuperated ICRH cycle based cogeneration system obtained higher value of the specific work compared to the other cycles studied.

3 The economic analysis, conducted for one power-to-heat ratio value, suggested that a high size ($P_{el}=100$ MW) cogenerative system utilizing nonrecuperated ICRH gas turbine will provide better return on the investment compared to the other investigated gas turbine cycles.

4 For a given load condition (three load cases investigated), each investigated cycle was found to have a limited range of the power-to-heat ratio values achievable. This implied that some power-to-heat ratio values, at a given load, may not be achievable for all the cycles.

The importance of power-to-heat ratio in comparing different cycles used in cogeneration system was appropriately identified by Bhargava et al. [11]. To fairly and appropriately compare co-

Contributed by the International Gas Turbine Institute (IGTI) of THE AMERICAN SOCIETY OF MECHANICAL ENGINEERS for publication in the ASME JOURNAL OF ENGINEERING FOR GAS TURBINES AND POWER. Paper presented at the International Gas Turbine and Aeroengine Congress and Exhibition, New Orleans, LA, June 4–7, 2001; Paper 01-GT-206. Manuscript received by IGTI, December 2000, final revision, March 2001. Associate Editor: R. Natole.

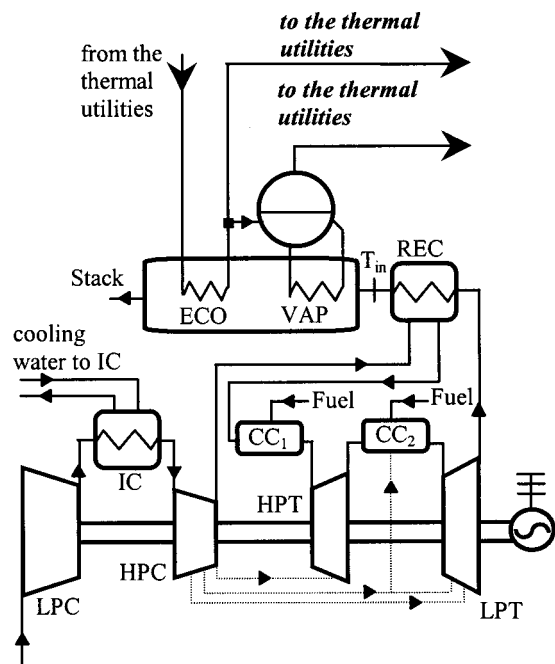


Fig. 1 Schematic layout of the recuperated ICRH gas turbine in cogenerative application (dotted lines represent GT cooling flow streams)

generation systems utilizing different cycles, it was noted that their power-to-heat ratio must be the same. However, the earlier investigation by the authors ([11]) did not address the effects of power-to-heat ratio on the thermo-economic performance for a cogeneration system utilizing recuperated ICRH gas turbine cycle. Additionally, it is not evident from the earlier work ([11]) if the economic results observed for a large size cogeneration system, summarized in the observation 3 above, will be valid for medium and small size cogeneration systems.

Therefore, emphasis of the present paper is to conduct a comprehensive thermo-economic optimization analysis of the recuperated ICRH gas turbine cycle in cogenerative applications.

To realize the aforesaid objective, the thermo-economic optimization analyses of the cogenerative systems equipped with recuperated ICRH gas turbine cycle have been performed for the three load cases.

The effects of fuel cost, electric sale price, and steam sale price on the economics of recuperated ICRH cycle-based cogeneration systems covering a wide range of power-to-heat ratio values achievable have been examined. It must be mentioned that the thermo-economic analyses results for the nonrecuperated ICRH, recuperated Brayton and simple Brayton cycles are included in the paper for comparison purpose and also to show relative thermo-economic performance changes with the use of recuperated ICRH gas turbine in cogeneration applications.

Thermodynamic Analysis

The Plant Layout. Figure 1 shows a schematic layout of the single-spool recuperated ICRH gas turbine cycle in a cogenerative application. The thermodynamic analyses of cogeneration systems utilizing recuperated ICRH gas turbine were performed by adopting the assumptions and the methodology described by Bhargava et al. [11].

In particular, these analyses have been performed for the three gas turbine sizes: 5 MW, 20 MW, and 100 MW electric power output; and each of the gas turbine is defined by the values of key design parameters as reported in Table 1. The values of polytropic efficiency parameters for compressors and turbines, given in Table 1, are

Table 1 Key design parameters for the three gas turbine sizes investigated

Size (MW)	TiT (°C)	η_{pc}	η_{pt}
5	1050	0.88	0.87
20	1200	0.90	0.89
100	1350	0.91	0.90

representative of the selected gas turbine sizes based on the current technology while operating at the design-load condition. The same holds true for the selected values of turbine inlet temperature given in Table 1. The thermodynamic analyses results presented here assumes no supplementary firing of heat recovery steam generator. This approach is taken to limit the number of parameters affecting performance evaluation of an already complex cycle. The thermal host is supplied with two thermal streams at a pressure of 1.7 MPa (247 Psig) having different enthalpy content: the first stream at the economizer outlet as a hot water at 199°C; and the second stream, at the vaporizer outlet as saturated steam (1.7 MPa at 204°C).

Methodology. As mentioned before, the methodology to find the best value of Energy Saving Index (ESI_B), for a given cycle and at a given value of power-to-heat ratio, has been described by Bhargava et al. [11]. The key steps of the above-mentioned methodology, for a given cycle and load case, are briefly summarized below:

- A value of the exhaust gas temperature (T_{in} , see Fig. 1) at the inlet of heat recovery steam generator (HRSG) is set.
- For an assigned overall cycle pressure ratio (β_{TOT}) and for the selected value of T_{in} , the values of electric efficiency and ESI versus specific power are evaluated. In this case, for every low pressure compressor (LPC) pressure ratio the corresponding value of high pressure turbine (HPT) pressure ratio is found within the imposed bounds of β_{TOT} and T_{in} .
- Based on the above discussed two steps, for an assigned T_{in} value, it is possible to get many cycle configurations (for each β_{TOT} value). Since for a cogeneration system, it would be important to consider configurations corresponding to the maximum value of ESI (ESI_{Max}), for each β_{TOT} the values of ESI_{Max} and the corresponding electric efficiency are then evaluated (by means of the above steps). Among all the β_{TOT} values and for the assigned value of T_{in} , the best value of ESI_{Max} (ESI_B) is selected. Subsequently, the values of electric efficiency and P_{el}/Q_{th} ratio are obtained corresponding to the ESI_B value identified.
- The thermodynamic performance for different values of T_{in} are subsequently calculated by following the above steps and finding the corresponding values of ESI_B , electric efficiency and P_{el}/Q_{th} ratio.

The results obtained, by using the above described thermodynamic analysis steps, for medium size ($P_{el} = 20$ MW) cogeneration systems using recuperated ICRH gas turbine cycle are shown in Fig. 2. It must be noted that the main purpose of including Fig. 2 here is to show the results of steps used in identifying plausible configurations for a given cycle at a given load.

For each curve (at a selected value of T_{in}), the minimum and maximum values of cycle overall pressure ratio achievable are reported in Fig. 2. It must be noted that, for comparison purpose, the results for the recuperated Brayton cycle are also included in Fig. 2. It is evident that a significant (approximately three percentage point) increase in the value of ESI_B can be achieved with the use of recuperated ICRH gas turbine cycle compared to the recuperated Brayton cycle.

For the recuperated ICRH cycle at a given load, Fig. 2 also shows that the values of ESI_{Max} and subsequently ESI_B increase as the values of T_{in} decrease. For a given load, this observed trend is associated with the increase in power-to-heat ratio and η_{el} with the decrease in T_{in} values. Furthermore, there exists an optimum

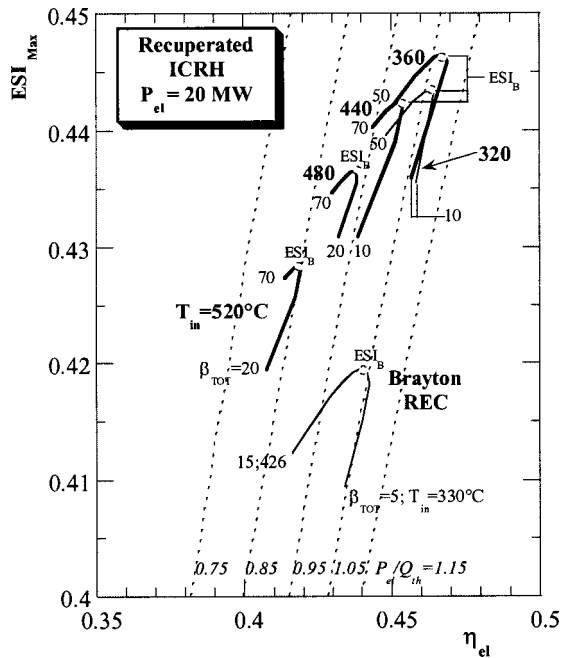


Fig. 2 ESI_{Max} versus η_{el} for different β_{TOT} as a function of T_{in} for medium size recuperated ICRH gas turbine-based cogeneration systems

value of T_{in} , for the recuperated ICRH cycle at a given load, below which the values of ESI_{Max} and ESI_B decrease (see Fig. 2). Since, ESI_{Max} (or ESI_B) is a function of η_{el} and η_{th} , this implies decrease in the values of η_{el} and η_{th} , for T_{in} value less than its optimum value which can be clearly seen in Fig. 2.

It must be mentioned that realizing manufacturing difficulties which may be encountered with the use of very high overall cycle pressure ratio, in the present study the cycle configurations are selected by limiting the overall cycle pressure ratio value to 50. Therefore, in such cases where for a given T_{in} the overall cycle pressure ratio corresponding to ESI_B was higher than 50, the selected value of ESI_B equals the value of ESI_{Max} corresponding to the overall cycle pressure ratio of 50.

Thermodynamic Analyses Results. Using the thermodynamic optimization analysis steps described above, the investigation was performed for the three load cases reported in Table 1, the results of which are discussed here. It must be reiterated that the values of electric efficiency and the P_{el}/Q_{th} ratio, presented in various figures, are those corresponding to the cycle configurations supplying the ESI_B values as explained in step 3 of the methodology.

For the high size ($P_{el}=100$ MW) cogeneration systems, it is evident that a recuperated ICRH gas turbine-based cogeneration system provides higher value of electric efficiency at all the values of power-to-heat ratios considered in the present study (see Fig. 3). This trend of electric efficiency versus power-to-heat ratio is also true for the other two load cases investigated in the present study as shown in Figs. 4 and 5.

The main reason for this observed higher thermodynamic performance can be attributed to the fact that in a recuperated ICRH gas turbine, higher air temperature exists at entry to the high pressure combustor (CC1) because of waste heat recovery through the recuperator, and results in the decrease in fuel consumption in the combustor CC1.

For the high size ($P_{el}=100$ MW) cogeneration systems using the Brayton recuperated cycle, the variation of power-to-heat ratio is found small (1.025 to 1.094) compared to the other cycles investigated as shown in Fig. 3. The optimization results show weak influence of the variation of overall cycle pressure ratio on the

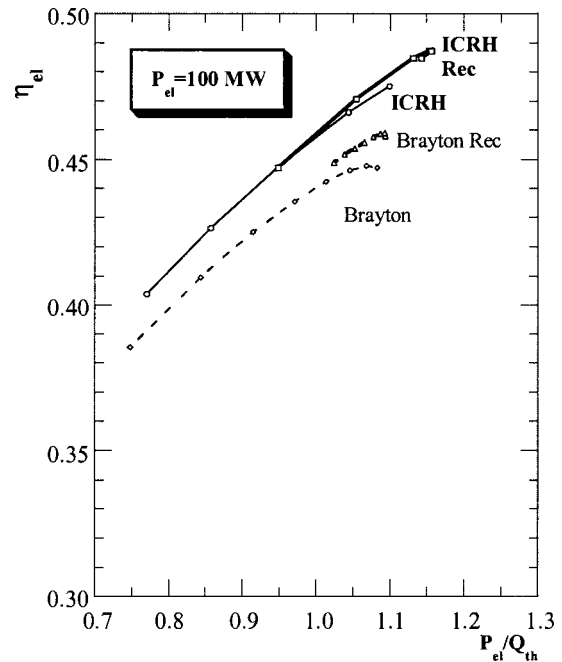


Fig. 3 η_{el} versus P_{el}/Q_{th} for the four cycles considered (high size—100 MW)

values of power-to-heat ratio, ESI_{Max} and η_{el} . One of the plausible reasons is a very small change in T_{in} values (395°C to 444°C) as the overall cycle pressure ratio changed from 8 to 15.

It is interesting to note that the recuperated and nonrecuperated ICRH gas turbine-based cogeneration systems provide similar thermodynamic performance over a wide range of power-to-heat ratio for the three load cases examined in the study (see Figs. 3–5).

However, the optimum value of power-to-heat ratio is higher for the cogeneration systems using a recuperated ICRH gas tur-

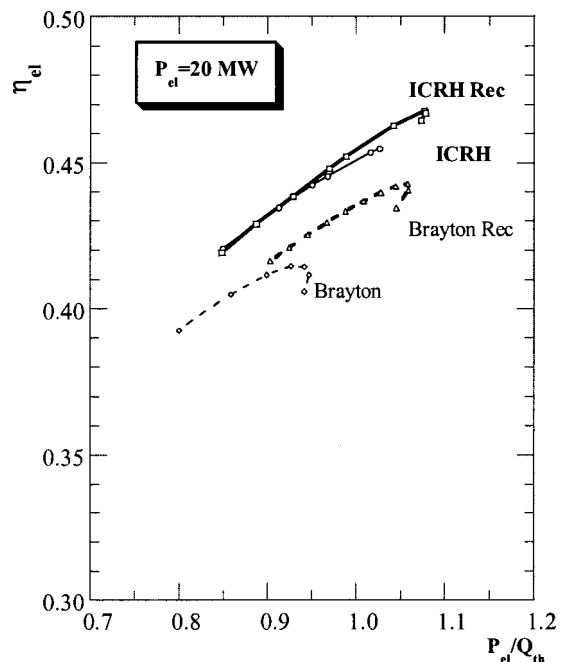


Fig. 4 η_{el} versus P_{el}/Q_{th} for the four cycles considered (medium size—20 MW)

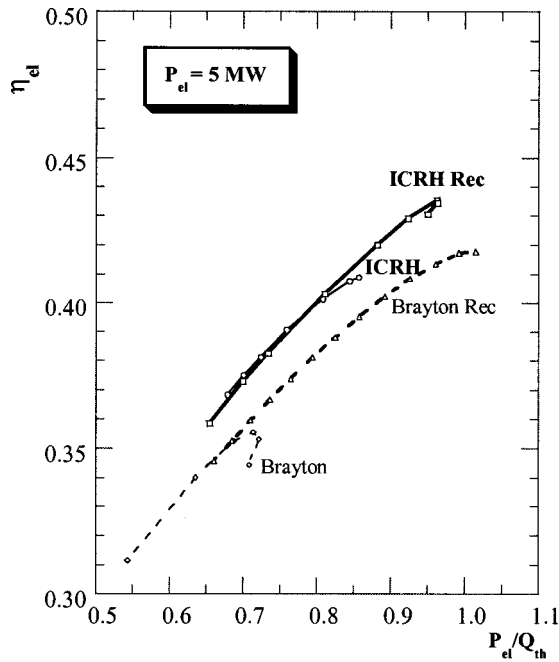


Fig. 5 η_{el} versus P_{el}/Q_{th} for the four cycles considered (low size—5 MW)

bine, except for low load case as is evident from Fig. 5, compared to the cogeneration systems using a nonrecuperated ICRH gas turbine including the other cycles studied. The high value of P_{el}/Q_{th} ratio obtainable with the recuperated ICRH gas turbine-based cogeneration system compared to the cogeneration systems using nonrecuperated ICRH and Brayton cycles examined is essentially associated with the use of the recuperator which decreases temperature (T_{in}) of the gas at the HRS inlet and consequently decreases thermal energy available at the HRS inlet and to the thermal utility.

For the medium and small load cases, the Brayton cycle is found to have comparatively small power-to-heat ratio range as shown in Figs. 4 and 5. This suggests that the Brayton cycle will be better suited in cogeneration applications with high thermal load requirements compared to the other cycles.

The advantage of using recuperated ICRH gas turbine in a cogeneration application is clearly evident from the variation of best values of Energy Saving Index (ESI_B), a direct measure of fuel savings in a cogeneration plant, versus power-to-heat ratio as shown in Figs. 6–8 for the three load cases. It is clearly observed that a significant amount of energy savings can be achieved over a wide range of power-to-heat ratio values by employing nonrecuperated or recuperated ICRH cycle compared to the other cycles. Furthermore, the variation of ESI_B values reveals that use of the recuperated ICRH gas turbine in a cogeneration system will provide higher values of energy savings for plants with low thermal power (high P_{el}/Q_{th} ratio) needs, particularly, in comparison to the simple Brayton or recuperated Brayton cycle.

It is evident, based on the thermodynamic analyses results presented here (particularly, see Figs. 6–8), that the recuperated ICRH gas turbine will be more beneficial in cogeneration applications especially with low-power generation capacity as indicated by comparatively higher increase in the ESI_B value at a given value of P_{el}/Q_{th} ratio with respect to the Brayton cycle. The comparison of ESI_B values for the three load cases, at a fixed value of P_{el}/Q_{th} ratio, suggests somewhat higher improvement in fuel savings for the recuperated ICRH cycle with respect to the Brayton cycle for a low load case system as shown in Fig. 9. It may be noted that to achieve appropriate comparison of ESI_B

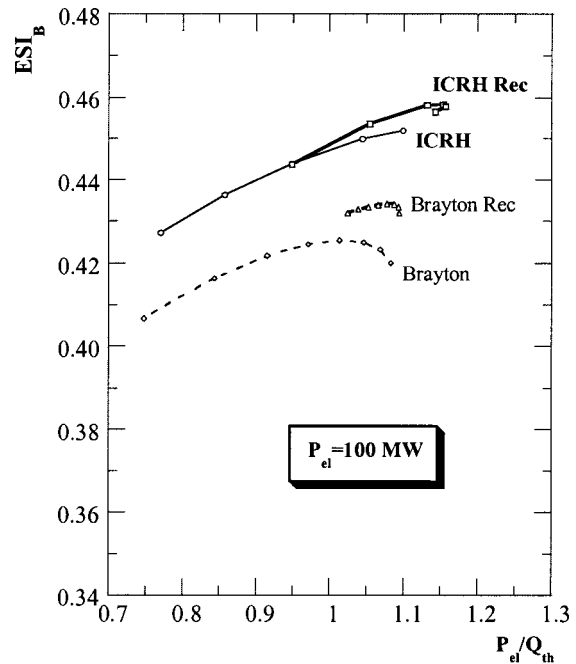


Fig. 6 ESI_B versus P_{el}/Q_{th} for the four cycles considered (high size—100 MW)

values for all the cycles at a given load, the value of P_{el}/Q_{th} used in Fig. 9 corresponds to the maximum value of ESI_B achieved for the Brayton cycle.

In comparison to the other cycles studied and for all the load cases examined, the recuperated ICRH cycle shows higher thermal efficiency over the range of power-to-heat ratio values achievable as is evident for midsize ($P_{el}=20$ MW) case shown in Fig. 10.

For all the load cases examined, it is further observed that the recuperated ICRH cycle achieves the highest value of specific

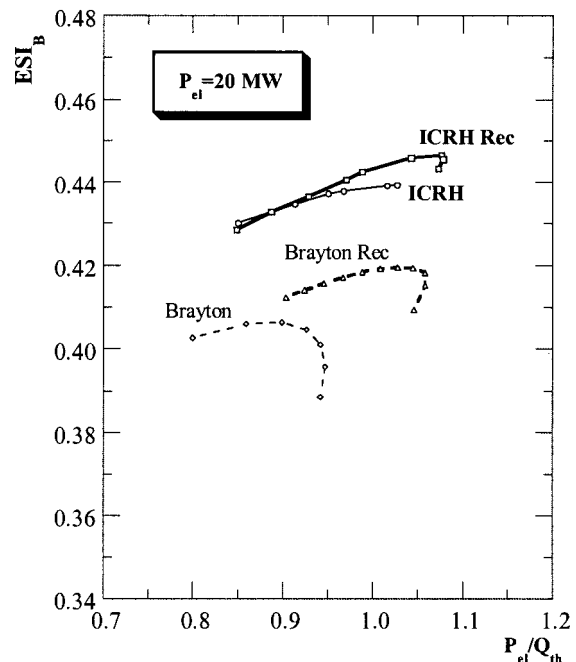


Fig. 7 ESI_B versus P_{el}/Q_{th} for the four cycles considered (medium size—20 MW)

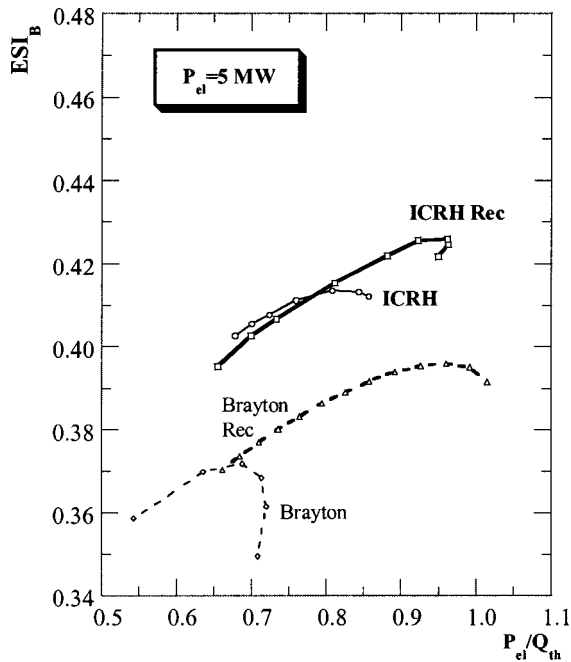


Fig. 8 ESI_B versus P_{el}/Q_{th} for the four cycles considered (low size—5 MW)

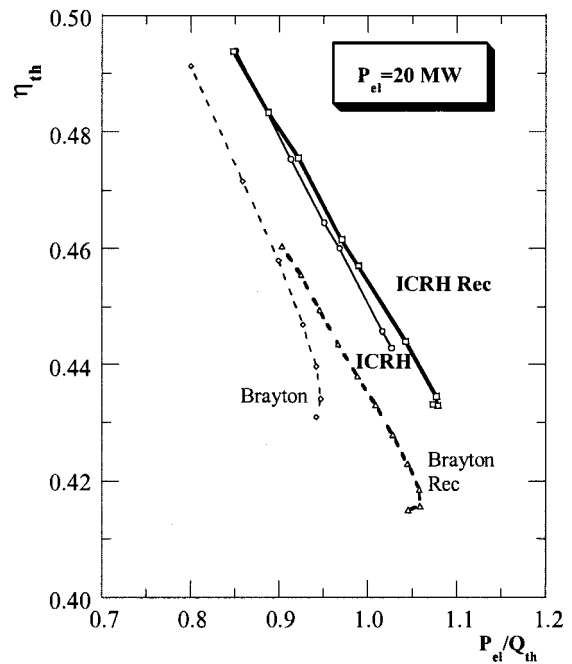


Fig. 10 η_{th} versus P_{el}/Q_{th} for the four cycles considered (medium size—20 MW)

work (see Fig. 11) at a given value of power-to-heat ratio compared to the other cycles with few exceptions. This clearly implies that, for a given value of power-to-heat ratio and a load value (or TIT), the recuperated ICRH cycle will allow to reduce size (dimensions) of the machine. The exception is that for some load cases, there exists a power-to-heat ratio value below which ICRH cycle will have higher value of specific work compared to the recuperated ICRH cycle as can be seen in Fig. 11.

For all the load cases examined, the recuperated ICRH cycle provides higher electric efficiency, compared to the other cycles, while maintaining a low value of the overall cycle pressure ratio as is evident from Fig. 12. This suggests that implementation of the recuperated ICRH cycle in a cogeneration system will allow to design a machine which has high work density and high electric efficiency at low value of the overall pressure ratio (see Table 2) compared to the other cycles. Furthermore, as evident from Fig. 12, the recuperated ICRH cycle shows a good amount of gain (for example, 8% at $\beta_{TOT}=20$ for a low load case) in electric effi-

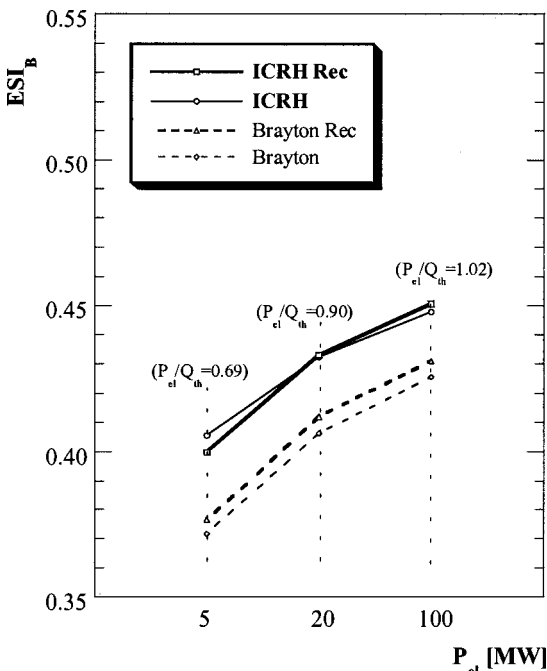


Fig. 9 ESI_B versus P_{el} for the four cycles and for the three load cases considered (P_{el}/Q_{th} ratio constant for each load case and equal to the value maximizing ESI_B for the Brayton cycle)

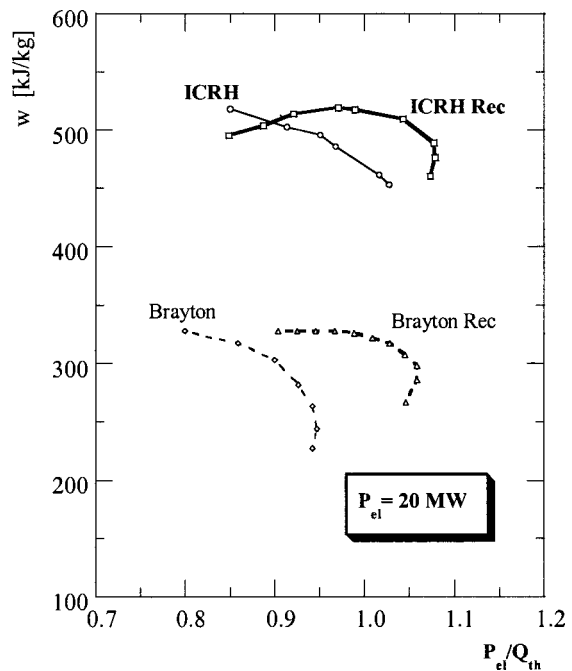


Fig. 11 Specific work versus P_{el}/Q_{th} for the four cycles considered (medium size—20 MW)

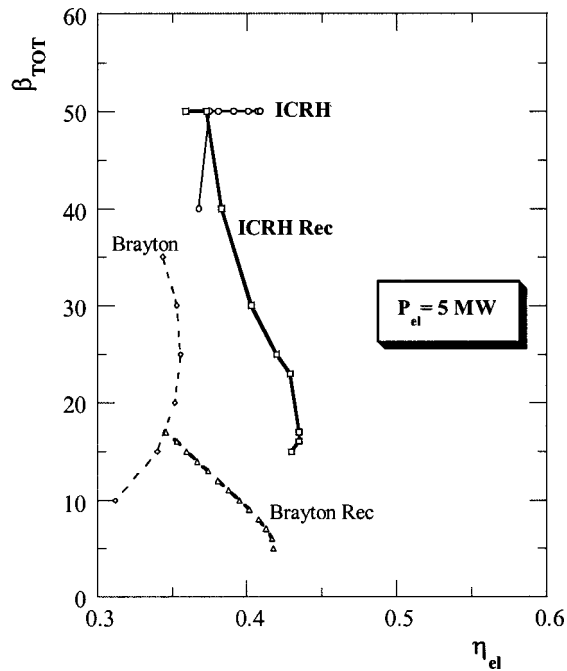


Fig. 12 β_{TOT} versus η_{el} for the four cycles considered (low size—5 MW)

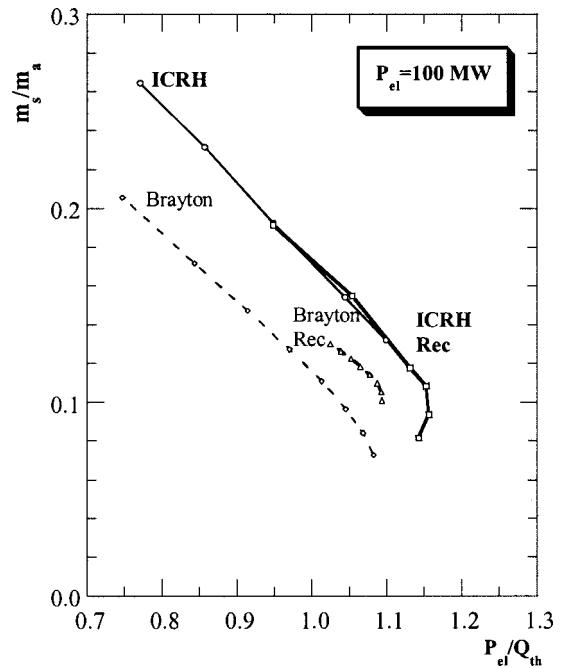


Fig. 13 m_s/m_a versus P_{el}/Q_{th} for the four cycles considered (high size—100 MW)

ciency at a low value of the overall cycle pressure ratio in comparison to the simple Brayton cycle (see also Table 2). For the three load cases examined, the optimum (corresponding to the maximum value of electric efficiency for each load case—see Figs. 3–5) values of the key thermodynamic parameters for the four cycles studied are summarized in Table 2.

The low optimum values of the overall cycle pressure ratio for the recuperated ICRH cycle compared to the ICRH cycle for all the three load cases studied are evident from Table 2. This study also shows that for the power-to-heat ratio values for which ICRH cycle becomes comparative to the recuperated ICRH cycle, ICRH cycle requires a high value of the overall cycle pressure ratio (see Fig. 12). Similarly, to achieve high value of electric efficiency for the simple Brayton cycle, for a given load case, high value of the overall cycle pressure ratio is required as is evident from Fig. 12 and Table 2.

In the design and optimization of a cogeneration system, the knowledge of steam produced is an important parameter. A comparison of steam generated for different cycles examined in the

present study for high, medium and small size cogeneration systems are shown in Figs. 13, 14, and 15, respectively.

For appropriate comparison of the four cycles investigated, it was necessary to normalize the steam mass flow rate (m_s) by the air mass flow rate at the gas turbine inlet (m_a). For the load cases examined, the normalized steam flow rate values are observed to be higher for the recuperated ICRH gas turbine cycle over a wide range of P_{el}/Q_{th} ratio compared to the other cycles investigated. This observed trend can be attributed, for a given value of P_{el}/Q_{th} and gas turbine size, to high specific work capacity associated with the recuperated ICRH cycle compared to the other cycles.

Furthermore, the variation of actual steam flow rate for four cycles shows different results in comparison to the normalized steam flow as is evident from Fig. 16. For all the three load cases, except small size case ($P_{el}=5$ MW), the trend in variation of the actual steam mass flow rate is as anticipated, namely lowest steam flow rate for the recuperated ICRH cycle in comparison to the

Table 2 Optimum thermodynamic parameters—full-load cases

	η_{el} (Max)	ESI _B	W (kJ/kg)	P_{el}/Q_{th}	β_{TOT}	β_{LPC}	β_{HPT}
High Size							
ICRH Rec	0.487	0.458	575	1.15	30	4.6	1.9
ICRH	0.475	0.452	540	1.01	50	3.0	1.6
Brayton Rec	0.459	0.434	385	1.09	10	-	-
Brayton	0.448	0.423	323	1.07	50	-	-
Medium Size							
ICRH Rec	0.467	0.445	488	1.08	25	4.8	1.9
ICRH	0.455	0.439	455	1.03	50	3.2	1.5
Brayton Rec	0.440	0.415	299	1.06	7	-	-
Brayton	0.414	0.405	282	0.93	35	-	-
Low Size							
ICRH Rec	0.435	0.426	385	0.96	17	4.2	2.0
ICRH	0.409	0.412	333	0.86	50	3.8	1.5
Brayton Rec	0.413	0.396	238	0.96	7	-	-
Brayton	0.356	0.368	217	0.71	25	-	-

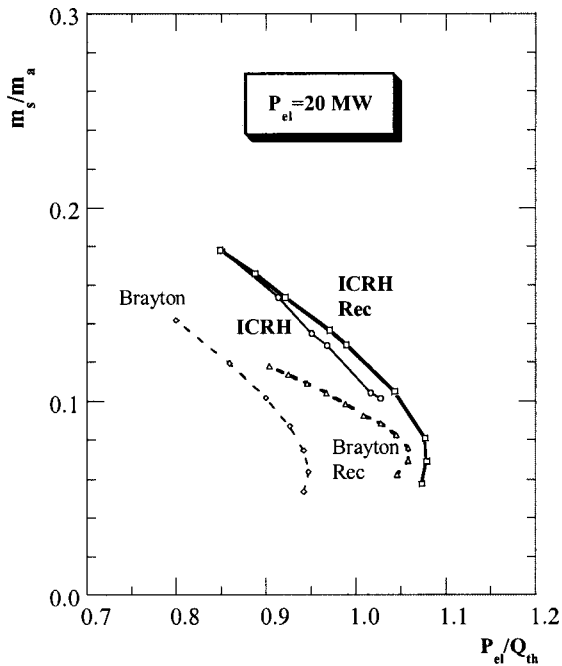


Fig. 14 m_s/m_a versus P_{el}/Q_{th} for the four cycles considered (medium size—20 MW)

other cycles. For small size case, the amount of steam generated is lowest for the cogeneration system using ICRH cycle compared to the other cycles.

It may be noted that the amount of actual steam generated will have an important impact on the economic analysis as will be evident from the discussion presented in the Economic Analysis section.

In summarizing the thermodynamic optimization analyses, it is evident that a cogeneration system using the recuperated ICRH gas turbine cycle can achieve maximum thermodynamic perfor-

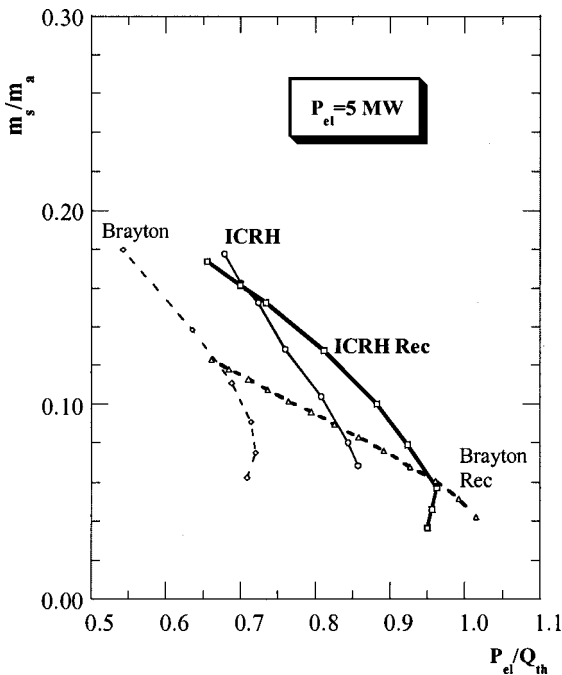


Fig. 15 m_s/m_a versus P_{el}/Q_{th} for the four cycles considered (low size—5 MW)

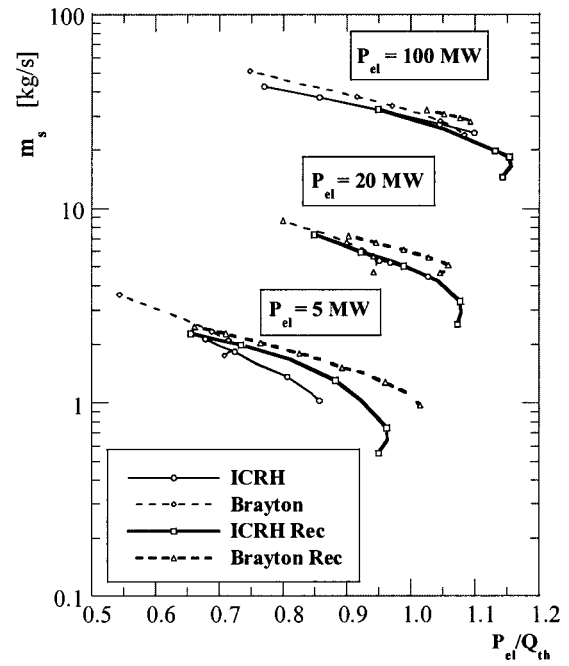


Fig. 16 m_s versus P_{el}/Q_{th} for the four cycles and for the three load cases

mance (indicated by high values of electric efficiency and Energy Saving Index) at the highest value of P_{el}/Q_{th} ratio.

Also, for a given load case, the highest amount of normalized steam flow can be produced corresponding to the lowest value of P_{el}/Q_{th} ratio (representing maximum thermal power) for the recuperated ICRH gas turbine cycle-based cogeneration system. This study clearly shows that implementation of the recuperated ICRH cycle in a cogeneration system will allow to design a gas turbine which has high work density and high electric efficiency at low value of the overall pressure ratio compared to the other cycles.

A careful economic analysis will determine if the cogeneration systems with high thermodynamic performance materialize into economically viable systems. The results of economic analyses for different cycles at the three load conditions are discussed next.

Economic Analysis

The economic analysis is performed relative to the performance and cycle configurations identified using thermodynamic optimization analysis and the results presented in Figs. 3–8. The values of main economic parameters, assumed for the economic analysis, are presented in Table 3.

The economic analyses have been performed for different combinations of the fuel cost, electric sale price and steam sale price. Because of the space limitations, only selective charts have been included here. For a fixed values of the fuel cost (\$3/MSCF) and steam sale price (\$7/kpph), first effects of electric sale price have been evaluated, the results for which are given in Figs. 17–22. The results for two values of electric sale price (4.5 and 5.5 Cents/kWh) are presented in the paper.

For the high load ($P_{el}=100$ MW) case, DCRR values versus P_{el}/Q_{th} ratio are reported at an electric sale price of 4.5 and 5.5 cents/kWh in Figs. 17 and 20, respectively. It is evident that the recuperated ICRH cycle provides lowest return on the investment than the other cycles in spite of the fact that it showed highest thermodynamic performance (as seen earlier in Figs. 3 and 6).

The observed poor economic performance of the recuperated ICRH cycle is mainly attributed to the increased equipment cost and the decreased revenues associated with steam generated in comparison to the other cycles.

Table 3 Main economic parameters assumed for the economic analysis

Parameter	Unit	Selected Value
Plant utilization factor	%	85
Plant economic life	years	20
Loan term	years	20
Debt interest rate	APR	15
Depreciation period	years	10
Construction period	years	1.5
Escalation rate	%	5
Fuel gas cost	\$/MSCF	3.0
Utility avoided cost	cents/kWh	4.5
Local taxes and insurance	% of total investment cost	2.5
Auxiliary power consumption	% of gross power generated	1.5
Income taxes	flat rate, % of net revenues	45

For the high load case examined, it is possible to develop an economically viable system using recuperated or nonrecuperated ICRH cycle provided the power-to-heat ratio values are equal or higher than 1.05.

For a medium size ($P_{el} = 20$ MW) cogeneration system, nonrecuperated ICRH cycle has been found economically preferable in comparison to the other cycles for the power-to-heat ratio values higher than 0.95 and a suitable electric sale price as shown in Figs. 18 and 21. Also, the recuperated ICRH cycle can be economically viable if the power-to-heat ratio is equal or higher than 1.05 and the electric sale price 5.5 Cents/kWh or higher (see Figs. 18 and 21). It is further noted that the simple Brayton cycle is limited in power-to-heat ratio range and the discount cash flow rate of return (DCRR) value decreases at a faster rate with the increase in power-to-heat ratio values compared to the other cycles (see Figs. 18 and 21). Also, the Brayton cycle based cogeneration systems show better economic performance at the lower values (less than 0.95) of power-to-heat ratio compared to the other cycles studied.

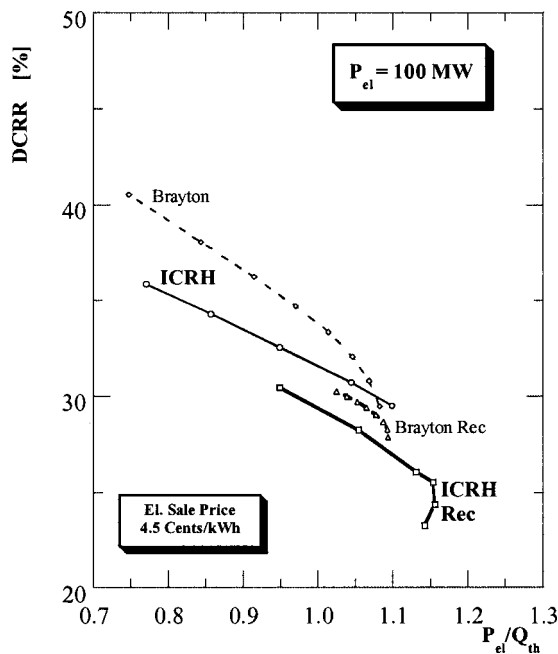


Fig. 17 DCRR versus P_{el}/Q_{th} for the four cycles considered (high size—100 MW)

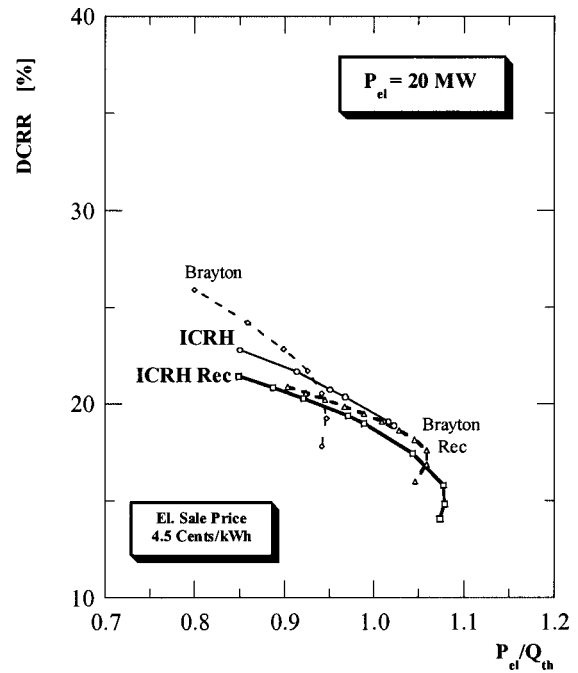


Fig. 18 DCRR versus P_{el}/Q_{th} for the four cycles considered (medium size—20 MW)

For a small-size ($P_{el} = 5$ MW) cogeneration system, a particular cycle can be selected depending on the power-to-heat ratio requirement as shown in Figs. 19 and 22. For this load case also, as was observed with the medium load case, the Brayton cycle has a narrow range of power-to-heat ratio and the DCRR values decrease at a faster rate as the power-to-heat ratio value increases compared to the other cycles. Similar to the midsize case, the Brayton cycle-based cogeneration systems for small size case

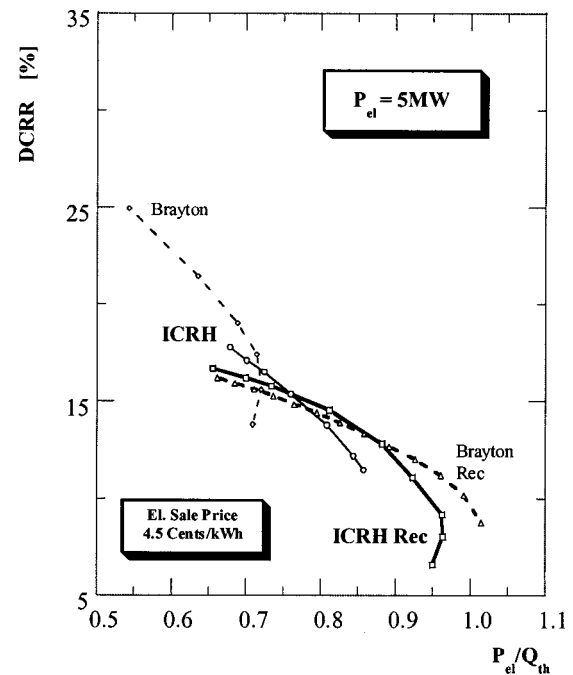


Fig. 19 DCRR versus P_{el}/Q_{th} for the four cycles considered (low size—5 MW)

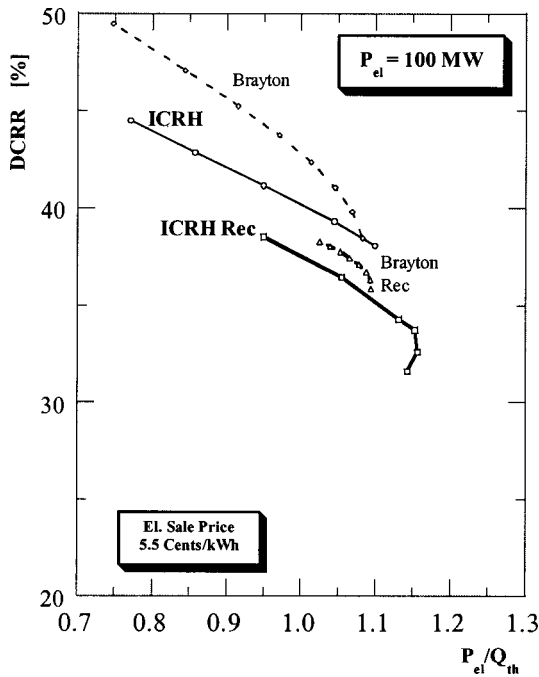


Fig. 20 DCRR versus P_{el}/Q_{th} for the four cycles considered (high size—100 MW)

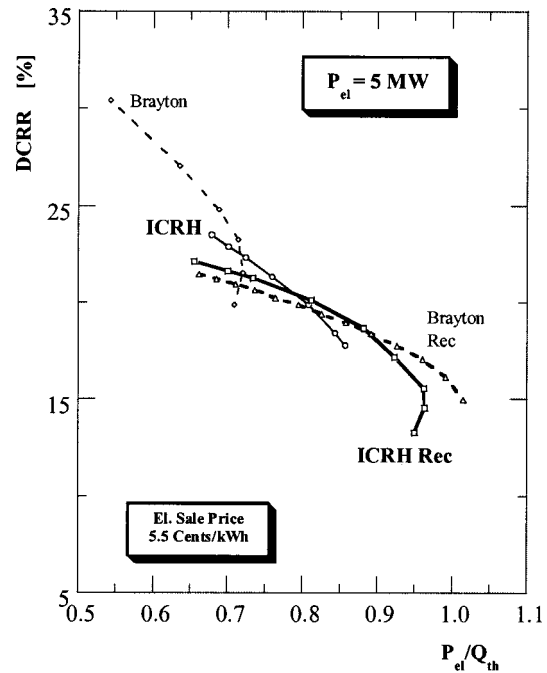


Fig. 22 DCRR versus P_{el}/Q_{th} for the four cycles considered (low size—5 MW)

($P_{el}=5$ MW) show better economic performance at the lower values (less than 0.7) of power-to-heat ratio compared to the other cycles studied.

It is quite evident that at the electric sale price of 4.5 cents/kWh for the small load case, not all the investigated cycle will be considered economically viable because of low return on the investment.

The effect of increase in fuel cost on economic performance is to reduce the values of DCRR for each cycle as shown in Fig. 23 for a high load case. The trends in variation of DCRR values are

same for different values of the fuel cost examined and the Brayton cycle shows higher values of DCRR over a wide range of power-to-heat ratio values (see Figs. 20 and 23).

The steam sale price showed more pronounced effect on the economic performance (see Fig. 24) for the small load case. Co-generation systems using recuperated ICRH and ICRH cycles can become economically viable at certain values of power-to-heat ratio. For the small load case ($P_{el}=5$ MW), the results obtained further show that the electric sale price higher than 5.5 cents/kWh

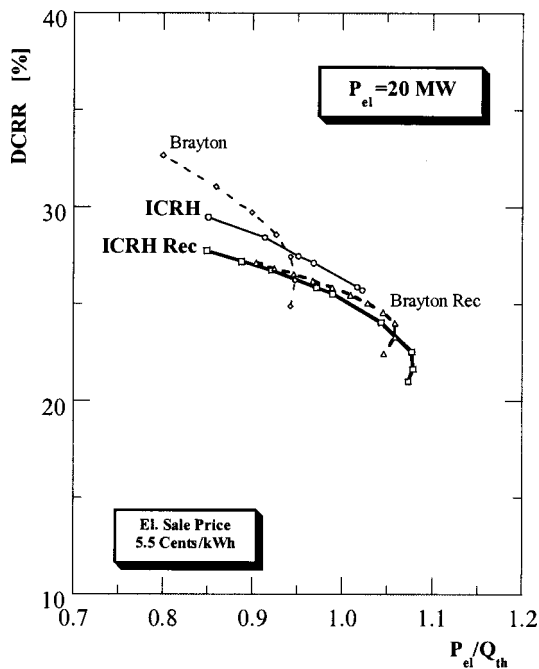


Fig. 21 DCRR versus P_{el}/Q_{th} for the four cycles considered (medium size—20 MW)

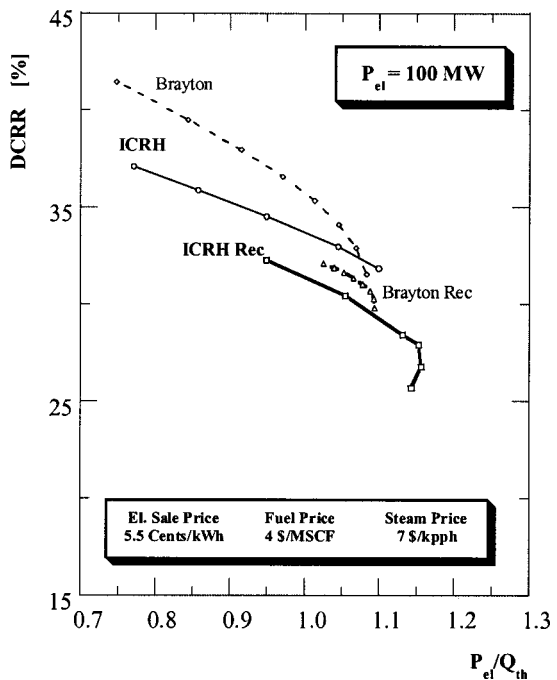


Fig. 23 DCRR versus P_{el}/Q_{th} for the four cycles considered (high size—100 MW)

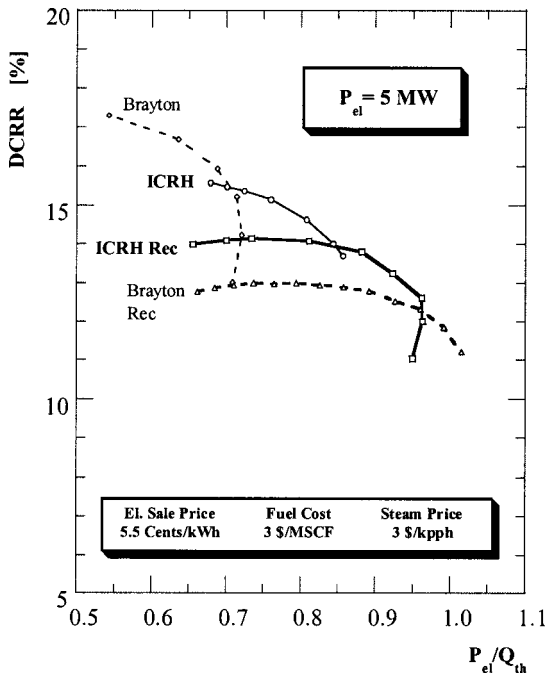


Fig. 24 DCRR versus P_{el}/Q_{th} for the four cycles considered (low size—5 MW)

will be required for the recuperated ICRH cycle based cogeneration system to be economically preferable at the high P_{el}/Q_{th} values.

Concluding Remarks

In the present paper, a comprehensive approach for the thermoeconomic performance optimization of a recuperated intercooled reheat gas turbine for cogenerative applications has been presented covering a wide range of power-to-heat ratio values achievable. In addition, effects of electric sale price, steam sale price, and fuel cost in selecting an appropriate cycle, among the four cycles investigated at a given load, have been presented. To show relative changes in the thermoeconomic performance for the recuperated ICRH gas turbine cycle, results for ICRH, recuperated Brayton and simple Brayton cycles are also included in the paper.

It is clearly observed that, for the three load cases and P_{el}/Q_{th} ratio of 0.9 or less, the recuperated and nonrecuperated ICRH gas turbine-based cogeneration systems have higher thermodynamic performance compared to the recuperated or simple Brayton cycle. Furthermore, for P_{el}/Q_{th} ratio greater than 0.9, recuperated ICRH gas turbine based cogeneration systems have the highest values of electric efficiency and Energy Saving Index compared to the other cycles for all the three load cases examined.

From the thermodynamic performance point of view, this study suggests that the recuperated ICRH gas turbine will be more suitable for small size cogeneration systems (5 MW or less) as indicated by the higher incremental value of ESI_B with respect to the simple Brayton cycle (about three percentage point).

For the load cases examined, the recuperated ICRH gas turbine cycle permits wider power-to-heat ratio range compared to nonrecuperated ICRH and Brayton cycles, a characteristic beneficial to the cogeneration applications.

This study clearly shows that implementation of the recuperated ICRH cycle in a cogeneration system will permit to design a gas turbine which has the high specific work capacity and high electric efficiency at low value of the overall cycle pressure ratio compared to the other cycles studied.

For the medium and low load cases, the Brayton cycle has a narrow range of power-to-heat ratio, and the values of DCRR

decrease rapidly with the increase in the value of P_{el}/Q_{th} ratio. This implies that the Brayton cycle will be better suited in cogeneration applications with high thermal load requirements compared to the other cycles.

The advantages of recuperated ICRH cycle are also seen in the normalized steam mass flow rate produced (referred to gas turbine inlet air mass flow rate) which has the highest value in comparison to the other cycles for different load cases examined and at different values of P_{el}/Q_{th} ratio. This implies that for a given air flow rate and power requirements, recuperated ICRH gas turbine will allow higher steam flow production.

For the load cases investigated, ICRH and recuperated ICRH-based cogeneration systems will be economically preferable, compared to the other cycles, provided the thermal load requirements are small (high power-to-heat ratio values). The steam sale price showed more pronounced effect on the economic performance.

The observed poor economic performance of the recuperated ICRH cycle, for the three load cases examined, is mainly attributed to the increased equipment cost and the decreased revenues associated with steam generated in comparison to the other cycles.

Acknowledgment

The authors would like to thank Prof. Giorgio Negri di Montenegro for his valuable comments and Andrea De Pascale for his help during thermodynamic and economic calculations. The first author would like to also thank the management of Universal Enso for their continued encouragement and financial support.

Nomenclature

ESI = Energy Saving Index := $(F^* - F)/F^* = 1 - 1/(\eta_{el}/\eta_{el}^* + \eta_{th}/\eta_{th}^*)$ where, the variables with the superscript* refer to values for η_{th} and η_{el} taken equal to 0.8 and 0.37, respectively

F = LHV fuel energy supplied in a cogenerative plant

F^* = total LHV fuel energy supplied in the two separate plants producing the same amount of electric and thermal power as that of the cogenerative plant

m_a = air mass flow rate at the gas turbine inlet

m_s = steam mass flow rate

P_{el} = electric power output

Q_{th} = thermal power supplied to the thermal host

T = temperature

T_{in} = temperature at inlet to the HRSG

TIT = inlet temperature to the first-stage turbine rotor

β_{TOT} = overall cycle pressure ratio

η_{el} = LHV electric efficiency := P_{el}/F

η_{pc} = polytropic compression efficiency

η_{pe} = polytropic expansion efficiency

η_{th} = LHV thermal efficiency := Q_{th}/F

Acronyms

APR = annual percentage rate for the debt

CC₁ = high pressure combustor

CC₂ = low pressure combustor

DCRR = discount cash flow rate of return

ECO = economizer

GT = gas turbine

HPC = high pressure compressor

HPT = high pressure turbine

HRSG = heat recovery steam generator

IC = intercooler

ICRH = intercooled reheat

LHV = lower heating value

LPC = low pressure compressor

LPT = low pressure turbine

MSCF = 1000 standard cubic foot

REC = recuperator

VAP = vaporizer

References

- [1] Smith, D., 1999, "First H System Gas Turbine Planned for Baglan," *Mod. Power Syst.*, May, pp. 37–42.
- [2] Casper, R. L., 1993, "Application of the LM-6000 for Power Generation and Cogeneration," ASME Paper No. 93-GT-278.
- [3] Abe, T., Sugiura, T., Okunaga, S., Nojima, K., Tsutsui, Y., and Matsunuma, T., 2000, "Research and Development of Practical Industrial Cogeneration Technology in Japan," ASME Paper No. 2000-GT-0655.
- [4] Rice, I. G., 1980, "The Combined Reheat Gas Turbine/Steam Turbine Cycle, Part I—A Critical Analysis of the Combined Reheat Gas Turbine Steam Turbine Cycle," ASME J. Eng. Gas Turbines Power, **102**, pp. 35–41.
- [5] Rice, I. G., 1987, "Thermodynamic Evaluation of Gas Turbine Cogeneration Cycles, Part II—Complex Cycle Analysis," ASME J. Eng. Gas Turbines Power, **109**, pp. 8–15.
- [6] El-Masri, M. A., 1986, "On Thermodynamics of Gas Turbine Cycles, Part II—A Model for Expansion in Cooled Turbines," ASME J. Eng. Gas Turbines Power, **108**, pp. 151–159.
- [7] El-Masri, M. A., 1987, "Thermodynamics and Performance Projections for Intercooled/Reheat/Recuperated Gas Turbine Systems," ASME Paper No. 87-GT-108.
- [8] Macchi, E., Bombarda, P., Chiesa, P., Consonni, S., and Lozza, G., 1991, "Gas Turbine Based Advanced Cycles for Power Generation. Part B: Performance Analysis of Selected Configurations," International Gas Turbine Congress, Yokohama, Oct.
- [9] Farmer, R., 1993, "Reheat GTs Boost 250 and 365 MW Combined Cycle Efficiency to 58%," *Gas Turbine World*, Sept.–Oct.
- [10] Negri di Montenegro, G., Gambini, M., and Peretto, A., 1995, "Reheat and Regenerative Gas Turbines for Feed Water Repowering of Steam Power Plant," ASME Turbo Expo, Houston, June 5–8.
- [11] Bhargava, R., Bianchi, M., Negri di Montenegro, G., and Peretto, A., 2000, "Thermo-Economic Analysis of an Intercooled, Reheat and Recuperated Gas Turbine for Cogenerative Applications: Part I—Base Load Operation," ASME Paper No. 2000-GT-0316.

Thermoeconomic Analysis of an Intercooled, Reheat, and Recuperated Gas Turbine for Cogeneration Applications—Part II: Part-Load Operation

R. Bhargava

Universal Ensco, Inc.,
1811 Bering Drive,
Houston, TX 77057

G. Negri di Montenegro

A. Peretto

DIEM—University of Bologna,
Viale Risorgimento 2,
Bologna 40136, Italy

The knowledge of off-design performance for a given gas turbine system is critical particularly in applications where considerable operation at low load setting is required. This information allows designers to ensure safe operation of the system and determine in advance thermoeconomic penalty due to performance loss while operating under part-load conditions. In this paper, thermoeconomic analysis results for the intercooled reheat (ICRH) and recuperated gas turbine, at the part-load conditions in cogeneration applications, have been presented. Thermodynamically, a recuperated ICRH gas turbine-based cogeneration system showed lower penalty in terms of electric efficiency and Energy Saving Index over the entire part-load range in comparison to the other cycles (nonrecuperated ICRH, recuperated Brayton and simple Brayton cycles) investigated. Based on the comprehensive economic analysis for the assumed values of economic parameters, this study shows that a midsize (electric power capacity 20 MW) cogeneration system utilizing nonrecuperated ICRH cycle provides higher return on investment both at full-load and part-load conditions, compared to the other same size cycles, over the entire range of fuel cost, electric sale, and steam sale values examined. The plausible reasons for the observed trends in thermodynamic and economic performance parameters for four cycles and three sizes of cogeneration systems under full-load and part-load conditions have been presented in this paper. [DOI: 10.1115/1.1477195]

Introduction

A phenomenal growth in power generation market worldwide combined with the deregulation and increasing gas prices is making power plant developers and designers to give a careful look at the economics of power generation systems. It may be interesting to note that in the last 12 months, in some parts of the U.S. the gas prices have tripled or more. In such circumstances, complex cycles, namely, nonrecuperated and recuperated intercooled reheat (ICRH) cycles which were prohibitive earlier because of the high initial investment cost in spite of their better thermodynamic performance, can become attractive and viable proposition.

There are many process plants where flexibility in power generation and steam generation is essential. In such applications the complete knowledge of off-design performance for a given gas turbine system is critical. This information permits designers to ensure that there is a sufficient margin between compressor surge line and the operating line while operating under off-design conditions resulting in safe operation of the system. Furthermore, off-design analysis will allow to determine in advance economic penalty due to loss in performance as a result of part-load operation. It should also be observed that in a cogeneration application, the part-load working conditions will realize different values of electric-to-thermal power ratio and subsequently will impact the economics of the power generation system. Therefore, it becomes evident that prediction of the part-load performance of a cogeneration system is of fundamental importance.

The selection, size, and cost of the two heat exchangers, intercooler and recuperator, is critical for the complex gas turbine cycle discussed in this paper. An interesting discussion on the available technologies relating to the intercoolers and recuperators has been recently presented by Saidi et al. [1] and McDonald [2], respectively.

In the previous work of the authors (Bhargava et al. [3]), thermoeconomic performance analysis of recuperated ICRH gas turbine cycle in a cogeneration application at the full-load condition was addressed. It was shown that the cogeneration system with recuperated ICRH cycle realizes highest thermodynamic performance, under full-load condition, in comparison to the other gas turbine cycles (nonrecuperated ICRH, recuperated Brayton and, simple Brayton cycle). On the contrary, the economic analysis, conducted for the large size ($P_{el}=100$ MW) cogeneration systems with one power-to-heat ratio value, revealed that the discount cash flow rate of return (DCRR) values were highest for the nonrecuperated ICRH cycle compared to the other cycles studied.

The main objective of the present study, therefore, is to evaluate thermodynamic performance of the recuperated ICRH cycle in a cogeneration application operating under off-design conditions. This objective is achieved by identifying cycle configurations that maintain high thermodynamic performance also at the part-load conditions. Subsequently, a detailed economic analysis has been performed considering three different part-load operating scenarios, to evaluate effects of fuel cost, electric sale price and steam sale price on the DCRR values. It must be noted that a similar thermoeconomic analysis has also been performed for three other gas turbine cycles (namely, nonrecuperated ICRH, recuperated Brayton, and simple Brayton cycle) for comparison purposes.

Contributed by the International Gas Turbine Institute (IGTI) of THE AMERICAN SOCIETY OF MECHANICAL ENGINEERS for publication in the ASME JOURNAL OF ENGINEERING FOR GAS TURBINES AND POWER. Paper presented at the International Gas Turbine and Aeroengine Congress and Exhibition, New Orleans, LA, June 4–7, 2001; Paper 01-GT-207. Manuscript received by IGTI, Dec. 2000, final revision, Mar. 2001. Associate Editor: R. Natole.

Table 1 Key design parameters for the three gas turbine sizes investigated

Size (MW)	TIT(°C)	η_{pc}	η_{pe}
5	1050	0.88	0.87
20	1200	0.90	0.89
100	1350	0.91	0.90

Part-Load Thermodynamic Analysis

The Design Performance and Configurations. The thermodynamic analyses have been performed for three gas turbine sizes of 5, 20, and 100 MW electric power output: each of the gas turbine is defined by the value of key design parameters as reported in Table 1. The values of polytropic efficiency for compressors and turbines, given in Table 1, are representative of the selected gas turbine sizes based on the current technology.

For the three sizes of cogeneration systems, the main thermodynamic performance parameters obtained at the full-load condition, for the four cycles investigated, and subsequently used in the off-design analysis are reported in Table 2 (Bhargava et al. [3]). The thermodynamic performance for each load case, summarized in Table 2, corresponds to the specific value of electric-to-thermal power ratio that was chosen such that all the four cycles can be compared at the same value.

Off-Design Modeling Technique. In this section, a brief description of the off-design thermodynamic analysis technique, including assumptions made, for a cogeneration system utilizing recuperated ICRH gas turbine, has been presented. A schematic layout of the recuperated ICRH gas turbine cycle in a cogenerative application is shown in Fig. 1. As noted earlier, to show advantages and limitations of the recuperated ICRH cycle compared to the other cycles, the off-design analyses have also been performed for the three other cycles, namely, nonrecuperated ICRH, recuperated Brayton, and simple Brayton cycle. The complete thermodynamic analysis has been accomplished by utilizing a commercial software package.

The part-load operating conditions have been realized by simulating the inlet air mass flow rate change by adjusting the inlet guide vanes (IGV), as it is commonly done on the actual machines. To simplify the analysis, a linear correlation has been assumed between air mass flow rate at the low pressure compressor (LPC) inlet and the IGV angle as expressed by Eq. (1). Moreover, isentropic efficiency of the LPC is assumed to change linearly with the IGV angle as given by Eq. (2). It must be noted that both parameters α and γ , assumed constant in the present study for all the four cycles, have a value equal to 0.01 and 0.003, respectively.

To analyze the high pressure compressor (HPC) at the part-load condition, the value of inlet mass flow function is assumed constant and equal to its value corresponding to the full-load condition (design condition). Equation (3) is used to estimate the value of pressure at the HPC inlet under part-load condition. This assumption of constant mass flow function implies a vertical line on a pressure ratio versus mass flow function compressor performance map. Also, the values of isentropic efficiency of HPC,

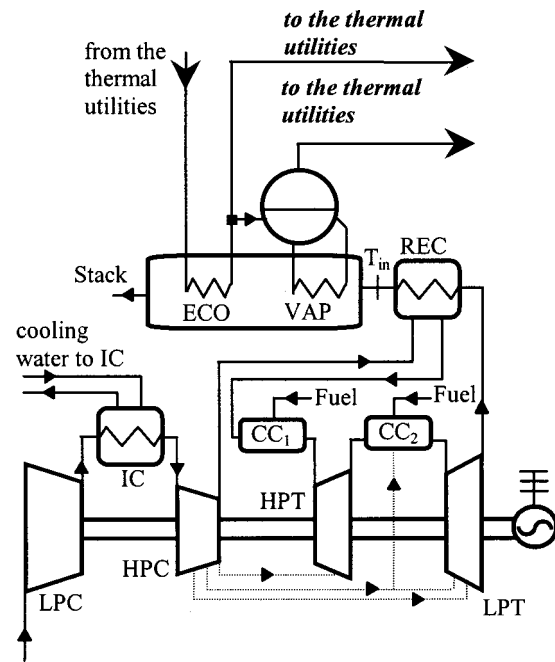


Fig. 1 Schematic layout of the recuperated ICRH gas turbine in cogenerative application (dotted lines represent GT cooling flow streams)

under various part-load conditions, are assumed constant and equal to the design value (full-load case). Pressure at the exit of HPC, $p_{HPC\ out}$, is obtained by adding to the pressure at the high pressure turbine (HPT) inlet, $p_{HPT\ in}$, the pressure drops across the first combustor, Δp_{CC1} , as shown in Eq. (4).

For analyzing high and low-pressure turbine sections under part-load conditions, both HPT and low pressure turbine (LPT) have been assumed to work in choking condition. As a result, the values of mass flow function for both HPT and LPT, under different part-load conditions, are constant and equal to their respective design values. The values of pressure at inlet to the HPT and LPT, at different part-load conditions, have been calculated using Eq. (5) and Eq. (7), respectively. It must be observed that on the basis of constant mass flow function at the HPT and LPT inlets, the HPT pressure ratio is insignificantly affected by the part-load operation and maintains its value very close to the design value. However, the LPT pressure ratio, even if it decreases from its design value, it maintains a value that ensures the constant mass flow function at the LPT inlet.

$$\text{for LPC} \begin{cases} m_a = m_{a0}(1 - \alpha IGV) & (1) \\ \eta_{is\ LPC} = \eta_{is\ 0,LPC}(1 - \gamma IGV) & (2) \end{cases}$$

$$\text{for HPC} \begin{cases} p_{HPC\ in} = \frac{m_{HPC\ in} \sqrt{T_{HPC\ in}}}{MFF_{0,HPC\ in}} & (3) \\ p_{HPC\ out} = p_{HPT\ in} + \Delta p_{CC1} & (4) \end{cases}$$

Table 2 Design performance for the three size cogeneration systems

Type of Cycle	$P_{el}=100\ MW$ $P_{el}/Q_{th}=1.05$			$P_{el}=20\ MW$ $P_{el}/Q_{th}=0.95$			$P_{el}=5\ MW$ $P_{el}/Q_{th}=0.70$		
	η_{el0} (%)	ESI ₀ (%)	β_{TOT}	η_{el0} (%)	ESI ₀ (%)	β_{TOT}	η_{el0} (%)	ESI ₀ (%)	β_{TOT}
Brayton	44.7	42.5	40.8	41.2	39.7	44.1	35.4	37.1	21.8
Brayton REC	45.3	43.3	13.2	42.6	41.6	12.8	35.7	37.6	15.4
ICRH	46.6	44.5	50.0	44.2	43.7	50.0	37.5	40.6	50.0
ICRH REC	47.0	45.3	50.0	44.5	44.0	50.0	37.3	40.3	50.0

$$\text{for HPT} \begin{cases} p_{\text{HPT in}} = \frac{m_{\text{HPT in}} \sqrt{T_{\text{HPT in}}}}{\text{MFF}_{0_{\text{HPT in}}}} & (5) \\ p_{\text{HPT out}} = p_{\text{LPT in}} + \Delta p_{\text{CC2}} & (6) \end{cases}$$

$$\text{for LPT} \begin{cases} p_{\text{LPT in}} = \frac{m_{\text{LPT in}} \sqrt{T_{\text{LPT in}}}}{\text{MFF}_{0_{\text{LPT in}}}} & (7) \\ p_{\text{LPT out}} = p_{\text{amb}} + \Delta p_{\text{out}} & (8) \end{cases}$$

As a consequence, values of isentropic efficiency for the HPT and LPT have been assumed constant and equal to their design values at different part-load conditions (Cohen et al. [4]).

The value of pressure at HPT discharge, $p_{\text{HPT out}}$, is obtained by adding to the pressure at the LPT inlet, $p_{\text{LPT in}}$, the pressure drops across the second combustor, Δp_{CC2} , as shown in Eq. (6). Pressure at the LPT discharge, $p_{\text{LPT out}}$, has been determined using Eq. (8) by considering applicable pressure losses (Δp_{out}) given by the sum of pressure drop across recuperator, pressure drop across the exhaust stack, and pressure drop across the HRSG.

The LPT stage expansion ratio is determined by means of the stage enthalpy drop, Δh_i , by using Eq. (9):

$$\Delta h_i = \Psi_i u^2. \quad (9)$$

Assuming that the average wave speed, u , has the same value for all the stages, Eq. (9) may be also written as

$$\Delta h_i = \Psi_i \frac{\sum_{j=1}^{n_{\text{LPT}}} \Delta h_j}{\sum_{j=1}^{n_{\text{LPT}}} \Psi_j} \quad (10)$$

where n_{LPT} is the number of stages in the LPT expander. Under part-load operating conditions, the value of Ψ_i for each stage is assumed equal to its design value (Bhargava et al. [3]). As a consequence, the stage enthalpy drop Δh_i , and the stage expansion pressure ratio, have been iteratively calculated by means of Eq. (10).

During off-design performance evaluation, for the surface areas of various heat exchangers, the values calculated at the full-load condition were considered (Bhargava et al. [3]). Also, the values of effectiveness and outlet temperature for a given heat exchanger, at the part-load conditions, have been calculated utilizing a commonly used ε -NTU method (Kays and London [5] and Rohsenow et al. [6]).

The amounts of required cooling air flows, for hot gas path and the most stressed components, have been evaluated: at the design load following the work of Benvenuti et al. [7] and at off-design conditions by assuming that each cooling flow is in choking condition.

During the off-design analysis for various cycles and load cases examined, it was ensured that the gas turbine outlet temperature is always below 650°C , so as not to impose excessive mechanical and thermal stresses in the last stage of the gas turbine expander. Moreover, the stack temperature, in all the cases was maintained higher than 75°C .

Finally, in the entire off-design analysis study, the values of TiT at the HPT and LPT inlets are maintained equal to their design values for each size case as defined in Table 1.

Off-Design Thermodynamic Results. In Fig. 2, values of change in electric efficiency, expressed in percentage with respect to the design values (as given in Table 2), at different part-load conditions are reported for the four cycles and the high load case ($P_{e1} = 100 \text{ MW}$). For each cycle, the lower value of part-load condition is limited by the constraints described earlier.

The recuperated ICRH cycle distinctively shows not only the smallest decrement in the electric efficiency, at different part-load conditions, but also has the smallest rate of decrease in its value compared to the other cycles examined in the present study. This

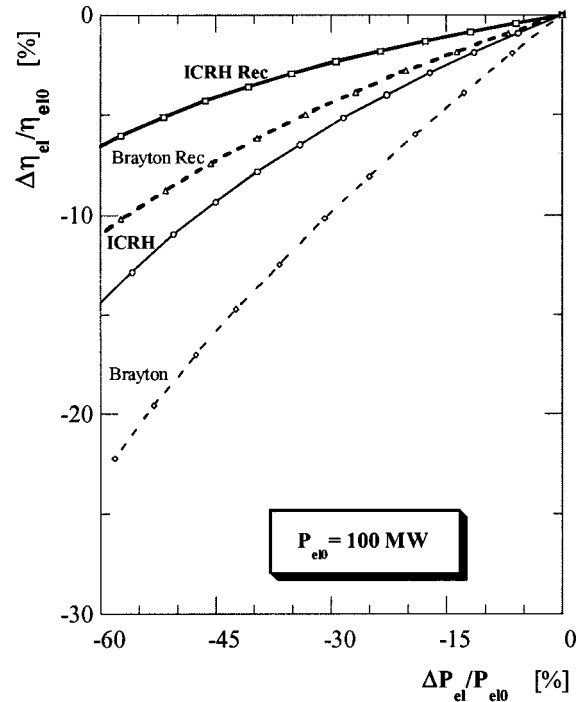


Fig. 2 $\Delta \eta_{e1} / \eta_{e10}$ versus $\Delta P_{e1} / P_{e10}$ for high-size cogeneration plant

behavior of the recuperated ICRH cycle is beneficial in applications where the system requires operation under part-load conditions.

Furthermore, both recuperated cycles, recuperated ICRH and Brayton, have the lowest decrease in electric efficiency as compared to the nonrecuperated cycles. The observed trend in variation of the electric efficiency values, at the part-load conditions, can be attributed to the following reason: at a given part-load condition, the value of overall cycle pressure ratio decreases and the LPT outlet temperatures increases, resulting in an increased heat exchange between air at the HPC discharge and the flue gases at the LPT discharge in presence of the recuperator. This additional heat exchange, because of the presence of the recuperator, decreases the amount of specific fuel energy (fuel energy per unit air mass flow rate) required and consequently contributing to a less decrease in electric efficiency of the recuperated cycles compared to the nonrecuperated cycles. The decrease in specific fuel energy consumption for the recuperated cycles compared to the nonrecuperated cycles at part-load conditions is clearly seen in Fig. 3. The values of specific fuel energy for four cycles at design load condition, for large load case ($P_{e1} = 100 \text{ MW}$), are also included in Fig. 3. For the nonrecuperated ICRH and Brayton cycles, it is further noted that the specific fuel energy increases at the part-load conditions as is evident from Fig. 3.

Another trend, namely, the change in electric efficiency of the ICRH cycle in comparison to the recuperated Brayton cycle under part-load conditions, as shown in Fig. 2, needs explanation. The performance of ICRH and recuperated Brayton cycle at the full-load condition showed higher electric efficiency for the ICRH gas turbine-based cogeneration system compared to the recuperated Brayton cycle (see Table 2). However, under part-load conditions, recuperated Brayton cycle shows better performance compared to the ICRH cycle as is evident from Fig. 2. The main reason for this observed trend is attributed to considerable decrease in specific

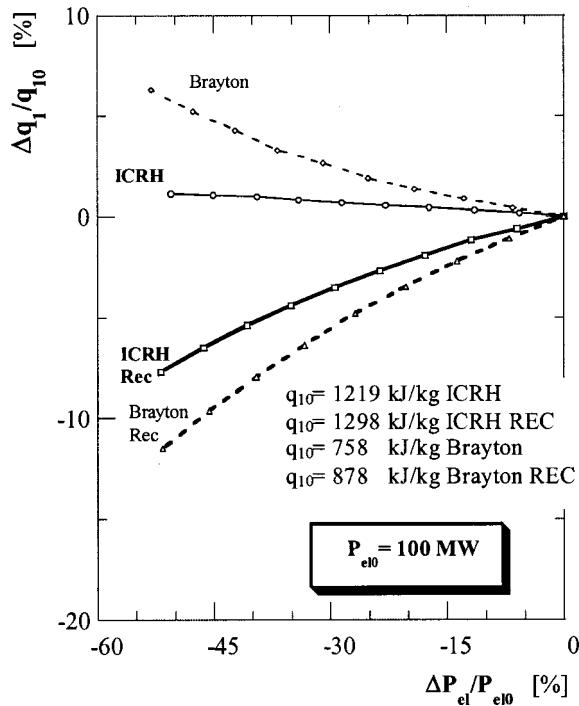


Fig. 3 $\Delta q_1/q_{10}$ versus $\Delta P_{el}/P_{el0}$ for high-size cogeneration plant

fuel energy for the recuperated Brayton cycle in comparison to that for the ICRH cycle at different part-load conditions as shown in Fig. 3.

It should also be observed from Fig. 2, that the ICRH cycle has a lower decrease in electric efficiency, at the part-load conditions, than the Brayton cycle. This may be attributed to two factors:

1 The decrease in specific power is lower for the nonrecuperated ICRH cycle than the Brayton cycle (see Fig. 4). This is be-

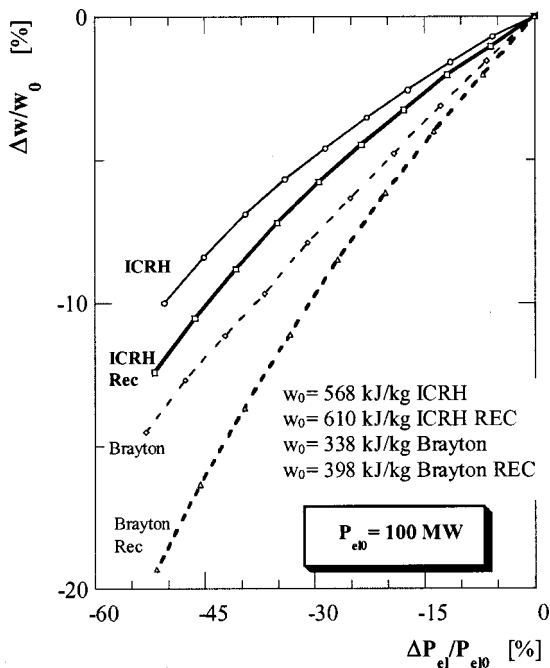


Fig. 4 $\Delta w/w_0$ versus $\Delta P_{el}/P_{el0}$ for high-size cogeneration plant

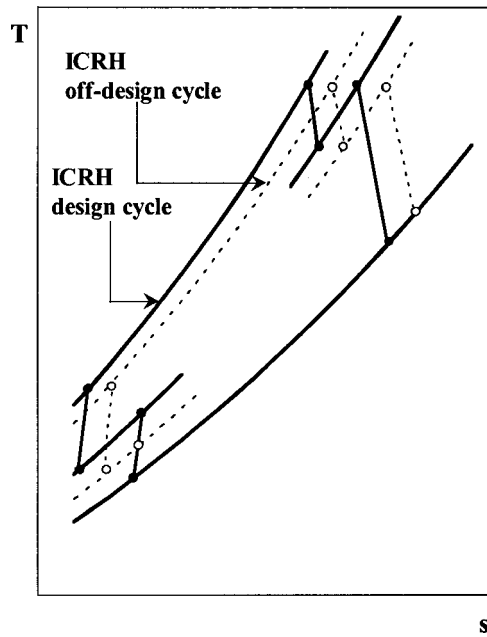


Fig. 5 Modifications to ICRH cycle due to part-load operation

cause, for an assigned electric power percentage variation, it was found that the variation of specific power (Δw) for ICRH results very close to Brayton values but the relative variations are higher for Brayton cycle having lower design specific power than ICRH (see w_0 values in Fig. 4).

2 Under part-load conditions, the change (increase) in specific fuel energy is negligible for the nonrecuperated ICRH cycle with respect to its design value (see Fig. 3). Consequently, the specific fuel energy required for the combustor CC1 also does not change appreciably under part-load conditions. Furthermore, the assumption of constant mass flow function at the inlet of HPT and LPT results in insignificant variation in expansion ratio for the HPT and inlet temperature to the combustor CC2 (see Fig. 5). As a result, under part-load conditions and in comparison to the Brayton cycle, the ICRH cycle has minimum decrease in $\Delta w/w_0$, (see Fig. 4) and the minimum increase in $\Delta q_1/q_{10}$ (see Fig. 3). Consequently, in comparison to the Brayton cycle, the ICRH cycle shows smaller decrease in $\Delta \eta_{el}/\eta_{el0}$ values under part-load conditions as shown in Fig. 2.

For a high size ($P_{el0} = 100$ MW) case, the change in Energy Saving Index value is found lowest, at all the part-load conditions, for the recuperated ICRH cycle in comparison to the other cycles examined as is evident from Fig. 6. This aforesaid result, combined with its full-load performance as given in Table 2, clearly implies that the high-size cogeneration systems utilizing recuperated ICRH cycle maintains high values of ESI both at full-load and part-load conditions in comparison to the other cycles.

Therefore, it is unambiguously clear that the recuperated ICRH cycle-based cogeneration systems will be thermodynamically better not only at the full-load condition but also at the part-load conditions, compared to the other cycles examined, a beneficial requirement for the cogeneration systems.

In spite of the fact that the cogeneration systems utilizing ICRH cycle showed higher penalty in terms of electric efficiency, compared to the recuperated Brayton cycle as discussed earlier and seen in Fig. 2, the changes in ESI values, under part-load conditions, are lower for the ICRH cycle. The main reason being availability of increased thermal energy for the utilities under part-load conditions for the ICRH cycle as shown in Fig. 7.

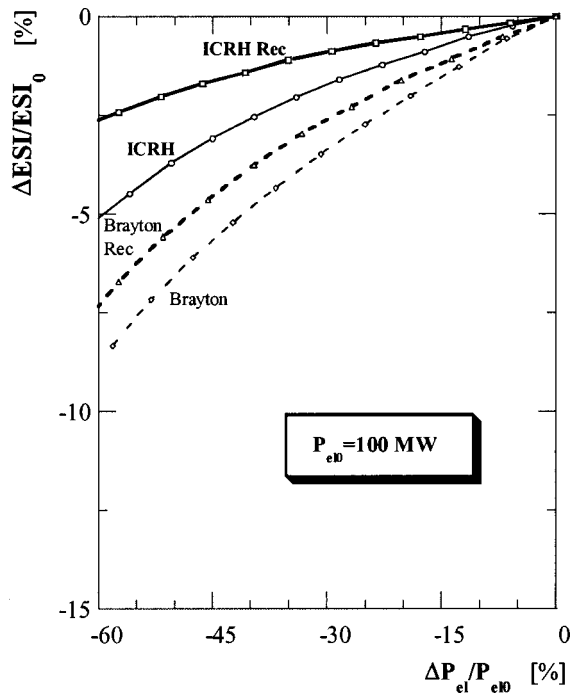


Fig. 6 $\Delta ESI/ESI_0$ versus $\Delta P_{el}/P_{el0}$ for high-size cogeneration plant

On the other hand, use of recuperation in recuperated Brayton cycle reduces thermal energy available for the utilities under part-load conditions (see Fig. 7).

The low penalization in terms of ESI for the ICRH cycle is also confirmed, if the variation in thermal efficiency under part-load conditions is examined (see Fig. 8). It is evident from Fig. 8 that, under part-load conditions, the increase in thermal efficiency is much greater for the ICRH cycle than the recuperated Brayton

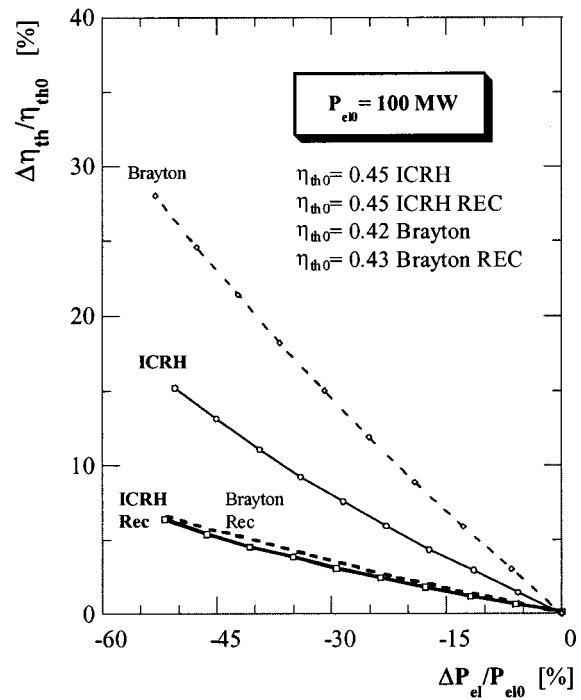


Fig. 8 $\Delta \eta_{th}/\eta_{th0}$ versus $\Delta P_{el}/P_{el0}$ for high-size cogeneration plant

cycle. It is interesting yet equally important to note from Fig. 8 in combination with Figs. 2 and 6, that the Brayton cycle has the highest thermal efficiency increase, but also the highest penalty in terms of ESI and electric efficiency, compared to the other cycles under part-load conditions. On the contrary, recuperated ICRH has the lowest increase in thermal efficiency, and the lowest decrease in the values for ESI and electric efficiency. This observed trend is mainly attributed to the fact that for the ESI value, not only ther-

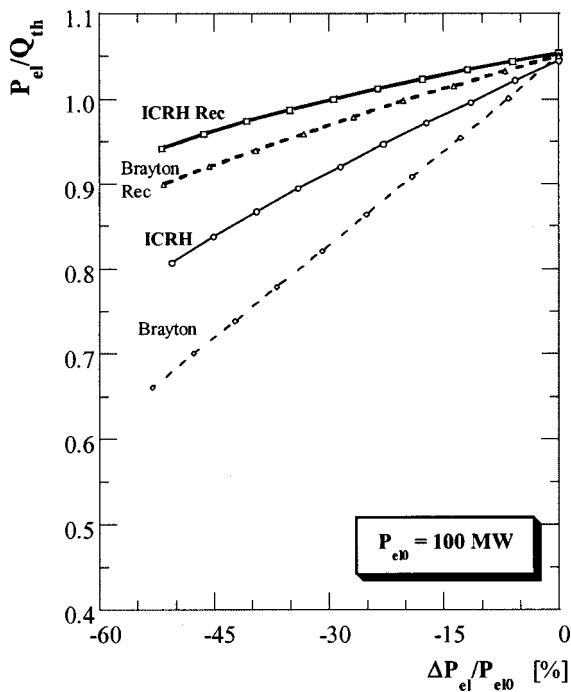


Fig. 7 P_{el}/Q_{th} versus $\Delta P_{el}/P_{el0}$ for high-size cogeneration plant

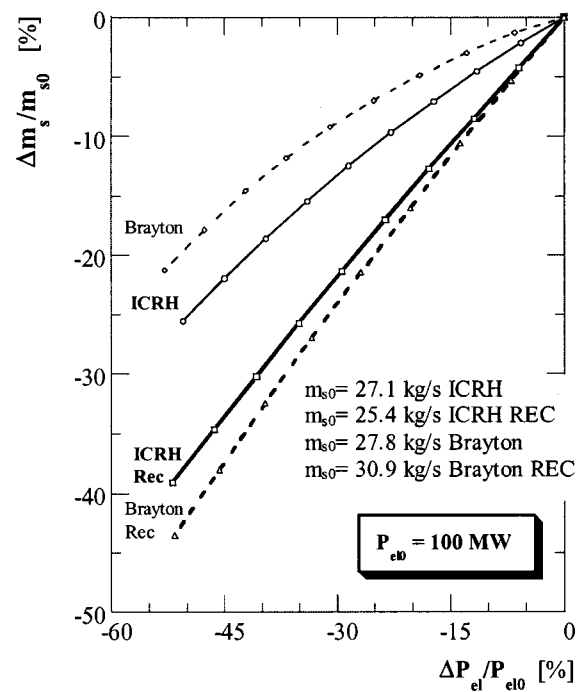


Fig. 9 $\Delta m_s/m_{s0}$ versus $\Delta P_{el}/P_{el0}$ for high-size cogeneration plant

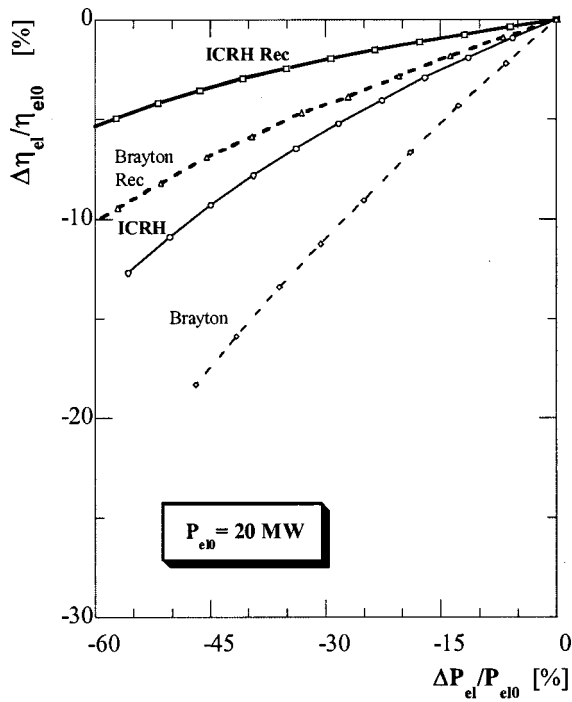


Fig. 10 $\Delta\eta_{el}/\eta_{el0}$ versus $\Delta P_{el}/P_{el0}$ for medium-size cogeneration plant

mal efficiency is important for its determination, but also electric efficiency plays a significant role.

It should also be noted from Fig. 7, that the recuperated cycles, under part-load conditions, have relatively smaller variation in the thermal-to-power ratio compared to the nonrecuperated cycles. This may be explained considering that, for recuperated cycles, the electric power reduction leads to a reduction of specific power (see Fig. 4) and not an appreciable increase in specific thermal power, available for the utilities, due to recuperation. As a conse-

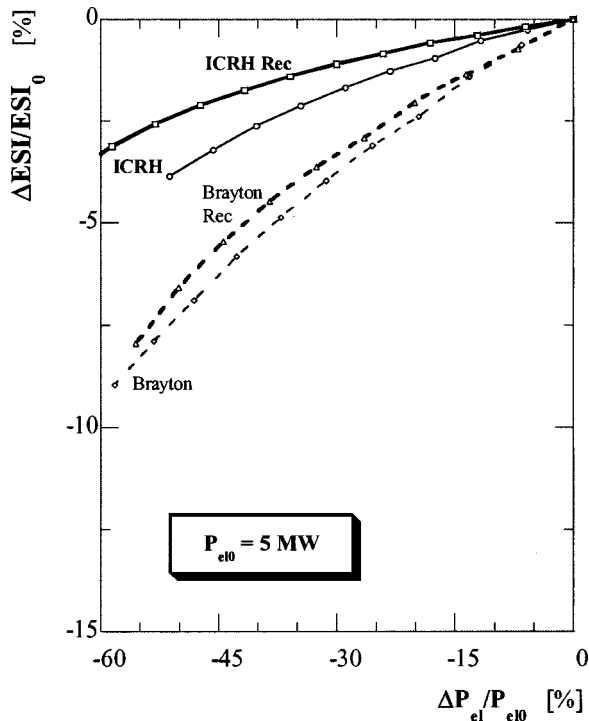


Fig. 11 $\Delta ESI/ESI_0$ versus $\Delta P_{el}/P_{el0}$ for low-size cogeneration plant

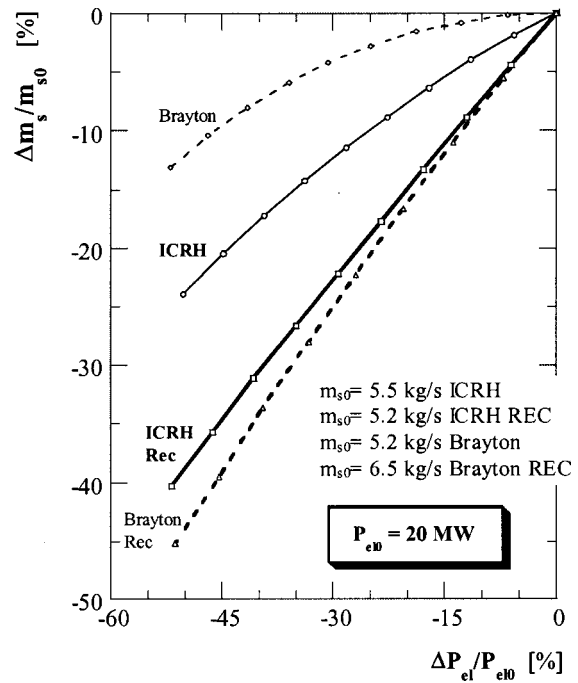


Fig. 12 $\Delta m_s/m_{s0}$ versus $\Delta P_{el}/P_{el0}$ for medium-size cogeneration plant

quence, P_{el}/Q_{th} , for recuperated cycles, is less affected by electric power variation than nonrecuperated cycles for which a decrease in electric power is accompanied by an increase in specific thermal power.

The changes in steam mass flow rate values (expressed as percentage with respect to the design value) for a large-size case ($P_{el0}=100$ MW), under part-load conditions, clearly show that the nonrecuperated cycles have smaller penalty compared to the recuperated cycles as is evident from Fig. 9. This is a consequence

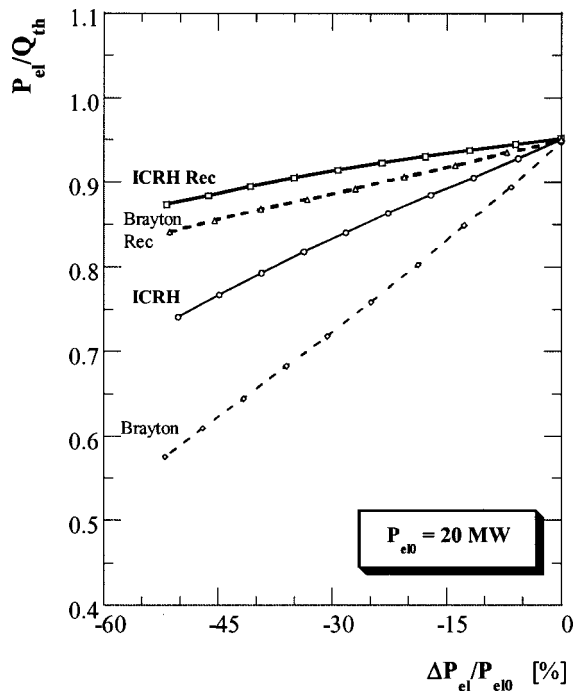


Fig. 13 P_{el}/Q_{th} versus $\Delta P_{el}/P_{el0}$ for medium-size cogeneration plant

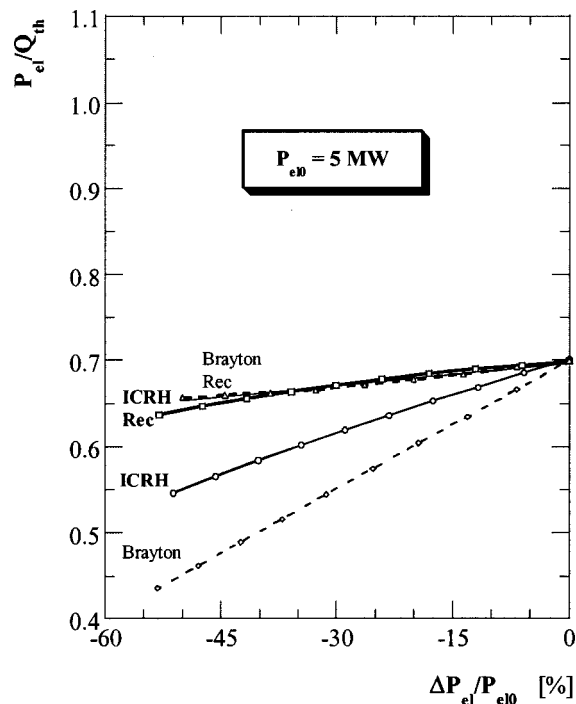


Fig. 14 P_{el}/Q_{th} versus $\Delta P_{el}/P_{el0}$ for low-size cogeneration plant

of the fact, as discussed earlier and shown in Fig. 7, that there is a increase in thermal power available for the utility for nonrecuperated cycles compared to the recuperated cycles under part-load conditions.

The selected results of thermodynamic performance for mid size ($P_{el0}=20$ MW) and small size ($P_{el0}=5$ MW) cases, under part-load conditions, are shown in Figs. 10–14. A closer look of these results suggests that the trends in variation of various thermodynamic performance parameters are similar for the three sizes of cogeneration systems examined in the present study. Furthermore, the magnitude of changes in various performance parameters, except power-to-heat ratio, have not been found affected by the system's size under part-load conditions. However, the values of power-to-heat ratio for different size systems are different for obvious reason, chief reason being differences in the values of TiT for the three load cases.

Economic Analysis

The Design Economic Data. The values of various parameters used in conducting economic analysis are reported in Table 3. It is important to note that the values given in Table 3 are project dependent and, therefore, the presented results should be viewed accordingly.

First, the economic analyses were conducted at the full-load condition for high, medium, and small-size cases. The results of economic analyses for thermodynamically optimum configura-

Table 3 Main economic parameters assumed for the economic analysis

Parameter	Unit	Selected Value
Plant utilization factor		85
Plant economic life	years	20
Loan term	years	20
Debt interest rate	APR	15
Depreciation period	years	10
Construction period	years	1.5
Escalation rate	%	5
Fuel gas cost	\$/MSCF	3.0
Utility avoided cost	cents/kWh	4.5
Local taxes and insurance cost	% of total investment cost	2.5
Auxiliary power consumption	% of gross power generated	1.5
Income taxes	flat rate, % of net revenues	45

tions, at the full-load condition, for the three load cases considered are summarized in Table 4. The results presented in Table 4 are for a specific value of power-to-heat ratio for each load case. A more detailed study for the range of power-to-heat ratio values for these load cases has been presented in a companion paper (Bhargava and Peretto [8]).

Assumptions for Off-Design Economic Analysis. The economic analysis of a cogeneration system under off-design conditions is quite involved, for the simple fact that the plant may not operate at a given part-load condition for the entire operational period in a given year. Therefore, some reasonable assumptions need to be made to simplify the economic analysis. For the present study, a cogeneration system, of a given size and utilizing a given cycle, is assumed to operate under one of the four possible working scenarios during a year (Fig. 15):

- 1 at design load (full load) for the entire operational period in a year.
- 2 for 75 percent of the operational period in a year at the design load and 25 percent of the operational period in a year at 50 percent of the design load.
- 3 for 50 percent of the operational period in a year at the design load and 50 percent of the operational period in a year at 50 percent of the design load.
- 4 for 25 percent of the operational period in a year at the design load and 75 percent of the operational period in a year at 50 percent of the design load.

This approach allows to simulate a cogeneration plant, in a year, to operate at the design load or part-load condition with a time-sharing scheme as described by the four scenarios. Obviously, the plant energy generated in a year (kWh/year) decreases when passing from scenario 1 to scenario 4. At the same time the yearly heat rate increases. The main purpose of examining the scenario 1 is to evaluate comparative effect of part-load operation on the economic performance.

Table 4 Design economic data for the three size cogeneration systems

Type of Cycle	$P_{el}=100$ MW $P_{el}/Q_{th}=1.05$		$P_{el}=20$ MW $P_{el}/Q_{th}=0.95$		$P_{el}=5$ MW $P_{el}/Q_{th}=0.70$	
	DCRR (%)	GPO (year)	DCRR (%)	GPO (year)	DCRR (%)	GPO (year)
ICRH REC	49.85	2.1	35.63	3.1	27.38	4.0
ICRH	52.96	2.0	37.58	2.9	29.51	3.7
Brayton REC	49.63	2.1	35.03	3.0	26.07	4.3
Brayton	54.96	1.9	37.18	2.9	29.95	3.7

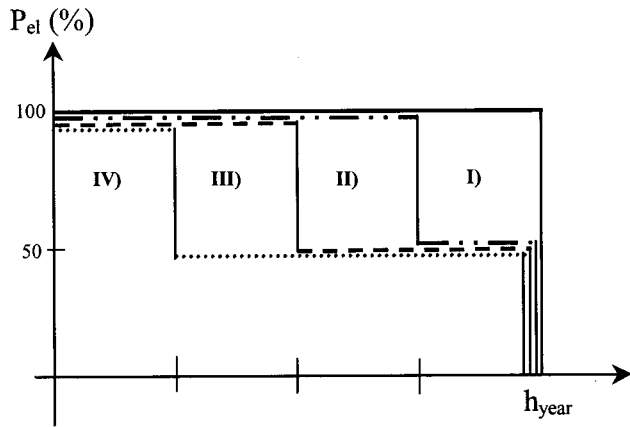


Fig. 15 Four different scenarios assumed for the plants working in off-design condition

The economic analysis has been performed for each scenario where an average power produced in a year is obtained from Eq. (11) given below:

$$P_{av} = P_0 \frac{h_0}{h_{year}} + P_{50 \text{ percent}} \frac{h_{50 \text{ percent}}}{h_{year}} \quad (\text{MW}) \quad (11)$$

where P_0 and $P_{50 \text{ percent}}$ are the power produced at design load and 50 percent of the design load, respectively; h_0 and $h_{50 \text{ percent}}$ are the working hours, in a year, at design load and 50 percent of the design load, respectively; h_{year} are the plant working hours in a year (considering the plant utilization factor).

The value of yearly fuel consumption is obtained using Eq. (12) given below:

$$M_{fuel} = c_1 \left(\frac{P_0 h_0}{\eta_{el0} \text{LHV}} + \frac{P_{50 \text{ percent}} h_{50 \text{ percent}}}{\eta_{el50 \text{ percent}} \text{LHV}} \right) \quad (\text{MSCF/year}) \quad (12)$$

where η_{el0} and $\eta_{el50 \text{ percent}}$ are the plant electric efficiency at design load and 50 percent of the design load, respectively, and c_1 is a constant to obtain the fuel consumption in MSCF/year.

The value of steam generated in a year is obtained by the following equation:

$$m_{sy} = c_2 (m_{s0} h_0 + m_{s50 \text{ percent}} h_{50 \text{ percent}}) \quad (\text{kg/year}) \quad (13)$$

where c_2 is a constant to obtain the mass steam generated in kg/year.

For a given size cogeneration system utilizing a specific cycle, first the average values of power generated, fuel consumed and steam produced have been calculated by using Eq. (11), Eq. (12), and Eq. (13), respectively. Subsequently, the economic analysis has been performed using the assumed values of economic parameters given in Table 3.

Economic Analysis Results. A comprehensive economic analysis has been performed for the four scenarios described above by evaluating effects of fuel cost, electric sale price, and steam sale price using the assumed values of key economic parameters. It is important to reiterate that the results should be viewed with the understanding that the return on investment values are based on the assumptions used in this study for economic parameters including equipment costs. It must be noted that a large number of charts were generated as a result of the comprehensive economic analysis, but only selected charts are presented in the paper because of space limitations.

It should be noted that the trends in variation of economic performance have been found same for all the scenarios examined mainly because the same part-load condition has been used in scenarios 2 to 4. Furthermore, the key difference in these scenarios is that the values of rate of return on investment (DCRR)

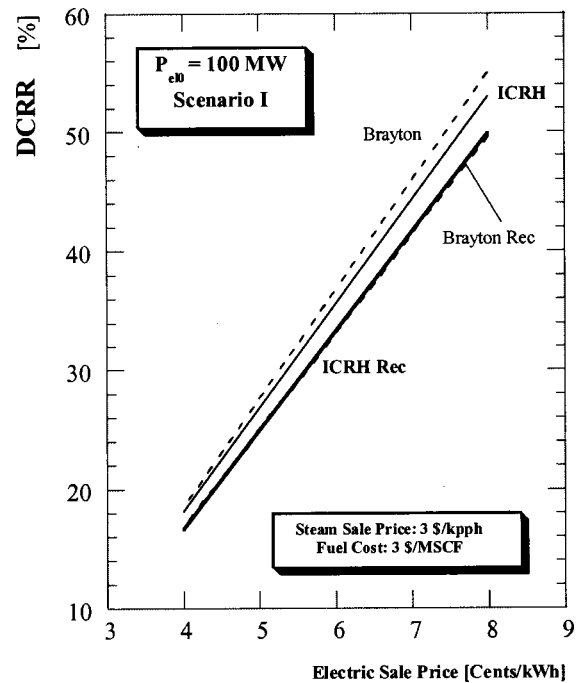


Fig. 16 DCRR versus electric sale price for high-size cogeneration plant (scenario 1)

decrease mainly because the quantities of both electric energy and thermal energy sold reduce as the operating condition changes from scenario 1 to scenario 4.

Economic Analysis Results—Scenario 1. For the scenario 1 (i.e., full-load condition) and large-size ($P_{e10} = 100 \text{ MW}$) case, simple Brayton cycle achieves better return on investment compared to the other cycles for the entire range of fuel cost, electric sale price and steam sale price: The effects of electric and steam sale prices on DCRR values are shown in Fig. 16 and Fig. 17,

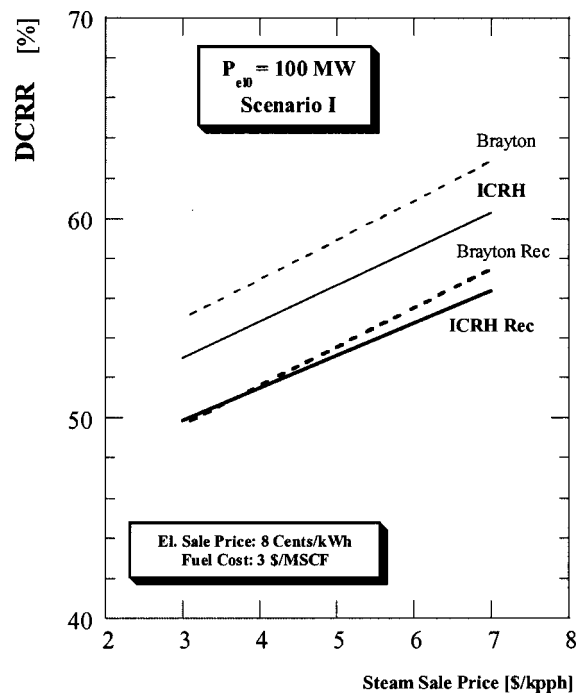


Fig. 17 DCRR versus steam sale price for high-size cogeneration plant (scenario 1)

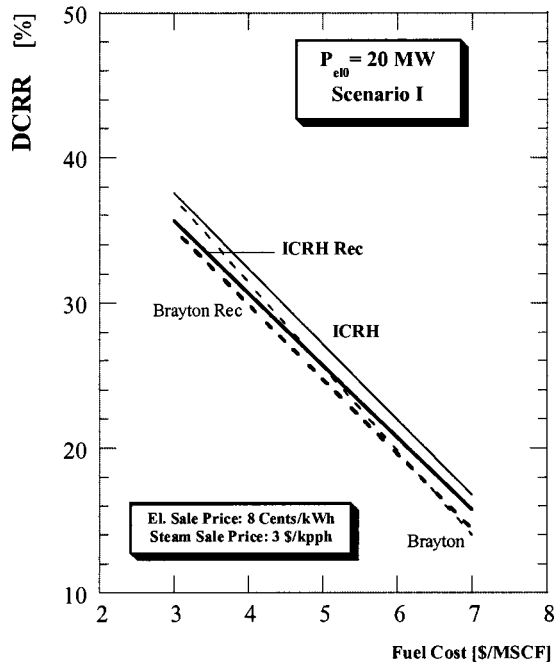


Fig. 18 DCRR versus fuel cost for medium size cogeneration plant (scenario 1)

respectively. The main reason for poor economic performance of the recuperated ICRH cycle, compared to the simple Brayton cycle, is considerably increased equipment cost and the lost revenues from steam sale. For the recuperated ICRH cycle, the effect of these two factors could not be offset by its relative increased thermodynamic performance.

However, for the medium size ($P_{e10}=20$ MW) case, nonrecuperated ICRH cycle achieves higher return on investment for the entire range of electric sale price, steam sale price and fuel cost values examined in the present study: for example, the effects of fuel cost on the DCRR values are shown in Fig. 18. Also, economic performance of the recuperated ICRH cycle, compared to the recuperated and simple Brayton cycles, becomes competitive (even though still lower than nonrecuperated ICRH cycle) as the fuel cost increases (see Fig. 18). This trend in economic performance for the medium size nonrecuperated ICRH cycle can be attributed to the observed higher increase in thermodynamic performance, compared to the large size case, which has been found sufficient to overcome the increased equipment cost for the nonrecuperated cycle (see Table 2 and Bhargava et al. [3]). The poor economic performance of the recuperated ICRH cycle, compared to the nonrecuperated ICRH cycle, for midsize case is mainly due to the increased equipment cost and lost revenues associated with the reduced steam production.

For the small-size case ($P_{e10}=5$ MW) at the full-load, the nonrecuperated ICRH cycle achieves better economic performance for the range of fuel cost as shown in Fig. 19. Also, the recuperated ICRH cycle can be economically viable at higher fuel cost even though the DCRR values are lower than the nonrecuperated ICRH cycle. The lower values of DCRR, corresponding to the fuel cost of \$6/MSCF and higher observed in Fig. 19, suggest a need for high electric sale price for the small size cogeneration systems to be economically viable.

Economic Analysis Results—Scenario 4. For the large-size case under part-load condition in scenario 4, nonrecuperated ICRH cycle achieves better economic performance for almost the entire range of fuel cost and electric sale values examined: for example, the effects of fuel cost on the DCRR values are shown in Fig. 20. This improved performance of the nonrecuperated ICRH cycle, at least compared to the simple Brayton cycle can be asso-

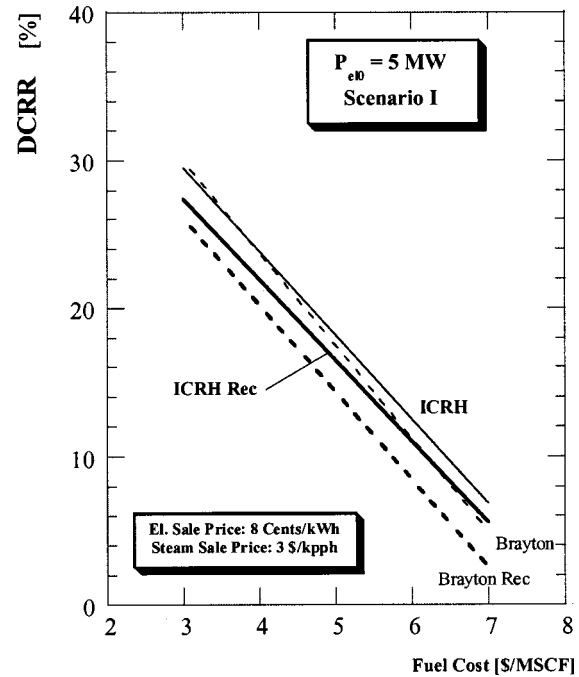


Fig. 19 DCRR versus fuel cost for low-size cogeneration plant (scenario 1)

ciated with lower penalty in terms of electric efficiency for the nonrecuperated ICRH cycle as discussed earlier (see Fig. 2). The poor economic performance of the recuperated ICRH cycle, compared to the nonrecuperated ICRH cycle, can be mainly attributed to the increased equipment cost associated with recuperated ICRH cycle in spite of its improved part-load thermodynamic performance as is evident from Fig. 2. Another interesting result to observe from Fig. 20 is the improved economic performance of

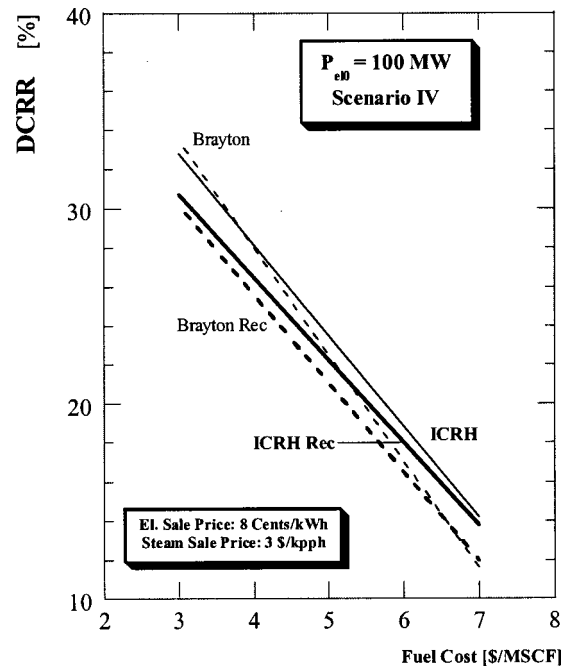


Fig. 20 DCRR versus fuel cost for high-size cogeneration plant (scenario 4)

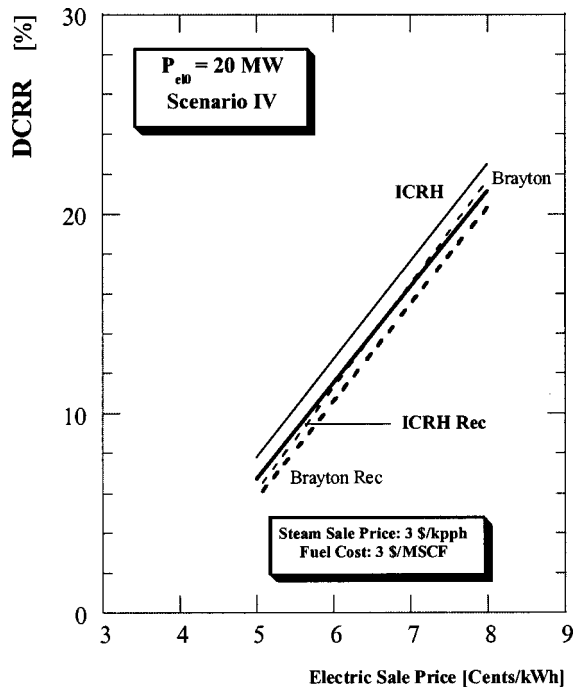


Fig. 21 DCRR versus electric sale price for medium-size cogeneration plant (scenario 4)

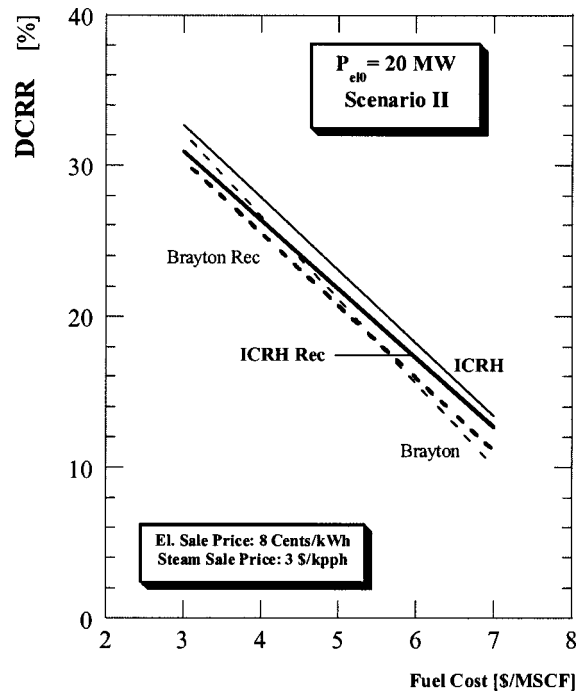


Fig. 23 DCRR versus fuel cost for medium-size cogeneration plant (scenario 2)

the recuperated ICRH cycle with the fuel cost higher than \$5/MSCF in comparison to the other cycles except the nonrecuperated ICRH cycle.

The midsize nonrecuperated ICRH cycle under part-load conditions, compared to the other midsize cycles, has been observed to achieve higher economic performance over the entire range of cost structure investigated: for example, the effects of electric sale price on the DCRR values are shown in Fig. 21. Also, the recuperated ICRH cycle performs economically better at the part-load

condition compared to the recuperated and simple Brayton cycles mainly because of its comparatively lower penalty in thermodynamic performance (see Fig. 10).

For the small-size case and under part-load condition, the nonrecuperated ICRH cycle economically outperforms other cycles over the entire range of fuel cost (see Fig. 22) for given values of electric sale price (8 Cents/kWh) and steam sale price (\$3/kpph).

The higher economic performance of the nonrecuperated ICRH cycle, in spite of its poor thermodynamic performance, compared

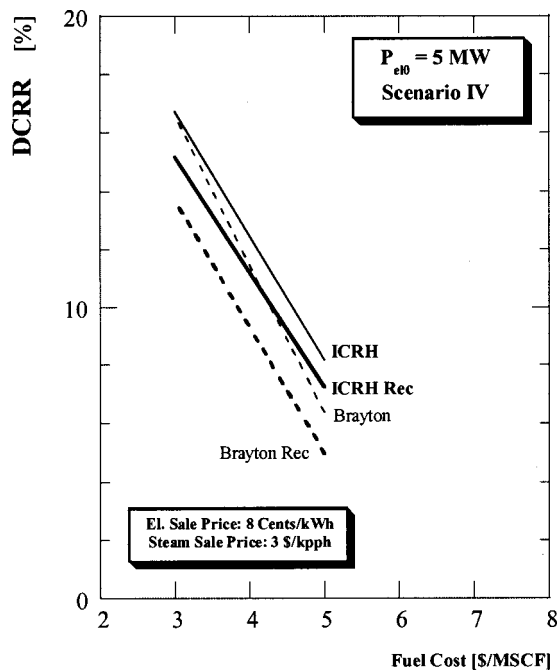


Fig. 22 DCRR versus fuel cost for low-size cogeneration plant (Scenario 4)

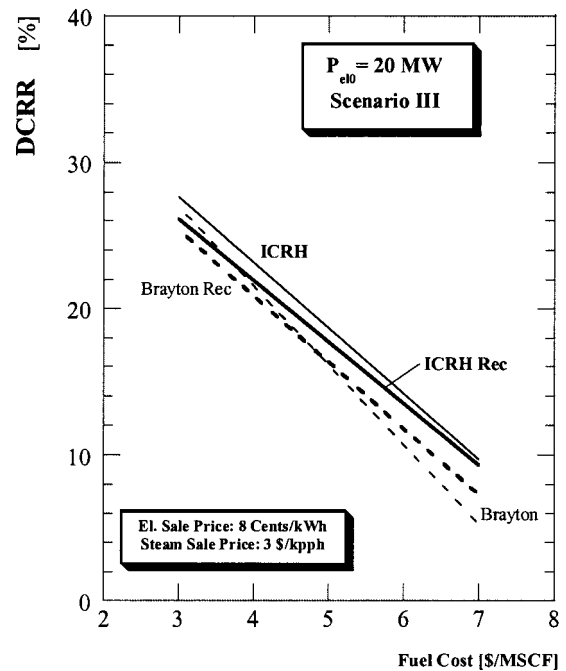


Fig. 24 DCRR versus fuel cost for medium-size cogeneration plant (scenario 3)

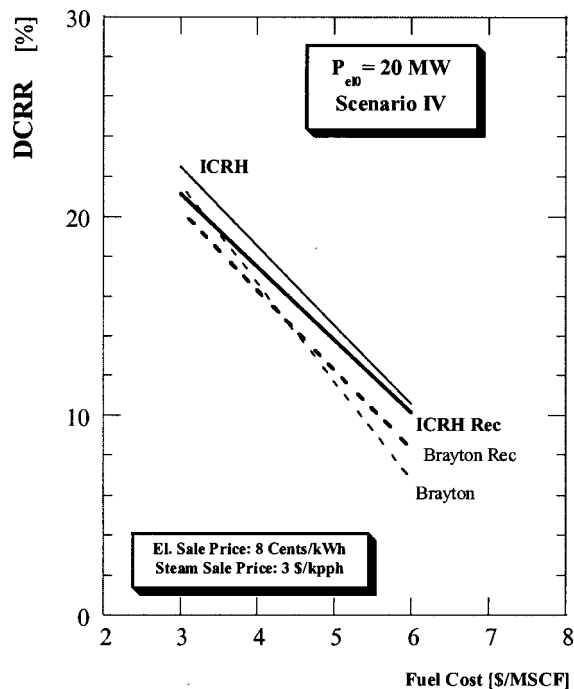


Fig. 25 DCCR versus fuel cost for medium-size cogeneration plant (scenario 4)

to the recuperated ICRH cycle, is mainly due to its reduced equipment cost and increased revenues associated with steam production (see Fig. 12).

Effects of Fuel Cost on Economic Performance. The effects of fuel cost on the DCCR values for midsize ($P_{e10} = 20$ MW) load case for all the part-load scenarios, shown in Figs. 23–25, reveal some interesting observations: (a) the ICRH cycle has the highest DCCR values in comparison to the other cycles over the entire range of the fuel cost values examined; (b) the differences in the DCCR values increase in comparison to the Brayton cycle, particularly at the high fuel cost values, as the operating hours in a year for the part-load conditions increase; and (c) the recuperated ICRH cycle becomes economically attractive at higher values of fuel cost and with unit operating under part-load condition for longer duration in a year. Also, the value of fuel cost corresponding to which the recuperated ICRH cycle achieves higher economic performance (compared to the other cycles except the nonrecuperated ICRH cycle) decreases as the yearly generated energy decreases at a part-load condition.

In summarizing the economic analysis results, it is obvious that the midsize nonrecuperated ICRH cycle, compared to the other cycles, achieves higher return on investment under full-load and part-load conditions over the entire range of fuel cost, electric sale, and steam sale values.

The main reason for poor economic performance of midsize recuperated ICRH cycle, compared to the same-size nonrecuperated ICRH cycle, under part-load operation are two folds: higher equipment cost and increased penalty in steam generation.

The obtained results also show that the differences in DCCR values for the four cycles, when considering effects of fuel and electric sale prices and operating under full-load and part-load conditions, are small (less than 2–4 percent) as is evident, for example, from Figs. 16, 18–21. This observed trend can be attributed to the small differences in thermodynamic performance for different cycles at a given operating condition and the selected value of power-to-heat ratio. For example, the maximum values of difference in electric efficiency between Brayton and recuperated ICRH cycle are 2.3 percent, 3.3 percent, and 1.9 percent for 100 MW, 20 MW, and 5 MW load cases, respectively, at the full-load

operating condition as is evident from Table 2. Furthermore, the differences in electric efficiency values between recuperated and nonrecuperated ICRH cycles are less than 0.5 percent for the three load cases examined (see Table 2).

It is evident that the part-load analyses at different values of power-to-heat ratio are required to obtain complete understanding of the economic performance for the cycles investigated here.

Conclusions

A systematic approach to conduct thermo-economic analysis for the recuperated ICRH cycle and its comparison with the other cycles (nonrecuperated ICRH, recuperated Brayton and simple Brayton cycles) in cogeneration applications has been presented in this paper. Based on the thermoeconomic analysis approach presented and implemented for three sizes of cogeneration systems, the following concluding remarks can be made:

1 In cogeneration applications of the three sizes considered, the recuperated ICRH cycle shows the lowest amount of penalty in terms of electric efficiency and energy saving index at different part-load conditions in comparison to the other cycles investigated.

2 The lower amount of penalty in terms of electric efficiency for the recuperated Brayton cycle in comparison to the nonrecuperated ICRH and Brayton cycles, under part-load conditions for all the three load cases, has been attributed to the considerable decrease in specific fuel energy for the recuperated Brayton cycle.

3 The thermal efficiency increase of the recuperated ICRH and recuperated Brayton cycle, in cogeneration applications at different part-load conditions for all the three load cases, are lowest as compared to the nonrecuperated cycles (simple Brayton and ICRH cycle). The main reason being that these two cycles have lowest values of thermal energy available for the thermal utility because of the use of recuperator in the cycle.

4 For the large load case ($P_{e1} = 100$ MW) under full-load and part-load conditions, simple Brayton cycle shows higher economic performance for the range of fuel cost, electric sale price and steam sale price in spite of its poor thermodynamic performance, compared to the other cycles with few exceptions. The main reason for the higher economic performance for the Brayton cycle can be attributed to the lowest equipment cost, higher steam generation capacity both of which offset increased penalty in terms of electric efficiency. However, the ICRH cycle provides better economic performance, compared to the other cycles under part-load conditions, for fuel cost higher than 4 \$/MSCF. The reason for the observed trend, under part-load condition for the large-load case, can be associated with highest performance penalty of the Brayton cycle compared to the other cycles.

5 For a midsize cogeneration system, the nonrecuperated ICRH cycle provides higher return on investment, both at the full-load and part-load operations, for the entire range of fuel cost, electric sale, and steam sale values examined in the present study in spite of the fact that its thermodynamic performance has been found lower than the recuperated ICRH cycle. These observed differences are mainly attributed to the increased equipment cost and decreased revenues from steam sale for the recuperated ICRH cycle.

6 For the small load case ($P_{e1} = 5$ MW) under full-load and part-load conditions, the ICRH cycle shows better economic performance for the range of fuel cost and electric sale price compared to the other cycles.

7 The obtained results also show that the differences in DCCR values for the four cycles, when considering effects of fuel and electric sale prices and operating under full-load and part-load conditions, are small (less than 2–4 percent). This observed trend can be attributed to the small differences in thermodynamic performance for different cycles at a given operating condition and the selected value of power-to-heat ratio. For example, the maximum values of difference in electric efficiency between Brayton

and recuperated ICRH cycle are 2.3 percent, 3.3 percent, and 1.9 percent for 100 MW, 20 MW, and 5 MW load cases, respectively, at the full-load operating condition.

8 The recuperated ICRH cycle showed better economic performance, compared to the simple Brayton and recuperated Brayton cycles under part-load conditions at all the load cases examined, at the higher fuel cost values.

Acknowledgment

The authors would like to thank Andrea De Pascale for his help during thermodynamic and economic calculations. The first author would like to also thank the management of Universal Ensco for their continued encouragement and financial support.

Nomenclature

- ESI = Energy Saving Index: $= (F^* - F) / F^* = 1 - 1 / (\eta_{el} / \eta_{el}^* + \eta_{th} / \eta_{th}^*)$ where the variables with the superscript * refer to values for η_{th} and η_{el} taken equal to 0.8 and 0.37, respectively
- F = LHV fuel energy supplied in a cogenerative plant
- F^* = total LHV fuel energy supplied in the two separate plants producing the same amount of electric and thermal power as that of the cogenerative plant
- IGV = inlet guide vane
- m = mass flow rate
- MFF = mass flow function: $= m \sqrt{T/p}$
- p = pressure
- P_{el} = electric power output
- Q_{th} = thermal power to the utilities
- q_1 = specific fuel energy: $= F/m_a$
- T = temperature
- T_{in} = temperature at inlet to the HRSG
- TiT = inlet temperature to the first-stage turbine rotor
- u = average blade speed
- w = specific power: $= P_{el}/m_a$
- β_{TOT} = overall cycle pressure ratio
- β_{HPT} = HPT pressure ratio
- β_{LPC} = LPC pressure ratio
- Δh = stage specific enthalpy drop
- η_{el} = LHV electric efficiency: $= P_{el}/F = w/q_1$
- η_{th} = LHV thermal efficiency: $= Q_{th}/F$
- η_{pc} = polytropic compression efficiency
- η_{pe} = polytropic expansion efficiency
- Ψ = aerodynamic loading parameter: $= \Delta h/u^2$

Subscripts and Superscripts

- 0 = design case
a = air
in = inlet
out = outlet

Acronyms

- APR = annual percentage rate
CC₁ = high pressure combustor
CC₂ = low pressure combustor
DCRR = discount cash flow rate of return
ECO = economizer
GT = gas turbine
GPO = gross payout period
HPC = high pressure compressor
HPT = high pressure turbine
HRSG = heat recovery steam generator
IC = intercooler
ICRH = intercooled reheat
LHV = lower heating value
LPC = low pressure compressor
LPT = low pressure turbine
MSCF = 1000 standard cubic foot
REC = recuperator
VAP = vaporizer

References

- [1] Saidi, A., Sunden, B., and Eriksson, D., 2000, "Intercoolers in Gas Turbine Systems and Combi-Processes for Production of Electricity," ASME Paper No. 2000-GT-0234.
- [2] McDonald, C. F., 2000, "Low Cost Recuperator Concept for Microturbine Applications," ASME Paper No. 2000-GT-167.
- [3] Bhargava, R., Bianchi, M., Negri di Montenegro, G., and Peretto, A., 2000, "Thermo-economic Analysis of an Intercooled, Reheat and Recuperated Gas Turbine for Cogeneration Applications: Part 1—Base Load Operation," ASME Paper No. 2000-GT-0316.
- [4] Cohen, H., Rogers, G. F. C., and Saravanamuttoo, H. I. H., 1987, "Gas Turbine Theory," 3rd Ed., Longman Singapore Publishers (Pte) Ltd., Singapore, pp. 292–293.
- [5] Kays, W., and London, L., 1964, *Compact Heat Exchangers*, 2nd Ed., McGraw-Hill, New York.
- [6] Rohsenow, W. M., Hartnett, J. P., and Ganic, E. N., 1985, *Handbook of Heat Transfer Applications*, 2nd Ed., McGraw-Hill, New York.
- [7] Benvenuti, E., Bettocchi, R., Cantore, G., Negri di Montenegro, G., and Spina, P. R., 1993, "Gas Turbine Cycle Modeling Oriented to Component Performance Evaluation from Limited Design or Test Data," ASME—Cogen Turbo, Bournemouth, UK, Sept. 21–23.
- [8] Bhargava, R., and Peretto, A., 2001, "A Unique Approach for Thermo-economic Optimization of an Intercooled, Reheat and Recuperated Gas Turbine for Cogeneration Applications," ASME Paper No. 2001-GT-0206.

Conformable Eddy-Current Sensors and Arrays for Fleetwide Gas Turbine Component Quality Assessment

N. Goldfine

D. Schlicker

Y. Sheiretov

A. Washabaugh

V. Zilberstein

T. Lovett

JENTEK Sensors, Inc.,
110-1 Clematis Avenue,
Waltham, MA 02453-7013
e-mail: jentek@shore.net

The conformable Meandering Winding Magnetometer (MWM[®]) eddy current sensors and MWM-arrays provide new inspection capabilities for gas turbine components. The sensors provide measurements of coating thickness and absolute electrical conductivity, which can capture features of interest for a population of components, e.g., for tracking fleetwide trends in quality and aging, failure evaluations, and correlating failure origins to features of specific fleet population segments. Inspection applications include metallic and nonmetallic coating thickness and porosity measurement, detection of cracks on complex surfaces, imaging and detection of small flaws, thermal degradation monitoring, and cold work quality assessment. For example, the U.S. Air Force uses the MWM for cold work quality control on all of the C-130 propeller blades that go through the Warner Robins ALC. For P-3 and C-130 propeller blades, trend analysis is being performed fleetwide. This paper describes MWM technology advances for absolute property measurements and specific capability demonstrations. Multifrequency quantitative inversion methods used for coating characterization are also used for characterization of process-affected zones, such as shot peen quality or titanium alpha case characterization.

[DOI: 10.1115/1.1477196]

1 Introduction and Background

In service, effective monitoring of critical gas turbine components blades and vanes for condition and remaining life assessment is essential to address both safety and cost concerns. Cost-effective condition assessment and remaining life prediction for overlay coatings and thermal barrier coatings (TBCs) require an accurate, practical, and fieldable nondestructive method that provides relevant information about thickness and degradation of the coatings as well as degradation of the substrate.

Conventional nondestructive testing equipment has a limited capability to characterize TBCs as it can measure no more than two variables independently, typically coating thickness and liftoff where liftoff is defined as the proximity of the material under test to the eddy current sensor. This is a severe limitation, as many coated systems require measurement of additional parameters, such as the coating porosity (electrical conductivity) and/or the substrate conductivity. As indicated by Auld and Moulder [1], for conventional eddy-current sensors “nominally identical probes have been found to give signals that differ by as much as 35%, even though the probe inductances were identical to better than 2%.” Characterization of overlay coatings and TBCs with conventional eddy current sensors is rendered impractical by this lack of sensor reproducibility, difficulty in modeling of the complex winding interactions with layered media, and effects of liftoff and probe tilt on complex shaped components. These limitations for curved parts have been overcome through a combination of conformable sensors and independent determination of liftoff and other variables using the MWM.

Using a spatially periodic field conformable eddy-current sensor such as the MWM and a quantitative model-based inversion algorithm, a nondestructive method has been developed for char-

acterization of nonmagnetizable metallic coatings on nonmagnetizable substrates ([2]). The current method permits independent and simultaneous measurement of three unknown variables; in the case of TBCs, these unknowns include ceramic topcoat thickness, metallic bond coat porosity, and metallic bond coat thickness. It is applicable for manufacturing quality control of overlay coatings and TBCs and for in-service inspection of those coating/substrate combinations that do not become magnetizable in service. The method also works for some weakly magnetic coatings ([3]).

The MWM Sensor—The MWM is an inductive, eddy-current-based sensor designed specifically for nondestructive material characterization. The sensor consists of a meandering primary winding for creating the magnetic field and secondary windings located on both sides of the primary for sensing the response. The windings are typically fabricated onto a thin and flexible substrate, producing a conformable sensor. Micro-fabrication techniques are employed to produce the MWM sensors, resulting in essentially identical sensors. The winding pattern of the sensor permits the interactions of the periodic magnetic field with multiple layered media to be modeled accurately. This significantly reduces calibration requirements. For example, in some situations an “air calibration” can be used to measure a component’s absolute electrical conductivity without calibration standards. For characterization of coatings with MWM, standards with coatings are not required; calibration is performed on a reference part having the approximate properties of the substrate, such as an uncoated section of material at the blade root. Figure 1 provides schematics of (a) a single sensing element sensor, (b) an MWM-array sensor with four sensing elements, and (c) a deeper penetration MWM-array with multiple differential and absolute sensing elements. Scanning with MWM sensors or with MWM-arrays provides the capability for imaging the material properties and conditions.

The Measurement Grid-Based Inversion Methods—The MWM sensor response is converted into material or geometric properties using measurement grids. These grids are used to map the magnitude and phase of the transimpedance into unknown properties of interest. The grids are two-dimensional databases, which can be

Contributed by the International Gas Turbine Institute (IGTI) of THE AMERICAN SOCIETY OF MECHANICAL ENGINEERS for publication in the ASME JOURNAL OF ENGINEERING FOR GAS TURBINES AND POWER. Paper presented at the International Gas Turbine and Aeroengine Congress and Exhibition, New Orleans, LA, June 4–7, 2001; Paper 01-GT-212. Manuscript received by IGTI, Dec. 2000; final revision, Mar. 2001. Associate Editor: R. Natole.

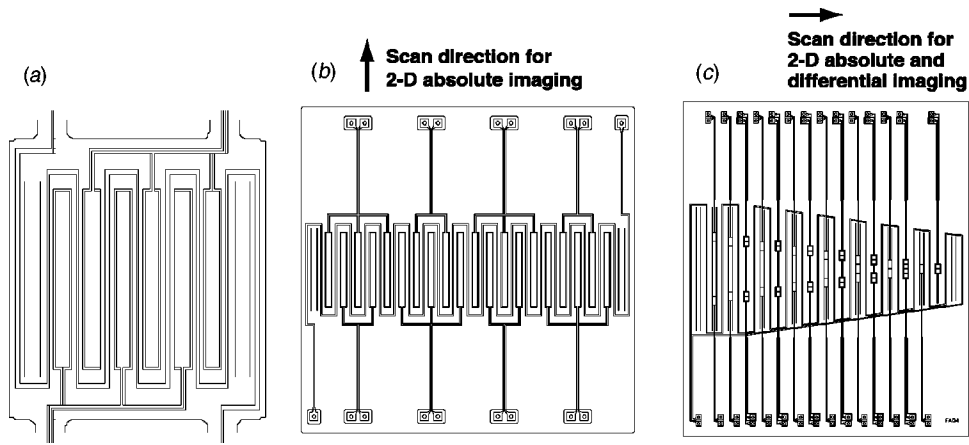


Fig. 1 (a) Single-sensing element MWM sensor, (b) MWM-array, and (c) tapered MWM-array

displayed graphically to support procedure development. Typically, grids relate two measured parameters to two unknowns, such as the electrical conductivity and liftoff, or metallic coating thickness and liftoff. Three-dimensional versions of the measurement grids, called grid lattices, are discussed in Section 2.1.

For overlay coatings and TBCs, the MWM with inversion algorithm first provides a measure of effective absolute conductivity as a function of frequency and liftoff. Then, for the metallic bond coat or overlay coating, thickness and porosity are determined. In the case of TBCs, the liftoff provides a measure of ceramic coating thickness to within $\pm 2 \mu\text{m}$; reproducibility of better than $\pm 1.5 \mu\text{m}$, day to day, has recently been demonstrated by NASA Glenn Research Center using the MWM and grid methods for ceramic thickness measurements ([4]).

Earlier Results—The MWM technology has shown the capability to measure nondestructively the coating thickness for a variety of as-manufactured MCrAlY coatings, aluminide coatings, and other metallic coatings on various substrates. For example, the MWM can be used to monitor thermal degradation of the overlay coatings and bond coats for PtAl coating ([5]). In one study, MWM measurements on high-nickel Alloy U520 components correlated with the degree of increasing sigma phase precipitation in well-characterized samples provided by Westinghouse Power Corporation ([6,7]). In another study, the MWM was used to characterize embrittled Alloy 718 samples provided by Idaho National Engineering and Environmental Laboratory.

MWM resistivity measurements were found to be repeatable and correlated well with specimen high-temperature exposure time ([6]). The thermal degradation evidenced by decreases in resistivity has been shown to cause reduction in material toughness ([8]).

2 Characterization of Coatings and Substrate Materials

2.1 Grid Lattices and Multiple-Frequency Algorithm for Determination of Three Variables. A multiple-frequency algorithm has been developed for the independent determination of three properties associated with the coating evaluation. This algorithm has successfully been applied to as-manufactured coatings and has the potential for evaluating service-aged coatings. In this algorithm, three-dimensional grid lattices are used. The lattices are sets of two-dimensional measurement grids, where each grid describes the sensor response to changes in coating thickness and liftoff at a given coating conductivity. The lattices shown in Fig. 2 contain coating thickness—liftoff grids for four values of the coating conductivity at 1 MHz and 6.31 MHz. Within each grid, the spacing between the grid points indicates the sensitivity for independently estimating the coating thickness and liftoff. The grid spacing depends on the difference between the coating and substrate conductivities. The lattices of Fig. 2 are relatively coarse for visualization purposes, with only 140 lattice points (seven coating

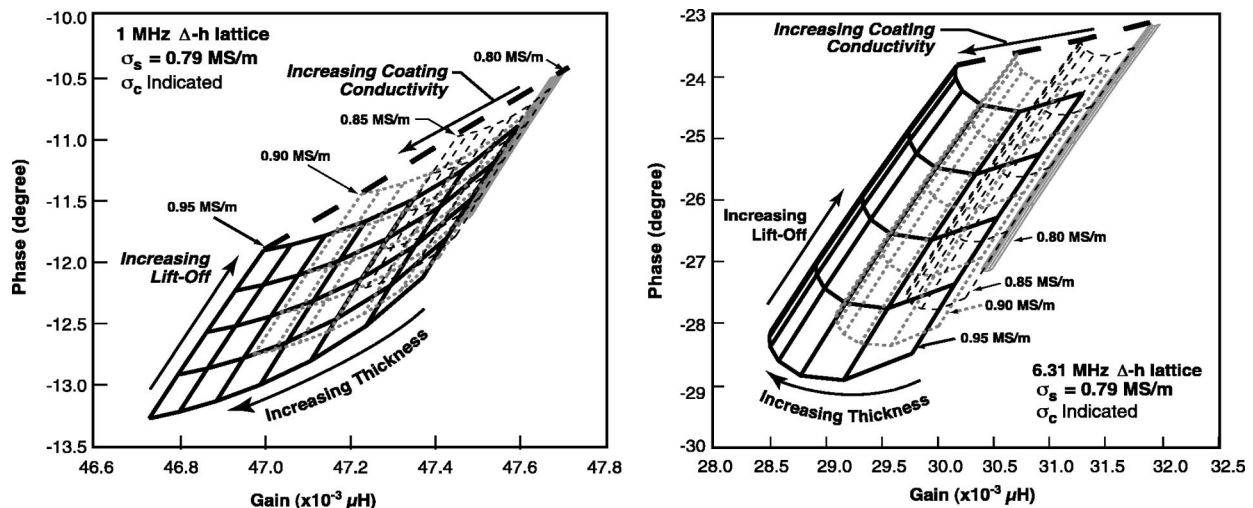
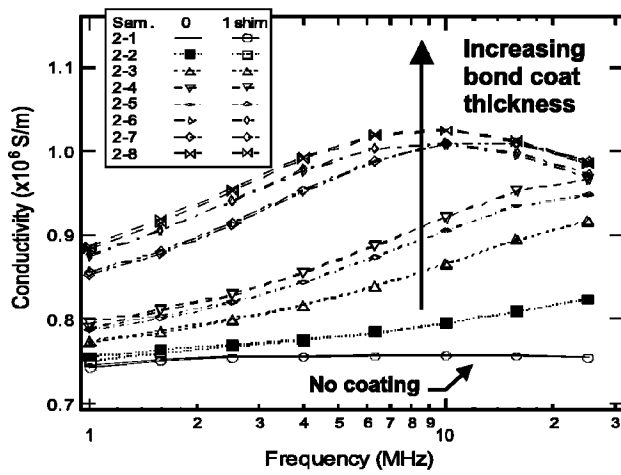
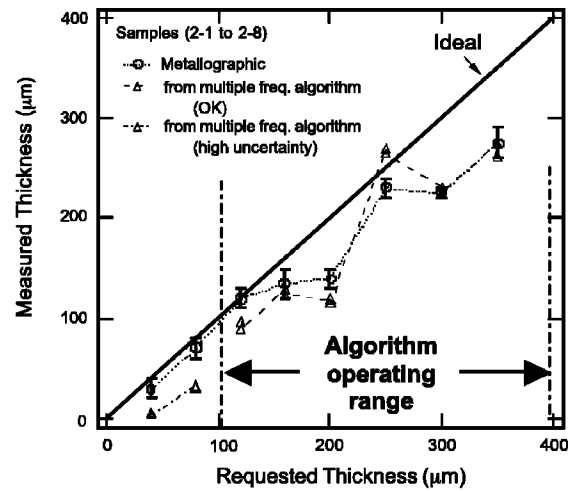


Fig. 2 Coating thickness—liftoff grid lattices for MCrAlY coating family



(a)



(b)

Fig. 3 MWM results for MCrAlY on IN 738; (a) multiple-frequency MWM effective conductivity data for different coating thicknesses, (b) MWM metallic bond coat thickness results compared to metallography thickness and requested thickness (ideal). The samples were provided by Innogy Ltd.

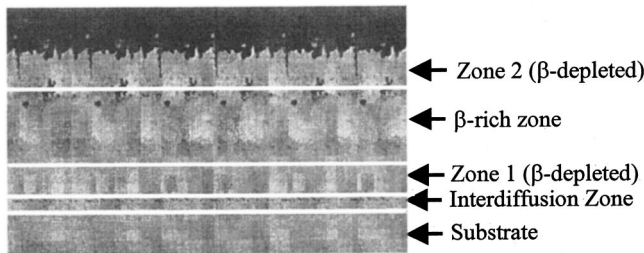


Fig. 4 Schematic representation of a degraded MCrAlY coating

thicknesses, five liftoffs, and four coating conductivities), whereas a typical lattice has on the order of 20,000 points.

2.2 Thickness Measurements on As-Manufactured Samples. For components with conductive coatings, the effective electrical conductivity near the surface is measured with a wide-frequency range instrument. It is essential that this instrument provides accurate impedance magnitude and phase at each frequency for a wide range of operating conditions (a commercially available JENTEK multiple frequency impedance instrument was used for this purpose). Typical results are shown in Fig. 3(a). For the uncoated samples, the conductivity is constant with frequency. For the coated samples, the low-frequency response tends toward the substrate conductivity as the skin depth of the magnetic field becomes large compared to the coating thickness. The high frequency response becomes small compared to the coating conductivity as the skin depth of the magnetic field approaches the coating thickness ([9]).

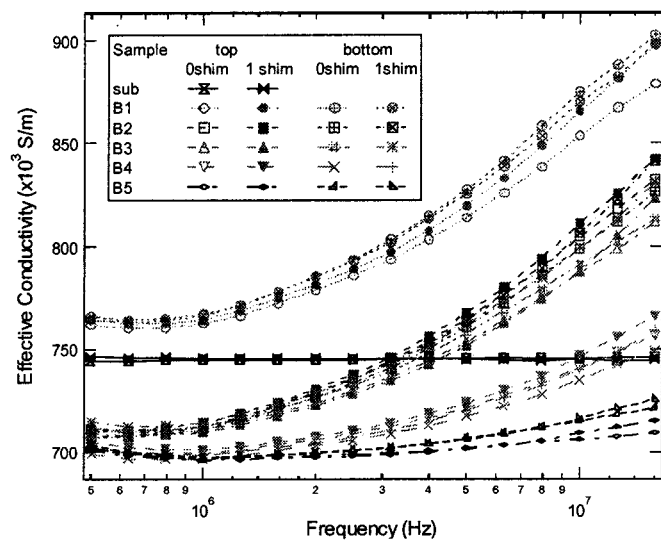
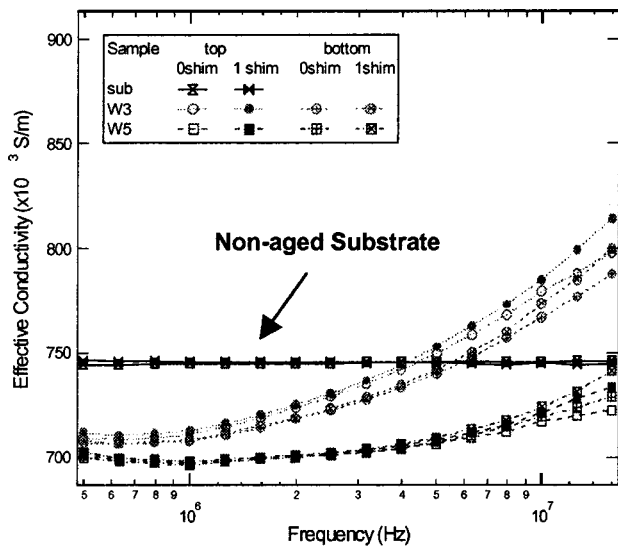


Fig. 5 MWM multiple-frequency measurements for both sides of blind test samples

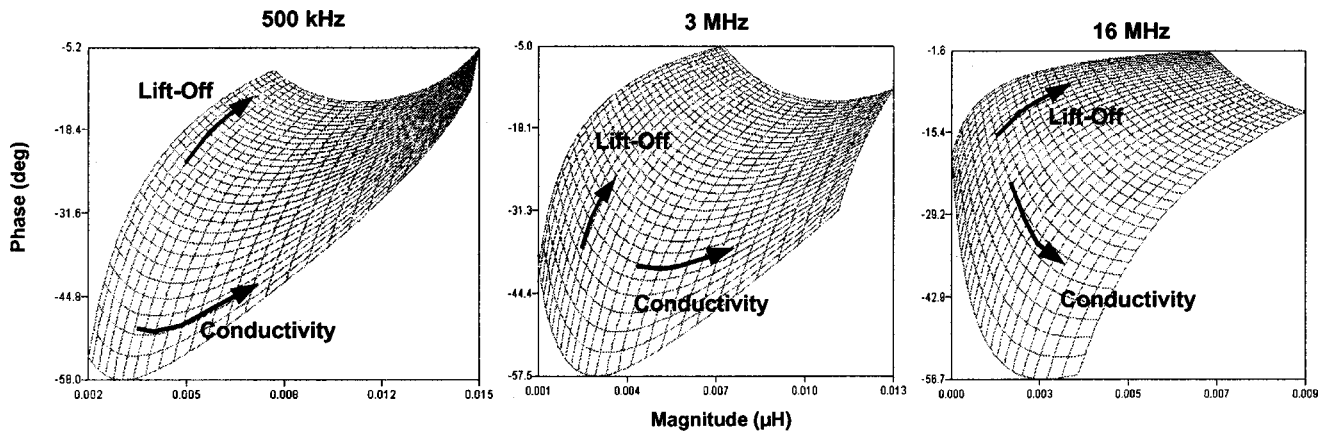


Fig. 6 Representative conductivity/liftoff measurement grids used for characterization of the coated samples in the EPRI round robin. These grids assume a uniform conductivity, i.e., no coating.

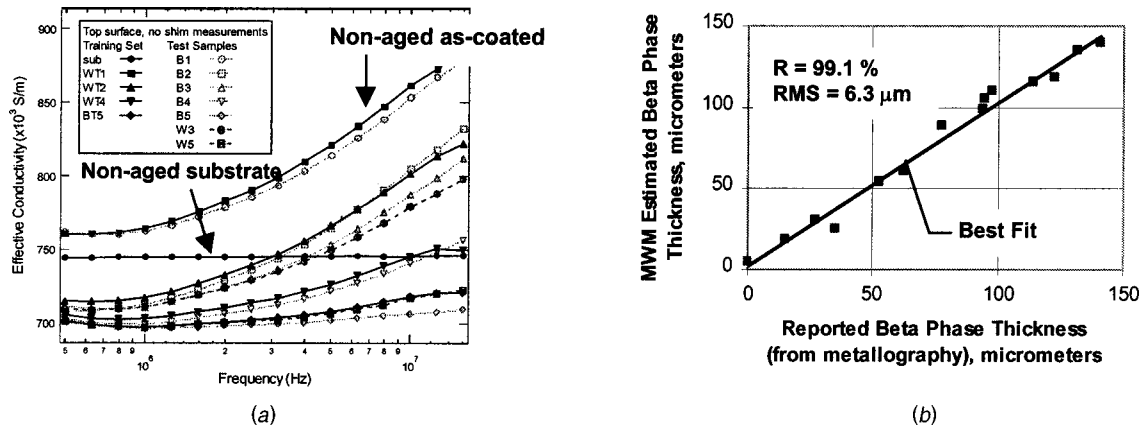


Fig. 7 (a) Comparison of the MWM multifrequency effective conductivity measurements for training set and blind test samples on one side of each sample without a shim, (b) MWM measured beta-phase layer thickness versus reported beta-phase layer thickness for blind test set

Table 1 Comparison of the layer thickness values estimated based on the MWM measurements with reported metallographic data. The training set consisted of samples WT1, WT2, WT4, and BT5. The blind test set was comprised of samples B1 through B5, W3, and W5. (Zone 1—internal β -depleted zone, Zone 2—external β -depleted zone).

Sample	Side	Coating Thickness Reported by EPRI, μm			Coating Thickness Estimated from MWM measurements, μm		
		Zone 2	β -phase	Zone 1	Zone 2	β -phase	Zone 1
WT1	T	0.0	134.4	0.0	0.7	136.4	0.0
WT1	B	0.0	136.2	0.0	2.6	134.5	0.0
WT2	T	20.1	122.7	0.0	21.7	115.2	0.2
WT2	B	22.9	115.1	0.0	17.5	119.6	0.0
WT4	T	47.1	57.0	33.7	41.3	64.0	31.8
WT4	B	43.1	61.2	36.5	43.8	57.6	35.7
BT5	T	56.0	27.8	54.0	55.9	26.1	55.2
BT5	B	51.4	23.1	54.7	57.0	23.1	57.0
B1	T	0.0	132.0	0.0	1.8	135.3	0.0
B1	B	0.0	140.9	0.0	0.0	139.6	0.0
B2	T	14.5	122.4	8.9	18.7	118.4	0.0
B2	B	11.6	114.2	8.1	21.6	115.5	0.0
B3	T	17.9	94.6	14.9	25.6	105.1	6.5
B3	B	19.7	98.0	16.8	23.8	109.6	3.7
B4	T	37.5	62.6	34.0	42.7	60.3	34.0
B4	B	33.2	52.6	38.1	45.2	53.8	38.1
B5	T	118.7 (reported as Zone 1; includes Zone 2; no β)			64.0	4.8	68.2
B5	B	48.5	15.2	61.5	58.6	19.0	59.5
W3	T	26.4	94.4	15.4	28.0	98.6	10.4
W3	B	27.9	78.0	19.1	32.0	88.2	16.9
W5	T	50.2	35.2	46	56.4	24.8	55.9
W5	B	46.9	27.6	45.9	54.3	30.3	52.6
				RMS error (μm)	6.57	6.31	6.78

The data in Fig. 3(b) shows a comparison of the measured coating thickness values with those requested from the manufacturer. For a few of these samples, the actual MCrAlY coating thickness, determined by destructive metallographic measurements, was substantially different than the nominal thickness requested from the coating supplier. The data suggest that MWM with grid methods provided an accurate coating thickness measurement when compared to the metallographic measurements on the same samples. For MCrAlY coatings, the MWM coating thickness values are generally reliable in the 100 to 250 μm (4 to 10 mil) range.

2.3 MWM Characterization of Service-Aged MCrAlY Coatings¹. The MWM was recently used to characterize artificially degraded MCrAlY coatings. This characterization was conducted as a part of Electric Power Research Institute (EPRI) round robin testing. The objective was to demonstrate the capability to provide a quantitative assessment of coating degradation for MCrAlY coatings used on combustion turbine blades. MWM measurements were initially performed on five training set samples. These included one noncoated GTD-111 as-machined specimen and four samples with PWA 286 coating on both “top” and “bottom” surfaces. According to information provided in the test protocol, three of the four coated samples in the training set were aged.

After completing measurements on the training set, multiple frequency MWM measurements were performed on seven samples provided for the blind test. For each sample, four MWM measurements were made, i.e., two on each side of the sample, one with the sensor placed directly on the surface, and another with a 25- μm (0.001-in.) thick insulating shim. The data were processed with quantitative, model-based inversion methods to estimate the thicknesses of the top three coating layers shown in Fig. 4.

MWM results for the blind test samples are shown in Fig. 5. The effective conductivity was obtained at each frequency using conductivity/liftoff measurement grids. Figure 6 shows the measurement grids for three of the frequencies. The flat conductivity response in Fig. 5 corresponds to the baseline (reference) response of the nonaged substrate. Measurements with and without an insulating shim placed between the MWM sensor and the sample provide very similar results, indicating that the measured effective conductivity is not affected by liftoff. Figure 7(a) shows MWM measured effective conductivity for the coatings on the top surface of the samples, without a shim, for both the training set and blind test samples. The uppermost curve corresponds to the as-coated sample. The aged samples from the training set show a progression of decreasing effective conductivity across the frequency range reflecting the effects of degradation due to aging. The effective conductivities of the blind test samples are similar to those measured on the training set samples, which suggests that the training set samples adequately represent the blind test samples and that estimation methods based on the training set data should apply to the blind test samples. The MWM measurement results were analyzed using an estimation algorithm based on a model for the sensor response to obtain the various layer thicknesses. Table 1 shows a summary of the estimation results comparing the MWM measurements to the reported layer thickness values based on metallographic measurements ([10]). The numbers beneath the table indicate the root-mean-square (RMS) of the errors between the metallographic data and the MWM based estimates for each layer of the blind test samples. The RMS error of the β -phase zone thickness estimates based on the MWM measurements is about 6 μm (see Fig. 7(b)).

¹The authors would like to thank Mr. Kenji Krzywosz of EPRI NDT Center for his review of this section.

3 Characterization of Process-Affected Zones

3.1 Alpha Case Thickness Measurement in Titanium Alloys. Alpha case can form at the surface of titanium alloys as the result of aggressive machining or during cooling of titanium castings in a mold. This oxygen-rich phase is relatively brittle and can provide initiation sites for cracks. To demonstrate the MWM capability to detect alpha case and quantify its thickness, measurements were performed on cast titanium samples with varying alpha case thickness. One of these samples is a stair-step cast sample, supplied by Howmet, that has eight regions with reported alpha case thicknesses of 5.1 to 24.5 mils. The alpha case thickness varies along the surface due to the differences in cooling rates associated with the sample thickness variations.

Two methods, multiple-frequency measurements and single-frequency measurements, have been used to estimate the thickness of the alpha case. For the single frequency measurements, it was assumed that the alpha case can be represented as a discrete layer on the titanium alloy substrate and that the conductivities of both phases are known so that coating thickness/lift-off measurements grids could be used. Figure 8 presents results of the alpha case thickness estimation from single frequency measurements. The value of the MWM measurement at each point is a weighted average of two neighboring regions since the sensor footprint has a finite width.

3.2 Shot Peening Process Quality Control Monitoring. Shot peening is a commonly used process for introducing compressive residual stresses at the surface of fatigue-critical areas of components. In this process, a high-velocity stream of shot or a special flapper tool is used to plastically deform a near-surface layer. The intensity of the shot peening process is generally measured with Almen strips placed at various positions around the part. Within the plastically deformed (cold-worked) layer, high compressive residual stresses are locked in. The electrical conductivity of the cold worked layer is lower than the conductivity of the underlying base metal, which can be detected with the MWM.

Figure 9 shows the results of multiple frequency MWM measurements for two aluminum alloys. The plot on the left shows the results for Al 2024 samples prepared by Boeing while the plot on the right shows the results for Al 7076 propeller blades provided by Warner Robins. In these measurements, the unpeened sample conductivity was essentially constant with frequency. For the peened samples, the effective conductivity varies with frequency. The thickness of the process-affected zone can be estimated based on the multiple frequency data, assuming that the processed zone is a discrete layer over an unprocessed substrate. The estimated affected zone thickness is shown in Fig. 10 for both the Boeing and Warner Robins samples.

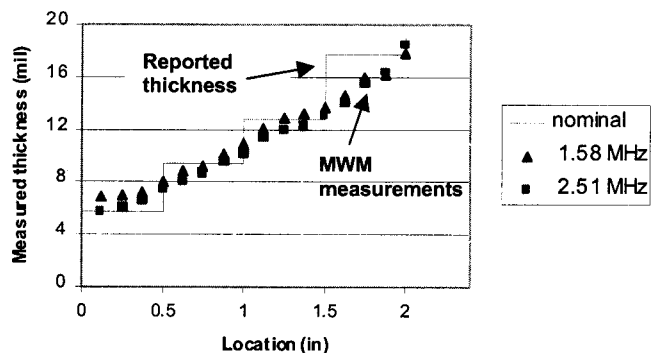


Fig. 8 MWM measured and reported nominal alpha case thickness over the stair-step cast sample

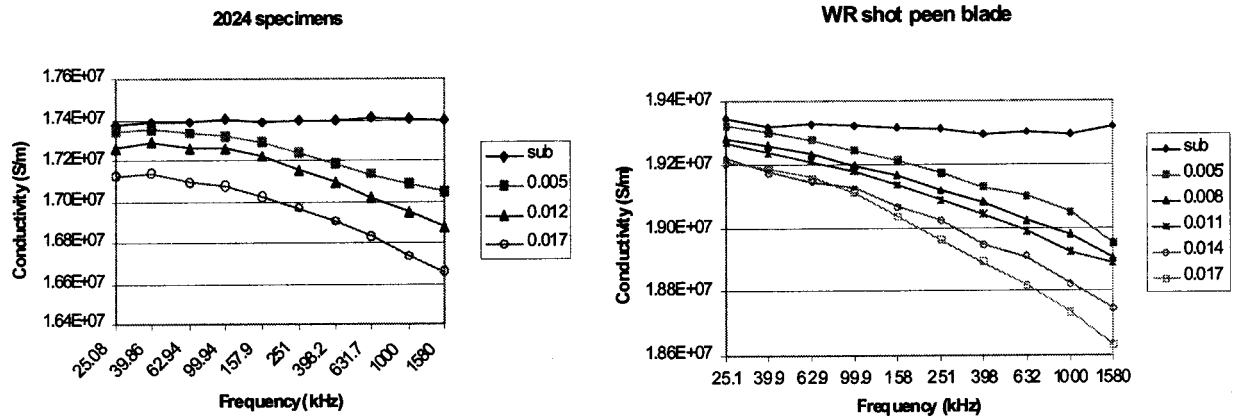


Fig. 9 Multiple-frequency measurements of shot-peened aluminum components. The indicated Almen intensities are given in scale A.

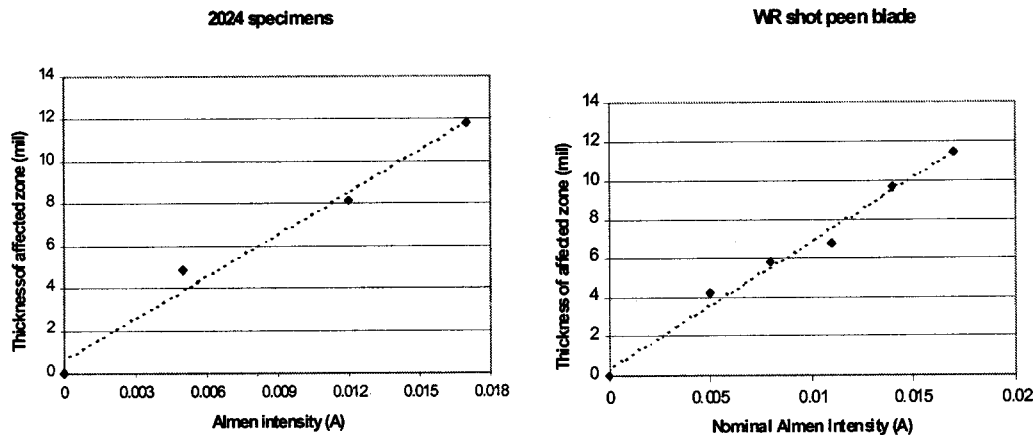


Fig. 10 Estimated effective thickness of the shot peen process-affected zone versus Almen intensity

For quality control monitoring during manufacturing processes, it is generally more desirable to monitor the intensity of the shot peening process directly on the peened surfaces rather than indirectly with Almen strips. This can be accomplished using a simplified, two-frequency approach, through the ratio of effective conductivities measured at a relatively high frequency and a relatively low frequency. This method has provided good results for aluminum alloys and is expected to work for gas turbine component materials as well.

4 Conclusion

The key advantage of MWM sensors is the capability to provide consistent absolute property data for a population of inspected components. The MWM sensor has the potential to become an efficient monitoring and diagnostics tool for fleetwide quality assessment of gas turbine components. The MWM sensors and MWM-arrays can provide traceable information on changes in the coating and potentially in the substrate in terms of absolute physical properties of interest. It is an effective and affordable method for building a database of coating performance to support trend analysis and engineering/maintenance/procurement decisions within a utility or for a fleet of gas turbines.

References

- [1] Auld, B. A., and Moulder, J. C., 1999, "Review of Advances in Quantitative Eddy Current Nondestructive Evaluation," *J. Nondestruct. Eval.*, **18**(1).
- [2] Goldfine, N. J., 1993, "Magnetometers for Improved Materials Characterization in Aerospace Applications," *Mater. Eval.*, **Mar.**, pp. 396-404.
- [3] Goldfine, N. J., Lovett, J. T., and Sheiretov, Y., 1995, "Dielectrometers and Magnetometers, Suitable for in-situ Inspection of Ceramic and Metallic Coated Components," *SPIE Conference on Nondestructive Evaluation of Aging Infrastructure*.
- [4] Miller, R. A., 2000, private communication.
- [5] Goldfine, N. J., Zombo, P. J., and Miller, R. A., 1999, gas turbine materials.
- [6] Goldfine, N., Washabaugh, A., Walrath, K., Zombo, P., and Miller, R. 1998, "Conformable Eddy Current Sensors and Methods for Gas Turbine Inspection and Health Monitoring," *Gas Turbine Materials Technology, Proc. ASM International Gas Turbine Technology Conference*, ASM International, Materials Park, OH.
- [7] Goldfine, N. J., and Zombo, P. J., 1994, "Combustion Turbine Blade Coating Characterization Using a Meandering Winding Magnetometer," *Fall 1994 American Society of NDT Conference*.
- [8] Radavich, J. F., and Korth, G. E., 1992, "High-Temperature Degradation of Alloy 718 After Longtime Exposures," *Superalloys 1992*, S. D. Antolovich et al., eds., Minerals, Metals, & Materials Society, pp. 497-506.
- [9] Goldfine, N., Sheiretov, Y., Washabaugh, A., and Zilberstein, V., 2000, "Materials Characterization and Flaw Detection for Metallic Coating Repairs," *Insight*, **42**(12), pp. 809-814.
- [10] performance demonstration protocol for round robin testing of combustion turbine blade coatings, 2000, EPRI NDT Center.

Real-Time On-Line Performance Diagnostics of Heavy-Duty Industrial Gas Turbines

S. C. Gülen

GE Power Systems,
1 River Road,
Schenectady, NY 12345

P. R. Griffin

Thermoflow Incorporated,
29 Hudson Road,
Sudbury, MA 01776

S. Paolucci

MASSPOWER,
General Electric Company,
750 Worcester Street,
Indian Orchard, MA 01151

This paper describes the results of real-time, on-line performance monitoring of two gas turbines over a period of five months in 1997. A commercially available software system is installed to monitor, analyze and store measurements obtained from the plant's distributed control system. The software is installed in a combined-cycle, cogeneration power plant, located in Massachusetts, USA, with two Frame 7EA gas turbines in Apr. 1997. Vendor's information such as correction and part load performance curves are utilized to calculate expected engine performance and compare it with measurements. In addition to monitoring the general condition and performance of the gas turbines, user-specified financial data is used to determine schedules for compressor washing and inlet filter replacement by balancing the associated costs with lost revenue. All measurements and calculated information are stored in databases for real-time and historical trending and tabulating. The data is analyzed ex post facto to identify salient performance and maintenance issues. [DOI: 10.1115/1.1413465]

1 Introduction

Even under the best possible operating conditions, the performance of a gas turbine is subjected to deterioration due to compressor fouling and corrosion, inlet filter clogging, thermal fatigue, and oxidization of hot gas path components such as combustion liners and turbine blades.

The performance degradation attributed to compressor fouling is mainly due to deposits formed on the compressor blades by particles carried in by the air that are not large enough (typically a few microns diameter) to be blocked by the inlet filter. Depending on the environment, these particles may range from dust and soot particles to water droplets or even insects. These deposits result in a reduction of compressor mass flow rate, efficiency, and pressure ratio which in turn causes a drop in gas turbine's power output while increasing its heat rate. This type of degradation is by far the dominant mode. Indeed, several studies of heavy-duty industrial gas turbines suggest that the decrease in output can easily reach five percent after a month's operation (e.g., [1]).

Fortunately, compressor fouling is a "recoverable" degradation in that it can be alleviated by periodic on-line and/or off-line compressor washes. In an on-line wash, distilled water is injected into the compressor while the gas turbine is running such that water droplets impact the blades at high speeds to loosen and partially remove deposits. However, complete performance recovery can only be achieved by an off-line wash where distilled water (sometimes mixed with a special detergent) is sprayed into the gas turbine while being rotated by the starter at the crank speed.

Inlet filter clogging reduces gas turbine air flow and compressor inlet pressure and thus adversely affects gas turbine performance. Replacing the old filter with a new one can recover the lost performance.

The performance degradation associated with hot gas path components is influenced by myriad factors such as fuel quality, number of starts, amount of water/steam injection etc. and it is commonly referred to as "nonrecoverable." Typically, for a base load machine this type of degradation can be 0.2–0.3 percent of the

nominal (when new and clean) rating after a month's operation ([2]). The only remedy for nonrecoverable degradation is an engine overhaul.

Although the benefits of compressor washing and inlet filter replacement are undoubted, the frequency of on-line and off-line washes and the type of detergent solvents to be used (if at all) and when to replace the filter are widely debated issues. It is essential to develop maintenance schedules based on the characteristics of the engine and its operating environment and/or cycle in order to balance the maintenance costs with lost revenue and extra fuel costs ([3]).

In this paper, results obtained from an on-line monitoring system for two industrial gas turbines will be presented in a way to clarify the general issues enumerated in the preceding paragraph. The monitoring system itself, results and financial benefits thereof specific to the installation site were the subject of an earlier paper by Gülen et al. [4].

2 Plant Description

The 245-MW gas-fired combined-cycle cogeneration power plant consists of two GE PG7121EA gas turbines with evaporative inlet coolers, one 72-MW condensing, dual admission/dual extraction, axial exhaust steam turbine, and two heat recovery steam generators (HRSGs). The plant is designed to deliver up to 150,000 lb/hr of steam to a steam host at 675 psia and 750°F and injection steam to the gas turbines at 310 psia and 550°F for NO_x control. Plant construction started in Oct. 1991, and it was commercially operating by July 1993.

Both gas turbines are primarily controlled by GE Mark IV Speedtronic control systems which are connected to the overall plant distributed control system (DCS). The on-line performance monitoring system was installed in Apr. 1997 and interfaces with the DCS to obtain gas turbine data tags.

3 System Description

The software system used for performance monitoring and subsequent data analysis is a complete unattended on-line real-time performance monitoring system that is designed to track the current and historic technical and financial performance of a gas turbine. The operating principle of the software is shown in Fig. 1.

Contributed by the International Gas Turbine Institute (IGTI) of THE AMERICAN SOCIETY OF MECHANICAL ENGINEERS for publication in the ASME JOURNAL OF ENGINEERING FOR GAS TURBINES AND POWER. Paper presented at the International Gas Turbine and Aeroengine Congress and Exhibition, Munich, Germany, May 8–11, 2000; Paper 00-GT-312. Manuscript received by IGTI, Nov. 1999; final revision received by ASME Headquarters, Feb. 2000. Associate Editor: D. Wisler.

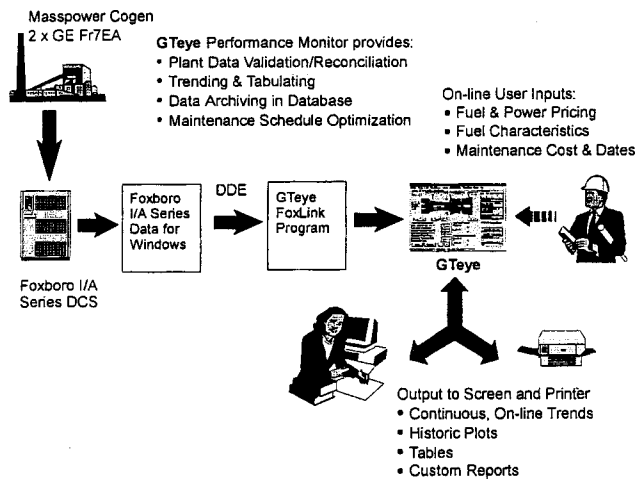


Fig. 1 How the on-line real-time performance monitoring system works

The performance monitoring suite consists of separate modules for gas turbine model configuration, on-line performance monitoring, data trending, and tabulating.

All software modules are 32-bit Windows programs designed to run on IBM-compatible personal computers (PC) with Windows 95 or NT operating systems (OS). The on-line monitoring module interacts with the plant's DCS via a special software module. The interface mechanism is the dynamic data exchange (DDE) protocol. A proprietary Windows program provided by the DCS manufacturer is the data source in the DDE conversation and the data link module is the data destination.

At a user-specified interval, the data link module requests updated values for each of the gas turbine data tags identified during the gas turbine model configuration phase. The updated values are stored in an ASCII data file that is continuously queried by the main monitoring module. When the module finds that its input file contains new data, it reads and processes the new data. In the application described herein the monitoring module reads a new data every ten seconds and averages data in intervals of one minute, one hour and one day. For more details of the software description, the reader is referred to Gülen et al. [4].

4 Gas Turbine Performance

The performance expected from the gas turbine at its undeteriorated condition at prevailing site and loading conditions can be found as follows:

$$Y_{j,x} = Y_{j,b} \prod_{i=1}^7 X_{ij} \quad (1a)$$

where Y_j is a performance parameter of the gas turbine guaranteed by the manufacturer when the gas turbine was (i) in its new and clean condition at the time of the acceptance test, or (ii) in its condition at the time of any performance test which is going to be used as a benchmark. The subscripts x and b denote expected and baseline values, respectively. The four cardinal gas turbine performance parameters are listed in Table 1. X_{ij} are the correction

Table 1 Cardinal gas turbine performance parameters, Y_j

j	GT Parameter Y_j
1	gross output at generator terminals
2	gross heat rate at generator terminals
3	exhaust gas temperature
4	exhaust gas mass flow rate

Table 2 Correction factor to Y_j , X_{ij}

i	Correction in Y_j for
1	ambient Temperature (or Compressor Inlet Temperature if there are inlet coolers and/or heaters)
2	ambient Pressure
3	ambient Humidity (or compressor inlet humidity if there are inlet coolers)
4, 5	inlet and exhaust pressure drops
6, 7	water/steam injection

factors at a given value of a specific turbine operation parameter, i , which, when multiplied with the baseline value of a turbine performance parameter Y_j , reflect the change in Y_j due to a change in i (see Table 2).

When the gas turbine is running at part load, the performance of the gas turbine is calculated as

$$Y_{j,x} = \Pi_j \left(Y_{j,b} \prod_{i=1}^7 X_{ij} \right) \quad (1b)$$

where Π_j is the part load correction factor to the gas turbine performance parameter Y_j . For the gas turbine power output, i.e., $j=1$, Π_j is the gas turbine's loading factor expressed as a fraction. For the others, Π_j is determined from manufacturer's part load correction curves.

4.1 Compressor Performance. For a given speed, there is a characteristic line that describes the flow versus pressure ratio relationship for any axial or centrifugal compressor. This line has an upper limit that is referred to as the surge point and a lower limit that is commonly called as the choke or stonewall point. At the given speed, a compressor can operate in a stable fashion only between these two points. Above the surge point, airflow within the compressor will reverse directions rapidly, thereby leading to severe vibration and equipment damage. Below the choking point, flow will not increase and compressor operation will become unpredictable. The collection of characteristic lines over a certain range of rotational speeds comprises the performance map of a given compressor. The performance map usually also includes lines of constant adiabatic efficiency which are referred to as efficiency contours.

The compressor performance map is a very useful diagnostic tool that lends itself to engine performance monitoring with the most readily available measurements. The manufacturer's performance map for the compressors of their gas turbine can be specified during model configuration phase. Unfortunately, few turbine manufacturers publish such data. Although compressor maps for certain engines can be found in the literature, they are few and far between and not easy to locate. A representative compilation is available in a commercial software, GasTurb 8.0 ([5]). One can certainly construct a compressor map from the operational data. However, this would require a reliable set of historic DCS data that is usually not the case.

When flow, rotational speed and compressor delivery pressure are expressed in nondimensional terms, effects of any changes in the compressor air inlet conditions and physical properties are eliminated. Furthermore, such normalized performance maps of a variety of compressors are found to be nearly identical (e.g. see [6]). The relevant flow, speed, and pressure rise parameters, respectively, are defined as follows:

$$\Phi = \frac{\dot{m} \sqrt{RT_0}}{P_0} \bigg/ \left(\frac{\dot{m} \sqrt{RT_0}}{P_0} \right)_{\text{design}} \quad (2a)$$

$$N = \frac{N}{\sqrt{RT_0}} \bigg/ \left(\frac{N}{\sqrt{RT_0}} \right)_{\text{design}} \quad (2b)$$

$$\Pi = \frac{p_2}{p_0} / \left(\frac{p_2}{p_0} \right)_{\text{design}} \quad (2c)$$

where \dot{m} is the compressor air mass flow rate, p is the pressure, T is the temperature, N is the rotational speed, and R is the gas constant. Subscripts 0 and 2 refer to compressor inlet and exit, respectively.

5 Gas Turbine Performance Degradation

5.1 Compressor Fouling. The difference between expected and measured powers gives the lost kilowatts due to gas turbine degradation. However, this information does not enable one to separate the effects of compressor fouling (recoverable) from those of hot gas path degradation (nonrecoverable).

The monitoring software algorithm utilizes the fact that nonrecoverable performance degradation proceeds at a rate that is approximately one order of magnitude slower than that for recoverable degradation by attributing the lost power entirely to compressor fouling. The effect of nonrecoverable degradation is introduced by using a user-specified *recovery factor*, that is

$$P_{\text{lost}} = \phi^n P_x - P_a \quad (3)$$

where ϕ is the recovery factor for power output, P_a is the actual measured power output, and n is the number of the off-line compressor wash since on-line monitoring started. Thus, we account for the fact that each off-line compressor wash restores only a fraction (equal to ϕ) of the power output previously restored by the preceding crank wash, and n^{th} off-line compressor wash restores only ϕ^n fraction of the original (baseline) power output.

A similar consideration applies to the heat rate; i.e., each off-line wash restores the heat rate to a level slightly higher than that restored by the preceding wash. In that case, extra fuel burned can be expressed as

$$F_{\text{extra}} = f_a - \phi^n \phi'^n f_x \quad (4)$$

where ϕ' is the recovery factor for the heat rate, f_a and f_x are actual and expected fuel mass flow rates, respectively. The values of ϕ and ϕ' used herein are 0.998 and 1.005, respectively.

The average linear rate of change of power lost due to compressor fouling at a given time t can be found from

$$\Pi = \frac{2}{t^2} \int_0^t P_{\text{lost}}(t) dt. \quad (5)$$

Similarly, for the average linear rate of change of the extra fuel burned due to compressor fouling

$$\Phi = \frac{2}{t^2} \int_0^t F_{\text{extra}}(t) dt. \quad (6)$$

It can then be shown that the optimum time to do an off-line compressor wash is given by

$$\tau^* = \sqrt{\frac{2C_m}{\Pi C_p + \Phi C_f}} \quad (7)$$

where C_m , C_p , and C_f are cost of maintenance, power sale price, and fuel purchase price, respectively, and τ^* is the time from the last compressor off-line wash. The on-line monitoring software uses these formulas in its algorithm to continuously update the estimated off-line compressor wash dates as new data is received and processed.

Note that, although compressor fouling is detrimental to gas turbine output and heat rate, it actually decreases the fuel consumption at full load. For a typical Frame 7 machine, a 2.5 percent decrease in compressor efficiency and five percent reduction in air mass flow results in a 7.5 percent decrease in output and a 2.9 percent increase in heat rate whereas the fuel consumption drops by 4.8 percent. The net financial impact, however, is almost always negative unless the fuel purchase price is extremely high

and/or power sale price is too low. The beneficial effect of an engine degradation on fuel expenditure is somewhat counterintuitive and deserves a closer look. This point and the condition under which the net financial impact can even be positive are expounded on in the Appendix.

5.2 Inlet Filter Fouling. For a gas turbine, neglecting leakage and assuming no blow-off during normal operation, the mass flow rate of air entering the compressor is equal to

$$\dot{m}_{\text{air}} = \dot{m}_{\text{exh}} - \dot{m}_{\text{fuel}} - \dot{m}_{\text{inj}}. \quad (8)$$

From the baseline values of exhaust gas, fuel, and steam/water injection mass flow rates we determine a flow coefficient C for the inlet filter such that

$$\dot{m}_{\text{air}} = C \frac{(\rho \Delta p_{\text{in}}^{nc})^n}{\mu^m} \quad (9)$$

where ρ is the density of inlet air, μ is the viscosity and $\Delta p_{\text{in}}^{nc}$ is the new and clean inlet pressure loss across the inlet filter. Exponents m and n have different values for laminar and turbulent flow regimes. Using C and the measured values of fuel and steam/water mass flow rates along with the exhaust mass flow rate determined from the engine part load curves in the above equations, a pressure drop across the filter is calculated. This pressure drop would only result with a filter that was new and clean. Lost generating capacity due to inlet filter fouling is found as follows:

$$P_{\text{lost}} = P_x \left(\frac{X_{41}^{nc}}{X_{41}} - 1 \right). \quad (10)$$

The superscript nc denotes that the correction factor X_{41} (see Table 2) is calculated using the new and clean inlet pressure drop obtained from Eq. (9). The resulting value is then used to evaluate the impact of filter clogging on gas turbine's performance as described in Section 6.2.

The filter replacement dates are estimated using the same logic and formulas presented above for compressor wash schedule by replacing the lost power and extra fuel terms by their corresponding definitions. Similar considerations described at the end of Section 5.1 apply to effects of inlet filter fouling as well.

6 On-Line Monitoring Results

At the time the monitoring system was installed in the plant, both gas turbines were nearly four years old. Thus, nominal base-load performance data was specified using the average of several full-load measurements prior to monitoring system installation. Inlet filters for both gas turbines were installed in Nov. 1995, seventeen months prior to the installation. Off-line compressor washes were performed on gas turbines A and B on Apr. 28 and 19 1997, respectively. Also in April, gas turbine B was taken off line for a hot gas path inspection and compressor discharge packing replacement. The firing temperature was upgraded by 15 deg.

Two on-line monitor modules run separately for each gas turbine in unattended mode on a PC with a Microsoft® Windows NT OS in the plant's administration building. The data acquired by the software and calculated performance parameters are written into Microsoft® Access databases that are stored in a dedicated folder on the plant owner's wide area network. For the analysis presented herein, the data is downloaded via modem to a remote PC and the monitoring module is run in the off-line (calculator) mode. The figures in the paper are generated using the Trend module and the daily-average data in the databases.

6.1 Compressor Performance. The monitoring system is used to track the compressor degradation and optimize the maintenance schedule. One specific goal was to assess the effectiveness of on-line washes and the benefit of using detergents. An on-line compressor wash program was developed in order to achieve this objective. Between May 5 and June 24 1997, both gas turbines had on-line washes with distilled water only. From June

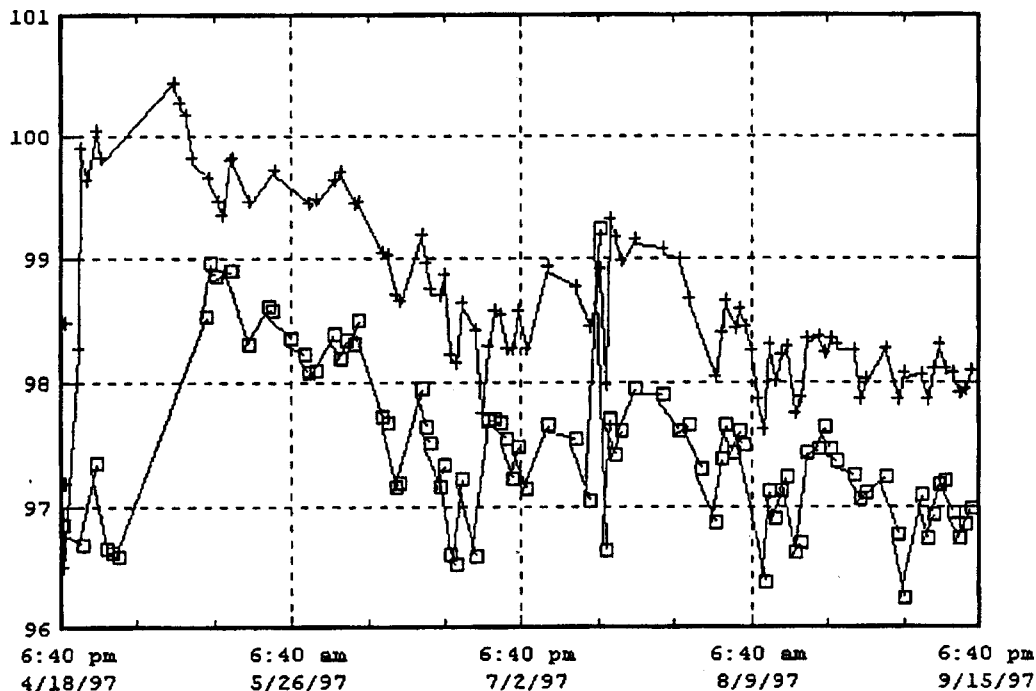


Fig. 2 Capacity factor for units A (symbol □) and B (symbol +)

24 on, gas turbine A compressor was subjected to on-line washes with detergent three times a week while gas turbine B was kept on water-only washing program.

Trends of the capacity factor¹ for both units shown in Fig. 2 indicated several facts:

- for both units engine degradation progressed at a rate of roughly one percent a month.
- after about two months engine degradation stabilized at a the level of two percent.
- there was no discernible benefit associated with using detergent in on-line washes as opposed to using distilled water only, and
- there was a constant one percent difference between units A and B although both engines were identical.

During the same period, the heat rates for both gas turbines increased roughly by one percent. These findings indicate that the compressor fouling observed in both gas turbines is consistent with the lower end of the spectrum of observations for heavy industrial gas turbines as reported in the literature. The results supported the use of on-line water washes to limit compressor degradation and the previously reported exponential law behavior of compressor fouling due to the stabilization of the deposits on the blades (e.g., see, [3]).

The average linear rate of deterioration of output for both gas turbines as observed in capacity factor trends was calculated to be approximately 0.7 kW per hour. The average linear rate of decrease in the fuel mass flow rate, on the other hand, was found to be 0.2 lb/h per hour. Substituting these rates into Eq. (6) along with the financial information, the next crank wash was estimated to be 2400 hours from the last one.

Compressor discharge measurements for unit A corrected for the ambient conditions are shown in Fig. 3. Same trends are observed for unit B as well. There is a four–five percent decrease in the corrected discharge pressure that stabilizes after two months similar to the trend observed in output degradation. The corrected discharge temperature (CDT) shows an unexpected-trend in that it

¹Capacity factor, expressed as a percentage, is defined as the ratio of the measured power output to the expected power output.

first decreases and then increases. This in turn results in decreasing and increasing compressor adiabatic efficiency trend. This result, at first puzzling, can be explained by examining the hourly trends of the corrected CDT and the adiabatic efficiency in Fig. 4.

The four on-line water wash periods can be clearly identified by the pronounced spikes in the hourly-averaged trends of Fig. 4.

These spikes are due to the inter-cooling effect of the evaporating water droplets as they are compressed and heated within the compressor. The increase in efficiency and decrease in CDT between the on-line washes can also be clearly seen. The spikes are (about 1.5 percent in efficiency and five–ten deg in CDT) major enough to cause a strong bias in daily averages. Thus, in the period following the off-line wash when the compressor was thoroughly clean the water washes bias the daily averages to the extent that they show the compressor getting progressively “cleaner.” The intercooling effect slowly decreases over time as deposits build up and the daily-averaged plots start revealing the expected deterioration trends.

For a quick evaluation of the compressor degradation, pressure and flow parameters can be plotted on the compressor performance map as shown in Fig. 5. Note that the horizontal and vertical axes are normalized and corrected compressor air mass flow parameter (Eq. 2a) and pressure rise parameter (Eq. 2c), respectively.

The performance map in the figure is the default map used by the monitoring software that is based on the generic map presented in Saravanamuttoo and MacIsaac [6] and it should be a reasonably close approximation of a Frame 7 gas turbine’s axial compressor. In Fig. 5, it can be seen that for the same period as in Fig. 2 there is a five percent drop in compressor air mass flow parameter and a eight percent drop in compressor pressure rise parameter. The trend displayed on the map in Fig. 5 represents a shift in the operating point to the left and downward. Clearly, the shift in the speed line and partially the trends in the mass flow and pressure rise parameters are due to the increase in ambient temperature and humidity. Typically, for a 7EA the decrease in mass flow and pressure rise parameters due to a four percent increase in ambient temperature (absolute) and 40 percent increase in relative

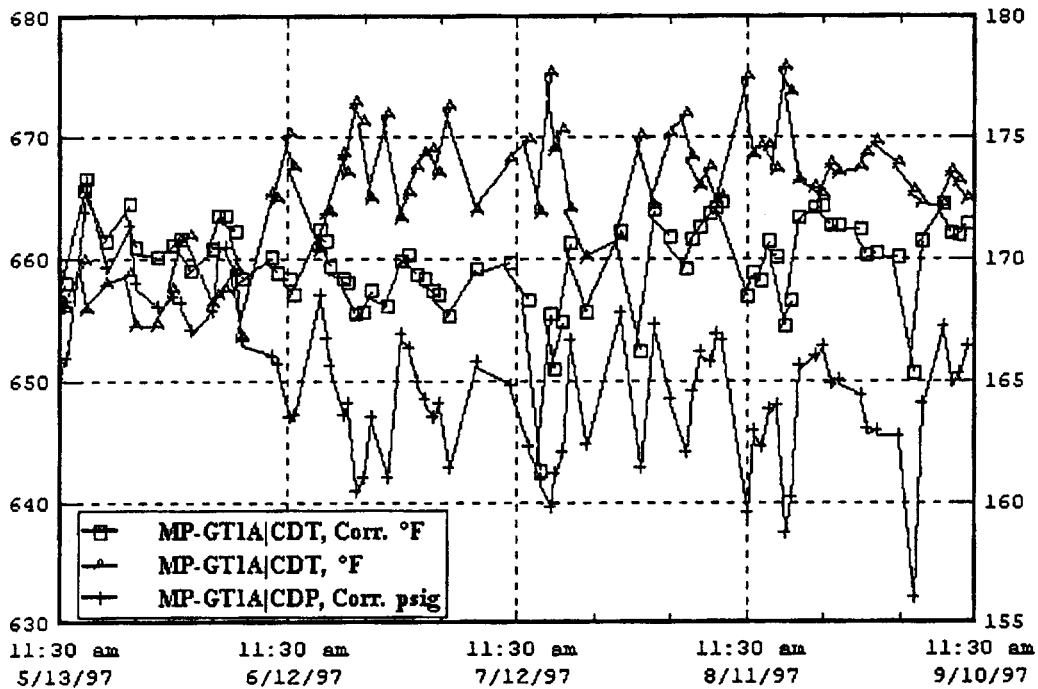


Fig. 3 Compressor discharge data (corrected) for unit A. (Left axis=°F and right axis=psig.)

humidity would be 3.6 percent and 5.6 percent respectively. The significant difference in measured values is clearly attributable to compressor fouling.

6.2 Inlet Filter Performance. Each gas turbine has a single-stage self-cleaning intake air filtration system with an evaporative cooler downstream. The inlet filter utilizes cylindrical filter elements that are sequentially cleaned by reverse flow pulses of compressed air. The operational pressure drop is between two and three inches of H₂O and the cleaning cycle starts when the

pressure drop across the elements reaches the upper limit. The evaporative cooler consists of a direct-contact, irrigated media utilizing cross-fluted cellulose pads impregnated with anti-rot salts and rigidifying saturants with an operational pressure drop of 0.25 in. H₂O.

For both gas turbines, between 5/1/97 and 9/28/97, the trends shown in Fig. 6 indicated a performance degradation of roughly 25 kW per month due to inlet filter clogging. During this period the inlet pressure drop (inlet filter plus evaporative cooler) in-

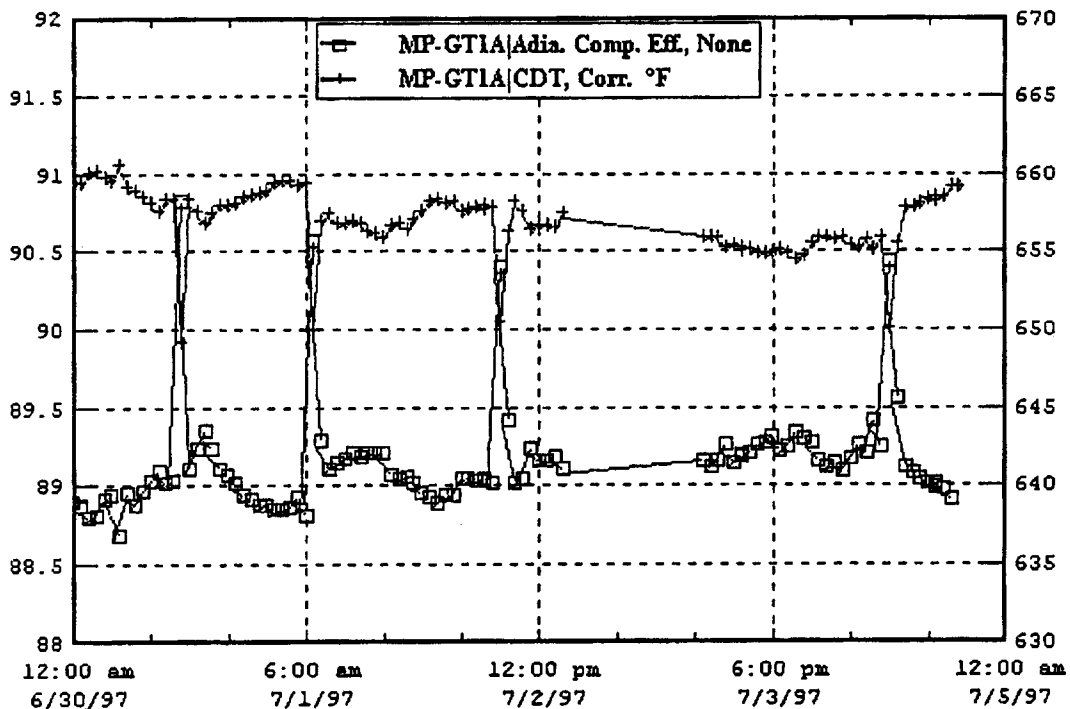


Fig. 4 Hourly trends of corrected CDT and adiabatic efficiency for unit A

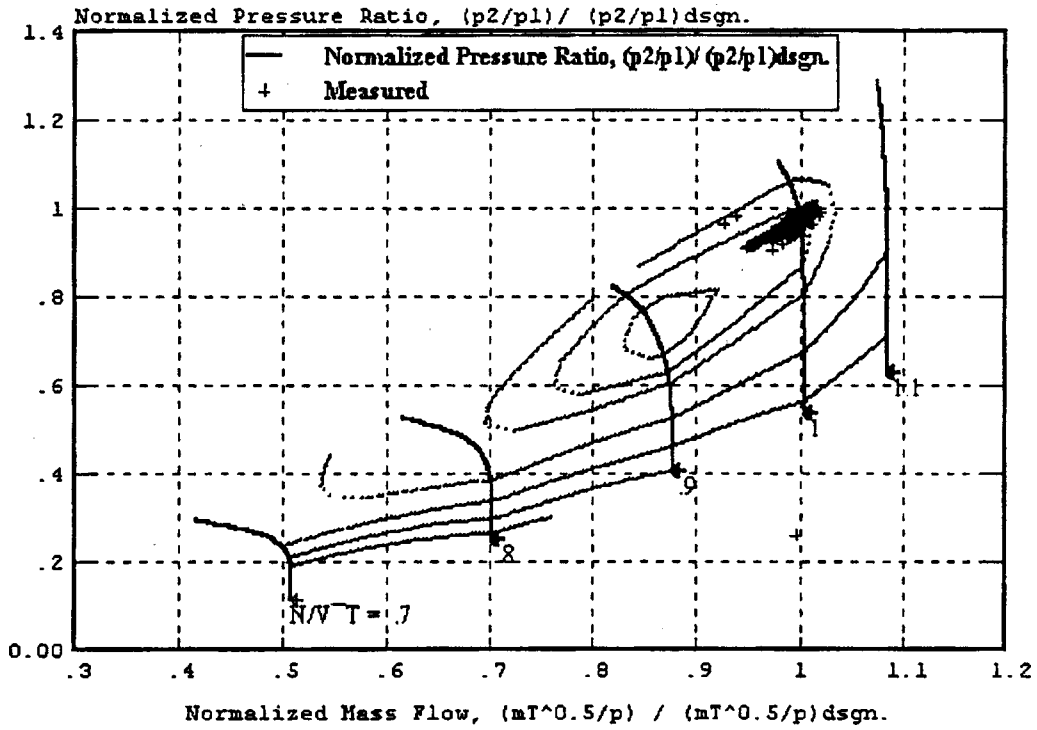


Fig. 5 Normalized and corrected compressor performance parameters for unit A

creased from 2.9 to 3.1 in. H₂O for unit A. Unit B displayed the same trend, but the measured drops were on the average 0.05 in H₂O higher.

For both gas turbines A and B, the trends shown in Fig. 7 indicated less fuel burned due to inlet filter clogging at a rate of roughly 9 lb/h per month. Balancing the effects of both performance changes (converted into monetary terms using user-defined

power prices and fuel costs) with the cost of filter replacement, a filter replacement date of 2.7 years from the last replacement date (end of 1995 for both units) has been predicted.

However, samples of filter units sent to its manufacturer and an independent consultant for testing revealed that they were deteriorated to the point of performing below minimum filtering speci-

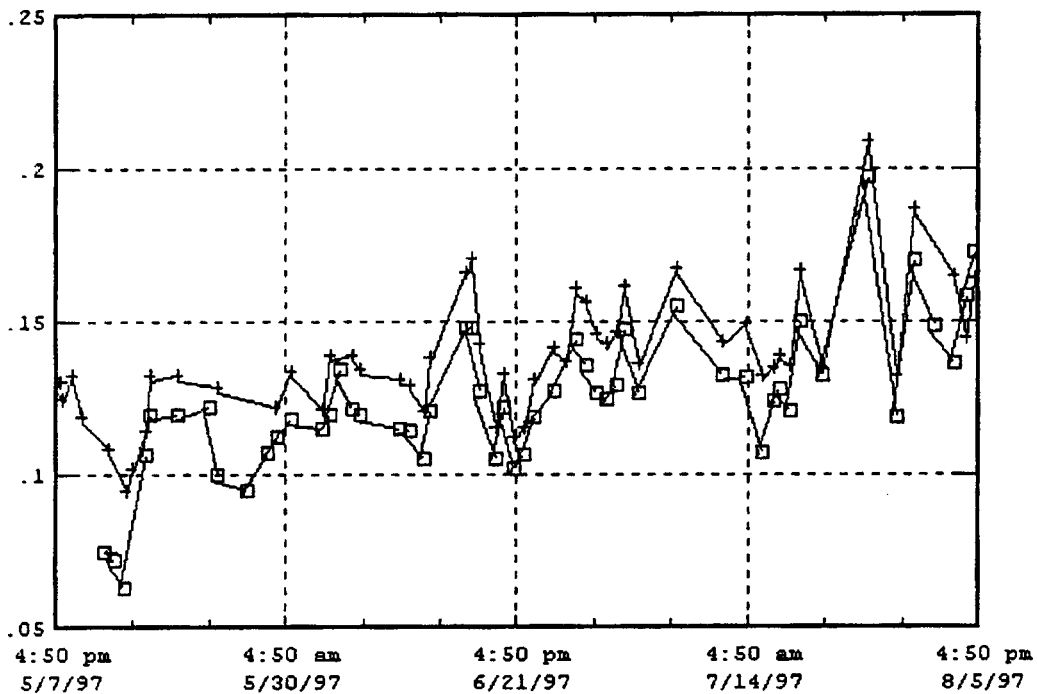


Fig. 6 Lost power generating capacity [MW] due to inlet filter fouling for units A (symbol □) and B (symbol +)

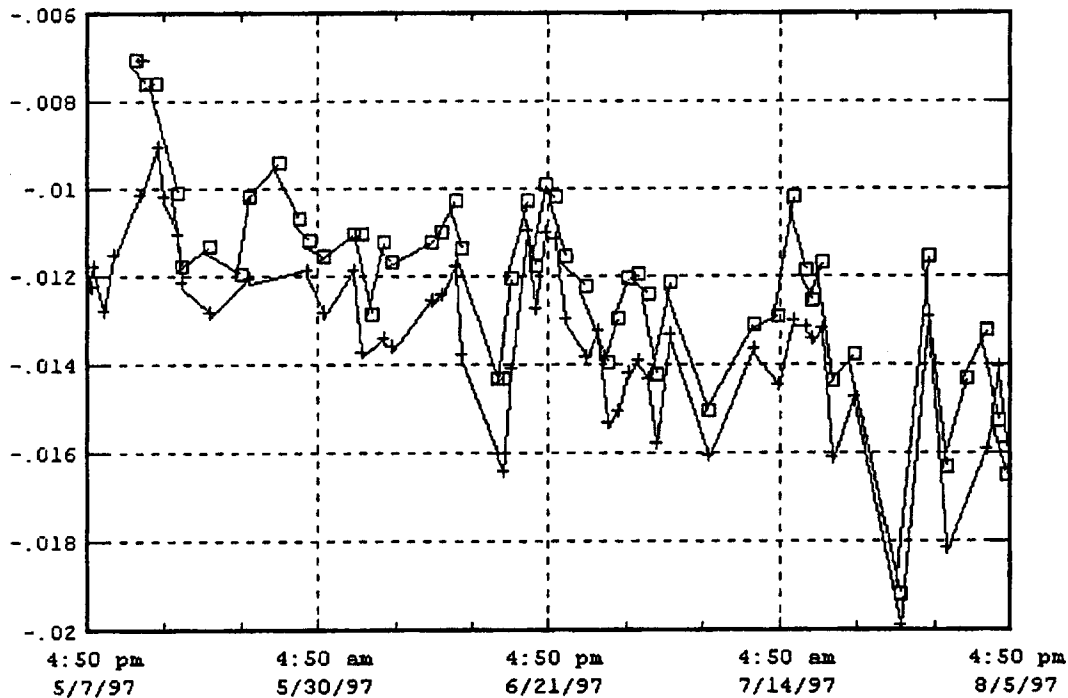


Fig. 7 Extra fuel burned [lb/s] due to inlet filter clogging for units A (symbol □) and B (symbol +)

cations. These findings prompted the decision to replace the inlet filters in the summer of 1999. This experience clearly demonstrates that the pressure drop by itself is not a sufficient criterion to determine inlet filter performance degradation.

6.3 Gas Turbine Performance. During monitoring it was observed that gas turbine B had a consistently higher output than gas turbine A. On the average, the difference was roughly one percent of the nominal baseline output as shown in Fig. 2. Over the time period considered, i.e., approximately 2000 hours of operating between 5/1/97 and 9/28/97, this translated to a lost power production of nearly 1800 MWh. For an annual service factor² of 80 percent at base load this is equivalent to an annual loss of 6300 MWh.

The trend plot shown in Fig. 8 implied that, although both gas turbines had identical temperature control curves, gas turbine A exhaust temperature as calculated by the monitoring software was roughly three deg below the control value.

To investigate this trend further, a quick visual diagnosis has been obtained from the exhaust temperature map utility of the Trend module as shown in Fig. 9. These plots are intended to be used in determining faulty combustors or fuel injectors using the known swirl angle for a particular engine. Indeed, it can be seen that unit A has two “hot” spots, i.e., thermocouples 1 and 12.

From Figs. 8–9, it is quite clear that the “hot” thermocouples at the exhaust duct of gas turbine A cause a bias in the control exhaust temperature signal of gas turbine A (which is an average of eighteen thermocouples). In other words, the exhaust temperature control signal is higher than the actual exhaust temperature and thus results in underfiring. The monitoring system’s sensor validation detected the two outliers, thermocouples 1 and 12, and re-calculated an average exhaust temperature that is a better representation of the actual value and pointed to the source of the problem.

Exhaust temperature of gas turbine B, on the other hand, either corresponded to the control temperature or was one degree higher (Fig. 10). The exhaust temperature plot in Fig. 11 indicated a

“cold” spot for unit B. The “cold” thermocouple 5 at the exhaust duct of unit B has the opposite effect of the “hot” ones in unit A; i.e. the control signal is lower than the actual exhaust temperature resulting in over-firing although the bias was not as severe in unit B as in unit A. Consequently, everything else being the same, an exhaust temperature difference of four deg corresponds to a seven deg difference in firing temperature and roughly 0.6 percent difference in the power output.

On the other hand, when we factor in the 0.35 percent lower polytropic compressor efficiency for unit B and a 0.35 percent increase in turbine efficiency,³ this results in power output deficiency of roughly 1 percent for unit A and an decrease of 12 deg in turbine inlet temperature.⁴ Performance tests conducted in Apr. and May of 1997 qualitatively agree with these observations based on the analysis of the stored data.

Unit A turbine section was overhauled in Oct. 1998 during a major scheduled outage. This resulted in an increase in turbine efficiency as confirmed by a performance test conducted in Nov. 1998. Furthermore, firing temperature of unit A was also increased by 11 deg. Test results confirmed that unit A output increased substantially to the point that it exceeded unit B output by roughly 0.5 MW.

6.4 Combustor Performance. An important diagnostic parameter that is calculated by the monitoring software is the shape factor. Also known as the profile factor, this parameter is the ratio of the maximum exhaust thermocouple reading to the average of all exhaust temperature thermocouples. It is a measure of the exhaust temperature spread that is the difference between highest and lowest thermocouple readings. Excessive and sudden changes or consistent upward trends in the shape factor may indicate combustor or fuel distribution problems. As can be seen in Fig. 12, unit A combustor shape factor displayed such an upward trend.

From the exhaust temperature map of Fig. 9, thermocouples 1

³Note that turbine efficiency calculations require proprietary information and thus not included in the analysis algorithm. The assumption was based on the fact that a hot gas path inspection and maintenance was performed on unit B in April 1997.

⁴This analysis was carried out by using the GE7121EA gas turbine model of a commercially available heat balance software, GT PRO.

²Service factor is the operational use expressed as a percentage on an annual basis (8760 hours.)

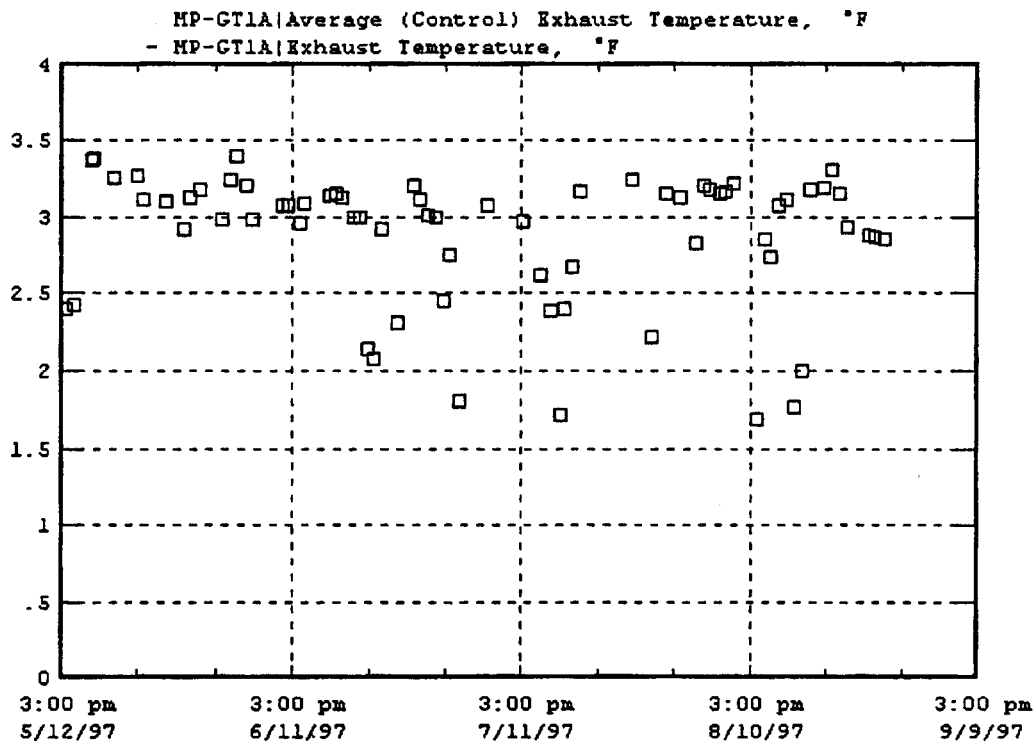


Fig. 8 Deviation of average exhaust temperature from DSC control temperature signal [°F] for unit A

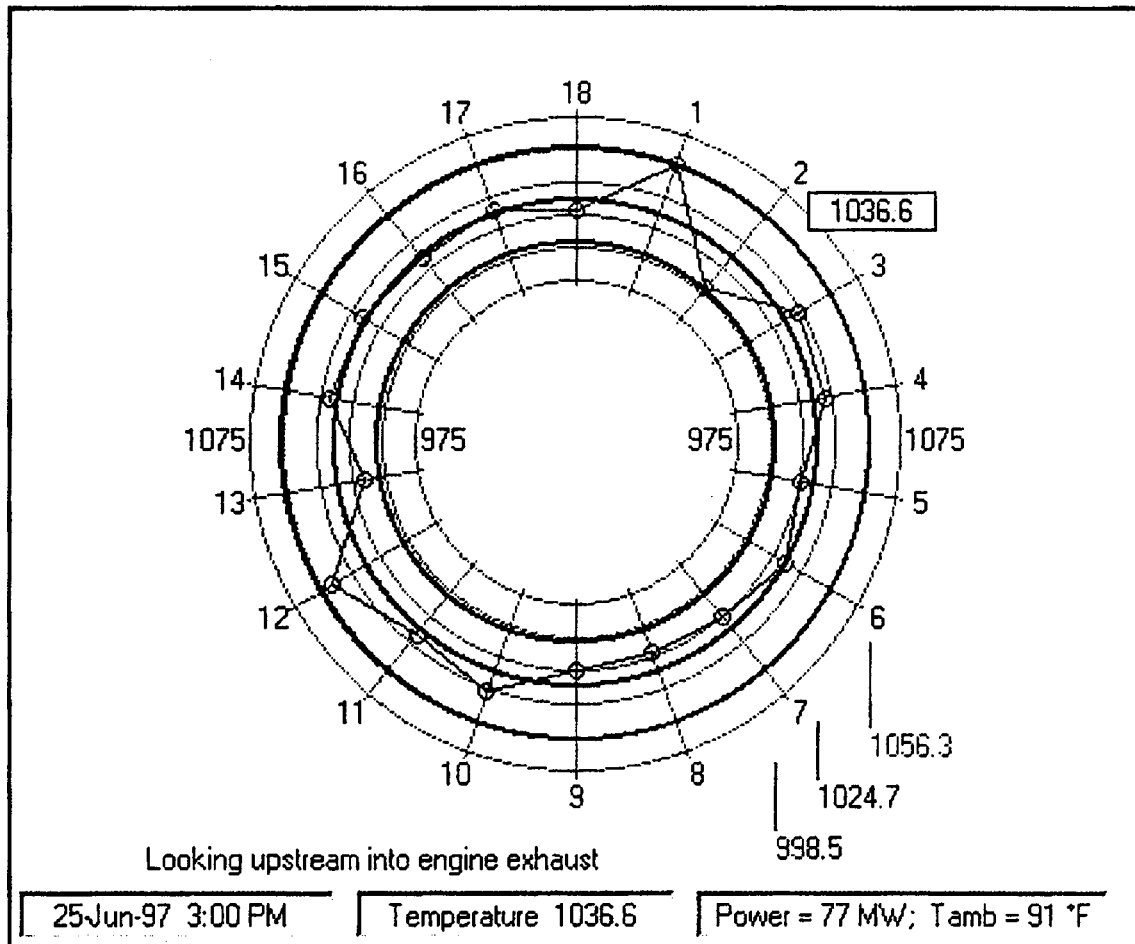


Fig. 9 Exhaust temperature profile for turbine A

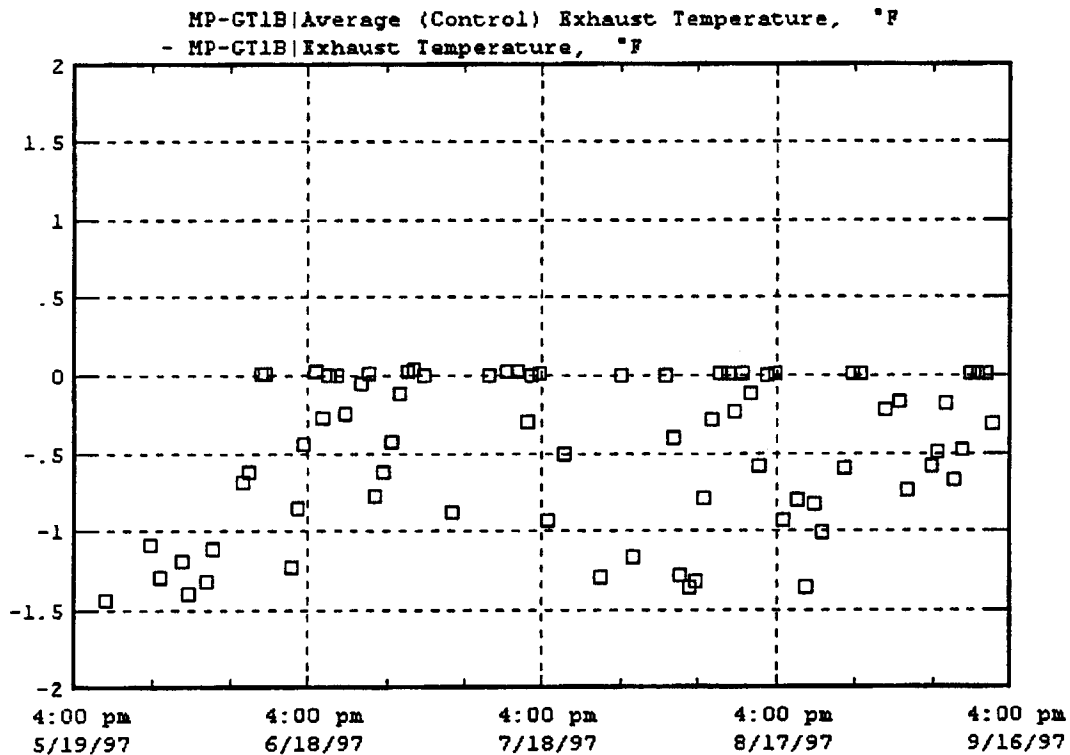


Fig. 10 Deviation of average exhaust temperature form DCS control temperature signal [°F] for unit B

and 2 are identified as the highest and lowest reading sensors, respectively. The plot of the difference between the two thermocouples, i.e., the spread, shows a clear upward trend in Fig. 13. A combustor inspection is required when this spread reaches a value of 70 deg. The trend in Fig. 13 indicated that this particular level of deterioration would be reached in about five to six months.

7 Summary and Conclusions

A real-time on-line performance monitoring system was installed in a combined cycle cogeneration power plant with two Frame 7 gas turbines. The program runs continuously and unattended in a real-time on-line mode to monitor two gas turbines. Collected data is stored in database files on a network and is available to local and remote users for historical plots, real-time monitoring, and other data analysis purposes. The software analyzes data for predicting off-line compressor wash and filter replacement scheduling. The software also calculates gas turbine parameters such as shape factor and compressor efficiency that can be used for on-line or off-line diagnostic as well as prognostic purposes.

The results highlighted several important aspects of gas turbine operation and maintenance:

- regular on-line washing performed three times a week with demineralized water keeps compressor fouling at a minimum. No benefits were observed for using detergent in on-line washes. This is to be expected because the primary cleaning mechanism in the on-line wash is the water droplet impact on the first five-six row blades that loosens the deposits. There is ample evidence in the literature that for typical frame engines the degradation in output can reach ten percent or more in 2,000 hours of base load operation. In the plant discussed herein the degradation in the same period was about two percent.
- the previously observed exponential law trend in output degradation was confirmed by the trends of this paper. In the absence of on-line washing, the mechanism was thought to be the stabilization of the thickness and shape of the blade deposits. In ma-

chines with regular on-line water washes, the mechanism can be the re-deposition of the dirt loosened from the front rows of blades on the back rows or a combination of the two.

- over short term, performance degradation due to filter pressure drop is negligible as compared to compressor fouling. In this study, over 2000 hours of base load operation the lost generating capacity due to excess inlet filter pressure drop was measured roughly to be 70 MWh (at a rate of 25 kW per month). This translates to roughly five percent of the lost generation capacity due to compressor fouling in the same period (at a rate of 0.7 kW/h or 500 kW per month.)
- inlet filter fouling is a long-term maintenance consideration. Most filters have a manufacturer recommended life of two years. In this project it was discovered that excess inlet pressure loss is one consideration in deciding whether to replace the inlet filter not. It is also important to ensure that filter elements are healthy enough to perform their job of blocking microscopic particles contributing to compressor blade deposits.
- an important performance degradation source can be the combustor problems. This was demonstrated by the underfiring of unit A. This problem, if not remedied, could lead to an annual lost generating capacity equivalent to 7800 MWh at base load. Most gas turbine controllers such as GE's Speedtronic Mark IV are able to detect and discard bad thermocouple readings to generate a reliable control signal. However, if the individual deviations (due to possible combustor problems) are not excessive, the resulting bias of a few degrees can still result in significant loss of output. Thus identifying and continuously trending exhaust thermocouple spread can pinpoint problems resulting from presently mild deviations that can lead to potentially serious engine problems or result in lost revenue.

In order to put these results into dollars and cents, consider an 80 MW base load unit with a service factor of 80 percent and power sale price of 3¢/kWh. The fuel cost is assumed to be \$2/MMBtu and the total cost of an off-line wash is estimated at \$10,000 including labor, materials and downtime. Regular on-line

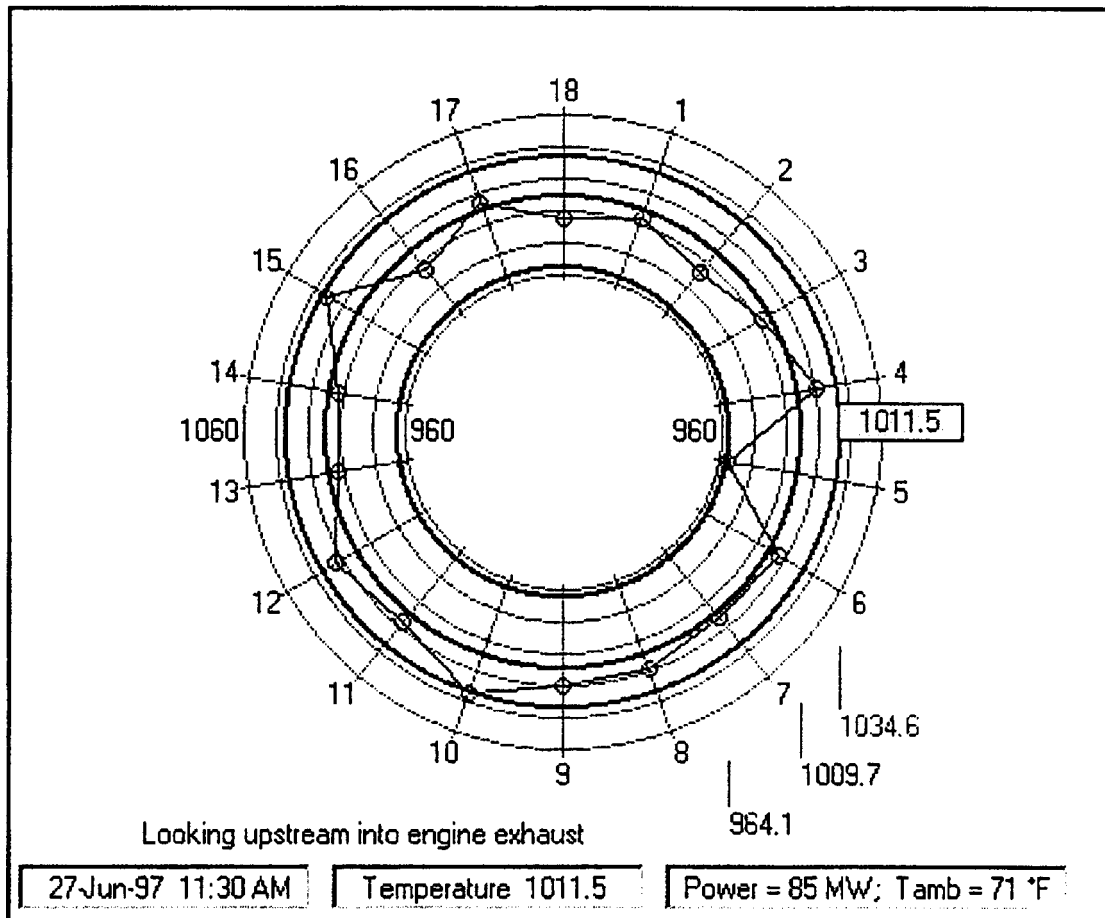


Fig. 11 Exhaust temperature profile for turbine B

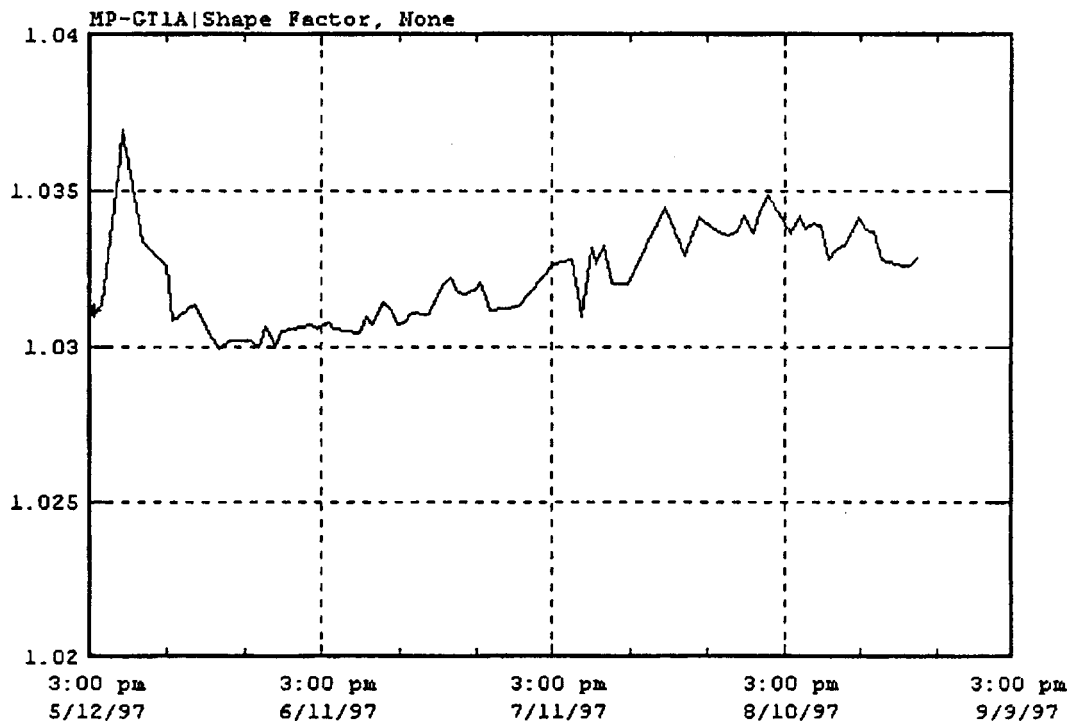


Fig. 12 Combustor shape factor for unit A

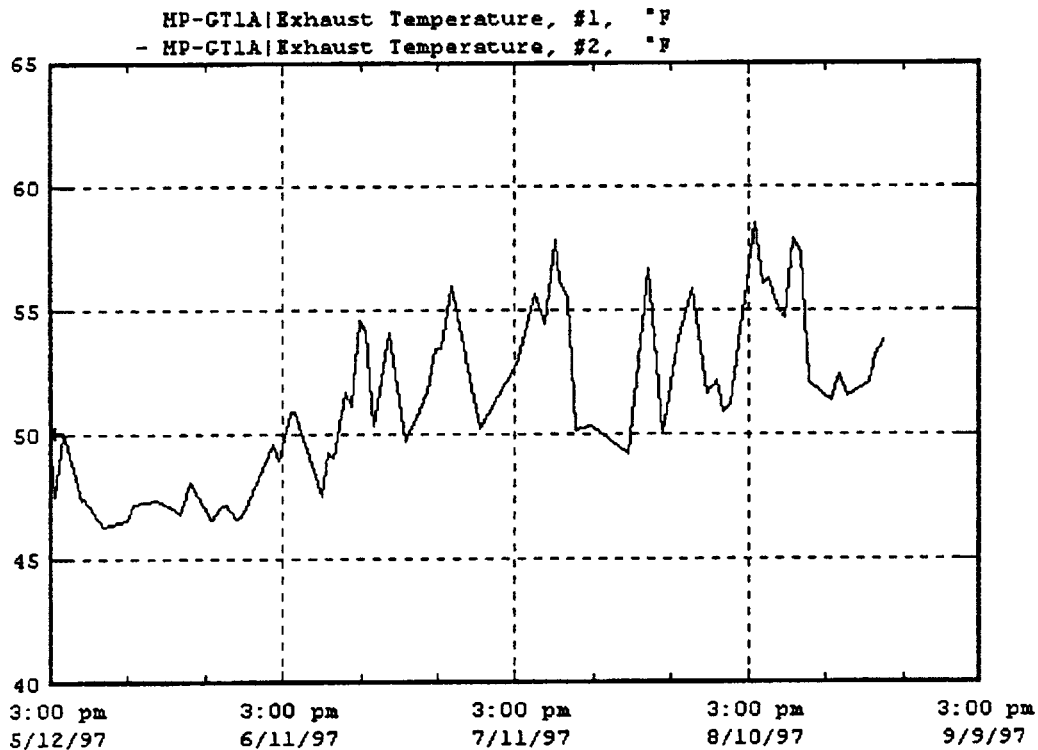


Fig. 13 Exhaust temperature spread for unit A

washing would recover \$200,000 worth of power generation capacity. Compressor fouling, if not remedied by off-line washes, would result in \$300,000 worth of lost power generating capacity annually assuming a two percent capacity factor loss with an exponential law trend. Performing an off-line compressor wash at intervals of 1500 hours would save the operator \$20,000 annually.

The savings will increase with increasing engine size, service factor, and fouling rate. The savings will be directly proportional to power sale price and inversely proportional to fuel costs and off-line wash expenses. For the example numbers cited above, a software package that would estimate the optimum off-line wash interval would pay for itself in six months at a licensing cost of \$10,000. This payback period would be proportional to the savings if only compressor maintenance is taken into consideration and could be even much shorter if the software helps to shed light on situations similar to that described in Section 6.3.

For a discussion of the actual benefits of the system in the site of installation the reader is referred to Gülen et al. [4].

Appendix

The following relationship exists between the efficiency and power output of a gas turbine:

$$\frac{1}{\eta} \propto \frac{fLHV}{P} \quad (A1)$$

where η is the engine's thermal efficiency and LHV is the lower heating value of the fuel. With some algebra, one can show that

$$\frac{\Delta f}{f_0} = \frac{\left(1 + \frac{\Delta P}{P_0}\right)}{\left(1 + \frac{\Delta \eta}{\eta_0}\right)} - 1 \quad (A2)$$

where subscript 0 denotes the new and clean state of the engine and Δ denotes a change in the particular quantity. Compressor degradation results in a decrease in power output ($\Delta P < 0$) and an increase in heat rate. Since the heat rate is equivalent to $3412/\eta$,

this translates into a decrease in the engine's thermal efficiency ($\Delta \eta < 0$). Thus, both terms in parentheses on the RHS of Eq. (A2), as well as their ratio, are always less than unity because in relative terms $|\Delta P|$ is always greater than $|\Delta \eta|$. Equation (A2) then implies that Δf is always less than zero, i.e., fuel mass flow rate at full load decreases with increasing compressor fouling.

This conclusion can also be reached qualitatively starting from the fact that, since a fouled compressor has a lower efficiency and higher discharge temperature, a smaller amount of fuel is required to reach a set firing temperature.

In monetary terms, the total cost of engine degradation due to compressor fouling over a time period of τ is

$$\Delta C_{\text{tot}} = (C_f \Delta f - C_p \Delta P) \tau \quad (A3)$$

Equation (A3) suggests that the total cost can be negative, i.e., one could actually even save money due to compressor fouling. This would happen in the possible—albeit unlikely—event that

$$\frac{C_f}{C_p} > \frac{\Delta P}{\Delta f} \quad (A4)$$

In order to give a numerical example, consider a typical frame 7EA with 84,920 kW output and 10,212 Btu/kWh heat rate. When compressor fouling leads to a pressure ratio decrease of two percent, engine output will drop by five percent (i.e., about 4.25 MW) whereas heat rate will increase by two percent (e.g., see Fig. 23 in [7]). This implies a 3.1 percent decrease in fuel mass flow rate, i.e. about 27 MMBtu/h. Thus if C_f in [\$/MMBtu] is greater than 158 times C_p in [\$/kWh], there will be a saving due to this degradation. In other words, if the power sale price is three cents per kWh, the owner will save money because of compressor fouling if the fuel purchase price is higher than \$4.74 per MMBtu. The same will hold true if the power sale price is less than 1.6 cents per kWh if the fuel purchase price is 2.5 \$/MMBtu.

Note that these statements hold only for a gas turbine operating at full load. Same kilowatts as in a new and clean engine can

always be produced at the expense of extra fuel consumption in a degraded engine running at part load. In that case $\Delta P=0$ in Eq. (A2) such that

$$\frac{\Delta f}{f_0} = \frac{1}{1 + \frac{\Delta \eta}{\eta_0}} - 1. \quad (A5)$$

Since $\Delta \eta/\eta$ is always negative and less than unity in magnitude, Δf is always greater than zero.

References

- [1] Diakunchak, I. S., 1991, "Performance Deterioration in Industrial Gas Turbines," ASME Paper No. 91-GT-228.
- [2] Flashberg, L. S., and Haub, G. L., 1992, "Measurement of Combustion Turbine Non-Recoverable Degradation," ASME Paper No. 92-GT-264.
- [3] Tarabrin, A. P., Schurovsky, V. A., Bodrov, A. I., and Stalder, J.-P., 1998, "An Analysis of Axial Compressor Fouling and a Blade Cleaning Method," ASME J. Turbomach., **120**, pp. 256–261.
- [4] Gülen, S. C., Griffin, P. R., and Paolucci, S., 1999, "Real-Time, On-Line Performance Monitoring of Two Heavy Duty Industrial Gas Turbines," *POWER-GEN 99*, New Orleans, LA.
- [5] Kurzke, Joachim, 1998, GasTurb 8.0, "A Program to Calculate Design and Off-Design Performance of Gas Turbines," <http://www.gasturb.de/>
- [6] Saravanamuttoo, H. I. H., and Maclsaac, B. D., 1983, "Thermodynamic Models for Pipeline Gas Turbine Diagnostics," ASME J. Eng. Power, **105**, pp. 875–884.
- [7] Hoelt, R. F., 1993, "Heavy Duty Gas Turbine Operating and Maintenance Considerations," GER-3620, GE I&PS.

Delamination Cracking in Thermal Barrier Coating System

Y. C. Zhou¹

Fracture Research Institute,
Tohoku University,
Sendai 980-8579, Japan and
Institute of Fundamental Mechanics and
Materials Engineering,
Xiangtan University,
Xiangtan, Hunan 411105, P. R. China
e-mail: zhou@rift.mech.tohoku.ac.jp

T. Hashida

Fracture Research Institute,
Tohoku University,
Sendai 980-8579, Japan

Delamination cracking in thermal barrier coating (TBC) system is studied with the newly developed theoretical model. A semi-infinite long interface crack is pre-existing. The thermal stress and temperature gradient in TBC system are designated by a membrane stress P and a bending moment M . In this case, the effects of plastic deformation, creep of ceramic coating, as well as thermal growth oxidation and temperature gradient in TBC system are considered in the model due to the fact that these effects are considered in the calculation of thermal stress. The energy release rate, mode I and mode II stress intensity factors, as well as mode mixed measure ψ , are derived. The emphatic discussion about PSZ/Ni-alloy reveals that the TBC system may not fail in the form of coating delamination during the period of heat hold. However, the failure may be in the form of coating delamination during cooling or in the heating period during the second cycle or later cycles. The conclusion is consistent with the experimental observations. The delamination of ceramic coating is induced by the compressive load in the coating.

[DOI: 10.1115/1.1477194]

Introduction

Thermal barrier ceramic coating (TBC) is used to protect an alloy operating at high temperature, for example, at 1500°C and so that high thermal efficiency for an advanced gas turbine could be achieved [1]. A TBC provides performance, efficiency, and durability benefits by reducing turbine cooling air requirements and lowering metal temperatures. Previous work has demonstrated that there are some important effects on TBC life. The effects are thermal fatigue ([2–4]), thermal growth oxidation (TGO) between the bond coat and thermal barrier ceramic coating [5–7], and the surface roughness of the bond coat ([7,8]), as well as oxygen and sulfur penetration along the grain boundary ([9]). As we know, a TBC system is used to provide thermal insulation to critical air-cooled components by overlaying a strain-tolerant ceramic top coating. In this case, there must be a temperature gradient in the thickness direction of the TBC system. The temperature gradient has an important effect on the TBC system failure mechanism, such as the initiation and propagation of a surface crack or interface crack as observed in the experiment ([10,11]). However, the failure mechanism of the TBC system is the combined results of oxidation, residual stress, and thermal mechanical fatigue as well as the creep of the TBC system ([12]). Their nonlinear coupled effects govern the service life.

Generally the composition of TGO is similar to a brittle ceramic such as alumina (Al_2O_3). The cycles of high-temperature loading and unloading not only make TGO thick but also create microvoids and microcracks initiate in the TGO. Subsequently, the degradation of the TGO will induce the spallation or delamination of the thermal barrier ceramic coatings. The previous experimental and theoretical studies showed that the macrocrack would have been formed in the thermally grown oxide layer due to the aforementioned effects ([6–7]). As long as the microcrack forms, it may propagate along interface or kink out of the plane of the crack at an angle. Therefore, mixed-mode cracking is an important damage mechanism in the TBC system. However, the analysis of a mixed-mode crack is very complicated for theoretical as well as experimental analyses. Fortunately, the basic ideas founded by previous researchers such as Sih et al. [13], Rice et al.

[14], Dundurs [15], and Erdogan [16], and the results of the delamination of thin films and coatings from a substrate studied by Evans and Hutchinson [17], and Hutchinson and Suo [18] can be used to investigate the failure mechanism of the TBC system operating at high temperature.

The purpose of the investigation is to study the failure mechanism of a TBC system by exploring the energy release rate, thermal stress intensity factors, and the relative amount of mode II to mode I at the crack tip for the thermal mixed crack. In the model, the TBC system with an interface crack is assumed as a composite beam. With the composite theory ([19]), the energy release rate is expressed by a thermal strain and mechanical loads such as membrane stress P and bending moment M . The membrane stress P and bending moment M are calculated with integrating the thermal stress along the thickness direction of the TBC system with a temperature gradient. On the other hand, in the calculation of thermal stress, the combined effects of plastic deformation, creep of ceramic coating as well as thermal growth oxidation and temperature gradient in TBC system were considered ([12]). Subsequently, in the model, the delamination in the TBC system is the combined effects of plastic deformation and creep of ceramic coating, as well as thermal growth oxidation and temperature gradient.

Stress With Interface Crack

To consider the contribution of thermal stress and temperature gradient on the mixed-mode crack propagation, a theoretical model is proposed. The system consists of a ceramic coating of material No. 1 with thickness of h deposited on a substrate of material No. 2 with thickness of H . Each material is taken to be isotropic and linearly elastic. An interface crack is pre-existing. The problem is asymptotic in that two material layers are infinitely long and the crack is semi-infinite. The structure is loaded as shown in Fig. 1(a), where the membrane stresses P are loads per unit thickness and the bending moments M are moments per unit thickness. The temperature gradient along the y -direction and the temperature-dependent physical parameters are also considered in the analysis.

Constitutive Equations. The thermal stresses are considered to be two-dimensional. The general Hook's constitutive relation in a two-dimensional state can be written as ([20])

$$\varepsilon_{xx} = \frac{1}{2\mu} \left[\sigma_{xx} - \frac{1}{4}(3 - \kappa)(\sigma_{xx} + \sigma_{yy}) \right] + E_{xx} + \eta E_{zz} \quad (1)$$

¹To whom correspondence should be addressed.

Contributed by the IGTI Technical Committee of THE AMERICAN SOCIETY OF MECHANICAL ENGINEERS for publication in the ASME JOURNAL OF ENGINEERING FOR GAS TURBINES AND POWER. Manuscript received by the IGTI Technical Committee July 2000; final revision received by the ASME Headquarters September 2001. Associate Editor: J. Conner.

$$\varepsilon_{yy} = \frac{1}{2\mu} \left[\sigma_{yy} - \frac{1}{4}(3-\kappa)(\sigma_{xx} + \sigma_{yy}) \right] + E_{yy} + \eta E_{zz}. \quad (2)$$

In the above, equation E is used to denote the eigenstrain which may be a plastic strain and thermal expansion strain, as defined by Mura [21]. The eigenstrain E_{zz} is the normal strain perpendicular to the plane that is of interest. In the present study, only the eigenstrain of thermal expansion strain is considered. Therefore, $E_{xx} = E_{yy} = E_{zz} = \alpha \vartheta$, where $\vartheta = T(y) - T_0$, $T(y)$ and T_0 are, respectively, the operating temperature of the TBC system and room temperature and α is thermal expansion coefficient. Moreover, ν and μ denote the Poisson's ratio and shear moduli, respectively, $\kappa = 3 - 4\nu$, $\eta = \nu$ for plane strain, and $\kappa = (3 - \nu)/(1 + \nu)$, $\eta = 0$ for plane stress.

Stress Fields. The stresses far behind or ahead of the crack tip can be obtained by using the composite beam theory ([19]). In the model, the material properties are all temperature-dependent. In this case, the position of neutral axis can be first determined and they are expressed by $\Delta_1 h$, $\Delta_2 h$, and $\Delta_3 h$ as shown in Fig. 1. The stresses can be obtained for the upper beam far behind the crack tip denoted by $i=1$ when the beam is loaded by the membrane stress P_1 and bending moment M_1 as shown in Fig. 1(a). The stress comes from three parts, the first one is due to the strain of the neutral axis, the second one is due to the curvature, and third one is due to the thermal strain. With the same manipulating method, the stresses can be obtained for the lower beam far behind the crack tip denoted by $i=2$ and the composite beam far ahead of the crack tip denoted by $i=3$. Therefore, the stresses can be written as

$$\sigma_{xx}^{(i)}(P_i, M_i) = \frac{8\mu_j}{1 + \kappa_j} \left[\varepsilon_{xx0}^{(i)}(P_i) + K^{(i)}(M_i) \left(y + \frac{1}{2} \Delta_i h \right) - (E_{xx}^{(j)} + \eta^{(j)} E_{zz}^{(j)}) \right]. \quad (3)$$

In the expression, $j=1$ and 2 present the coating and substrate, respectively. In the above expression, $\varepsilon_{xx0}^{(i)}$, $K^{(i)}$, and Δ_i are defined as

$$\varepsilon_{xx0}^{(i)}(P_i) = e_1^{(i)} + e_3^{(i)} \frac{P_i C_1}{h} \quad K^{(i)}(M_i) = \left(s_1^{(i)} + s_3^{(i)} \frac{M_i C_1}{h^2} \right) \frac{1}{h} \\ \Delta_i = - \left(- \frac{1}{\eta_0} \right)^{i(i-1)/i!} \frac{\omega_2^i}{\omega_1^i} \quad (4)$$

where

$$e_1^{(i)} = \frac{\varphi_1^i}{\omega_1^i} \quad e_3^{(i)} = (-1)^i \frac{1}{8\omega_1^i} (\Sigma \eta_0)^{i(i-1)/i!} \\ s_1^{(i)} = 4J_i (-\eta_0)^{i(i-1)/i!} \left(\varphi_2^i - \frac{\omega_2^i \varphi_1^i}{\omega_1^i} \right) \\ s_3^{(i)} = (-1)^i \frac{1}{J_i} [\Sigma (\eta_0)^3]^{i(i-1)/i!} \quad (5)$$

where $\varepsilon_{xx0}^{(i)}$ and $K^{(i)}$ are the strain of the neutral axis and the curvature for beam i , respectively. The nondimensional material parameters such as ω_k^i , φ_k^i , and J_i are defined in Appendix A. The following dimensionless quantities, such as the geometrical parameter η_0 , bimaterial parameters Σ are used,

$$\eta_0 = \frac{h}{H}, \quad \Sigma = \frac{C_2}{C_1}, \quad (6)$$

where C is defined as $C = [\kappa(\bar{T}) + 1]/\mu(\bar{T})$, \bar{T} is the average temperature over the coating or substrate. Inspecting the expressions (4), (5) and (A2), one can see that the strain of the neutral axis comes from two parts. One is expressed by $e_1^{(i)}$ and it is the

contribution of thermal strain, i.e., temperature gradient along the thickness direction. Another is the contribution of mechanical loads such as P_i . This case is the same for the curvature of the beam. On the other hand, one can see that the contribution of thermal strain to the strain of the neutral axis and curvature comes from the expression φ_k^i . The contribution of mechanical loads to the strain of neutral axis and curvature comes from the expression ω_k^i .

In line with the treatment of Zuo and Hutchinson [22], the failure of the TBC system can be induced by equivalent loads P and M as shown in Fig. 1(b) by using the superimposition method. The equivalent loads P , M , and M^* are given by

$$P = P_1 + 8\varepsilon_{xx0}^{(3)}(P_3) \frac{h}{C_1} \omega_1^1 + 4K^{(3)}(M_3) \frac{h^2}{C_1} (\omega_2^1 + \Delta_3 \omega_1^1) \\ - 8 \frac{h}{C_1} \varphi_1^1 \quad (7)$$

$$M = M_1 + 4\varepsilon_{xx0}^{(3)}(P_3) \frac{h^2}{C_1} (\omega_2^1 + \Delta_1 \omega_1^1) + 8K^{(3)}(M_3) \frac{h^3}{C_1} \left[\frac{1}{3} \omega_3^1 \right. \\ \left. + \frac{1}{2} \Delta_1 \omega_2^1 + \frac{1}{4} (\Delta_1)^2 \omega_1^1 \right] - 4 \frac{h^2}{C_1} (\varphi_2^1 + \Delta_1 \varphi_1^1) \quad (8)$$

$$M^* = M + \frac{1}{2} Ph(\Delta_2 - \Delta_1). \quad (9)$$

Once the solution to the problem in Fig. 1(b) is obtained, the solution to the problem in Fig. 1(a) can be readily constructed by reinterpreting P and M . Inspecting expressions (7)–(9), one can see again that the equivalent loads P and M come from two parts. One is the contribution of thermal strain and the other is the contribution of mechanical loads such as P_i and M_i . The insertion of thermal strain in constitutive Eqs. (1)–(2) results in the different form for the energy release rate with the case of nonthermal strain in constitutive equations as discussed in the following.

Energy Release Rate

The energy release rate can be computed exactly within the context of plane stress or plane strain by taking the difference between the energy stored in the structure per unit length far ahead and far behind the crack tip,

$$G = \lim_{\Gamma' \rightarrow 0} \int_{\Gamma'} \left(W n_1 - \sigma_{ij} n_i \frac{\partial u_j}{\partial x_1} \right) d\Gamma', \quad (10)$$

where W is stress work, σ_{ij} and u_i are the Cartesian components of the stress and displacement, n_i is the unit vector normal to Γ' , and $d\Gamma'$ is the arc length as depicted in Fig. 1(b). As we know, the value of the J -integration is independent on the integral path. In this case, the path of the J -integration is chosen as depicted in Fig. 1(b) and the J -integral is

$$G = \int_{\Gamma} (W - \sigma_{xx} \varepsilon_{xx}) dy. \quad (11)$$

The strain energy density W is defined as the mechanical work of strain,

$$W = \frac{1}{2} (\sigma_{ij} \varepsilon_{ij} - \alpha \vartheta \sigma_{kk}) \\ = \frac{1}{2} \sigma_{xx} [\varepsilon_{xx} - (1 + \eta) \alpha \vartheta] \\ + \frac{1}{2} \sigma_{yy} [\varepsilon_{yy} - (1 + \eta) \alpha \vartheta] + \eta \mu \frac{7 - \kappa}{3 - \kappa} (\alpha \vartheta)^2. \quad (12)$$

Therefore, the energy release rate is obtained as

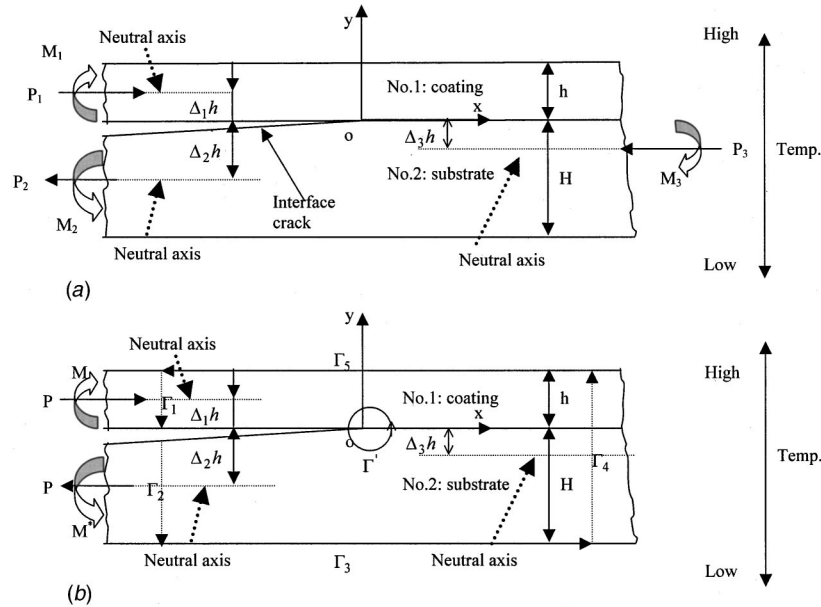


Fig. 1 Conventions and geometry for the analysis of delamination cracking in the TBC system; (a) the delamination cracking in the TBC system is induced by the membrane stresses P_i ($i=1,2,3$) and bending moments M_i ($i=1,2,3$), (b) the failure of the TBC system can be induced by equivalent loads P and M

$$G = \frac{P^2 C_1}{h} \frac{1}{2} \left[E_3^{21} + \frac{1}{s_3^{(2)}} (\bar{\Delta}_1)^2 \right] + \frac{M^2 C_1}{h^3} \frac{1}{2} S_3^{21} + \frac{P M C_1}{h^2} \bar{\Delta}_3 + P \frac{1}{2} (E_1^{21} + \bar{\Delta}_1) + \frac{M}{h} \frac{1}{2} S_1^{21} \quad (13)$$

where the related nondimensional parameters are defined as

$$E_k^{ij} = e_k^{(i)} - e_k^{(j)} \quad S_k^{ij} = s_k^{(i)} - s_k^{(j)} \quad \bar{\Delta}_k = \frac{1}{2} s_k^{(2)} (\Delta_2 - \Delta_1) \quad (14)$$

In order to analyze the stress intensity factors as in the next section, the energy release rate is rewritten in another useful form as

$$G = \frac{h}{C_1} \left[\Pi_1 \left(\frac{P C_1}{h} \right)^2 + \Pi_2 \left(\frac{M C_1}{h^2} \right)^2 + \Pi_3 \left(\frac{P M C_1^2}{h^3} \right) + \Pi_4 \left(\frac{P C_1}{h} \right) + \Pi_5 \left(\frac{M C_1}{h^2} \right) \right] \quad (15)$$

where the coefficients such as Π_i , ($i=1, \dots, 5$) can be known by comparing the above two expressions of the energy release rate in (13) and (15). Inspecting the equivalent loads P and M in expressions (7) and (8), we find that the equivalent loads are consisted of two parts. The first part is the general mechanical loads such as P_1, M_1, P_2, M_2, P_3 , and M_3 . The second part is thermal load or the named eigenload. In expression (15), the first term, second term, and third term are the second-order function of nondimensional quantities $P C_1/h$ and $M C_1/h^2$. The dependence of the energy release rate on the second-order function form of nondimensional loads is the same as that case of nonconsidering thermal strain in a constitutive relation ([22]). But the fourth term and fifth term are the linear function of nondimensional quantities $P C_1/h$ and $M C_1/h^2$. The dependence of the energy release rate on the linear function form of nondimensional loads is due to the thermal strain in the constitutive relation. The form of the energy release rate is different from the results obtained by Zuo and Hutchinson [22] in which the thermal strain is not considered.

Stresses Intensity Factors

The above energy release rate can reflect the composite effect of loads on crack propagation. However, crack propagation should be in mixed mode form for interface crack problems. In order to know the effect of the loading mode on crack propagation, for example, to understand which mode, whether mode I or mode II dominates the crack propagation, we must know the stress intensity factors. The TBC system is not an isotropic material and the system can be considered as a transverse isotropic body. For generally anisotropic materials, Hooke's law can be written as

$$\varepsilon_i = \sum_{j=1}^6 B_{ij} \sigma_j + \varepsilon_i^{\text{eign}}, \quad j=1, \dots, 6 \quad (16)$$

where $\varepsilon_i^{\text{eign}}$ is assumed to be an eigenstrain as defined by [21]. The standard correspondence is adopted ([23,24]) and $[B_{ij}]$ is a six-by-six symmetric matrix, referred to as the compliance matrix, with 21 independent elements. The TBC system described in Fig. 1 may be assumed as transverse isotropic materials and the compliance matrix has only five independent elements ([23,24]). It is assumed that the symmetry plane is normal to the y -axis as described in Fig. 1. The components $[B_{ij}]$ are determined by five parameters which are parameter η_0 , shear modulus μ_1, μ_2 (or Young's modulus E_1, E_2) and Poisson ratio ν_1, ν_2 of material 1 and material 2. The compliance matrix $[B_{ij}]$ is obtained by connecting the relation of engineering constants $E_T, E_L, \mu_A, \mu_T, \nu_A$, and ν_T for the transverse isotropic materials and engineering constants μ_1, μ_2 (or E_1, E_2), ν_1 , and ν_2 for the bimaterial system as discussed in references [23,24]. The details of compliance matrix $[B_{ij}]$ are given in Appendix B. In this case, the stress-strain relation for the deformation in the (x, y) plane can be reduced to

$$\varepsilon_i = \sum_{j=1,2,6} b_{ij} \sigma_j + \varepsilon_i^{\text{eign}}, \quad i=1,2,6 \quad (17)$$

where $b_{ij} = B_{ij}$ for plane stress and $b_{ij} = B_{ij} - B_{i3} B_{j3} / B_{33}$ for plane strain.

The complex interface stress intensity factor $k = k_1 + ik_2$ has real and imaginary parts k_1 and k_2 , respectively, which play similar roles to the conventional mode I and mode II intensity factors. For the anisotropic body in which zero eigenstrain exists, the energy release rate is obtained by Sih, Paris, and Irwin [13] and Suo [25] and G only depends on two (rather than three) nondimensional elastic parameters

$$\lambda = \frac{b_{11}}{b_{22}}, \quad \rho = \frac{2b_{12} + b_{66}}{2\sqrt{b_{11}b_{22}}}. \quad (18)$$

The energy release rate is related to the stress intensity factors of mode I, K_I and Mode II, K_{II} by

$$G = \pi b_{11} s \lambda^{-1/4} (\lambda^{-1/2} K_I^2 + K_{II}^2) \quad (19)$$

where the constant s is defined by

$$s = \sqrt{\frac{1 + \rho}{2}}. \quad (20)$$

However, for the problem studied in the present case, the eigenstrain should contribute to the energy release rate as discussed above. The energy release rate is not only dependent on the second-order function of nondimensional quantities PC_1/h and MC_1/h^2 , but also dependent on the linear function of nondimensional quantities PC_1/h and MC_1/h^2 . In this case, the energy release rate is assumed in the form

$$G = \pi b_{11} s \lambda^{-1/4} k(k + A) \quad (21)$$

where k is a complex interface stress intensity factor and A is a complex constant. By comparing Eq. (19) and Eq. (21), the complex stress intensity factor k can be written as

$$k = k_1 + ik_2 = \lambda^{-1/2} K_I + iK_{II}. \quad (22)$$

Equating the two energy release rate expressions (15) and (21), one can obtain the following relation:

$$|k|^2 = \frac{h}{b_{11}C_1} \frac{\lambda^{1/4}}{\pi s} \left[\Pi_1 \left(\frac{PC_1}{h} \right)^2 + \Pi_2 \left(\frac{MC_1}{h^2} \right)^2 + 2 \cos \alpha_0 \sqrt{\Pi_1 \Pi_2} \left(\frac{MC_1}{h^2} \right) \right] \quad (23)$$

where

$$\cos \alpha_0 = \frac{\Pi_3}{2\sqrt{\Pi_1 \Pi_2}}. \quad (24)$$

Let the complex stress intensity factor k be

$$k = \sqrt{\frac{h}{b_{11}C_1} \frac{\lambda^{1/4}}{\pi s}} \left[a \sqrt{\Pi_1} \left(\frac{PC_1}{h} \right) + b \sqrt{\Pi_2} \left(\frac{MC_1}{h^2} \right) \right] \quad (25)$$

where a and b are nondimensional complex numbers. On the similar lines of discussion given by Suo and Hutchinson [22], the complex numbers a and b do not depend on loads P and M , but only depend on geometric parameter η_0 and Dundurs' parameters $\bar{\alpha}$ and $\bar{\beta}$,

$$\bar{\alpha} = \frac{\Gamma(\kappa_2 + 1) - (\kappa_1 + 1)}{\Gamma(\kappa_2 + 1) + (\kappa_1 + 1)}, \quad \bar{\beta} = \frac{\Gamma(\kappa_2 - 1) - (\kappa_1 - 1)}{\Gamma(\kappa_2 + 1) + (\kappa_1 + 1)}, \quad (26)$$

where $\Gamma = \mu_1/\mu_2$. The complex numbers a and b can be expressed as

$$a = \cos \phi + i \sin \phi, \quad b = \cos(\phi + \alpha_0) + i \sin(\phi + \alpha_0). \quad (27)$$

In the above expressions, only one parameter ϕ is not known. The angle ϕ was determined by Suo and Hutchinson [22] and Hutchinson et al. [26] with integral equation methods in which the semi-infinite interface crack was represented by a distribution of dislocations lying along the negative x -axis. The numerical solu-

tion of the integral equation had been carried and the numerical results were given in tabular form ([22,26]). The angle ϕ depends on η_0 and ρ only, i.e., $\phi = \phi(\eta_0, \rho)$ and the excellent approximation with a numerical fit is $\phi = 0.1584\bar{\alpha} + 0.0630\bar{\beta}$. Therefore, we have

$$k_1 = \sqrt{\frac{h}{b_{11}C_1} \frac{\lambda^{1/4}}{\pi s}} \left[\sqrt{\Pi_1} \left(\frac{PC_1}{h} \right) \cos \phi + \sqrt{\Pi_2} \left(\frac{MC_1}{h^2} \right) \cos(\phi + \alpha_0) \right] \quad (28)$$

$$k_2 = \sqrt{\frac{h}{b_{11}C_1} \frac{\lambda^{1/4}}{\pi s}} \left[\sqrt{\Pi_1} \left(\frac{PC_1}{h} \right) \sin \phi + \sqrt{\Pi_2} \left(\frac{MC_1}{h^2} \right) \sin(\phi + \alpha_0) \right]. \quad (29)$$

The relative amount of mode II to mode I at the crack tip is measured by the angle ψ as

$$\psi = \tan^{-1} \frac{K_{II}}{K_I} = \tan \left[\frac{\lambda^{-1/2} \frac{\sqrt{\Pi_1} \left(\frac{PC_1}{h} \right) \sin \phi + \sqrt{\Pi_2} \left(\frac{MC_1}{h^2} \right) \sin(\phi + \alpha_0)}{\sqrt{\Pi_1} \left(\frac{PC_1}{h} \right) \cos \phi + \sqrt{\Pi_2} \left(\frac{MC_1}{h^2} \right) \cos(\phi + \alpha_0)}}{\lambda^{-1/2} \frac{\sqrt{\Pi_1} \left(\frac{PC_1}{h} \right) \sin \phi + \sqrt{\Pi_2} \left(\frac{MC_1}{h^2} \right) \sin(\phi + \alpha_0)}{\sqrt{\Pi_1} \left(\frac{PC_1}{h} \right) \cos \phi + \sqrt{\Pi_2} \left(\frac{MC_1}{h^2} \right) \cos(\phi + \alpha_0)}} \right]. \quad (30)$$

Calculated Results and Discussions

Calculated Model. In this section the results of the calculated energy release rate and thermal stress intensity factors (TSIFs) for the TBC system operating at high temperature conditions are given in detail to the possible extent. The main idea for the calculated model is the following: (1) The thermal stress is first calculated and the details such as the theoretical model and the constitutive equation, as well as material parameters, are given in [12]. (2) The membrane stress P_i and bending moment M_i are second calculated by integrating the thermal stress along the thickness direction of the TBC system with a temperature gradient and the formulas are given in expression (33). (3) The equivalent loads such as membrane stress P and bending moment M are third calculated according to Eqs. (7) and (8). (4) The energy release rate, stress intensity factors, and mixed mode are finally calculated according to (15), (28), (29), and (30), respectively.

The TBC system for thermal stress calculation is illustrated schematically in Fig. 2. The ceramic coating system is assumed to be partially stabilized ZrO_2 by 8wt% Y_2O_3 (PSZ) over a NiCrAlY bond coat sprayed on SUS340 stainless steel or Ni-superalloy substrate. In the laser heating/cooling fatigue experiment, one found that the interface delamination cracks in TBC system always occurred just above the interface between bond coat NiCrAlY layer and PSZ layer ([4]). The interface delamination for thermal barrier ceramic coating exposed to laser heating is shown in Fig. 3. In the test, the coating was exposed to six thermal fatigue cycles and the exposed time for every cycle was 70 s and the highest temperature on coating and substrate was 1200°C and 600°C, respectively. On the other hand, the elastic parameters for NiCrAlY bond coat and stainless steel SUS304 substrate are very close. Therefore, the combination of bond coat and SUS304 stainless steel is thought as a substrate in the following discussions. The material of substrate SUS340 stainless steel has thermal and elastic properties similar to Ni-based superalloys. Therefore, the real characterization of TBC system is reflected by the assumption that the substrate of Ni-alloy is considered to be plastic and creep in the calculation of thermal stress fields ([12]). In order to study the effect of the constitutive model of substrate on TBC system failure induced by

delemination, the substrate of steel is assumed to be elastic. The ceramic coating PSZ is considered to be elastic and creep. TGO is considered in the calculation of the thermal stress field and it is assumed to be elastic. The bond coat is considered to be elastic-perfectly plastic. Generally, TBC system is not a plane plate. There must be a curvature in some place, for example, the leading edge of a gas turbine blades is winding. It is assumed that the TBC system is a cylindrical shell with four layers which are the substrate, bond coat, thermal grown oxidation as well as the ceramic coating as schemed in Fig. 2. The thickness of the substrate, bond coat, and ceramic coating is, respectively, 0.20 cm, 0.01 cm, and 0.035 cm. The inner radius of the cylindrical shell is 0.2 cm. In order to investigate the effect of TGO on the failure mechanism of the TBC system, the initial thickness of TGO is assumed to be 45 μm and the evolution of TGO thickness is given by Zhou and Hashida [12]. The system is considered to be in plane-strain condition. The mechanical parameters are all temperature-dependent as given by Zhou and Hashida [12].

Loads in the TBC System with Interface Crack. The loads P_1 , M_1 , P_3 , and M_3 are defined as

$$\begin{aligned}
 P_1 &= - \int_0^h \sigma_{\theta\theta}(y+r_4, t) dy \\
 M_1 &= - \int_0^h \sigma_{\theta\theta}(y+r_4, t) \left(y + \frac{1}{2} \Delta_1 h \right) dy \\
 P_3 &= - \int_{-H}^0 \sigma_{\theta\theta}(y+r_4, t) dy \\
 M_3 &= - \int_{-H}^0 \sigma_{\theta\theta}(y+r_4, t) \left(y + \frac{1}{2} \Delta_3 h \right) dy \quad (32)
 \end{aligned}$$

where $\sigma_{\theta\theta}(r, t)$ are circumferential stresses which have the same effect as σ_{xx} studied in the above and the analytical and numerical results of $\sigma_{\theta\theta}(r, t)$ are obtained by Zhou and Hashida [11]. r_4 is the inner radius of the ceramic coating as described in Fig. 2 and Δ_1 or Δ_3 is defined in expression (4). The temperature fields are also the same as that in [12] and the temperatures on ceramic and substrate surfaces with one cycle of heating, heat hold, and cooling are given in Fig. 4.

Figure 5 shows the histories of membrane stresses P_1 , P_3 , and P . Note that the negative value of P_1 designates the ceramic coating to be in the tensile state according to Fig. 1(a). It is seen that membrane stresses P_3 are less than loads P_1 both in Ni-alloy and steel substrates. During the period of heating and holding the heat, the ceramic coating is in the tensile state and the substrate is in the compressive state. However, ceramic coating is in the compressive state and the substrate is in the tensile state for the TBC system during the cooling period. Generally, the residual loads of P_1 become larger. By analyzing the constitutive equation discussed by Zhou and Hashida [12], it is concluded that the higher creep rate of PSZ coating results in the higher residual loads of P_1 in the PSZ ceramic coating. Figure 6 shows the histories of bending moments M_1 , M_3 , and M . During the period of heating and holding the heat, the values of M_1 and M_3 are both negative. The related values are positive on the end of cooling. The same reasons of ceramic creep result in the high positive residual loads M_1 for PSZ coating on the end of cooling. The values of equivalent loads M in both studied TBC systems are negative during the period of heating and holding the heat and those are positive on every end of cooling.

The Effect of Temperature Gradient on TBC System Failure. Temperature gradient has an important effect on the failure mechanism of the TBC system as described in [4,10]. It is reasonable to assume the different linear temperature distribution along the thickness direction by inspecting the temperature fields in the TBC system [12]. The temperature at the outer surface of the

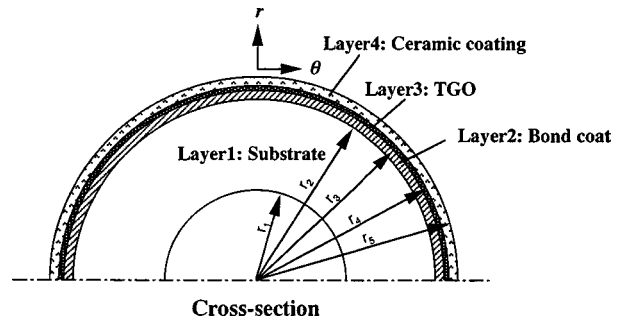


Fig. 2 Scheme of the analytical model for thermal stresses fields in the TBC system operating at high temperature

ceramic coating is 1000°C, and the temperature at the inner surface of substrate is 700°C. The temperature in the interface between material No. 1 and material No. 2 (Fig. 1) reflects the level of the temperature gradient. In order to have the concept of stress intensity factors, the energy release rate as derived in (15) is expressed by K_i as

$$K_i = \frac{1}{b_{11}} \frac{\lambda^{1/4}}{\pi s} G \quad (33)$$

The dimension of K_i is $\text{MPa}\cdot\text{m}^{1/2}$ and therefore, K_i is the mixed stress intensity factor (MSIF).

Figure 7 shows the TSIFs K_i , k_1 , and k_2 as a function of temperature on the interface of bi-materials, where the original loads are $P_1 = -7.0 \text{ MPa}\cdot\text{cm}$, $M_1 = -7.0 \times 10^{-3} \text{ MPa}\cdot\text{cm}^2$, $P_3 = 4.0 \text{ MPa}\cdot\text{cm}$, and $M_3 = -1.0 \text{ MPa}\cdot\text{cm}^2$. The original loads are typical loads for the PSZ/Ni-alloy TBC system operating at the heat hold period. In the figure, the experimental value of interface fracture toughness is also plotted, where the TBC system was partially stabilized ZrO_2 by 8wt% Y_2O_3 over a NiCrAlY bond coat sprayed on a SUS 304 stainless steel substrate ([27]). As shown in Fig. 7 for the PSZ/Ni-alloy system, the mediate interface temperature results in negative energy release rate, i.e., zero MSIF. For a PSZ/steel system with an elastic substrate, the high interface temperature results in zero MSIF. The negative mode I SIF shown in Fig. 7 means that the TBC system will not fail in the form of a mode I crack. It is seen that the temperature gradient does have an important effect on TSIFs. By inspecting Dundurs' parameters $\bar{\alpha}$ and $\bar{\beta}$, one finds that $\bar{\alpha}$ and $\bar{\beta}$ both decrease with

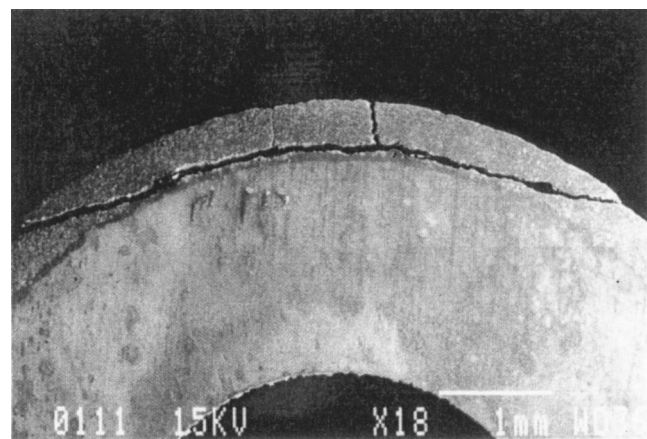


Fig. 3 SEM micrographs showing interface delamination cracking for thermal barrier ceramic coating subjected to six thermal fatigue cycles, where the exposed time for every cycle was 70 s and the highest temperature on the coating and substrate was 1200°C and 600°C, respectively

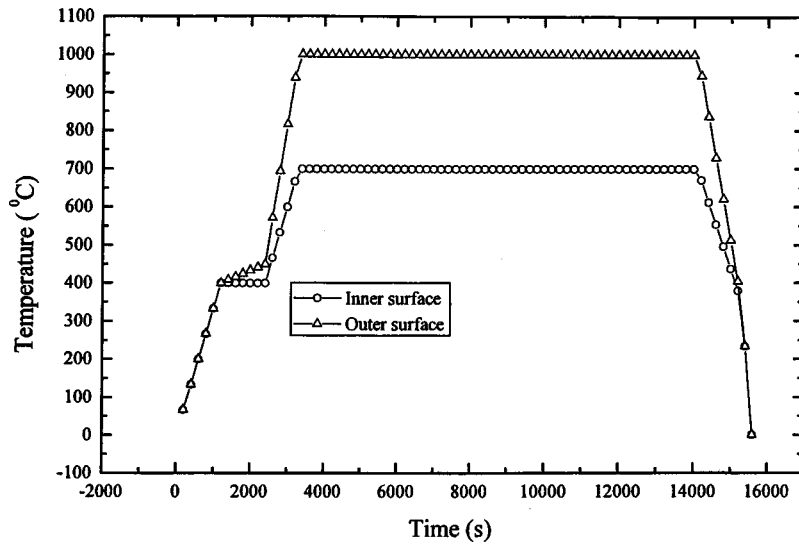
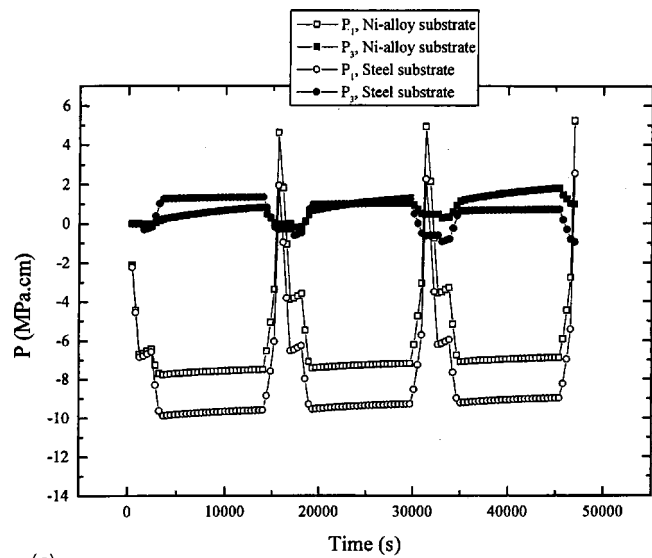


Fig. 4 Boundary conditions of temperature for the TBC system at the typical operating state

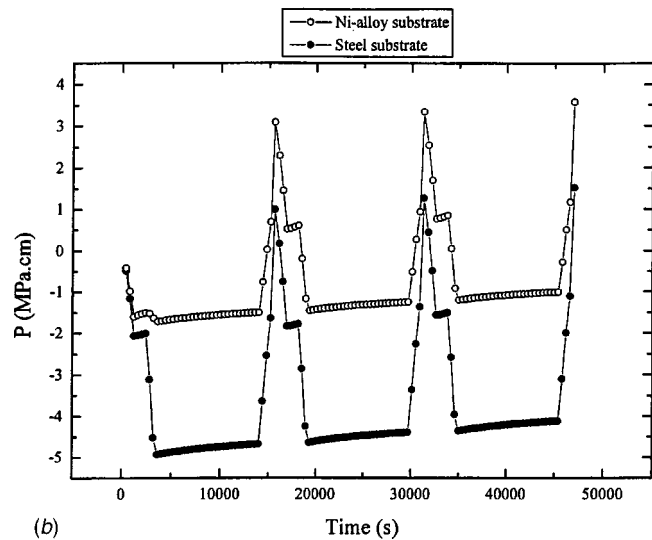
increasing interface temperature as shown in Fig. 8. There should be a correlation between K_i and Dundurs' parameters $\bar{\alpha}$ and $\bar{\beta}$, which is not known at present and it may be obtained by nondimensional analysis.

Failure Evolution. Figure 9 shows the histories of TSIFs for PSZ/Ni-alloy and PSZ/steel TBC systems. The temperature histories on outer and inner surfaces are shown in Fig. 4. Note that in the model Ni-alloy is in the plastic state and steel is in the elastic state. The difference of the constitutive model results in the different characterizations of TSIF in Ni-alloy and steel substrates. Let us focus on the characterizations of TSIFs for the PSZ/Ni-alloy system. The MSIF during the period of heat hold is lower than that during the period of cooling for PSZ/Ni-alloy system. The MSIF in the heat hold becomes lower and lower for the system operating with three cycles of heating/cooling. Generally, the MSIF during the period of the heat hold is lower than the interface fracture toughness K_{ic} . This means that interface crack may not propagate for the system during the heat hold period. However, the MSIF becomes higher and higher for the system during the cooling period. The MSIF may be higher than the interface fracture toughness K_{ic} . Therefore, the interface crack may propagate during cooling or during the heating period for the second or later cycles. It is concluded that the TBC system may not fail in the form of interface delamination during the period of heat hold, but it may fail in the form of interface delamination during cooling or during the heating period for the second cycle or after the second cycle. The conclusion is consistent with the experimental observations as shown in [4,10]. In [4,10], one has the fact that the interface delamination may take place during heating or cooling period and even on the end of cooling in which the temperature gradient along the thickness direction was zero.

The failure evolution of PSZ/Ni-alloy in the form of interface delamination may be explained by inspecting the characterization of equivalent loads P and M as shown in Figs. 5 and 6. The coating is in the tensile state during heating for the first cycle or during heat hold. These type of loads cannot lead to coating delamination. However, due to plastic and creep behavior of the ceramic and substrate, the coating is in the compressive state when the system is cooling. The compression of ceramic coating is similar to the condition of the blister test ([27]). Although the new heating cycle may relax the compressive loads, the compressive load is so high that not all the compressive load is relaxed. The residual compressive load in the coating is sufficient to cause delamination. Therefore, the interface delamination is caused by

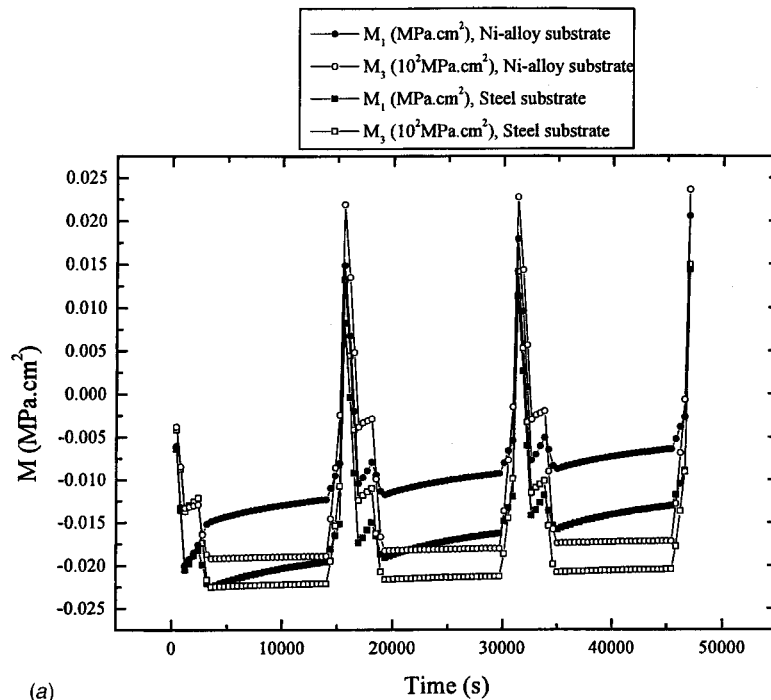


(a)

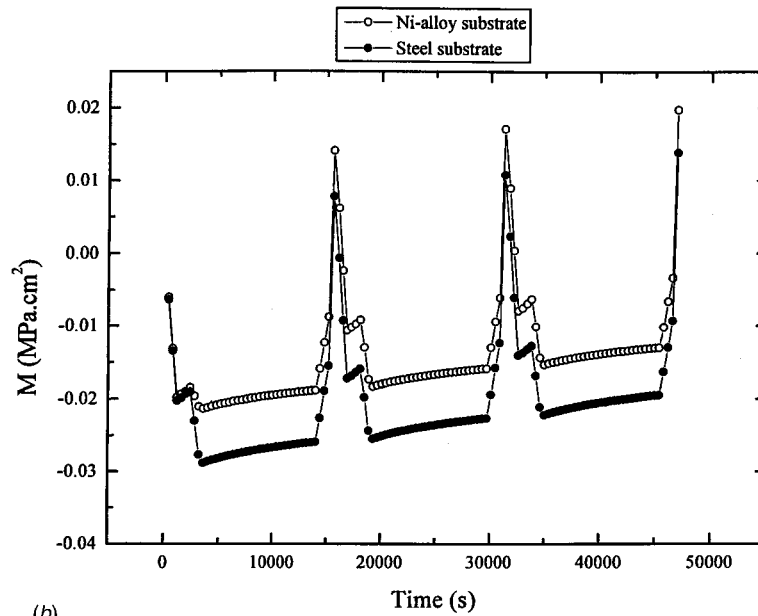


(b)

Fig. 5 Histories of membrane stresses; (a) original membrane stresses P_1 and P_3 , (b) equivalent membrane stresses P



(a)



(b)

Fig. 6 Histories of bending moments; (a) original bending moments M_1 and M_3 , (b) equivalent bending moments M

compressive loading in the coating. TSIFs for mode I and mode II shown in Fig. 9 reveal that the interface delamination crack in the period of heating or cooling is a mixed mode. Neither the mode I nor mode II crack singly dominates the crack propagation.

Conclusions

Delamination cracking in the thermal barrier coating system is studied in the present paper. A theoretical model concerning interface delamination cracking in the TBC system at operating state is proposed. In the model, a semi-infinite long interface crack is pre-existing. The thermal stress and temperature gradient in the TBC system are designated by a membrane stress P and a bending moment M . In this case, the coupled effect of plastic deformation,

creep of ceramic coating, as well as thermal growth oxidation and temperature gradient in the TBC system was considered in the model. The energy release rate, mode I and mode II stress intensity factors, as well as mode mixed measure ψ are derived. Temperature gradient has an important effect on the failure mechanism of the TBC system. There should be correlation of K_I with Dundurs' parameters $\bar{\alpha}$ and $\bar{\beta}$. The numerical results of TSIFs reveal some same results as obtained in the experimental test. For example, the TBC system may not fail in the form of coating delamination during the period of heat hold, but it may fail in the form of coating delamination during cooling or in the heating period for the second cycle or later cycles according to the model. In the experiment ([4,10]), one has the fact that the interface

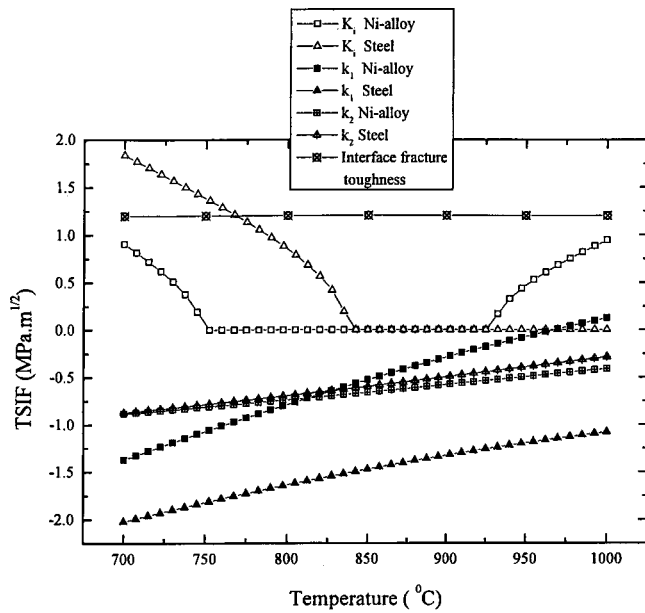


Fig. 7 TSIFs K_I , K_{II} , and K_{III} as a function of temperature on the interface of bimetals, where the original loads $P_1 = -7.0 \text{ MPa.cm}$, $M_1 = -7.0 \times 10^{-3} \text{ MPa.cm}^2$, $P_3 = 4.0 \text{ MPa.cm}$, and $M_3 = -1.0 \text{ MPa.cm}^2$

delamination may take place during the heating or cooling period and even on the end of cooling in which the temperature gradient along the thickness direction was zero. Due to plastic and creep behavior of the ceramic and substrate, the coating is in the compressive state when the system is cooling. The interface delamination is caused by compressive loading in the coating. The interface delamination crack during the period of heating or cooling is a mixed mode. Neither mode I nor mode II crack singly dominates the crack propagation.

Acknowledgment

The collaborative research grant for foreign researchers in Japan is provided to first author YCZ by JSPS (Japan Society for the Promotion of Science). This support is gratefully acknowledged. A part of this work was supported by the Grant-in-Aid for COE (Center of Excellence) Research (No. 11CE2003), the Japan Min-

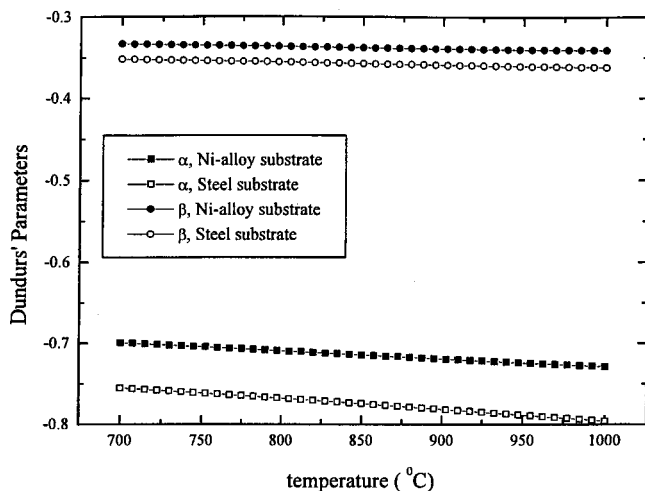
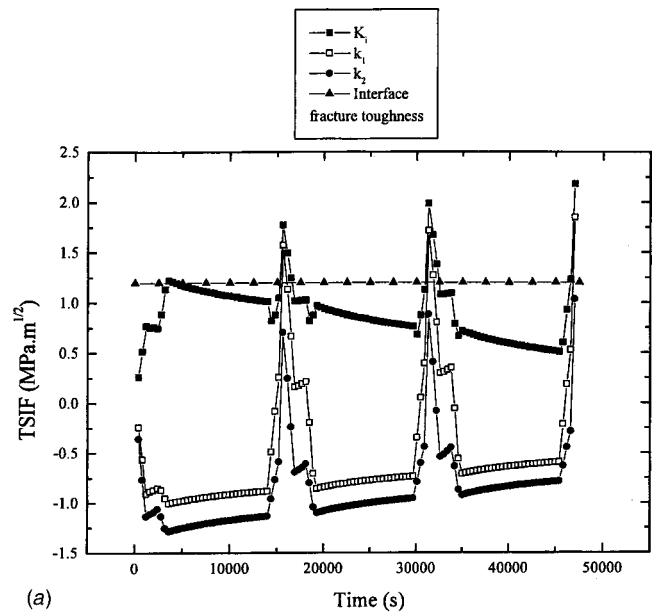
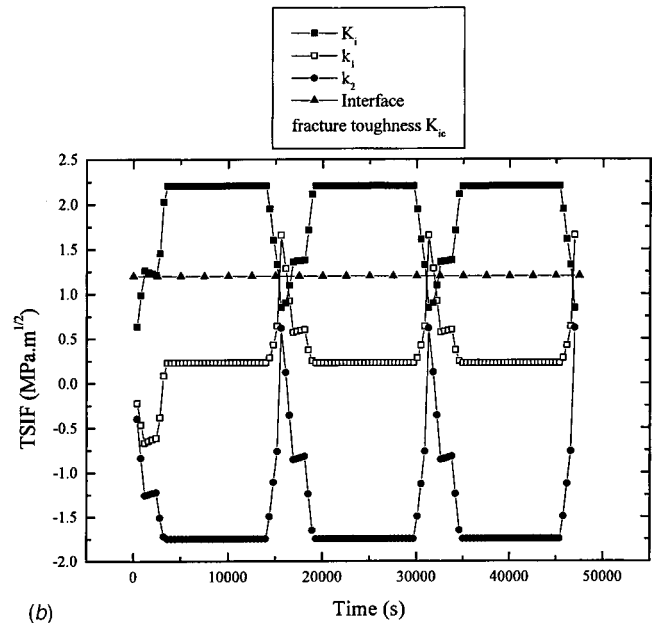


Fig. 8 Dundurs' parameters $\bar{\alpha}$ and $\bar{\beta}$ as a function of temperature on the interface of bimetals



(a)



(b)

Fig. 9 Histories of TSIFs in TBC coating system; (a) Ni-alloy substrate, (b) steel substrate

istry of Education, Science, Sports and Culture under Grant-in-Aid for Joint Research with the private sector. The authors express their appreciation for the grant. The authors show their sincere gratitude to the referees for their careful proofreading and many valuable suggestions.

Appendix A

In this Appendix, the following material parameters such as ω_k^j and φ_k^j are defined:

$$\omega_k^j = \int_{-H}^h \left[\frac{\mu_1}{1 + \kappa_1} \frac{C_1}{h^k} \delta_{j1} \gamma_1(y) + (-1)^{k+1} \frac{\mu_2}{1 + \kappa_2} \frac{C_2}{H^k} \delta_{j2} \gamma_2(y) \right] \times ky^{k-1} dy, \quad k=1,2,3 \quad j=1,2 \quad (A1)$$

$$\varphi_k^j = \int_{-H}^h \left[\frac{\mu_1}{1+\kappa_1} \frac{C_1}{h^k} (E_{xx}^{(1)} + \eta^{(1)} E_{zz}^{(1)}) \delta_{j1} \gamma_1(y) + (-1)^{k+1} \right. \\ \left. \times \frac{\mu_2}{1+\kappa_2} \frac{C_2}{h^k} (E_{xx}^{(2)} + \eta^{(2)} E_{zz}^{(2)}) \delta_{j2} \gamma_2(y) \right] k y^{k-1} dy \\ k=1,2 \quad j=1,2 \quad (A2)$$

$$\omega_k^3 = \omega_{ik}^2 + (-1)^{k+1} \Sigma (\eta_0)^k \omega_k^1, \\ \varphi_k^3 = \varphi_1^2 + (-1)^{k+1} \Sigma (\eta_0)^k \varphi_k^1, \quad k=1,2 \quad (A3)$$

In the above expressions, the related functions are defined as

$$\delta_{ij} = \begin{cases} 1 & i=j \\ 0 & i \neq j \end{cases} \quad \gamma_1(y) = \begin{cases} 0 & -H < y < 0 \\ 1 & 0 < y < h \end{cases} \\ \gamma_2(y) = \begin{cases} 1 & -H < y < 0 \\ 0 & 0 < y < h \end{cases} \quad (A4)$$

$$\frac{1}{j_i} = \frac{8}{3} \omega_3^i - 2 \frac{(\omega_2^i)^2}{\omega_1^i} \quad i=1,2,3. \quad (A5)$$

Appendix B

In this Appendix, the compliance matrix in Eq. (29) for the TBC system is given.

$$[B] = \begin{bmatrix} \frac{1}{E_T} & -\frac{\nu_A}{E_T} & -\frac{\nu_T}{E_T} & 0 & 0 & 0 \\ -\frac{\nu_A}{E_T} & \frac{1}{E_L} & -\frac{\nu_A}{E_L} & 0 & 0 & 0 \\ -\frac{\nu_T}{E_T} & -\frac{\nu_A}{E_L} & \frac{1}{E_T} & 0 & 0 & 0 \\ 0 & 0 & 0 & \frac{1}{\mu_A} & 0 & 0 \\ 0 & 0 & 0 & 0 & \frac{2(1+\nu_T)}{E_T} & 0 \\ 0 & 0 & 0 & 0 & 0 & \frac{1}{\mu_A} \end{bmatrix} \quad (B1)$$

where

$$E_T = \frac{E_1 \eta_0 + E_2}{1 + \eta_0}, \quad E_L = \frac{(1 + \eta_0) E_1 E_2}{E_1 + E_2 \eta_0} \\ \mu_A = \frac{(1 + \eta_0) \mu_1 \mu_2}{\mu_1 + \mu_2 \eta_0} \quad \nu_A = \frac{\nu_1 \eta_0 + \nu_2}{1 + \eta_0} \quad \nu_T = 1 - \nu_A + \frac{1 - 2\nu_A}{2} \frac{E_T}{E_L} \\ - \frac{3}{2} \frac{1}{1 + \eta_0} \left[\frac{E_T}{E_1} (1 - 2\nu_1) \eta_0 + \frac{E_T}{E_2} (1 - 2\nu_A) \right]. \quad (B2)$$

References

- [1] Yuri, I., Hisamatsu, T., Watanabe, K., and Etori, Y., 1997, "Structural Design and High Pressure Test of a Ceramic Combustor for 1500°C Class Industrial Gas Turbine," ASME J. Eng. Gas Turbines Power, **119**, pp. 506–511.
- [2] Kokini, K., and Takeuchi, Y. R., 1996, "Surface Thermal Cracking of Thermal Barrier Coatings Owing to Stress Relaxation: Zirconia vs. Mullite," Surf. Coat. Technol., **82**, pp. 77–82.
- [3] Zhu, D. M., and Miller, R. A., 1998, "Investigation of Thermal High Cycle and Low Cycle Fatigue Mechanisms of Thick Thermal Barrier Coatings," Mater. Sci. Eng., A, **245A**, pp. 212–223.
- [4] Jian, C. Y., 1996, "Study on Evaluation Method of Ceramic Coating System for Gas Turbine Rotator Blades," Doctor's thesis, Tohoku University.
- [5] Tolpygo, V. K., Dryden, J. R., and Clarke, D. R., 1998, "Determination of the Growth Stress and Strain in α -Al₂O₃ Scales During the Oxidation of Fe-22Cr-4.8Al-0.3Y Alloy," Acta Mater., **46**(3), pp. 927–937.
- [6] Ogawa, K., Minkov, D., Shoji, T., Sato, M., and Hashimoto, H., 1999, "NDE of Degradation of Thermal Barrier Coating by Means of Impedance Spectroscopy," NDT & E Int., **32**, pp. 177–185.
- [7] Gell, M., et al., 1999, "Mechanism of Spallation in Platinum Aluminide/Electron Beam Physical Vapor-Deposited Thermal Barrier Coatings," Metall. Trans. A, **30A**(2), pp. 427–435.
- [8] He, M. Y., Evans, A. G., and Hutchinson, J. W., 1998, "Effects of Morphology on the Decohesion of Compressed Thin Films," Mater. Sci. Eng., **245**, pp. 168–181.
- [9] Bernstein, H. L., and Allen, J. M., 1992, "Analysis of Cracked Gas Turbine Blades," ASME J. Eng. Gas Turbines Power, **114**, pp. 293–301.
- [10] Zhou, Y. C., and Hashida, T., 2000, "Coupled Effects of Temperature Gradient and Oxidation on the Thermal Barrier Coating Failure," *Life Assessment of Hot Section Gas Turbine Components*, R. Townsend, et al., eds., Cambridge University Press, London, UK, pp. 155–1720.
- [11] Zhou, Y. C., and Hashida, T., 2002, "Thermal Fatigue in Thermal Barrier Coating," JSME Int. J., **A45**, pp. 57–64.
- [12] Zhou, Y. C., and Hashida, T., 2001, "Coupled Effects of Temperature Gradient and Oxidation on the Thermal Stress in Thermal Barrier Coating," Int. J. Solids Struct., **38**, pp. 4235–4264.
- [13] Sih, G. C., Paris, P. C., and Irwin, G. R., 1965, "On Cracks in Rectilinearly Anisotropic Bodies," Int. J. Fract. Mech., **1**, pp. 189–203.
- [14] Rice, J. R., and Sih, G. C., 1965, "Plane Problems of Cracks in Dissimilar Media," ASME J. Appl. Mech., **32**, pp. 418–423.
- [15] Dundurs, J., 1969, "Edge-Bonded Dissimilar Orthogonal Elastic Wedges," ASME J. Appl. Mech., **36**, pp. 650–652.
- [16] Erdogan, F., 1965, "Stress Distribution in Bonded Dissimilar Materials With Cracks," ASME J. Appl. Mech., **32**, pp. 403–410.
- [17] Evans, A. G., and Hutchinson, J. W., 1984, "On the Mechanics of Delamination and Spalling in Compressed Films," Int. J. Solids Struct., **20**, pp. 455–466.
- [18] Hutchinson, J. W., and Suo, Z., 1992, "Mixed Mode Cracking in Layered Materials," Adv. Appl. Mech., **29**, pp. 63–191.
- [19] Timoshenko, S. P., and Gere, J. M., 1972, *Mechanics of Materials*, D. Van Nostrand, New York.
- [20] Dundurs, J., 1990, "Boundary Conditions at Interfaces," *Micromechanics and Inhomogeneous*. G. J. Weng, et al., eds., Springer-Verlag, New York, pp. 109–114.
- [21] Mura, T., 1982, *Micromechanics of Defects in Solid*, Martinus Nijhoff Publishers, The Hague.
- [22] Suo, Z., and Hutchinson, J. W., 1990, "Interface Crack Between Two Elastic Layers," Int. J. Fract., **43**, pp. 1–18.
- [23] Whitney, J. M., and McCullough, R. L., 1990, *Micromechanical Materials Modeling*, Vol. 2, Technomic Lancaster, PA.
- [24] Lekhnitskii, S. G., 1963, *Theory of Elasticity of an Anisotropic Elastic Body*, Holden-Day, Oakland, CA.
- [25] Suo, Z., 1990, "Delamination Specimens for Orthotropic Materials," ASME J. Appl. Mech., **57**, pp. 627–634.
- [26] Hutchinson, J. W., Mear, M. E., and Rice, J. R., 1987, "Crack Paralleling an Interface Between Dissimilar Materials," ASME J. Appl. Mech., **54**, pp. 828–832.
- [27] Zhou, Y. C., Hashida, T., and Jian, C. Y., 2002, "Determination of Interface Fracture Toughness in Thermal Barrier Coating System by Blister Tests," ASME J. Eng. Mater. Tech., **124**, in press.

Designing Hot Working Processes of Nickel-Based Superalloys Using Finite Element Simulation

R. Kopp

M. Tschirnich

M. Wolske

Institute of Metal Forming,
Intzestr. 10,
D-52056, Aachen, Germany

J. Klöwer

Krupp VDM GmbH,
D-58742 Altena, Germany

Knowledge of correct flow stress curves of Ni-based alloys at high temperatures is of essential importance for reliable plastomechanical simulations in materials processing and for an effective planning and designing of industrial hot forming schedules like hot rolling or forging. The experiments are performed on a computer controlled servohydraulic testing machine at IBF. To avoid an inhomogeneous deformation due to the influence of friction and initial microstructure, a suitable specimen geometry and lubricant is used and a thermal treatment before testing has to provide a microstructure, similar to the structure of the material in the real process. The compression tests are performed within a furnace, which keeps sample, tools, and surrounding atmosphere on the defined forming temperature. The uniaxial compressions were carried out in the range of strain rates between 0.001 and 50 s⁻¹ and temperatures between 950 and 1280°C. Furthermore, two-stage step tests are carried out to derive the work hardening and softening behavior as well as the recrystallization kinetics of the selected Ni-based alloys. At the end of this work a material model is adapted by the previously determined material data. This model is integrated into the Finite Element program LARSTRAN/SHAPE to calculate a forging process of the material Alloy 617. [DOI: 10.1115/1.1494096]

1 Introduction

At the company Krupp VDM the nickel-based alloys alloy C263, alloy X, and alloy 617 were deformed in a hot rolling process. To obtain the demand of forces in the different rolling steps, the calculation of flow stress is obviously necessary.

With respect to this demand Krupp VDM and IBF analyzed these three nickel-based alloys with respect to their plastic deformation behavior. In the first step uniaxial compression tests were carried out on the servohydraulic testing system at IBF. One-stage step tests were performed to determine the flow curves of the three materials in dependence to temperature and strain rate. Double-stage step tests were carried out to see the flow stress level in the second step in dependence to different holding times between the steps.

In addition to that a joint research project sponsored by the Deutsche Forschungsgesellschaft (DFG) was installed to develop new nickel-based alloys for high-temperature applications in stationary power generations. Here, the increase of efficiency of steam gas power generations are the main goal of manufacturers and carrier of stationary power plants. One effective way is to exceed the operation up to higher steam gas parameters, e.g., temperature and pressure. Next to other solutions does this demand led to new material developments.

With assistance of finite element method microstructure simulations will allow to predict the best manufacturable material group. Herewith, a prediction of local plastomechanical, thermal, or microstructural conditions is possible. The number of extensive trials can be reduced significantly while programs are available to simulate the microstructural characteristics.

2 Experimental Procedure

2.1 Materials. In the present study the commercial nickel-based alloys alloy C-263, alloy X, and alloy 617 were investigated. The chemical compositions are given in Table 1. The physical properties are given in Table 2.

2.2 Flow Stress Testing. For finite element method simulations of hot rolling and forming processes the knowledge of the flow stress is necessary to improve the accuracy of the numerical calculation. Besides, accurate values of the material properties (e.g., density, specific heat capacity, and thermal conductivity) and boundary conditions (e.g. friction, radiation, and heat transfer between workpiece and tools) have to be put in finite element method to achieve a higher quality of simulation.

Flow stress testing at IBF was performed at the computer-controlled, 1200-kN servohydraulic testing system, manufactured by the company SERVOTEST LTD., with which uniaxial hot compression tests up to temperatures of 1280°C and strain rates of 100/s could be obtained. Throughout the measurements the specimen, tools, and surrounding atmosphere could be held at a constant forming temperature by a furnace, installed in the testing system. After correction for dissipation heat, fully isothermal flow stress curves were obtained. Before compression all specimen were annealed for 15 min in the machine furnace to attain the accurate forming temperature.

Cylindrical compression samples, 16-mm diameter by 24-mm high, were machined. To eliminate friction as far as possible, Ras-tegaev specimen were used ([1]). The recessed end faces of the specimen were filled with glass lubricant. Herewith it was possible to relate the observed microstructure to a particular homogeneous forming condition. Constant strain rate is arranged by setting the crosshead velocity of the testing machine via displacement control. Therefore, uniform forming conditions within the specimen were ensured for the whole series of the tests.

At the company Krupp VDM the three nickel-based alloys were deformed in a hot rolling process. To obtain the demand of forces in the different rolling steps, the calculation of flow stress is obviously necessary. To ensure the same forming conditions as in the

Contributed by the International Gas Turbine Institute (IGTI) of THE AMERICAN SOCIETY OF MECHANICAL ENGINEERS for publication in the ASME JOURNAL OF ENGINEERING FOR GAS TURBINES AND POWER. Paper presented at the International Gas Turbine and Aeroengine Congress and Exhibition, New Orleans, LA, June 4–7, 2001; Paper 01-GT-429. Manuscript received by IGTI, December 2000, final revision March 2001. Associate Editor: R. Natole.

Table 1 Chemical compositions of investigated Ni-based alloys of Krupp VDM

	Alloy 617	Alloy C-263	Alloy X
Chemical Compositions in wt-%			
im	bal.	bal.	bal.
Cr	20–23	19–21	20.5–23.5
Fe	max. 2	max. 0.7	17–20
Mo	8–10	5.6–6.1	8–10
C	0.05–0.1	0.04–0.08	0.05–0.15
Ti	0.2–0.6	1.9–2.4	-
Co		19–21	0.5–2.5
Al	0.6–1.5	0.3–0.6	max. 0.1
Others	Co: 10–13	Al+Ti: 2.4–2.8	Si: max. 1 W: 0.2–1

rolling process, hot compression tests were carried out in a temperature range from 900°C to 1280°C for the three nickel-based alloys. For all materials, but in dependence to the strain rates at the corresponding temperatures of the process, the strain rates were set to 0.01/s, 0.1/s, 1/s, 10/s, and 50/s. In the double-stage

Table 2 Physical properties of investigated Ni-based alloys

	Alloy 617	Alloy C-263	Alloy X
Physical Properties at Room Temperature			
Density (g/cm ³)	8.4	8.4	8.3
Specific heat (J/Kg K)	420	426	435
Heat conductivity (W/m K)	13.4	11.7	11.3
Electrical resistivity (m Ω cm)	122	115	115
Thermal expansion 20–300°C (10 ⁻⁶ K)	13.1	12.5	14.3
Modulus of elasticity (kN/mm ²)	212	222	205

step tests only strain rates with 10/s were used. Thermal treatment before testing has to provide a microstructure, similar to the structure of the material in the real process. Therefore the samples were heated to 1100°C and then held on this temperature for two hours, followed by 20 minutes on 1250°C.

The compressed samples were rapidly pushed out of the forming zone by a pneumatic cylinder and quenched in water spray just after deformation with assistance of a quenching unit, which is directly connected to the upsetting machine as shown in Fig. 1.

The measured flow curves of the one stage step and double stage step testing at three characteristic temperatures are shown in Fig. 2 for all tested materials, respectively.

Analyzing the flow curves it becomes obvious, that there is a strong dependence on both the strain rate and the temperature in case of all materials. These effects should be illustrated with alloy 617 at 1100°C, where compression tests with the whole range of strain rates were performed. At the lowest strain rate (0.01/s) a maximal flow stress of 125 N/mm² occurs at a strain of 0.3. At the highest strain rate (50/s) the maximal flow stress increases up to 490 N/mm² at a strain of about 0.4. To show the dependence of the flow stress level on the temperature, the flow curves with a strain rate of 10/s are compared at a strain of 0.5. The flow stress is reaching 215 N/mm² at 1250°C, then increasing to 400 N/mm² at 1100°C and finally rising to 550 N/mm² at 1000°C.

The double-stage step compression tests were carried out with different holding times between the two steps, varying from 5 to 25 seconds. It becomes obvious that there is no significant influence of the holding time. In all cases the static recrystallization attains nearly 100%. Because of this correspondence only one flow curve per alloy is pictured, exemplary at 1100°C.

2.3 Metallography. Metallographical investigations are needed for microstructure models in form of the initial microstructural state and dynamically recrystallized grain sizes after deformation to fit the model equations. Here, alloy 617 was supplied by Saarschmiede GmbH Freiformschmiede for microstructure investigations. The as-forged material has undergone a two-step heat treatment before flow stress testing.

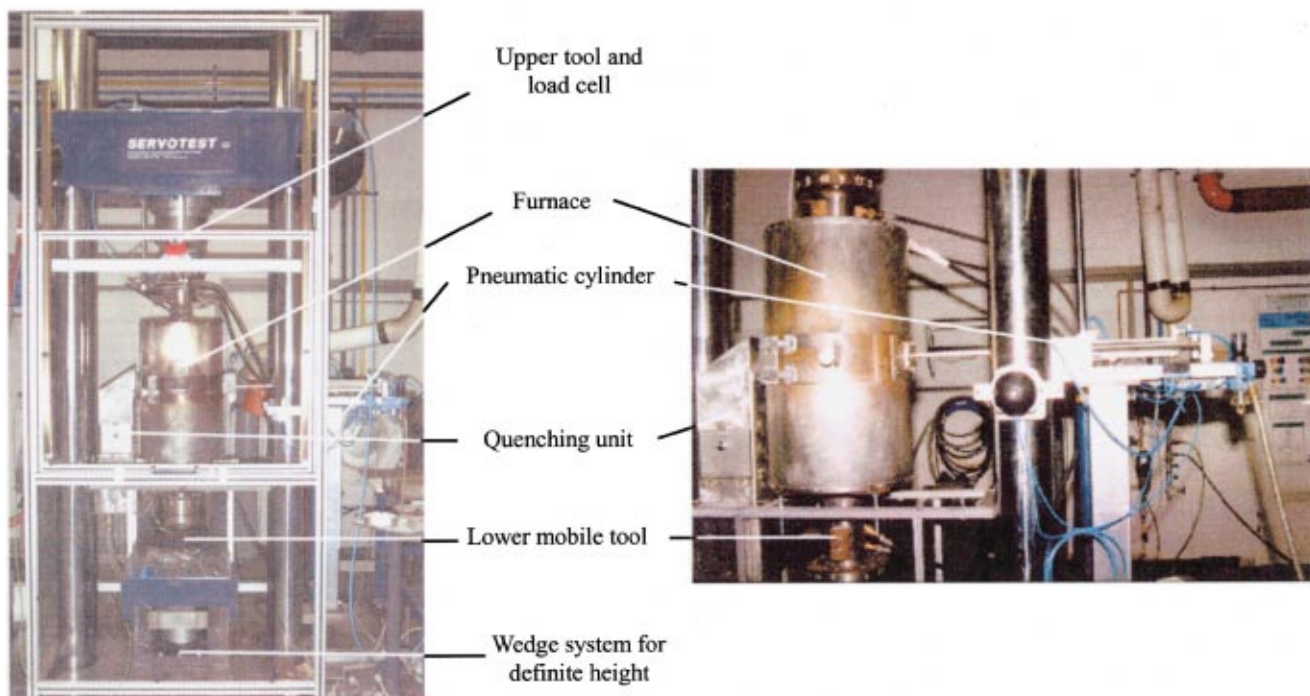


Fig. 1 Computer-controlled servohydraulic upsetting system with integrated quenching unit at IBF. Left:total system. Right:detail of quenching unit.

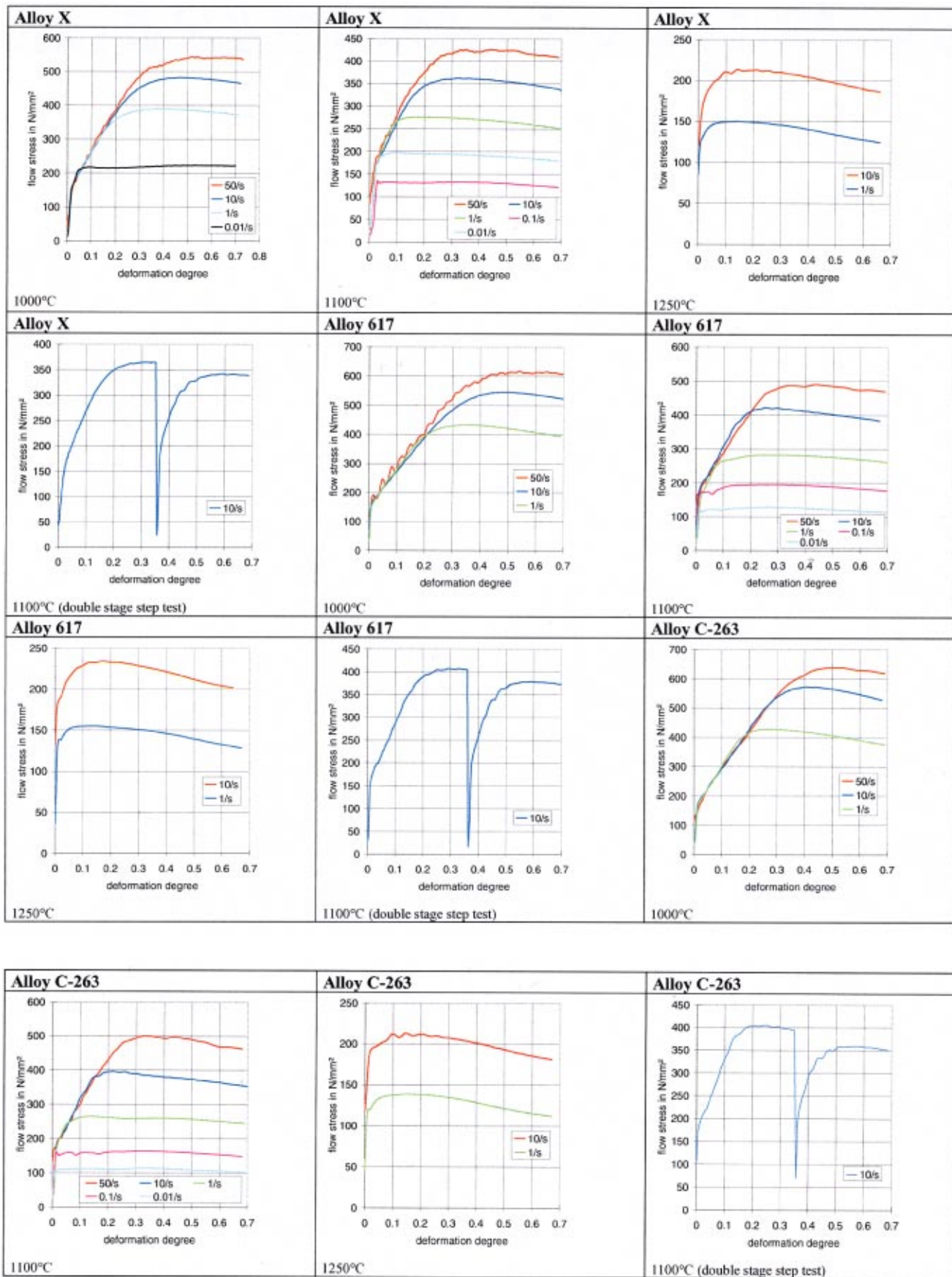


Fig. 2 Measured flow curves for alloy C-263, alloy X, and alloy 617 at 1000, 1100, and 1250°C

The observed specimen of alloy 617 were etched in a V_2A mordant at 60°C for 2 to 5 minutes resp. 20 minutes. The determined initial grain size is 223 μm (ASTM 1.4).

The microstructural state of compressed samples was as well observed. The specimen were prepared with the same etching as the for the observation of the initial state. Under forming conditions leading to partial recrystallization, characteristic “necklace” structures were observed. This phenomenon is characteristic for dynamically recrystallized nickel-based alloys ([2]).

Microstructure observation was done over the whole range of forming conditions. This was necessary to fit the model’s prediction of average grain size and recrystallized fraction. The combined influence of strain rate and temperature was taken into consideration by use of the Zener-Hollomon-parameter Z ,

$$Z = \dot{\epsilon} \cdot \exp\left(\frac{Q_{\text{def}}}{R \cdot T}\right) \quad (1)$$

where R is the universal gas constant, T the temperature in K , and $\dot{\epsilon}$ the strain rate.

3 Determination of Material Data

Isothermal flow stress curves have been calculated by an iterative method for providing material models on the basis of empirical equations. From the measured data the activation energy for hot deformation Q_{def} was calculated in a first step at the prevailing maximum of each flow curve. In the next step the dependence of

the maximum flow stress on forming temperature and strain rate was formulated by use of Z . Activation energy for hot deformation was found to be 411.8 kJ/mol for alloy 617.

The dynamic recrystallized grain size d_{dyn} decreases with increasing forming conditions, represented by the Zener-Hollomon-parameter Z . The measured value of d_{dyn} has been calculated by using following equation:

$$d_{\text{dyn}} = 0.0008 \cdot Z^{-0.0915} \quad (\text{alloy 617}). \quad (2)$$

The dynamic recrystallized grain size does not depend on the initial grain size but could described in dependence from the hot working conditions, as reported by various authors ([3–5]).

The dynamic recrystallized fraction X_{dyn} , which corresponds to the dynamic recrystallized grain size d_{dyn} could be expressed by an Avrami-type equation ([6]). Because the coefficients of the equations have an effect on each other during a simulation a combined interdependence optimization was carried out to determine the whole set of coefficients. This could be realized automatically with a program developed at IBF. A complete description of the model’s equations for the investigated Ni-based alloys could be found in [7].

4 Microstructure Simulation and Validation

To simulate microstructural evolution, a microstructure model program called STRUCSIM was used with coupling to the finite element method code ‘LARSTRAN/SHAPE.’ STRUCSIM receives ac-

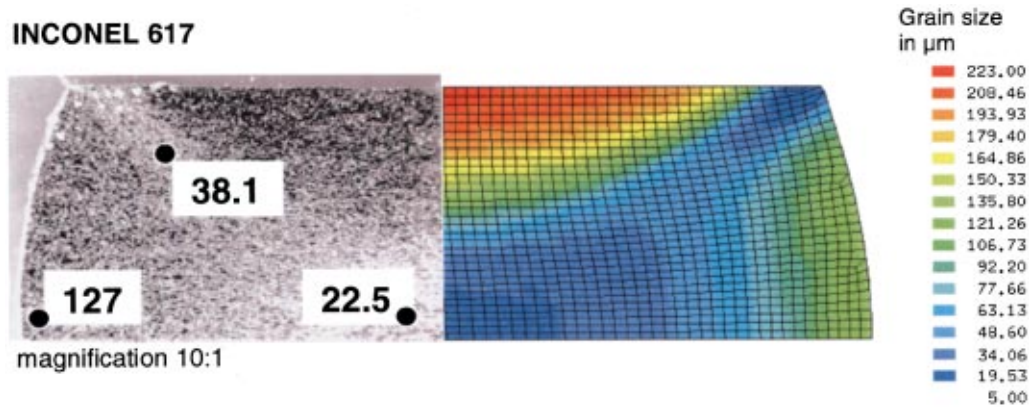


Fig. 3 Comparison of dynamically recrystallized grain size between experiment (left) and simulation (right) of compression of alloy 617 at 950°C and 10/s. Measured grain sizes in μm and the position of observation are marked in the micrograph.

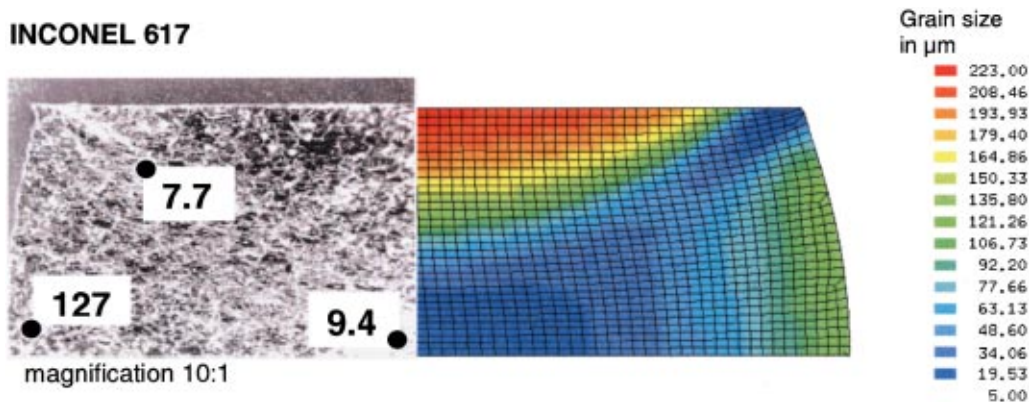


Fig. 4 Comparison of dynamically recrystallized grain size between experiment (left) and simulation (right) of compression of alloy 617 at 1150°C and 10/s. Measured grain sizes in μm and the position of observation are marked in the micrograph.

tual local forming conditions (strain, strain rate, and temperature) from LARSTRAN/SHAPE and simulates microstructural changes based on the forming data. The flow stress depending on the microstructure is estimated by STRUCSIM and feed back to the finite element method ([8,9]).

For validation of the developed microstructure models, selected experimental compression tests were simulated by a coupled finite element method-STRUCSIM simulation. The material data, as density, thermal conductivity, and specific heat capacity, were taken from product information of Inco Alloys Int., Inc. The values for boundary conditions have been set in case of heat transfer from workpiece to the tool to $a=0.0011$ and in case of the radiation coefficient to $e=0.86$. Coulomb's friction coefficients have been set by comparing the bulged finite element method shape with the contour of the experimental samples. The temperature of the tools and the surrounding atmosphere was held at the respective forming temperature. Thus, the influence of heat loss by radiation or heat transfer on the forming state is relatively low in contrast to the friction coefficient which becomes important value, e. g., for bulging of the sample.

Figure 3 illustrates a comparison between micrograph and simulation of microstructure for a compression test with alloy 617 at a temperature of 950°C and a strain rate of 10/s. The model prediction was as well validated at a temperature which represents the starting temperatures of forging. Here, the compression at a temperature of 1150°C and a strain rate of 10/s is shown in Fig. 4.

Forming with a strain rate of 10/s at 950°C as well as at 1150°C leads to similar microstructure distributions. The simulated average grain size shows fine grains from 5 μm up to 19.5 μm in the center of the sample and coarser grain with original grain size beneath the tool. The prediction of this microstructure model is quite acceptable as presented by the measured grain sizes in the left part of the figure. The average dynamically recrystallized fraction rises under both forming conditions from about 6% under the tool up to 95% in the center of the sample.

5 Conclusions

On the basis of Rastegaev hot compression tests friction-eliminated stress-strain curves were recorded for the Nickel-base alloys alloy C263, alloy X, and alloy 617. The testing parameters as strain rate and temperature cover the industrial range of hot rolling processes at Krupp VDM. The determined flow curve data has been temperature corrected by eliminating the softening effect caused by dissipation heat.

On the basis of empirical equations a microstructure model has been developed for an as forged and two-step heat treated alloy 617. This model describes the microstructural changes due to DRX quantitatively. Coupled to finite element method, the incremental calculation of flow stress and recrystallization kinetics provides an improved analysis of microstructural evolution. The model validation was shown up on the basis of simulated compression tests within the temperature range of the industrial production of open-die forged power generation components as, e. g., turbine shafts. The microstructure of the tested material was predicted reasonably well by the respective model under above mentioned forming conditions.

Process simulations of large free-forging components could be performed with assistance of these microstructure simulations. A determination of the best manufacturable Ni base alloy for large forging components will be possible with this simulation tool.

Acknowledgments

The authors would like to acknowledge the financial support given by the Deutsche Forschungsgemeinschaft (DFG), Germany, within the joint research project "Herstellungs- und Lebensdauermodelle für den Einsatz von Ni-Basis-Werkstoffen in Dampfturbinen oberhalb 700°C" (DT5).

References

- [1] Herbertz, R., and Wiegels, H., 1981, "Der Zylinderstauchversuch—ein geeigertes Verfahren zur Fließkurvenermittlung?" *Stahl & Eisen*, **101**, p. 89.
- [2] Brand, A. J., Karhausen, K., and Kopp, R., 1996, "Microstructural Simulation of Nickel Base Alloy Inconel 718 in Production of Turbine Discs," *Mater. Sci. Technol.*, **12**, p. 963.
- [3] Roberts, W., Boden, H., and Ahlblom, B., 1979, "Dynamic Recrystallization Kinetics," *Met. Sci.*, **13**, p. 195.
- [4] McQueen, H. J., and Bourell, D. L., 1987, "Summary Review of Comparative Hot Workability of Metals in Different Crystal Structures," *Proc. Conf. on Formability and Metallurgical Structure*, Sachdev and Embury, eds., TMS, Warrendale, PA, p. 341.
- [5] Sellars, C. M., 1979, "The Physical Metallurgy of Hot Working," *Hot Working and Forming Processes*, C. M. Sellars and G. J. Davies, eds., TMS, London, p. 3.
- [6] Luton, M. J., and Sellars, C. M., 1969, "Dynamic Recrystallization in Nickel and Nickel-Iron Alloys During High Temperature Deformation," *Acta Metall.*, **17**, p. 1033.
- [7] Kopp, R., and Wolske, M., 2000, "Microstructure Simulation of Ni Based Alloys," *Proc. IVa Conferência Internacional de Forjamento*, Porto Alegre/Brazil, p. 42.
- [8] Karhausen, K., 1994, "Integrierte Prozeß- und Gefügesimulation bei der Warmumformung," Dr.-Ing. thesis, Institute of Metal Forming, Aachen, Germany.
- [9] Karhausen, K., and Kopp, R., 1992, "Model for Integrated Process and Microstructure Simulation in Hot Forming," *Steel Res.*, **63**, p. 247.

Series of Parallel Arrangement in a Two-Unit Compressor Station

S. Ohanian

R. Kurz

e-mail: kurz_rainer_x@soltarturbines.com

Solar Turbines, Inc.,
9330 Skypark Court,
San Diego, CA 92123

This paper discusses how to determine the arrangement of compressors in a two-unit gas pipeline station where there is no standby unit. The compressors are driven by variable speed drivers such as gas turbines or variable frequency electric motors. Both series and parallel arrangements are analyzed in a transient simulation mode to determine which operation mode is more advantageous. Among the assumptions in this paper are the performance characteristics of the compressor. It will be outlined how these performance characteristics influence the conclusions. [DOI: 10.1115/1.1478074]

Introduction

The pressure and flow characteristics of pipelines as well as other factors may influence the arrangement of compressors in a station. This study will define a pipeline system under typical conditions and discuss the system behavior for two compressors piped either in parallel and in series configuration (Fig. 1). At the design point, it is possible to achieve a good station efficiency with either the series or the parallel arrangement of the two compressors. If circumstances require the shutdown of one of the compressors, significant differences between the two layouts become visible. The simulation results confirm the expectations that the series compressor design is the better selection, due to the fact that, with one unit out of service, the remaining unit will operate in a more efficient region of its performance map compared to the parallel design compressor. If one compressor is out of service, it will be shown that the decay in pipeline outlet pressure at the city gate (i.e., the transfer point for the pipeline) will be slower with the series compressor design and higher flow will be available for load distribution at this point.

Simulation Model

The simulation was performed with the aid of the unsteady-state module (USM) to the Stoner Workstation Service (SWS) for Windows (SWSg-USM). This program provides digital computer simulation of the transient gas flow behavior in a piping system (Stoner [1,2]). The analysis procedure allows to calculate the time-varying flows, pressures, power, and other variables and can determine the response of the system due to these and other variables.

The program solves the time-dependent mass conservation

$$\frac{\partial W}{\partial x} + A \frac{\partial \rho}{\partial t} = 0$$

where the through-flow area A is constant. The density is calculated from

$$\frac{p}{\rho} = ZRT.$$

The momentum balance is satisfied by

$$\rho A dx \left(\frac{DV}{Dt} \right) = pA - \left(pA + \frac{\partial}{\partial x} (pA) \right) dx - \pi D \frac{\rho \cdot f_{DW} V |V|}{2D} dx$$

for a pipeline with no differences in elevation.

Contributed by the International Gas Turbine Institute (IGTI) of THE AMERICAN SOCIETY OF MECHANICAL ENGINEERS for publication in the ASME JOURNAL OF ENGINEERING FOR GAS TURBINES AND POWER. Paper presented at the International Gas Turbine and Aeroengine Congress and Exhibition, New Orleans, LA, June 4–7, 2001; Paper 01-GT-230. Manuscript received by IGTI, December 2000, final revision, March 2001. Associate Editor: R. Natole.

The resulting system of equations is solved by the method of characteristics (Stoner [2]).

Time steps in the computational domain have a direct relationship with the wave speed and the length of the pipeline computational segment called “base length.” In this system, the average wave speed is 325 m/s (1065 ft/sec). With a base length of 1.61 km (1 mile), the time increment needs to be approximately five seconds.

Compressor maps for the relationships between flow, head and efficiency, based on actual centrifugal compressor performance, can be implemented into the simulation. The compressor models specifically cover the traditional and active portions of the compressor map from surge to choke. The program has capabilities to recognize surge and choke conditions (recycle flow, generate excess head, etc.) within bounds of available power and speed, but does not include specific performance data beyond surge and choke limits. Therefore, it finds the initial compressor speed line at a given flow and calculates the corresponding head, then determines whether the available power is adequate to meet the operation. The computations near the choke limit are approximations. Nevertheless, they correctly show that after the shutdown of one of the two compressors, the parallel compressor operates in choked condition and is less efficient than the series compressor.

Simulation Model Assumptions

A sample pipeline with a single station is the base configuration for this study. The simulation model assumes the following:

- pipeline is 508 mm (20 in.) diameter, 192 miles long, and buried.
- compressor station is located approximately in the middle of the pipeline. Nodes C1S and C1D represent the station suction and discharge.
- pipeline inlet pressure (INLET node, Fig. 1) is constant 104.6 bara (1517 psia).
- station discharge pressure is limited to 104.6 bara (1517 psia, assumed maximum pipeline operating pressure)
- the required outlet flow at the city gate (OUTLET node, Fig. 1) is $391 \cdot 10^3 \text{ Nm}^3/\text{h}$ (350 mmscfd) at a pressure of approximately 56.6 bara (820 psia).
- city gate can tolerate a pressure decay to 41.4 bara (600 psia). Below that setpoint, load shedding must occur, which is not desired.

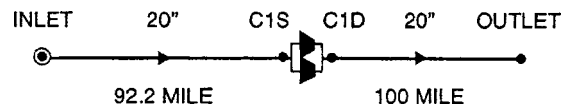


Fig. 1 Pipeline schematic series/parallel study

The simulation is based on two-stage compressors for parallel arrangement and single-stage compressors for series arrangement. The compressor casing is the same for both arrangements, but the internal rotor consists of two impellers for each parallel compressor and a single impeller for each series compressor. For the series compressors, both the low-pressure unit and the high-pressure unit have the same impeller design. The predicted head capacity maps with speed and isentropic efficiency lines of the selected impellers are used in the computer model.

Other parameters used in the model are as follows:

Gas specific gravity	0.6
Pipe internal diameter	495.3 mm (19.5 in.)
Internal roughness (internally coated pipe)	0.018 mm (0.0007 in.)
Average flowing temperature	26.7°C (80°F)
Pipeline profile	Flat
Available power per unit	3580 kW (4800 hp)
Flow equation	Fundamental, or general flow
Base length	1.61 km (1.0 mile)
Time interval	5 s
Gas viscosity	1.2E-05 Ns/m ² (0.25E-6 lbs/ft ²)
Max. compressor speed	14,300 rpm

Figure 1 shows the pipeline schematic with designation of the nodes.

In buried pipelines, the temperature profile depends on surrounding soil temperature, insulation, thermal conductivity, overall heat transfer coefficient, and other factors. Those calculations would become cumbersome for transient flow analysis; therefore, it is assumed that flow is isothermal and flowing gas temperature is a constant 26.7°C (80°F).

The fundamental flow equation

$$Q = C \cdot \frac{T_b}{P_b} \cdot e \cdot D_i^{2.5} \left[\frac{p_1^2 - p_2^2 - \frac{0.0375 \cdot SG \cdot (H_2 - H_1) \cdot p_a^2}{Z_a \cdot T_a}}{SG \cdot T_a \cdot L \cdot Z_a \cdot f_{DW}} \right]^{0.5}$$

(also called the general flow equation; $C=47880$ for flow Q in m³/h and otherwise SI Units; Hyman et al. [3]) is widely used in the pipeline industry. This equation is computationally efficient, requiring fewer resources compared to other equations and uses the Darcy Weisbach friction factor f_{DW} calculated as a function of Reynolds number. It is believed that this equation is very accurate for calculating frictional losses in fluid flow.

It is assumed that fuel usage and station yard piping losses are the same for both series and parallel arrangements and they are, therefore, not considered in this study.

The behavior of pressures and flows for the pipeline and the compressors is presented in both graphic and tabular format, assuming that one of the units is shut down at time 1.0 hour from a steady-state condition.

Under steady-state conditions with 391*10³ Nm³/h (350 mmscfd) flow, the station suction pressure is calculated to be approximately 62.1 bara (900 psia) and the pipe outlet pressure approximately 56.8 bara (823 psia). When one unit is taken out of service, the pressure at this point will start to decrease below the required level if the pipe outlet flow is maintained at 391*10³ Nm³/h (350 mmscfd). It will be demonstrated that with the remaining series compressor, the decrease in pipe outlet pressure will be slower compared to the parallel compressor, allowing more time for the station operators to take any remedial action. If the offline compressor is not put back into service for a prolonged time, the series compressor will deliver more flow at the pipe outlet compared to the parallel compressor.

Table 1 Operating conditions, parallel arrangement

Time, hr	1.0	7.26
Head, kJ/kg (ft lb _f /lb _m)	70.17 (23475)	32.55 (10891)
Capacity, m ³ /min (acfm)	51.56 (1822)	68.71 (2428)
Speed, rpm	13116	11997
Efficiency (%)	83.44	64.72
Surge margin (%)	35.0	50.0

Parallel Arrangement

In the parallel arrangement, each compressor is designed to compress 195.5*10³ Nm³/h (175 mmscfd) flow (or half of the 391*10³ Nm³/h (350 mmscfd) station flow) from 62.1 bara (900 psia) suction pressure to 104.6 bara (1517 psia) discharge pressure. The compressor rotors are identical, and each compressor includes the two-stage rotor required for the production of total head.

When one unit is down, the other unit, subject to available power, tries to pump more flow than its share of 195.5*10³ Nm³/h (175 mmscfd). Due to the flow range limitation, the compressor operates near the choke (stonewall or sonic limit) with reduced head and efficiency. With the station flow reduced and the upstream pressure (inlet to the pipeline) held constant, the station suction pressure starts to rise as the upstream section of the pipeline is packed with gas.

At the same time, the station discharge pressure starts to fall because the remaining compressor is not able to reach the desired discharge pressure of 104.6 bara (1517 psia) due to power limitation. Consequently, the pipeline outlet pressure at the city gate starts to fall. The line pack (volume of gas stored in the pipe or inventory) in the downstream section of the pipeline is reduced as gas is taken from the pack to maintain the required outlet flow of 391*10³ Nm³/h (350 mmscfd). At time 7.26 hours, the pipe outlet pressure reduces to the 41.4 bara (600 psia) minimum requirements.

The parameters of the compressor at time 1.0 hour and 7.26 hours are shown in Table 1. Note the low compressor efficiency and high surge margin at time 7.26 hours as the compressor tries its hardest to pump as much gas as it can.

Table 2 shows a summary of the pressures, flows, and line pack for the parallel arrangement.

Pack 1 is the line pack in the upstream pipe section between the pipe inlet and the compressor station, and Pack 2 is the line pack in the downstream pipe section between the compressor station and pipe outlet.

Figures 2–6 illustrate the behavior of the pipeline and the compressors from time 1.0 hour to time 7.26 hours. The pipe inlet flow shown in Fig. 4 dips slightly after one compressor is taken out of service. This is attributed to the shock wave traveling back from the compressor station to the pipe inlet, causing momentary disruption of flow; however, the flow is recovered quickly and reduced again due to the limitation of the remaining compressor.

Series Arrangement

In the series arrangement, the compressors are designed to compress the full station flow of 391*10³ Nm³/h (350 mmscfd) at approximately half of the total required head. The low pressure (LP) compressor pumps 391*10³ Nm³/h (350 mmscfd) of gas from 62.1 to 81.3 bara (900 to 1179 psia) and the high-pressure (HP) compressor takes the pressure to 104.6 bara (1517 psia). No intercooler is used between the LP and HP compressors.

As mentioned previously, both LP and HP compressors have identical single-stage rotors; however, the location of the steady-state operating point on the compressor maps at time 0–1.0 hour is different. Although the same mass flow of 391*10³ Nm³/h (350

Table 2 Summary for parallel arrangement

Time Hrs	Pipe Inlet press. Bara (psia)	Pipe inlet Flow $10^3 \text{ Nm}^3/\text{h}$ (MMSCFD)	Line Pack Pack 1 10^6 Nm (MMSCF)	Station Inlet Press. Bara (psia)	Station Flow $10^3 \text{ Nm}^3/\text{h}$ (MMSCFD)	Station Outlet Press. Bara (psia)	Pipe Outlet Press. Bara (psia)	Pipe Outlet Flow $10^3 \text{ Nm}^3/\text{h}$ (MMSCFD)	Line Pack Pack 2 10^6 Nm^3 (MMSCF)
0-1.0	104.6 (1517)	391 (350)	2.58 (96.2)	62.1 (900)	391 (350)	104.6 (1517)	56.8 (823)	391 (350)	2.71 (101)
2.0	104.6 (1517)	378 (338)	2.68 (100)	72.1 (1046)	305 (273)	97.1 (1408)	56.1 (813)	391 (350)	2.60 (97)
4.0	104.6 (1517)	346 (309)	2.76 (103)	75.2 (1090)	326 (292)	94.8 (1375)	50.6 (734)	391 (350)	2.47(92)
6.0	104.6 (1517)	336 (301)	2.79 (104)	76.3 (1106)	329 (295)	92.6 (1342)	45.0 (652)	391 (350)	2.33 (87)
7.26	104.6 (1517)	333 (298)	2.79 (104)	76.6 (1110)	331 (296)	91.1 (1321)	41.4 (600)	391 (350)	2.25 (84)

mmscfd) is passing through both compressors, the actual inlet flow going to the HP unit is lower, mainly due to higher pressure, and the duty point moves close to the surge line.

When one unit is down, the remaining unit cannot develop sufficient head to remain running. It goes into recycling mode until the rise in station suction pressure and decline in discharge pressure permit operation of the unit (at approximately time 1.15 to 1.25 hours in this system). Although some time is lost in this process, the decline in pipeline outlet pressure is slower since the compressor operates in a more efficient region of its operating range. The 41.4 bara (600 psia) minimum pipe outlet pressure at the city gate is reached at time 10.10 hours, which is 2.84 hours more time for any remedial action compared to the parallel scheme.

The parameters of the compressor at time 1.0 and 10.10 hours are shown in Table 3. Note superior compressor efficiency at time 10.1 hours compared to the efficiency of the parallel compressor at time 7.26 hours.

A summary of pressures, flows, and line pack for the series arrangement is shown in Table 4. Figures 7-13 illustrate the behavior of the pipeline and the compressors in series arrangement from time 1.0 hour to time 10.10 hours. The compressor flow and speed chattering shown in Figs. 8 and 10 are due to computational noise as compressor control is shifted from minimum flow to maximum head near the surge line, until such time that there is sufficient head to resume normal operation.

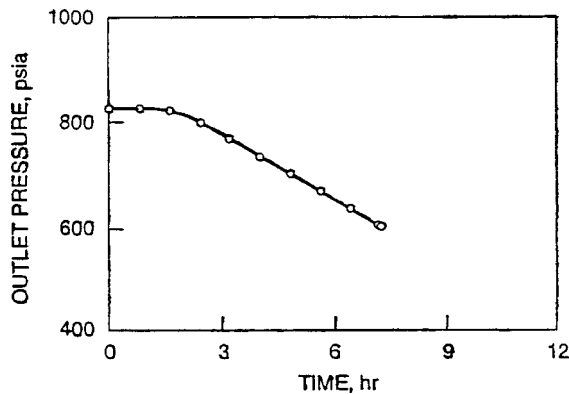


Fig. 2 Parallel scenario pipe outlet pressure

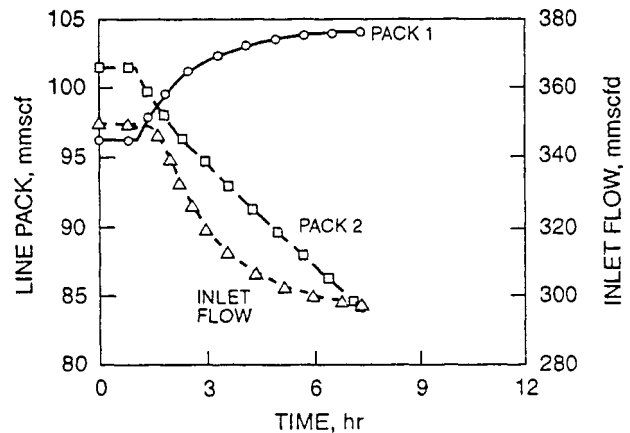


Fig. 4 Parallel scenario line pack and inlet flow

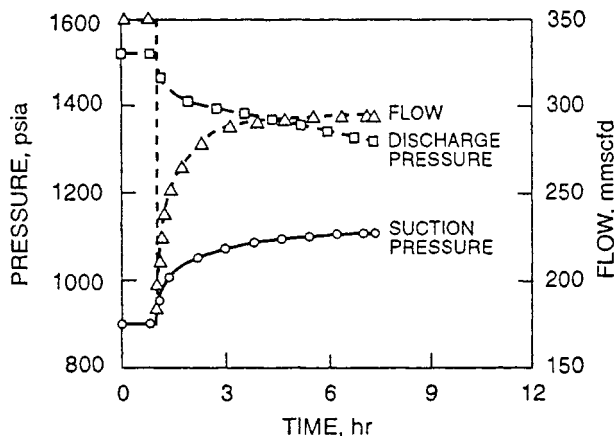


Fig. 3 Parallel scenario station pressure/flow

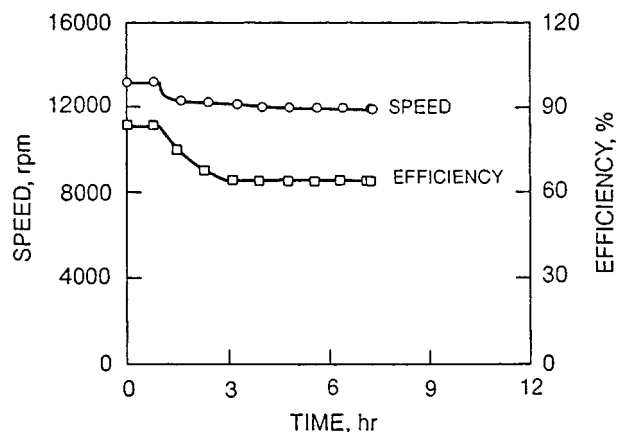


Fig. 5 Parallel scenario compressor speed and efficiency

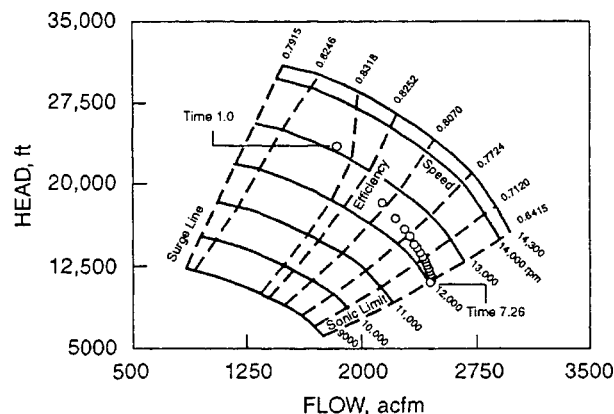


Fig. 6 Parallel scenario two-stage compressor map operating point time 1.0 to 7.26 hours

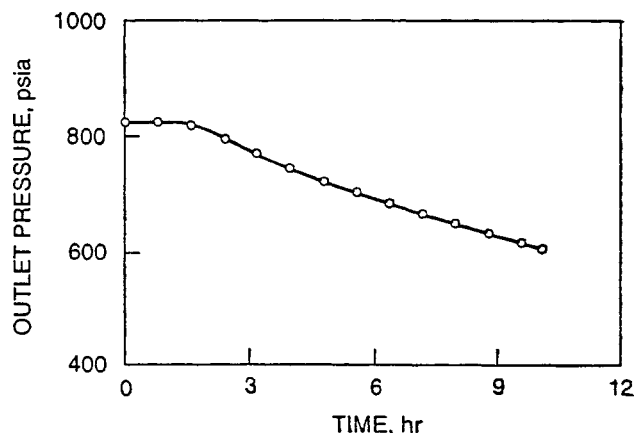


Fig. 7 Series scenario pipe outlet pressure

Table 3 Operating conditions, series arrangement

Time, hr	1.0		10.10
Unit	LP	HP	LP
Suction Press.	62.1	81.3	70.4
Bara (psia)	(900.0)	(1179.0)	(1021.0)
Disch. Press.	81.3	104.6	94.6
Bara (psia)	(1179.0)	(1517.0)	(1372.0)
Head kJ/kg	35.23	35.2	38.04
(ft-lb _f /lb _m)	(11785)	(11776)	(12727)
Capacity	(3644)	(2960)	(2934)
m ³ /min (acfm)			
Speed, rpm	13512	12949	13348
Efficiency, %	83.6	84.0	83.5
Surge Margin %	36.0	25.0	21.0

Long-Term Effect

In order to show the long-term effect with only one unit in operation, the simulation is continued at some reduced flows for each scenario. With the series compressor, the flow is reduced to $362.5 \times 10^3 \text{ Nm}^3/\text{h}$ (324.5 mmscfd) at the pipeline outlet at time 10.1 hours. The pipeline outlet reaches a steady pressure of 44.6 bara (647 psia) at time 15 hours (Fig. 13). With the parallel compressor arrangement a flow of $362.5 \times 10^3 \text{ Nm}^3/\text{h}$ (324.5 mmscfd) is not possible due to choked condition of the remaining compressor. The flow in this case is reduced to approximately

$330.5 \times 10^3 \text{ Nm}^3/\text{h}$ (296 mmscfd) (Fig. 14). The pipeline outlet pressure in this case settles out to 47.9 bara (694 psia) at time 12 hours. This flow is 9.6% lower than the $362.5 \times 10^3 \text{ Nm}^3/\text{h}$ (324.5 mmscfd) achievable with the series compressor.

Compressor Requirements

The study of both scenarios suggests certain requirements for the compression system (Fig. 15). Beyond the quest for higher compressor peak efficiencies, the operating requirements set forth in this study as well as in other references (Kurz and Cave [4]) require a compressor capable of operating over a wide operating range at high efficiency.

Wide operating range in a centrifugal compressor can be achieved by a combination of means.

Aerodynamic theory suggests a strong relationship between operating range, efficiency and impeller backsweep (Cumpsty [5]). However, there is a practical limit to the amount of backsweep. In particular, increasing backsweep reduces the capability of an impeller of given tip speed to make head.

However, with the capability to use two impellers in a casing, this perceived disadvantage can be eliminated. The operating range is further increased by the use of a vaneless diffuser.

This study assumes a two stage compressor for the parallel application. While it is acknowledged that the required head could have been produced by a single-stage compressor, this single-stage machine would probably exhibit a lower efficiency and operating range.

Table 4 Summary for series arrangement

Time Hrs	Pipe Inlet press. Bara (psia)	Pipe inlet Flow 10 ³ Nm ³ /h (MMSCFD)	Line Pack Pack 1 10 ⁶ Nm ³ (MMSCF)	Station Inlet Press. Bara (psia)	Station Flow 10 ³ Nm ³ /h (MMSCFD)	Station Outlet Press. Bara (psia)	Pipe Outlet Press. Bara (psia)	Pipe Outlet Flow 10 ³ Nm ³ /h (MMSCFD)	Line Pack Pack 2 10 ⁶ Nm ³ (MMSCF)
0-1.0	104.6 (1517)	391 (350)	2.57 (96)	62.1 (900)	391 (350)	104.6 (1517)	56.8 (823)	391 (350)	2.71 (101)
1.15	104.6 (1517)	391 (350)	2.63 (98)	70.3 (1019)	307 (274)	98.3 (1425)	56.7 (822)	391 (350)	2.68(100)
2.0	104.6 (1517)	374 (335)	2.68(100)	71.2 (1033)	329 (295)	97.9 (1420)	55.8 (810)	391 (350)	2.60(97)
4.0	104.6 (1517)	355 (318)	2.73(102)	71.9 (1043)	351 (315)	97.4 (1412)	51.3 (743)	391 (350)	2.52(94)
6.0	104.6 (1517)	354 (317)	2.73 (102)	71.6 (1038)	357 (320)	96.6 (1400)	47.6 (690)	391 (350)	2.44(91)
7.26	104.6 (1517)	355 (318)	2.71 (101)	71.2 (1033)	359 (322)	95.9 (1391)	45.6 (661)	391 (350)	2.39(89)
10.1	104.6 (1517)	358 (321)	2.71(101)	70.4 (1021)	362 (325)	94.6 (1372)	41.4 (600)	391 (350)	2.31(86)

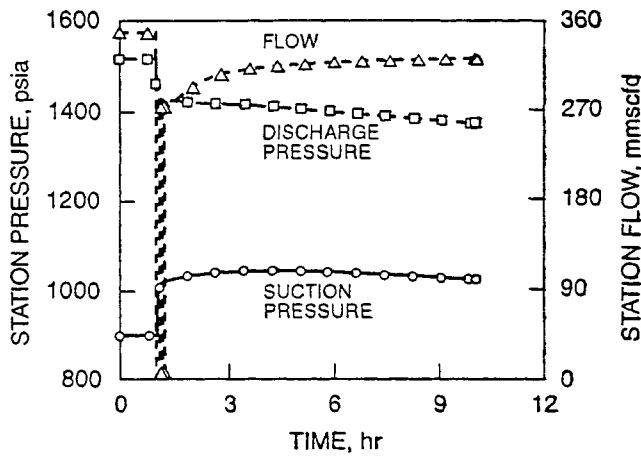


Fig. 8 Series scenario station pressure flow

Alternatives

While this study contains a number of assumptions, most of them are close to real operating scenarios. Certainly, the selection of the compressor design points may seem somewhat arbitrary.

If, for example, the two-stage parallel compressors were selected using higher flow impellers with a surge margin of 17% instead of 35%, the remaining compressor would not choke out as quickly and would settle out with a flow of approximately

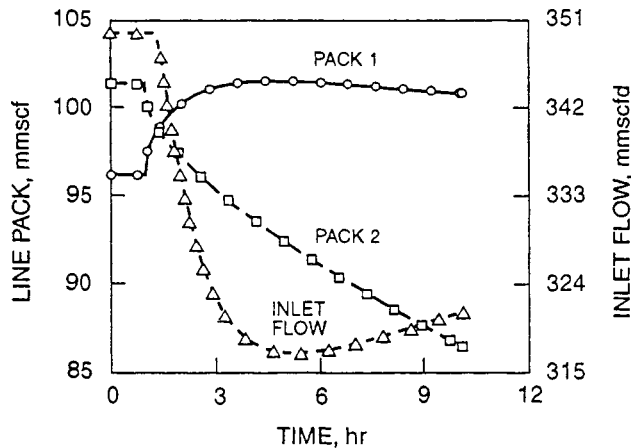


Fig. 9 Series scenario line pack and inlet flow

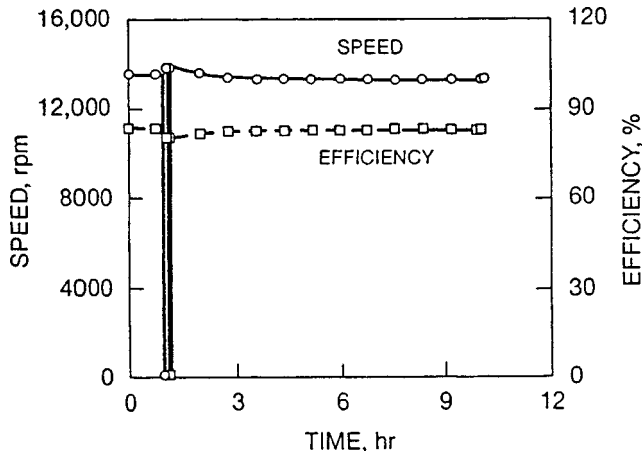


Fig. 10 Series scenario LP compressor speed and efficiency

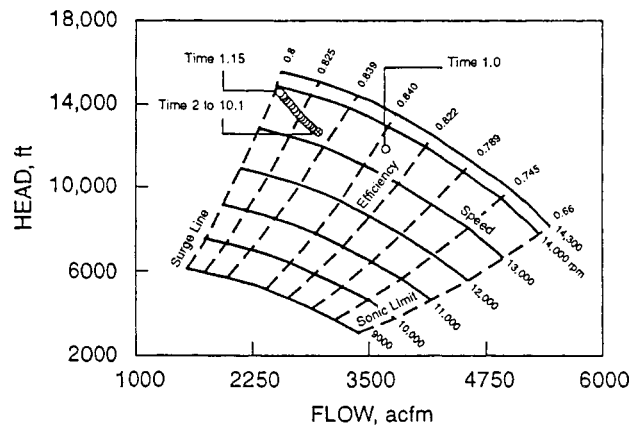


Fig. 11 Series scenario one-stage compressor map LP operating point time 1.0 to 10.10

$352 \times 10^3 \text{ Nm}^3/\text{h}$ at 45.8 bara (315 mmscfd at 664 psia) pipe outlet pressure. This is still 3% lower than the flow achievable with the series compressor. However, such a design point would not fall into the area of best efficiency for the compressor.

Finally, the operating companies may not desire such a low surge margin for their normal operating point, which is generally designated to be a point at which the compressor will run most of the time, but instead may prefer enough surge margin to cover other off-design low-flow conditions.

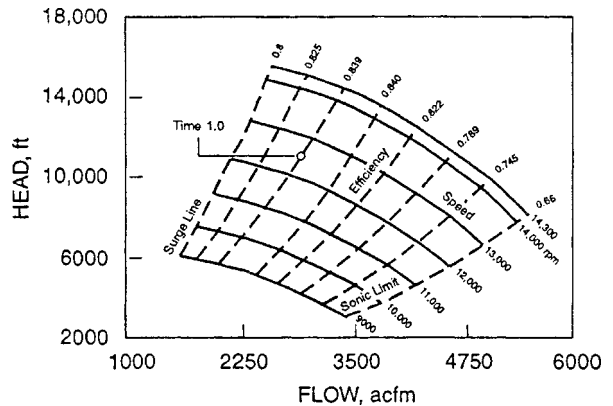


Fig. 12 Series scenario one-stage compressor map HP operating point time 1.0

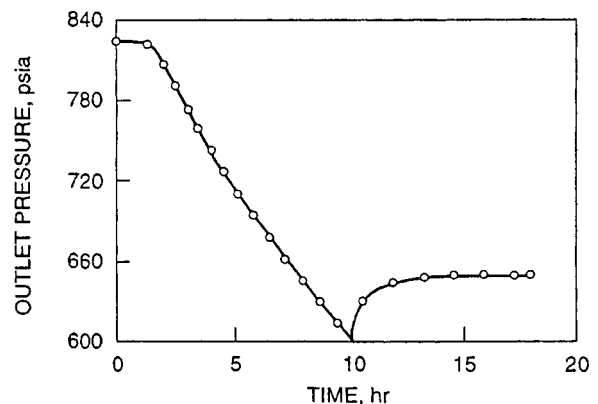


Fig. 13 Series scenario outlet pressure with 324.5 mmscfd flow at time 10.1 hours

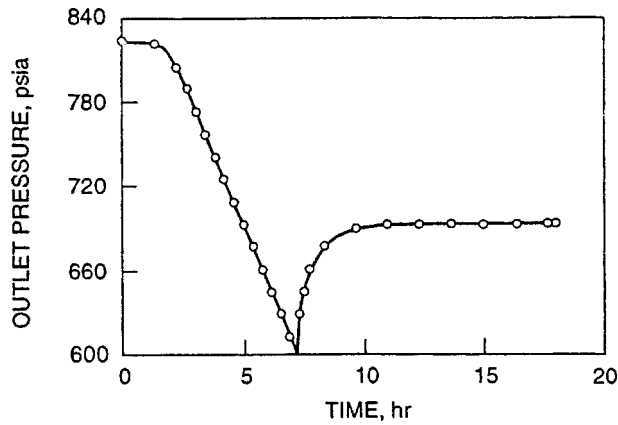


Fig. 14 Parallel scenario outlet pressure with 296 mmscf flow at time 7.26 hours

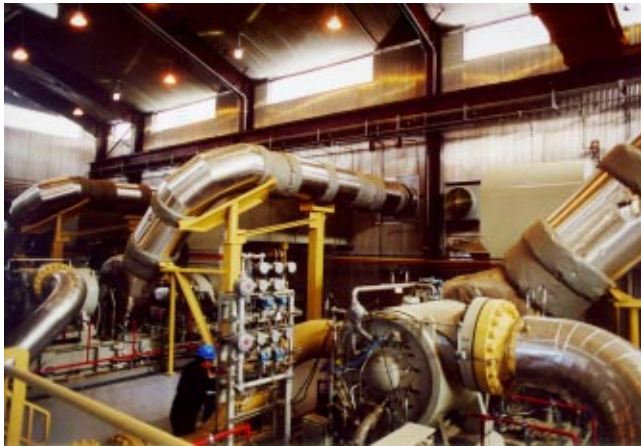


Fig. 15 Typical compressor station with multiple centrifugal compressors

Conclusions

This paper addresses the behavior of the pipeline system under the assumed conditions and confirms the advantage of series operation in a two-unit station without a standby unit.

Pipeline pressure/flow characteristics may differ and other considerations such as future growth, standby philosophy, availability, reliability, flexibility, and other factors may influence the arrangement of compressor sets. However, the results and considerations presented form a basis for decisions on the subject.

Acknowledgments

The authors wish to thank Alex Hollis of Stoner Associates for his support and valuable comments regarding this and other pipeline studies.

Nomenclature

- A = area
- C = constant
- D = diameter
- e = pipeline efficiency
- f_{DW} = Darcy Weisbach friction factor
- SG = specific gravity relative to air
- H = elevation
- L = length
- p = pressure
- Q = volumetric flow (capacity)
- R = gas constant
- T = temperature
- t = time
- V = flow velocity
- W = mass flow
- x = distance coordinate
- Z = compressibility factor
- ρ = density

Subscripts

- a = average
- b = base condition for standard state
- i = inner

References

- [1] Stoner Associates Incorporated, 1996, *Stoner Workstation Service User's Guide* Version 1.6, Stoner, Carlisle, PA.
- [2] Stoner Associates Incorporated, 1999, *SynerGEE Gas 3.1: Unsteady State Module*, Stoner, Carlisle, PA.
- [3] Hyman, S. I., Stoner, M. A., Karnitz, M. A., 1975, "Gas Flow Formulas—An Evaluation," *Pipeline Gas J.*, Dec.
- [4] Kurz, R., and Cave, M., 2000, "Compressors and Compressor Control," *Hydrocarb. Eng.*, 5(9).
- [5] Cumpsty, N. A., 1989, *Compressor Aerodynamics*, Longman, Essex, UK, pp. 263–265.

A Comparison of Two Finite Element Reduction Techniques for Mistuned Bladed Disks

F. Moyroud
Research Assistant

T. Fransson
Professor,
e-mail: fransson@egi.kth.se

Royal Institute of Technology,
Chair of Heat and Power Technology,
Brinellvägen 60,
S100 44 Stockholm, Sweden

G. Jacquet-Richardet
Professor,
Institut National des Sciences Appliquées,
Laboratoire de Mécanique des Structures,
20 Avenue Albert Einstein,
69 621 Villeurbanne Cedex, France
e-mail: jacquet@lmst.insa-lyon.fr

The high performance bladed disks used in today's turbomachines must meet strict standards in terms of aeroelastic stability and resonant response level. One structural characteristic that can significantly impact on both these areas is that of bladed disk mistuning. To predict the effects of mistuning, computationally efficient methods are much needed to make free-vibration and forced-response analyses of full assembly finite element (FE) models feasible in both research and industrial environments. Due to the size and complexity of typical industrial bladed disk models, one must resort to robust and systematic reduction techniques to produce reduced-order models of sufficient accuracy. The objective of this paper is to compare two prevalent reduction methods on representative test rotors, including a modern design industrial shrouded bladed disk, in terms of accuracy (for frequencies and mode shapes), reduction order, computational efficiency, sensitivity to intersector elastic coupling, and ability to capture the phenomenon of mode localization. The first reduction technique employs a modal reduction approach with a modal basis consisting of mode shapes of the tuned bladed disk which can be obtained from a classical cyclic symmetric modal analysis. The second reduction technique uses Craig and Bampton substructure modes. The results show a perfect agreement between the two reduced-order models and the nonreduced finite element model. It is found that the phenomena of mode localization is equally well predicted by the two reduction models. In terms of computational cost, reductions from one to two orders of magnitude are obtained for the industrial bladed disk, with the modal reduction method being the most computationally efficient approach. [DOI: 10.1115/1.1415741]

Introduction

A bladed disk is made of a certain number of sectors assembled around a rotational axis. When the sectors are identical, the bladed disk is a so-called cyclic symmetric or rotationally periodic structure. Cyclic symmetry is widely used to reduce full assembly finite element models of bladed disks to a single sector to predict the behavior of the entire assembly. Unfortunately, experience shows that blade-to-blade geometric and structural variations may occur during the manufacturing process and as a consequence of in-service wear. This phenomena, known as mistuning, is shown to have a large impact on the aeroelastic and resonant response of bladed disks ([1,2]).

Numerical predictions of the effects of mistuning on the free vibrations and forced response of bladed disks have been mostly performed with spring-mass models, with a few degrees-of-freedom per sector ([3–9]). These models have the advantage to make the problem computationally tractable while capturing the essential features. However, they are often difficult to correlate with actual bladed disk finite element models. On the other hand, full assembly finite element models may be a possible choice but the computational cost (CPU and memory) is prohibitively high, especially in the framework of Monte-Carlo simulations which involve the analysis of a large number of mistuning configurations.

Techniques have been developed and individually validated to reduce the cost of full assembly finite element models. For example, component mode synthesis methods are presented in

[10–16] and modal reduction methods in [17,18]. Validations have been performed mostly on simplified bladed disks and on a few industrial bladed disks (Table 1).

In this paper, two reduction techniques are selected and compared. The first method is based on a modal decomposition of a full assembly mistuned bladed disk where the modal basis consists of a set of tuned mode shapes obtained from a cyclic symmetric modal analysis ([18]). The second method is based on a Craig and Bampton substructuring and reduction of the full assembly bladed disk where the substructures are the sectors of the bladed disk ([10,19,20]). One advantage of these two reductions is to be applicable to unshrouded as well as shrouded bladed disks without any particular extension. The Craig and Bampton reduction method can be used for the limiting cases of fully stuck and fully slipping shroud interfaces, as well as for a transition of the interfaces between these two conditions when including friction constraints.

For the two selected reduction techniques, the present work looks at a range of technical issues. (1) The relative accuracy of the reduced-order models is studied on representative test cases.

Table 1 Test rotors for the validation of reduced-order models

Reference	Test Geometry
[10]	Cyclic symmetric plate
[12]	Industrial rotor
[13]	Simplified test rotor
[14]	Simplified test rotor
[15]	Cyclic symmetric plate
[16]	Test (shrouded) rotor
[22]	Simplified test rotor
[26]	Cyclic symmetric plate
[27]	Cyclic symmetric plate
[28]	Industrial turbine
[29]	Research compressor

Contributed by the International Gas Turbine Institute (IGTI) of THE AMERICAN SOCIETY OF MECHANICAL ENGINEERS for publication in the ASME JOURNAL OF ENGINEERING FOR GAS TURBINES AND POWER. Paper presented at the International Gas Turbine and Aeroengine Congress and Exhibition, Munich, Germany, May 8–11, 2000; Paper 00-GT-362. Manuscript received by IGTI Nov. 1999; final revision received by ASME Headquarters Feb. 2000. Associate Editor: D. Wisler.

Three test cases are considered: (a) an axisymmetric annular plate, (b) a cyclic symmetric annular plate exhibiting strong mode localizations when mistuned, and (c) a typical modern design industrial bladed disk. For all three test geometries, the comparison between nonreduced finite element model and reduced-order models is quantified. (2) The efficiencies of the reductions are compared not only in terms of degrees-of-freedom but also in terms of computational times. (3) More specific issues are discussed such as program vectorization and improved reanalysis algorithms to enhance computational efficiency in the framework of Monte Carlo simulations. (4) The effects of mistuning on an industrial structure at rest and at nominal rotational speed are also studied.

Background Theory

The small-amplitude free vibrations of a rotating bladed disk assembly around its static position are governed by the following finite element based system of equations,

$$\mathbf{M}\{\ddot{\delta}\} + \mathbf{G}\{\dot{\delta}\} + \mathbf{K}\{\delta\} = \{0\}, \quad (1)$$

where \mathbf{M} denotes the mass matrix, \mathbf{G} the gyroscopic or Coriolis matrix, and \mathbf{K} the stiffness matrix (including centrifugal softening and stiffening terms). $\{\delta\}$ is the finite element vector of dynamic displacements.

Cyclic Symmetric Model. A tuned bladed disk is viewed as an assembly of N cyclic symmetric sectors. The sectors are numbered $0, \dots, s, \dots, N-1$ where 0 denotes a reference sector. The dynamic displacements of the full assembly are decomposed in travelling wave coordinates as follows:

$$\{\delta^i\} = \mathbf{E}\{\hat{\delta}^{tw}\}_0, \quad (2)$$

where $\{\delta^i\}$ denotes a vector of *individual blade coordinates* and $\{\hat{\delta}^{tw}\}_0$ a vector of *travelling wave coordinates* based on the reference sector. The matrix \mathbf{E} is defined as follows:

$$\mathbf{E} = [\mathbf{e}_0, \dots, \mathbf{e}_n, \dots, \mathbf{e}_{N-1}], \quad (3)$$

where \mathbf{e}_n are vectors of \mathbf{C}^N ,

$$\mathbf{e}_n = \langle 1 e^{j1\beta_n} \dots e^{j(N-1)\beta_n} \rangle^T, \quad (4)$$

for $n=0, \dots, N-1$. $\beta_n = 2\pi n/N$ is the interblade phase angle or phase difference between consecutive sectors.

Combining (1) and (2) gives the equations governing the free vibrations of the tuned assembly in terms of travelling wave coordinates ([21])

$$\hat{\mathbf{M}}_{0,n}^{tw}\{\hat{\delta}_n^{tw}\}_0 + \hat{\mathbf{G}}_{0,n}^{tw}\{\hat{\delta}_n^{tw}\}_0 + \hat{\mathbf{K}}_{0,n}^{tw}\{\hat{\delta}_n^{tw}\}_0 = \{0\}, \quad (5)$$

for $n=0, \dots, N^{cs}$ where $N^{cs} = N/2$ (resp. $(N-1)/2$) if N is even (resp. odd). The systems of equations, Eq. (5), are uncoupled and solved individually. N^{cs} sets of frequencies $\omega_{m,n}$ and mode shapes $\{\hat{\Phi}_{m,n}^{tw}\}_0$ of the tuned bladed disk are obtained, with $m=0, \dots, M-1$. m is related to the blade mode shape (spanwise harmonics), and n to the assembly mode shape (circumferential harmonics). For an axisymmetric structure, m and n are, respectively, the numbers of nodal circles and nodal diameters.

Mistuning Patterns. Numerically, the symmetry of a tuned bladed disk can be destroyed in several ways. The approach adopted in this work consists in perturbing the Young's moduli (E) of the finite elements of a certain number of sectors of the bladed disk by a scaling factor ε . If $\{E^{(tun)}\}_0$ is the vector of Young's moduli of the elements on the reference sector of the tuned bladed disk, the selected *stiffness mistuning* pattern can be described as follows:

$$\{E^{(mis)}\}_s = (1 + \varepsilon_s)\{E^{(tun)}\}_0, \quad (6)$$

for $s=0, \dots, N-1$ where $\{E^{(mis)}\}_s$ denotes the vector of Young's moduli of the elements belonging to sector s of the mistuned bladed disk and ε_s is a mistuning coefficient. This method has the advantage to characterize a mistuning pattern with a set of N

parameters. These parameters can be set in a deterministic manner to study a few mistuning configurations, or extracted from a population of randomly generated reals in the framework of Monte Carlo simulations. Other strategies to generate mistuning patterns are found in the literature, for example a set of punctual masses is used in [22].

The following mistuning patterns are considered for the applications,

- mistuning of the reference sector, this belongs to the class of *partial mistuning*,

$$\varepsilon_0 \neq 0 \quad \text{and} \quad \varepsilon_s = 0 \quad \text{for } s = 1, \dots, N-1,$$

- alternate mistuning of consecutive sectors, this belongs to the class of *harmonic mistuning*,

$$\varepsilon_0 \neq 0 \quad \text{and} \quad \varepsilon_s = -\varepsilon_{s-1} \quad \text{for } s = 1, \dots, N-1.$$

Reduction Techniques

The objective is here to produce systematic reductions of a full assembly finite element model to achieve fast and accurate predictions of the dynamic behavior of mistuned structures. The modal decomposition method and the Craig and Bampton substructuring and reduction method considered in this work are first presented. The improvements made to the programming algorithms to enhance computational efficiency in the framework of Monte Carlo simulations are then discussed. The two reduction techniques and the optimization schemes can cope with a wide range of mistuning patterns, and are not limited to the simplified mistuning patterns chosen for the applications.

Modal Decomposition/Reduction Method. The modal decomposition method is based on the assumption that the mode shapes of a mistuned bladed disk, Φ^i , can be expressed as a linear combination of a set of mode shapes of the tuned bladed-disk, $\Phi^{i,tun}$. The approach is well founded and accurate if the modal basis is complete in terms of its circumferential harmonic (nodal diameters) and spanwise harmonic (blade mode shapes) contents. The algorithm developed consists of the following steps:

1 Cyclic symmetric modal analysis on a reference sector of the tuned bladed disk according to Eq. (5). A fixed number M of blade mode shapes is retained for all traveling waves.

2 Transform the previously determined mode shapes from travelling wave coordinates to individual blade coordinates using Eq. (2).

3 Project the vector of dynamic displacements of the mistuned bladed disk along the modal basis.

$$\{\delta\} = \Phi^{i,tun}\{q\}, \quad (7)$$

where $\{q\}$ is a vector of modal coordinates.

4 Project/reduce the finite element mass, gyroscopic and stiffness matrices ($\mathbf{X}=\mathbf{M}, \mathbf{G}, \mathbf{K}$) of the mistuned bladed disk,

$$\mathbf{x} = \Phi^{i,tun,T} \mathbf{X} \Phi^{i,tun}, \quad (8)$$

where $\mathbf{x}=\mathbf{m}, \mathbf{g}, \mathbf{k}$ are the modal/reduced matrices.

5 Extract the eigenvalues and vectors \mathbf{q} of the system of modal equations,

$$\mathbf{m}\{\ddot{q}\} + \mathbf{g}\{\dot{q}\} + \mathbf{k}\{q\} = \{0\}. \quad (9)$$

6 Calculate the corresponding mode shapes Φ^i of the mistuned bladed disk using Eq. (7).

Substructuring and Reduction Method. The bladed disk is decomposed into substructures, where a substructure is a $360/N$ degrees sector of the bladed disk. The finite element system of equations of a substructure is projected along a basis of Craig and Bampton substructure modes ([19]) which consists of (1) *static modes* associated with the left and right-hand side boundary

degrees-of-freedom of the substructure, (2) *internal vibrational modes* of the substructure clamped along the left and right-hand side boundaries.

For a substructure with n_L left-hand side boundary degrees-of-freedom, n_I internal degrees-of-freedom and n_R right-hand side boundary degrees-of-freedom, the Craig and Bampton basis consists of $n_L + m_I + n_R$ vectors where m_I is the number of substructure internal mode shapes retained, $m_I \ll n_I$. The reduction order is highly dependent on the number of degrees-of-freedom, n_L and n_R , at the substructure interfaces.

The following algorithm is applied to the assembly of N substructures:

1 Calculate the Craig and Bampton substructure modes \mathbf{T}_0^{cb} in *cylindrical coordinates* on the reference sector/substructure of the *tuned bladed disk*,

$$\mathbf{T}_0^{cb} = [\Phi_{L,0}, \Phi_{I,0}, \Phi_{R,0}], \quad (10)$$

where $\Phi_{L,0}$ and $\Phi_{R,0}$ are the static modes and $\Phi_{I,0}$ the dynamic modes of the (reference) substructure.

2 Project the nodal displacements of every substructure of the *mistuned* bladed disk along the Craig and Bampton basis,

$$\{\delta\}_s = \mathbf{T}_0^{cb} \{\delta^{cb}\}_s, \quad (11)$$

for $s=0, \dots, N-1$. For the tuned bladed disk, $\mathbf{T}_s^{cb} = \mathbf{T}_0^{cb}$ in cylindrical coordinates.

3 Calculate the reduced matrices of all Craig and Bampton substructures,

$$\mathbf{X}_s^{cb} = \mathbf{T}_0^{cb,T} \mathbf{X}_s \mathbf{T}_0^{cb}, \quad (12)$$

where $\mathbf{X}_s = \mathbf{M}_s, \mathbf{G}_s, \mathbf{K}_s$ are the finite element (nonreduced) matrices of substructure s , and $\mathbf{X}_s^{cb} = \mathbf{M}_s^{cb}, \mathbf{G}_s^{cb}, \mathbf{K}_s^{cb}$ the corresponding Craig and Bampton (reduced) matrices, with $s=0, \dots, N-1$.

4 Assemble the N reduced matrices. \mathbf{X}^{cb} is obtained from $\mathbf{X}_0^{cb}, \dots, \mathbf{X}_{N-1}^{cb}$ for $\mathbf{X} = \mathbf{M}, \mathbf{G}, \mathbf{K}$.

5 Extract the eigenvalues and vectors Φ^{cb} of the reduced system of equations,

$$\mathbf{M}^{cb} \{\delta^{cb}\} + \mathbf{G}^{cb} \{\delta^{cb}\} + \mathbf{K}^{cb} \{\delta^{cb}\} = \{0\}. \quad (13)$$

6 Calculate the mode shapes in individual blade and cylindrical coordinates according to Eq. (11).

Computational Performance Optimization. Experience shows that the calculation of reduced matrices, Eqs. (8) or (12), for new perturbations of the bladed disk is a computationally intensive task. For example, for the modal decomposition method, the calculation of the modal matrices represents between 50 percent and 80 percent of the total computational cost of a re-analysis. Therefore, improvements in the associated programming and calculation algorithms may result in large computational performance gains.

In this work, the computational cost of the reduced matrices has been reduced in two ways. First, the in-house developed program has been implemented on vector supercomputers, such as CRAY J90, C90 and Fujitsu VX. Vectorization or vector processing combines a specialized hardware architecture (using vector registers of finite length), a programming style and a vectorizing compiler to operate efficiently on large arrays (vectors) of data. The calculation of reduced matrices can be broken into series of vector operations and therefore theoretically 100% vector efficiency can be achieved, leading to large reductions in execution time. Secondly, the computational cost is further reduced by calculating the reduced matrices from the element matrices rather than from the assembled matrices. The reduced matrices are first calculated for the tuned configuration. Then, for a given mistuning configuration, contributions to the reduced matrices are evaluated for the limited set of finite elements which are mistuned. For the modal reduction method, this can be written as follows:

$$\Delta \mathbf{x} = \sum_s \sum_{e \text{ pert.}} \Phi_{(s,e)}^{i,\text{tun},T} \Delta \mathbf{X}_{(s,e)} \Phi_{(s,e)}^{i,\text{tun}}, \quad (14)$$

where $\Delta \mathbf{X}_{(s,e)}$ is the perturbation of the elemental matrix $\mathbf{X}_{(s,e)}$ (for element e of sector s) from the tuned state,

$$\Delta \mathbf{X} = \mathbf{X} - \mathbf{X}^{\text{tun}}. \quad (15)$$

The reduced matrix, Eqs. (8), is calculated as follows:

$$\mathbf{x} = \Phi^{i,\text{tun},T} \mathbf{X}^{\text{tun}} \Phi^{i,\text{tun}} + \Delta \mathbf{x}, \quad (16)$$

where only the term $\Delta \mathbf{x}$ is recalculated, according to Eq. (14), for a given perturbation of the tuned bladed disk. A similar technique is used to evaluate the Craig and Bampton reduced matrices, Eq. (12).

Simple Geometries

Test Geometries. Two test geometries, AXI and CYCL, with different intersector coupling strengths are selected. AXI is the axisymmetric annular plate shown in Fig. 1. CYCL is an annular plate with 20 cyclic symmetric sectors, Fig. 2. The plates have an inner radius (r_i) of 10 cm, an outer radius (r_o) of 20 cm, and a thickness (h) of 3 mm. The constitutive material is titanium

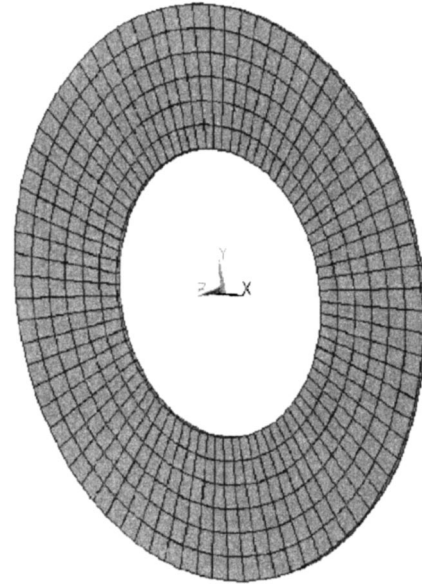


Fig. 1 AXI plate

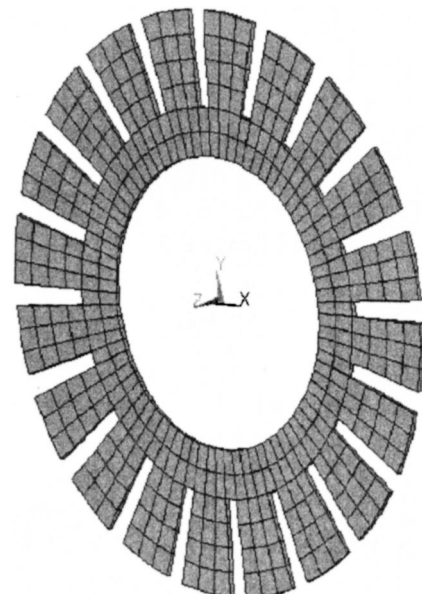


Fig. 2 CYCL plate

Table 2 Sizes of the CS, direct FEM, MR, and CBSR models

Models	AXI	CYCL
CS (ref.)	1188	1020
Direct FEM (ref.)	10080	9600
MR reduction	80	80
CBSR reduction	2080	880

with the following mechanical properties: $E=1.1 \cdot 10^{11}$ N/m², $\rho=4430$ kg/m³ and $\nu=0.35$. The plates are clamped and free, respectively, along the inner and outer radii.

The AXI plate is a cyclic symmetric structure with a strong intersector elastic coupling strength. In a similar fashion, the CYCL plate is a cyclic symmetric structure with a weak intersector elastic coupling strength. The AXI (resp. CYCL) plate can be viewed as a simplified model of a continuously shrouded (resp. unshrouded) bladed disk.

Models. The following four models are compared: (1) CS: cyclic symmetric modal analysis according to Eq. (5); (2) direct FEM: full assembly non-reduced modal analysis according to Eq. (1); (3) MR: full assembly modal analysis with the modal reduction method according to Eqs. (7)–(9); (4) CBSR: full assembly modal analysis with the Craig and Bampton substructuring and reduction method according to Eqs. (10)–(13).

The direct FEM analyses are performed with ANSYS.¹ The two reduced-order models (MR, CBSR) have been implemented in an in-house developed finite element code. The cyclic symmetric modal analyses of the AXI and CYCL plates are based on assemblies of 20 sectors, i.e., $N=20$.

Reduction Orders. The full assembly finite element models of the AXI and CYCL plates are shown in Figs. 1 and 2. The mesh of the AXI plate consists of 480 H20 solid elements (isoparametric second-order three-dimensional hexahedral elements with 20 nodes) and 3760 nodes. For the CYCL plate, there are 400 H20 elements and 3600 nodes.

The sizes of the CS, direct FEM, MR and CBSR models are reported in Table 2. For the MR analysis, the modal basis consists of 80 full assembly modes, including first/second/third bending mode shapes with 0 to 10 nodal diameters (twin mode shapes included). For the CBSR analysis of the AXI plate, the Craig and Bampton basis consists of 90 left and 90 right-hand side static modes and 14 dynamic modes per substructure. For the CBSR analysis of the CYCL plate, the basis consists of 30 left and 30 right-hand side static modes and 14 dynamic modes per substructure.

The MR method gives a 99 percent reduction of the number of degrees-of-freedom from the nonreduced full assembly model (direct FEM). This is the largest reduction obtained. The CBSR method leads to a 80–90 percent reduction. Note that the numbers of degrees-of-freedom of the CBSR and CS models are about the same (Table 2). The size of the cyclic symmetric model (CS) is about $2/N$ times that of the parent finite element model (direct FEM).

Free Vibrations of the Tuned Plates. The frequencies of the tuned plates are given in Table 3 for the first bending (1B) or zero nodal circle modes with 0 to 6 nodal diameters. The same frequencies are predicted with the four models. For the AXI plate, the predicted frequencies also compare very well with the analytical solution for thin annular plates. For tuned assemblies, the nodal diameter pattern provides a convenient way to group mode shapes. In this case, the cyclic symmetric model has the strong advantage to provide a systematic ordering of modes as a function of the number of nodal diameters whereas the full assembly models give the modes ordered according to increasing frequencies.

¹ANSYS, Swanson Analysis Systems, Inc., USA.

Table 3 Frequencies of the tuned AXI and CYCL plates for modes with 0 nodal circle (1B) and 0 to 6 nodal diameters.*: blade mode and nodal diameter patterns.

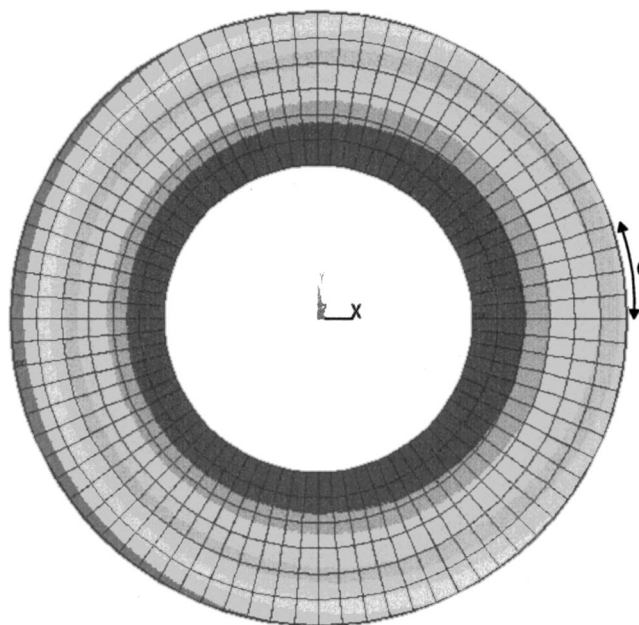
AXI		CYCL	
Modes (*)	(Hz)	Modes (*)	(Hz)
1 (1B-0D)	248.9	1 (1B-0D)	252.6
2, 3 (1B-1D)	252.7	2, 3 (1B-1D)	254.1
4, 5 (1B-2D)	275.1	4, 5 (1B-2D)	258.9
6, 7 (1B-3D)	340.1	6, 7 (1B-3D)	267.8
8, 9 (1B-4D)	462.8	8, 9 (1B-4D)	281.1
10, 11 (1B-5D)	643.1	10, 11 (1B-5D)	298.2
12, 13 (1B-6D)	875.7	12, 13 (1B-6D)	317.1

Table 4 Comparison of the first five frequencies of the mistuned AXI and CYCL plates

Mode	AXI, $\epsilon_0=+10\%$		CYCL, $\epsilon_0=-10\%$	
	Direct FEM (Ref.)	MR, CBSR	Direct FEM (Ref.)	MR, CBSR
1	249.38	249.38	250.68	250.63
2	252.88	252.88	253.28	253.23
3	253.97	253.97	254.06	254.00
4	275.57	275.57	257.93	257.87
5	276.08	276.08	258.79	258.72

Free Vibrations of the Mistuned Plates. The AXI and CYCL plates are partially mistuned with up to ten percent stiffness perturbation of the reference sectors, -10 percent $\leq \epsilon_0 \leq +10$ percent and $\epsilon_s=0$ for $s=1, \dots, N-1$. A perturbation of ten percent is large compared to actual mistuning patterns of industrial rotors. However, the objective of this work is to demonstrate that the selected reduction models are robust and can handle a wide range of mistuning patterns.

• **AXI Plate.** The frequencies of the mistuned AXI plate predicted with the direct FEM (reference), MR and CBSR models are given in Table 4 for the first five modes. Unlike the tuned case, mistuned modes are not characterized in terms of number of nodal diameters because they usually result from the combination of several nodal diameters. The frequencies predicted without and

**Fig. 3** First mode shape of the mistuned AXI plate ($\epsilon_0=+10$ percent). 0 indicates the reference sector.

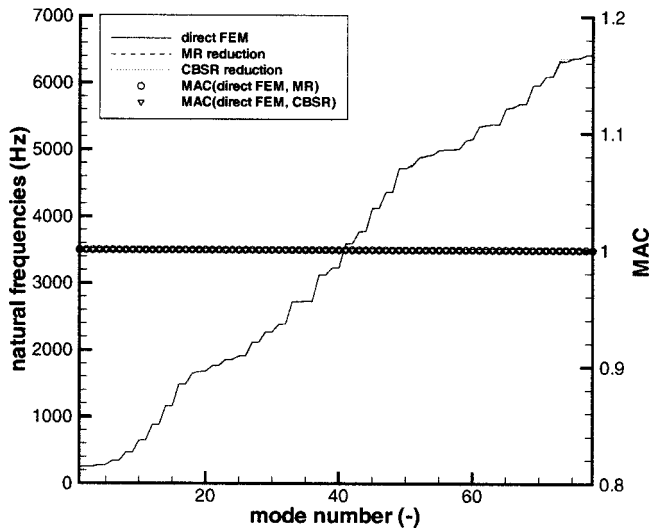


Fig. 4 Comparison of lowest 78 modes of the mistuned AXI plate ($\epsilon_0 = +10$ percent) with and without reduction

with reduction (Table 4) are in excellent agreement. They can be compared to the tuned frequencies of the 1B-0D, 1B-1D, and 1B-2D modes (Table 3). In the present case, the mistuned frequencies differ very little from the tuned frequencies. The first mode shape of the mistuned plate is shown in Fig. 3. This is a dominant zero nodal diameter first bending (1B-0D). The same mode shape is predicted with the direct FEM, MR, and CBSR models. A traveling wave decomposition gives three dominant circumferential harmonics, a zero nodal diameter for 87.6 percent, a first nodal diameter for 11.2 percent, and a second nodal diameter for 1.2 percent.

Figure 4 is a comparison of the lowest 78 frequencies of the mistuned AXI plate predicted with and without reduction. The direct FEM, MR, and CBSR models compare excellently well over the entire range of modes. Figure 4 also quantifies the comparison between mode shapes in terms of MAC (Modal Assurance Criterion [23]). A MAC of 1 indicates a perfect agreement between the pairs of mode shapes.

Figure 5 shows the variations of the first frequency as a function of the mistuning strength ϵ_0 , for variations from -10 percent

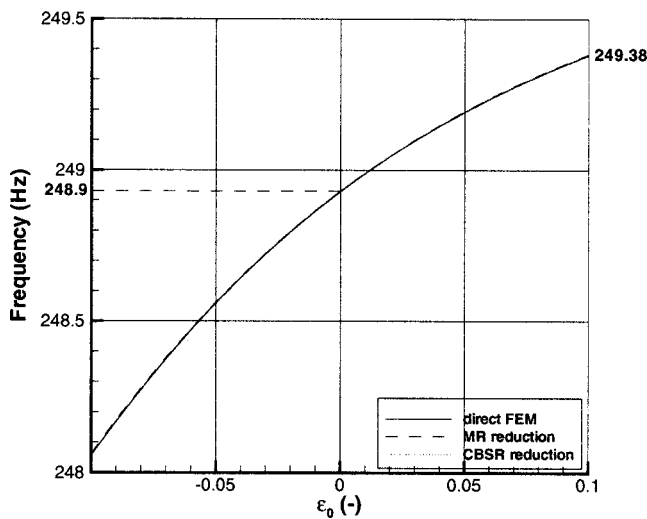


Fig. 5 Comparison of first natural frequency of the AXI plate as a function of ϵ_0

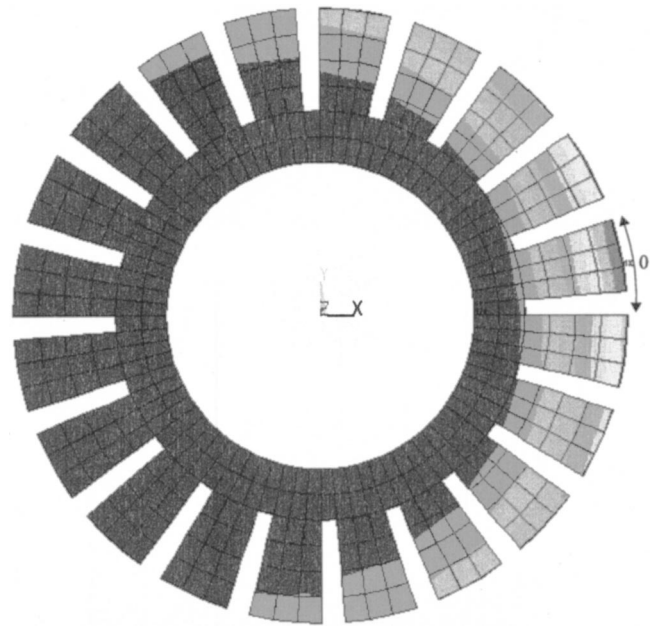


Fig. 6 First mode shape of the mistuned CYCL plate ($\epsilon_0 = -10$ percent). 0 indicates the reference sector.

to $+10$ percent. The results with and without reduction are here again in excellent agreement. It is important to note that the frequency is not a linear function of ϵ_0 . The degree of nonlinearity is a measure of the sensitivity of a particular mode to mistuning.

CYCL Plate. Looking now at Table 4 and Figs. 6–8, the conclusions previously given for the AXI plate can be transposed to the CYCL plate. Regarding the sensitivity of the first mode shape to mistuning, Fig. 6 shows a strong mode localization on a few blades around the mistuned (reference) sector. The phenomena of mode localization typically occurs for disordered or mistuned systems with weak coupling between the system components (i.e., sectors), for example see [6].

Overall, the results obtained on the AXI and CYCL plates clearly demonstrate the ability of the modal reduction method to predict strongly localized modes, provided a sufficient number of circumferential harmonics (or nodal diameters) are included in the modal basis.

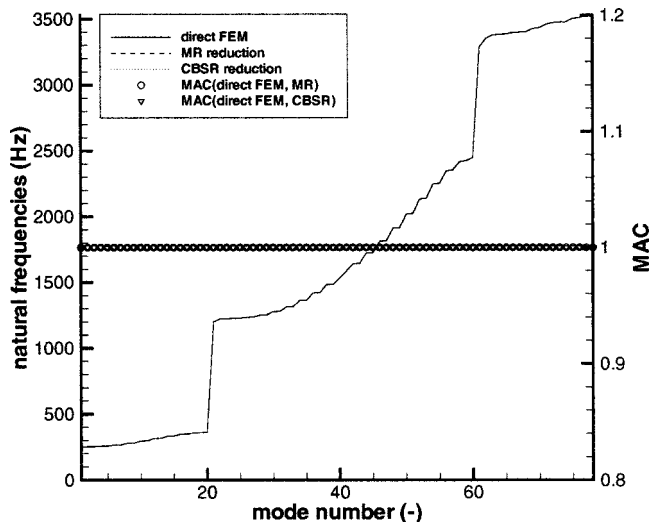


Fig. 7 Comparison of lowest 78 modes of the mistuned CYCL plate ($\epsilon_0 = -10$ percent) with and without reduction

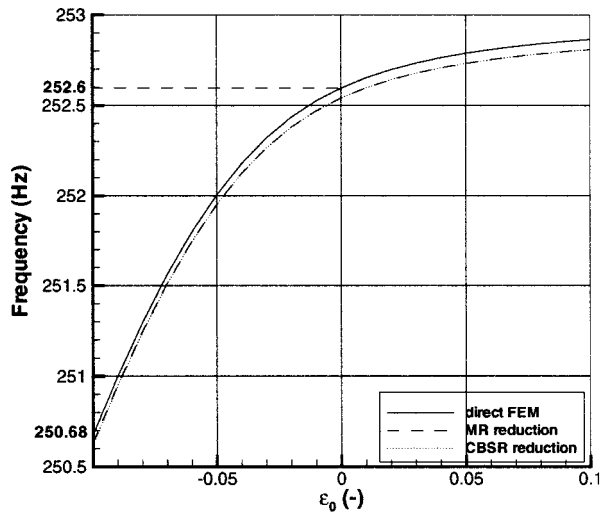


Fig. 8 Comparison of first natural frequency of the CYCL plate as a function of ϵ_0

Industrial Bladed Disk

Description of the Fan. The industrial test case selected is the *DCAHMI transonic shrouded fan* shown in Fig. 9(b) which belongs to a first fan stage of a modern aeroengine. The rotor has 30 blades with an aspect ratio of 3.4 and part-span shrouds located at about 60 percent span. Additional geometrical parameters are reported in Table 5. The constitutive material is titanium with the following mechanical properties: $E = 1.1 \cdot 10^{11} \text{ N/m}^2$, $\rho = 4430 \text{ kg/m}^3$, and $\nu = 0.35$. The DCAHMI rotor exhibits many of the characteristics of modern high-performance turbomachinery designs. The structural and aeroelastic behaviors of the tuned rotor have been previously studied in [20,24,25]. Here, it is proposed to study the sensitivity of the first frequencies and mode shapes of the rotor to the combination of mistuning strength and centrifugal stiffening.

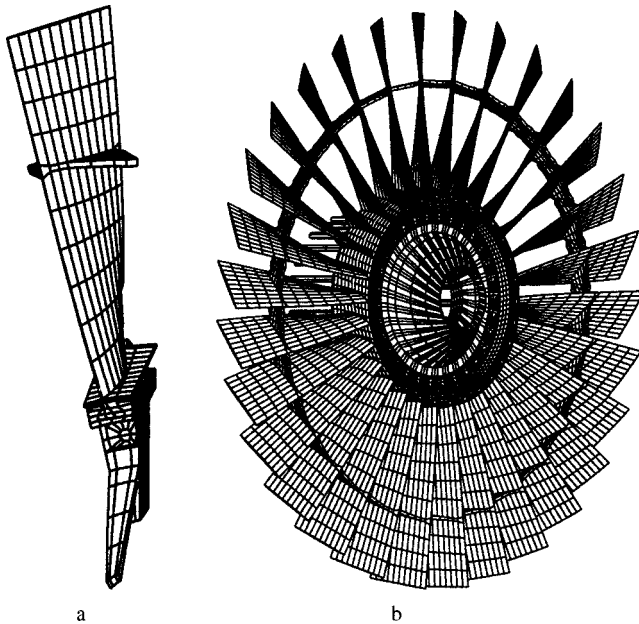


Fig. 9 (a) 12 deg sectorial mesh and Craig and Bampton substructure, (b) full assembly mesh

Table 5 Geometrical parameters (AR: aspect ratio, HTR: hub-tip ratio)

Parameters	DCAHMI
Number of blades	30
Average radius, hub and tip (m)	0.195 and 0.509
Average blade length (m)	0.314
Average chord (m)	0.090
Stagger, hub and tip (deg)	10.8 and 57.2
AR (-)	3.4
HTR (-)	0.38
Twist (deg)	46.4

Table 6 Statistics of the CS, direct FEM, MR, and CBSR models applied to an industrial bladed-disk. †: CPU time of a CRAY J90 vector computer, ◇: tuned bladed-disk, ⊕: mistuned bladed-disk with perturbations of sector 0 only, ♣: 150 modes=10 modes/nodal diameter×15 diameters, ♠: with vectorization.

	CS	Direct FEM	MR	CBSR
Number of DOF	21 666	304 650	120	23 640
Alloc. memory	88 Mb	728 Mb	670 Mb	1.1 Gb
Disk space	500 Mb	4.6 Gb	1 Gb	1 Gb
Static Analysis				
CPU mins (†)	9	3400	9	9
Modal Analysis (◇)				
Nb. of modes calc.	150 (♣)	20	120	210
CPU mins	105	600 (♠)	138 (♠)	405 (♠)
CPU mins per mode	0.7	30	1.15	1.93
Reanalysis (⊕)				
CPU mins per mode	NA	30	0.275	1.6

Modeling. The same MR and CBSR reduction models compared on the AXI and CYCL plates are applied to the present industrial rotor. The full assembly finite element modeling is performed with the ABAQUS² code.

Two meshes are considered, the 12 degrees sectorial mesh shown in Fig. 9(a) and the full assembly mesh shown in Fig. 9(b). The finite element is a 20-node hexaedral element. The sectorial mesh used for the cyclic symmetric modal analyses consists of 3624 nodes and 534 elements. The full assembly mesh has 102,210 nodes and 16,020 elements. To avoid the problem of "artificial numerical mistuning," the full assembly mesh is generated by copying and rotating the reference cyclic symmetric mesh sector (Fig. 9(a)) $N-1$ times around the rotational axis.

It should be noted that, in this presentation, the shroud-to-shroud interfaces are modeled as being continuous, i.e. the contacts are fully stuck.

Reduction Orders for Full Assembly Modal Analyses. The number of degrees-of-freedom of the full assembly models without reduction (direct FEM model) and with reduction (MR and CBSR models) are reported in Table 6. With 4 blade modes retained for all nodal diameters giving a total of 120 modes, the MR model has about 2500 times fewer degrees of freedom than the FEM model. The CBSR model gives about 13 times less degrees-of-freedom. In the present case, the CBSR and CS models have about the same number of degrees-of-freedom. The Craig and Bampton basis consists of 774 static modes and 14 dynamic modes per substructure. 98 percent of the degrees-of-freedom left after reduction are associated with the Craig and Bampton substructure static modes.

The reduction of the number of degrees-of-freedom may be quite different from the CPU time reduction depending on the computational cost of performing the reduction (i.e., calculating

²ABAQUS, Hibbitt, Karlsson & Sorensen, Inc., USA.

Table 7 First tuned frequencies (Hz) at 8000 rpm sorted by increasing order.*: blade mode and nodal diameter patterns

Mode (*)	CS (Ref.)	Direct FEM (Ref.)	MR, CBSR
1 (1B-0D)	171.62	171.17	171.62
2,3 (1B-1D)	314.39	313.90	314.39
4,5 (1B-2D)	321.81	321.36	321.81
6 (2B-0D)	325.42	324.71	325.42
7,8 (1B-3D)	346.08	345.67	346.08
9,10 (1B-4D)	367.71	367.35	367.71
11,12 (1B-5D)	380.81	380.45	380.81

the reduced matrices). The performances obtained with the in-house developed code and ABAQUS both in serial mode on a CRAY J90 vector supercomputer are listed in Table 6. The computational times with the direct FEM, MR, and CBSR models are given with full vectorization. For the present implementation of the MR and CBSR models, full vectorization (i.e., above 90 percent vector efficiency) decreases the CPU time by a factor 7–10. The MR (resp. CBSR) modal analysis of the tuned bladed disk requires about 4.4 (resp. 1.5) times less CPU time than the direct FEM modal analysis for the extraction of six (resp. ten) times as many modes. For a reanalysis of the partially mistuned bladed disk, the direct FEM model is about 109 (resp. 19) times more expensive than the reduced MR (resp. CBSR) model. The cost of full assembly reduced analyses is therefore clearly attractive. The main drawback is that, despite significant CPU time reductions, a large amount of (primary) memory is still necessary.

Modes of Tuned Bladed Disk at 8000 rpm. The first 12 frequencies of the tuned rotor predicted with the CS, direct FEM, MR, and CBSR models are given in Table 7. The results show the presence of twin modes with perfectly identical frequencies. A

Table 8 First frequencies at 0 rpm for $\epsilon_0 = -10$ percent

Mode	Direct FEM (Ref.)		MR, CBSR (Hz)
	(Hz)	$\Delta_{r-m} \omega$ (%)	
1	112.64	-0.17	112.66
2	212.29	-0.96	212.30
3	214.31	-0.02	214.31
4	214.87	-0.20	214.86
5	215.26	-0.02	215.24
6	220.35	-0.62	220.34
7	221.70	-0.02	221.68
8	225.25	-1.21	225.25
9	228.03	-0.01	227.98
10	228.85	-1.20	228.84
11	231.66	-0.05	231.63
12	231.77	-0.01	231.75

very good agreement is found between the cyclic symmetric analysis, the nonreduced (direct FEM) and reduced (MR, CBSR) order modeling of the full assembly. The marginal differences between the Direct FEM and other models are purely down to how nonlinear effects are treated in ABAQUS and the in-house FE code for the determination of the pre-stressed state of the blades under the combined effects of centrifugal stiffening and softening. A MAC of 1 is obtained between the pairs of mode shapes predicted with and without reductions for the first 210 modes. Figure 10 is a contour plot of the axial component of the second mode shape of the tuned bladed disk, which corresponds to a first bending of the blades with one nodal diameter (1B-1D).

Looking now at the CPU performances obtained for the tuned bladed disk (Table 6), the least computational cost per mode is obtained with the cyclic symmetric model. The MR and CBSR analyses of the full assembly are slightly more expensive than the CS analysis of a reference sector. The CBSR analysis is more

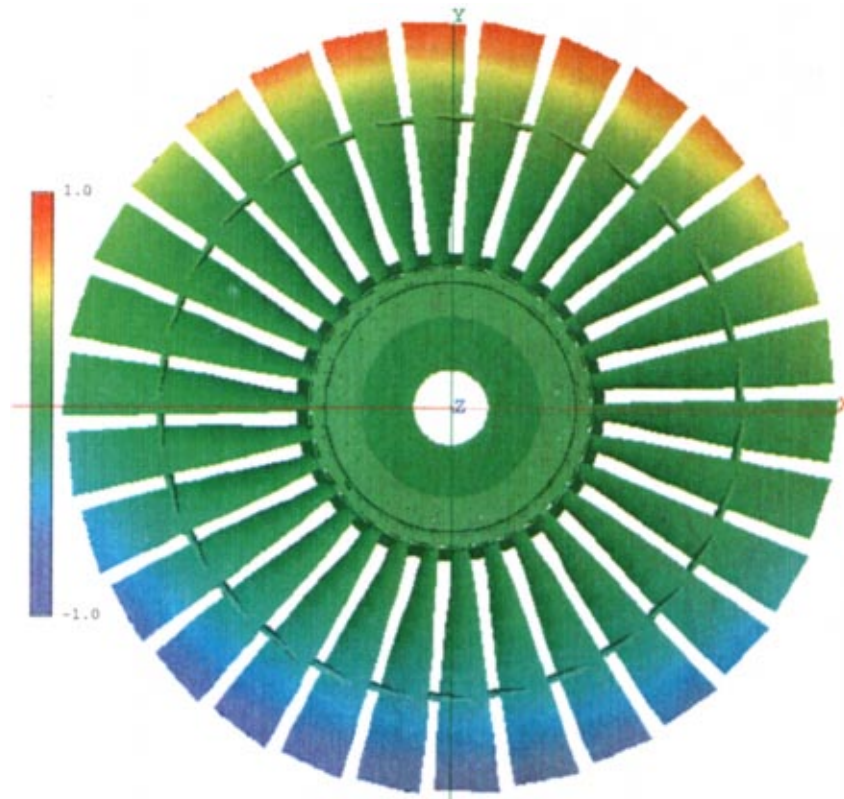


Fig. 10 Axial component of the second mode shape (1B-1D) at 8000 rpm for the tuned bladed disk, CBSR model

Table 9 First frequencies at 0 rpm for $\varepsilon_0 = +10$ percent

Mode	Direct FEM (Ref.)		MR, CBSR (Hz)
	(Hz)	$\Delta_{t-m}\omega$ (%)	
1	113.01	0.16	113.03
2	214.38	0.01	214.37
3	214.65	0.14	214.64
4	215.35	0.03	215.33
5	215.93	0.29	215.92
6	221.77	0.02	221.75
7	222.20	0.20	222.18
8	228.08	0.03	228.03
9	228.37	0.14	228.36
10	231.66	0.02	231.63
11	231.78	0.00	231.76
12	231.92	0.06	231.89

Table 10 First frequencies at 0 rpm for alternate mistuning with $\varepsilon_s = \pm 10$ percent

Mode	Direct FEM (Ref.)		MR (Hz)	CBSR (Hz)
	(Hz)	$\Delta_{t-m}\omega$ (%)		
1	112.73	-0.09	112.81	112.75
2	210.58	-1.76	210.72	210.57
3	210.58	-1.76	210.72	210.57
4	211.29	-1.86	211.39	211.28
5	211.29	-1.86	211.39	211.28
6	215.87	-2.64	215.94	215.85
7	215.87	-2.64	215.94	215.85
8	219.80	-3.61	219.85	219.77
9	219.80	-3.61	219.85	219.77
10	222.17	-4.10	222.21	222.14
11	222.17	-4.10	222.21	222.14
12	223.51	-3.57	223.56	223.49

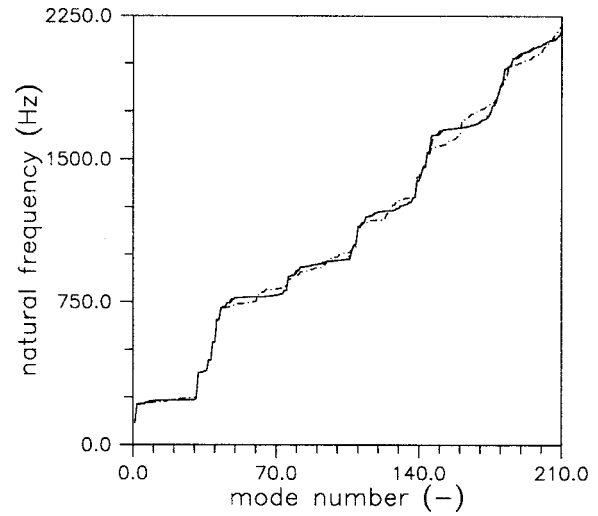


Fig. 11 Lowest 210 natural frequencies predicted with CBSR reduced-order model of the full assembly at rest, solid line: tuned, dashed line: $\varepsilon_0 = -10$ percent, dotted line: $\varepsilon_0 = +10$ percent, dotted-dashed line: alternate ten percent mistuning

expensive than the MR analysis but remains considerably more efficient than the direct FEM analysis.

Modes of Mistuned Bladed Disk at Rest. The free vibrations of the mistuned bladed disk at rest are predicted with and without reductions for three mistuning patterns, corresponding respectively to a ten percent decrease in stiffness of sector 0 ($\varepsilon_0 = -10$ percent), a ten percent increase in stiffness of sector 0

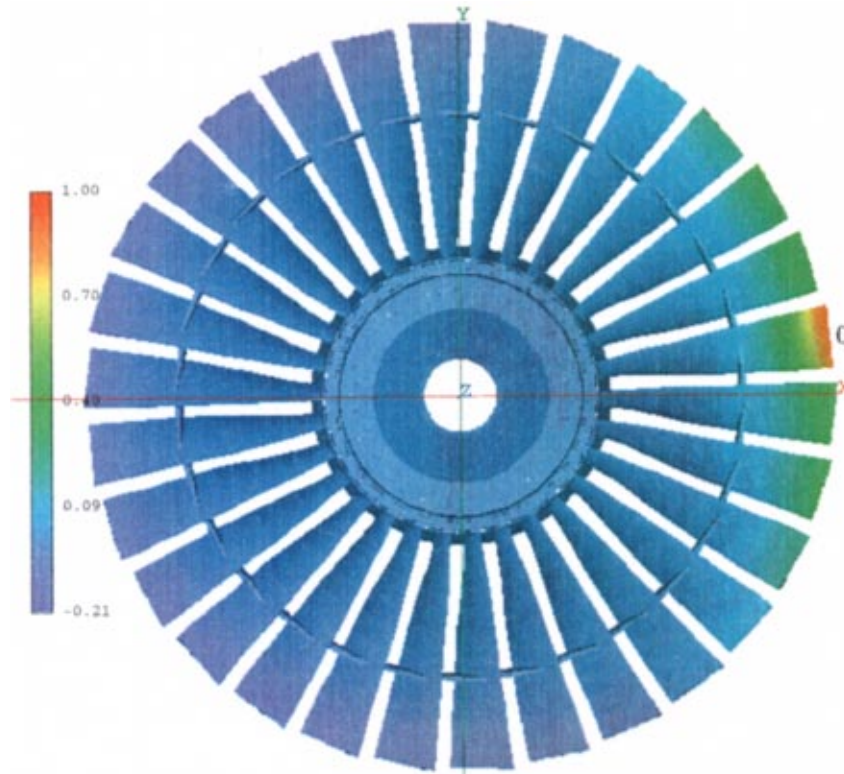


Fig. 12 Axial component of the second mode shape at 0 rpm for partial mistuning with $\varepsilon_0 = -10$ percent, CBSR model. 0 denotes the reference sector.

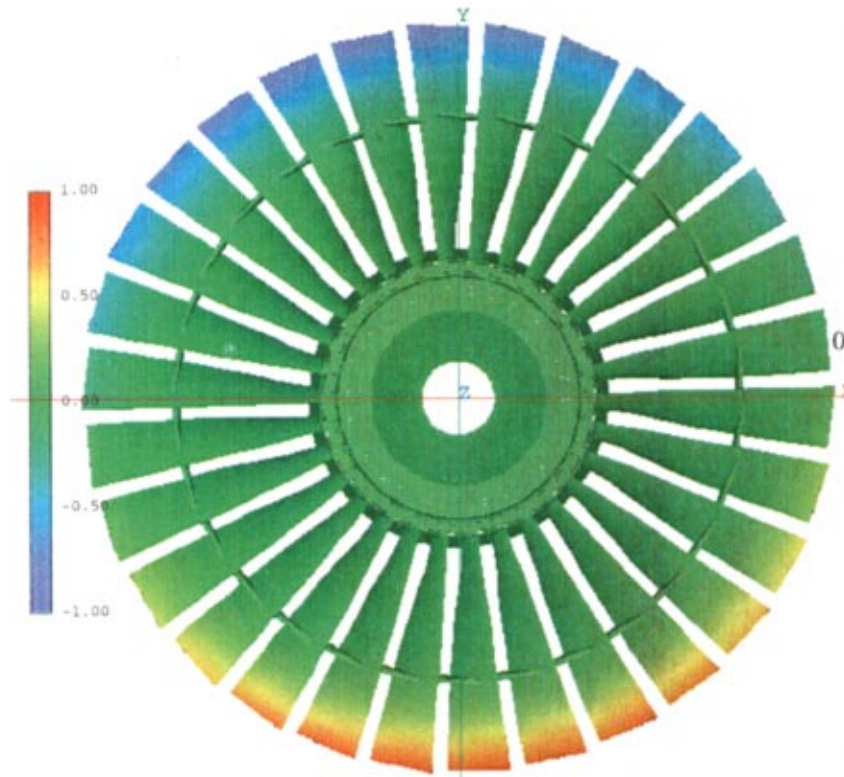


Fig. 13 Axial component of the second mode shape at 0 rpm for partial mistuning with $\varepsilon_0 = +10$ percent, CBSR model. 0 indicates the reference sector.

($\varepsilon_0 = +10$ percent), and ten percent alternate perturbations of the sectors ($\varepsilon_s = \pm 10$ percent). The frequencies of the first twelve modes are reported in Table 8 for $\varepsilon_0 = -10$ percent, in Table 9 for $\varepsilon_0 = +10$ percent, and in Table 10 for $\varepsilon_s = \pm 10$ percent.

The following sensitivity parameter is used in Tables 8–10 to quantify the differences between the tuned and mistuned frequencies:

$$\Delta_{l-m}\omega = \frac{\omega^{\text{mistuned}} - \omega^{\text{tuned}}}{\omega^{\text{tuned}}} \quad (17)$$

Small differences are observed between the tuned and mistuned frequencies and little variations between the different mistuning patterns. This statement also applies to the first 210 frequencies of the bladed-disk as shown in Fig. 11. It is also interesting to note the presence of pairs of identical frequencies in Table 10. Due to

the repetitive nature of the alternate mistuning pattern and because N is even, this mistuned bladed disk is a cyclic symmetric structure with $N/2$ sectors. The alternate mistuning also leads to the largest variations of the $\Delta_{l-m}\omega$ parameter.

Tables 8–10 demonstrates the level of accuracy sustainable by the two reduced order models in terms of frequency on an industrial application. This also translates nicely to the mode shapes which are indistinguishable both visually and in terms of MAC. The MR model is behaving exceptionally well given that it combines both the largest reduction order and accuracy.

The second mode shape of the mistuned bladed disk is shown in Fig. 12 for $\varepsilon_0 = -10$ percent, and in Fig. 13 for $\varepsilon_0 = +10$ percent. For the -10 percent perturbation, the vibration is strongly localized around the mistuned (reference) sector. The minimum and maximum normalized axial components are respectively $+1.0$ (right-hand side) and -0.21 (left-hand side) produc-

Table 11 First frequencies at 8000 rpm for $\varepsilon_0 = -10$ percent

Mode	Direct FEM (Ref.)		MR, CBSR (Hz)
	(Hz)	$\Delta_{l-m}\omega$ (%)	
1	171.02	-0.09	171.33
2	313.28	-0.19	313.05
3	313.83	-0.02	314.31
4	320.85	-0.16	320.74
5	321.25	-0.03	321.67
6	324.36	-0.11	324.96
7	345.15	-0.14	344.73
8	345.57	-0.02	345.95
9	366.77	-0.15	365.57
10	367.30	-0.01	367.64
11	379.77	-0.17	377.14
12	380.42	0.00	380.76

Table 12 First frequencies at 8000 rpm for $\varepsilon_0 = +10$ percent

Mode	Direct FEM (Ref.)		MR, CBSR (Hz)
	(Hz)	$\Delta_{l-m}\omega$ (%)	
1	171.31	0.08	171.90
2	313.96	0.02	314.45
3	314.37	0.15	315.14
4	321.47	0.04	321.94
5	321.80	0.14	322.59
6	325.09	0.12	326.04
7	345.75	0.03	346.20
8	346.10	0.13	346.93
9	367.40	0.02	367.78
10	367.75	0.11	368.51
11	380.47	0.01	380.85
12	380.81	0.10	381.46

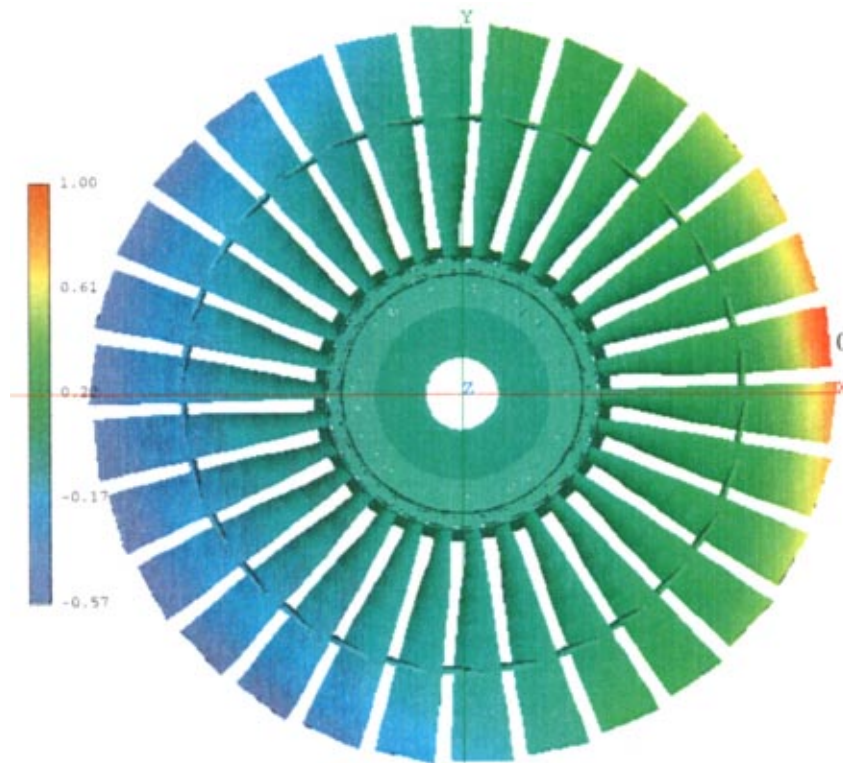


Fig. 14 Axial component of the second mode shape at 8000 rpm for partial mistuning with $\varepsilon_0 = -10$ percent, CBSR model. 0 indicates the reference sector.

ing a pronounced asymmetry. For $\varepsilon_0 = +10$ percent, the same mode shape is tuned and its nodal diameter is aligned along the mistuned sector (Fig. 13). Despite weak to strong sensitivities of the mode shapes to mistuning, the mistuned frequencies (Tables 8–10, Fig. 11) differ very little from the tuned frequencies.

Modes of Mistuned Bladed Disk at 8000 rpm. The frequencies of the first twelve modes of the mistuned bladed disk at 8000 rpm are given in Tables 11 and 12 for partial mistuning with $\varepsilon_0 = -10$ percent and $\varepsilon_0 = +10$ percent, respectively. Based on the direct FEM predictions, the $\Delta_{l-m}\omega$ parameter varies from -0.19 percent (mode 2 of Table 11) to 0.15 percent (mode 3 of Table 12). The frequencies of the bladed disk are therefore here again very little affected by the selected mistuning patterns. The results obtained with the MR and CBSR models are compared in Tables 11 and 12. A perfect agreement is found.

For $\varepsilon_0 = -10$ percent, the second mode shape predicted with the CBSR reduction is shown in Fig. 14. It has a one nodal diameter pattern very similar to the second tuned mode of Fig. 10. However, it is not cyclic symmetric since the minimum axial component is -0.57 (left-hand side) for a maximum of 1.0 (right-hand side). For $\varepsilon_0 = +10$ percent, the second mode shape of the mistuned bladed-disk shown in is nearly identical to the tuned mode shape of Fig. 10. Overall, these results show that the second mode shape of the DCAHM1 bladed disk is much more sensitive to negative than positive stiffness perturbations.

Comparison of the Modes at Rest and 8000 rpm. It is interesting to see that the sensitivities of the bladed disk to mistuning at rest and 8000 rpm are very different. At rest, the second mode shape of the -10 percent partially mistuned bladed disk (Fig. 12) displays a strong localization of the vibration around the mistuned (reference) sector. At 8000 rpm, the mode shape (Fig. 14) is clearly asymmetric but retains a strong one-nodal diameter

pattern. This can be explained by the fact that the rotational speed has a strong stiffening effect which tends to average out the perturbations in stiffness introduced by mistuning.

Summary and Conclusions

A comparison of two classical reduction techniques applied to full assembly free vibration analyses of mistuned bladed disks was presented. The first reduction employs a modal reduction approach with a modal basis consisting of a set of tuned mode shapes. The second reduction uses a Craig and Bampton substructuring and reduction approach. The two reduced-order models are compared on three representative test rotors, including a modern design industrial shrouded bladed disk, in terms of accuracy (for frequencies and mode shapes), reduction order, computational efficiency, sensitivity to intersector elastic coupling, and ability to capture the phenomenon of mode localization.

The two reduction methods can accurately predict the first tuned and mistuned modes of two annular plates, with respectively strong and weak intersector elastic coupling strengths, with reductions of the number of degrees-of-freedom from 80 percent to 99 percent compared to the nonreduced full assembly finite element approach. The results did not show any sensitivity of the two reduced order models to the intersector elastic coupling strength. Besides, strongly localized mode shapes are accurately predicted with the modal reduction method, provided a sufficient number of circumferential harmonics are included in the modal basis.

For the industrial shrouded bladed disk, the behaviors of the reduced-order models were studied for several mistuning arrangements with ten percent stiffness variations from the nominal state for two rotational speeds. The frequencies and mode shapes of the tuned and mistuned bladed disks predicted with the direct finite element model, modal reduction model and Craig and Bampton

model compare perfectly well at rest. A very good agreement is found at 8000 rpm. Besides, the two reduction methods are shown to be computationally efficient with reduction in computational times from 1 to 2 orders of magnitude. A comparison of the modes of the tuned and mistuned bladed disks leads to several interesting conclusions. The frequencies of the bladed disk are found to be much less sensitive to stiffness mistuning than the mode shapes. The second mode shape is very sensitive to negative stiffness perturbations (−10 percent) and almost insensitive to positive stiffness perturbations (+10 percent). The second mode shape is also much more sensitive to mistuning at rest than at 8000 rpm.

In an industrial environment, both reduction models can be used to achieve substantial analysis cost reductions. For the modeling of the industrial bladed disk with fully stuck shroud interfaces presented in this paper, the modal reduction approach is clearly the most efficient. However, the Craig and Bampton approach remains competitive since a wider range of shroud-to-shroud constraints can be used, including the limiting cases of full stick and full slip conditions ([20]), as well as for a transition between these two states when incorporating shroud friction constraints.

Acknowledgments

The authors wish to acknowledge the contributions of Mr. Hans Mårtensson and Dr. Gabor Csaba at Volvo Aero Corporation (Trollhättan, Sweden). The financial supports from the French “Direction des Recherches Etudes et Techniques de la Délégation Générale de l’Armement” (DRET/DGA Grant No. 961003/A000/DRET/DS/SR2) and from the Swedish “Nationella Flygtekniska Forsknings Programmet” (NFFP Grant No. 342) are gratefully acknowledged. This work was also supported with computing resources by the Swedish Council for Planning and Coordination of Research (FRN) and Paralleldator Centrum (PDC), Royal Institute of Technology (Stockholm, Sweden).

References

- [1] Srinivasan, A. V., 1997, “Flutter and Resonant Vibration Characteristics of Engine Blades,” *ASME J. Eng. Gas Turbines Power*.
- [2] Slater, J., Minkiewicz, G., and Blair, A., 1999, “Forced Response of Bladed Disk Assemblies—A Survey,” *Shock Vib. Dig.*, **31**, No. 1, pp. 17–24.
- [3] Huang, W., 1981, “Free Forced Vibration of Closely Coupled Turbomachinery Blades,” *AIAA J.*, **19**, No. 7, pp. 918–924.
- [4] Huang, W., 1982, “Vibration of Some Structures With Periodic Random Parameters,” *AIAA J.*, **20**, No. 7, pp. 1001–1008.
- [5] Sinha, A., 1986, “Calculating the Statistics of Forced Response of a Mistuned Bladed Disk Assembly,” *AIAA J.*, **24**, No. 11, pp. 1797–1801.
- [6] Wei, S.-T., 1988, “Effects of Structural Irregularities on the Dynamics of Cyclic Structures,” Ph.D. dissertation, University of Michigan.
- [7] Cai, C., and Lin, Y., 1992, “Statistical Distribution of Frequency Response in Disordered Periodic Structures,” *AIAA J.*, **30**, No. 5, pp. 1400–1407.
- [8] Mignolet, M., and Lin, C., 1993, “The Combined Closed Form Perturbation

- Approach to the Analysis of Mistuned Bladed Disks,” *ASME J. Turbomach.*, **115**, No. 4, pp. 771–780.
- [9] Mignolet, M., and Lin, C.-C., 1996, “A Novel Limit Distribution for the Analysis of Randomly Mistuned Bladed Disks,” *ASME Paper 96-GT-414*.
- [10] Irretier, H., 1983, “Spectral Analysis of Mistuned Bladed-Disk Assemblies by Component Mode Synthesis,” *Vibrations of Bladed Disk Assemblies*, ASME, New York.
- [11] Zheng, Z.-C., and Wang, F.-R., 1985, “Dynamic Analysis of Blade Groups Using Component Mode Synthesis,” *Vibrations of Blades and Bladed Disk Assemblies*, ASME, New York, pp. 97–103.
- [12] Kruse, M. J., and Pierre, C., 1996, “Dynamic Response of an Industrial Turbomachinery Rotor,” *AIAA Paper 96-2820-CP*.
- [13] Kruse, M. J., and Pierre, C., 1996, “Forced Response of Mistuned Bladed-Disks Using Reduced-Order Modelling,” *AIAA Paper 96-1545-CP*.
- [14] Castanier, M., Ottarsson, G., and Pierre, C., 1997, “A Reduced-Order Modeling Technique for Mistuned Bladed-Disks,” *ASME J. Vib. Acoust.*, **119**, No. 3, pp. 439–447.
- [15] Yang, M.-T., and Griffin, J., 1997, “A Reduced Order Approach for the Vibration of Mistuned Bladed-Disk Assemblies,” *ASME J. Eng. Gas Turbines Power*, **119**, No. 1, pp. 161–167.
- [16] Bladh, R., Castanier, M., and Pierre, C., 1998, “Reduced Order Modeling and Vibration Analysis of Mistuned Bladed-Disk Assemblies With Shrouds,” *ASME Paper 98-GT-484*.
- [17] Lin, C.-C., 1994, “Forced Response of Mistuned Bladed Disks: Identification and Prediction,” Ph.D. thesis, Arizona State University.
- [18] Yang, M.-T., and Griffin, J., 1999, “A Reduced Order Model of Mistuning Using a Subset of Nominal System Modes,” *ASME Paper 99-GT-288*.
- [19] Craig, R., and Bampton, M., 1968, “Coupling of Substructures for Dynamic Analyses,” *AIAA J.*, **6**, No. 7, pp. 1313–1319.
- [20] Jacquet-Richardet, G., Moyroud, F., and Fransson, T., 1997, “An Influence of Shroud Design on the Dynamic and Aeroelastic Behaviors of Bladed-Disk Assemblies,” *ASME Paper 97-GT-191*.
- [21] Jacquet-Richardet, G., Ferraris, G., and Rieutord, P., 1996, “Frequencies and Modes of Rotating Flexible Bladed Disc-Shaft Assemblies: A Global Cyclic Symmetric Approach,” *J. Sound Vib.*, **191**, No. 5, pp. 901–915.
- [22] Slater, J., and Blair, A., 1996, “A Design Strategy for Preventing High Cycle Fatigue by Minimizing Sensitivity of Bladed-Disks to Mistuning,” Technical Report, Wright State University, Mechanical Engineering Materials Science and Engineering, Dayton, OH.
- [23] Allemang, R. J., and Brown, D. L., 1986, “A Correlation Coefficient for Modal Vector Analysis,” *Proceedings of the 1st International Modal Analysis Conference*, Orlando, FL, Society for Experimental Mechanics, pp. 461–467.
- [24] Moyroud, F., Jacquet-Richardet, G., and Fransson, T., 1996, “A Modal Coupling of Fluid and Structure Analyses for Turbomachine Flutter. Application to a Fan Stage,” *ASME Paper 96-GT-335*.
- [25] Moyroud, F., 1998, “Fluid-Structure Integrated Computational Methods for Turbomachinery Blade Flutter and Forced Response Predictions,” Ph.D. thesis, Royal Institute of Technology/Institute National des Sciences Appliquées.
- [26] Kruse, M., and Pierre, C., 1997, “An Experimental Investigation of Vibration Localization in Bladed-Disks, Part I: Free Response,” *ASME Paper 97-GT-501*.
- [27] Kruse, M., and Pierre, C., 1997, “An Experimental Investigation of Vibration Localization in Bladed-Disks, Part II: Forced Response,” *ASME Paper 97-GT-502*.
- [28] Berthillier, M., Dupont, C., Chanez, P., and Saurat, F., 1998, “Réponse Forcée Aéroélastique des Aubes de Turbomachines,” *Revue Française de Mécanique*, **4**, pp. 265–275.
- [29] Kenyon, J., and Minkiewicz, G., 1998, “Mistuning Characteristics of a Bladed Rotor From a Two-stage Transonic Compressor,” *AIAA Paper 98-3721*.

Effects of Wheel-Shaft-Fluid Coupling and Local Wheel Deformations on the Global Behavior of Shaft Lines

D. Lornage

E. Chatelet

G. Jacquet-Richardet

e-mail: georges.jacquet@insa-lyon.fr

Laboratoire de Mécanique des Structures,
INSA de Lyon, Bât. J. D'Alembert,
8, rue des Sciences,
69621 Villeurbanne Cedex, France

Rotating parts of turbomachines are generally studied using different uncoupled approaches. For example, the dynamic behavior of shafts and wheels are considered independently and the influence of the surrounding fluid is often taken into account in an approximate way. These approaches, while often sufficiently accurate, are questionable when wheel-shaft coupling is observed or when fluid elements are strongly coupled with local structural deformations (leakage flow between wheel and casing, fluid bearings mounted on a thin-walled shaft, etc.). The approach proposed is a step toward a global model of shaft lines. The whole flexible wheel-shaft assembly and the influence of specific fluid film elements are considered in a fully three-dimensional model. In this paper, the proposed model is first presented and then applied to a simple disk-shaft assembly coupled with a fluid film clustered between the disk and a rigid casing. The finite element method is used together with a modal reduction for the structural analysis. As thin fluid films are considered, the Reynolds equation is solved using finite differences in order to obtain the pressure field. Data are transferred between structural and fluid meshes using a general method based on an interfacing grid concept. The equations governing the whole system are solved within a time-marching procedure. The results obtained show significant influence of specific three-dimensional features such as disk-shaft coupling and local disk deformations on global behavior. [DOI: 10.1115/1.1492830]

Introduction

Increasing requirements concerning the performances, reliability, and security of turbomachines cannot be satisfied fully without accurate knowledge of the behavior of their rotating parts. This knowledge is usually obtained through numerical models that account for the main physical phenomena. Among these, the effects of fluid-structure interactions are of major importance, since they govern system stability and have significant influence on its dynamic characteristics (vibrational frequencies and amplitudes, critical speeds, etc.). Within this context, the goal of this study is to develop a general modeling procedure, adapted to the analysis of the dynamic behavior of shaft lines coupled with fluid films.

The general effect on rotordynamics of fluid films, occurring for example in hydrodynamic journal bearings, thrust bearings and seals (Childs [1], Frêne et al. [2], Diewald and Nordmann [3], Iwatsubo et al. [4], etc.), has been studied widely. More specifically, Desbordes et al. [5] analyzed the influence of pad elastic deformations on the trajectory inside a tilting pad bearing, Berger [6] showed that thrust bearing defects may have a significant effect and Van de Vandere and De Kraker [7] analyzed the influence of bearing compliance. The effect of leakage flow between wheels and casing has been pointed out by Childs [8,9]. All these approaches are based on classical rotordynamics hypotheses (Lalanne and Ferraris [10]), which consider only shaft bending-torsional flexibility and cannot account efficiently for effects that may be significant such as wheel shaft coupling, local wheel deformations or cross-sectional deformations of hollow thin-walled shafts.

Concerning fluid-structure coupling, different types of tech-

nique can be used. Coupling is strong when both domains are modeled using fully compatible discretizations and numerical schemes. Associated with the arbitrary Lagrangian Eulerian (ALE) concept, well adapted for dealing with moving boundaries, strong coupling is efficient but supposes the development of very specific tools (Bendiksen [11]). Alternative coupling techniques, which are slightly less strong, consider fluid and structural equations alternatively, with data used as a boundary condition between the two domains. These techniques are much more flexible and allow the use of independent existing tools.

The coupling technique considered in this study is the latter, associated to an interfacing grid to facilitate and systemize data transfers between fluid and structure. The basic models are based on a fully three-dimensional discretization of both domains, allowing all types of global or local deformations. The global coupled problem is solved using a time-marching procedure, after projection on the uncoupled structural mode shapes at rest. The advantages of this reduction are twofold. It permits a necessary major reduction in computational effort and it increases the efficiency of the retained coupling technique.

In this paper, the proposed procedure is first described and then applied to a simple disk-shaft system. The application allows validation and shows the significant effects that disc-shaft coupling or local disk deformations can have on the global behavior of a rotor.

Numerical Model

Structural Dynamic Behavior. The structure is discretized using the finite element method and studied with respect to the rotating frame, allowing the processing of complex shaped non-axisymmetric cases. The equations, governing the motion of the structure rotating in a fluid environment, are derived from the internal energies (kinetic, potential, dissipation) as well as from the work done by the external forces, by applying the Lagrange's equations. The system obtained is the following:

Contributed by the International Gas Turbine Institute (IGTI) of THE AMERICAN SOCIETY OF MECHANICAL ENGINEERS for publication in the ASME JOURNAL OF ENGINEERING FOR GAS TURBINES AND POWER. Paper presented at the International Gas Turbine and Aeroengine Congress and Exhibition, New Orleans, LA, June 4-7, 2001; Paper 01-GT-233. Manuscript received by IGTI, December 2000, final revision, March 2001. Associate Editor: R. Natole.

$$[M]\{\ddot{\delta}\} + [C + C_n + C_r]\{\dot{\delta}\} + [K_E + K_S + K_G + K_A + K_C n]\{\delta\} = \{F(\delta, \dot{\delta}, \ddot{\delta})\} \quad (1)$$

where $\{\ddot{\delta}\}$, $\{\dot{\delta}\}$, and $\{\delta\}$ are, respectively, the nodal acceleration, velocity, and displacement vectors. $[M]$ and $[K_E]$ are the standard mass and elastic stiffness matrices. $[C]$, $[K_S + K_G + K_A]$ are linked to the effect of rotation, $[C_n + C_r]$ and $[K_C n]$ are matrices accounting for damping, and $\{F\}$ is the nodal forces vector. The effects of rotation are divided into gyroscopic effects $[C]$, stress stiffening $[K_G]$, and spin softening $[K_S]$ effects, and into effects induced by rotational speed variations $[K_A]$. Two types of damping are considered: internal or rotating damping, $[C_r]$, and non-rotating damping, $[C_n]$ and $[K_C n]$. $\{F\}$ accounts for classical forces (weight, unbalance, etc.) as well as forces induced by the fluid. The developments leading to these motion equations are not presented here but can be found in Genta [12], Jacquet-Richardet et al. [13], and Hsieh and Abel [14].

A direct solution of Eq. (1) has major drawbacks. First, when considering real structures, the number of degrees-of-freedom needed for an accurate analysis is large, leading to prohibitive computer costs. Secondly, fluid effects must be transferred into nodal equivalent forces, leading generally to information losses. Thirdly, a full fluid and structural model, using compatible meshes and numerical procedures, is often not desirable as it supposes the use of very specific tools. As shown below, these drawbacks can be overcome by considering a modal approach coupled with the use of an interfacing grid concept.

Modal Reduction. Let us consider the undamped structure at rest in a vacuum. Thus, in this case, Eq. (1) reduces to

$$[M]\{\ddot{\delta}\} + [K_E]\{\delta\} = \{0\}. \quad (2)$$

The solution of this system, done directly or by using a cyclic symmetrical approach, gives a set of mode shapes $\{\Phi_{ij}\}$, which can be grouped into a modal matrix $[\Phi]$. Assuming that the unknown displacements $\{\delta\}$ can be written as a linear combination of these basic shapes, then

$$\{\delta\} = [\Phi]\{q\}. \quad (3)$$

Equation (1) becomes

$$[m]\{\ddot{q}\} + [c]\{\dot{q}\} + [k]\{q\} = \{f\} \quad (4)$$

where $[m]$, $[c]$, and $[k]$, respectively, modal mass, damping, and stiffness matrices, are full matrices obtained from

$$[m] = [\Phi]^T [M] [\Phi] \\ [c] = [\Phi]^T [C + C_n + C_r] [\Phi] \quad (5)$$

$$[k] = [\Phi]^T [K_E + K_S + K_G + K_A + K_C n] [\Phi].$$

Similarly, disregarding forces induced by the fluid, the modal forces vector is obtained from

$$\{f\} = [\Phi]^T \{F\}. \quad (6)$$

Equation (4) is solved within a time-marching procedure with information passing between fluid and structural domains through an interface grid. In addition to the reduction in computational effort, the modal approach gives two other important advantages. First, modal quantities can be obtained using different original meshes and numerical schemes. Secondly, structural damping can be introduced in its modal form using, for example, experimental results. This reduction has been validated with respect to numerical and experimental reference results in Jacquet-Richardet et al. [13,15].

Fluid-Structure Coupling and Solution. The coupled system is composed of a structural domain, a fluid domain and the associated fluid structure interface. The structure is discretized using finite elements, for example, an efficient 20 nodes volume

isoparametric element. For the fluid domain, various discretization techniques are used classically: finite elements, finite volumes, finite differences and the mesh is often very fine (much more than the structural mesh). Consequently, the two meshes are usually not compatible at the interface, both considering the type of discretization technique and the mesh density. To maintain fluid and structure mesh properties, an interface grid concept is used.

Modal quantities are physical quantities and thus are independent of the mesh used, provided the latter is fine enough. Consequently, if mode shapes and fluid-induced pressures are known on a grid, situated at the interface between the two domains but independent from the original meshes, the modal forces induced by the fluid can be obtained simply from

$$\{f\} = [\Phi_I]^T \{F_I\} \quad (7)$$

where $[\Phi_I]$ is the projection of mode shapes onto the interface grid and $\{F_I\}$ the nodal equivalent forces calculated from the pressure field, considering the intrinsic shape functions of the interface grid.

The interface grid considered is constituted with planar four-noded finite elements. It is linked to the undeformed interface, rotates with the structure and is as fine as the finest mesh, which is usually the fluid mesh. This grid gives obvious advantages in terms of efficiency because, in this case, basic meshes can be constructed independently, considering only the convergence requirements of each domain. It gives also advantages in terms of flexibility, because, for coupling, nothing needs to be known concerning the intrinsic characteristics of the original elements used. The only information needed is the location of nodes and the associated nodal displacements for the structure and pressures for the fluid, information which is easily available when using existing codes.

The coupling process implies several transfers between the original and interface grids:

- mode shapes from the structural mesh $[\Phi_S]$ to the interface grid $[\Phi_I]$,
- structural displacements and velocities, calculated using $[\Phi_I]$, $\{q\}$, and $\{\dot{q}\}$ according to (3), from the interface grid to the fluid mesh, and
- pressures from the fluid mesh to the interface grid.

The first transfer is done only once and is quite simple as it concerns data with smooth spatial variations. The two other transfers should be done for each time step but can be simple if the original fluid mesh is consistent with the interface grid. To perform a transfer from a grid G_s (s : source) to a grid G_t (target) of a physical field (pressure, displacements, etc.), the following algorithm is used:

- After locating the fluid/structure interface nodes of grid G_s , a new grid is established to connect these nodes with linear two-dimensional triangular elements. The resulting grid allows independence from the characteristics of G_s .
- Each node of grid G_t is then paired with a triangular cell and an interpolation/extrapolation scheme is used to compute the new values of the transferred field on G_t .

A full description of the transfer algorithm can be found in Moyroud et al. [16].

Equation (4) is solved using the Runge-Kutta's time-marching procedure of the fourth order. Very efficient for finding numerical solution of differential equations, this procedure is generally quite stable and accurate. For linear systems, the time step Δt used, shall verify $\Delta t < 1/10f_{\max}$, where f_{\max} is the highest frequency retained in the modal basis. However, due to the highly nonlinear property of hydrodynamic forces, the time step considered for the application is $\Delta t = 10^{-6}$ s, a value significantly lower than the classical limit ($1/10f_{\max} = 3.10^{-5}$ s).

The main steps of the solution technique are summarized in Fig. 1. The dependency of matrices upon rotational speed is fully

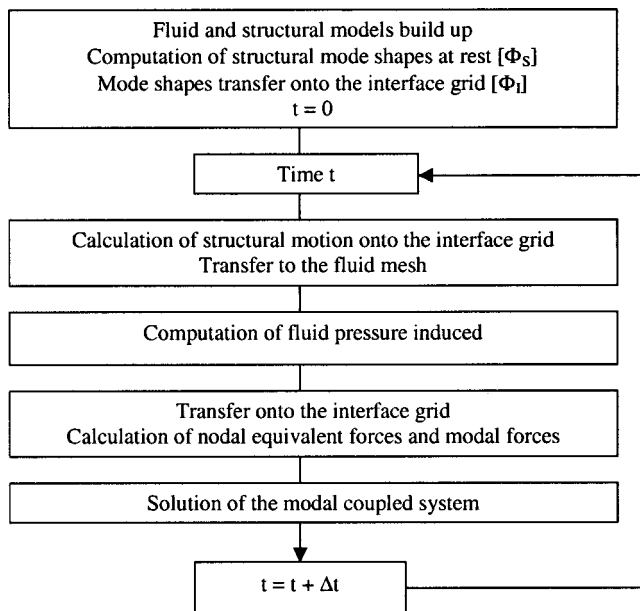


Fig. 1 Solution procedure

taken into account at each time step. For the application, where the effect of stress stiffening is not significant, the associated matrix has been linearized.

Fluid Model. The procedure proposed can be used whatever the fluid model. However, in order to keep the computational effort at an acceptable level, the application has been limited to cases involving thin fluid films where inertial effects are neglected and the flow is supposed to be laminar. For an incompressible fluid, without an effect of temperature, the pressure in the film is governed by the classical Reynolds equation. In a cylindrical frame, this equation is written as

$$\begin{aligned} & \frac{\partial}{\partial r} \left[r \frac{h^3}{\mu} \frac{\partial p}{\partial r} \right] + \frac{\partial}{\partial \theta} \left[\frac{h^3}{\mu r} \frac{\partial p}{\partial \theta} \right] \\ &= 6r(U_1 - U_2) \frac{\partial h}{\partial r} + 6r(V_1 - V_2) \frac{\partial h}{\partial \theta} \\ &+ 6h \left[\frac{\partial}{\partial r} (r(U_1 + U_2)) + \frac{\partial}{\partial \theta} (V_1 + V_2) \right] + 12r(W_2 - W_1) \end{aligned} \quad (8)$$

where μ is the fluid dynamic viscosity, h is the film thickness, and p the pressure in the fluid. U_i , V_i , W_i ($i=1,2$) are, respectively, the wheel ($i=1$) and casing ($i=2$) velocities in r (radial), θ (circumferential), and z (axial) directions.

Equation (8), associated with the Reynolds boundary conditions in the θ -direction is solved using finite differences associated with a Gauss-Seidel iterative process with over relaxation (Frêne et al. [2]).

Application

The main goal of the application presented here is to validate the proposed technique and to use it in order to show the possible effects of wheel-shaft-fluid couplings within rotating assemblies. Consequently, the case considered is kept simple, while remaining as representative as possible.

Description. The structure is composed of a shaft clamped at both ends and a disk mounted at 70% of shaft length. The dimensions of the shaft are the following: length $L=1.0$ m, inner radius $R_i=0.01$ m and outer radius $R_e=0.04$ m. The disk radius is R_d

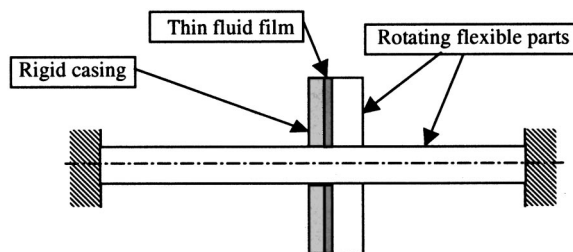


Fig. 2 Coupled disk-shaft-fluid system

$=0.2$ m and its thickness is $e=0.02$ m. Both shaft and disk are made of steel (Young's modulus $E=2.10^{11}$ Pa, density $\rho=7800$ kg/m³). The fluid film is clustered between the disk and a rigid casing (Fig. 2). Its thickness is $C=0.1$ mm and the fluid dynamic viscosity is $\mu=0.001$ Pa.s.

The structural mesh, presented in Fig. 3, is composed of 288 isoparametric 20 nodes finite elements, thus 2160 nodes. The fluid finite difference mesh, presented in Fig. 4, is composed of 1512 nodes. For this particular test case, the interface grid is originally superimposed on the fluid mesh, leading to a simple pressure transfer. The mode shapes kept for the modal reduction are chosen to allow all structural motions: bending, longitudinal and torsional shaft motions, disk motions, and coupled disk-shaft motions. A convergence study has shown that, for the case considered, 20 mode shapes are sufficient to give good results.

Validation of the Method. To validate the method, a three-dimensional rigid disk model is obtained by multiplying the stiffness of each disk element by 10,000. Then, the results obtained using the proposed approach are compared with those given by a classical rotordynamics one-dimensional approach, based on a beam finite element model of the shaft and a direct integration of fluid pressures induced by rigid disk motions into equivalent forces and moments. The four first frequencies of the isolated rotor at rest, obtained using both models, are presented in Table 1. These frequencies, associated with shaft bending, torsional, and longitudinal mode shapes, are in good agreement.

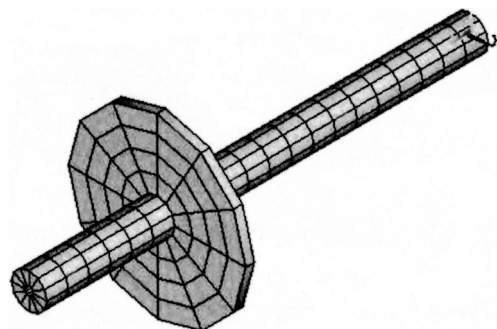


Fig. 3 Structural finite element mesh

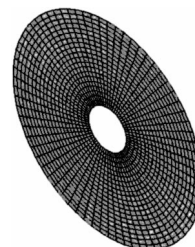


Fig. 4 Fluid finite difference mesh

Table 1 Frequencies of the isolated rigid disk flexible shaft system at rest

	1D	3D Rigid Disk	Δ (%)
1st bending (Hz)	278.	281.	1.1
2nd bending (Hz)	738.	745.	1.0
1st torsion (Hz)	316.	314.	-0.6
1st longitudinal (Hz)	1912.	1912.	0.0

Both isolated and coupled rotors are then considered under rotation with a constant vertical force $F_y = -1000$ N applied on the shaft at disk level, and an unbalance equal to 100 g.cm applied on the disk. In this case, since the structure is symmetric, only the forward whirling bending mode can be excited. Discrepancies in the stationary equilibrium vertical position of shaft midline at disk level (y) and in the two first bending frequencies of the structure rotating at 10,000 rpm, obtained from both one-dimensional and three-dimensional models, are presented in Table 2. Here, too, agreement remains very good.

The full unbalance response is presented in Fig. 5 for an increase of rotation speed from 15,000 to 25,000 rpm in two seconds at constant angular acceleration (5000 rpm/s). The response in the vertical direction (y) is reported.

The results presented confirm the considerable effect of fluid, which induces an increase of 26% in critical speed (from 17,950 rpm to 22,650 rpm) and a decrease of 20% in the amplitude at resonance (from 576 μm to 459 μm).

Effect of Disk Flexibility. The results obtained when disk flexibility is accounted for are presented in Table 3 (FD), where they are compared to those associated with the three-dimensional rigid disk model (RD). The effect of disk flexibility appears clearly. This effect remains low when the structure is isolated but is considerable for the whole fluid-structure coupled system. In this case, the rigid disk model underestimates the static displacement by a factor of about 30% and overestimates the first fre-

Table 2 Rigid disk system under rotation at $\Omega = 10,000$ rpm: discrepancies in equilibrium position and frequencies

	Isolated (%)	Coupled (%)
y (μm)	-2.6	-2.1
F_1 (Hz)	1.0	1.4
F_2 (Hz)	1.1	0.6

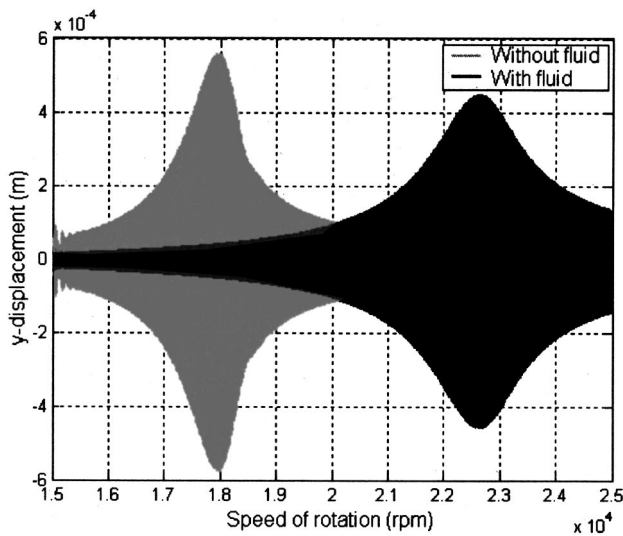


Fig. 5 Unbalanced response of the isolated and coupled systems (vertical displacement—rigid disk model)

Table 3 Influence of disk flexibility (RD: 3D Rigid Disk—FD: 3D Flexible Disk). $\Omega = 10,000$ rpm

	Isolated			Coupled		
	RD	FD	Δ (%)	RD	FD	Δ (%)
y (μm)	-7.5	-7.6	1.3	-5.23	-6.75	29.1
f_1 (Hz)	288.	288.	0.0	375.	320.	-14.7
f_2 (Hz)	763.	735.	-3.7	830.	801.	-3.5

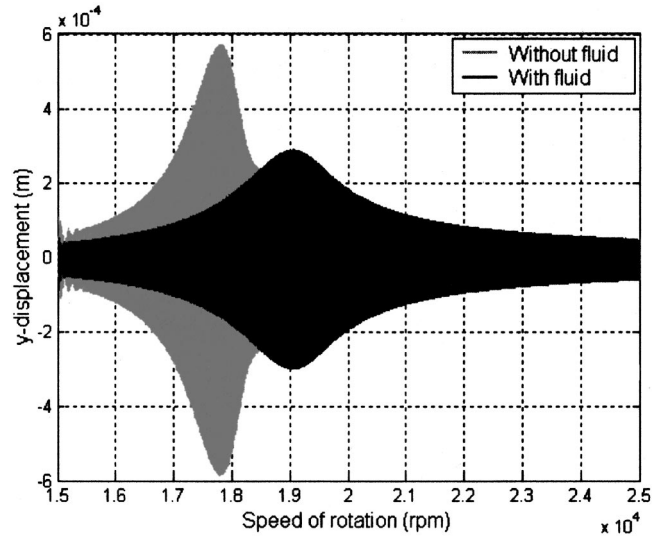


Fig. 6 Unbalanced response of the isolated and coupled systems (vertical displacement—three-dimensional flexible disk model)

Table 4 Discrepancies induced by the rigid disk hypothesis when considering fluid influence (Ω_{crit} critical speed, y_{max} maximal displacement of the response)

	Rigid Disk—Flexible Shaft		Δ (%)
	Isolated	Coupled	
Ω_{crit} (rpm)	17950.	22650.	26.2
$ y_{\text{max}} $ (μm)	576.	459.	-20.3
Flexible Disk—Flexible Shaft			
	Isolated	Coupled	Δ (%)
Ω_{crit} (rpm)	17800.	19050.	7.0
$ y_{\text{max}} $ (μm)	586.	301.	-48.6

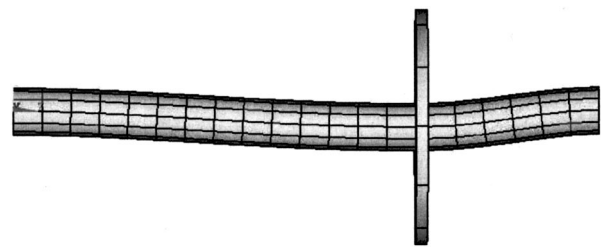


Fig. 7 Deformed shape of the rigid disk—flexible shaft assembly with fluid influence. $\Omega = 10,000$ rpm.

quency by a factor of 15%. The unbalance response obtained with the flexible disk model is given in Fig. 6. When comparing the results presented in Fig. 6 to those already shown in Fig. 5, it appears clearly that the rigid disk model overestimates the critical speed of the rotor as well as the displacement at resonance. These results are confirmed quantitatively when examining Table 4,

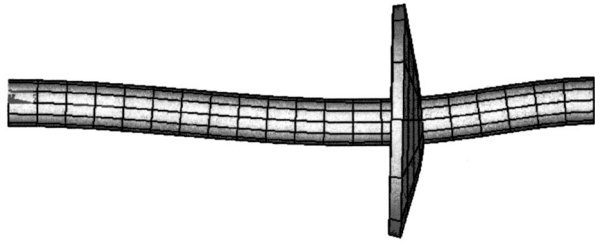


Fig. 8 Deformed shape of the flexible disk—flexible shaft assembly with fluid influence. $\Omega = 10,000$ rpm.

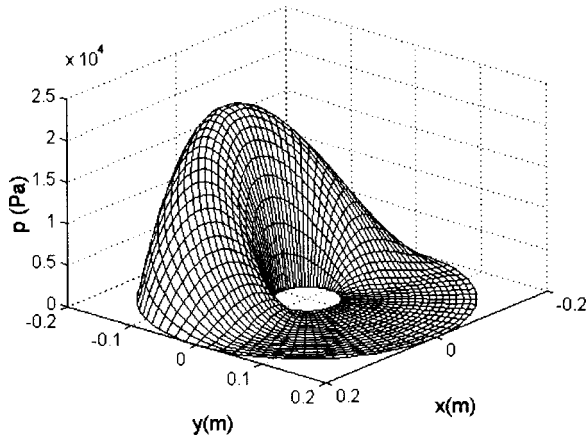


Fig. 9 Pressure field at the interface. Rigid disk—flexible shaft assembly. $\Omega = 10,000$ rpm.

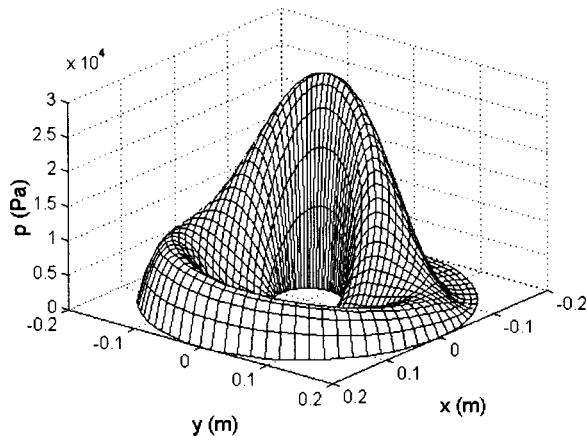


Fig. 10 Pressure field at the interface. Flexible disk—flexible shaft assembly. $\Omega = 10,000$ rpm.

which summarizes fluid effects as well as the associated discrepancies induced by the rigid disk hypothesis.

The deformed shape of the coupled disk-shaft assembly is illustrated in Fig. 7 for the rigid disk configuration and in Fig. 8 for the flexible disk configuration. Displacements are multiplied by a factor of 5000. The associated pressure fields are presented in Figs. 9 and 10, respectively. When examining those figures, the influence of disk flexibility appears clearly.

Conclusion

The classical rotordynamics approach, which considers only shaft flexibility and assumes that wheels mounted on it remain rigid, has proven its efficiency for solving many practical cases. In particular, this method is well adapted to the study of slender solid

shafts coupled with fluid bearings. However, when shafts are short, hollow thin walled, or when considering the effect of leakage flows which take place between wheels and casings, the effect of coupling between the fluid and local structural motions can be significant and requires examination.

The proposed procedure is based on a global three-dimensional model of the coupled fluid-wheel-shaft assembly. Its major interest lies in the integration of a modal reduction, associated with an interface grid concept, which allows a major reduction in computational effort and leads to efficient coupling between fluid and structural models developed independently using existing available tools.

The procedure is applied to a simple shaft-disk-thin fluid film assembly. A rigid three-dimensional model is considered first in order to perform a validation by comparison of the results obtained to those given by a rotordynamics one-dimensional approach. The influence of disk flexibility is then highlighted. For the case considered, the rigid wheel shaft model significantly overestimates both the critical speeds and displacements caused by an unbalance.

References

- [1] Childs, D. W., 1993, *Turbomachinery Rotordynamics Phenomena, Modeling and Analysis*, John Wiley and Sons, New York.
- [2] Frêne, J., Nicolas, D., Degueurce, B., Berthe, D., and Godet, M., 1990, *Lubrification Hydrodynamique-Paliers et Butées*, Eyrolles, Paris.
- [3] Diewald, W., and Nordmann, R., 1989, "Dynamic Analysis of Centrifugal Pump Rotors With Fluid Mechanical Interactions," *ASME J. Vib., Acoust., Stress, Reliab. Des.*, **111**(4), pp. 370–378.
- [4] Iwatsubo, T., Sheng, B. C., and Ono, M., 1990, "Experiment of Static and Dynamic Characteristics of Spiral Grooved Seals," 6th Workshop Rotordynamic Instability Problems in High Performance Turbomachinery, Texas A&M University, College Station, TX.
- [5] Desbordes, H., Fillon, M., Chan Hew Wai, C., and Frêne, J., 1994, "Dynamic Analysis of Tilting-Pad Journal Bearing—Influence of Pad Deformations," *ASME J. Tribol.*, **116**(3), pp. 621–628.
- [6] Berger, S., 1999, "Etude du comportement dynamique non linéaire d'un rotor monté sur éléments fluides: caractérisation des étanchéités—influence des butées," Thèse de doctorat, Université de Poitiers, France.
- [7] Van de Vrande, B. L., and De Kraker, B., 1999, "Influence of Bearing Compliance on Long-Term Nonlinear Rotordynamics," *Proceedings of the 1999 ASME Design Engineering Technical Conferences*, Las Vegas, NV, DETC99/VIB-8043, ASME, New York.
- [8] Childs, D. W., 1989, "Fluid-Structure Interaction Forces at Pump-Impeller-Shroud Surfaces for Rotordynamic Calculations," *ASME J. Vib., Acoust., Stress, Reliab. Des.*, **111**(3), pp. 216–225.
- [9] Childs, D. W., 1991, "Fluid-Structure Interaction Forces at a Pump-Impeller-Force Axial Analysis," *ASME J. Vib. Acoust.*, **113**(1), pp. 108–115.
- [10] Lalanne, M., and Ferraris, G., 1998, *Rotordynamics Prediction in Engineering*, 2nd Ed., John Wiley and Sons, Chichester, UK.
- [11] Bendiksen, O. O., 2000, "Transonic Bending Flutter in Rotors and Cascades," *Proc. 9th International Symposium on Unsteady Aerodynamics, Aeroacoustics and Aeroelasticity of Turbomachines*, Lyon, France.
- [12] Genta, G., 1995, *Vibration of Structures and Machines—Practical Aspects*, Springer-Verlag, New York.
- [13] Jacquet-Richardet, G., Ferraris, G., and Rieutord, P., 1996, "Frequencies and Modes of Rotating Flexible Bladed Disk-Shaft Assemblies: A Global Cyclic Symmetry Approach," *J. Sound Vib.*, **191**(5), pp. 901–915.
- [14] Hsieh, S.-H., and Abel, J. F., 1995, "Comparison of Two Finite Element Approaches for Analysis of Rotating Bladed-Disk Assemblies," *J. Sound Vib.*, **182**(1), pp. 91–107.
- [15] Jacquet-Richardet, G., and Rieutord, P., 1998, "A Three-Dimensional Fluid-Structure Coupled Analysis of Rotating Flexible Assemblies of Turbomachines," *J. Sound Vib.*, **209**(1), pp. 61–76.
- [16] Moyroud, F., Cosme, N., Jocker, M., Fransson, T. H., Lornage, D., and Jacquet-Richardet, G., 2000, "A Fluid-Structure Interfacing Technique for Computational Aeroelastic Simulations," *Proc. 9th International Symposium on Unsteady Aerodynamics, Aeroacoustics and Aeroelasticity of Turbomachines*, Lyon, France, Presses Universitaires de Grenoble, Grenoble, pp. 721–738.

Measurements Versus Predictions for the Dynamic Impedance of Annular Gas Seals—Part I: Test Facility and Apparatus

M. P. Dawson

Senior Engineer
Pratt and Whitney,
400 Main Street,
M/S 162-20,
East Hartford, CT 06108

D. W. Childs

Jordan Professor of Mechanical Engineering

C. G. Holt

Research Assistant

S. G. Phillips

Research Engineer
Turbomachinery Laboratory,
Texas A&M University,
College Station, TX 77843-3123

An experimental facility and apparatus are described for measuring the dynamic impedance and leakage characteristics of annular gas seals. The apparatus currently has a top speed of 29,800 rpm and can accommodate seal diameters up to 114.3 mm. The air-supply system can provide up to 13.79 MPa (2000 psi) of pressure at the seal inlet. Test seals are configured in a back-to-back arrangement inside the stator and air enters a central inlet annulus at two opposed radial positions. Labyrinth seals and bleed ports located outboard of each test seal are used to control the pressure drop across the test seals. Two orthogonal, external hydraulic shakers are used to excite the test stator at frequencies up to 400 Hz. At a given operating condition, the apparatus can measure the rotordynamic impedance of a pair of identical seals over a broad frequency range using a single pseudo-random excitation waveform. Measurements are also made of seal leakage rates and upstream and downstream temperatures and pressures.

[DOI: 10.1115/1.1478075]

Introduction

Smooth-rotor/honeycomb-stator annular seals have been used successfully on a retrofit basis in replacing labyrinth seals to eliminate rotordynamic instabilities in centrifugal compressors (Zeidan et al. [1], Gelin et al. [2], and Childs and Moyer [3]) and steam turbines (Armstrong and Perricone [4]). However, initial efforts to develop a reliable analysis to predict the rotordynamic behavior of these seals were not successful. These efforts focused on the development of a one-control-volume bulk-flow model for plain (smooth) annular seals that utilized modified friction factors to account for seal surface roughness and included compensations for entrance and exit losses (Nelson [5], Elrod et al. [6], and Ha and Childs [7]). All of these models yield reaction-force/relative displacement motion of the form

$$-\begin{Bmatrix} f_{xg} \\ f_{yg} \end{Bmatrix} = \begin{bmatrix} K & k \\ -k & K \end{bmatrix} \begin{Bmatrix} x \\ y \end{Bmatrix} + \begin{bmatrix} C & c \\ -c & C \end{bmatrix} \begin{Bmatrix} \dot{x} \\ \dot{y} \end{Bmatrix} + M \begin{Bmatrix} \ddot{x} \\ \ddot{y} \end{Bmatrix}, \quad (1)$$

where the stiffness (K and k), damping (C and c), and inertia (M) coefficients are frequency independent. The inertia term is assumed to be negligible for labyrinth gas seals.

Childs [7], in an authors' reply, proposed a two-control-volume model approach for honeycomb annular gas seal analysis with an additional control volume to account for the capacitance of the gas in the honeycomb cells. Subsequently, Kleynhans and Childs [8] developed a numerical solution for the two-control-volume model that predicts strongly frequency-dependent rotordynamic coefficients. The two-control-volume model results indicate that the conventional frequency-independent coefficient model of Eq. (1) is not valid for honeycomb seals and provides a possible explanation for prior poor correlation between predictions and measurements.

However, previous experimental measurements were inadequate to evaluate the predictions from this new analysis because

of the limited excitation frequency range (only 40 to 70 Hz) of the available data (Childs et al. [9]). To evaluate the new model, a test facility and apparatus were developed to measure the dynamic impedance of annular gas seals over the broader excitation frequency range of 40 to 440 Hz. Part II of this paper presents measurements illustrating the frequency-dependent nature of honeycomb seal impedance and compares these measurements with predictions from the analysis of Kleynhans and Childs [8]. This paper provides the details of the test facility and apparatus design and operation in measuring the static characteristics and dynamic impedance of annular gas seals.

Test Facility and Apparatus

The seal tests were performed using the annular gas seal test stand (AGSTS) recently constructed by the Turbomachinery Laboratory at Texas A&M University. The AGSTS was constructed by modifying an existing hydrostatic bearing rig (HBR) to test hybrid hydrostatic-hydrodynamic bearings. A description of the HBR test stand can be found in Childs and Hale [10].

As illustrated in Fig. 1, The AGSTS rotor is supported in two hydrostatic bearings. Two nominally identical test seals are arranged facing each other inside the test stator and used in each test. High-pressure air enters in the center of the stator and discharges axially across the test seals. A closeup of the test section stator is provided in Fig. 2. Back-pressure labyrinth seals maintain pressure downstream of the test seals. The seal pressure ratio can be varied independently of supply pressure via bleed lines that are connected to each back-pressure annulus.

The target pressure ratios are 0.4 and 0.6, which are representative of the pressure ratios across the balance pistons of through-flow and back-to-back compressors, respectively. Static pressure and temperature are recorded in the center inlet annulus between the seals and in each of the back-pressure annuli between the test seals and the outer labyrinth seals. Swirl brakes are located immediately upstream of the exit labyrinths to minimize the seal's preswirl and the attendant cross-coupled stiffness coefficients. The flexible hose connecting the test stator

Contributed by the International Gas Turbine Institute (IGTI) of THE AMERICAN SOCIETY OF MECHANICAL ENGINEERS for publication in the ASME JOURNAL OF ENGINEERING FOR GAS TURBINES AND POWER. Paper presented at the International Gas Turbine and Aeroengine Congress and Exhibition, New Orleans, LA, June 4–7, 2001; Paper 01-GT-237. Manuscript received by IGTI, December 2000, final revision, March 2001. Associate Editor: R. Natole.

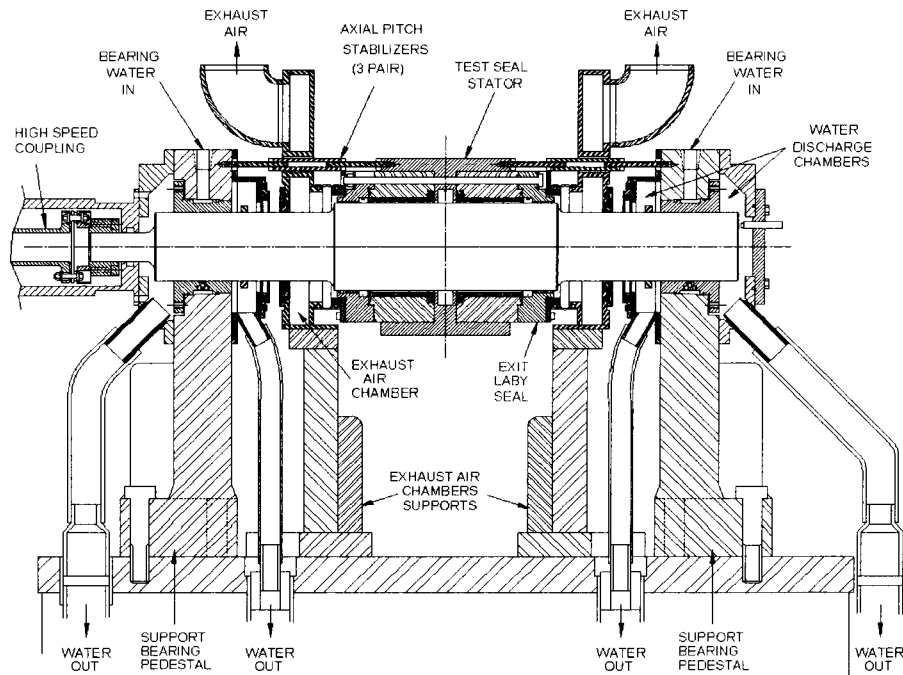


Fig. 1 The annular gas seal test stand

to the bearing pedestal provides a radially flexible containment for the lower pressure air conditions down stream of the test section.

Returning to Fig. 1, a pair of stabilizer arrays, each containing three equally spaced stabilizers, connects the test stator to each bearing pedestal. They prevent the stator from pitching during excitation, ensuring that it remains coaxial with the rotor, and

provide axial position control. The pitch stabilizers were designed to be stiff enough to control pitch yet flexible enough to allow radial movement of the stator.

The diameter of the rotor at the test section is 114.3 mm (4.500 in.). Each test seal has an L/D ratio of 0.75 (85.7 mm (3.375 in.) long). Seals are tested using compressed air with a maximum available supply pressure of 13.79 MPa (2000 psi). The high-pressure capability was not completed at the time the present tests were completed; hence test results cited in Part II are for a maximum supply pressure of 1.72 Mpa (250 psi). Test results with a supply pressure of 6.89 Mpa (1000 psi) have been completed subsequently and will be reported in the future. The stator inlet pressure is governed using an electronically controlled valve. Seal leakage flow rate is measured using a flow meter upstream of the stator. The rotor is driven by a 93.2 Kw (125 Hp) variable speed electric motor through a 7:1 ratio speed-increasing gear-box via a flexible disk coupling and has a maximum speed of 29,800 rpm.

The rotor is supported by two hybrid hydrostatic-hydrodynamic bearings using 7.58 MPa (1100 psi) water supplied by a centrifugal pump and flow loop left intact from the previous hydrostatic bearing rig (HBR). Accumulators are in place to provide pressurized bearings during coast-down in the event of pump failure. The first critical speed for the bearings/rotor-stator assembly is predicted to be near 30,000 rpm.

As with the HBR, the AGSTS has been designed to facilitate rapid testing of multiple seal configurations. The flexible coupling allows easy removal of the test rotor from the stand, and the stator design allows quick installation and removal of test seals. A complete seal test takes typically one week including assembly, calibration, testing, and disassembly of the test apparatus. Actual seal dynamic testing is managed by software and usually takes only a few hours. Data reduction is also expedited using software. A comprehensive logic-controlled monitoring and fault detection system provides partially or totally unassisted safe shutdowns to protect the test facility and apparatus.

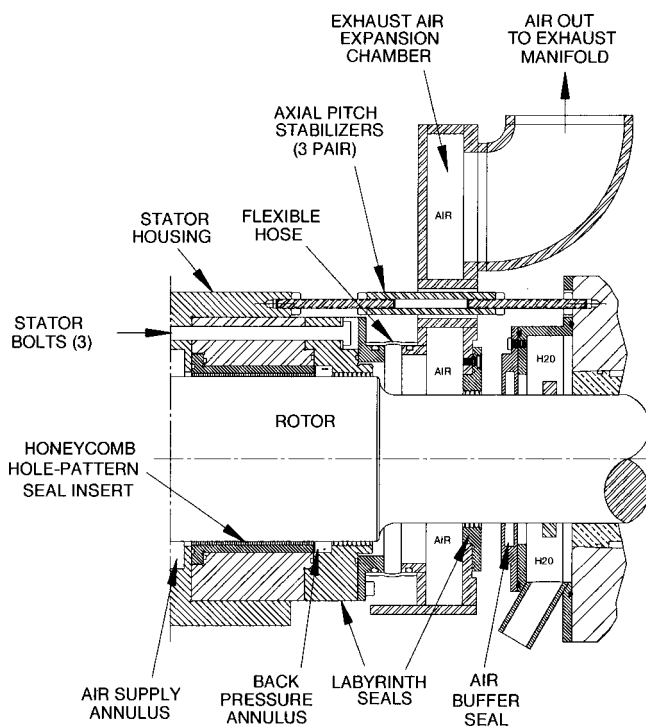


Fig. 2 Closeup of stator section

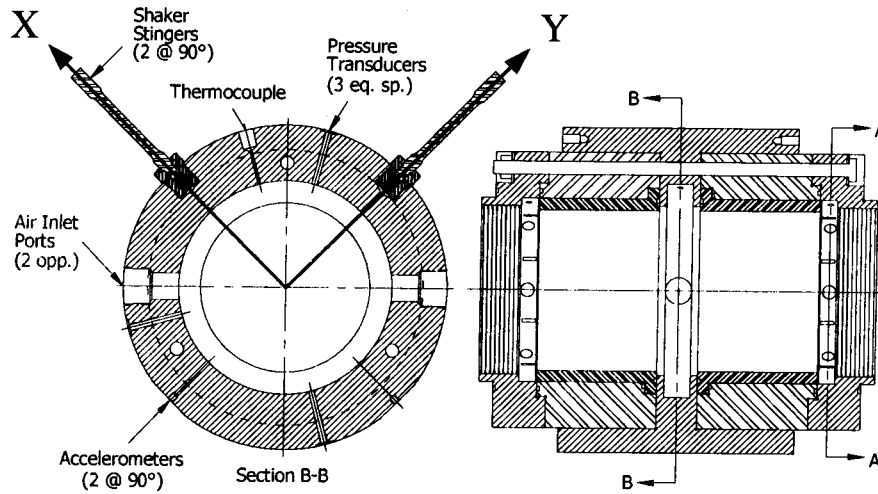


Fig. 3 Cross section of test stator: inlet annulus

Impedance Identification

Two hydraulic shakers, mounted orthogonal to one another, are attached to the test stator via isolation “stingers.” The “stingers,” as shown in Fig. 3, were designed using guidelines from Mitchell and Elliott [11]. The shakers can apply dynamic loads up to 4,450 N (1000 lb.) at frequencies up to 1000 Hz. The seal reaction forces are measured as the stator is excited using the hydraulic shakers. The equation of motion for the stator mass M_s in Fig. 3 is

$$M_s \begin{Bmatrix} \ddot{x}_s \\ \ddot{y}_s \end{Bmatrix} = \begin{Bmatrix} f_x \\ f_y \end{Bmatrix} + \begin{Bmatrix} f_{xg} \\ f_{yg} \end{Bmatrix}, \quad (2)$$

where \ddot{x}_s and \ddot{y}_s are the (measured) orthogonal stator accelerations, f_x and f_y are the (measured) shaker component input forces, and f_{xg} and f_{yg} are the (measured) annular gas seal reaction forces.

The stator is simultaneously shaken at multiple discrete frequencies using a predetermined pseudo-random waveform. The pseudo-random waveform is an ensemble of discrete sinusoids with frequencies every 10 Hz from 40 out to a potential maximum of 440 Hz. The phase of the sinusoids is optimized to provide a composite loading function with a high spectral-line energy to crest-factor ratio. Childs and Hale [10] provide a more in-depth discussion of the power cross spectral density method used to calculate a frequency-response function \mathbf{H}_{ij} . The elements of the frequency-response function are related to the stiffness and damping coefficients of Eq. (1) by the following expressions (assuming inertia $M=0$):

$$\mathbf{H}_{xx} = \mathbf{H}_{yy} = K + j(\Omega C) \quad (3)$$

$$\mathbf{H}_{yx} = -\mathbf{H}_{xy} = k + j(\Omega c). \quad (4)$$

Utilizing a PC-controlled data acquisition system, the AGSTS measures 32 100 millisecond time samples of force, acceleration, and displacement. These time samples are transformed to the frequency domain and averaged. In combining Eqs. (1) and (2), the results of the transformation and averaging yield

$$\begin{Bmatrix} \mathbf{F}_x - M_s \mathbf{A}_x \\ \mathbf{F}_y - M_s \mathbf{A}_y \end{Bmatrix} = \begin{bmatrix} \mathbf{H}_{xx} & \mathbf{H}_{xy} \\ \mathbf{H}_{yx} & \mathbf{H}_{yy} \end{bmatrix} \begin{Bmatrix} \mathbf{X} \\ \mathbf{Y} \end{Bmatrix}, \quad (5)$$

where

$$\mathbf{H}_{xx} = \mathbf{H}_{yy} = \mathbf{D}(j\Omega) \quad (6)$$

$$\mathbf{H}_{xy} = -\mathbf{H}_{yx} = \mathbf{E}(j\Omega). \quad (7)$$

In turn, the frequency-dependent direct $\mathbf{D}(j\Omega)$ and cross-coupled $\mathbf{E}(j\Omega)$ impedances can be expressed in terms of frequency-dependent stiffness $K(j\Omega)$ and $k(j\Omega)$ and damping $C(j\Omega)$ and $c(j\Omega)$ as shown below:

$$\mathbf{D}(j\Omega) = K(\Omega) + j\Omega C(\Omega) \quad (8)$$

$$\mathbf{E}(j\Omega) = k(\Omega) + j\Omega c(\Omega). \quad (9)$$

The frequency-dependent impedances $\mathbf{D}(j\Omega)$ and $\mathbf{E}(j\Omega)$ are determined for each seal test case. Since Eq. (5) has four unknowns and only two equations, two independent orthogonal dynamic loads are applied to yield the four necessary equations to solve for the impedance. The two independent excitations are obtained by alternately exciting the stator in each orthogonal direction (x and y). In addition to providing the excitation necessary to measure the dynamic impedance of the test seals, the shakers are also used to maintain the static position of the stator at a given eccentricity with respect to the rotor.

Six high-sensitivity inductance-type proximity transducers, located in each back-pressure annulus shown in Fig. 4, record the relative motion of the stator with respect to the rotor for each axis of excitation. These proximity probes are used to determine both the static position and dynamic motion of the stator relative to the rotor. Accelerometers and load cells are used to measure stator acceleration and reaction forces. The dynamic measurements obtained from the proximity transducers, the load cells, and the accelerometers are used to determine frequency-dependent direct $\mathbf{D}(j\Omega)$ and cross-coupled $\mathbf{E}(j\Omega)$ impedances of the test seals.

Prior to starting a test, the proximity probes, accelerometers, load cells, pressure transducers, thermocouples, and flow meter are calibrated with the data acquisition system. With the hydrostatic bearings operational and air flowing through the seals, the stator is centered on the rotor using the hydraulic shakers by lightly “bumping” the stator against the rotor in each orthogonal direction. The center of the rotor is set as the midpoint of the distances the stator travels in each direction. Finally, inlet and back pressures are set/adjusted along with the rotor speed to the desired steady-state condition. Once at a steady-state operating condition, the stator is alternately excited in orthogonal directions using a predetermined pseudo-random waveform.

In addition to tests performed with the test seals inside the stator, another set of “baseline” tests is performed with the test seals removed. The supply pressure for the baseline tests is reduced to match the pressure upstream of the exit labyrinth seals during regular tests and is set to around 40% to 60% of the normal

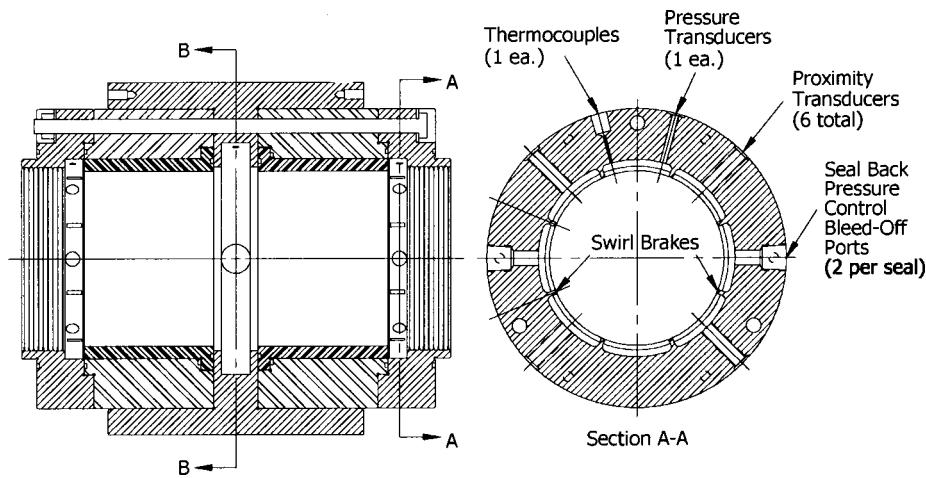


Fig. 4 Cross section of test stator: back-pressure annulus

supply pressure. These tests establish the impedance for the baseline test stand—including the back-pressure labyrinth seals, the pitch and yaw stabilizers, the hydraulic shaker stingers, etc. Subtracting the baseline impedance from the overall test impedance yields the impedance of the seals alone.

Uncertainty Analysis

The primary concerns for uncertainty with the results presented are instrumentation (load cells, motion probes, accelerometers, pressure transducers, thermocouples, flow meters). Efforts to minimize transducer and instrumentation uncertainty were observed carefully. Motion probes, pressure transducers, thermocouples, and flow meters were calibrated before operation in the new AGSTS.

Static parameter uncertainties (shaft speed, pressure, and flow rate), used either as inputs for the prediction code or as comparisons of measurement to prediction, have been estimated by Kurtin et al. [12] for the HBR test rig and apply to the AGSTS as well. The static parameter uncertainties are listed in Table 1.

Table 1 Static parameter uncertainties

Parameter	Uncertainty
Shaft speed	± 10 rpm
Pressure	± 0.003747 MPa
Flow rate	± 0.177 liters/min
Eccentricity ratio	± 0.03

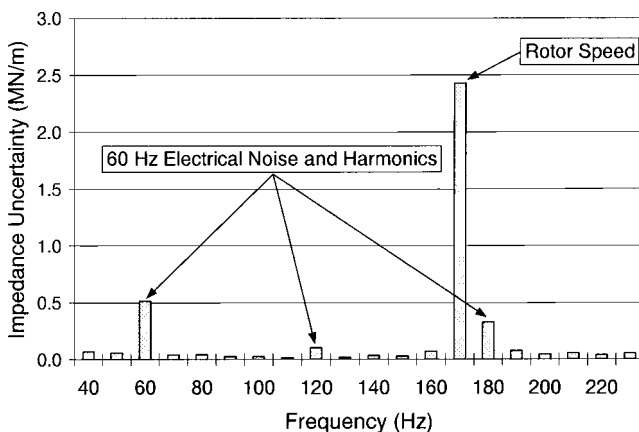


Fig. 5 AGSTS typical uncertainty spectrum

The seal impedance is obtained by exciting the stator with a pseudo-random waveform (ensemble of sinusoidal excitations) 32 times and then averaging the resultant individual impedances in the frequency domain. The uncertainty of the resultant impedances varies strongly with excitation frequency; e.g., a data point near running speed has a high degree of uncertainty because the imbalance excitation is not accounted for in parameter identification. Hence, conventional static uncertainty analyses are not appropriate. For the dynamic measurements, an uncertainty test was performed for each seal by running ten identical tests (each containing 32 excitations) to obtain an average and ± 1 standard deviation at each frequency of interest. In Part II of this research paper, the results for each frequency are shown with error bars that represent a ± 1 standard deviation for each frequency.

Figure 5 shows a typical uncertainty spectrum for an annular gas seal test conducted using the AGSTS. As one can see, high-precision error occurs at 60 Hz, 120 Hz, and 170 Hz, and these frequencies are omitted from the data presented in Part II of this paper. Very low precision at 180 Hz can be attributed to the close proximity to 170 Hz running speed. The 180 Hz frequency is also the second harmonic of electrical noise. Due to the introduced error of electrical noise and close proximity to running speed, the 180 Hz frequency contribution is also removed from the impedance data.

Summary and Comments

The AGSTS has been developed and used to test annular gas seals over an extended frequency range. Measurements include static (pressure, flow, and temperature) and dynamic (force, acceleration, and displacement) seal characteristics. The test facility and apparatus was developed to evaluate the two-control-volume model of Ha and Childs [7] and predictions by Kleynhans and Childs [8] of strongly frequency-dependent reaction-force/motion models. Comparisons between analytical predictions and measured seal impedance and leakage flow rate are presented for a honeycomb seal in Part II of this paper.

Nomenclature

- A_x, A_y = Fourier transformed components of stator acceleration (L/T^2)
- C, c = direct and cross-coupled damping coefficients (FT/L)
- C_{eff} = effective damping coefficient (FT/L)
- $C(\Omega), c(\Omega)$ = frequency-dependent direct and cross-coupled damping (FT/L)
- $D(j\Omega)$ = complex direct impedance (F/L)
- $E(j\Omega)$ = complex cross-coupled impedance (F/L)

f_x, f_y = stator excitation input force components (F)
 $\mathbf{F}_x, \mathbf{F}_y$ = Fourier transformed components of f_x and f_y (F)
 f_{xg}, f_{yg} = annular gas seal reaction force components (F)
 $\mathbf{H}_{ij}(j\Omega)$ = frequency-response functions (F/L)
 $j = \sqrt{-1}$
 K, k = direct and cross-coupled stiffness coefficients (F/L)
 K_{eff} = effective stiffness coefficient (FT/L)
 $K(\Omega), k(\Omega)$ = frequency-dependent direct and cross-coupled stiffness (F/L)
 M = direct inertia coefficient (M)
 M_s = stator mass (M)
 x, y = seal/rotor relative motion in orthogonal directions (L)
 \mathbf{X}, \mathbf{Y} = Fourier transformed components of seal/rotor relative motions in orthogonal directions (L)
 Ω = excitation frequency ($1/L$)

Subscripts

s = stator
 x, y = motion direction (L)

References

- [1] Zeidan, F., Perez, R., and Stephenson, E., 1993, "The Use of Honeycomb Seals in Stabilizing Two Centrifugal Compressors," *Proceedings of the 22nd Turbomachinery Symposium*, Turbomachinery Laboratory, Texas A&M University, pp. 3–15.
- [2] Gelin A., Pugnet, J., Bolusset, D., and Freiz, P., 1996, "Experience in Full Load Testing Natural Gas Compressors for Rotordynamic Improvements," ASME Paper No. 96-GT-378.
- [3] Childs, D., and Moyer, D., 1985, "Vibration Characteristics of the HPOTP (High-Pressure Oxygen Turbopump) of the SSME (Space Shuttle Main Engine)," ASME J. Eng. Gas Turbines Power, **107**, pp. 152–159.
- [4] Armstrong, J., and Perricone, F., 1996, "Turbine Instability Solution—Honeycomb Seals," *Proceedings of the 25th Turbomachinery Symposium*, Turbomachinery Laboratory, Texas A&M University, pp. 47–56.
- [5] Nelson, C., 1984, "Analysis for Leakage and Rotordynamic Coefficients of Surface-Roughened Tapered Annular Gas Seals," ASME J. Eng. Gas Turbines Power, **106**, pp. 927–934.
- [6] Elrod, D., Childs, D., and Nelson, C., 1990, "An Annular Gas Seal Analysis Using Empirical Entrance and Exit Region Friction Factors," ASME J. Tribol., **112**, pp. 254–258.
- [7] Ha, T., and Childs, D., 1994, "Annular Honeycomb-Stator Turbulent Gas Seal Analysis Using New Friction-Factor Model Based on Flat Plate Tests," ASME J. Tribol., **116**, pp. 352–360.
- [8] Kleyhans, G., and Childs, D., 1997, "The Acoustic Influence of Cell Depth on the Rotordynamic Characteristics of Smooth-Rotor/Honeycomb-Stator Annular Gas Seals," ASME J. Eng. Gas Turbines Power, **119**, pp. 949–957.
- [9] Childs, D., Nelson, C., Nicks, C., Scharer, J., Elrod, D., and Hale, K., 1986, "Theory Versus Experiment for the Rotordynamic Coefficients of Annular Gas Seals: Part I—Test Facility and Apparatus," ASME J. Tribol., **108**, pp. 426–432.
- [10] Childs, D., and Hale, K., 1994, "A Test Apparatus and Facility to Identify the Rotordynamics Coefficients of High-Speed Hydrostatic Bearings," ASME J. Tribol., **116**, pp. 337–344.
- [11] Mitchell, L., and Elliott, K., 1984, "How to Design Stingers for Vibration Testing of Structures," *Sound Vib.*, **Apr**, pp. 14–18.
- [12] Kurtin, K. A., Childs, D. W., San Andrés, L. A., and Hale, R. K., 1993, "Experimental Versus Theoretical Characteristics of a High-Speed Hybrid (Combination Hydrostatic and Hydrodynamic) Bearing," ASME J. Tribol., **115**, pp. 160–169.

Measurements Versus Predictions for the Dynamic Impedance of Annular Gas Seals—Part II: Smooth and Honeycomb Geometries

M. P. Dawson

Senior Engineer
Pratt and Whitney,
400 Main Street,
M/S 162-20,
East Hartford, CT 06108

D. W. Childs

Jordan Professor of Mechanical Engineering
Turbomachinery Laboratory,
Texas A&M University,
College Station, TX 77843-3123

Results are presented from tests conducted using an experimental test facility to measure the leakage and dynamic impedance of smooth and honeycomb straight-bore annular gas seals. The test seals had a 114.3 mm (4.500 in.) bore with a length-to-diameter ratio of 0.75 and a nominal radial clearance of 0.19 mm (0.0075 in.). The honeycomb cell depth for both seals was 3.10 mm (0.122 in.), and the cell width was 0.79 mm (0.031 in.). Dynamic impedance and leakage measurements are reported using air at three supply pressures out to 1.72 Mpa (250 psi), three speeds out to 20,200 rpm, and exit-to-inlet pressure ratios of 40% and 50%. Comparisons to the predictions from the two-control-volume model of Kleynhans and Childs [1] are of particular interest. This model predicts that honeycomb seals do not fit the conventional frequency independent model for smooth annular gas seals. The experimental results verify this new theory. Numerical predictions from a computer program incorporating the new two-control-volume model of Kleynhans and Childs [1] correlate well with both measured seal leakage and dynamic impedances for the honeycomb seals. [DOI: 10.1115/1.1478076]

Introduction

Since the 1960s, smooth-rotor/honeycomb-stator annular seals have been used in process centrifugal compressors where they were employed as direct replacements for aluminum labyrinth seals that were being consumed by the process fluid. As it turned out, honeycomb seals had significantly less leakage compared to conventional see-through labyrinth seals at same clearances. Figure 1 provides an isometric view of a honeycomb seal and rotating shaft.

In addition to reducing leakage, honeycomb seals have been employed widely to eliminate instabilities in centrifugal compressors and steam turbines. Despite the favorable field experience with honeycomb seals, efforts to develop a reliable analysis proved unsuccessful. These efforts used a single-control-volume bulk-flow model for plain (smooth) annular seals and modeled honeycomb stator surfaces only by friction factor definitions, netting the following frequency-independent model for the reaction force components:

$$-\begin{Bmatrix} f_{xg} \\ f_{yg} \end{Bmatrix} = \begin{bmatrix} K & k \\ -k & K \end{bmatrix} \begin{Bmatrix} x \\ y \end{Bmatrix} + \begin{bmatrix} C & c \\ -c & C \end{bmatrix} \begin{Bmatrix} \dot{x} \\ \dot{y} \end{Bmatrix} + M \begin{Bmatrix} \ddot{x} \\ \ddot{y} \end{Bmatrix}, \quad (1)$$

where the annular gas seal reaction forces f_{xg} and f_{yg} are related to the relative orthogonal seal/rotor displacements x and y by the frequency-independent fluid (gas) stiffness (K and k), damping (C and c), and inertia (M) coefficients. The fluid inertia term is assumed to be negligible for annular gas seals.

A New Approach. In light of the limited success predicting rotor dynamic force coefficients with the conventional frequency-independent model of Eq. (1), Childs, in the author response in Ha

and Childs [1], proposed a two-control-volume model approach for honeycomb annular gas seal analysis. Subsequently, Kleynhans and Childs [2] developed bulk-flow solutions for the two-control-volume analysis that comprises a traditional flow-through control volume with an adjacent radial-flow control volume to model flow in and out of the honeycomb cells. The two-control-volume model is illustrated in Fig. 2.

The additional control volume drops the effective acoustic velocity of the gas passing through the seal so that the seal's first acoustic natural frequency drops into the frequency range of interest for rotor dynamics (below the running speed). Kleynhans and Childs' [2] two-control-volume analysis utilizes a general transfer function model of the form

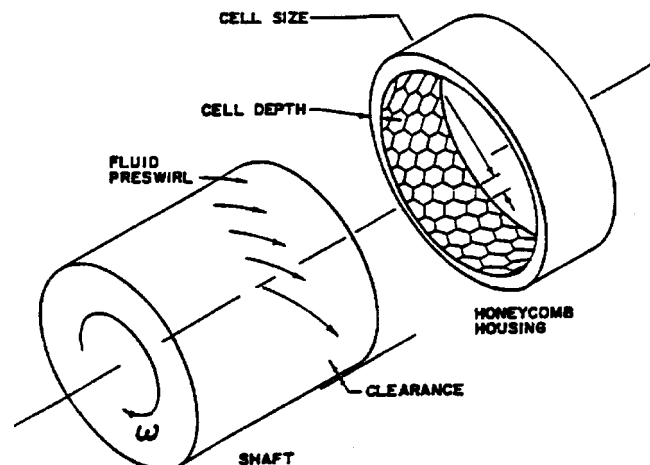


Fig. 1 Honeycomb annular seal and rotating shaft

Contributed by the International Gas Turbine Institute (IGTI) of THE AMERICAN SOCIETY OF MECHANICAL ENGINEERS for publication in the ASME JOURNAL OF ENGINEERING FOR GAS TURBINES AND POWER. Paper presented at the International Gas Turbine and Aeroengine Congress and Exhibition, New Orleans, LA, June 4–7, 2001; Paper 01-GT-238. Manuscript received by IGTI, December 2000, final revision, March 2001. Associate Editor: R. Natole.

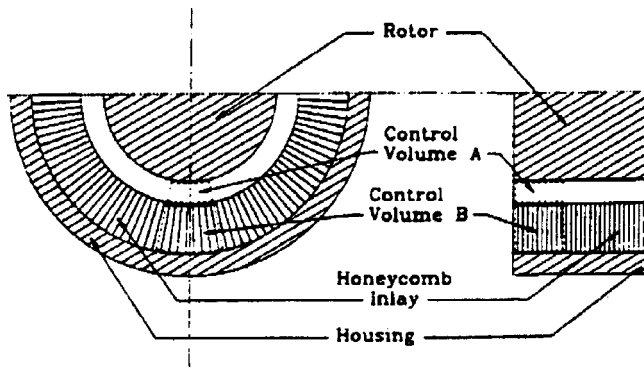


Fig. 2 Two-control-volume model: cross sections of honeycomb seal stator and rotor

$$-\begin{Bmatrix} \mathbf{F}_x(j\Omega) \\ \mathbf{F}_y(j\Omega) \end{Bmatrix} = \begin{bmatrix} \mathbf{D}(j\Omega) & \mathbf{E}(j\Omega) \\ -\mathbf{E}(j\Omega) & \mathbf{D}(j\Omega) \end{bmatrix} \begin{Bmatrix} \mathbf{X}(j\Omega) \\ \mathbf{Y}(j\Omega) \end{Bmatrix}. \quad (2)$$

The frequency-dependent stiffness and damping coefficients are defined in terms of the real and imaginary components of the direct and cross-coupled impedances $\mathbf{D}(j\Omega)$ and $\mathbf{E}(j\Omega)$ via

$$\mathbf{D}(j\Omega) = K(\Omega) + j\Omega C(\Omega) \quad (3)$$

and

$$\mathbf{E}(j\Omega) = k(\Omega) + j\Omega c(\Omega). \quad (4)$$

The effective stiffness and damping coefficients defined by

$$K_{\text{eff}} = K(\Omega) + \Omega c(\Omega) \quad (5)$$

and

$$C_{\text{eff}} = C(\Omega) - \frac{k(\Omega)}{\Omega}, \quad (6)$$

are useful for comparing the rotordynamic performance of two seals.

Previous experimental measurements were not adequate to evaluate the merit of this new two-control-volume analysis because of the limited excitation frequency range (only 40 to 70 Hz) of the data. To evaluate this new analysis, the test facility and apparatus described in Part I of this paper were developed and used to measure the dynamic impedances $\mathbf{D}(j\Omega)$ and $\mathbf{E}(j\Omega)$ of smooth and honeycomb annular gas seals. These tests were conducted over a broader excitation frequency range of 40 to 230 Hz.

This paper presents measurements illustrating the frequency-dependent nature of honeycomb annular gas seal impedance contrasted to the frequency-independent nature of smooth annular gas seal impedance. The measured honeycomb seal impedance and leakage data are then compared with predictions from ISOT-SEAL, a computer program incorporating the two-control-volume analysis of Kleynhans and Childs [2]. Subsequent publications will provide test results for convergent, tapered-bore honeycomb seals and hole-pattern seals.

Prior Test Results

Benckert and Wachter [3] first measured annular gas seal coefficients with labyrinth seals at the University of Stuttgart. Although their apparatus only yielded direct and cross-coupled stiffness coefficients, they were able to ascertain that eliminating the circumferential fluid flow within an annular seal clearance would reduce destabilizing cross-coupled seal forces.

Childs et al. [4] performed tests comparing a variety of honeycomb annular gas seals with labyrinth and smooth-surface seal configurations. Comparatively, these results showed that honeycomb seals offered minimum leakage and maximum stability (large direct damping and small cross-coupled stiffness).

Table 1 Seal geometry

Seal Parameter	Dimension
Diameter	114.30 mm
Length	85.70 mm
Radial clearance	0.19 mm
Cell depth (honeycomb seals)	3.10 mm
Cell width (honeycomb seals)	0.79 mm

Table 2 Seal test cases

Inlet Pressure, P_e (MPa)	Pressure Ratio, P_x/P_e	Speed, ω (rpm)
0.69	0.4	10,000
	0.6	15,000
		20,000
1.21	0.4	10,000
	0.6	15,000
		20,000
1.72	0.4	10,000
	0.6	15,000
		20,000

Seal Geometry and Test Cases

Using the procedures detailed in Part I of this paper, seal tests were performed using the annular gas seal test stand (AGSTS) recently developed within the authors' laboratory. The leakage flow rate and overall frequency response functions $\mathbf{D}(j\Omega)$ and $\mathbf{E}(j\Omega)$ (impedances) were measured for a pair of identical constant-clearance honeycomb annular gas seals along with a pair of smooth, straight-bore seals. Note that smooth seals are not used in compressors because of excessive leakage. They were tested here to contrast their frequency-independent behavior with the frequency-dependent nature of the honeycomb seals.

The honeycomb seal data were obtained to evaluate the predictions from the new two-control-volume model. The impedance measurements obtained with the smooth seals were included to demonstrate the validity of the frequency-independent coefficient model of Eq. (1). Both the smooth and honeycomb test seals had the same geometry with the exception of the honeycomb cells. Their geometry is summarized in Table 1.

Both tests seals had an L/D ratio of 0.75 and a C_r/R ratio of 0.0033. Although the seals were tested over an excitation frequency range of 40 to 440 Hz, data are reported only up to 230 Hz because of an unanticipated stator pitch mode that invalidated the data above 230 Hz. Subsequently, the pitch stabilizers were redesigned to be stiffer and data is currently being retained up to 380 Hz.

Each of the two pairs of annular gas seals was tested in the centered position only. Results were obtained for each test seal for three seal inlet pressures, two pressure ratios, and three speeds totaling 18 tests. Pressure ratio is defined as the ratio of seal exit to inlet pressure P_x/P_e . The test matrix is presented in Table 2.

In addition to the 18 test cases for each of the two test seals, an additional set of tests was performed with the test seals removed. This second set of tests established the impedance for the "baseline" test stand—including the back-pressure labyrinth seals, the pitch and yaw stabilizers, and the hydraulic shaker stingers. Subtracting this "baseline" impedance from the test impedance yields the impedance of the seals alone.

Computational Predictions

Plots of nondimensional radial I_r and tangential I_θ impedance versus frequency are shown in Figs. 3 and 4, respectively, as calculated for a typical honeycomb seal using the new two-control-volume analysis of Kleynhans and Childs [2]. Impedance is shown for increasing nondimensional honeycomb cell depths h_d .

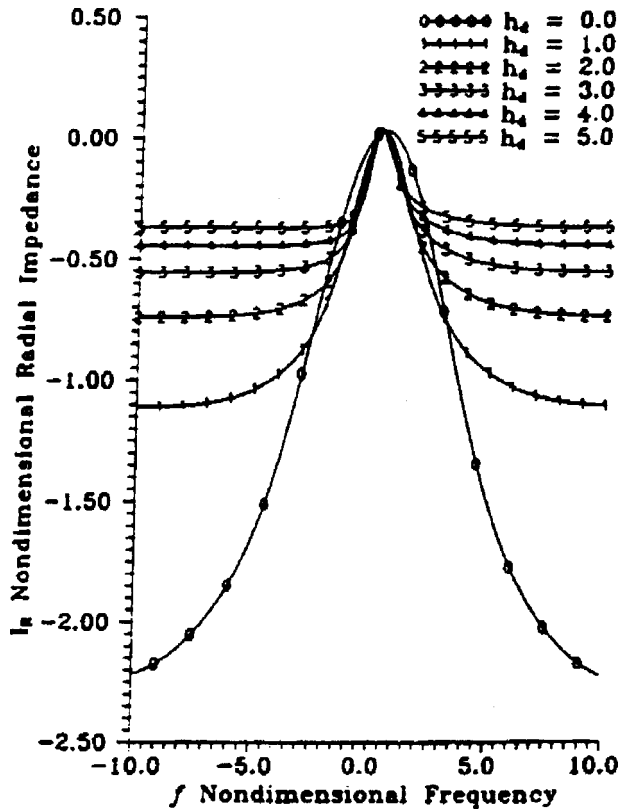


Fig. 3 Nondimensional radial impedance predictions

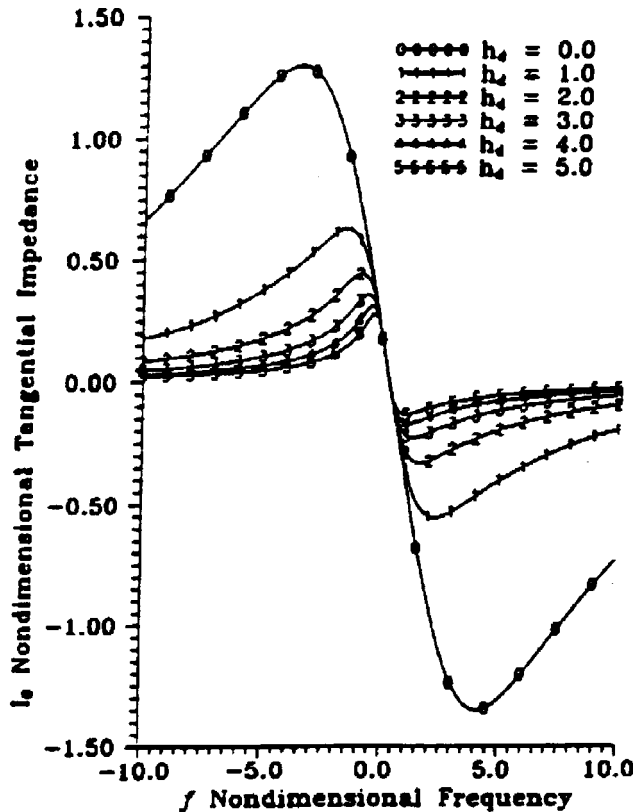


Fig. 4 Nondimensional tangential impedance predictions

Table 3 Example honeycomb seal parameters for Fig. 3

Seal Parameter	Dimension/Value
Inlet pressure	1.83 MPa
Exit pressure	0.44 MPa
Inlet temperature	29°C
Speed	15,960 rpm
Seal diameter	101.0 mm
Seal length	101.0 mm
Seal clearance	0.20 mm
Cell width	1.59 mm

The nondimensional honeycomb cell depth h_d is defined as the ratio of the effective honeycomb cell depth H_d to the seal radial clearance C_r .

The honeycomb seal parameters used in the calculation of the impedances shown in Figs. 3 and 4 are summarized in Table 3. The seal parameters in Table 3 are similar, but do not correspond to the test seals. The effective cell depth H_d is defined in Eq. (7) as the ratio of total honeycomb cell volume to seal surface area. This relationship accounts for the double-foil thickness present on two of each of the six honeycomb cell walls.

$$\frac{\text{Volume}}{\text{Area}} = H_d = \frac{3C_d(C_w - t)^2}{C_w(3C_w + 2t)} \quad (7)$$

The nondimensional frequency f is defined as the rotor precession frequency Ω divided by the rotor rotational frequency ω . The radial I_r and tangential I_θ impedance are defined in Eqs. (8) and (9) in terms of the seal force coefficients K , k , C , c , and M .

$$I_r(f) = (K - Mf^2) + cf \quad (8)$$

$$I_\theta(f) = k - Cf \quad (9)$$

As defined by Kleynhans [5], Eqs. (8) and (9) are nondimensionalized by multiplying the force coefficients by the radial seal clearance C_r and dividing by inlet pressure P_e , rotor radius R , and seal length L . The damping terms are additionally multiplied by the rotor rotational frequency ω and the mass term is additionally multiplied by ω^2 for nondimensionalization.

The Laplace transform model of Eq. (2) proposed by Kleynhans and Childs [2] requires the forms of the direct $\mathbf{D}(j\Omega)$ and cross-coupled $\mathbf{E}(j\Omega)$ impedances to be obtained from the radial I_r and tangential I_θ impedance solutions. For positive excitation frequencies, I_r and I_θ can be expressed in terms of $\mathbf{D}(j\Omega)$ and $\mathbf{E}(j\Omega)$ using the relationships shown in Eqs. (10) and (11).

$$\mathbf{D}(i\Omega) = -\text{Re}[I_r] - \text{Im}[I_\theta] \quad (10)$$

$$\mathbf{E}(i\Omega) = \text{Re}[I_\theta] - \text{Im}[I_r] \quad (11)$$

Looking at Figs. 3 and 4 for $h_d = 0.0$ (i.e., a smooth seal), the conventional frequency-independent coefficient model of Eq. (1) is sufficient over a wide frequency range as noted by the quadratic and linear portions of the I_r and I_θ curves, respectively. As the hole depth increases, the valid frequency range of the frequency-independent coefficient model decreases; i.e., the quadratic and linear ranges, respectively, of radial impedance I_r and tangential I_θ become smaller.

Kleynhans and Childs [2] developed ISOTSEAL (constant temperature, two-control-volume annular gas seal code) to predict frequency-dependent stiffness and damping coefficients and leakage. ISOTSEAL was used here to predict seal leakage flow rate and direct $\mathbf{D}(j\Omega)$ and cross-coupled $\mathbf{E}(j\Omega)$ impedances.

ISOTSEAL uses a two-control-volume solution for determining the seal impedance and then first attempts a conventional (single-control-volume) model curve fit. If the curve fit correlates well, the program will output conventional frequency-independent force

coefficients. Otherwise, it will output frequency-dependent coefficients. The conventional model is likely appropriate for short honeycomb seals with shallow cell depths.

The ISOTSEAL input data includes the operating conditions, seal geometry, entrance losses and exit recovery factors, and empirical rotor and stator friction coefficients used in the program's Blasius shear stress model. The empirical values for the Blasius rotor friction coefficients (n_r and m_r) were obtained from Yamada's [6] test data for smooth seals. The empirical values for the Blasius stator friction coefficients (n_s and m_s) are based on flat-plate friction factor data from Ha et al. [7] and were developed for this specific honeycomb geometry.

The effective cell depth H_d , defined in Eq. (7), of the honeycomb cells is referred to in ISOTSEAL as the cell volume to area ratio. Using the cell width, actual cell depth, and measured foil thickness ($t=0.10$ mm), a cell-volume-to-area ratio of 2.2 mm was calculated and used in the analysis of the honeycomb seals.

When running ISOTSEAL, the inlet preswirl ratio and entrance loss coefficients were set to zero. The preswirl ratio is the ratio of the tangential velocity component of the gas inside the seal clearance to the tangential velocity component of the rotor ($R\omega$). Setting the preswirl ratio to zero implies zero fluid (gas) rotation immediately upstream of the test seals. As discussed in Part I, the stator was designed to minimize preswirl by (1) having air enter the annulus radially at opposite sides of the stator and (2) making the cross-sectional area of the annulus as large as possible.

The entrance-loss coefficient accounts for head drops in excess of the inlet velocity-head loss, and Kleynhans [5] found the best correlation between predictions and measurements for this setting. The exit recovery factor accounts for a recovery of pressure immediately downstream of the seal exit. A recovery factor of 1.0 implies no recovery, and this value was used, also based on Kleynhans [5] results.

The entrance loss and exit recovery factors are empirical values that effect the computation of the inlet and outlet seal pressures used in the solution the pressure field inside the seal clearance. The predicted seal impedance is calculated from the seal reaction forces that are determined by integrating the pressure field of the seal surface area.

All three parameters have little to no effect on seal leakage predictions, and Childs et al. [4] showed that preswirl does not significantly effect dynamic seal characteristics for honeycomb seals with an L/D ratio greater than 1/3. Table 4 provides a sample list of the input parameters for ISOTSEAL from one test case of the honeycomb seals.

Table 4 Sample parameters used in ISOTSEAL

Input Parameter	Metric Units
Reservoir pressure	1.72 MPa (250 psia)
Sump pressure	0.69 MPa (100 psia)
Reservoir temperature	28.89°C (84°F)
Rotational speed	20,200 rpm
Seal diameter	114.3 mm (4,500 in.)
Seal length	85.7 mm (3,375 in.)
Inlet clearance	0.19 mm (7.5 mils)
Exit clearance	0.19 mm (7.5 mils)
Cell volume/area ratio	2.20 mm (87 mils)
Inlet preswirl ratio	0.000
Entrance loss coefficient	0.000
Exit recovery factor	1.000
Absolute viscosity	1.876e-5 N-s/m ² (1.260e-5 lbm/ft-s)
Molecular weight	28.96
Specific heat ratio	1.400
Compressibility factor	1.000
Tolerance percentage	0.010
No. Integration steps	100.0
n_r	0.0586
m_r	-0.2170
n_s	0.0785
m_s	-0.1101

Experiment Results

When discussing seal test cases throughout this section, reference will be made to various operating conditions. Low speed (LS), medium speed (MS), and high speed (HS) refer to the three journal rotational speeds of 10,200, 15,200, and 20,200 rpm, respectively. Similarly, the three inlet pressures of 0.69, 1.21, and 1.72 MPa are referred to as the low pressure (LP), medium pressure (MP) and high pressure (HP) cases, respectively.

Leakage Flow Rate. On average, the ISOTSEAL program overpredicted the measured honeycomb seal leakage flow rate by 11%. Tables 5 and 6 display the experimental and predicted honeycomb seal leakage flow rate data at 40% and 50% pressure ratio. The best correlation between experiment and theory was observed at LS, LP, and 40% pressure ratio with the program overpredicting leakage flow rate by just over 4%.

In general, the leakage flow rate predictions conform well to the measured leakage data. Although the authors have not investigated the impact that modifying the preswirl ratio and entrance loss and exit recovery factors would have on the predicted leakage correlation to the measured data, they believe the correlation would be significantly improved.

Impedance Measurements. Given the large amount of test data obtained from all eighteen seal test cases and the limited space with which to present it, only a portion of the impedance test data will be presented. Impedance data are supplied for HS, HP case at 40% pressure ratio for each set of test seals. The excitation frequency ranges from 40 to 230 Hz. Output comparison to larger-magnitude waveforms show that the impedances are linear and independent of the input magnitudes. Centered results are presented for excitation and motion in the X-Z plane. Almost identical results were obtained for the Y-Z plane.

Figure 5 shows the measured real and imaginary components of the direct $\mathbf{D}(j\Omega)$ and cross-coupled $\mathbf{E}(j\Omega)$ impedance for the smooth and honeycomb seals. As defined in Eq. (3), $K(\Omega) = \text{Re}[\mathbf{D}]$ and $\Omega C(\Omega) = \text{Im}[\mathbf{D}]$ where Ω is the excitation frequency. One can see that $K(\Omega)$ increases with frequency for the honeycomb seals while remaining comparatively constant for the

Table 5 Experiment versus predictions for leakage flow rates of the honeycomb seals at 40% pressure ratio

Condition	Experiment (kg/s)	Theory (kg/s)	Change (%)
LS, LP	0.0306	0.0333	8.81%
MS, LP	0.0305	0.0328	7.33%
HS, LP	0.0279	0.0321	14.99%
LS, MP	0.0572	0.0615	7.51%
MS, MP	0.0536	0.0606	13.00%
HS, MP	0.0504	0.0595	18.00%
LS, HP	0.0836	0.0874	4.49%
MS, HP	0.0790	0.0861	8.97%
HS, HP	0.0737	0.0844	14.57%

Table 6 Experiment versus predictions for leakage flow rates of the honeycomb seals at 50% pressure ratio

Condition	Experiment (kg/s)	Theory (kg/s)	Change (%)
LS, LP	0.0300	0.0326	8.73%
MS, LP	0.0288	0.0320	11.18%
HS, LP	0.0263	0.0312	18.70%
LS, MP	0.0541	0.0586	8.30%
MS, MP	0.0517	0.0575	11.21%
HS, MP	0.0492	0.0562	14.13%
LS, HP	0.0797	0.0836	4.94%
MS, HP	0.0754	0.0822	8.98%
HS, HP	0.0712	0.0803	12.83%

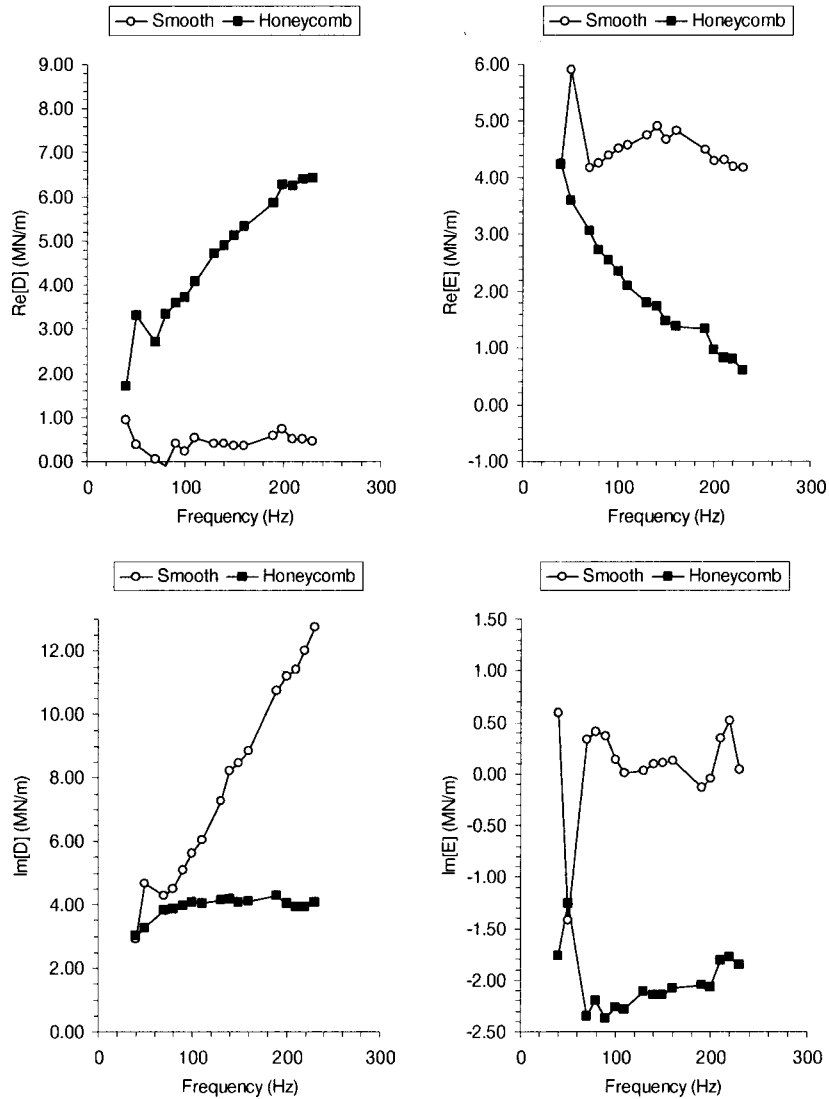


Fig. 5 Measured real and imaginary components of direct $D(j\Omega)$ and cross-coupled $E(j\Omega)$ impedance versus frequency at HS, HP, and 40% pressure ratio for smooth and honeycomb seals

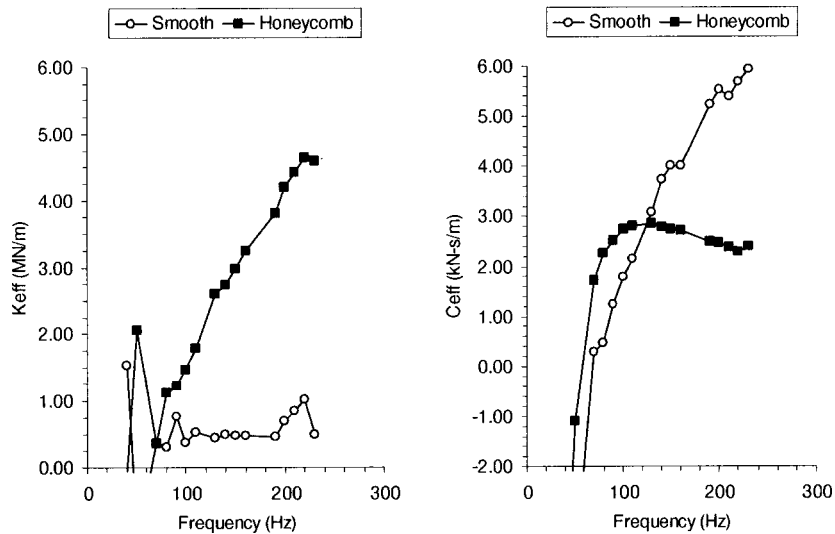


Fig. 6 Experimental effectiveness stiffness K_{eff} and effective damping C_{eff} versus frequency at HS, HP, and 40% pressure ratio

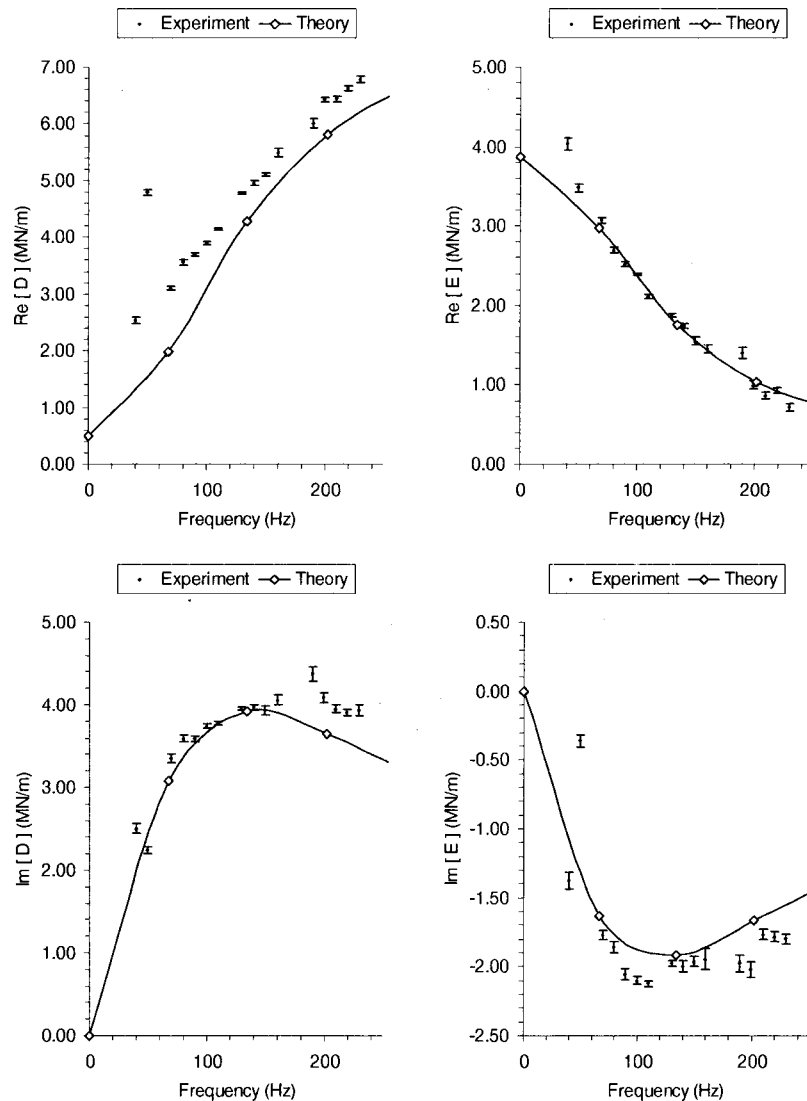


Fig. 7 Experimental and theoretical real and imaginary components of direct $D(j\Omega)$ and cross-coupled $E(j\Omega)$ impedance versus frequency at HS, HP, and 50% pressure ratio for the honeycomb seals

smooth seals. For the smooth seals, the $\text{Im}[D]$ increases linearly with frequency while remaining comparatively flat for the honeycomb seals.

The low-frequency “jump” shown in Fig. 5 corresponds to a low-frequency radial natural frequency of the stator assembly. It is present in most of the test data and is probably spurious.

The impedance characteristics exhibited by the smooth seals validate the use of frequency-independent K and C coefficients in Eq. (1). However, the direct stiffness and damping coefficients $K(\Omega)$ and $C(\Omega)$ of the honeycomb seals exhibit strong frequency-dependence and clearly do not follow the conventional model of Eq. (1).

Equation (4) defines $k(\Omega) = \text{Re}[E]$ and $\Omega c(\Omega) = \text{Im}[E]$. Through the measurements of $k(\Omega)$, one again sees the frequency-dependent behavior of the honeycomb seals compared to the frequency-independent nature of the smooth seals. Looking at $\text{Im}[E]$, c is more or less frequency independent for Ω greater than 70 Hz.

Equations (5) and (6) define effective stiffness K_{eff} and damping C_{eff} in terms of the real and imaginary components of D and E and the excitation frequency Ω . Figure 6 compares the measured K_{eff} and C_{eff} between the smooth and honeycomb seals. The hon-

eycomb seals exhibit a K_{eff} that increases with Ω while K_{eff} remains quite flat for the smooth seals. The honeycomb seals have significantly more K_{eff} than the smooth seals. The C_{eff} of a seal is reduced by the cross-coupled stiffness, $k = \text{Re}[E]$. Looking at Fig. 6, one can see that the smooth seal has the larger C_{eff} , averaging approximately double the effective damping of the honeycomb seals.

However, the honeycomb seals exhibit a larger C_{eff} than the smooth seals up to a frequency of approximately 120 Hz. Note that C_{eff} for the honeycomb seals increases up to a “break” frequency and then begins to slowly decrease. When centrifugal compressors are either unstable during operation or predicted to be unstable at the design-review stage, the first rotor mode is normally the unstable “culprit.” Hence, in seeking to stabilize an otherwise unstable compressor, placing the peak effective damping at or near the compressor rotor’s first natural frequency is frequently the design objective. Increasing the honeycomb cell depth will reduce the “break” frequency.

Comparison to Predictions. This section compares the measured impedance data for the honeycomb seals with theoretical predictions from ISOTSEAL. Overall, impedance predictions cor-

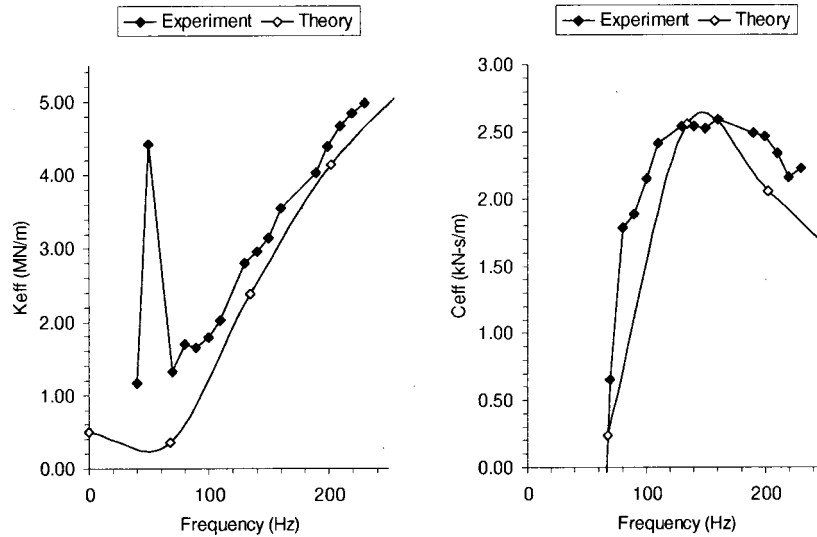


Fig. 8 Experimental and theoretical effective stiffness K_{eff} and damping C_{eff} versus frequency at HS, HP, and 50% pressure ratio for the honeycomb seals

related well across all of the test cases over the frequency range 40 to 230 Hz. Of all the eighteen test cases, the HS, HP, 50% pressure ratio data shown in Fig. 7 correlated best with predictions. The error bars shown in Fig. 7 represent the uncertainty associated with the measured impedance at each frequency as discussed in Part I of this paper.

As noted in Part I, each test spectra is the average of 32 pseudo-random excitations. Cross-spectral-density analysis is used to develop each of the individual transfer functions within the average to eliminate response motion that is not related to the input excitation force. The error bars represent the standard deviations from ten independent tests. Unlike standard “static” uncertainty calculations, they are strongly frequency-dependent. Large error bars appear near the running speed, where the imbalance force is producing spurious response amplitudes. Similarly, large error bars appear at the line frequency of 60 Hz and its multiples. Finally, large error bars appear at higher frequencies where the stator begins a pitching motion. Hence, the authors’ experience is that the error bars provide an accurate measure of the accuracy and repeatability of the test results.

In general, ISOTSEAL under-predicted $K(\Omega) = \text{Re}[\mathbf{D}]$, varying an average of 12% with respect to the measured data. While tending to underpredict $\Omega C(\Omega) = \text{Im}[\mathbf{D}]$, predictions at low-frequency overshoot the measurements. Predictions for the cross-coupled impedance \mathbf{E} did not correlate as well as those of the direct impedance \mathbf{D} . Overall, ISOTSEAL underpredicted $k(\Omega) = \text{Re}[\mathbf{E}]$ and overpredicted $\Omega c(\Omega) = \text{Im}[\mathbf{E}]$, with the least difference observed at HS and HP. Predictions for $k(\Omega) = \text{Re}[\mathbf{E}]$ deviated by an average of 31%, while the predictions for $\Omega c(\Omega) = \text{Im}[\mathbf{E}]$ deviated by an average of only 22%.

Figure 8 provides a comparison of the experimental effective stiffness K_{eff} and damping C_{eff} measurements of the honeycomb seals with predictions from ISOTSEAL.

Generally, the K_{eff} and C_{eff} predictions correlate well with measurements. Overall, K_{eff} and C_{eff} are under predicted for the honeycomb seals. The predicted “break” frequencies also agree well with the measurements. The frequency-dependence of the honeycomb seal force coefficients is particularly visible looking at C_{eff} .

Summary, Conclusions, and Comments

Two sets of annular gas seals were successfully tested using the recently constructed AGSTS located at the authors’ laboratory. The dynamic impedance measurements demonstrate the validity of the conventional frequency-independent model of Eq. (1) for

smooth seals, while clearly disproving its use for honeycomb seals, which demonstrated strong frequency-dependent force coefficients K , C , and k .

Seal leakage and dynamic impedance predictions correlate very well with the honeycomb seal measurements. The measured impedance data are very consistent as demonstrated by the small standard of deviation (error bars in Fig. 7) calculated for each frequency data point across ten identical tests performed for each seal.

Of greatest significance is the fact that the measured honeycomb seal impedance validates the frequency-dependent force coefficients predicted by the two-control-volume annular gas seal analysis of Kleynhans and Childs [1]. Subsequent test work with the AGSTS has been performed at elevated pressures to 6.89 MPa (1000 psi). The details of these results will be reported in the future and generally support the predictions of Kleynhans and Childs [1].

The authors are presenting test data in terms of frequency-dependent stiffness and damping coefficients, and many available rotordynamic codes require seal or bearing descriptions in this format. However, Kleynhans and Childs [1] provide lead-lag transfer-function descriptions for $\mathbf{D}(j\Omega)$ and $\mathbf{E}(j\Omega)$, and this is certainly the more efficient modeling approach.

Nomenclature

- C, c = direct and cross-coupled damping coefficients (FT/L)
- C_d = honeycomb cell depth (L)
- C_{eff} = effective damping coefficient (FT/L)
- C_r = radial seal clearance (L)
- C_w = honeycomb cell width (L)
- $C(\Omega), c(\Omega)$ = frequency-dependent direct and cross-coupled damping (FT/L)
- $\mathbf{D}(j\Omega)$ = complex direct impedance (F/L)
- $\mathbf{E}(j\Omega)$ = complex cross-coupled impedance (F/L)
- $\mathbf{F}_x, \mathbf{F}_y$ = Fourier transformed components of f_{xg} and f_{yg} (F)
- f_{xg}, f_{yg} = annular gas seal reaction force components (F)
- \hat{h}_d = nondimensional honeycomb cell depth H_d/C_r
- H_d = effective honeycomb cell depth of Eq. (9) (L)
- I_r, I_θ = radial and tangential seal impedance (F/L)
- j = $\sqrt{-1}$
- K, k = direct and cross-coupled stiffness coefficients (F/L)

K_{eff} = effective stiffness coefficient (F/L)
 $K(\Omega), k(\Omega)$ = frequency-dependent direct and cross-coupled stiffness (F/L)
 L = seal length (L)
 M = direct inertia coefficient (M)
 n_r, m_r = Blasius rotor friction coefficients
 n_s, m_s = Blasius stator friction coefficients
 P_e, P_x = seal inlet and exit pressures (F/L^2)
 R = rotor radius (L)
 t = honeycomb foil thickness (L)
 x, y = seal/rotor relative motion in orthogonal directions (L)
 \mathbf{X}, \mathbf{Y} = Fourier transformed components of seal/rotor relative motions in orthogonal directions (L)
 ω = rotor rotational frequency ($1/L$)
 Ω = excitation frequency ($1/L$)

Subscripts

s = stator
 x, y = motion direction (L)

References

- [1] Ha, T., and Childs, D., 1994, "Annular Honeycomb-Stator Turbulent Gas Seal Analysis Using New Friction-Factor Model Based on Flat Plate Tests," *ASME J. Tribol.*, **116**, pp. 352–360.
- [2] Kleynhans, G., and Childs, D., 1997, "The Acoustic Influence of Cell Depth on the Rotordynamic Characteristics of Smooth-Rotor/Honeycomb-Stator Annular Gas Seals," *ASME J. Eng. Gas Turbines Power*, **19**, pp. 949–957.
- [3] Benckert, H., and Wachter, J., "Flow Induced Spring Coefficients of Labyrinth Seals for Application in Rotor Dynamics," *Rotordynamic Instability Problems in High-Performance Turbomachinery*, Proceedings of a workshop held at Texas A&M University, May 12–14, NASA cp 2133, pp. 189–212.
- [4] Childs, D., Nelson, C., Nicks, C., Scharer, J., Elrod, D., and Hale, K., 1986, "Theory Versus Experiment for the Rotordynamic Coefficients of Annular Gas Seals: Part 1—Test Facility and Apparatus," *ASME J. Tribol.*, **108**, pp. 426–432.
- [5] Kleynhans, G., 1996, "A Two-Control-Volume Bulk-Flow Rotordynamic Analysis for Smooth-Rotor/Honeycomb-Stator Gas Annular Seals," dissertation, Mechanical Engineering, Texas A&M University, pp. 55–57.
- [6] Yamada, Y., 1962, "Resistance of Flow Through an Annulus With an Inner Rotating Cylinder," *Bull. JSME*, **5(1)**, pp. 302–310.
- [7] Ha, T., Morrison, G., and Childs, D., 1992, "Friction-Factor Characteristics for Narrow Channels With Honeycomb Surfaces," *ASME J. Tribol.*, **114**, pp. 714–721.

Using Guided Balls to Auto-Balance Rotors

H. L. Wettergren

Department of Mechanical Engineering,
Linköping University,
SE-58183 Linköping, Sweden
e-mail: hakwe@ikp.liu.se

By using balancing balls constrained to move in a circular groove filled with oil, the vibration of rotating machinery can, under certain circumstances, be reduced. This paper shows that the damping from the oil reduces the instability region, i.e., the conditions when the balancing balls don't find their equilibrium positions. However, the instability region seems to increase with increasing number of balancing balls. The critical ball damping ratio is highest just above the natural frequency and then rapidly decreases. Consequently, since the region between instability and critical damping is quite small, the ball damping should be made as small as possible without getting too close to the instability threshold. Bearing damping has a large effect on the instability region. High bearing damping will suppress the instability. The time it takes to reach the asymptotically stable position seems to increase with increasing number of balls. Keeping this time low is one of the most important things when designing a balancing ring.

[DOI: 10.1115/1.1479335]

Introduction

In many rotating machines the unbalance of the rotor changes with time. In some of these machines this happens rapidly, for instance in a grinding wheel or in a basket in a laundry machine. Consequently, there is a need for balancing these machines during operation.

One example of how to do this is described in Gosiewski [1,2] where an active control of the vibration is used. The correction masses may be pistons or cylinders of pneumatic or hydraulic servos. This method is relatively expensive. In many applications there is a need for simpler methods.

One well-known example of this is the Lablanc balancer from 1916. The Lablanc balancer consists of a cylindrical chamber partly filled with a heavy liquid. The dynamic balancing machine is described by Thearle [3] and analyzed by Inoue et al. [4]. The machine only reduces the vibration when the rotation frequency is higher than its critical speed. Thearle improved it by introducing a flanged annular ring surrounding and attached to the washing machine basket in such a position that the extracted liquid enters the inside of the ring. Therefore at low speeds, below the critical speed, little liquid is present in the balance ring and consequently it will not significantly increase the vibration.

It has for many years been known that, by using balls moving freely in a circular groove on a rotor, the rotor's vibrations can be reduced. Even here, this is only possible when the rotation frequency is higher than its critical speed. The centrifugal force on the balancing balls act to move them into a rest position and consequently change the unbalance, see Fig. 1.

On the shaft, which should be balanced, the balancing element is mounted concentric with the center axis. Due to the centrifugal forces, the two balls will move the balancing balls away to a circumferential position from the center of gravity. As a result the center of gravity will change.

Hand-held rotary power tools are examples of machinery where, for instance, Lindell [5] has successfully used balls for auto balancing. Auto-balanced power tools are today commercially used. In that paper Lindell also explained the balancing mechanism of the device with two balls and established that the

balls will move to the exact circumferential location inside the groove to neutralize the rotor balance completely.

The behavior of the rotor due to this auto balancing is, however, poorly analyzed, but work does exist.

Högfors [6] found that auto balancing is possible for nonplane rotors.

Rajalingham et al. [7] analyzed under which conditions unbalanced flexible vertical rotors could be neutralized by automatic balancing. They found that it was only possible at speeds higher than the critical speed. However, there exist unstable regions above this speed where the ball could not find its equilibrium position.

Rajalingham and Rakheja [8] extended the work and also considered the friction in the contact between the ball and the groove.

The last three papers have studied the perturbed motion from steady state and not studied the time-varying motion.

In this paper the behavior of the rotor and balancing ball(s) will be studied. This is first done with one ball and then with two balls. Two balls cover most of the principles with more than one ball. The paper only covers rotors with isotropic bearings.

One Guided Ball

The system to be used in this paper is shown in Fig. 2. The mass of the stiff shaft and the ring without the ball is m . The ends of the shaft are mounted in two isotropic bearings with stiffness k and damping c . The behavior of this kind of system has been known since the middle of the 19th century when Rankine in 1869 extended Euler's over 100-years-old theory of lateral vibrations, and since Jeffcott in 1919 established the concept of shaft whirl.

In Fig. 3 the cross section of the balancing ring can be seen. The coordinates (x, y) of the rotor center are referred to a fixed reference. The balancing ball, with radius r and mass m_b , moves in a circular path with radius a . The angular position of the ball is $\Omega t + \psi$ where Ω is the rotation frequency of the shaft. The groove in the ring is partly filled with oil. This oil gives a damping force acting on the ball in the opposite direction to the relative motion between the ball and the ring.

The governing equations for the rotor and the balancing ball, seen in Figs. 2 and 3, can be written in the x -direction as

$$(m + m_b)\ddot{x} + 2c\dot{x} + 2kx - m_b a (\dot{\psi} + \Omega)^2 \cos(\psi + \Omega t) - m_b a \ddot{\psi} \sin(\psi + \Omega t) = m e \Omega^2 \cos(\Omega t) \quad (1)$$

and in the y -direction as

Contributed by the International Gas Turbine Institute (IGTI) of THE AMERICAN SOCIETY OF MECHANICAL ENGINEERS for publication in the ASME JOURNAL OF ENGINEERING FOR GAS TURBINES AND POWER. Paper presented at the International Gas Turbine and Aeroengine Congress and Exhibition, New Orleans, LA, June 4-7, 2001; Paper 01-GT-243. Manuscript received by IGTI, December 2000, final revision, March 2001. Associate Editor: R. Natole.

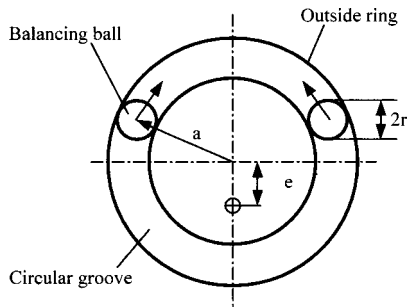


Fig. 1 Balancing ring

$$(m + m_b)\ddot{y} + 2c\dot{y} + 2ky - m_b a(\psi + \Omega)^2 \sin(\psi + \Omega t) + m_b a \ddot{\psi} \cos(\psi + \Omega t) = m e \Omega^2 \sin(\Omega t) \quad (2)$$

The analysis of the ball becomes more complicated, if the ball may both roll and slip. If there is more than one ball the contact force between them also affects the system's behavior. In this paper it is assumed that the ball rolls on the radius $(a + r)$. The moment equation for the ball about the contact point, marked with "A" in Fig. 3, becomes

$$m_b a \ddot{\psi} r + c_{ball} a \dot{\psi} r + m_b \ddot{y} \cos(\psi + \Omega t) r - m_b \dot{x} \sin(\psi + \Omega t) r + j_b \frac{a}{r} \ddot{\psi} = 0 \quad (3)$$

It is shown in Rajalingham and Rakheja [8] that if c_{ball} and c are equal to zero, the steady-state solution is

$$\sqrt{x_0^2 + y_0^2} = \frac{\Omega^2 (m e + m_b a \cos \psi_0)}{2k - (m + m_b) \Omega^2}, \text{ and } \psi_0 = 0 \text{ or } \pi. \quad (4)$$

When the rotation is below the natural frequency the asymptotic stable solution for the ball always is $\psi_0 = 0$. If the rotation is higher than the natural frequency the stable solution is $\psi_0 = \pi$.

If we let the mass unbalance $(m \cdot e)$ be equal to the unbalance added by the ball $(m_b \cdot a)$, then with $\psi_0 = \pi$, the deflection be-

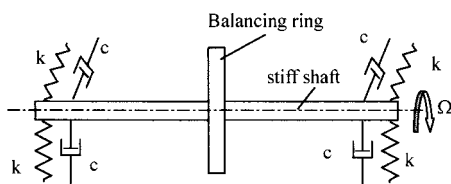


Fig. 2 Rotor with balancing ring

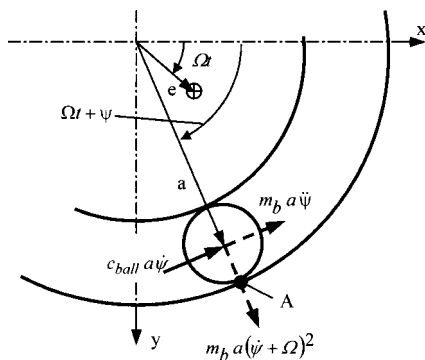


Fig. 3 One guided ball

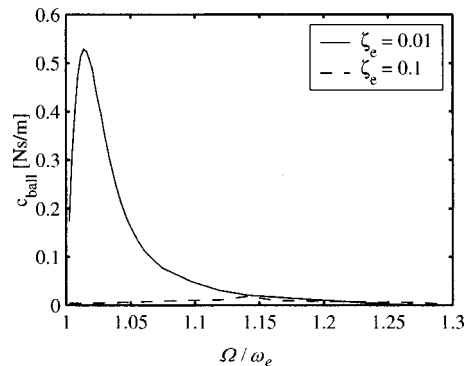


Fig. 4 Amount of ball damping to avoid instability

comes zero. Consequently, when the rotation is higher than the first critical speed the deflection may become zero. According to Rajalingham and Rakheja [8] the ball cannot, with the values of the parameters chosen in this paper, find this stable position if

$$\Omega < 1.28 \cdot \sqrt{\frac{2k}{(m + m_b)}} \quad (5)$$

Equations (1)–(3) may be solved numerically with methods based on the Runge-Kutta-Fehlberg (R-K-F) method. The equations have to be written as a first-order system as

$$[M(t, q)] \cdot \{\dot{q}\} = \{F(t, q)\} \quad (6)$$

where both the mass matrix and the right-hand side become state and time-dependent. The state vector may for instance be expressed as

$$\{q\} = \{x \quad \dot{x} \quad y \quad \dot{y} \quad \psi \quad \dot{\psi}\}^T. \quad (7)$$

We introduce the external damping ratio, conventionally defined as

$$s_e = \frac{c}{2 \sqrt{k \left(\frac{m}{2} + \frac{m_b}{2} \right)}} \quad (8)$$

Since there are two bearings and a stiff shaft half of the masses are lumped on each bearing.

Since Eqs. (1)–(3) are nonlinear the results may not be generally valid. Unless otherwise noted the following numerical data are used in the calculations in this paper: $\rho = 7850 \text{ kg/m}^3$, $d = 0.016 \text{ m}$, $r = 0.005 \text{ m}$, $a = 0.02 \text{ m}$, $k = 395 \text{ N/m}$.

The first analysis concerns the well-known and abundantly investigated instability region just above the critical speed as was described in the introduction of this paper. Fig. 4 shows the amount of ball damping required to avoid instability for different amounts of external damping. The theoretical value from Eq. (5) does not seem to be so important. The system may be stable much earlier and the instability does not seem to be a problem, especially if the external damping is high.

From Fig. 4 it is noted that the amount of damping to avoid instability for the ratio of rotational to eigenfrequency of 1.1 is $c_{ball} = 0.050 \text{ Ns/m}$. With this amount of ball damping, the ratio of deflection to eccentricity is calculated. For rotational frequencies lower than the critical speed, the ratio is in principle doubled since the ball unbalance is chosen to be the same as the eccentricity. In this example the region between the eigenfrequency and $\Omega / \omega_e = 1.1$ the ball cannot find its stable position. For higher rotational frequencies the deflection is zero.

From Figs. 4 and 5 it is noted that the amount of ball damping seems to be important. For a single degree-of-freedom system, critical damping represents the limit for allowing the system close

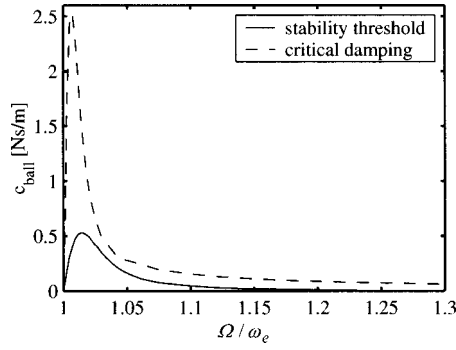


Fig. 5 Critical ball damping and the stability threshold when one guided ball is used

find its equilibrium position in the shortest possible time. This means that the mass never crosses the steady-state position but only approaches it asymptotically.

In the following section, a similar definition for the ball damping is used. The critical ball damping, ζ_{ball} , is taken to be the damping where the ball reaches 180 deg in the shortest time without overshooting it. Figure 5 illustrates this condition when the external bearing damping, ζ_e , is equal to 0.01. In the same figure, the stability threshold from Fig. 4 for the lowest possible ball damping is plotted for comparison. Figure 6 illustrates the ball position for four different ball dampings when $\Omega/\omega_e = 1.1$ and when the start position for the ball is $\psi = 60$ deg. The lowest damping, $\zeta_{ball} = 0.2$, gives an unstable system. The ball will just continue to rotate in the ring. The figure also illustrates why too much damping should be avoided. The time it takes to reach 180 deg increases when $\zeta_{ball} > 1$.

Consequently, since the region between instability and critical damping is quite small, the ball damping should be as small as possible without getting too close to the instability threshold.

Two Guided Balls

The drawback with using one guided ball is that the size of the eccentricity has to be known in advance. This is of course seldom the case and if it is, then the machine can be balanced using conventional balancing technique. Instead a number of balls, greater than one, and whose total effective unbalance is greater than the maximum expected shaft unbalance, has to be used. In this paper the behavior with two guided balls is studied.

The equations of motion described in Eqs. (1)–(3) have to be extended because there are two balls instead of one and because contact between the balls may occur (see Fig. 7).

In the same manner as for one guided ball the governing equations for the rotor and the balancing, seen in Fig. 7, can be written in the x -direction as

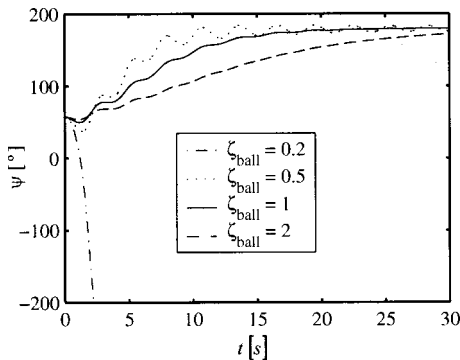


Fig. 6 Ball position as a function of time

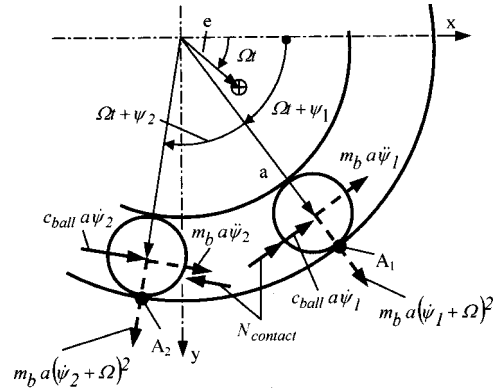


Fig. 7 Two guided balls

$$(m + 2m_b)\ddot{x} + 2c\dot{x} + 2kx - m_b a (\dot{\psi}_1 + \Omega)^2 \cos(\psi_1 + \Omega t) - m_b a \ddot{\psi}_1 \sin(\psi_1 + \Omega t) - m_b a (\dot{\psi}_2 + \Omega)^2 \cos(\psi_2 + \Omega t) - m_b a \ddot{\psi}_2 \sin(\psi_2 + \Omega t) = m e \Omega^2 \cos(\Omega t) \quad (9)$$

and in the y -direction as

$$(m + 2m_b)\ddot{y} + 2c\dot{y} + 2ky - m_b a (\dot{\psi}_1 + \Omega)^2 \sin(\psi_1 + \Omega t) + m_b a \ddot{\psi}_1 \cos(\psi_1 + \Omega t) - m_b a (\dot{\psi}_2 + \Omega)^2 \sin(\psi_2 + \Omega t) + m_b a \ddot{\psi}_2 \cos(\psi_2 + \Omega t) = m e \Omega^2 \sin(\Omega t). \quad (10)$$

The moment equation for the balls when they are in contact becomes, for the first ball

$$m_b a \ddot{\psi}_1 r + c_{ball} a \dot{\psi}_1 r + m_b \ddot{y} \cos(\psi_1 + \Omega t) r + N_{contact} r - m_b \ddot{x} \sin(\psi_1 + \Omega t) r + j_b \frac{a}{r} \ddot{\psi}_1 = 0 \quad (11)$$

and for the second ball

$$m_b a \ddot{\psi}_2 r + c_{ball} a \dot{\psi}_2 r + m_b \ddot{y} \cos(\psi_2 + \Omega t) r - N_{contact} r - m_b \ddot{x} \sin(\psi_2 + \Omega t) r + j_b \frac{a}{r} \ddot{\psi}_2 = 0. \quad (12)$$

The contact force is obtained from Hertz contact theory, i.e., the stiffness of the contact is

$$k_{ball} = \frac{2^{3/2} \cdot r^{1/3} \cdot E}{3 \cdot 4^{1/3} \cdot (1 - \nu)}. \quad (13)$$

Three possible cases exist.

$$(1) \text{ If } (\psi_2 - \psi_1) < 2 \frac{r}{a} \Rightarrow N_{contact} = ((\psi_2 - \psi_1)a - 2r)^{3/2} \cdot k_{ball}. \quad (14)$$

This means that the contact is as shown in Fig. 7, however, the ball with index 2 may also move almost a whole lap more than the ball with index 1. The contact force will then be in the opposite direction, i.e.,

$$(2) \text{ If } (\psi_2 - \psi_1) > 2\pi - 2 \frac{r}{a} \Rightarrow N_{contact} = -((\psi_2 - \psi_1)a - 2r - 2\pi a)^{3/2} \cdot k_{ball}. \quad (15)$$

(3) Otherwise, if none of these two conditions is fulfilled the contact force is zero.

Let each of the two ball unbalances be $m_b a = 0.8 \cdot m e$ and keep the rest of the numerical data from the shaft/bearing system used

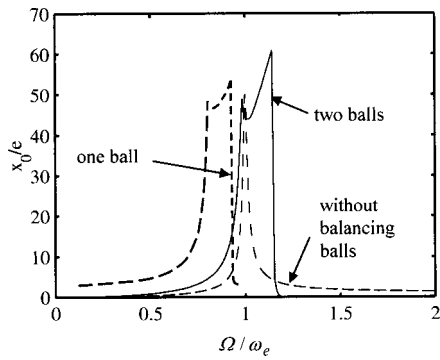


Fig. 8 Deflection with and without balancing balls as a function of rotational frequency for $c_{ball}=0.050$ Ns/m

previously with one guided ball. Figure 8 shows the ratio of deflection to eccentricity ratio. For rotational frequencies lower than the critical speed the ratio is in principle 2.6 times the deflection without balls. This is due to the fact that each ball unbalance is 0.8 times the mass unbalance and that the asymptotically stable position of the balls is in the same direction as the eccentricity. The location of balls will be in a row near 0 deg. In the region between the eigenfrequency and $\Omega/\omega_e = 1.15$, the ball cannot find its stable position. For higher rotational frequencies the deflection is zero.

It seems that the more balancing balls used the larger the instability region will be.

The asymptotically stable position for rotational frequencies higher than the eigenfrequency will now depend on the ratio between the mass unbalance and the guided ball unbalance. The asymptotically stable positions will of course not be 180 deg when more than one balancing ball is used. Therefore the critical ball damping is defined as the damping used when the ball reaches its asymptotically stable position in the shortest time without overshooting it. Figure 9 illustrates this when the external bearing damping, ζ_e , is equal to 0.01. In the same figure the stability threshold is plotted for the lowest possible ball damping.

A comparison between Figs. 5 and 9 gives that the amount of damping to obtain instability is a few percent higher for the balancing ring with two balls than with one ball. This is valid for all rotational frequencies except those just above the critical frequency, where the amount of damping to avoid instability is higher than that which is practically available.

The same conclusion is reached for the balancing ball critical damping ratio. Figure 10 illustrates the ball position for four different ball damping as a function of time when $\Omega/\omega_e = 1.1$. The lowest damping gives an unstable system. Note that ζ_{ball} is different than that used in Fig. 6. The starting positions for the balls are

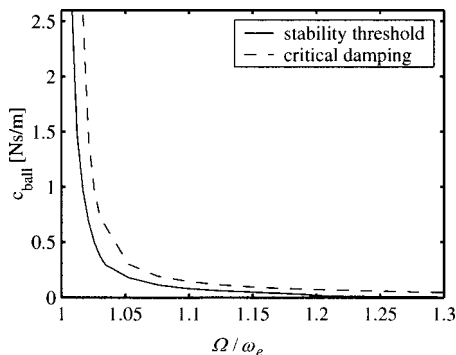


Fig. 9 Critical damping and the stability threshold when two guided balls are used

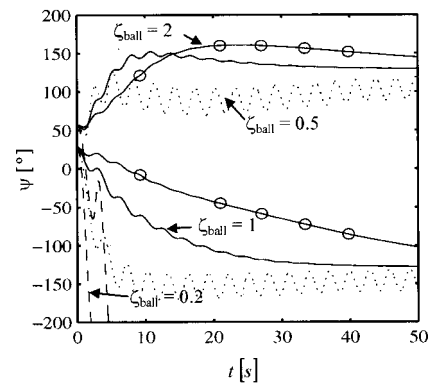


Fig. 10 Ball positions as a function of time

$\psi_1 = 30$ deg and $\psi_2 = 6$ deg. Since there are two balls with $m_b \cdot a = 0.8 \cdot m_e$ the asymptotically stable position will be $\psi_1 = -128.68$ deg and $\psi_2 = 128.68$ deg.

As can be seen in Fig. 10, it is not unequivocal how to define the critical damping factor when more than one ball is used. In this paper the critical damping factor is chosen so that the one ball is taken as subcritically damped and the other critically damped. In that way, the vibration will vanish faster than if it is chosen to be supercritically damped.

A comparison between Fig. 6 and Fig. 10 suggests that the time it takes to reach the asymptotically stable position seems to increase with increasing number of balls. Keeping this time low is one of the most important objectives when designing a balancing ring. For instance if the washing in a laundry machine changes position and it takes tenths of seconds to reach the new asymptotically stable position, the usefulness of the balancing ring substantially will be very limited.

Conclusion

By using balancing balls constrained to move in a circular groove filled with oil the vibration of rotating machinery can under certain circumstances be reduced. The conclusions from this study can be summarized:

At least two balls, whose total unbalance is greater than the expected rotor unbalance, are required.

The damping from the oil reduces the instability region, i.e., the region where the balancing balls don't find their equilibrium position.

In the instability region the ball(s) will continuously rotate in the groove.

The critical damping ratio is highest just above the natural frequency and then rapidly decreases. Consequently, since the region between instability and critical damping is quite small, the ball damping should be as small as possible without getting too close to the instability threshold.

Bearing damping has a large effect on the instability region. High bearing damping will suppress the instability.

The theoretically calculated rotational frequency when the system becomes stable, which can be found in the literature, is of minor interest since damping changes the behavior drastically.

The time it takes to reach the asymptotically stable position seems to increase with increasing number of balls.

The instability region seems to increase with increasing number of balancing balls.

Nomenclature

- A = ball contact point
- a = radius of the ball orbit
- c = bearing damping
- c_{ball} = ball damping
- d = diameter of the shaft

E = modulus of elasticity
 e = eccentricity
 $\{F(t, q)\}$ = right-hand side in R-K-F
 k = bearing stiffness
 k_{ball} = contact stiffness between balls
 $\{M(t, q)\}$ = bending moment
 m = mass of the rotor without the balls
 m_b = mass of the ball
 N = force between balls
 $\{q\}$ = state vector
 r = radius of the ball
 t = time
 x, y, z = Cartesian coordinate system
 x_0, y_0 = amplitudes of the shaft
 ζ_{ball} = ball damping ratio
 ζ_e = bearing damping ratio
 μ = coefficient of friction
 ρ = density
 ν = Poisson number
 ψ = angular position of the ball

ψ_0 = stable angular
 Ω = rotational frequency
 ω_e = resonance frequency

References

- [1] Gosiewski, Z., 1985, "Automatic Balancing of Flexible Rotors, Part I: Theoretical Background," *J. Sound Vib.*, **100**(1), pp. 551–567.
- [2] Gosiewski, Z., 1987, "Automatic Balancing of Flexible Rotors, Part II: Synthesis of System," *J. Sound Vib.*, **114**(4), pp. 103–119.
- [3] Thearle, E. L., 1950, "Automatic Dynamic Balancing, Part I—The Lablanc Balancer," *Mach. Des.*, **11**, pp. 103–106.
- [4] Inoue, J., Araki, Y., and Hayashi, S., 1967, "On the Self-Synchronization of Mechanical Vibrators," *Trans. JSME*, **32**(234), pp. 184–193.
- [5] Lindell, H., 1996, "Vibration Reduction on Hand-Held Grinders by Automatic Balancing," *Central Euro. J. Public Health*, **4**, pp. 43–45.
- [6] Högfors, C., 1984, "Autobalancing," XVI Congress of Theoretical Applied Mechanics, Lyngby.
- [7] Rajalingham, C., Bhat, R. B., and Rakheja, S., 1998, "Automatic Balancing of Flexible Vertical Rotors Using a Guided Ball," *Int. J. Mech. Sci.*, **40**(9), pp. 825–834.
- [8] Rajalingham, C., and Rakheja, S., 1998, "Whirl Suppression in Hand-Held Power Tool Rotors Using Guided Rolling Balancers," *J. Sound Vib.*, **217**(3), pp. 453–466.

Estimation of Distributed Unbalance of Rotors

T. Yang
C. Lin

Department of Mechanical Engineering,
Yuan Ze University,
Neili, Taoyuan, Taiwan

Mass unbalance commonly causes vibration of rotor-bearing systems. Lumped mass modeling of unbalance was adapted in most previous research. The lumped unbalance assumption is adequate for thin disks or impellers, but not for thick disks or shafts. Lee et al. (Lee, A. C., et al., 1993, "The Analysis of Linear Rotor-Bearing Systems: A General Transfer Matrix Method," ASME J. Vib. Acoust., 115, pp. 490-497) proposed that the unbalance of shafts should be continuously distributed. Balancing methods based on discrete unbalance models may not be very appropriate for rotors with distributed unbalance. A better alternative is to identify the distributed unbalance of shafts before balancing. In this study, the eccentricity distribution of the shaft is assumed in piecewise polynomials. A finite element model for the distributed unbalance is provided. Singular value decomposition is used to identify the eccentricity curves of the rotor. Numerical validation of this method is presented and examples are given to show the effectiveness of the identification method. [DOI: 10.1115/1.1479336]

Introduction

Vibration is common to the rotor-bearing systems of rotating machinery. Serious vibration not only generates noise and degrades the performance of the machines, but also decreases the service life and reliability of the machines, and even causes dangerous problems. The causes of rotor vibration are diversified and complicated. Mass unbalance is the most frequent cause of the vibration of rotating machinery.

Reasons that may produce unbalance include assembly error, unsymmetric geometry, material inhomogeneity, and manufacturing tolerance, which all may cause mass centers not to align with the rotating axes of the rotors. Extensive studies concerning unbalance have been done, but most of them are concentrated on the discrete (or lumped) unbalance ([1]). Methods of balancing the rotors may be categorized into modal balancing methods ([2-4]), and influence coefficient balancing methods ([5-7]). To reduce the tedious work of replacing trial masses and overcome the limitation of planar modes, the unified balancing method ([8,9]) was developed to integrate the two aforementioned balancing methods.

However, very little attention was devoted to the topics of distributed unbalance. The distributed unbalance of a rotor is lumped into a finite number of discrete unbalanced "disks" and the rotor is balanced based on the method for discrete unbalance by Little and Pilkey [10]. Lee et al. [11] proposed that the mass unbalance of shafts should be continuously distributed. Lumped unbalance models are suitable for thin disks or impellers, but do not seem appropriate for shafts or thick disks ([11]). Modeling the distributed unbalance with equivalent lumped unbalance masses and balancing the rotor with several corrective masses does not seem to be the best approach. A better approach would be identifying the distribution of the shaft unbalance and correcting the unbalance with a counter distributed mass ([12]).

Lee and Shin [12] suggested that the curves of the shaft eccentricity should be finite and piecewise continuous. Representing the mass eccentricity curves in Fourier series, they used the modified transfer matrix method to identify the unbalance distribution of the shaft and verify the balancing effects. Their unbalance identification derivation using Fourier series is very involved and also not very suitable for the popular finite element programs of rotor-

dynamic analyses ([13]). This paper used polynomial curves for eccentricity distribution with finite element modeling in the eccentricity identification derivation of shafts. The merits of our approach are the derivation is straightforward and easy to incorporate into the existing finite element rotordynamic programs.

Finite Element Modeling

The coordinate systems used in this paper are depicted in Fig. 1, where XYZ is the fixed frame, and xyz the rotating frame. The rotor rotates about the z -axis with an angular velocity Ω counterclockwise. u, v, w are the displacements of the rotor in the X, Y, Z directions, θ_x and θ_y the rotational angles in X and Y -axes.

Figure 2 shows a cross section of the shaft with mass center M_c , geometric center G_c , eccentricity e , and phase angle of the unbalance ϕ_u . Assuming the eccentricity curves are finite, piecewise continuous, and of m -degree polynomials, the local eccentricity distribution for each shaft element $f(s)$ can be expressed as

$$f(s) = \sum_{i=0}^m (a_i + jb_i) \left(\frac{s}{l}\right)^i = x(s) + jy(s) \quad (1)$$

where $j = \sqrt{-1}$.

$$x(s) = \sum_{i=0}^m a_i \left(\frac{s}{l}\right)^i, \quad \text{and} \quad y(s) = \sum_{i=0}^m b_i \left(\frac{s}{l}\right)^i.$$

The unbalance forces are modeled with the beam shape functions by following the common finite element procedure. In the fixed frame, the unbalance forces are

$$\begin{aligned} \{Q^e\} &= \int_0^l \mu \Omega^2 [\Psi]^T \begin{Bmatrix} x(s) \\ y(s) \end{Bmatrix} \cos \Omega t + \begin{Bmatrix} -y(s) \\ x(s) \end{Bmatrix} \sin \Omega t \, ds \\ &= \{Q_c^e\} \cos \Omega t + \{Q_s^e\} \sin \Omega t \end{aligned} \quad (2)$$

where

$$\{Q_c^e\} = \int_0^l \mu \Omega^2 [\Psi]^T \begin{Bmatrix} \sum_{i=0}^m a_i \left(\frac{s}{l}\right)^i \\ \sum_{i=0}^m b_i \left(\frac{s}{l}\right)^i \end{Bmatrix} ds,$$

Contributed by the International Gas Turbine Institute (IGTI) of THE AMERICAN SOCIETY OF MECHANICAL ENGINEERS for publication in the ASME JOURNAL OF ENGINEERING FOR GAS TURBINES AND POWER. Paper presented at the International Gas Turbine and Aeroengine Congress and Exhibition, New Orleans, LA, June 4-7 2001; Paper 01-GT-245. Manuscript received by IGTI, Dec. 2000, final revision, March 2001. Associate Editor: R. Natole.

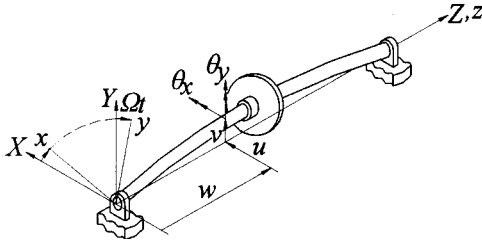


Fig. 1 Coordinate systems of the rotor-bearing system

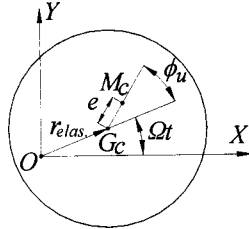


Fig. 2 Eccentricity of a shaft cross section

$$\{Q_s^e\} = \int_0^l \mu \Omega^2 [\Psi]^T \begin{bmatrix} -\sum_{i=0}^m b_i \left(\frac{s}{l}\right) \\ \sum_{i=0}^m a_i \left(\frac{s}{l}\right) \end{bmatrix} ds$$

$$[\Psi]^T = \begin{bmatrix} N_1 & 0 & 0 & N_2 & N_3 & 0 & 0 & N_4 \\ 0 & N_1 & -N_2 & 0 & 0 & N_3 & -N_4 & 0 \end{bmatrix}^T$$

$N_1 \sim N_4$ are the shape functions for Timoshenko beams ([13]). Integration results of $\{Q_c^e\}$ and $\{Q_s^e\}$ were given in Lin [14].

The unbalance of disks is modeled as lumped unbalance. The disk unbalance forces in the fixed frame are

$$\{Q^d\} = m_d \Omega^2 \begin{Bmatrix} x_d \\ y_d \\ 0 \\ 0 \end{Bmatrix} \cos \Omega t + m_d \Omega^2 \begin{Bmatrix} -y_d \\ x_d \\ 0 \\ 0 \end{Bmatrix} \sin \Omega t \quad (3)$$

where m_d is the disk mass, $x_d = e_d \cos(\phi_d)$, $y_d = e_d \sin(\phi_d)$, e_d eccentricity, ϕ_d phase angle of the unbalance of the disk.

Rotor-bearing systems usually contain shafts, disks, and bearings. The finite element models of these three major parts can be assembled by using the common finite element procedure ([13,15]). The system equation is

$$[M]_{d \times d} \{\ddot{q}\}_{d \times 1} + [C]_{d \times d} \{\dot{q}\}_{d \times 1} + [K]_{d \times d} \{q\}_{d \times 1} = \{Q\}_{d \times 1} \quad (4)$$

where $d = (n+1) \times 4$, n is the total number of the shaft elements, $[M]$ system inertia matrix; $[C]$ system damping matrix; $[K]$ system stiffness matrix; and $\{Q\}$ external forces, including external loadings and unbalance forces.

Derivation of Identification Equations

In the steady-state responses of the lateral vibration of a shaft, the elliptical orbit of a node on the shaft can be expressed as

$$u(t) = U_c \cos \Omega t + U_s \sin \Omega t \quad (5a)$$

$$v(t) = V_c \cos \Omega t + V_s \sin \Omega t \quad (5b)$$

so we can represent the nodal displacements of the rotor as

$$\{q\} = \{q_c\} \cos \Omega t + \{q_s\} \sin \Omega t \quad (6)$$

where

$$\{q_c\} = \{U_{c1} V_{c1} \theta_{xc1} \theta_{yc1} \cdots U_{c(n+1)} V_{c(n+1)} \theta_{xc(n+1)} \theta_{yc(n+1)}\}^T$$

$$\{q_s\} = \{U_{s1} V_{s1} \theta_{xs1} \theta_{ys1} \cdots U_{s(n+1)} \theta_{s(n+1)} \theta_{xs(n+1)} \theta_{ys(n+1)}\}^T$$

The synchronous external forces on the rotor can be expressed as

$$\{Q\} = \{Q_c\} \cos \Omega t + \{Q_s\} \sin \Omega t \quad (7)$$

where

$$\{Q_c\} = \{Q_{xc1} \ Q_{yc1} \ M_{xc1} \ M_{yc1} \cdots \ Q_{xc(n+1)} \ Q_{yc(n+1)} \ M_{xc(n+1)} \ M_{yc(n+1)}\}^T$$

$$\{Q_s\} = \{Q_{xs1} \ Q_{ys1} \ M_{xs1} \ M_{ys1} \cdots \ Q_{xs(n+1)} \ Q_{ys(n+1)} \ M_{xs(n+1)} \ M_{ys(n+1)}\}^T$$

Substituting Eqs. (6) and (7) into Eq. (4) yields

$$[T_{\text{sys}}]_{8(n+1) \times 8(n+1)} \{\bar{q}\}_{8(n+1) \times 1} = \{\bar{Q}\}_{8(n+1) \times 1} \quad (8)$$

where

$$[T_{\text{sys}}] = \begin{bmatrix} [K] - \Omega^2 [M] & \Omega [C] \\ -\Omega [C] & [K] - \Omega^2 [M] \end{bmatrix}$$

$$\{\bar{Q}\} = \begin{Bmatrix} \{Q_c\} \\ \{Q_s\} \end{Bmatrix}; \quad \{\bar{q}\} = \begin{Bmatrix} \{q_c\} \\ \{q_s\} \end{Bmatrix}$$

If the mass eccentricity curve is assumed as an m -degree polynomial in space and projected into the x - z and y - z planes, there will be $2(m+1)$ real unknown coefficients totally. $8(n+1)$ equations can be found by modeling the shaft with n elements. So, a necessary condition in modeling the shaft is $8(n+1) \geq 2(m+1)$, which must be satisfied in order to identify the eccentricity curve.

The eccentricity of a shaft can reasonably be divided into a limited number of piecewise curves, called the global eccentricity curves. There may be just one global eccentricity curve through-

out the shaft or several piecewise global eccentricity curves, not necessarily connected for the adjacent curves, due to abrupt changes in properties or geometry along the shaft. The eccentricity curve for each shaft element is called the local eccentricity. Obviously, the local eccentricity curves should match the global eccentricity curve(s), and same degrees of polynomials should be assigned to the matched global and local eccentricity curves. The global eccentricity curve may be

$$X(z) = \sum_{i=0}^m A_i z^i \quad (9a)$$

$$Y(z) = \sum_{i=0}^m B_i z^i \quad (9b)$$

where $X(z)$ is the projection of the global eccentricity curve on the x - z plane, and $Y(z)$ the projection of the global eccentricity curve on the y - z plane.

The local eccentricity curve for a shaft element may be represented as

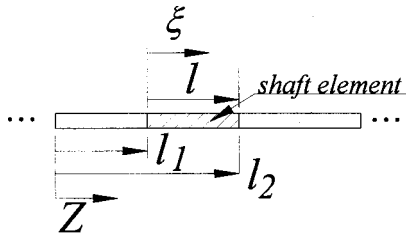


Fig. 3 Global and local coordinates

$$x(\xi) = \sum_{i=0}^m a_i \xi^i \quad (10a)$$

$$y(\xi) = \sum_{i=0}^m b_i \xi^i \quad (10b)$$

where

$$\xi = \frac{s}{l}, \quad 0 < \xi < 1.$$

In the following derivation, the eccentricity curves are assumed in polynomials of degree 3 for illustration. Similar procedures can be derived for polynomials of arbitrary degrees. The global eccentricity curve can be

$$X(z) = A_3 z^3 + A_2 z^2 + A_1 z + A_0 \quad (11a)$$

$$Y(z) = B_3 z^3 + B_2 z^2 + B_1 z + B_0 \quad (11b)$$

and the local eccentricity

$$x(\xi) = a_3 \xi^3 + a_2 \xi^2 + a_1 \xi + a_0 \quad (12a)$$

$$y(\xi) = b_3 \xi^3 + b_2 \xi^2 + b_1 \xi + b_0 \quad (12b)$$

where

$$\xi = \frac{s}{l}, \quad 0 \leq \xi \leq 1.$$

On the same shaft element, the local and global eccentricity curves should be matched. Thus, the values and derivatives of the local and global eccentricity curves at the nodes of the element are required to be equal, so

$$X(l_1) = x(0) = a_0 \quad (13)$$

$$X'(l_1) = x'(0) = \frac{a_1}{l} \quad (14)$$

$$X(l_2) = x(1) = \frac{a_3}{l^3} + \frac{a_2}{l^2} + \frac{a_1}{l} + a_0 \quad (15)$$

$$X'(l_2) = x'(1) = \frac{3a_3}{l^3} + \frac{2a_2}{l^2} + \frac{a_1}{l} \quad (16)$$

$$Y(l_1) = y(0) = b_0 \quad (17)$$

$$Y'(l_1) = y'(0) = \frac{b_1}{l} \quad (18)$$

$$Y(l_2) = y(1) = \frac{b_3}{l^3} + \frac{b_2}{l^2} + \frac{b_1}{l} + b_0 \quad (19)$$

$$Y'(l_2) = y'(1) = \frac{3b_3}{l^3} + \frac{2b_2}{l^2} + \frac{b_1}{l} \quad (20)$$

where $l = l_2 - l_1$, l_1 , l_2 are the z -coordinates of the nodes of the element, see Fig. 3. “ $'$ ” denotes the derivative with respect to z .

Rearranging Eqs. (13)–(20), we can obtain

$$\begin{Bmatrix} X(l_1) \\ X'(l_1) \\ X(l_2) \\ X'(l_2) \\ Y(l_1) \\ Y'(l_1) \\ Y(l_2) \\ Y'(l_2) \end{Bmatrix} = \begin{bmatrix} 0 & 0 & 0 & 1 & 0 & 0 & 0 & 0 \\ 0 & 0 & 1/l & 0 & 0 & 0 & 0 & 0 \\ 1/l^3 & 1/l^2 & 1/l & 1 & 0 & 0 & 0 & 0 \\ 3/l^3 & 2/l^2 & 1/l & 0 & 0 & 0 & 0 & 0 \\ 0 & 0 & 0 & 0 & 0 & 0 & 0 & 1 \\ 0 & 0 & 0 & 0 & 0 & 0 & 1/l & 0 \\ 0 & 0 & 0 & 0 & 1/l^3 & 1/l^2 & 1/l & 1 \\ 0 & 0 & 0 & 0 & 3/l^3 & 2/l^2 & 1/l & 0 \end{bmatrix} \times \begin{Bmatrix} a_3 \\ a_2 \\ a_1 \\ a_0 \\ b_3 \\ b_2 \\ b_1 \\ b_0 \end{Bmatrix}. \quad (21)$$

Inverting the matrix gives

$$\begin{Bmatrix} a_3 \\ a_2 \\ a_1 \\ a_0 \\ b_3 \\ b_2 \\ b_1 \\ b_0 \end{Bmatrix} = \begin{bmatrix} 2 & l & -2 & l & 0 & 0 & 0 & 0 \\ -3 & -2l & 3 & -l & 0 & 0 & 0 & 0 \\ 0 & l & 0 & 0 & 0 & 0 & 0 & 0 \\ 1 & 0 & 0 & 0 & 0 & 0 & 0 & 0 \\ 0 & 0 & 0 & 0 & 2 & l & -2 & l \\ 0 & 0 & 0 & 0 & -3 & -2l & 3 & -l \\ 0 & 0 & 0 & 0 & 0 & l & 0 & 0 \\ 0 & 0 & 0 & 0 & 1 & 0 & 0 & 0 \end{bmatrix} \times \begin{Bmatrix} X(l_1) \\ X'(l_1) \\ X(l_2) \\ X'(l_2) \\ Y(l_1) \\ Y'(l_1) \\ Y(l_2) \\ Y'(l_2) \end{Bmatrix}. \quad (22)$$

Equation (22) can be written in short as

$$\{u_3^e\} = [T_l^e] \{\alpha^e\} \quad (23)$$

where $\{\alpha^e\}$ is the vector for the eccentricity values and derivatives at the nodes, and $\{u_3^e\}$ is the coefficient vector of the local eccentricity curve.

Extending the procedure to polynomials of degree m and assembling the element equations gives us the equation for all the local eccentricity coefficients,

$$\{u_m\}_{2n(m+1) \times 1} = [T_l]_{2n(m+1) \times 2(m+1)} \{\alpha\}_{2(m+1) \times 1}, \quad (24)$$

where n is the total number of shaft elements and $[T_l]$ is the assembly of element matrices $[T_l^e]$.

$$\{u_m\} = \{ \{u_{m1x}^e\}^T \{u_{m1y}^e\}^T \cdots \{u_{mnx}^e\}^T \{u_{mny}^e\}^T \}^T$$

$$\{u_{mnx}^e\} = \{a_{mn}, \cdots, a_{1n}, a_{0n}\}^T, \quad \{u_{mny}^e\} = \{b_{mn}, \cdots, b_{1n}, b_{0n}\}^T$$

a_{ij} and b_{ij} are the local eccentricity coefficients of degree i in element j , $i = 0 \sim m$, $j = 0 \sim n$.

$$\{\alpha\} = \{ \{\alpha^e(0)\} \cdots \{\alpha^e(l_n)\} \}^T, \quad \{\alpha^e(l_j)\} = \begin{Bmatrix} \{\alpha_x^e(l_j)\} \\ \{\alpha_y^e(l_j)\} \end{Bmatrix}$$

$$\{\alpha_x^e(l_j)\} = \{X(l_j), X'(l_j), \dots, X^{(k)}(l_j)\}^T$$

$$\{\alpha_y^e(l_j)\} = \{Y(l_j), Y'(l_j), \dots, Y^{(k)}(l_j)\}^T$$

$k = (m-1)/2$ and m is an odd number.

If m is an even number, the derivatives up to order of $m/2$ of the local and global eccentricity curves are matched at one node of the element while only the derivatives up to order of $m/2 - 1$ are matched at the other node.

Similarly, the values and derivatives of the global eccentricity curves at the nodes of the shaft element are

$$X(l_1) = A_3 l_1^3 + A_2 l_1^2 + A_1 l_1 + A_0 \quad (25)$$

$$X'(l_1) = 3A_3 l_1^2 + 2A_2 l_1 + A_1 \quad (26)$$

$$X(l_2) = A_3 l_2^3 + A_2 l_2^2 + A_1 l_2 + A_0 \quad (27)$$

$$X'(l_2) = 3A_3 l_2^2 + 2A_2 l_2 + A_1 \quad (28)$$

$$Y(l_1) = B_3 l_1^3 + B_2 l_1^2 + B_1 l_1 + B_0 \quad (29)$$

$$Y'(l_1) = 3B_3 l_1^2 + 2B_2 l_1 + B_1 \quad (30)$$

$$Y(l_2) = B_3 l_2^3 + B_2 l_2^2 + B_1 l_2 + B_0 \quad (31)$$

$$Y'(l_2) = 3B_3 l_2^2 + 2B_2 l_2 + B_1 \quad (32)$$

where l_1 and l_2 are the z -coordinates of the nodes of the shaft element, Fig. 3.

Combining Eqs. (25)–(32) yields

$$\begin{Bmatrix} X(l_1) \\ X'(l_1) \\ X(l_2) \\ X'(l_2) \\ Y(l_1) \\ Y'(l_1) \\ Y(l_2) \\ Y'(l_2) \end{Bmatrix} = \begin{bmatrix} l_1^3 & l_1^2 & l_1 & 1 & 0 & 0 & 0 & 0 \\ 3l_1^2 & 2l_1 & 1 & 0 & 0 & 0 & 0 & 0 \\ l_2^3 & l_2^2 & l_2 & 1 & 0 & 0 & 0 & 0 \\ 3l_2^2 & 2l_2 & 1 & 0 & 0 & 0 & 0 & 0 \\ 0 & 0 & 0 & 0 & l_1^3 & l_1^2 & l_1 & 1 \\ 0 & 0 & 0 & 0 & 3l_1^2 & 2l_1 & 1 & 0 \\ 0 & 0 & 0 & 0 & l_2^3 & l_2^2 & l_2 & 1 \\ 0 & 0 & 0 & 0 & 3l_2^2 & 2l_2 & 1 & 0 \end{bmatrix} \times \begin{Bmatrix} A_3 \\ A_2 \\ A_1 \\ A_0 \\ B_3 \\ B_2 \\ B_1 \\ B_0 \end{Bmatrix} \quad (33)$$

Equation (33) can be written in short as

$$\{\alpha^e\} = [T_L^e] \{U_3\} \quad (34)$$

where $\{\alpha^e\}$ contains the values and derivatives of the eccentricity at the nodes, and $\{U_3\}$ is the coefficient vector for the global eccentricity curve.

Extending the procedure to the polynomials of degree m and assembling from the element equations yields the equation for all the global eccentricity coefficients,

$$\{\alpha\}_{2n(m+1) \times 1} = [T_L]_{2n(m+1) \times 2n(m+1)} \{U_m\}_{2n(m+1) \times 1} \quad (35)$$

where

$$\{\alpha\} = \{\{\alpha^e(0)\} \cdots \{\alpha^e(l_n)\}\}^T$$

$$\{U_m\} = \begin{Bmatrix} \{U_{mx}\} \\ \{U_{my}\} \end{Bmatrix},$$

$$\{U_{mx}\} = \{A_m, A_{m-1}, \dots, A_2, A_1, A_0\}^T,$$

and

$$\{U_{my}\} = \{B_m, B_{m-1}, \dots, B_2, B_1, B_0\}^T.$$

$k = (m-1)/2$ and m is an odd number. The derivation of $[T_L]$ for an even degree m is similar as explained in the previous section.

From Eqs. (24) and (35), we have the relations between the coefficients of local and global eccentricity curves

$$\{u_m\} = [T_L][T_L] \{U_m\}. \quad (36)$$

The relations between the coefficients of the eccentricity curves and the unbalance forces for each element can be obtained by using Eq. (2) as

$$\{Q_c^e\} = \Omega^2 [QD_c^e] \{u_3^e\} \quad (37a)$$

$$\{Q_s^e\} = \Omega^2 [QD_s^e] \{u_3^e\} \quad (37b)$$

where

$$\{u_3^e\} = \{a_3, a_2, a_1, a_0, b_3, b_2, b_1, b_0\}^T$$

$$[QD_c^e] = \frac{\mu}{1+\Phi} [[QD_{c0}^e] + \Phi [QD_{c1}^e]]$$

$$[QD_s^e] = \frac{\mu}{1+\Phi} [[QD_{s0}^e] + \Phi [QD_{s1}^e]]$$

$$\Phi = \frac{12EI}{KGA l^2}$$

$$[QD_{c0}^e] = \begin{bmatrix} \frac{l}{28} & \frac{l}{15} & \frac{3l}{20} & \frac{l}{2} & 0 & 0 & 0 & 0 \\ 0 & 0 & 0 & 0 & \frac{l}{28} & \frac{l}{15} & \frac{3l}{20} & \frac{l}{2} \\ 0 & 0 & 0 & 0 & \frac{-l^2}{105} & \frac{-l^2}{60} & \frac{-l^2}{30} & \frac{-l^2}{12} \\ \frac{l^2}{105} & \frac{l^2}{60} & \frac{l^2}{30} & \frac{l^2}{12} & 0 & 0 & 0 & 0 \\ \frac{3l}{14} & \frac{4l}{15} & \frac{7l}{20} & \frac{l}{2} & 0 & 0 & 0 & 0 \\ 0 & 0 & 0 & 0 & \frac{3l}{14} & \frac{4l}{15} & \frac{7l}{20} & \frac{l}{2} \\ 0 & 0 & 0 & 0 & \frac{l^2}{42} & \frac{l^2}{30} & \frac{l^2}{20} & \frac{l^2}{12} \\ \frac{-l^2}{42} & \frac{-l^2}{30} & \frac{-l^2}{20} & \frac{-l^2}{12} & 0 & 0 & 0 & 0 \end{bmatrix}$$

$$[QD_{c1}^e] = \begin{bmatrix} \frac{l}{20} & \frac{l}{12} & \frac{l}{6} & \frac{l}{2} & 0 & 0 & 0 & 0 \\ 0 & 0 & 0 & 0 & \frac{l}{20} & \frac{l}{12} & \frac{l}{6} & \frac{l}{2} \\ 0 & 0 & 0 & 0 & \frac{-l^2}{60} & \frac{-l^2}{40} & \frac{-l^2}{24} & \frac{-l^2}{12} \\ \frac{l^2}{60} & \frac{l^2}{40} & \frac{l^2}{24} & \frac{l^2}{12} & 0 & 0 & 0 & 0 \\ \frac{l}{5} & \frac{l}{4} & \frac{l}{3} & \frac{l}{2} & 0 & 0 & 0 & 0 \\ 0 & 0 & 0 & 0 & \frac{l}{5} & \frac{l}{4} & \frac{l}{3} & \frac{l}{2} \\ 0 & 0 & 0 & 0 & \frac{l^2}{60} & \frac{l^2}{40} & \frac{l^2}{24} & \frac{l^2}{12} \\ \frac{-l^2}{60} & \frac{-l^2}{40} & \frac{-l^2}{24} & \frac{-l^2}{12} & 0 & 0 & 0 & 0 \end{bmatrix}$$

$$[QD_{s0}^e] = \begin{bmatrix} 0 & 0 & 0 & 0 & \frac{-l}{28} & \frac{-l}{15} & \frac{-3l}{20} & \frac{-l}{2} \\ \frac{l}{28} & \frac{l}{15} & \frac{3l}{20} & \frac{l}{2} & 0 & 0 & 0 & 0 \\ \frac{-l^2}{105} & \frac{-l^2}{60} & \frac{-l^2}{30} & \frac{-l^2}{12} & 0 & 0 & 0 & 0 \\ 0 & 0 & 0 & 0 & \frac{-l^2}{105} & \frac{-l^2}{60} & \frac{-l^2}{30} & \frac{-l^2}{12} \\ 0 & 0 & 0 & 0 & \frac{3l}{14} & \frac{4l}{15} & \frac{7l}{20} & \frac{l}{2} \\ \frac{3l}{14} & \frac{4l}{15} & \frac{7l}{20} & \frac{l}{2} & 0 & 0 & 0 & 0 \\ \frac{l^2}{42} & \frac{l^2}{30} & \frac{l^2}{20} & \frac{l^2}{12} & 0 & 0 & 0 & 0 \\ 0 & 0 & 0 & 0 & \frac{l^2}{42} & \frac{l^2}{30} & \frac{l^2}{20} & \frac{l^2}{12} \end{bmatrix}$$

$$[QD_{s1}^e] = \begin{bmatrix} 0 & 0 & 0 & 0 & \frac{-l}{20} & \frac{-l}{12} & \frac{-l}{6} & \frac{-l}{2} \\ \frac{l}{20} & \frac{l}{12} & \frac{l}{6} & \frac{l}{2} & 0 & 0 & 0 & 0 \\ \frac{-l^2}{60} & \frac{-l^2}{40} & \frac{-l^2}{24} & \frac{-l^2}{12} & 0 & 0 & 0 & 0 \\ 0 & 0 & 0 & 0 & \frac{-l^2}{60} & \frac{-l^2}{40} & \frac{-l^2}{24} & \frac{-l^2}{12} \\ 0 & 0 & 0 & 0 & \frac{-l}{5} & \frac{-l}{4} & \frac{-l}{3} & \frac{-l}{2} \\ \frac{l}{5} & \frac{l}{4} & \frac{l}{3} & \frac{l}{2} & 0 & 0 & 0 & 0 \\ \frac{l^2}{60} & \frac{l^2}{40} & \frac{l^2}{24} & \frac{l^2}{12} & 0 & 0 & 0 & 0 \\ 0 & 0 & 0 & 0 & \frac{l^2}{60} & \frac{l^2}{40} & \frac{l^2}{24} & \frac{l^2}{12} \end{bmatrix}$$

When polynomials of degree m are used, Eqs. (37a) and (37b) will have the form as

$$\begin{Bmatrix} [Q_c^e] \\ [Q_s^e] \end{Bmatrix} = \Omega^2 \begin{bmatrix} [QD_c^e] \\ [QD_s^e] \end{bmatrix} \{u_m^e\}. \quad (38)$$

Assembling the element equations, we obtain

$$\{Q\} = \Omega^2 [QD] \{u_m\}. \quad (39)$$

Substituting Eqs. (36) and (39) into Eq. (8), we can write

$$[T_{sys}]_{p \times p} \{\tilde{q}\} = \Omega^2 [QD]_{p \times q} [T_l]_{q \times q} [T_L]_{q \times r} \{U_m\} \quad (40)$$

where

$$p = 8(n+1); \quad q = 2n(m+1); \quad r = 2(m+1).$$

Equation (40) relates the coefficients of the global eccentricity curves to the vibration response. The above procedure can be extended to a shaft with a complicated geometry, where the eccentricity curves can be assumed as finite and piecewise polynomials.

Reforming Eq. (40) gives

$$\{\tilde{q}\} = \Omega^2 [T_{sys}]^{-1} [QD] [T_l] [T_L] \{U_m\} = \Omega^2 [T]_{p \times r} \{U_m\} \quad (41)$$

where

$$p = 8(n+1), \quad r = 2(m+1), \quad \text{and} \quad [T] = [T_{sys}]^{-1} [QD] [T_l] [T_L].$$

Eq. (41) is used to identify the coefficients of the eccentricity curve, $\{U_m\}$. In Eq. (41), $[T_{sys}(\Omega)]$ can be obtained from finite element modeling; $[T_l]$, $[T_L]$, and $[QD]$ are obtained from Eqs. (24), (35), and (39); $\{\tilde{q}\}$ is the vibration responses, and can be measured from experiments.

If a disk on the shaft also has unbalance, the eccentricity coefficients to be identified become

$$\{U\} = \begin{Bmatrix} \{U_m\} \\ \{U^d\} \end{Bmatrix}. \quad (42)$$

where

$$\{U^d\} = \begin{Bmatrix} x_d \\ y_d \end{Bmatrix},$$

and $\{U_m\}$ is the eccentricity coefficient vector for the shaft. The disk unbalance should be inserted into the corresponding rows of the nodes where the disk is located in the finite element model. So, the matrices of Eq. (41) are modified as

$$[QD_c^d] = \begin{bmatrix} \vdots & \vdots \\ 0 & \vdots \\ [QD_c] & 0 \\ 0 & m_d \\ \vdots & 0 \\ \vdots & \vdots \\ \vdots & \vdots \end{bmatrix}_{(p/2) \times (q+2)} \quad (43)$$

$$[QD_s^d] = \begin{bmatrix} \vdots & \vdots \\ \vdots & 0 \\ [QD_s] & -m_d \\ m_d & 0 \\ 0 & \vdots \\ \vdots & \vdots \end{bmatrix}_{(p/2) \times (q+2)} \quad (44)$$

$$[T_l^d] = \begin{bmatrix} [T_l] & \{\tilde{0}\} & \{\tilde{0}\} \\ \{\tilde{0}\} & 1 & 0 \\ \{\tilde{0}\} & 0 & 1 \end{bmatrix}_{(q+2) \times (q+2)} \quad (45)$$

$$[T_L^d] = \begin{bmatrix} [T_L] & \{\tilde{0}\} & \{\tilde{0}\} \\ \{\tilde{0}\} & 1 & 0 \\ \{\tilde{0}\} & 0 & 1 \end{bmatrix}_{(q+2) \times (q+2)} \quad (46)$$

Solution Considerations

Suppose a rotor-bearing system contains d disks and h shaft segments of unbalance, in which each shaft segment for unbalance is uniform in geometry and property. If a polynomial of degree m_i is assumed for the eccentricity distribution of the i th segment, then in the finite element modeling, the total number of the shaft elements n must satisfy

$$8(n+1) \geq \sum_{i=1}^h 2(m_i+1) + 2d \quad (47)$$

where the identification equation is

$$\{\tilde{q}\} = \Omega^2 [T]_{p \times t} \{U\} \quad (48)$$

and

$$p = 8(n+1); \quad t = \sum_{i=1}^h 2(m_i+1) + 2d.$$

Eq. (47) is of the form

$$[A]\{x\} = \{b\} \quad (49)$$

where

$$\{b\} = \{\tilde{q}\}; \quad [A] = \Omega^2 [T(\Omega)]; \quad \{x\} = \{U\}.$$

Methods of least square fitting or singular value decomposition ([16,17]) can be used to solve Eq. (49), especially when $[A]$ is not rectangular.

In industrial rotating machines, not all the nodal locations along the length of the shaft can be measured by the sensors. Most of the locations are covered by casings or shields due to structural designs or safety considerations. Sensor signals can only be acquired at the locations exposed, or from the sensors pre-installed. From the observations of the nonzero off-diagonal terms of $[T]$, we know that the vibration response at each node is influenced by the unbalance at all the other nodes. The unbalance message at each node transmits along the shaft and shows its effects in the vibration response at all locations. Theoretically, the unbalance distribution along the shaft can be uncovered with enough measurement information at a single node.

To overcome the lacking of measurable locations, which makes the number of equations less than the number of unknowns, measurements are made at different operating speeds. This is possible because unbalance mass distributions do not change with operating speeds. By assuming signals are taken from w degrees-of-freedom at an operating speed Ω ,

$$\{q^*(\Omega)\} = \Omega^2 [T^*(\Omega)]_{2w \times t} \{U\} \quad (50)$$

where

$$\{q^*(\Omega)\} = \{q_{1c} \cdots q_{wc} q_{1s} \cdots q_{ws}\}_{2w \times t}^T,$$

w is the number of the measurement degrees-of-freedom, $w \leq 4(n+1)$. $[T^*(\Omega)]$ is the matrix with the rows corresponding to the measurement degrees-of-freedom.

Let the operating speeds for measurement be $\Omega_1, \Omega_2, \dots, \Omega_k$. Eq. (50) is expanded to become

$$\begin{Bmatrix} \{q^*(\Omega_1)\} \\ \{q^*(\Omega_2)\} \\ \vdots \\ \{q^*(\Omega_k)\} \end{Bmatrix} = \begin{bmatrix} \Omega_1^2 [T^*(\Omega_1)] \\ \Omega_2^2 [T^*(\Omega_2)] \\ \vdots \\ \Omega_k^2 [T^*(\Omega_k)] \end{bmatrix}_{2kw \times t} \{U\} \quad (51)$$

In order to solve the equation, the number of speeds k has to satisfy

$$2kw \geq t. \quad (52)$$

Results and Discussion

The aim of this paper is to study the feasibility of the proposed identification theory. The system for illustration is a high damping and anisotropic rotor-bearing system. The rotor model for simulations is depicted in Fig. 4. Related geometry data are given in Table 1. As stated in Table 2, the shaft eccentricity distributions are chosen arbitrarily in polynomials of degree three for demonstration, while the unbalance masses of disks are lumped. The eccentricity curve of the shaft is divided into two global eccentricity segments. The xz (and yz) projections of the eccentricity curve are shown in Fig. 5.

In the first example, four shaft elements (Fig. 4) are used in finite element modeling to fulfill the requirement of Eq. (47), so we have 18 unknown coefficients, 2 for the disks and 16 for the shaft. The four degrees-of-freedom of the middle point, node 3, are measured and eight equations are obtained. So, at least three operating speeds are necessary for the identification work. Table 3 shows the identification results with operating speeds, 9000, 9100, and 9200 rpm (rounded up to six significant digits). The results show high accuracy of agreement with an averaged coefficient error, $3.163 \times 10^{-4}\%$. The accurate results of identification are

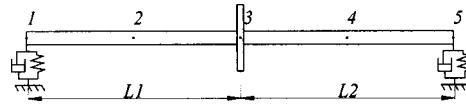


Fig. 4 Rotor model and four elements in finite element modeling

Table 1 Rotor data

Shaft
Outer Diameter : 0.01 m
$L1 = 0.2m$, $L2 = 0.2m$
$E = 2.07 \times 10^7 \text{ N/m}^2$, $G = 8.0 \times 10^{10} \text{ N/m}^2$
$\rho = 7750 \text{ kg} \cdot \text{m}^3$
Disk
Outer Diameter : 0.1 m
Thickness : 0.005 m
Mass : 0.3043 kg
Density : $\rho = 7750 \text{ kg} \cdot \text{m}^3$
Bearings
$K_{xx} = 1 \times 10^7 \text{ N/m}$, $K_{xy} = 1 \times 10^6 \text{ N/m}$
$K_{yx} = 1 \times 10^6 \text{ N/m}$, $K_{yy} = 1 \times 10^7 \text{ N/m}$
$C_{xx} = 500 \text{ N} \cdot \text{s/m}$, $C_{xy} = 50 \text{ N} \cdot \text{s/m}$
$C_{yx} = 50 \text{ N} \cdot \text{s/m}$, $C_{yy} = 500 \text{ N} \cdot \text{s/m}$

Table 2 Eccentricity data

Operating Speeds : 9000, 9100, 9200, (9300) rpm
Disk eccentricity :
$x_d = -1 \times 10^{-6} \text{ m}$, $y_d = 1 \times 10^{-6} \text{ m}$
Shaft Eccentricity :
Segment 1 ($L = 0 \sim 0.2 \text{ m}$)
$x(\tilde{z}) = 0.00533\tilde{z}^3 - 0.0016\tilde{z}^2 + 0.000107\tilde{z} - 1 \times 10^{-6} \text{ m}$
$y(\tilde{z}) = 0.00533\tilde{z}^3 - 0.0016\tilde{z}^2 + 0.000107\tilde{z} - 1 \times 10^{-6} \text{ m}$
Segment 2 ($L = 0.2 \sim 0.4 \text{ m}$)
$x(\tilde{z}) = 0.00533\tilde{z}^3 - 0.0016\tilde{z}^2 + 0.000107\tilde{z} - 1 \times 10^{-6} \text{ m}$
$y(\tilde{z}) = 0.00533\tilde{z}^3 - 0.0016\tilde{z}^2 + 0.000107\tilde{z} - 1 \times 10^{-6} \text{ m}$
$\tilde{z} = z - 0.2$

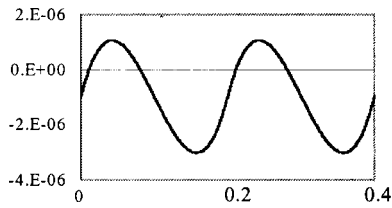


Fig. 5 $xz(yz)$ projection of eccentricity

Table 3 Identification results, noise free

	Exact	Estimated (4 elements)	Estimated (20 elements)
Disk			
x_d	-1.00×10^{-6}	-1.00000×10^{-6}	-1.00000×10^{-6}
y_d	1.00×10^{-6}	1.00000×10^{-6}	1.00000×10^{-6}
Shaft			
Segment 1	A_{31}	5.33×10^{-3}	5.33000×10^{-3}
	A_{21}	-1.60×10^{-3}	-1.60000×10^{-3}
	A_{11}	1.07×10^{-4}	1.07000×10^{-4}
	A_{01}	-1.00×10^{-6}	-1.00000×10^{-6}
	B_{31}	5.33×10^{-3}	5.32998×10^{-3}
	B_{21}	-1.60×10^{-3}	-1.60000×10^{-3}
	B_{11}	1.07×10^{-4}	1.07000×10^{-4}
	B_{01}	-1.00×10^{-6}	-0.99997×10^{-6}
Segment 2	A_{32}	5.33×10^{-3}	5.33000×10^{-3}
	A_{22}	-1.60×10^{-3}	-1.60000×10^{-3}
	A_{12}	1.07×10^{-4}	1.07000×10^{-4}
	A_{02}	-1.00×10^{-6}	-0.99999×10^{-6}
	B_{32}	5.33×10^{-3}	5.33001×10^{-3}
	B_{22}	-1.60×10^{-3}	-1.60000×10^{-3}
	B_{12}	1.07×10^{-4}	1.07001×10^{-4}
	B_{02}	-1.00×10^{-6}	-1.00002×10^{-6}
Ave Error (%)		3.163×10^{-4}	1.002×10^{-4}
Condition Number		2.240×10^{11}	3.891×10^{10}

due to the sufficient measurement information and the noise-free condition. To improve the identification accuracy, the shaft is modeled with 20 shaft elements, which is more accurate in finite element modeling than four elements. The improved finite element model of the rotor is shown in Fig. 6. Again, the middle point, node 11, is measured and the results are compared with those of the previous case. Table 3 shows that the averaged coefficient error reduced to 1.002×10^{-4} %. This improvement is due to the decrease of the condition number of $[T_{sys}]$, where the condition number is reduced from 2.240×10^{11} to 3.891×10^{10} .

Noise inevitably pollutes the signals in field measurements and enlarges the identification errors. Simulations are conducted with added noise of NSR=1% into the signals. 400 sets of signals are averaged. Table 4 shows the comparison of the results of two-point (nodes 6 and 16) and three-point (nodes 6, 11, and 16) measurements. The averaged coefficient error is reduced from 2.164% to 0.229% with more points in measurement. Next, The simulation is done for four operating speeds, 9000, 9100, 9200,

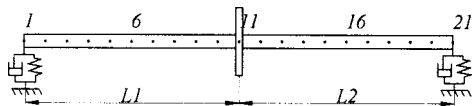


Fig. 6 Rotor model and 20 elements in finite element modeling

Table 4 Identification results, NSR=1%

	Exact	Estimated (2 nodes)	Estimated (3 nodes)
Disk			
x_d	-1.00×10^{-6}	-1.00729×10^{-6}	-1.00134×10^{-6}
y_d	1.00×10^{-6}	0.99159×10^{-6}	1.00010×10^{-6}
Shaft			
Segment 1	A_{31}	5.33×10^{-3}	5.40007×10^{-3}
	A_{21}	-1.60×10^{-3}	-1.64639×10^{-3}
	A_{11}	1.07×10^{-4}	1.08100×10^{-4}
	A_{01}	-1.00×10^{-6}	-1.01236×10^{-6}
	B_{31}	5.33×10^{-3}	5.40586×10^{-3}
	B_{21}	-1.60×10^{-3}	-1.61767×10^{-3}
	B_{11}	1.07×10^{-4}	1.08107×10^{-4}
	B_{01}	-1.00×10^{-6}	-1.01325×10^{-6}
Segment 2	A_{32}	5.33×10^{-3}	5.25603×10^{-3}
	A_{22}	-1.60×10^{-3}	-1.57299×10^{-3}
	A_{12}	1.07×10^{-4}	1.04011×10^{-4}
	A_{02}	-1.00×10^{-6}	-0.90399×10^{-6}
	B_{32}	5.33×10^{-3}	5.24015×10^{-3}
	B_{22}	-1.60×10^{-3}	-1.56728×10^{-3}
	B_{12}	1.07×10^{-4}	1.03390×10^{-4}
	B_{02}	-1.00×10^{-6}	-0.88459×10^{-6}
Ave Error (%)		2.614	0.299

and 9300 rpm. The results are shown in Table 5. As expected, the averaged coefficient error is reduced from 2.614% to 2.087%. The increase of the measurement points and the number of operating speeds would add more information into the identification equation and improve the accuracy of the results. Based on this reasoning, it is likely that increasing the distances between sensors will also improve the accuracy of identification.

Table 5 Identification results, NSR=1%

	Exact	Estimated* (3 speeds)	Estimated** (4 speeds)
Disk			
x_d	-1.00×10^{-6}	-1.00729×10^{-6}	-1.00624×10^{-6}
y_d	1.00×10^{-6}	0.99159×10^{-6}	0.99425×10^{-6}
Shaft			
Segment 1	A_{31}	5.33×10^{-3}	5.40007×10^{-3}
	A_{21}	-1.60×10^{-3}	-1.64639×10^{-3}
	A_{11}	1.07×10^{-4}	1.08100×10^{-4}
	A_{01}	-1.00×10^{-6}	-1.01236×10^{-6}
	B_{31}	5.33×10^{-3}	5.40586×10^{-3}
	B_{21}	-1.60×10^{-3}	-1.61767×10^{-3}
	B_{11}	1.07×10^{-4}	1.08107×10^{-4}
	B_{01}	-1.00×10^{-6}	-1.01325×10^{-6}
Segment 2	A_{32}	5.33×10^{-3}	5.25603×10^{-3}
	A_{22}	-1.60×10^{-3}	-1.57299×10^{-3}
	A_{12}	1.07×10^{-4}	1.04011×10^{-4}
	A_{02}	-1.00×10^{-6}	-0.90399×10^{-6}
	B_{32}	5.33×10^{-3}	5.24015×10^{-3}
	B_{22}	-1.60×10^{-3}	-1.56728×10^{-3}
	B_{12}	1.07×10^{-4}	1.03390×10^{-4}
	B_{02}	-1.00×10^{-6}	-0.88459×10^{-6}
Ave Error (%)		2.614	2.087

Conclusions

The proposed identification procedure for distributed unbalance of the rotor was validated to be effective for high damping and anisotropic rotor-bearing systems. The eccentricity distributions of the shaft are assumed in finite and piecewise polynomials while the unbalance masses of the disks are assumed lumped. Measurement of the response is only needed at a few locations along the length of the shaft. Effective means, such as increasing the number of operating speeds, enlarging the speed intervals, measuring at multipoints and increasing the distances among sensors, can improve the accuracy of identification, especially under noisy environments. The procedure is based on finite element modeling and is easy to integrate into existing finite element programs for rotordynamic analyses.

Nomenclature

- a, b = coefficient of the local eccentricity curve
 A, B = coefficient of the global eccentricity curve
 e = eccentricity of the shaft
 ϕ_u = phase angle of the unbalance of the shaft
 $x(s)$ = projection of the local eccentricity curve on the x - z plane, $x = e(s) \cos \phi_u(s)$
 $y(s)$ = projection of the local eccentricity curve on the y - z plane, $y = e(s) \sin \phi_u(s)$
 e_d = eccentricity of the disk
 ϕ_d = phase angle of the unbalance of the disk
 x_d = projection of the disk eccentricity on the x - z plane, $x_d = e_d \cos(\phi_d)$
 y_d = projection of the disk eccentricity on the y - z plane, $y_d = e_d \sin(\phi_d)$
 l = length of a shaft element
 m_d = mass of the disk
 $\{q\}$ = nodal displacement
 $\{Q\}$ = unbalance force
 $[T]$ = see Eq. (47)
 $[T_l]$ = see Eqs. (23) and (24)
 $[T_L]$ = see Eqs. (34) and (35)
 $[T_{\text{sys}}]$ = system matrix, see Eq. (8)
 $\{u_m\}$ = vector of the local eccentricity coefficients
 $\{U_m\}$ = vector of the global eccentricity coefficients
 $\{U^d\}$ = vector of the eccentricity of the disk
 s = local coordinate in a shaft element, $0 \leq s \leq l$
 ξ = s/l , $0 < \xi < 1$

Superscript

- d = disk
 e = element
 $*$ = values obtained on a specific speed

Subscript

- i = degree
 j = element number
 c = cosine term
 s = sine term

References

- [1] Darlow, M. S., 1989, *Balancing of High-Speed Machinery*, Springer-Verlag, New York.
- [2] Bishop, R. E. D., and Parkinson, A. G., 1972, "On the Use of Balancing Machines for Flexible Rotors," *ASME J. Eng. Ind.*, **94**, pp. 561–576.
- [3] Kellenberger, W., 1972, "Should a Flexible Rotor be Balanced in N or $(N + 2)$ planes?" *ASME J. Eng. Ind.*, **94**(2), pp. 548–560.
- [4] Saito, S., and Azawa, T., 1983, "Balancing of Flexible Rotors by the Complex Modal Method," *ASME J. Vib., Acoust., Stress, Reliab. Des.*, **105**, pp. 94–100.
- [5] Goodman, T. P., 1964, "A Least-Square Method for Computing Balance Corrections," *ASME J. Eng. Ind.*, **86**, pp. 273–279.
- [6] Lund, J. W., and Tonnesen, J., 1972, "Analysis and Experiments on Multiplane Balancing of a Flexible Rotor," *ASME J. Eng. Ind.*, **94**, pp. 233–242.
- [7] Tessarzik, J. M., Badgley, R. H., and Anderson, W. J., 1972, "Flexible Rotor Balancing by the Exact Point-Speed Influence Coefficient Method," *ASME J. Eng. Ind.*, **94**, pp. 148–158.
- [8] Darlow, M. S., Smalley, A. J., and Parkinson, A. G., 1981, "Demonstration of a Unified Approach to the Balancing of Flexible Rotors," *ASME J. Eng. Power*, **103**, pp. 101–107.
- [9] Parkinson, A. G., Darlow, M. S., and Smalley, A. J., 1980, "A Theoretical Introduction to the Development of a Unified Approach to Flexible Rotor Balancing," *J. Sound Vib.*, **68**(4), pp. 489–506.
- [10] Little, R. M., and Pilkey, W. D., 1976, "A Linear Programming Approach for Balancing Flexible Rotors," *ASME J. Eng. Ind.*, **98**, pp. 1030–1035.
- [11] Lee, A. C., Shih, Y. P., and Kang, Y., 1993, "The Analysis of Linear Rotor-Bearing Systems: A General Transfer Matrix Method," *ASME J. Vib. Acoust.*, **115**, pp. 490–497.
- [12] Lee, A. C., and Shin, Y. P., 1997, "Identification of The Unbalance Distribution in Flexible Rotors," *Int. J. Mech. Sci.*, **39**, pp. 841–857.
- [13] Nelson, H. D., 1980, "A Finite Rotating Shaft Element Using Timoshenko Beam Theory," *ASME J. Mech. Des.*, **102**, pp. 793–803.
- [14] Lin, C., 1999, "Identification of Distributed Unbalance on Bent Rotors," Master thesis, Department of Mechanical Engineering, Yuan Ze University, Taiwan.
- [15] Nelson, H. D., and McVaugh, J. M., 1976, "The Dynamics of Rotor-Bearing Systems Using Finite Elements," *ASME J. Eng. Ind.*, **98**, pp. 593–600.
- [16] Leon, S. J., *Linear Algebra With Application 4th*, Prentice-Hall, Englewood Cliffs, NJ.
- [17] Hasan, W. M., and Viola, E., 1997, "Use of The Singular Value Decomposition Method To Detect Ill-Conditioning of Structural Identification Problems," *Comput. Struct.*, **63**(2), pp. 267–275.

Transient Rotordynamic Modeling of Rolling Element Bearing Systems

A. Liew

Postgraduate Student

N. Feng

Lecturer

E. J. Hahn

Professor

e-mail: e.hahn@unsw.edu.au

School of Mechanical and
Manufacturing Engineering,
The University of New South Wales,
Sydney, NSW 2052, Australia

Nonlinearity effects in rolling element bearings arise from Hertzian contact force deformation relationships, clearance between rolling elements and races, and the bearing-to-housing clearance. Assuming zero bearing-to-housing clearance, a simplified earlier analysis showed that rotor bearing systems (RBSs) with deep groove ball bearings can give rise to chaotic motion and jump. This paper extends the bearing model to include rolling element centrifugal load, angular contacts and axial dynamics; and illustrates their effects in a rigidly supported rigid RBS and a flexibly supported flexible RBS, the latter modeling an existing test rig. Results are presented on the effect of bearing preload on the unbalance response up to a speed of 18,000 rpm. [DOI: 10.1115/1.1479337]

Introduction

Rolling element bearings are widely used in rotating machinery where high reliability and low power consumption are primary concerns. In the dynamic analysis of rotor bearing systems (RBSs) with rolling element bearings, special modeling of the bearing characteristics is occasionally needed. This is not only because the bearing flexibility may be significant but also because of nonlinearity effects due to the Hertzian force deformation relationship, the varying stiffness resulting from load transmission via a finite number of rolling elements, the presence of clearance between the rolling elements and the bearing races, and the bearing-to-housing clearance.

Past investigations to predict the vibration behavior of such RBSs have been concerned with the determination of the stiffness and damping provided by these bearings under constant unidirectional loading situations. Thus, measurements under quasi-static conditions of the vertical and horizontal positions of rotors supported by ball bearings by Tamura and Taniguchi [1] agreed with predictions by Meldau [2]. Sunnersjö [3] extended this work to include rotor inertia effects and considered the possibility of positive clearance between the rolling elements and the bearing races. No unbalance loading was considered and the rotor was rigid. Experimental work provided qualitative agreement in locating resonance peaks which were at the ball passing frequency. The review paper by Stone [4] noted that the most important parameters affecting stiffness and damping were bearing type, axial preload, radial clearance/interference, and to a lesser extent, speed and lubricant. Whereas the investigations by Sunnersjö [3] were primarily concerned with roller bearings, which have a virtually linear force deformation characteristic ([5]), the investigations by Fukata et al. [6] were concerned with ball bearings for which the characteristic is nonlinear ([5]). Though restricting consideration to negative and zero radial clearance, sub/superharmonic resonances, beats and chaotic vibration possibilities were predicted, all in the absence of unbalance. Using a simpler expression for the ball bearing reaction force, Saito [7] investigated the effect of radial clearance on an unbalanced Jeffcott rotor, and predicted multistable solution possibilities. Tiwari et al. [8] carried out a detailed study of unbalance effects on ball bearing supported rigid rotors and again predicted nonsynchronous response. El-Saeidy

[9] extended the system modeling to flexible rotors, though the theoretical results were restricted to a symmetric balanced Jeffcott rotor with zero and positive bearing-to-housing clearance. Chaotic motions were again predicted. Assuming deep groove ball bearings, zero bearing-to-housing clearance, and neglecting ball inertia effects, Feng and Hahn [10] carried out a parametric study on the effect of radial clearance and unbalance loading using the model of a proposed experimental rig as the RBS. These investigations showed that the aforementioned nonlinear effects, including multistable operation (jump) were indeed possible. However, assurance of zero or negative clearance between the balls and the races is in practice frequently achieved by using preloaded angular contact ball bearings, the modeling of which is significantly more complicated than that for deep groove ball bearings. Also, it is unclear whether centrifugal load effects can justifiably be neglected.

Though centrifugal load effects on angular contact bearings were considered in earlier investigations ([11,12]), these neglected unbalance loading and did not, to the authors' knowledge, consider whether contact was maintained in the presence of centrifugal load. Also, previous transient analyses ([6,8,10]) were restricted to deep groove ball bearings, thereby avoiding the significant increase in computational effort involved in considering the additional degrees-of-freedom (DOF) necessarily present with angular contact bearings. Hence, this paper extends the earlier work by Feng and Hahn [10] to incorporate rolling element centrifugal load effects as well as axial and tilting stiffness effects, necessarily present with angular contact ball bearings. To simplify the analysis, it will still be assumed that the bearing-to-housing clearance is zero. It is recognized that this assumption may need to be revisited in light of evidence to the contrary, for with such clearance multistable, subharmonic, quasi-periodic and chaotic response ([13]) and even instability ([14]) have been predicted. Additionally, transient ball motion effects are ignored.

Modeling

The equations of motion for a RBS may be written as

$$M\ddot{\mathbf{X}} + C\dot{\mathbf{X}} + \mathbf{K}\mathbf{X} = \mathbf{G}(\mathbf{X}, \dot{\mathbf{X}}, t) \quad (1)$$

where the total nonlinear bearing forces (\mathbf{f}), gravity load and unbalance load constitute the function \mathbf{G} .

Four different models for evaluating the bearing forces are summarized below, viz. two or five degrees-of-freedom (DOF), with or without rolling element centrifugal load. The five-degree-of-

Contributed by the International Gas Turbine Institute (IGTI) of THE AMERICAN SOCIETY OF MECHANICAL ENGINEERS for publication in the ASME JOURNAL OF ENGINEERING FOR GAS TURBINES AND POWER. Paper presented at the International Gas Turbine and Aeroengine Congress and Exhibition, New Orleans, LA, June 4-7, 2001; Paper 01-GT-255. Manuscript received by IGTI, December 2000, final revision, March 2001. Associate Editor: R. Natole.

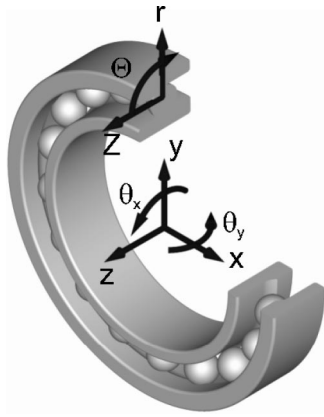


Fig. 1 5DOF model coordinate systems

freedom (DOF) modeling follows that of de Mul et al. [12] in that it is assumed that ball gyroscopic effects considered by Jones [11] may be ignored. All four models consider individual ball rolling elements and use Hertzian contact theory ([5]) to model the non-linear stiffness of the bearing. Whereas complicated functions are used for stiffness, constant damping is used to represent the effects of lubrication and friction. Cage influences are ignored though the spacing of the rolling elements is assumed constant.

Two-Degrees-of-Freedom Model Without Inertia (2DOF).

This was the model investigated previously ([10]). Of the five DOF shown in Fig. 1, only the x and y DOF are used. Contact or loss of contact is considered for each rolling element. Ignoring rolling element centrifugal load effects, the inner and outer race contact deformations can be combined so that the overall contact deformation for the j th rolling element, δ_j , is given by

$$\delta_j = x \cos \phi_j + y \sin \phi_j - c_i - c_e. \quad (2)$$

Summing the contact forces for each rolling element in the x and y directions gives

$$\begin{cases} f_x \\ f_y \end{cases} = K_p \sum \gamma_j \delta_j^n \begin{cases} \cos \phi_j \\ \sin \phi_j \end{cases} \quad (3)$$

where

$$\gamma_j = \begin{cases} 1 & \text{for } \delta_j > 0 \\ 0 & \text{for } \delta_j \leq 0 \end{cases} \quad \text{and} \quad \phi_j = \frac{2\pi(j-1)}{n_b} + \omega_c t + \phi_0. \quad (4)$$

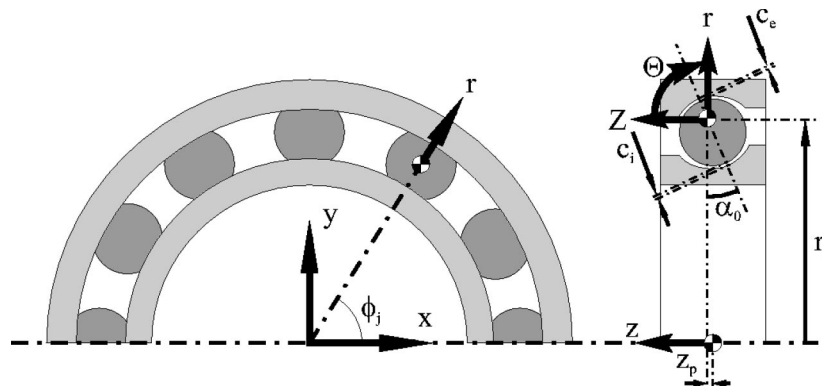


Fig. 2 5DOF model parameters

Two-Degrees-of-Freedom Model With Inertia (2DOF+i).

This model can be considered a simplification of the 5DOF model with centrifugal load effects included ([12]). Since the inner race and outer race contact forces are no longer equal, the contact deformations can no longer be combined. Hence for each ball

$$\frac{m_{re} \omega_c^2 D_p}{2} = F_e - F_i = K_{pe} \delta_e^n - K_{pi} \delta_i^n \quad (5)$$

and

$$\delta_i + \delta_e = \delta. \quad (6)$$

Elimination of δ_e gives

$$g(\delta_i) = \frac{m_{re} \omega_c^2 D_p}{2} + K_{pi} \delta_i^n - K_{pe} (\delta - \delta_i)^n = 0. \quad (7)$$

Equation (7) is a nonlinear equation in δ_i (δ is known for a given inner race position) that may be solved by some appropriate technique such as the Newton-Raphson algorithm. With known δ_i , all parameters, including the inner and outer race contact forces, can be obtained and transformed into the global degrees-of-freedom.

Note that when inertia is ignored, contact is lost when δ is negative but with centrifugal load, the inner race can lose contact even though there is still contact with the outer race. The critical value of δ when contact is lost, δ_c , occurs when $\delta_i = 0$. Hence contact with the inner race is lost when $\delta \leq \delta_c$, where

$$\delta_c = \left(\frac{m_{re} \omega_c^2 D_p}{2K_{pe}} \right)^{1/n}. \quad (8)$$

Five-Degrees-of-Freedom Model (5DOF).

As shown in Fig. 1, this model ([11,12]) includes not only the radial displacements of the inner race but also the rotations about the x and y -axes and the axial displacement. Two coordinate systems are used. The inner race coordinate system ($x, y, z, \theta_x, \theta_y$) corresponds to the degrees-of-freedom of the rotor at this point and has its origin at the center of the bearing. The local rolling element coordinate system (r, Z, Θ) defines the position of the inner race center of curvature for each rolling element and has its origin at the nominal position of the inner race center of curvature. The outer race center of curvature is used as a reference point. Figure 2 shows the various parameters used. Note that r_p , the radial coordinate of the nominal center of curvature of the inner race, is not related to D_p .

For the j th ball, the displacement of the inner race center of curvature, \mathbf{u} , is related to the displacement of the inner race, \mathbf{d} (treated as a known input quantity for the forcing function) according to

$$\mathbf{u} = \{u_r \ u_z \ u_\Theta\}^T = [\mathbf{R}]\mathbf{d} = [\mathbf{R}]\{x \ y \ z \ \theta_x \ \theta_y\}^T \quad (9)$$

where

$$[\mathbf{R}] = \begin{bmatrix} \cos \phi_j & \sin \phi_j & 0 & -z_p \sin \phi_j & z_p \cos \phi_j \\ 0 & 0 & 1 & r_p \sin \phi_j & -r_p \cos \phi_j \\ 0 & 0 & 0 & -\sin \phi_j & \cos \phi_j \end{bmatrix}_{3 \times 5} \quad (10)$$

All surfaces are assumed to be curves with only one radius of curvature. Figure 3(a) shows the geometry of the centers of curvatures of the inner race, of the outer race and of the center of the rolling element, before and after the known deflection of the inner race \mathbf{u} . Hence

$$l_{0i} = r_i - \frac{D_b}{2} - c_i, \quad l_{0e} = r_e - \frac{D_b}{2} - c_e \quad (11)$$

$$\tan \alpha = \frac{(l_{0i} + l_{0e}) \sin \alpha_0 + u_z}{(l_{0i} + l_{0e}) \cos \alpha_0 + u_r} = \frac{a}{b} \quad (12)$$

$$l_i + l_e = \sqrt{a^2 + b^2}. \quad (13)$$

Comparing $l_i + l_e$ with the nominal distance and the nominal clearance yields the overall contact deformation

$$\delta = l_i + l_e - l_{0i} - l_{0e} - c_i - c_e. \quad (14)$$

If the contact deformation is positive, then the contact load is calculated via the standard Hertzian contact relationship, otherwise contact is lost and no load is transmitted, so that

$$Q = \begin{cases} K_p \delta^{1.5} & (\text{for } \delta > 0) \\ 0 & (\text{for } \delta \leq 0). \end{cases} \quad (15)$$

Hence, the contact forces for the j th rolling element in the two coordinate systems are given by

$$\mathbf{Q} = \{Q_r \quad Q_z \quad Q_\theta\}^T = \{-Q \cos \alpha \quad -Q \sin \alpha \quad 0\}^T \quad (16)$$

and

$$\mathbf{F} = \{F_x \quad F_y \quad F_z \quad M_x \quad M_y\}^T = [\mathbf{R}]^T \mathbf{Q}. \quad (17)$$

Summing the contact forces for each rolling element gives the nonlinear forcing function, $\mathbf{f}(\mathbf{d})$. Note that if $\alpha_0 = 0$ and the θ_x , θ_y and z degrees-of-freedom are ignored, $\mathbf{f} = \{f_x, f_y\}^T$ as in Eq. (3).

Five-Degrees-of-Freedom Model With Inertia (5DOF+i).

Inclusion of rolling element centrifugal load means that inner and outer race contacts may have different contact angles. The equations of dynamic equilibrium become

$$\begin{cases} g_r \\ g_z \end{cases} = \begin{cases} Q_i \cos \alpha_i - Q_e \cos \alpha_e + \frac{m_{re} \omega_c^2 D_p}{2} \\ Q_i \sin \alpha_i - Q_e \sin \alpha_e \end{cases} = \begin{cases} 0 \\ 0 \end{cases} \quad (18)$$

where

$$Q_i = K_{pi} \delta_i^n \quad (\text{for } \delta_i > 0) \quad (19)$$

and

$$Q_e = K_{pe} \delta_e^n \quad (\text{for } \delta_e > 0). \quad (20)$$

From Fig. 3(b) one has the geometric relationships

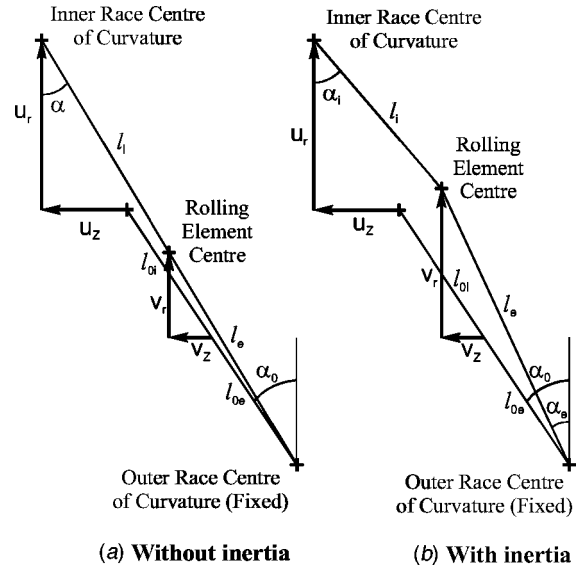


Fig. 3 Contact geometry

$$l_i = \frac{l_{0i} \cos \alpha_0 + u_r - v_r}{\cos \alpha_i} = \frac{l_{0i} \sin \alpha_0 + u_z - v_z}{\sin \alpha_i} \quad (21)$$

$$l_e = \frac{l_{0e} \cos \alpha_0 + v_r}{\cos \alpha_e} = \frac{l_{0e} \sin \alpha_0 + v_z}{\sin \alpha_e} \quad (22)$$

and

$$\delta_i = l_i - l_{0i} - c_i, \quad \delta_e = l_e - l_{0e} - c_e. \quad (23)$$

For a given inner ring position (\mathbf{u}) one now has two nonlinear equations for the two unknown rolling element positions v_r and v_z . These may again be solved by the Newton-Raphson technique extended to two unknowns, i.e.,

$$\mathbf{v} = \begin{cases} v_r \\ v_z \end{cases}_{i+1} = \begin{cases} v_r \\ v_z \end{cases}_i - \begin{bmatrix} \frac{\partial g_r}{\partial v_r} & \frac{\partial g_r}{\partial v_z} \\ \frac{\partial g_z}{\partial v_r} & \frac{\partial g_z}{\partial v_z} \end{bmatrix}_i^{-1} \begin{cases} g_r \\ g_z \end{cases}_i. \quad (24)$$

Reference [12] presents analytical expressions for these partial derivatives. As with the 2DOF+i model, careful attention needs to be paid to the conditions under which contact occurs. In absence of contact, the equations of dynamic equilibrium (18) reduce to

$$\begin{cases} -Q_e \cos \alpha_e + \frac{m_{re} \omega_c^2 D_p}{2} \\ -Q_e \sin \alpha_e \end{cases} = \begin{cases} 0 \\ 0 \end{cases} \quad (25)$$

giving

$$\alpha_e = 0 \quad \text{and} \quad Q_e = \frac{m_{re} \omega_c^2 D_p}{2}. \quad (26)$$

In other words the outer race provides the reaction to the rolling element centrifugal force and its contact angle becomes zero. To determine if contact occurs, the above condition can be assumed and the corresponding inner race contact deformation can be calculated. From Eqs. (20) and (26)

$$\delta_e = \left(\frac{m_{re} \omega_c^2 D_p}{2K_{pe}} \right)^{2/3}. \quad (27)$$

Table 1 Known bearing parameters

$\omega_c = 0.4398 \times \omega_s$ rad/s	$n_b = 18$	$D_p = 52$ mm
$D_b = 6.35$ mm	$\alpha_0 = 15$ deg	

Substituting into Eq. (23) yields

$$l_e = \delta_e + l_{0e} + c_e = \left(\frac{m_{re} \omega_c^2 D_p}{2K_{pe}} \right)^{2/3} + l_{0e} + c_e \quad (28)$$

and substituting Eq. (26) into Eq. (22) yields

$$v_z = -l_{0e} \sin \alpha_0 \quad \text{and} \quad v_x = l_e - l_{0e} \cos \alpha_0. \quad (29)$$

Using these elements of \mathbf{v} , for given \mathbf{u} , it is possible to calculate the inner race deflection from Eqs. (21) and (23). If δ_i is negative then contact does not occur. If, on the other hand, δ_i is positive, then contact does occur and the iterative solution for the rolling element position must be pursued as above. One can then calculate contact loads Q_i and Q_e and hence obtain \mathbf{Q}_i and \mathbf{Q}_e as in Eq. (16). As for the 5DOF model, the contact load vectors are transformed back into the global coordinate system and summed for all rolling elements.

Transient Solution Method. In light of earlier nonsynchronous responses with the 2DOF model ([10]), the bearing models were implemented into in-house transient analysis software which uses fixed-step fourth-order Runge-Kutta integration. In all solutions the time step size was considered sufficient when halving it no longer changed results. The maximum number of points per cycle required was 3000. Solutions were continued until a repetitive solution was obtained. In the case of chaotic results, the solution was continued until the envelope of the orbit remained constant.

Sample Calculations

All sample calculations used data pertinent to NSK/RHP angular contact bearing 7908CTDULP4 as these are the bearings to be used in the test rig. Tables 1 and 2 give the relevant bearing parameters. Note that the cage velocity ω_c could, if desired, be obtained by measurement rather than using the formula in Table 1. An arbitrary linear damping coefficient of 1000 Ns/m was assumed at all degrees-of-freedom associated with the bearings. For 2DOF modeling, the 5DOF were maintained (with the linear damping) but the nonlinear bearing forces were only applied to the relevant degrees-of-freedom. This eliminated any differences between modeling techniques except for those due to the different bearing models.

Single Bearing Model. A simple single-bearing model is used to demonstrate the effect of rolling element centrifugal load. Only 5DOF models were used because of the ease of applying preload. The axial and rotational motions associated with the 5DOF modeling are negligible in this example and hence the

Table 2 Estimated bearing parameters

$r_i = 3.2086$ mm	$r_o = 3.3655$ mm
$r_p = 25.5315$ mm	$z_p = 8.4375$ mm
$c_o = 1$ μ m	$c_i = 1$ μ m
$K_{pi} = 3.8832 \times 10^{10}$ Nm ^{-1.5}	
$K_{po} = 2.0821 \times 10^{10}$ Nm ^{-1.5}	
$m_{re} = 1.0524$ g (sphere volume \times 7850 kg/m ³)	

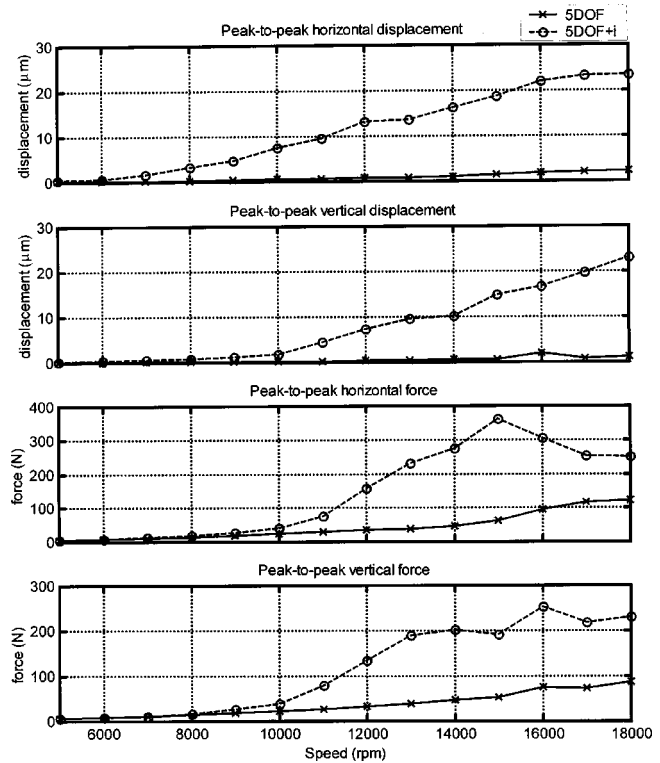


Fig. 4 Effect of inertia on peak-to-peak response

2DOF models can be tuned to give similar results. A 2 kg rotor was used with $I_d = 0.01$ kgm², $I_p = 0$, an unbalance of 1×10^{-5} kgm and a bearing preload of 19.5N. The rotor was modeled in five degrees-of-freedom with stiffness provided by the bearing model.

Figure 4 shows the peak-to-peak response of the single-bearing

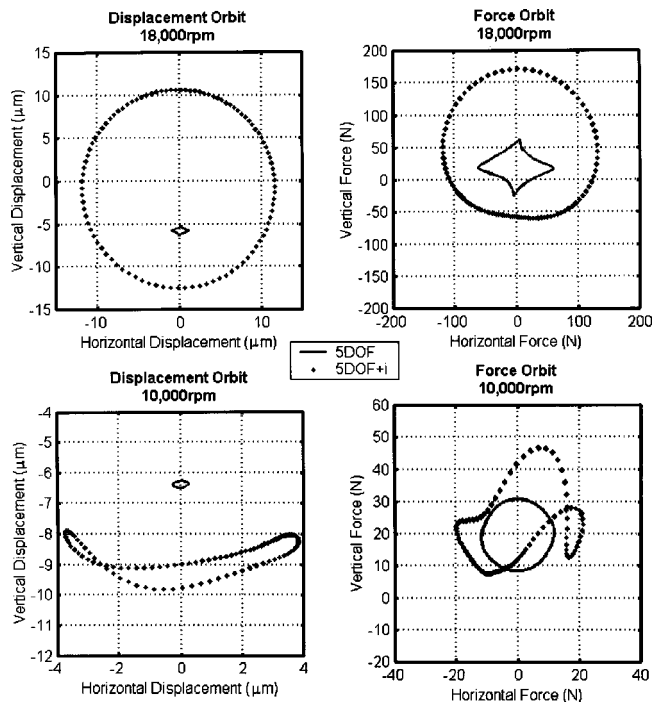


Fig. 5 Effect of inertia on bearing orbits

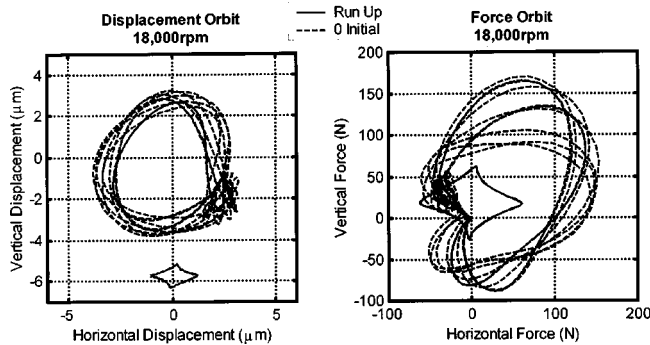


Fig. 6 Two solutions at 18,000 rpm (5DOF model)

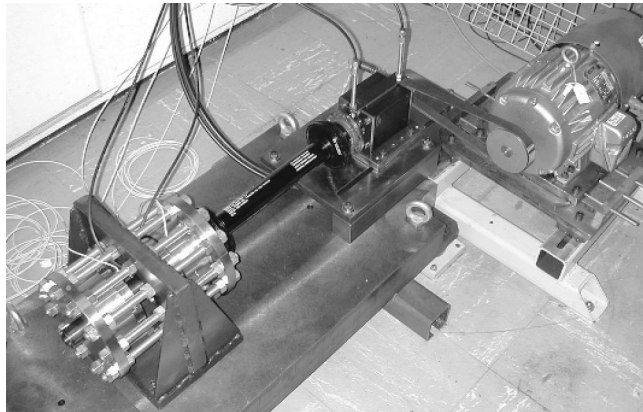


Fig. 7 Photograph of test rig

Table 3 Test rig model parameters

Mass No.	DOF	Mass (kg)	Span Data		
			Length (mm)	Outer ϕ (mm)	Inner ϕ (mm)
1	1,2	0.3425			
2	3-6,25	0.6744	106.0	39.00	0.023
3	7-10,26	0.6235	108.5	39.00	0.023
4	11,12	0.8093	39.70	39.00	0.023
5	13,14	0.2430	65.80	55.90	0.040
6	15,16	0.2441	9.70655	3.6211	0.000
7	17,18	0.2441	268.0	46.18	0.044
8	19,20	0.3290	9.70655	3.6211	0.000
9	-	0.3290	44.00	6.505	0.060
Ped 1	21,22	$m_p = 10$ kg	$c_p = 1$ Ns/m	$k_p = 16.5$ MN/m	
Ped 2	23,24	$m_p = 10$ kg	$c_p = 1$ Ns/m	$k_p = 16.5$ MN/m	

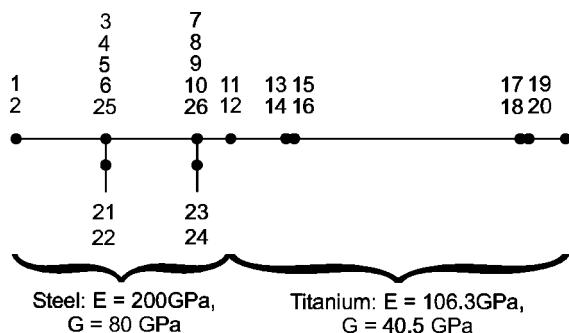


Fig. 8 Lumped mass model of test rig

Table 4 Clearance for 2DOF models

Preload (N)	2DOF and 2DOF+i model clearances (μm)	
	c_i	c_e
19.5	-0.20695	-0.31356
100	-0.59794	-0.90597

model at speeds ranging from 5000 rpm to 18,000 rpm in increments of 1000 rpm. Because of the nature of some of the nonperiodic motions, peaks in Fig. 4 do not indicate resonance values. Figure 5 compares orbits at 18,000 rpm and 10,000 rpm. The presence of centrifugal load has the effect of introducing additional clearance. At 18,000 rpm, with the unbalance load dominant, a circular orbit is achieved whereas at 10,000 rpm, when neither unbalance nor gravity load are predominant, the unbalance load is insufficient to cause the rotor to maintain a full circular orbit but is sufficient to cause looping.

The results at successive speed were obtained by using the results of the previous speed as the initial condition. Multiple solutions could be obtained by changing the initial condition; e.g., changing the input angle of inclination of the rotor (θ_x) resulted in different solutions for the higher speeds. Figure 6 shows the run up solution at 18,000 rpm compared to a solution obtained by using an all zero initial condition. Here, the zero initial condition solution is chaotic. These multiple solutions result from the bearing nonlinearity and should be avoided, as far as possible, by appropriate selection of system parameters.

Test Rig Model. Figure 7 shows a photograph of the modeled test rig which is currently being commissioned. The test rig model is the same as that in [10] except three more degrees-of-freedom were added at each bearing as required by the 5DOF modeling. Table 3 gives the relevant parameters for the rotor system while

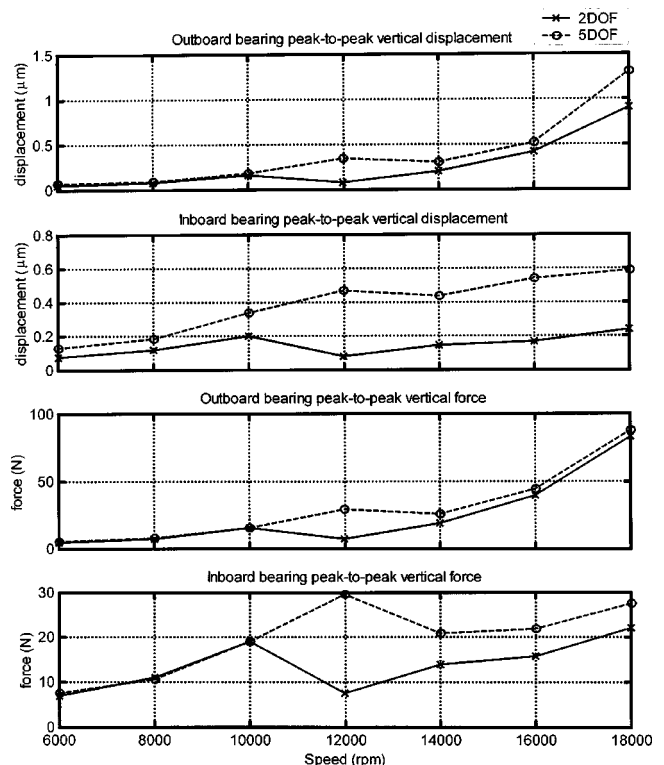


Fig. 9 Peak-to-peak response 19.5 N preload

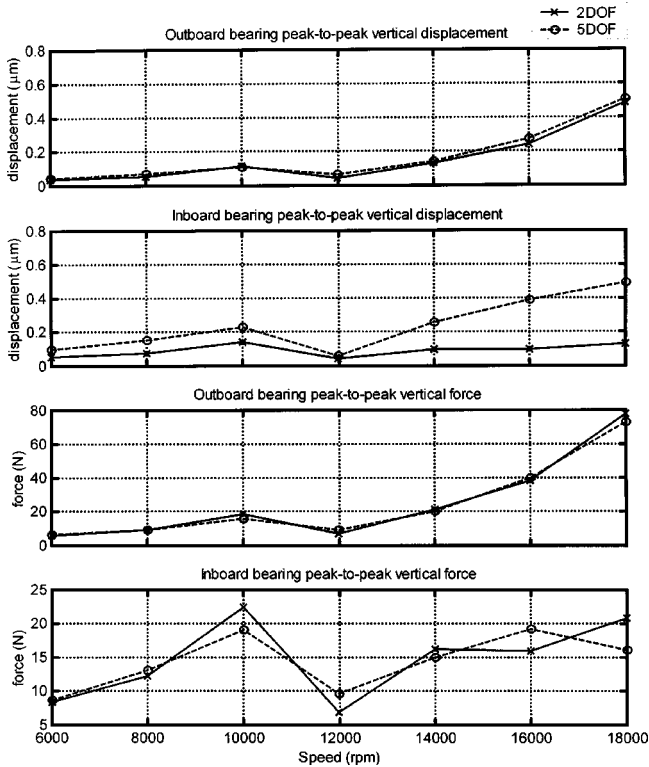


Fig. 10 Peak-to-peak response 100 N preload

the lumped mass model and degrees-of-freedom DOF are shown in Fig. 8. Note that DOF 25 and 26 are added axial degrees-of-freedom that have no stiffness, but have masses of 0.1 kg. The rotational degrees-of-freedom at masses 2 and 3 have I_d values of $7.130 \times 10^{-3} \text{ kgm}^2$ and $3.995 \times 10^{-3} \text{ kgm}^2$ respectively. To see if it is feasible to replace the 5DOF model with the simpler 2DOF model, the inner and outer race clearances caused by the applica-

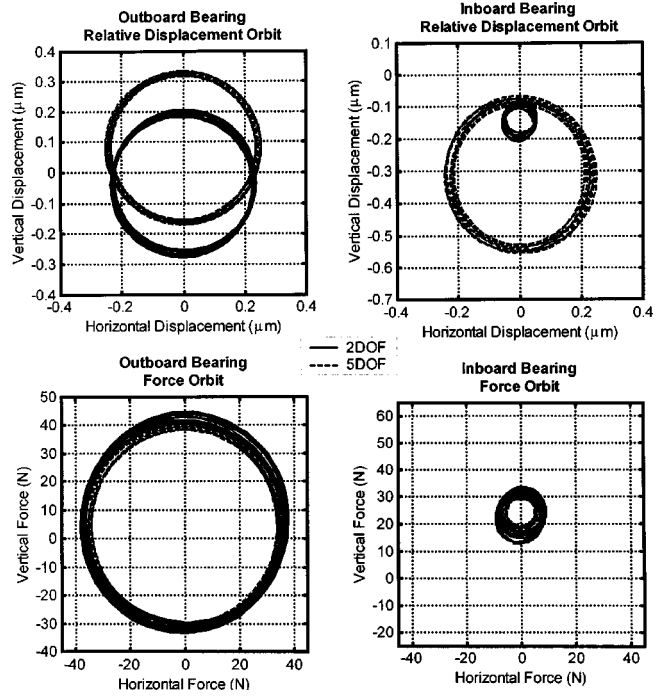


Fig. 12 Orbits at 18,000 rpm with 100 N preload

tion of preload in the 5DOF model were used as input data for the radial clearances in the equivalent 2DOF model. Table 4 shows these equivalent clearance values. There is of course no way in which such radial clearances could be assuredly achieved in any practical deep groove ball bearing assembly. Also in the 2DOF model, axial degrees-of-freedom became dummy degrees-of-freedom (i.e., not connected to other degrees-of-freedom in any way). In the 5DOF model, preloads were obtained by applying appropriate loads to the axial degrees-of-freedom. The 2DOF model uses DOF 3, 4, 7, and 8 while 5DOF model uses DOF 3 through 10, 25, and 26.

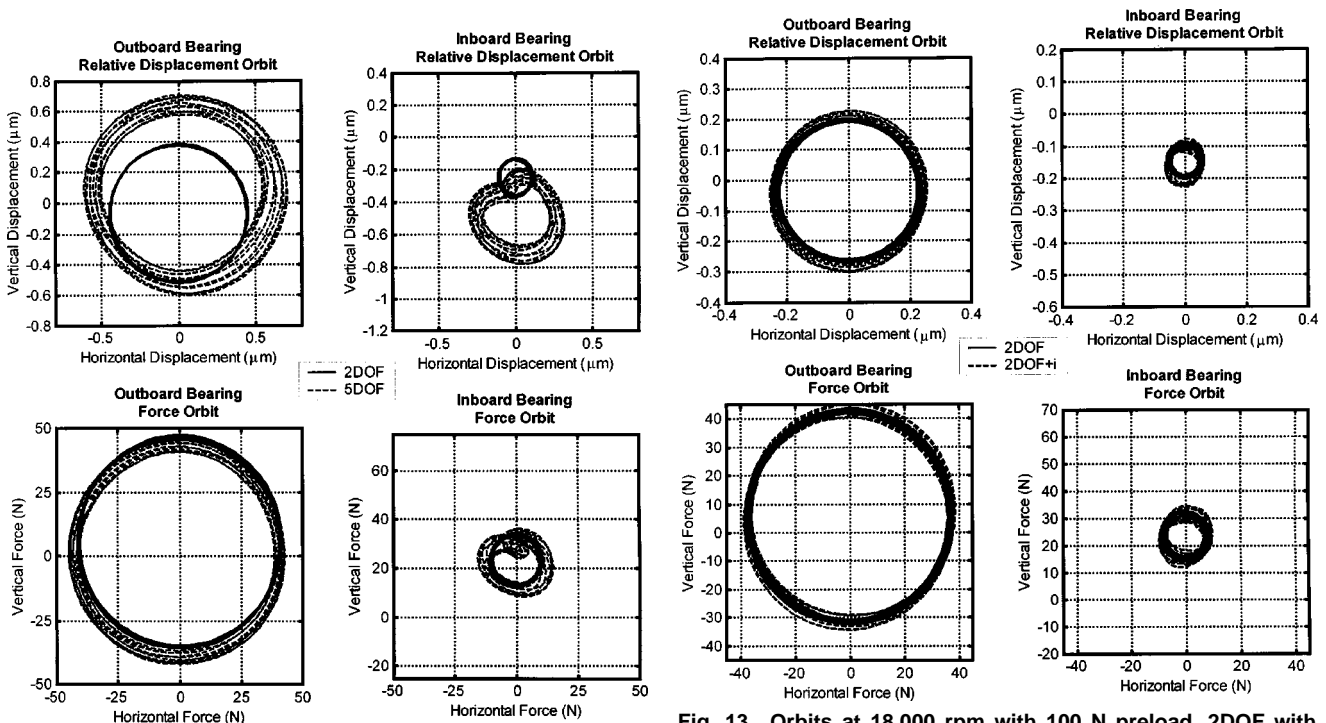


Fig. 11 Orbits at 18,000 rpm with 19.5 N preload

Fig. 13 Orbits at 18,000 rpm with 100 N preload, 2DOF with and without inertia

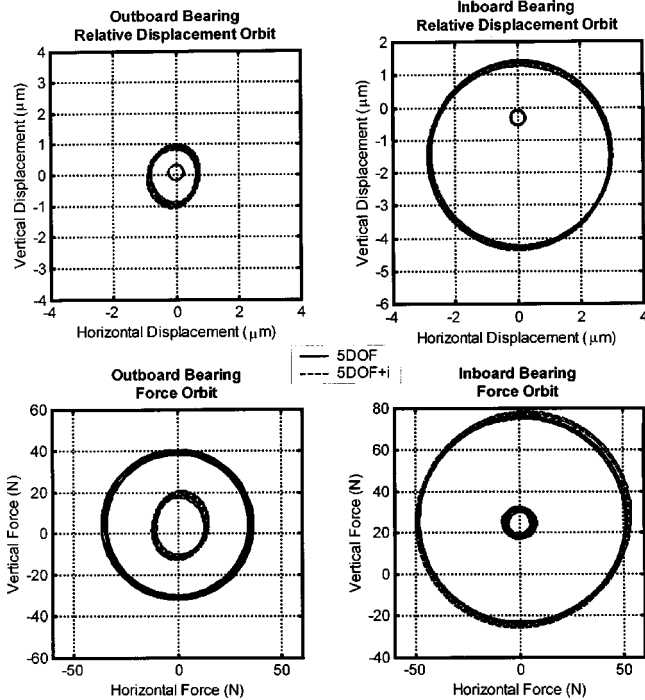


Fig. 14 Orbits at 18,000 rpm with 100 N preload, 5DOF with and without inertia

The system was loaded by gravity and a fixed unbalance of 1×10^{-5} kgm at DOF 11 and 12. The response was calculated at speeds ranging from 6000 rpm to 18,000 rpm in 2000 rpm increments.

Figures 9 and 10 compare the 2DOF and 5DOF models (without rolling element centrifugal load) in terms of peak-to-peak (maximum for ten cycles minus the minimum for ten cycles) response. Figure 9 shows the response for low preload (19.5 N) while Fig. 10 shows the response for medium preload (100 N). Only vertical displacements and forces are shown as the horizontal response is almost identical to the vertical response.

Of the many simulations performed, selected relative bearing orbits and forces are shown in Figs. 11 through 14 where the rotor speed is 18,000 rpm. Figures 11–12 compare solutions obtained with the 2DOF and 5DOF models for light (19.5 N) and medium (100 N) preloads in the absence of centrifugal load while the effect of centrifugal load on the 2DOF and 5DOF models is shown in Figs. 13 and 14. Note that in general the mean force remains vertical and relatively constant over the speed range but 2DOF and 5DOF models give different mean forces. Exceptions occur with light preload (19.5 N) at 12,000 rpm (close to a support natural frequency) and 18,000 rpm where the mean force distribution changes in the 5DOF model only. Figure 15 compares the computation times for 10 cycles of simulation at 1000 points per cycle, 18,000 rpm and 100 N preload, using an Intel Celeron 466 based PC.

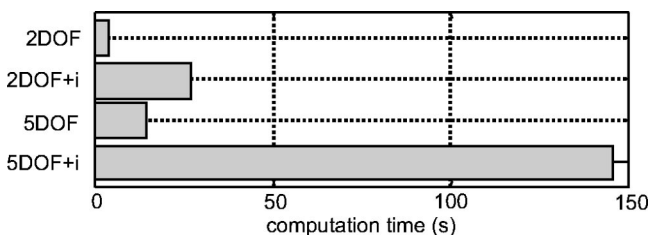


Fig. 15 Computation time comparison

Discussion

The effect of rolling element centrifugal load is most clearly displayed in the single bearing model. As expected, as speed increases, the effect of centrifugal load increases. More interestingly, as the unbalance force increasingly dominates the loading, the difference between the forces with and without centrifugal load decreases while the difference between displacements continues to increase. This can be explained by the centrifugal loading pushing the rolling elements into the outer race (Hertzian deformation) and hence increasing clearance that the shaft and inner race experience. Thus, when the rotor is simply moving around the bearing, the bearing force does not see the effect of the centrifugal load while the displacement does.

In the test rig model, the effect of rolling element centrifugal load is seen to be minimal on the 2DOF model (Fig. 13) compared to its effect on the 5DOF model (Fig. 14), although displacements and forces do increase slightly. Indeed, the need for the more complicated 5DOF models is not evident until more complicated multiple bearing systems are involved where rotational (θ_x, θ_y) and axial (z) motions may be significant at the bearings. Where these motions have negligible effect, the 2DOF models can be tuned to give very close results to the 5DOF models. This was possible in the single bearing model but not in the test rig model. Note that 2DOF modeling for the test rig was performed neglecting the angular contact, resulting in small differences between the clearance and stiffness of the models. However, the differences seen between the 2DOF and 5DOF models are largely due to the added axial and tilting stiffness of the 5DOF model as seen in both the peak to peak responses (Figs. 9 and 10) and the mean force distributions. This is particularly evident at 12,000 rpm where opposite dynamic response is predicted. The most significant effect of the 5DOF model is noticed at higher speeds where unbalance plays a larger role and at lighter preloads. Preload tends to reduce the effect of both the 5DOF modeling and the rolling element centrifugal load.

Conclusions

Transient analysis software has been gainfully applied to determine the vibration response of general rotor-bearing systems involving angular contact ball bearings; and in particular, to the test rig presently being commissioned to evaluate nonlinearity effects arising from such bearings. It will therefore be possible to predict system parameter combinations which give rise to undesirable vibration characteristics due to bearing nonlinearity, such as chaotic motions or multistable (jump) operation.

Numerical computations show that

- (i) inclusion of rolling element centrifugal load can significantly affect response results. Rolling element centrifugal load seems to increase the effective clearance or decrease the interference present in the bearing.
- (ii) the use of 5DOF rather than 2DOF models can significantly affect response results when there are rotational and axial displacements at the bearings.
- (iii) both the inclusion of ball centrifugal load effects and the extension of the 2DOF models to 5DOF models significantly increased the computational effort.

The need to utilize the computationally more demanding 5DOF model and the need to include rolling element centrifugal load effects when determining the vibration response of rotor bearing systems has been demonstrated.

Acknowledgments

This work was supported by the Aeronautical and Maritime Research Laboratories, DSTO (Australia) and the Australian Research Council.

Nomenclature

$c_{i,e}$ = inner, outer race clearances, respectively, in direction of contact [m]
 D_b = rolling element diameter [m]
 D_p = bearing pitch diameter [m]
 \mathbf{d} = inner race displacement vector = $\{x, y, z, \theta_x, \theta_y\}^T$ [m] or [rad]
 \mathbf{F} = bearing load vector per element [N] or [Nm]
 \mathbf{f} = total bearing load vector [N] or [Nm]
 $f_{x,y}$ = bearing force in x and y directions, respectively [N]
 \mathbf{G} = forcing function vector [N] or [Nm]
 g, g_r, g_z = dynamic equilibrium function(s)
 K_p = load-deflection factor for point contact [$\text{Nm}^{-1.5}$]
 l_{0i}, l_{0e} = nominal distance between rolling element center and inner, outer race centers of curvature, respectively [m]
 l_i, l_e = actual distance between rolling element center and inner, outer race centers of curvature, respectively [m]
 $\mathbf{M}, \mathbf{K}, \mathbf{C}$ = system mass, stiffness and damping + gyroscopic matrices
 m_p, k_p, c_p = support mass, stiffness and damping [$\text{kg}, \text{Nm}^{-1}, \text{Nsm}^{-1}$]
 m_{re} = rolling element mass [kg]
 n = load deformation index (1.5 for point contacts)
 n_b = number of rolling elements
 Q, Q_i, Q_e = contact load [N]
 $\mathbf{Q}, \mathbf{Q}_i, \mathbf{Q}_e$ = contact force vectors [N or Nm]
 $r_{i,e}$ = inner and outer race radii of curvature [m]
 r_p = radial distance from bearing center to nominal inner race center of curvature [m]
 \mathbf{u} = displacement of the inner race = $\{u_r, u_z, u_\theta\}^T$ [m or rad]
 \mathbf{v} = displacement of the rolling element = $\{v_r, v_z\}^T$ [m]
 \mathbf{X} = displacement vector of system DOF [m or rad]
 z_p = axial distance from bearing center to nominal inner race center of curvature [m]

α = contact angle [rad]
 α_0 = nominal contact angle [rad]
 δ = contact deformation or deflection [m]
 ϕ_j = angular location of the j th rolling element [rad]
 ω_c = cage angular velocity [rad/s]
 ω_s = shaft angular velocity [rad/s]

References

- [1] Tamura, A., and Taniguchi, O., 1960, "Ball Bearing Vibrations (1st Report)," *Trans. Jpn. Soc. Mech. Eng.*, **26**, pp. 19–25.
- [2] Meldau, E., 1951, "Die Bewegung der Achse von Wällagen bei geringen Drehzahlen," *Werkstatt und Betrieb* **7**, pp. 308–313.
- [3] Sunnersjö, C. S., 1978, "Varying Compliance Measurement of Rolling Bearings," *J. Sound Vib.*, **58**(3), pp. 363–373.
- [4] Stone, B. T., 1982, "The State of the Art in the Measurement of Stiffness and Damping of Rolling Element Bearings," *Annals of the CIRP* **21**(2), pp. 529–538.
- [5] Harris, T. A., 1966, *Rolling Bearing Analysis*, John Wiley and Sons, New York.
- [6] Fukata, S., Gad, E. H., Kondou, T., Ayabe, T., and Tamura, H., 1985, "On the Radial Vibration of Ball Bearings," *Bull. JSME*, **28**(239), pp. 899–904.
- [7] Saito, S., 1985, "Calculation of Non-linear Unbalance Response of Horizontal Jeffcott Rotors Supported by Ball Bearings With Radial Clearances," *ASME J. Vib., Acoust., Stress, Reliab. Des.*, **107**, pp. 416–420.
- [8] Tiwari, M., Gupta, K., and Prakash, Om., 1998, "Non-linear Dynamic Analysis of a Rigid Rotor Supported on Deep Groove Ball Bearings," *Proceedings of the 7th International Symposium on Transport Phenomena and Dynamics of Rotating Machinery*, Bird Rock Publishing, pp. 960–969.
- [9] El-Saeidy, F. M. A., 1998, "Finite Element Modeling of Rotor Shaft Rolling Element Bearing System with Consideration of Bearing Nonlinearities," *J. Vib. Control*, **4**, pp. 541–602.
- [10] Feng, N. S., and Hahn, E. J., 2000, "Rolling Element Bearing Non-Linearity Effects," *ASME Paper No. 2000-GT-391*.
- [11] Jones, A. B., 1960, "A General Theory for Elastically Constrained Ball and Radial Roller Bearings Under Arbitrary Load and Speed Conditions," *ASME J. Basic Eng.*, **82**(2), pp. 309–320.
- [12] de Mul, J. M., Vree, J. M., and Maas, D. A., 1989, "Equilibrium and Associated Load Distribution in Ball and Roller Bearings Loaded in Five DOF While Neglecting Friction Part 1: General Theory and Applications to Ball Bearings," *ASME J. Tribol.*, **111**, pp. 142–148.
- [13] Kahraman, A., and Singh, R., 1991, "Non-Linear Clearance of a Geared Rotor-Bearing System with Multiple Clearances," *J. Sound Vib.*, **144**(3), pp. 469–506.
- [14] Lin, Y. Q., 1993, "Rotor Instability Induced by Radial Clearance in Ball Bearing Support," *ASME Paper No. 93-GT-029*.

Optimum Design of Squeeze Film Dampers Supporting Multiple-Mode Rotors

A. El-Shafei

Associate Professor

R. Y. K. Yakoub

Department of Mechanical Design
and Production Engineering,
Cairo University,
Giza 12316, Egypt

In this paper a study of the optimum design of squeeze film dampers for multimode rotors is presented. The optimum design program obtains the best possible damper parameters for a given rotor to satisfy the minimization requirements for the objective function. The objectives are to minimize the amplitude response of the rotor at the critical speed, minimize the force transmitted to the support at the operating speed, or maximize the power dissipated by the damper. A combination of these objectives can also be used, with weighting factors to weigh the importance of each of these objectives. These are the possible objectives for the design of squeeze film dampers for aircraft engine applications. The basis of the optimum design program is an extremely fast algorithm which is able to quickly calculate the unbalance response of a rotor, for circular centered orbits of the journal in the damper. A commercial routine is used for the optimization, and is based on a complex direct search technique. The variation of the optimum clearance, length, and retainer spring stiffness are plotted against various rotor parameters. Recommendations for the design of squeeze film dampers are made. Applications of an aircraft engine illustrate the power of the developed algorithm. [DOI: 10.1115/1.1479338]

Introduction

Squeeze film dampers (SFDs) are usually designed based on rules of thumb. Most SFD designers would give a clearance value relative to the radius of the damper as their preferred choice for SFD design, even though there may be different objectives for the design of SFDs. Many SFDs are designed to provide damping while crossing critical speeds, but other SFDs are designed to provide stability to the rotor system. It is the objective of this paper to provide insight into the design process of SFDs, and clarify the competing objectives for the design of SFDs. The paper describes an optimum design procedure, for the selection of optimum SFD parameters to support different SFD design objectives.

The SFD literature is quite rich, ever since the invention of SFDs by Cooper [1]; however, the work on SFD optimization is relatively limited. Perhaps the first analysis of optimum design of SFDs is the work of Cunningham et al. [2] who optimized the stiffness and damping of an SFD as a support of a symmetric five-mass rotor. Their design objective was to reduce the rotor motions and forces transmitted to the support bearings. They used a single-mass flexible rotor analysis in their optimum design. Barrett et al. [3] derived an approximate formula to evaluate the optimum damping of SFD supporting multiple modes rotors. This formula was expressed as a function of the bearing stiffness and rotor modal stiffness at the rigid bearing critical speed. The optimum damping of SFD minimizes the rotor unbalance response and maximizes stability in the vicinity of the rotor first critical speed. They used the equivalent mass-spring model to evaluate the unbalance response of their system. Rabinowitz and Hahn [4] were able to obtain an optimum design chart for an SFD supporting flexible rotors based on the desired value of the vibration amplitude and the damper force. Later, Chen et al. [5] were successful addressing an automated optimization technique using nonlinear programming to obtain the optimum damper radial clearance, journal length, and the radius of the damper. They used

the finite element method to model their systems. Their design objective was to minimize the maximum damper force in a certain speed range. Natraj and Ashrafioun [6] studied the effect of rotor spin speed and the unbalance value on the optimal value of the bearing parameter. They derived analytical formulas based on the analysis of two-degree-of-freedom systems. More recently, Ramesh and Kirk [7] used a multidegree-of-freedom rotor model and presented an SFD design procedure to obtain optimum stability. Nyqvist and Larsson [8] presented an optimization method for the optimization of SFDs for stability problems by optimizing the location of the root locus. Each of the above researchers presented a useful algorithm, but either with limited objectives, or based on simple models. It is desirable to optimize the design of SFDs with different objectives and using data from actual multimode rotors.

In this paper a method to optimize the performance of SFDs supporting multiple modes rotors is presented. This method relies on the simulation of the unbalance response of the rotors through an extremely fast algorithm based on planar modal analysis theory and the assumption of circular motion ([9]). An objective function is constructed to describe different design objectives, which are to minimize the vibration amplitude, minimize the transmitted force to the machine support, and/or maximize the SFD power. The direct search method is used to find the minimal value of the objective function and the corresponding optimum design variables within two bounds. A numerical example is given to demonstrate different cases of design objectives. The optimum SFD parameters are obtained in each case using the developed method. The unbalance response of each case is compared to that of the baseline design. Simulations show that the developed optimization method achieves the specified design objectives.

Squeeze Film Damper Parameters

There are many parameters that control the behavior of squeeze film dampers (SFDs). Inspection of the nondimensional bearing parameter or inertia parameter ([10]), would reveal that the following design parameters affect the performance of an SFD: clearance, length, radius, viscosity of oil, density of oil, as well as the retainer spring stiffness, the configuration of the damper, and the supply pressure.

The damper configuration, including oil supply method and sealing type, dictate whether the damper will operate in the long

Contributed by the International Gas Turbine Institute (IGTI) of THE AMERICAN SOCIETY OF MECHANICAL ENGINEERS for publication in the ASME JOURNAL OF ENGINEERING FOR GAS TURBINES AND POWER. Paper presented at the International Gas Turbine and Aeroengine Congress and Exhibition, New Orleans, LA, June 4-7, 2001; Paper 01-GT-256. Manuscript received by IGTI, December 2000, final revision, March 2001. Associate Editor: R. Natole.

damper mode or short damper mode or anywhere in between ([11]). The oil supply pressure dictates whether the damper will operate uncavitated, cavitated, or with air entrainment. Usually the supply pressure in SFDs is large enough to reduce air entrainment, but possibly not large enough to eliminate cavitation. These are decisions an SFD designer is confronted with, however, for the purposes of this paper it is assumed that the design configuration and supply pressure are already established, based on previous experience or constraints in the damper design. Thus the damper design problem is reduced to selecting the appropriate SFD parameters.

Of the parameters mentioned in the first paragraph in this section, the choice of the type of oil, thus its viscosity and density, is most probably governed by considerations other than the damper design. Usually, the oil used for lubrication is used in the SFD. Moreover, the radius of the damper is almost always dictated by considerations other than the damper design. The radius is usually dictated by the rotor design, whether from the point of view of functionality, stress, or critical speed placement.

This leaves only three parameters that the SFD designer works with, to obtain the best possible performance from the SFD, namely the clearance C , the length L , and the retainer spring stiffness K_r . Of these, previous work ([12,13]), has shown that the clearance C has the largest effect on the amount of damping provided by an SFD; while the retaining spring is useful in providing a soft support. The optimum design algorithm presented herein, provides a method for the proper selection of these SFD parameters.

Simulation of Squeeze Film Damper Behavior

Because of the nonlinearity of squeeze film dampers (SFDs) it is possible to predict the behavior of SFDs by numerical integration, to obtain the unbalance response ([14]). However, this is quite time-consuming. Therefore various authors have resorted to try to predict the unbalance response of SFD supported rotors by various methods. Taylor and Kumar [15] predicted the response of a simple model of a rigid rotor on SFD by assuming circular centered orbits and manipulating the nonlinear algebraic equations to obtain a polynomial in frequency which when solved for various eccentricities results in the full unbalance response. This technique was extended by El-Shafei [10,16] to flexible rotors including fluid inertia effects in SFDs.

Until recently an SFD designer could not use the simulations of the unbalance response as a design tool, because the available technology either relied on extremely time-consuming numerical integration techniques, or relatively simple models. The designer

would try to predict the behavior of the SFD supported rotor using the simple models, then proceed to design the rotor-damper system, and at the end of the design process resort to numerical integration just to check the design.

Recent developments concentrated on overcoming this problem. Mclean and Hahn [17] tried to solve this problem for a multimode rotor system assuming circular centered orbits. However, their technique needs to be developed mathematically for each particular rotor, and the mathematics can be cumbersome for complicated rotors. A major development occurred recently by the authors ([9]), who used planar modal analysis, developed by Gunter et al. [18] and applied by Hathout et al. [19], to obtain the full nonlinear unbalance response of a multimode rotor supported on SFDs. This is an elegant algorithm based on planar modal analysis and the methodology of Taylor and Kumar [15] and El-Shafei [10,16] to obtain the full nonlinear unbalance response of multi-mode rotors supported on SFDs with a speed of 25 orders of magnitude faster than numerical integration. This algorithm only requires the knowledge of the undamped planar modes of any rotor, and would predict the full unbalance response in a matter of seconds.

The advent of such a fast algorithm allows the designer to use simulation as a design tool. Actually the authors used the algorithm to simulate the response of an aircraft gas turbine fan rotor (AGTFR) and design an SFD for the AGTFR all in a day's work ([9]). However, a huge amount of data are generated by the simulations, and an automated method is required to obtain the best possible design solution. Therefore an optimization methodology needs to be developed, which is precisely the objective of this paper.

Design Objectives of Squeeze Film Dampers and the Objective Function

The goals of using squeeze film dampers (SFDs) in high-speed high-performance rotors, such as aircraft gas turbine engines, are to utilize their capabilities in controlling vibrations. Controlling vibrations means that the vibration amplitudes are attenuated, transmitted forces to the bearings are reduced, and good stability characteristics are provided. It was found that SFDs have the ability to achieve these requirements. Meanwhile, it was also found that if the SFDs are poorly designed, they may act as magnifier devices for vibrations rather than attenuators. Moreover, it is desired to investigate the possibility of exploiting SFDs to their maximum, since it cannot be claimed that the performance of SFDs is optimal. Thus it is desired to find a method to perform an optimum design procedure for SFDs. At present, SFDs are de-

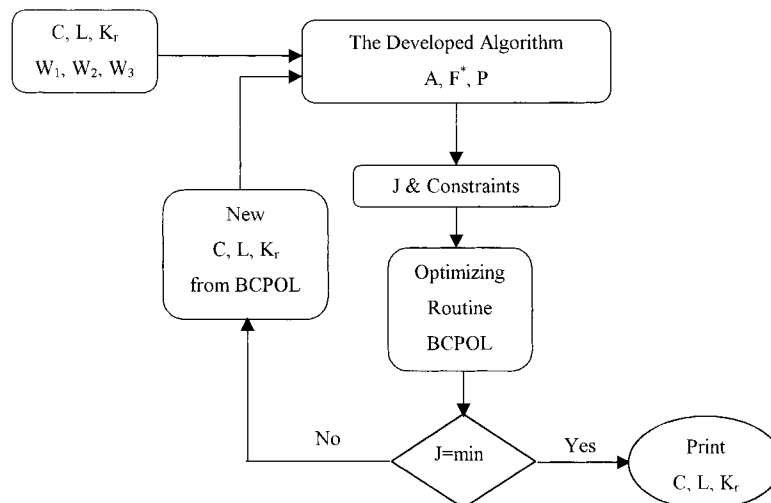


Fig. 1 Flow chart for the optimum design program

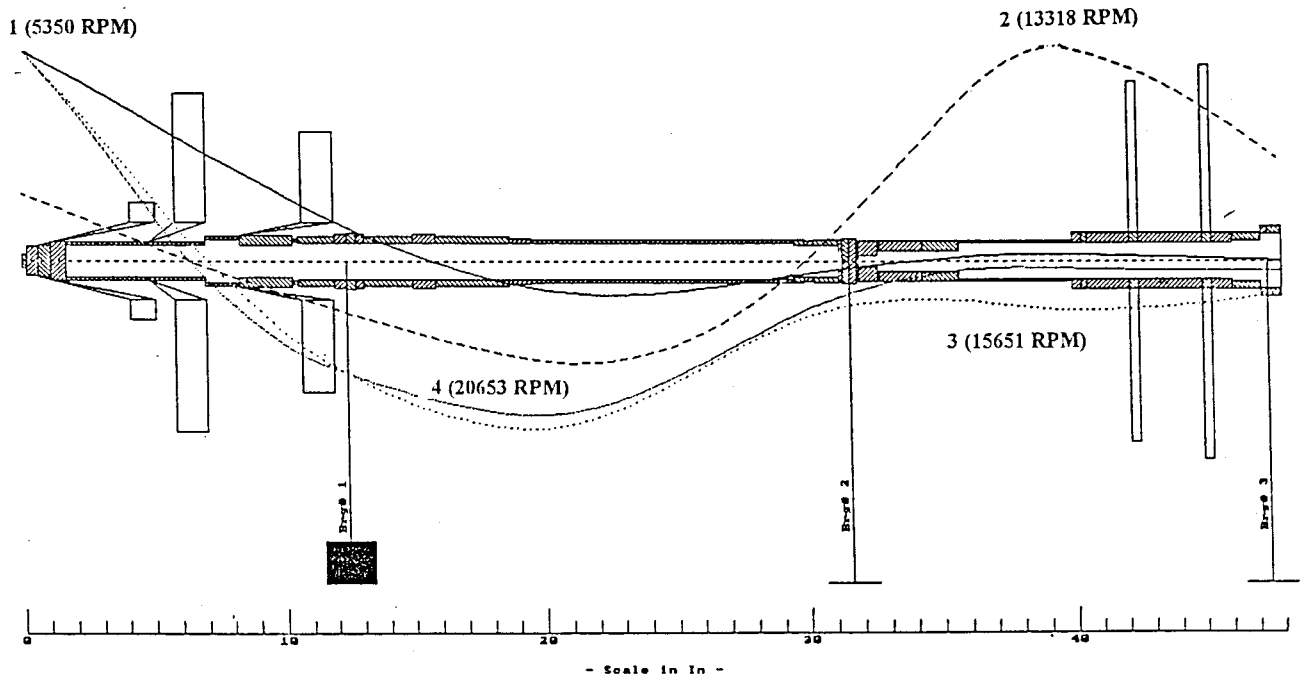


Fig. 2 Aircraft gas turbine fan rotor and its mode shapes

signed based on rules of thumb, which are extracted from the rules of journal bearing design. Even though these rules are widely recognized, they may not achieve the desired optimum performance of SFDs.

In summary, SFDs are used in rotating machinery for three main reasons:

- (a) to minimize the amplitude response at critical speeds,
- (b) to minimize the force transmitted to the support at operating speeds, and
- (c) to stabilize rotating machinery at onset of instability.

Actually in many cases these three objectives can be competing,

and many authors have worked on variable SFDs to satisfy these different design objectives ([19]), however, this is beyond the scope of the current paper.

To reduce the amplitude response at critical speeds, one would necessarily require a large amount of damping to reduce the amplification factor; while to reduce the force transmitted to the support a soft support needs to be designed with little damping to reduce the transmissibility. To stabilize a rotating machine, one needs a large amount of damping to move all eigenvalues to the right-hand side of the complex plane.

Based on the above, it is desirable to develop an objective function to represent all the above three design objectives, and to

Table 1 Different design objectives

Case Number	Design Objective	Objective Function
Case 1	minimize the maximum vibration amplitude (A), which is measured at the unbalanced disk (at the fan), (i.e., design objective 1)	$J = A_{\max}$ $W_1 = 1, W_2 = W_3 = 0$
Case 2	minimize the maximum transmitted force (F^*), design objective 2	$J = F^*_{\max}$ $W_2 = 1, W_1 = W_3 = 0$
Case 3	maximize the average SFD power in a certain speed range, the chosen speed range is from 12,000 (rpm) to 20,000 (rpm), which is the operating speed range of AGTFR, design objective 3	$J = \frac{1}{P_{\text{avg}}} \Big _{\Omega_1}^{\Omega_2}$ $W_3 = 1, W_1 = W_2 = 0$
Case 4	minimize the maximum A and the maximum F^* , design objectives 1 and 2 together	$J = A_{\max} + F^*_{\max}$ $W_1 = W_2 = 1, W_3 = 0$
Case 5	minimize the maximum A and maximize the P_{avg} over a speed range, design objectives 1 and 3 together	$J = A_{\max} + \frac{1}{P_{\text{avg}}} \Big _{\Omega_1}^{\Omega_2}$ $W_1 = W_3 = 1, W_2 = 0$
Case 6	minimize the maximum F^* and maximize P_{avg} over a speed range, design objectives 2 and 3 together	$J = F^*_{\max} + \frac{1}{P_{\text{avg}}} \Big _{\Omega_1}^{\Omega_2}$ $W_2 = W_3 = 1, W_1 = 0$
Case 7	minimize the maximum A , maximum F^* , and maximize P_{avg} in a speed range, design objectives 1, 2 and 3 combined	$J = A_{\max} + F^*_{\max} + \frac{1}{P_{\text{avg}}} \Big _{\Omega_1}^{\Omega_2}$ $W_1 = W_2 = 1, W_3 = 1$

Table 2 The optimum squeeze film damper (SFD) parameters for different cases

Case No.	C_{opt} (μm)	L_{opt} (mm)	Kr_{opt} (N/mm)	J_{min}	$J_{initial}$	Reduction %
Case 1	150.136	10.65	600	0.874	1.2422	29.64
Case 2	295.146	11.27	100	1.2138	3.25	62.65
Case 3	300	17.216	100	0.025	0.0619	59.61
Case 4	295.39	15.82	128.65	2.543	4.4922	43.39
Case 5	276	16.7	224.298	0.935	1.3041	28.3
Case 6	300	10.5	112.2	2.04	3.3119	38.65
Case 7	150	12.9	600	3.5	5.0	30

use the simulation algorithm of Yakoub and El-Shafei [9] to evaluate this objective function. This is quite straightforward for the first two objectives; however, for the third objective one encounters a problem. To really satisfy the third design objective, it is necessary to evaluate the system eigenvalues. However, this

is not possible from the unbalance response, which is our main simulation tool.

A possible approximate solution to this stability problem, is to consider the function of the SFD as a stabilizer. In this case the SFD would be required to remove as much energy as possible

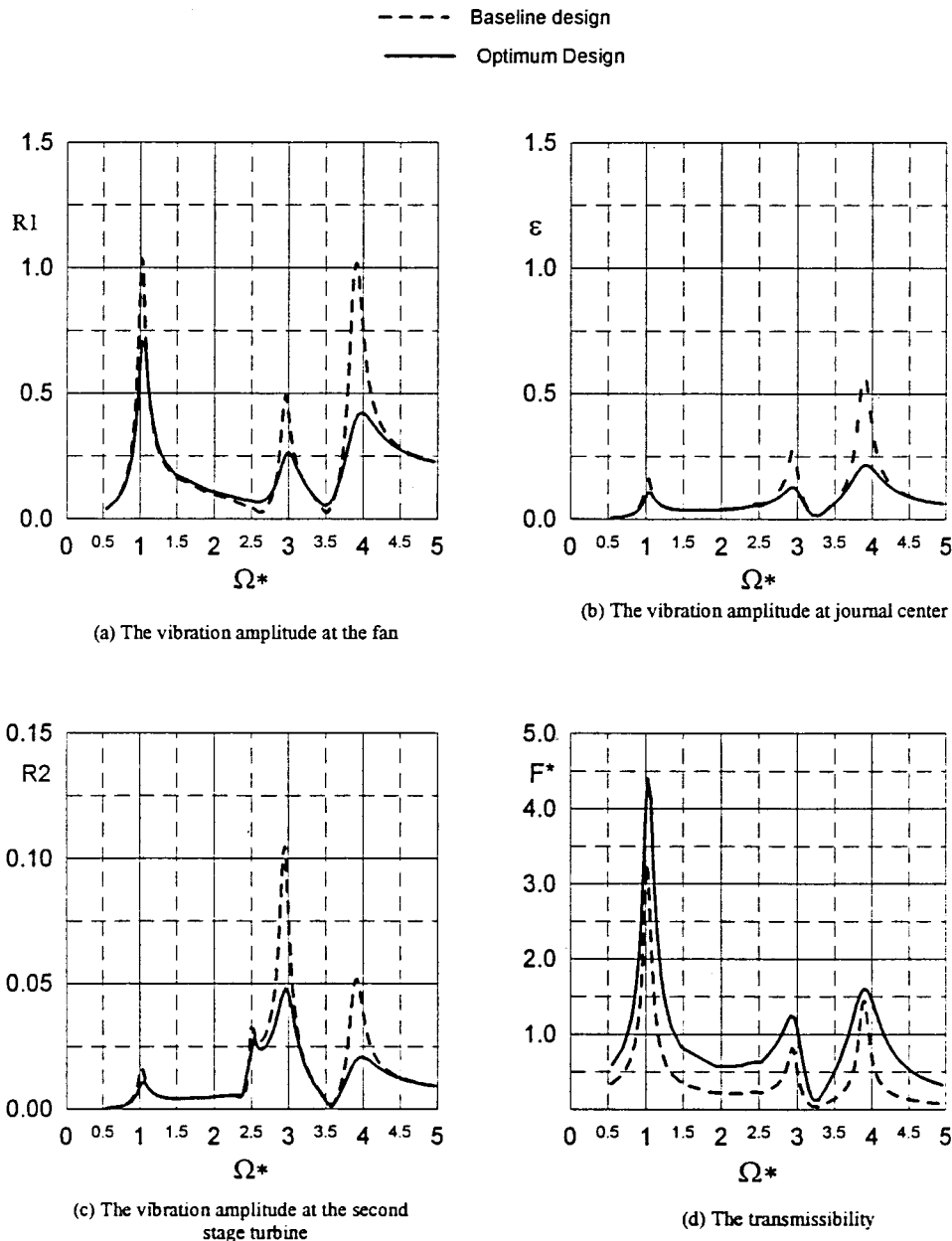


Fig. 3 The unbalance response of AGTFR supported on short SFD optimum design versus baseline design, Case 1 $W1=1.0$

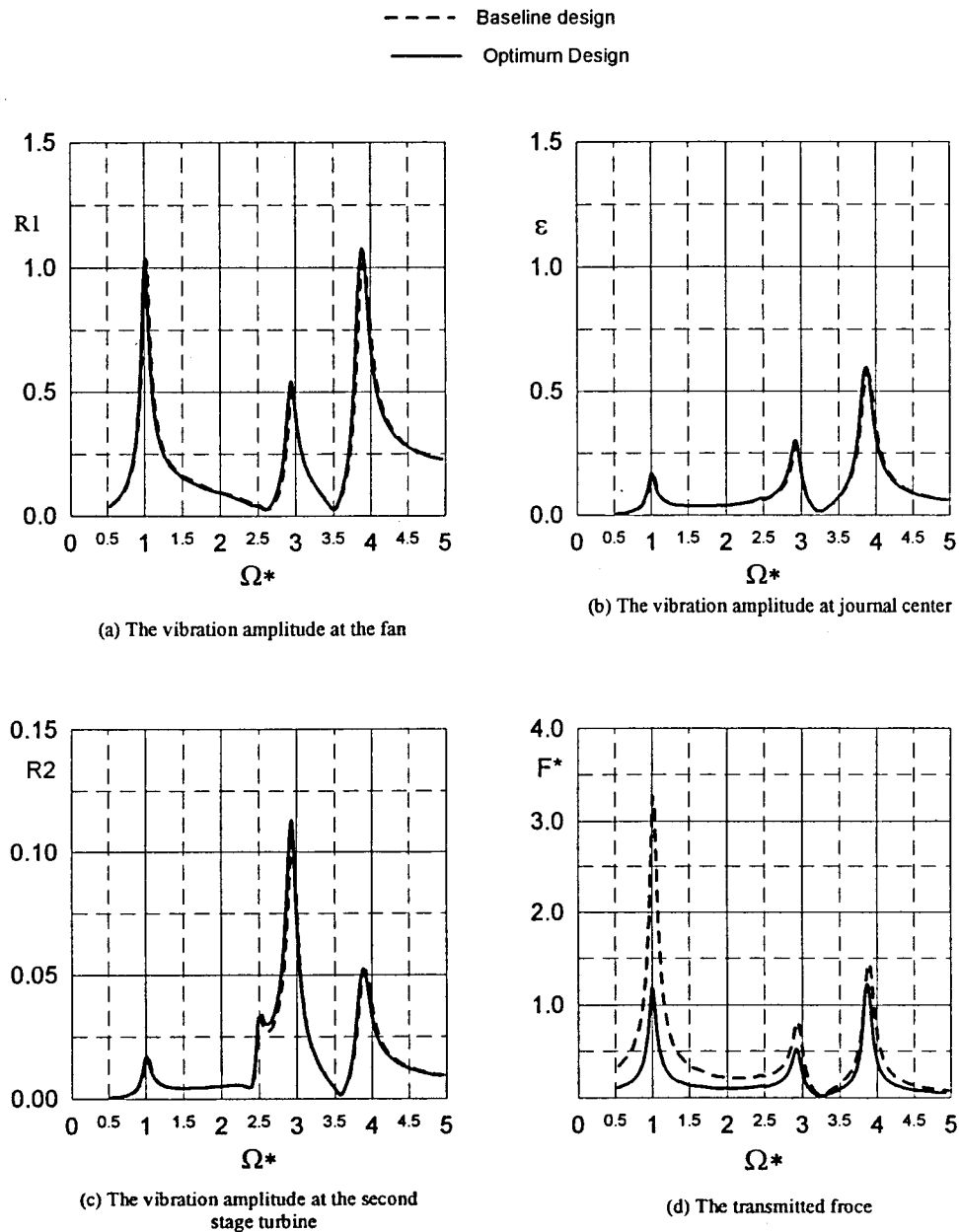


Fig. 4 The unbalance response of AGTFR supported on short SFD optimum design versus baseline design, Case 2, $W_2=1.0$

from the rotor system to stabilize it. Thus, if the SFD is designed to maximize the power removed during one cycle, one would approximate the necessary conditions of stability while only using the unbalance response simulations.

Thus, a possible objective function for the design of SFDs could be constructed as follows:

$$J = W_1 \times A + W_2 \times F^* + W_3 / P$$

where A is the maximum vibration amplitude on the rotor, F^* is the largest transmitted force at the damper, and P is the power removed in the damper at particular points. W_1 , W_2 , and W_3 are weighting factors. The weighting factors W_1 , W_2 , and W_3 can be defined according to the design objectives. For instance, to achieve the design objective of smallest vibration amplitude, then W_1 will take the value 1, while the other factors will be zero. In the case of more than one objective, the weighting factors can be

taken in such a way such that they emphasize the importance of each design objective to the overall design requirements.

Optimum Design Technique

In the optimum design process of squeeze film dampers (SFDs), it is desired to obtain the optimum damper radial clearance (C), the optimum length of the damper journal (L), and the optimum stiffness of the retainer spring (Kr). These design variables are confined within two bounds; lower and upper bounds. Thus the problem of optimum design can be formulated as follows:

$$\text{Min}(J) = W_1 \times A + W_2 \times F^* + W_3 / P \quad (1)$$

$$C_{\text{lower}} \leq C_{\text{opt}} \leq C_{\text{upper}} \quad (2)$$

$$L_{\text{lower}} \leq L_{\text{opt}} \leq L_{\text{upper}} \quad (3)$$

$$Kr_{\text{lower}} \leq Kr_{\text{opt}} \leq Kr_{\text{upper}} \quad (4)$$

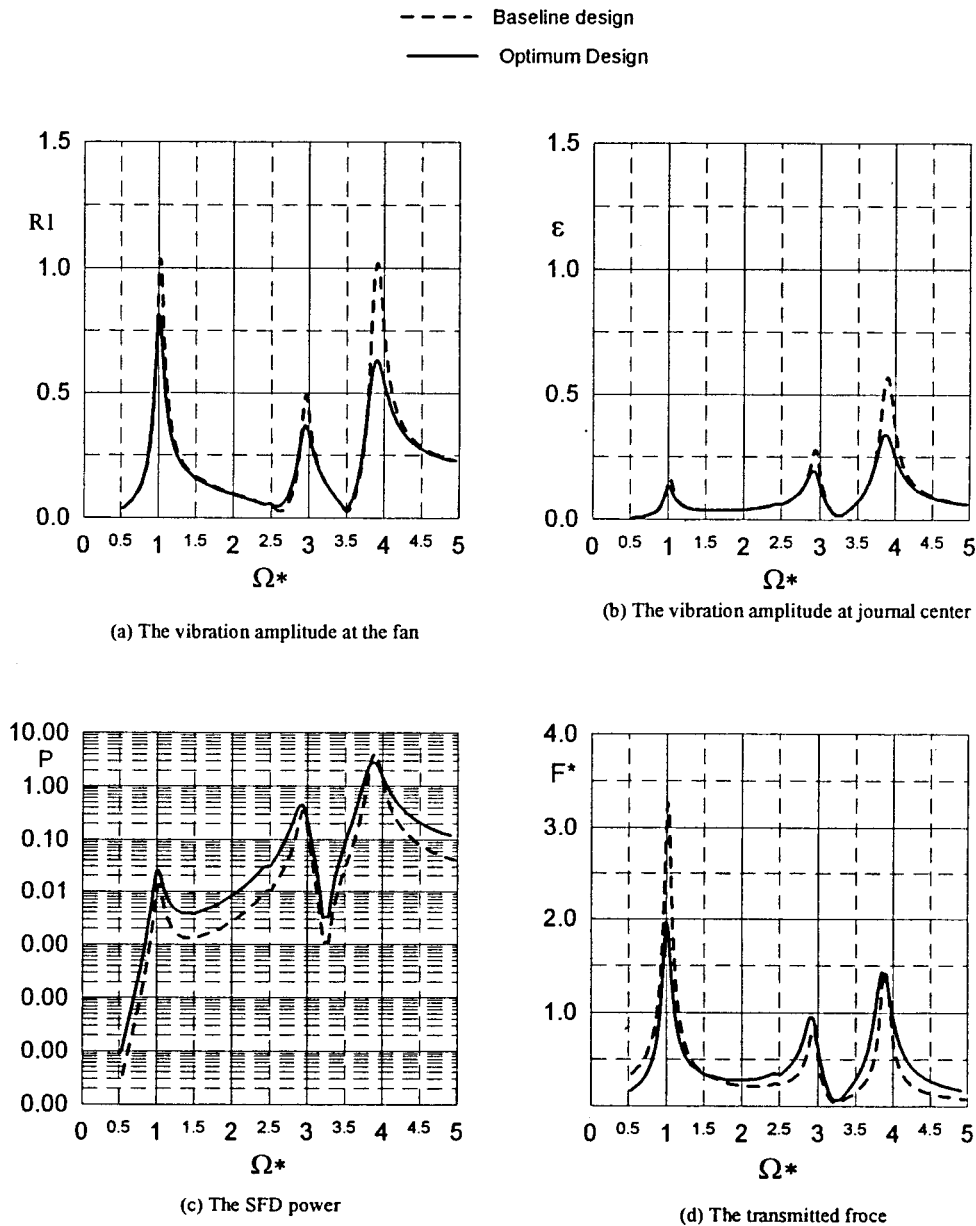


Fig. 5 The unbalance response of AGTFR supported on short SFD optimum design versus baseline design, Case 3, $W3=1.0$

where the subscripts lower, upper, and opt stand for the lower bound, upper bound, and the optimum value of the design variable, respectively.

These bounds are chosen to be indicative of the actual physical bounds on the design parameters. They should not be chosen arbitrarily, as this would constrain the optimization, and result in the loss of more "optimum" solutions. For example, the clearance lower bound should be determined by machining and assembly tolerances while the clearance upper bound should be determined by the view of the effectiveness of the SFDs. The length upper and lower bounds are actually determined by space limitations, while the stiffness lower bound should be determined by physical properties of soft springs, and the stiffness upper bound is determined by the need to avoid a hard mount.

In solving this problem, conventional optimization methods are not helpful since we do not have an analytical form for the objective function. This is because the objective function is evaluated based on the simulation of the system unbalance response, which

is the steady-state behavior at different spin speeds of the rotor. Thus gradient methods cannot be used in this case since the gradients of the objective function cannot be evaluated analytically, and finite difference gradient evaluation methods would not be effective in calculating the gradients numerically, since it would be very time-consuming.

As a solution for this problem, direct search methods are suggested to search for the optimum SFD parameters. Direct search methods are effective for low-order optimization problems, where the number of variables is limited to about 5. In the optimization problem defined by Eqs. (1) to (4), the search is confined to a three dimensional parameter space. The direct search method depends on changing the values of the design variables according to a certain formula (Complex method, IMSL routine BCPOL) ([20]) and evaluating the objective function that corresponds to those variables. The minimum value of the objective function and its corresponding variables are obtained by comparing the evaluated objective function values.

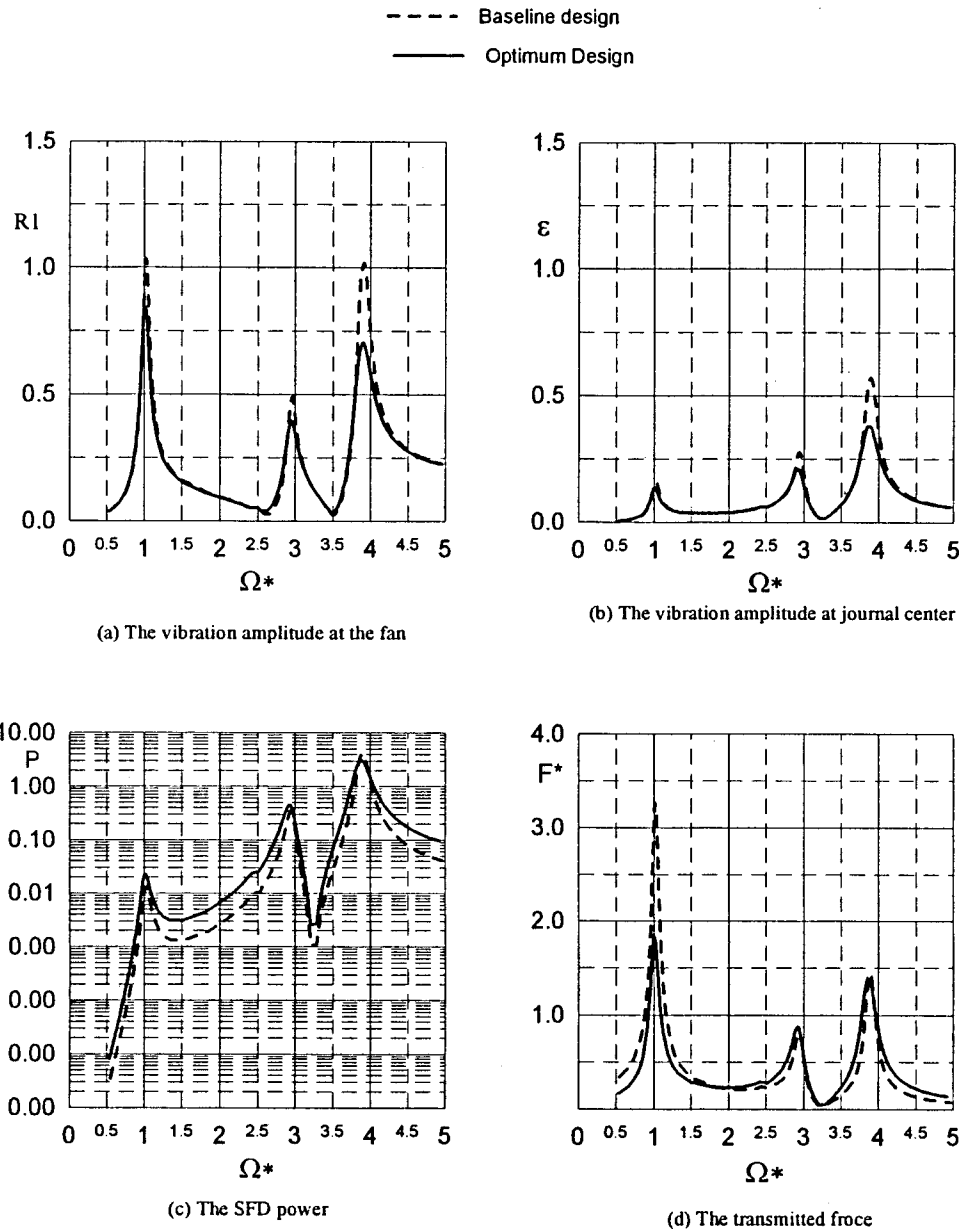


Fig. 6 The unbalance response of AGTFR supported on short SFD optimum design versus baseline design, Case 4, $W1=W2=1.0$

Briefly, a set of $2N$ points in an N -dimensional space is called a complex. The minimization process iterates by replacing the point with the largest function value by a new point with a smaller function value. The iteration continues until all the points cluster sufficiently close to a minimum. The method is based on function comparison, no smoothness is assumed ([20]).

The procedure of optimum design, which is illustrated in Fig. 1, can be summarized in the following steps:

1 Baseline design values of SFD parameters (C , L , Kr) are given between the lower and upper bounds.

2 The fast algorithm, described briefly above, is called to simulate the unbalance response (A , F^* , P) of a certain rotor.

3 The objective function is evaluated according to Eq. (1).

4 The parameters of SFD are changed according to an IMSL optimization routine BC POL which uses the complex method to find the minimum J through values comparison ([20]).

5 A new value of the objective function is obtained corresponding to the new SFD parameters. Then this value is compared to the previously obtained values to investigate the minimum value. The program will stop when the difference between two minimum values of the objective function is less than a certain tolerance (in this analysis, this tolerance is taken to be 10^{-6}).

It should be noted that these steps are linked together in a closed-form program to obtain the optimum parameters of an SFD supporting a certain rotor automatically.

Numerical Example

In order to demonstrate the automated routine, a typical aircraft gas turbine fan rotor (AGTFR), discussed by Yakoub and El-Shafei [9], is introduced here to improve its unbalance behavior through selecting and optimizing an SFD. The rotor exhibits four

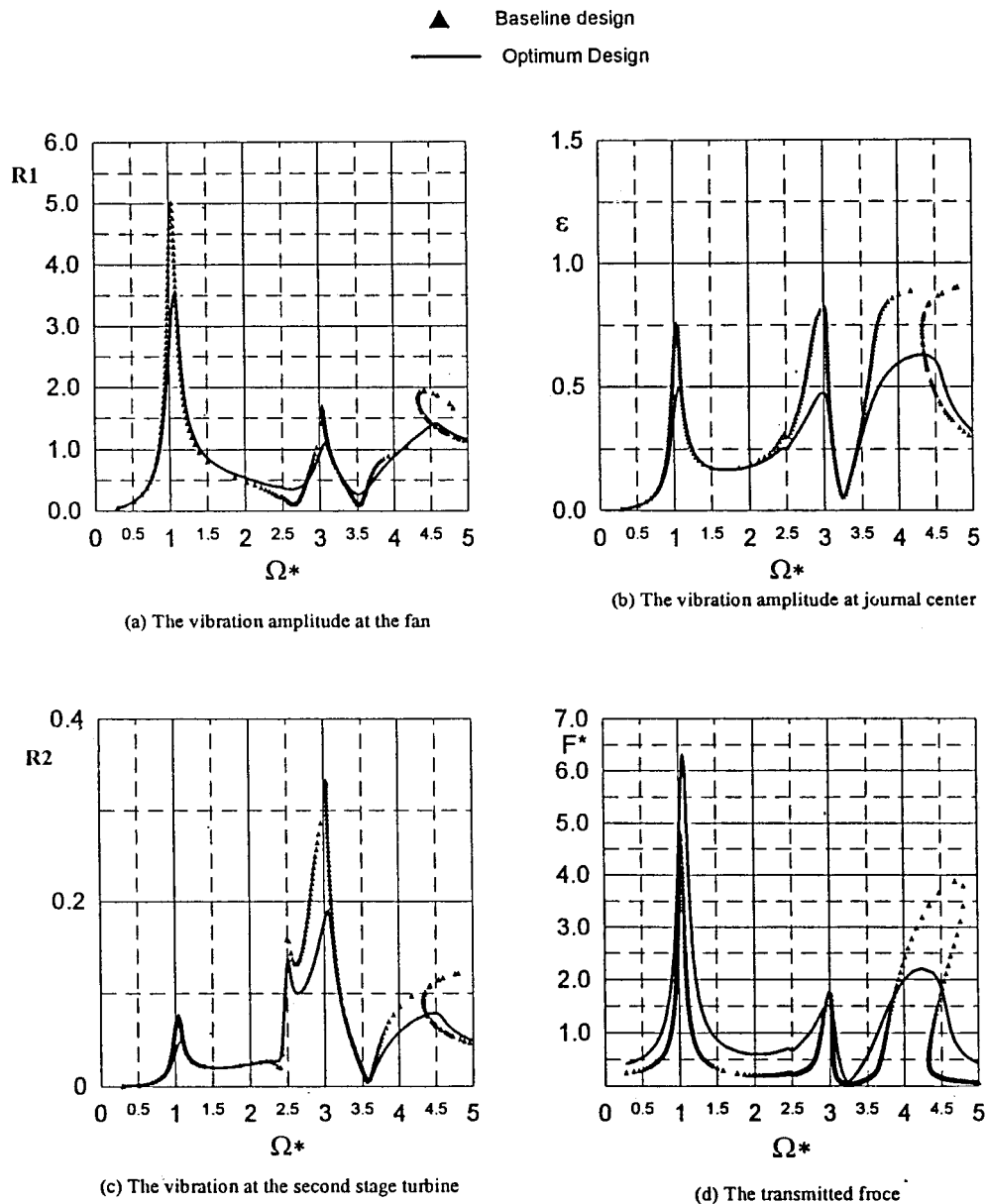


Fig. 7 The unbalance response of AGTFR supported on short SFD optimum design versus baseline design, Case 7, $W1=1.0$

critical speeds in the speed range up to 25,000 rpm. The rotor critical speeds and their associated mode shapes are illustrated in Fig. 2. An SFD is mounted on the fan end bearing with the following specifications:

- radial damper clearance (C) = 250 μm ,
- length of the damper journal (L) = 10 mm
- stiffness of the retainer spring (Kr) = 350 N/mm
- oil viscosity (μ) = 0.014 Ns^2/m

Different cases are taken to satisfy one of the previously mentioned design objectives or a combination of them. These cases are listed in Table 1. In each case, the optimum design process is conducted to obtain the corresponding optimum SFD parameters. The obtained optimum parameters are listed in Table 2 with their corresponding objective function value.

The design variables in each case are the damper radial clearance (C), the length of the journal (L), and the stiffness of the retainer spring (Kr). The bounds of these design variables are

$$C_{\text{lower}} = 150 \mu\text{m} \quad C_{\text{upper}} = 300 \mu\text{m}$$

$$L_{\text{lower}} = 10 \text{ mm} \quad L_{\text{upper}} = 30 \text{ mm}$$

$$Kr_{\text{lower}} = 100 \text{ N/mm} \quad Kr_{\text{upper}} = 600 \text{ N/mm.}$$

The unbalance response in each case is obtained to compare the performance of the AGTFR with the optimized damper to its performance with the baseline damper. Figure 3 shows the baseline unbalance response with the optimized damper in Case 1. The vibration amplitude at the fan (unbalance location) (R_1) is shown in Fig. 3(a), while Fig. 3(b) illustrates the vibration amplitude at the damper journal center (ϵ), and Fig. 3(c) shows the vibration amplitude at the second stage turbine (R_2). The damper force (F^*) is plotted in Fig. 3(d). It is obvious in this figure that the vibration amplitude (R_1) is reduced with a percentage of 29 in the optimized damper than in the baseline damper, which hugely satisfies the design objective of Case 1 (minimizing the maximum

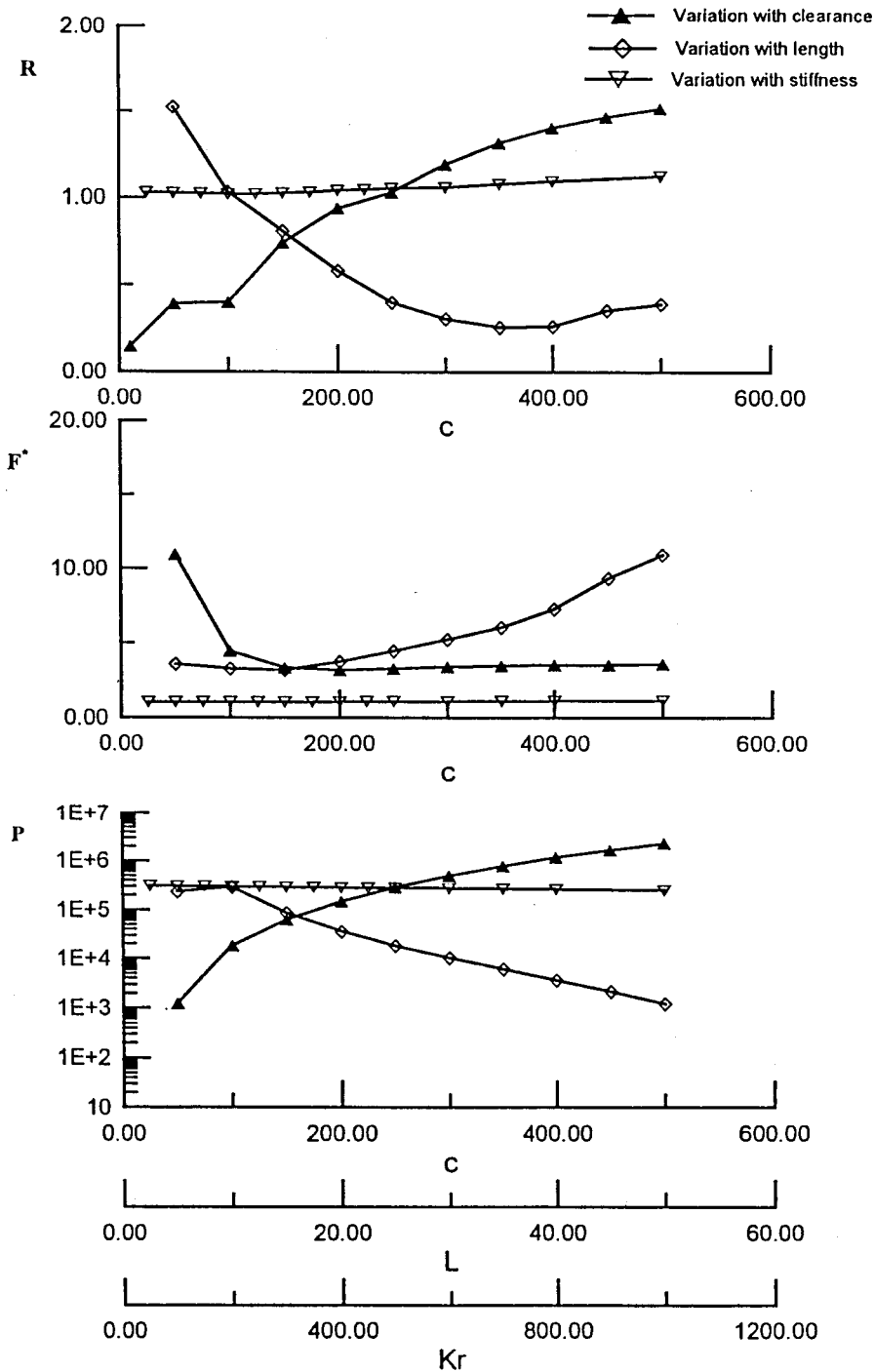


Fig. 8 Variation of objective functions with design parameters for AGTFR SU model

vibration amplitudes). Also the transmitted force (F^*) is reduced. The same quantities are also plotted in Fig. 4 to compare the optimized damper in Case 2 to the baseline damper. This figure shows that the design objective of minimizing the maximum transmitted force is achieved with a 62 percent reduction, while the vibration amplitudes are not changed. Case 3 is illustrated in Fig. 5. The objective of this case is to maximize the summation of the SFD power (P) over speed range $\Omega^* = 2.2$ to 4.0 (12,000–20,000 rpm). It is shown in both Table 2 and Fig. 5 that this objective is fulfilled, since the objective function has reduced from 0.0619 to 0.025. Also, both the vibration amplitudes and the transmitted force are reduced in this case.

Cases with more than one objective have been investigated using the developed optimization method. Case 4 combines two competing design objectives; the vibration amplitude and the transmitted force. Plots (a) and (d) of Fig. 6 show that both objectives are achieved. Table 2 illustrates the success of the optimization with competing objectives, for Cases 4 to 7. The corresponding figures for Cases 5 to 7 have been eliminated for brevity.

To give insight into the behavior of the optimization algorithm it should be stated that in general providing more damping is useful in controlling the amplitude of vibration but increases the force transmitted to the support. The amount of damping produced from an SFD is proportional to the length cubed and inversely

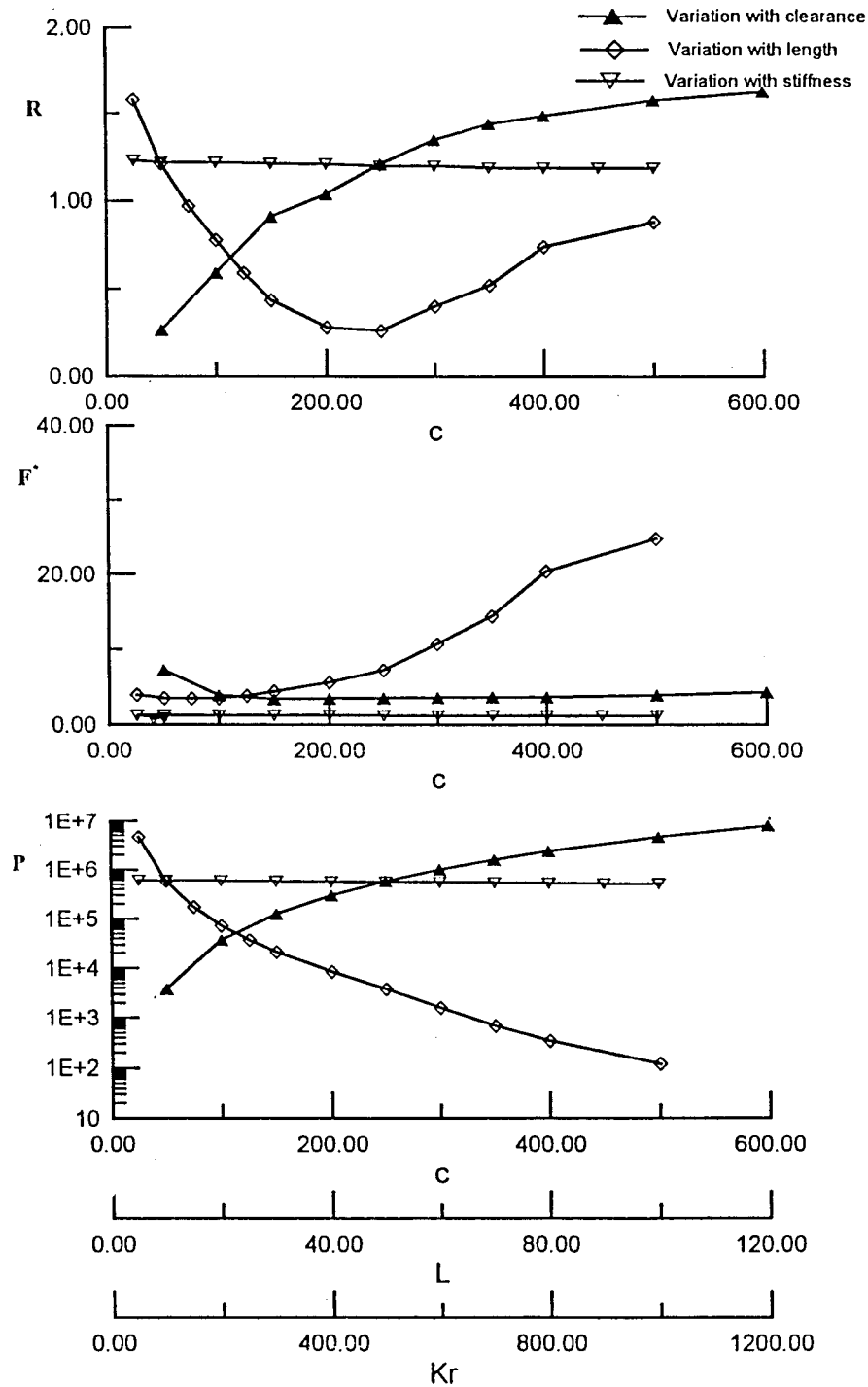


Fig. 9 Variation of objective functions with design parameters for AGTFR SC model

proportional to the clearance cubed. Examining Table 2, it can be seen that for Case 1 the optimization routine chose a small C and a small L (indicating large amount of damping), to control the amplitude of vibration, while for Case 2 the optimization routine chose a large C and a larger L (indicating small amount of damping), to control the transmitted force. In case of competing objectives, Case 4, the optimization routine chose a large C and an even larger L , thus striking a balance between both reducing the amplitude of vibration and reducing the transmitted force. This can be seen in Figs. 3, 4, and 6, where the result of the optimization is to reduce the amplitude of vibration (due to high damping) in Fig. 3 and to reduce the transmitted forces (due to lower damping) in

Fig. 4, while Fig. 6 represents middle grounds with moderate damping due to the competing objectives, but achieves the best possible solution given the design objectives. This physical insight is useful in interpreting Cases 1, 2, and 4. The same reasoning can be applied to interpret the other cases.

Figure 7 illustrates a different case which targets reducing the tendency of SFD to exhibit the jump resonance phenomenon. This phenomenon is usually associated with nonlinear systems. In the work presented in this paper, the jump phenomenon appears when the damper is short and cavitated ([10]). However, this nonlinear phenomenon is undesirable and it is required to prevent the possibility of its occurrence. Thus, in this case, the design objective is

to minimize the maximum vibration amplitude such that the jump resonance would disappear. This objective is achieved as shown in Fig. 7.

Figures 8 and 9 illustrate the variation of different objective functions for the AGTFR with the optimized values, for uncavitated and cavitated dampers, respectively. Note the multiple horizontal scales in these figures for each parameter. In both figures the baseline parameters are fixed, while only one parameter is varied. Thus, it is possible to plot a two-dimensional plot rather than a four-dimensional space to obtain the true optimum values without restrictions. The above figures can only be used as guidance, and only in Case 2 are the design parameters fixed, and then again for only one objective.

Conclusion

This paper presented a method to obtain the optimum parameters of SFDs supporting multiple mode rotors. These parameters are the damper radial clearance, the journal length, and the stiffness of the retainer spring. The developed method relies on the direct search method which minimizes a function subjected to bounded constraints. An objective function is developed to express the specified design objectives. These objectives are to minimize the vibration amplitude, minimize the transmitted force, and/or maximize the SFD power. The objective function is evaluated through the rotor simulations. These simulations are obtained from an already developed fast algorithm. This algorithm is based on using the planar modal analysis theory and the assumption of circular motion. Several design objectives are tested and the unbalance response is investigated in each case. Demonstrations show that the optimized damper achieves the specified design objective in each case.

Acknowledgment

Fruitful discussions with Prof. M. Elaraby are acknowledged.

Nomenclature

A	= nondimensional vibration amplitude
C	= damper radial clearance, m
C_{lower}	= lower bound of the radial clearance, m
C_{opt}	= optimum value of the radial clearance, m
C_{upper}	= upper bound of the radial clearance, m
F^*	= transmitted force, nondimensional
J	= objective function, nondimensional
Kr	= stiffness of the retainer spring, N/m
Kr_{lower}	= lower bound of the retainer spring stiffness, m
Kr_{opt}	= optimum value of the retainer spring stiffness, m
Kr_{upper}	= upper bound of the retainer spring, m
L	= journal length, m
L_{lower}	= lower bound of the journal length, m
L_{opt}	= optimum value of the journal length, m

L_{upper}	= upper bound of the journal length, m
P	= SFD power, nondimensional
$P_{\text{avg}} \Omega_1$	= average power dissipated in the speed range Ω_1 to Ω_2 , nondimensional
R	= journal radius, m
R_1, R_2, \dots	= amplitude of rotor vibration, nondimensional
W_1, W_2, W_3	= weighting factors, nondimensional
ε	= eccentricity ratio in damper, nondimensional
Ω^*	= nondimensional rotor speed

References

- [1] Cooper, S., 1963, "Preliminary Investigation of Oil Films for the Control of Vibration," *Lubrication and Wear Convention*, I. Mech. E., London, pp. 305–315.
- [2] Cunningham, R. E., Fleming, D. P., and Gunter, E. J., 1975, "Design of a Squeeze-Film Damper for a Multi-Mass Flexible Rotor," ASME Paper No. 75-DET-40.
- [3] Barrett, L. E., Gunter, E. J., and Allaire, P. E., 1978, "Optimum Bearing Support Damping for Unbalance Response and Stability of Rotating Machinery," ASME J. Eng. Power, **100**, pp. 89–94.
- [4] Rabinowitz, M. D., and Hahn, E. J., 1982, "Optimal Design of Squeeze Film Supports for Flexible Rotors," ASME Paper No. 82-GT-232.
- [5] Chen, W. J., Rajan, M., Rajan, S. D., and Nelson, H. D., 1988, "The Optimal Design of Squeeze Film Dampers for Flexible Rotor Systems," ASME J. Mech., Transm., Autom. Des., **110**, pp. 166–174.
- [6] Nataraj, C., and Ashrafiun, H., 1993, "Optimal Design of Centered Squeeze Film Dampers," ASME J. Vibr. Acoust., **115**, pp. 210–215.
- [7] Ramesh, K., and Kirk, R. G., 1995, "Design Procedure for Evaluating Stability of Turbomachinery Supported on Squeeze Film Dampers," ASME J. Tribol., **117**, pp. 742–744.
- [8] Nyqvist, J. J., and Larsson, R., 1996, "Solution to Stability Problems in Steam Turbines by Optimization of a Squeeze Film Damper," I. Mech. E. International Conference on Vibrations in Rotating Machinery, Paper C500/022/96, pp. 641–650.
- [9] Yakoub, R. Y., and El-Shafei, A., 1998, "A Fast Method to Obtain the Non-linear Response of Multi-Mode Rotors Supported on Squeeze Film Dampers Using Planar Modes, Part I and Part II," ASME Paper Nos. 98-GT-412 and 98-GT-413.
- [10] El-Shafei, A., 1990, "Unbalance Response of a Jeffcott Rotor Incorporating Short Squeeze Film Dampers," ASME J. Eng. Gas Turbines Power, **112**, pp. 445–453.
- [11] Tecza, J. A., Giordano, J. C., Zorzi, E. S., and Drake, S. K., "Squeeze Film Damper Technology: Part 2—Experimental Verification Using a Controlled Orbit Test Rig," ASME Paper No. 83-GT-248.
- [12] White, D. C., 1972, "The Dynamics of a Rigid Rotor Supported on Squeeze Film Dampers," *Conference on Vibrations of Rotating Machinery*, Proc. I. Mech. E., London, pp. 213–229.
- [13] Mohan, S., and Hahn, E. J., 1974, "Design of Squeeze Film Damper Supports for Rigid Rotors," ASME J. Eng. Ind., **96**, pp. 976–982.
- [14] Taylor, D. L., and Kumar, B. R. K., 1980, "Nonlinear Response of Short Squeeze Film Dampers," ASME J. Lubr. Technol., **102**, pp. 51–58.
- [15] Taylor, D. L., and Kumar, B. R. K., 1983, "Closed Form Steady State Solution for the Unbalance Response of a Rigid Rotor in Squeeze Film Damper," ASME J. Eng. Power, **105**, pp. 551–559.
- [16] El-Shafei, A., 1991, "Unbalance Response of Jeffcott Rotor Incorporating Long Squeeze Film Dampers," ASME J. Vibr. Acoust., **113**, pp. 85–94.
- [17] Mclean, L. J., and Hahn, E. J., 1983, "Unbalance Behavior of Squeeze Film Damped Multi-Mass Flexible Rotor Bearing Systems," ASME J. Lubr. Technol., **105**, pp. 22–28.
- [18] Gunter, E. J., Choy, K. C., and Allaire, P. E., 1978, "Modal Analysis of Turborotors Using Planar Modes-Theory," J. Franklin Inst., **305**(4), pp. 221–243.
- [19] Hathout, J. P., El-Shafei, A., and Youssef, R., 1997, "Active Control of Multi-Mode Rotor-Bearing System Using HSFDs," ASME J. Tribol., **119**, pp. 49–56.
- [20] IMSL MATH/LIBRARY-FORTRAN subroutines for Mathematical Application, Version 1.0, Apr. 1987.

A Framework for Flutter Clearance of Aeroengine Blades

A. Khalak¹

Gas Turbine Laboratory,
Massachusetts Institute of Technology,
Cambridge, MA 02139
e-mail: akhalak@alum.mit.edu

A framework for flutter operability assessment, based upon a new set of similarity parameters, has been developed. This set consists of four parameters which embrace both the performance characteristics in terms of corrected mass flow and corrected speed, and the flight condition in terms of inlet temperature and density (or, equivalently, inlet pressure). It is shown that a combined mass-damping parameter, g/ρ^ , novel in the field of turbomachinery aeroelasticity, can summarize the individual effects of mechanical damping, g , and blade mass ratio, μ . A particular selection of four nondimensional parameters, including g/ρ^* and a compressible reduced frequency parameter, K^* , allows for a decoupling of corrected performance effects from purely aeroelastic effects, for a given machine and a specific modeshape. This view of flutter operability is applied to the analysis of full-scale engine data. The data exhibits the trend that increasing K^* and increasing g/ρ^* have stabilizing effects, which is consistent with previous work in flutter stability. We propose that these trends hold generally, and apply the trends towards constructing a flutter clearance methodology, a test procedure which satisfies the requirements for comprehensive flutter stability testing. [DOI: 10.1115/1.1492832]*

Introduction

To assure reliability and safety of jet propulsion, the potential for blade flutter must be eliminated from the turbomachinery stages. The current predictive models for aeroengine flutter are typically computationally intensive, and it is difficult to ensure high fidelity. A contributor to the complexity of this problem is that there are a large number of relevant physical parameters.

Rig and engine testing are therefore necessary in any engine development program to ensure that flutter does not occur in the operational regime. The relevant regime for assessing performance (i.e., pressure ratio and efficiency) is typically measured in terms of corrected mass flow, \dot{m}_c , and corrected speed. For a given machine, these are equivalent to the axial and tangential blade relative Mach number, respectively. Flutter stability, however, is not solely described by these variables, but requires other variables as well. In particular, the flight condition in terms of inlet temperature and pressure is known to influence flutter stability. In the present research, we address the effects upon flutter stability from the full (nondimensional) set of parameters which span the operating space for a given flowpath geometry.

Aeroelastic problems in turbomachines have been studied for over 50 years. The AGARD Manual on Aeroelasticity ([1]) summarizes the accomplishments in the field through the late 1980s. Since then there has been considerable further research, particularly in the area of computational flow simulations. More recent reviews describe the state of understanding through the 1990s ([2–4]).

The problem of flight condition effects upon flutter stability was first identified by Jeffers and Meece [5] in the context of a fan flutter problem during the development of the F100 engine. While flutter tests at sea level ambient conditions initially suggested that the engine would not flutter, later flight and ground tests confirmed that changes in inlet temperature and density led to a flutter problem in the initial design. Further laboratory testing ([6]) corroborated these results on the F100. Such behavior is shown schematically in Fig. 1. A more comprehensive parameter study of the

effects of flight condition was included in experiments on an annular cascade ([7]) which focused upon choke flutter in midstage compressors. This study also showed temperature effects to be a significant contributor to stability, but did not find inlet density to be a significant factor. Using the current results, we propose that the discrepancy in the density effects between these studies was a result of differing blade root attachments, as will be explained.

Other publicly available experimental flutter tests (see [8,9] also in [1], Chap. 20) varied the performance conditions in terms of corrected speed, N_c , and corrected mass flow, \dot{m}_c , but did not explore the effects of flight condition. Stargardter showed that the classical procedure of correlating flutter onset with reduced velocity, U^* , and flow incidence angle was not valid in his tests. Since Stargardter's tests were conducted at constant inlet temperature and density, increases in reduced velocity, U^* , resulted in Mach number increases as well. The classical correlation procedure could not account for such mixing of Mach number effects and reduced velocity effects, which underscores the need to account for *all* the relevant parameters in assessing aeroengine flutter stability.

This paper focuses upon developing a rational methodology for flutter clearance; that is, for determining that flutter does not occur in the intended operating regime of a given engine. To accomplish this, we develop a minimal parameter space in terms of similarity parameters. Further, parameters are selected which separate the effects of performance point and of flight condition. A set of full-scale engine test data, provided by the Volvo Corporation, is analyzed using this new framework. Finally, we describe a flutter clearance procedure.

Stability Boundary Representation

For flutter clearance, we must assess the flutter stability boundary of a given machine. Srinivasan [4] identifies the following governing parameters: Mach number, M , flow angle, α , reduced frequency, k , temperature, T , and density, ρ . The blade mechanical damping, g , is also a factor. For flutter stability, these six parameters can be summarized by four similarity parameters. We propose a set of four that are especially useful for stability boundaries. These four are corrected mass flow, \dot{m}_c , corrected speed, N_c , and two new parameters, reduced damping, g/ρ^* , and compressible reduced frequency, K^* . Note that the vibrational mode-shapes are presumed to be specified, and that each relevant mode-shape should be considered.

¹Current address: Alphatech, 50 Mall Road, Burlington, MA 01803.

Contributed by the International Gas Turbine Institute (IGTI) of THE AMERICAN SOCIETY OF MECHANICAL ENGINEERS for publication in the ASME JOURNAL OF ENGINEERING FOR GAS TURBINES AND POWER. Paper presented at the International Gas Turbine and Aeroengine Congress and Exhibition, New Orleans, LA, June 4–7, 2001; Paper 01-GT-270. Manuscript received by IGTI, December 2000, final revision, March 2001. Associate Editor: R. Natole.

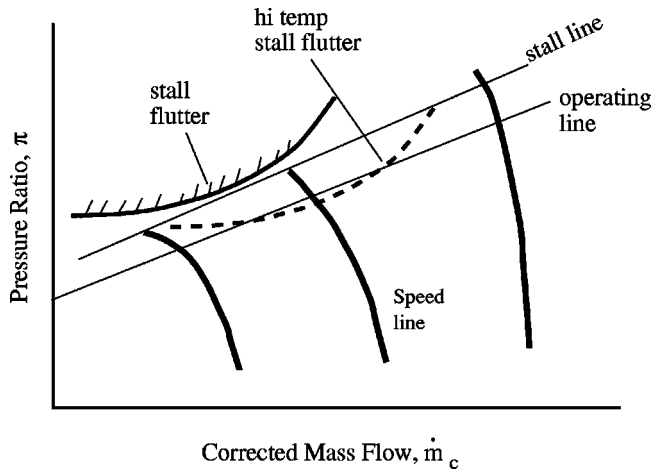


Fig. 1 Schematic of performance map with stall flutter boundary. Changes in the thermodynamic conditions can move the boundary, as shown.

Development of Parameters. The parameter development begins with the linear stability criterion for single-mode flutter of a tuned rotor. Note that complications such as mistuning (with a specified amount and pattern) and nonlinearities will not change the governing parameters, though they can alter the form of the stability criterion. We begin with the structural equation (see Crawley [1], Chap. 19, or Försching [3]) of a specific mode, η , on blade j ,

$$\frac{1}{\omega_0^2} \ddot{\eta}_j + (1 + ig) \dot{\eta}_j = \frac{F_j}{cm_0 \omega_0^2} \quad (1)$$

where ω_0 is the modal natural frequency, F is the fluid force, c is the chord, and m_0 is the modal mass. The imaginary damping term, ig , presumes that η is complex with an imaginary part phase-lagged by 90 deg from the real part (true for positive frequencies).

For a tuned rotor, the use of interblade phase coordinates ([10]) decouples the fluid forces between blades. For interblade phase, σ_j , we use the following model for the fluid forces:

$$\frac{F_{\sigma_j}}{c^2 \rho U^2} = [l_{\sigma_j}(M, \alpha, k)] \eta_{\sigma_j} + \text{h.o.t.} \quad (2)$$

where U is inlet blade-relative velocity, k is the reduced frequency, and l is a nondimensional force coefficient. For the linear stability criterion, the higher-order terms are neglected. Models for l_{σ_j} are often based upon numerical solutions of unsteady flow over a cascade and are typically computationally intensive. In general, such a model includes the Prandtl number, Pr , the Reynolds number, Re , and the Rossby (rotation) number, Ro , as parameters ([11]). For an axial-flow machine, however, Ro is equivalent to the corrected speed, N_c , which can be deduced from M and α ([12]). Furthermore, Re is typically large enough (i.e., $> 10^6$) for aeroengine applications such that variations do not impact flutter. This view is corroborated by Isomura [13], whose vibrating cascade computations were insensitive to Re in this regime. Also, the experiments of Jutras et al. [8], confirmed that a geometrically scaled-down version of a front-stage fan (i.e., with lower Reynolds number) gave the same results in terms of performance and flutter as the full size version, demonstrating the Reynolds number insensitivity experimentally. Therefore, we list l as a function of M , α , and k alone.

Substituting the expression (2) into the interblade-phase version of the structural equation, (1), one obtains a linear, second-order equation for η . Using a harmonic time-dependence, $\eta = \eta_0 e^{i\omega t}$, one obtains the following equation for ω :

$$-\left(\frac{\omega}{\omega_0}\right)^2 \frac{1}{\rho^*} + \frac{1}{\rho^*} + i \frac{g}{\rho^*} = \frac{1}{k^2} l_{\sigma_j}(M, \alpha, k) \quad (3)$$

where ρ^* is a fluid inertia parameter, $c^3 \rho / m_0$, which is equivalent to the traditionally defined mass ratio, $\mu = 4 / \pi \rho^*$. We prefer ρ^* since it highlights the dependence upon inlet density. For linear stability, $\text{Im}(\omega)$, must be positive for all possible interblade phases, σ_j . Taking the imaginary part of (3), we find the following criterion for stability:

$$g / \rho^* > \frac{1}{k^2} \max\{\text{Im} l_{\sigma_j}(M, \alpha, k)\}. \quad (4)$$

The stability criterion, (4), demonstrates that the parameter space is four-dimensional: $(g / \rho^*, k, M, \alpha)$, and specifically that the separate physical parameters of damping, g , and fluid inertia, ρ^* , may be combined into a single parameter for purposes of stability. We term this new parameter, g / ρ^* , the *reduced damping*. Although this combination is novel in the context of turbomachinery flutter, it is not an entirely new idea, and has been applied in bluff-body interactions ([14,15]). It should be recognized that the vibration-induced fluid force coefficient, l , is independent of g / ρ^* , but still depends on M , α , and k .

Implications of g / ρ^* . This result has some important implications to aeroengine flutter. For example, the reduced damping parameter summarizes the interdependent effects of mass and damping as discussed in the parametric study of Försching [3].

An estimate of the fluid inertia at sea level is $\rho^* \sim O(0.01)$, for a metal fan blade in bending. The mechanical damping depends upon whether the vibrating blade rubs against other surfaces, causing friction. Srinivasan [4,16] estimates that the frictional damping in bending for inserted metal blades is of order $g \sim O(0.01)$, while material damping alone (i.e., no friction) gives $g \sim O(0.0001)$. Thus, with friction, g / ρ^* is of the same order as the fluid term (3) and is significant towards assessing stability. Without friction, g / ρ^* is much smaller than the fluid term, and is therefore not significant.

This observation helps explain the discrepancy in density effects between the experiments on the F100 and the annular cascade experiments, as mentioned in the introduction. The F100 engine had the inserted blades with frictional damping, while the annular cascade had a special root attachment [17] with no rubbing or friction. Thus, the presence of density effects upon flutter stability in the F100, should be expected since $g / \rho^* \sim O(1)$, while the absence of density effects in the annular cascade should also be expected since $g / \rho^* \sim O(0.01)$ was too small to be relevant in this case. Note that these “density effects” (i.e., g / ρ^* effects) are considered for constant M , α , and k .

Decoupling Performance From Flight Condition. Using the parameter space developed above, we can fully describe flutter stability for a given structural mode and flowpath geometry, throughout its operational regime. Although the above parameters (M , α , k , and g / ρ^*) span this space, we find it more convenient to use another set of four parameters for operability assessment. First, it is useful to use the corrected mass flow, \dot{m}_c and corrected speed, N_c , which are equivalent to Mach number, M , and flow angle, α , for a given geometry.

The main reason, however, is to separate the performance effects from the flight condition effects. Specifying the modal parameters (which fixes ω_0) and the flight condition (which fixes T), the parameters M and k become linearly proportional, making their individual effects indistinguishable. To address this, we replace k with K^* , a parameter which depends only upon the modal parameters and the flight condition, defined as

$$K^* = \frac{k}{M} = \frac{\omega_0 c}{\sqrt{\gamma R T}} \quad (5)$$

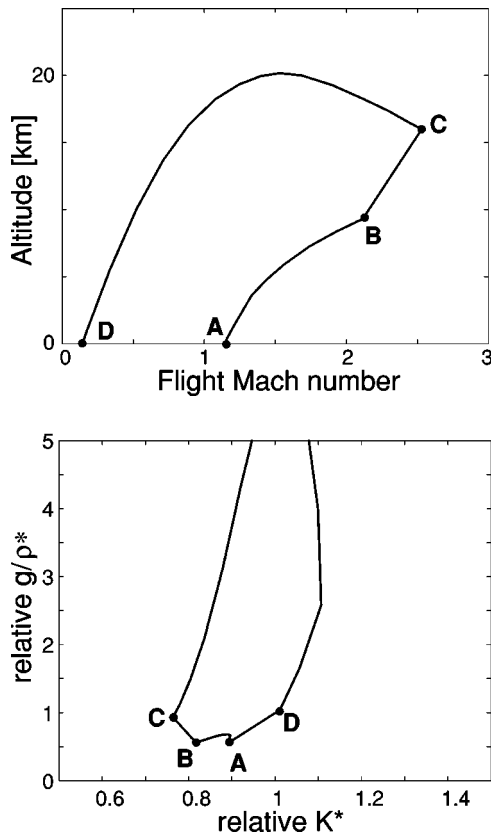


Fig. 2 Flight envelopes for typical supersonic aircraft of flight Mach number versus altitude (adapted from McCormick [18]). The corresponding plot of $(K^*, g/\rho^*)$ is shown, assuming a front stage with an ideal inlet and constant modal parameters. The $(K^*, g/\rho^*)$ plot is normalized such that sea level static conditions are at point D, location (1,1).

where γ is the ratio of specific heats, R is the gas constant, and T is the temperature. Physically, K^* is the ratio between the acoustic timescale and the oscillation timescale. For constant modal parameters (m_0, g, ω_0) , using the parameter set $(\dot{m}_c, N_c, K^*, g/\rho^*)$ decouples the performance effects from the flight condition. The first two parameters, (\dot{m}_c, N_c) , alone account for the corrected performance, and the latter two, $(K^*, g/\rho^*)$, alone account for the flight condition in terms of inlet temperature and density.

In the case of a front stage with an ideal inlet and given modal parameters, T and ρ can be expressed in terms of the aircraft flight Mach number, M_f , and altitude, a . Figure 2 shows this relationship for a typical supersonic aircraft (taken from McCormick [18]).

Using K^* , the stability criterion (4) can be rewritten as follows:

$$g/\rho^* > \frac{1}{K^{*2}} \max\{\text{Im } l'_{\sigma_j}(M, \alpha, K^*)\} \quad (6)$$

where l' is the fluid force, F , nondimensionalized by $\gamma c^2 p_0$, with p_0 being the inlet static pressure, as compared to l which is nondimensionalized with the dynamic pressure. It can be mathematically proven using the implicit function theorem that for constant modal parameters, K^* , or a function thereof, is the only replacement for k which decouples the performance from the flight condition (see Khalak [19]).

Varying Modal Parameters. Sometimes the modal parameters vary with operating condition, notably in the case of centrifugal stiffening. To maintain the separation of performance effects and flight condition effects, the parameters K^* and g/ρ^* ,

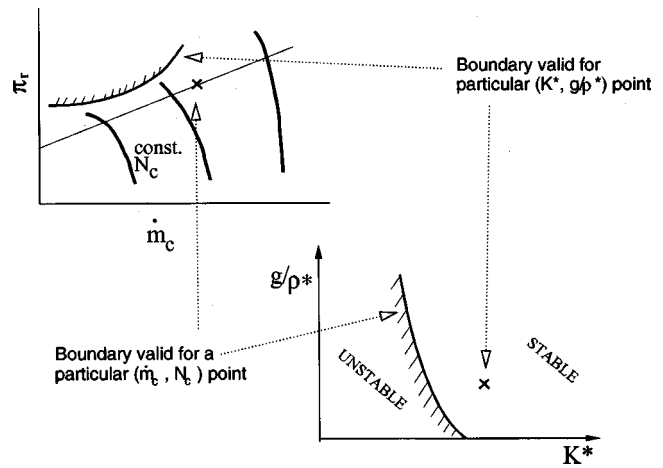


Fig. 3 Dual view of performance map and K^*-g/ρ^* map. Two simultaneous views depict a point (denoted by the \times) in relation to the flutter boundary in the four parameter space, $(\dot{m}_c, N_c, K^*, g/\rho^*)$. Movement of the \times on one set of axes affects the flutter boundary location on the other set of axes. A full description of the operating point requires an \times on both axes.

which were defined for constant modal parameters, should be generalized. In the case of centrifugal stiffening, for example, we can generalize K^* using the *unrotating* natural frequency (i.e., at rest) in the definition of K^* . This retains only the speed-independent effects of frequency in K^* , and maintains the separation of performance from flight condition. Generalizations to other dependencies of the modal parameters should be based on the specific form of the dependency.

Flutter Boundaries. The four parameters, $(\dot{m}_c, N_c, K^*, g/\rho^*)$, offer a view of flutter stability which completes the performance map view of Fig. 1, in which the flutter boundary moves with changes in inlet temperature. In general, the flutter boundary on the performance map can move with changes in K^* and g/ρ^* . A useful diagram is a simultaneous view of the performance map, of pressure ratio, π_r , versus corrected mass flow, \dot{m}_c , on a pair of axes, and a K^*-g/ρ^* map on another pair of axes, as shown in Fig. 3.

In the dual plots of Fig. 3, an \times is drawn on each map to fully specify the operating point, and the boundary is shown by the hatched curves. Movement of the operating point, \times , on one map affects the position of the flutter boundary on the other map. For example, if there is an increase in inlet temperature at constant corrected performance, the \times moves on the K^*-g/ρ^* map, and the boundary moves on the performance map.

Conversely, for changes in corrected performance, the boundary on the K^*-g/ρ^* map moves. Figure 4 shows this behavior for a two-dimensional subsonic linearized-unsteady potential flow model as described in Hall [20] for a cascade in the 10th Standard Configuration. This model was used to compute l' in the stability criterion (6), for a fixed inlet flow angle, α , and varying inlet relative Mach numbers from $M=0.4$ to $M=0.7$.

The flutter boundary on the K^*-g/ρ^* map, for a given performance point as in Figs. 3 and 4, is downward sloping. Thus, increases in g/ρ^* and in K^* are stabilizing. That increasing g/ρ^* is stabilizing can be seen by inspection of the stability criterion, (6). Increasing K^* is stabilizing as well, although this trend ultimately has an empirical basis. By similarity, an increase in K^* (for constant g/ρ^* , \dot{m}_c , and N_c) is equivalent to an increase in the modal frequency, ω_0 , whose stabilizing effect is established in design practice (Chap. 22 of [1]). Moreover, models in many special cases exhibit this tendency, such as those for cascades in potential flow ([21]), inviscid cascades with strong shocks ([22]),

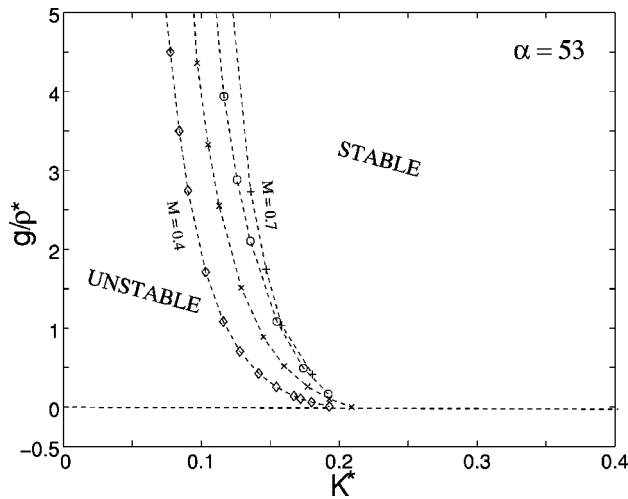


Fig. 4 Boundaries on K^*-g/ρ^* map using linearized-unsteady compressible potential model (Hall [20]) in 10th Standard Configuration. The effect of increasing Mach number at constant (K^* , g/ρ^*) is destabilizing.

and fully stalled cascades in incompressible flow ([23]). These trends in K^* and g/ρ^* can be used to assist in data interpretation and testing.

Application to Full-Scale Engine Tests

The above framework was applied to the interpretation of full scale engine tests. First, development tests upon an early multi-mission aircraft engine are discussed, and then a particular case of fan flutter data, provided by the Volvo Corporation, from full-scale engine tests is treated in detail.

Figure 5 shows a summary of results from flutter testing on several fan builds for a multimission aircraft engine. In each case, the flutter occurred at approximately the same point on the operating map (at part speed); therefore, only the data on the K^*-g/ρ^*

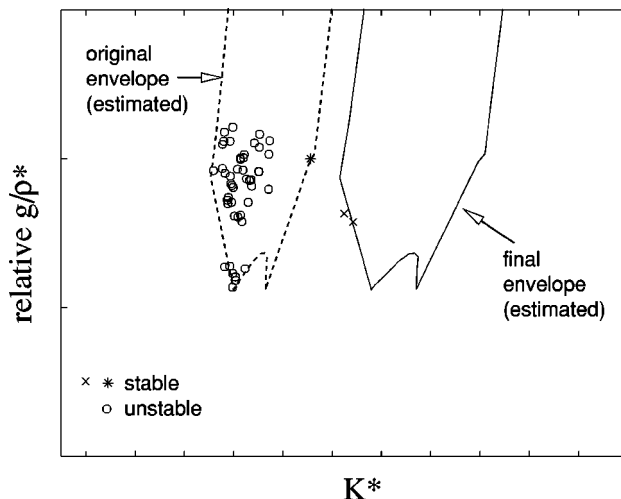


Fig. 5 Fan data on K^*-g/ρ^* map, for early multimission aircraft. A \circ indicates a flutter point, while * and \times are stable points. The dashed envelope is estimated from the “generic” aircraft shown in Fig. 2, anchored on the sea level static (SLS) rig tests on the original design, *. The original design (and several minor design variations) were unstable at flight conditions other than SLS, shown in the cluster of \circ 's. The eventual redesign, corresponding to the solid envelope, was tested to be stable at all relevant flight conditions, \times .

map is shown. Although the actual flight envelope was not available, the “generic” supersonic envelope from Fig. 2 is used. Initial rig testing at SLS (*) indicated that the engine would be stable, but engine testing at other flight conditions (cluster of \circ 's) exhibited a flutter. Several minor modifications to the design were tested (also in the cluster of \circ 's), but none of these increased K^* enough for stability. The final redesign, \times , did significantly increase K^* , and it is clear that the corresponding flight envelope is completely to the right of the SLS (*) point. This view shows that the stable measurements of the SLS rig test were actually consistent with the engine tests at other flight conditions, a point which was not apparent otherwise.

Volvo Data. The Volvo engine test data of fan flutter in the second bending mode are rare in the sense that the full four-dimensional parameter space was explored. For each combination of parameters, the frequency and magnitude of a stress signal associated with blade vibrations was recorded. The mechanical damping, g , was not explicitly measured, but it was known that there was friction at the root attachment and the part-span shroud. In the current analysis, it is assumed that the value of g was constant, and the subsequent values of g/ρ^* listed for this data are normalized relative to the sea-level static condition at $g/\rho^*=1$.

Due to centrifugal stiffening, the rotating natural frequency, ω_{rot} , differed from the unrotating natural frequency, ω_{rest} . In the computation of K^* , the unrotating frequency, ω_{rest} , was used as described in the previous section, which ensures that flight condition effects and performance effects remain decoupled. However, one would expect the oscillation frequency in flutter to be ω_{rot} .

To distinguish between stable points and flutter points, both the frequency and magnitude information was used, since some of the vibrations were a result of upstream forcing. The median stress measured in the flutter region was about 45 MPa. The criteria used to separate the data into stable and flutter data are as follows:

Stress > 1 MPa	Freq. within 2% of ω_{rot}	Category
No	-	Stable
Yes	No	Discard
Yes	Yes	Flutter

The data were sampled at locations on the K^*-g/ρ^* map, each with a cluster spanning a portion of the performance map. Each cluster did not necessarily contain enough data, alone, to obtain an accurate estimate of the stability boundary. However, data from other clusters could be used to generate upper and lower bounds for stability and thus lead to an accurate boundary. Here, we use the trend identified in the previous section that increases in g/ρ^* and in K^* are stabilizing.

Figure 6 shows the stability boundary estimate for the cluster, or “analysis box,” with $0.68 < K^* < 0.69$, and $0.74 < g/\rho^* < 0.75$. The stability boundary is a polynomial constructed using a support vector machine (SVM) classification algorithm (see Khalak [19] for details). Stable points lie on one side of the boundary (a lower bound) and unstable points lie on the other (upper bound). The lower bound of stable points is formed from the stable points in the analysis box (*) and the stable points (+) from regions of equal or lower stability, $K^* < 0.69$ and $g/\rho^* < 0.75$. Conversely, the upper bound of unstable points is taken from measurements in the box (\circ) and unstable points (\triangleright) from regions of equal or greater stability, i.e., $K^* > 0.68$ and $g/\rho^* > 0.74$.

Results of Volvo Data Analysis. The trends in the flutter boundary with changes in K^* and g/ρ^* are shown in Fig. 7(a). As expected, an increase in g/ρ^* stabilizes the flutter boundary, moving the flutter region away from the operating region. The range of movement with g/ρ^* is striking since it spans nearly half the speedline for a change in g/ρ^* from 0.6 to 1.0. For example,

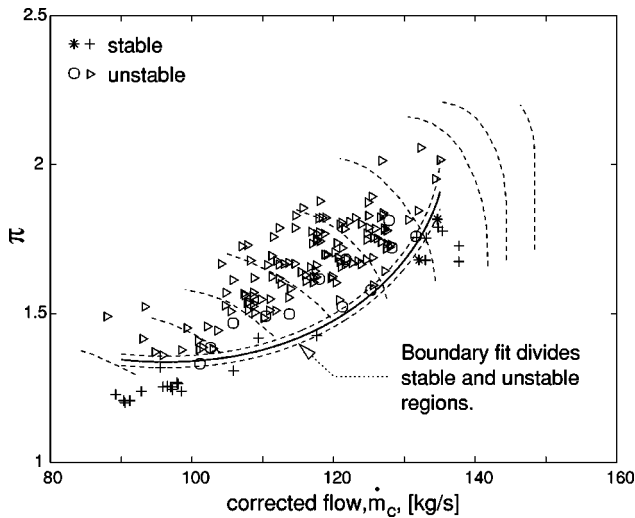


Fig. 6 Example of stability boundary, for $(0.68 < K^* < 0.69$ and $0.74 < g/\rho^* < 0.75)$, with \circ in flutter, and $*$ stable. Data outside this $(K^*, g/\rho^*)$ analysis box, $+$ points at lower K^* and g/ρ^* , and \triangleright at higher K^* and g/ρ^* , are used to generate upper and lower bounds for the stability curve. The dashed lines indicate the uncertainty in the boundary estimation process.

at 83% corrected speed on Fig. 7(a), a change in the reduced damping, g/ρ^* , from 0.6 to 1 leads to an increase in the pressure ratio at the boundary of about 15%.

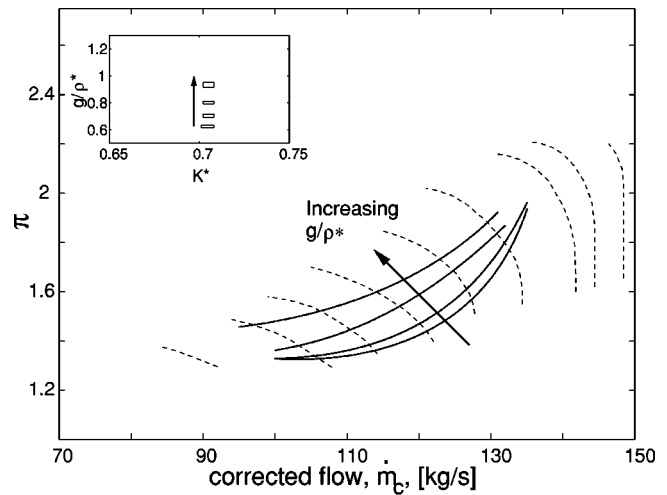
The case of changing K^* is shown in Fig. 7(b) for $g/\rho^* \approx 1$, for values of K^* from 0.68 to 0.75. Increasing the compressible reduced frequency, K^* , tends to stabilize the boundary, as expected. The stabilizing effect of increasing K^* is prominent at lower corrected speeds.

In the context of corrected performance, flight condition effects are reducible to changes in the inlet stagnation pressure. For flutter stability, however, the inlet pressure alone cannot always account for the flight condition effects. In the case of the supersonic aircraft of Fig. 2, for example, there are independent variations in K^* and g/ρ^* with flight condition. To demonstrate that flight condition effects are not merely reducible to inlet pressure effects, analysis boxes at the same inlet pressure and varying inlet temperature are compared in Fig. 8.

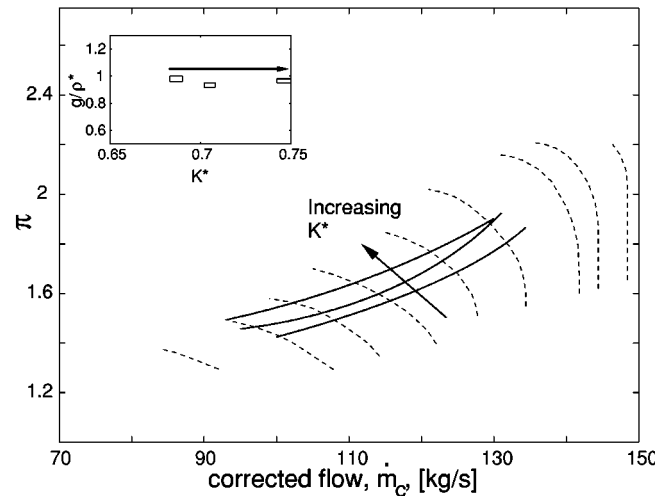
Instead of looking at the flutter boundaries on the performance map, we can also look at the dual view of the boundary on the K^*-g/ρ^* map. This view is useful since, for given structural quantities, it is understandable in terms of the flight envelope of the aircraft powered by the engine, as depicted in Fig. 2.

We consider boundaries on the K^*-g/ρ^* map, as shown in Fig. 9, at a constant point on the corrected performance map (\dot{m}_c, N_c), similar to those depicted in Figs. 3 and 4. For each of the 11 points (■) on the K^*-g/ρ^* map, a flutter boundary was estimated on the performance map. Then, for any given performance map point, each of the 11 points could be classified as either stable or unstable depending upon its corresponding boundary location. The dashed boundaries of Fig. 9 divide the stable ■'s from the unstable ■'s for a specific performance map point. In particular, the dashed boundaries correspond to a corrected speed of $N_c = 74\%$, for various critical pressure ratios, π_{cr} .

This series of boundaries gives an indication of the coupled effects of K^* and g/ρ^* . The boundaries tend to curve downward, being flatter for lower K^* and lower g/ρ^* , but steeper for higher K^* and higher g/ρ^* . The curvature in the boundaries indicates that the sensitivity changes as one moves in the parameter space. Similar behavior was observed for other values of N_c .



(a)



(b)

Fig. 7 Flutter boundaries (a) with constant $K^*=0.705$, and varying g/ρ^* , and (b) with constant $g/\rho^* \approx 1$, and varying K^* . Each boundary corresponds to one of the analysis boxes of the inset plots. The trend for increasing g/ρ^* , is stabilizing, as is the trend for increasing K^* .

Flutter Clearance

Flutter clearance refers to the testing procedure performed to ensure that the engine blades will not flutter throughout the intended operating regime. The testing environment for aeroengine flutter is harsh on the measurement equipment and the machine being tested, making it important to minimize the required testing effort.

The design of a flutter test, can be framed in terms of a *test matrix*, or a testing schedule, which spans the relevant factors. In this case, the factors are given by the similarity variables: ($\dot{m}_c, N_c, K^*, g/\rho^*$). The requirement for flutter clearance is that *the machine must be stable for every combination of parameters, ($\dot{m}_c, N_c, K^*, g/\rho^*$), that it is designed to encounter*. Testing every permutation of parameters is performed in a so-called “full factorial” test.

Although this would satisfy the requirement, it is neither practical nor essential for flutter clearance. Using the concept that flutter stability increases with increases in K^* and g/ρ^* , the test matrix can be simplified. At a given $(K^*, g/\rho^*)$ location, a stable

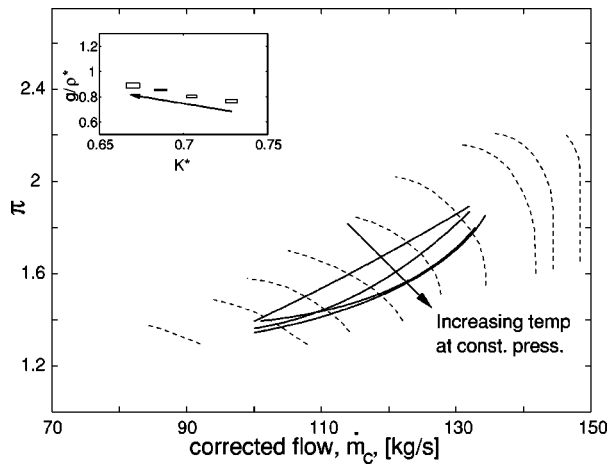


Fig. 8 Effect of temperature at a constant pressure. A series of flutter boundaries are shown corresponding the same pressure (within 2%) and varying temperature. Increasing in temperature, at constant pressure, destabilizes the flutter boundary, showing that inlet pressure is not the only relevant flight condition.

measurement also holds for higher values of $(K^*, g/\rho^*)$, and an unstable measurement is relevant for lower values of $(K^*, g/\rho^*)$. This principle is outlined in Fig. 10.

Using this trend, we can modify the above stability requirement in the following manner: *for every performance point of operation, (\dot{m}_c, N_c) , the machine is stable at $(\min K^*, \min(g/\rho^*))$, where min denotes the minimum value encountered for the given (\dot{m}_c, N_c) .* The behavior at this minimum $(K^*, g/\rho^*)$ pair must be estimated by some reliable means, the most straightforward of which is to take experimental measurements there.

To illustrate, a flutter clearance example is presented for a supersonic aircraft, using the Volvo engine data for the stability characteristics in nondimensional form; however, since different structural parameters and a different flight envelope is used, the results are not related to any real case. This fictitious example is meant only to demonstrate the flutter clearance methodology, rather than to precisely simulate any specific application.

Example: High Speed Aircraft. We consider a front stage fan of a high-speed (i.e., supersonic) aircraft with the following

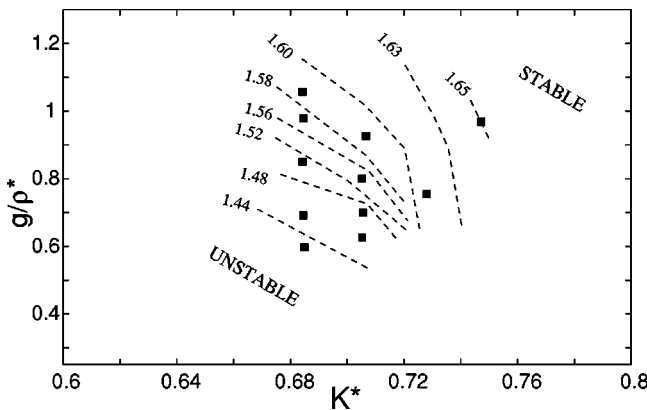


Fig. 9 Family of flutter boundaries on K^*-g/ρ^* map, for 74% corrected speed, and various critical pressure ratios, π_{cr} . The boundary resolution is limited by sampling of $(K^*, g/\rho^*)$ points (represented by ■'s).

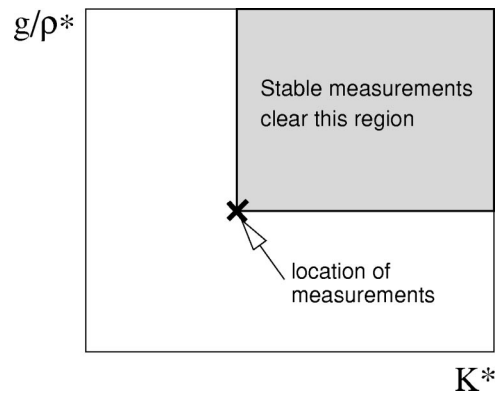


Fig. 10 Schematic of flutter clearance rule on K^*-g/ρ^* map

assumptions, for simplicity: (a) the mechanical damping does not vary significantly during operation, (b) the relevant modeshape has been identified.

The value of K^* is taken to be 0.8 at sea level static (SLS) conditions, and the mechanical damping remains unchanged from the Volvo data. Furthermore, we assume that SLS testing does not indicate flutter.

The minimal region for clearance on the K^*-g/ρ^* map depends upon the mission requirements, which for a high-speed aircraft are relatively sophisticated, and are based upon accomplishing specific scenarios. For this simplified example, the re-

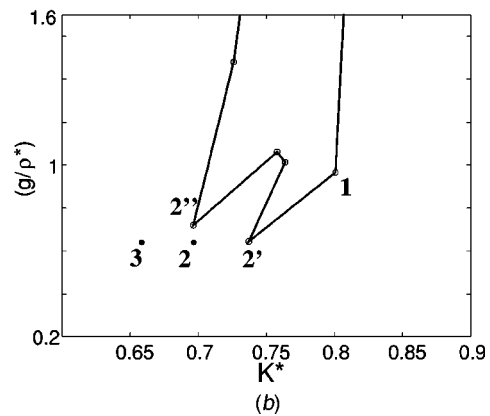
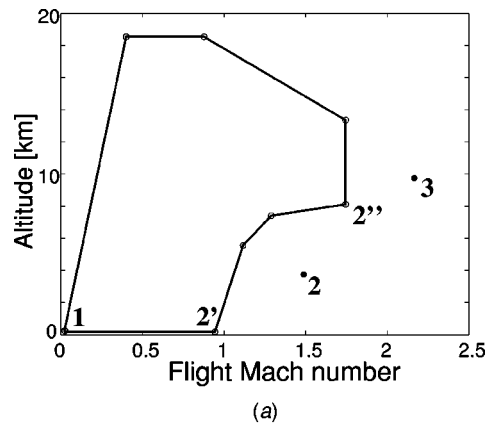


Fig. 11 Flight requirements for example in terms of Mach number versus altitude (a) and region on K^*-g/ρ^* map (b). The sea level static condition is assumed to be at $(K^*, g/\rho^*) = (0.8, 1)$. The critical points, 2' and 2'' are labeled on both plots.

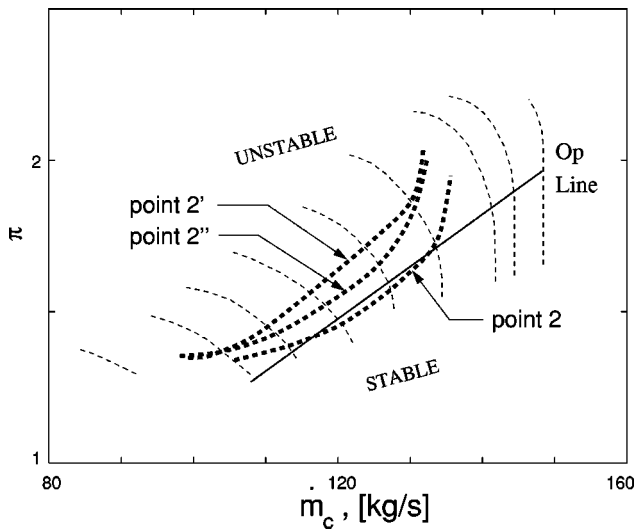


Fig. 12 Flutter boundaries for clearance example. The tests are performed at four points: first, at sea level static (point 1), then at point 2, where a flutter occurs on the operating line, then at points 2' and 2'', which establish that the minimally acceptable envelope is clear, but is close to a flutter event on the operating line at point 2.

quirements are depicted in Fig. 11(a). Minimum required Mach numbers are specified for low altitude (takeoff and climb), and for higher altitudes (cruise and supersonic dash). There are two critical points for the purposes of flutter, labeled 2' and 2'', respectively. The corresponding region on the K^*-g/ρ^* map is shown in Fig. 11(b). Furthermore, for this simplified example, we require that the operating line be clear of flutter throughout the entire specified region of the K^*-g/ρ^* map. A more sophisticated approach might require a desired flutter margin, or limit the range of the operating line depending upon the values of K^* and g/ρ^* .

It is proposed to test the engine successively at the numbered points: 1, 2, and 3 on the K^*-g/ρ^* map, depicted on Fig. 11(b). At each point, the engine should be run along the operating line to check for possible intersections with the flutter boundary. This type of testing requires the capability to adjust the values of K^* and g/ρ^* , which may be accomplished by setting the temperature and the pressure of the inlet flow to achieve the desired K^* and g/ρ^* . Using the principle shown in Fig. 10, if point 2 is confirmed to be clear of flutter, then the entire region in Fig. 11(b) is clear. However, if a flutter event occurs at point 2, then the minimal region may still be cleared if points 2' and 2'' are clear.

The relationship between the flutter boundary and the operating line, using the Volvo data, is depicted in Fig. 12. By assumption, point 1 (the SLS point) does not exhibit flutter. However, point 2 would show a flutter event on the operating line. Further testing at points 2' and 2'', however, would reveal that the operating line is clear throughout the minimally acceptable range of flight conditions, but that extensions beyond this minimally acceptable range (e.g., to point 2) can lead to a flutter event.

Summary and Conclusions

A framework for flutter stability was developed for the case of an axial-flow machine with specified flowpath geometry and a particular modeshape. Such a framework can be described in terms of four nondimensional parameters, by combining the mechanical damping and the fluid inertia into a single reduced damping parameter, g/ρ^* , a novel development in the context of turbomachinery flutter. Consideration of the reduced damping

implies that density effects upon flutter are only significant in the case of significant mechanical damping, usually achieved with frictional supports.

Besides corrected performance, flight condition in terms of inlet temperature and density influences flutter stability. In general, the performance can be described by \dot{m}_c and N_c , while the flight condition for given modal parameters corresponds to the similarity parameters K^* and g/ρ^* . Increasing g/ρ^* has a stabilizing effect on flutter, a trend which is based in the analytical form of the stability criterion. Increasing K^* is also stabilizing, which has been shown to hold in a variety of idealized cases, but whose application to aeroengines is ultimately empirical.

The framework was used in the interpretation of full-scale flutter data, showing how one could quantify the trends in a real case. In particular, the data also exhibited the trend that increasing K^* and g/ρ^* were both stabilizing influences towards flutter. Also, it was shown that these quantities affect flutter differently, and that inlet pressure is not the only relevant inlet condition, but rather that two thermodynamic states (e.g., temperature and density) must be specified.

Finally, these concepts were applied to the problem of flutter clearance testing. The basic requirement to confirm that the machine is stable at every point of operation, can be simplified by utilizing the trend that increasing K^* and g/ρ^* is stabilizing. This suggests the location of critical points in the required operating regime for clearance testing.

Acknowledgment

The author would like to acknowledge the generosity of the Volvo Corporation in supplying the fan flutter test data. The advice and support of Prof. Jack Kerrebrock of M.I.T. were essential. This work was supported by a grant from AFOSR, Grant #F49620-00-1-0014, Tom Beutner, Contract Monitor, as well as a National Science Foundation Fellowship.

Nomenclature

a	= altitude
c	= blade chord
g	= (non-dimensional) modal mechanical damping
g/ρ^*	= reduced damping
k	= classical reduced frequency, $c\omega_0/U$
l	= vibration-induced fluid force coefficient
\dot{m}_c	= corrected mass flow
m_0	= modal mass
p_0	= inlet air pressure
F	= vibration-induced fluid forces
K^*	= compressible reduced frequency, $c\omega_0/\sqrt{\gamma RT}$
M	= characteristic inlet Mach number
M_f	= aircraft flight Mach number
N_c	= corrected speed
R	= gas constant
T	= inlet air temperature
U	= characteristic inlet velocity
U^*	= classical reduced velocity, $1/k$
α	= characteristic inlet flow angle
γ	= ratio of specific heats
η	= nondimensional modal coordinate
ω	= (complex) vibrational frequency
ω_0	= modal frequency
π_r	= pressure ratio
ρ	= inlet air density
ρ^*	= fluid inertia parameter, $c^3\rho/m_0$

References

- [1] Sisto, F., and Carta, F. O., eds., 1988, *AGARD Manual on Aeroelasticity in Axial-Flow Turbomachines*, **1 and 2**, AGARDograph No. 298.
- [2] Verdon, J. M., 1993, "Review of Unsteady Aerodynamic Methods for Turbo-

- machinery Aeroelastic and Aeroacoustic Applications," *AIAA J.*, **31**, pp. 235–250.
- [3] Försching, H., 1994, "Aeroelastic Stability of Cascades in Turbomachinery," *Prog. Aerosp. Sci.*, **30**, pp. 213–266.
- [4] Srinivasan, A. V., 1997, "Flutter and Resonant Vibration Characteristics of Engine Blades," *ASME J. Eng. Gas Turbines Power*, **119**, pp. 742–775.
- [5] Jeffers, J. D., and Meece, C. E., 1975, "F100 Fan Stall Flutter Problem Review and Solution," *J. Aircr.*, **12**, pp. 350–357.
- [6] Mehlic, C. M., Hurrel, H. G., Dicus, J. H., Lubomski, J. F., Kurkov, A. P., and Evans, D. G., 1977, "Experimental Results and Data Format of Preliminary Fan Flutter Investigation Using YF100 Engine," Technical Report, NASA TM SX-3444.
- [7] Jutras, R. R., Stallone, M. J., and Bankhead, H. R., 1980, "Experimental Investigation of Flutter in Mid-Stage Compressor Designs," AIAA Paper 80-0786.
- [8] Jutras, R. R., Fost, R. B., Chi, R. M., and Beacher, B. F., 1983, "Subsonic/Transonic Stall Flutter Investigation of a Rotating Rig," Technical Report, NASA CR-174625.
- [9] Stargardt, H., 1979, "Subsonic/Transonic Stall Flutter Study," Technical Report, NASA CR-165356.
- [10] Lane, F., 1956, "System Mode Shapes in the Flutter of Compressor Blade Rows," *J. Aerosp. Sci.*, pp. 54–66.
- [11] Gerolymos, G. A., 1993, "Coupled Three-Dimensional Aeroelastic Stability Analysis of Bladed Disks," *ASME J. Turbomach.*, **115**, pp. 791–799.
- [12] Kerrebrock, J. L., 1992, *Aircraft Engines and Gas Turbines*, M.I.T. Press, Cambridge, MA.
- [13] Isomura, K., 1996, "A Numerical Investigation of Flutter in a Transonic Fan," Technical Report, GTL Report 223, M.I.T. Gas Turbine Laboratory.
- [14] Vickery, B. J., and Watkins, R. D., 1964, "Flow-Induced Vibrations of Cylindrical Structures," *Proceedings of the First Australian Conference on Hydraulics and Fluid Mechanics*, R. Silvester ed., Pergamon Press, New York.
- [15] Scruton, C., 1965, "On the Wind-Excited Oscillations of Towers, Stacks, and Masts," *Proceedings of the Symposium on Wind Effects on Buildings and Structures*, Her Majesty's Stationary Office, London, pp. 798–836.
- [16] Srinivasan, A. V., Cutts, D. G., and Sridhar, S., 1981, "Turbojet Engine Blade Damping," Technical Report, NASA CR-165406.
- [17] Rakowski, W. J., Ellis, D. H., and Bankhead, H. R., 1978, "A Research Program for the Experimental Analysis of Blade Instability," AIAA/SAE 14th Joint Propulsion Conference.
- [18] McCormick, B., 1995, *Aerodynamics, Aeronautics, and Flight Mechanics*, John Wiley and Sons, New York.
- [19] Khalak, A., 2000, "Parametric Dependencies of Aeroengine Flutter for Flutter Clearance Applications," Ph.D. thesis, M.I.T., Cambridge, MA.
- [20] Hall, K. C., 1993, "Deforming Grid Variational Principle for Unsteady Small Disturbance Flows in Cascades," *AIAA J.*, **31**, pp. 777–787.
- [21] Whitehead, D. S., 1960, "Force and Moment Coefficients for Aerofoils Vibrating in Cascade," Technical Report R&M 3254, British ARC.
- [22] Goldstein, M. E., Braun, W., and Adamczyk, J. J., 1977, "Unsteady Flow in a Supersonic Cascade With Strong In-Passage Shocks," *J. Fluid Mech.*, **83**, pp. 569–604.
- [23] Chi, R. M., 1980, "Unsteady Aerodynamics in Stalled Cascade and Stall Flutter Prediction," ASME Paper 80-C2/AERO-1.

Eigen solutions of Grouped Turbo Blades Solved by the Generalized Differential Quadrature Method

J. H. Kuang¹

Professor

e-mail: kuang@mail.nsysu.edu.tw

M. H. Hsu

Graduate Student

Department of Mechanical Engineering,
National Sun Yat-Sen University,
Kaohsiung 80424, Taiwan

The eigenvalue problems of grouped turbo blades were numerically formulated by using the generalized differential quadrature method (GDQM). Different boundary approaches accompanying the GDQM to transform the partial differential equations of grouped turbo blades into a discrete eigenvalue problem are discussed. Effects of the number of sample points and the different boundary approaches on the accuracy of the calculated natural frequencies are also studied. Numerical results demonstrated the validity and the efficiency of the GDQM in treating this type of problem. [DOI: 10.1115/1.1492833]

Introduction

With the increasing availability of various numerical methods, e.g., the finite difference method, the finite element method and the boundary element method, the static, and dynamic solutions for many complicated structures have now become achievable. However, to look for an alternative efficient technique is still of prime interest. The concept of differential quadrature method (DQM) was introduced by Bellman et al. [1,2]. In last 20 years, the DQM had been used extensively to solve a variety of problems in different fields of science and engineering. The DQM has been shown to be a powerful contender in solving initial and boundary value problems and thus has become an alternative to the existing methods. Chen and Zhong [3] pointed out that the differential quadrature method is more efficient for nonlinear problems than the traditional finite element and finite difference methods. In order to derive the weighting coefficients in a more explicit way, a generalized differential quadrature method (GDQM) was proposed by Quan and Chang [4,5] and Shu and Richards [6]. The GDQM is rather convenient in comparison with the DQM. In the GDQM, Li and Lam [7] pointed out that there is no restriction on the distribution and the number of discrete grid points used in the approximation process and the weighting coefficients are determined by using a simple recurrence relationship instead of solving a set of linear algebraic equations.

The DQM or the GDQM have been used extensively to solve a variety of engineering problems. One of the fields among which one can find extensive applications of DQM is structural mechanics. Bert et al. [8–12] and Han and Liew [13] analyzed static and free vibration of beams, rectangular and annular plates by using the DQM. Malik and Bert [14] implemented the DQM multiple boundary conditions to free vibration of plates. Striz et al. [15] used the quadrature element method for static analysis. Du et al. [16] used the GDQM for buckling analysis.

In the design of turbomachinery, the trend is toward higher efficiency, so complex shape of blade in turbo machinery is unavoidable. Due to the complexity of turbo blade shapes, a pretwisted taper beam has been used to approximate it. The natural frequencies of a single tapered and pretwisted turbo blade were calculated by Rao [17,18], Hodges et al. [19], Abrate [20], and Dawson et al. [21,22] by using the Rayleigh-Ritz method. Gupa and Rao [23] applied the finite element method for finding the frequencies of natural vibration of doubly tapered and twisted

beams. Swaminathan and Rao [24] solved the vibrations of a rotating, pretwisted, and tapered blade. Subrathmanyam et al. [25,26] determined the natural frequencies and the mode shapes of a uniform pretwisted cantilever blade by using the Reissner method. Chen and Keer [27] analyzed the transverse vibrations of a rotating pretwisted Timoshenko beam subjected to an axial loading. Storti and Aboelnaga [28] studied the transverse deflections of a straight tapered symmetric beam attached to a rotating hub as a model for the bending vibration of blades in turbomachinery. Wagner [29] calculated the forced vibration response of sub-systems with different natural frequencies and damping, attached to a foundation with finite stiffness or mass. Griffin et al. [30,31,32] solved dynamic responses of frictionally damped turbine blades. Wagner and Griffin [33,34] analyzed the harmonic response of grouped blade and flexible disk systems.

To improve the dynamic behavior of a rotating shroud blade disk, the blades are shrouded and grouped together frequently. The dynamic characteristics of the grouped blades are of considerable importance in turbomachinery designs. To analyze the blade group effect on the dynamic behavior of a turbodisk, periodically grouped blades are assumed. For simplicity, the tapered pretwisted beams are used to approximate the blades. In this study, the GDQM is employed to formulate the corresponding eigenvalue problems in matrix form. The Chebyshev-Gauss-Lobatto point distribution on each blade is employed. The integrity and computational efficiency of the GDQM in this problem will be demonstrated through a series of case studies. The effect of the number of sample points on the numerical results is studied. Numerical results solved from different boundary approaches of the GDQM are also compared and discussed.

Generalized Differential Quadrature Method (GDQM)

The basic concept of the differential quadrature method is that the derivative of a function at a given point can be approximated as a weighted linear sum of the functional values at all of the sample points in the domain of that variable. Using this approximation, the differential equation is then reduced into a set of algebraic equations. The number of equations is dependent upon the selected number of the sample points. As for any polynomial approach, the accuracy of the solution using in this method may be improved by increasing the number of sample points. Possible oscillations in numerical results arising from higher-order polynomials can be avoided by using numerical interpolation methods.

For a function $f(r)$, GDQM approximation for the m th order derivative at the i th sample point is given by

¹To whom correspondence should be addressed.

Contributed by the International Gas Turbine Institute (IGTI) of THE AMERICAN SOCIETY OF MECHANICAL ENGINEERS for publication in the ASME JOURNAL OF ENGINEERING FOR GAS TURBINES AND POWER. Paper presented at the International Gas Turbine and Aeroengine Congress and Exhibition, New Orleans, LA, June 4–7, 2001; Paper 01-GT-273. Manuscript received by IGTI, December 2000, final revision, March 2001. Associate Editor: R. Natole.

$$\frac{d^m}{dx^m} \begin{Bmatrix} f(r_1) \\ f(r_2) \\ \vdots \\ f(r_N) \end{Bmatrix} \cong [D_{ij}^{(m)}] \begin{Bmatrix} f(r_1) \\ f(r_2) \\ \vdots \\ f(r_N) \end{Bmatrix} \quad \text{for } i, j = 1, 2, \dots, N \quad (1)$$

in which $f(r_i)$ is the functional value at the sample point r_i , and $D_{ij}^{(m)}$ are the weighting coefficients of m th order differentiation attached to these functional values.

To overcome the numerical ill conditions in determining the weighting coefficients $D_{ij}^{(m)}$, a Lagrangian interpolation polynomial was introduced by Quan et al. [4,5] and Shu and Richards [6], which is

$$f(r) = \frac{M(r)}{(r-r_i)M_1(r_i)} \quad \text{for } i = 1, 2, \dots, N \quad (2)$$

where

$$M(r) = \prod_{j=1}^N (r-r_j),$$

$$M_1(r_i) = \prod_{j=1, j \neq i}^N (r_i-r_j) \quad \text{for } i = 1, 2, \dots, N.$$

Substituting Eq. (2) into Eq. (1) leads to

$$D_{ij}^{(1)} = \frac{M_1(r_i)}{(r_i-r_j)M_1(r_j)} \quad \text{for } i, j = 1, 2, \dots, N \text{ and } i \neq j \quad (3)$$

and

$$D_{ii}^{(1)} = - \sum_{j=1, j \neq i}^N D_{ij}^{(1)} \quad \text{for } i = 1, 2, \dots, N. \quad (4)$$

Once the sample points, i.e., r_i for $i = 1, 2, \dots, N$, are selected, the coefficients of the weighting matrix can be obtained from Eqs. (3) and (4). For the second or the higher order derivatives, the weighting coefficients can be obtained by using the following recurrence relation:

$$D_{ij}^{(m)} = m \left(D_{ii}^{(1)} - \frac{1}{r_i-r_j} \right) D_{ij}^{(m-1)} \quad \text{for } i, j = 1, 2, \dots, N \text{ and } i \neq j \quad (5)$$

and

$$D_{ii}^{(m)} = - \sum_{j=1, j \neq i}^N D_{ij}^{(m)} \quad \text{for } i = 1, 2, \dots, N. \quad (6)$$

It should be emphasized that the number of the test functions must be greater than the highest order of derivative in the governing equations, i.e., $N > m$.

Formulation of the Eigenvalue Problem

The periodic shrouded blade structure as shown in Fig. 1 consists of a rigid hub and a cyclic assembly of N_G grouped blades. In each blade group, the blade is coupled with the adjacent one through a shroud. A massless spring k is assumed to model the function of this shroud. Every blade is coupled by a spring k to the adjacent one. In this paper, it is assumed that the cross section of the blade is symmetric about two principal axes and only the flexural bending is able to occur. The kinetic energy of the s th blade, due to the lateral bending vibration [35,36], is

$$T_s^e = \frac{1}{2} \int_0^L \rho A \left[\left(\frac{\partial u_s}{\partial t} \right)^2 + \left(\frac{\partial v_s}{\partial t} \right)^2 + (\Omega v_s)^2 \right] dr. \quad (7)$$

Consider the cross-sectional area of the tapered pretwist blade at position r to be

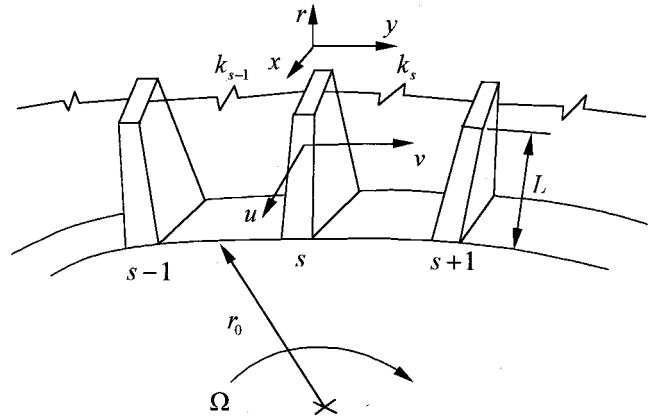


Fig. 1 Geometry of the grouped turbo blade system

$$A(r) = b_0 t_0 \left(1 - \alpha \frac{r}{L} \right) \left(1 - \beta \frac{r}{L} \right) \quad (8)$$

where ρ is the density of the blade, b_0 and t_0 denote, respectively, the breadth and thickness at the root of blade, as shown in Fig. 2, and

$$\alpha = \frac{b_0 - b_1}{b_0}; \quad \beta = \frac{t_0 - t_1}{t_0} \quad (9)$$

where b_1 and t_1 denote, respectively, the breadth and thickness at the blade tip. The strain energy of the s th blade is

$$U_s^e = \frac{1}{2} \int_0^L E \left[I_{yy} \left(\frac{\partial u_s}{\partial r} \right)^2 + 2I_{xy} \left(\frac{\partial u_s}{\partial r} \right) \left(\frac{\partial v_s}{\partial r} \right) + I_{xx} \left(\frac{\partial v_s}{\partial r} \right)^2 \right] dr + \frac{1}{2} \int_0^L \int_r^L \rho A \Omega^2 (r+r_0) dr \left[\left(\frac{\partial u_s}{\partial r} \right)^2 + \left(\frac{\partial v_s}{\partial r} \right)^2 \right] dr. \quad (10)$$

In this equation, r_0 is the radius of the hub, Ω is the rotational speed, I_{xx} , I_{yy} , and I_{xy} are the moments of area. Consider the tapered blade to be pretwisted with a uniform twist angle θ and then the moments of area at the position r can be derived as

$$I_{xx} = I_{XX} \cos^2 \left(\frac{r}{L} \theta \right) + I_{YY} \sin^2 \left(\frac{r}{L} \theta \right) \quad (11)$$

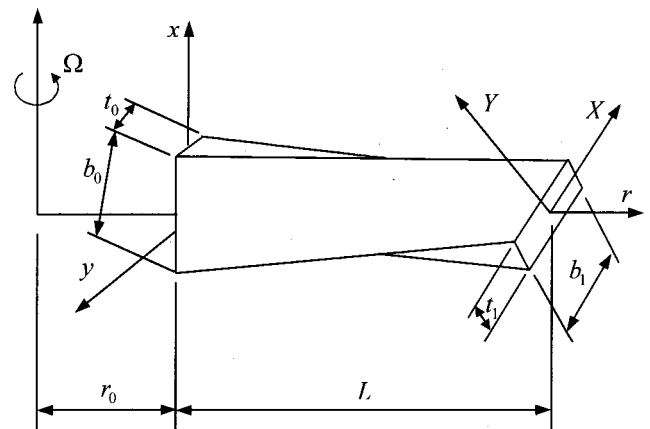


Fig. 2 Geometry of the pretwisted taper beam

$$I_{yy} = I_{XX} \sin^2\left(\frac{r}{L}\theta\right) + I_{YY} \cos^2\left(\frac{r}{L}\theta\right) \quad (12)$$

$$I_{xy} = (I_{YY} - I_{XX}) \sin\left(\frac{r}{L}\theta\right) \cos\left(\frac{r}{L}\theta\right) \quad (13)$$

where L is the length of the tapered blade.

$$I_{XX} = \frac{b_0 t_0^3}{12} \left(1 - \alpha \frac{r}{L}\right) \left(1 - \beta \frac{r}{L}\right)^3 \quad (14)$$

$$I_{YY} = \frac{b_0^3 t_0}{12} \left(1 - \alpha \frac{r}{L}\right)^3 \left(1 - \beta \frac{r}{L}\right) \quad (15)$$

The total kinetic and strain energies of N_G blade disk are

$$T^e = \sum_{s=1}^{N_G} T_s^e \quad \text{and} \quad U^e = \sum_{s=1}^{N_G} U_s^e. \quad (16)$$

By using the Hamilton principle of motion the equations of motion of the s th blade can be derived as

$$\begin{aligned} E \frac{\partial^2 I_{yy}}{\partial r^2} \frac{\partial^2 u_s}{\partial r^2} + 2E \frac{\partial I_{yy}}{\partial r} \frac{\partial^3 u_s}{\partial r^3} + EI_{yy} \frac{\partial^4 u_s}{\partial r^4} + E \frac{\partial^2 I_{xy}}{\partial r^2} \frac{\partial^2 v_s}{\partial r^2} \\ + 2E \frac{\partial I_{xy}}{\partial r} \frac{\partial^3 v_s}{\partial r^3} + EI_{xy} \frac{\partial^4 v_s}{\partial r^4} - \rho \Omega^2 \frac{\partial}{\partial r} \left[\int_r^L A(r+r_0) dr \right] \frac{\partial u_s}{\partial r} \\ - \rho \Omega^2 \left[\int_r^L A(r+r_0) dr \right] \frac{\partial^2 u_s}{\partial r^2} + \rho A \frac{\partial^2 u_s}{\partial t^2} = 0 \end{aligned} \quad (17)$$

for $s = 1, 2, \dots, N_G$

$$\begin{aligned} E \frac{\partial^2 I_{xx}}{\partial r^2} \frac{\partial^2 v_s}{\partial r^2} + 2E \frac{\partial I_{xx}}{\partial r} \frac{\partial^3 v_s}{\partial r^3} + EI_{xx} \frac{\partial^4 v_s}{\partial r^4} + E \frac{\partial^2 I_{xy}}{\partial r^2} \frac{\partial^2 u_s}{\partial r^2} \\ + 2E \frac{\partial I_{xy}}{\partial r} \frac{\partial^3 u_s}{\partial r^3} + EI_{xy} \frac{\partial^4 u_s}{\partial r^4} - \rho \Omega^2 \frac{\partial}{\partial r} \left[\int_r^L A(r+r_0) dr \right] \frac{\partial v_s}{\partial r} \\ - \rho \Omega^2 A v_s - \rho \Omega^2 \left[\int_r^L A(r+r_0) dr \right] \frac{\partial^2 v_s}{\partial r^2} + \rho A \frac{\partial^2 v_s}{\partial t^2} = 0 \end{aligned} \quad (18)$$

for $s = 1, 2, \dots, N_G$.

The corresponding boundary conditions are

$$u_s(0,t) = 0; \quad v_s(0,t) = 0; \quad \frac{\partial u_s(0,t)}{\partial r} = 0 \quad (19)$$

$$\frac{\partial v_s(0,t)}{\partial r} = 0; \quad \frac{\partial^2 u_s(L,t)}{\partial r^2} = 0; \quad \frac{\partial^2 v_s(L,t)}{\partial r^2} = 0 \quad (20)$$

$$\frac{\partial^3 u_s(L,t)}{\partial r^3} = 0$$

and

$$EI_{xx} \frac{\partial^3 v_s(L,t)}{\partial r^3} + kv_{s-1}(L,t) - 2kv_s(L,t) + kv_{s+1}(L,t) = 0 \quad (21)$$

for $s = 1, 2, \dots, N_G$.

By employing the differential quadrature method (derived in the Appendix), the equations of motion of the grouped blades can be discretized in a dimensionless form as

$$[C_{ij}] \{\bar{W}_s(\bar{r}_j)\} = \bar{\omega}^2 \{\bar{W}_s(\bar{r}_i)\} \quad \text{for } s = 1, 2, \dots, N_G \quad (22)$$

where

$$\begin{Bmatrix} \bar{W}_s(\bar{r}_1) \\ \bar{W}_s(\bar{r}_2) \\ \vdots \\ \bar{W}_s(\bar{r}_N) \\ \bar{W}_s(\bar{r}_{N+1}) \\ \bar{W}_s(\bar{r}_{N+2}) \\ \vdots \\ \bar{W}_s(\bar{r}_{2N}) \end{Bmatrix} = \begin{Bmatrix} \bar{U}_s(\bar{r}_1) \\ \bar{U}_s(\bar{r}_2) \\ \vdots \\ \bar{U}_s(\bar{r}_N) \\ \bar{V}_s(\bar{r}_1) \\ \bar{V}_s(\bar{r}_2) \\ \vdots \\ \bar{V}_s(\bar{r}_N) \end{Bmatrix} \quad \text{for } s = 1, 2, \dots, N_G \quad (23)$$

$$\begin{aligned} C_{ij} = \frac{d^2 \bar{I}_{yy}(\bar{r})}{d\bar{r}^2} \Big|_{\bar{r}=\bar{r}_i} D_{ij}^{(2)} + 2 \frac{d \bar{I}_{yy}(\bar{r})}{d\bar{r}} \Big|_{\bar{r}=\bar{r}_i} D_{ij}^{(3)} + \bar{I}_{yy}(\bar{r}_i) D_{ij}^{(4)} \\ - \bar{\Omega}^2 \left\{ \frac{d}{d\bar{r}} \left[\int_{\bar{r}}^1 \bar{A}(\bar{r})(\bar{r} + \bar{r}_0) d\bar{r} \right] \right\} \Big|_{\bar{r}=\bar{r}_i} D_{ij}^{(1)} - \bar{\Omega}^2 \left[\int_{\bar{r}}^1 \bar{A}(\bar{r})(\bar{r} \right. \\ \left. + \bar{r}_0) d\bar{r} \right] \Big|_{\bar{r}=\bar{r}_i} D_{ij}^{(2)} \quad \text{for } i \\ = 3, 4, \dots, N-2 \end{aligned} \quad (24)$$

and $j = 1, 2, \dots, N$

and

$$\begin{aligned} C_{ij} = \frac{d^2 \bar{I}_{xy}(\bar{r})}{d\bar{r}^2} \Big|_{\bar{r}=\bar{r}_i} D_{i,j-N}^{(2)} + 2 \frac{d \bar{I}_{xy}(\bar{r})}{d\bar{r}} \Big|_{\bar{r}=\bar{r}_i} D_{i,j-N}^{(3)} \\ + \bar{I}_{xy}(\bar{r}_i) D_{i,j-N}^{(4)} \quad \text{for } i \\ = 3, 4, \dots, N-2 \end{aligned} \quad (25)$$

and $j = N+1, N+2, \dots, 2N$

$$\begin{aligned} C_{ij} = \frac{d^2 \bar{I}_{xy}(\bar{r})}{d\bar{r}^2} \Big|_{\bar{r}=\bar{r}_{i-N}} D_{i-N,j}^{(2)} + 2 \frac{d \bar{I}_{xy}(\bar{r})}{d\bar{r}} \Big|_{\bar{r}=\bar{r}_{i-N}} D_{i-N,j}^{(3)} \\ + \bar{I}_{xy}(\bar{r}_{i-N}) D_{i-N,j}^{(4)} \quad \text{for } i = N+3, N+4, \dots, 2N-2 \end{aligned} \quad (26)$$

and $j = 1, 2, \dots, N$

$$\begin{aligned} C_{ij} = \frac{d^2 \bar{I}_{xx}(\bar{r})}{d\bar{r}^2} \Big|_{\bar{r}=\bar{r}_{i-N}} D_{i-N,j-N}^{(2)} + 2 \frac{d \bar{I}_{xx}(\bar{r})}{d\bar{r}} \Big|_{\bar{r}=\bar{r}_{i-N}} D_{i-N,j-N}^{(3)} \\ + \bar{I}_{xx}(\bar{r}_{i-N}) D_{i-N,j-N}^{(4)} - \bar{\Omega}^2 \frac{d}{d\bar{r}} \left[\int_{\bar{r}}^1 \bar{A}(\bar{r})(\bar{r} \right. \\ \left. + \bar{r}_0) d\bar{r} \right] \Big|_{\bar{r}=\bar{r}_{i-N}} D_{i-N,j-N}^{(1)} - \bar{\Omega}^2 \left[\int_{\bar{r}_{i-N}}^1 \bar{A}(\bar{r})(\bar{r} \right. \\ \left. + \bar{r}_0) d\bar{r} \right] D_{i-N,j-N}^{(2)} \quad \text{for } i \\ \neq j, \quad i = N+3, N+4, \dots, \\ 2N-2 \quad \text{and } j = N+1, N+2, \dots, 2N \end{aligned} \quad (27)$$

Table 1 Percentage differences of the calculated lowest natural frequency $\bar{\omega}_1$ with different number of sample points

Methods		Percentage Difference* (%)										
		Number of Sample Points										
		7	8	9	10	11	13	15	16	17	18	20
δ -Interval	$\delta=10^{-2}$	1.82	2.07	2.04	2.04	2.04	2.04	2.04	2.04	2.04	2.05	2.04
Method	$\delta=10^{-4}$	-0.19	0.02	0.00	2.04	2.04	2.04	2.04	0.00	0.00	2.04	0.02
	$\delta=10^{-5}$	5.54	0.00	3.27	5.34	0.59	6.88	8.70	5.60	-24.51	0.31	2.04
	$\delta=10^{-6}$	396.8	291.2	308.6	355.9	364.1	344.4	320.6	429.0	355.1	320.6	322.7
Proposed GDQM		-0.85	0.08	0.00	0.00	0.00	0.00	0.00	0.00	0.00	0.00	0.00

* $\left(\text{Difference}(\%) = \frac{\text{GDQM} - \text{Kuang et al. [40]}}{\text{Kuang et al. [40]}} \times 100\% \right)$

$$C_{ii} = \frac{d^2 \bar{I}_{xx}(\bar{r})}{d\bar{r}} \Big|_{\bar{r}=\bar{r}_{i-N}} D_{i-N,i-N}^{(2)} + 2 \frac{d \bar{I}_{xx}(\bar{r})}{d\bar{r}} \Big|_{\bar{r}=\bar{r}_{i-N}} D_{i-N,i-N}^{(3)} \quad [K]\{\bar{W}_i\} = \bar{\omega}^2 \{\bar{W}_i\} \quad (35)$$

$$+ \bar{I}_{xx}(\bar{r}_{i-N}) D_{i-N,i-N}^{(4)} - \bar{\Omega}^2 \bar{A}(\bar{r}_{i-N}) - \bar{\Omega}^2 \left\{ \frac{d}{d\bar{r}} \left[\int_{\bar{r}}^1 \bar{A}(\bar{r}) (\bar{r} + \bar{r}_0) d\bar{r} \right] \right\} \Big|_{\bar{r}=\bar{r}_{i-N}} D_{i-N,i-N}^{(1)} - \bar{\Omega}^2 \left[\int_{\bar{r}_{i-N}}^1 \bar{A}(\bar{r}) (\bar{r} + \bar{r}_0) d\bar{r} \right] \Big|_{\bar{r}=\bar{r}_{i-N}} D_{i-N,i-N}^{(1)} \quad (28)$$

The boundary conditions of a clamped-free blade at the root can be rearranged into the matrix form as

$$\begin{bmatrix} 1 & 0 & 0 & \dots & 0 & 0 \\ D_{11}^{(1)} & D_{12}^{(1)} & D_{13}^{(1)} & \dots & D_{1,N-1}^{(1)} & D_{1,N}^{(1)} \end{bmatrix} \{\bar{U}_x(\bar{r}_j)\} = \begin{bmatrix} 0 \\ 0 \end{bmatrix} \quad \text{for } j=1,2,\dots,N \quad \text{and } s=1,2,\dots,N_G \quad (29)$$

$$\begin{bmatrix} 1 & 0 & 0 & \dots & 0 & 0 \\ D_{11}^{(1)} & D_{12}^{(1)} & D_{13}^{(1)} & \dots & D_{1,N-1}^{(1)} & D_{1,N}^{(1)} \end{bmatrix} \{\bar{V}_s(\bar{r}_j)\} = \begin{bmatrix} 0 \\ 0 \end{bmatrix} \quad \text{for } j=1,2,\dots,N \quad \text{and } s=1,2,\dots,N_G. \quad (30)$$

The boundary conditions at the free end are

$$\begin{bmatrix} D_{N,1}^{(2)} & D_{N,2}^{(2)} & D_{N,3}^{(2)} & \dots & D_{N,N-1}^{(2)} & D_{N,N}^{(2)} \\ D_{N,1}^{(2)} & D_{N,2}^{(2)} & D_{N,3}^{(2)} & \dots & D_{N,N-1}^{(2)} & D_{N,N}^{(2)} \end{bmatrix} \begin{Bmatrix} \bar{U}_s(\bar{r}_j) \\ \bar{V}_s(\bar{r}_j) \end{Bmatrix} = \begin{bmatrix} 0 \\ 0 \end{bmatrix} \quad \text{for } j=1,2,\dots,N \quad \text{and } s=1,2,\dots,N_G \quad (31)$$

$$[D_{N,1}^{(3)} \ D_{N,2}^{(3)} \ D_{N,3}^{(3)} \ \dots \ D_{N,N-1}^{(3)} \ D_{N,N}^{(3)}] \{\bar{U}_s(\bar{r}_j)\} = 0 \quad \text{for } j=1,2,\dots,N \quad \text{and } s=1,2,\dots,N_G \quad (32)$$

$$[D_{N,1}^{(3)} \ D_{N,2}^{(3)} \ D_{N,3}^{(3)} \ \dots \ D_{N,N-1}^{(3)} \ D_{N,N}^{(3)}] \{\bar{V}_s(\bar{r}_j)\} + [\bar{k}] \{\bar{V}_{s-1}(\bar{r}_N)\} - 2[\bar{k}] \{\bar{V}_s(\bar{r}_N)\} + [\bar{k}] \{\bar{V}_{s+1}(\bar{r}_N)\} = 0 \quad \text{for } j=1,2,\dots,N \quad \text{and } s=1,2,\dots,N_G. \quad (33)$$

From above equations, an eigenvalue problem can be derived as

$$\begin{bmatrix} K_{bb} & K_{bi} \\ K_{ib} & K_{ii} \end{bmatrix} \begin{Bmatrix} \bar{W}_b \\ \bar{W}_i \end{Bmatrix} = \bar{\omega}^2 \begin{bmatrix} 0 & 0 \\ 0 & I \end{bmatrix} \begin{Bmatrix} \bar{W}_b \\ \bar{W}_i \end{Bmatrix} \quad (34)$$

where $\{\bar{W}_b\}$ and $\{\bar{W}_i\}$ are the dimensionless displacements at the boundary and the interior degrees-of-freedom, respectively. Equation (34) can be rearranged into a reduced eigenproblem

with

$$[K] = [K_{ii} - K_{ib} \cdot K_{bb}^{-1} \cdot K_{bi}]. \quad (36)$$

Generally, the matrix $[K_{bb}]$ is not singular.

Choice of the Sample Points

The selection of sample points always played an important role ([37,38]) in the solution accuracy of the DQM. For a structural problem, the most convenient method is to peak up the sample points in an equal space sample point distribution ([39]). However, some very poor accuracy results were obtained by using this equally spaced distribution. An unequally spaced sample point distribution, i.e., Chebyshev-Gauss-Lobatto distribution ([9]), has been used to improve the calculation accuracy. For convenience, the δ -interval method ([10,39]) has been used frequently to deal with the multiple boundary conditions in the beam and the plate problems. However, the selection of the value of δ plays a significant role in the accuracy of the solutions of DQM equations. In this paper, we just give up this δ -interval method and deal with the boundary conditions directly on the boundary points. By using the Chebyshev-Gauss-Lobatto points distribution, the unequally spaced inner points of each blade are distributed as

$$\bar{r}_i = \frac{1}{2} \left[1 - \cos \left(\frac{(i-1)\pi}{N-1} \right) \right] \quad \text{for } i=2,3,\dots,N-1. \quad (37)$$

The boundary points of the clamped-free blades are defined as

$$\bar{r}_1 = 0; \quad \bar{r}_N = 1 \quad (38)$$

where $\bar{r}_i = r_i/L$.

Results and Discussion

A model of the bladed disk with a rigid hub attached to 60 uniform blades is assembled. The shroud ring segments on the blade tips couple the blades. There are six uniform blades in a group. The feasibility of GDQM for the grouped blades was studied first. The effect of the number of sample points on the solution accuracy was studied. The results solved by the GDQM formulation proposed in this paper and those solved by using the δ -interval were also compared. Table 1 lists the percentage differences of the calculated lowest natural frequencies of the stationary grouped blades system with the results solved from the Galerkin method ([40]). The parameters of the blades are: $\bar{r}_0 = 0.5$, $\bar{k} = 0.1$, $\alpha = \beta = 0.0$, $\theta = 0$ deg, and $\bar{\Omega} = 0.0$. Different number of sample points for each blade, i.e., 7, 8, 9, 10, 11, 13, 15, 16, 17, 18, and 20, were selected for accuracy analysis. Results indicated that the lowest natural frequencies calculated by using the proposed GDQM formulation with different sample points all agree very well with the results solved by using Galerkin method. However, the frequencies solved by using the traditional DQM with the δ -interval boundary conditions are dependent upon the se-

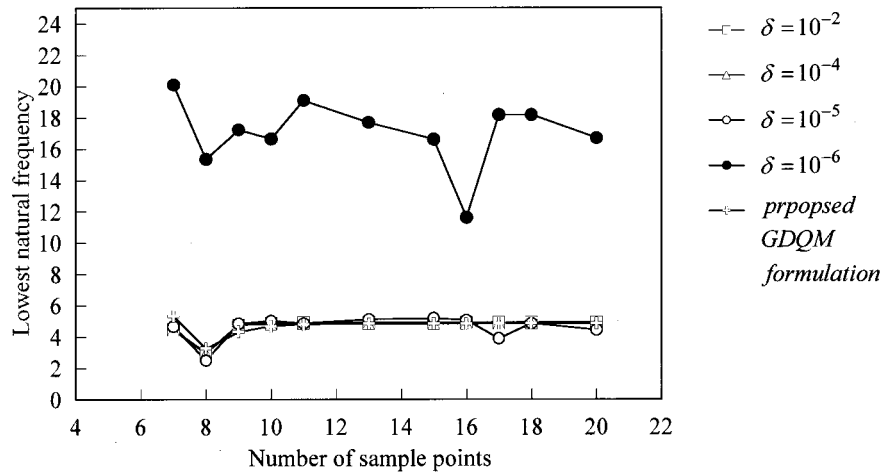


Fig. 3 The calculated lowest natural frequencies of a grouped turbo blade disk with a rotating speed of $\bar{\Omega} = 1.5$

lected value of the δ -interval and the number of sample points. The noticeable differences, i.e., 291% to 429%, were calculated as the δ -interval was not selected properly. A value of $\delta = 10^{-6}$ might introduce the ill condition in computation in this case. However, there is no this kind of difficulty in the proposed GDQM because no δ is required in the formulation. A comparison between the required calculating time for the GDQM and the Galerkin method indicated that a 40 percent computation cost reduction can be achieved for the case with seven sample points.

Figure 3 shows the variation of the calculated lowest natural frequencies of a rotating turbodisk with different number of sampling points. The nondimensional parameters of the rotating disk system are: $\bar{b}_0 = 0.1$, $\bar{r}_0 = 0.02$, $\bar{r}_1 = 0.2$, $\bar{k} = 0.1$, and $\bar{\Omega} = 1.5$. The taper angles α and β are assumed to be 0.5, the total twist angle θ is 45 deg. Similarly, results of this rotating pretwisted taper-blade system are sensitive to the value of the selected δ -interval and the number of sample points. Figure 4 shows the effect of the rotation speed on the calculated lowest natural frequencies of a taper-blade disk with different pretwist angles. The dimension parameters of the blade are $\bar{b}_0 = 0.1$, $\bar{r}_0 = 0.02$, $\bar{r}_1 = 0.2$, $\bar{k} = 0.1$, and $\alpha = \beta = 0.5$. Numerical results indicate that the calculated lowest natural frequencies were increased as the rotation speed is increased. A

higher natural frequency was calculated for the grouped blades system with a larger total pretwist angle. Figure 5 shows the effect of the shroud stiffness \bar{k} on the natural frequencies of the grouped blades system. The parameters of the pretwisted turbodisk system are: $\bar{b}_0 = 0.1$, $\bar{r}_0 = 0.02$, $\bar{r}_1 = 0.2$, $\alpha = \beta = 0.5$, $\theta = 45$ deg, and $\bar{\Omega} = 0.0$. Results show that a strong shroud may increase the natural frequencies of a grouped turboblade system significantly.

Generally, results calculated from the proposed GDQM formulation have the satisfactory accuracy and the solution accuracy is not so sensitive to the number of sample points. In previous cases, nine sample points for each blade can provide a convergent calculated result.

Concluding Remarks

In this work, a GDQM formulation on the eigenvalue problem of a turbodisk with grouped pretwist-tapered blades is provided. Results calculated for the stationary and rotating cases indicate that the GDQM is valid for solving such a complicate engineering problem without using a large number of degrees-of-freedom. In the proposed formulation, the multiple boundary conditions are directly applied on the boundary points and thus there is no need

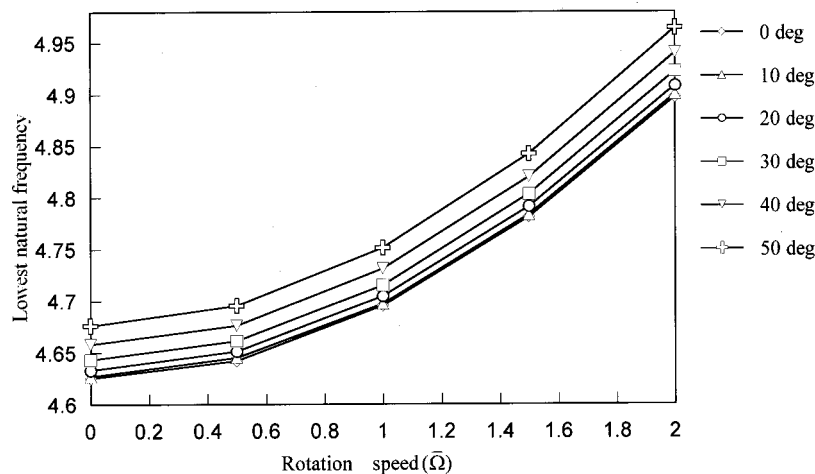


Fig. 4 The lowest natural frequencies ($\bar{\omega}_1$) of the rotating turbo disk with different pretwist angles

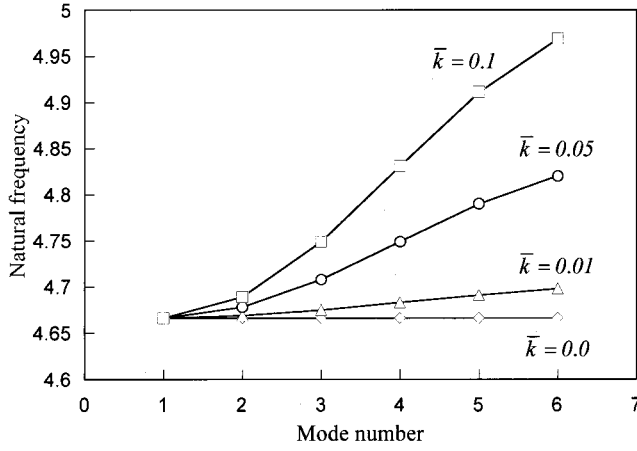


Fig. 5 The calculated natural frequencies of the grouped turbo disk with different shroud stiffness \bar{k}

to select a nearby point as the δ -interval method does. In other words, the accuracy of the calculated results will be independent of the value of δ -interval. This approach is convenient for solving problems governed by the fourth or higher-order differential equations. The accuracy of the calculated natural frequencies can be improved significantly by employing the Chebyshev-Gauss-Lobatto sample point equation. Besides this problem there are numerous other applications those can be modeled by using the GDQM. This method still offers a rich source of interesting the boundary value problems to be solved. The simplicity of the formulation makes it a good candidate for modeling more complicated applications.

Acknowledgments

This material is based upon work supported by the National Science Council of R.O.C. under Grant NSC88-TPC-7-110-010 to the National Sun Yat-Sen University.

Nomenclature

- A = cross-section area of the blade
- \bar{A} = dimensionless cross-section area of the blade
- b_0 = width at the blade root
- b_1 = width at the blade tip
- $D_{ij}^{(m)}$ = weighting coefficient of the m th order differentiation
- E = Young's modulus
- I_{xx}, I_{yy}, I_{xy} = moment of inertia
- k = shroud stiffness
- \bar{k} = dimensionless shroud stiffness
- L = length of the tapered blade
- N = number of sample points
- N_G = total number of blades
- r_0 = outer diameter of disk
- t_0 = thickness at the blade root
- t_1 = thickness at the blade tip
- T_s^e = kinetic energy of the s th blade
- u_s, v_s = elastic deflections of the s th blade
- \bar{U}_s, \bar{V}_s = dimensionless deflections of the s th blade
- U_s^e = strain energy of the s th blade
- α, β = taper ratio
- θ = twist angle
- ρ = density of the blade
- ω = natural frequency
- $\bar{\omega}$ = dimensionless natural frequency

- Ω = rotating speed
- $\bar{\Omega}$ = dimensionless rotating speed

Appendix

Consider the displacements to be of the form

$$u_s(r,t) = U_s(r) \exp(i\omega t) \quad \text{for } s = 1, 2, \dots, N_G \quad (A1)$$

$$v_s(r,t) = V_s(r) \exp(i\omega t) \quad \text{for } s = 1, 2, \dots, N_G. \quad (A2)$$

Equations (17) and (18) can be simplified to

$$\begin{aligned} E \frac{d^2 I_{yy}}{dr^2} \frac{d^2 U_s}{dr^2} + 2E \frac{dI_{yy}}{dr} \frac{d^3 U_s}{dr^3} + EI_{yy} \frac{d^4 U_s}{dr^4} + E \frac{d^2 I_{xy}}{dr^2} \frac{d^2 V_s}{dr^2} \\ + 2E \frac{dI_{xy}}{dr} \frac{d^3 V_s}{dr^3} + EI_{xy} \frac{d^4 V_s}{dr^4} - \rho \Omega^2 \frac{d}{dr} \left[\int_r^L A(r) \right. \\ \left. + r_0 \right] \frac{dU_s}{dr} - \rho \Omega^2 \left[\int_r^L A(r+r_0) dr \right] \frac{d^2 U_s}{dr^2} \\ = \omega^2 \rho A U_s \quad \text{for } s = 1, 2, \dots, N_G \quad (A3) \end{aligned}$$

$$\begin{aligned} E \frac{d^2 I_{xx}}{dr^2} \frac{d^2 V_s}{dr^2} + 2E \frac{dI_{xx}}{dr} \frac{d^3 V_s}{dr^3} + EI_{xx} \frac{d^4 V_s}{dr^4} + E \frac{d^2 I_{xy}}{dr^2} \frac{d^2 U_s}{dr^2} \\ + 2E \frac{dI_{xy}}{dr} \frac{d^3 U_s}{dr^3} + EI_{xy} \frac{d^4 U_s}{dr^4} - \rho \Omega^2 A V_s - \rho \Omega^2 \frac{d}{dr} \left[\int_r^L A(r) \right. \\ \left. + r_0 \right] \frac{dV_s}{dr} - \rho \Omega^2 \left[\int_r^L A(r+r_0) dr \right] \frac{d^2 V_s}{dr^2} \\ = \omega^2 \rho A V_s \quad \text{for } s = 1, 2, \dots, N_G. \quad (A4) \end{aligned}$$

For simplicity, Eqs. (A3) and (A4) can be rewritten in dimensionless forms as

$$\begin{aligned} \frac{d^2 \bar{I}_{yy}(\bar{r})}{d\bar{r}^2} \frac{d^2 \bar{U}_s}{d\bar{r}^2} - 2 \frac{d\bar{I}_{yy}(\bar{r})}{d\bar{r}} \frac{d^3 \bar{U}_s}{d\bar{r}^3} + \bar{I}_{yy}(\bar{r}) \frac{d^4 \bar{U}_s}{d\bar{r}^4} + \frac{d^2 \bar{I}_{xy}(\bar{r})}{d\bar{r}^2} \frac{d^2 \bar{V}_s}{d\bar{r}^2} \\ + 2 \frac{d\bar{I}_{xy}(\bar{r})}{d\bar{r}} \frac{d^3 \bar{V}_s}{d\bar{r}^3} + \bar{I}_{xy}(\bar{r}) \frac{d^4 \bar{V}_s}{d\bar{r}^4} - \bar{\Omega}^2 \frac{d}{d\bar{r}} \left[\int_{\bar{r}}^1 \bar{A}(\bar{r})(\bar{r} \right. \\ \left. + \bar{r}_0) d\bar{r} \right] \frac{d\bar{U}_s}{d\bar{r}} - \bar{\Omega}^2 \left[\int_{\bar{r}}^1 \bar{A}(\bar{r})(\bar{r} + \bar{r}_0) d\bar{r} \right] \frac{d^2 \bar{U}_s}{d\bar{r}^2} \\ = \bar{\omega}^2 \bar{U}_s \quad \text{for } s = 1, 2, \dots, N_G \quad (A5) \end{aligned}$$

$$\begin{aligned} \frac{d^2 \bar{I}_{xx}(\bar{r})}{d\bar{r}^2} \frac{d^2 \bar{V}_s}{d\bar{r}^2} + 2 \frac{d\bar{I}_{xx}(\bar{r})}{d\bar{r}} \frac{d^3 \bar{V}_s}{d\bar{r}^3} + \bar{I}_{xx}(\bar{r}) \frac{d^4 \bar{V}_s}{d\bar{r}^4} + \frac{d^2 \bar{I}_{xy}(\bar{r})}{d\bar{r}^2} \frac{d\bar{U}_s}{d\bar{r}} \\ + 2 \frac{d\bar{I}_{xy}(\bar{r})}{d\bar{r}} \frac{d^3 \bar{U}_s}{d\bar{r}^3} + \bar{I}_{xy}(\bar{r}) \frac{d^4 \bar{U}_s}{d\bar{r}^4} - \bar{\Omega}^2 \bar{A}(\bar{r}) \bar{V}_s \\ - \bar{\Omega}^2 \frac{d}{d\bar{r}} \left[\int_{\bar{r}}^1 \bar{A}(\bar{r})(\bar{r} + \bar{r}_0) d\bar{r} \right] \frac{d\bar{V}_s}{d\bar{r}} - \bar{\Omega}^2 \left[\int_{\bar{r}}^1 \bar{A}(\bar{r})(\bar{r} \right. \\ \left. + \bar{r}_0) d\bar{r} \right] \frac{d^2 \bar{V}_s}{d\bar{r}^2} = \bar{\omega}^2 \bar{V}_s \quad \text{for } s = 1, 2, \dots, N_G \quad (A6) \end{aligned}$$

with

$$\bar{r} = \frac{r}{L}; \quad \bar{r}_0 = \frac{r_0}{L}; \quad \bar{I}_{xx}(\bar{r}) = \frac{I_{xx}}{I_o} \quad \text{and} \quad I_o = \frac{b_0 t_0^3}{12} \quad (A7)$$

$$\bar{I}_{yy}(\bar{r}) = \frac{I_{yy}}{I_o}; \quad \bar{I}_{xy}(\bar{r}) = \frac{I_{xy}}{I_o} \quad (A8)$$

$$\bar{A}(\bar{r}) = \frac{A}{A_0} \text{ and } A_0 = b_0 t_0 \quad (A9)$$

$$\bar{U}_s = \frac{U_s}{L} \text{ and } \bar{V}_s = \frac{V_s}{L} \text{ for } s = 1, 2, \dots, N_G \quad (A10)$$

$$\bar{\omega} = \omega \sqrt{\frac{\rho A_0 L^4}{EI_o}} \text{ and } \bar{\Omega} = \Omega \sqrt{\frac{\rho A_0 L^4}{EI_o}} \quad (A11)$$

The corresponding nondimensional boundary conditions are

$$\bar{U}_s(0) = 0 \text{ and } \bar{V}_s(0) = 0 \text{ for } s = 1, 2, \dots, N_G \quad (A12)$$

$$\frac{d\bar{U}_s(0)}{d\bar{r}} = 0 \text{ and } \frac{d\bar{V}_s(0)}{d\bar{r}} = 0 \text{ for } s = 1, 2, \dots, N_G \quad (A13)$$

$$\frac{d^2\bar{U}_s(1)}{d\bar{r}^2} = 0 \text{ and } \frac{d^2\bar{V}_s(1)}{d\bar{r}^2} = 0 \text{ for } s = 1, 2, \dots, N_G \quad (A14)$$

$$\frac{d^3\bar{U}_s(1)}{d\bar{r}^3} = 0 \text{ for } s = 1, 2, \dots, N_G \quad (A15)$$

and

$$\frac{d^3\bar{V}_s(1)}{d\bar{r}^3} + \bar{k}\bar{V}_{s-1}(1) - 2\bar{k}\bar{V}_s(1) + \bar{k}\bar{V}_{s+1}(1) = 0 \quad (A15')$$

for $s = 1, 2, \dots, N_G$.

The dimensionless shroud stiffness is $\bar{k} = kL^3/EI$. Substituting Eq. (1) into Eqs. (A5)–(A6), the differential equations can be derived as

$$\{C_{ij}\}\{\bar{W}_s(\bar{r}_j)\} = \bar{\omega}^2\{\bar{W}_s(\bar{r}_i)\} \text{ for } s = 1, 2, \dots, N_G \quad (A16)$$

References

- [1] Bellman, R., and Casti, J., 1971, "Differential Quadrature and Long-Term Integration," *J. Math. Anal. Appl.*, **34**, pp. 235–238.
- [2] Bellman, R. E., Kashef, B. G., and Casti, J., 1972, "Differential Quadrature: A Technique for Rapid Solution of Nonlinear Partial Differential Equations," *J. Comput. Phys.*, **10**, pp. 40–52.
- [3] Chen, W., and Zhong, T., 1997, "The Study on the Nonlinear Computations of the DQ and DC Methods," *Numer. Methods Part. Differ. Eqs.*, **13**, pp. 57–75.
- [4] Quan, J. R., and Chang, C. T., 1989, "New Insights in Solving Distributed System Equations by the Quadrature Method—I. Analysis," *Comput. Chem. Eng.*, **13**, pp. 779–788.
- [5] Quan, J. R., and Chang, C. T., 1989b, "New Insights in Solving Distributed System Equations by the Quadrature Method—II. Numerical Experiments," *Comput. Chem. Eng.*, **13**, pp. 1017–1024.
- [6] Shu, C., and Richards, B. E., 1992, "Application of Generalized Differential Quadrature to Solve Two-Dimensional Incompressible Navier-Stokes Equations," *Int. J. Numer. Methods Fluids*, **15**, pp. 791–798.
- [7] Li, H., and Lam, K. Y., 1998, "Frequency Characteristics of a Thin Rotating Cylindrical Shell Using the Generalized Differential Quadrature Method," *Int. J. Mech. Sci.*, **40**(5), pp. 443–459.
- [8] Bert, C. W., Jang, S. K., and Striz, A. G., 1988, "Two New Approximate Methods for Analyzing Free Vibration of Structural Components," *Int. J. Numer. Methods Eng.*, **28**, pp. 561–577.
- [9] Bert, C. W., and Malik, M., 1996, "Free Vibration Analysis of Tapered Rectangular Plates by Differential Quadrature Method: A Semi-analytical Approach," *J. Sound Vib.*, **190**(1), pp. 41–63.
- [10] Bert, C. W., Wang, X., and Striz, A. G., 1993, "Differential Quadrature for Static and Free Vibration Analysis of Anisotropic Plates," *Int. J. Solids Struct.*, **30**, pp. 1737–1744.
- [11] Bert, C. W., Wang, X., and Striz, A. G., 1994, "Static and Free Vibration Analysis of Beams and Plates by Differential Quadrature Method," *Acta Mech.*, **102**, pp. 11–24.
- [12] Bert, C. W., Wang, X., and Striz, A. G., 1994, "Convergence of the DQ Method in the Analysis of Anisotropic Plates," *J. Sound Vib.*, **170**, pp. 140–144.
- [13] Han, J. B., and Liew, K. M., 1999, "Axisymmetric Free Vibration of Thick Annular Plates," *Int. J. Mech. Sci.*, **41**, pp. 1089–1109.
- [14] Malik, M., and Bert, C. W., 1996, "Implementing Multiple Boundary Conditions in the DQ Solution of Higher-Order PDE Application to Free Vibration of Plates," *Int. J. Numer. Methods Eng.*, **39**, pp. 1237–1258.
- [15] Striz, A. G., Chen, W., and Bert, C. W., 1994, "Static Analysis of Structures by the Quadrature Element Method (QEM)," *Int. J. Solids Struct.*, **31**, pp. 2807–2818.
- [16] Du, H., Liew, K. M., and Lim, M. K., 1996, "Generalized Differential Quadrature Method for Buckling Analysis," *J. Eng. Mech.*, **122**(2), pp. 95–100.
- [17] Rao, J. S., 1972, "Flexural Vibration of Pretwisted Tapered Cantilever Blades," *J. Eng. Ind.*, **94**, No. 1, pp. 343–346.
- [18] Rao, J. S., 1977, "Vibration of Rotating, Pretwisted and Tapered Blades," *Mech. Mach. Theory*, **12**, pp. 331–337.
- [19] Hodges, D. H., Chung, Y. Y., and Shang, X. Y., 1994, "Discrete Transfer Matrix Method for Non-uniform rotating beams," *J. Sound Vib.*, **169**, pp. 276–283.
- [20] Abrate, S., 1995, "Vibrations of Non-uniform Rods and Beams," *J. Sound Vib.*, **185**(4), pp. 703–716.
- [21] Dawson, B., 1968, "Coupled Bending-Bending Vibrations of Pre-twisted Cantilever Blading Treated by Rayleigh-Ritz Energy Method," *J. Mech. Eng. Sci.*, **10**, pp. 381–386.
- [22] Dawson, B., and Carneige, W., 1969, "Model Curves of Pretwisted Beams of Rectangular Cross-Section," *J. Mech. Eng. Sci.*, **11**, pp. 1–13.
- [23] Gupa, R. S., and Rao, S. S., 1978, "Finite Element Eigenvalue Analysis of Tapered and Twisted Timoshenko Beams," *J. Sound Vib.*, **56**(2), pp. 187–200.
- [24] Swaminathan, M., and Rao, J. S., 1977, "Vibrations of Rotating, Pretwisted and Tapered Blades," *Mech. Mach. Theory*, **12**, pp. 331–337.
- [25] Subrahmanyam, K. B., Kulkarni, S. V., and Rao, J. S., 1981, "Coupled Bending-Bending Vibrations of Pre-twisted Cantilever Blading Allowing for Shear Deflection and Rotary Inertia by the Reissner Method," *Int. J. Mech. Sci.*, **23**(9), pp. 517–530.
- [26] Subrahmanyam, K. B., and Rao, J. S., 1982, "Coupled Bending-Bending Vibrations of Pretwisted Tapered Cantilever Beams Treated by the Reissner Method," *J. Sound Vib.*, **82**(4), pp. 577–592.
- [27] Chen, W. R., and Keer, L. M., 1993, "Transverse Vibrations of a Rotating Twisted Timoshenko Beam Under Axial Loading," *ASME J. Vibr. Acoust.*, **115**, pp. 285–294.
- [28] Storti, D., and Aboelnaga, Y., 1987, "Bending Vibrations of a Class of Rotating Beams With Hypergeometric Solutions," *ASME J. Appl. Mech.*, **54**, pp. 311–314.
- [29] Wagner, J. T., 1967, "Coupling of Turbomachine Blade Vibrations Through the Rotor," *ASME J. Eng. Gas Turbines Power*, **89**, pp. 502–512.
- [30] Griffin, J. H., 1980, "Friction Damping of Resonant Stresses in Gas Turbine Engine Airfoils," *ASME J. Eng. Gas Turbines Power*, **102**, pp. 329–333.
- [31] Griffin, J. H., and Sinha, A., 1985, "The Interaction Between Mistuning and Friction in the Forced Response of Bladed Disk Assemblies," *ASME J. Eng. Gas Turbines Power*, **107**, pp. 107–205.
- [32] Sinha, A., and Griffin, J. H., 1984, "Effects of Static Friction on the Forced Response of Frictionally Damped Turbine Blades," *ASME J. Eng. Gas Turbines Power*, **106**, pp. 65–69.
- [33] Wagner, L. F., and Griffin, J. H., 1996, "Forced Harmonic Response of Grouped Blade Systems: Part I—Discrete Theory," *ASME J. Eng. Gas Turbines Power*, **118**, pp. 130–136.
- [34] Wagner, L. F., and Griffin, J. H., 1996, "Forced Harmonic Response of Grouped Blade Systems: Part II—Application," *ASME J. Eng. Gas Turbines Power*, **118**, pp. 137–145.
- [35] Anderson, G. L., 1975, "On the Extensional and Flexural Vibration of Rotating Bars," *Int. J. Non-Linear Mech.*, **10**, pp. 223–236.
- [36] Young, T. H., 1991, "Dynamic Response of a Pretwisted, Tapered Beam With Non-constant Rotating Speed," *J. Sound Vib.*, **167**(3), pp. 529–539.
- [37] Sherbourne, A. N., and Pandey, M. D., 1991, "Differential Quadrature Method in the Buckling Analysis of Beams and Composite Plates," *Comput. Struct.*, **40**, pp. 903–913.
- [38] Shu, C., and Du, H., 1997, "A Generalized Approach for Implementing General Boundary Conditions in the GDQ Free Vibration Analysis of Plates," *Int. J. Solids Struct.*, **34**(7), pp. 837–846.
- [39] Jang, S. K., Bert, C. W., and Striz, A. G., 1989, "Application of Differential Quadrature to Static Analysis of Structural Components," *Int. J. Numer. Methods Eng.*, **28**, pp. 561–577.
- [40] Kuang, J. H., and Huang, B. W., 2000, "Mode Localization in a Grouped Bladed Disk," *ASME Paper No. 00-GT-369*.

T. Berruti
S. Filippi
M. M. Gola

Dip. Ing. Meccanica,
Politecnico di Torino,
Corso Duca degli Abruzzi 24,
10129 Torino, Italy

S. Salvano
FIAT AVIO,
Via Nizza 312,
10127 Torino, Italy

Friction Damping of Interlocked Vane Segments: Experimental Results

Experimental methods and results of the stator bladed segment of an aircraft engine are presented. Investigation concerns the energy dissipation due to friction between contact surfaces of adjacent segments. The influence of the force normal to the contact surface (due to interference between adjacent segments) on friction damping is shown. Moreover, the experiments show the nature of friction at contact surfaces. The parameters of a contact model to be used in a numerical analysis have been identified from the experiments. [DOI: 10.1115/1.1494097]

Introduction

The present paper deals with a six-vanes segment of a low-pressure stage of an aircraft engine ([1]). As shown in Fig. 1 the vanes are grouped in segments and they are connected at their ends by the “outer platform” (external stator radius) and by the “inner platform” (internal stator radius). The outer platform of each segment is fixed to the engine casing, the inner platform is in contact (on surfaces normal to the turbine axis) with the inner platforms of the two neighboring segments. A normal force is applied on these contact surfaces by means of an elastic pre-deformation of the segment (pre-twist). During operation the relative slipping of the surfaces generates the friction that is used to reduce the vibrations. Slipping takes place mainly in the hoop direction. In the present paper the experimental tests performed on an ad hoc designed ([1]) experimental setup will be illustrated.

The performed measurements have two main scopes:

- to investigate the quantity of energy dissipated for friction and its relation with the force normal to the contact surface;
- to identify the contact behavior in order to find out an empirical contact model to be used in the numerical analysis with HBM ([2]) (harmonic balance method).

Interpretation and treatment of experimental data to find out an empirical contact model has been attempted in two parallel ways: determination of the physical parameters of the contact model (contact stiffness and friction coefficient) and direct determination of the contact quantities required by a numerical model solved by HBM.

Experimental Setup

The test rig (Fig. 2), designed to hold the segment and transducers, has been deeply described in paper ([1]). The outer platform of the segment is clamped to an aluminum frame, the inner platform is in contact through the two contact surfaces with two instrumented supports mounted on a pivoting cradle. The rotation of the cradle induces a twist to the segment and, as a consequence, a normal force on the contact surfaces.

As in normal operating condition, the segments are twisted and a normal force is applied on the contact surfaces of neighboring segments. The sum of displacements of the two ends of the lower

platform after twisting is defined “interlocking” ([1]). Different “interlocking” values correspond to different normal contact surface values.

Contact Force. The contact forces are determined by the two supports instrumented with strain gages. A picture of a support is shown in Fig. 3. As described in ([1]) the support acts as a bending transducer (SGF strain gages) to detect the force normal to the contact (z or engine axial direction) and as a traction transducer (SGT strain gages) to detect the force tangential to the contact surface (x or engine circumferential direction). The contact surface of the support has curvature radius 2.5 mm and length 30 mm. The segment contact surface is plane. Technical data of these transducers obtained after static calibration ([1]) are listed in Table 1.

Contact Displacements. Instruments and methods of measurement of relative displacement of the contact surfaces have been changed respect to the previous set up ([1]) (mainly by elimination of the laser device). In the new set up (Fig. 4) two accelerometers (B and B') are glued on the platform near the contact surfaces, and two accelerometers (A and A') are glued on the supports. The displacements are obtained by integrating twice the signals from accelerometers. The relative displacement of the contact surfaces is obtained as difference of integrated signals from $A-B$ and $A'-B'$.

The accelerometer have been accurately calibrated: the pairs of accelerometers A and B and A' and B' mounted back to back are mounted as close as possible on a shaker head. A range of frequency up to 3000 Hz has been explored. After this calibration the error on the relative displacements ($A-B$ and $A'-B'$) has been estimated ≤ 2 percent of the absolute displacements (B and B').

Dynamic Force Calibration. The measurement of the tangential force by the strain gages is influenced by the dynamic of the system. An example is shown in Fig. 5, a normal contact force is imposed at 24 N, the segment is excited at the first resonance frequency (212.5 Hz). The tangential force determined by the strain gages through the static calibration is the light curve of Fig. 5. Components with frequency higher than excitation are due to the nonlinear behavior of the contact. A correction has been applied to keep into account this dynamic effects as it will be shown.

With

A : coeff. from static calibration

$e(t)$: signal from SGT

$f(t)_{\text{static}}$: contact tangential force

$$f(t)_{\text{static}} = A \cdot e(t) \quad F_{\text{static}}(\omega) = \text{FFT}(f(t)_{\text{static}})$$

Contributed by the International Gas Turbine Institute (IGTI) of THE AMERICAN SOCIETY OF MECHANICAL ENGINEERS for publication in the ASME JOURNAL OF ENGINEERING FOR GAS TURBINES AND POWER. Paper presented at the International Gas Turbine and Aeroengine Congress and Exhibition, New Orleans, LA, June 4–7, 2001; Paper 01-GT-432. Manuscript received by IGTI, Dec. 2000, final revision, Mar. 2001. Associate Editor: R. Natole.

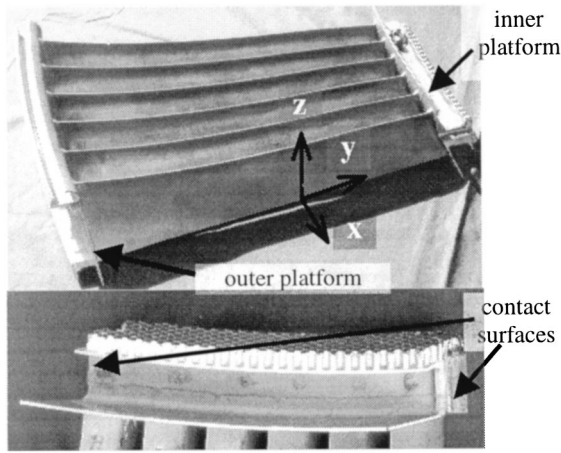


Fig. 1 Stator segment contact surfaces

$$F(\omega)_{\text{dyn}} = F_{\text{static}}(\omega) \cdot \left[1 - \left(\frac{\omega}{\omega_n} \right)^2 + 2i\zeta \left(\frac{\omega}{\omega_n} \right) \right] \quad \text{if } \left(\frac{\omega}{\omega_n} \right) \leq 1$$

$$F(\omega)_{\text{dyn}} = 0 \quad \text{if } \left(\frac{\omega}{\omega_n} \right) > 1$$

$$f(t)_{\text{dyn}} = \text{AFFT}(F(\omega)_{\text{dyn}})$$

where $\omega_n = 1575$ Hz: resonance frequency of the support (x direction) ([1]), the value of damping ratio of the support has been assumed $\xi = 10^{-3}$.

The force obtained after this dynamic calibration is the thick line in Fig. 5: Self-excited components at high frequency are eliminated.

Plan of Experiments

A sketch of the experimental set up is shown in Fig. 6.

The dynamic tests have been performed for different values of contact normal force and excitation force.

Contact normal force. At design, the value of the contact force deriving from a given interlocking is calculated numerically (Nasran finite element method model of the segment). In the experi-

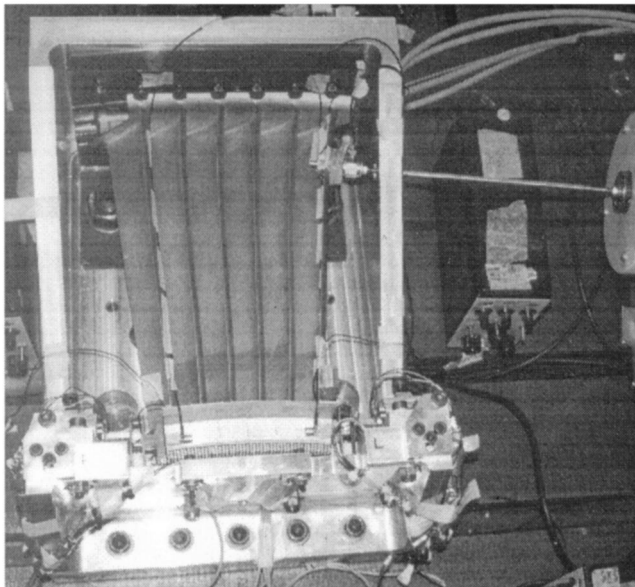


Fig. 2 Test rig image

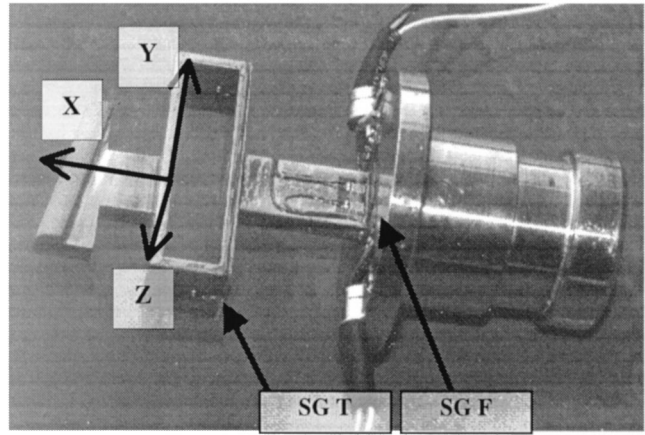


Fig. 3 Picture of a support instrumented with strain gages

ments, the desired contact normal force (equal for both the supports) is applied by rotating the cradle carrying the supports and measured through the strain gages SGF. The cradle is locked when the desired contact normal force is obtained.

The tested values of contact normal force correspond to interlocking values that can be imposed to the segment on the engine. The nominal interlocking normally used for the engine in service nom. = 0.4 mm corresponds to a contact force of 97 N. Interlocking values lower than nom./4 have not been tested since they are not to be used, mainly to be well away from loss of contact and consequently 'chattering' of the contact surfaces.

Excitation force. The segment is excited by a shaker through a stinger as shown in Fig. 6. Excitation near the fixed platform has

Table 1 Technical data of supports (force transducers)

Support L			
Traction transducer			
Traction load		Bending load	
Sensitivity	Linearity	Sensitivity	Linearity
5.16 mV/N	0.03%	0.18	2%
Bending transducer			
Bending load		Traction load	
Sensitivity	Linearity	Sensitivity	Linearity
13.16 mV/N	0.09%	0.10	2%
Support R			
Traction transducer			
Traction load		Bending load	
Sensitivity	Linearity	Sensitivity	Linearity
5.15 mV/N	0.05%	0.18	3%
Bending transducer			
Bending load		Traction load	
Sensitivity	Linearity	Sensitivity	Linearity
12.87 mV/N	0.07%	0.01	31%

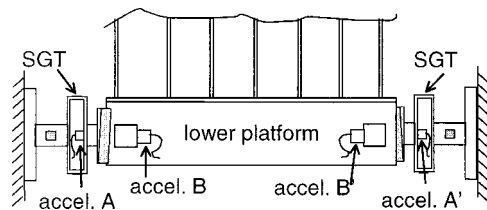


Fig. 4 Position of the accelerometers near the contact surfaces

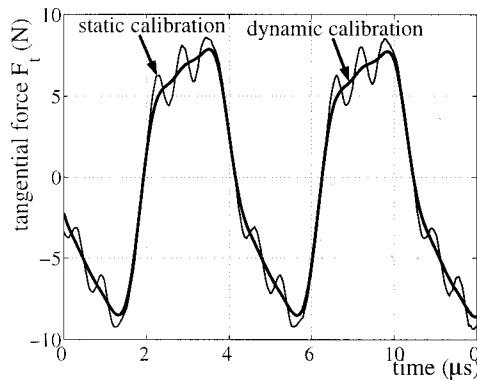


Fig. 5 Tangential contact force (determined through static and dynamic calibration)

been chosen in order to keep the excitation force almost constant during the test. Excitation ‘force drop out’ would have happened with the shaker positioned near the lower platform due to the greatest displacement of the excitation point. As shown in Fig. 6 an accelerometer (E) is placed aligned with the load cell on the other side of the vane, in order to detect (after integration) the displacement in the excitation point. The different values of exciting force imposed for different interlocking configurations are listed in Table 2.

Experimental Procedure. An interlocking value is imposed. The desired excitation force is applied (measured by the load cell) at 100 Hz. A ‘sweep’ is performed between 100 and 300 Hz in order to identify the position of the first resonance peak (displacement mainly in hoop direction) ([1]).

Different numbers of frequency values (10 to 20, equally spaced) depending on the peak form are selected around the resonant peak.

The system is excited by a sinusoidal signal for each frequency value, the signals from the transducers (strain gages, accelerometers, and load cell) are acquired after a time long enough for the transient to expire (3 s). It has been verified that the amplitude of

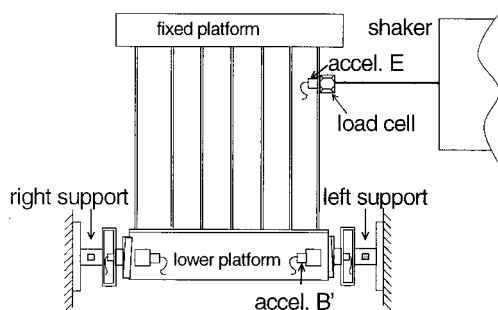


Fig. 6 Experimental setup

Table 2 Plan of experiments: excitation force values (sinusoidal force amplitude) for different interlocking configurations

Interlocking values			
nom./4	nom./2	nom.	2-nom.
20 N	20 N	20 N	20 N
40 N	40 N	40 N	40 N
60 N	60 N	60 N	-
80 N	80 N	80 N	80 N

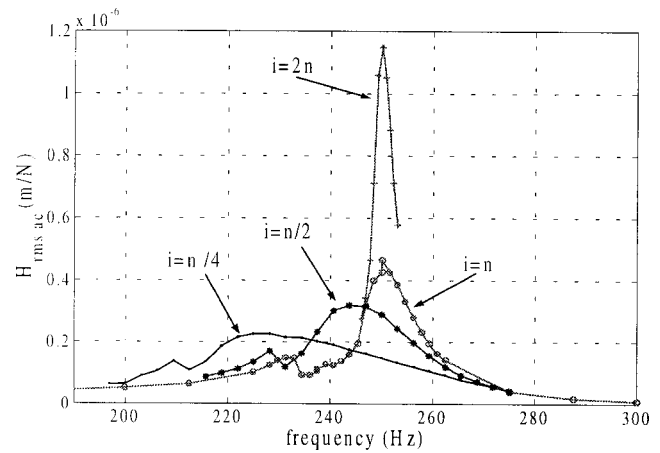


Fig. 7 Receptance of the system for different interlocking values. Excitation force 80 N_{pk}

the excitation force for the frequency range in which measurements are performed varies of about 5 percent. The acquisition system is DIFA DSA220.

For each given interlocking value the procedure is repeated for the excitation values of Table 2.

Repeatability of the measurements has been checked by running a further full set of acquisitions at nominal interlocking (nom.), after having disassembled the experimental device.

Frequency Sweep: System Receptance. For the different interlocking values and fixed excitation force (80 N_{pk}) the receptance of the system obtained from signals of the accelerometer B' and the load cell (Fig. 6) are shown in Fig. 7. As it could be expected, by increasing the interlocking value the segment is more constrained (higher friction force is applied) as a consequence the first resonance frequency increases. Moreover, it can be immediately seen that the receptance drastically decreases with the decrease of interlocking value. This damping is due to the friction that is generated at the contact surfaces.

Integration of measured contact tangential force versus relative displacement gives the energy dissipated for friction.

Friction Dissipated Energy. In Fig. 8 the tangential contact force is plotted versus the relative displacement for right (light curves) and left (dark curves) support, in resonance condition for the listed interlocking and excitation force values. The area of the cycles is the dissipated energy for friction.

At fixed interlocking value (columns of Fig 8) the slipping displacement increases with increment of excitation. For the case of excitation force equal to 80 N_{pk} these results are summarized in Fig. 9. The total dissipated energy has been calculated as the sum of areas of hysteresis cycle of support right and support left. The input energy has been calculated from the integration of force (from load cell of Fig. 6) versus displacement of the point of force application. The ratio of dissipated energy and total energy is plotted in Fig. 9 versus the excitation frequency for the different interlocking values. At resonance condition the ratio is at maximum for the lowest interlocking value (nom./4), as it can be noticed, in fact, in this case, at the resonant condition almost 80 percent of the input energy is dissipated by friction.

Friction Model

The aim is to obtain an empirical contact model from these experimental data to be used for the numerical calculation of segments with friction contacts.

The definition of an empirical contact model is made difficult by the fact that the contact behavior changes with different interlocking conditions. In fact, as it is shown in Figs. 8, 10, and 11,

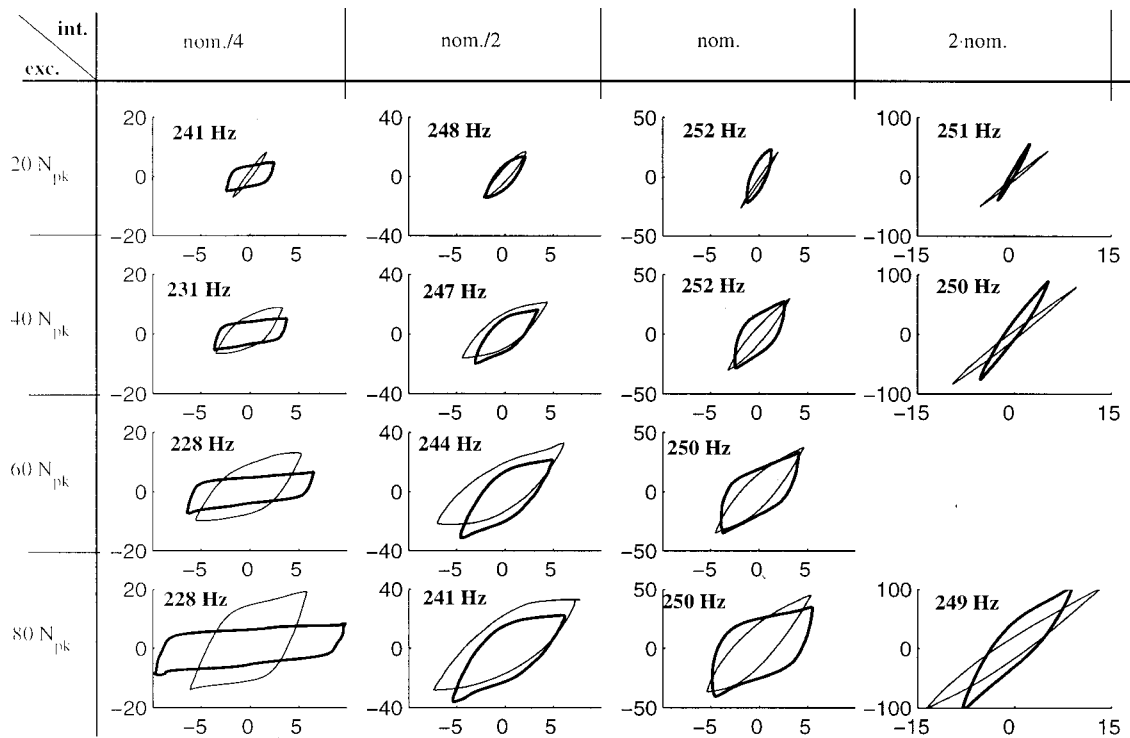


Fig. 8 Tangential contact force (N) (hoop direction) versus relative displacement (μm) for different interlocking and excitation values, resonance condition. Light line: right support, dark line: left support.

the shape of the cycles changes from almost Coulomb law of gross slip ($i = n/4$) to a behavior of partial slip or microslip (interl. = $2 \cdot \text{nom.}$) in the same range of displacement amplitude ($\approx 10 \mu m$) ([3–5]). Moreover, for the same interlocking value, the contact behavior can change since the contact is not a point contact but a linear contact (the experimental setup reproduces the geometry “as designed” for the real case): Differences of position of contact of the support surface relative to the segment surface can change the contact behavior. This is confirmed by the differences of friction behavior between the left and right support for the same interlocking value. The approach to the modeling of the contact goes along two different lines of thought:

- determination of the physical parameters (contact stiffness and friction coefficient), in order to allow reconstruction of

the cycle at known displacements and interlocking force. Fourier representation for HBM will numerically follow.

- direct determination of the factors for the HBM force/displacement ellipse at the contact, as a function of displacement and interlocking force.

Determination of Contact Parameters

Contact Stiffness. The “contact stiffness” is defined as the tangent to the friction cycle when the relative motion inverts direction as shown in Fig. 12. The contact stiffness can be determined for each cycles of Fig. 8 from the measurement of contact tangential force through SGT strain gages and from the measurement of relative displacement through accelerometers.

The stiffness values are obtained by interpolation of the portions (linear) of cycle where inversion of motions takes place. The

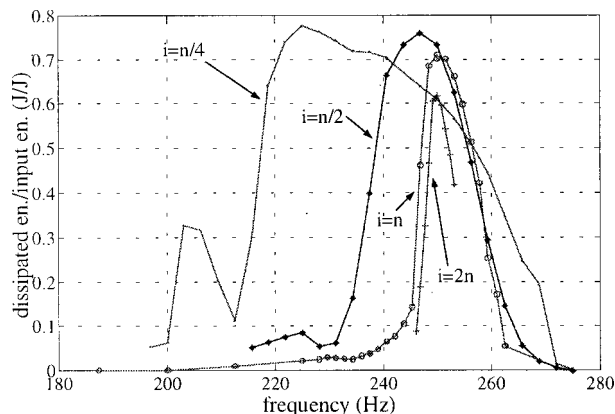


Fig. 9 Ratio of dissipated energy for friction and input energy versus frequency for different interlocking values. Excitation force $80 N_{pk}$.

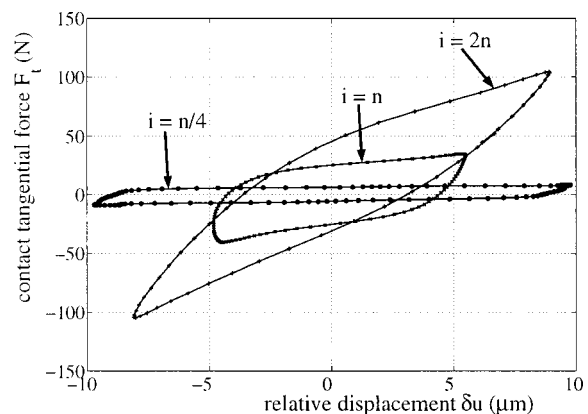


Fig. 10 Hysteresis cycles in resonant condition for different interlocking values. Excitation force $80 N_{pk}$.

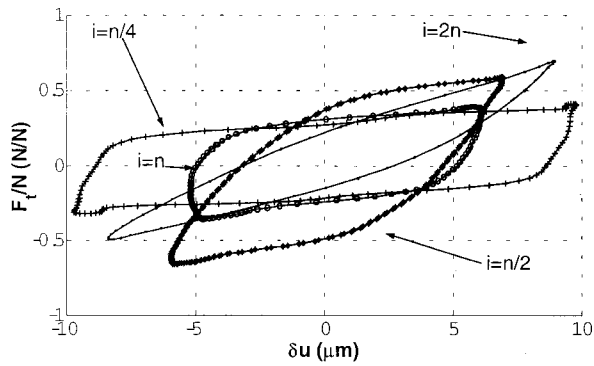


Fig. 11 Ratio of tangential force and normal contact force for different interlocking values. Support left. Resonance condition. Excitation frequency 80 Npk.

values of the contact stiffness for cycles around resonance are listed in Table 3. Considering the possible sources of errors in the measurement of displacement (accelerometers linearity, sensibility variation with frequency, transversal sensibility, and misalignment errors in accelerometers mounting), it has been estimated that, in the worst case, the values of k_c^M (measured contact stiffness) listed in Table 3 are inside the error interval: $0.7 \cdot k_c^M \div 1.6 \cdot k_c^M$.

From the values of Table 3 the following considerations can be drawn:

- the values are of the order of magnitude of $10 \text{ N}/\mu\text{m}$.
- left support shows values of stiffness on average double than right support.
- it is not evident a trend of the contact stiffness with the interlocking, the stiffness for interlocking nom. is higher than for interlocking 2-nom., the repetition of the experiment for interlocking nom. has confirmed this high value of stiffness.

In order to evaluate the meaning of the measured “contact stiff-

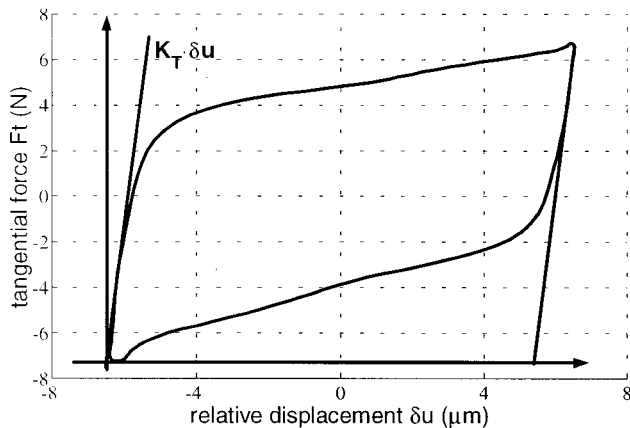


Fig. 12 Contact stiffness

Table 3 k_c^M : measured contact stiffness (N/m) for right and left support. Excitation force 80 Npk.

Interlocking values			
nom./4	nom./2	nom.	2-nom.
f:220÷240Hz	f:230÷250Hz	f:248÷252Hz	f:248÷251Hz
right: $8 \frac{\text{N}}{\mu\text{m}}$	right: $9 \frac{\text{N}}{\mu\text{m}}$	right: $11 \frac{\text{N}}{\mu\text{m}}$	right: $9 \frac{\text{N}}{\mu\text{m}}$
left: $8 \frac{\text{N}}{\mu\text{m}}$	left: $12 \frac{\text{N}}{\mu\text{m}}$	left: $26 \frac{\text{N}}{\mu\text{m}}$	left: $17 \frac{\text{N}}{\mu\text{m}}$

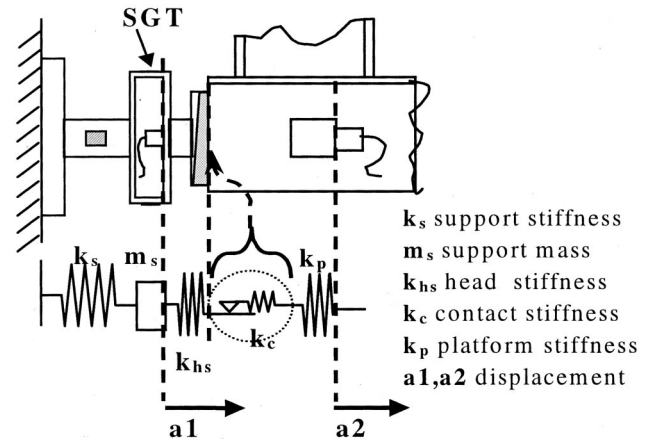


Fig. 13 Model with mass and stiffness in the measurement area

ness” of Table 3 the support and platform around the contact zone has been modeled by means of masses and springs (Fig. 13). This clearly shows that:

- the force determined through the strain gages SGT (after static and dynamic calibration) is the tangential force in the contact since the springs are in series;
- the relative displacement $a1-a2$ is the sum of displacement due to deformation of k_{hs} , displacement due to contact slipping and displacement due to deformation of k_c , assuming that the deformation of k_p is negligible.

The value of $k_{hs} = 100 \text{ N}/\mu\text{m}$ has been calculated from a finite element method (Nastran) of the support. According to the model of Fig. 13, the measured “contact stiffness” is the series of the stiffness k_c and k_{hs} . If only static calibration had been performed, the force determined through SGT would have been different from the contact tangential force because of the mass m_s . Through dynamic calibration the effect of the mass m_s is kept into account (but still neglecting the force components with frequencies greater than ω_n ; see the section Dynamic Force Calibration). The values of measured “contact stiffness” (k_c^M) listed in Table 3 are one order of magnitude smaller than k_{hs} . Therefore it can be assumed that $k_c^M \approx k_c$.

Friction Coefficients. Figure 11 shows the ratio of tangential and normal contact force for different interlocking values, for the same excitation force (80 N_{pk}).

For the cycles with a more bilinear hysteresis shape, the linear parts where gross slip occurs give the value of the friction coefficient as sketched in Fig. 14. These lines of gross slip are not

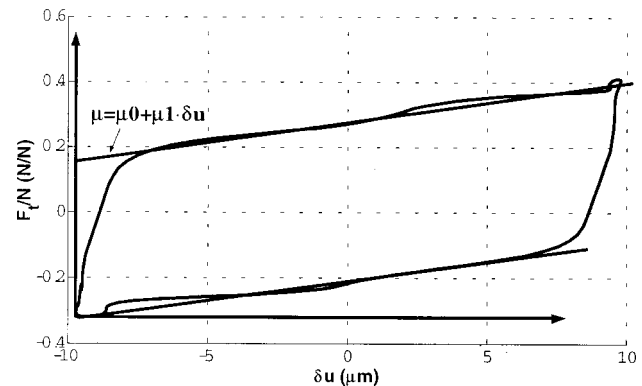


Fig. 14 Linear behavior of gross slip

Table 4 Friction coefficients μ_0 and μ_1 for right and left support. Excitation force 80 Npk.

Right support				
int.	nom./4	nom./2	nom.	nom. bis
freq (Hz)	220÷240	230÷250	248÷252	248÷252
μ_0 (mean)	0.42	0.43	-	0.13
μ_0 (st.dev)	0.05	0.17	-	0.12
μ_1 (mean) (μm^{-1})	0.02	0.01	-	0.03
μ_1 (st.dev) (μm^{-1})	0.01	0.01	-	0.01
Left support				
μ_0 (mean)	0.14	0.34	0.16	0.19
μ_0 (st.dev)	0.05	0.05	0.05	0.05
μ_1 (mean) (μm^{-1})	0.01	0.02	0.02	0.06
μ_1 (st.dev) (μm^{-1})	0.001	0.01	0.01	0.01

horizontal, as it could be expected by a Coulomb friction; instead friction coefficient varies with relative displacement. From this observation the law assumed for the friction coefficient is $\mu = \mu_0 + \mu_1 \cdot \delta u$ (Fig. 14).

For a fixed excitation force (80 N_{pk}) and different interlocking values the values of μ_0 and μ_1 for cycles around resonance have been calculated; the selected cycles are those where portions of gross slip occur. The parameters μ_0 and μ_1 have been calculated both for the portion of cycles with increasing displacement and decreasing displacement. The mean values and standard deviations of μ_0 and μ_1 (on cycles around resonance) obtained for each interlocking condition have been listed in Table 4. For the case interl.=2·nom., μ_0 and μ_1 cannot be calculated since all the cycles show a behavior where only microslip is present (no gross slip) as evident in Fig. 8. From the values of Table 4 the following observations can be drawn:

- the values of coefficients μ_0 and μ_1 show a high scatter; there is no evidence of a trend of these friction parameters with interlocking;
- for the same value of interlocking there is a difference in the mean value of μ_0 for support left and right (see the case of nom./4, right 0.42, left 0.14);
- for the same value of interlocking and same support, the standard deviation of μ_0 can be of the same order of magnitude of the mean value (see the case nom. bis μ_0 mean=0.13, μ_0 st. dev.=0.12);
- for the case *interlocking nom./right support* μ_0 and μ_1 have not been determined since the cycles obtained did not show gross slip behavior (see Fig. 6, row 4 column 3 right support); during the repetition at interlocking nom. (after disassembly and assembly of the segment on the rig) gross slip took place and μ_0 and μ_1 could then be determined;
- by comparison of the cases *interlocking nom./left support* and its repeated nom., it can be noticed that the mean value of μ_0 and μ_1 in the repetition test have changed, in particular the mean value of μ_1 is three times higher;
- standard deviation increases with interlocking. That is with lower normal forces friction tends to a more stable gross slip behavior, accordingly with friction measurements found in literature ([3,4]).

Figure 15 shows that when two cycles are detected for the same excitations force and the same interlocking value for two frequencies corresponding to the same level of receptance amplitude (the frequency has been changed without stopping the test), the relative displacement is the same but the friction coefficient μ_0 varies of almost 20 percent.

It can be concluded that while the contact stiffness can be determined at least as an order of magnitude, the friction coefficients μ_0 and μ_1 show an uncontrolled scatter.

It is suspected that the scatter may be due to:

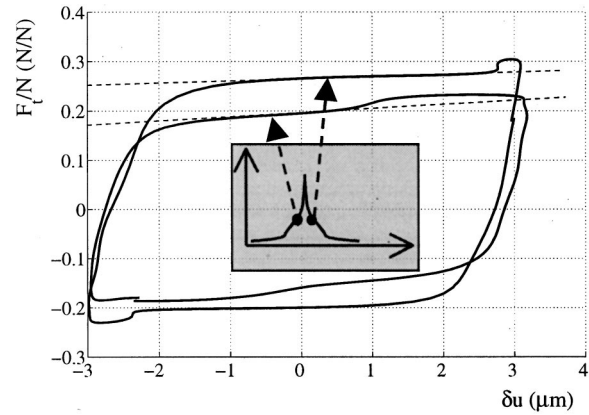


Fig. 15 Ratio of tangential force and normal contact force for different frequency around resonance: evidence of friction coefficients variation

- friction behavior in mixed slip regime ([3]);
- lack of reproducibility of contact condition, since the contact is not a point contact but a linear contact;
- wear.

The conclusion is that even in accurately controlled conditions, this approach was not successful, even though it gave at least orders of magnitudes of parameters. Perhaps a more complete and refined contact model could explain this behavior ([6,7]).

Fourier Expansion

The numerical model of segments with friction contact will be solved by means of HBM. This method implies the Fourier expansion of the tangential contact force. As in the majority of work in the literature ([8–13]), the truncation to the first harmonic term is adopted.

In view of the future numerical calculation the experimental tangential contact force and the relative tangential displacement have been expanded in Fourier series and truncated at the first harmonic order. This calculation has been performed for each set of experimental measurements (Table 2). As an example, in Fig. 16 it is shown that the approximation of the hysteresis cycles with the ellipses are derived by the amplitude of force and displacement expanded in Fourier series and truncated at the first term.

In Figs. 17 and 18 the coefficients of tangential force are plotted versus the amplitude of relative displacement for different interlocking values for the case of left support. In the graphs the values

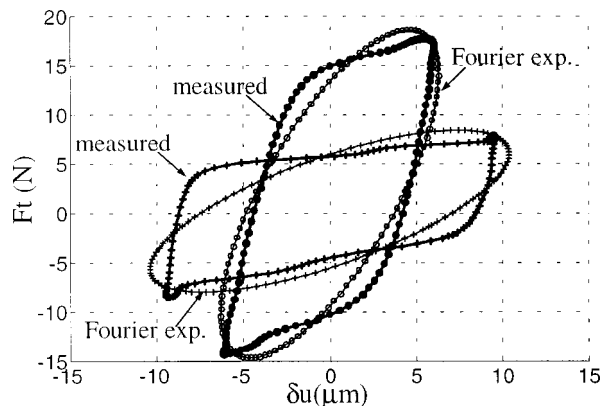


Fig. 16 Example of measured hysteresis cycles and ellipses obtained after Fourier (1st order approx.) of force and displacement

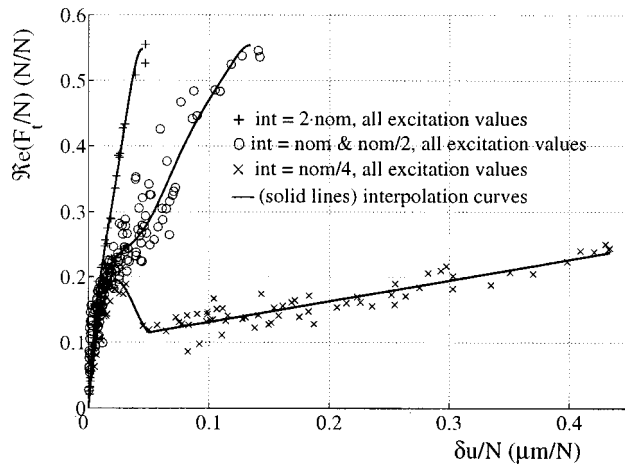


Fig. 17 Real part of Fourier expansion of tangential force on mean normal force versus the amplitude of relative displacement on mean normal force for different interlocking values. Left support.

of forces and displacements are divided by the mean value of the contact normal force. The following observations hold:

- the experimental points show a distribution that leads to an interpolation in three different families of interlocking values: $n/4$, $n/2$ and n , $2n$.
- the points refer to all the conditions of Table 2 (different excitation frequencies and amplitudes), however these quantities seem not to have influence on the trend of the interpolating curve, the parameter which characterizes these curves is the interlocking value.
- the interpolated curve of the real part for the case $n/4$ (Fig. 17) has the typical shape of the real part of the tangential contact force in Coulomb friction behavior as found in the

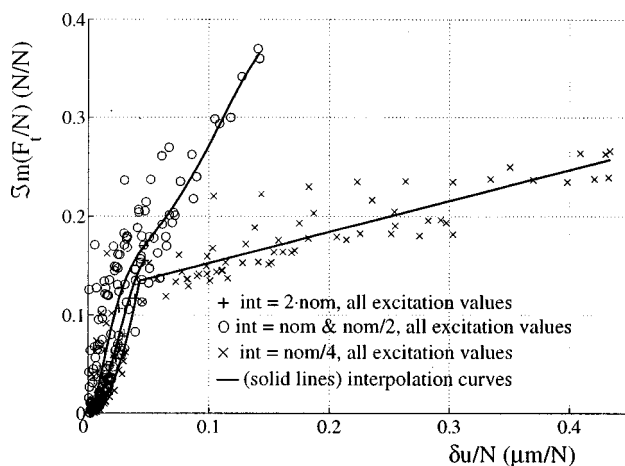


Fig. 18 Imaginary part of tangential force Fourier expansion versus the amplitude of relative displacement for different interlocking values. Left support.

literature ([10]). In fact, for interlocking $n/4$ support left (Fig. 8) the cycles show a more Coulomb behavior than for the other interlocking cases.

- both for imaginary and real parts the curve interpolating the points at interlocking $n/4$ behaves differently from the other curves.

These curves interpolating imaginary and real parts for different interlocking values can be used in the numerical analysis. The proposed method consists in using these curves during the numerical HBM solution: For a given value of displacement amplitude the curves give the corresponding values of real and imaginary part of the contact tangential force.

Conclusions

A purposely made experimental setup has allowed accurate laboratory measurements of forces and displacements at the point where a turbine vane sector is normally in contact with neighboring sectors.

An attempt was made to relate physical parameters of the contact (tangential stiffness friction and dissipated energy) to interlocking force and sliding displacement, under the typical resonant and near resonance condition. It was concluded that the most viable approach is to relate directly the real and imaginary parts of the I term from the Fourier expansion of tangential force, with the total displacement range. Experimental points then fall on curves whose parameters is the interlocking force.

Acknowledgments

This work has been financially supported by Fiat Avio.

References

- [1] Berruti, T., Filippi, S., Goglio, L., and Gola, M. M., 2000, "A Test Rig for Frictionally Damped Bladed Segments," 45th ASME Gas Turbine and Aeroengine Congress and Exhibition, Munich (Germany).
- [2] Berruti, T., Filippi, S., Goglio, L., and Gola, M. M., 1999, "Forced Vibrations of Frictionally Damped Stator Segments," 44th ASME Gas Turbine and Aeroengine Congress and Exhibition, Indianapolis, IN.
- [3] Fouvry, S., Kapsa, Ph., and Vincent, L., 1997, "Developments of Fretting Sliding Criteria to Qualify the Local Friction Coefficient Evolution Under Partial Slip Condition," *Tribology for Energy Conservation*, D. Dawson et al., eds., Tribol. Ser., **34**, pp. 161–172.
- [4] Fouvry, S., Kapsa, Ph., and Vincent, L., 1995, "Analysis of Sliding Behavior for Fretting Loading, Determination of Transition Criteria," *Wear*, **185**, pp. 35–46.
- [5] Waterhouse, R. B., 1981, *Fretting Fatigue*, Waterhouse, ed., Applied Science Pub., UK.
- [6] Sextro, W., 2000, "The Calculation of the Forced Response of Shrouded Blades With Friction Contacts and Its Experimental Verification" 45th ASME Gas Turbine and Aeroengine Congress and Exhibition, Munich (Germany).
- [7] Csaba, G., 1999, "Modeling of a Microslip Friction Damper Subjected to Translation and Rotation," 44th ASME Gas Turbine and Aeroengine Congress and Exhibition, Indianapolis, IN.
- [8] Sanliturk, K. Y., Imregun, M., and Ewins, D. J., 1997, "Harmonic Balance Vibration Analysis of Turbine Blades With Friction Dampers," *ASME J. Vib. Acoust.*, **119**, pp. 96–103.
- [9] Sanliturk, K., and Ewins, D. J., 1996, "Modeling Two-Dimensional Friction Contact and Its Application Using Harmonic Balance Method," *J. Sound Vib.*, **193**(2), pp. 511–523.
- [10] Menq, C. H., Griffin, J. H., and Bielak, J., 1986, "The Influence of a Variable Normal Load on the Forced Vibration of a Frictionally Damped Structure," *ASME J. Eng. Gas Turbines Power*, **108**, pp. 300–305.
- [11] Sanliturk, K. Y., Ewins, D. J., and Stanbridge, A. B., 1999, "Underplatform Dampers for Turbine Blades: Theoretical Modeling, Analysis and Comparison of Experimental Data," 44th ASME Gas Turbine and Aeroengine Congress and Exhibition, Indianapolis, IN.
- [12] Menq, C. H., Griffin, J. H., and Bielak, J., 1986, "The Forced Response of Shrouded Fan Stages," *ASME J. Vib. Acoust.*, **108**, pp. 50–55.
- [13] Menq, C. H., Griffin, J. H., and Bielak, J., 1986, "The Influence of Microslip on Vibratory Response, Part I: A New Microslip Model, Part II: A Comparison With Experimental Results," *J. Sound Vib.*, **107**, pp. 279–293 (295–307).

Three Practical Examples of Magnetic Bearing Control Design Using a Modern Tool

M. Spirig
J. Schmied

Delta JS AG,
Technoparkstr. 1,
Zurich CH-8005, Switzerland

P. Jenckel
U. Kanne

LUST Antriebstechnik,
Lahnau D-35633, Germany

The use of magnetic bearing in industrial applications has increased due to their unique properties. Nowadays efficiency and predictability in handling rotors on magnetic bearings is asked with the same standard as conventional rotors on oil or roller bearings. First of all one must be aware of the special technical properties of magnetic bearing designs. The dynamic behavior of the rotor combined with requirements of the application define the desired bearing characteristic. With modern tools covering the mechanical aspects as well as the electronic controllers and their digital implementation on a DSP, these properties can be designed. However, despite the use of such efficient tools engineering practice is needed. Therefore this paper summarizes the major steps in the control design process of industrial applications. Three rotors supported on magnetic bearing with their specific dynamic behavior are presented: a very small high speed spindle (120,000 rpm); a small industrial turbo molecular pump rotor (36,000 rpm); and a large multistage centrifugal compressor (600 to 6300 rpm). The results of the analyses and their experimental verification are given. [DOI: 10.1115/1.1417483]

1 Introduction

1.1 Technical Considerations in Magnetic Bearing Design.

The allowable rotor vibrations in magnetic bearing applications are limited, e.g., due to small clearances, bearing capacity limits, limited driving torque when crossing critical speeds, etc., and therefore have to be specified. Design specifications for the rotor damping and the location of critical speeds, such as API 617, can be used as guidelines. However, they do not cover all aspects. Basic questions in the case of any rotating machine design are as follows ([1]):

- Where are the critical speeds? Are critical speeds within the operating speed range? How many critical speeds must be crossed during the run up of the rotor?
- What is the necessary damping of the natural modes of the rotor in order to ensure safe run up and operation? How can it be achieved?
- What is the necessary stiffness of the bearing? How can it be achieved?

These questions have higher significance in the magnetic bearing design, especially because of the limited specific bearing capacity. At low frequencies the capacity is around 0.3–1 MPa, because of the magnetic saturation of the material. It is even further reduced at higher frequencies due to the limited voltage of the power amplifiers ([2,3]). Excessive bearing loads lead to a contact of the rotor with the auxiliary bearings. Normally they are ball bearings or bushings with a low friction surface. Each contact wears them out more and more. That is why loads, which can occur during a rotor lifetime, have to be considered very carefully in the design process.

An optimal damping is mandatory for any robust rotor design. In most applications the damping has to be provided by the bearing. In order to enable a magnetic bearing to do this, all natural modes, which must be well damped (normally all modes below the maximum operating speed), must be observable and control-

lable. Sufficient damping force must be provided by a controller design, which yields the appropriate amplitude and phase angle of the bearing transfer function. A damping characteristic is achieved for phase angles $0 \text{ deg} < \phi < 90 \text{ deg}$ or $-180 \text{ deg} > \phi > -270 \text{ deg}$ (see the figure with bearing transfer functions).

In some applications a sufficient stiffness force is also important, e.g., to resist high fluid forces, which normally have very low frequencies. With speed the behavior of a rotor may change due to gyroscopic effects or due to changes in the fluid forces. A robust controller design as presented in Section 2 for the three different rotors must take all this into account.

1.2 Tools for the Rotordynamic Analyses. Software tools suited for the engineering of magnetic bearing applications must comprise a structural part describing the rotor ([4–6]) as well as a mechatronic part describing the magnetic bearing and the combined rotor bearing system. A relatively simple practical way of

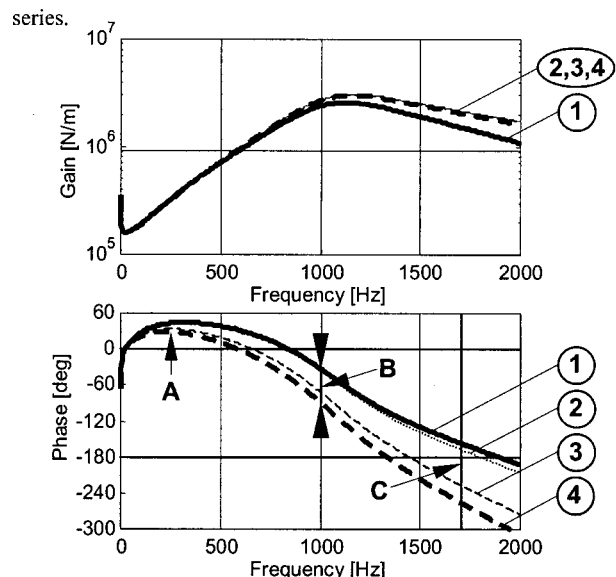


Fig. 1 Bearing transfer function of the high speed rotor

Contributed by the International Gas Turbine Institute (IGTI) of THE AMERICAN SOCIETY OF MECHANICAL ENGINEERS for publication in the ASME JOURNAL OF ENGINEERING FOR GAS TURBINES AND POWER. Paper presented at the International Gas Turbine and Aeroengine Congress and Exhibition, Munich, Germany, May 8–11, 2000; Paper 00-GT-407. Manuscript received by IGTI Nov. 1999; final revision received by ASME Headquarters Feb. 2000. Associate Editor: D. Wisler.

looking at the combined system is described in [7]. The necessary software capabilities are listed in the following:

- The structural part has to consider: gyroscopic effects,
 - rotor fluid interaction, such as labyrinth induced excitations,
 - dynamics of flexible parts mounted on the rotor, such as disks, and
 - flexibility of stator parts.
- The mechatronic part has to consider:
 - noncollocation of sensors and actuators,
 - magnetic pull (negative stiffness) of magnetic actuators,
 - digital controllers, taking into account the antialiasing filter, a time delay and the AD conversion,
 - characteristics of the hardware components of magnetic bearings (sensors and amplifiers),
 - separate sensors as well as separate controllers for displacement and velocity, and
 - coupling of bearings and/or axes by means of controllers, e.g., different controllers for tilting and translation rotor modes.

A comprehensive tool is illustrated in [1] and [8]. It also includes a controller design part, which allows to create the transfer function with the required amplitude and phase by combining standard controller components, e.g., modified PID controllers (see Appendix), first and second-order filters, and all pass, notch, and analogue Butterworth filters.

1.3 Typical Engineering Procedure. The major steps in the control design process are

- modeling the structural part in a similar way as in case of conventional bearings (see Tables 1 and 2).
- studying the basic behavior of the rotor, including the analyses of natural frequencies of the rotor at standstill and at speed for different bearing stiffness coefficients, as well as the analyses of the damping ratios (see Appendix) of natural modes for different bearing damping coefficients.
- define the requirements and/or determine the properties of the electronic hardware and software as listed in Section 1.2.
- design of the controller transfer function ([3]), taking into account the basic behavior of the rotor as well as the requirements of the application (Section 2).
- study the actual behavior of the combined system in a closed loop analysis ([1] Section 3).

This procedure is demonstrated in detail for three applications in the next sections.

2 Rotors, Applications Requirements, and Controllers

The first step in the design procedure is to model the rotor structure and study its basic behavior ([5]). The main data of the three very different rotors are summarized in Table 1. Table 2 shows the dimensions, the mass and stiffness diameters, the locations of the supports (triangles) and the arrangement of the nodes. Also the concentrated masses and the flexible disk of the third rotor are visible.

The lower part of Table 2 shows the mode shapes of the free rotors at standstill, which will be important in the later controller design. The long vertical lines indicate the actuator locations and

the shorter vertical lines the sensor locations. The natural frequencies and the range of the frequencies as the rotor starts rotating up to its maximum speed are listed above the mode shapes.

2.1 Rotor 1: Small High-Speed Rotor. The first rotor is a very small spindle realized in a research project ([1]). It rotates supercritically at the very high speed of 120,000 rpm = 2000 cps.

Basic Behavior of the Rotor (Table 2). The natural frequency of the free rotor's first bending mode is at 1714 Hz. In order to cross this mode considerable damping forces have to be provided by the bearings at an extremely high frequency.

The Electronic Hardware and Software. Digital hardware is used to implement the controller. Due to the high frequency range of this small rotor the phase losses of the electronic components are quite important (B in Fig. 1). At 1714 Hz they consist of the following components:

- The time delay is one period of the sampling rate, i.e., it is 96 μ s, which corresponds to 59 deg. Within this time the A/D conversion as well as the signal processing takes place.
- The zero-order hold behavior ([9]) of the digital controller with a sampling rate of 10,400 Hz adds another 30 deg.
- The amplifier, i.e., the current controller has more than 45 deg.

The magnetic bearings each have a negative stiffness of about 53,000 N/m. The motor also has a negative stiffness in the same order of magnitude. Hence the stiffness of the bearings created by the controller should be at least around 2–3 10^5 N/m in order to safely compensate these negative stiffnesses.

Design of the Controller. Due to the above-mentioned phase losses it is impossible to damp the first bending mode with a phase angle above 0 deg. This could only be achieved by a phase angle below –180 deg. The transfer function of the bearings is shown in Fig. 1. Both bearings have the same function. The figure contains several curves, which demonstrate the influence of various effects.

1 Controller with its analogue transfer function digitally transformed by the “first-order hold” (FOH, [9]) method. This is how it is programmed in the processor. The FOH method gives a good approximation to the analogue transfer function. The amplifier characteristic is also included and FOH transformed as well. The curve is composed of the following elements:

- A modified PID element (see the “base” function in the Appendix) to damp the rigid-body modes by phase lead (A).
- A second-order filter at 1100 Hz to lower the phase below –180 deg in order to damp the first bending mode at 1714 Hz (C).
- A second-order filter at 2200 Hz approximating the amplifier.

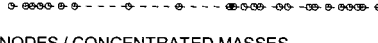
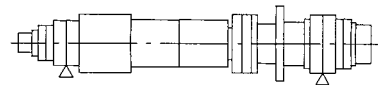
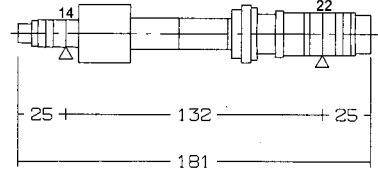
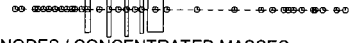
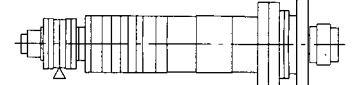
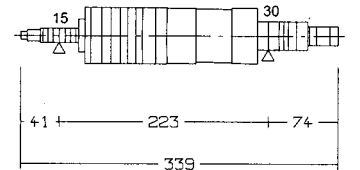
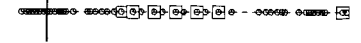
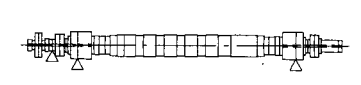
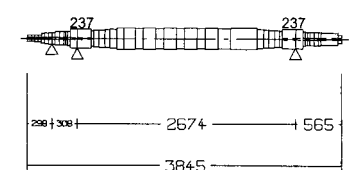
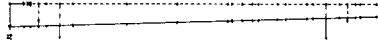
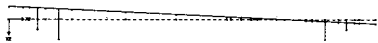
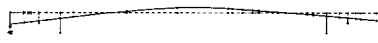
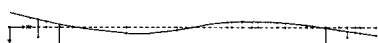
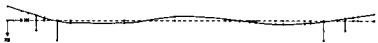
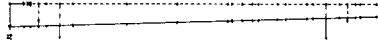
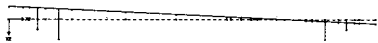
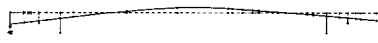
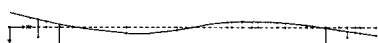
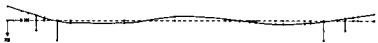
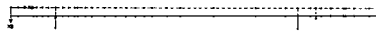

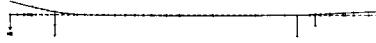
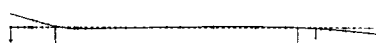

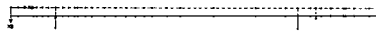

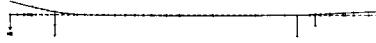
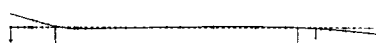

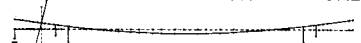


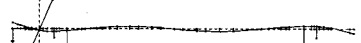
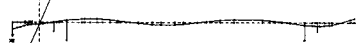
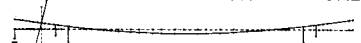


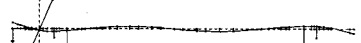
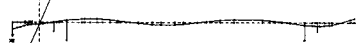
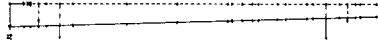
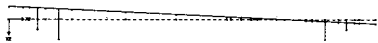
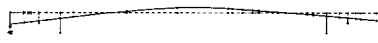
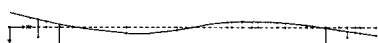
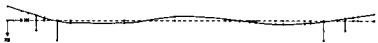
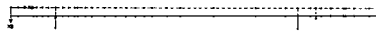

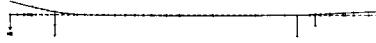
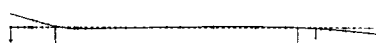

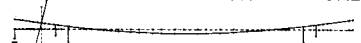


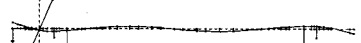
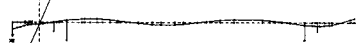
2 The controller and amplifier in their analogue form including an analogue antialiasing filter of first order at the frequency of 5200 Hz. This filter has almost no influence in the frequency range up to 2000 Hz.

3 The analogue form of the controller, amplifier and antialiasing filter (curve 2) plus the time delay of 96 μ s, which lowers the phase angle significantly.

Table 1 Summary of the main rotor data

	High Speed Spindle		Turbo Molecular Pump		Centrifugal Compressor	
Mass	0.68	kg	6.3	kg	$2.1 \cdot 10^3$	kg
Polar Moment of Inertia	$6.2 \cdot 10^{-5}$	kgm^2	$1.6 \cdot 10^{-2}$	kgm^2	$4.1 \cdot 10^1$	kgm^2
Diametral Moment of Inertia	$1.5 \cdot 10^{-3}$	kgm^2	$4.0 \cdot 10^{-2}$	kgm^2	$2.2 \cdot 10^3$	kgm^2
Rotor Diameter (Bearing)	14 / 22	mm	15 / 30	mm	237	mm
Rotor Length	181	mm	344	mm	3845	mm
Bearing Span	132	mm	223	mm	2674	mm
Max. continuous speed	120000	rpm	36000	rpm	6300	rpm

Table 2 Rotor models, mode shapes, and natural frequencies

High Speed Spindle	Turbo Molecular Pump	Centrifugal Compressor																																																																																																																																																
 NODES / CONCENTRATED MASSES  MASS DIAMETER  DIMENSIONS / STIFFNESS DIAMETER	 NODES / CONCENTRATED MASSES  MASS DIAMETER  DIMENSIONS / STIFFNESS DIAMETER	 NODES / DISK / CONCENTRATED MASSES  MASS DIAMETER  DIMENSIONS / STIFFNESS DIAMETER																																																																																																																																																
Mode Shapes (at standstill) and Natural Frequencies of the Free Rotors ((Hz))																																																																																																																																																		
<table border="1"> <thead> <tr> <th></th> <th>Standstill</th> <th colspan="2">n = 2000 Hz</th> </tr> <tr> <th></th> <th></th> <th>backward</th> <th>forward</th> </tr> </thead> <tbody> <tr> <td><u>parallel</u></td> <td>0.0</td> <td>0.0</td> <td>0.0</td> </tr> <tr> <td></td> <td></td> <td></td> <td></td> </tr> <tr> <td><u>tilting</u></td> <td>0.0</td> <td>0.0</td> <td>77.4</td> </tr> <tr> <td></td> <td></td> <td></td> <td></td> </tr> <tr> <td><u>1. bending</u></td> <td>1714.3</td> <td>1582.9</td> <td>1856.0</td> </tr> <tr> <td></td> <td></td> <td></td> <td></td> </tr> <tr> <td><u>2. bending</u></td> <td>5543.9</td> <td>5330.3</td> <td>5764.7</td> </tr> <tr> <td></td> <td></td> <td></td> <td></td> </tr> <tr> <td><u>3. bending</u></td> <td>10281.9</td> <td>9979.9</td> <td>10588.0</td> </tr> <tr> <td></td> <td></td> <td></td> <td></td> </tr> </tbody> </table>		Standstill	n = 2000 Hz				backward	forward	<u>parallel</u>	0.0	0.0	0.0					<u>tilting</u>	0.0	0.0	77.4					<u>1. bending</u>	1714.3	1582.9	1856.0					<u>2. bending</u>	5543.9	5330.3	5764.7					<u>3. bending</u>	10281.9	9979.9	10588.0					<table border="1"> <thead> <tr> <th></th> <th>Standstill</th> <th colspan="2">n = 600 Hz</th> </tr> <tr> <th></th> <th></th> <th>backward</th> <th>forward</th> </tr> </thead> <tbody> <tr> <td><u>parallel</u></td> <td>0.0</td> <td>0.0</td> <td>0.0</td> </tr> <tr> <td></td> <td></td> <td></td> <td></td> </tr> <tr> <td><u>tilting</u></td> <td>0.0</td> <td>0.0</td> <td>228.8</td> </tr> <tr> <td></td> <td></td> <td></td> <td></td> </tr> <tr> <td><u>1. bending</u></td> <td>1195.7</td> <td>1110.7</td> <td>1275.9</td> </tr> <tr> <td></td> <td></td> <td></td> <td></td> </tr> <tr> <td><u>2. bending</u></td> <td>1501.7</td> <td>1344.8</td> <td>1724.5</td> </tr> <tr> <td></td> <td></td> <td></td> <td></td> </tr> <tr> <td><u>3. bending</u></td> <td>2641.4</td> <td>2446.8</td> <td>2851.4</td> </tr> <tr> <td></td> <td></td> <td></td> <td></td> </tr> </tbody> </table>		Standstill	n = 600 Hz				backward	forward	<u>parallel</u>	0.0	0.0	0.0					<u>tilting</u>	0.0	0.0	228.8					<u>1. bending</u>	1195.7	1110.7	1275.9					<u>2. bending</u>	1501.7	1344.8	1724.5					<u>3. bending</u>	2641.4	2446.8	2851.4					<table border="1"> <thead> <tr> <th></th> <th>Standstill</th> <th colspan="2">n = 105 Hz</th> </tr> <tr> <th></th> <th></th> <th>backward</th> <th>forward</th> </tr> </thead> <tbody> <tr> <td><u>1. bending</u></td> <td>64.3</td> <td>61.4</td> <td>67.2</td> </tr> <tr> <td></td> <td></td> <td></td> <td></td> </tr> <tr> <td><u>2. bending</u></td> <td>154.3</td> <td>143.4</td> <td>163.3</td> </tr> <tr> <td></td> <td></td> <td></td> <td></td> </tr> <tr> <td><u>3. bending</u></td> <td>255.2</td> <td>228.9</td> <td>275.1</td> </tr> <tr> <td></td> <td></td> <td></td> <td></td> </tr> <tr> <td><u>4. bending</u></td> <td>356.9</td> <td>321.0</td> <td>397.4</td> </tr> <tr> <td></td> <td></td> <td></td> <td></td> </tr> <tr> <td><u>disk mode</u></td> <td>488.1</td> <td>454.8</td> <td>538.1</td> </tr> <tr> <td></td> <td></td> <td></td> <td></td> </tr> </tbody> </table>		Standstill	n = 105 Hz				backward	forward	<u>1. bending</u>	64.3	61.4	67.2					<u>2. bending</u>	154.3	143.4	163.3					<u>3. bending</u>	255.2	228.9	275.1					<u>4. bending</u>	356.9	321.0	397.4					<u>disk mode</u>	488.1	454.8	538.1				
	Standstill	n = 2000 Hz																																																																																																																																																
		backward	forward																																																																																																																																															
<u>parallel</u>	0.0	0.0	0.0																																																																																																																																															
																																																																																																																																																		
<u>tilting</u>	0.0	0.0	77.4																																																																																																																																															
																																																																																																																																																		
<u>1. bending</u>	1714.3	1582.9	1856.0																																																																																																																																															
																																																																																																																																																		
<u>2. bending</u>	5543.9	5330.3	5764.7																																																																																																																																															
																																																																																																																																																		
<u>3. bending</u>	10281.9	9979.9	10588.0																																																																																																																																															
																																																																																																																																																		
	Standstill	n = 600 Hz																																																																																																																																																
		backward	forward																																																																																																																																															
<u>parallel</u>	0.0	0.0	0.0																																																																																																																																															
																																																																																																																																																		
<u>tilting</u>	0.0	0.0	228.8																																																																																																																																															
																																																																																																																																																		
<u>1. bending</u>	1195.7	1110.7	1275.9																																																																																																																																															
																																																																																																																																																		
<u>2. bending</u>	1501.7	1344.8	1724.5																																																																																																																																															
																																																																																																																																																		
<u>3. bending</u>	2641.4	2446.8	2851.4																																																																																																																																															
																																																																																																																																																		
	Standstill	n = 105 Hz																																																																																																																																																
		backward	forward																																																																																																																																															
<u>1. bending</u>	64.3	61.4	67.2																																																																																																																																															
																																																																																																																																																		
<u>2. bending</u>	154.3	143.4	163.3																																																																																																																																															
																																																																																																																																																		
<u>3. bending</u>	255.2	228.9	275.1																																																																																																																																															
																																																																																																																																																		
<u>4. bending</u>	356.9	321.0	397.4																																																																																																																																															
																																																																																																																																																		
<u>disk mode</u>	488.1	454.8	538.1																																																																																																																																															
																																																																																																																																																		

4 Curve 3 digitally transformed by the “zero-order hold” (ZOH, [9]) method. The transfer function including the ZOH behavior gives an additional phase loss.

Curve 2 to 4 are only plotted for design purposes of the controller, to show the phase losses (B in Fig. 1). The actual closed loop model is built by the digital bearing transfer function transformed by first-order hold (thick solid curve 1) combined with the ZOH transformed model of the rotor with the analogue antialiasing filter switched in series.

2.2 Rotor 2: Industrial Turbo Molecular Pump (TMP).

The second rotor is an industrial turbo molecular pump. It runs at a maximum speed of 36,000 rpm.

Basic Behavior of the Rotor (Table 2). Due to the shape including the large disks with blades the ratio of the polar moment of inertia to the transverse moment of inertia is quite high (see Table 1). Therefore the gyroscopic effect is quite extreme, as can be seen in Fig. 2. The forward tilting mode frequency rises with the speed from 0 to 250 Hz.

Beside the rotor modes, blade modes between 600 and 800 Hz play a role, although they are not coupled with rotor modes to a high extent. However, in the testing phase it turned out, that they had to be considered in the controller design. In the theoretical model they are assumed as rigid.

The first elastic rotor mode is at a frequency of 1200 Hz.

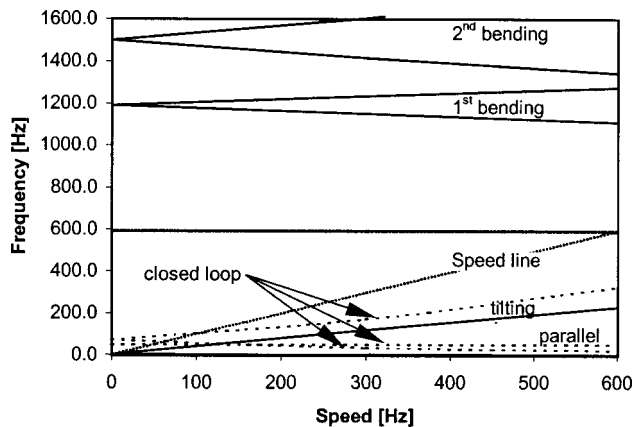


Fig. 2 Natural frequencies of the modes versus speed for the free and supported rotor

The Electronic Hardware and Software. Also in this application the phase losses of the electronic components, i.e., of the amplifier, the antialiasing filter of second order at 4450 Hz, the time delay of 64 μ s and of the digital controller sampling rate of 8900 Hz cannot be neglected.

The magnetic pull of the bearing in this case is $2.4 \cdot 10^5$ N/m for the upper bearing (left in Table 2) and $3.0 \cdot 10^5$ N/m for the lower bearing (right in Table 2).

Design of the Controller. The transfer function of the bearings is shown in Fig. 3 in the same way as in Fig. 1. The basic design ideas are:

- A The range with positive phase is enlarged up to 330 Hz, in order to damp the widely spread tilting modes. This is done with a phase lead part of a PID element at 170 Hz (see the “base” function in the Appendix).
- B In order to provide damping at the frequency of the blade modes the phase has to be dropped rapidly below -180 deg. This is achieved by a second order element in the denominator (phase lag element in the “base” function in the appendix), which has a frequency of 520 Hz. This has also the effect of reducing the amplitude.

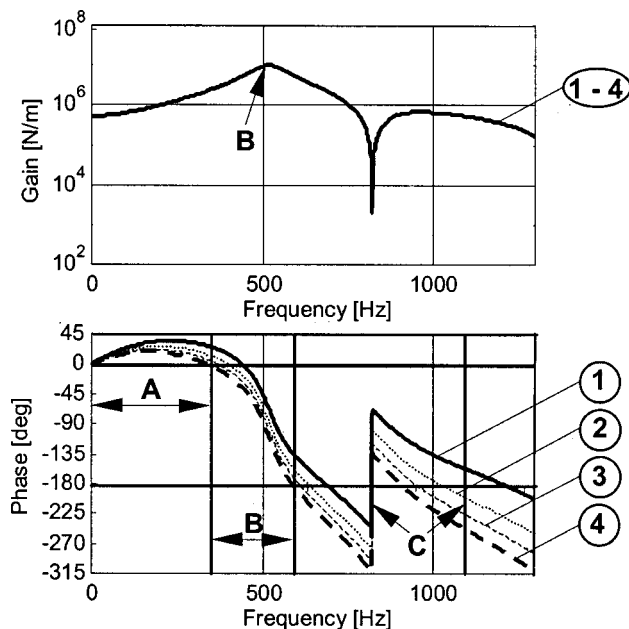


Fig. 3 Bearing transfer function of the TMP

- C In order to provide damping for the rotor mode at 1200 Hz the fast phase loss, which would drop even below -360 deg is interrupted by a notch filter at 820 Hz.

2.3 Rotor 3: Large Industrial Centrifugal Compressor.

The third rotor is a large industrial multistage centrifugal compressor [8]. It is driven by a 23 MW variable speed synchronous electric motor, with a wide operating speed range from 600 rpm to 6300 rpm.

Basic Behavior of the Rotor (Table 2). At low frequencies the rotor is exposed to considerable fluid forces.

The first bending mode is at 64 Hz. Hence it is in the operating speed range and requires special attention.

The frequency of the one nodal diameter vibration mode of the axial bearing disk is at 490 Hz. It had to be considered in the model for the controller design, since it strongly interacts with rotor modes. In the second and higher bending modes the flexible disk tilts more than a rigid disk would (see the mode shapes in Table 2). This has the effect of considerably increasing the gyroscopic effect. In Figs. 4 and 5 the natural frequencies are presented as a function of the bearing stiffness at different speeds for a rigid and a flexible disk. The comparison of both results show, that the frequency difference between forward and backward whirl as well as the frequency regions where the bearing has to provide damping increase considerably in case of the flexible disk.

The Electronic Hardware and Software. As in the previous cases, the controller is implemented on a digital system with a sampling rate of 10,000 Hz. The phase losses due to the digitalization and the hardware are considered, however, in this case they are not as important as in the previous cases, due to the lower frequencies.

The magnetic pull of the actuator, which has to be compensated by the controller, has a value of $1.57 \cdot 10^7$ N/m.

Design of the Controller. Figure 6 shows the magnetic bearing transfer function including the sensor, the antialiasing filter, the controller, the amplifier, the actuator, and the time delay.

Important features of the controller are:

- A To resist the high fluid forces at low frequencies the stiffness has to be above a certain limit.
- B In order to damp the rigid-body modes, which are mostly affected by the destabilising labyrinth seal forces, the phase is increased by an extra filter at 18 Hz.
- C To prevent saturation of the amplifier the amplitudes at high frequencies are reduced with a second-order low pass filter. The phase decreases below 0 deg, which yields a negative

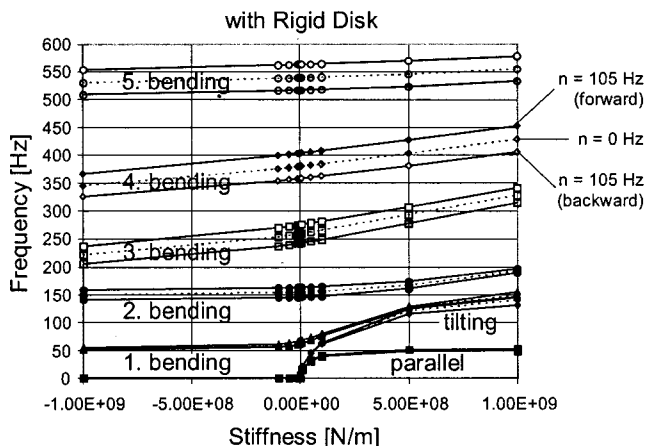


Fig. 4 Natural frequencies of the modes versus bearing stiffness and speed (rigid fixed disk)

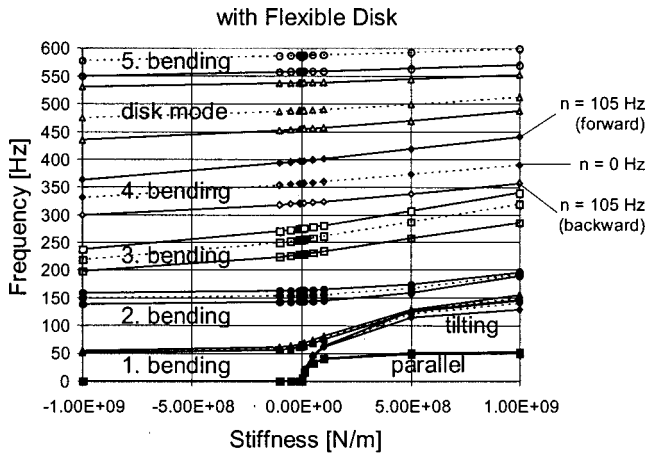


Fig. 5 Natural frequencies of the modes versus bearing stiffness and speed (flexible disk)

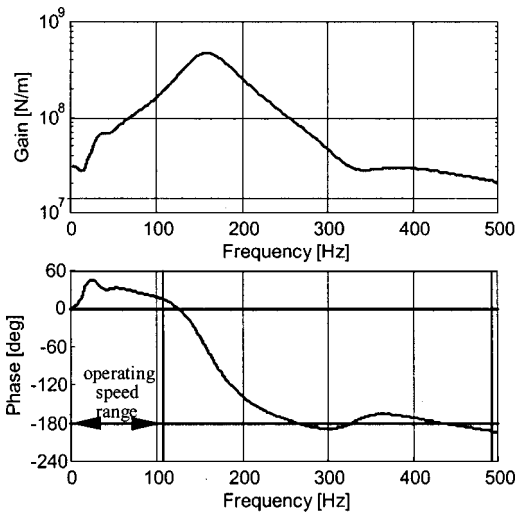


Fig. 6 Bearing transfer function of the large centrifugal compressor

damping force for the second bending mode. However, this mode has a node slightly inside the outboard sensor. The deflections at the sensor and the actuator have reverse sign and thus the mode is slightly damped. At higher frequencies the bearing provides a damping force thanks to the phase angle below -180 deg.

The overall controller transfer function is an 18th-order polynomial. It is designed by the bearing manufacturer using his own controller design software. To fully optimize the controller for this application the transfer function is synthesized with complex rather than simple poles and zeros. Digital controller hardware is essential to the implementation of this type of controller transfer function.

3 Closed-Loop Behavior

Once a controller is designed considering the basic rotor behavior and the application requirements, the actual behavior of the combined system can be studied. The comparison between analysis and measurements can bring up possible deficiencies of the model. Often this helps to complete the model and thus improves iteratively the prediction and the behavior of the final closed loop system. The degree of agreement between reality and prediction depends mainly on the complexity of the rotor, e.g., shrunk parts,

elasticity of parts mounted on the rotor, etc., and how accurate it can be modeled. A fine tuning after implementation of the controller may be necessary.

In the following sections the calculated closed loop behavior and the experimental verification of the analysis are presented for the three rotors:

- First the calculated eigenvalues composed of the natural frequency (+ forward, - backward whirling) and the damping ratio of the combined rotor bearing system at standstill and nominal speed are listed for each case. Tables 3–5 contain the eigenvalues, which can be assigned to the rotor. Besides that some eigenvalues are caused by controller poles, which interact with the rotor. This interaction can change their frequency and damping ratio. The eigenvalues caused by the controller with a damping ratio below 20 percent are also shown in the tables.
- Second examples of the calculated and measured responses to force or unbalance excitation are given.

3.1 Rotor 1: High Speed Rotor. In Table 3 can be seen that the rigid modes are well damped. The first forward whirling bending mode at speed has a damping ratio of only 2.5 percent. This has to be improved, among others by a higher gain. The higher gain can only be realized with a balance compensation system as the tests showed. At this moment such a system is being optimised. A speed of 1600 Hz has been reached.

Table 3 Natural frequencies and damping ratios

Mode	n = 0 [Hz]		n = 2000 [Hz]	
	Frequency [Hz]	Damping Ratio [%]	Frequency [Hz]	Damping Ratio [%]
parallel	89.7	29.5	- 88.7 + 89.9	29.7 29.6
tilting	145.9	49.7	- 100.1 + 229.5	45.8 43.6
1 st bending	1709.6	3.9	- 1534.4 + 1787.5	4.1 2.5
2 nd bending	4856.2	0.6	- 4635.4 + 5069.7	0.7 0.6

Table 4 Natural frequencies and damping ratios

Mode/Pole [Hz], [%]	n = 0 [Hz]		n = 600 [Hz]	
	Frequency [Hz]	Damping Ratio [%]	Frequency [Hz]	Damping Ratio [%]
parallel	38.7	17.0	- 38.4 + 38.5	16.8 16.9
tilting	70.2	24.7	- 13.5 + 296.8	9.5 9.7
contr. pole 520, 10	481.2	12.4	- 431.9 + 495.1	16.6 11.5
contr. pole 520, 10	512.0	11.0	- 511.2 + 513.0	11.1 11.0
contr. pole 820, 17	801.6	16.9	- 799.0 + 803.5	16.9 17.0
contr. pole 820, 17	809.9	17.7	- 809.6 + 810.0	17.6 17.7
1 st bending	1193.3	0.3	- 1107.7 + 1274.1	0.4 0.3
contr. pole 1400, 18.6	1373.1	18.8	- 1372.7 + 1373.4	18.8 18.7
contr. pole 1400, 18.6	1374.9	18.6	- 1374.7 + 1375.1	18.6 18.6
2 nd bending	1501.0	0.2	- 1344.3 + 1724.4	0.3 0.1

Table 5 Natural frequencies and damping ratios

Speed	n = 0 [Hz]		n = 105 [Hz]	
	Frequency [Hz]	Damping Ratio [%]	Frequency [Hz]	Damping Ratio [%]
parallel	12.6	25.8	-12.6 +12.6	25.8
tilting	14.0	28.8	- 13.8 + 14.1	28.9
contr. pole 35.8, 40	35.8	18.5	- 35.7 + 35.9	18.3 18.7
1 st bending	81.2	19.8	- 77.3 + 84.7	21.0 19.2
contr. pole 161, 20	130	6.8	- 129 + 131	7.8 6.5
contr. pole 161, 20	131	9.5	- 131 + 132	12.3 15.5
2 nd bending	155	1.4	- 143 + 164	1.5 1
3 rd bending	250	0	- 223 + 272	0 0
4 th bending	355	0	- 320 + 396	0 0
Rotor disk mode	488	0	- 454 + 538	0 0
4 th bending	587	0	- 558 + 631	0 0

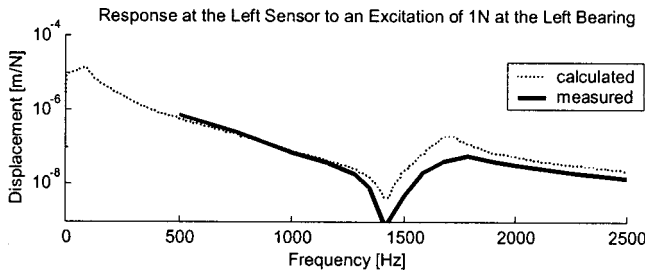


Fig. 7 Measured and calculated responses at standstill

The closed-loop behavior at standstill is confirmed by comparison of calculated and measured transfer functions with an excitation by the bearing. Figure 7 shows the response at the left sensor location to an excitation of 1 N at the left bearing. The resonance of the rotor's first bending at 1709 Hz as well as the frequency of the anti resonance agree well.

The damping of the bending mode ≈ 6 percent is higher in the measurement. Possible reasons for this are the inner damping of the rotor and the external damping of the surrounding air.

3.2 Rotor 2. Small Industrial Turbo Molecular Pump.

The modes within the speed range shown in Table 4 are well damped. The higher modes are stable with low damping ratios.

For this rotor the behavior is confirmed by a comparison of a calculated and measured transfer function.

Figure 8 shows a good agreement of the responses at the left sensor location to an excitation of 1N at the left bearing.

The resonances of the tilting mode as well as of the parallel mode are well visible. In addition, the measurement at 300 Hz shows the influence of the unbalance, which is not included in the load case of the calculation. In the region of 700 to 800 Hz the calculated curve deviates from the measured curve. This is probably due to elastic blade modes, which are not considered in the model.

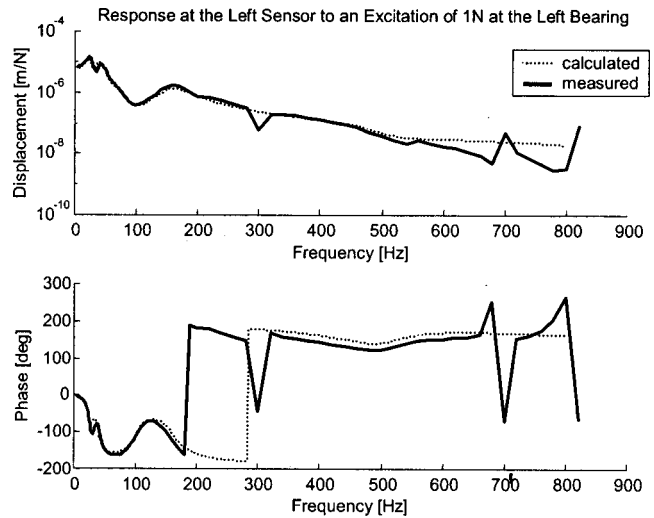


Fig. 8 Measured and calculated responses at 300 cps

3.3 Rotor 3: Large Industrial Centrifugal Compressor.

In Table 5 all damping ratios of the modes below the maximum speed are very well damped. The first bending mode, which is within the operating speed range, has a damping ratio of 20 percent. This complies with the specification according to API 617 for compressors, although its application to compressors supported on magnetic bearings is controversial.

Figure 9 shows the calculated and measured bearing response of the right bearing to an unbalance magnitude of G2, i.e. 3300 gmm are applied at the thrust disk and 2700 gmm at the coupling. This distribution yields a good excitation for the first bending mode. The maximum force below the maximum speed of 6300 rpm remains below the dynamic capacity of 20,000 N peak-peak.

The agreement between measurement and calculation is good. The calculated force at higher speeds, where the compressor never runs, increases due to the controller dominated pole at 130 Hz, which has a relatively low damping. Also the measured force remains at a high level up to maximum speed for the same reason.

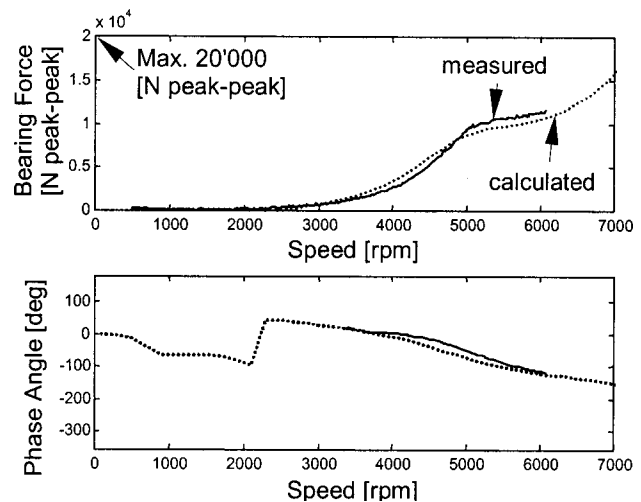


Fig. 9 DE bearing response to an unbalance G2 (peak-peak amplitude)

4 Conclusions

Efficiency and predictability in handling rotors on magnetic bearings is achieved by using a modern design tool ([1,8]). The typical design procedure is presented. Its main steps are

- the study of the mechanical part, i.e., modeling the rotor structure and investigate its basic behavior.
- the study of the mechatronic part, i.e., defining the requirements or determining the properties of the electronic hardware and software.
- the design of the controller, i.e., generating the bearing transfer function considering the gain as well as the phase.
- the study and interpretation of the closed loop behavior.

This procedure is iterative and needs engineering practice. Therefore the paper presents three applications.

- A very small high-speed spindle running at a maximum speed of 120,000 rpm, which is above the natural frequency of the free rotor's first bending mode at 1714 Hz. Because of this high speed, the phase losses of the electronic components and of the digitizing process are of special importance.
- A small, industrial turbo molecular pump rotor running at a maximum speed of 36,000 rpm. Due to its shape this rotor has a pronounced gyroscopic effect. For this reason the frequency range between the forward and backward tilting mode is widely spread from 0 to 320 Hz. Above that, elastic blade modes in the region of 600 to 800 Hz had to be considered for the controller design.
- A large industrial multistage centrifugal compressor with an operating speed range from 600 rpm to 6300 rpm. This rotor is subject to high fluid forces at low frequency, has its first bending mode within the operating speed and has a flexible axial bearing disk, which strongly interacts with the rotor modes and which played an important role for the controller design.

The result of the design process is the transfer function of the bearing controller and the prediction of the closed-loop behavior. The extent of predictability depends on the complexity of the rotor and how accurate it can be modelled. The accuracy also depends on tolerances, which play an important role, especially in case of the small rotors. However, a model always helps to accelerate and improve the design, even for cases where the theoretical model is not a complete representation of the reality. In some cases the final implementation of the controller may require a fine tuning.

For all three presented rotors a comparison of calculation and measurement has been carried out. The result can be summarized as follows:

- For the high-speed spindle the measured performance of the bearing is better than predicted. The higher damping ratio of the first bending mode is probably due to damping effects, which are not part of the model.
- For the turbomolecular pump good agreement is achieved apart from elastic blade modes, which were not considered.

They are rigidly modeled, since they did not seem to interact with the rotor. In this regard the model turned out to be insufficient.

- For the industrial turbocompressor the theoretical prediction is very good, after the elasticity of the axial bearing disk has been taken into account.

Acknowledgments

The authors wish to thank the Swiss Federal Institute of Technology ETH and Sulzer Electronics for their cooperation in the high-speed spindle research project. We also thank Federal Mogul Magnetic Bearings and Demag Delaval for their support concerning the industrial turbo compressor project. Special thanks to Frits de Jongh for the excellent coordination during the project and for the unbalance response measurements.

Appendix

Definition of the Damping Ratio.

$$D = \frac{\text{Re}(\text{Eigenvalue})}{|\text{Eigenvalue}|} \approx \frac{\log(\text{Decrement})}{2 \cdot \pi} \approx \frac{1}{2 \cdot \text{Ampl.Factor}}$$

Base Function (MEDYN Function "Base" [1]). The base function is a modified PID-controller. The function has the following structure:

$$F_{\text{base}} = \frac{\left(P_{n1} + \frac{(P_{n1} + P)s}{2\pi f_{n1}} \right) \left(1 + \frac{s}{2\pi f_{n2}} \right)}{\left(1 + \frac{s}{2\pi f_{d1}} \right) \left(1 + \frac{s}{2\pi f_{d2}} \right)} + \frac{(P_{n1} + P)2\pi f_{in}}{s} + P$$

phase lead/lag 1 phase lead/lag 2 integrator P-part

References

- [1] Schmied, J., and Betschon, F., 1998, "Engineering for Rotors Supported on Magnetic Bearings," *Proceedings of the 6th International Symposium on Magnetic Bearings*, Boston.
- [2] Maslen, E., et al., April 1989, "Practical Limits to the Performance of Magnetic Bearings: Peak Force, Slew Rate, and Displacement Sensitivity," ASME J. Tribol.
- [3] Proceedings of MAG '97, Session 6 & 7, 1997, "Industrial Conference and Exhibition on Magnetic Bearings," University of Virginia, Technomic, Lancaster, PA.
- [4] Lund, J. W., 1974, "Stability and Damped Critical Speeds of a Flexible Rotor in Fluid-Film Bearings," J. Eng. Ind.
- [5] Klement, H. D., 1993, "Berechnung der Eigenfrequenz und Stabilität von Rotoren mit MADYN," VDI Bericht Nr. 1082.
- [6] Nelson, H. D., and Vaugh, J. M., 1976, "The Dynamics of Rotor-Bearing Systems Using Finite Elements," J. Eng. Ind.
- [7] Schoeneck, K. A., and Hustak, J. F., 1987, "Comparison of Analytical and Field Experience for a Centrifugal Compressor Using Active Magnetic Bearings," IMechE C104/87.
- [8] Schmied, J., Nijhuis, A. B. M., and Shultz, R. R., 1999, "Rotordynamic Design Considerations for the 23MW NAM-GLT Compressor with Magnetic Bearings," IMechE Fluid Machinery Symposium, The Hague.
- [9] Franklin, G. F., Powell, J. D., and Workman, M. L., 1994, *Digital Control of Dynamic Systems*, 2nd Ed., Addison-Wesley, New York.

Application of Foil Bearings to Turbomachinery Including Vertical Operation

J. F. Walton II

H. Hesmat

Mohawk Innovative Technology, Inc.,
Albany, NY 12205
e-mail: jwalton@miti.cc

A review is made of the function of compliant surface bearings in serving the needs of modern turbomachinery. This service extends over a wide spectrum of severe operational and environmental conditions such as extreme low and high temperatures, speeds over 100,000 rpm, and the use of cryogenics as lubricants. The importance of using appropriate simulators that duplicate the actual equipment in evaluating the application of compliant bearings is demonstrated via two specific examples; one, a simulator to evaluate bearings for an air cycle machine and another for an advanced cryogenic device. In view of the known difficulties in using hydrodynamic bearings in vertical machines a new preloaded compliant journal bearing design is offered which performs as well with a vertically mounted shaft as it does in horizontal operation. In terms of the location of the first two rigid-body criticals, the test data show the compliant bearing's vertical operation to be at most 15 percent lower than for the horizontal case, whereas the maximum vibrational amplitude stayed the same for both modes of operation. This new class of hydrodynamic compliant surface journal bearings now makes possible development of oil-free machines capable of all attitude operation, such as aircraft gas turbine engines undergoing severe pitch maneuvers or machines that must be operated vertically due to space constraints. [DOI: 10.1115/1.1392986]

Introduction

With the advent of ever more sophisticated machinery operating in the most diverse and extreme environments, there is a wide range of applications and conditions where conventional bearings, be they of the fluid film or rolling element types, are not capable of meeting the extreme demands imposed on them. Previous bearing requirements of adequate load capacity or low power losses have given way to demands that the bearings function at extremely low or high temperatures or speeds in atmospheres ranging from vacuum to cryogenic fluids of negligible viscosity, all of which demands not just a simple advancement on existing designs but a breakthrough in bearing concepts required to meet the needs of these new technologies.

Compliant surface bearings combine a number of inherent features that make them prime candidates for most of these extreme applications. Combining as they do the elements of both hydrodynamic and elastic operation, their structure enables the designer to achieve the following goals: deliberate variation of fluid film shape in response to changes in speed; load and directional variation in stiffness and damping; and a built-in flexibility to yield and absorb unexpected rotor excursions. They thus offer solutions to a wide gamut of problems attending turbomachinery, air cycle machines ([1]) cryogenic turbopumps ([2]) advanced gas turbines ([3,4]) compressor ([5]), and similar modern equipment. In this kind of machinery compliant bearings have been used in speeds exceeding 120,000 rpm and loads in excess of 100 psi, and has proved to be resistant to the most adverse environmental conditions ([6,7]).

One of the major problems attending the use of rigid surface hydrodynamic bearings is that they become unstable when operated with vertical shafting. Unloaded as they are in that mode, such bearings have zero stiffness and no damping ability leading

to system instability known as half-frequency whirl. Supported partly by external agencies and partly by internal funding, MiTi has developed a preloaded compliant journal bearing design which overcomes this basic difficulty ([8,9]). Using an appropriate simulator running at speeds up to 60,000 rpm, tests were run in both the horizontal and vertical orientations yielding excellent results for the new design. The test data for vertical operation proved to be as good as for the horizontal case. Thus in addition to these bearings tolerating high speeds, temperatures, and extreme shaft excursions, they are also stable when applied in vertical machines.

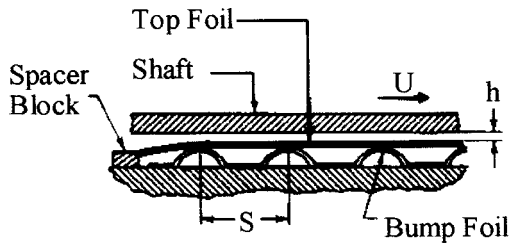
Compliant Surface Bearings (CSB)

The compliant surface bearing (CSB) combines features of fluid dynamics and elastic response which makes for a number of unique features of this device. The basic elements of such a bearing are shown in Fig. 1. One of its essential features is that it possesses a twofold mechanism for imparting stiffness and damping to the bearing. One is via the bump and top foils which are equivalent to a spring support; the other is its hydrodynamic action resulting from the fluid film between the runner or journal and the top foil. Because a CSB surface will deform as hydrodynamic pressure is generated, the bearing can be constructed to deform in an advantageous manner for a particular application, be it high load capacity, high speed operation, or stability. Frictional damping can also be introduced through the rubbing of its component parts. This takes place via relative motion between the bumps and the adjacent upper and lower surfaces producing what is known as Coulomb friction.

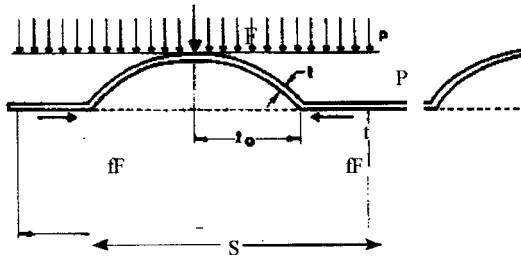
The construction of a CSB consist of two parts; a smooth top foil which constitutes the bearing surface, and a flexible corrugated foil strip formed by a series of bumps to provide resilient support to this surface. The bump foil strip is welded or otherwise fixed at one end of the bearing housing with its other end free. Consequently the bumps near the free end have a higher deflection, whereas the fixed end has a higher stiffness.

Journal Bearings. As shown in Fig. 2(a) a single top foil, which may extend up to 360 deg, forms the equivalent of a full

Contributed by the International Gas Turbine Institute (IGTI) of THE AMERICAN SOCIETY OF MECHANICAL ENGINEERS for publication in the ASME JOURNAL OF ENGINEERING FOR GAS TURBINES AND POWER. Paper presented at the International Gas Turbine and Aeroengine Congress and Exhibition, Indianapolis, IN, June 7–10, 1999; ASME Paper 99-GT-391. Manuscript received by IGTI Oct. 1998; final revision received by the ASME Headquarters Mar. 1999. Associate Editor: D. Wisler.



(a) Basic Elements of Bearing



(b) Configuration of Bump Foil

96-0022 b

Fig. 1 Elements of compliant surface bearing

bearing. Figure 2(b), on the other hand, forms the equivalent of a multipad journal bearing. Here the clearance geometry required to generate a hydrodynamic film is provided by the elastic deflection of the foils. As speed increases the top and bump foils are radially deflected forming a converging wedge. Thus a proper shape for hydrodynamic action is generated without the need for prior machining. Furthermore, this convergence becomes more pronounced with increasing speed and load. The more pronounced convergence enhances stability through a reduction of the bearing's cross-coupling dynamic coefficients ([10,11]). The overall merits of the CSB's versus conventional designs is illustrated in the analytical results obtained for two equivalent designs. Figure 3 shows that due to foil compliance, a CSB has a more uniform film thickness resulting in a larger h_{min} and, correspondingly, a more uniform pressure distribution with lower peak pressures. The latter will result in lower stresses and lower peak temperatures.

Thrust Bearings. Figure 4 shows the configuration of compliant surface thrust bearing. All the characteristics stated in connection with the journal bearing apply here as well, except that the film thickness is different. Initially, the bearing is given an appropriate converging shape, in most cases that of a composite surface, that is one in which the leading portion has a constant slope, fol-

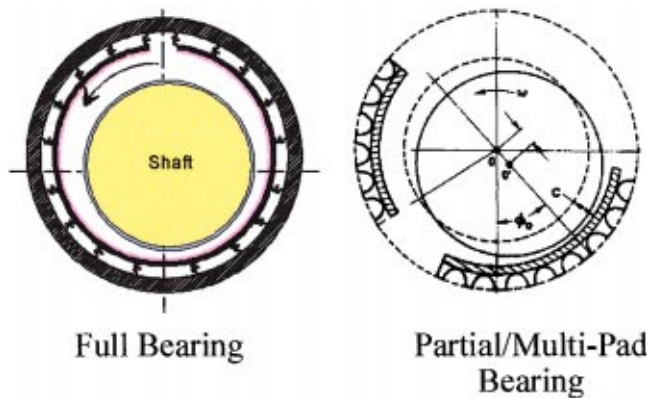
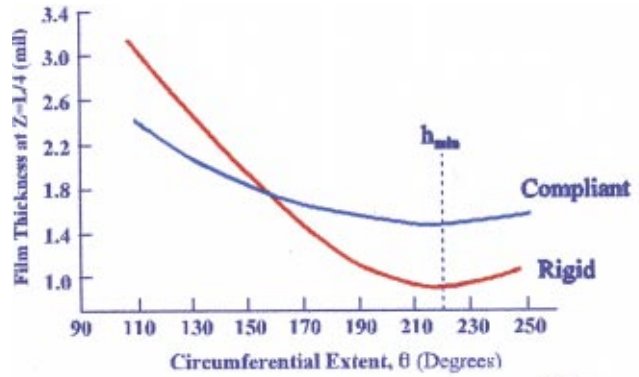
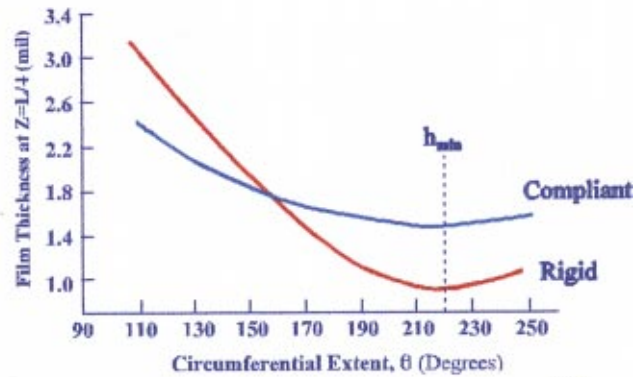


Fig. 2 Compliant surface journal bearing types



(a) Film Shape

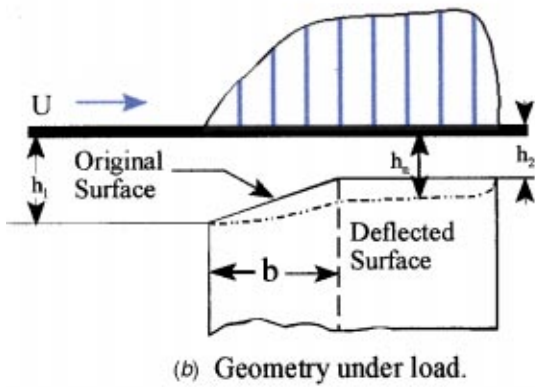
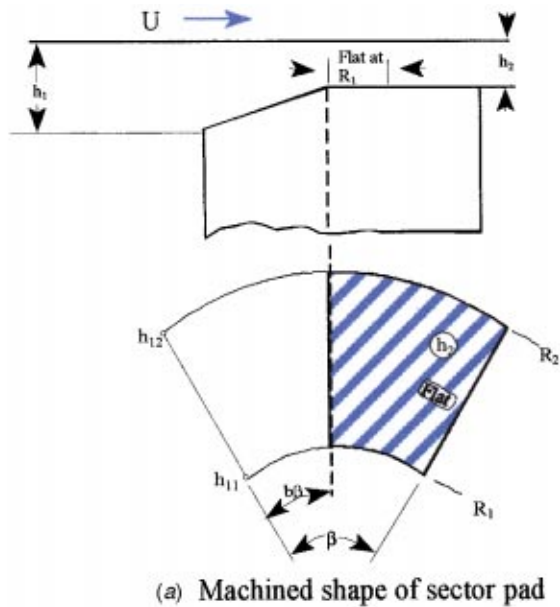


(b) Pressure Profile

Fig. 3 The hydrodynamics of rigid and compliant surface bearings

lowing which the surface is parallel to the runner. When loaded, the original shape is modified producing essentially three regions; an initial converging wedge, then a more or less parallel section, and an extremely narrow periphery at the sides and the exit which represents the domain of minimum film thickness. A cross section of such a film at $r = \text{const.}$ in both its original shape and after deflection is given in Fig. 4(b). In an optimization study of a gas lubricated CSB the optimum dimensions were found to be a pad having the geometry of $(R_2/R_1) = 2$ and $\beta = 45$ degrees with its geometry as designated in Fig. 4 ([10]). In rigid thrust bearings the ramp portion is usually of the order of 70–80 percent of the total bearing arc. With CSBs the parameter “b” that denotes the fraction of pad angle occupied by the ramp is much smaller, of the order of one half or less. Likewise the optimum ratio (h_1/h_2) which in rigid bearings is around 2.2, is much higher in compliant bearings.

Advanced Designs. The construction of CSBs lends itself to a number of modifications that can enhance the particular performance characteristic in accordance with operational requirements. The bump foil design can be manipulated to provide a wide range of desirable dynamic characteristics. One such arrangement can vary the stiffness in both the radial and circumferential directions is shown in Fig. 5. The stiffness gradients permit the formation of a variable hydrodynamic wedge in accordance with variations in load and speed. As speed increases the particular arrangement can be made to increase convergence which enhances stability when it is most needed. In one such application an advanced air lubricated journal bearing reached speeds of 132,000 rpm carrying a load of 100 psi ([7]). Much of the above applies also to thrust bearings.

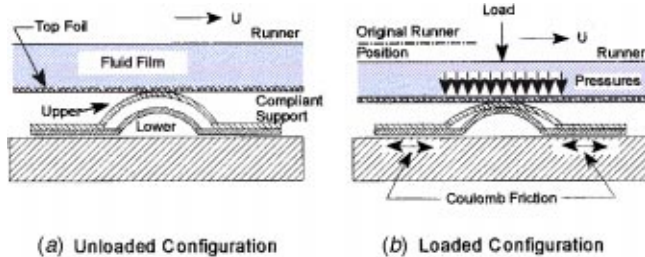


98-0340

Fig. 4 Compliant surface thrust bearing

Such a bearing can be constructed with a foil possessing stiffness elements at the trailing edge, as portrayed in Fig. 5(b). The stiffening elements placed between top and bump foils provide a variable stiffness gradient from the leading to trailing edge yielding the desired convergence wedge.

A CSB can also be made to incorporate internal damping and thus enhance stability. This can be done by affecting the Coulomb friction due to the relative motion between the top and bump surfaces, as well as between the bump foil and the housing as sketched in Fig. 6. This relative motion occurs when the bearing is



96-0320

Fig. 5 Bearing construction for variable stiffness

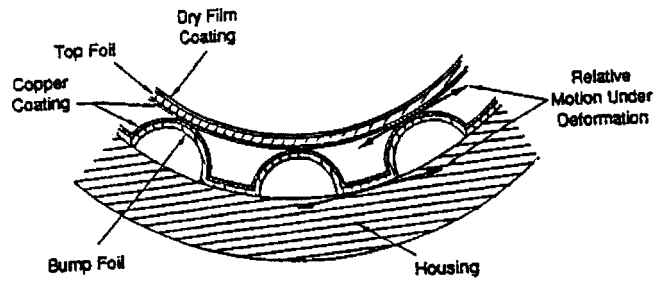
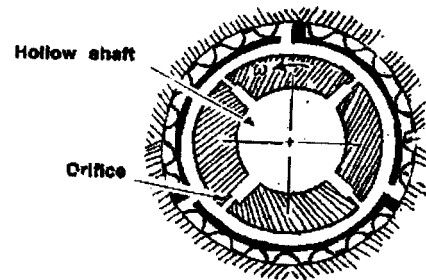


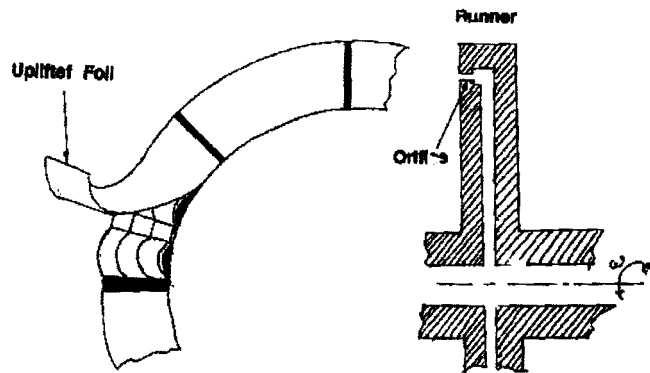
Fig. 6 Mechanisms of Coulomb friction

loaded and the foils are deflected. To improve the friction characteristics of this relative motion, the rubbing surfaces may be sputter-coated with copper, silver, or some other high friction material. Sometime the surfaces of the journal and mating top foil are coated with a dry lubricant to minimize friction upon startup and shutdown. To further enhance stability the bump foils can be split axially along circumferential lines to improve alignment and axial compliance.

Hybrid Bearings. The essence of hydrostatic compliant journal bearing fed with lubricant through the rotating shaft is shown in Fig. 7(a). A hydrostatic thrust bearing fed through eight orifices which yields more or less the optimum square pad configuration is shown in Fig. 7(b). The pressurized fluid can, of course, be either a liquid or a gas. An example of the kind of loads such a thrust bearing can support for a given supply pressure is shown in Table 1.



(a) Journal Bearing



(b) Thrust Bearing

Fig. 7 Hybrid hydrostatic/hydrodynamic compliant surface bearings

Table 1 Hybrid thrust bearing load capacity as function of supply pressure ($R_2/R_1=1.4 P_a=250$ psia)

Ps, psia	Ps/Pa	W, lbs
1000	4	1650
2000	8	4620
3000	12	6040

Foil Bearing Applications

Operational Areas. CSBs have been applied successfully in a wide spectrum of turbomachinery equipment. The use of these bearings reduces system complexity and maintenance costs and increases efficiency and operating life. Since CSBs will deform as hydrodynamic pressure is generated the bearings can be constructed to suit specific applications.

By selecting material combinations and proper elastic foundations, optimized design can be achieved for best performance under given operating conditions. CSBs offer the following advantages as compared to conventional rigid hydrodynamic gas bearings:

(a) *Higher Load Capacity.* In terms of the usual load-to-film thickness relation, the foil bearing will, for a given load, have a higher minimum film thickness.

(b) *Lower Power Losses.* The prevalence of higher film thicknesses results in lower viscous shear losses. With gas as a lubricant they have minimal power losses.

(c) *Tolerance to High Temperatures.* Higher film thickness and proper response to loadings yields a much lower temperature rise in the fluid film. A CSB is also less likely to suffer from thermal distortion.

(d) *High Speed Operation.* Due to their ability to yield under load they can endure substantially higher surface velocities.

(e) *Tolerance of Debris.* The bearing's conformity makes it possible to tolerate and eject foreign matter that may enter the clearance space.

(f) *Self-Alignment.* Due to the flexibility of the entire bearing assembly it can easily accommodate misalignment as well as any unexpected excursions of the runner or journal be it due to acceleration, shock, or any other unexpected maneuver.

(g) *Tolerant of Thermal Gradients.* Due to the bearings compliance in all three axes thermal gradients are more readily accommodated.

However, as already indicated above, the most important attribute of CSB's is their ability to respond to the dynamic requirements of the system they serve. Bearing stiffness is primarily a

Table 2 Industrial usage of foil bearings air cycle machines

Application	Journal Bearing Diameter (in)	Rotor Weight (lb)
General aviation ACM	0.8	0.55
F-16 and F-18 ACM	1.2	1.3
A7E cooling turbine	1.5	1.5
C-5A Tire Pump—Turbocompressor	1.0	2.5
	1.4	2.8
727 cooling turbine	1.8	4.3
53A cooling turbine	1.8	5
F-14 turbine compressor	1.9	6
F-15 ACM	2.0	7
767 ACM	2.0	9
DC-10 three-wheel ACM	1.375	10
747-ACM		
Gas Turbines		
AGT 101 advanced	1.3	3.0
Automobile gas turbine	1.8	5.0
Navy APU turbine	1.5	9.0
18-kW closed-cycle gas Turbine	3.0	35
GTCP 165		

function of the elastic properties of the foils. This provides great flexibility for tuning the stiffness to meet the specific needs of the machine. A field of variable spring coefficients distributed in the circumferential, radial or, in journal bearings, the axial directions enables the designer to reach optimum conditions from a rotordynamic standpoint. This would yield desirable performance in terms of the location of system resonances and of minimizing vibrations either at or outside the encountered critical speeds. The elastic structure also provides high shock absorbing capacity. In a certain sense a CSB duplicates one of nature's ingenious mechanisms imparted to human and animal joints when under increased load or during shock the stiffness and damping of a joint is automatically boosted to enable it to absorb the impact before damage is caused to the joint. A CSB likewise produces higher stiffness and higher damping capacity the higher the applied load.

Industrial Applications. The most successful foil bearing applications to date have been in air cycle machines for cabin pressurization and cooling. One such typical application is shown in Fig. 8. On the Boeing 747 they have accumulated more than a million flight hours and demonstrated a mean interval between replacements in excess of 100,000 hours. They are also being used on the FALCON-2000 and the MIRAGE military aircraft. For these applications the bearings were required to operate at close to 100,000 rpm with dynamic loads exceeding the steady load by an order of magnitude. A particularly successful area of application has been the field of cryogenic devices where due to extreme

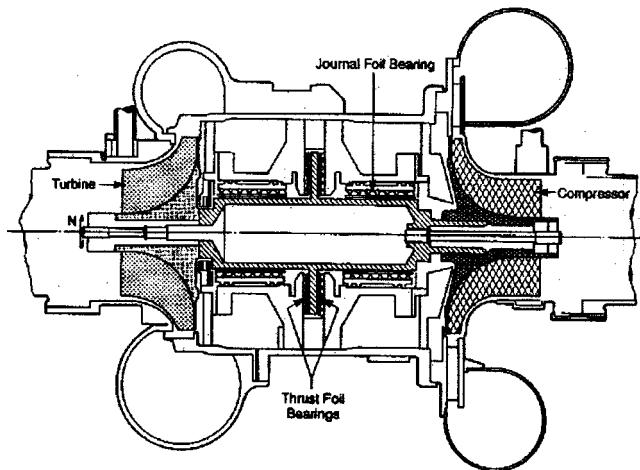


Fig. 8 Air cycle machine with compliant surface bearings

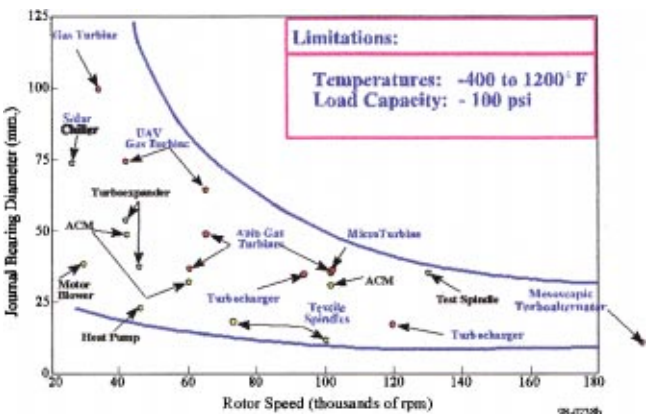


Fig. 9 Spectrum of industrial applications using compliant surface bearings

temperatures and the low viscosity of cryogenics, conventional hydrodynamic or rolling-element bearings have difficulty operating or lasting for any appreciable length of time. Some of the CSBs tested for application in the SSME turbopumps have demonstrated the ability to carry loads up to 300 psi, with a damping capability of 40 lb-sec/in. They ran successfully up to 50,000 rpm, 50 percent above the system's bending critical.

The spectrum of industrial air cycle machine and gas turbine applications employing self-acting hydrodynamic compliant surface bearings is shown in Table 2. A mapping of past and potential applications in terms of rotational speeds involved is given in Fig. 9.

MiTi Simulators

In order to evaluate performance of complex turbomachines to be equipped with compliant surface bearings it is MiTi's practice to construct simulators that are as much as possible dynamic duplicates of the configurations of the actual machines. Two such examples will be cited here to illustrate the equipment and instrumentation employed and the performance data recorded in studying CSB equipped machinery.

Air Cycle Machine Simulator. When a simulator is built it is endeavored that it have a mass distribution and inertia close to the prototype. Figure 10 shows a simulator which was built to evaluate journal bearings for an air cycle machine. The rotor was driven by an air turbine and its lateral motion measured with four displacement probes. Two probes were mounted orthogonally in a plane between the bearings and the other two toward the end of the rotor simulating the turbine. A tachometer measured the speed of the simulated compressor. A tradeoff study was then conducted to evaluate system response to different bearing positions, levels

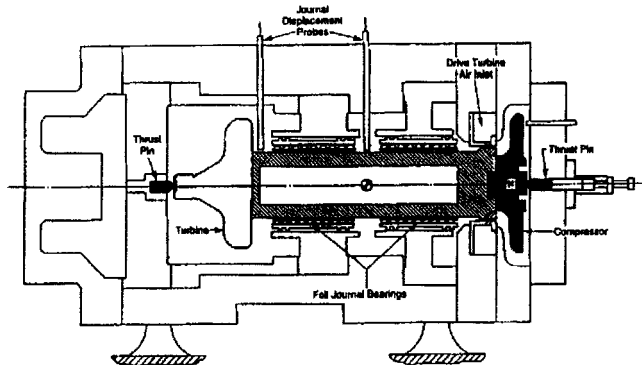


Fig. 10 Simulator for air cycle machine

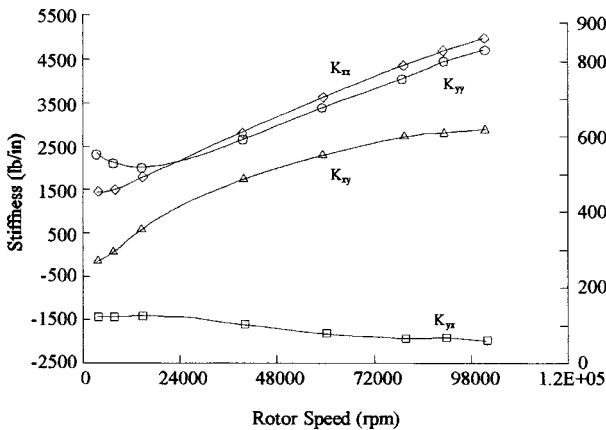


Fig. 11 Stiffness of bearings for air cycle machine (ACM) application

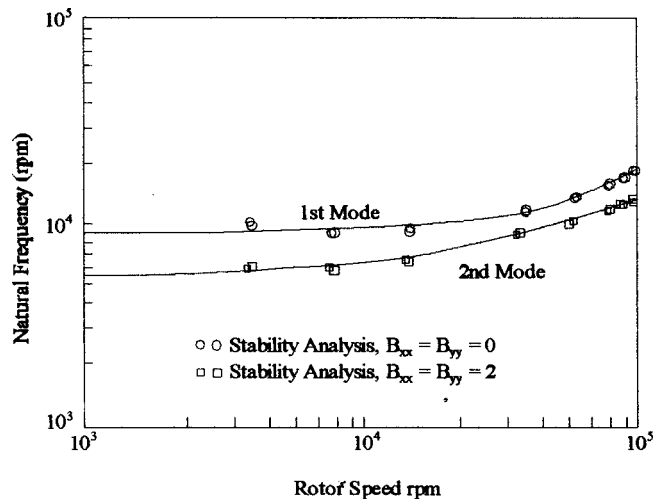


Fig. 12 Critical speeds and damping coefficients of air cycle machine (ACM) bearings

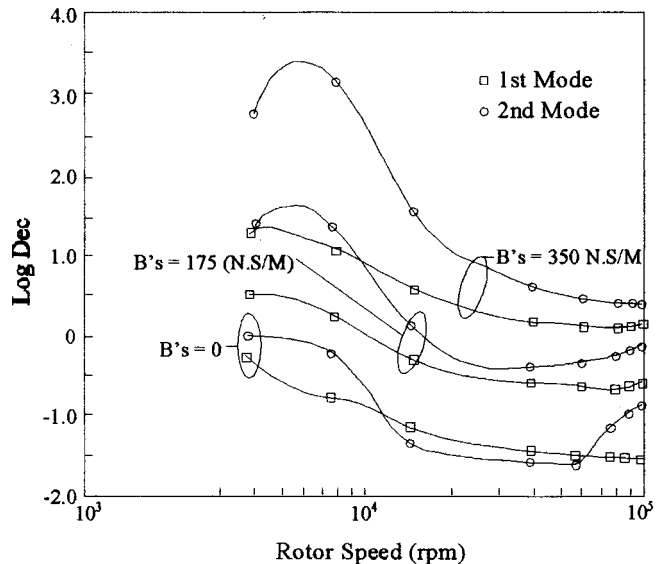


Fig. 13 Log decrement of air cycle machine (ACM) bearings

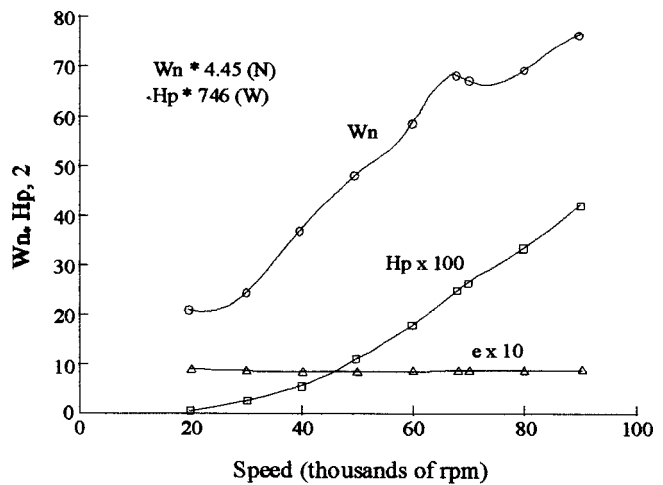


Fig. 14 Performance characteristics of the air cycle machine (ACM) bearings

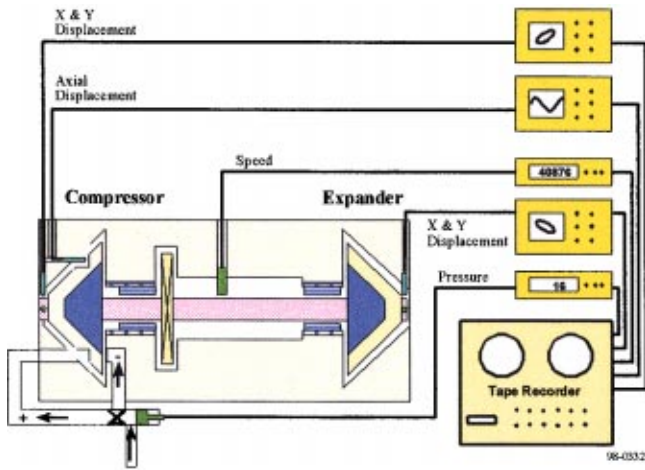


Fig. 15 Simulator for the cryogenic device

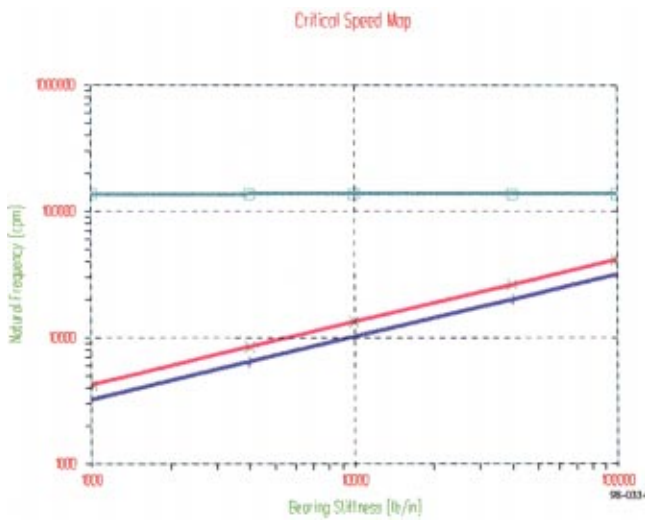


Fig. 16 Calculated critical speeds for the cryogenic rotor system

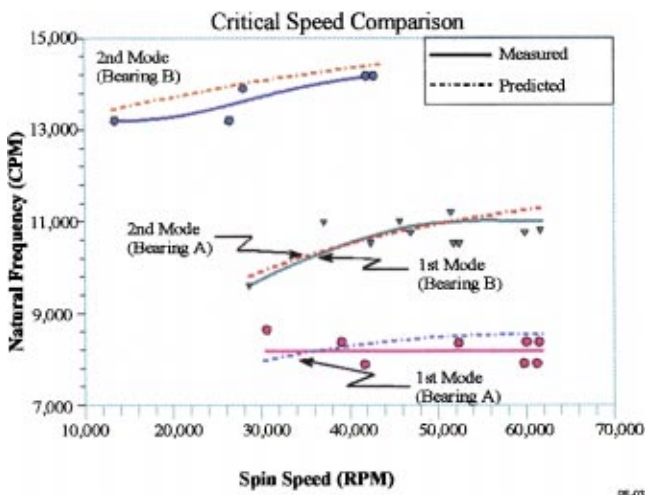


Fig. 17 Measured critical speeds of cryogenic rotor system

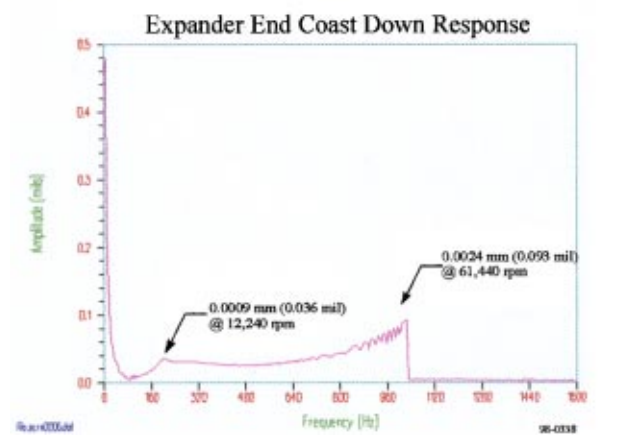
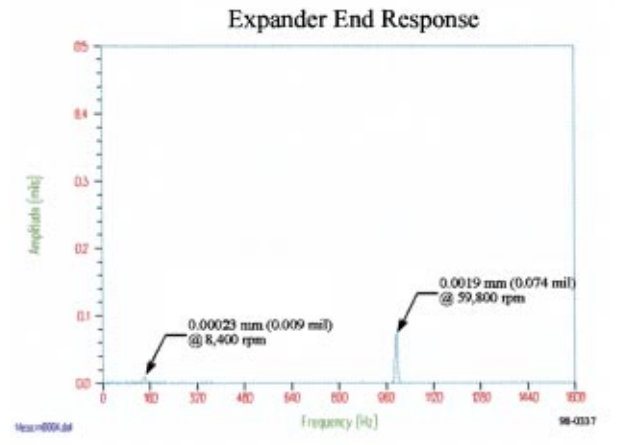
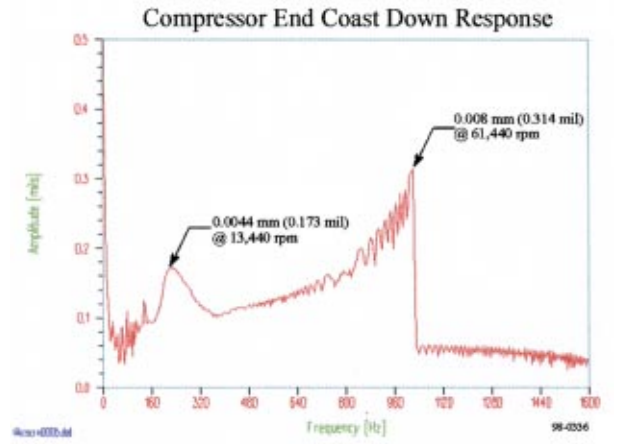
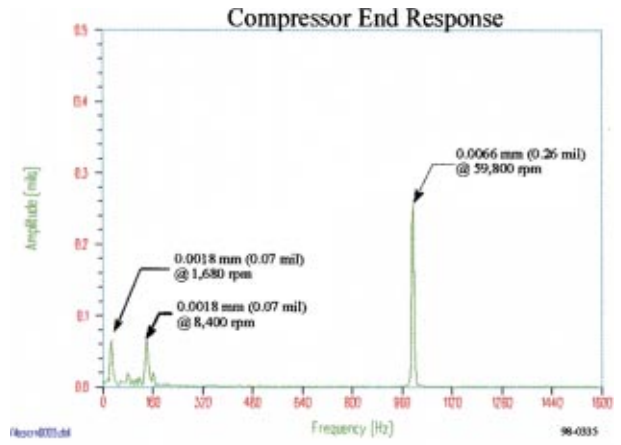


Fig. 18 Instantaneous and peak hold vibration plots for the cryogenic rotor system

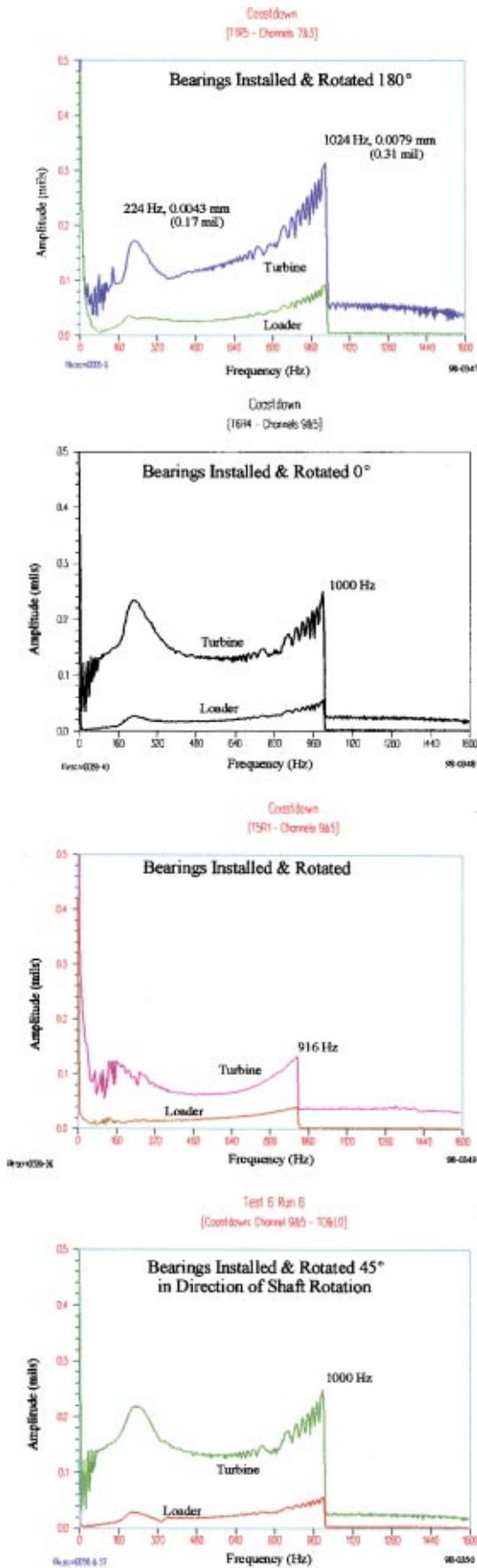


Fig. 19 Peak hold coast down for the different bearing angular orientations

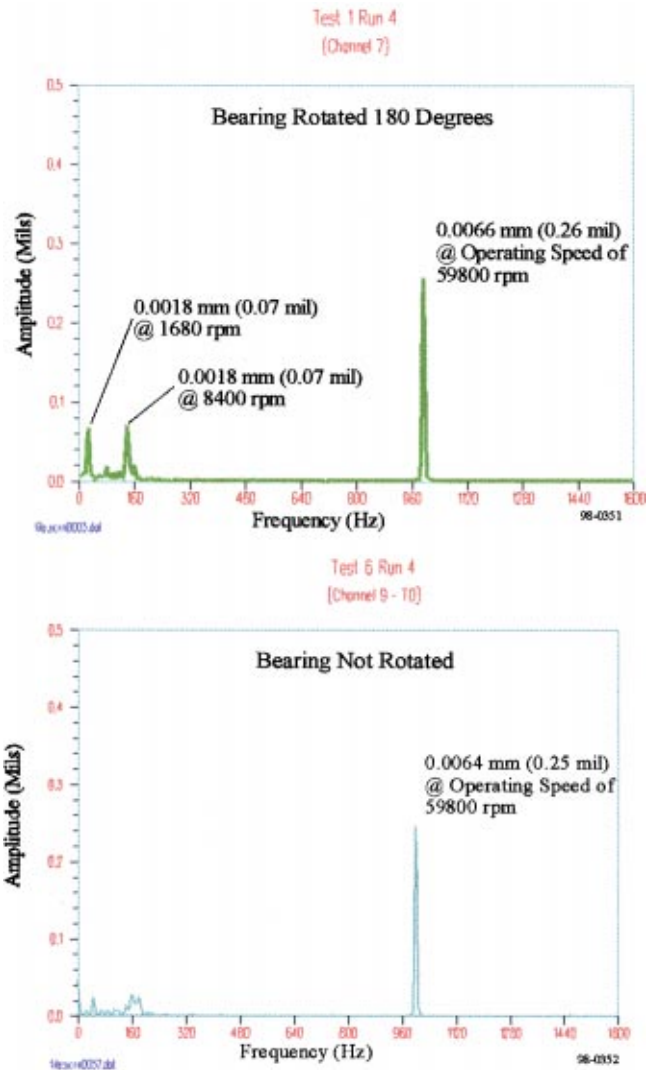


Fig. 20 Instantaneous fast Fourier transform (FFT) plots for two different bearing angular orientations

of bearing stiffness and damping and rotor unbalance. These characteristics were recorded for speeds up to 100,000 rpm and temperatures up to 300°F.

Figure 11 represents the bearings' dynamic characteristics while Fig. 12 shows plots of the first two rigid-body criticals as a function of speed and bearing damping coefficients ranging from zero to 350 N-sec/m (2 lb-sec/in.). Using the obtained stiffness and damping coefficients, frequency of vibration, log decrement, and precession direction for the conical and translatory modes were predicted. Figure 13 shows the rotor-bearing system stability map for speeds up to 100,000 rpm.

This mapping indicates the level of damping required to achieve a positive, that is a stable, value of the log decrement for the two most troublesome rigid-body modes. Figure 14 summarizes the compliant bearings' predicted performance in terms of load, eccentricity ratio and power loss as a function of speed. Thus the entire range of performance and dynamic characteristics for the system have been specified.

Cryogenic Test Rig. A schematic representation of the test rig designed to simulate a cryogenic turboexpander is shown in Fig. 15. The rotor, supported by a pair of compliant journal as well as a thrust bearing, is driven by an integral impulse-type air turbine. The impulse turbine was selected because it imparts very

Table 3 Simulator bearing performance versus design requirements

Design Category	Design Requirements	Demonstrated
Start/stop cycles (bearing static load)	5000 (Static Load <2psi)	0.76 psi Static Load-Expander 1.03 psi Static Load—Brake 90 start-stop cycles completed with no visible distress— In excess of 30,000 Start-Stop cycles demonstrated in similar applications
Maximum speed	48,000 rpm	70,000 rpm
Operating thrust load	±45. lb. @48,000 rpm	Greater than ±120 lb.
Axial motion limit	0.1524 mm (0.006 in.) At 48,000 rpm	±0.147 mm (0.0058 in) at 80 lb. load and 30,000 rpm
Allowed dynamic radial motion	0.102 ±.0254 mm (0.004±0.001 in.)	0.051 mm (0.002 in.), during start up. Max nominal motion of 0.0084 mm (0.00033 in.), during shut down at ≈330 Hz (19,800 rpm), Max steady state motion at 1000 Hz=0.0064 mm (0.00025 in.)
Allowed static liftoff motion	0.051 mm (0.002 in.)	<0.051 mm (0.002 in.)
Allowed cooling flow	6 CFM @40 psi & 70°F	5 CFM @10 psi Maximum-Nominal flow 1-2 CFM to prevent contamination exhaust
Critical speed	Operating range free of critical speeds	Critical speeds at 8,400 10,560 and 13,200 rpm <i>f</i> (stiffness)
Stability	stable throughout operating speed range	Steady state vibrations at subsynchronous rigid body mode frequencies controlled and limited in magnitude.

little thrust load during operation thereby allowing a test configuration to be assembled for testing at known thrust loads levels. To ensure dynamic similarity between the test rig and the actual intended application, the inertia properties of the turbine wheel were designed to match as closely as possible the expander wheel. The simulated compressor/brake was also designed to match the inertia properties of actual application and was used with corresponding seals for load testing of the thrust bearing. Cooling air at pressures ranging from 2 to 10 psi and a temperature of 20°C was supplied at the outer radius of the thrust bearing at a rate of 1–2 cfm. The simulator was instrumented with a magnetic pickup to determine rotor speed, two sets of eddy current displacement probes to measure the rotor displacement orbit near each journal bearing and one probe to measure axial motion. All probe outputs were recorded on a racal store-14 FM multitrack magnetic tape. The rotor orbits were displayed on an oscilloscope and a fast Fourier Transform signal analyzer was used to locate resonant and harmonic frequencies.

The predicted and measured critical speeds for the rotor in the horizontal orientation are shown in Figs. 16 and 17. Figures 18 through 20 summarize the test results. Figure 18 presents both instantaneous and peak fast Fourier transform FFT plots of rotor vibrations up to a speed of 61,400 rpm. It shows that vibrations on the brake end are larger than on the expander side. In each case subsynchronous vibrations are present but they are significantly weaker than the synchronous component which is itself quite small—a maximum of 0.008 mm (0.314 mils). The coast-down plot also indicates that the rigid-body critical speeds are well damped as evidenced by the broad peak at about 13,400 rpm (the second mode). Tests were also run for the bearings installed at different angular orientations (i.e., free end of bearing top foil located at different angular position relative to rotor gravity load) to find a preference in terms of system behavior. Changing the bearing angular orientation was achieved by rotating its support shell inside the simulator bearing housing. Altering the angular orientation of the bearing with respect to the gravity load affects the formation of the converging wedge and hence bearing perfor-

mance as was noted above. As shown in Figs. 19 and 20 the rotor remained stable and under control throughout the range of speeds tested regardless of bearing angular position.

Table 3 summarizes the overall performance of the CSB equipped simulator vis-a-vis the specified turboexpander requirements. All major specifications were successfully met over a range of speeds up to 70,000 rpm. Thus, for example, the maximum demonstrated thrust bearing load capacity of 120 lbs exceeded the 45 lbs load requirement while speeds used were beyond the requirement of 48,000 rpm. While a maximum axial motion of 6 mils was set at the operating load of 45 lbs this restriction was not exceeded even at loads at 80 lbs, almost double the specified condition.

Vertical Operation

Problem With Vertical Shafts. One of the major problems encountered in hydrodynamic bearing operation is when they are used with vertically mounted shafts. In horizontal shafting there is always at least some static load due to gravity and therefore journal bearings operate at some eccentricity which helps produce a convergent clearance and thus hydrodynamic pressures. In vertical operation the effects of gravity are absent and, as is well known from both theory and experience, a centrally operated shaft is liable to produce instability referred to either as half-frequency whirl or oil whip. If one were to calculate the spring and damping coefficients in a conventional bearing one would note that as the eccentricity of the journal approaches zero so, too, do the stiffness and damping of the bearing.

It is in view of this common difficulty with conventional hydrodynamic bearing designs that an attempt was made to design a compliant journal bearing which would overcome this inherent problem. For this purpose the simulator described in Section 4.2 was turned 90 deg on its side and mounted on a pedestal enabling it to operate with a vertically mounted rotor equivalent to a zero radial load. The bearings tested were circular compliant bearings with the inner foil inserted in such a way as to given it an initial

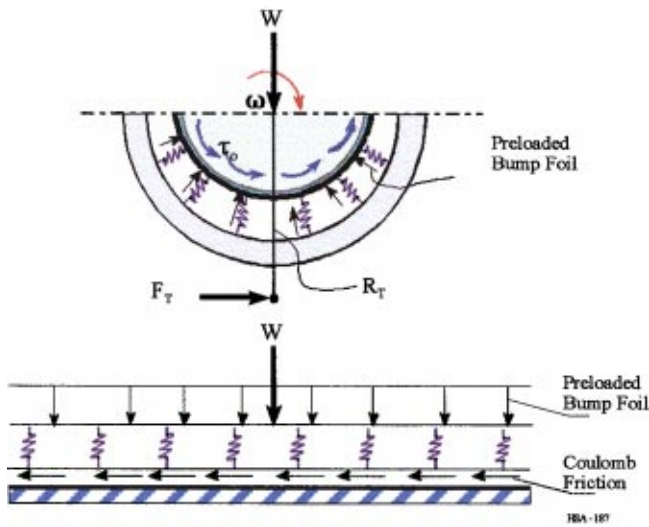


Fig. 21 The preloaded compliant journal bearing

preload. The preloaded bearing is shown in Fig. 21 while the test rig, stood on its end, was the one previously shown in Fig. 15.

Test Results With Vertical Operation. Measurements were taken of the shaft excursions versus rotor speed over a range up to 60,000 rpm with the rotor in both vertical and horizontal orientations. From Figs. 22 and 23, the effect of rotor orientation on the first and second rigid-body critical speeds can be determined. With the rotor horizontal and the dead weight or rotor gravity load supported by the bearings, the first two critical speeds were observed at 260 Hz (15,600 rpm) and 315 Hz (18,900 rpm). The maximum rotor excursion for both of these modes was approximately 0.0061 mm (0.24 mils). For the rotor in the vertical orientation (i.e., zero gravity load on the bearings), the first and second critical speeds were observed at 220 Hz (13,200 rpm) and 280 Hz (16,800 rpm) respectively. The maximum rotor excursion occurred at the second critical speed during the coast down and was approximately 0.0066 mm (0.26 mils). These results are indeed impressive in that the stiffness and damping characteristics of the pre-loaded compliant surface gas bearing in the vertical operation

Comparison of Rotor Response for Vertical and Horizontal Orientation

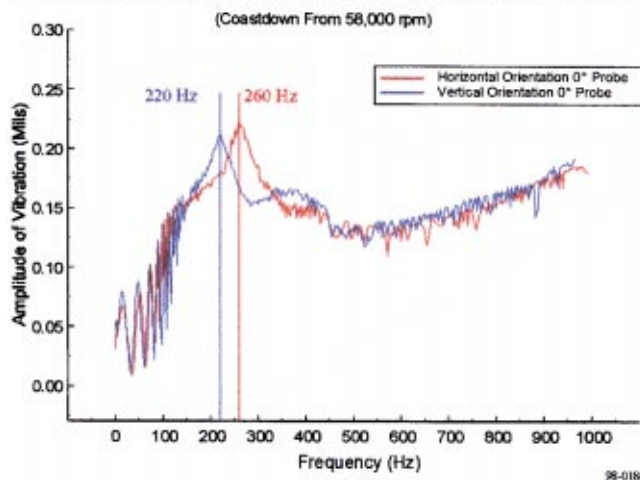


Fig. 22 Comparison of horizontal and vertical rotor operation, Mode 1

Table 4 Comparison of measured and calculated critical speeds

	Measured, rpm		Calculated, rpm	
	Mode 1	Mode 2	Mode 1	Mode 2
Horizontal Operation $K_{xx}=21,500$ lb/in	15,600	18,900	14,573	19,033
Vertical Operation $K_{xx}=16,000$ lb/in	13,200	16,800	12,620	16,392

differed little from the horizontal setup. Specifically, the critical speed variations were less than 15 percent and vibration amplitudes almost none at all.

Next, using appropriate values of spring constants, a lower one for the vertical and a higher one for the horizontal case a stability analysis was run to calculate predicted critical speeds for both rotor orientations. For the horizontal case a $K_{xx}=21,000$ lbs/in. was used whereas for the vertical case $K_{xx}=16,000$ lbs/in. Table 4 shows the results of the calculated two modes versus the measured data as recorded in Figs. 22 and 23. The impressive closeness of results attests again to the reliability of the stiffness values assigned to the compliant bearings as well as of the analytical methods used to calculate the stability criteria of critical speeds, log decrements, etc. The same stability analysis used to calculate the data in Table 4 was employed to obtain the damping required for stable operation, namely a positive log decrement value. This yielded a required damping of 2–3 lbs-sec./in. In a coast-down test the rotor in vertical operation remained stable throughout the range of decreasing speeds. This provided a solid indication that the Coulomb friction built into the preloaded foil elements provided sufficient damping to impart stability to the system over its entire range of operation.

Figure 24 provides a qualitative representation of the stability behavior of a system equipped with preloaded CSBs running with a vertical shaft. The first thing to note is that on such a plot conventional bearings would show zero values for their stiffness and thus criticals at very low speeds. With negligible damping in such bearings the rotor would most likely become unstable with high amplitudes of vibration posing a serious threat to the installation. For a horizontal rotor position the criticals would be relatively high on the curves corresponding to high values of bearing stiffness. For vertical operation the locations of the first and sec-

Comparison of Rotor Response for Vertical and Horizontal Orientation

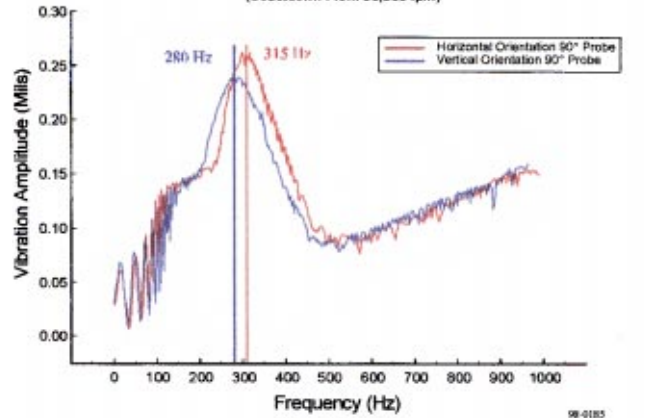


Fig. 23 Comparison of horizontal and vertical coast-downs, Mode 2

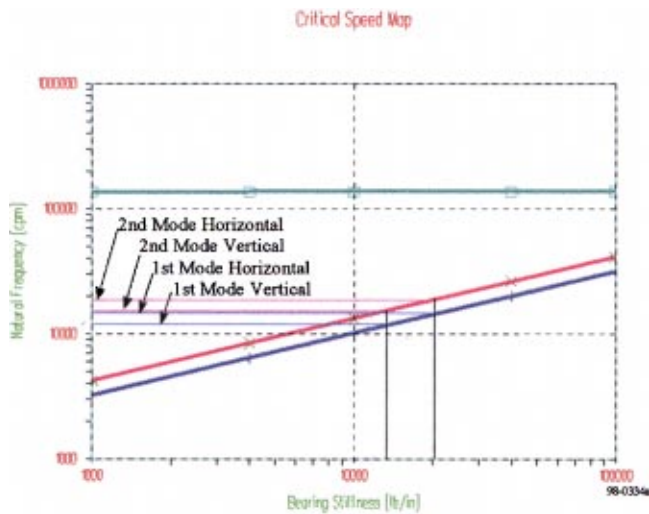


Fig. 24 Generalized plot of rotor critical speeds for horizontal and vertical operation

ond modes would be lower as will the values of bearing stiffness. However, they would be not far from those encountered in horizontal operation.

Conclusions

This paper has presented results of an analytical and experimental investigation into the application of compliant surface gas bearings to advanced oil-free rotating machinery. Investigations of an air cycle machine were presented showing close correlation between design and practical implementation in an operating machine. This was followed by a presentation of design and test results for a cryogenic turboexpander. Good correlation was achieved between predicted and measured critical speeds for the turboexpander supported on compliant surface hydrodynamic gas bearings. In particular, it was shown that the rotor could be operated in either the vertical or horizontal orientation with little difference in dynamic performance of the rotor system. The demonstrated all attitude capability overcomes the major half-frequency whirl limitation observed in conventional hydrodynamic bearings and thereby provides opportunities for developing a whole a new

class of oil-free machines. This demonstration therefore confirms the successful implementation of a new class of pre-loaded compliant surface hydrodynamic gas bearings that are suitable for use in oil-free rotating machinery independent of operating orientation. This new class of bearings now makes possible development of oil-free aircraft gas turbine engines capable of transitioning from level flight to a vertical operation without experiencing instability. Further the ability to operate with the bearing at different angular orientations will also permit aircraft roll operations with little or no degradation in performance. Other machines that must be operated vertically due to space constraints such as some cryogenic pumps or turbochargers will also benefit from this bearing design.

Acknowledgments

The authors would like to thank Mohawk Innovative Technology, Inc. for the technical and financial support for this effort. Mr. Michael Tomaszewski is also acknowledged for his support in the testing, data reduction and fabrication and installation of the bearings. Finally, the authors would like to thank Prof. Oscar Pinkus for his invaluable contributions and support in preparing this paper.

References

- [1] Emerson, T. P. 1976, "The Application of Foil Air Bearing Turbomachinery in Aircraft Environmental Control Systems," ASME Paper No. 78-ENAS-18.
- [2] Heshmat, H., Shapiro, W., and Artiles, A., 1992, "Application of Compliant Fluid Film Bearings to the High Pressure Oxygen Turbopump of the SSME," *Proc. of Adv. Earth-to-Orbit*, NASA, May 19–22.
- [3] Suriano, F. I., 1981, "Gas Lubricated Turbine End Foil Bearing Development Program," Paper No. AFWAL-TR-81-2119.
- [4] Zorzi, E. S., and Koepsel, W. F., 1976, "Gas Lubricated Foil Bearing Development for Advanced Turbomachines," *AFAPL-TR-76-1-D14*, Vols. I and II.
- [5] Heshmat, H., 1992, "Gas Lubricated Foil Bearings for Heat Pumps with Counterrotating Heat Exchangers," ASME Paper No. 82-DET-139.
- [6] Heshmat, H., Shapiro, W., and Gray, S., 1992, "Development of Foil Journal Bearings for High Load Capacity and High Speed Whirl Stability," *ASME J. Lubr. Technol.*, **104**, No. 2.
- [7] Heshmat, H., and Hermel, P., 1992, "Compliant Foil Bearing Technology and Their Application to High Speed Turbomachinery," *Proc. of 19th Leeds-Lyons Symposium*.
- [8] Ku, C. P. R., and Heshmat, H., 1992, "Compliant Foil Structural Stiffness Analysis, Part I: Theoretical Model," *ASME J. Tribol.*, **114**, No. 2.
- [9] Ku, C. P. R., and Heshmat, H., 1992, "Compliant Foil Structural Stiffness Analysis: Part II: Experimental Investigation," *ASME J. Tribol.*, **115**, pp. 364–369.
- [10] Heshmat, H., Walowit, J., and Pinkus, O., 1983, "Analysis of Gas Lubricated Compliant Journal Bearings," *ASME J. Lubr. Technol.*, **105**, No. 4.
- [11] Heshmat, H., 1991, "Analysis of Compliant Foil Bearings with Spatially Variable Stiffness," Paper Numbers AIAA-91-2102 and -2103.

Applying the Representative Interactive Flamelet Model to Evaluate the Potential Effect of Wall Heat Transfer on Soot Emissions in a Small-Bore Direct-Injection Diesel Engine

C. Hergart¹

Diesel Powertrain Systems,
Ford Research Center Aachen,
Süsterfeldstrasse 200,
52072 Aachen, Germany

N. Peters

Institut für Technische Mechanik,
Rheinisch-Westfälische Technische
Hochschule,
Templegraben 64,
52062 Aachen, Germany
e-mail: n.peters@itm.rwth-aachen.de

Capturing the physics related to the processes occurring in the two-phase flow of a direct-injection diesel engine requires a highly sophisticated modeling approach. The representative interactive flamelet (RIF) model has gained widespread attention owing to its ability of correctly describing ignition, combustion, and pollutant formation phenomena. This is achieved by incorporating very detailed chemistry for the gas phase as well as for the soot particle growth and oxidation, without imposing any significant computational penalty. This study addresses the part load soot underprediction of the model, which has been observed in previous investigations. By assigning flamelets, which are exposed to the walls of the combustion chamber, with heat losses calculated in a computational fluid dynamics (CFD) code, predictions of the soot emissions in a small-bore direct-injection diesel engine are substantially improved. It is concluded that the experimentally observed emissions of soot may have their origin in flame quenching at the relatively cold combustion chamber walls. [DOI: 10.1115/1.1473147]

Introduction

In attempting to meet future stringent emission legislation, three-dimensional modeling of the combustion in a direct injection (DI) diesel engine has become a valuable tool for engineers to develop an understanding of the processes governing the formation of the major pollutants, NO_x and soot. Optimized computer models also allow engine developers to quickly perform trend studies, varying several parameters independently from each other.

The RIF model ([1]) offers a way of separating the numerical effort associated with solving the turbulent flow from that of the chemistry. The model is based on the laminar flamelet concept for non-premixed combustion ([2]), which views a turbulent flame as an ensemble of thin, locally one-dimensional laminar flamelets. These flamelets are strained and stretched by the turbulent flow field, but maintain their inner structure. The chemistry is solved in a one-dimensional flamelet code, where profiles of species and temperature are calculated as functions of a conserved scalar, the mixture fraction. This enables very detailed chemical mechanisms of fuels similar to diesel to be incorporated in the analysis. Processes relevant to NO_x and soot chemistry can be resolved with arbitrary accuracy. In the current investigation a model fuel comprising 70% (by volume) n-decane and 30% α -methyl-naphthalene is used to represent diesel. The reaction mechanism includes 509 elementary reactions and 109 species.

¹To whom correspondence should be addressed. Currently at Institut fuer Technische Mechanik, RWTH Aachen, Templegraben 64, 52062 Aachen, Germany. e-mail: cahe@itm.rwth-aachen.de

Contributed by the Internal Combustion Engine Division of THE AMERICAN SOCIETY OF MECHANICAL ENGINEERS for publication in the ASME JOURNAL OF ENGINEERING FOR GAS TURBINES AND POWER. Manuscript received by the ICE Division May 2001; final revision received by the ASME Headquarters November 2001. Associate Editor: D. Assanis.

The model has been extensively validated in the past against engine experiments in heavy-duty ([3]) as well as light-duty DI diesel engines ([4–6]). Ignition delay, peak cylinder pressure, and emissions of NO_x were found to be in excellent agreement with the experiments. For soot, the agreement was found to be satisfactory at higher loads and high exhaust gas recirculation (EGR) rates ([3,4]). Soot predictions at part load proved to be more of a challenge, primarily due to the rather small amounts emitted in the exhaust. Engine-out soot is governed by the difference of two large numbers representing the processes of formation and oxidation. Typically 90–95% of the soot formed is subsequently oxidized ([7]). Essentially, the model suggested that, at part load under relatively high-swirl conditions, the oxidation ought to be sufficiently efficient as to completely oxidize all soot available. Experiments, however, indicated small amounts of soot emitted under the part load conditions examined. Optical measurements ([7,8]) have shown that soot-abundant regions are present at the relatively cold combustion chamber walls, mainly in the bowl, at early stages of the combustion process. The objective of this paper is to investigate the influence of wall heat transfer on the soot oxidation process. This is done in the framework of the RIF model by introducing an additional term—the enthalpy defect—in the flamelet temperature equation, which is directly coupled to the total convective wall heat transfer calculated in the computational fluid dynamics (CFD) code.

The mathematical basis of the RIF model, its interaction with the CFD code, KIVA-3V, and the chemistry model will be discussed in the first section of the paper. Next, the experimental setup, relevant engine data, and the operating conditions will be outlined. Finally, preceding the conclusions of the study, simulations applying the extended model will be compared to part load experimental data performed on a single-cylinder version of the FORD DIATA diesel engine equipped with a first-generation Bosch common-rail injection system.

The Representative Interactive Flamelet (RIF) Model

Flamelet Code. As mentioned in the Introduction, the RIF model is based on the laminar flamelet concept. In order for it to be applicable, the chemical time scales have to be very small compared to the turbulent ones and the reaction zone has to be much smaller than the size of a Kolmogorov eddy, ensuring the inner structure of the flamelet to remain undistorted by turbulence. The governing equations for species and temperature are transformed by relating them to a conserved scalar, the mixture fraction, denoted Z . The mixture fraction ranges between zero and one, corresponding to pure oxidizer and fuel, respectively. The iso-surface of stoichiometric mixture fraction, denoted Z_{st} , defines the location of the flame surface. Scalar profiles, given as functions of the mixture fraction, are assumed to be attached to the flame surface. This enables statistical moments of reactive scalars to be obtained from the statistical distribution of the conserved scalar. Hence, it is not necessary to solve separate transport equations for the chemical species in the CFD code.

The definition of the mixture fraction employed here is governed by the following transport equation ([9]):

$$\rho \frac{\partial Z}{\partial t} + \rho v_\alpha \frac{\partial Z}{\partial x_\alpha} - \frac{\partial}{\partial x_\alpha} \left(\rho D_Z \frac{\partial Z}{\partial x_\alpha} \right) = 0 \quad (1)$$

where ρ is the density, v_α the flow velocity, and D_Z the diffusion coefficient of the mixture fraction Z . D_Z can in principle be chosen arbitrarily, but it can be shown that the flamelet temperature equation can be considerably simplified if D_Z is set equal to the thermal diffusivity. It should be noted that this definition of Z is different from that resulting from the Schvab-Zeldovich formalism, which would only allow Lewis numbers equal to unity for all species in the flamelet equations. Hence differential diffusion can be considered using the current concept, which has been discussed at length by Pitsch and Peters [10].

Following the technique described by Peters [2], the following *flamelet equations* can be derived, assuming unity species Lewis numbers, Le_i .

Temperature:

$$\begin{aligned} \rho \frac{\partial T}{\partial t} - \rho \frac{\chi}{2} \frac{\partial^2 T}{\partial Z^2} - \rho \frac{\chi}{2 c_p} \frac{\partial T}{\partial Z} \frac{\partial c_p}{\partial Z} - \sum_i^N \rho \frac{\chi}{2} \frac{c_{pi}}{c_p} \frac{\partial Y_i}{\partial Z} \frac{\partial T}{\partial Z} \\ + \frac{1}{c_p} \sum_i^N \dot{m}_i h_i - \frac{1}{c_p} \frac{\partial p}{\partial t} - \frac{\dot{q}_R}{c_p} - \frac{\dot{q}_{\Delta h}}{c_p} = 0 \end{aligned} \quad (2)$$

Species:

$$\rho \frac{\partial Y_i}{\partial t} - \rho \frac{\chi}{2} \frac{\partial^2 Y_i}{\partial Z^2} - \dot{m}_i = 0 \quad (3)$$

where terms containing derivatives of Z in directions nonperpendicular to the flame front have been neglected, since they are small to leading order. N is the number of chemical species, p is the pressure, T is the temperature, c_{pi} , \dot{m}_i , h_i , and Y_i are the heat capacities at constant pressure, the chemical production terms, the enthalpies, and the mass fractions of species i , respectively. The temperature equation has two source terms—due to radiation, \dot{q}_R , and due to wall heat losses the flamelet may be exposed to, $\dot{q}_{\Delta h}$. Radiation is calculated according to the following expression:

$$\dot{q}_R = -4 \sigma_s T^4 (\alpha_{p,CO_2} p_{CO_2} + \alpha_{p,H_2O} p_{H_2O} + \alpha_{p,s} f_v) \quad (4)$$

where σ_s is the Stefan-Boltzmann constant, α_{p,CO_2} , α_{p,H_2O} , and $\alpha_{p,s}$ are the radiation coefficients for CO_2 , H_2O , and soot, respectively. p_{CO_2} and p_{H_2O} , designate the partial pressures for CO_2 and H_2O , respectively. f_v is the soot volume fraction. The radiation coefficient for soot was taken from Hubbard and Tien [11] and the ones for CO_2 and H_2O from Müller [12]. The enthalpy defect, $\dot{q}_{\Delta h}$, accounting for the flamelet heat losses is calculated as

$$\dot{q}_{\Delta h}^l(Z) = \alpha^l (T^l(Z) - T_{wall}) \quad (5)$$

where α is the heat transfer coefficient pertaining to flamelet l and T_{wall} is the wall temperature. Interactions between soot-containing regions and the wall primarily occurs at the bowl lip, where the temperature was estimated to be 520 K under the conditions investigated here. Spatial variations of the piston wall temperature were not considered in the present study. The flamelet temperature distribution over Z is given by $T^l(Z)$. The heat transfer coefficient appearing in Eq. (5) is calculated from the following expression (see Appendix):

$$\alpha^l = \frac{\dot{Q}_{WHF}^l}{\int V_w \bar{\rho} \bar{T}_l \int_0^1 \frac{1}{\rho} (T^l(Z) - T_{wall}) \bar{P} dZ dV_w} \quad (6)$$

where it has been assumed that the heat transfer coefficient is independent of Z . \dot{Q}_{WHF}^l is the total wall heat transfer ascribed to flamelet l . \bar{T}_l , \bar{P} , and V_w is the probability of finding flamelet l , the mixture fraction probability density function (PDF), and the volume of the mixture close to the wall, respectively. The flamelet wall exposure is determined by solving transport equations for marker particles representing elements of fluid, to which the flamelets are attached. This will be further discussed in the next section.

The parameter, χ , appearing in the flamelet equations is the scalar dissipation rate, which describes the impact of the turbulent flow field on the laminar flamelet. It is defined as

$$\chi = 2 D_Z \left(\frac{\partial Z}{\partial x_\alpha} \right)^2 \quad (7)$$

This is a difficult quantity to extract from a calculation of a turbulent flow, since it requires knowledge of the instantaneous value of Z . Furthermore, it is important that the gradual homogenization of the mixture is reflected in the scalar dissipation rate ([13]). An expression derived by Pitsch [9], accounting for the displacement of the boundaries in mixture fraction space, was employed in this study to obtain the conditional averaged scalar dissipation rate used in the flamelet equations:

$$\langle \chi | Z \rangle = \langle \chi_{st} \rangle \underbrace{\left(\frac{Z}{Z_{st}} \right)^2 \frac{\ln(Z/Z_{max})}{\ln(Z_{st}/Z_{max})}}_{f(Z)/f(Z_{st})} \quad (8)$$

where it has been assumed that the left-hand boundary remains fixed at $Z=0$. The ensemble average of the conditional scalar dissipation rate at stoichiometric mixture is calculated from the following expression:

$$\langle \chi_{st} \rangle = \frac{\bar{\chi}}{\int_{Z=0}^{Z=1} \frac{f(Z)}{f(Z_{st})} \bar{P}(Z, x, t) dZ} \quad (9)$$

where $\bar{\chi}$ is modeled according to Jones and Whitelaw [14]:

$$\bar{\chi} = c_\chi \frac{\bar{\varepsilon}}{\bar{k}} \widetilde{Z}''^2 \quad (10)$$

where $\bar{\varepsilon}$, \widetilde{Z}''^2 , \bar{k} , is the turbulent dissipation, mixture fraction variance, and turbulent kinetic energy, respectively. The constant c_χ expresses the time scale ratio for dissipation of scalar and velocity fluctuations. A value of 2.0 for c_χ is used in the current study.

The pressure, the mean conditional scalar dissipation rate at stoichiometric mixture, and the enthalpy defect constitute the flamelet parameters, required in order to solve the flamelet equations.

Computational Fluid Dynamics (CFD) Code. In this investigation the KIVA-3V code was used to solve the governing equations for the turbulent, reactive two-phase flow. A detailed documentation of the computer program is contained in a series of manuals ([15–18]). The $k-\varepsilon$ turbulence model was employed in the current study. KIVA-3V was modified such that an equation for the total specific enthalpy, including species heat of formation, is solved instead of the specific internal energy. The temperature is solved for iteratively via the species mass fractions. The specific enthalpy equation appears in the following form:

$$\bar{\rho} \frac{D\tilde{h}}{Dt} = \frac{Dp}{Dt} + \nabla \cdot \left(\frac{\mu_t}{Sc_t} \nabla \tilde{h} \right) + \bar{\rho} \tilde{\varepsilon} + \tilde{Q}_s + \tilde{q}_R \quad (11)$$

where ρ , h , p , μ_t , Sc_t , and ε is the density, enthalpy, pressure, turbulent dynamic viscosity, turbulent Schmidt number, and turbulence dissipation, respectively. \tilde{Q}_s and \tilde{q}_R are the Favre averages of the source terms due to spray and radiation. It should be noted that, as opposed to the case of considering the internal energy, no transport equations for the turbulent mean values of the species need to be solved in order to compute the heat flux vector.

If several flamelets are present in the calculation, additional transport equations are solved for marker particles representing fluid elements attached to the individual flamelets. This allows the flamelets to be followed in their path through the turbulent flow field. The transport equations have the following appearance:

$$\frac{\partial(\bar{\rho}\tilde{I}_l)}{\partial t} + \nabla \cdot (\bar{\rho}\tilde{I}_l\tilde{v}) - \nabla \cdot \left(\bar{\rho} \frac{\mu_t}{Sc_l} \nabla \tilde{I}_l \right) = 0 \quad (12)$$

assuming molecular diffusion to be negligible compared to the turbulent one. A complete derivation of this equation is given by Barths et al. [19]. μ_t is the turbulent viscosity and Sc_l is the turbulent Schmidt number. I_l is the Favre averaged mass fraction of particle l within the total number of particles, n_l .

Since \tilde{I}_l expresses the probability of finding flamelet l at location \mathbf{x} and time t in the combustion chamber, the condition

$$\sum_{l=1}^{n_l} \tilde{I}_l = 1 \quad (13)$$

holds everywhere.

Turbulent mean values of the species mass fractions are calculated by summing up the solutions pertaining to the various flamelets, weighted by the probability of finding a flamelet at that location in the flow field. Mathematically, this is expressed as

$$\tilde{Y}_i(\mathbf{x}, t) = \sum_{l=1}^{n_l} \tilde{I}_l(\mathbf{x}, t) \cdot \left(\int_0^1 Y_{i,l}(Z, \tilde{\chi}_{Z,l}, t) \tilde{P}(Z; \mathbf{x}, t) dZ \right) \quad (14)$$

where $\tilde{P}(Z)$ is the Favre averaged mixture fraction PDF, describing the statistics of the conserved scalar in the turbulent flow field, and $\tilde{\chi}_Z$ is short for $\langle \chi | Z \rangle$. Girimaji [20] has shown that the β PDF is appropriate in capturing the nature of the relevant mixing processes in non-premixed combustion. This function has the attractive feature of being fully determined by its first two moments, \tilde{Z} and \tilde{Z}''^2 . It has the following mathematical form:

$$\tilde{P}(Z) = \frac{Z^{\alpha-1}(1-Z)^{\beta-1}}{I} \quad (15)$$

where I is the normalization factor

$$I = \int_{Z=0}^{Z=1} Z^{\alpha-1}(1-Z)^{\beta-1} dZ = \frac{\Gamma(\alpha)\Gamma(\beta)}{\Gamma(\alpha+\beta)} \quad (16)$$

with the parameters

$$\alpha = \tilde{Z} \left[\frac{\tilde{Z}(1-\tilde{Z})}{\tilde{Z}''^2} - 1 \right] \quad (17)$$

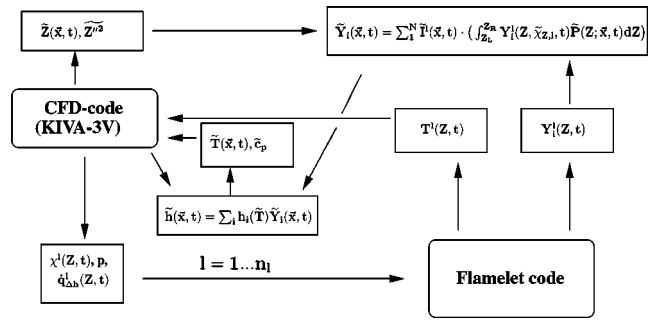


Fig. 1 Interaction between flamelet code and CFD code

$$\beta = (1 - \tilde{Z}) \left[\frac{\tilde{Z}(1 - \tilde{Z})}{\tilde{Z}''^2} - 1 \right]. \quad (18)$$

Since the turbulent mean values of the mixture fraction and its variance are needed in order to obtain $\tilde{P}(Z)$, transport equations for these have to be solved in the CFD code. They have the following form:

$$\frac{\partial(\bar{\rho}\tilde{Z})}{\partial t} + \frac{\partial(\bar{\rho}\tilde{v}_\alpha\tilde{Z})}{\partial x_\alpha} = \frac{\partial}{\partial x_\alpha} \left(\frac{\mu_t}{Sc_Z} \frac{\partial\tilde{Z}}{\partial x_\alpha} \right) + \bar{\rho}^s \quad (19)$$

$$\frac{\partial(\bar{\rho}\tilde{Z}''^2)}{\partial t} + \frac{\partial(\bar{\rho}\tilde{v}_\alpha\tilde{Z}''^2)}{\partial x_\alpha} = \frac{\partial}{\partial x_\alpha} \left(\frac{\mu_t}{Sc_{Z''^2}} \frac{\partial\tilde{Z}''^2}{\partial x_\alpha} \right) + 2 \frac{\mu_t}{Sc_{Z''^2}} \left(\frac{\partial\tilde{Z}}{\partial x_\alpha} \right)^2 - \bar{\rho}\tilde{\chi}. \quad (20)$$

Here Sc_Z and $Sc_{Z''^2}$ are the turbulent Schmidt numbers for \tilde{Z} and \tilde{Z}''^2 , respectively. In the current study both were set equal to 0.9.

Figure 1 illustrates how the flamelet code, solving the previously presented flamelet equations, interacts with the KIVA-3V program. The parameters needed to solve the flamelet equations, i.e., the mean conditional scalar dissipation rate at stoichiometric mixture, the mean pressure, and the enthalpy defect are calculated in every time-step of the CFD code and provided to the flamelet code. In addition to this, the enthalpy level in the flamelet has to be initiated the first time the flamelet code is called from the CFD code. The flamelet code produces laminar flamelet profiles, which are functions of Z only. Turbulent mean values are calculated through the procedure described above, i.e., weighting with the mixture fraction PDF, and are subsequently used to calculate the turbulent mean value of the temperature via an iterative procedure as indicated. The turbulent mean values of species, temperature, and heat capacity are finally fed back to the CFD code, which completes one computational time-step. The time-steps in the flamelet code are determined by the chemical activity, and are made sufficiently small to resolve the fastest chemical processes. During ignition, for example, a time-step in the flamelet code is typically the order of hundreded times smaller than the time-step in the CFD code.

Chemistry Model

In the reaction mechanism for n-decane used in the current work, the C_1-C_2 as well as the oxyhydrogen (O/H) chemistry was mainly taken from Baulch et al. [21]. The low-temperature kinetics have been taken from Benson [22] and Chevalier et al. [23]. In developing a reaction mechanism for α -methyl-naphthalene, Shaddix et al. [24] used the power of analogy arguing that its oxidation proceeds in a manner similar to that of toluene (C_7H_8) for which the reaction mechanism is known ([25]). Pitsch et al. [26] reduced the starting mechanism for α -methyl-naphthalene and combined it with the reduced mecha-

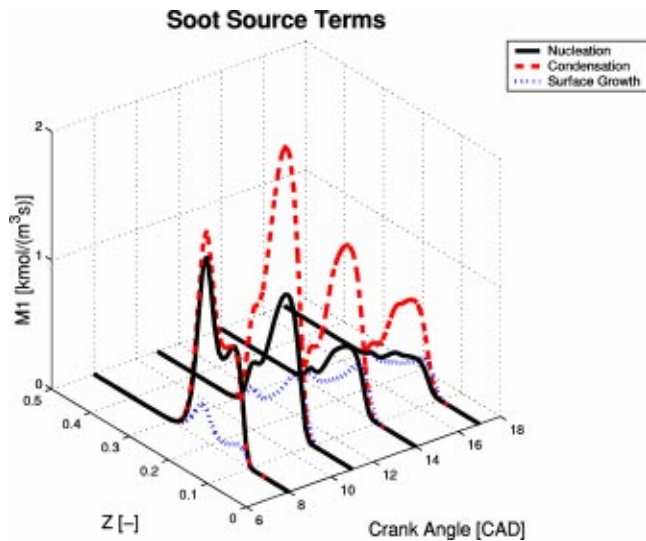


Fig. 2 Soot source terms as a function of engine crank angle in a direct-injection diesel engine

nism for n-decane. This combined mechanism is the basis for the one employed in the current work. The NO_x -mechanism used in the current study was taken from [27] and integrated into the combined reaction mechanism of n-decane and α -methyl-naphthalene. It accounts for thermal, prompt, and nitrous oxide contributions to NO_x formation, as well as NO_x reburn by hydrocarbon radicals and amines (NH_x).

The chemistry describing the formation of benzene was taken from Frenklach and Warnatz [28] and Miller and Melius [29], who included a pathway via propargyl (C_3H_3). The formation of benzene is followed by an H-abstraction/ C_2H_2 -addition sequence. This process is described in the chemistry of the gas phase up to the fourth aromatic ring. The second step in the soot model is the further growth of these small PAH. Since accounting for all possible structures of the resulting PAH would become computationally prohibitive applying standard numerical techniques, a statistical description referred to as linear lumping was proposed by Frenklach [30]. This method is based on the assumption that the growth of the PAH can approximately be described as a polymerization divided into polymerization steps consisting of a sequence of identical reactions. In one polymerization step the first PAH is thermodynamically always the most stable. Frenklach proposed solving transport equations for the PAH moments.

The first soot particles are formed when two polycyclic-aromatic hydrocarbons (PAH) coagulate. This is designated particle inception. The further growth due to coagulation, condensation of PAH onto the surface of the particles, and heterogeneous surface growth as well as oxidation by molecular oxygen and OH radicals is to a large extent fully analogous to that of the PAH. Hence, a statistical approach is used to solve for the size distribution of the soot particles [31,32]. Transport equations for the first two moments, representing particle number density and soot volume fraction, are solved in the flamelet code.

Figure 2 displays the source terms (oxidation not included) to the first soot moment as a function of time resulting from a simulation of the combustion process in a DI diesel engine under the conditions investigated in the current study. Injection started at 2.0 deg before top dead center (TDC) and the first soot starts to form in small amounts at approximately 2.0 deg after TDC. The source term due to particle coagulation has been omitted, since this process does not contribute to the growth in soot volume fraction, and is thus equal to zero at all times. It is seen that, apart from the initial phase of particle inception, condensation of PAH onto the soot particle surface is the dominating process. It should be em-

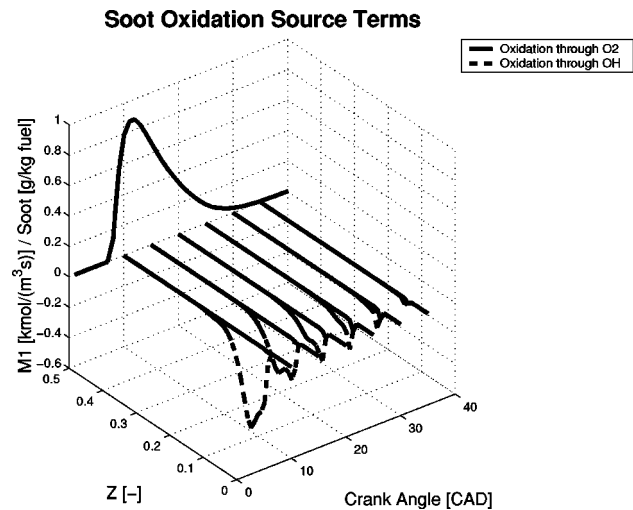


Fig. 3 Source terms owing to oxidation through OH-radicals and molecular oxygen, respectively. Additionally, total soot versus engine crank angle is shown in a case of not including any source term in the temperature equation accounting for flamelet heat losses.

phasized that this process is treated separately from surface growth in the current model. Figure 3 shows the total soot as a function of engine crank angle and the source terms owing to oxidation by OH radicals and molecular oxygen, respectively. The figure clearly demonstrates that oxidation by OH radicals is the dominating process under conditions relevant for diesel engine combustion.

Experiments

Experiments were performed on a single-cylinder version of the FORD DIATA engine, which is a small-bore DI diesel engine equipped with a Bosch common rail injection system capable of producing a maximum injection pressure of 1350 bar. Basic engine data is summarized in Table 1. Part load investigations at approximately 13–14 percent of full load—equivalent to 3 bar indicated mean effective pressure (IMEP)—varying the rail pressure at a constant EGR rate (30 percent) and SOI (2 deg before TDC) were conducted in order to validate the model. The operating conditions are compiled in Table 2. The cylinder pressure was measured with a flush mounted quartz sensor from Kistler (type 6061B), NO_x using a chemiluminescent detector (CLD) (Thermo Electron Corporation, Environmental Instruments Model 10), and for soot a 415 smokemeter from AVL was used. EGR was controlled by manually operating a valve.

The rate of injection is a very important input to the spray model. Therefore, measurements in an injection rate meter were performed at conditions corresponding to the relevant part load operating point. Figure 4 shows the measured injection rate pro-

Table 1 Engine specifications

Engine	Single-cylinder FORD DIATA
Displacement	300 cc
Bore	70.0 mm
Stroke	78.0 mm
Connecting rod	132.6 mm
Compression ratio	19.5
No. of valves	4
Injector nozzle	6-hole
Nozzle hole diameter	0.124 mm
Hydraulic flow rate	250 [cm^3 /(30 s) at 100 bar]
Spray cone angle	150 deg
Injector protrusion	1 mm

Table 2 Part load operating conditions

Engine speed	2000 rpm
Fuel	diesel
Injected fuel mass	5.0 mg
Trapped mass	350 mg
Global equivalence ratio	0.25
EGR rate	30%
Start of injection (ATDC)	-2
Injection duration	6.0, 7.0, 8.0°
Intake valve closing (IVC)	-150° ATDC
Exhaust valve opening (EVO)	160° ATDC
Rail pressures	600, 800, 1000 bar

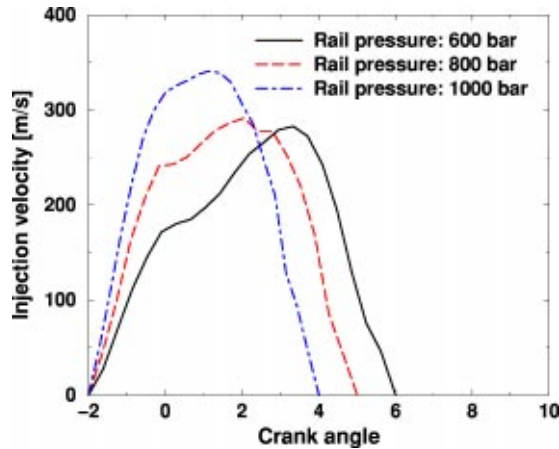


Fig. 4 Injection rates at part load corresponding to various rail pressures. The measurements were performed using an EVI injection rate meter. Crank angles apply to an engine speed of 2000 rpm.

files corresponding to rail pressures of 600, 800, and 1000 bar, respectively. The back pressure was 50 bar. These shapes were used as input in the simulations to be presented.

The thermophysical properties of the two-component fuel used in the simulations are very similar to those of diesel. The densities of the model fuel and diesel are 817 kg/m^3 and 840 kg/m^3 , respectively. Cetane numbers are also similar, 53 for diesel and 56 for the two-component fuel. Barths et al. [33] showed that the two-component model fuel displays very similar performance and emission characteristics to diesel.

Results and Discussion

In the following, the results of the numerical analysis will be presented and compared with the measured data on cylinder pressure, apparent heat release rate, NO_x , and soot. Due to the centrally located, vertical injector equipped with a 6-hole nozzle, only a 60-deg sector of the combustion chamber was simulated. This provided a significant saving in the total computational effort. Figure 5 shows the computational grid employed in the simulations. The grid resolution is 0.9 mm, 3.5 mm, and 3.3 deg in the radial, axial, and azimuthal directions, respectively. Three different rail pressure were tested: 600, 800, and 1000 bar. Figures 6–11 show the pressure traces and heat release rates for the different cases. As one would expect, the greatest heat release rate is observed for the high-pressure case.

Interestingly, there is no significant difference in ignition delay between the three cases. Higher injection pressures produce finer sprays and overall leaner mixtures. Hence, when the mixture auto-ignites more mixture at stoichiometric is available in the high-pressure case. The fact that the mixture is more homogeneous at higher injection pressures has important implications for the soot, as displayed in Fig. 12. The low soot emissions at higher injection pressures are a result of less formation, which is clearly demon-

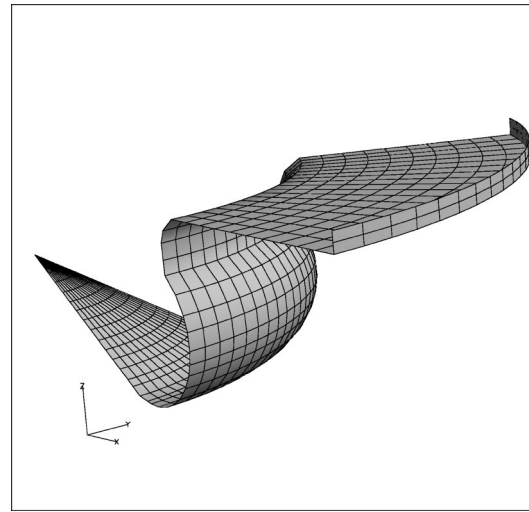


Fig. 5 Computational grid used in the simulations

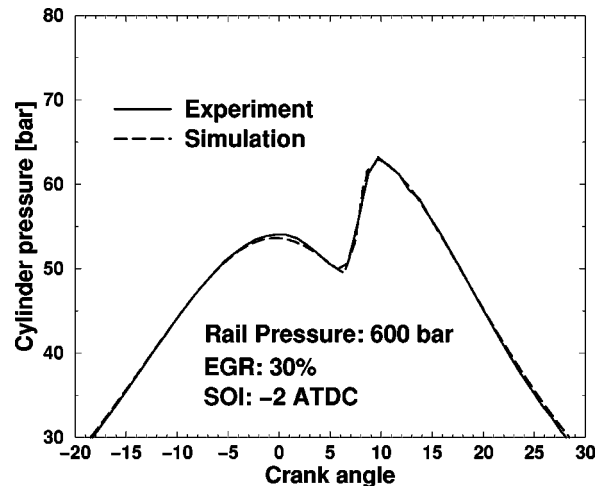


Fig. 6 Pressure trace 600 bar case

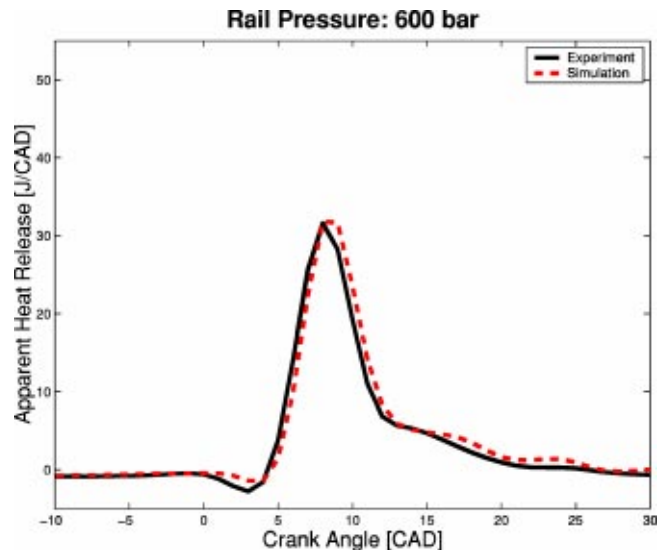


Fig. 7 Heat release 600 bar case

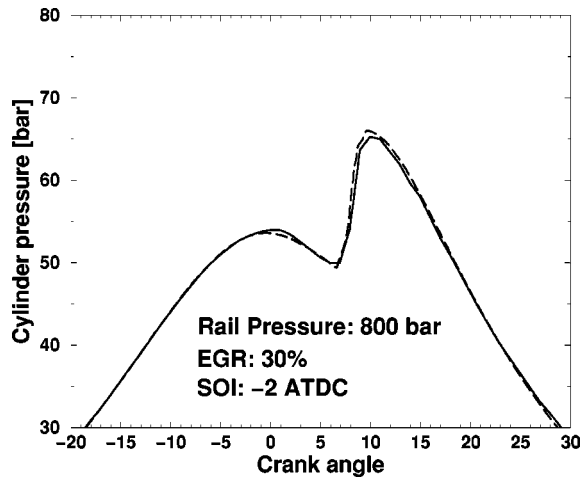


Fig. 8 Pressure trace 800 bar case

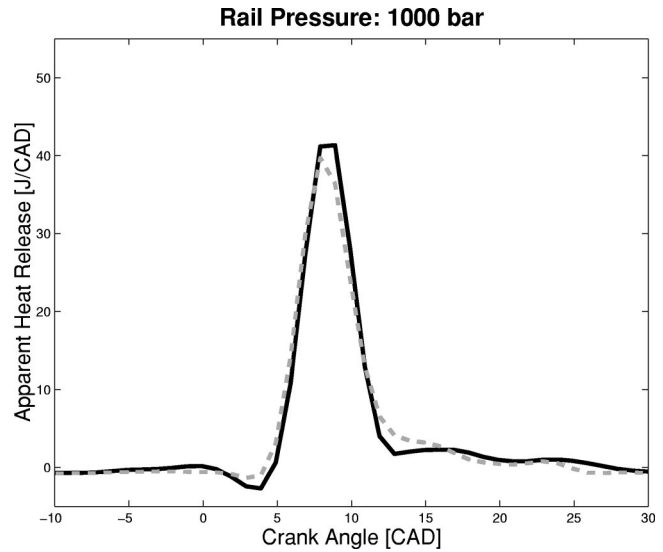


Fig. 11 Heat release 1000 bar case

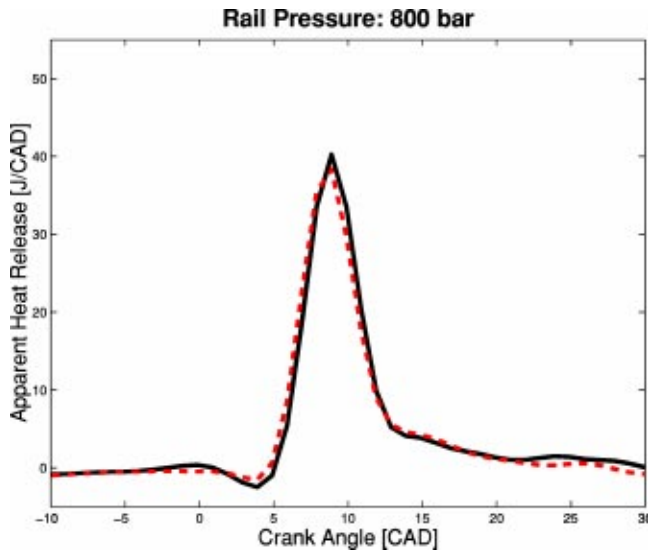


Fig. 9 Heat release 800 bar case

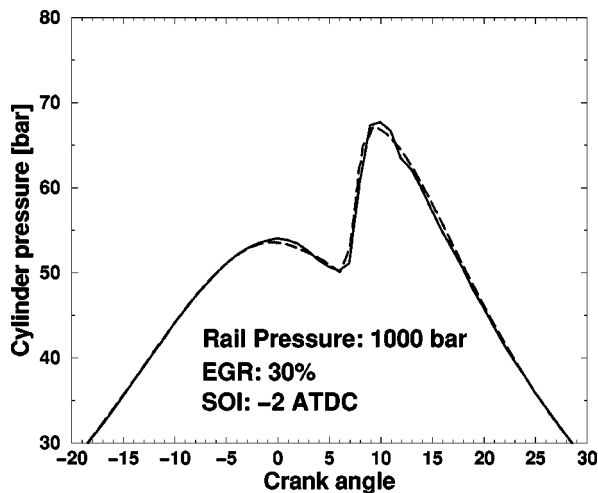


Fig. 10 Pressure trace 1000 bar case

strated by Fig. 13. The computations suggest a more modest decrease in soot with increasing injection pressure than that observed in the experiments. Regarding the other pollutant considered here, it may appear counter-intuitive that NO_x , also, decreases with increasing injection pressure, as seen in Fig. 14. However, studying the heat release traces, shown in Figs. 7, 9, 11, it can be concluded that the combustion duration gets shorter as the injection pressure increases, i.e., the residence time at high temperature is reduced. Although the peak heat release rate is greater at higher injection pressures, normally leading to more NO_x , the reduction in combustion duration can not be compensated for. This simultaneous reduction of NO_x and soot is one example of the ample potential of a common-rail injection system. It should, however, be noted that more energy is required to operate the high-pressure fuel pump the higher the injection pressure gets, which is reflected in a higher overall fuel consumption.

Whereas the computational results are given in units of gram soot per kg fuel, i.e., soot emission index (SEI), the experimental data was obtained in units of filter smoke number (FSN). Normally, smoke numbers are converted to soot concentrations in units of mg/m^3 applying some correlation ([34]).

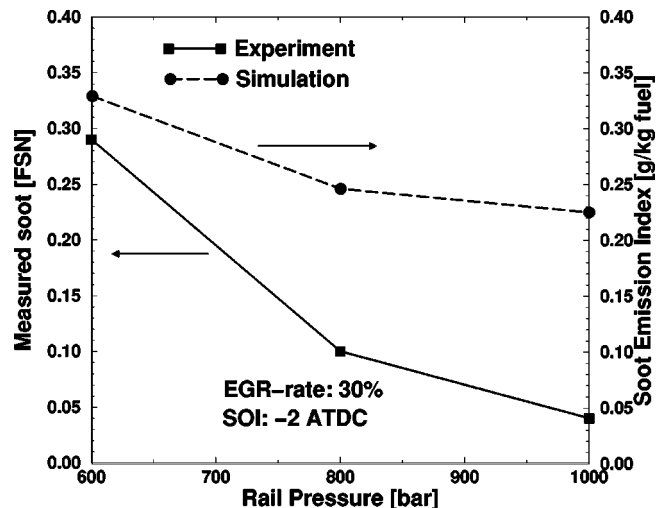


Fig. 12 Comparison of measured and predicted soot

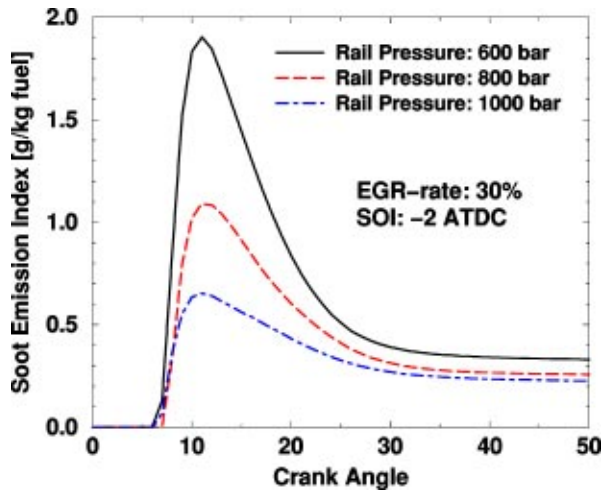


Fig. 13 Soot versus degree crank angle at different injection pressures, EGR rate=30% and SOI=2ATDC

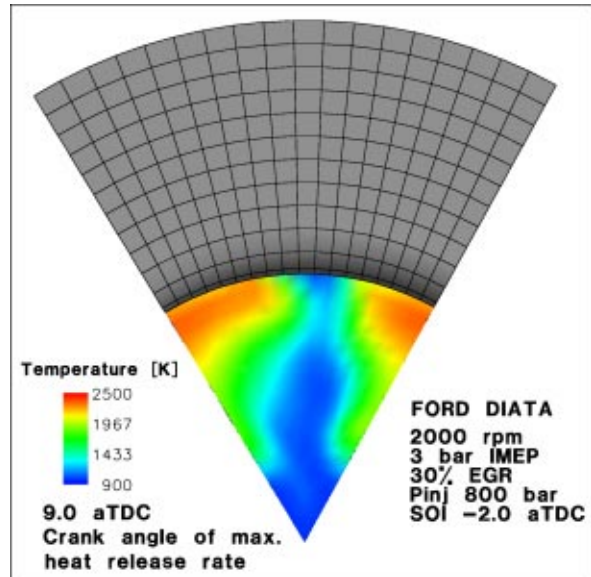


Fig. 16 Spatial distribution of temperature at the cutplane given by Fig. 15 at the crank angle of maximum heat release rate

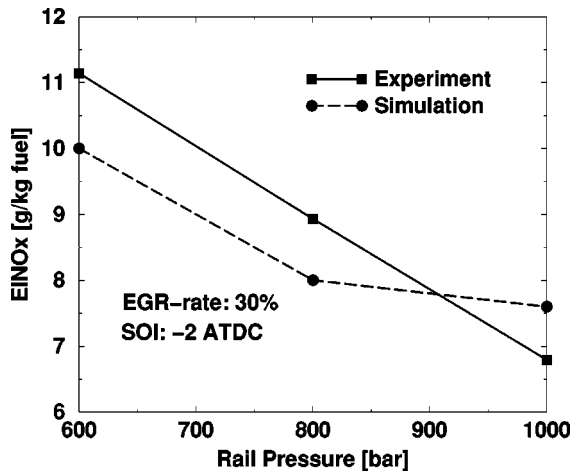


Fig. 14 Comparison of measured and predicted NO_x

Due to the uncertainties in these correlations at the low soot concentrations considered here, such a conversion was not found meaningful here.

In the following, spatial distributions of the temperature and some relevant scalars will be shown in a plane cutting through the spray as indicated in Fig. 15. Figures 16 and 17 display the distributions of temperature and NO_x at the crank angle corresponding to maximum heat release rate (9 deg ATDC, compare Fig. 9). The figures show the expected close correlation between high-temperature regions and high concentrations of NO_x . An important observation is that NO_x is produced in a diffusion-controlled flame under close to stoichiometric conditions. Hence, it would appear incorrect to relate it to a premixed burn, which is sometimes seen in the literature.

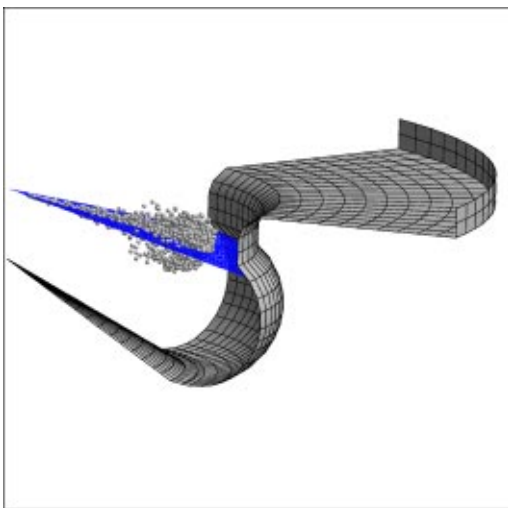


Fig. 15 Cutplane through spray. Spatial distributions of temperature and some selected scalars will be shown in this plane.

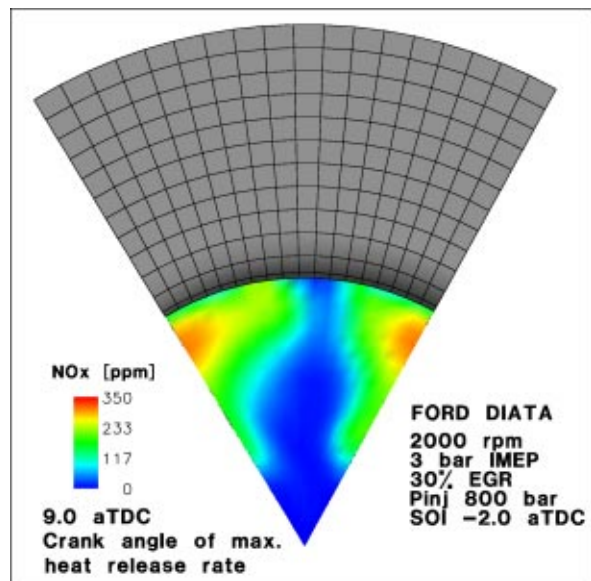


Fig. 17 Spatial distribution of NO_x in the cutplane given by Fig. 15 at the crank angle of maximum heat release rate

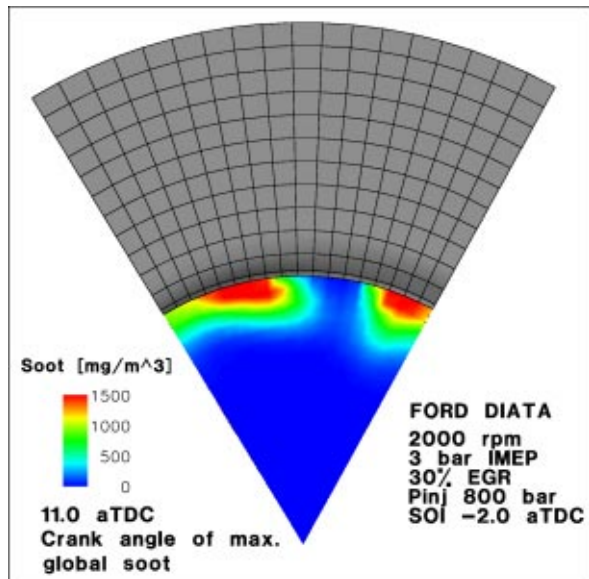


Fig. 18 Spatial distribution of soot in the cutplane given by Fig. 15 at the crank angle of maximum cylinder soot concentration

Figures 18 and 19 show the distributions of soot and OH at the crank angle of maximum soot concentration. Soot is formed in locally rich regions of relatively high temperature. The figures indicate that soot and OH radicals, which are primarily responsible for oxidizing the soot, coexist spatially at the crank angle corresponding to the maximum abundance of soot in the cylinder, 11 deg ATDC. This is in agreement with experimental data obtained from laser sheet imaging performed by Dec [35].

In the simulations performed here, wall flamelets were initiated continuously starting at a crank angle when burning, soot-abundant mixture with a volume equal to approximately 4 percent of the total cylinder charge had reached the combustion chamber wall. These regions are located close to the bowl lip. The residence time at the wall is accounted for by solving transport equations in the CFD code for marker particles representing the indi-

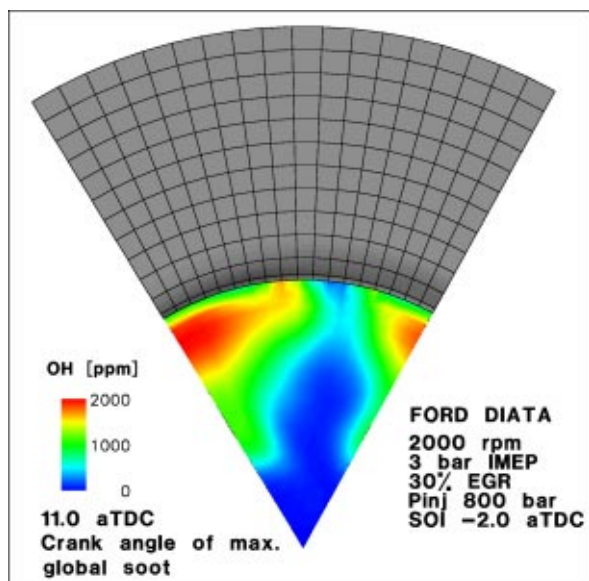


Fig. 19 Spatial distribution of OH in the cutplane given by Fig. 15 at the crank angle of maximum cylinder soot concentration

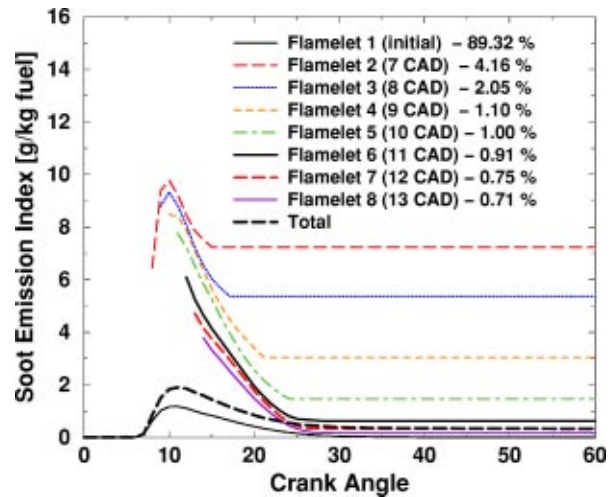


Fig. 20 Soot histories for individual flamelets applying a multiple wall flamelet strategy. Injection pressure: 1000 bar, EGR rate 30%, start of injection 2 deg before TDC.

vidual flamelets. Figure 20 shows the histories of the soot emission index (SEI) for the individual flamelets present in the calculation in the 1000 bar case. Applying more than eight flamelets did not lead to any significant changes in the soot predictions. In the case illustrated, excluding the eighth flamelet would only involve a 0.4 percent change in total predicted engine-out soot. It is interesting to note that the largest flamelet, containing almost 90 percent of the total cylinder volume, is only responsible for a very small fraction of the total soot emitted—approximately equivalent to what would have been predicted with no enthalpy defect present in the analysis. Due to its large volume and limited wall exposure, the enthalpy defect of this flamelet is very small. Soot oxidation in the regions covered by this flamelet proceeds very efficiently. Figure 21 shows the in-cylinder soot concentration versus crank angle applying the new model compared to the previous model not accounting for the wall heat losses. It is apparent that the old model essentially predicts complete oxidation of the soot formed. Hence, the analysis suggests that, for the part load operating point investigated here, flamelet wall quenching is a main contributor to the observed soot emissions. In cases where the in-cylinder density is higher, or in large-bore heavy-duty engines, the interaction of burning mixture with walls is not as strong, and

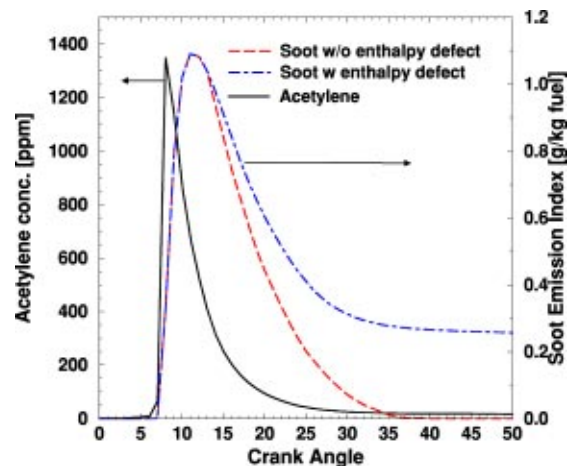


Fig. 21 In-cylinder soot versus engine crank angle comparing previous model with extended model accounting for wall heat losses

consequently the effects addressed in the current analysis are expected to be less pronounced. Experience has shown that the predictions of engine-out NO_x are relatively accurate, provided that the heat release is captured correctly. A major uncertainty in the model is in the prediction of the formation of NO_2 from NO . However, this does not influence the predictions of total NO_x . Regarding the soot predictions, it is difficult to estimate the error in the predictions, since no quantitative comparison could be undertaken as discussed above. Nevertheless, the results shown confirm that the model yields the correct qualitative response to changes in the operating conditions investigated in the present study.

Conclusion

Combustion at part load in a small-bore DI diesel engine was modeled using the representative interactive flamelet model. By realizing that combustion in a conventional diesel engine takes place in thin, locally one-dimensional flamelets whose chemistry is fast, the numerical effort associated with the treatment of the chemistry can be separated from that of the turbulent flow. This enables the approach to incorporate chemistry of arbitrary complexity without sacrificing the accuracy with which the fluid dynamics is treated. KIVA-3V was used to solve the governing equations of the turbulent reactive two-phase flow.

In view of the substantial interaction between regions of burning mixture and the combustion chamber walls in the investigated small-bore engine, the objective of the current study was to analyze the influence of wall heat transfer on engine-out soot emissions. For this purpose a new flamelet parameter, the enthalpy defect, was introduced in the model. It was shown that the enthalpy defect can be directly linked to the total wall heat loss calculated in KIVA-3V.

Applying the model to simulate a part load operating point in the small-bore FORD DIATA engine varying the injection pressure confirmed the ability of the RIF model to accurately predict ignition delay, peak cylinder pressure, and apparent heat release rate. Regarding the emissions, the model was able to capture the nonconventional behavior of simultaneous reduction of NO_x and soot displayed when applying common-rail technology. Furthermore, the analysis suggests that, for the part load operating point investigated, flame quenching at relatively cold combustion chamber walls, mainly located close to the bowl lip, is responsible for the bulk of the emitted soot. The effect is likely to be less significant in engines of larger bore.

Nomenclature

Acronyms

CFD = computational fluid dynamics
 CLD = chemiluminescent detector
 DI = direct injection
 DIATA = direct injection aluminum through-screw assembly
 EGR = exhaust gas recirculation
 FSN = filter smoke number
 HSDI = high-speed direct injection
 IMEP = indicated mean effective pressure
 PAH = polycyclic-aromatic hydrocarbons
 PDF = probability density function
 RIF = representative interactive flamelet
 SEI = soot emission index
 SOI = start of injection
 TDC = top dead center

Variables

α^l = heat transfer coefficient of flamelet l ($\text{W}\cdot\text{m}^{-3}\cdot\text{K}^{-1}$)
 χ = scalar dissipation rate (s^{-1})
 c_{pi} = spec. heat capacity for species i ($\text{J}\cdot\text{kg}^{-1}\cdot\text{K}^{-1}$)
 D_Z = diff. coefficient for mixture fraction, Z ($\text{m}^2\cdot\text{s}^{-1}$)
 ε = turbulent dissipation ($\text{m}^2\cdot\text{s}^{-3}$)

$\dot{q}_{\Delta h}$ = enthalpy defect ($\text{J}\cdot\text{m}^{-3}\cdot\text{s}^{-1}$)
 h_i = specific enthalpy of species i ($\text{J}\cdot\text{kg}^{-1}$)
 \tilde{I}_l = flamelet probability
 Le_i = Lewis number for species i
 \dot{m}_i = chemical production rate for species i ($\text{kg}\cdot\text{s}^{-1}$)
 μ_t = turbulent dynamic viscosity ($\text{kg}\cdot\text{m}^{-1}\cdot\text{s}^{-1}$)
 p = pressure (Pa)
 \dot{q}_R = heat loss due to radiation ($\text{J}\cdot\text{m}^{-3}\cdot\text{s}^{-1}$)
 \dot{Q}_{WHF} = vol.-integr. wall heat transf. per unit time ($\text{J}\cdot\text{s}^{-1}$)
 \dot{Q}_{WHF}^l = vol.-integr. wall heat transf. per unit time of flamelet l ($\text{J}\cdot\text{s}^{-1}$)
 ρ = density, ($\text{kg}\cdot\text{m}^{-3}$)
 T = temperature (K)
 k = turbulent kinetic energy ($\text{m}^2\cdot\text{s}^{-2}$)
 $T^l(Z)$ = flamelet temperature over Z (K)
 v_α = component in α -direction of the velocity ($\text{m}\cdot\text{s}^{-1}$)
 x_α = α -component of spatial coordinate x (m)
 Y_i = mass fraction of species i
 Z = mixture fraction
 $\frac{Z_{st}}{Z}$ = mixture fraction at stoichiometric mixture
 Z'^2 = mixture fraction variance

Constants

c_χ = time-scale ratio for scalar dissipation and velocity fluctuations, 2.0
 Sc_l = turbulent Schmidt number in the transport equation for the flamelet marker particles, 0.9
 Sc_t = turbulent Schmidt number, 0.9
 Sc_Z = Schmidt number in the transport equation for the turbulent mean value of the mixture fraction, 0.9
 $Sc_{Z'^2}$ = Schmidt number in the transport equation for the turbulent mean value of the mixture fraction variance, 0.9

Appendix

Introducing an Enthalpy Defect to Account for Wall Heat Transfer. Assuming unity Lewis numbers, the following equation can be derived for the enthalpy in the flamelet:

$$\rho \frac{\partial h_Z}{\partial t} - \rho \frac{\chi}{2} \frac{\partial^2 h_Z}{\partial Z^2} - \frac{\partial p}{\partial t} = 0 \quad (21)$$

where the subscript Z on the enthalpy is used in order to emphasize that this enthalpy originates from the flamelet solution and is a function of the mixture fraction only. This will be shown later to have an important implication. In Eq. (21) the source term due to radiation has been neglected only for the purpose of making the discussion to follow more transparent.

The transport equation for the turbulent mean value of the enthalpy, neglecting radiation, is

$$\bar{\rho} \frac{D\bar{h}}{Dt} = \frac{Dp}{Dt} + \nabla \cdot \left(\frac{\mu_t}{Sc_t} \nabla \bar{h} \right) + \bar{\rho} \bar{\varepsilon} + \bar{Q}_s \quad (22)$$

where p is the mean pressure, ε is the viscous dissipation, and \bar{Q}_s is the source term due to evaporation. The tilde sign designates Favre averages. μ_t and Sc_t is the turbulent dynamic viscosity and the Schmidt number, respectively. In the current analysis focus will be on processes that are of importance at times when there is little or no evaporation. Heat loss due to viscous dissipation (the third term on the right-hand side of Eq. (22)) can safely be neglected for the purpose of this discussion. In the following it will be shown how the remaining wall heat flux can be accounted for by introducing an additional source term in the flamelet enthalpy equation. The enthalpy equation becomes

$$\rho \frac{\partial h_Z}{\partial t} - \rho \frac{\chi}{2} \frac{\partial^2 h_Z}{\partial Z^2} - \frac{\partial p}{\partial t} - \dot{q}_{\Delta h} = 0 \quad (23)$$

where $\dot{q}_{\Delta h}$ expresses a heat loss per unit volume and time. The equivalent transport equation for the Favre-averaged turbulent mean can be derived from Eq. (23) by considering the transport equation for the mixture fraction probability density function (PDF):

$$\bar{\rho} \frac{\partial \bar{P}}{\partial t} + \bar{\rho} \bar{\mathbf{v}} \cdot \nabla \bar{P} = \nabla \cdot (\bar{\rho} D \nabla \bar{P}) - \frac{1}{2} \frac{\partial^2}{\partial Z^2} (\bar{\chi}_Z \bar{P}) \quad (24)$$

where D is the sum of the turbulent and molecular diffusion coefficients. $\bar{\chi}_Z$ denotes the ensemble averaged conditional scalar dissipation rate, which is often found in the literature written as $\langle \chi | Z \rangle$. Following the procedure described by Peters [36], Eq. (24) is multiplied by h_Z , obtained from the flamelet solution, and integrated over the mixture fraction space. h_Z may be moved underneath all spatial derivatives.

$$\begin{aligned} \bar{\rho} \int_0^1 h_Z \frac{\partial \bar{P}}{\partial t} dZ + \bar{\rho} \bar{\mathbf{v}} \cdot \nabla \bar{h}_Z \\ = \nabla \cdot (\bar{\rho} D_t \nabla \bar{h}_Z) - \frac{\bar{\rho}}{2} \int_0^1 h_Z \frac{\partial^2}{\partial Z^2} (\bar{\chi}_Z \bar{P}) dZ \end{aligned} \quad (25)$$

Assuming that both the value of $\bar{\chi}_Z \bar{P}$ and its derivative are zero at both limits of the integral ([37,38]), the last term in Eq. (25) can be transformed applying partial integration twice. Hence,

$$\bar{\rho} \int_0^1 h_Z \frac{\partial \bar{P}}{\partial t} dZ + \bar{\rho} \bar{\mathbf{v}} \cdot \nabla \bar{h}_Z = \nabla \cdot (\bar{\rho} D_t \nabla \bar{h}_Z) - \bar{\rho} \int_0^1 \frac{\bar{\chi}_Z}{2} \frac{\partial^2 h_Z}{\partial Z^2} \bar{P} dZ. \quad (26)$$

The last term on the right-hand side of Eq. (26) is identified as the diffusion term in the flamelet equation, which leads to the following expression:

$$\begin{aligned} \bar{\rho} \int_0^1 h_Z \frac{\partial \bar{P}}{\partial t} dZ + \bar{\rho} \bar{\mathbf{v}} \cdot \nabla \bar{h}_Z \\ = \nabla \cdot (\bar{\rho} D_t \nabla \bar{h}_Z) - \bar{\rho} \int_0^1 \left(\frac{\partial h_Z}{\partial t} - \frac{1}{\rho} \frac{\partial p}{\partial t} - \frac{1}{\rho} \dot{q}_{\Delta h} \right) \bar{P} dZ. \end{aligned} \quad (27)$$

Here it is implied that the scalar dissipation rate used in the flamelet equations is equal to the conditional scalar dissipation rate as featured in the mixture fraction PDF transport equation. Rearranging and simplifying Eq. (27) it is cast in its final form, assuming zero pressure gradients, following the low Mach number approximation:

$$\bar{\rho} \frac{D \bar{h}_Z}{D t} = \frac{D p}{D t} + \nabla \cdot (\bar{\rho} D_t \nabla \bar{h}_Z) + \bar{\rho} \int_0^1 \frac{1}{\rho} \dot{q}_{\Delta h} \bar{P} dZ. \quad (28)$$

As mentioned already, the enthalpy calculated in the flamelet, h_Z is a function of Z . Since there is no diffusion of the conserved scalar across the boundaries of the computational domain, integrating Eq. (28) over the whole volume will yield zero for the second term on the right-hand side, representing the enthalpy diffusion. Comparison with the volume-integrated enthalpy equation solved in the CFD code (Eq. (22)), neglecting the contributions from viscous dissipation and evaporation, will force the following equality:

$$\begin{aligned} \int_V \nabla \cdot \left(\frac{\mu_t}{Sc_t} \nabla \bar{h} \right) dV = \int_V \bar{\rho} \int_0^1 \frac{1}{\rho} \dot{q}_{\Delta h} \bar{P} dZ dV \\ \Leftrightarrow \quad (29) \\ \underbrace{\int_S \left(\frac{\mu_t}{Sc_t} \nabla \bar{h} \right) \cdot dS}_{\dot{Q}_{WHF}} = \int_{V_w} \bar{\rho} \int_0^1 \frac{1}{\rho} \dot{q}_{\Delta h}(Z) \bar{P} dZ dV_w \end{aligned}$$

where Gauss' theorem has been used to convert the volume integral into a surface integral. The integral on the left-hand side is equal to the global wall heat flux per unit time, \dot{Q}_{WHF} . V_w represents the volume of the wall regions. Extending the current analysis to allow for multiple flamelets is straightforward. The global heat flux per unit time, \dot{Q}_{WHF} is distributed over n_l flamelets used to represent the combustion chamber based on their relative wall mass fraction. With n_l flamelets included in the analysis, the following entity holds:

$$\dot{Q}_{WHF} = \sum_l^{n_l} \dot{Q}_{WHF}^l \quad (30)$$

where superscript l is used to represent the flamelets. Considering an individual flamelet, Eq. (29) now takes the form

$$\dot{Q}_{WHF}^l = \int_{V_w} \bar{\rho} \bar{T}_l \int_0^1 \frac{1}{\rho} \dot{q}_{\Delta h}^l(Z) \bar{P} dZ dV_w. \quad (31)$$

\bar{T}_l is the probability of finding flamelet l at the wall. The heat flux transferred to the wall is given by the following expression:

$$\dot{q}_{\Delta h}^l(Z) = \alpha^l (T^l(Z) - T_{wall}) \quad (32)$$

where α is the heat transfer coefficient pertaining to flamelet l and T_{wall} is the wall temperature. Inserting Eq. (32) into (31) and rearranging, it is possible to determine the flamelet heat transfer coefficient:

$$\alpha^l = \frac{\dot{Q}_{WHF}^l}{\int_{V_w} \bar{\rho} \bar{T}_l \int_0^1 \frac{1}{\rho} (T^l(Z) - T_{wall}) \bar{P} dZ dV_w} \quad (33)$$

where it has been assumed that the heat transfer coefficient is independent of Z .

References

- [1] Peters, N., Müller, U. C., Pitsch, H., and Wan, Y. P., 1995, "Modellierung der Schadstoffbildung bei der dieselmotorischen Verbrennung," *5th Symposium: The Working Process of the Internal Combustion Engine*, Graz, Austria, Sept., pp. 51–67.
- [2] Peters, N., 1984, "Laminar Diffusion Flamelet Models in Non-Premixed Turbulent Combustion," *Prog. Energy Combust. Sci.*, **10**, pp. 319–339.
- [3] Hasse, C., Barths, H., and Peters, N., 1999, "Modeling the Effect of Split Injection in Diesel Engines Using Representative Interactive Flamelets," SAE Technical Paper 1990-01-3547.
- [4] Pitsch, H., Barths, H., and Peters, N., 1996, "Three-Dimensional Modeling of NO_x and Soot Formation in DI Diesel Engines Using Detailed Chemistry Based on the Interactive Flamelet Approach," SAE Technical Paper 962057.
- [5] Barths, H., Pitsch, H., and Peters, N., 1997, "Comparison of the Representative Interactive Flamelet Model and the Magnussen Model for Combustion and Pollutant Formation in DI Diesel Engine to Experiments," *Proceedings of the third International Conference on High Performance Computing in the Automotive Industry*, M. Sheh, ed.
- [6] Hergart, C., Barths, H., and Peters, N., 1999, "Modeling the Combustion Process in a Small-Bore Diesel Engine Using a Model Based on Representative Interactive Flamelets," SAE Technical Paper 1999-01-3550.
- [7] Schwarz, V., König, G., Dittrich, P., and Binder, K., 1999, "Analysis of Mixture Formation, Combustion and Pollutant Formation in HD Diesel Engines using Modern Optical Diagnostics and Numerical Simulation," SAE Technical Paper 1999-01-3647.
- [8] Miles, P. C., "The Influence of Swirl on HSDI Diesel Combustion at Moderate Speed and Load," SAE Technical Paper 2000-01-1829.
- [9] Pitsch, H., 1998, "Modellierung der Zündung und Schadstoffbildung bei der dieselmotorischen Verbrennung mit Hilfe eines interaktiven Flamelet-Modells," Ph.D. thesis, Rheinisch-Westfälische Technische Hochschule, Institut für Technische Mechanik, Feb.
- [10] Pitsch, H., and Peters, N., 1998, "A Consistent Formulation for Non-Premixed Combustion Considering Differential Diffusion Effects," *Combust. Flame*, **114**, pp. 26–40.
- [11] Hubbard, G. L., and Tien, C. L., 1978, "Infrared Mean Absorption Coefficient of Luminous Flames and Smoke," *ASME J. Heat Transfer*, **100**, pp. 235–239.
- [12] Müller, U. C., 1989, "Der Einfluß von Strahlungsverlusten auf die thermische NO-Bildung in laminaren CO—H₂-Diffusionsflammen," Diploma thesis, RWTH Aachen.
- [13] Hergart, C., 2001, "Modeling Combustion and Soot Emissions in a Small-Bore Direct-Injection Diesel Engine," Ph.D. thesis, Rheinisch-Westfälische Technische Hochschule, Institut für Technische Mechanik.

- [14] Jones, W. P., and Whitelaw, J. H., 1982, "Calculation Methods for Turbulent Flows: A Review," *Combust. Flame*, **48**, p. 1.
- [15] Amsden, A. A., O'Rourke, P. J., and Butler, T. D., "KIVA-II: A Computer Program for Chemically Reactive Flows With Sprays," Los Alamos National Labs., U.S.A.
- [16] Amsden, A. A., "A KIVA Program with Block-Structured Mesh for Complex Geometries," Los Alamos National Labs., U.S.A.
- [17] Amsden, A. A., "A Block-Structured KIVA Program for Engines with Vertical or Canted Valves," Los Alamos National Labs., U.S.A.
- [18] Amsden, A. A., "KIVA-3V, Release 2, Improvements to KIVA-3V," Los Alamos National Labs., U.S.A.
- [19] Barths, H., Hasse, C., Bikas, G., and Peters, N., 2000, "Simulation of Combustion in DI Diesel Engines Using an Eulerian Particle Flamelet Model," *Twenty-Eighth Symposium (International) on Combustion*, The Combustion Institute, Pittsburgh, submitted for publication.
- [20] Girimaji, S. S., 1991, "Assumed β -pdf Model for Turbulent Mixing: Validation and Extension to Multiple Scalar Mixing," *Combust. Sci. Technol.*, **78**, p. 177.
- [21] Baulch, D. L., Cobos, C. J., Cox, R. A., Frank, P., Hayman, Th. Just, Kerr, J. A., Murrells, T., Pilling, M. J., Troe, J., Walker, R. W., and Warnatz, J., 1992, "Evaluated Kinetic Data for Combustion Modelling," *J. Phys. Chem. Ref. Data*, **21**, pp. 411–429.
- [22] Benson, S. W., 1981, *Prog. Energy Combust. Sci.*, **7**, pp. 125–134.
- [23] Chevalier, C., Pitz, W. J., Warnatz, J., Westbrook, C. K., and Melenk, H., 1992, "Hydrocarbon Ignition: Automatic Generation of Reaction Mechanisms and Application to Modeling of Engine Knock," *Twenty-Fourth Symposium (International) on Combustion*, The Combustion Institute, Pittsburgh, PA, pp. 93–101.
- [24] Shaddix, C. R., Brezinsky, K., and Glassman, I., 1992, "Oxidation of 1-Methylnaphthalene," *Twenty-Fourth Symposium (International) on Combustion*, The Combustion Institute, Pittsburgh, PA, pp. 683–690.
- [25] Emdee, C. R., Brezinsky, K., and Glassman, I., 1992, "A Kinetic Model for the Oxidation of Toluene Near 1200 K," *J. Phys. Chem.*, **96**, pp. 2151–2161.
- [26] Pitsch, H., and Peters, N., 1995, "Reduced Kinetics of Multicomponent Fuels to Describe the Auto-Ignition, Flame Propagation and Post Flame Oxidation of Gasoline and Diesel Fuels," Periodic Report, project FK.2, IDEA-EFFECT, 6th period 01.07.95-31.12.95.
- [27] Hewson, J. C., and Bollig, M., 1996, "Reduced Mechanisms for NO_x Emissions From Hydrocarbon Diffusion Flames," *Twenty-Sixth Symposium (International) on Combustion*, The Combustion Institute, Pittsburgh, PA.
- [28] Frenklach, M., and Warnatz, J., 1987, "Detailed Modeling of PAH Profiles in a Sooting Low-Pressure Acetylene Flame," *Combust. Sci. Technol.*, **51**, p. 265.
- [29] Miller, J. A., and Melius, C. F., 1992, "Kinetic and Thermodynamic Issues in the Formation of Aromatic Compounds in Flames of Aliphatic Fuels," *Combust. Flame*, **91**, pp. 21–39.
- [30] Frenklach, M., 1985, *Chem. Eng. Sci.*, **40**(10), pp. 1843–1849.
- [31] Frenklach, M., and Harris, S. J., 1987, *J. Colloid Interface Sci.*, **118**, pp. 252–261.
- [32] Mauß, F., 1998, "Entwicklung eines kinetischen Modells der Rußbildung mit schneller Polymerization," Ph.D. thesis, Rheinisch-Westfälische Technische Hochschule, Institut für Technische Mechanik, Feb.
- [33] Barths, H., Pitsch, H., and Peters, N., 1999, "Three-Dimensional Simulation of DI Diesel Combustion and Pollutant Formation Using a Two-Component Reference Fuel," *Oil Gas Sci. Technol.*, **54**, pp. 233–244.
- [34] Muntean, G. G., 1999, "A Theoretical Model for the Correlation of Smoke Number to Dry Particulate Concentration in Diesel Exhaust," SAE Technical Paper 1999-01-0515.
- [35] Dec, J. E., and Tree, A. R., 2001, "Diffusion-Flame/Wall Interactions in a Heavy-Duty DI Diesel Engine," SAE Technical Paper 2001-01-1295.
- [36] Peters, N., 2000, *Turbulent Combustion*, Cambridge University Press, Cambridge, UK.
- [37] Peters, N., and Janicka, J., 1982, "Prediction of Turbulent Jet Diffusion Flame Lift-Off Using a PDF Transport Equation," *Nineteenth Symposium (International) on Combustion*, The Combustion Institute, Pittsburgh, PA, pp. 367–374.
- [38] Girimaji, S. S., 1992, "On the Modelling of Scalar Diffusion in Isotropic Turbulence," *Phys. Fluids*, **11**, Nov., pp. 2529–2537.